

[Handwritten signature]

[Handwritten initials]

AGARD-CP-366

AGARD-CP-366

AGARD

ADVISORY GROUP FOR AEROSPACE RESEARCH & DEVELOPMENT

7 RUE ANCELLE 92200 NEUILLY SUR SEINE FRANCE

AD-A156 047

AGARD CONFERENCE PROCEEDINGS No.366

Aerodynamics and Acoustics of Propellers

This document has been approved
for public release and sale; its
distribution is unlimited.

DTIC
ELECTE
JUN 20 1985
[Handwritten 'S' and 'A' with propeller symbol]

DTIC FILE COPY

NORTH ATLANTIC TREATY ORGANIZATION



DISTRIBUTION AND AVAILABILITY
ON BACK COVER

85 06 19 061

NORTH ATLANTIC TREATY ORGANIZATION
ADVISORY GROUP FOR AEROSPACE RESEARCH AND DEVELOPMENT
(ORGANISATION DU TRAITE DE L'ATLANTIQUE NORD)

AGARD Conference Proceedings No.366
AERODYNAMICS AND ACOUSTICS OF PROPELLERS

THE MISSION OF AGARD

The mission of AGARD is to bring together the leading personalities of the NATO nations in the fields of science and technology relating to aerospace for the following purposes:

- Exchanging of scientific and technical information;
- Continuously stimulating advances in the aerospace sciences relevant to strengthening the common defence posture;
- Improving the co-operation among member nations in aerospace research and development;
- Providing scientific and technical advice and assistance to the North Atlantic Military Committee in the field of aerospace research and development;
- Rendering scientific and technical assistance, as requested, to other NATO bodies and to member nations in connection with research and development problems in the aerospace field;
- Providing assistance to member nations for the purpose of increasing their scientific and technical potential;
- Recommending effective ways for the member nations to use their research and development capabilities for the common benefit of the NATO community.

The highest authority within AGARD is the National Delegates Board consisting of officially appointed senior representatives from each member nation. The mission of AGARD is carried out through the Panels which are composed of experts appointed by the National Delegates, the Consultant and Exchange Programme and the Aerospace Applications Studies Programme. The results of AGARD work are reported to the member nations and the NATO Authorities through the AGARD series of publications of which this is one.

Participation in AGARD activities is by invitation only and is normally limited to citizens of the NATO nations.

The content of this publication has been reproduced directly from material supplied by AGARD or the authors.

Published February 1985

Copyright © AGARD 1985
All Rights Reserved

ISBN 92-835-0374-0



*Printed by Specialised Printing Services Limited
40 Chigwell Lane, Loughton, Essex IG10 3TZ*

THEME

The propeller has become a focus of attention after being neglected for many years. It has long been appreciated that the propeller is a most efficient means of propulsion up to Mach No. 0.6 for old technology propellers. However, this efficiency has been realized at the expense of high noise and vibration levels.

The resurgence of interest in propeller technology that started in the mid-1970's, has brought with it several interesting developments, among which the propfan is perhaps the most novel. Recent studies indicate that the propfan can operate with an aerodynamic efficiency of 80% at Mach No. 0.8 and that makes it a very serious contender to the fan-jet in a speed regime that has hitherto been its exclusive domain. The advent of the supercritical airfoil is another significant recent development that is already beginning to influence modern propeller design.

The propfan has near field noise problems at cruise because blade extremities become supersonic. This will require novel means to reduce cabin noise level to acceptable standards, without incurring excessive weight penalties.

It was intended that the symposium should provide a "state of the art review" of the following areas: aerodynamic design and testing of modern propellers, acoustic and vibration environmental problems and their solutions, and considerations in the integration of propeller-airframe.

* * * *

Après avoir été négligée pendant des années, l'hélice est redevenue un centre d'attention. On reconnaît depuis longtemps qu'elle constitue un moyen de propulsion très efficace jusqu'à Mach 0,6 lorsqu'il s'agit d'une hélice de technologie ancienne. Toutefois, cette efficacité a été obtenue au prix de niveaux élevés de bruit et de vibrations.

Le regain d'intérêt pour la technologie des hélices a commencé à se manifester vers le milieu des années 70 et s'est accompagné de plusieurs développements intéressants, parmi lesquels le turbopropulseur avec soufflante est peut-être le plus original. De récentes études indiquent que le turbopropulseur avec soufflante peut avoir un rendement aérodynamique de 80% à Mach 0,8, ce qui en fait un sérieux concurrent du turboréacteur à soufflante pour une gamme de vitesses qui a été jusqu'ici son domaine exclusif. L'apparition récente du profil aérodynamique critique constitue encore un développement important qui commence déjà à influencer sur la conception des hélices modernes.

Le turbopropulseur avec soufflante pose des problèmes de champ proche au régime de croisière où les extrémités des pale deviennent supersoniques. Il faudra donc trouver des solutions nouvelles pour réduire le niveau de bruit en cabine et atteindre des normes acceptables sans pénalités excessives au plan pondéral.

L'objectif du Symposium était de rendre compte de l'état de l'art dans les domaines suivants: conception et essais aérodynamiques des hélices de technologie moderne, problèmes d'environnement aux plans de l'acoustique et des vibrations, solutions à ces problèmes, et considération sur l'intégration des hélices à la cellule.

Accession For	
NTIS GRA&I	<input checked="" type="checkbox"/>
DTIC TAB	<input type="checkbox"/>
Unannounced	<input type="checkbox"/>
Justification	
Distribution/	
Availability Codes	
Dist	Special

BTIC
COPY
INSPECION
8

AI

FLUID DYNAMICS PANEL

Dr L.Roberts
Joint Institute for Aeronautics and Acoustics
Department of Aeronautics and Astronautics
Stanford University
Stanford
California 94305, USA

Dipl. Ing. P.W.Sacher
Messerschmitt-Bölkow-Blohm-GmbH
UF FE 122
Postfach 80 11 60
D-8000 München 80
Federal Republic of Germany

PROGRAMME COMMITTEE MEMBERS

Mr L.H.Ohman (Chairman)
Head, High Speed Aerodynamics Lab.
National Aeronautical Establishment
National Research Council, Montreal Road
Ottawa, Ontario K1A 0R6, Canada

Dr Ir. H.Tijdeman
National Aerospace Laboratory NLR
Anthony Fokkerweg 2
1059 CM Amsterdam
Netherlands

Professor L.Bjørnø
The Acoustics Lab. — Bldg 352
Technical University of Denmark
Bygning 404 — Lundtoftevej 100
DK-2800 Lyngby, Denmark

Mr D.H.Peckham
Aerodynamics Department
Royal Aircraft Establishment
Farnborough, Hants GU14 6TD, UK

M.C.Dujarric
STPA/EG
4 Avenue de la Porte d'Issy
76996 Paris Armées, France

Dr R.A.Kilgore
MS 287 — Transonic Aerodynamics Division
NASA Langley Research Center
Hampton
Virginia 23665, USA

Professor Dr Ing. B.Laschka
Institut für Strömungsmechanik
der Tech. University
Bienroder Weg 3
D-3300 Braunschweig
Federal Republic of Germany

Professor Ir. H.Wittenberg (PEP)
Dept. of Aerospace Engineering
Delft University of Technology
Klyverweg 1
2629 HS Delft
Netherlands

PANEL EXECUTIVE

Robert H.Rollins, II
Fluid Dynamics Panel Executive
7 rue Ancelle
92200 Neuilly-sur-Seine
France

CONTENTS

	Page
THEME	iii
FLUID DYNAMICS PANEL	iv
	Reference
<u>SESSION I – PROPELLER ANALYSIS AND DESIGN I</u>	
A REVIEW OF ADVANCED TURBOPROP TRANSPORT ACTIVITIES by R.H.Lange	1
METHODES AERODYNAMIQUES UTILISEES EN FRANCE POUR L'ETUDE DES HELICES POUR AVIONS RAPIDES par J.M.Bousquet	2
DESIGN CONCEPT AND PERFORMANCE PREDICTION TECHNIQUE FOR POTENTIAL FLOWS AROUND ADVANCED PROPELLERS by T.S.Luu and R.Collercandy	3
Paper 4 withdrawn	
<u>SESSION I – PROPELLER ANALYSIS AND DESIGN II</u>	
REVIEW OF ARA RESEARCH INTO PROPELLER AERODYNAMIC PREDICTION METHODS by A.J.Bocci and J.I.Morrison	5
PROFILS MODERNES POUR HELICES par A.M.Rodde, J.J.Cuny et J.J.Thibert	6
AERODYNAMICS OF WIDE-CHORD PROPELLERS IN NON-AXISYMMETRIC FLOW by J.B.H.M.Schulten	7
ON THE AERODYNAMICS OF INSTALLED PROPELLERS by M.E.Eshelby	8
A UNIFIED APPROACH FOR THE AERODYNAMICS AND ACOUSTICS OF PROPELLERS IN FORWARD MOTION by A.Das	9
THEORETICAL ANALYSIS OF LINEARIZED ACOUSTICS AND AERODYNAMICS OF ADVANCED SUPERSONIC PROPELLERS by F.Farassat	10
A GENERAL THEORY OF ARBITRARY MOTION AERODYNAMICS USING AN AEROACOUSTIC APPROACH by L.N.Long and G.A.Watts	11
<u>SESSION II – PROPELLER TESTING</u>	
SUMMARY OF RECENT NASA PROPELLER RESEARCH by D.C.Mikkelson, G.A.Mitchell and L.J.Bober	12
COMPORTEMENT DYNAMIQUE D'UN PROP-FAN par J.M.Besson et D.Petot	13
PERFORMANCE EVALUATION OF FULL SCALE PROPELLERS BY WIND TUNNEL TEST by D.J.Barber	14
ETUDE DU SILLAGE 3D D'UNE HELICE AERIENNE par D.Favier et C.Maresca	15

	Reference
INVESTIGATIONS OF MODERN GENERAL AVIATION PROPELLERS by H.Zimmer, R.Hoffmann and K.H.Horstmann	16
AERODYNAMIC AND STRUCTURAL ASPECTS OF PROPELLER AND DRIVE FOR A 1/3 SCALE MODEL WIND TUNNEL PROGRAMME by R.M.Bass, B.Munnikma and J.van Hengst	17
<u>SESSION III – PROPELLER AIRFRAME INTEGRATION</u>	
SOME CONSIDERATIONS IN PROPELLER AND AIRFRAME INTEGRATION by B.Eggleston	18
LES PROBLEMES D'INTEGRATION DES HELICES A LA CELLULE D'UN AVION ET, PLUS PARTICULIEREMENT, D'UN BIMOTEUR DE FORTE PUISSANCE par R.Taisseire	19
A FLOW MODEL FOR WINGS/BODY PROPELLER INTERFERENCE* by A.Emerati and G.M.Lilley	20
WIND TUNNEL INVESTIGATION OF THE INTERACTION OF PROPELLER SLIPSTREAM WITH NACELLE/WING/FLAP COMBINATIONS by A.S.Aljabri and A.C.Hughes	21
AN ASYMPTOTIC THEORY FOR THE INTERFERENCE OF LARGE ASPECT RATIO SWEEPED WINGS AND MULTIPLE PROPELLER SLIPSTREAMS by R.K.Prabhu, C.H.Liu and S.N.Tiwari	22
<u>SESSION IV – PROPELLER ACOUSTICS I</u>	
DEVELOPMENT OF MODERN TURBOPROP ENGINES by H.I.H.Saravanamuttoo	23
AEROACOUSTIC WIND TUNNEL MEASUREMENTS ON PROPELLER NOISE by F.R.Grosche and H.Stiewitt	24
SOME AEROACOUSTIC WINDTUNNEL MEASUREMENTS, THEORETICAL PREDICTIONS, AND FLIGHT TEST CORRELATIONS ON SUBSONIC AIRCRAFT PROPELLERS by W.G.Trebbles, J.Williams and R.P.Donnelly	25
AN INVESTIGATION OF IN-FLIGHT NEAR-FIELD PROPELLER NOISE GENERATION AND TRANSMISSION by H.Bonneau, D.F.Wilford and L.Wood	26
FULL-SCALE FLIGHT AND MODEL-SCALE WINDTUNNEL TEST ON THE NEARFIELD NOISE CHARACTERISTICS OF AIRCRAFT PROPELLERS by H.H.Heller, M.Kallergis and B.Gehlar	27
<u>SESSION IV – PROPELLER ACOUSTICS II</u>	
CABIN NOISE REDUCTION FOR A NEW DEVELOPMENT TURBOPROP COMMUTER AIRCRAFT by A.Carbone, A. Paonessa, L.Lecce and F.Marulo	28
PROPELLER AIRCRAFT CABIN VIBRATION AND NOISE-EXCITATION, SOURCES AND PATHS by R.E.Donham, F.J.Balena, E.Z.Bochary and O.K.Liehr	29
THE STATE OF THE ART IN PROP-FAN AND PROPELLER NOISE by F.B.Metzger	30
APPLICATION OF ACTIVE NOISE CONTROL TO MODEL PROPELLER NOISE by M.Salikuddin, H.K.Tanna, R.H.Burrin and W.E.Carter	31

*Not available at time of printing

ROUND TABLE DISCUSSION

Reference

RTD

1-1

A REVIEW OF ADVANCED TURBOPROP TRANSPORT ACTIVITIES

by

Roy H. Lange
Manager, Advanced Concepts Department
Dept. 72-79, Zone 419
Lockheed-Georgia Company
Marietta, Georgia 30063

SUMMARY

The application of advanced technologies shows the potential for significant improvement in the fuel efficiency and operating costs of future transport aircraft envisioned for operation in the 1990s time period. One of the more promising advanced technologies is embodied in an advanced turboprop concept originated by Hamilton Standard and NASA and known as the propfan. The concept features a highly loaded, multibladed, variable pitch propeller geared to a high pressure ratio gas turbine engine. The blades have high sweepback and advanced airfoil sections to achieve 80 percent propulsive efficiency at $M=0.80$ cruise speed. Aircraft system studies have shown improvements in fuel efficiency of 15-20 percent for propfan advanced transport aircraft as compared to equivalent turbofan transports. Beginning with the Lockheed C-130 and Electra turboprop aircraft, this paper presents an overview of the evolution of propfan aircraft design concepts and system studies. These system studies include possible civil and military transport applications and data on the performance, community and far-field noise characteristics and operating costs of propfan aircraft design concepts. NASA Aircraft Energy Efficiency (ACEE) program propfan projects with industry are reviewed with respect to system studies of propfan aircraft and recommended flight development programs.

INTRODUCTION

Lockheed involvement in propeller aircraft is exemplified by the successful turboprop aircraft programs of the C-130H Hercules and its civil counterpart, the L-100-30, and the Model 188 Electra and its military counterpart, the P-3 Orion, shown in Figure 1. These aircraft utilize propellers with the latest state-of-the-art for their time of development. For this propeller technology, the highest cruise speeds attainable with good efficiency were limited to Mach 0.60 (360 knots). The jet engines introduced in the 1960s provided high subsonic speed capability which was desired by the civil and military transport aircraft operators. The improvements in fuel consumption brought about by the low by-pass-ratio followed by the high by-pass-ratio turbofan engines combined with increased reliability further consolidated the use of these engines on all new transport aircraft up to the present time. There was no comparable technology development for advanced propellers.

The dramatic increases in fuel prices since 1973 resulted in fuel costs becoming an increasingly larger part of the direct operating costs of aircraft as shown in Figure 2. The prediction of fuel prices shown here was made before the present world oil situation, so the \$2 per gallon fuel price for 1985 may not occur. Nevertheless, it is expected that fuel costs will constitute at least 65 percent of the direct operating costs of aircraft from the present time onward. Therefore, the increasing fuel costs provided the motivation for serious consideration of advanced technologies directed toward increased fuel efficiency of transport aircraft. Since the early 1970s the industry and government agencies, including the Air Force, Navy, NASA, and others worked jointly in programs on the development and timely application of advanced technologies. The NASA Aircraft Energy Efficiency, ACEE, program initiated in 1973, was a joint program with industry on advanced technologies for aircraft fuel efficiency (References 1,2). This NASA program provided the impetus for the development of an advanced turboprop concept initiated in 1975 by the Hamilton Standard division of United Technologies and known as the propfan (Reference 3). The propfan concept utilizes technologies to achieve 80 percent propulsive efficiency at $M=0.80$ (480 knots). Moreover, aircraft system studies have shown fuel savings of about 20 percent as compared to counterpart aircraft powered by turbofan engines. An excellent review of the NASA advanced turboprop program is contained in Reference 4.

There are several technical issues which must be resolved before the propfan can be utilized on production aircraft; these include the propeller structural integrity, the aerodynamic interference effects and installed performance, and cabin noise. This paper presents an overview of propfan aircraft design concepts and system studies and tests directed toward the resolution of the technical issues. The system studies include civil and military transport applications and data on the performance, noise, and operating costs of propfan aircraft design concepts. NASA propfan projects with industry including the Propfan Test Assessment, PTA, program are also reviewed.

PROPFAN TECHNOLOGY

The propfan concept shown in Figures 3 and 4 features a highly loaded, multibladed, variable pitch propeller geared to a high pressure ratio gas turbine engine. The propeller blades have tip sweep and advanced airfoil sections to achieve the design goals of 80 percent propulsive efficiency at $M=0.80$ cruise speed. High subsonic speed wind-tunnel tests on a 24.5 inch diameter propfan have verified the predicted 80 percent

propulsive efficiency at $M=0.80$ speeds (References 5-7). The comparison of propulsive efficiencies of turbofan and turboprop systems of Figure 5 shows the higher efficiency of the propfan (advanced turboprop) over that for the Electra-type turboprops and the turbofans in the Mach 0.60 to 0.80 range. At $M=0.8$ the propfan is projected to have a propulsive efficiency about 15 percent greater than that for a high-bypass ratio turbofan, and the improvement is even larger at $M=0.70$. The relatively thin, sweptback, and large number of propeller blades are required to increase efficiency, reduce noise, and absorb the high engine power requirements for high subsonic cruise speeds (Reference 8).

As noted earlier, there are several technical issues to be resolved before the expected performance gains can be realized in an installation of a propfan on a transport aircraft. The aerodynamic/propulsion interference for a propfan installation on a transport aircraft wing is illustrated in Figure 6. The propfan rotation produces a non-uniform flow including an upwash on one side of the wing leading edge and a downwash on the other. In addition, there is an increase in velocity over the wing which, though small, could be troublesome on a supercritical airfoil which has mixed subsonic and supersonic flow fields. On a sweptback wing there is additional interference and nonuniform flow since the inboard propfan blade is nearer to the leading edge of the wing than is the outboard propfan blade. Wind tunnel tests have been conducted at the NASA Ames 14-foot tunnel as shown in Figure 7 with a propfan mounted on a semispan sweptback wing in order to assess the aerodynamic interference and installation drag effects for a Mach number range of 0.60 to 0.85 for the Hamilton Standard SR-2 (unswept) eight-blade propfan geometry (References 9,10). The analysis of these experimental data, and comparison with advanced computational methods for relevant wing/nacelle/slipstream parameters, was performed under contract to the NASA Ames Research Center by the Lockheed-Georgia Company (Reference 11). These and continuing research activities will provide for more accurate estimates of the installed performance of propfan propulsive systems on transport aircraft.

The previous discussion of interference effects of the propfan has been directed to the normal or generic installation of the propfan on the wing of the aircraft. Alternative propfan locations on the aircraft for both tractor and pusher arrangements are feasible as depicted in Figure 8, and the aft-mounted arrangements eliminate the undesirable interference effects associated with the wing-mounted installations. Studies have been made of these alternative propfan locations, and, for example, on a short-to-medium range aircraft, the ranking of most desirable locations is: first, horizontal tail aft mounted; second, wing mounted; and third, aft fuselage pylon mounted (Reference 12). The alternative propfan installations have their own peculiar problem areas such as the engine-out considerations for the wing-tip mounted installation, weight and balance for the aft-mounted installations, and wing torsion considerations for wing-mounted pusher installations.

PROPFAN AIRCRAFT SYSTEM STUDIES

There have been continuing studies of the effects on performance and operating costs for the application of propfan propulsion systems on transport aircraft. Aircraft systems studies must address the design integration of all aspects of the propfan propulsion system, and, as illustrated in Figure 9, the major areas include the engine, gearbox and propeller mechanical components, propeller/nacelle integration, installation aerodynamics, and the cabin environments of noise and vibration. It is not the intent in this paper to discuss the complex and interactive design efforts in each of the major areas shown in Figure 9, but rather to review the major results of several system studies.

The initial propfan aircraft system studies were performed by Boeing, Douglas, and Lockheed in the NASA funded studies on Reducing the Energy of the Commercial Air Transportation (RECAT) system reported in 1976 (References 13-19). In general, the results of these design system studies for medium-range transports showed fuel savings of 15 to 20 percent for wing-mounted propfan aircraft as compared to counterpart turbofan powered aircraft for the same mission characteristics and cruising at $M=0.80$. The fuel savings represent a reduction in direct operating costs ranging from 5 to 10 percent for a fuel cost of 60 cents per gallon. An excellent review of the status of propfan technology at the end of 1977 is provided in Reference 20. Lockheed and Douglas propfan concepts are shown in Figure 10.

Recent system studies of the propfan cargo aircraft conducted by Lockheed have included company-funded and NASA-funded efforts. The NASA-funded study emphasized the prediction of aircraft noise and noise footprints in the terminal area for fuel-efficient propfan cargo aircraft. Parametric variations of aircraft and propeller characteristics were investigated for Mach numbers of 0.60 to 0.80 to determine their effects on noise-print areas, fuel consumption, and direct operating costs. Optimized aircraft were selected and compared with counterpart turbofan aircraft to provide a basis for comparison of the two propulsion systems (References 21,22). In these studies the engine thrust and horsepower levels were sized for $M=0.80$ cruise conditions and the take-off field lengths were a fall out of this sizing process. Two-engine aircraft with cargo payloads from 30,000 pounds to 60,000 pounds and a four-engine aircraft with a payload of 135,000 pounds were investigated. An artist's sketch of the two engine aircraft is presented in Figure 11. Representative results of the study in Figure 12 at a cruise Mach number of 0.75 show significant improvements in block fuel, fuel efficiency, direct operating costs (DOC) and field length for propfan aircraft as compared to that for equivalent turbofan aircraft.

These improvements are 20 percent and 18 percent for block fuel and 14 percent and 8 percent in DOC for the two and four engine aircraft, respectively. An interesting performance improvement is the reduction in field length of 21 percent and 38 percent which are useful in STOL capability and reduced community noise.

The far-field noise characteristics of the two and four engine propfan and turbofan aircraft are compared with the FAR 36 Stage 3 requirements in Figure 13. As shown, all configurations comply with the regulations with the propfan aircraft showing lower noise levels than the turbofan aircraft. The improved airfield performance of the propfan aircraft in achieving larger climb-out angles at takeoff is reflected in the lower noise levels shown on the chart for the takeoff fly-over noise as compared to the turbofan aircraft. It is also seen that noise for the approach fly-over condition is more difficult to reduce for both types of propulsion systems.

Although the aircraft comply with the FAR 36 Stage 3 noise criteria of Figure 13, the size of the total area affected by the noise is of importance in dealing with effects of aircraft noise on the community around an airport. In the study reported in References 21,22, calculations were made of the noise footprints for noise levels of 70, 80, and 90 EPNdB. The results showed that the propfan aircraft had smaller noise footprints at 90 EPNdB than that for the turbofan aircraft; but the reverse was true for the two lower noise levels. Whereas these results are of interest, it is felt that the data would be more meaningful for aircraft which are designed to greater detail and depth than that for the aircraft reported in this study.

The near-field noise for the cabin of the aircraft involves the determination of the amount of noise attenuation material required in the fuselage to provide the desired passenger comfort level. In order to obtain noise data for the propfan, flight tests were made in 1981 at the NASA Dryden Flight Research Facility on a JetStar aircraft with a 24.5 inch diameter propfan mounted above the fuselage as shown in Figure 14. The noise was measured by microphones mounted on the surface of the fuselage. Additional noise data will be obtained at larger scale in the NASA/Lockheed Propfan Test Assessment program which will be discussed later in this paper.

An obvious approach to minimizing the swirl interference of the propfan is the use of counter rotation as depicted in Figure 15. The use of counter rotation propellers is not new, of course, and has been used in the past on aircraft such as the Convair R3Y-1, Northrop XB-35, Avro Shackleton, Tupolev TU-20 Bear, and others. These previous systems were faced with complexity, weight and costs as compared to their single rotation installations. Recent activities sponsored by NASA, therefore, are directed to determine whether the performance benefits of a current state-of-the-art counter rotation propfan installation would provide substantial benefits to offset the complexity, weight and cost of a single rotation system (see Reference 23).

Aircraft design system studies were performed on M=0.8 cruise speed, 100 passenger transports with a maximum range of 1300 nautical miles. In order to determine the benefits due to counter rotation, aircraft were designed to perform the identical mission and with single and counter rotation propfan installations. A general arrangement of the counter rotation propfan transport is shown in Figure 16. Engine performance data are based on the Pratt and Whitney STS 589 turboshaft engine. Design parameters for the system study include 82dBA cabin noise level limit and FAR 36 - Stage 3 exterior noise constraints. An in-line differential planetary gearbox was selected for the counter rotation system and the offset compound idler arrangement was selected for the single rotation system. These gearbox determinations are based on a separate study on reduction gear concepts reported in Reference 24.

For a 400 nautical mile range, the advanced counter rotation propfan transport shows a fuel savings of 8 percent and a reduction in direct operating costs, DOC, of 2.5 percent as compared to a counterpart advanced single rotation propfan transport. It is felt that the benefits due to counter rotation merit continued research and development activities. Furthermore, no serious problems have been identified that might prevent the realization of these benefits.

TECHNOLOGY READINESS

In order to establish technology readiness in the late 1980's for the propfan, it became abundantly clear early in the program that flight tests of a propfan installation on a generic transport aircraft would be required to resolve some of the major concerns relative to structural integrity, installed performance, and noise and vibration. Accordingly, as part of the NASA Advanced Turboprop program, funded studies were awarded to Douglas Aircraft Company and the Lockheed-Georgia Company for system studies of candidate testbed aircraft to accomplish the flight test program (References 25,26). These testbed aircraft are required to cruise at M=0.80 to 30,000 feet altitude. The major objective of these studies is to determine to what extent demonstration of technology readiness can be accomplished by means of a flight testbed aircraft. Candidate propeller drive systems and aircraft combinations were selected and a program plan including schedules and costs were developed. Douglas Aircraft studied several versions of the DC-9 as the testbed aircraft. Lockheed-Georgia surveyed NASA inventory aircraft including the C-141A, KC-135A, JetStar, B-52B, and Gulfstream II. The Lockheed recommended testbed system included an Allison XT-701 turboshaft engine with 8070 sea level static horsepower, a T56A-14 gearbox,

Hamilton Standard 9 foot diameter propfan, and the Gulfstream II aircraft. The results of this testbed study provided a significant input to the successful Lockheed proposal to the NASA Lewis Research Center in October 1983 for the Propfan Test Assessment program.

Another purpose of the Advanced Turboprop Testbed System Study was to identify technical areas of concern which can best be resolved by means of large-scale flight research. As compared with previous wind tunnel and small-scale flight tests of the propfan as described previously, the large scale flight research testbed aircraft provides operating conditions fully representative of flight operations at $M=0.80$ and 30,000 feet in altitude and also at some off-design flight conditions. This flight research output is essentially that for the Propfan Test Assessment program. A review of the flight research output data and applications toward the resolution of the major technical issues of concern is provided in Figure 17. The technical data output is arranged into three major areas: (a) verification of design methodology, (b) scale effects, and (c) correlation of wind-tunnel and flight tests. Hamilton Standard was awarded a NASA contract in 1983 to design, fabricate, and ground test a 9-foot diameter propfan for the Large-Scale Advanced Propeller (LAP) program. Thus the LAP program and the Propfan Test Assessment (PTA) programs will be closely coordinated and together should establish the technology readiness of the propfan in the late 1980s. The Lockheed PTA system depicted in Figure 18 includes the Gulfstream II aircraft, the Hamilton Standard 9-foot diameter propfan, and the Allison 570-M78 engine and drive system. The Allison 570-M78 is an industrial derivative of the XT-701 engine previously mentioned. According to the PTA schedule, flight test data will be generated in 1984 (see Reference 27).

CONCLUDING REMARKS

One of the more promising advanced technologies for improved efficiency of future transport aircraft is the Hamilton Standard and NASA propfan concept which has the potential for fuel savings of 15-20 percent over that for an equivalent advanced turbofan transport at $M=0.80$ cruise speed. Vital to the successful application of the propfan is the resolution of major technical issues of structural integrity, installed propfan performance, and noise and vibration. These issues are being addressed in several NASA/industry laboratory, ground, and wind tunnel test programs. Large-scale activities include the NASA/Hamilton Standard Large-Scale Advanced Propeller, LAP, program initiated in 1983. The NASA/Lockheed Propfan Test Assessment, PTA, program will begin in mid 1984 and culminate with flight tests of a large-scale propfan, engine and gearbox arrangement on the Gulfstream II transport in 1987. These large-scale programs, properly funded, should resolve the technical issues and establish technology readiness for the propfan in the late 1980s.

REFERENCES

1. Kramer, J.J., "Planning a New Era in Air Transport Efficiency," Aeronautics and Astronautics, July/August 1978, pp. 26-28.
2. Nored, D.D., "Propulsion," Aeronautics and Astronautics, July/August 1978, pp. 47-54.
3. Gatzert, B.S., and Hudson, S.M., "General Characteristics of Fuel Conservation Prop-Fan Propulsion System," SAE Paper No. 751085, November 1975.
4. Dugan, James F., Miller, Brent A., Garber, Edwin J., and Sargerser, David A., "The NASA High-Speed Turboprop Program," NASA TM81561, October 1980.
5. Rohrbach, C., "A Report on the Aerodynamic Design and Wind Tunnel Test of a Prop-Fan Model," AIAA Paper 76-667, July 1967.
6. Mikkelsen, D.C., et al, "Design and Performance of Energy Efficient Propellers for Mach 0.8 Cruise," SAE Paper 770458, March 1977.
7. Rohrbach, C., Metzger, F.B., Black, D.M., and Ladden, R.M., "Evaluation of Wind Tunnel Performance Testings of an advanced 45° Swept Eight-Bladed Propeller at Mach Numbers from 0.45 to 0.85," NASA CR3505, March 1982.
8. Welge, H. Robert, "Prop-Fan Integration at Cruise Speeds," AGARD Paper 33 presented at AGARD Symposium on Aerodynamics of Power Plant Installations, Toulouse, France, May 11-14, 1981.
9. Smith, Ronald C. and Levin, Alan D., "Propfan Installation Aerodynamics of a Supercritical Swept Wing Transport Configuration," AIAA Paper 81-1563, July 1981.
10. Levin, Alan D., and Smith, Ronald C., "Propfan Propulsion Integration Test Techniques," AIAA Paper No. 82-0577, March 1982.
11. Aljabri, Abdulla S., and Swearingen, John M., "Analysis of Mach Number 0.8 Turboprop Slipstream Wing/Nacelle Interactions," NASA CR166419, prepared by the Lockheed-Georgia Company, December 1982.
12. Goldsmith, I.M., and Bowles, J.V., "Potential Benefits for Propfan Technology on Derivatives of Future Short-to-Medium Range Transport Aircraft," AIAA paper 80-1090, June 30 - July 2, 1980.
13. Foss, R.L., and Hopkins, J.P., "Fuel Conservation Potential for the Use of Turboprop Powerplanes," SAE Paper 760537, May 1976.
14. Hopkins, J.P., and Wharton, H.E., "Study of the Cost/Benefit Tradeoffs for Reducing the Energy Consumption of the Commercial Air Transportation System," LR-27769-1, Lockheed-California Company, NASA CR-137927, 1976.
15. Hopkins, J.P., "Study of the Cost/Benefit Tradeoffs for Reducing the Energy Consumption of the Commercial Air Transportation System," LR-27769-2, Lockheed-California Company, NASA CR-137926, 1976.
16. Stern, J.A., "Aircraft Propulsion - A Key to Fuel Conservation: An Aircraft Manufacturer's View," SAE Paper 760538, May 1976.
17. Kraus, E.F., "Cost/Benefit Tradeoffs for Reducing the Energy Consumption of Commercial Air Transportation System. Vol. I: Technical Analysis," MDC-J7340 - Vol. 1, Douglas Aircraft Company, Inc., NASA CR-137923, 1976. Van Abkoude, J.C., "Cost/Benefit Tradeoffs for Reducing the Energy Consumption of Commercial Air Transportation System. Vol. II: Market and Economic Analyses," MDC-J7340 - Vol. 2, Douglas Aircraft Company, Inc., NASA CR-137925, 1976.
18. Anon, "Energy Consumption Characteristics of Transports Using the Prop-Fan Concept: Summary," D6-75780, Boeing Commercial Airplane Company, NASA CR-137938, 1976.
19. Anon, "Energy Consumption Characteristics of Transports Using the Prop-Fan Concept: Final Report," D6-75780, Boeing Commercial Airplane Company, NASA CR-137937, 1976.
20. Dugan, J.F., Miller, B.A., and Sargerser, D.A., "Status of Advanced Turboprop Technology," NASA CP 2036, CTOL Transport Technology, pp. 139-166, February 28-March 3, 1978.
21. Muehlbauer, J.C., et al, "Turboprop Cargo Aircraft Systems Study," NASA CR 165813, prepared by the Lockheed-Georgia Company, November 1981.
22. Muehlbauer, J.C., and Morris, S.J., "Advanced Turboprop Cargo Aircraft Systems Study," AIAA Journal of Aircraft, Vol. 20, No. 6, June 1983, pp. 523 - 529.

23. Strack, W.C., Knip, G., Weisbrich, A.L., Godston, J., and Bradley, E.S., "Technology and Benefits of Aircraft Counter Rotation Propellers," NASA Technical Memorandum 82983, Oct. 1982.
24. Godston, J. and Kish, J., "Selecting the Best Reduction Gear Concept for Prop-Fan Propulsion Systems," AIAA Paper 82-1124, Joint Propulsion Conference, Cleveland, Ohio, June 1982.
25. Goldsmith, I.M., "Advanced Turboprop Testbed Systems Study," NASA CR167895, prepared by Douglas Aircraft Company, July 1982.
26. Bradley, E.S., et al, "Advanced Turboprop Testbed Systems Study," NASA CR167928, prepared by the Lockheed-Georgia Company, July 1982.
27. Arndt, William E., "Propfans Go Full Scale," Aerospace America, January 1984, pp. 100 - 103.

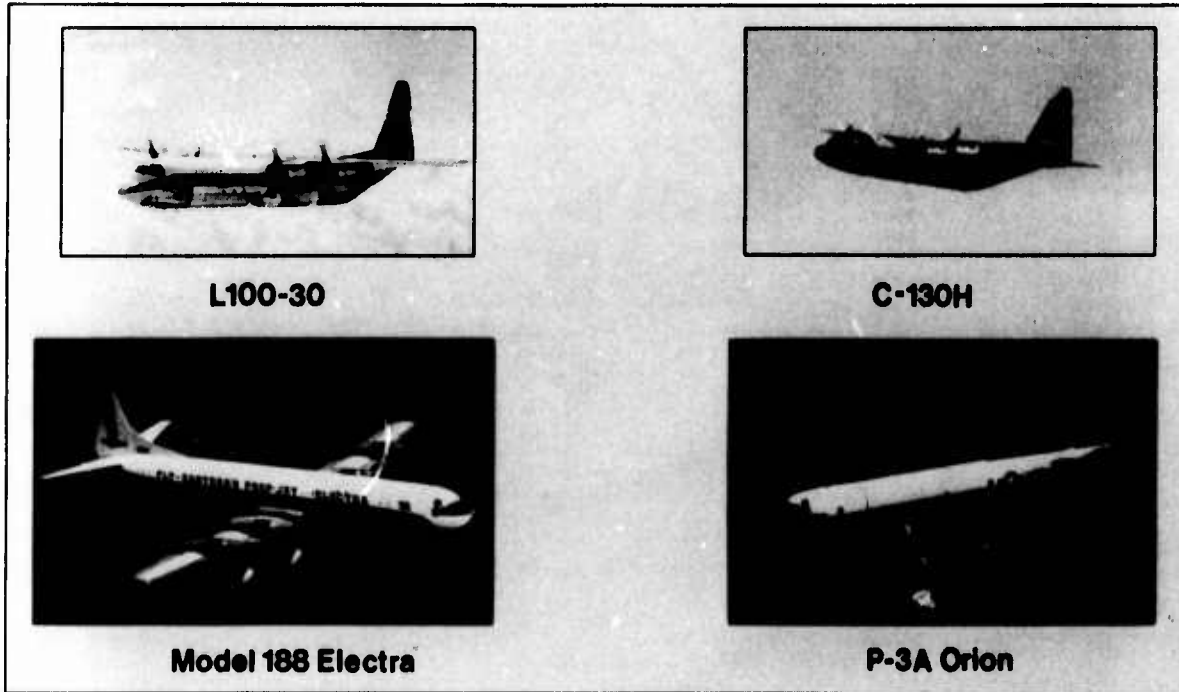


Figure 1. Lockheed Turboprop Aircraft. Clockwise from top left: L-100-30, C-130H, Model 188 Electra, P-3 Orion

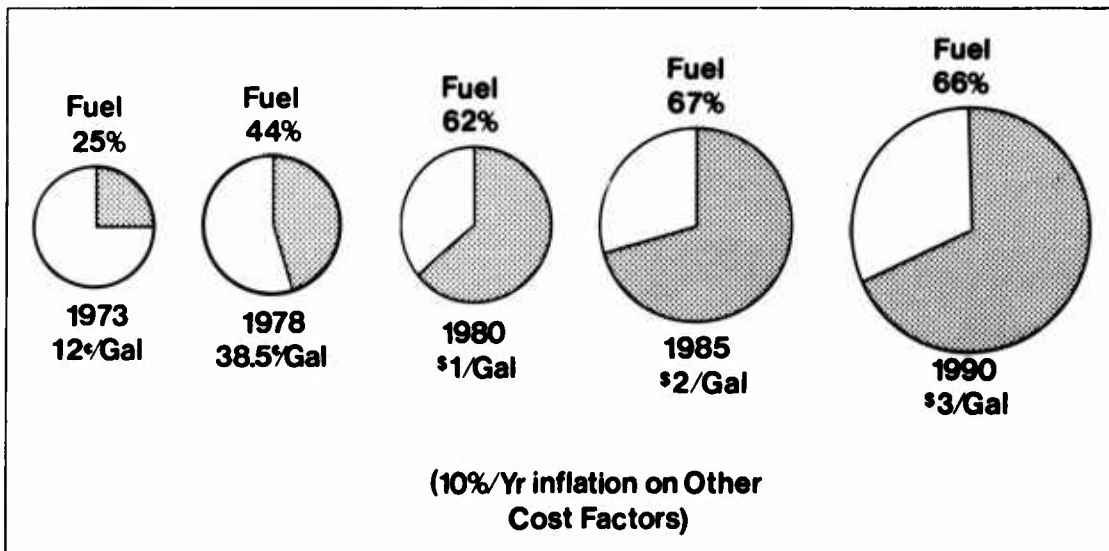


Figure 2. Fuel as a Percentage of Direct Operating Cost (DOC)

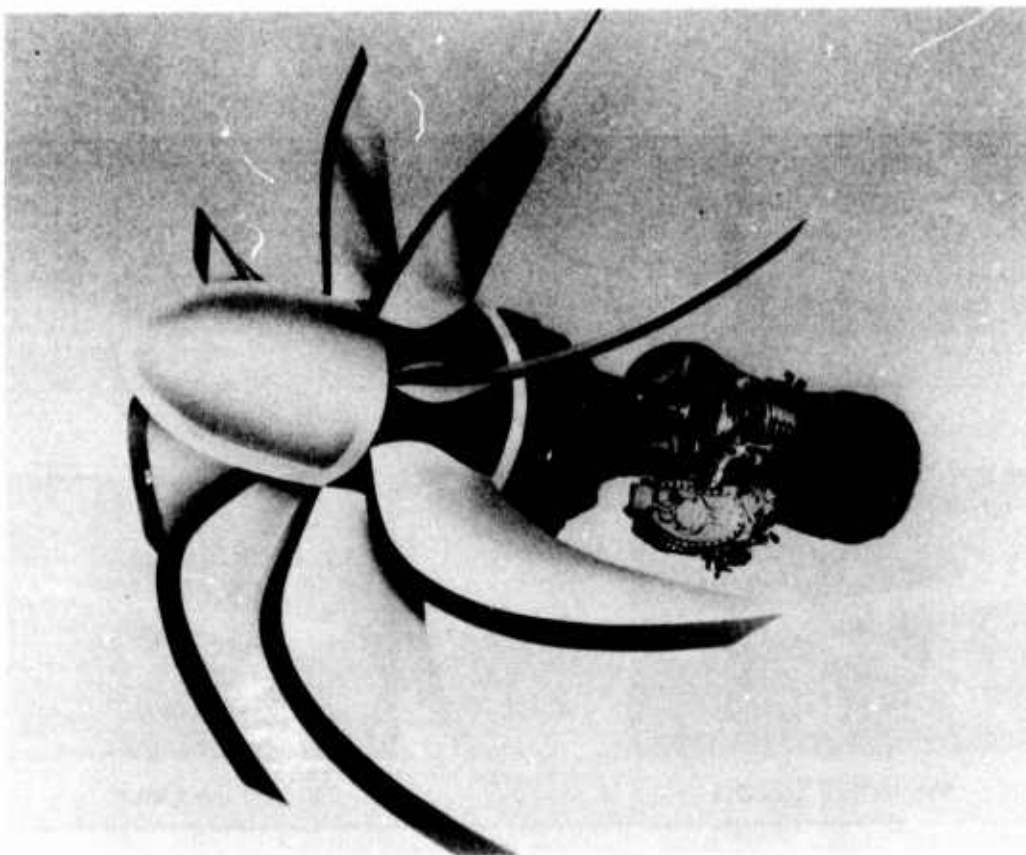


Figure 3. Propfan Propulsion



Figure 4. Propfan Mounted in NASA Wind Tunnel

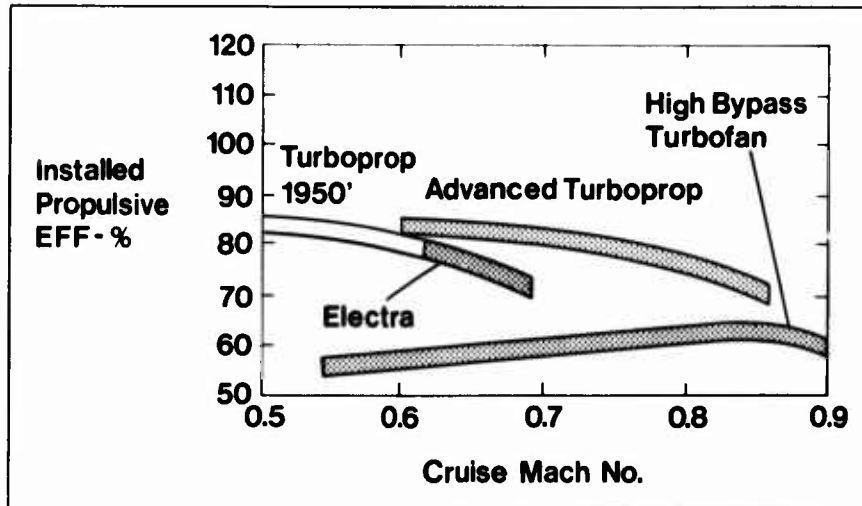


Figure 5. Propulsive Efficiency Comparison

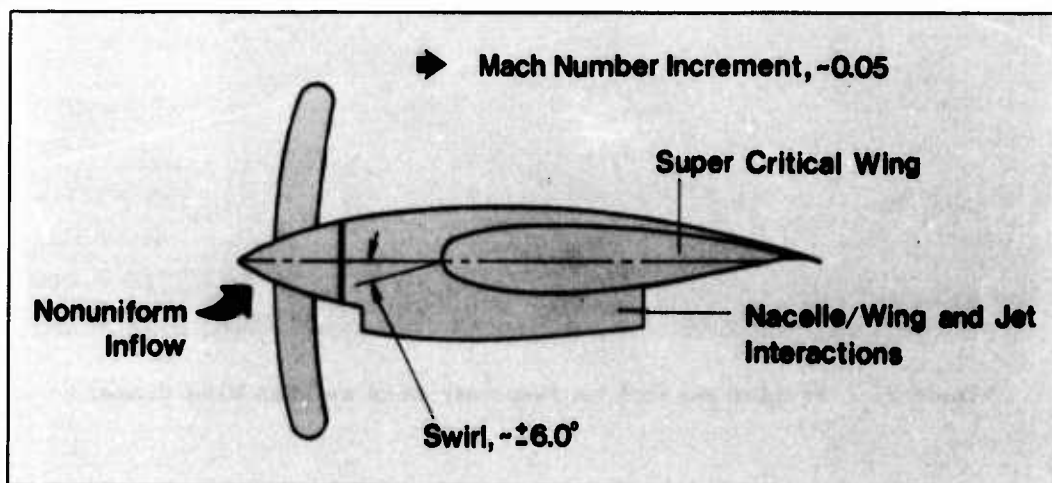


Figure 6. Aero/Propulsive Interference



Figure 7. Propfan Mounted on Sweptback Wing in NASA Wind Tunnel

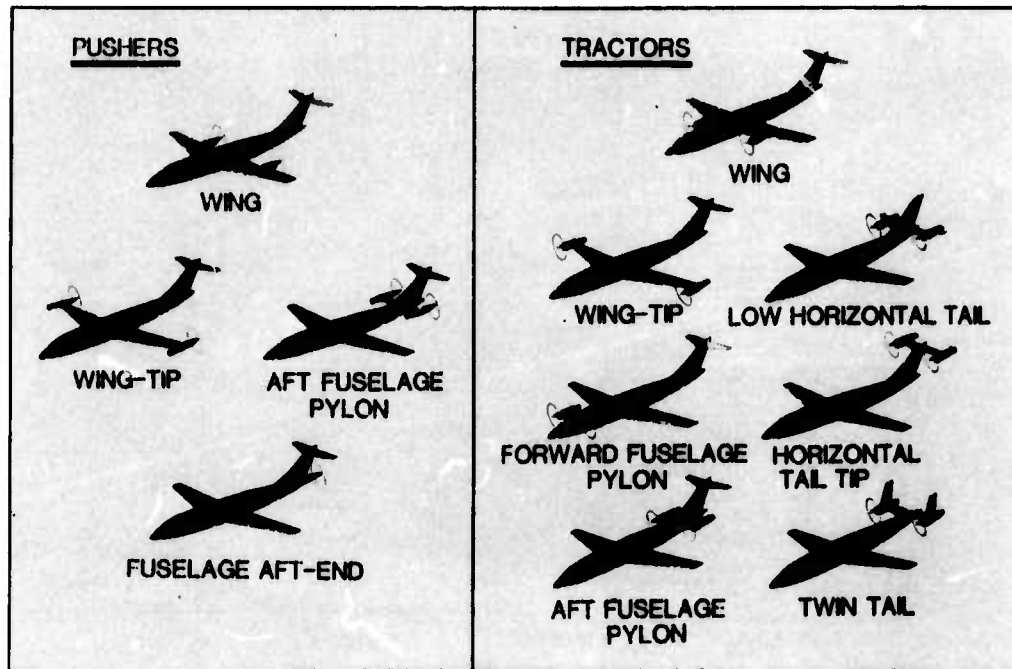


Figure 8. Alternate Propfan Installations

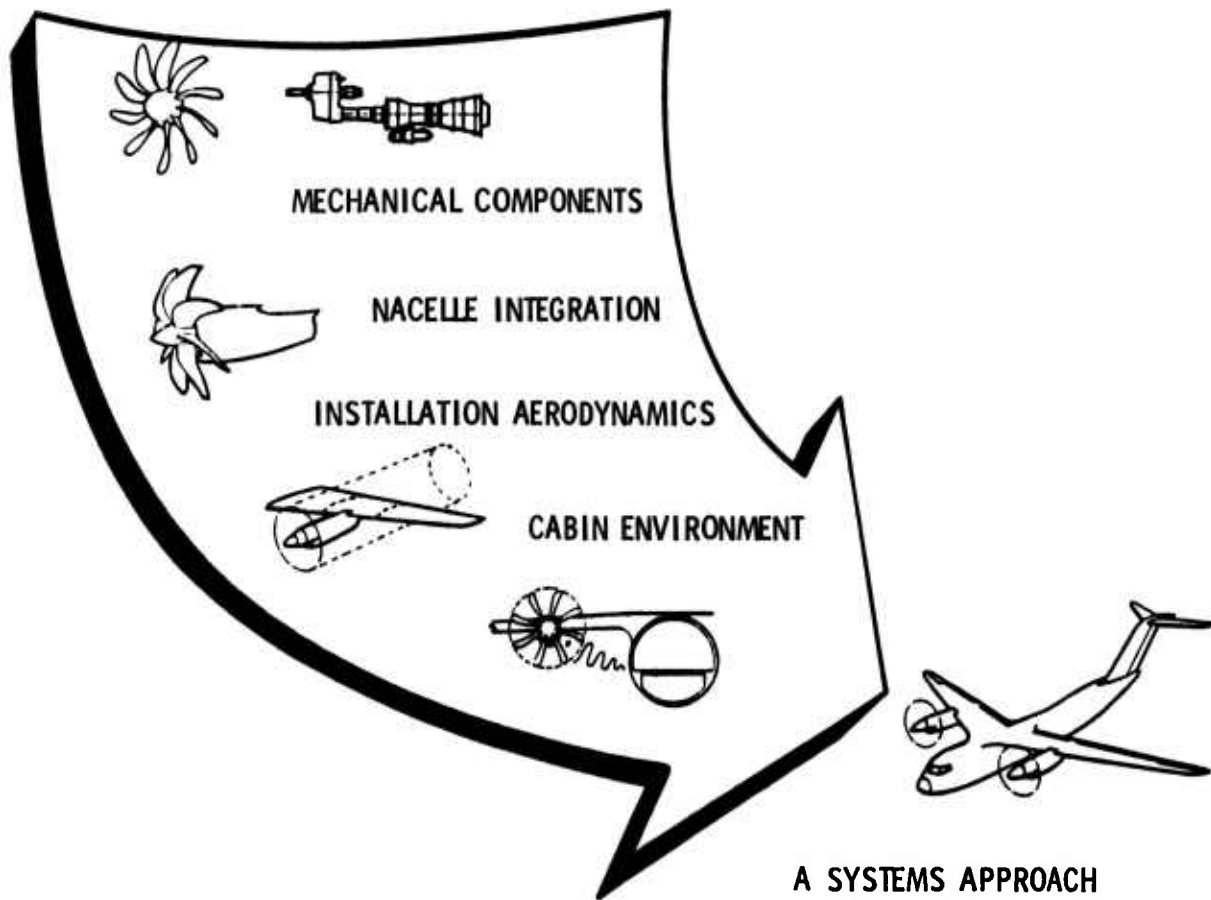


Figure 9. Propfan Design Integration



Figure 10. Propfan Concepts in the NASA RECAT Study

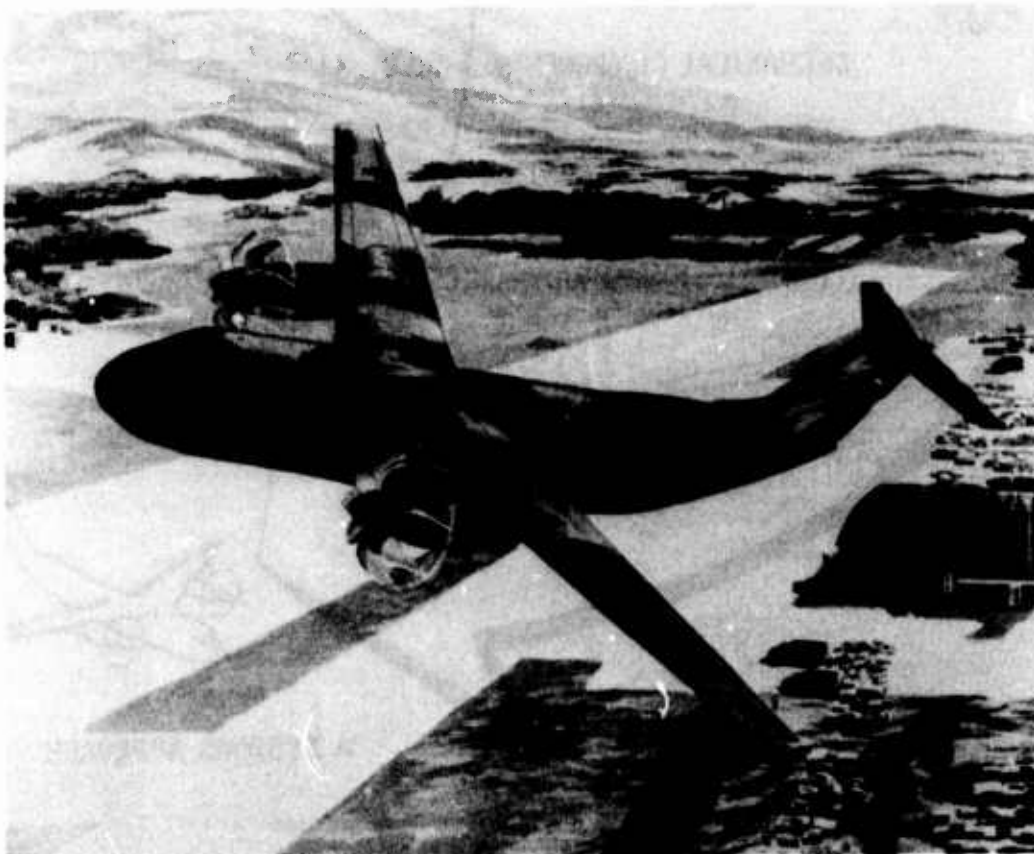


Figure 11. Propfan Cargo Aircraft. Payload - 60,000 Lb, $M=0.75$

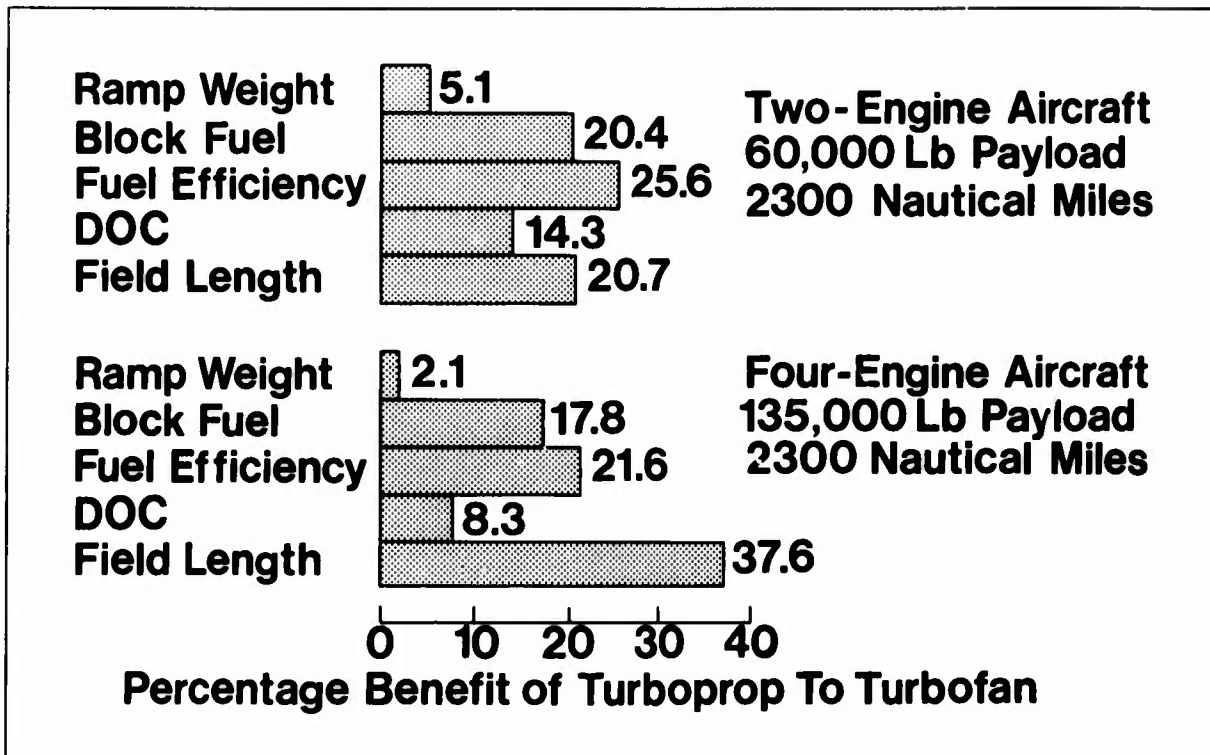


Figure 12. Performance Comparison of Propfan and Turbofan Cargo Aircraft, M=0.75

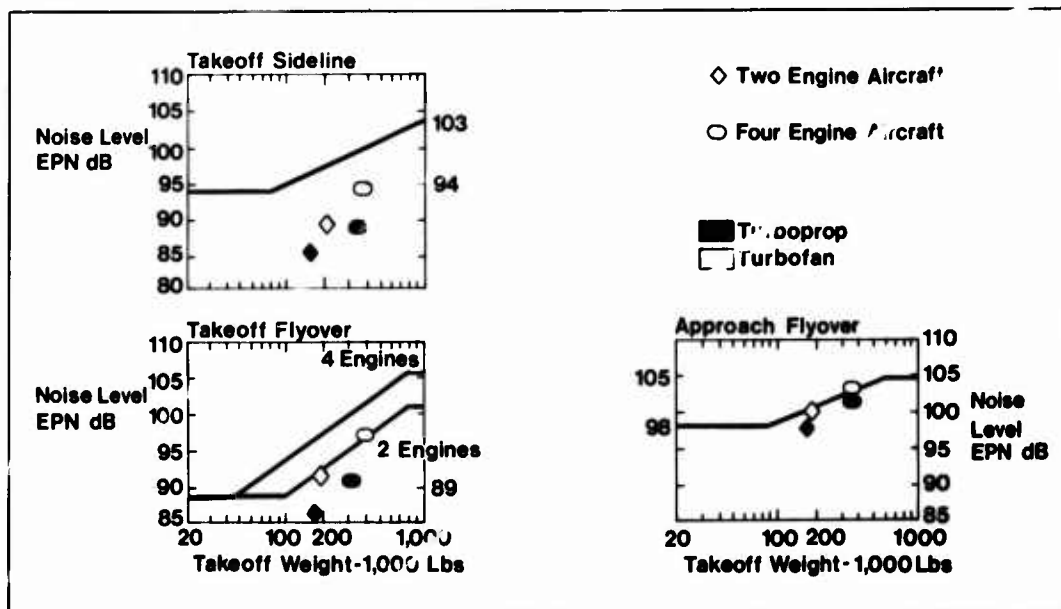


Figure 13. FAR 36 Stage 3 Noise Limits and Noise Levels

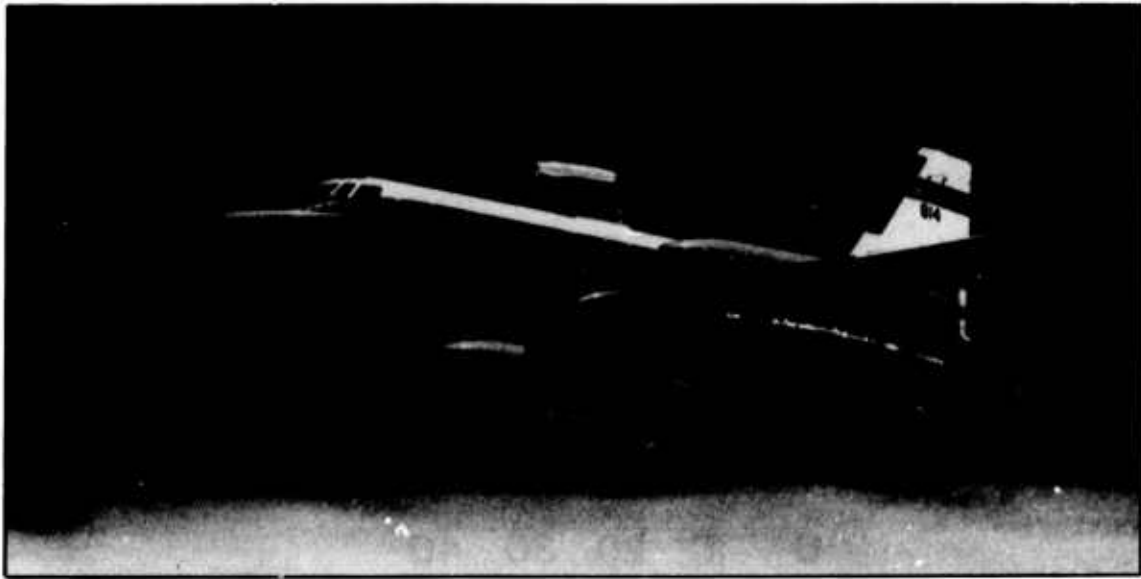


Figure 14. NASA JetStar Propfan Testbed

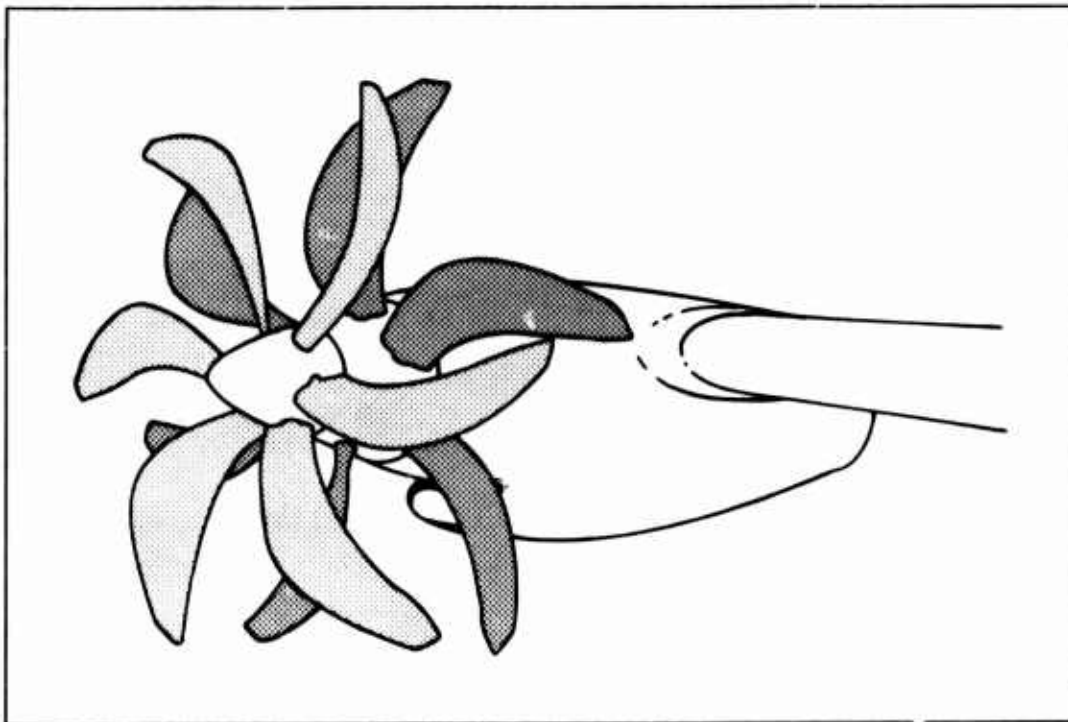


Figure 15. Counter Rotation Propfan

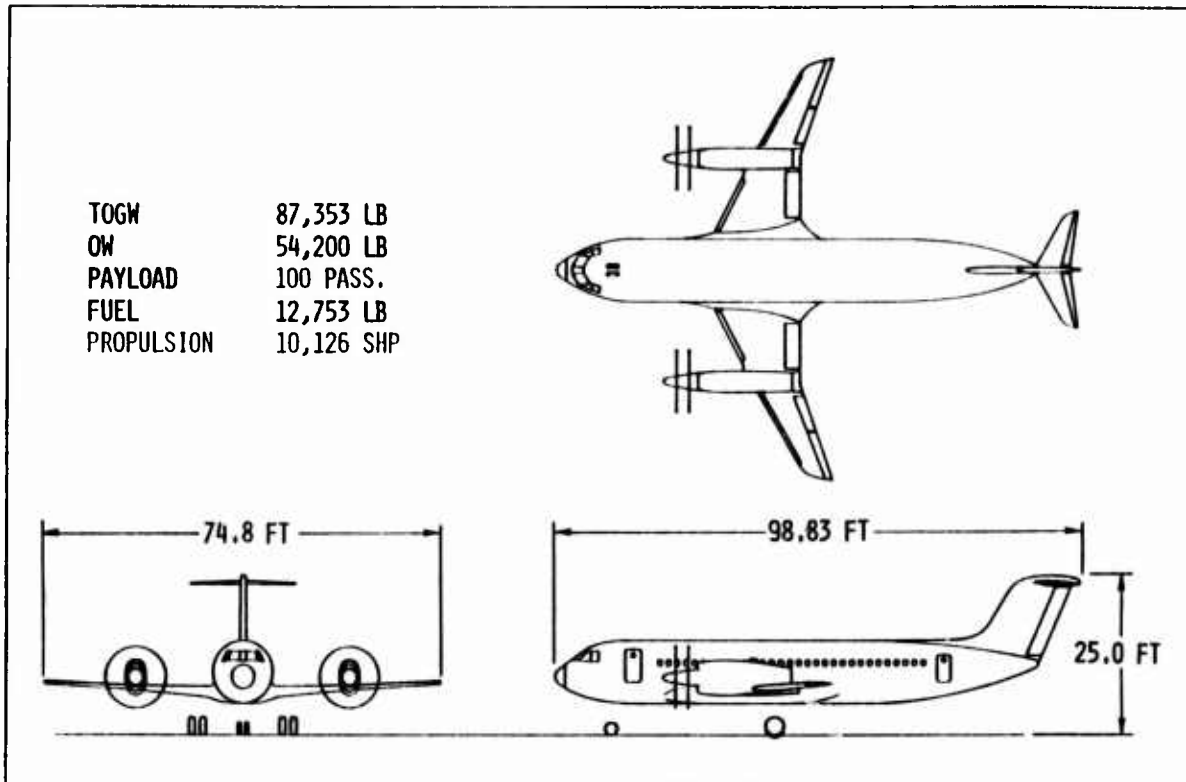


Figure 16. M=0.8 Counter Rotation Propfan Transport

Large Scale Flight Research Output

Provides Credible Data Base for Representative Operating Conditions

- **Verifies Analytical and Design Methodology**
 - Propeller Aeroelastics and Dynamics
 - Fuselage Noise/Vibration Attenuation
 - Propeller Noise Generation and Propagation
 - Propeller Performance
 - Installation Aerodynamics
- **Establishes Scaling Effects**
- **Establishes Wind Tunnel/Flight Correlation**

Figure 17. Output Data from Large Scale Flight Research



Figure 18. Lockheed Propfan Test Assessment Aircraft

METHODES AERODYNAMIQUES UTILISEES EN FRANCE
 POUR L'ETUDE DES HELICES POUR AVIONS RAPIDES *

par

J.M. BOUSQUET

Office National d'Etudes et de Recherches Aérospatiales (ONERA)

92320 Châtillon - FRANCE

RESUME

Les recherches menées en France sur les hélices pour avions rapides portent particulièrement sur le développement de méthodes de calcul. Parallèlement, et en application de ces méthodes, une hélice de 1 mètre de diamètre a été définie pour essai dans la soufflerie S1 de l'ONERA à Modane.

Dans le domaine de l'Aérodynamique, les méthodes disponibles vont des théories simples adaptées à l'avant-projet et à l'optimisation de l'hélice, à des méthodes plus sophistiquées adaptées à la prévision fine des caractéristiques de l'écoulement tridimensionnel transsonique sur les pales. Les différentes méthodes sont présentées, et leurs résultats comparés avec des résultats d'expériences disponibles. Des résultats de calcul par une méthode de résolution des équations d'Euler tridimensionnelles sont ensuite utilisés pour mettre en évidence les risques de blocage en embase de pales des hélices pour avion rapide.

AERODYNAMIC METHOD USED IN FRANCE
 FOR ADVANCED FAST PROPELLER STUDY

ABSTRACT

French researches on advanced fast propellers concern the development of calculation methods. As an application of these methods, a 1 meter diameter propeller has been designed to be tested in S1 Modane ONERA Wind Tunnel.

Aerodynamic methods used in this study, go from simple ones adapted for project and optimisation of the propeller, to very sophisticated ones able to predict the characteristics of the tridimensional transonic flow on the blades. The different methods are presented, and their results are compared with existant test data. Results obtained by tridimensional Euler code are also used to illustrate the blockage risks near the root of advanced fast propellers.

TABLE DES MATIERES -

NOTATIONS

- 1 - INTRODUCTION
- 2 - METHODES DE CALCUL AERODYNAMIQUE D'HELICES
 - 2.1 - Méthodes de Ligne Portante (LP et LPC)
 - 2.2 - Méthode de Surface Portante incompressible
 - 2.3 - Méthode de Surface Portante compressible
 - 2.4 - Méthode Euler tridimensionnelle
- 3 - APPLICATION DES METHODES
 - 3.1 - Hélices classiques
 - 3.2 - Hélices pour Avion Rapide
 - 3.2.1 - Comparaison des différentes méthodes
 - 3.2.2 - Analyse de l'écoulement sur l'hélice HT1 à l'aide de la méthode Euler
- 4 - PERSPECTIVES
- 5 - CONCLUSION

NOTATIONS -

- B : Nombre de pales
 C : Célérité du son

* Etude effectuée avec le soutien financier de la DRET du Ministère Français de la Défense.

C_z : Coefficient de portance (profil) C_x : Coefficient de traînée (profil)

D : Diamètre de l'hélice

 F_z : Portance

M : Nombre de Mach

n : Fréquence de rotation

P : Puissance

R : Rayon de l'hélice

 r : Rayon

T : Traction

V : Vitesse

 $W(\xi)$: Vitesse relative α : Incidence β : Calage γ : Paramètre d'avancement η : Rendement λ_0 : Pas réduit du sillage ξ : Rayon réduit (ou diamètre réduit) ξ_0 : Rayon réduit (ou diamètre réduit) du moyeu ρ : Masse volumique τ : Coefficient de traction χ : Coefficient de puissance Ω : Vitesse de rotation

$$C_z = \frac{F_z}{\frac{1}{2} \rho W^2}$$

$$n = \frac{\Omega}{2\pi}$$

$$W = V \sqrt{1 + \frac{\pi^2}{\gamma^2} \xi^2}$$

$$\gamma = \frac{V_0}{nD} = J$$

$$\eta = \frac{\delta T}{\chi}$$

$$\tau = \frac{T}{\rho n^2 D^4} = C_T$$

$$\chi = \frac{P}{\rho n^3 D^6} = C_P$$

1 - INTRODUCTION -

L'objectif des études sur les hélices pour avions rapides se situe dans le contexte général des économies d'énergies à réaliser sur les avions de transport futurs.

Il est indéniable que la propulsion par hélices bénéficie d'un regain d'intérêt, à cause, essentiellement, de l'augmentation continue du prix du carburant et de son influence croissante sur le DOC (Direct Operating Cost) des avions de transport [1]. Le renouveau potentiel des hélices concerne les avions de faible capacité et faible vitesse traditionnellement équipés d'hélices classiques (commuter), mais également des avions plus rapides qui pourraient dans le futur être équipés d'hélices transsoniques [2]. Ce concept hélice transsonique est de nouveau d'actualité à la suite des études sur les prop-fans menées depuis 1975 aux Etats-Unis par la NASA et Hamilton Standard. Les premiers résultats très encourageants de ces recherches mettent en concurrence, d'un point de vue économique, la propulsion par hélice rapide et la propulsion traditionnelle par turboréacteur [3].

Le programme de recherche relatif aux hélices pour avions rapides, lancé par les Services Officiels Français en Mars 1982, est un des moyens choisis pour améliorer les performances des avions équipés de turbopropulseurs, et pour moderniser la conception des hélices. Ce programme orienté principalement vers le développement d'hélices très complexes, conduira à des progrès dont devraient bénéficier tous les types d'hélices.

L'opération "Hélice pour Avions Rapides" (CHARME), effectuée en collaboration entre l'AEROSPATIALE Division Avions, l'AEROSPATIALE Division Hélicoptères, RATIER-FIGEAC et l'ONERA, est structurée autour de la définition et l'essai d'une maquette d'hélice de 1 mètre de diamètre dans la soufflerie S1 Modane. Dans cette opération, l'ONERA a la charge du développement de méthodes de calcul nouvelles (Aérodynamique, Acoustique, Aéroélasticité), de la définition aérodynamique de la maquette, et de l'exécution de l'essai à Modane (Figure 1).

L'éventuel succès de ce type de propulsion dépend de nombreux paramètres, parmi lesquels trois semblent déterminants : les performances, la tenue structurale (ainsi que la fiabilité) et le niveau de bruit.

Pour définir de telles hélices, il faut disposer de méthodes de calcul de niveaux de spécificité différents. Des méthodes simples doivent être utilisées au stade de l'avant-projet pour effectuer le choix des paramètres de définition ; des méthodes plus sophistiquées sont employées au stade du projet pour affiner la définition des hélices et préciser les caractéristiques locales de fonctionnement.

Les méthodes de calcul aérodynamiques décrites dans ce document couvrent ces deux finalités. Les méthodes basées sur la théorie de la Ligne Portante sont bien adaptées pour l'avant-projet, et permettent d'accéder aux performances globales de l'hélice à partir des caractéristiques de fonctionnement bidimensionnel des profils. Les méthodes de calcul tridimensionnel, plus fines mais plus restrictives dans la mesure où elles sont basées sur l'hypothèse de fluide parfait, sont ensuite utilisées pour vérifier la validité des hypothèses des méthodes de Ligne Portante.

Dans la première partie de ce document, les différentes méthodes de calcul aérodynamique d'hélices sont décrites ; l'accent est mis sur les hypothèses relatives à chacune des méthodes.

Dans la seconde partie, on présente des applications de ces méthodes : d'abord sur des hélices classiques pour lesquelles les différentes théories fournissent des résultats voisins ; puis sur des hélices pour avions rapides, où les écarts entre les méthodes sont commentés. Des résultats de calcul par la méthode de résolution des équations d'Euler tridimensionnelles sont ensuite utilisés pour décrire l'évolution des phénomènes transsoniques sur les pales, particulièrement les risques de blocage de l'écoulement en embase.

Dans la dernière partie de ce document, les autres études menées à l'ONERA dans le cadre de l'opération CHARME sont commentées, notamment le futur essai dans la soufflerie SIMA de la maquette d'hélice HT3.

2 - METHODES DE CALCUL AERODYNAMIQUE D'HELICES -

Les études sur les hélices pour avion rapide ont débuté à l'ONERA en 1979 [2]. D'abord orientées sur des méthodes simples dérivées des méthodes de calcul d'hélices classiques (Ligne Portante), les recherches ont porté sur des méthodes plus sophistiquées pour prendre en compte la géométrie tridimensionnelle des hélices en flèche. Cette évolution dans les méthodes est assez comparable aux développements effectués parallèlement aux Etats-Unis [4, 5].

Comme il est fait classiquement pour les voilures tournantes, les équations de la mécanique des fluides sont écrites dans un référentiel tournant à la vitesse Ω de rotation de l'hélice. La figure 2 présente ce référentiel relatif, dans lequel les composantes de la vitesse de l'écoulement sont stationnaires pour une hélice sans incidence.

Les différentes méthodes disponibles ou en cours de développement sont présentées par ordre de complexité décroissante sur la figure 3.

2.1 - Méthodes de Ligne Portante - (LP et LPC)

Le programme de calcul de ligne portante L.P. utilisé dans ces études a été développé par COURJARET de l'AEROSPATIALE.

Le calcul des vitesses induites y est effectué soit en utilisant les formules de HIRSCH [6], soit par intégration numérique. Les caractéristiques des profils sont interpolées dans un fichier de polaires expérimentales de profils bidimensionnels. L'originalité de cette méthode réside dans le calcul exact du pas réduit de chacun des tourbillons hélicoïdaux du sillage à l'aide d'un processus itératif.

Pour traiter le cas de pales d'hélices comportant de la flèche, le programme L.P. a été modifié d'une part en incorporant la théorie simplifiée de l'attaque oblique pour le fonctionnement des profils, et d'autre part en introduisant une ligne portante courbe dans le calcul tourbillonnaire. Sur la figure 4, on compare les répartitions de circulation pour une ligne portante droite et pour une ligne portante courbe typique, pour les mêmes répartitions de pas de sillage. On remarque que l'incurvation de la ligne portante se traduit par un décalage du maximum de circulation vers l'extrémité de la pale, et par une inflexion dans les zones médianes.

L'interaction avec une nacelle est également prise en compte dans ces deux programmes, par les techniques proposées par GLAUERT [7] pour la détermination des tractions apparentes et nettes (figure 5).

2.2 - Méthode de Surface Portante incompressible (LUU) -

Cette méthode a été développée par LUU du LIMSI pour les hélices marines [8].

Dans cette méthode tridimensionnelle incompressible, les pales et leurs sillages sont modélisés par des singularités. Chaque pale est modélisée par des répartitions de sources (effet d'épaisseur) et de doublets (effet de cambrure) ; les sillages sont représentés par des répartitions de doublets. Dans la version initiale du programme, l'ensemble des singularités était réparti sur la surface hélicoïdale représentative du point de fonctionnement ; plus récemment, des modifications ont été apportées pour prendre en compte la géométrie exacte des pales de l'hélice. Le pas réduit local à l'origine du sillage est calculé itérativement, pour tenir compte de la répartition radiale des vitesses induites au niveau des pales.

Dans la version du programme utilisée, le carénage de moyeu est traité comme un cylindre infini. Les pertes de traînée de profil ne sont pas prises en compte dans les calculs.

2.3 - Méthode tridimensionnelle compressible (COSTES) -

Ce programme de calcul a été développé par J.J. COSTES de la Direction des Structures de l'ONERA.

L'écoulement tridimensionnel sans choc autour de pales de formes quelconques est calculé par résolution de l'équation des petites perturbations du potentiel des vitesses :

$$(1-M_0^2) \frac{\partial^2 \varphi}{\partial \sigma^2} - 2 \frac{\partial^2 \varphi}{\partial \xi \partial \sigma} + \frac{1+\mu^2}{\mu^2} \frac{\partial^2 \varphi}{\partial \xi^2} + \frac{\partial^2 \varphi}{\partial \mu^2} + \frac{1}{\mu} \frac{\partial \varphi}{\partial \mu} = 0$$

où φ est le potentiel de perturbation

M_0 est le nombre de Mach amont

$$\mu, \sigma \text{ sont les coordonnées réduites} \quad \mu = \frac{\Omega r}{V_0} \quad \sigma = \frac{\Omega \xi}{V_0}$$

$$\text{et } \xi \text{ la coordonnée hélicoïdale} \quad \xi = \theta - \sigma$$

Cette équation est résolue par différences finies dans un domaine compris entre deux pales. Le moyeu n'est pas modélisé dans cette méthode. Les pertes de trainée de profil ne sont pas prises en compte dans le calcul des performances de l'hélice.

2.4 - Méthode Euler 3D -

Cette méthode a été initialement développée pour les turbomachines par J. BROCHET [10] et [11]. La présente adaptation au cas des hélices est assez similaire à la méthode EULER développée aux Etats-Unis [12].

Dans l'hypothèse de fluide parfait, les équations d'Euler décrivant le comportement d'une particule le long d'une ligne de courant relative s'écrivent :

$$1 \begin{cases} a) \operatorname{div}(\rho \bar{W}) = 0 \\ b) \operatorname{div}(\rho \bar{W} \otimes \bar{W} + p \bar{I}) + \rho \bar{F} = 0 \\ c) \operatorname{div}(\rho I \bar{W}) = 0 \end{cases}$$

où I désigne la rothalpie $I = h(p, \rho) + W^2/2 - \Omega^2 r^2/2$
et \bar{F} est la somme des accélérations d'entraînement et de Coriollis

$$\bar{F} = 2\Omega \bar{e}_3 \wedge \bar{W} - \Omega^2 \bar{e}_r$$

\bar{e}_3 et \bar{e}_r sont les vecteurs unitaires axiaux et radiaux du référentiel tournant.

Ce problème stationnaire est d'abord transformé en un problème pseudo-instationnaire par introduction d'une variable "temps" fictive, qui permet de construire un procédé itératif convergent vers la solution stationnaire. Le système pseudo-instationnaire est construit en remplaçant l'équation de l'énergie (c) par la condition de rothalpie uniforme $I = \text{cte}$ et en traitant les formulations instationnaires exactes des équations de continuités (a) et de quantité de mouvement (b).

$$2 \begin{cases} a) \frac{\partial \rho}{\partial t} + \bar{\nabla} \cdot (\rho \bar{W}) = 0 \\ b) \frac{\partial \rho \bar{W}}{\partial t} + \bar{\nabla} \cdot (\rho \bar{W} \otimes \bar{W} + p \bar{I}) + \rho \bar{F} = 0 \end{cases}$$

Les 4 inconnues du problème sont la masse volumique ρ et les 3 composantes de la quantité de mouvement relative $\rho \bar{W}$. La pression statique est déterminée par la condition de rothalpie uniforme $I = \text{cte}$ et par la relation thermodynamique :

$$p(\rho, \rho \bar{W}) = \frac{\gamma-1}{\gamma} \left(I + \frac{\Omega^2 r^2}{2} \right) \rho - \frac{\gamma-1}{2\gamma} \frac{(\rho \bar{W})^2}{\rho}$$

Le système 2 est complété par un ensemble de conditions aux limites et de conditions initiales.

Des considérations de périodicité permettent de limiter le domaine de calcul à l'espace compris entre deux pales consécutives (figure 6).

Les conditions limites basées sur la résolution d'équations de compatibilité [9] sont du type :

- périodicité sur les surfaces latérales, sauf sur les pales où l'on applique une condition de glissement relatif,
- glissement relatif sur le moyeu,
- vitesse absolue uniforme et axiale dans le plan amont,
- condition de pression (équilibre radial simplifié) ou de non réflexion des ondes acoustiques sur le plan aval,

- condition de glissement relatif, de pression uniforme ou de non réflexion des ondes acoustiques sur le carter fictif suivant les applications (soufflerie ou atmosphère illimitée).

3 - APPLICATION DES METHODES -

3.1 - Hélices classiques -

Pour des hélices classiques, fonctionnant à des nombres de Mach modérés, les méthodes préalablement décrites fournissent des résultats très voisins. C'est ce que montre la figure 7 où sont comparés les résultats de calcul avec les valeurs expérimentales obtenues dans la soufflerie S1 de Modane, sur l'hélice quadripale Marquis. Pour un paramètre d'avancement $\gamma = 1,72$, l'évolution du coefficient de traction \mathcal{T} en fonction du coefficient de puissance χ est bien prévue par le calcul ; le calcul par la méthode Ligne Portante est en meilleur accord avec l'expérience que les méthodes tridimensionnelles (LUU et COSTES) dans lesquelles les pertes de traînée de profils ne sont pas prises en compte.

Les répartitions calculées de charges en envergure sont très voisines pour toutes les méthodes. Sur la figure 8 sont comparées les répartitions de C_z des profils calculées par les méthodes tridimensionnelles LUU et COSTES, pour un paramètre d'avancement $\gamma = 1,72$ et un coefficient de puissance $\chi = 0,22$. L'accord entre les deux méthodes est très bon, sauf en embase de pale où de légers écarts apparaissent, dus à la prise en compte différente du carénage de moyeu.

La validité de ces méthodes de calcul a été contrôlée pour des hélices plus rapides. Dans ce cas, les pertes de traînée deviennent importantes en raison du fonctionnement en régime transsonique des profils. La figure 9 montre que la méthode Ligne Portante reste bien adaptée pour la prévision des performances globales de ces hélices. La comparaison porte sur l'hélice NACA 4 (5) (05) 041 essayée jusqu'à des nombres de Mach de 0,83, en présence d'une nacelle moteur [13]. L'évolution du rendement apparent calculé par la méthode Ligne Portante est en bon accord avec l'expérience, la performance étant néanmoins légèrement surévaluée dans le calcul. On présente également sur cette figure les résultats de calculs de l'hélice isolée (minimum-body) au même calage que précédemment ; le rendement isolé est très inférieur (de l'ordre de $\Delta \eta \sim - 0,08$) au rendement apparent calculé, traduisant l'importance de la prise en compte de la nacelle dans le calcul des performances de l'hélice.

3.2 - Hélices pour avion rapide -

Les hélices rapides, ou hélices transsoniques, diffèrent essentiellement des hélices classiques par deux caractéristiques : des pales comportant de la flèche et une forte charge au disque. Ces deux caractéristiques particulières découlent des grands nombres de Mach visés pour la croisière ($0,7 \leq Mo \leq 0,8$).

La mise en flèche des pales est destinée à retarder l'apparition des phénomènes transsoniques, pénalisants pour la performance et le niveau acoustique des hélices ; en contrepartie, cette géométrie particulière engendre des problèmes d'ordre structural et aéroélastique qui ne peuvent être résolus que par l'emploi de nouvelles technologies (matériaux composites).

La forte charge au disque est imposée par des contraintes d'architecture d'avion, et a pour conséquence la transmission des grandes puissances nécessaires au vol rapide à des hélices de faible diamètre. Les effets de la charge au disque sont illustrés par la figure 10 résultat d'une étude paramétrique effectuée à l'aide de la méthode de Ligne Portante. Dans cette étude, seules sont considérées les pertes "tourbillonnaires", en négligeant les pertes de traînée de profil. Les pertes dues à l'accroissement de vitesse axiale (rendement de Froude), celles dues à la rotation résiduelle du sillage (nombre de pales ∞) et celles dues au nombre fini de pales augmentent toutes avec la charge au disque.

En conséquence, pour conserver un bon rendement à ce type d'hélices très chargées, il est essentiel de disposer d'un grand nombre de pales ; la minimisation des pertes dues à la rotation résiduelle du sillage par redresseur ou hélice controrotative peut également s'avérer intéressante.

3.2.1 - Comparaison des différentes méthodes -

Pour ces hélices d'un type nouveau, la validité de la méthode ligne portante courbe (LPC) a été testée par comparaison avec les résultats expérimentaux du prop-fan SRI [14] comportant 8 pales. Sur la figure 11, on compare l'évolution des rendements nets calculé et expérimental, en fonction du nombre de Mach, pour un paramètre d'avancement $\gamma = 3,14$ et un coefficient de puissance $\chi = 1,85$. Le rendement net calculé est inférieur au rendement expérimental ($\Delta \eta \sim - 0,025$). Cette sous-évaluation peut être due à la mauvaise connaissance de la géométrie de l'hélice et de ses déformations en essai, ou au peu de données disponibles concernant les caractéristiques aérodynamiques des profils très minces dont l'hélice SRI est dotée en extrémité de pale ($e/l \sim 0,02$) ; des incertitudes peuvent également résider dans la détermination des rendements nets calculé et expérimental.

On a également reporté sur la figure 11 les résultats du calcul de l'hélice HT3 définie à l'ONERA, comportant 12 pales, qui sera essayée dans la soufflerie S1 de Modane. Les performances calculées de cette hélice réalisent l'objectif fixé d'un rendement $\eta \sim 0,8$ au nombre de Mach $Mo = 0,75$.

Sur la figure 12, sont comparées les répartitions de portance calculées par toutes les méthodes disponibles sur la même configuration de fonctionnement d'une hélice HT1, à 12 pales comportant de la flèche. Il est à remarquer que dans la configuration étudiée, la répartition de C_z comporte un minimum dans la partie médiane de la pale ($\xi \sim 0,65$). Les calculs effectués par les méthodes tridimensionnelles (LUU, COSTES et EULER) sont très proches dans la zone d'extrémité de la pale ($\xi > 0,65$) ; les écarts en embases de pale sont dus aux prises en compte différentes du moyeu

(glissement relatif sur moyeu cylindrique pour LUJ et EULER, absence de moyeu pour COSTES). La méthode LPC restitue bien l'allure de la répartition de C_z ; le niveau de portance est toutefois surévalué. Par contre, la méthode LP ne décèle aucun minimum sur la répartition de charge en envergure.

Cet exemple montre l'importance des effets tridimensionnels sur les pales d'hélices rapides, justifiant l'emploi de méthodes sophistiquées pour la prévision des caractéristiques précises de l'écoulement sur les pales.

3.2.2 - Analyse de l'écoulement sur l'hélice HT1 à l'aide de la méthode Euler -

Cette étude a pour but de montrer l'influence des paramètres de fonctionnement et de définition sur les caractéristiques de l'écoulement autour des pales d'une hélice d'avion rapide. Les exemples de calcul présentés concernent l'hélice HT1 ; tous les calculs ont été effectués à iso-géométrie de pale (aucune déformation, aucun changement de pas ou de vrillage).

3.2.2.1 - Effet du paramètre d'avancement -

A iso-nombre de Mach d'entraînement (ici $Mo = 0,7$), l'augmentation de la vitesse de rotation de l'hélice (ou diminution du paramètre d'avancement γ), se traduit par une augmentation du nombre de Mach relatif et de l'incidence géométrique de tous les profils de la pale. Il en résulte, comme le montre la figure 13, une augmentation globale des niveaux de C_z sur les pales, et donc une augmentation de la puissance absorbée par l'hélice.

L'importance de la zone d'écoulement supersonique à l'extrados des pales augmente (figure 14) ; le choc est relativement faible dans les régions médianes et d'extrémité de pales à $\gamma \sim 3,38$ et est localisé vers les 40% des cordes de la pale. A $\gamma = 2,94$, le choc se raidit et se trouve vers les 60% de la corde. Parallèlement, à l'intrados se crée une région supersonique en embase de pale (figure 15), associée au blocage de l'écoulement dans le canal interpales que l'on discerne nettement au rayon relatif $\xi = 0,369$ (figure 16).

L'installation d'un blocage en embase de pales s'effectue de manière assez continue lors de l'augmentation de la vitesse de rotation.

3.2.2.2 - Effet du nombre de Mach -

A iso-paramètre d'avancement γ (ici $\gamma = 3,15$), l'augmentation du nombre de Mach de l'écoulement se traduit essentiellement par une augmentation du nombre de Mach relatif d'attaque de tous les profils, l'incidence géométrique restant constante. Il en résulte, comme le montre la figure 17, une augmentation globale des niveaux de C_z des profils de la pale entre $Mo = 0,6$ et $Mo = 0,7$. Le passage à $Mo = 0,75$ se traduit également par une augmentation des C_z des profils d'extrémité de pale ; par contre, en embase de pale, l'intensification du phénomène de blocage s'accompagne d'une chute assez marquée du coefficient C_z .

La zone d'écoulement supersonique se développe rapidement à l'extrados des pales (figure 18) entre $Mo = 0,7$ et $Mo = 0,75$, le choc confiné dans les 50% en corde à $Mo = 0,7$, atteignant 80% en corde à $Mo = 0,75$ sur toute la pale ; les niveaux de Mach relatif maximum augmentent principalement en embase de pale.

A l'intrados (figure 19), le développement de la zone supersonique est lui aussi rapide entre $Mo = 0,7$ et $Mo = 0,75$. Ce développement est principalement dû à un blocage de plus en plus important des zones d'embase de pale ; la trace du choc assez oblique par rapport à l'axe de la pale est conditionnée par la géométrie tridimensionnelle, et particulièrement l'évolution du vrillage des profils.

Ce phénomène de blocage des embases est détaillé sur la figure 20 pour des coupes cylindriques au rayon relatif $\xi = 0,369$. A $Mo = 0,75$ un choc fort se développe à l'arrière des profils. Ce blocage s'étend d'ailleurs assez loin radialement comme le montre la figure 21 au rayon relatif $\xi = 0,795$.

Des tendances analogues auraient pu être relevées en augmentant suffisamment la vitesse de rotation (§ 3.2.2.1), mais cependant de façon moins nette en raison de l'augmentation de l'incidence géométrique des profils sur toute la pale.

3.2.2.3 - Effet du nombre de pales -

La raison principale du blocage de l'écoulement dans les configurations précédemment présentées lorsque le nombre de Mach d'entraînement atteint $Mo = 0,7$, réside dans le faible pas relatif des profils d'embase de pale. Une des solutions envisageables pour éviter ce phénomène pénalisant pour les performances de l'hélice, peut être de diminuer le nombre de pales.

Les figures 22 et 23 comparent des calculs de l'hélice HT1 à 12 et 10 pales, à $Mo = 0,7$ et $\gamma = 3,15$. Alors que les nombres de Mach maximaux à l'extrados des pales sont très voisins (figure 22), le blocage présent au rayon relatif $\xi = 0,369$ de la configuration 12 pales a disparu de la configuration 10 pales (figure 23).

Ainsi, à même géométrie, une configuration comportant un plus faible nombre de pales (et donc un pas relatif des profils d'embase de pale plus important) est elle préférable. La puissance et la traction sont par contre plus faibles.

Dans le problème de définition d'une telle hélice un compromis doit être recherché entre le grand nombre de pales nécessaire pour l'adaptation des profils d'extrémité de pales et les risques de blocage en embase.

3.2.2.4 - Effet du diamètre de moyeu -

Une autre alternative pour diminuer les risques de blocage d'embase, peut consister à augmenter le diamètre de moyeu.

Dans la comparaison présentée sur les figures 24 et 25, les profils d'embase de pale de l'hélice HT1 ont été masqués par un carénage cylindrique positionné au rayon relatif $\xi_0 = 0,483$ (au lieu de $\xi_0 = 0,346$ pour l'hélice HT1). La figure 24 montre que cette modification affecte peu l'organisation de l'écoulement sur l'extrados des pales pour $\xi > 0,5$. La figure 25 confirme qu'aucun blocage n'est présent dans la configuration $\xi_0 = 0,483$.

Cette solution peut s'avérer intéressante pour les hélices à grand nombre de pales, la structure de l'écoulement étant assez peu sensible à cette diminution de l'allongement relatif des pales. Par contre, la chute de puissance observée est comme pour la diminution du nombre de pales, assez importante ; un effet semblable se produit sur la traction, la comparaison étant effectuée pour une même géométrie des pales.

3.2.2.5 - Effet d'un carénage de moyeu de diamètre évolutif -

La solution la plus satisfaisante pour minimiser les problèmes de blocage des profils, est certainement de profiter de l'obstruction naturelle que constitue la nacelle du turbomoteur, pour ralentir l'écoulement en embases de pale. L'influence du carénage est étudiée à $Mo = 0,7$, pour un paramètre d'avancement $\gamma \sim 3,06$.

La figure 26 montre les lignes iso-Mach relatif sur l'extrados de la pale, et dans un canal inter-pales au rayon relatif $\xi = 0,346$. On remarque la large région supersonique s'étendant jusqu'à environ 60% de la corde sur l'extrados de la pale. Le nombre de Mach est voisin de 1,25 dans les zones externes de la pale, atteignant 1,4 en embase. Comme le montre la coupe cylindrique (développée) à $\xi = 0,346$, un choc intense barre le canal inter-pales.

Les mêmes calculs menés sur une combinaison hélice/carénage sont présentés sur la planche 27. Les nombres de Mach atteints sur l'extrados de la pale sont du même ordre que ceux atteints sur l'hélice seule : 1,25 en extrémité et 1,4 en embase. Mais la position du choc s'est beaucoup avancée en embase de pale. De plus, comme le montre la coupe conique (développée) au rayon $\xi = 0,37$, la zone supersonique est confinée au voisinage du bord d'attaque des profils, le choc ne barrant plus le canal inter-pales.

Il est à noter que le maillage utilisé pour cette étude est moins dense que les maillages utilisés pour les autres études du § 3.2.2 ; il en résulte des valeurs un peu plus faibles du nombre de Mach relatif dans les mêmes conditions de fonctionnement.

Cette étude tridimensionnelle confirme clairement qu'une forme de carénage de moyeu adaptée, améliore de façon notable le fonctionnement des embases de pales.

4 - PERSPECTIVES -

Comme il a été vu, les méthodes de calcul aérodynamique qui sont développées permettent de mieux comprendre le fonctionnement complexe des pales d'hélice, constituant ainsi un outil précieux pour la conception d'hélices mais aussi pour l'analyse des résultats d'essais.

Les différentes méthodes actuellement disponibles constituent une bonne base pour l'étude d'hélices isolées sans incidence. Cet éventail doit cependant être complété par des méthodes en cours de développement ou de validation, parmi lesquelles on peut citer la méthode du potentiel complet du LMSI [15], et pour les cas de vol à faible vitesse la méthode instationnaire de mise en équilibre du sillage [16]. Pour valider ces différentes méthodes, un certain nombre d'expériences très détaillées sont nécessaires comme par exemple les mesures de sillage effectuées à l'IMFM [17], ou encore l'essai de la maquette HT3 à SI Modane.

La conception de cette maquette de 1 mètre de diamètre est le fruit de la collaboration de l'ONERA et de l'Aérospatiale, dans les domaines de l'Aérodynamique et des Structures [18], l'étude des problèmes acoustiques étant menée de concert [19].

Le cahier des charges de cette hélice, fixé par l'Aérospatiale Toulouse, est de $Mo = 0,75$ à $Z = 10\ 700$ m d'altitude avec une charge au disque de 250 Kw, et une vitesse périphérique de 220 m/s. Pour équiper cette hélice de 12 pales en flèche, de nouveaux profils ayant de bonnes caractéristiques transsoniques ont été définis. Un profil très mince OH2204 de 3,5% d'épaisseur relative a d'ailleurs été essayé dans la soufflerie S3MA ; il présente de très bonnes performances transsoniques ($M_{dx} > 0,9$ à $C_z \sim 0,3$), supérieures à celles du profil de référence NACA 16 304 (Fig. 28) ; on remarque que les deux profils ont des caractéristiques équivalentes à $Mo = 0,6$ correspondant à des régimes de montée hélice ($C_z \text{ max} \sim 1,1$).

Pour la définition de cette hélice, des calculs conjoints aérodynamiques et structuraux ont permis d'étudier précisément les déformations des pales sous l'effet des efforts centrifuges et aérodynamiques. La figure 29 montre les iso-Mach relatif sur l'extrados des pales de l'hélice HT3, calculées par la méthode EULER.

Cette hélice HT3 sera essayée en 1985 dans la grande soufflerie SI de Modane de l'ONERA. Une vue générale du dispositif d'essai est donnée sur la figure 30 [20]. L'objectif de ces essais sera de vérifier les bonnes performances globales de l'hélice, mais également de fournir des informations nombreuses et précises pour la validation des méthodes de calcul. A cet égard, outre la balance 6 composantes,

L'instrumentation sera composée de capteurs de pression sur les pales, sur la casserole de moyeu et sur les carénages ; le sillage sera détaillé par sondage à l'aide de sondes directionnelles miniatures (stationnaire et instationnaire). De nombreuses jauges de contraintes seront implantées sur les pales et parties mécaniques. Des micros seront également disposés dans la veine, pour l'étude des problèmes acoustiques.

Les développements ultérieurs de l'opération CHARME seront consacrés à l'amélioration des méthodes de calcul qui en aérodynamique concerneront principalement l'étude des effets visqueux et des interactions avec l'avion [21] et les autres éléments de la propulsion (entrées d'air...). L'effort sera en outre porté sur une intégration encore plus poussée de toutes les méthodes de définition, afin de réaliser une meilleur optimisation de l'hélice en fonction de contraintes aussi interdépendantes que la performance, la fiabilité et le niveau de bruit.

5 - CONCLUSION -

Les méthodes de calcul aérodynamique disponibles permettent de couvrir l'ensemble des phases de la conception d'hélices rapides : depuis l'avant-projet où des méthodes simples sont utilisées avec des méthodes de calcul acoustique et structural, jusqu'à la vérification finale nécessitant l'emploi de méthodes tridimensionnelles transsoniques.

L'ensemble de ces méthodes a été utilisé pour définir l'hélice HT3 de 1 mètre de diamètre, qui sera essayée dans la soufflerie S1 de Modane. Les résultats de cet essai fourniront de très utiles informations pour vérifier les méthodes de calcul, mais également pour s'assurer des bonnes caractéristiques de ce type d'hélices à grand nombre de Mach en ce qui concerne les performances, le niveau acoustique et la tenue structurale.

Les développements futurs de ces recherches seront orientés vers une meilleure prise en compte de l'ensemble des effets complexes dont ces hélices sont le siège, afin d'optimiser l'intégration des ensembles propulsifs sur les avions de transport futurs équipés d'hélices.

REFERENCES -

- 1 D. BERGER - P. JACQUET
Vers un renouveau de l'hélice en Aéronautique.
19ème Colloque AAAF - Marseille 1982.
- 2 J.M. BOUSQUET
Hélices pour vol économique à grandes vitesses.
Aéronautique et Astronautique n° 88 1981-3
ONERA - TP 1981-55.
- 3 B.S. GATZEN
Advanced turboprop propulsion technology.
VKI Lecture Series n° 82/10 (24-28 mai 1982).
- 4 L.J. BOBER - G.A. MITCHELL
Summary of advanced methods for predicting high speed propeller performance.
NASA - TM 81409.
- 5 J.P. SULLIVAN
Advanced theoretical treatments of propeller aerodynamics.
VKI Lecture Series n° 82/08 (24/28 mai 1982).
- 6 R. HIRSCH
Détermination et calcul des hélices d'avion optima simples et coaxiales.
Publications Scientifiques et Techniques du Ministère de l'Air N° 220 (1948) et n° 225 (1949).
- 7 H. GLAUERT
Airplane propellers dans Aerodynamic theory.
Volume IV - DURAND Dover Publications (1963).
- 8 T.S. LUU
Calcul de l'hélice marine subcavitante par la méthode des singularités.
ATMA 1970.
- 9 H. VIVIAND - J.P. VEUILLOT
Méthodes pseudo-instationnaires pour le calcul d'écoulements transsoniques.
Publication ONERA n° 1978-4.
- 10 J. BROCHET
Calcul numérique d'écoulements internes tridimensionnels transsoniques.
La Recherche Aérospatiale n° 1980-5.
- 11 M. ENSELME - J. BROCHET - J.P. BOISSEAU
Low cost three-dimensional flow computations using a mini-system.
AIAA Paper N° 81-1013.

- 12 L.J. BOBER - D.S. CHAUSSEE - P. KUTLER
Prediction of highspeed propeller flow fields using a three dimensional Euler analysis.
AIAA 83-0188 et NASA TM 33065.
- 13 REYNOLDS - SAMMONDS - KENYON
An investigation of a four blade single rotation propeller in combination with an NACA 1 -
Serie D -
Type cowling at Mach numbers up to 0.83.
NACA RM A 53 B06 - 1953.
- 14 BLACK - MENTHE - WAINAUSKI
Aerodynamic design and performance testing of an advanced 30° swept, eight bladed propeller
at Mach numbers from 0.2 to 0.85.
NASA CR 3047.
- 15 T.S. LUU - R. COLLERCANDY
Design concept and Performance Prediction Technic for potential flows around advanced propellers.
Agard Symposium on Aerodynamics and Acoustics of Propellers.
Toronto - 1-4 octobre 1984.
- 16 B. CANTALOUBE - S. HUBERSON
Nouvelle Approche par méthode de tourbillons ponctuels pour la prédiction de performance
de rotors en vol stationnaire et d'avancement.
ONERA TP 1983-120.
- 17 D. FAVIER - C. MARESCA
Etude du Sillage 3D d'une hélice aérienne.
Agard Symposium on Aerodynamics and Acoustics of Propellers.
Toronto - 1-4 octobre 1984.
- 18 J.M. BESSON - D. PETOT
Comportement dynamique d'un rotor de prop-fan.
Agard Symposium on Aerodynamics and Acoustics of Propellers.
Toronto - 1-4 octobre 1984.
- 19 H. GOUNET - S. LEWY
Contribution à l'étude théorique et expérimentale du bruit d'hélice.
ONERA TP 1982-122.
- 20 G. LECLERE - J. N. REMANDET
Moyens d'essais d'hélices et de rotors de l'ONERA.
AAAF - 19ème Colloque d'Aérodynamique Appliquée - Marseille - Novembre 1982.
- 21 C. KIRKMAN - A. ROUSSEAU - M. YERMIA
Calcul du Souffle moyen d'une hélice et de son influence sur les performances d'un avion.
ONERA TP 1982-120.

**PROGRAMME DE RECHERCHE
SUR LES HELICES POUR AVIONS RAPIDES**

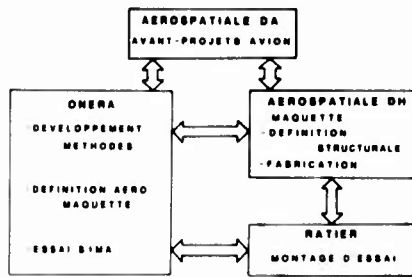
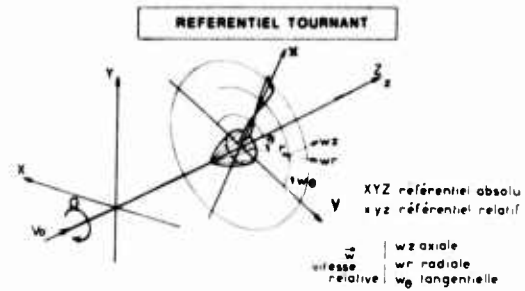


Fig. 1



ECOULEMENT STATIONNAIRE DANS LE REFERENTIEL TOURNANT

Fig. 2

METHODES 3D DE CALCUL D'HELICES

EQUATION	HYPOTHESES	PROGRAMME	CPU CYBER 750
EULER	• FLUIDE PARFAIT	BROCHET	2-3 HEURES
POTENTIEL	• IRROTATIONNEL	→ LIMSI	
	• SILLAGE		
LIGNE PORTANTE	• PROFILS MINCES	J.J. COSTES	~ 15 mn
	• SUBSONIQUE		
SINGULARITES	• INCOMPRESSIBLE	LUU (LMS)	
	• SILLAGE		
LIGNE PORTANTE	• COMPRESSIBILITE ET EFFETS VISQUEUX	LP	~ 10 s
	• PROFILS 3D	LPC	

Fig. 3

INFLUENCE D'UNE LIGNE PORTANTE COURBE

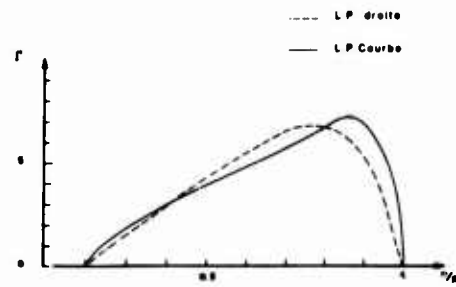


Fig. 4

HELICE INTERACTIONNEE

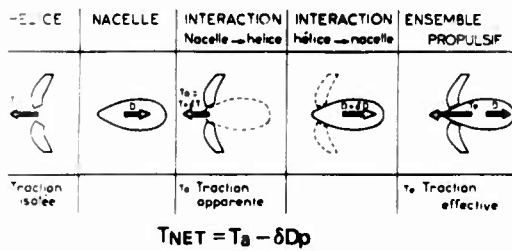


Fig. 5

HELICES TRANSSONIQUES. CALCUL EULER

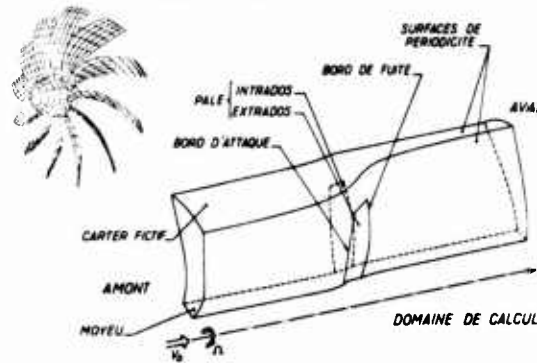


Fig. 6

HELICE MARQUIS

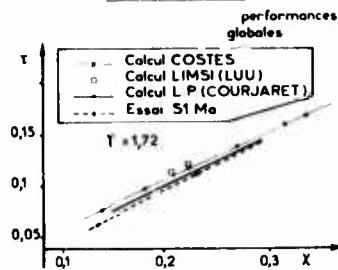


Fig. 7

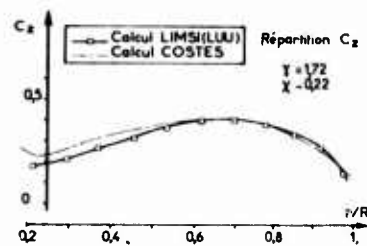


Fig. 8

CALCUL DE L'HELICE NACA 4(6)(05)041
 $M_0 = 0,83$

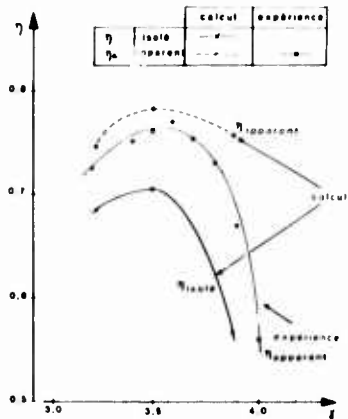


Fig. 9

RENDEMENT THÉORIQUE DE L'HELICE

VOL DE CROISIÈRE $M = 0,8$ 35000 FT
 VITESSE DE ROTATION PÉRIPHÉRIQUE 200m/s

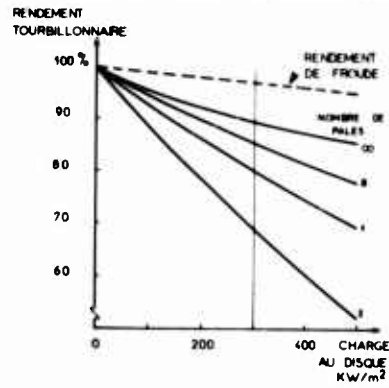


Fig. 10

EVALUATION DE LA METHODE LPC SUR DES HELICES RAPIDES.
 $\gamma = 3,14$ $z = 1,85$

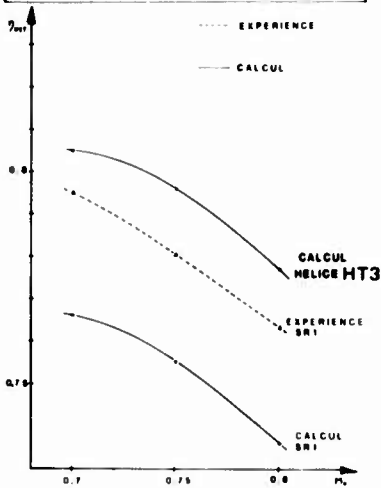


Fig. 11

COMPARAISON DES METHODES DE CALCUL D'HELICES(HT1)

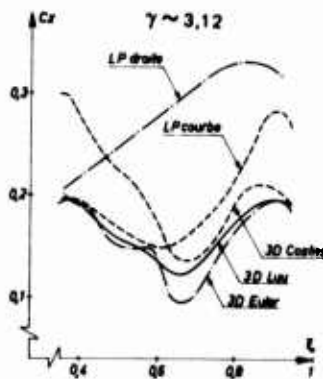


Fig. 12

HELICE HT1 CALCUL EULER 3D
EFFET DU PARAMETRE D'AVANCEMENT
 $M_0 = 0,7$

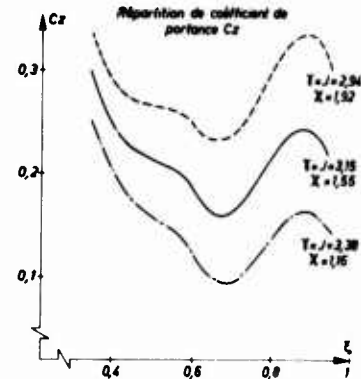


Fig. 13

Hélice HT1. Calcul Euler 3D
Effet du paramètre d'avancement $M_0 = 0,7$.
Iso-Mach relatif extrados.

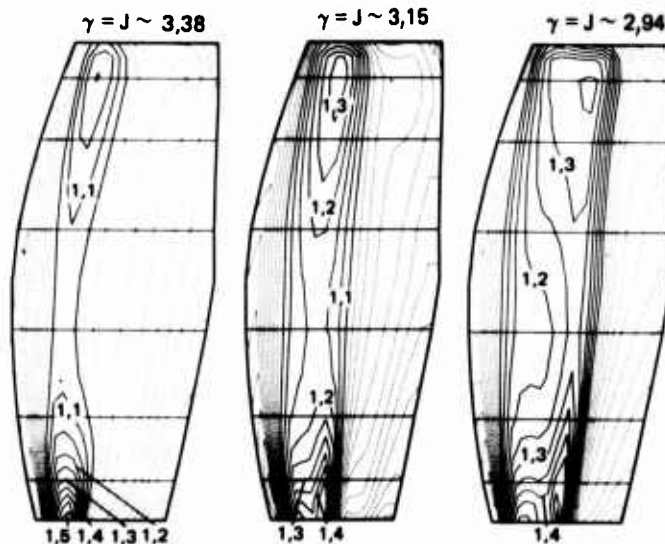


Fig. 14

Hélice HT1. Calcul Euler 3D
 Effet du paramètre d'avancement $M_0 = 0,7$.
 Iso-Mach relatif intrados.

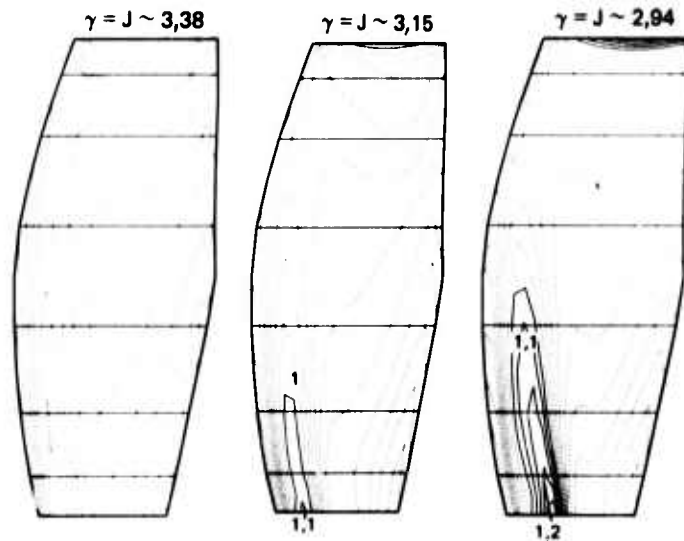


Fig. 15

Hélice HT1. Calcul Euler 3D
 Effet du paramètre d'avancement $M_0 = 0,7$.
 Iso-Mach relatif $\xi = 0,369$.

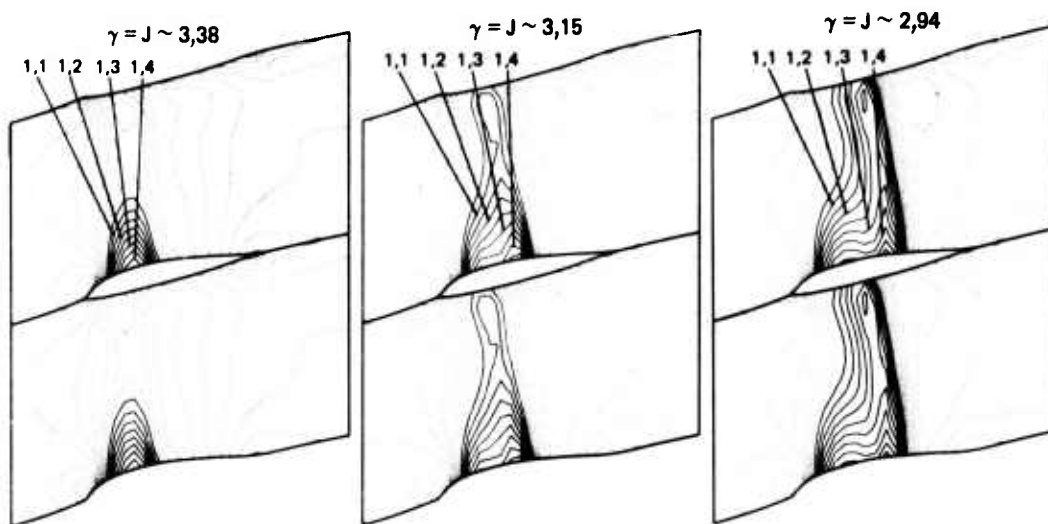


Fig. 16

HELICE HT1 CALCUL EULER 3D
 EFFET DU NOMBRE DE MACH
 $\gamma = J = 3,15$

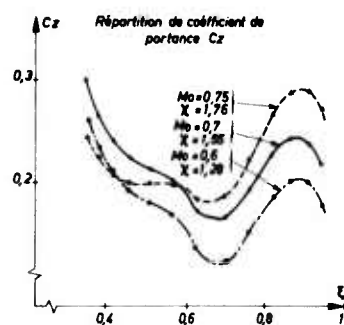


Fig. 17

Hélice HT1. Calcul Euler 3D - $\gamma = J = 3,15$
 Effet du nombre de Mach
 Iso-Mach relatif extradors.

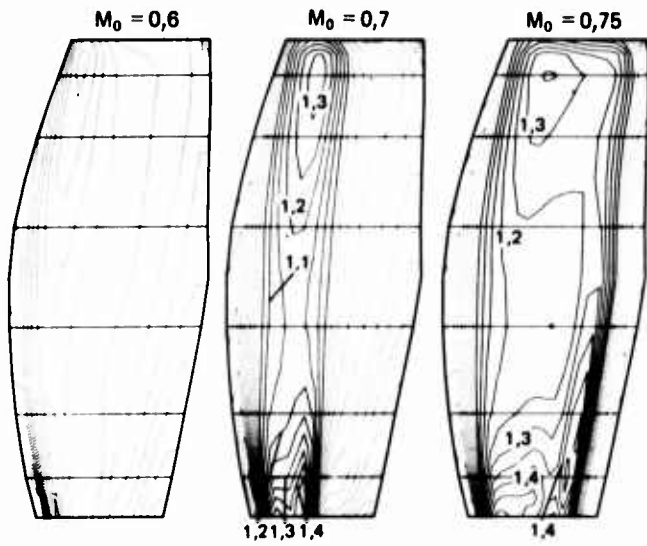


Fig. 18

Hélice HT1. Calcul Euler 3D - $\gamma = J = 3,15$
 Effet du nombre de Mach
 Iso-Mach relatif intrados.

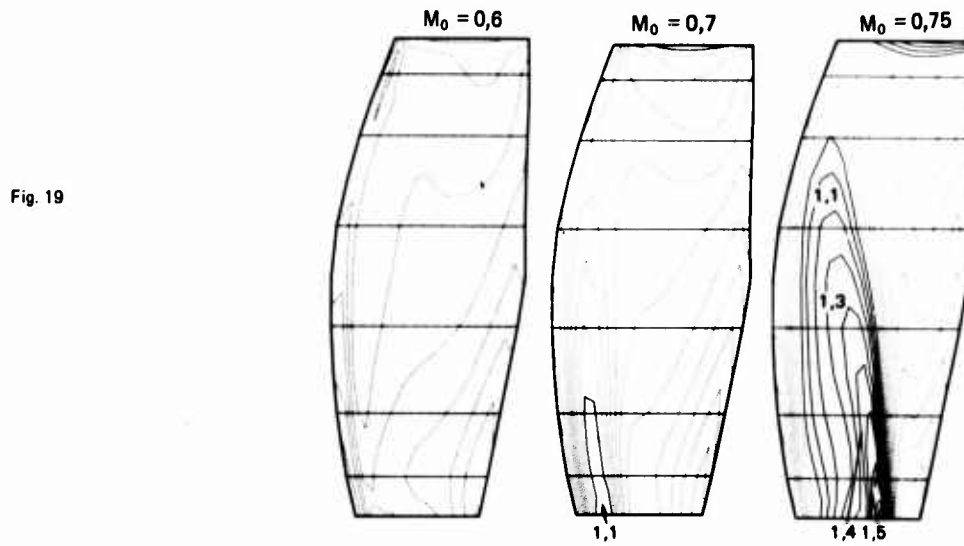


Fig. 19

Hélice HT1. Calcul Euler 3D - $\gamma = J = 3,15$
 Effet du nombre de Mach
 Iso-Mach relatif $\xi = 0,369$.

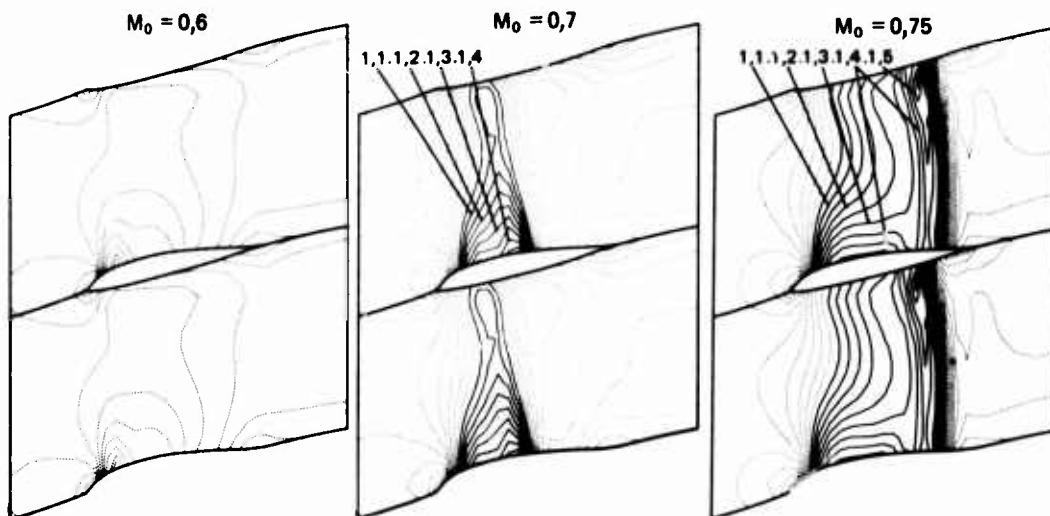


Fig. 20

Hélice HT1. Calcul Euler 3D - $\gamma = J = 3,15$
 Effet du nombre de Mach
 Iso-Mach relatif $\xi = 0,795$.

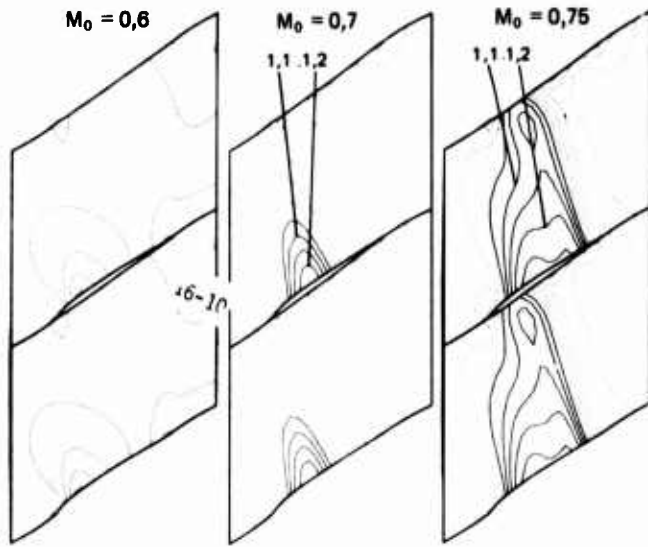


Fig. 21

Hélice HT1. Calcul Euler 3D - $\gamma = J = 3,15$ $M_0 = 0,7$
 Effet du nombre de pales
 Iso-Mach relatif extrados.

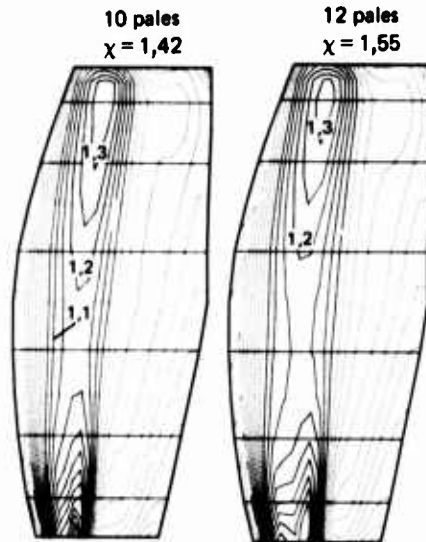


Fig. 22

Hélice HT1. Calcul Euler 3D - $\gamma = J = 3,15$ $M_0 = 0,7$
 Effet du nombre de pales
 Iso-Mach relatif $\xi = 0,369$.

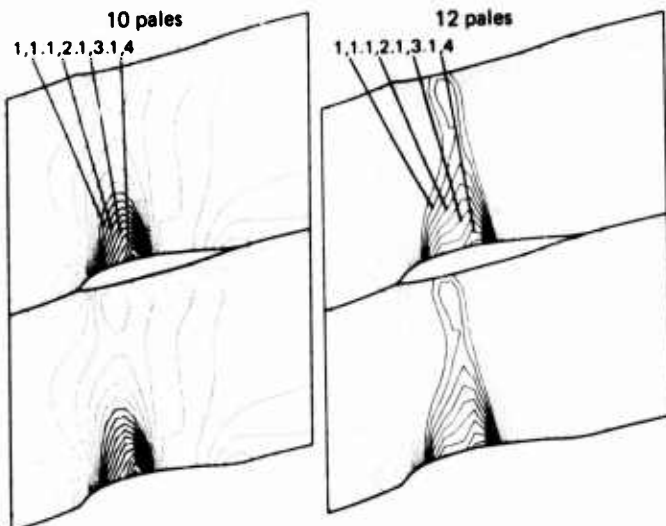


Fig. 23

Hélice HT1. Influence du diamètre de moyeu.
 Calcul Euler 3D - $M_0 = 0,7 - \gamma = J \sim 3,15$.
 Iso-Mach relatif extradoss.

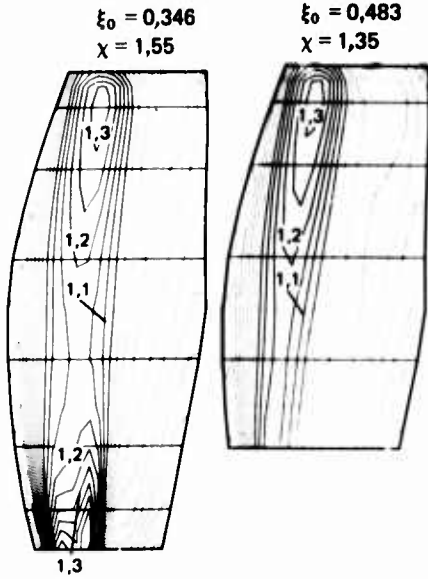


Fig. 24

Hélice HT1. Influence du diamètre de moyeu.
 Calcul Euler 3D - $M_0 = 0,7 - \gamma = J \sim 3,15$.
 Iso-Mach relatif $\xi = 0,538$.

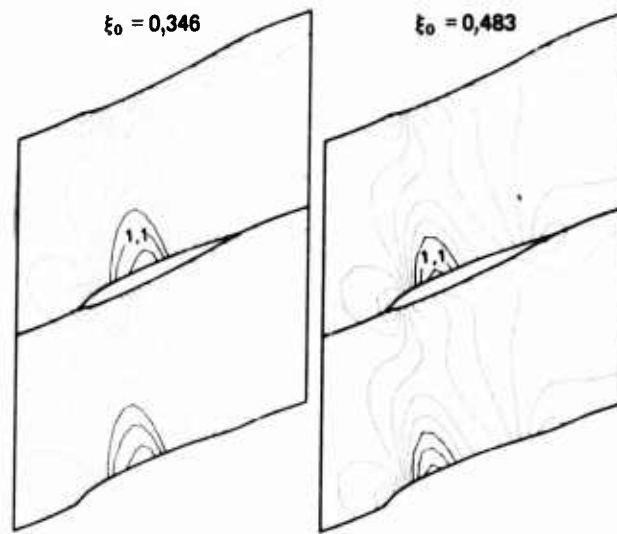


Fig. 25

CALCUL EULER - HELICE HT1
 $M_0 = 0,7 \quad \gamma \sim 3,06$

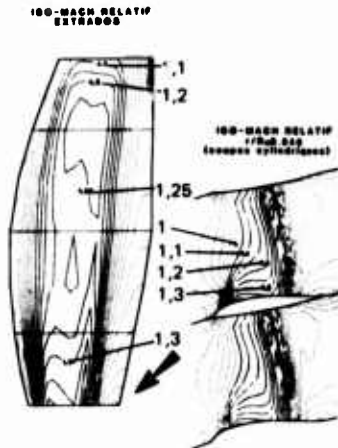


Fig. 26

CALCUL EULER.HELICE HT1 + CARENAGE CE
 $M_0 = 0,7 \quad \gamma \sim 3,06$

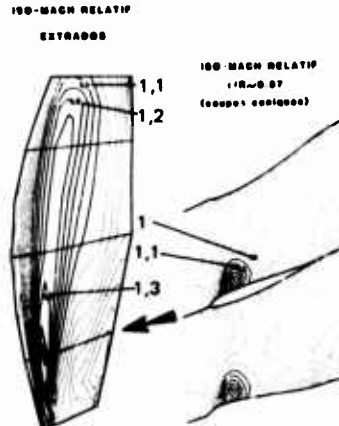


Fig. 27

PERFORMANCES GLOBALES DES PROFILS OH2204
 ET NACA 16304

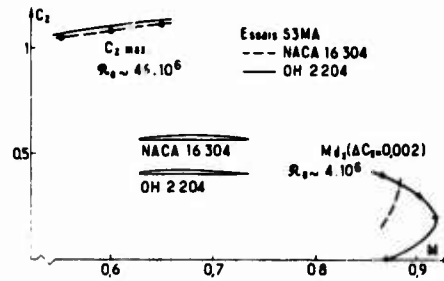


Fig. 28

CALCUL EULER - HELICE HT3
 EFFET DU NOMBRE DE MACH

$\gamma \sim 3,06$
 100-MACH RELATIF EXTRADOSS

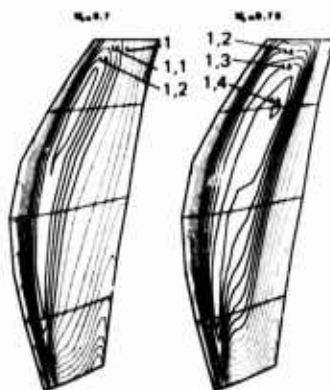


Fig. 29

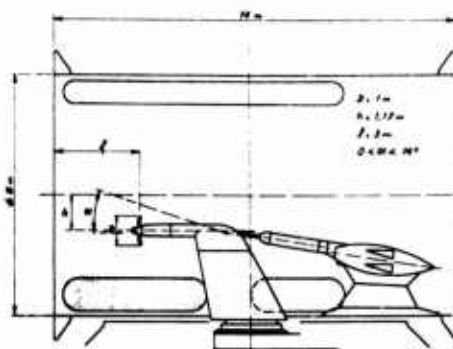


Fig. 30

DESIGN CONCEPT AND PERFORMANCE PREDICTION TECHNIC
FOR POTENTIAL FLOWS AROUND ADVANCED PROPELLERS

Thoai-Sum LUU and Ranjit COLLERCANDY

L.I.M.S.I. (C.N.R.S.)
B.P. 30
91406 ORSAY CEDEX (FRANCE)

ABSTRACT

The design concept and performance prediction technic for potential flows around advanced propellers are presented.

The design of propellers is based on the panel method, applied to the lifting surface theory in which the flow is supposed to be incompressible.

A transonic performance prediction technic is developed where the resulting potential equation is solved by a finite difference approximate factorization method in a body fitted grid system. Both two and three dimensional results are presented.

1. INTRODUCTION

This paper discusses the computation of the potential flow around propellers of the type "Prop-Fan". The geometrical complications such as skew, rake and radial pitch variations of the blades are taken in to consideration. Both, design of propellers and prediction of steady propeller characteristics are presented.

The design of propellers is carried out by the panel method, applied to the lifting surface theory, in which the flow is supposed to be incompressible. Any spanwise reference line characterizing the blade contour may be given, which in turn can be determined from the structural criteria. The flow field is generated by a doublet/source panel representation of the blades with the elements located on the chord-line surface of the blade, the pitch variation of which is obtained by an iterative procedure. The chordwise distribution of the loading can be adjusted to give any desired pressure distribution over the blade to avoid the boundary layer separation. The spanwise distribution of the circulation can either be considered optimum or else imposed to avoid the brutal changes in circulation in the radial direction to minimize the noise. The pitch of the trailing vortex sheet is trimmed according to the induced velocity deduced during the calculation. Moreover, this analysis permits to obtain a preliminary performance estimation of the propeller.

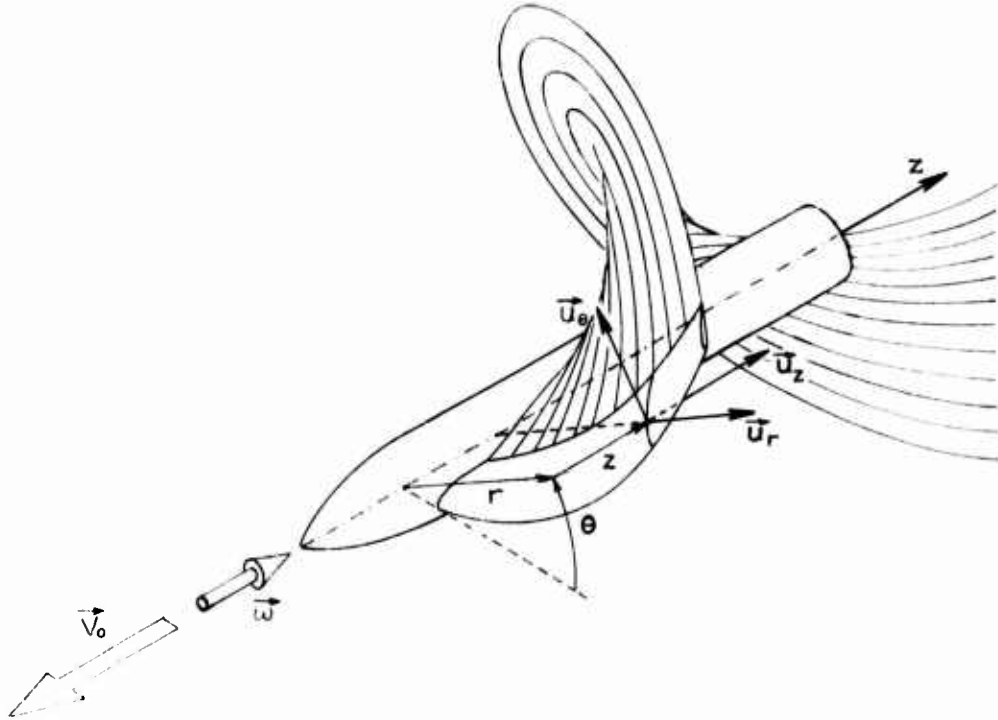
The advanced propellers, like Prop-Fan, usually operates at Mach 0.8. The flow around such propellers become transonic and it is essential to study the performances of these propellers taking in to account the actual flow conditions. Two and three dimensional transonique potential flow theories around such propellers are developed. Thus, the transonic potential equation expressed in the general curvilinear coordinates is cast in the conservative form. To ensure a good quality solution of transonic flow, it is preferable to use an approximately orthogonal coordinate system having one of the three axis almost aligned with the local relative flow direction. The curvilinear coordinates constituted by the stream lines and equipotential lines corresponding to the two dimensional incompressible flow at each cylindrical section are constructed using the singularity method. Thus, the local domain of dependance of the equation can be taken in to account in the difference scheme better than other type of networks. The grid system utilized in the three dimensional calculation is obtained by superimposing these two dimensional networks at each cylindrical surface of constant radius. The stacking of the two dimensional network to the three dimensional grid system is carried out in a typical way to avoid the sudden variations in the coordinates. Introducing the concept of artificial density, an approximate factorization technic is used to solve the resulting potential equation.

This work was carried out under contract DRET n° 81-512 of the French Ministry of Defense.

PRECEDING PAGE BLANK-NOT FILMED

2. GENERAL GOVERNING EQUATIONS

Let us consider a screw propeller operating in an inviscid fluid which is otherwise at rest. The screw moves forward with a velocity $-V_0 \vec{u}_z$ and rotates with an angular velocity $-\omega \vec{u}_z$. The relative advance velocity of the blade element is then given by $\vec{V}_{adv} = -V_0 \vec{u}_z - \omega r \vec{u}_\theta$.



As the flow is supposed to be irrotational, the absolute velocity can be derived from the velocity potential ϕ : $\vec{V} = \nabla \phi$. Then the relative fluid velocity \vec{W} can be written as $\vec{W} = \nabla \phi - \vec{V}_{adv}$. This velocity is steady with respect to a moving frame fixed to the propeller and hence the time derivative of taken with respect to this moving frame becomes zero.

The continuity equation implies that $\nabla \cdot (\rho \vec{W}) = 0$ which in turn can be expressed as

$$\nabla \cdot (\rho (\nabla \phi - \vec{V}_{adv})) = 0 \quad (2.1)$$

This equation is considered as the equation governing the potential ϕ . In the incompressible case, this equation reduces to

$$\nabla^2 \phi = 0 \quad (2.2)$$

Introducing the rothalpy I defined by

$$I = h + \frac{W^2}{2} - \frac{\omega^2 r^2}{2} \quad (2.3)$$

when the flow is compressible; or by

$$I = \frac{p}{\rho} + \frac{W^2}{2} - \frac{\omega^2 r^2}{2} \quad (2.4)$$

when the flow is supposed to be incompressible, the momentum equation leads to

$$(\nabla \times \vec{V}) \times \vec{W} + \nabla I = 0 \quad (2.5)$$

Since $\nabla \times \vec{V} = 0$, this equation becomes

$$\nabla I = 0 \quad (2.6)$$

which implies that I is constant in the whole field. This equation will be utilized later to calculate the pressure p or the density ρ in the field.

On the blade surfaces of the propeller and on the hub surface, the flow tangency condition implies that

$$\vec{W} \cdot \vec{n} = 0 \quad (2.7a)$$

or

$$\frac{\partial \phi}{\partial n} = -\vec{V}_{adv} \cdot \vec{n} \quad (2.7b)$$

where \vec{n} is the unit vector normal to the surface under consideration.

At the trailing edge of the blades and on the vortex sheets issuing from it, the potential jump $\phi^+ - \phi^-$ corresponds to the circulation around the blade section at a radius r : $\Gamma(r) = \phi^+ - \phi^-$. This circulation is defined when the Kutta-Joukowski condition (zero loading at the trailing edge) is respected.

3. DESIGN PROBLEM

Although there is no major theoretical difficulty in developing a nonlinear theory to design a screw propeller, the thin lifting surface theory is used in the computation for the sake of time savings. Thus, the Neumann condition (2.7b) on the surface of the blade is transposed to the trace of the blade. The trace of the blade is the surface generated by the helicoidal chords at different cylindrical sections of constant radius; and the free vortex sheet is the surface generated by the helicoidal free vortex lines issuing from the trailing edge of the blades. The pitch of the free vortex line for each radius is determined according to the induced velocity deduced during the computation.

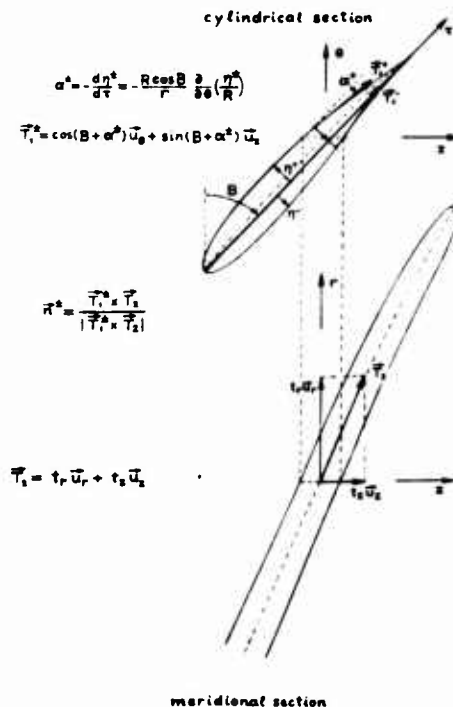
Let τ denote the curvilinear abscissa taken on the helicoidal chord at a cylindrical section of the blade; the forme of the blade section is then defined by $\eta^\pm(\tau)$, the signs \pm referring respectively to the upper and lower surfaces. The tangential vector \vec{T}_1^\pm of the cylindrical section is given by:

$$\vec{T}_1^\pm = \cos(B + \alpha^\pm) \vec{u}_\theta + \sin(B + \alpha^\pm) \vec{u}_z \quad (3.1)$$

where $B(r)$ denotes the pitch angle of the blade at the radius r . As τ is related to the angular abscissa θ by the relation $d\tau = r d\theta / \cos B$ we have

$$\alpha^\pm = -\frac{d\eta^\pm}{d\tau} = -\frac{d\eta^\pm}{d\theta} \frac{d\theta}{d\tau} = -\frac{R \cos B}{r} \frac{\partial}{\partial \theta} \left(\frac{\eta^\pm}{R} \right) \quad (3.2)$$

where R denotes the radius of the propeller.



Let \vec{T}_2 represent the tangential vector in the local meridional section of the blade, then we have $\vec{T}_2 = t_r \vec{u}_r + t_z \vec{u}_z$. Because of the small thickness of the blade, we can admit that \vec{T}_2 taken on the upper or lower surface at the same abscissa τ is identical with the vector taken on the trace of the blade. Then the unit-normal vector of the blade surface is given by :

$$\begin{aligned} \vec{n}^\pm &= \frac{\vec{T}_1^\pm \times \vec{T}_2}{|\vec{T}_1^\pm \times \vec{T}_2|} = \frac{t_z \cos(B + \alpha^\pm) \vec{u}_r + t_r \sin(B + \alpha^\pm) \vec{u}_\theta - t_r \cos(B + \alpha^\pm) \vec{u}_z}{\{t_r^2 + [t_z \cos(B + \alpha^\pm)]^2\}^{1/2}} \\ &= n_r^\pm \vec{u}_r + n_\theta^\pm \vec{u}_\theta + n_z^\pm \vec{u}_z \end{aligned} \quad (3.3)$$

For the practical computations, we introduce a local orthogonal frame work defined by the unit vectors $(\vec{n}^\pm, \vec{\tau}^\pm, \vec{b}^\pm)$, where $\vec{\tau}^\pm$ is identical to \vec{T}_1^\pm and \vec{b}^\pm is defined by the relation

$$\vec{b}^\pm = \frac{\vec{n}^\pm \times \vec{T}_1^\pm}{|\vec{n}^\pm \times \vec{T}_1^\pm|} = \frac{[n_\theta^\pm \sin(B + \alpha^\pm) - n_z^\pm \cos(B + \alpha^\pm)] \vec{u}_r - n_r^\pm \sin(B + \alpha^\pm) \vec{u}_\theta + n_r^\pm \cos(B + \alpha^\pm) \vec{u}_z}{\{n_r^{\pm 2} + [n_\theta^\pm \sin(B + \alpha^\pm) - n_z^\pm \cos(B + \alpha^\pm)]^2\}^{1/2}} \quad (3.4)$$

Moreover, the thin lifting surface approximation suggests replacing $\cos(B + \alpha^\pm)$ in these relations by $\cos B$. Posing $W_0 = (V_0^2 + \omega^2 r^2)^{1/2}$ and $\beta = \tan^{-1}(V_0/\omega r)$, the flow tangential condition on the blades becomes

$$\begin{aligned} \frac{1}{\omega R} \left(\frac{\partial \phi}{\partial n} \right)^\pm &= \frac{t_r}{\{t_r^2 + (t_z \cos B)^2\}^{1/2}} \frac{W_0}{\omega R} \sin(\beta - B - \alpha^\pm) \\ &= \frac{t_r}{\{t_r^2 + (t_z \cos B)^2\}^{1/2}} \frac{W_0}{\omega R} \left\{ \frac{R \cos B}{r} \frac{\partial}{\partial \theta} \left(\frac{\eta^\pm}{R} \right) + B - \beta \right\} \end{aligned} \quad (3.5)$$

In order to generate the flow field, a source distribution q is applied on the trace of the blades S and a normal-axis doublet $\Delta\phi = \phi^+ - \phi^-$ distribution is applied on the trace of the blades and on the free vortex sheets $S + \Sigma$. This can be represented as (1)

$$\frac{\phi(P)}{\omega R^2} = -\frac{1}{4\pi} \int_S \frac{q(M)}{\omega R} \frac{R}{d(M,P)} \frac{dS_M}{R^2} + \frac{1}{4\pi} \int_{S+\Sigma} \frac{\Delta\phi(M)}{\omega R^2} \left\{ \frac{\partial}{\partial n} \frac{R}{d(M,P)} \right\}_M \frac{dS_M}{R^2} \quad (3.6)$$

On the blade surface, we have ϕ_n^\pm given by

$$\frac{\phi_n^\pm(P)}{\omega R} = \pm \frac{q(P)}{2\omega R} - \frac{1}{4\pi} \int_S \frac{q(M)}{\omega R} \left\{ \frac{\partial}{\partial n} \frac{R}{d(M,P)} \right\}_P \frac{dS_M}{R^2} + \frac{1}{4\pi} \int_{S+\Sigma} \frac{\Delta\phi(M)}{\omega R^2} \left\{ \frac{\partial}{\partial n} \left\{ \frac{\partial}{\partial n} \frac{R}{d(M,P)} \right\}_M \right\}_P \frac{dS_M}{R^2} \quad (3.7)$$

where the integral sign \oint represents the integration with suppression of the local effects.

Taking the difference $\phi_n^+ - \phi_n^-$ and from (3.5), we have

$$\frac{1}{\omega R} (\phi_n^+ - \phi_n^-) = \frac{q}{\omega R} = \frac{t_r}{\{t_r^2 + (t_z \cos B)^2\}^{1/2}} \frac{W_0}{\omega R} \frac{R \cos B}{r} \frac{\partial}{\partial \theta} \left(\frac{e}{R} \right) \quad (3.8)$$

Similarly, the half sum $(\phi_n^+ + \phi_n^-)/2$ can be defined as

$$\begin{aligned} \frac{0.5(\phi_n^+ + \phi_n^-)}{\omega R} &= -\frac{1}{4\pi} \int_S \frac{q(M)}{\omega R} \left\{ \frac{\partial}{\partial n} \frac{R}{d(M,P)} \right\}_P \frac{dS_M}{R^2} + \frac{1}{4\pi} \int_{S+\Sigma} \frac{\Delta\phi(M)}{\omega R^2} \left\{ \frac{\partial}{\partial n} \left\{ \frac{\partial}{\partial n} \frac{R}{d(M,P)} \right\}_M \right\}_P \frac{dS_M}{R^2} \\ &= \frac{t_r}{\{t_r^2 + (t_z \cos B)^2\}^{1/2}} \frac{W_0}{\omega R} \left\{ \frac{R \cos B}{r} \frac{\partial}{\partial \theta} \left(\frac{\eta_c}{R} \right) + \beta - B \right\} \end{aligned} \quad (3.9)$$

where $e(r, \theta)$ and $\eta_c(r, \theta)$ represent respectively the thickness and the camber of the blade, and we have $\eta^\pm = \eta_c \pm 0.5e$.

For a direct problem, the complete geometrical definition of the propeller is specified, and the integral eqn.(3.9) serves to determine the doublet density $\Delta\phi$ on the trace of the blades. Moreover, the Kutta-Joukowski condition implies that the value of $\phi^+ - \phi^-$ on the vortex sheet is equal to its value defined along the trailing edge.

For the design problem, in general the thickness of the blades is specified; then the density q of the source applied on the presumed trace of the blade is determined by eqn. (3.8). The bound vortex distribution on the blades and radial distribution of the free vortex on the wake have to be specified according to the desired loading distribution on the blades. So, the density of the normal-axis doublet $\Delta\phi$

on the trace of the blades as well as on the free vortex wakes is determined accordingly. The flow field is then generated by the discrete source and doublet distributions and the normal derivative on the trace of the blades can be computed. By integrating eqn; (3.9) and noting that : $\eta_c(\theta_{LE}) - \eta_c(\theta_{TE}) = 0$, the pitch angle $B^{(n+1)}$ is deduced for $(n+1)^{th}$ iterative cycle by :

$$B^{(n+1)} = \frac{-0.5}{\theta_{LE} - \theta_{TE}} \frac{1}{W_0} \int_{\theta_{LE}}^{\theta_{TE}} \frac{[t_r^2 + (t_z \cos B^{(n)})^2]^{1/2}}{t_r} \left(\frac{\partial \phi^+}{\partial n} + \frac{\partial \phi^-}{\partial n} \right) d\theta + \beta \quad (3.10)$$

where the subscripts LE and TE denote respectively the leading edge and the trailing edge. On the right-hand side, $B^{(n)}$ denotes the pitch angle obtained during the previous iterative cycle, from which the trace of the blade has been defined. The camber of the blade is then given by :

$$\frac{\eta_c(\theta)}{R} = \frac{r}{R \cos B^{(n+1)}} \left\{ \frac{0.5}{W_0} \int_{\theta_{LE}}^{\theta} \frac{[t_r^2 + (t_z \cos B^{(n)})^2]^{1/2}}{t_r} \left(\frac{\partial \phi^+}{\partial n} + \frac{\partial \phi^-}{\partial n} \right) d\theta + (B^{(n+1)} - \beta)(\theta - \theta_{LE}) \right\} \quad (3.11)$$

Figure 1 shows the geometry of a 12 bladed propeller designed by the present method. Figure 2 shows the division of the trace of the blades where the discretized source and doublet distributions are applied. Using the finite difference to compute \vec{W} , the pressure distribution in the form of a dimensionless coefficient

$$K_p = \frac{p - p_0}{0.5 \rho V_0^2} = -2 \left(\frac{\omega R}{V_0} \right)^2 \left\{ \frac{V_0}{\omega R} \vec{u}_z + \frac{r}{R} \vec{u}_\theta \right\} \frac{\nabla \phi}{\omega R} - \left(\frac{\omega R}{V_0} \right)^2 \left(\frac{\nabla \phi}{\omega R} \right)^2 \quad (3.12)$$

deduced from $I = \text{constant}$ as a function of ω is shown in fig. 3. For more detailed descriptions of this method, the readers are invited to consult the references [1] to [3].

4. TRANSONIC PERFORMANCE PREDICTIONS

Even though, the above analysis permits to obtain an approximate idea of the global performance of the propeller, it is essential to take in to consideration the compressibility effects in order to obtain a precise idea of the flow structure, because the advanced propellers, like Prop-Fan, are usually assigned to operate at a cruising Mach number of about 0.8. In addition to this, the high number of blades used for this type propeller may create the choking phenomenon especially near the hub section where the passage between the blades becomes quite narrow. Thus, two and three dimensional transonic potential theories are developed [4].

In this paper, we present only the three dimensional analysis around such propellers. The governing equation for ϕ is given by (2.1). As the flow is isentropic, we can derive from (2.3) and (2.6) the following relations for a calorifically perfect gaz :

$$\frac{p}{p_0} = \left[1 + \frac{\gamma-1}{2} M_0^2 \left\{ 1 + \frac{\omega^2 r^2}{V_0^2} - \frac{W^2}{V_0^2} \right\} \right]^{\frac{1}{\gamma-1}} \quad (4.1)$$

$$M = \frac{W}{a} = M_0^2 \left(\frac{W}{V_0} \right)^2 \left\{ 1 + \frac{\gamma-1}{2} M_0^2 \left\{ 1 + \frac{\omega^2 r^2}{V_0^2} - \frac{W^2}{V_0^2} \right\} \right)^{-1} \quad (4.2)$$

$$K_p = \frac{2}{\gamma M_0^2} \left\{ \left[1 + \frac{\gamma-1}{2} M_0^2 \left(1 + \frac{\omega^2 r^2}{V_0^2} - \frac{W^2}{V_0^2} \right) \right]^{\frac{\gamma}{\gamma-1}} + 1 \right\} \quad (4.3)$$

The compressible potential equation (2.1) is expressed in a general curvilinear coordinates ξ^1, ξ^2, ξ^3 in the conservation form. It is well known that this equation is elliptic where the flow is subsonic and becomes hyperbolic where the relative Mach number is supersonic. In order to ensure stability of the numerical scheme when the flow becomes locally supersonic, we use the concept of artificial density; the solution is then obtained by finite difference approximate factorization tecnics.

The finite difference grid system used in the computation is obtained by stacking H-type two dimensional networks composed of streamlines and equipotential lines. At each cylindrical section of the blade. The creation of such a network is achieved by solving the incompressible potential flow around the two dimensional cascade corresponding to the section, using the combinaison of the singularity method and the finite difference method described in [5] and [6]. The pitch of the trailing vortex sheet is supposed to be constant in the radial direction and is determined from a preliminary calculation carried out by lifting line theory around the propeller. This arrangement is used in the computation in order to simplify the far down-stream boundary condition as will be seen later.

The coordinate system ξ^1, ξ^2, ξ^3 related to the body fitted grid system is defined with the mesh sizes $\Delta \xi^1, \Delta \xi^2, \Delta \xi^3$ normalized to unity. The $\xi^3 = \text{cte}$ surfaces correspond to the cylindrical surfaces of constant radius r . The streamlines and the equipotential lines defined with an adequate level at different cylindrical blade section serve to generate the $\xi^2 = \text{cte}$ and the $\xi^1 = \text{cte}$ surfaces respectively.

Once the surfaces ξ^1, ξ^2, ξ^3 are defined the nodal coordinates $z, \theta, r (z^1, z^2, z^3)$ can be determined. The coefficients of the transformation matrix $(z_{\xi^i}^j)$ can be obtained from finite differences. Using the relation

$$z_{\xi^m}^i \xi_{\xi^j}^m = \delta_j^i$$

the coefficients $\xi_{\xi^j}^m$ can then be deduced by the inversion of the above matrix.

The Jacobian is defined as

$$J = \frac{\partial(\xi^1, \xi^2, \xi^3)}{\partial(z^1, z^2, z^3)} = \left[\frac{\partial(z^1, z^2, z^3)}{\partial(\xi^1, \xi^2, \xi^3)} \right]^{-1}$$

In the coordinate system $z^i (z, \theta, r)$, the components of the metric tensor are given by

$$\begin{aligned} (g_{11})_z &= 1 & (g_{22})_z &= r^2 & (g_{33})_z &= 1 \\ (g^{11})_z &= 1 & (g^{22})_z &= \frac{1}{r^2} & (g^{33})_z &= 1 \end{aligned}$$

and the element of the Levi-Chivita tensor is $(\sqrt{g})_z = r$.

In the coordinate system ξ^i , the elements of the metric tensor are obtained from

$$\begin{aligned} (g_{ij})_{\xi} &= \frac{\partial z^1 \partial z^1}{\partial \xi^i \partial \xi^j} + \frac{\partial z^2 \partial z^2}{\partial \xi^i \partial \xi^j} r^2 + \frac{\partial z^3 \partial z^3}{\partial \xi^i \partial \xi^j} \\ (g^{ij})_{\xi} &= \frac{\partial \xi^i \partial \xi^j}{\partial z^1 \partial z^1} + \frac{\partial \xi^i \partial \xi^j}{\partial z^2 \partial z^2} \frac{1}{r^2} + \frac{\partial \xi^i \partial \xi^j}{\partial z^3 \partial z^3} \end{aligned} \quad (4.4)$$

and the Levi-Chivita tensor becomes

$$(\sqrt{g})_{\xi} = \frac{(\sqrt{g})_z}{J} = \frac{r}{J}$$

In the ξ^1, ξ^2, ξ^3 coordinate system, the contravariant components W^i of \vec{W} are given by

$$\begin{aligned} W^1 &= g^{1m} \phi_{\xi^m} + \xi_{\xi^1}^1 V_0 + \xi_{\xi^2}^1 \omega \\ W^2 &= g^{2m} \phi_{\xi^m} + \xi_{\xi^1}^2 V_0 + \xi_{\xi^2}^2 \omega \\ W^3 &= g^{3m} \phi_{\xi^m} \end{aligned} \quad (4.5)$$

and the covariant components W_i are defined as

$$\begin{aligned} W_1 &= \phi_{\xi^1} + \xi_{\xi^1}^1 V_0 + \xi_{\xi^2}^1 \omega r^2 \\ W_2 &= \phi_{\xi^2} + \xi_{\xi^1}^2 V_0 + \xi_{\xi^2}^2 \omega r^2 \\ W_3 &= \phi_{\xi^3} + \xi_{\xi^1}^3 V_0 + \xi_{\xi^2}^3 \omega r^2 \end{aligned} \quad (4.6)$$

The continuity equation becomes

$$\frac{\partial}{\partial \xi^i} \left(\frac{\rho r W^i}{J} \right) = 0 \quad (4.7)$$

where W^i are replaced by (4.5) and becomes the governing equation for the potential ϕ . The density ρ is determined by (4.1) where $|\vec{W}|^2$ is given by $W^i W_i$.

Let us introduce the following notations to represent the backward and forward finite differences

$$\overleftarrow{\delta}_{\xi^1} F_{i,j,k} = \frac{F_{i,j,k} - F_{i-1,j,k}}{\xi_i^1 - \xi_{i-1}^1}$$

$$\overrightarrow{\delta}_{\xi^1} F_{i,j,k} = \frac{F_{i+1,j,k} - F_{i,j,k}}{\xi_{i+1}^1 - \xi_i^1}$$

The potential equation governing ϕ written in the discretised form may be represented by the operator $\mathbb{L} \phi_{i,j,k}$:

$$\mathbb{L} \phi_{i,j,k} = \overleftarrow{\delta}_{\xi^1} \left(\frac{\bar{p} r W^1}{J} \right)_{i+1/2,j,k} + \overrightarrow{\delta}_{\xi^2} \left(\frac{\hat{p} r W^2}{J} \right)_{i,j+1/2,k} + \overleftarrow{\delta}_{\xi^3} \left(\frac{\hat{p} r W^3}{J} \right)_{i,j,k+1/2} = 0 \quad (4.8)$$

where W^i are related to ϕ_{ξ^i} by (4.5), and the finite difference approximation of ϕ_{ξ^i} , for example at the point $i+1/2, j, k$ is given by

$$\begin{aligned} (\phi_{\xi^1})_{i+1/2,j,k} &= \frac{\phi_{i+1,j,k} - \phi_{i-1,j,k}}{\xi_{i+1}^1 - \xi_{i-1}^1} \\ (\phi_{\xi^2})_{i+1/2,j,k} &= \frac{1}{2} \left[\frac{\phi_{i+1,j+1,k} - \phi_{i+1,j-1,k} + \phi_{i,j+1,k} - \phi_{i,j-1,k}}{\xi_{j+1}^2 - \xi_{j-1}^2} \right] \\ (\phi_{\xi^3})_{i+1/2,j,k} &= \frac{1}{2} \left[\frac{\phi_{i+1,j,k+1} - \phi_{i+1,j,k-1} + \phi_{i,j,k+1} - \phi_{i,j,k-1}}{\xi_{k+1}^3 - \xi_{k-1}^3} \right] \end{aligned}$$

Moreover, in order to ensure stability of the scheme in the supersonic zones and to produce the effect of artificial viscosity necessary for the resolution, we have introduced in the operator $\mathbb{L} \phi_{i,j,k}$ the concept of retarding the density. The appropriate choice of retarding the density \bar{p} , \hat{p} , \hat{p} respectively in the directions ξ^1 , ξ^2 , and ξ^3 are given by [7]

$$\begin{aligned} \bar{p}_{i+1/2} &= \begin{cases} (1-\nu) \rho_{i+1/2} + \nu \rho_{i-1/2} & \text{if } W_{i+1/2,j,k}^1 > 0 \\ (1-\nu) \rho_{i+1/2} + \nu \rho_{i+3/2} & \text{if } W_{i+1/2,j,k}^1 < 0 \end{cases} \\ \hat{p}_{j+1/2} &= \begin{cases} (1-\nu) \rho_{j+1/2} + \nu \rho_{j-1/2} & \text{if } W_{i,j+1/2,k}^2 > 0 \\ (1-\nu) \rho_{j+1/2} + \nu \rho_{j+3/2} & \text{if } W_{i,j+1/2,k}^2 < 0 \end{cases} \\ \hat{p}_{k+1/2} &= \begin{cases} (1-\nu) \rho_{k+1/2} + \nu \rho_{k-1/2} & \text{if } W_{i,j,k+1/2}^3 > 0 \\ (1-\nu) \rho_{k+1/2} + \nu \rho_{k+3/2} & \text{if } W_{i,j,k+1/2}^3 < 0 \end{cases} \end{aligned} \quad (4.9a)$$

in which the factor ν is defined by

$$\nu = \min \{ \max \{ (M^2 - 1) c, 0 \}, 1 \} \quad (4.9b)$$

where c represents a user specified constant.

The three-level approximate factorization procedure used to solve the potential equation can then be written as

$$\left\{ \alpha - \overleftarrow{\delta}_{\xi^1} \left(\frac{\bar{p} r q^1}{J} \right)_{i+1/2,j,k} \right\} \overrightarrow{\delta}_{\xi^1} \left\{ \alpha - \overrightarrow{\delta}_{\xi^2} \left(\frac{\hat{p} r q^2}{J} \right)_{i,j+1/2,k} \right\} \overleftarrow{\delta}_{\xi^2} \left\{ \alpha - \overleftarrow{\delta}_{\xi^3} \left(\frac{\hat{p} r q^3}{J} \right)_{i,j,k+1/2} \right\} \overrightarrow{\delta}_{\xi^3} \delta \phi_{i,j,k}^{(n)} = \sigma \alpha^2 \mathbb{L} \phi_{i,j,k}^{(n)} \quad (4.10)$$

where $\delta \phi_{i,j,k}^{(n)}$ represents the nodal correction after each iterative cycle and σ is the relaxation parameter. The α appearing in this relation is a time like acceleration parameter and the choice of α greatly affects the convergence of the numerical scheme. In practice, it is best to use a small sequence of acceleration parameters running between the minimum and maximum values obtained from a simple two dimensional Von-Neumann analysis. Even though, this choice was adopted because of its simplicity, it was found that this choice is still effective in the three dimensional computations. The parameter σ is taken to be 2.5

On the blade surface, the flow tangency condition requires that the contravariant velocity component W^2 on this surface be zero. Thus, the derivatives ϕ_{ξ^2} at the blade surface, in the expression (4.8), are calculated using the blade boundary condition $W^2 = 0$ and we have

$$(\phi_{\xi^2})_{blade} = - \frac{1}{q^{22}} \{ q^{21} \phi_{\xi^1} + q^{23} \phi_{\xi^3} + \xi_{\xi^1}^2 V_0 + \xi_{\xi^2}^2 \omega \} \quad (4.11)$$

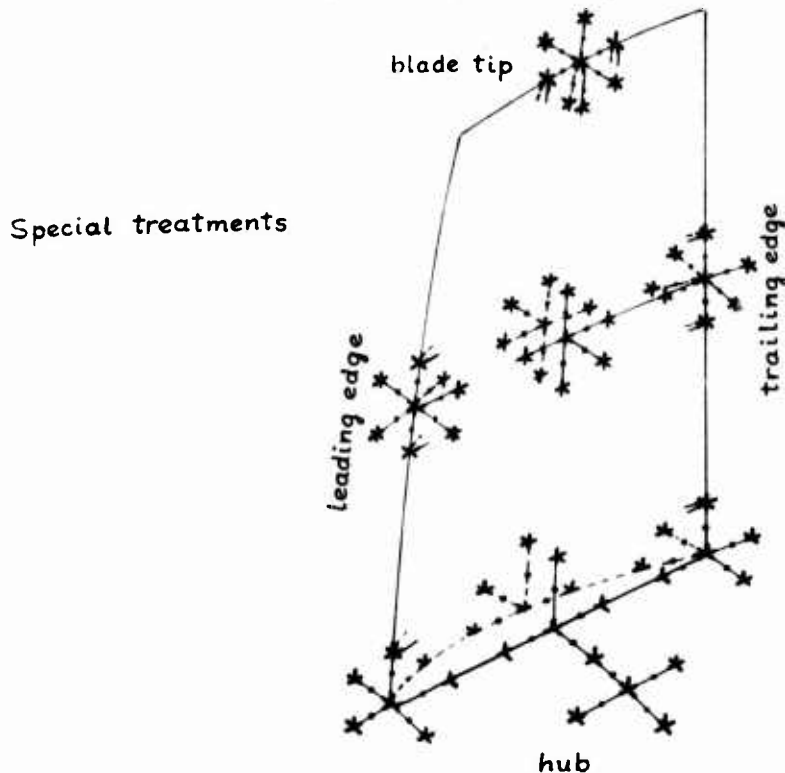
Similarly, on the hub surface, the flow tangency condition implies that $W^3 = 0$. Thus, the derivatives ϕ_{ξ^3} at the hub surface in the expression (4.8) are evaluated from

$$(\phi_{\xi^3})_{hub} = -\frac{1}{g^{33}} (g^{31} \phi_{\xi^1} + g^{32} \phi_{\xi^2}) \quad (4.12)$$

On the other hand, at the intersection between the hub and the blade, we have simultaneously the two flow tangency conditions : $w^2=0$ and $w^3=0$. This leads to determine the derivatives ϕ_{ξ^2} and ϕ_{ξ^3} from the following relations

$$(\phi_{\xi^2})_{hub/blade} = -\left(1 - \frac{g^{32}g^{23}}{g^{22}g^{33}}\right)^{-1} \frac{1}{g^{22}} \left[(g^{21} - \frac{g^{22}g^{31}}{g^{33}}) \phi_{\xi^1} + \xi_{\xi^1}^2 V_0 + \xi_{\xi^1}^2 \omega \right] \quad (4.13a)$$

$$(\phi_{\xi^3})_{hub/blade} = -\left(1 - \frac{g^{32}g^{23}}{g^{22}g^{33}}\right)^{-1} \frac{1}{g^{33}} \left[(g^{31} - \frac{g^{32}g^{21}}{g^{22}}) \phi_{\xi^1} - \frac{g^{32}}{g^{22}} (\xi_{\xi^1}^2 V_0 + \xi_{\xi^1}^2 \omega) \right] \quad (4.13b)$$



On the vortex wake issuing from the trailing edge, we must also admit the jump in the potential which corresponds the circulation around the blade section $\Gamma(r)$. On this vortex sheet, the derivatives ϕ_{ξ^1} and ϕ_{ξ^2} are both continuous while the derivative ϕ_{ξ^3} becomes discontinuous. Thus, we obtain two values of $|\vec{w}|$ on the upper and lower surfaces of this sheet and consequently leading to two values of ρ^+ and ρ^- . In the computation, at these grid points on the vortex sheet, the value used for ρ is the average value of those taken from the upper and the lower faces of this sheet.

The Kutta-Joukowski condition implies that the loading has to be reduced to zero at the trailing edge (TE) of the blade :

$$(w^1 w_1 + w^3 w_3)_{TE-\epsilon}^+ = (w^1 w_1 + w^3 w_3)_{TE-\epsilon}^- \quad (4.14)$$

This leads to a relation which serves to determine the value of $\phi^+ - \phi^-$ at the trailing edge.

Since the computation is limited in a single blade sector, the periodicity condition of the potential ϕ

$$\phi(z, \theta \pm \frac{2\pi}{N_p}, r) = \phi(z, \theta, r) \quad (4.15)$$

has to be applied on the boundary surfaces $\xi^2 = cte$ of the grid system.

At the far upstream as well as for the boundary surface $\xi^3 = cte$ having a radius far off from the propeller, the absolute fluid velocity has to be reduced to zero : $\nabla \phi = 0$. As the potential ϕ at these regions being arbitrary, we can admit that $\phi = 0$ at these regions.

And, finally, as the trailing vortex sheet is supposed to have the same pitch for all radius of the blade, the potential Φ induced by the free vortex presents a character of helicoidal symmetry [8] at the far down-stream side around the free vortex sheets. This condition requires that Φ must be constant following any helicoidal line. For the grid system considered, we should have $\Phi_{\xi} = 0$.

The transonic computation is carried out on the propeller defined by the panel method. Figures 4 to 6 show the type of grid system utilized for the finite difference calculations.

For the numerical applications, we have first developed a two dimensional code around a cylindrical section of the blade to study the different problems concerning the boundary conditions. The fig. 8 represents the iso-Mach curves obtained at the hub section of the blades. The continued lines correspond to the supersonic iso-Mach curves while the dotted lines correspond to subsonic curves. At the hub, we note that, in the two dimensional calculation, the choking phenomenon appears at a cruising Mach number $M_0 = 0.7$. The second test of this code was carried out at a radius $r/R = 0.7$. The fig. 9 represents the different levels of the iso-Mach curves at this section. This figure shows that supersonic region developed from the maximum thickness point reaching quite near to the trailing edge, this phenomenon is responsible for the high wave drags.

In the three dimensional code, the first test case was carried out by imposing the cruising Mach number to zero in the the code, in order to check the results obtained by the three dimensional singularity method (design problem) and the finite difference method (direct problem). The fig. 7 represents the circulation distribution on the blades obtained by these methods.

To reduce the cost of computations, the final three dimensional transonic computation was carried out on a coarse mesh system of 55 X 14 X 24 nodal points. The figs. 10 to 13 represent the iso-Mach curves obtained at different sections of the blade at a cruising Mach number 0.8. The choking phenomenon found at the hub section in the two dimensional analysis did not appear in the three dimensionnal computations. This is due the radial components of the velocity becoming more important in the three dimensional computations. Moreover, these radial effects are observed at different sections of the blade. The fig. 14 represents the absolute velocity field in the far downstream. We note the rolling up of the flow at the tip of the vortex sheet and also the importance of the radial effects near to the hub surface. Finally, the fig. 15 represents the comparison of the two and three dimensional results at the section $r/R = 0.7$ for a cruising Mach number 0.8.

5. CONCLUSION

A design method using the singularities distributions to generate the flow field is presented. This method permits to determine the geometrical parameters of the propeller in the zero Mach range, while the skew and rake angles, the form of the developed contour of the blade, the thickness and the bound vorticity distribution may be prescribed. To analyse the operation of the propellers in the transonic range, the full potential transonic finite difference method is developed; this offers the possibility to estimate the performanec of the propeller in the design and off-design conditions

REFERENCES

- [1] - LUU, T.S.
"Calcul de l'hélice marine subcavitante par la méthode des singularités", ATMA Paris, session 1970
- [2] - LUU, T.S. and DULIEU, A.
"Calcul de l'hélice fonctionnant en arrière d'un corps à symétrie axiale", ATMA Paris, session 1977
- [3] - LUU, T.S. and COLLERCANDY, R.
"Calcul de l'hélice du type Prop-Fan", Rapport contrat DRET Paris, Fev. 1983.
- [4] - COLLERCANDY, R.
"Etude et Calcul théorique d'écoulements transsoniques autour d'une hélice propulsive du type Prop-Fan", Thèse de Docteur-Ingénieur, presented at the University of Pierre and Marie CURIE, Paris, July 1984.

- [5] - LUU, T.S. and COULMY, G.
 "Calcul de l'écoulement transsonique avec choc à travers une grille d'aubes", ATMA Paris, Session, 1975
- [6] - LUU, T.S. and COULMY, G.
 "Relaxation solution for the transonic flow through a cascade", Symposium Transsonicum II, IUTAM, Göttingen, Sept. 1975.
- [7] - HOLST, T.L.
 "Fast conservative algorithm for solving the transonic full potential equation", AIAA Journal, Vol 18, N° 12, 1980
- [8] - SIESTRUNCK, R.
 "Le développement moderne de la théorie de l'hélice", ED. Gauthier-Villars, Paris 1947

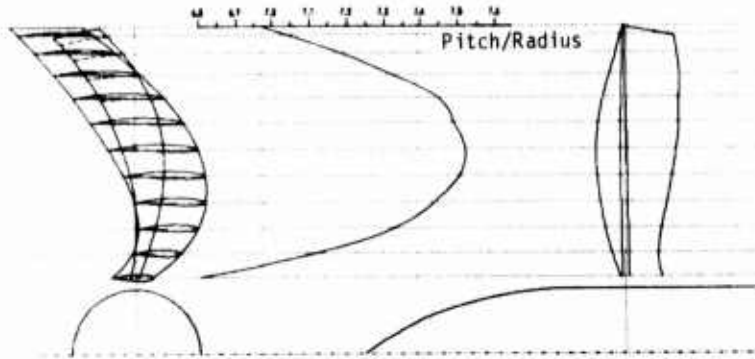


Fig.1 Geometry of a 12 bladed propeller designed by the panel method.

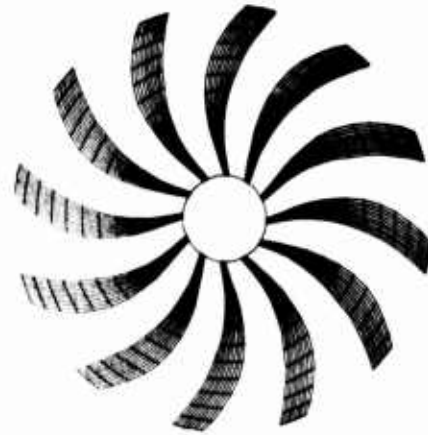


Fig.2 Division of the blades into inducing elements.

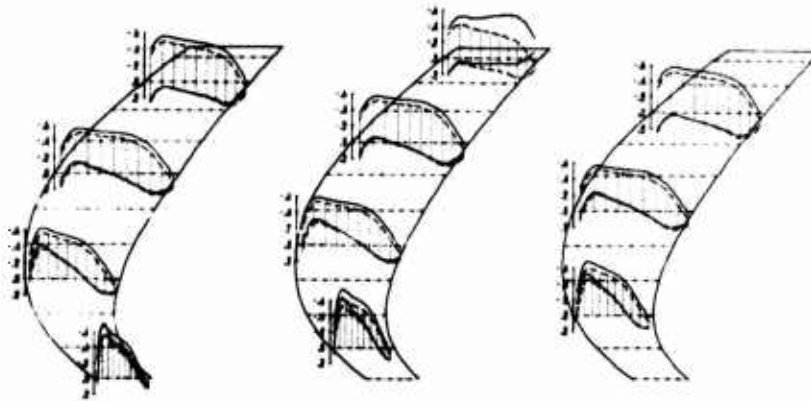


Fig.3 Pressure coefficient distributions. (panel method)

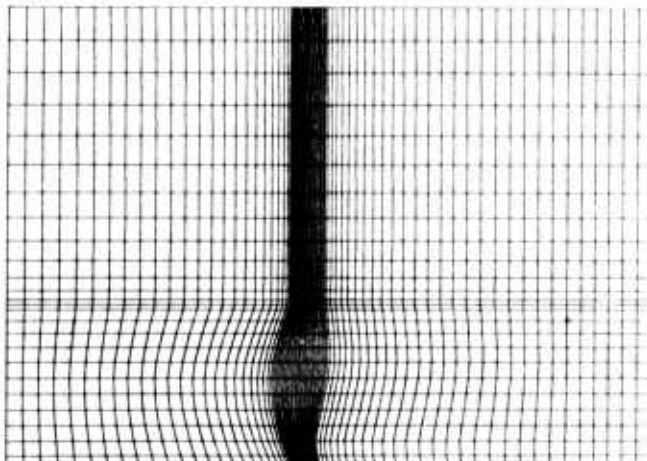


Fig.4 Grid system (coordinates z,r of ξ^2 surface around the blade).

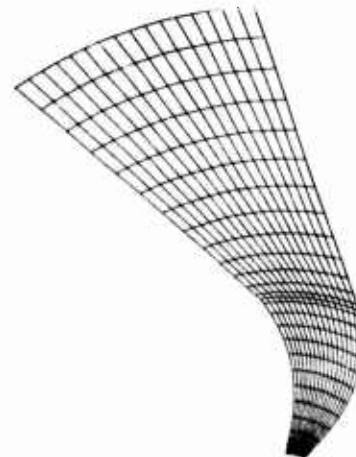


Fig.5 Grid system (section z constant).

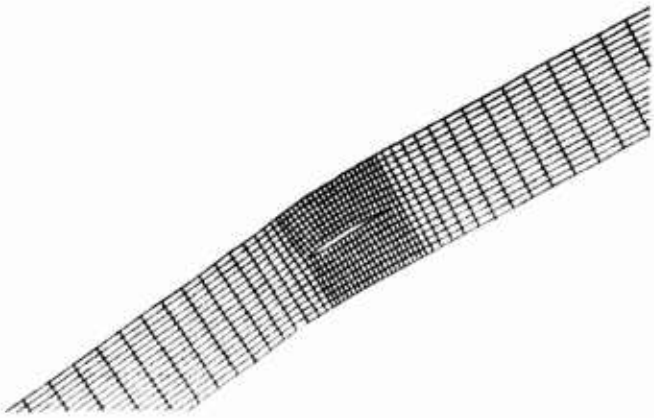
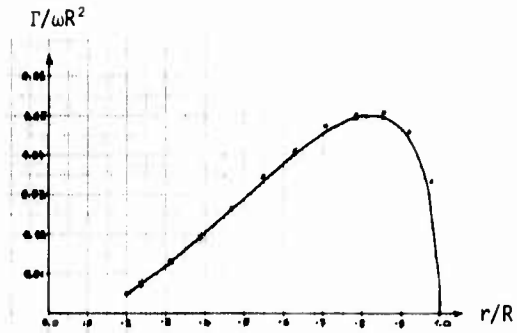
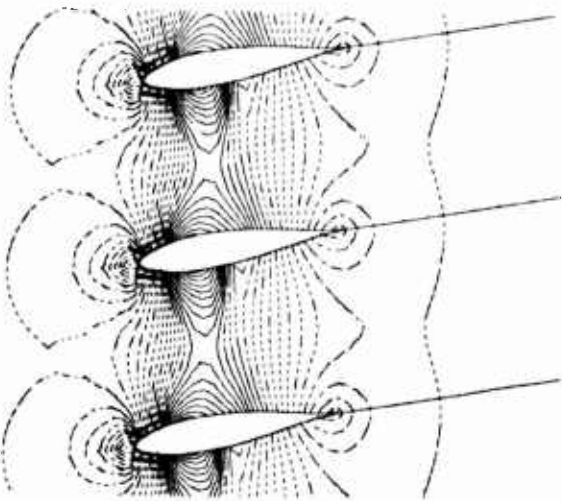
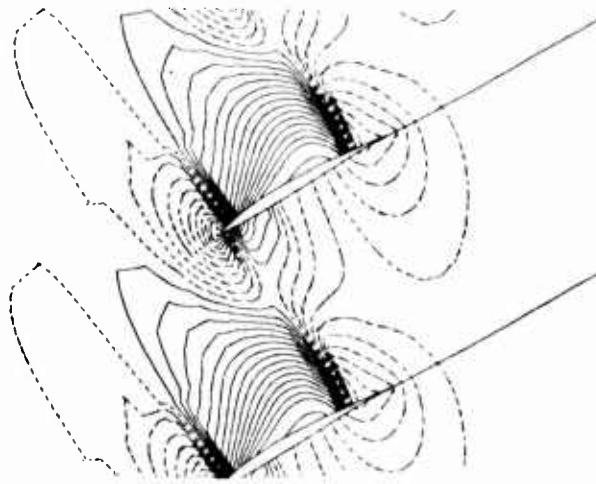
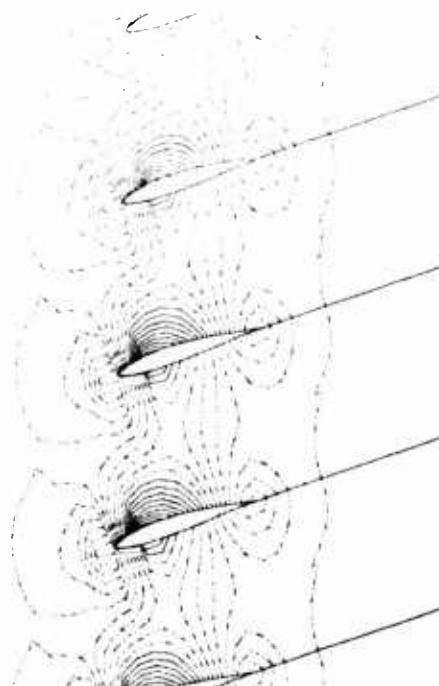


Fig.6 Grid system (network on the cylindrical section)

Fig.7 Comparisons of the circulation distributions Panel/Finite differences at $M_0 = 0$.Fig.8 2D iso-Mach curves $r/R = 0.2$, $M_0 = 0.7$ Fig.9 2D iso-Mach curves $r/R = 0.7$, $M_0 = 0.8$ Fig.10 3D iso-Mach curves $r/k = 0.2$, $M_0 = 0.8$ Fig.11 3D iso-Mach curves $r/R = 0.4$, $M_0 = 0.8$

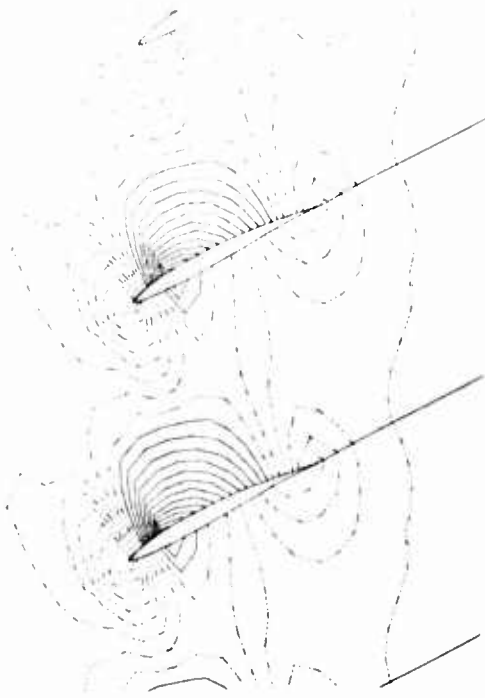


Fig.12 3D iso-Mach curves $r/R = 0.6$, $M_o = 0.8$

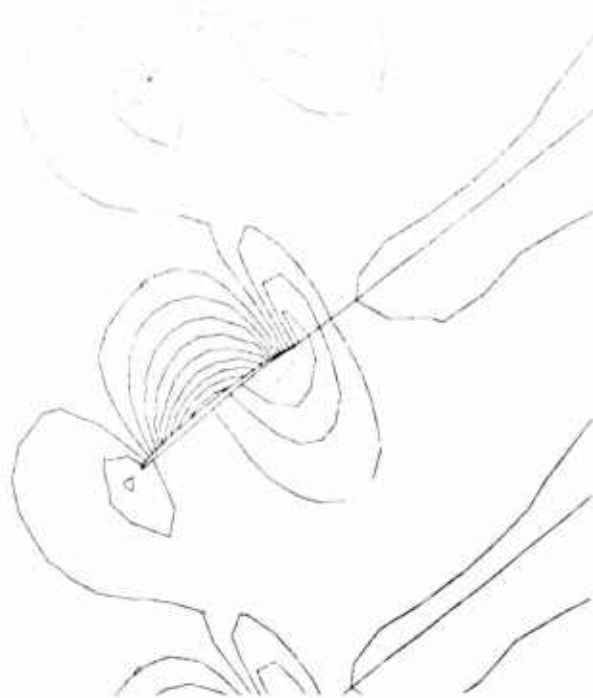


Fig.13 3D iso-Mach curves $r/R = 0.8$, $M_o = 0.8$

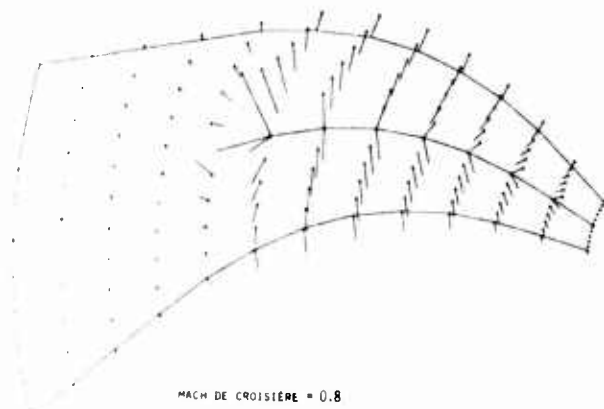


Fig.14 Absolute velocity distributions far downstream.

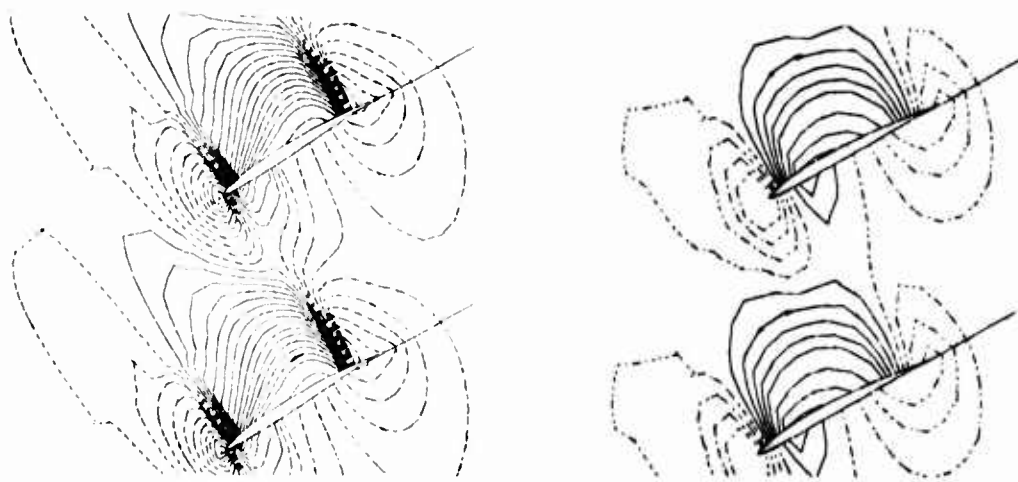


Fig.15 Comparisons of 2D and 3D computations $r/R=0.7$, $M_o=0.8$

A REVIEW OF ARA RESEARCH INTO PROPELLER
AERODYNAMIC PREDICTION METHODS

A J Bocci, J I Morrison
Aircraft Research Association Ltd,
Manton Lane, Bedford MK41 7PF, UK

SUMMARY

A research programme is being followed at ARA, aimed at providing methods capable of predicting the performance of a range of propeller configurations of practical interest. An improved wake method involving a numerical solution to Goldstein's wake flow model has been developed and the effects of removing Goldstein's limiting assumptions are illustrated. The representation of ARA-D aerofoil data for use with the wake methods is considered, covering the wide range of geometry and flow conditions likely to be encountered on operating blades. The importance of finite blade effects is discussed and a tip relief correction is shown to improve predictions of experimental blade pressures and loadings. A method has been developed to calculate the flow induced by a prescribed wake vortex sheet and some of the issues arising in calculating the flow development from the propeller disc downstream are illustrated. A three-dimensional method involving solution of the compressible potential flow equation has been developed, capable of predicting the blade flow in some detail for general multi-blade configurations. Comparisons with experiment are shown for two-blade cases.

NOTATION

a	Axial velocity increment at propeller disc, fraction of advance velocity
a'	Rotational velocity increment at propeller disc, fraction of advance velocity
c	Section chord length
C _D	Drag coefficient
C _{L0}	Design lift coefficient, defines camber of NACA series 16 sections
C _L	Lift coefficient
C _N	Force coefficient normal to chord
C _p	Pressure coefficient or power coefficient
G	Goldstein's loading function, $G \equiv pr\omega/2\pi w$
J	Advance ratio, $J \equiv 2\pi V/\omega D$
K ₁	Camber factor used in definition of ARA-D sections
M	Mach number
p	Blade number or flow field pressure
q	Flow field velocity relative to axes rotating with blade
r	Radial coordinate
R	Blade radius
R _c	Chord Reynolds number
t/c	Section thickness/chord
V	Propeller advance velocity
W	Blade element onset flow velocity
W ₀	Blade element helical velocity
w ₁	Blade element interference velocity due to wake
w	Wake displacement velocity
x/c	Non-dimensional distance along chord
z	Axial coordinate opposite to propeller direction
α	Blade element effective incidence
Γ	Wake vortex strength
θ	Cylindrical polar coordinate, right hand screw downstream
κ	Lock's loading function
μ	Radial coordinate in transformed wake plane
ξ	Circumferential coordinate in transformed wake plane
ρ	Flow field density
ϕ	Blade element onset flow angle
ϕ_0	Blade element helix angle, or wake helix angle for light loading, $\phi_0 \equiv \tan^{-1} (V/\omega r)$
ϕ_1	Wake helix angle for heavy loading $\phi_1 = \tan^{-1} (V+W/\omega r)$
ϕ	Velocity potential
ω	Angular velocity of propeller rotation, right hand screw upstream
∇	Vector first differential
Suffix:	Bar denotes mean or vector quantities
H	Pertaining to helical flow

1 INTRODUCTION

In recent years, Dowty Rotol propellers incorporating new blade aerofoils have been specified for a number of aircraft. The aerofoils, referred to as the ARA-D series, were developed at the Aircraft Research Association and are described in Refs 1 and 2. The present paper is concerned with describing subsequent work at ARA involving the development of theoretical methods for propeller performance prediction.

The major effects of blade aerofoil characteristics on propeller performance can be considered in the context of classical methods involving simple wake models and blade element theory. The methods are usually believed to provide a reasonably accurate performance prediction, particularly for relatively low solidity propellers with two, three or four blades. This belief has been broadly confirmed by experience gained over the years in using the classical Lock/Goldstein theory in conjunction with the NACA series 16 data bank developed at Dowty Rotol, and comparing with known propeller performance. However, the aerofoil data cannot be regarded as purely two-dimensional, containing features representative of what might be expected on a finite rotating blade, and these differences from two dimensions can have a significant effect

on propeller performance estimates in certain conditions. It follows that there is a need to allow for such blade effects when new aerofoil data is introduced, and one objective of the work described here is to ensure that this is the case with the ARA-D data.

Inherent in the classical methods are certain approximations and assumptions and the methods cannot be expected to predict the details of the flow associated with rotating blades with great accuracy, even if the overall propeller performance prediction is adequate. These limitations may become more significant in the more highly disc loaded cases envisaged for some applications. Consequently, another objective of the work has been to develop more advanced methods which could predict the flows in greater detail and could be used as alternatives to the classical methods if and when necessary. An interim description of the work was contained in Ref 2.

Fig 1 illustrates the scheme which is being followed in the work, which is aimed at providing acceptable flow predictions for the range of configurations shown. The boxes defined by solid lines indicate the particular areas of research effort which will be referred to here. This may be summarised as follows.

A method has been developed to provide a finite difference solution for the flow between regular wake screw surfaces, with the limiting assumptions of Goldstein removed. This is discussed in section 2.

The propeller performance prediction may be obtained by combining the inflow velocities given by the wake method with the blade element lift and drag data, according to the velocity diagram. The ARA-D two-dimensional aerofoil data, obtained from experimental tests on a limited number of aerofoils, is represented by empirical mathematical formulae for interpolation or extrapolation purposes, over a comparable range of geometric and flow conditions to the ACA series 16 data bank. The representation of the data is considered in section 3.

The two-dimensional aerofoil data should be modified when applied to the blade elements, to take account of conditions on the finite, rotating blade. A tip relief correction has been derived which gives pressure distributions and loadings consistent with those in experimental tests on pressure tapped blades. Towards the root, the spinner/nacelle shaping may influence flow field velocities and cascade effects may be significant. These finite blade effects are discussed in section 4. Centrifugal effects on the development of the viscous layers may be significant but are not considered here.

The assumption of a regular screw surface downstream of the same diameter as the propeller, forms the basis for the classical methods. In practice, the surfaces are unlikely to be regular, with a natural tendency to contract due to loading. To investigate such effects, and their influence on propeller disc inflow velocities, a method has been developed to calculate the flow induced by a prescribed wake vortex sheet. This is considered briefly in section 5. The method could be adapted to give a first order approximation to the interaction of the wake with the finite nacelle or fuselage, wing, or other parts of the aircraft.

In order to predict the blade flow in greater detail, three-dimensional methods involving solution of the compressible potential flow equation have been investigated. Results from a method limited to the two-blade case were shown in Ref 2. Another method has been developed to deal with multi-blade cases, unswept or swept, and including the effect of a finite, circular spinner/nacelle. This is discussed in section 6.

2 AN IMPROVED WAKE METHOD

An example of the screw surfaces traced out by a four-blade propeller moving forward with right-hand screw is shown in Fig 2a. The screw surfaces of a propeller with p blades of radius R , moving with velocity V and angular velocity ω , are given by the equation

$$\theta - \frac{\omega z}{V} = 0, \frac{2\pi}{p} \dots \frac{2\pi(p-1)}{p} \quad \text{for } r < R$$

Here, r, θ, z are right-hand cylindrical polar coordinates fixed in space, with the z axis coincident with the propeller axis and opposite to the propeller direction.

The ideal wake is a screw surface comprising trailing vortex filaments which move downstream with a uniform displacement velocity w . The filaments actually move normal to themselves but this is visually indistinguishable from downstream displacement. It is straightforward to show that the ideal wake corresponds to minimum energy loss per unit time (see eg Ref 3).

Goldstein (Ref 4) gave an exact solution for the incompressible potential flow between the wake surfaces, subject to a normal velocity boundary condition on the surfaces written as

$$w \cos \phi_0 = \frac{\partial \phi}{\partial z} \cos \phi_0 - \frac{1}{r} \frac{\partial \phi}{\partial \theta} \sin \phi_0$$

where ϕ_0 is the wake helix angle, see Fig 2a, and ϕ is the velocity potential. Goldstein took the wake helix angle to be the same as the propeller helix, ie $\phi_0 = \tan^{-1}(V/\omega r)$, which is only true in the limit of infinitely light loading. A substitution, $\xi = \theta - \omega z/V$, is used to transform the wake into a two-dimensional plane. The additional transformation $\mu = \omega r/V$ enables Laplace's potential flow equation, $\nabla^2 \phi = 0$, to be written

$$\mu^2 \frac{\partial^2 \phi}{\partial \xi^2} + \mu \frac{\partial \phi}{\partial \mu} + (1 + \mu^2) \frac{\partial^2 \phi}{\partial \xi^2} = 0 \quad (1)$$

and the boundary condition becomes

$$\frac{\partial \phi}{\partial \xi} = \frac{-\mu^2}{1+\mu^2} \cdot \frac{wV}{\omega} \quad (2)$$

Goldstein obtained a solution for the velocity potential in terms of a series solution involving Bessel functions, with the wake loading given by the discontinuity in ϕ across the screw surface. The solution was limited to the two or four blade case with zero centre body radius and expressed in terms of a light loading function $G \equiv \rho\omega/2\pi W$, where Γ is the wake vortex strength at a given radial location.

Lock (Ref 5) extended Goldstein's method to deal with a range of blade number from two to six. He assumed a wake helix angle equal to the blade element onset flow angle ϕ (see Fig 1) and tabulated an alternative function κ against ϕ at standard radial stations, related to Goldstein's function by

$$\kappa = G/\cos^2 \phi \quad (3)$$

Lock made use of an approximate function of Prandtl (see eg Ref 3) to interpolate or extrapolate values of κ for blade number other than two or four.

Morrison, Ref 6, has developed a computational method which provides a numerical solution to equations (1) and (2), with a non-zero centrebody radius forming an additional boundary. An example of the type of grid used in the numerical scheme is shown in Fig 2b, for a four-blade case. An additional radial transformation is included to bring the infinite far-field, at which the flow velocity is zero, in to a finite distance, to form the computational boundary. The equations are put in central difference form and equation (1) solved by line relaxation, sweeping through the grid in a radial direction from the centre body boundary out to the boundary corresponding to infinity.

Advantages of Morrison's method include the ability to deal with any number of blades and to take account of a non-zero centrebody radius. Also, an option is available of providing a solution to Goldstein's equations expressed in terms of the true wake helix angle, which we will refer to here as ϕ_1

$$\phi_1 = \tan^{-1} \left(\frac{V+W}{\omega r} \right)$$

This will be referred to as the heavy loading mode.

Morrison's method can be used to examine the accuracy of the classical ideal wake solutions. Fig 3 shows examples of calculations by the method, with a sufficiently refined grid to ensure numerical accuracy.

Fig 3a shows the effect of centrebody radius on Goldstein's light loading function for two blades, with the zero body radius solution precisely matching the original, given in Ref 4. The implication of this result is that the values of κ tabulated in Ref 5 are incorrect towards the root in the general case of non-zero body radius.

Fig 3b shows typical examples of checks carried out on the accuracy of the interpolated or extrapolated κ values tabulated in Ref 5. In these checks, a wake helix angle of ϕ_0 or ϕ_1 was assumed in equation (3), as appropriate. It can be seen that, in general, the accuracy is good, with a maximum error of about 10% near to the tip noted in some cases.

Fig 3c shows examples of a trend towards much higher efficiency at lower advance ratios when the switch from the light to heavy loading mode is made. This is of considerable significance to propeller performance estimates.

The methods discussed so far provide a solution for the ideal wake of a propeller with given radius, blade number and operating conditions. To use the methods for a practical propeller calculation, the blade element onset flow conditions may be linked to conditions in the wake according to the blade element velocity diagram, see Fig 1. Usually, the interference velocity w_1 at the blade element is assumed to be one half of the normal sheet velocity in the wake, and directed normal to W , the onset flow velocity. The calculation proceeds in an iterative fashion, since the interference velocity influences blade loading and hence the wake solution. In order to deal with non-ideal loading distributions, isolated blade elements are assumed. This means that a converged solution may be obtained for each element in turn, with the interference velocity calculated as if the element were part of an ideal loading distribution. In the case of Morrison's method, a perturbation to an ideal loading distribution is assumed. The isolated blade element assumption also implies that the lift and drag coefficients may be obtained from two-dimensional aerofoil data.

3 AEROFOIL DATA REPRESENTATION

The NACA series 16 data bank used at Dowty Roto1 consists of tables of lift and drag coefficient at discrete steps of thickness/chord, camber (C_d), Mach number and incidence, over the ranges indicated in Fig 1.

Seven members of the ARA-D family of aerofoils, of thickness/chord ranging from 4% to 20% and of varying camber factor (K1), featured in the main series of experimental tests in the ARA 18" x 8" 2D wind tunnel. The aerofoils were tested transition free, at Reynolds numbers relevant, as far as possible, to blade flow conditions, and measurements were taken at incidences well into the stall, over a Mach number range up to the limit, $M \approx 0.85$, of the normal tunnel operating range, for which the open-area ratio ensures blockage-free conditions. To create a data bank comparable with NACA series 16, tests on a far larger number of aerofoils would have been required, over a wider range of flow conditions.

A fundamental feature of the ARA-D aerofoil family (Ref 1) is the geometric definition by simple mathematical expressions. The continuous shape variation with thickness/chord ensures a reasonably linear variation of aerodynamic properties, with the camber factor (K1) having a similar effect. It has proved possible to approximate the lift and drag data by curves defined by mathematical formulae, allowing interpolation or extrapolation of the data to any geometry or flow condition. Fig 4 shows examples of the accuracy of representation of the data for two aerofoils from the ARA-D family. To assess the quality of the curve fitting, some interpretation of the experimental data is necessary.

At the lower Mach numbers the results for the 8% t/c section are sensitive to Reynolds number but such Reynolds number sensitivity is less likely for the 4% t/c section due to the leading edge separation characteristics in the stall. As the stall develops, the existence of separated flow over a significant chordwise extent sets a limit to the incidence for which the data may be regarded as valid. This is because the separated flow is likely to develop in a three-dimensional manner which may be influenced by the tunnel wall boundary layer. At the highest Mach numbers in both cases, few experimental drag values are available since the shock wave on the aerofoil penetrates well into the flow field, with the result that the wake exceeds the width of the drag measuring rake outside a small incidence range. At these Mach numbers, the lift continues to increase with incidence as the stall develops, although more slowly than in attached flow conditions.

The examples show that in conditions corresponding to attached flow, the curve fitting is of adequate accuracy for propeller calculations. As separations develop, the curves follow the trends, but not the details, of the data variation; in these conditions the curves are biased towards Reynolds numbers most representative of typical blade operating conditions. At high Mach numbers and/or incidences, where the experimental data is limited or non-existent, the curves extrapolate smoothly but arbitrarily. These examples are typical of the accuracy of representation of the data for the aerofoils in the main test series.

For sections differing significantly in thickness/chord or camber from those tested and for higher Mach numbers than the limit of the ARA 2D tunnel, the curve fitting formulae have been calibrated as far as possible against the results of theoretical calculations by a viscous supercritical method, Ref 7, referred to as VGK. The method can be expected to give results in close agreement with experiment, at a given aerofoil lift coefficient, but difficulties arise because the calculated lift curve slope is typically somewhat steeper than given in 2D wind tunnel tests and the method is restricted to essentially attached flow conditions. Also, the method cannot deal with shocks located at the trailing edge, typical of sonic or supersonic free stream Mach numbers. For these reasons, other approaches to obtaining the data were required.

Fig 5a shows some results from recent tests carried out in the ARA 18" x 8" 2D tunnel on an extremely thick ARA-D aerofoil, representative of the upper limit of thickness which might apply close to the root. The section would be expected to feature significant flow separations in many practical blade operating conditions. The wing chord was only two inches (5.1 cm) to allow the low Reynolds numbers typical of blade roots to be achieved, and an attempt was made to ensure two-dimensional flow as far into the stall as possible by isolating the tunnel wall boundary layer using large end plates. The curves given by the formulae at $M = 0.4$ can be seen to give a fair prediction of the experimental results at incidences below the stall; the flow development in the stall is very sensitive to Reynolds number and cannot be represented adequately by a single curve.

The $C_L - \alpha$ curves at $M \approx 0.65$ represent conditions with fully separated flow aft of the shock, giving very high drag (not shown). This could have a significant adverse effect on propeller efficiency and illustrates the risk involved in operating with thick root sections beyond their drag rise Mach number. It should be noted that such an aerofoil would not normally be used for high speed propeller applications: advanced ARA-D aerofoils have been developed for this purpose.

Lift and drag data for supersonic Mach numbers may be obtained from calculations by the inviscid method of Ref 8. In such conditions the aerofoil shock waves are located at, or very close to the trailing edge and it has been found that inviscid theory is acceptable. This is illustrated by check comparisons for aerofoil NPL 2211 (Ref 9), for which test results, in the form of surface static pressures, but not wake drag measurements, are available for Mach numbers up to 1.4. Fig 5b shows the close match of pressures between theory and experiment in a comparison at $M = 1.0$ and there is a similar close match at other incidences and supersonic Mach numbers, not shown. Lift coefficients compare closely between theory and experiment and this also applies to pressure drag coefficients if the integration of experimental pressures follows the theoretical curve around the leading edge, where experimental points are sparse. The drag coefficient is taken to be given to adequate accuracy by the pressure drag coefficient, with an increment to allow for skin friction which depends on the extent of laminar flow assumed. From the results of such calculations for thin, low cambered ARA-D aerofoils, a supersonic data bank has been constructed, consisting of lift and drag coefficients at a limited number of discrete values of thickness/chord, camber, Mach number and incidence. This approach has been adopted since attempts to modify the curve fitting formulae to fit the supersonic data points were unsuccessful. It is planned to carry out tests on an ARA-D aerofoil up to supersonic Mach numbers in another wind tunnel, to check the accuracy of the supersonic data bank. An important part of such an exercise is to ensure the consistency of experimental data between wind tunnels.

The ARA-D aerofoil data representation by mathematical formulae, with a switch to a small supersonic data bank when necessary, gives instant data of reasonable accuracy. This is very much to be preferred to the search through a large data bank such as NACA series 16 when used in an iterative fashion as part of a wake method calculation, particularly when finite blade effects are introduced.

4 FINITE BLADE EFFECTS

The accuracy of the classical wake methods with the isolated blade element assumption can be assessed by comparing pressure distributions on the rotating blade with those on the corresponding two-dimensional aerofoil, at equivalent flow onset conditions. A series of wind tunnel tests on full scale propellers with pressure tapped blades was carried out in the early post-war years by NACA, and provides data suitable for such an assessment. The propellers had two blades (or one blade for some tests) incorporating NACA series 16 sections, with the range of geometries sketched in Fig 6. Pressures were recorded at a number of radial stations, each station in a separate run, and were corrected for centrifugal forces on the columns of air in tubes set radially in the blades. Refs 10, 11, 12, 13, 14, which should be consulted for full details of the experimental configurations and tests, contain tables of pressures at each radial station for various combinations of free stream velocity, rotational velocity and blade angle.

Ref 2 included examples demonstrating a major tip effect on blade pressures, with a reduction in section loading and an increase in (effective) drag rise Mach number compared with two dimensions. The

pressures were taken from the results for the blade referred to as blade 1 in Fig 6. Examination of the results for the complete range of blades shows that the tip effect is also manifest as a reduction in lift curve slope, as illustrated in Fig 7a. Points on the curves correspond to different radial stations having the same geometry and helical Mach number, with the curve for the inboard stations closely matching two dimensions. The incidence shown allows for inflow and the effect of blade deflection under load.

A tip relief correction has been developed, principally as a change to the effective section geometry, which is consistent with the trends observed in the experiments. The effect of the correction is shown in Fig 7b, for two radial stations near the tip of blade 1. The 2D theoretical calculations are by the method of VGK, Ref 7, and it can be seen that the main features of the blade pressures are represented when the tip relief correction is included in the geometry used for the calculations, with a substantial improvement in lift coefficient prediction. The comparisons are reasonably typical of the tip regions of the blades shown in Fig 6, at most flow conditions, although incidence corrections are sometimes necessary.

The tip relief correction may be included in the wake methods, mainly by modifying the section geometry used to obtain the blade element lift and drag data. Calculations by Morrison's method, with and without tip relief included, are compared with experimental data from the NACA blade tests in Fig 8. In the theory, the experimental blade angle was matched and the blade deflection under load included in the specified twist. The Mach number of the free stream flow was also matched and the experimental loading at each station corrected to the average value of advance ratio (J) used in the theory. In the case of blade 1 the introduction of tip relief has clearly brought the theoretical loadings closely into line with experiment. In the case of blade 5 the trend of the tip relief correction seems plausible but the comparison is obscured by the discrepancy on the main part of the blade, for which no explanation could be found. It may be that the experimental values are unreliable since, in addition to the loading corrections for advance ratio, further corrections were required to account for discrepancies in experimental blade angle.

The inclusion of tip relief in the wake methods can have a significant effect on predicted efficiency, by changing lift/drag for the tip sections. Finite blade effects associated with the root can also be important, particularly the influence of spinner/nacelle shaping on disc plane flows and the cascade effects associated with increased blade number. Some points of interest arising from the inclusion of root effects in the wake methods are illustrated in Fig 9 and will be discussed briefly.

The effect of spinner/nacelle shaping on flow field velocities may be calculated to first order by a method such as that described in Ref 15, with the shape represented by a body of revolution. Several issues arise when the influence on flow field velocities is introduced into the wake methods. For example, consider Fig 9a, which shows a sketch of the root region of a modern composite blade with a cuff extending nearly to the spinner side. The spinner/nacelle shape would influence the flow over the whole blade chord, rather than just the blade axis as assumed in the wake methods. Also, the spanwise positions of the calculation stations must be considered. Fine grid calculations by Morrison's method are found to give a much better definition of the rapid radial variation in spinner/nacelle influence, blade planform and section geometry than the widely spaced x stations used in Lock/Goldstein calculations. However, the definition of conditions at the spinner/blade junction remains uncertain, with the true flow following the spinner profile and the possibility of large viscous effects.

An allowance for cascade effects towards the root may be necessary, even for a relatively limited number of blades. Fig 9b shows a comparison of calculated pressures in free air and in a cascade, according to subcritical inviscid theory (Ref 16). The section thickness/chord and the gap in the cascade case are representative of the root region of a four-blade propeller. This comparison illustrates the fact that mild cascade effects can be allowed for by a reduction of section loading. However, the two-dimensional approach may not be representative of the three-dimensional flow development. This might be anticipated in cases where the spinner/nacelle profile has a significantly three-dimensional influence on the flow but, according to the theory, it can also apply to cases with a parallel body assumed. This is illustrated by Fig 9c, which shows results for four-blade propellers differing mainly in design loading distribution. Blade loadings according to Morrison's method are compared with those calculated by a three-dimensional field method to be discussed later. The moderate root loading case shows a fair measure of consistency between the theoretical predictions when the cascade effect is introduced into the wake method. This is not true of the high root loading case, where the three-dimensional method gives a much lower loading than that resulting from the isolated blade element assumption in the wake method, and the cascade correction has a marginal effect only. It should be noted that supercritical flow development at the root is of only minor significance in these examples.

The above considerations apply to conditions at the blade elements, with the inflow calculated assuming the wake model of the classical methods.

5 WAKE SHEET INDUCED VELOCITIES

The vortex sheets shed by the blades of a rotating propeller form helical surfaces which move downstream, varying in pitch and radius. Eventually, the sheets may roll up into discrete vortices. The ideal wake, of the same diameter as the propeller, forms the basis for the classical methods and it may be that a more realistic wake model is required, which could include the effects of interaction with the aircraft geometry.

A method (Ref 17) has been developed at ARA to calculate the flow due to a prescribed wake vortex sheet, by direct integration of the velocities induced by the vortex filaments comprising the sheets. The aim of the work is to carry out a systematic investigation of the flow between the propeller disc and the downstream wake. Here we will consider several points of interest arising from the validation of the method and its use to predict wake convergence.

The basic version of the method takes an ideal wake solution given by the Morrison method, for a propeller with a given number of blades at a given operating condition. The velocity induced by the vortex filaments, of strength corresponding to the ideal loading, is calculated using the Biot-Savart law (eg Ref 18). For this purpose, grids are defined on the sheet surfaces by lines following the direction of the

vortex filaments and by radial lines at equal intervals along the helix axis. An example of the type of grid in a two blade case is shown in Fig 10a. The induced velocity at a point in the field is calculated by integrating the contributions from the filaments at each grid intersection point on the wake sheets. It should be noted that a centrebody is not included in the basic version of the method, since a singularity distribution would be required on the surface of the body to avoid flow leakage.

To illustrate the results of calculations by the method, it is convenient to consider velocities induced at points in a plane normal to the axis, following a circumferential line from one sheet to another at a given radius, as in Fig 10a, with the velocities expressed in axial (V_z), swirl (V_θ) and radial (V_r) components. Fig 10b shows a comparison with an ideal wake solution on a circumferential line at half the wake radius and includes the corresponding results in an upstream propeller disc plane where the wake sheets are cut off. It is interesting to note that, in such calculations, most of the induced velocity contribution arises from the sheets in the immediate vicinity of the calculation point, and has almost vanished within two or three complete rotations.

The wake comparison is very close, except on the sheets where the integration is very sensitive to the position of the point relative to the local grid. The results shown were calculated with the point mid-way between radial lines but the most appropriate choice of point position has not been resolved. The point position should be chosen to ensure a balance of the large velocity contributions from adjacent grid points, which become singular as the grid point is approached. In this respect, grid refinement is not helpful. For the present, it has been accepted that the sheet velocities are not calculated with complete accuracy by the method.

Velocities on the sheets in the disc plane are, as would be expected, one half of those in the wake, with the exception of radial velocity V_r . Between the sheets, velocities in the disc plane vary in a different manner to those in the wake. The value of V_r is zero on the sheet in the wake, since it is the mean of velocities of opposite sign on either side of the sheet. The non-zero value of V_r in the disc plane on the sheet indicates contraction.

Theodorsen (Ref 19) provides a correlation of wake contraction for two and four blades (and an infinite number), derived using expressions bearing some similarity to those in the present method but with light loading assumed. An extensive range of calculations of radial velocity V_r at the edge of the sheet, from the disc plane to the far wake, has been carried out using the method, to provide a new correction valid for any number of blades and for both heavy and light loading modes. The trends of the correlation are shown in Fig 10c. It should be noted that, for high blade number and low advance ratio J , the values of forward velocity V and displacement velocity w may be such as to give a wake contraction of over 50%. Calculations on a pre-contracted wake are necessary to check whether or not this is a genuine trend and to give information on the interference velocity at the blade.

So far, the discussion has mainly concerned enhancements of the classic wake methods which assume, in part, that the propeller blade is represented by a lifting line.

6 FIELD METHOD FOR THREE-DIMENSIONAL BLADE FLOW

The flow field about a rotating, advancing propeller with an axisymmetric spinner/nacelle, in isolation, is irrotational except for the bound vorticity on the blades and the shed vorticity concentrated in the wake sheets. Relative to a blade-fixed coordinate system, the flow is steady, and may be described by a rotational flow of constant vorticity throughout, and an irrotational perturbation flow. In vector notation the rotational flow has a velocity component $\bar{q}_H = \bar{V} - \bar{\omega} \times \bar{r}$, where the vector directions are consistent with the system defined in section 2, and the irrotational flow has a velocity component $\nabla\phi$, where ϕ is a perturbation velocity potential. A complete description of the flow field may be obtained by solving the compressible potential flow equation subject to boundary conditions on the blade surfaces and in the far field. Density ρ , and velocity \bar{q} , are related in the solution by a form of Bernoulli's equation

$$\frac{dp}{\rho} + \frac{1}{2} \bar{q} \cdot \bar{q} - \frac{1}{2} (\bar{\omega} \times \bar{r})^2 = \text{constant.}$$

Ref 2 included a comparison of calculated and experimental pressures on a rotating blade. The pressures were calculated from a compressible potential flow solution, broadly following the approach described above, using an adaptation of a wing/body code (Ref 20). A transformation from a rotational to a sheared flow allowed the grid system of the original wing/body code to be used for the flow field solution. A disadvantage of the method was the effective restriction to two blades, due to the grid system used.

Wing/body codes solving the compressible potential flow equation with alternative grid systems have been investigated in recent work at ARA, with a view to dealing with the general multi-blade case. A grid system of the O-C type has been found suitable for the purpose and Fig 11 shows the transformations involved in adapting the grid to deal with increasing blade number. The front view shows that the planes of symmetry between the blades are rotated as blade number is increased, with a compression of the circular grid. The blade section grid actually wraps around the circular grid. The blade section grid progressively distorts as blade number is increased and so a shearing transformation is used to return to a reasonably orthogonal grid. The grid system naturally follows the contour of an axisymmetric centrebody of arbitrary shape, and remains acceptable with the introduction of blade sweep.

With the multi-blade grid system, the method can be used to provide a solution to the potential flow equation, subject to boundary conditions on the centrebody and in the far field, and periodic boundary conditions on the planes of symmetry. A transformation from a rotational to a sheared flow field is again used.

Fig 12 shows a comparison of pressures calculated by the method with experimental pressures on NACA blade 1. In the theory, viscous effects were crudely represented by slightly modifying section profiles. Blade angle was matched, allowing for blade deflection under load, and experimental pressures at each station were corrected to the average value of advance ratio (J) used in the theory. The comparison is generally close, with the main differences probably due to the simplified viscous representation in the

theory. Also, the fact that the flow equations are solved in non-conservative form is likely to be associated with the error in shock position on the outer station. The differences are responsible for a prediction of loading which is not quite as good as that given by the wake method at the same flow condition, already shown in one of the comparisons in Fig 8.

The effect of increasing blade number, keeping the blade angle fixed, is shown in Fig 13, comparing blade loadings with those given by the wake method. The trends in the comparisons are the same, with the differences consistent with the improved representation of root and tip effects which would be expected of the 3D theory.

Fig 14 shows a comparison of theoretical and experimental pressures on NACA blade 1 at the flow condition of the other comparison in Fig 8. The same section profiles were used as for the calculation shown in Fig 12. The comparison is reasonably close, except for the supercritical flow region on the outer station and the appreciable overestimate of loading. In this case, the predicted loading distribution is less accurate than that given by the wake method and it is likely that this is largely a consequence of an inadequate viscous representation. The comparisons are typical of others, not shown here, on the NACA pressure tapped blades. Converged solutions have also been obtained showing a plausible representation of the effects of blade sweep and spinner/nacelle shaping, as well as increased blade number. Detailed experimental information is required to validate the method in these respects.

7 CONCLUDING REMARKS

- 1) A research programme is being carried out at ARA to provide methods suitable for the prediction of propeller aerodynamic characteristics. The majority of the methods are currently in use for propeller design and performance prediction.
- 2) An improved wake method has been developed to supersede Lock/Goldstein, giving the correct solution for arbitrary blade number and for the centre body effect on inflow. The accuracy of the method ensures that it forms a satisfactory basis for comparison with the more advanced, three-dimensional methods.
- 3) The representation of the ARA-D lift and drag data variation by curves defined by mathematical formulae, for use in the wake methods, is a practical alternative to wind tunnel testing of a very large number of aerofoils. Difficulties arise in representing the extremes of operating conditions, where the wind tunnel data is usually very limited. Work to improve the data representation is continuing.
- 4) A number of finite blade effects have been identified, partly from an analysis of early tests on NACA pressure tapped blades. These effects can have a significant influence on propeller performance estimates.
- 5) A method has been developed to give a direct calculation of the flow induced by prescribed wake vortex sheets. The method is being used to investigate the wake development between the propeller disc plane and far downstream, and could be adapted to give a first approximation to the effects of wake interaction with the aircraft geometry.
- 6) A method has been developed to calculate the three-dimensional compressible flow about a multi-bladed propeller, unswept or swept, including the effect of a finite, circular spinner/nacelle. Some further development is required, in particular to take better account of viscosity, including centrifugal effects.
- 7) Finally, it is worth noting that work, not discussed here, is being carried out at ARA to define more advanced ARA-D aerofoils. This is partly in response to a need to improve their applicability to high forward speed cases and partly due to a better understanding of three-dimensional effects on rotating blades.

ACKNOWLEDGEMENT

The work described in the paper was carried out under contract to Dowty Rotor Ltd, partially supported by the Department of Trade and Industry.

REFERENCES

- 1 A J Bocci, A New Series of Aerofoil Sections suitable for Aircraft Propellers, Aeronautical Quarterly, Vol 28, February 1977.
- 2 A J Bocci, Advances in the Aerodynamic Design of Propeller Blades, ARA Memo 241, 1982.
- 3 W F Durand, Aerodynamic Theory, Dover Publications Inc, 1963.
- 4 S Goldstein, On the Vortex Theory of Screw Propellers, Proc Roy Soc A, 1929, pp 123, 440.
- 5 C N H Lock, R C Pankhurst, J F C Conn, Strip Theory Method of Calculation for Airscrews on High Speed Aeroplanes, ARC R&M 2035, 1945.
- 6 J I Morrison, A Numerical Treatment of the Vortex Theory of Screw Propellers, ARA unpublished note, 1982.
- 7 M R Collyer, R C Lock, Prediction of Viscous Effects in Steady Transonic Flow past an Aerofoil, Aeronautical Quarterly, Vol 30, 1979.
- 8 A Jameson, Iterative Solution of Transonic Flows over Airfoils and Wings, including flows at Mach 1, Communications on Pure and Applied Mathematics, Vol XXVII, 1974, pp 283-309.

- 9 P G Wilby, The Pressure Drag of an Aerofoil with Six Different Round Leading Edges at Transonic and Low Supersonic Speeds, NPL Aero Rpt 1180, 1966.
- 10 J D Maynard, M P Murphy, Pressure Distributions on the Blade Sections of the NACA 10-(3)(066)-033 Propeller under Operating Conditions, NACA RM L9L12, 1950.
- 11 W H Gray, R M Hunt, Pressure Distributions on the Blade Sections of the NACA 10-(3)(049)-033 Propeller under Operating Conditions, NACA RM L9L23, 1950.
- 12 P J Johnson, Pressure Distributions on the Blade Sections of the NACA 10-(3)(090)-03 Propeller under Operating Conditions, NACA RM L50A26, 1950.
- 13 A J Evans, W Luchuk, Pressure Distributions on the Blade Sections of the NACA 10-(5)(066)-03 Propeller under Operating Conditions, NACA RM L50B21, 1950.
- 14 A J Evans, Propeller Section Aerodynamic Characteristics determined by measuring the Section Surface Pressures on an NACA 10-(3)(08)-03 Propeller under Operating Conditions, NACA RM L50H03, 1950.
- 15 T J Baker, F A Ogle, A Computer Program to Compute Transonic Flow over an Axisymmetric Solid Body, ARA Memo 197, 1977.
- 16 M G Edwards, User's Guide to Multi-Aerofoil and Cascade Program (MAF), ARA unpublished document.
- 17 R W Sterland, The Calculation of the Induced Velocity due to a Propeller Wake, ARA Model Test Note E26/1, 1984.
- 18 L M Milne-Thomson, Theoretical Hydrodynamics, Macmillan & Co Ltd, 1962.
- 19 T Theodorsen, Theory of Propellers, McGraw-Hill Bk Co, 1948.
- 20 T J Baker, C R Forsey, A Fast Algorithm for the Calculation of Transonic Flow over Wing/Body Combinations, AIAA Journal, Vol 21, No 1, 1983, pp 60-67.

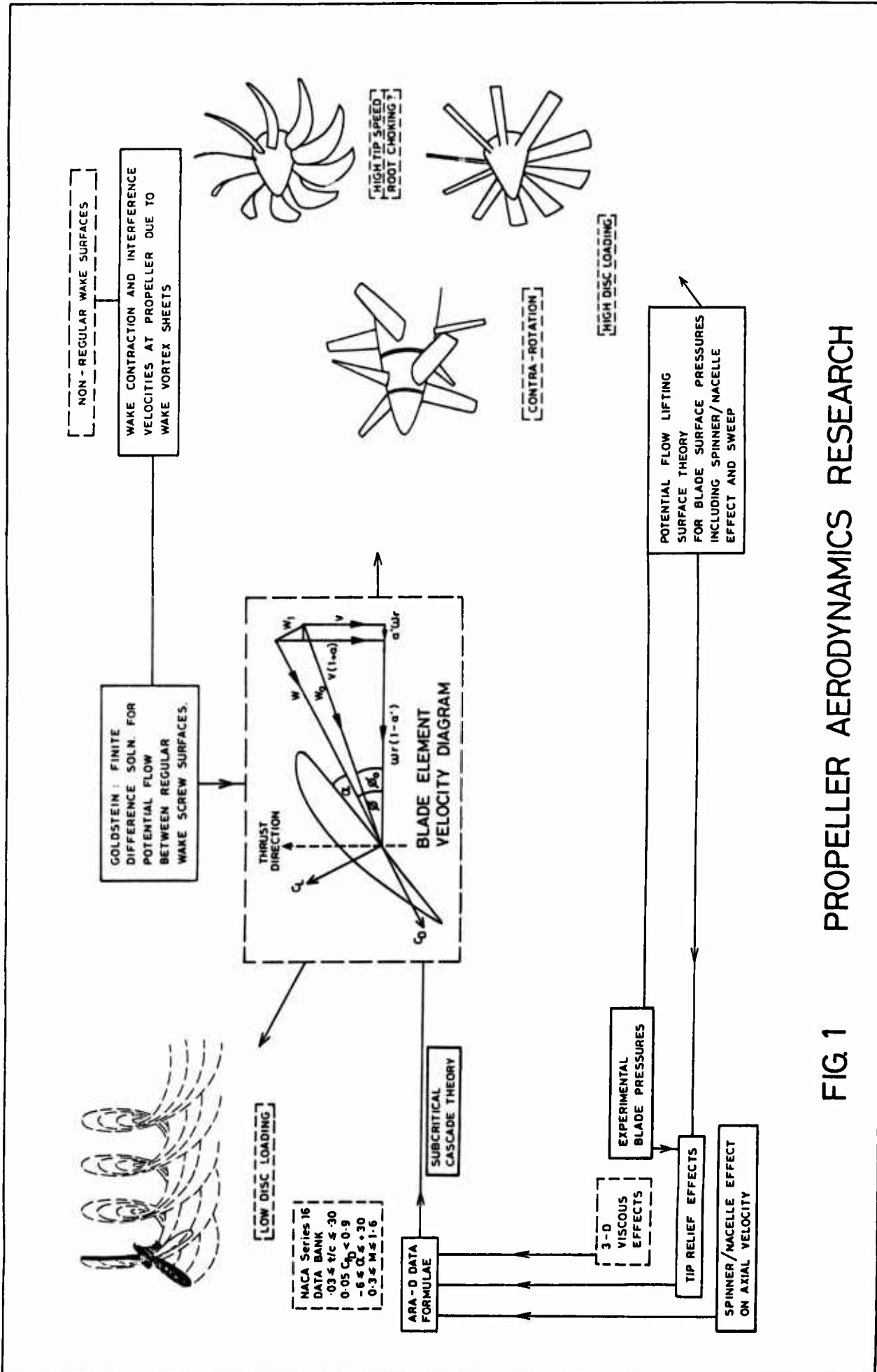
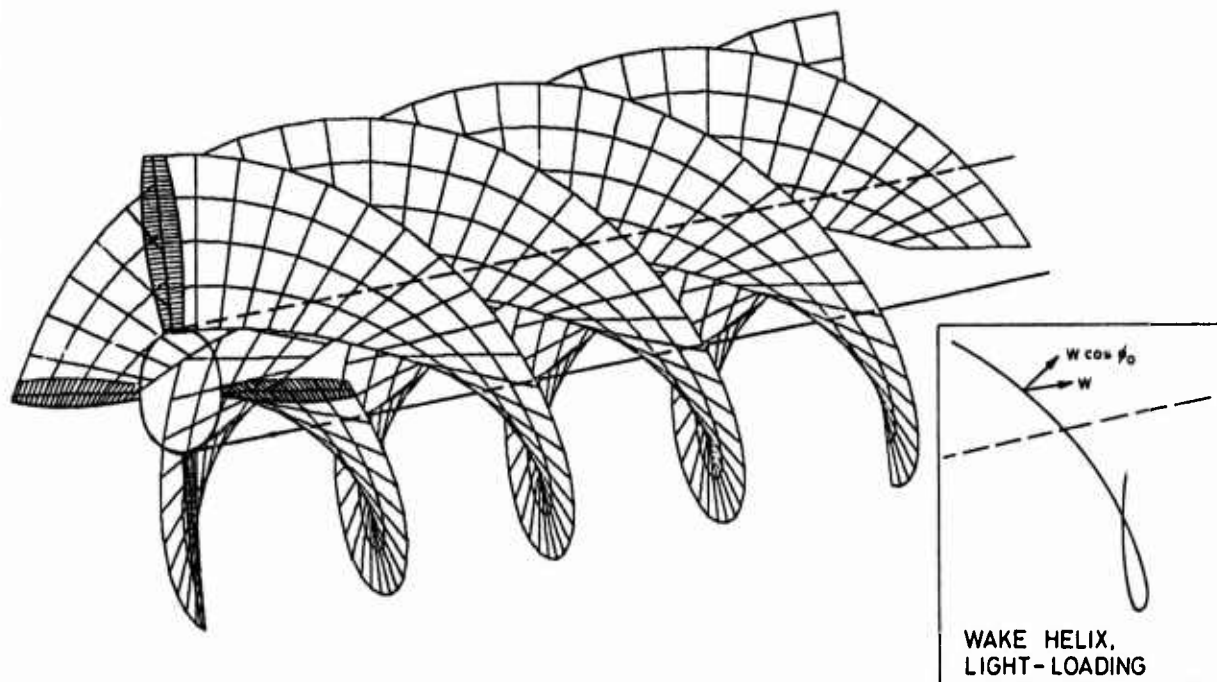
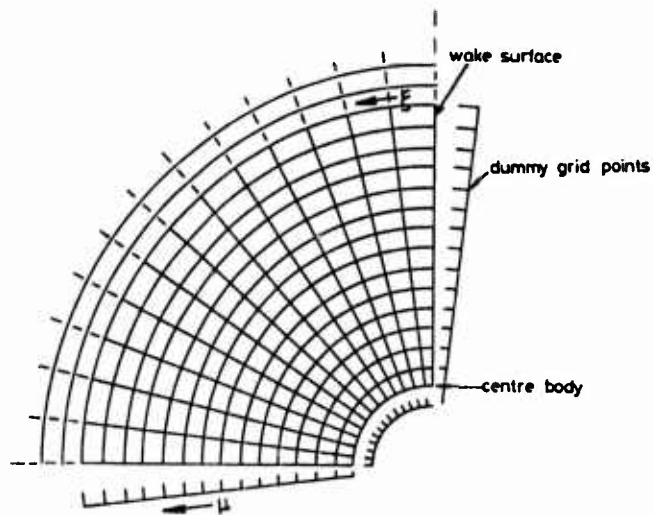


FIG 1 PROPELLER AERODYNAMICS RESEARCH

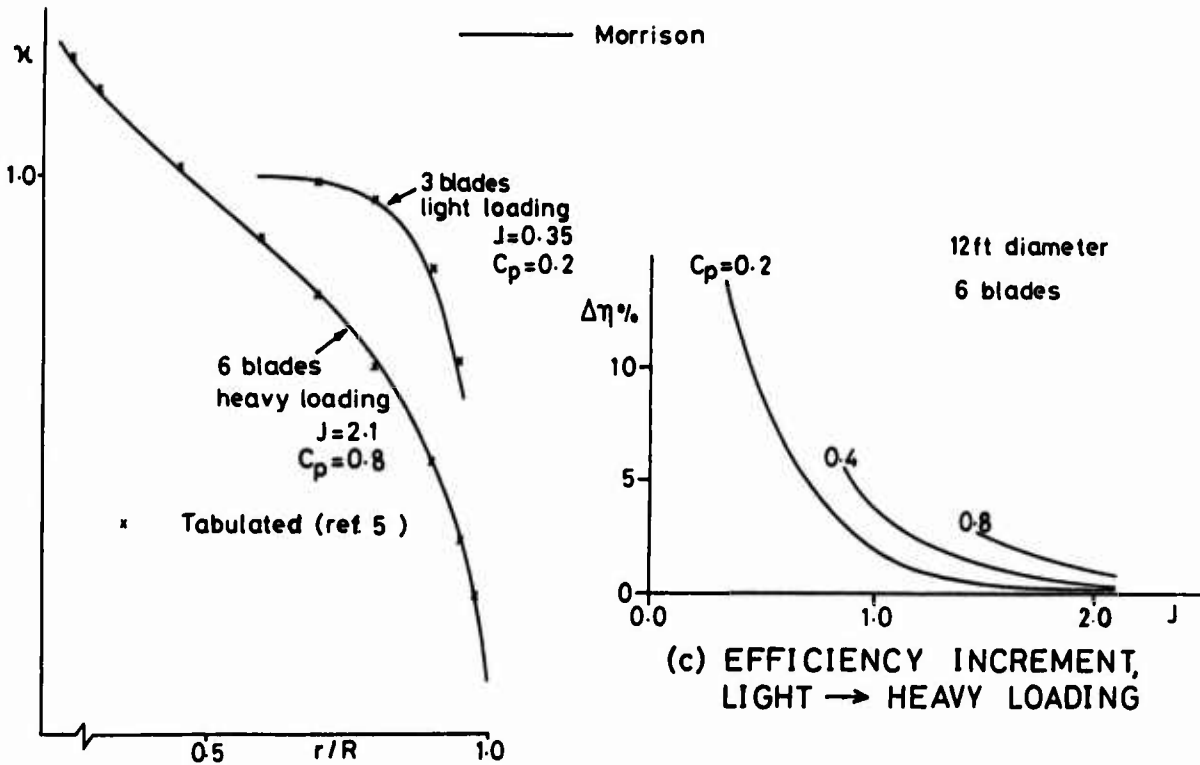
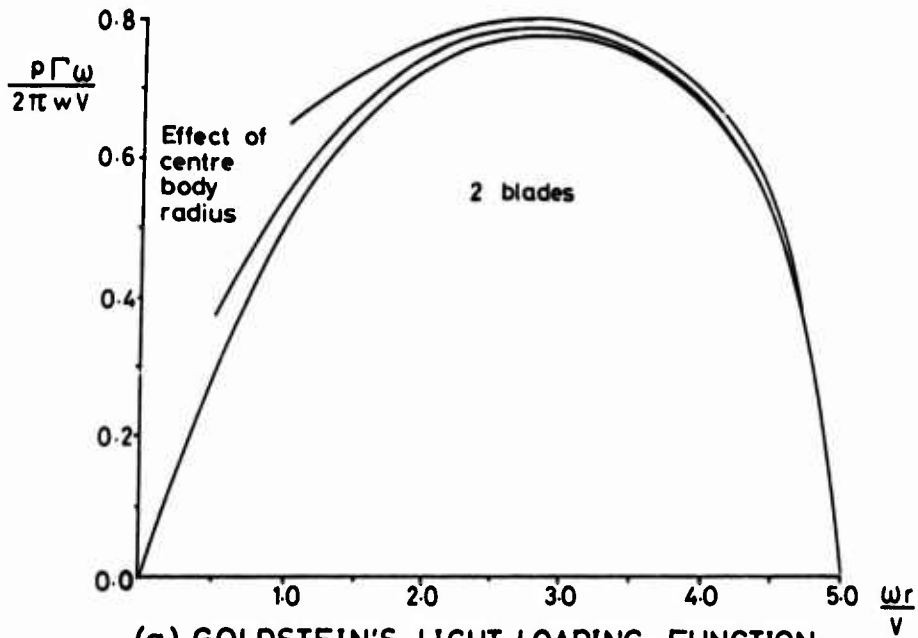


(a) PROPELLER SCREW SURFACES



(b) GRID IN TRANSFORMED WAKE PLANE

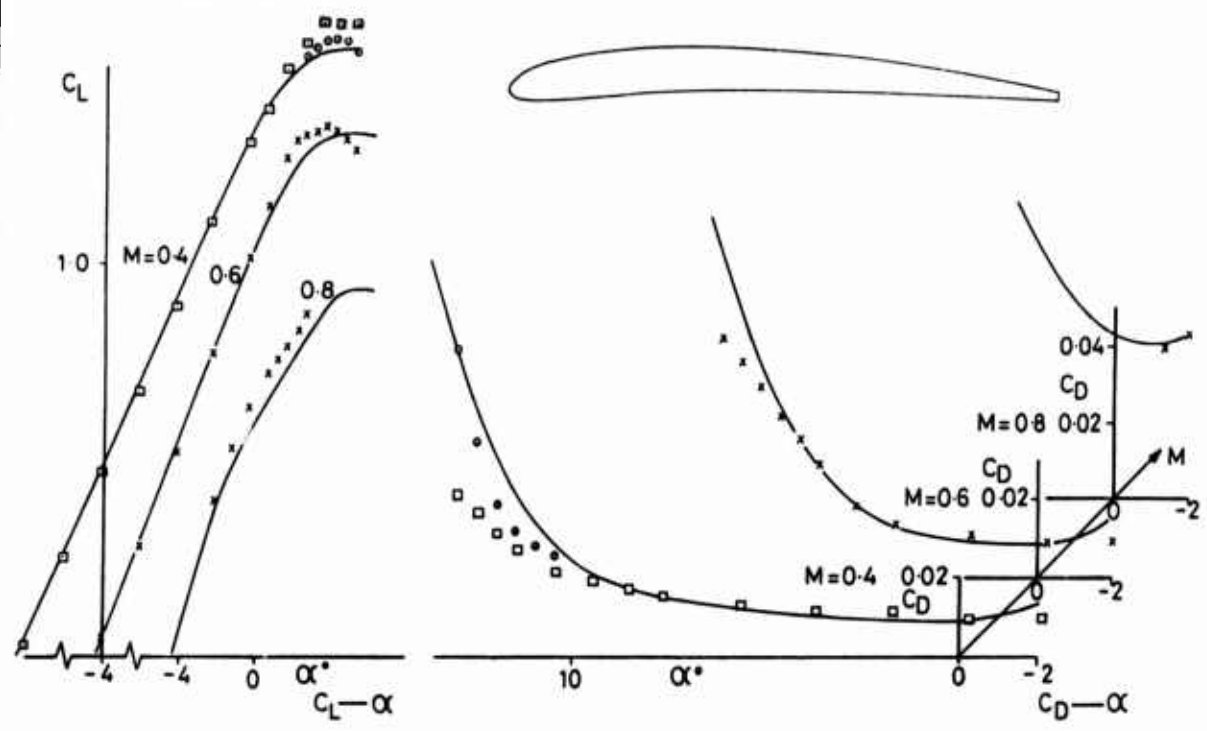
FIG. 2 WAKE MODELLING



(c) EFFICIENCY INCREMENT, LIGHT \rightarrow HEAVY LOADING

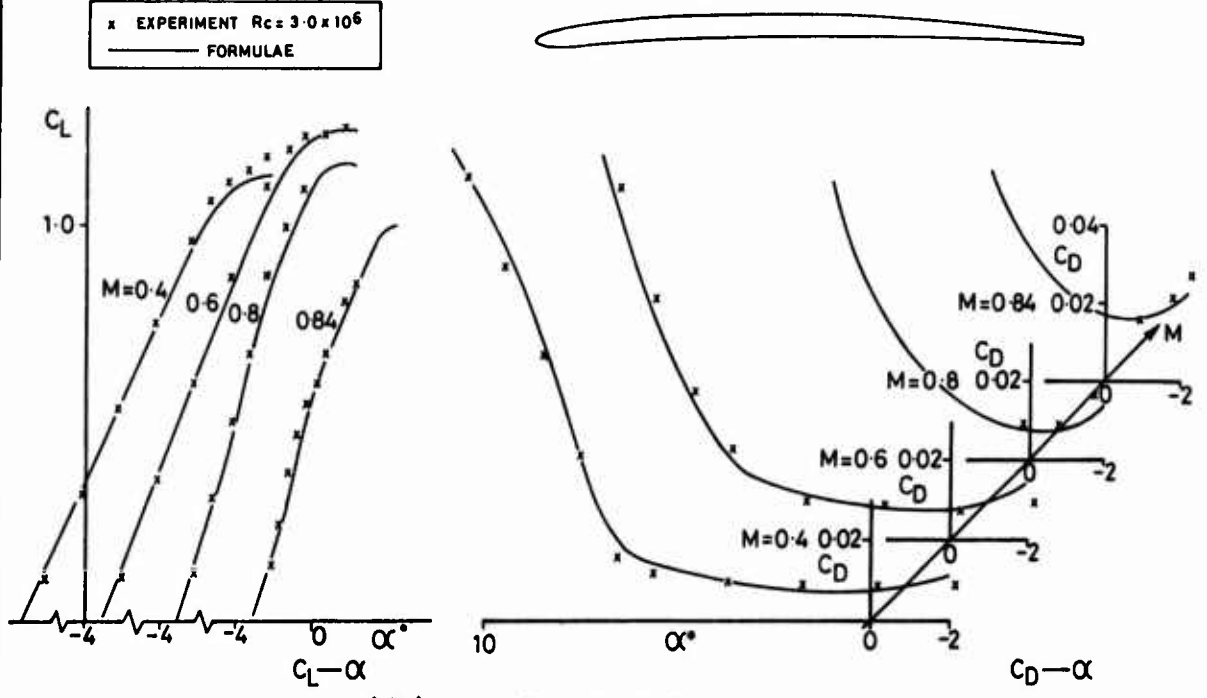
FIG 3 IDEAL WAKE SOLUTIONS

$Rc \times 10^{-6}$	
EXPERIMENT	x 3.5
	□ 2.4
	○ 1.5
FORMULAE	—



(a) $t/c=8\%$ $K1=1.0$

x	EXPERIMENT $Rc=3.0 \times 10^6$
—	FORMULAE



(b) $t/c=4\%$ $K1=0.5$

FIG. 4 AEROFOIL DATA COMPARISONS

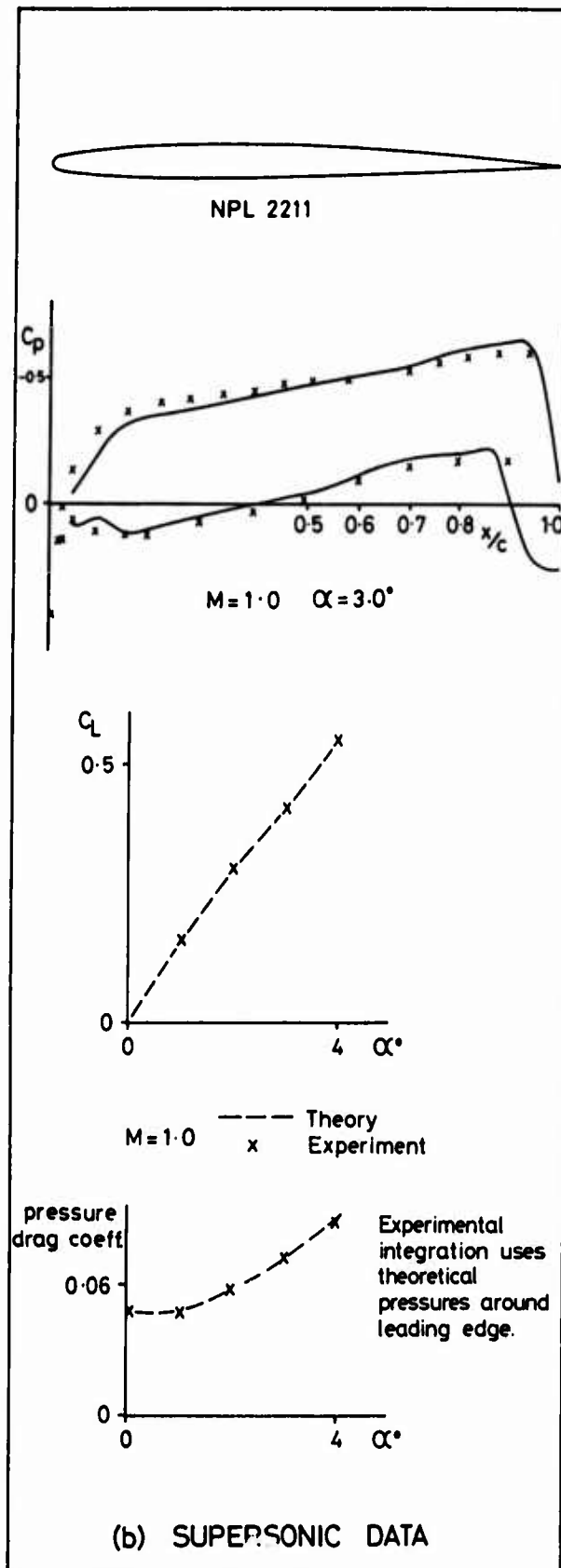
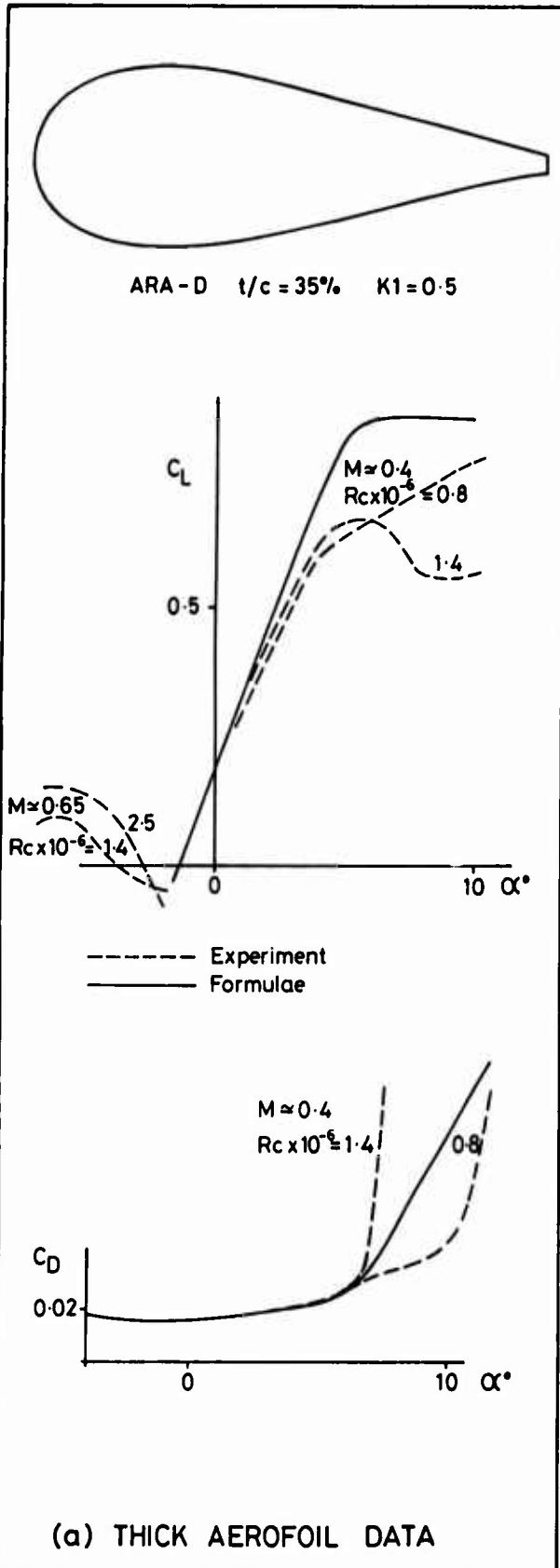
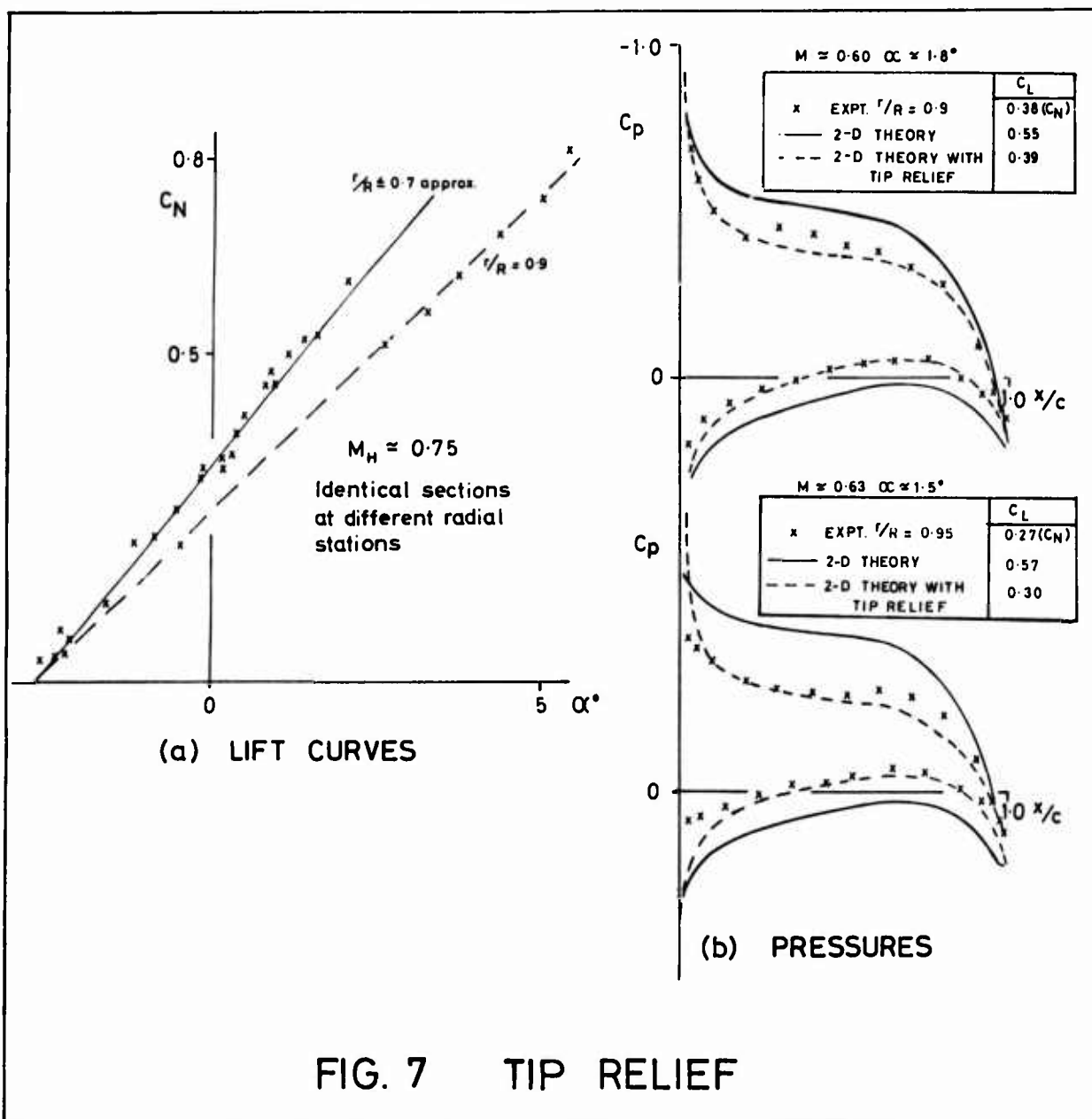
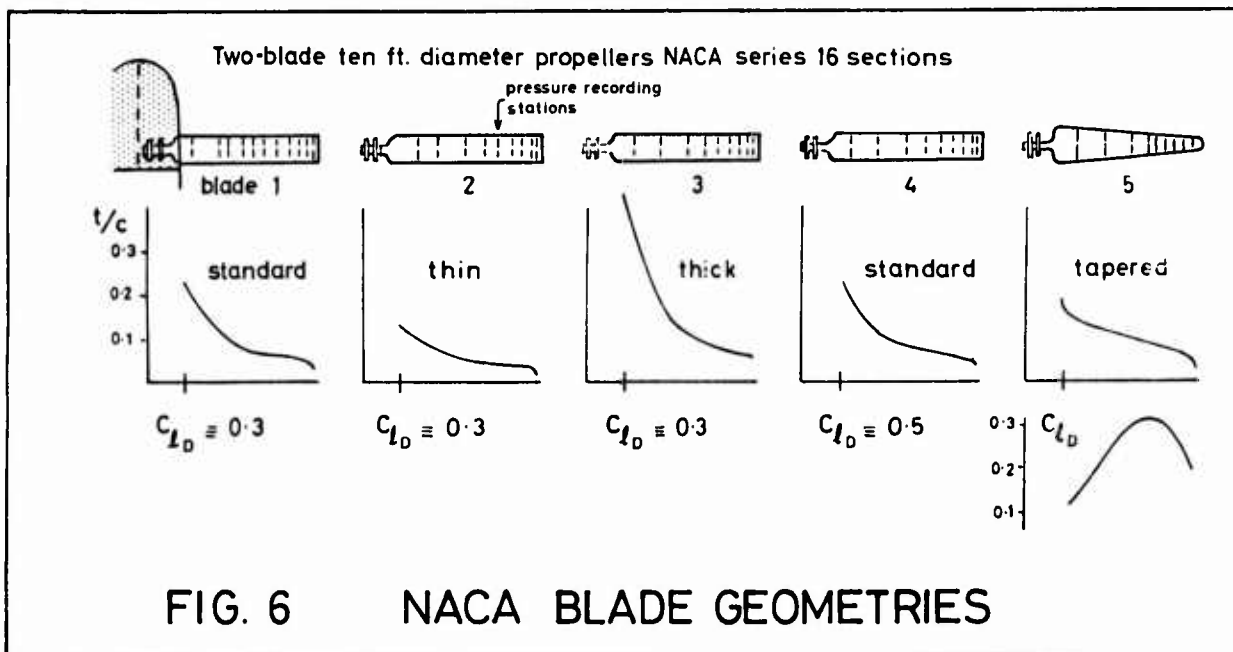
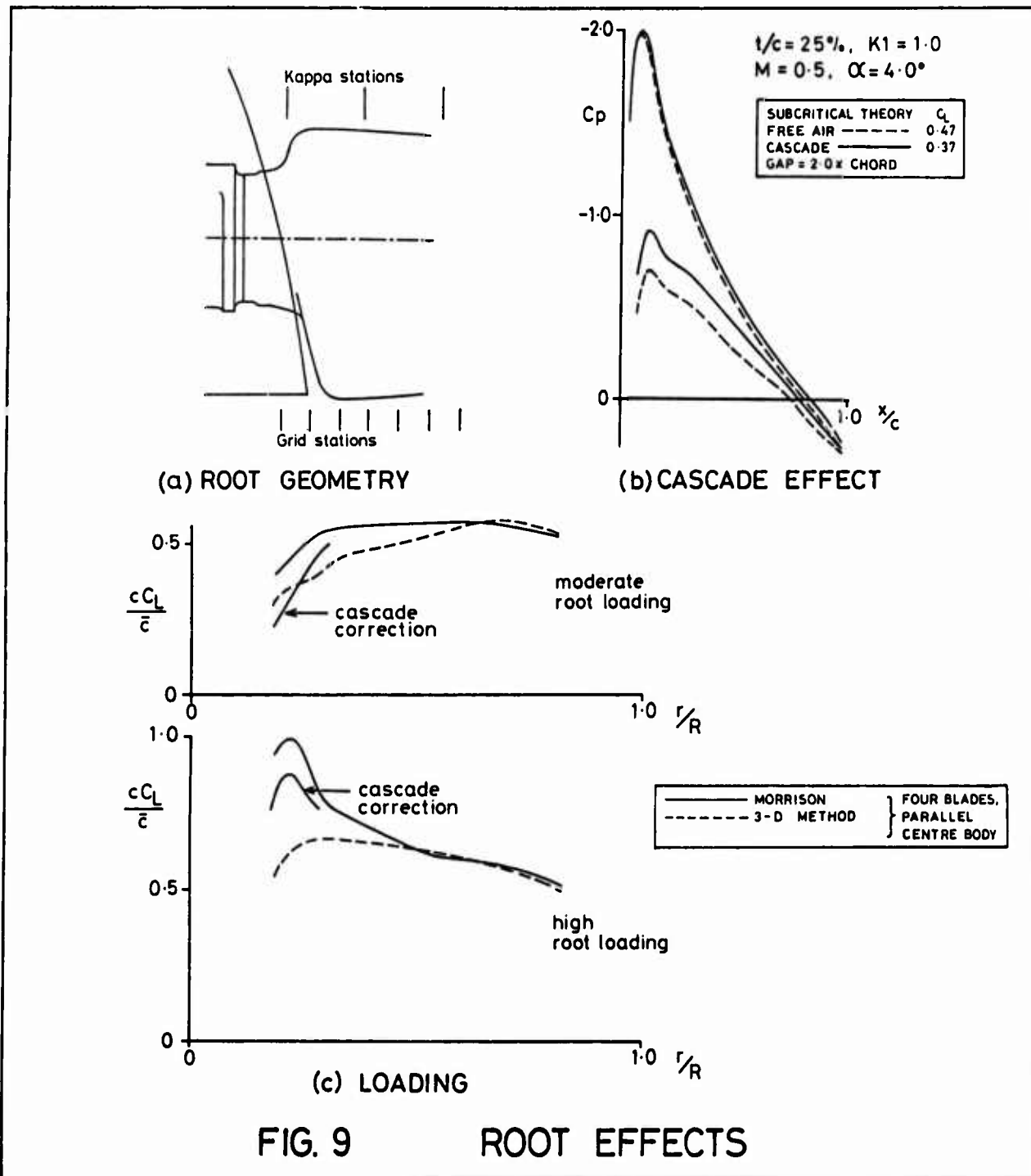
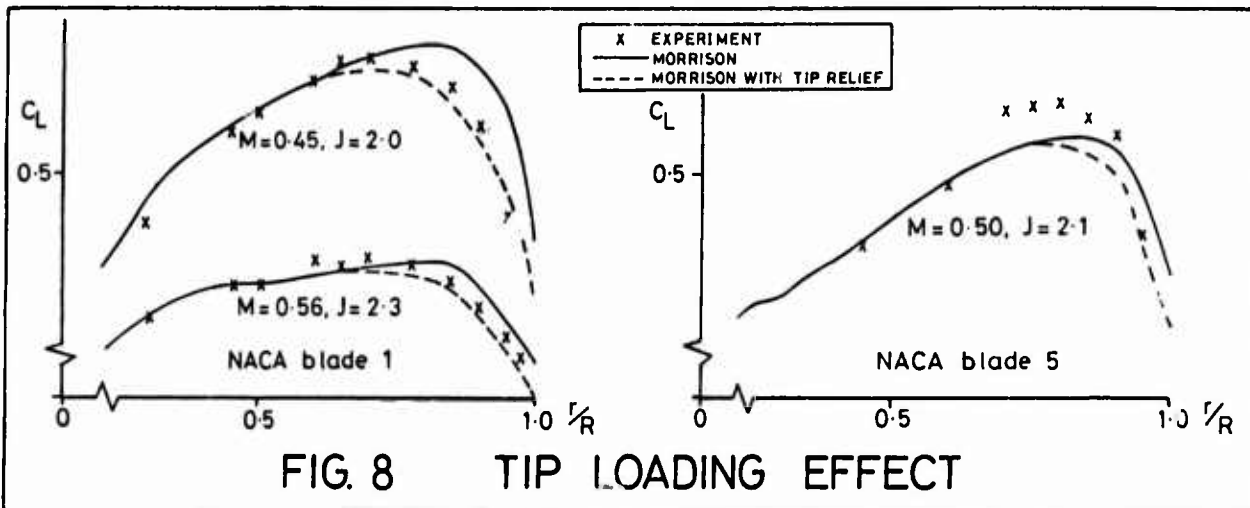
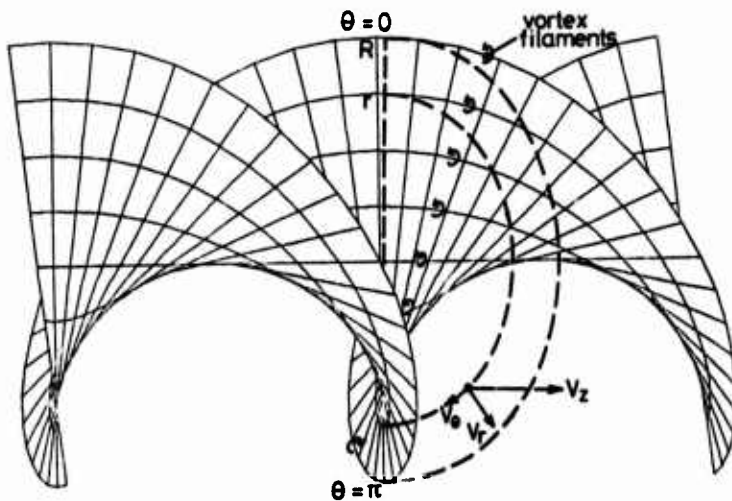


FIG. 5 EXTENDED AEROFOIL DATA

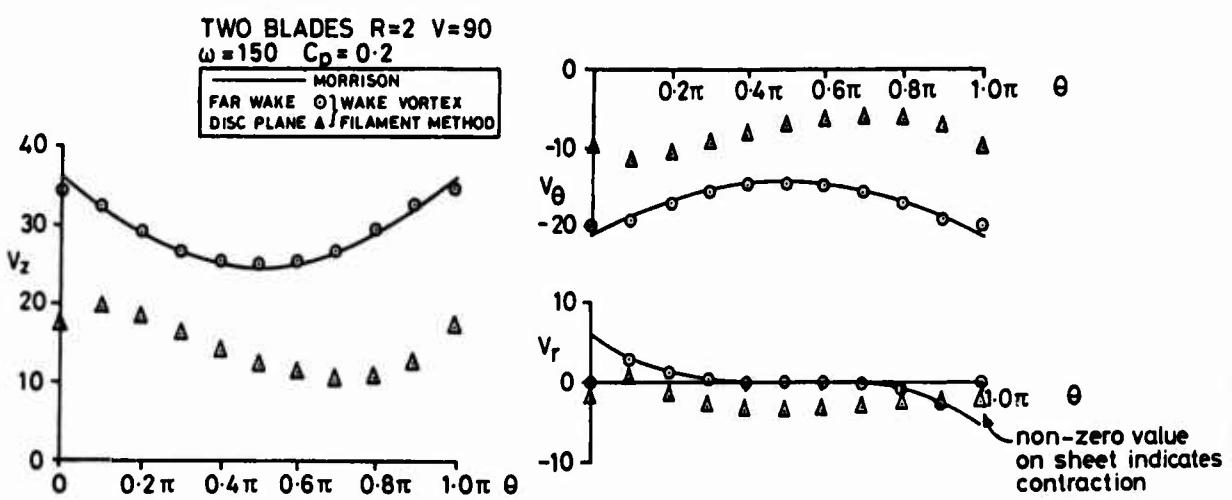




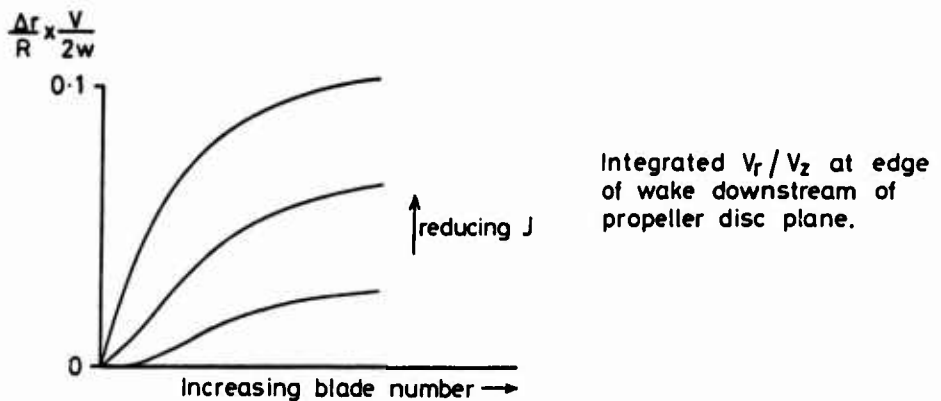


Two blades
Ideal wake

(a) WAKE GRID

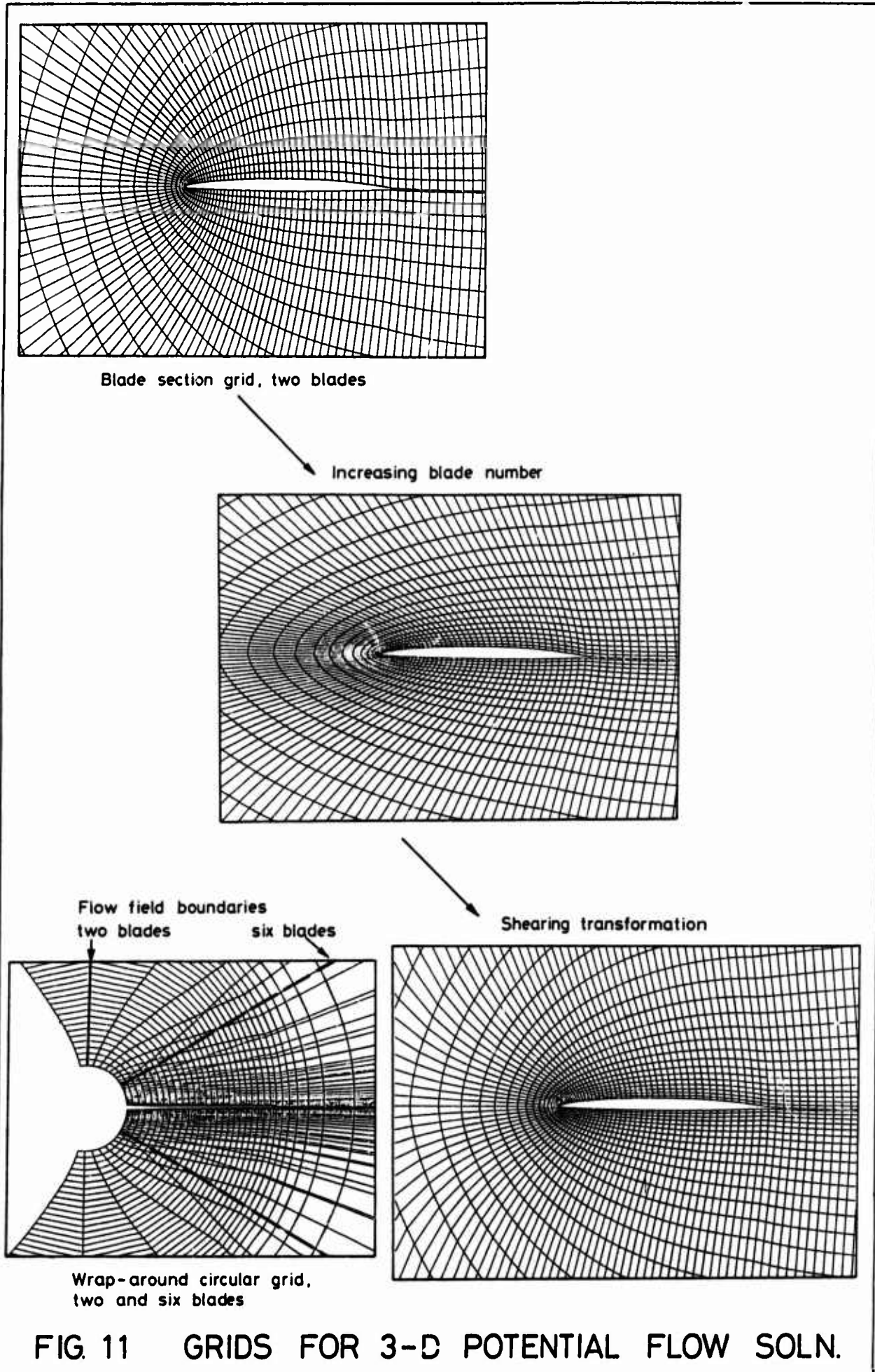


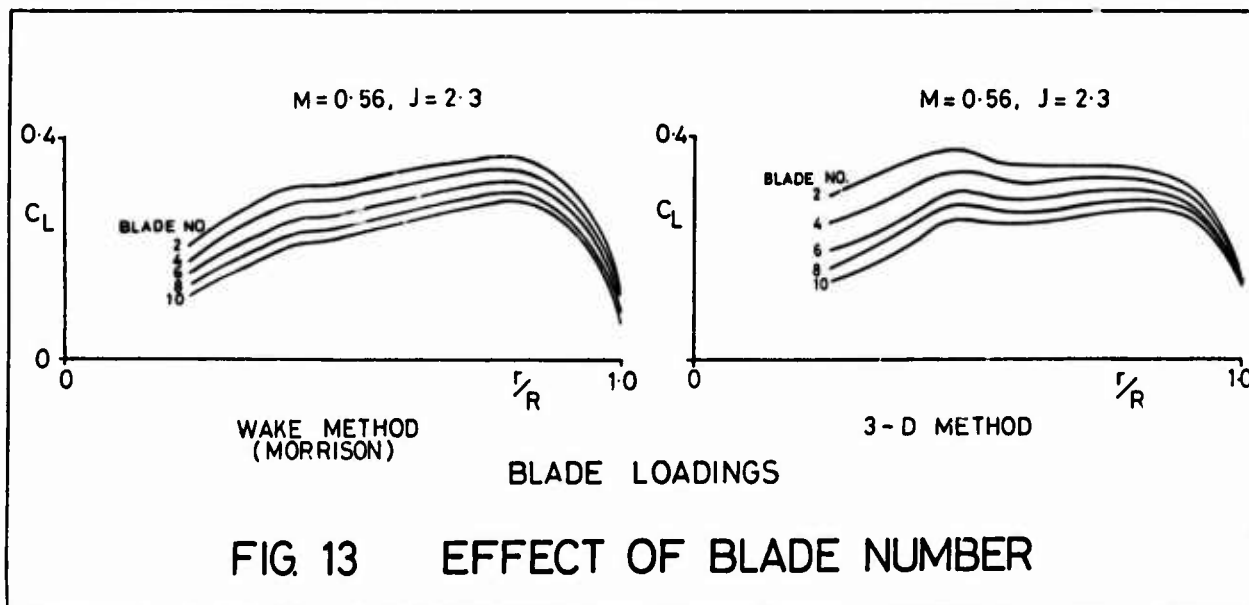
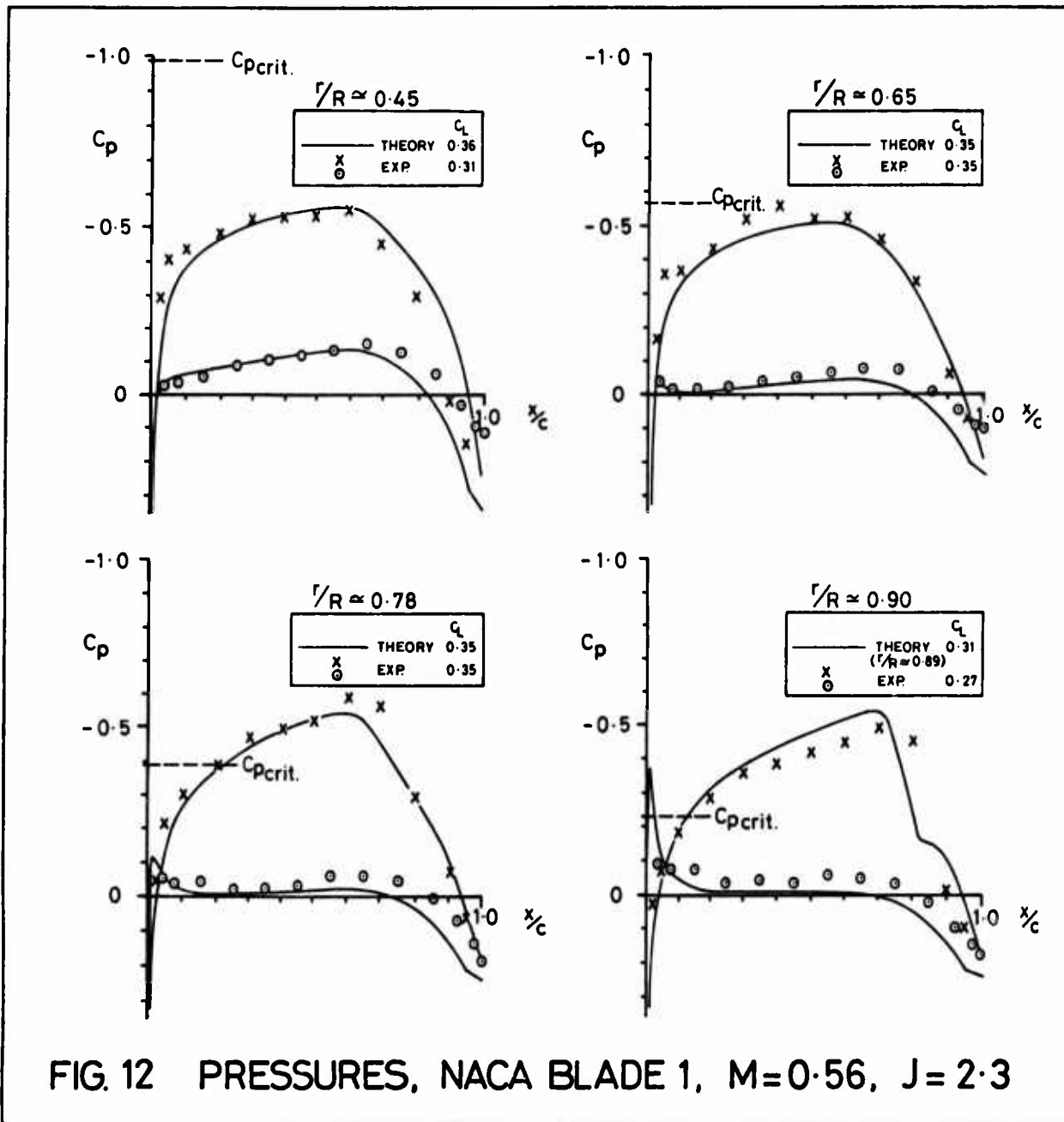
(b) VELOCITIES AROUND CIRCUMFERENTIAL LINE $r/R = 0.5$



(c) WAKE SHEET CONTRACTION

FIG 10 WAKE SHEET INDUCED VELOCITIES





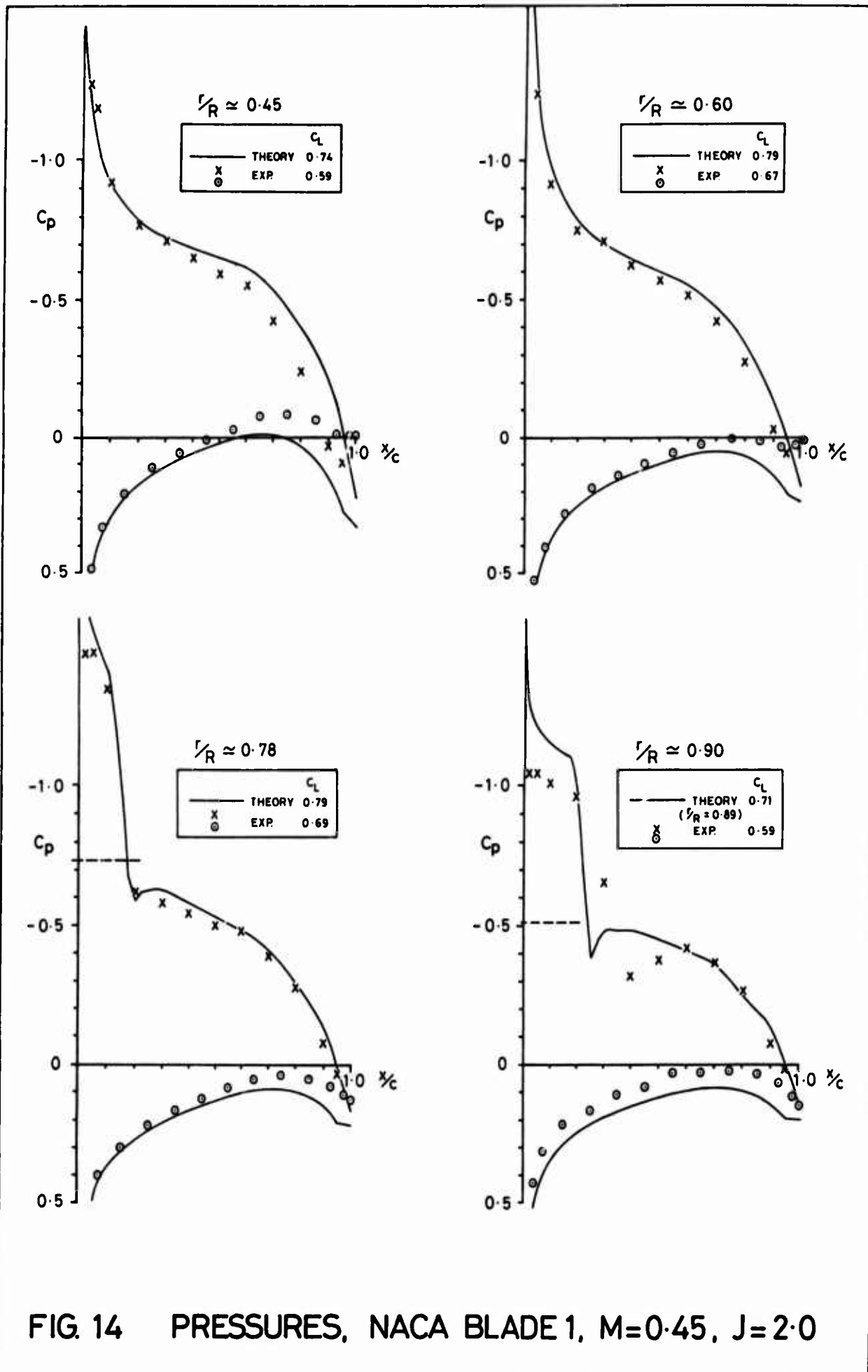


FIG. 14 PRESSURES, NACA BLADE 1, $M=0.45$, $J=2.0$

PROFILS MODERNES POUR HELICES
 Mme A.M. RODDE[✶] et MM. J.J. CUNY^{✶✶} et J.J. THIBERT[✶]

RESUME

En 1982, l'ONERA et la Société RATIER-FIGEAC ont entrepris la définition d'une nouvelle famille de profils aérodynamiques, adaptés aux pales d'hélices.

Au total, quatre profils ont été définis avec des épaisseurs relatives de 4, 7, 12 et 20%.

Des essais en soufflerie ont permis de vérifier les gains de performances aérodynamiques escomptés par comparaison avec un profil NACA 16707 de référence, soit :

- Gain de finesse en croisière : 43%
- Gain de finesse en montée : 8%
- Amélioration du C_z maximal : 15%
- Mach critique équivalent mais avec un plus faible niveau de traînée.

La première application de ces nouveaux profils se fera sur une pale tout composite destinée à l'avion TRANSALL.

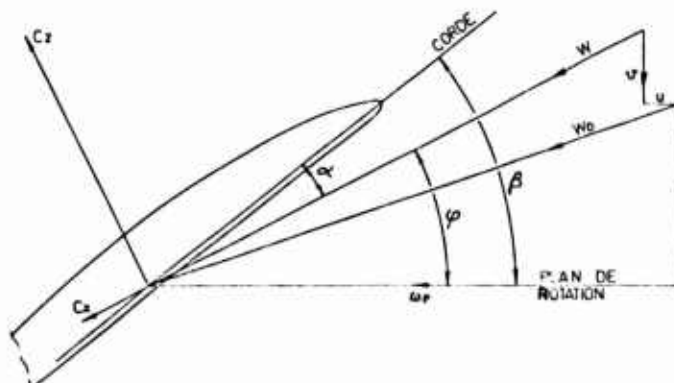
LISTE DES SYMBOLES -

C	corde de référence du profil
C_z	coefficient de portance
C_x	coefficient de traînée de sillage
C_m	coefficient de moment à 25% de la corde
Re	nombre de Reynolds rapporté à la corde
K_p	coefficient de pression
F	finesse du profil
φ	angle entre le vecteur vitesse et le plan de rotation

1 - INTRODUCTION -

La nature des profils aérodynamiques utilisés sur les hélices aériennes a varié au cours des temps en fonction de l'évolution des technologies de fabrication et des performances des avions. Des profils comme le Clark Y, à l'intrados plan, ou encore le RAF 6 et le NACA 24 00-34 ont équipé toute la génération des hélices en bois. L'apparition des pales métalliques a entraîné une diminution générale de l'épaisseur des profils ainsi que l'utilisation, en extrémité de pale principalement, des profils de la série NACA 16. Ce type de profil, encore largement utilisé de nos jours, cède progressivement la place à des profils modernes dont la conception est dérivée de celle des nouveaux profils pour ailes d'avions ou pour pales d'hélicoptères.

Ces nouveaux profils sont définis à l'aide des méthodes récentes de calcul qui permettent une évaluation plus précise de leurs caractéristiques aérodynamiques, notamment en écoulement transsonique. Les améliorations des performances des hélices qui en découlent sont notables, surtout aux basses vitesses. En effet, l'impact de la finesse des profils sur le rendement des hélices est d'autant plus important que la vitesse d'avancement est faible.



[✶] ONERA, 29 av. de la Division Leclerc 92320 CHATILLON (FRANCE)
^{✶✶} Ste RATIER FIGEAC 46100 FIGEAC (FRANCE)

En première approximation, le rendement élémentaire d'une tranche s'exprime par :

$$\eta = \kappa \cdot \operatorname{tg} \varphi \cdot \frac{(F - \operatorname{tg} \varphi)}{(F + \operatorname{cotg} \varphi)}$$

ce qui est équivalent au premier ordre à :

$$\eta \approx \kappa \cdot \operatorname{tg} \varphi \left(1 - \frac{1}{F} \left(\operatorname{tg} \varphi + \frac{1}{\operatorname{tg} \varphi} \right) \right)$$

On constate que le terme multiplicateur de l'inverse de la finesse est d'autant plus grand que la vitesse est petite. Le minimum de la fonction $\left(\operatorname{tg} \varphi + \frac{1}{\operatorname{tg} \varphi} \right)$ est atteint pour $\varphi = 45^\circ$.

Dans la pratique, l'intégration en envergure du rendement, ou des autres grandeurs aérodynamiques, donne une valeur moyenne correspondant aux grandeurs obtenues à 70% du rayon. D'autre part, l'angle $\varphi = 45^\circ$ à 0,7R correspond à un paramètre d'avancement très important (de l'ordre de 2,2), rarement atteint par les hélices classiques. On peut en conclure que l'impact d'une petite variation de la finesse des profils est d'autant moins importante que la vitesse d'avancement est grande.

En ce qui concerne la définition des nouveaux profils, l'accent a été mis sur la portance maximale au Mach de décollage et sur la finesse au Mach de montée tout en préservant tant les finesesses aux Mach et Cz moyens de croisière que les Mach critiques. Indirectement, une amélioration des performances en croisière est obtenue par la diminution des cordes rendue possible par l'augmentation du Cz maximal.

La technologie des hélices en matériaux composites mise au point par RATIER-FIGEAC nécessite une épaisseur de bord de fuite importante de façon à faciliter le drapage des tissus et à préserver leur résistance au niveau du contournement. Nous avons donc introduit, au stade de définition des profils, une contrainte d'épaisseur de bord de fuite. Nous avons pris en compte, pour cela, les cordes minimales et maximales rencontrées sur les différentes pales réalisées par RATIER et nous avons fixé une épaisseur de culot de 0,9%, ce qui représente un compromis acceptable tant pour le mécanicien que pour l'aérodynamicien.

La philosophie générale qui a présidé à la conception des profils HOR peut se résumer par les propositions suivantes :

- Portance maximale au Mach de décollage.
- Finesse maximale aux Mach et Cz de montée.
- Finesse au moins comparable à celle des profils NACA 16 aux Mach et Cz de croisière.
- Mach critique à faible Cz supérieur au Mach maxi de fonctionnement.
- Epaisseur de bord de fuite importante.

Aucune condition particulière concernant la position du maître couple ou le coefficient de moment des profils n'a été imposée car, en comparaison avec les profils NACA 16, les profils modernes ne peuvent que diminuer les torsions d'origine aérodynamique. Les profils NACA 16 ont en effet un maître couple très reculé puisque situé à 50% de la corde et, avec les cambrures utilisées sur les hélices, ils ont également un Cm important. Les profils modernes ont tendance à avoir un maître couple donc un axe mécanique beaucoup plus proche du bord d'attaque ce qui diminue considérablement la part de la torsion due au bras de levier de la portance, l'autre part provenant des Cm restant du même ordre de grandeur que pour les profils de référence. Sans imposer de contraintes sur le Cm et le maître couple, nous étions assurés de ne pas augmenter, voire de diminuer, les contraintes de torsion dans les pales. Cette absence de contrainte donne une certaine liberté pour la conception des profils puisque les contraintes en Cm sont très pénalisantes pour la portance maximale et le fait de pouvoir déplacer le maître couple vers l'arrière sur les sections les plus fines permet une augmentation du Mach critique de ces sections.

2 - CAHIER DES CHARGES -

La première phase de cette étude a consisté à fixer un cahier des charges le plus précis possible. Nous sommes partis de l'examen statistique de la géométrie et des conditions de fonctionnement d'hélices connues. En effet, la position en envergure d'un profil d'épaisseur donnée n'est pas uniquement fonction de contraintes aérodynamiques mais également de contraintes mécaniques et vibratoires. Une approche uniquement aérodynamique du problème aurait risqué de conduire à des profils inutilisables car non adaptés aux conditions de fonctionnement réellement rencontrées sur les hélices.

Cette approche statistique a permis de constater que la géométrie des pales est relativement peu variable d'une hélice à l'autre. Nous avons choisi, pour notre étude, de prendre en compte les trois points de fonctionnement fondamentaux des hélices : le décollage, la montée et la croisière. Chacun de ces trois points de fonctionnement a une grande importance pour les performances de l'avion. La traction au décollage détermine le couple distance de décollage-masse au décollage. Le rendement en montée détermine parfois la masse décollable (cas de panne moteur sur bimoteur), parfois simplement un temps de montée donc la rentabilité du vol. Le rendement de croisière détermine, bien entendu, la dépense en carburant pendant le vol.

Le premier travail a consisté à choisir l'épaisseur relative des profils de référence. Nous avons constaté que, sur nos hélices, les épaisseurs d'extrémité de pale ne descendent que rarement en dessous de 4%, principalement pour des raisons structurales. Nous avons donc pris cette valeur comme épaisseur relative minimale. Comme il nous était possible, compte tenu des impératifs économiques, d'étudier au total quatre profils, nous avons donc trois autres épaisseurs relatives à choisir.

L'estimation des performances de profils d'épaisseur relative supérieure à 20% étant difficile du fait de la présence de décollements, nous avons pris cette valeur comme limite supérieure.

Les deux profils restants ont été choisis avec des épaisseurs de 7 et 12%. Ces valeurs permettent une répartition régulière en envergure. De plus, les conditions de fonctionnement de ces deux sections sont relativement sévères ce qui permet une bonne optimisation de la zone de corps de pale où elles se situent.

Partant de ces considérations, nous avons tracé les réseaux de courbes de fonctionnement aérodynamique de diverses hélices. Le premier faisceau fig. 1 nous a donné la répartition des nombres de Mach en fonction de la position en envergure choisie pour les profils, pour les trois conditions de fonctionnement choisies. Nous en avons déduit une valeur moyenne du Mach de fonctionnement pour les profils de 4, 7, 12 et 20% d'épaisseur relative.

Les nombres de Mach ainsi obtenus sont vus par des profils tridimensionnels et en rotation. Ces deux éléments ont une influence favorable sur le Mach critique, influence qui est malheureusement difficile à chiffrer. Nous avons donc décidé de prendre un nombre de Mach de référence réduit de $\Delta M = 0,05$ pour le profil d'extrémité de pale (4% d'épaisseur) et de $\Delta M = 0,03$ pour le profil de 7% d'épaisseur. Ces nouvelles valeurs de nombre de Mach seront appelées par la suite "Mach bidimensionnels" et serviront de valeur de référence pour les essais en soufflerie.

En ce qui concerne les C_z de fonctionnement des différentes sections ils ont été soit déduits des courbes de performances d'hélices connues soit recalculés à partir des géométries et des données de puissance et de vitesses. Les plages ainsi obtenues sont tracées fig. 2. Pour le cas du décollage nous avons obtenu une zone de C_z maximal des profils NACA 16, la largeur de cette zone correspondant aux variations du C_z maximal en fonction des cambrures utilisées. Nos valeurs-objectifs ont été mises délibérément au-delà du maximum observé sur les profils classiques.

La courbe de C_z en montée définit une large zone de fonctionnement. Là encore, nous avons choisi de nous situer à des valeurs importantes de portance de façon à insister sur les caractéristiques de finesse à fort C_z .

La courbe au point de croisière définit une plage de fonctionnement plus réduite. Nos valeurs-objectifs ont, cette fois, été choisies au niveau de C_z le plus bas rencontré sur les hélices étudiées. Ce choix de C_z d'adaptation relativement faible conduit à des profils peu cambrés possédant une plage de bon fonctionnement en C_z plus étendue que les profils du type NACA 16.

Les objectifs de finesse, pour les cas de montée et de croisière ont été plus délicats à cerner. Il est difficile, en effet, de connaître, de façon réaliste, les traînées des profils NACA 16 aux C_z et Mach de références. Nous avons fait pour cela une compilation des résultats expérimentaux de provenances diverses et nous en avons tiré un objectif réaliste (fig. 3). Les finesses demandées au point de montée sont autour de 100 pour les profils de 7 et 12% et autour de 65 pour les profils de 4 et 20%.

Les finesses-objectifs au point de croisière sont décroissantes en fonction de l'épaisseur, de 60 pour le 4% à 40 pour le 20%.

Nous sommes conscients du fait que ces valeurs sont globalement assez élevées mais elles constituent un objectif réaliste et, surtout, elles mettent bien en valeur les points-clés de cette étude.

Le cahier des charges ainsi obtenu pour les différents profils est présenté fig. 4. Les plages de nombre de Reynolds figurant dans ce cahier des charges correspondent aux valeurs extrêmes de Reynolds rencontrées sur les hélices étudiées.

Pour les essais en soufflerie, nous désirions disposer d'un profil de référence, du type NACA 16, pour pouvoir quantifier les écarts de performance de façon indiscutable. Nous avons choisi un profil NACA 16 707 de 7% d'épaisseur avec un C_z d'adaptation de 0,7. Cette dernière valeur est très importante et correspond au maximum de ce que l'on rencontre sur les hélices. Elle a cependant été choisie car elle permet une comparaison de la portance maximale du profil HOR 07 et de sa finesse à fort C_z avec celles d'un profil classique très cambré.

3 - DEFINITION DES PROFILS HOR -

Quatre profils ont été définis pour répondre au cahier des charges. Leur appellation est HORxx, HOR désignant le nom de la famille et les 2 derniers chiffres l'épaisseur relative. Les dessins de ces 4 profils sont présentés figure 5.

Les performances des profils ont été calculées à l'aide d'un programme de calcul [Réf. 1] résolvant l'équation complète du potentiel à l'aide d'un schéma non conservatif avec prise en compte des effets visqueux par épaissement du profil. L'épaisseur relativement forte du bord de fuite des profils HOR (épaisseur de 0,9% de la corde fixée par le cahier des charges pour des raisons technologiques) conduit avec ce type de calcul à certaines imprécisions au niveau du bord de fuite et par conséquent dans la détermination des coefficients globaux de traînée et de moment.

Une méthode de calcul développée à l'O.N.E.R.A. [Réf. 2] qui permet une approche de forte interaction visqueuse pour les couches limites et le sillage a également été utilisée pour le calcul de certaines configurations où il existe des décollements d'étendue limitée notamment pour les calculs à faible C_z pour lesquels les fortes survitesses au niveau du bord d'attaque des profils provoquent un bulbe de décollement.

Pour chaque position en envergure, les objectifs fixés par le cahier des charges sont :

- à faible nombre Mach un C_z max élevé supérieur à celui du profil NACA 16 de même épaisseur relative et de cambrure adaptée correspondant aux conditions de décollage. L'estimation du C_{zmax} des 2 profils les

plus épais 20 et 12% d'épaisseur relative a été effectuée en utilisant comme critère la valeur du K_p mini à l'extrados au décrochage déduite des essais en soufflerie sur des profils similaires. Pour les profils les plus minces, où il existe un choc à l'extrados, c'est le nombre de Mach avant le choc qui a été utilisé pour estimer le C_{zmax} des profils ;

- une finesse élevée à un niveau de C_z intermédiaire (condition de montée) ;
- un nombre de Mach de divergence de traînée ($dC_x/dM \approx 0.4$) et une finesse équivalents à ceux des profils NACA 16 (conditions de croisière).

Les performances des profils HOR dans ces 2 configurations ont été directement déduites des calculs, de nombreuses comparaisons calcul-expérience ayant montré que les performances (C_x , M_{dx} , répartition de pressions) étaient bien prévues.

Les Profils HORxx ont été définis en choisissant une loi d'épaisseur et une loi de cambrure :

- une loi d'épaisseur dont le maximum se situe vers 25% de la corde (fig. 6), position très avancée par rapport aux profils NACA 16 ce qui entraîne un accroissement favorable du rayon de bord d'attaque ;
- une loi de cambrure avec un maximum à 50% de la corde (fig. 6) et dont le niveau est adapté aux conditions de fonctionnement imposées par le cahier des charges.

Les lois ainsi définies ont été légèrement modifiées au cours du processus itératif de définition des profils les plus minces afin d'adapter avec plus de précision ces profils aux demandes du cahier des charges.

3.1 - Définition des profils pour les sections les plus internes de la pale -

Pour ces profils HOR20 et HOR12 épais respectivement de 20 et de 12% les lois d'épaisseur et de cambrure prévues n'ont pas été modifiées.

Les répartitions de pression calculées dans les 3 configurations caractéristiques de vol du profil HOR20 tracées fig. 7 montrent le bon comportement du profil dans tous les domaines de vol :

- faible niveau de survitesse au voisinage du C_{zmax} ;
- niveau de traînée conforme au cahier des charges dans les conditions de montée et de croisière où même $M = 0.5$, le calcul ne décèle aucun décollement.

La comparaison des répartitions calculées dans les mêmes conditions sur les profils HOR12 et NACA 16912, choisi comme profil de référence à cette section de pale tracées figure 8 permet de constater que l'avancement du maître couple du profil HOR12 à 25% de la corde permet :

- au voisinage du décrochage une recompression par choc au niveau du bord d'attaque où la couche limite est encore mince suivie d'une recompression dont le gradient diminuant progressivement permet d'éviter la forte recompression au niveau du bord de fuite observées sur le profil NACA 16912.
- à faible niveau de C_z et fort nombre de Mach (condition de croisière) d'éviter la forte survitesse au bord d'attaque intrados existant sur le profil NACA du fait de son faible rayon de bord d'attaque.

3.2 - Définition du profil pour les sections à mi-envergure (HOR07)

Pour le profil de 7% d'épaisseur relative, les lois d'épaisseur et de cambrure ont été légèrement modifiées. La partie arrière du profil a été surépaissie à partir de 40% de la corde pour augmenter la charge du profil. Le maximum de la loi de cambrure a été augmenté pour améliorer le C_z max ($y/c_{max} = 4,6\%$) et légèrement déplacé vers le bord d'attaque pour ne pas trop pénaliser le profil en transsonique par recul du choc.

Les répartitions de pression calculées sont comparées figure 9 avec celle du profil NACA 16707. Dans la configuration du décollage la forte survitesse de bord d'attaque existant sur le profil NACA est remplacée par une zone de survitesses plus modérées, terminée par un choc et suivie d'une recompression dont le gradient diminue vers le bord de fuite. Pour la configuration de croisière, la survitesse intrados est très réduite et l'avance de la survitesse maximum extrados de 70% de la corde à 30% permet une recompression moins forte pour la couche limite dans la seconde moitié du profil.

3.3 - Définition de profil pour les sections d'extrémité de pale (HOR04)

Pour le profil HOR04 de 4% d'épaisseur relative le maître couple du profil a été légèrement reculé ($x/c = 30\%$ de la corde) et le maximum de la cambrure limité ($y_c/c = 1,6\%$) pour ne pas pénaliser les performances à fort nombre de Mach et à faible C_z .

Les répartitions de pression tracées figure 10 montrent :

- dans les conditions de décollage une zone supersonique limitée par un choc précédé par une recompression isentropique qui permet de limiter l'intensité du choc.
- en montée, le plateau de pression obtenu permet d'avoir un point de transition assez reculé.
- au niveau du C_z de croisière la survitesse au bord d'attaque intrados reste limitée, et le choc à l'extrados relativement faible.

4 - PERFORMANCES DES PROFILS DE LA FAMILLE HOR -

Les essais des 3 profils HOR12, HOR07 et HOR04 ainsi que ceux du profil NACA 16707 de 7% d'épaisseur relative ont été effectués à la soufflerie S3 de Modane.

Les maquettes qui ont été utilisées ont une corde de 200 mm et sont équipées de 90 prises de pression statique pour les profils de 12 et 7% d'épaisseur relative et de 50 prises pour le profil de 4%. Les essais ont eu lieu en veine perméable, en transition naturelle et à une pression génératrice variable permettant de respecter les nombres de Reynolds des différents cas de fonctionnement fixés par le cahier des charges correspondant à une utilisation sur hélice de grand diamètre.

Les coefficients globaux des profils C_z , C_x , C_m ont été déterminés par intégration des mesures de pression sur le profil et dans le sillage. Les résultats présentés sont les résultats corrigés des effets de parois haute et basse de la soufflerie par une méthode de signatures [Réf. 3].

Le profil HOR20 de 20% d'épaisseur relative a été essayé à la soufflerie S10 du CEAT sur une maquette de 500 mm de corde non équipée de prises de pression. Les efforts globaux de portance et de moment de tangage ont été déduits des pesées et la traînée a été déterminée à l'aide de sondages de pression dans le sillage du profil.

4.1 - Profil d'emplanture HOR20 -

Les performances mesurées du profil HOR20 (figure 11) montrent que les exigences du cahier des charges ont été atteintes ($C_z \text{ max} = 1,59$ à $M = 0,2$, $M_{dx} = 0,5$ à $C_z = 0,4$) sauf en ce qui concerne la finesse de croisière.

Comparativement aux performances qui avaient été estimées par le calcul, le $C_z \text{ max}$ et le nombre de Mach de divergence de traînée sont bien prévus mais les niveaux de la traînée en montée et en croisière sont fortement sous-estimés.

4.2 - Profil HOR12 -

La figure 12 qui récapitule les performances globales du profil HOR12 de 12% d'épaisseur relative montre les bonnes performances obtenues pour le $C_z \text{ max}$ (1,68 à $M = 0,45$) et le nombre de Mach de divergence de traînée ($M_{dx} = 0,69$ à $C_z = 0,4$) tout en conservant des niveaux de finesse en accord avec le cahier des charges.

La comparaison calcul-expérience des performances globales ou des répartitions de pressions obtenues dans les 3 configurations caractéristiques de vol (figure 13) montre une bonne concordance générale, mais la présence d'un bord de fuite épais ($e/c = 0,9\%$ de la corde) qui n'est pas prise en compte par le calcul par couplage faible conduit à des niveaux de pressions erronés au bord de fuite du profil et par conséquent à des coefficients de traînée calculés trop faibles. En effet, la présence de ce culot épais conduit à un K_p expérimental au bord de fuite voisin de 0 valeur inférieure à celle fournie par le calcul ou mesurée sur des profils à culot moins épais $K_p \sim 0,15$. Traduit en traînée cet écart de K_p donne un $\Delta C_x \sim 0,0013$.

Cette estimation bien que grossière, montre cependant que, en retranchant ce ΔC_x au C_x mesuré, on retrouve un niveau de traînée voisin de celui calculé.

4.3 - Profil HOR07 -

Les performances du profil HOR07 peuvent être comparées directement à celles du profil NACA 16707 essayé dans les mêmes conditions à la soufflerie S3 de Modane. On notera toutefois que le profil NACA n'a pas de culot au bord de fuite.

Les résultats du profil HOR07 sont supérieurs à ceux du profil NACA 16707 sur tous les points figurant au cahier des charges (figure 14) :

- amélioration de 15% du $C_z \text{ max}$ à $M = 0,55$
- nombres de Mach de divergence de traînée équivalents des 2 profils mais obtenus à un C_x plus faible sur le HOR07 malgré la forte épaisseur de son bord de fuite.
- amélioration de la finesse de montée (+8%)
- amélioration de la finesse de croisière (+43%) qui reste toutefois inférieure à celle du cahier des charges.

Figure 15 où sont tracées les répartitions de pression mesurées sur les 2 profils, et celle calculée sur le HOR07 on notera au voisinage du $C_z \text{ max}$ la survitesse plus faible obtenue sur le HOR07 et la forme plus adaptée de la recompression qui la suit. Les répartitions de pression obtenues dans les conditions de montée et de croisière sont bien reproduites par le calcul mais le coefficient de traînée est comme pour le HOR12 nettement sous-estimé du fait de la forte épaisseur de bord de fuite.

La méthode de calcul [ref.2] comprenant une approche de forte interaction visqueuse pour les couches limites et le sillage et qui prend en compte les faibles décollements qui apparaissent au voisinage du bord d'attaque intrados dans la configuration de croisière permet de calculer avec une meilleure précision l'évolution de la traînée en fonction du nombre de Mach (fig. 16).

Une nouvelle méthode de définition de profils utilisant les techniques d'optimisation numérique ayant été développée à l'O.N.E.R.A. [Réf. 4], une application a été effectuée sur le profil HOR07 conduisant à un profil légèrement modifié HOR07 ϕ (figure 17).

En effet, compte tenu des résultats obtenus sur le HOR07 il a semblé possible de le modifier de la manière suivante :

- modifier l'extrados pour diminuer l'intensité du choc dans les conditions de décollage montée ($M = 0,55$ $C_z = 1,35$) et augmenter ainsi le C_z max ;
- modifier l'intrados pour diminuer l'intensité du choc dans les conditions de croisière ($M = 0,7$ $C_z \approx 0,4$) et augmenter ainsi le nombre de Mach de divergence de traînée.

La technique utilisée est basée sur l'optimisation numérique. L'organigramme de la méthode de calcul employée est présenté figure 18.

Le programme est constitué de trois modules indépendants :

- a) un programme de calcul aérodynamique fournissant pour une géométrie et des conditions à l'infini amont (Mach et incidence) les caractéristiques aérodynamiques (pressions, C_z , C_x , C_m) compte tenu des effets visqueux [Réf. 1] .
- b) une bibliothèque de fonctions de modification de la géométrie du profil initial. Cette bibliothèque est constituée de 6 polynômes de Legendre modifiant la géométrie entre 0 et 50% de la corde et assurant les continuités de pentes et de courbure à $x/c = 0$ et $X/c = 0,50$.
- c) un programme d'optimisation numérique dont le rôle est de choisir la combinaison optimale des fonctions de modification (6 variables de décision) pour obtenir les objectifs visés compte tenu des contraintes imposées.

Le profil ainsi obtenu HOR07 ϕ ne présente que de faibles différences géométriques avec le profil HOR 07 initial ; toutefois la vérification expérimentale qui a été effectuée à la soufflerie S3 de Modane a montré que le profil HOR07 ϕ possédait des performances légèrement supérieures à celles du profil HOR07.

La comparaison des performances des 2 profils aux points d'optimisation montre dans les conditions de montée figure 19 une réduction du coefficient de traînée ($\Delta C_x = 21\%$). Dans les conditions de croisière figure 20 on obtient une réduction favorable de la survitesse intrados bien qu'elle ne se traduise pas par une diminution de la traînée.

C'est donc ce profil optimisé qui a été retenu pour la génération de la pale.

4.4 - Profil d'extrémité de pale HOR04 -

Les performances du profil de 4% d'épaisseur relative sont tracées figure 21. Le C_z max obtenu dans les conditions de décollage est d'environ 1,15, le nombre de Mach de divergence de traînée au C_z de croisière est de 0,845. Les finesses dans les conditions de montée et de croisière sont inférieures à celles fixées par le cahier des charges. Pour ce profil de très faible épaisseur relative on notera que les performances déduites des essais sont nettement inférieures à l'estimation qui en avait été faite. La comparaison des répartitions de pression mesurées et calculées montrent (figure 22) que le saut de pression à travers le choc est en général mal restitué et que le niveau de pression calculé au bord de fuite est fortement erroné ce qui entraîne une mauvaise estimation de la traînée de ce profil.

5 - COMPARAISONS DES PROFILS HOR AVEC DES PROFILS D'HELICE RECENTS -

A titre indicatif les performances des profils de la famille HOR sont comparées figure 23 et 24 avec celles de profils d'hélice récents : profils ARAD développés par l'ARA conjointement avec DOWTY [Réf. 5] et profil HSl développé par Hamilton-Standard [Réf. 6] .

Cette comparaison est toutefois à faire avec prudence, les conditions d'essais (Soufflerie-Reynolds) et les performances complètes de ces profils n'étant pas connues avec précision. De plus pour une même épaisseur relative le cahier des charges n'est pas nécessairement identique, les objectifs pouvant être orientés plus précisément sur une configuration de vol.

Le profil HOR12 possède un C_z max à $M = 0,45$ et une finesse de montée supérieurs à ceux du profil ARAD13 de 13% d'épaisseur relative.

Pour les profils de 7 et de 6% d'épaisseur relative le profil HOR07 a un C_z max légèrement plus faible que celui du profil ARAD6 mais supérieur à celui du profil HSl et du profil de référence NACA 16707. Le profil HOR07 a une finesse de montée supérieure à celle du profil ARAD6.

Pour les profils de plus faible épaisseur relative, la comparaison fait apparaître que le C_z max du profil HOR04 est inférieur à celui du profil ARAD4 mais le nombre de Mach de divergence de traînée est supérieur.

Les 4 profils HOR permettent la définition complète d'une pale d'hélice répondant aux exigences principales imposées par le cahier des charges. Comparativement aux autres profils d'hélice connus, les profils HOR possèdent en bidimensionnel des performances supérieures à celles des profils NACA16 et des performances au moins égales à celles de profils plus récents définis par Dowty et Hamilton Standard.

6 - PERFORMANCES HELICES -

La première hélice à être équipée de nouveaux profils HOR sera l'hélice composite du TRANSALL C160, bi-turbopropulseur de transport équipé de moteurs Rolls Royce TYNE.

Les utilisateurs ont posé un Cahier des Charges qui prévoyait principalement une optimisation aérodynamique de l'hélice au point de croisière. Ce type d'exigence est très difficile à satisfaire car, généralement, une optimisation complète sur un point de croisière conduit à des pales de très faible facteur d'activité qui ne conviennent pas pour les points de montée et de décollage. Nous avons donc été obligés de composer avec ce Cahier des Charges ce qui nous a conduits à diminuer le facteur d'activité par rapport à la pale métallique existante d'environ 5%.

Malgré cette diminution des cordes, l'estimation des performances de l'hélice fait apparaître une amélioration de la traction de 9,45% au point fixe, 1,35% en montée et 1,4% en croisière. On notera que, pour obtenir un gain de rendement de 1,4% en croisière, nous avons augmenté la finesse des profils de plus de 20% (fig. 25).

En plus des améliorations de performances, la technologie de pales composites permet de gagner une masse de 400 Kg par avion.

7 - CONCLUSIONS -

La famille de profils HOR, définie en collaboration entre l'ONERA et RATIER-FIGEAC, possède des performances nettement supérieures à celles des profils classiques de la série NACA 16. L'utilisation de cette famille pour la définition de nouvelles hélices permet des gains substantiels pour tout le domaine de vol et, notamment, au décollage et en montée.

Nous pouvons résumer les points forts de ces profils ainsi :

- Forte portance maximale. Nous avons mesuré un C_z max supérieur à celui du profil de référence alors que ce dernier a une cambrure très importante.
- Bonne finesse à fort C_z , meilleure que le profil de référence.
- Finesse en croisière acceptable, surtout compte tenu de la traînée de culot que nous avons imposée par l'intermédiaire du bord de fuite épais.
- Maître couple autour de 25% de la corde ce qui centre la pale et diminue les torsions d'origine aérodynamique.
- Bord d'attaque à grand rayon et bord de fuite épais plus facile à réaliser et moins sensibles aux chocs.

REFERENCES -

- 1 J. BOUSQUET
Calculs bidimensionnels transsoniques avec couche limite.
AAAF 11ème Colloque d'aérodynamique appliquée (1974)
- 2 J. C. LEBALLEUR, P. GIRODROUX-LAVIGNE, M. LAZAREFF
Calcul en fluide visqueux de l'écoulement transsonique autour d'un profil de voilure.
O.N.E.R.A. RT 7/3073 AY (1982)
- 3 X. VAUCHERET
Corrections d'effets de parois en courant plan, méthode des signatures.
O.N.E.R.A. RT 180/1464 GN (1980)
- 4 J. RENEAUX
Méthode de définition de profils par optimisation numérique.
O.N.E.R.A. RSF 19/3369 AY (1983)
- 5 R.J. BOCCI
A new series of airfoil sections suitable for aircraft propellers.
Aeronautical Quarterly (1977)
- 6 ROHRBACH C., WAINASKY M.S.
Aerodynamic characteristics of an advanced technology propeller for commuter aircraft.
AIAA 81-1565

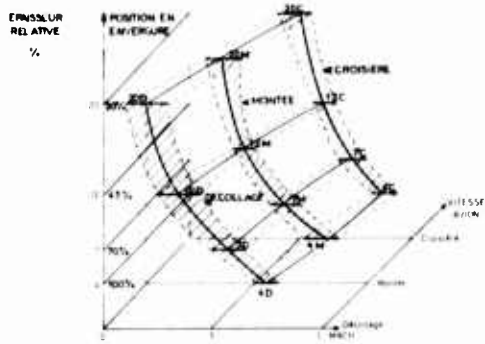


Fig. 1 : Nombres de Mach de fonctionnement des différents profils

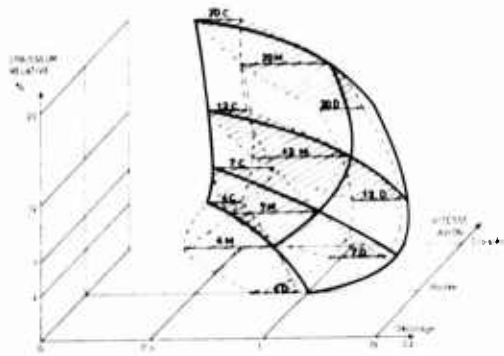


Fig. 2 : Coefficient de Portance

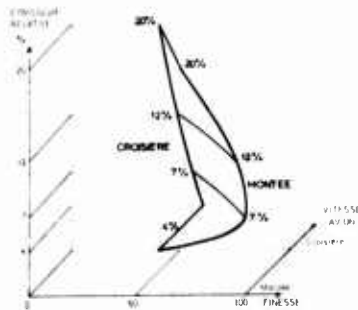


Fig. 3 : Finesse en montée et en croisière

	Épaisseur relative	4	7	12	20
Décollage	10^{-6} Reynolds	1,5 à 7,1	1,91 à 5	1,2 à 3,5	0,8 à 3
	Mach hélice	0,7 à 0,8	0,5 à 0,66	0,25 à 0,45	
	Mach bidim.	0,65 à 0,75	0,47 à 0,63	0,25 à 0,45	0,2
	Cz max bidimension.	1,2	1,6	1,65	1,5
Montée	10^{-6} Reynolds	1,65 à 7	2 à 5	1,4 à 4	1,4 à 2,7
	Mach hélice	0,72 à 0,87	0,57 à 0,70	0,4 à 0,5	
	Mach bidim.	0,67 à 0,82	0,54 à 0,67	0,4 à 0,5	0,35
	Cz	0,45 à 0,85	0,65 à 1,05	0,75 à 1,20	1,10
Croisière	Mach/Cz/finesse	0,77 0,85 60	0,60 1,05 100	0,45 1,20 95	0,35 110 70
	10^{-6} Reynolds	1,3 à 4	1,4 à 3,4	1,1 à 2,7	1 à 2
	Mach hélice	0,83 à 0,93	0,67 à 0,79	0,56 à 0,65	
	Mach bidim.	0,78 à 0,88	0,64 à 0,76	0,56 à 0,65	0,5
Croisière	Mdx	0,88	0,76	0,65	0,50
	Cz	0,35 à 0,50	0,38 à 0,65	0,35 à 0,52	0,30 à 0,50
	Mach/Cz/finesse	0,81 0,35 60	0,7 0,38 55	0,6 0,39 50	0,5 0,30 40

Fig. 4 : Cahier des charges

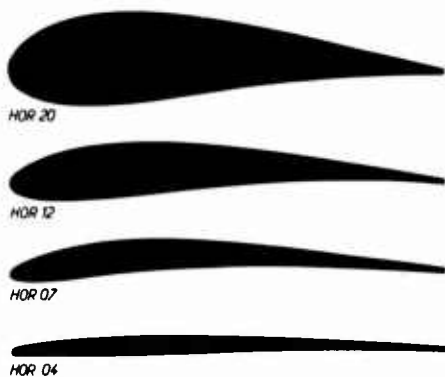


Fig. 5 : Dessin de la famille de profils HOR

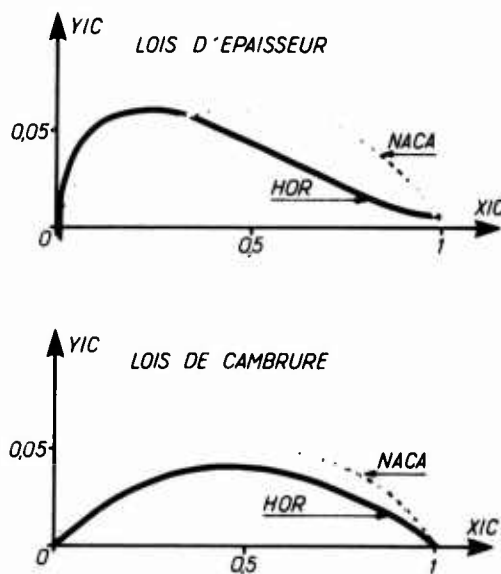


Fig. 6 : Loi de cambrure et loi d'épaisseur pour les profils HOR

REPARTITIONS DE PRESSION CALCULEES

PROFIL HOR20

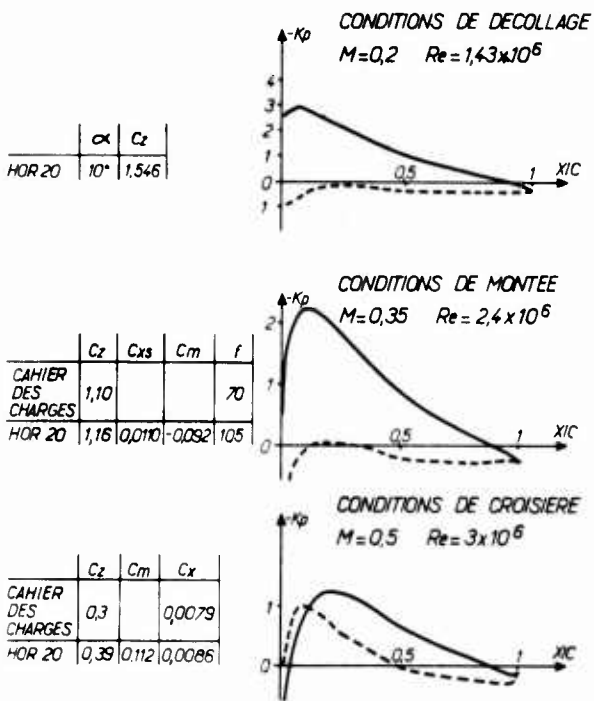


Fig. 7 : Répartitions de pression calculées Profil HOR 20

REPARTITIONS DE PRESSION CALCULEES
COMPARAISON HOR 12-NACA 16912

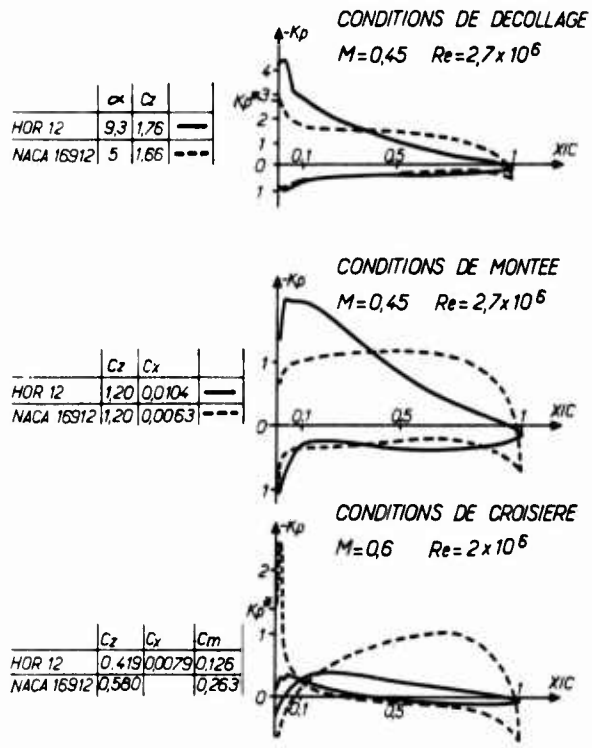
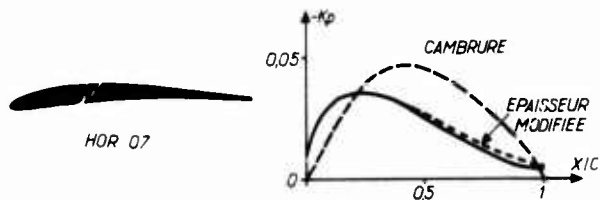


Fig. 8 : Répartitions de pression calculées Comparaison HOR 12-NACA 16912

PROFIL HOR 07



REPARTITIONS DE PRESSION CALCULEES
COMPARAISON HOR 07 - NACA 16707

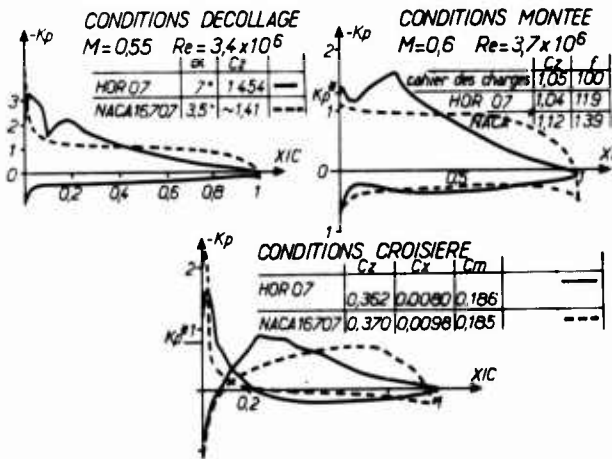
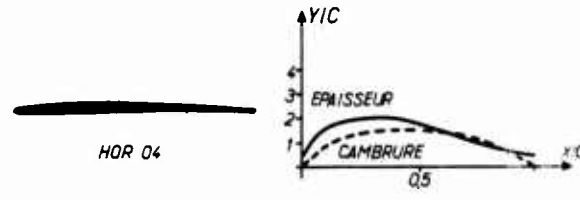


Fig. 9 : Répartitions de pression calculées Comparaison: HOR 07-NACA 16707

PROFIL HOR 04



REPARTITIONS DE PRESSION CALCULEES

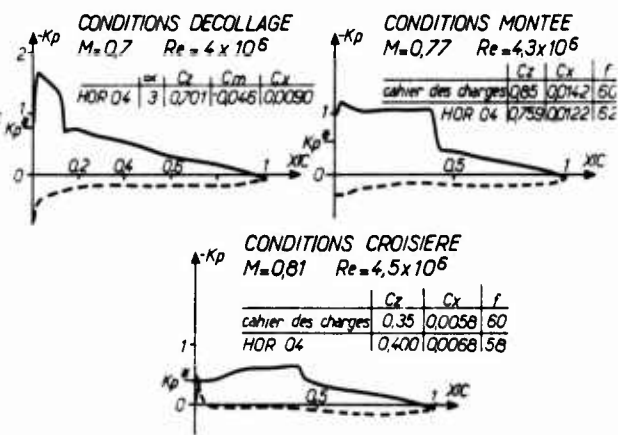


Fig. 10 : Répartitions de pression calculées Profil HOR 04

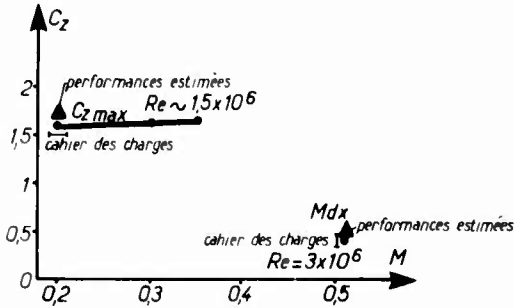
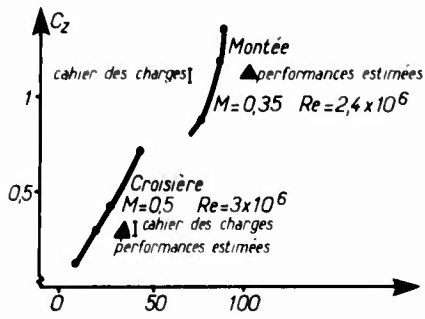


Fig. 11 : Performances globales - Profil HOR 20

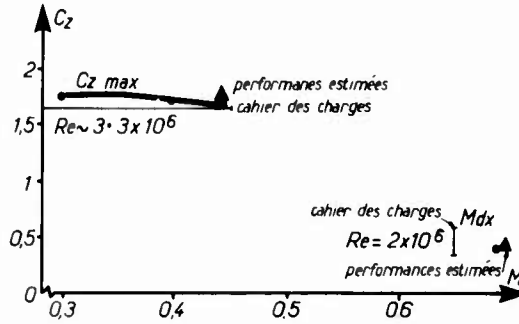
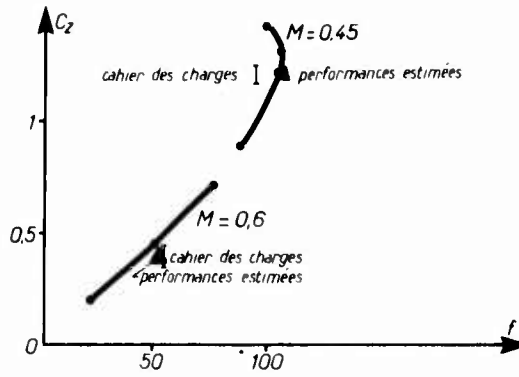


Fig. 12 : Performances globales - Profil HOR 12

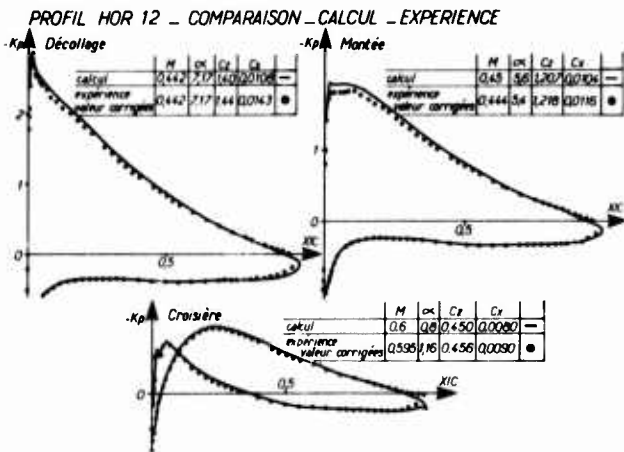


Fig. 13 : Comparaison Calcul-Expérience - Profil HOR 12

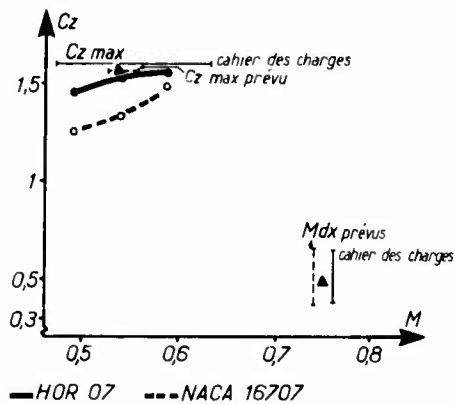
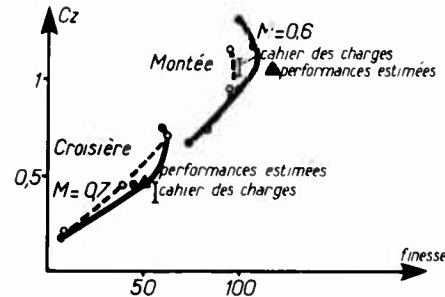


Fig. 14 : Performances globales
Profils HOR 07-NACA 1607

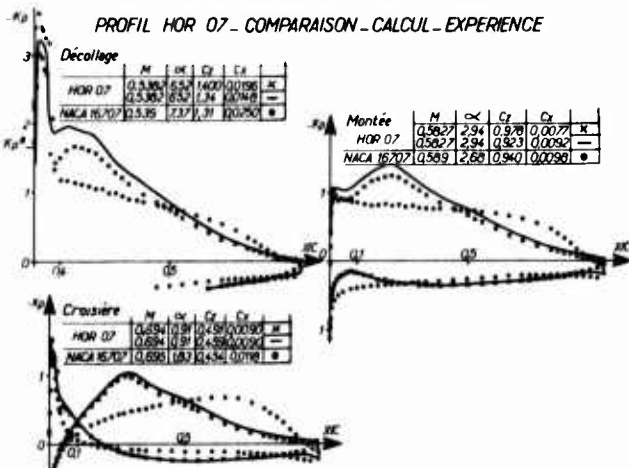


Fig. 15 : Comparaison Calcul-Expérience - Profil HOR 07

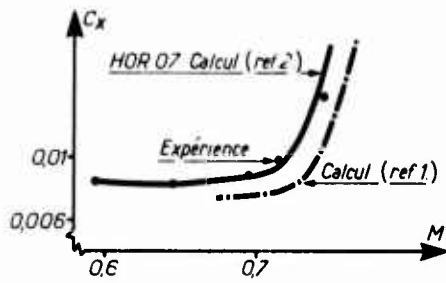


Fig. 16 : Mach de divergence de trainée - Profils HOR 07



Fig. 17 : Géométries du profil initial et du profil optimisé

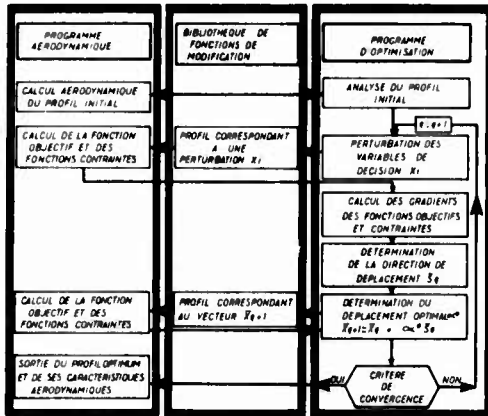


Fig. 18 : Organigramme - Optimisation numérique

PROFIL HOR 07 - PROFIL HOR 07 optimisé - MACH 0,55
CONDITIONS DE MONTEE

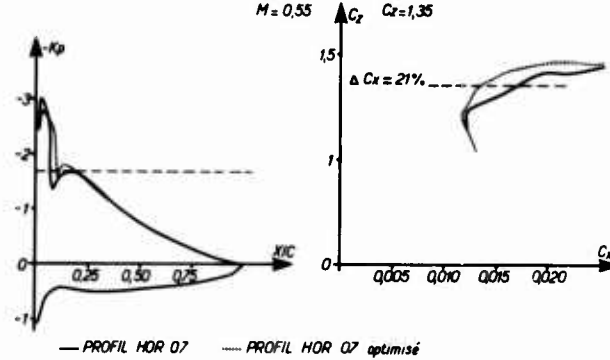


Fig. 19 : Comparaison des caractéristiques aérodynamiques expérimentales - Conditions de montée

PROFIL HOR 07 - PROFIL HOR 07 optimisé - MACH 0,70
CONDITIONS DE CROISIERE

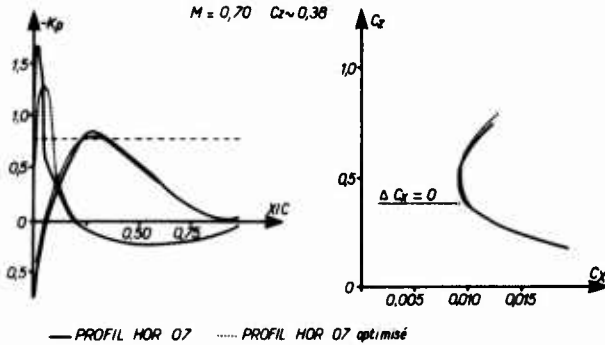


Fig. 20 : Comparaison des caractéristiques aérodynamiques expérimentales - Conditions de croisière

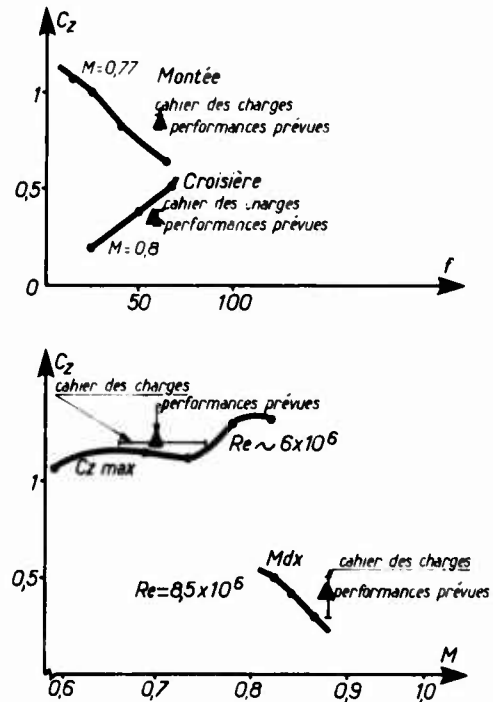


Fig. 21 : Performances globales - Profil HOR 04

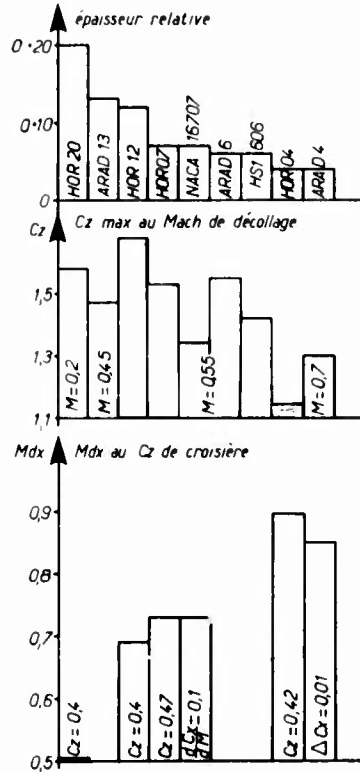
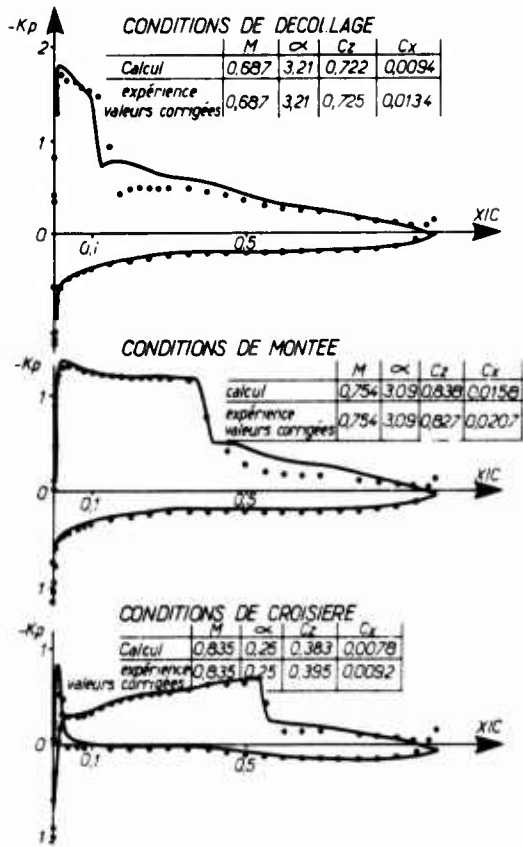
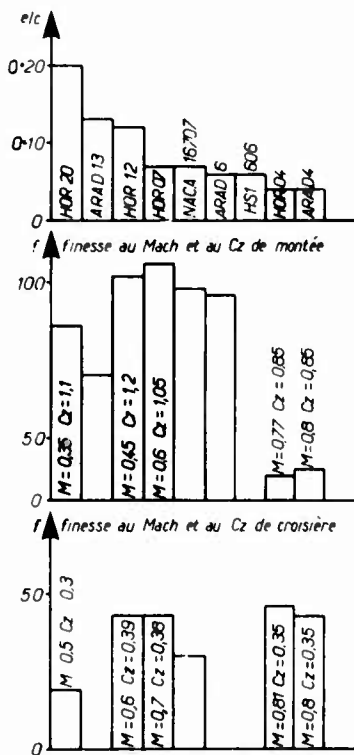


Fig. 22 : Comparaison Calcul-Expérience - Profil HOR 04 Fig. 23 : Récapitulation des performances globales



	VERSION METALLIQUE	VERSION COMPOSITE	GAIN RELATIF
POINT FIXE P = 5665 SHP H = 976 tr/mm V = 0 Z = 0	16 500 livres	18 060 livres	+ 9,45 %
DECOLLAGE P = 5735 SHP H = 976 tr/mm V = 100 Kts Z = 0	. 672	. 681	+ 1,3 %
MONTEE P = 4175 SHP H = 928 V = 130 Kts Z = 0	. 791	. 797	+ 0,8 %
P = 4420 SHP H = 928 V = 151 Kts Z = 9850 Ft	. 791	. 801	+ 1,25 %
P = 3380 SHP H = 864 V = 173 Kts Z = 16 400 Ft	. 822	. 833	+ 1,35 %
CROISIERE P = 3030 SHP H = 864 V = 270 Kts Z = 23 000 Ft	. 864	. 876	+ 1,4 %

fig. 25 : Estimation des performances de l'hélice

Fig. 24 : Récapitulation des performances globales

AERODYNAMICS OF WIDE-CORD PROPELLERS IN NON-AXISYMMETRIC FLOW

by

J.B.H.M. Schulten
National Aerospace Laboratory NLR
Anthony Fokkerweg 2, 1059 CM Amsterdam
The Netherlands

SUMMARY

A lifting surface analysis is presented for propellers in non-axisymmetric flow. Usually such conditions prevail for propellers installed on aircraft, wing upwash being the most common flow asymmetry. In the analysis the Euler equations linearized about a uniform subsonic main flow are solved after separation of variables in cylindrical coordinates. This solution is obtained via an integral equation for the force distribution over the upper and lower surfaces of the blades which replaces the action of the propeller on the surrounding fluid. The boundary condition of vanishing normal velocity is applied at the actual blade surfaces, thus leading to a non-helicoidal, unsteady lifting surface theory for propellers. Since the integral equation is solved most efficiently per circumferential Fourier component of the inflow distortion field, symmetric inflow is included naturally as the zeroth term of the Fourier series. General blade shapes can be handled as the blades may be swept both axially and azimuthally. There is no inherent limitation to the propeller tip Mach number. Apart from the calculation of the unsteady blade loading, expressions for the velocity and pressure fields are derived, in which the propeller slipstream appears explicitly as part of the complete velocity field in a form perfectly suited for wing interference calculations.

LIST OF SYMBOLS

$\vec{a}_n(\alpha, \gamma, r)$	= $(\alpha, -i\gamma J'_n(\gamma r)/J_n(\gamma r), n/r)$
$\vec{a}_n^*(\alpha, \gamma, \rho)$	= $(\alpha, i\gamma J'_n(\gamma \rho)/J_n(\gamma \rho), n/\rho)$
B	= number of blades
$\vec{b}_n(x-\xi, r, \gamma, \omega)$	= $\vec{a}_n([M\omega - \text{sgn}(x-\xi)\kappa(\gamma, \omega)]/\beta^2, \gamma, r)$
$\vec{b}_n^*(x-\xi, \rho, \gamma, \omega)$	= $\vec{a}_n^*([M\omega - \text{sgn}(x-\xi)\kappa(\gamma, \omega)]/\beta^2, \gamma, \rho)$
$\vec{c}_n(r, \gamma, \omega)$	= $\vec{a}_n(-\omega/M, \gamma, r)$
$\vec{c}_n^*(\rho, \gamma, \omega)$	= $\vec{a}_n^*(-\omega/M, \gamma, \rho)$
\vec{F}	= force field
\vec{f}	= force
G	= Green's function
$\vec{g}(x, r)$	= $(-r \frac{\partial \phi_0}{\partial x}, -r \frac{\partial \phi_0}{\partial r}, 1)$ normal to blade surface
\vec{H}_m	= $\vec{h}_m \text{sgn}[\sigma - s_L(\rho)]$
\vec{h}_m	= vector function defined in Eq. (14)
h	= hub radius
$\vec{i}_x, \vec{i}_r, \vec{i}_\theta$	= unit vectors in x, r, θ directions respectively (Fig. 1)
J_n, J'_n	= Bessel function of the first kind and order n, its derivative
J	= maximum j
j	= blade index; index of radial Galerkin projection
k	= circumferential Fourier index of distortion velocity component
L	= maximum ℓ
ℓ	= index of perimetral Galerkin projection
M	= main flow Mach number
m	= k - nB
\vec{n}	= unit normal on blade surface
n	= integer number
PJD	= pressure jump distribution
$P_{k\eta\lambda}$	= pressure jump Fourier coefficient
p	= pressure
$\Delta p_{k,j}$	= pressure jump across jth blade surface caused by kth distortion velocity component
$\Delta p_{k,0,i}$	= $\Delta p_{k,0}$ caused by ith frequency in kth distortion velocity component
r	= radial coordinate
s	= blade section perimetral coordinate
t	= time coordinate
\vec{v}	= velocity induced by propeller
$\vec{V}_{A,m}(x, \gamma)$	= Fourier-Hankel transformed acoustic velocity

$\vec{V}_{H,m}(\gamma)$	= Fourier-Hankel transformed hydrodynamic velocity, without factor $\exp[-i\kappa\omega/M]$
\vec{w}	= incident distortion velocity
x	= axial coordinate
α	= axial wave number
β	= $\sqrt{1-M^2}$
γ	= radial wave number
H	= maximum η
η	= index of radial Fourier expansion of pressure jump distribution
θ	= angular coordinate
$\kappa(\gamma, \omega)$	= $\omega \sqrt{1 - (\beta\gamma/\omega)^2}$ $(\beta\gamma)^2 \leq \omega^2$ = $-i \sqrt{(\beta\gamma)^2 - \omega^2}$ $(\beta\gamma)^2 > \omega^2$
Λ	= maximum λ
λ	= index of perimetral Fourier expansion of pressure jump distribution
v	= local normal coordinate
ξ	= axial source coordinate
ρ	= radial source coordinate
σ	= perimetral source coordinate
τ	= source time coordinate
φ	= angular source coordinate
φ_0	= angular blade surface coordinate of zeroth blade at $t = 0$
Ω	= circumferential tip Mach number
ω	= Helmholtz number (non-dimensional radian frequency)
$\omega_{k,i}$	= i th discrete frequency of k th Fourier component \vec{w}_k

Superscripts

(\sim)	= in time domain
$(\hat{\sim})$	= axially Fourier transformed variable
$(\bar{\sim})$	= radially Hankel transformed variable
$(\vec{\sim})$	= vector
$()^u$	= blade upper surface (Fig. 2)
$()^l$	= blade lower surface (Fig. 2)

Subscripts

A	= acoustic
f	= point force
H	= hydrodynamic
L	= leading edge
T	= trailing edge
c	= continuous

Other symbols

$\langle \cdot \cdot \rangle$	= inner product of two three-dimensional vectors
-------------------------------	--------------------------------------------------

1. INTRODUCTION

One of the first simplifications commonly made in theories on propeller aerodynamics is to assume a flow symmetric about the axis of rotation. This assumption certainly is convenient analytically yielding a problem no longer dependent on time in the coordinate system of the propeller. For propellers installed on aircraft, however, there are various circumstances to disturb the axi-symmetry of the flow.

When conventionally mounted in front of a wing, there is an upwash which obviously leads to a non-axisymmetric inflow to the propeller. If the wing is swept this upwash may be particularly effective on the side of smallest clearance between wing leading edge and propeller. Other sources of non-axisymmetric flow are an angle of attack of the propeller axis, fuselage flow displacement while pusher propellers are exposed to the flow distortions of the upstream airframe wake system. Furthermore, a very pronounced and highly periodic asymmetry is formed by the mutual aerodynamic interference of dual counter-rotation propellers. This configuration is interesting because of its efficiency potential resulting from the swirl recovery by the downstream propeller.

The cyclic loading arising from flow asymmetry may be a matter of concern with respect to the fatigue life of the blades. Also, upwash shifts the thrust line laterally which may have an adverse effect on the stability and control of the aircraft. And, of course, the generated acoustic field can be altered con-

siderably by inflow asymmetries. While the acoustic significance of installation effects has been recognized for some time, e.g., Tanna¹ et al., aerodynamic analyses so far have been focussed on the symmetric problem sufficient to study propulsion performance and efficiency.

The present paper deals with an analysis of the aerodynamics of a propeller in a uniform flow perturbed by a general, time-dependent, non-axisymmetric flow. It goes without saying that the symmetric case is thus included in the present analysis. While in the modeling of the problem a lifting line approximation may be attractive for conventional, unswept propeller blades of high aspect ratio's, the generously swept, wide-chord propellers now being considered for high subsonic cruise speeds do not match the asymptotics of a lifting line approximation very well. Therefore, in the present paper the flow around a wide-chord propeller is analyzed in terms of a lifting surface problem. Recently, an alternative lifting surface analysis for propellers was given by Hanson². His formulation, however, is biased to axis-symmetric flow. Also, the boundary conditions are applied at a mean helicoidal surface (linearized boundary conditions), whereas in the present method the actual upper and lower surfaces of the blades are used. Further, there are several other important points of diversity between Hanson's approach and the present one, the most of which will be touched upon at the appropriate place in the analysis.

2. ANALYSIS

2.1. Formulation of the problem

The present paper deals with an isolated propeller in a uniform, subsonic and inviscid main flow. This flow is parallel to the propeller axis and is perturbed by the rotating propeller blades as well as by some other, incident velocity distortion field. For this problem a non-dimensional formulation will be used throughout the paper by taking the propeller tip radius, the main flow mass density and its sound speed as scaling parameters. A stationary, cylindrical frame of reference (x, r, θ) is taken of which the x-axis is chosen coincident with the propeller rotational axis (Fig. 1) and positive in the direction of the main flow. Then the governing linearized Euler equations for small isentropic perturbations of the main flow are

$$\frac{\partial \tilde{p}}{\partial t} + M \frac{\partial \tilde{p}}{\partial x} + \nabla \cdot \tilde{v} = 0 \quad (1)$$

$$\frac{\partial \tilde{v}}{\partial t} + M \frac{\partial \tilde{v}}{\partial x} + \nabla \tilde{p} = \tilde{F} \quad (2)$$

The force field \tilde{F} in the momentum equation (2) represents the effect of the blades as it stands for the force distribution by which the blade surfaces push away the surrounding fluid. In this description the interior of the blades is assumed to be filled with the same medium. The final problem to be solved will be an integral equation for \tilde{F} , resulting from the condition of no fluid passing through the blade surfaces. Instead of linearizing this boundary condition by approximating the blades by helicoidal surfaces, here the actual shape is retained. So the present approach may be characterized as a non-helicoidal lifting surface theory.

The additional condition of outward radiation of the field will be satisfied by selecting the causal solution of an impulsive point source as the starting point of the analysis. Finally, since inviscid flow has been assumed, the flow behavior at the trailing edge is to be controlled by a Kutta condition.

2.2. Field of an impulsive point force

Elimination of the velocity \tilde{v} from equations (1) and (2) yields the following inhomogeneous, convected-wave equation for the pressure

$$\left[\nabla^2 - \left(M \frac{\partial}{\partial x} + \frac{\partial}{\partial t} \right)^2 \right] \tilde{p} = \nabla \cdot \tilde{F} \quad (3)$$

The first step to solve this equation is the construction of Green's function \tilde{G} for the differential operator acting on \tilde{p} in Eq. (3). In the present context, Green's function can be interpreted as the pressure field of an impulsive point source active at point (ξ, ρ, φ) and time τ (Fig. 1). It satisfies the following equation

$$\left[\nabla^2 - \left(M \frac{\partial}{\partial x} + \frac{\partial}{\partial t} \right)^2 \right] \tilde{G} = -\delta(x-\xi)\delta(r-\rho) \frac{\delta(\theta-\varphi)}{r} \delta(t-\tau) \quad (4)$$

The solution to Eq. (4) in spherical coordinates is given by

$$\tilde{G} = \frac{\delta(T-R)}{4\pi R} \quad (5)$$

where $T = \beta(t-\tau) + \frac{M(x-\xi)}{\beta}$ and $R = \sqrt{\left(\frac{x-\xi}{\beta}\right)^2 + r^2 + \rho^2 - 2r\rho \cos(\theta-\varphi)}$

In propeller acoustic theory this representation of Green's function has been used by Gutin³, Garrick and Watkins⁴, Van de Vooren and Zandbergen⁵, Farrasat⁶ and many other investigators. Also Hanson² starts from this representation to arrive eventually at a formulation in separated helicoidal coordinates.

In the present study, however, from the outset an alternative representation in separated, cylindrical coordinates is favored for both analytical convenience and physical transparency. This representation is directly obtained by taking (formally) integral transforms of Eq. (4) as follows

$$\int_{\varphi-\pi}^{\varphi+\pi} \int_{-\infty}^{\infty} \int_0^{\infty} \exp[-i(n\theta + \omega t + \alpha x)] r J_n(\gamma r) [Eq. (4)] dr dx dt d\theta \quad (6)$$

where J_n denotes the Bessel function of the first kind and order n . After carrying out the integrations in Eq. (6) the following expression for Green's function in wave number space ($n, \alpha, \gamma, \omega$) is obtained

$$\hat{G}_n(\alpha, \gamma, \omega | \xi, \rho, \varphi, \tau) = \frac{\exp[-i(n\varphi + \omega\tau + \alpha\xi)] J_n(\gamma\rho)}{\gamma^2 + \alpha^2 - (\omega + M\alpha)^2} \quad (7)$$

Here $(\bar{\quad})$ denotes a quantity transformed to the radial wave number domain (γ) and $(\hat{\quad})$ relates to the axial wave number domain (α). The subscript n indicates the circumferential Fourier-index. Taking inverse transforms and the Fourier series expansion of circumferential harmonics n , the following representation for Green's function in physical space is obtained

$$\begin{aligned} \hat{G}(x, r, \theta, t | \xi, \rho, \varphi, \tau) = & \frac{1}{(2\pi)^2} \int_{-\infty}^{\infty} \exp[in(\theta - \varphi)] \int_{-\infty}^{\infty} \exp[i\omega(t - \tau)] \int_0^{\infty} \gamma J_n(\gamma r) J_n(\gamma\rho) \\ & \times \frac{1}{2i\kappa(\gamma, \omega)} \exp\left\{\frac{i(x - \xi)}{\beta^2} [M\omega - \text{sgn}(x - \xi)\kappa(\gamma, \omega)]\right\} d\gamma d\omega \end{aligned} \quad (8)$$

$$\text{where } \kappa(\gamma, \omega) = \beta\sqrt{\gamma - \frac{\omega}{\beta}} \sqrt{\gamma + \frac{\omega}{\beta}}$$

(The square roots are defined as principal values, with branch cuts running from $\gamma = \frac{\omega}{\beta}$ to $-\infty$ and from $\gamma = -\frac{\omega}{\beta}$ to $+i\infty$, respectively.) In Eq. (8) the inverse transform $\alpha \rightarrow x$ has been performed by integrating along a contour, just above the real axis for $\alpha > \frac{M\omega}{\beta^2}$ and just below for $\alpha < \frac{M\omega}{\beta^2}$ ($\omega > 0$), such that the causal solution was selected. Alternatively, the inverse transform $\gamma \rightarrow r$ could have been done analytically, leaving the transform $\alpha \rightarrow x$ for numerical integration. The latter procedure leads to a formulation similar to those of S. Goldstein⁷, Kondo⁸ and Hanson².

The possibility of the present approach for propellers was already put forward by Davidson⁹ in the early fifties. A most interesting point of this formulation is the strong parallelism with the lifting surface theory for ducted fans (e.g. Refs. 10, 11, 12, 13). The inverse Hankel transform, i.e., the integration in γ , in the propeller problem just corresponds to the summation over radial modes in the fan problem.

For an impulsive point force of amplitude \vec{f} acting at $(\xi, \rho, \varphi, \tau)$ as the driving force field in Eq. (3), it is easily shown that its pressure field p_f is related to Green's function as follows

$$\hat{p}_{f,n}(\alpha, \gamma, \omega | \xi, \rho, \varphi, \tau) = -i \langle \vec{a}_n^*(\alpha, \gamma, \rho) \cdot \vec{f} \rangle \hat{G}_n(\alpha, \gamma, \omega | \xi, \rho, \varphi, \tau) \quad (9)$$

where the vector $\vec{a}_n^* = (\alpha, i\gamma J_n'(\gamma\rho)/J_n(\gamma\rho), n/\rho)$ originates from the divergence operator in the right hand side of Eq. (3). In the present context the main objective is to find the force distribution \vec{F} acting at the blade surfaces on the surrounding fluid. To this end, first the velocity field \vec{v}_f induced by a point force will be derived.

Similar to references 11 and 12, an important characteristic of the present approach is to retain the complete balance of forces $\vec{F} - \nabla p$ when determining the velocity from the momentum Eq. (2). If \vec{F} acts on the fluid via an interface, as has been assumed in the present model, it can be written as $\vec{F} = \Delta p \delta(v) \vec{n}$, where \vec{n} is the unit normal of the surface, v the local, normal coordinate and Δp the pressure jump across the surface. On the other hand, the pressure gradient ∇p equals $\nabla[\Delta p \text{sgn}(v)/2 + p_c] = \Delta p \delta(v) \vec{n} + \nabla p_c$, where p_c denotes the continuous part of the pressure. Now, at the surface, the net normal force (per unit volume) $\langle \vec{n} \cdot (\vec{F} - \nabla p) \rangle$ reduces to $-\frac{\partial p_c}{\partial v}$ since the two delta functions cancel out. Thus the pressure jump across the surface is exactly balanced by the concentrated surface force.

In contrast to this approach, Hanson² ignores the force term \vec{F} and consequently a singular kernel in the normal velocity integral is obtained. Of course, this singularity can be dealt with appropriately by separating regular and singular parts as shown, for instance, by Namba¹⁰ in the analogous problem of a ducted fan. However, Hanson's velocity integral still contains a non-uniform double limit which looks hard to handle numerically. The present approach seems both simpler and more straightforward physically.

Applying the same integral transform in x , θ and t as before to the linearized momentum Eq. (2) for an impulsive point force, yields

$$i(\omega + M\alpha) \hat{v}_{f,n} = \vec{f} \frac{\delta(r - \rho)}{r} \exp[-i(n\varphi + \omega\tau + \alpha\xi)] - (i\alpha, \frac{\partial}{\partial r}, \frac{in}{r}) \hat{p}_{f,n}(r) \quad (10)$$

This is, rewritten in terms of an inverse Hankel transform,

$$\hat{v}_{f,n} = \int_0^{\infty} \frac{\gamma J_n(\gamma r)}{i(\omega + M\alpha)} J_n(\gamma\rho) \exp[-i(n\varphi + \omega\tau + \alpha\xi)] \left[\vec{f} - \frac{\langle \vec{a}_n^*(\alpha, \gamma, \rho) \cdot \vec{f} \rangle \vec{a}_n(\alpha, \gamma, r)}{\gamma^2 + \alpha^2 - (\omega + M\alpha)^2} \right] d\gamma \quad (11)$$

The vector $\vec{a}_n = (\alpha, -i J_n'(\gamma r)/J_n(\gamma r), n/r)$ results from the gradient operator in Eq. (2). The inverse transform $\alpha \rightarrow x$ of Eq. (11) can again be carried out by complex contour integration similar to the way Green's function was obtained. In this case, however, an extra pole is encountered at $\alpha = -\omega/M$. This pole gives rise to a hydrodynamic velocity field, i.e., a purely convective field with a vanishing pressure component. Thus the velocity field in physical space becomes

$$\begin{aligned} \vec{v}_f(x, r, \theta, t | \xi, \rho, \omega, \tau) &= \frac{1}{(2\pi)^2 M} \sum_{n=-\infty}^{\infty} \exp[in(\theta-\varphi)] \int_{-\infty}^{\infty} \exp[i\omega(t-\tau)] \int_0^{\infty} \gamma J_n(\gamma r) J_n(\gamma \rho) \\ &\times \left[\exp\left[\frac{-i\omega}{M}(x-\xi)\right] H(x-\xi) \left\{ \vec{f} - \frac{\langle \vec{c}_n^*(\rho, \gamma, \omega) \cdot \vec{f} \rangle}{(\omega/M)^2 + \gamma^2} \vec{c}_n(r, \gamma, \omega) \right\} \right. \\ &\left. + \beta^2 \frac{\exp\left\{i(x-\xi) \left[\frac{M\omega - \text{sgn}(x-\xi)\kappa(\gamma, \omega)}{\omega/M - \text{sgn}(x-\xi)\kappa(\gamma, \omega)} \right] / \beta^2\right\}}{2\kappa(\gamma, \omega) [\omega/M - \text{sgn}(x-\xi)\kappa(\gamma, \omega)]} \langle \vec{b}_n^*(x-\xi, \rho, \gamma, \omega) \cdot \vec{f} \rangle \vec{b}_n(x-\xi, r, \gamma, \omega) \right] d\gamma d\omega \end{aligned} \quad (12)$$

This expression shows the hydrodynamic part of the velocity to depend on x only through $\exp(-\frac{i\omega}{M}x)$, i.e., with an axial wave number ω/M (the hydrodynamic wave number, or Strouhal number), independent of n and γ . Moreover it extends only downstream of the point force. The acoustic part of the velocity is characterized by a unique axial wave number for every n, γ combination and extends upstream as well as downstream of the point force.

2.3. Propeller velocity field

To construct the field of the complete propeller one first identifies the point force with the force exerted by a small blade surface element during the time $d\tau$. Let the upper and lower surface of the j th blade be given by $\varphi = \varphi_0^u(\xi, \rho) + \Omega\tau + j2\pi/B$ and $\varphi = \varphi_0^l(\xi, \rho) + \Omega\tau + j2\pi/B$, respectively. Further, the pressure jump across the blade surface is defined as $\Delta p = [p(\text{exterior}) - p(\text{interior})]$. Then, for an upper surface element of area $\|\vec{g}^u\| d\xi d\rho$ and outward unit normal vector $\vec{n} = -\vec{g}^u / \|\vec{g}^u\|$, one obtains

$$\vec{f}^u = -\vec{g}^u(\xi, \rho) \Delta p_j^u(\xi, \rho, \tau) d\xi d\rho d\tau \quad (13a)$$

and for a lower surface element

$$\vec{f}^l = \vec{g}^l(\xi, \rho) \Delta p_j^l(\xi, \rho, \tau) d\xi d\rho d\tau \quad (13b)$$

where $\vec{g}(\xi, \rho) = (-\rho \frac{\partial \varphi_0}{\partial \xi}, -\rho \frac{\partial \varphi_0}{\partial \rho}, 1)$.

Substitution of the blade surface coordinates and Eqs. (13a) and (13b) into Eq. (12) followed by summation and integration over the blades and the source time τ yields the velocity field of a complete propeller

$$\begin{aligned} \vec{v}(x, r, \theta, t) &= \frac{1}{(2\pi)^2 M} \sum_{n=-\infty}^{\infty} \exp(in\theta) \int_{-\infty}^{\infty} \exp(i\omega t) \int_0^{\infty} \gamma J_n(\gamma r) \sum_{j=0}^{B-1} \exp(-inj \frac{2\pi}{B}) \int_h^1 J_n(\gamma \rho) \\ &\times \left[\int_{x_L(\rho)}^{x_T(\rho)} \exp[-in\varphi_0^l(\xi, \rho)] \vec{h}_n^l(x, \gamma, \omega, \xi, \rho) \Delta p_j^l(\xi, \rho, \omega + n\Omega) d\xi \right. \\ &\left. - \int_{x_L(\rho)}^{x_T(\rho)} \exp[-in\varphi_0^u(\xi, \rho)] \vec{h}_n^u(x, \gamma, \omega, \xi, \rho) \Delta p_j^u(\xi, \rho, \omega + n\Omega) \right] d\rho d\gamma d\omega \end{aligned} \quad (14)$$

where

$$\begin{aligned} \vec{h}_n &= \exp\left[\frac{-i\omega}{M}(x-\xi)\right] H(x-\xi) \left\{ \vec{g}(\xi, \rho) - \frac{\langle \vec{c}_n^*(\rho, \gamma, \omega) \cdot \vec{g}(\xi, \rho) \rangle}{(\omega/M)^2 + \gamma^2} \vec{c}_n(r, \gamma, \omega) \right\} \\ &+ \beta^2 \frac{\exp\left\{i(x-\xi) \left[\frac{M\omega - \text{sgn}(x-\xi)\kappa(\gamma, \omega)}{\omega/M - \text{sgn}(x-\xi)\kappa(\gamma, \omega)} \right] / \beta^2\right\}}{2\kappa(\gamma, \omega) [\omega/M - \text{sgn}(x-\xi)\kappa(\gamma, \omega)]} \langle \vec{b}_n^*(x-\xi, \rho, \gamma, \omega) \cdot \vec{g}(\xi, \rho) \rangle \vec{b}_n(x-\xi, r, \gamma, \omega) \end{aligned}$$

In the following the response is considered of the propeller to a single circumferential Fourier component $\vec{w}_k(x, r, t) \exp(ik\theta)$ of an arbitrary incident velocity distortion field. Eventually the full response of the propeller is found by summation over the Fourier-index k . Since the $(j+1)$ th blade is exposed to the same flow as the j th blade except for a phase shift $k2\pi/B$, $\Delta p_{k,j}$ can be expressed in the PJD of the zeroth blade as

$$\Delta p_{k,j} = \exp(ikj2\pi/B) \Delta p_{k,0} \quad (15)$$

This allows the summation over the blades to be performed explicitly by using the identity

$$\sum_{j=0}^{B-1} \exp\left[ij(k-n) \frac{2\pi}{B}\right] = B \quad \text{if } k-n = \ell B \\ 0 \quad \text{if } k-n \neq \ell B \quad \text{for any integer } \ell$$

Further it is somewhat inconvenient to deal with separate PJD's for upper and lower surfaces. Therefore, Δp is expressed in the local coordinate σ which is the perimetral length along a blade section of constant radius (see Fig. 2) starting at the trailing edge on the upper surface ($\sigma=0$), passing the leading edge [$\sigma=s_L(\rho)$] and ending at the trailing edge on the lower surface [$\sigma=s_T(\rho)$]. Then φ_0 , ξ and ζ are single-values functions of σ .

Now Eq. (14) can be rewritten as

$$\begin{aligned} \vec{v}_k(x, r, \theta, t) = & \frac{B}{(2\pi)^2 M} \sum_{n=-\infty}^{\infty} \exp(im\theta) \int_{-\infty}^{\infty} \exp(i\omega t) \int_0^{\infty} \gamma J_m(\gamma r) \\ & \times \int_h^1 J_m(\gamma \rho) \int_0^{s_T(\rho)} \exp[-im\varphi_0(\sigma, \rho)] \vec{H}_m(x, \gamma, \omega, \sigma, \rho) \frac{\Delta p_{k,0}(\sigma, \rho, \omega + m\Omega)}{\sqrt{1 + (\rho \frac{\partial \varphi_0}{\partial \xi})^2}} d\sigma d\rho d\gamma d\omega \end{aligned} \quad (16)$$

where $m = k - nB$ and $\vec{H}_m = \vec{h}_m \text{sgn}[\sigma - s_L(\rho)]$.

2.4. Integral equation for Δp

Obviously, the boundary condition at the blade surfaces requires the normal components of induced velocity \vec{v} , incident velocity \vec{w} and axial velocity $M\vec{i}_x$ to be equal to the normal component of the surface velocity $\Omega r \vec{i}_\theta$ (see Fig. 3) and so

$$\begin{aligned} \langle \vec{n} \cdot (\vec{v} + \vec{w} + M\vec{i}_x) \rangle &= \langle \vec{n} \cdot \Omega r \vec{i}_\theta \rangle \\ \text{for } \begin{cases} \theta = \varphi_0^u(x, r) + \Omega t + j \frac{2\pi}{B} & \text{and } \theta = \varphi_0^l(x, r) + \Omega t + j \frac{2\pi}{B} \\ j = 0, 1, \dots, B-1 \\ h < r < 1, x_L(r) < x < x_T(r) \end{cases} \end{aligned} \quad (17)$$

In view of the linearity of the problem the total field can be built up from the components \vec{v}_k induced by each circumferential Fourier component \vec{w}_k of the incident velocity and thus

$$\langle \vec{n} \cdot \vec{v}_k \rangle = \langle \vec{n} \cdot [(\Omega r \vec{i}_\theta - M\vec{i}_x) \delta_{0,k} - \vec{w}_k \exp(ik\theta)] \rangle \quad (18)$$

Eq. (16) and the surface coordinates of Eq. (17) are substituted into Eq. (18). Then, taking the Fourier transform in time and introducing a perimetral coordinate s analogously to σ (Fig. 2), the following integral equation for Δp_k , irrespective of the blade index number j is obtained

$$\begin{aligned} \frac{B}{2\pi M} \sum_{n=-\infty}^{\infty} \exp[im\varphi_0(s, r)] \int_0^{\infty} \gamma J_m(\gamma r) \int_h^1 J_m(\gamma \rho) \\ \times \int_0^{s_T(\rho)} \exp[-im\varphi_0(\sigma, \rho)] \langle \vec{n}(s, r) \cdot \vec{H}_m(x, \gamma, \omega - m\Omega, \sigma, \rho) \rangle \frac{\Delta p_{k,0}(\sigma, \rho, \omega)}{\sqrt{1 + (\rho \frac{\partial \varphi_0}{\partial \xi})^2}} d\sigma d\rho d\gamma \end{aligned} \quad (19)$$

$$= \langle \vec{n}(s, r) \cdot [2\pi(\Omega r \vec{i}_\theta - M\vec{i}_x) \delta(\omega) \delta_{0,k} - \exp[ik\varphi_0(s, r)] \vec{w}_k(x, r, \omega - k\Omega)] \rangle$$

with $h < r < 1$, $0 < s < s_T(r)$.

This equation describes the relation between the pressure jump across the zeroth blade surface, the surface displacement velocity and the k th circumferential Fourier component of an incident velocity field.

Since Eq. (19) is formulated in the frequency domain it is most appropriate to study the response of a propeller to incoming turbulence. However, in most applications of practical interest the components $\vec{w}_k \exp(ik\theta)$ are steady or consist of a series of discrete tones as in the interaction of counter-rotation propellers. So when $\vec{w}_k(x, r, t) = \sum_i \vec{w}_{k,i}(x, r) \exp(i\omega_{k,i} t)$ the driving field in Eq. (19) is given by $2\pi \sum_i \vec{w}_{k,i}(x, r) \delta[\omega - (\omega_{k,i} + k\Omega)]$ and consequently the PJD due to a single i -component can be written as

$$\Delta p_{k,0,i}(\sigma, \rho, \omega) = 2\pi \Delta p_{k,0,i}(\sigma, \rho) \delta[\omega - (\omega_{k,i} + k\Omega)] \quad (20)$$

Thus the discrete tone version of Eq. (19) becomes

$$\begin{aligned}
& \frac{B}{2\pi M} \sum_{n=-\infty}^{\infty} \exp[im\varphi_0(s,r)] \int_0^{\infty} \gamma J_m(\gamma r) \int_h^1 J_m(\gamma \rho) \int_0^{s_T(\rho)} \exp[-im\varphi_0(\sigma,\rho)] \\
& \times \langle \vec{n}(s,r) \cdot \vec{H}_m^*(x,\gamma,\omega_{k,i} + nB\Omega, \sigma,\rho) \rangle \frac{\Delta p_{k,0,i}(\sigma,\rho)}{\sqrt{1 + (\rho \frac{\partial \varphi_0}{\partial \xi})^2}} d\sigma d\rho d\gamma \\
& = \langle \vec{n}(s,r) \cdot \left[(\Omega r \vec{i}_\theta - M \vec{i}_x) \delta_{0,k} \delta_{0,\omega_{k,i}} - \exp[ik\varphi_0(s,r)] \vec{w}_{k,i}(x,r) \right] \rangle \quad (21)
\end{aligned}$$

2.5. Some useful expressions

2.5.1. Pressure field

By comparing Eqs. (3) and (4) it is readily seen that the pressure field of a propeller can be found from

$$\tilde{p} = - \int_{-\pi}^{\pi} \int_{-\infty}^{\infty} \int_0^{\infty} \rho \tilde{G} \cdot \nabla_0 \cdot \tilde{F}(\xi,\rho,\varphi,\tau) d\rho d\xi d\tau d\varphi \quad (22)$$

where ∇_0 denotes the divergence operator with respect to the source coordinates. Using the Green function of Eq. (8) and the blade force distribution

$$\begin{aligned}
\tilde{F} &= \sum_{j=0}^{B-1} \left[\vec{g}^k(\xi,\rho) \Delta \tilde{p}_{k,j}^k(\xi,\rho,\tau) \frac{\delta[\varphi - \varphi_0^k(\xi,\rho) - \Omega\tau - j2\pi/B]}{\rho} \right. \\
&\quad \left. - \vec{g}^u(\xi,\rho) \Delta \tilde{p}_{k,j}^u(\xi,\rho,\tau) \frac{\delta[\varphi - \varphi_0^u(\xi,\rho) - \Omega\tau - j2\pi/B]}{\rho} \right] \quad (23)
\end{aligned}$$

in Eq. (22) yields:

$$\begin{aligned}
\tilde{p}_k &= \frac{-B}{(2\pi)^2} \sum_{n=-\infty}^{\infty} \exp(im\theta) \int_{-\infty}^{\infty} \exp(i\omega t) \int_0^{\infty} \frac{\gamma J_m(\gamma r)}{2\kappa(\gamma,\omega)} \int_h^1 J_m(\gamma \rho) \\
&\times \int_0^{s_T(\rho)} \exp[-im\varphi_0(\sigma,\rho)] \exp\{i(x-\xi)[M\omega - \text{sgn}(x-\xi)\kappa(\gamma,\omega)]/\beta^2\} \text{sgn}[\sigma - s_L(\rho)] \\
&\times \langle \vec{b}_m^*(x-\xi,\rho,\gamma,\omega) \cdot \vec{g}(\sigma,\rho) \rangle \frac{\Delta p_{k,0}(\sigma,\rho,\omega + m\Omega)}{\sqrt{1 + (\rho \frac{\partial \varphi_0}{\partial \xi})^2}} d\sigma d\rho d\gamma d\omega \quad (24)
\end{aligned}$$

The discrete tone version of the pressure field obtained after substituting Eq. (20) into Eq. (24) is

$$\begin{aligned}
p_{k,i}(x,r,\theta,t) &= \frac{-B}{2\pi} \exp(ik\theta) \exp(i\omega_{k,i}t) \sum_{n=-\infty}^{\infty} \exp[inB(\Omega t - \theta)] \int_0^{\infty} \frac{\gamma J_m(\gamma r)}{2\kappa(\gamma, nB\Omega + \omega_{k,i})} \\
&\times \int_h^1 J_m(\gamma \rho) \int_0^{s_T(\rho)} \exp[-im\varphi_0(\sigma,\rho)] \exp\{i(x-\xi)[M(nB\Omega + \omega_{k,i}) - \text{sgn}(x-\xi)\kappa(\gamma, nB\Omega + \omega_{k,i})]/\beta^2\} \\
&\times \text{sgn}[\sigma - s_L(\rho)] \langle \vec{b}_m^*(x-\xi,\rho,\gamma, nB\Omega + \omega_{k,i}) \cdot \vec{g}(\sigma,\rho) \rangle \frac{\Delta p_{k,0,i}(\sigma,\rho)}{\sqrt{1 + (\rho \frac{\partial \varphi_0}{\partial \xi})^2}} d\sigma d\rho d\gamma \quad (25)
\end{aligned}$$

2.5.2. Slipstream velocity

The discrete tone version of the complete velocity field Eq. (16) is found similarly to the pressure field above and is given by

$$\begin{aligned} \vec{v}_{k,i}(x,r,\theta,t) &= \frac{B}{2\pi M} \exp(ik\theta) \exp(i\omega_{k,i}t) \sum_{n=-\infty}^{\infty} \exp[inB(\Omega t - \theta)] \int_0^{\infty} \gamma J_m(\gamma r) \\ &\times \int_h^1 J_m(\gamma \rho) \int_0^{s_T(\rho)} \exp[-im\varphi_0(\sigma, \rho)] \vec{H}_m(x, \gamma, nB\Omega + \omega_{k,i}, \sigma, \rho) \frac{\Delta p_{k,0,i}(\sigma, \rho)}{\sqrt{1 + (\rho \frac{\partial \varphi_0}{\partial \xi})^2}} d\sigma d\rho d\gamma \end{aligned} \quad (26)$$

This expansion is valid everywhere and includes velocity components of both acoustic and hydrodynamic nature.

The hydrodynamic part, defined as the $\exp[-ix(nB\Omega + \omega_{k,i})/M]$ dependent term, appears explicitly in Eq. (26) when it is rewritten for an observer downstream of the propeller:

$$\begin{aligned} \vec{v}_{k,i}(x,r,\theta,t) &= \frac{B}{2\pi M} \exp(ik\theta) \exp(i\omega_{k,i}t) \sum_{n=-\infty}^{\infty} \exp[inB(\Omega t - \theta)] \\ &\times \left\{ \exp\left[-i \frac{nB\Omega + \omega_{k,i}}{M} x\right] \int_0^{\infty} \gamma J_m(\gamma r) \vec{v}_{H,m}(\gamma) d\gamma + \int_0^{\infty} \gamma J_m(\gamma r) \vec{v}_{A,m}(x, \gamma) d\gamma \right\} \end{aligned} \quad (27)$$

where

$$\begin{aligned} \vec{v}_{H,m}(\gamma) &= \int_h^1 J_m(\gamma \rho) \int_0^{s_T(\rho)} \exp[-im\varphi_0(\sigma, \rho)] \operatorname{sgn}[\sigma - s_L(\rho)] \exp\left[i \frac{nB\Omega + \omega_{k,i}}{M} \xi\right] \\ &\times \left\{ \vec{g}(\sigma, \rho) - \frac{\langle \vec{c}_m^*(\rho, \gamma, nB\Omega + \omega_{k,i}) \cdot \vec{g}(\sigma, \rho) \rangle}{\left(\frac{nB\Omega + \omega_{k,i}}{M}\right)^2 + \gamma^2} \vec{c}_m(r, \gamma, nB\Omega + \omega_{k,i}) \right\} \frac{\Delta p_{k,0,i}(\sigma, \rho)}{\sqrt{1 + (\rho \frac{\partial \varphi_0}{\partial \xi})^2}} d\sigma d\rho. \end{aligned}$$

The acoustic part $\vec{v}_{A,m}$ does not reveal new aspects so it is not reproduced here. Eq. (27) shows the hydrodynamic m-modes being convected downstream without any attenuation at Strouhal periodicity $\frac{nB\Omega + \omega_{k,i}}{M}$.

This contrasts to the acoustic velocity for which the axial behavior also depends on the radial wave number γ . Moreover, since the acoustic velocity is associated with pressure its magnitude decreases $\sim 1/|x|$ as $|x| \rightarrow \infty$. Therefore the unattenuated hydrodynamic field will dominate in the propeller slipstream beyond some distance. It is noted that the hydrodynamic field is bound to the trailing vorticity and on its own it is not a solution of the problem. It can only exist together with an associated acoustic field to satisfy the boundary condition at the blade surfaces.

2.5.3. Blade surface pressure

Sofar the present analysis has been concentrated on the pressure jump distribution p over the blade surfaces. Once the PJD is known the whole field is determined. However, there is one important exception; the interior and exterior blade surface pressures themselves. As the pressure is given by the Fourier series Eq. (24), this expression will yield the average of $p(\text{exterior})$ and $p(\text{interior})$ at a blade surface coordinate. Thus the exterior blade surface pressure is found from

$$\tilde{p}(\text{exterior}) = \tilde{p}[\text{Eq. (24)}] \Big|_{\theta = \varphi_0(s,r) + \Omega t} + \frac{1}{2} \Delta \tilde{p}_{k,0}(s,r,t) \quad (28)$$

The interior pressure may be found similarly but this pressure is, of course, only formal and not important in practice.

3. SOLUTION PROCEDURE

In the preceding analysis an integral equation for the PJD over the blade surfaces has been derived. The first step taken to solve the PJD from this equation is its expansion into a suitably chosen set of perimetral and radial basis functions. Here the following truncated Fourier double series has been adopted

$$\Delta p_{k,0}(\sigma, \rho, \omega) \approx \sqrt{M^2 + (\Omega \rho)^2} \sum_{\eta=1}^H \sin\left[\pi \eta \frac{\rho-h}{1-h}\right] \sum_{-\Lambda}^{\Lambda} P_{k\eta\lambda}(\omega) \exp\left[\frac{12\pi\lambda\sigma}{s_T(\rho)}\right] \quad (29)$$

The factor $\sqrt{M^2 + (\Omega \rho)^2}$ is added to improve the convergence of the series (29) as the PJD presumably scales on the relative, local main velocity.

Since the analysis leading to the integral equation is essentially for inviscid flow it does not define the PJD uniquely and a Kutta condition has to be added to ensure a symmetric flow at the trailing edge of the blades. As discussed in references 12 and 13, pointwise imposed conditions are insufficient to force a Fourier series to a local behavior if uniform convergence is not guaranteed. Therefore the Kutta condition is here applied as the requirement that the PJD expansion averaged over a small interval adjacent to the trailing edge must be equal for upper and lower surface. The size of the interval chosen is

the shortest perimetral wavelength occurring in the series (29), $s_T(\rho)/\Lambda$. This leads to the following equations for the Fourier coefficients $P_{k\eta\lambda}$

$$\int_{\lambda=-\Lambda}^{\Lambda} K_{\lambda} P_{k\eta\lambda}(\omega) = 0$$

for $\eta = 1, 2, \dots, H$ (30)

$$\text{where } K_{\lambda} = \begin{cases} [1 - \cos(2\pi\lambda/\Lambda)]/\lambda, & \lambda \neq 0 \\ 0, & \lambda = 0 \end{cases}$$

Now the following Galerkin projections are made of integral Eq. (19), or its discrete tone counterpart Eq. (21)

$$\int_h^1 \cos(\pi j \frac{r-h}{1-h}) \int_0^{s_T(r)} \cos[\frac{\pi \ell s}{s_T(r)}] [\text{Eq. (19)}] ds dr$$

($j = 0, 1, 2, \dots, J, \ell = 0, 1, 2, \dots, L$) (31)

Upon substitution of the approximating series (29), the projections Eqs. (31) turn into a set of $(J+1)(L+1)$ linear algebraic equations in the unknown pressure jump coefficients $P_{k\eta\lambda}(\omega)$. This set is completed by the H Eqs. (30) to satisfy the Kutta condition. Obviously, the number of equations must equal the number of unknowns, i.e., $2\Lambda H = (J+1)(L+1)$. After having approximated the infinite series over n in the integral equation [Eq. (19), Eq. (21)] by means of a Richardson extrapolation (e.g., see Ref. 14), the set of equations can be solved by standard matrix inversion techniques.

A computer program based on the above solution procedure is under development at NLR.

4. CONCLUSIONS

A non-helicoidal unsteady lifting surface theory has been formulated for propellers in a non-axisymmetric flow. The method in particular applies to wide-chord propellers with blades that may be swept both axially and azimuthally. Whereas an essentially subsonic forward velocity has been assumed there is no such limitation for the propeller tip speed. Though wing upwash may be considered the most common source of flow asymmetry, stronger inflow distortions may be expected in less usual configurations as pusher and dual, counter-rotation propellers, which are equally well covered by the present analysis. By a formulation in separated cylindrical coordinates and by the chosen sequence of inverse transforms a close analogy resulted with the modal approach in the lifting surface problem for a ducted fan. An inverse Hankel transform in the propeller problem just corresponds to the summation of radial modes in the fan problem. Consequently, similar transparent and relatively compact expressions for the field of a propeller have been obtained. The hydrodynamic velocity field downstream of the propeller (i.e., the slipstream) appears explicitly and in a form most appropriate for interference calculations.

5. REFERENCES

1. Tanna, H.K., Burrin, R.H. and Plumblee, H.E., "Installation Effects on Propeller Noise", AIAA Paper 80-0993, June 1980.
2. Hanson, D.B., "Compressible Helicoidal Surface Theory for Propeller Aerodynamics and Noise", AIAA Journal, Vol. 21, No. 6, June 1983, pp. 881-889.
3. Gutin, L., "On the Sound Field of a Rotating Propeller", NACA TM 1195, 1948 (From Phys. Zeitschrift der Sowjetunion, Bd. 9, Heft 1, 1936, pp. 57-71).
4. Garrick, I.E. and Watkins, C.E., "A Theoretical Study of the Effect of Forward Speed on the Free-space Sound Field around Propellers", NACA TN 3018, Oct. 1953.
5. Van de Vooren, A.I. and Zandbergen, P.J., "Noise Field of a Rotating Propeller in Forward Flight", AIAA Journal, Vol. 1, No. 7, July 1963, pp. 1518-1526.
6. Farassat, F., "Linear Acoustic Formulas for Calculation of Rotating Blade Noise", AIAA Journal, Vol. 19, No. 9, Sept. 1981, pp. 1122-1130.
7. Goldstein, S., "On the Vortex Theory of Screw Propellers", Proc. Roy. Soc. London, A 123, 1929, pp. 440-465.
8. Kondo, K., "On the Potential-Theoretical Fundamentals of the Aerodynamics of Screw Propellers at High Speed", Journal of the Faculty of Engineering, University of Tokyo, Vol. XXV, No. 1, 1957, pp. 1-39.
9. Davidson, R.E., "Linearized Potential Theory of Propeller Induction in a Compressible Flow", NACA TN 2983, Sept. 1953.
10. Namba, M., "Three-Dimensional Analysis of Blade Force and Sound Generation for an Annular Cascade in Distorted Flows", Journal of Sound and Vibration, Vol. 50, No. 4, 1977, pp. 479-508.

11. Lordi, J.A. and Homicz, G.F., "Linearized Analysis of the three-dimensional compressible flow through a rotating annular blade row", Journal of Fluid Mech., Vol. 103, 1981, pp. 413-442.
12. Schulten, J.B.H.M., "Sound Generated by Rotor Wakes Interacting with a Leaned Vane Stator", AIAA Journal, Vol. 20, No. 10, Oct. 1982, pp. 1352-1358.
13. Schulten, J.B.H.M., "Vane Stagger Angle and Camber Effects in Fan Noise Generation", AIAA Journal, Vol. 22, No. 8, Aug. 1984, pp. 1071-1079.
14. Bender, C.M. and Orszag, S.A., "Advanced Mathematical Methods for Scientists and Engineers", McGraw-Hill, 1978.

6. ACKNOWLEDGEMENTS

The present investigation was sponsored by the Netherlands Agency for Aerospace Programs (NIVR). The author gratefully acknowledges the many helpful discussions with Dr. S.W. Rienstra.

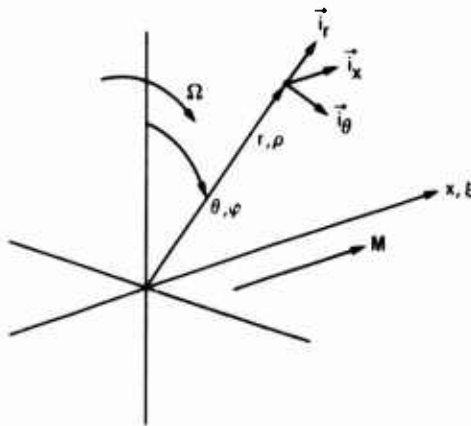


Fig. 1 Coordinate system

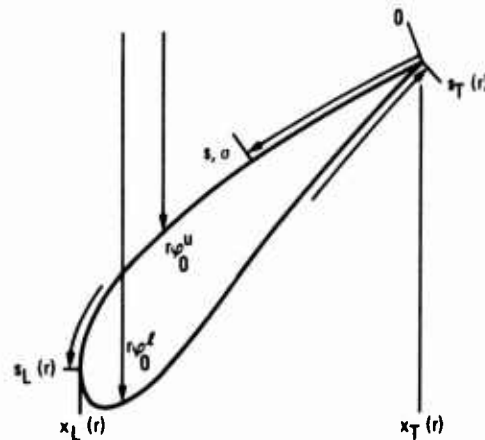


Fig. 2 Blade section perimetral coordinates

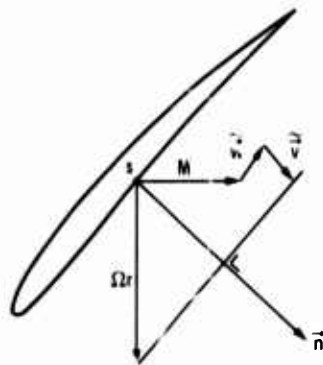


Fig. 3 Boundary condition in point s

ON THE AERODYNAMICS OF INSTALLED PROPELLERS

by
Martin E. Eshelby

College of Aeronautics
Cranfield Institute of Technology
Cranfield
Bedfordshire MK43 0AL
U.K.

SUMMARY

The majority of the research available on the aerodynamics of propellers is based on the isolated propeller on a test rig. When the propeller is installed on the aircraft there will be mutual influence between the airframe and the propeller and its slipstream, this paper examines two sources of that interference. Firstly, as the aircraft angle of attack changes with forward speed the angle of attack of the propeller also changes giving rise to forces and moments other than thrust and torque. Secondly the high energy slipstream may pass over the tailplane and so affect the tail lift force, and in consequence a pitching moment due to power may be produced. These two effects are considered separately and means are suggested to estimate their magnitude and their effect on the handling qualities of the aircraft.

NOTATION

A	Propeller disc area	Greek symbols
a	Axial velocity inflow factor	α angle of attack
a'	Angular velocity inflow factor	β Propeller blade pitch angle
B	Number of propeller blades	γ Flight path angle
b, b ₀	Blade chord, max. chord	δ_p Propeller incidence relative to wing
D; C _D	Propeller diameter, Drag; Drag coefficient	ϵ Downwash or upwash angle
E	Lift-drag ratio	θ Angular position of blade, wing vortex position angle (eqn.33)
J	Advance ratio V/nD	η Propeller efficiency, elevator angle
K	Coefficient (eqn. 30)	ψ Induced velocity angle
L, C _L	lift, lift coefficient	ρ, σ air density, relative density
M, C _M	Pitching moment, Pitching moment coefficient	ϕ wind angle relative to propeller disc
N, C _N	Yawing moment, Yawing moment coefficient	Ω Angular velocity of propeller
n	Propeller rotational speed (revs/sec)	ω Angular velocity of slipstream
P, C _P	Engine shaft power, power coefficient	Subscripts
Q, C _Q	Torque, Torque coefficient	o zero, datum
q	dynamic pressure $\frac{1}{2}\rho V^2$	x at radius x
r	radius	β blade
S, S _T	Wing area, Tailplane area	P power, propeller
s	wing semi-span	w wing
T	thrust	T tail
V	True airspeed	S slipstream
v _i	Induced velocity	
W	Aircraft weight	
x	non-dimensional radius 2r/D	
Y, C _Y	Sideforce, sideforce coefficient	
Z, C _Z	Normal force, normal force coefficient	

Part I. Propeller Performance in Asymmetric Flow

1.1 INTRODUCTION

There is a resurgence of interest in the use of propellers on the next generation of transport aircraft since they can be shown to give a better propulsive efficiency than turbojet or turbofan powerplants. However, since the last generation of propellers was developed there have been extensive developments in powerplant technology which have increased the power output of the engines and the operating speeds of the aircraft have generally increased. The next generation of propellers must absorb very much higher power input and operate over a larger speed range than their older counterparts and any secondary forces and moments produced by the propeller, hitherto neglected, may become large enough to significantly affect the handling or performance of the aircraft.

It has long been known^{1,2,3} that propellers under power produced forces along and moments about axes normal to their rotational axis but little has been done to evaluate these effects since the early 1940's because of the introduction of the turbojet engine which has dominated the civil and military transport scene since then. At that time attempts were made to estimate the lateral forces and moments due to the propeller in yaw based on a projected propeller disc area^{1,2} or by considering the propeller "fin effect" in which the propeller is assumed to produce forces which can be analysed in a similar manner to a vertical lifting surface at the propeller³. These approaches were based largely on empirical data and produced adequate allowances for the propeller and engine combinations which were being used towards the end of World War II. In neither case would the methods be considered suitable for application to current or future propeller designs and a method of estimation of the additional forces and moments which will take into account the variables of flight is required.

In all but a very few cases the propeller-engine combination can be considered rigidly fixed to the airframe so that there will be a fixed relationship between the angle of attack of the aircraft and that of the propeller with respect to the free stream flow direction. (In this paper the inevitable degree of flexibility of the structure and engine mounting will not be considered, but this can obviously be included in a more vigorous treatment.) Since the angle of attack of the aircraft is a function of its forward speed, or more strictly C_L , the direction of the flow relative to the propeller axis will also be a function of the angle of attack and in general the flow direction will not be axially into the propeller but along some direction in the xz plane, fig.1.1. This will lead to an asymmetric loading of the propeller disc which will give rise to the additional forces and moments.

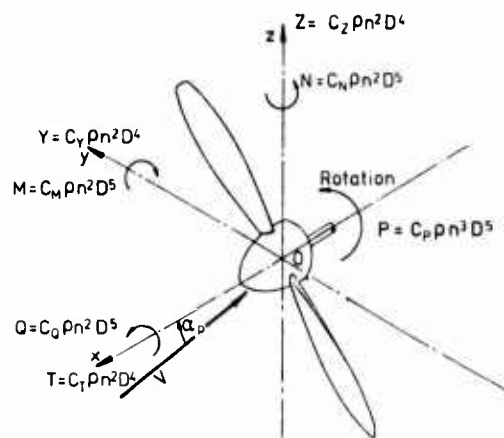


Fig 1.1 PROPELLER NOTATION & ASYMMETRIC FLOW

The simple momentum theory of the propeller considers only the forward speed of the propeller and the power input so that symmetry of disc loading is assumed and only the thrust is estimated. Clearly this approach is not sufficient to predict the performance of a propeller in asymmetric flow and a method is required which will take into account the effects of the cyclic variation in local angle of attack as the propeller rotates. If the basic geometric and sectional aerodynamic characteristics of the propeller blade are known then the strip theory can be applied. This method is well established^{4,5} and modern computing techniques enable the propeller performance to be established under the asymmetric loading conditions which occur in flight. Usually the only propeller variables known are the aircraft's forward speed, the rotational speed of the propeller and the gross power of the engine which are not sufficient for the analysis of the propeller by the strip theory. The local angle of attack of the propeller blade element will be required, as will the propeller efficiency, and the only means of obtaining this data is to calculate it by an iterative analysis which will compare the propeller performance estimated from the strip theory with a simple analysis based on the momentum theory. To achieve this the propeller performance must be defined in appropriate terms for each form of analysis.

1.2 ANALYSIS OF THE PROPELLER PERFORMANCE

Since a propeller is doing work on the airstream it will modify the flow vector giving rise to an increment in the effective forward speed of a blade element, this increment is known as the displacement velocity and is defined as the velocity of the screw surface in the direction of its axis⁵. It arises from the combination of the increase of the axial momentum of the flow through the propeller disc due to the thrust and the angular momentum imposed on the propeller slipstream due to the propeller torque reaction. The momentum theory can be used to provide a reliable average value of the inflow factor at the propeller disc (the axial interference) and an average angular momentum can be calculated from the gross shaft power delivered to the propeller and used to give an estimate of the rotational interference factor.

1.2.1 The Axial Interference Factor, a .

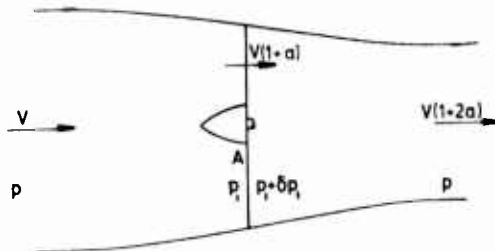


Fig 1.2 ACTUATOR DISC & MOMENTUM THEORY

Using the well known momentum theory⁶ the propeller is represented by an actuator disc of area A in a free stream of velocity V and pressure p , Fig.1.2. The thrust can be expressed in terms of the axial interference factor, a , as

$$T = 2A\rho V^2(1+a)a \quad 1)$$

Now from the definition of the propeller efficiency

$$\eta P = TV \quad 2)$$

eqn. 1) becomes

$$\eta P = 2A\rho V^3(1+a)a \quad 3)$$

which in coefficient form reduces to

$$\eta C_p = \frac{2A\rho V^3}{\rho n^3 D^5}(1+a)a = \frac{1}{2}\pi J^3(1+a)a \quad 4)$$

where J is the propeller tip advance ratio based on aircraft forward speed.

Solving 4) for a gives the approximate solution

$$a = 2\eta C_p / \pi J^3 \quad 5)$$

The axial inflow factor is thus a function of the propeller efficiency, η , and in any calculation it is necessary to estimate an initial value of η and to use an iterative process to find a .

1.2.2 Angular Velocity Interference Factor a'

The torque reaction of the propeller on the airstream will cause a rotation of the propeller slipstream about the propeller axis with an angular velocity ω in the direction of the propeller rotation. The angular velocity interference factor, a' , can be regarded as an apparent loss of propeller angular velocity, thus if the propeller angular velocity is Ω the effective rotational speed will be $\Omega - \omega$. Defining the angular velocity interference factor in terms of

$$\omega = \Omega a'$$

then the effective rotational speed of the propeller will be

$$\Omega(1 - a') \quad 6)$$

The magnitude of the angular velocity interference factor can be estimated by considering the torque reaction of the propeller on the flow through the propeller disc and the resultant change in angular momentum of the flow⁷. This leads to the result

$$a' = 4C_p / \{\pi^3 J(1+a)\} \quad 7)$$

which represents an average value of the angular velocity inflow factor over the propeller disc which can be estimated from known flight parameters.

1.2.3 Velocity Vector at the Propeller

Using the interference factors developed in sections 2.1 and 2.2 the velocity vectors at the propeller can be calculated for a blade element at radius x from the axis of rotation where

$$x = 2r/D$$

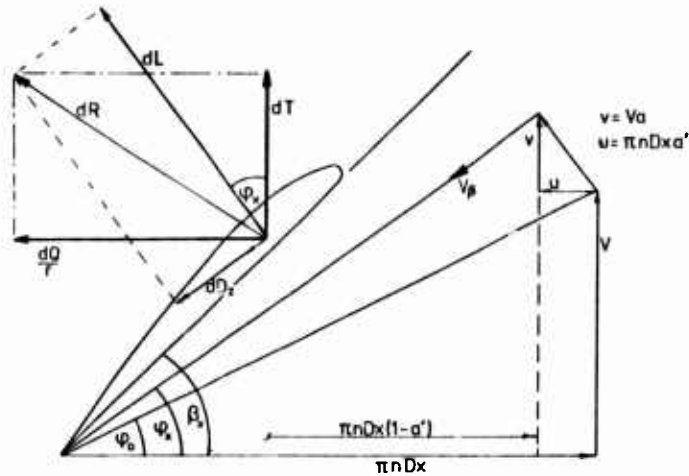


Fig 1.3 PROPELLER BLADE ELEMENT
FORCE & VELOCITY DIAGRAM

From fig.1.3 the apparent wind angle ϕ_0 to the propeller is given by

$$\tan \phi_0 = V/\pi n D x \quad 8)$$

whilst the actual wind angle ϕ_x relative to the blade element is given by

$$\tan \phi_x = \frac{V(1+a)}{\pi n D x(1-a')} \quad 9)$$

and the velocity component on the blade element can now be defined as

$$V_\beta = V(1+a)/\sin \phi_x \quad 10)$$

It should be noted that the values of the interference factors a and a' are average values for the propeller and do not follow the blade loading profile or any asymmetry of loading which may arise from the angle of attack of the propeller to the local flow direction.

1.2.4 Resolution of Blade Element Forces

From fig.1.3 the angle of attack of the propeller blade at radius x is the difference between the blade element pitch angle β_x and the airflow vector ϕ_x ,

$$\alpha_x = \beta_x - \phi_x \quad 11)$$

The blade element will produce a lift force normal to the local streamflow direction and a drag force in the streamwise direction and these forces can be resolved into a forward (axial) direction (thrust) dT , and a torque component dQ such that

$$dT = B\{dL \cos \phi_x - dD \sin \phi_x\} \quad 12)$$

and

$$dQ = Br\{dL \sin \phi_x + dD \cos \phi_x\} \quad 13)$$

where B is the number of propeller blades.

$$\text{Now } dL = \frac{1}{2} \rho V_\beta^2 C_{L_x} b dr$$

$$\text{and } dD = \frac{1}{2} \rho V_\beta^2 C_{D_x} b dr$$

Substituting $x = 2r/D$, putting the blade chord b in terms of the maximum chord b_0 and substituting for V_β from eqn. 10) gives, in coefficient form

$$\frac{dC_T}{dx} = \frac{b_0 B J^2 (1+a)^2}{4D \sin^2 \phi_x} \left\{ \frac{b}{b_0} C_{L_x} \cos \phi_x - \frac{b}{b_0} C_{D_x} \sin \phi_x \right\} \quad 14)$$

and

$$\frac{dC_Q}{dx} = \frac{\frac{1}{2} b_O B J^2 (1+a)^2}{4D \sin^2 \phi_x} x \left\{ \frac{b}{b_O} C_{Lx} \sin \phi_x + \frac{b}{b_O} C_{Dx} \cos \phi_x \right\} \quad 15)$$

These expressions for the blade element thrust and torque components are completely general and can be integrated over the propeller disc to give the gross thrust and torque coefficients.

1.2.5 The Propeller in Asymmetric Flow

The expression for wind angle, ϕ_x , relative to the blade element, eqn.9, applies only to flow which is parallel to the propeller axis. In flight the propeller will generally be at some angle of attack to the free stream and therefore a component of the forward speed will act in the plane of the propeller and will combine with the rotational velocity to produce a periodic variation of angle of attack as the propeller rotates. From fig.1.4 it can be seen that for the blade angular position θ the instantaneous axial velocity of the blade element at radius x will be,

$$V' = V(1+a) \cos \alpha_p \quad 16)$$

where α_p is the angle of attack of the propeller axis to the local flow.

The instantaneous rotational velocity will be

$$V'_x = \pi n D x (1-a') + V(1+a) \sin \alpha_p \sin \theta \quad 17)$$

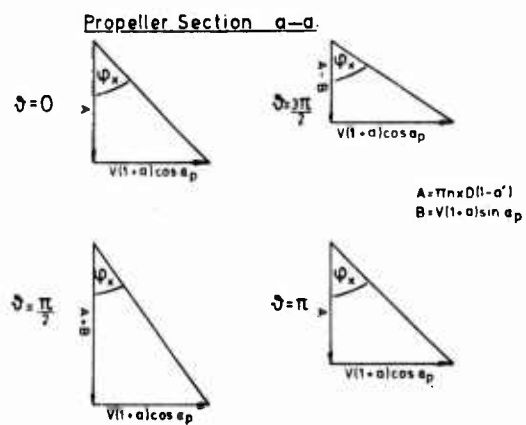
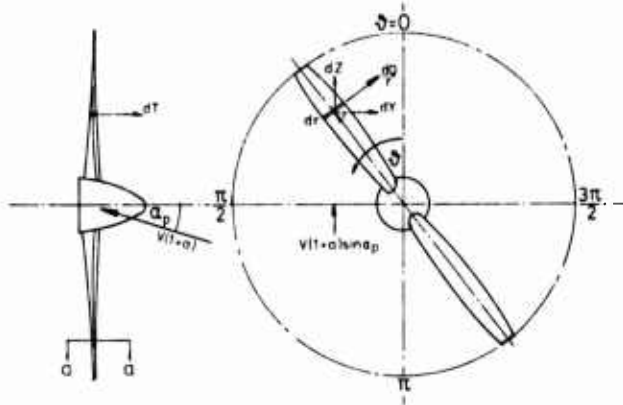


Fig 1.4 PROPELLER VELOCITY VECTORS AT ANGLE OF ATTACK

From eqns. 16) and 17) the instantaneous value of ϕ_x will become ϕ'_x given by

$$\tan \phi'_x = V'/V'_x \quad 18)$$

This leads to modified expressions for the thrust and torque coefficients, eqns. 14) and 15), which become

$$\frac{dC_T}{dx} = \frac{b_O B J^2 (1+a)^2}{4D \sin^2 \phi'_x} \left\{ \frac{b}{b_O} C_{Lx} \cos \phi'_x - \frac{b}{b_O} C_{Dx} \sin \phi'_x \right\} \cos^2 \alpha_p \quad 19)$$

and

$$\frac{dC_Q}{dx} = \frac{\frac{1}{2}b_o B J^2 (1 + a')^2 x}{4D \sin^2 \phi'_x} \left\{ \frac{b}{b_o} C_{L_x} \sin \phi'_x + \frac{b}{b_o} C_{D_x} \cos \phi'_x \right\} \cos^2 \alpha_p \quad (20)$$

and now have periodic variations which will cause an asymmetric loading over the propeller disc. Integrating the disc loading may produce forces which act in the plane of the disc and moments about axes normal to the propeller axis.

The torque force component dQ/r can be resolved into force components normal to the propeller axis, fig.1.4, giving the normal force

$$dZ = \frac{dQ}{r} \sin \theta \quad (21)$$

and the lateral force

$$dY = \frac{dQ}{r} \cos \theta \quad (22)$$

Similarly the thrust component dT will produce moments about the horizontal and vertical axes in the plane of the propeller disc, these being the pitching moment

$$dM = r dT \cos \theta \quad (23)$$

and the yawing moment

$$dN = r dT \sin \theta \quad (24)$$

The magnitude of these forces and moments can be established by integrating over the propeller disc; for example the normal force will be given by

$$Z = \frac{1}{2\pi} \int_0^1 \int_0^{2\pi} \frac{dQ}{r} \sin \theta dx d\theta \quad (25)$$

To perform the integration it is necessary to define the lift and drag characteristics of the propeller blade. These have been defined in terms of the local blade chord b in eqns. 19 and 20 as

$$\text{lift characteristic} = \frac{b}{b_o} C_{L_x} \quad (26)$$

$$\text{and drag characteristic} = \frac{b}{b_o} C_{D_x} \quad (27)$$

Since these characteristics depend on the design features of the propeller blade, e.g. aerofoil section, thickness, twist, chord distribution with span etc., the integral can only be performed for the particular propeller under consideration. The spanwise characteristics of lift and drag can be obtained either from the measured characteristics of the blade or by estimation from its geometric data.

1.3 PROPELLER EFFICIENCY

The propeller efficiency η is defined as the ratio of the work output to the work input,

$$\eta = TV/P = JC_T \pi / 2\pi C_Q \quad (28)$$

The ideal efficiency η_i can be shown⁶ to be

$$\eta_i = (1 - a') / (1 + a) \quad (29)$$

but can never be achieved in practice since the profile drag of the propeller is not represented, neither is the thrust uniformly distributed over the propeller disc. The actual efficiency will be a function of the engine power and propeller operating conditions, which determine a and a' , and can be found from eqn. 28). Since the efficiency is needed to determine a and a' an iterative process is used to calculate an efficiency which will satisfy the estimation of thrust and torque coefficients in terms of the overall propeller performance estimated from the momentum theory. To achieve this the ideal efficiency is factored to give an estimate of the efficiency with the blade drag and the estimated efficiency η_e becomes

$$\eta_e = K(1 - a') / (1 + a) \quad (30)$$

where

$$K = \tan \phi_x / (\tan \phi_x + E)$$

and E is the lift-drag ratio of the blade element. Since ϕ_x and E vary over the blade it is not possible to define a value of K which would be acceptable for the blade and an estimation must be used followed by an iterative procedure to establish a working value of K for any particular operating condition.

1.4. DETERMINATION OF PROPELLER OPERATING CONDITIONS

Since the propeller is assumed to be rigidly fixed to the aircraft the operating conditions of the propeller will be determined by the flight conditions of the aircraft and the engine power which can be regarded as independently variable.

The shaft power delivered to the propeller can be found from the engine operating conditions, usually defined by rotational speed and a parameter such as a pressure or temperature of the engine cycle, together with the pressure and temperature of the atmosphere at the test altitude. The engine manufacturers guaranteed performance charts or an engine calibration are needed for this purpose.

The flight conditions of the aircraft will determine the operating conditions of the propeller in terms of the free stream velocity and propeller angle of attack; these are determined from the weight of the aircraft and the lift equation which in steady flight gives

$$L = W \cos \gamma = \frac{1}{2} \rho V^2 S C_L$$

where γ is the flight path angle.

Thus by specifying a weight and speed in a given atmosphere the angle of attack of the aircraft is specified. The angle of attack of the propeller α_p can now be taken as

$$\alpha_p = \alpha - \delta_p \tag{32}$$

where δ_p is the propeller incidence relative to the wing zero lift line.

There will however be interference between the propeller and the aircraft, the main contribution to be considered will be from the wing. A wing mounted propeller will be in the upwash field of the wing which will contribute to the effective angle of attack of the propeller. The simplest approach to the estimation of the wing interference is to replace the wing by a bound vortex of strength Γ at the quarter chord line. This will produce an induced velocity v_i at a point on the propeller disc, fig.1.5, given by

$$v_i = L(\cos \theta_1 + \cos \theta_2) / 4\pi \rho s V r \tag{33}$$

and the resultant flow direction at the propeller disc will be

$$\alpha + \epsilon_p = \tan^{-1} \{ (v_i \cos \psi + V \sin \alpha) / (v_i \sin \psi + V \cos \alpha) \} \tag{34}$$

The angle of attack of the propeller blade element is

$$\alpha_p = \alpha - \delta_p + \epsilon_p \tag{35}$$

and the resultant velocity at the blade element is given by

$$V' = V(1 + a_w)$$

where

$$a_w = \frac{v_i}{V} \sin(\alpha + \psi)$$

This can be combined with the inflow factor to give a total inflow factor at the blade element leading to

$$V' = V(1 + a + a_w) \tag{36}$$

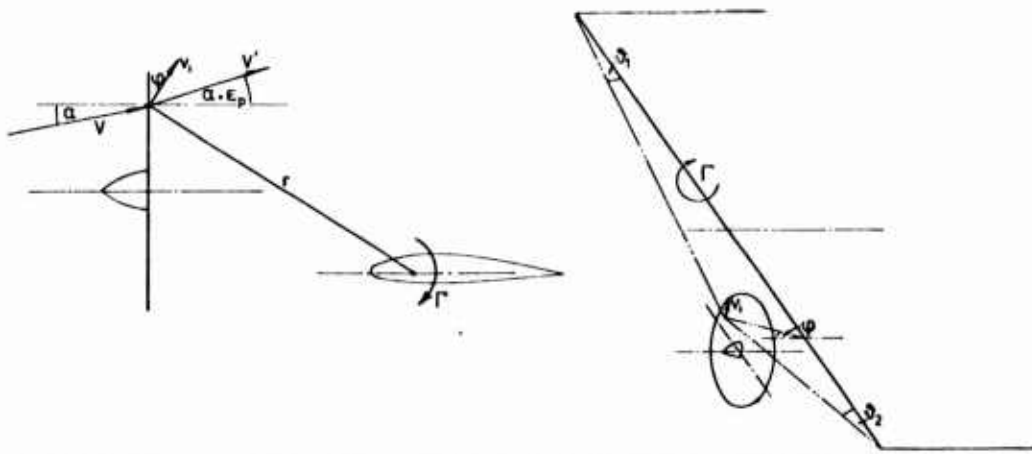


Fig 1.5 INDUCED VELOCITY AT THE PROPELLER DUE TO THE WING

Eqns. 35) and 36) now define the flow vector at each blade element. This will vary

over the wing since the upwash field is a function of the distance from the line vortex of the wing causing an asymmetric inflow vector field and a consequent variation of blade loading with angular position θ .

1.5 CALCULATION OF PROPELLER FORCES AND MOMENTS

The process of calculation of the propeller performance starts with a simple estimation of the thrust and torque coefficients based on the momentum theory,

$$\text{and } C_T = \eta C_p / J \quad (37)$$

$$C_Q = C_p / 2\pi \quad (38)$$

assuming a value for the propeller efficiency.

The thrust and torque coefficients are then calculated by integrating eqns. 19) and 20) over the propeller disc area. This involves a double integral, firstly calculating the blade loading by integrating along the blade span and secondly integrating a revolution of the blade round the propeller disc. Since the loading will depend on the angle of attack of the blade and the calculated inflow factors these parameters will have to be either estimated or calculated from estimated data. Having calculated C_T and C_Q by the integration the value of C_T can be compared with the value from the momentum theory, if these are not similar a correction can be made to the blade angle and an iterative process followed until convergence is achieved. When the thrusts calculated by each method agree within specified limits the propeller efficiency based on the calculated thrust and torque can be calculated from eqn. 28) and compared with the initial estimate. Correction can then be made to the propeller efficiency and the process repeated until thrust and torque coefficients calculated by the momentum theory and blade element theory agree. This state should now define the propeller loading and the normal forces and moments can be found by integrating the thrust and torque force components over the propeller disc.

1.6 CALCULATED PROPELLER PERFORMANCE

A twin engined light aircraft, which was the subject of a research task, was used as the model for the calculation of the propeller performance. Measurements of the engine power, aircraft speed and weight and the atmospheric pressure and temperature were used in the propeller simulation programme. The data is presented in terms of engine power coefficient and propeller advance ratio rather than in terms of the aircraft flight parameters since it is the propeller performance which is of prime interest. Fig.1.6 shows the performance.

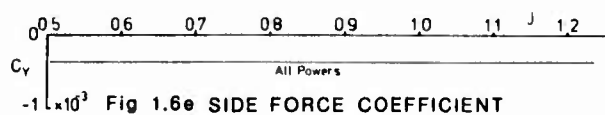
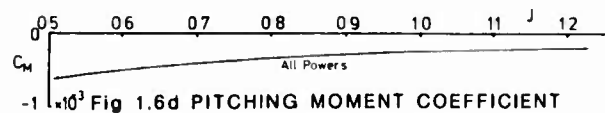
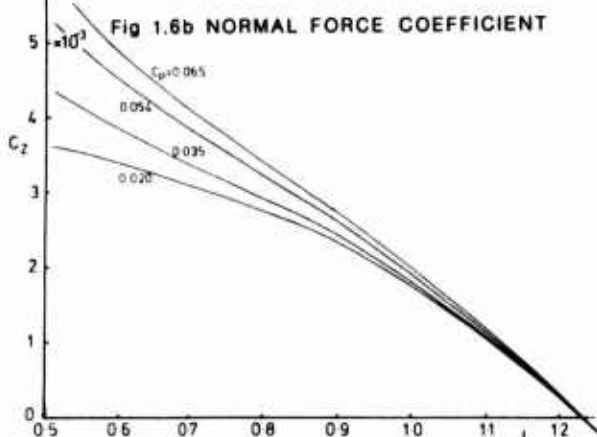
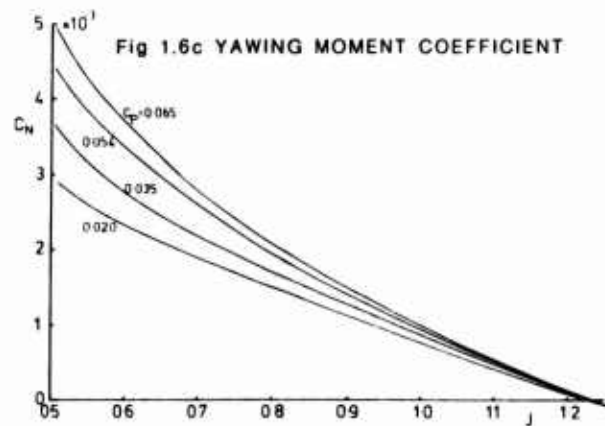
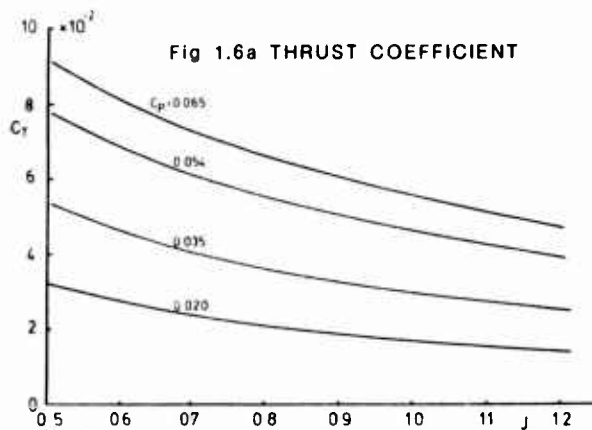


Fig 1.6 FORCES & MOMENTS DUE TO ASYMMETRIC FLOW

1.6.1 Thrust Coefficient, C_T

Since the thrust coefficient is related to the power coefficient by the expression

$$JC_T = \eta C_P$$

the curve of C_T against J for constant C_P should have a hyperbolic form. This is the case with the calculated values of C_T from the programme although variation in propeller efficiency causes some distortion of the pure hyperbolic curve, fig.1.6a. At all powers there is evidence of a decrease in propeller efficiency at low advance ratios which will tend to decrease the slope of the curve and prevent them from tending towards infinity as the advance ratio approaches zero.

1.6.2 Normal Force Coefficient, C_z

The normal force coefficient which arises from the integration of the torque force component of the blade element, is a function of angle of attack. It increases from zero at an advance ratio corresponding to a zero propeller angle of attack, fig.1.6k. The slope of the curve is almost linear, with the value of C_z decreasing as the advance ratio increases. The slight inflection of the curve is most probably due to the propeller efficiency changes with increasing advance ratio.

1.6.3 Yawing Moment Coefficient, C_N

The yawing moment coefficient is also primarily a function of angle of attack and arises mainly from the integration of the thrust force about the vertical axis in the plane of the propeller. It is zero at an angle of attack corresponding to the zero propeller angle of attack and increases as advance ratio decreases with a tendency to increasing slope at lower values of advance ratio, fig.1.6c.

1.6.4 Pitching Moment and Sideforce Coefficients, C_M , C_y

By symmetry these should be zero but due to the asymmetry caused by the wing circulation on the propeller disc located in a wing mounted installation there will be small pitching moments and sideforces. If the propeller is subject to a sideslip, which can be taken to be equivalent to a lateral angle of attack, then the sideforce and pitching moments would be of similar magnitude to the normal force and yawing moments, figs.1.6d and 1.6e.

1.6.5 Propeller Efficiency, η

The propeller efficiency is calculated in the programme as a part of the matching process between the integrated propeller performance and the momentum theory. From the calculated data a general propeller efficiency curve can be constructed, this takes the typical form of a 'rolling surface', fig.1.7. The maximum efficiency is seen to be a function of the two principle variables of the propeller performance, power coefficient and advance ratio.

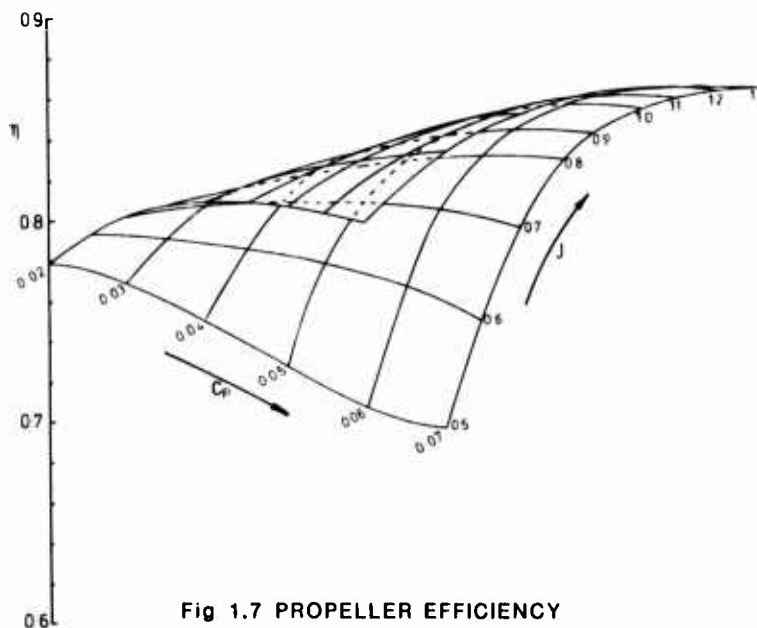


Fig 1.7 PROPELLER EFFICIENCY

1.7 CONCLUSION

The study of the propeller at an angle of attack to the airflow has shown that a considerable normal force and yawing moment can be expected to occur and that they are related to the aircraft angle of attack and engine power. The calculated propeller performance is based on a specific propeller-engine-aircraft combination and serves as an example of the levels of forces which might be produced. Other aircraft and powerplant combinations could be analysed by adapting the propeller and airframe characteristics to suit the case considered.

The study has only considered the effects of angle of attack on the propeller, whereas in general flight sideslip will also occur and will, by the same reasoning, produce a sideforce and a pitching moment. The sideslip could be included by adding a further term to account for the cyclic variation of blade angle of attack in the same manner as the aircraft angle of attack but 90° out of phase. The sideforce arising from the sideslip effect gives rise to the so-called propeller fin effect, but the pitching moment contributes to the longitudinal static stability and it is noticeable that it will be a nose up or nose down contribution depending on the direction of sideslip and propeller rotation.

Generally the magnitude of the contributions will increase with propeller angle of attack (or sideslip) and will be at a maximum at low forward speeds and high engine powers, on take-off or overshoot for example. These are notably high workload periods and substantial changes in power could cause significant changes in handling qualities which may not be fully appreciated.

Part II. Slipstream Interference Effects at the Tailplane

2.1 INTRODUCTION

A propeller under power produces a slipstream in which the energy of the flow is higher than the free stream. If the slipstream passes over some part of the aircraft then it will produce aerodynamic forces which will be dependent on the engine power and on the extent of interference between the slipstream and the airframe. One of the most significant areas of interference is between the propeller slipstream and the tailplane of the aircraft, fig.2.1. If the tailplane is wholly or partly immersed in the propeller slipstream then the tailplane lift forces will be modified by the high energy flow, this may lead to substantial changes of trim setting or static stability as power changes are made or to self-induced oscillations which could be unstable. Such phenomena had been observed during trials with light aircraft and an investigation into the prediction of such interference was initiated.

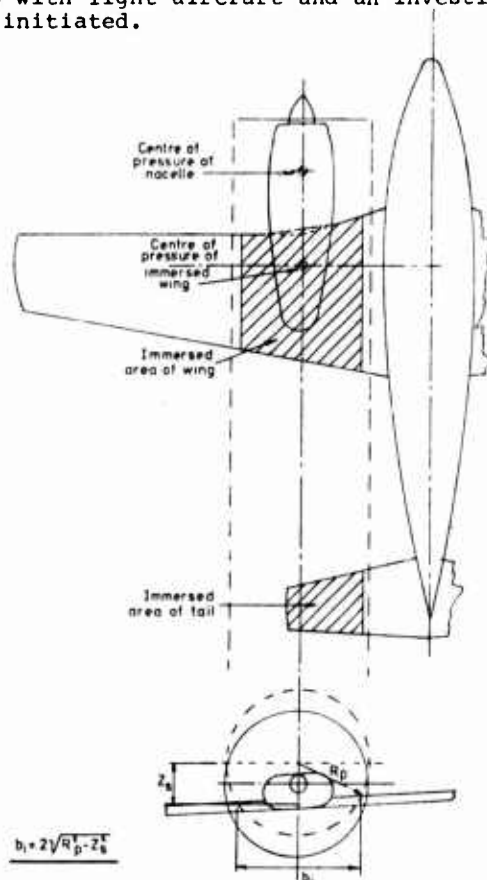


Fig 2.1 PROPELLER SLIPSTREAM INTERFERENCE

The prediction was required to provide information on the slipstream velocity at the tail and the extent of immersion of the tail in the slipstream. The velocity prediction was achieved by using the momentum theory of the propeller to estimate the slipstream velocity in the fully developed slipstream. The tailplane immersion was estimated by tracking the locus of a set of flow filaments assumed to emanate from the edge of the propeller disc downstream towards the tail. In this way the modification of the lift of the tailplane could be assessed and used to estimate the change to the pitching moment equation of the aircraft. Only the static forces are considered in this analysis although the method could be extended to the dynamic case.

2.2 OBSERVATION OF THE SLIPSTREAM-TAILPLANE INTERFERENCE EFFECTS

During the measurement of the longitudinal static stability of a twin-engined light aircraft it had been seen that the trim curves appeared to exhibit a change of slope which was dependent on engine power, fig.2.2. To investigate this phenomenon a pitot

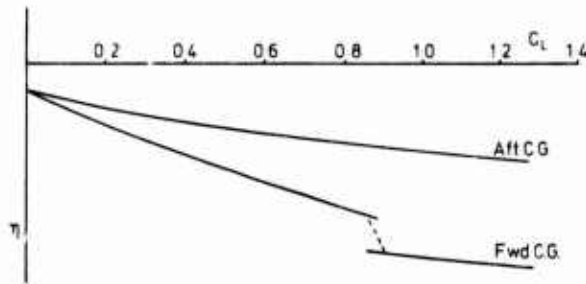


Fig 2.2 MEASURED STATIC STABILITY TRIM CURVES

tube was installed on the tailplane at mid semi-span projecting about 15cm ahead of the leading edge. The total pressure sensed by the tailplane pitot, q_T, was compared with the freestream total pressure, q, to give the slipstream energy factor, q_T/q, which can then be compared with the slipstream energy factor estimated from the engine power and lift coefficient. The experimental system is shown in fig.2.3.

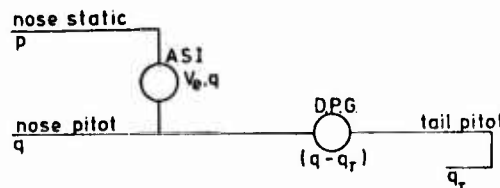


Fig2.3 PITOT-STATIC SYSTEM FOR SLIPSTREAM ENERGY MEASUREMENT

The estimated slipstream energy factor is calculated from the momentum theory of the propeller on the assumption that the slipstream is fully developed by the time it reaches the tail. On this assumption the slipstream energy factor can be shown to be given by

$$\frac{q_T}{q} = 1 + \frac{\eta P \sigma^{\frac{1}{2}}}{A} \left\{ \left(\frac{\delta^3}{W} \right) \frac{\rho C}{2} \right\}^{\frac{1}{2}} C_L^{\frac{3}{2}} \quad (39)$$

and the comparison with the observed slipstream energy factor is shown in fig.2.4 for a single sample of engine power over a range of lift coefficients. Two aircraft loadings

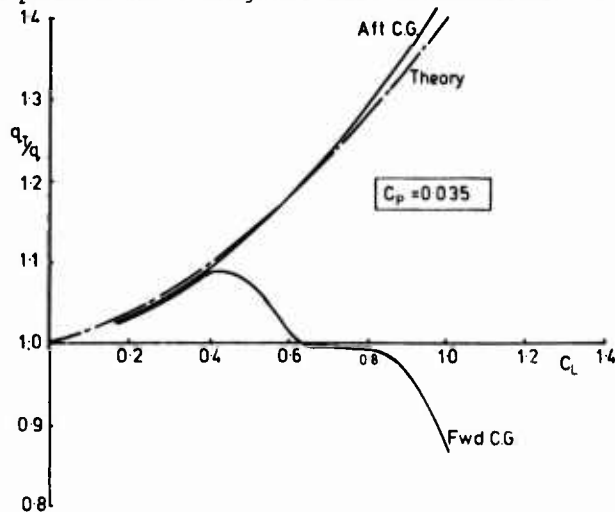


Fig 2.4 SLIPSTREAM ENERGY FACTOR

were used and, rather surprisingly, produced very different comparisons. At aft C.G. the measured and estimated values of the slipstream energy factor compared very closely whereas at forward C.G. the slipstream energy was seen to decrease to the freestream value after an initial rise with C_L , and then became an energy loss. Possible reasons for this will be discussed later in section 2.4.

Similar comparisons exist at other power settings and confirm that there is good correlation between the observed and estimated slipstream energy factor throughout the range of power and speed based on measurements taken at aft C.G. loading.

2.3. EXTENT OF TAILPLANE IMMERSION IN THE SLIPSTREAM

Since part of the tailplane is immersed in the propeller slipstream the lift of the tail will be modified by the high energy flow. Fig.2.5 shows the general effect of the interference between the tailplane and slipstream. In the freestream flow the tail-

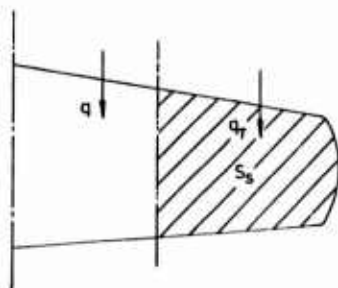


Fig 2.5 TAILPLANE IMMERSION IN SLIPSTREAM

plane lift would be given by

$$L_T = q S_T C_{L_T} \quad 40)$$

whereas if part of the tailplane is immersed in the high energy flow its lift would be

$$L_T = q S_T C_{L_T} \left\{ 1 + \left(\frac{q_T}{q} - 1 \right) \frac{S_S}{S_T} \right\} \quad 41)$$

where S_S is the area of the tail immersed in the slipstream. As the tail lift force is used to balance the aircraft pitching moment the angle of attack of the tailplane, or elevator control deflection, will be adjusted to give the same lift force under the influence of the slipstream as it would in its absence; this may lead to the peculiarities noted in the trim curves of the aircraft.

To determine the extent of the immersion of the tailplane in the propeller slipstream a computer programme was developed to simulate the flow path of a fluid filament issuing from a point on the propeller disc in the presence of the aircraft wing, fuselage and tail. This entailed the calculation of the instantaneous flow velocity at a point on the fluid filament, and the direction of the flow, to build up the locus of the fluid filament. By selecting points of origin of the fluid filament on the periphery of the propeller disc an approximation to the position of the slipstream relative to the tailplane can be made. The method of analysis is based on refs. 8,9,10, and 11.

In representing the aircraft for this purpose the lifting surfaces are replaced by simple bound vortices at the quarter chord with fully rolled up trailing vortices from their tips. The slipstream induced wing lift is included by the addition of a further bound vortex system at the quarter chord of the wing in the slipstream region; the vortex strength being a function of the engine power. The fuselage is represented by an aerofoil section body of revolution which displaces the local flow; no fuselage lift is assumed with increased angle of attack. The propeller slipstream is represented by an incremental velocity calculated by the actuator disc theory⁶. It is assumed that the inflow factor at the disc is half that of the developed slipstream at the tail and that a linear velocity gradient exists between them. No propeller slipstream rotation is included. The lift force generated by the tail is estimated from the pitching moment equation of the aircraft under power.

Using this simple model eight fluid filaments are used to determine the boundary of the propeller slipstream at the leading edge of the tailplane; fig.2.6 shows the predicted location of the slipstream for several values of lift coefficient and the two C.G. locations and power settings corresponding to fig.2.4. It can be seen that as the angle of attack of the aircraft increases the tailplane moves down through the slipstream from the upper portion through to the lower portion and the extent of the tailplane immersion decreases at the higher angles of attack. A small difference is noted between the slipstream position at forward and aft C.G., but not sufficient to account for the large differences in characteristics seen in fig.2.4.

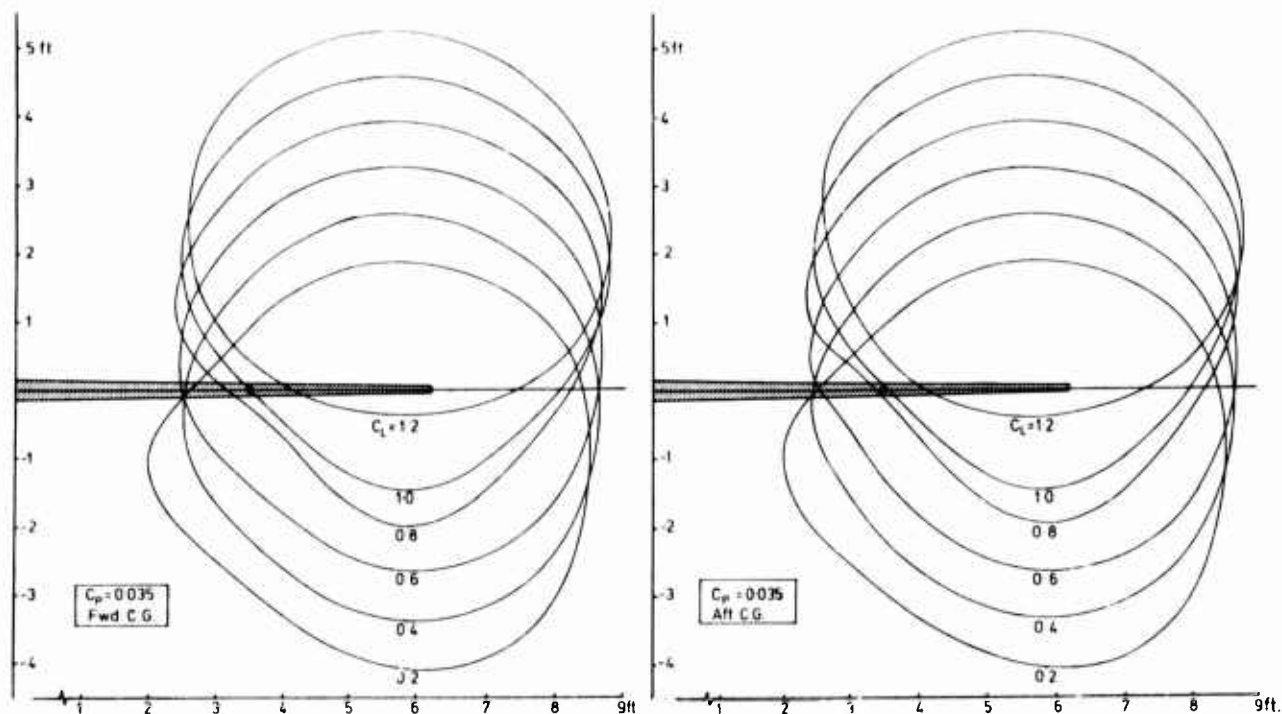


Fig 2.6 SLIPSTREAM POSITION AT THE TAILPLANE

2.4. DISCUSSION

Whilst it is appreciated that the model of the aircraft used to determine the slipstream locus is very simple it was sufficient for the purpose at the time which was to investigate observed power effects on the longitudinal trim curves of an aircraft; it was not intended to be an in depth analysis of some of the propeller characteristics it brought to light. Also the investigation was carried out as an addition to the original research and unfortunately there was insufficient time to do more than a very brief series of tests whilst the aircraft was still available. The instrumentation was minimal, being limited to flight deck displays and a single pitot tube installed on the tailplane for this part of the work.

The investigation showed that the slipstream energy at the tailplane could be predicted to a good accuracy by the momentum theory; this is shown by the measured value of the slipstream energy factor at aft C.G., fig.2.4. The forward C.G. case however showed quite a different trend which was not fully explained by the simulation. The loss of slipstream energy may have been due to the slipstream moving away from the pitot head region. The predicted slipstream position, fig.2.6, shows that the boundary is not far from the pitot head and a small degree of sideslip may well have brought the boundary across to the pitot. It is significant to note that different pilots were used to fly the forward and aft C.G. cases, firstly because their weights assisted the C.G. shift required and secondly to share the flying on the project in a fair manner. It has since been noted that their methods of achieving a zero sideslip state are not entirely similar and this could lead to sufficient asymmetry to cause the slipstream to shift laterally. Also no account was taken of the deflection of the tailplane during the change of C.G. or with C_L , as this is only of the order of 5° over the speed and C.G. range it would only move the pitot location by about 0.17ft (5cm) which is not considered to be likely to cause the effects observed.

The loss of energy in the slipstream at higher values of C_L and forward C.G. are a further enigma. It is thought unlikely to be caused by the wing wake since it does not occur at aft C.G. locations, although nacelle wake interference as a result of sideslip is a possibility. A further possibility arises from the propeller tip vortex system which has been seen to be very complicated¹². As the vortex system breaks up it may produce a very turbulent boundary to the slipstream within which the pitot tube will not register the total head of the flow. The relative motion of the pitot head and the boundary of the slipstream could be maintained over a substantial range of angle of attack given a small amount of sideslip.

Since only the one total pressure source was used in this investigation any conclusions drawn are limited to minimal evidence. The question must be asked, "What would be the effect of a similar tube mounted on the opposite tailplane?" It is possible that the characteristics of the slipstream energy factor curves at forward and aft C.G. could be reversed. If so the sideslip theory could be proved. Alternatively a series of total pressure sensors along the leading edge of the tailplane would determine more fully the extent of the tailplane immersion and its variation with power and angle of attack.

A UNIFIED APPROACH FOR THE AERODYNAMICS AND ACOUSTICS
OF PROPELLERS IN FORWARD MOTION

A. Das
Deutsche Forschungs- und Versuchsanstalt
für Luft- und Raumfahrt e.V.
Institut für Entwurfsaerodynamik
D-3300 Braunschweig-Flughafen
Germany

SUMMARY

The aerodynamics and the acoustics of moving bodies or surfaces follow the same basic laws of disturbance propagation and hence can be treated in a unified way. Further advancements of the propeller theories have two objectives - attaining better propulsive efficiency and producing less noise at high forward speeds. In the present contribution a unified aerodynamic and acoustic theory of propeller in forward motion is formulated and analyzed in detail describing, the aspect of disturbance propagation from singularities in arbitrary motion, derivation of the spatial and temporal dilatations concerned with the propagation process, generalized exposition of the solution method for aerodynamics and acoustics and an extended sweep technique to determine the inducing effect of moving surfaces. In view of the flow field of a propeller being not completely irrotational the use of pressure-potential proves to be more suitable in the numerical methods. The results of the analysis are illustrated extensively by diagrams.

NOTATIONS

Geometrical quantities

		R_o, R	radius of singularity element and field point of a blade
		R_H, R_T	hub- and tip-radius of a blade
		R'_1, R'	radial distance from field point projection to singularity elements and to the scanned contour
		v_o, v_v	volume of a singularity element and of the effective emission element
		x, y, z	cartesian coordinates
		\hat{x}	spatial sweep variable in space domain
		$\bar{x}, \bar{y}, \bar{z}$	rotated coordinates of moving singularity elements with the x-axis parallel to the trajectory at P.
		x', y', z'	coordinates of the rotated singularity surface used in the sweep technique
		α	incidence angle of a propeller blade
		γ_h	helix angle of the trajectory of a blade element
		ϑ_a	inclination angle of the radius vector r_a of a field point to the trajectory
		$\vartheta_o, \tilde{\vartheta}_o$	inclination angle of r_o to the trajectory of a singularity and to the Ma_P -vector of a moving field point
		$\vartheta_v, \tilde{\vartheta}_v$	inclination angle of r_v to the trajectory of a singularity and to the Ma_P -vector of a moving field point
		$\vartheta_{vx}, \vartheta_{vw}$	inclination angle of r_v to the velocity vectors Ma_x and Ma_w at P_v
		θ	angular position of a scanning segment for contour integration around a singularity surface (Fig.11)
B	number of blades		
c	local chord length of a blade		
d	maximum thickness of blade-aerofoil		
D	propeller diameter		
F_o	control surface or singularity surface		
F_v	emitting surface incorporating the spatial stretching effects		
$h_o; h_v$	radial distance of a field point from the trajectory of a singularity ($h_o \equiv h_v$)		
h_S	radial distance of a singularity from a given trajectory		
H	height of a field point normal to a singularity surface-element		
l_o, m_o, n_o	geometric dimensions related to the moving singularity elements		
l_v, m_v, n_v	geometric dimensions related to the effective emission elements		
P, P_o, P_v	locations of field point, singularity element and corresponding emission element		
r_a	radial distance of a field point in spherical polar coordinates		
r_o	radial distance between singularity and field point at the time instant t_o		
r_v	propagation radius or emission radius of a spherical wave		
r_v^*	effective propagation radius by including the spatial dilatation factor		

χ, χ'	inclination of a singularity surface to the trajectory based on original or rotated position (Fig.11)	t_o, t_v	momentary time for signals reaching a field point and the corresponding emission time of the signals
ψ_o, ψ	angular position of a singularity element and of a field point in the plane of the propeller	T_{ij}	stress tensor
		T	axial thrust force of a propeller
ψ_v	angular position of the emission element on the helical surface described by a propeller blade	$u'; v'; w'$	perturbation velocities in the medium
<u>Aeroacoustic and aerodynamic quantities</u>		v_n	velocity component normal to a moving surface
a	local sound velocity	V_S	velocity of a singularity element relative to the medium
a_∞	sound velocity in a homogeneous medium at rest	V_E	velocity of a field point relative to the medium
c_p	pressure coefficient	V_x, V_w	axial and circumferential velocity of moving blade elements
D	drag force	β	Mach number parameter ($\sqrt{ 1-Ma_S^2 }$)
D_o, D_v	singularity strength of a doublet	β_l, β_n	Mach number parameter based on the lengthwise and crosswise component of the motion of a singularity element inclined to the trajectory
G_{ij}	momentum flux or disturbance force per unit surface [kg/m sec ²]	Γ	circulation about a blade element
I_S, I_D	inducing functions comprising resultant perturbation at a field point due to unit singularity strength	γ	nondimensional circulation
k	wave number (ω/a_∞)	δ	Dirac delta-function for specifying the emitting positions and emitting times of signals from moving singularities
\tilde{k}, \bar{k}	reduced wave number ($\tilde{k} = k/\beta^2$) ($\bar{k} = k/Ma_x$)	$\hat{\epsilon}_o$	spatial compatibility parameter for fulfilling the kinematics of disturbance propagation
K_i	disturbance force per unit volume [kg/m ² sec ²]	ζ	aerofoil coordinate normal to the mean surface
L	lift force on a blade	κ	ratio of the specific heats
M	circumferential moment on a blade due to aerodynamic forces	$\hat{\kappa}_o$	temporal compatibility parameter to fulfill the kinematics of disturbance propagation
Ma_S	Mach number of a singularity element having the resultant velocity V_S	λ	speed ratio (V_x/V_w)
Ma_x, Ma_w	axial and circumferential Mach number of a moving blade element	ρ	local medium density in the disturbance field
Ma_l, Ma_n	Mach number component parallel and normal to a singularity surface element	ρ_∞	density of the undisturbed medium
Ma_E, \tilde{Ma}_E	Mach number and its component in the $P_o P P_v$ -plane of a moving field point	$\Delta\rho, \rho'$	density perturbation ($\rho - \rho_\infty$)
p	static pressure	$\sigma_V, \sigma_L, \sigma_N$	spatial dilatation factors (volumetric, lengthwise and crosswise due to effective stretching elements)
p_∞	static pressure in the undisturbed medium	σ_x, σ_w	spatial dilatation factors for stretching in the axial and circumferential directions
$\Delta p, p'$	perturbation pressure ($p - p_\infty$)	σ_R	spatial dilatation factor due to effective shifting of the emitting source-sink-elements
q_∞	nominal dynamic head as reference quantity	$\sigma_D; \sigma_D^*$	temporal dilatation factors yielding the Doppler effect at fixed or moving field points
Q	source flow per unit volume [kg/m ³ sec]	φ	disturbance potential in the propagation field
\bar{s}	nondimensional perturbation quantity for density and pressure		
S	singularity strength of a source		
\bar{t}	sweep variable in time domain		

ψ	summation of the non-linear terms of the wave equation	<u>Subscripts</u>	
ω_0	circular frequency of the rotating blades	o	notation for momentary time and for coordinates relating singularity and field point at a time t_0
ω_v, ω	circular frequency of the emitted signals and of the receiving signals	v	notation for radiation or emission quantities
Ω, Ω^*	singularity functions [1/sec; 1/m]	i, j, k	unit direction-vectors
		μ	emission locations of singularity elements
		n	normal vector

1. INTRODUCTION

The first aerodynamic theory of airscrews or propellers was based on the simple momentum theory, which is also known as the Rankine-Froude theory of marine-propellers. The shortcomings of this crude theory being evident, refinements were attempted by formulating an extended momentum theory and the blade element theory by N.E. Joukowski [1], A. Betz [2], S. Drzewiecki [3] and G.I. Taylor [4]. When the basic concepts of the wing theory were established, attempts were made to extend it to propeller aerodynamics, resulting in the first foundation of the simple vortex theory. For simplicity the assumption of infinite number of blades was introduced and the propeller wake was modelled with successive vortex rings being shed into it and with longitudinal vortex filaments being placed on the cylindrical wake surface. Formulations of propeller theories based on this concept are known from A. Betz [5], H. Glauert [6], E. Pistolesi [7] and Th. Bienen and Th.v. Kármán [8].

A more realistic modelling of the spiraling vortex wakes originating from the propeller blades was taken up by A. Lauth [9] and Th. Troller [10]; the theory was then fully established by S. Goldstein [11]. The application of the vortex theory of propellers has been described in detail in the contributions of H. Glauert [12], C.N.H. Lock [13], F. Weinig [14], Th. Theodorsen [15], W.L. Alexandrow [16] and O. Tietjens [17]. These treatments can be denoted as the prestage of the lifting line and lifting surface theories. During the period when more emphasis was put on the rotor and fan aerodynamics, these being in a way equivalent to propeller aerodynamics, the lifting surface theory was formulated more closely using integral equations and kernel function methods. However the solution of these analytical methods are quite involved.

With the evolution of the numerical fluid dynamics a large impetus was given to the airfoil and wing theories. Because of the more complex nature of the flow fields of propellers the introduction of these numerical methods for propeller aerodynamics lagged behind before they were taken up by H.L. Runyan [18] and more extensively formulated by D.B. Hanson [19] and F. Farassat [20].

Looking now into the development of the acoustic theories of propellers, they can be traced back to the early works of E.J.H. Lynam and H.A. Webb [21], G.H. Bryan [22] and W. Ernsthausen [23] [24], in which analyses of the noise sources on rotating blades and of the sound fields were described. After the fundamental work of L. Gutin [25] based on Fourier analysis of noise sources had been established a number of important contributions followed such as those by A.F. Deming [26] [27], E.Y. Yudin [28], H.H. Hubbard and L.W. Lassiter [29], and by A.A. Regier and H.H. Hubbard [30]. The effect of forward motion of a propeller on the sound field was first studied by I.E. Garrick and C.E. Watkins [31], and then further analyzed by A.I. van de Vooren and P.J. Zandbergen [32]. The collected papers of F.B. Metzger et. al., Ed. H.S. Ribner [33] describe the status of propeller noise research of that time.

While some further relevant papers on the subject were presented in the past years, of which the work of C.L. Morfey [34] is an example, a large impetus was initiated by D.B. Hanson [35] [36], P.A. Nystrom and F. Farassat [37] and by F. Farassat [38] who introduced the powerful methods of numerical fluid mechanics in this field. The two text books by P.M. Morse and K.U. Ingard [39] and of M.E. Goldstein [40] now often serve as references in acoustics.

With the increased forward motion of the propellers the emission and propagation of disturbances from the blades to the surrounding field and their reception at the field points becomes significantly modified. Some of the phenomena connected with the wave propagation from moving sources were first recognized in the electromagnetic fields, as is well known from the contribution of C. Doppler [41], W. Voigt [42] and H.A. Lorentz [43]. The spatial stretching effect caused by the translating motion of emitting elements was first derived by A. Liénard [44] and E. Wiechert [45] for moving electrons in an electromagnetic field. Both authors used the concept of shrinking spherical surfaces with the centers at the field point and their interception with the trajectory. Electromagnetic radiation from periodic sources in arbitrary motion was studied in detail by G.A. Schott [46]. For the solution of the wave equation in acoustics and electromagnetic fields the classical methods of S.D. Poisson [47], H.v. Helmholtz [48] and G. Kirchhoff [49] are very useful.

The effect of motion of singularities on the sound field was first studied by H. Hönl [50], H.G. Küssner [51], N. Rott [52], H. Billing [53] and H. Oestreicher [54]. A very significant contribution in the field of aeroacoustics was introduced by Sir James Light-hill [55] through the fact that the generalized Navier-Stokes equation was formulated as a wave equation calling for the existence of quadrupole terms, which fully established the treatment of aerodynamic sound generation. Further extensions of this basic work are due to N. Curle [56], M.V. Lowson [57] and to J.E. Ffowcs-Williams and D. Hawkings [58]. These contributions have also formed the foundations for some new numerical methods on propeller aerodynamics and acoustics. Also in two recent papers of the present author [59] [60] the problem of spatial- and temporal-dilatations in the propagation field of singularities in arbitrary motion, have been extensively dealt with. The analysis reveals the essential basic properties in the radiation fields and leads to more precise formulations and expositions of many of the classical concepts. Furthermore the invariant nature of the nondimensionalized field quantities as obtained from the solutions in physical space and in Lorentz space are established. Some numerical methods for the solution of aerodynamic and acoustic fields are outlined in [60], using a new sweeping technique for calculating the inducing functions of moving singularities.

The numerical methods within the framework of linearized theories used for calculating flows about bodies or wings of arbitrary configurations are known as panel methods. These have been developed originally for flows at low Mach numbers. The basic ideas and outlines are given in the contributions of J.L. Hess and A.M.O. Smith [61], Th.E. Labrujere et al. [62], W. Kraus [63] and J.L. Hess [64]. The extension of the method to unsteady flows are dealt with in the papers of E. Albanno and W.P. Rodden [65], J.A. Moore and W.P. Jones [66], W. Geissler [67] and L. Morino [68]. A direct numerical method for calculating flows about wings and bodies at high subsonic speeds has been worked out by H.H. Kohlmeier [69] by using the concepts given in [59] and [60]. For Mach numbers comprising transonic flows the numerical fluid dynamics solving the Euler-equations are in the course of development. A recent contribution pertaining to propeller flow fields has been presented by D.S. Chaussee and P. Kutler et al. [70].

The present contribution comprises three essential aspects which are of basic significance for propeller aerodynamics and acoustics, - i.e. (i) derivation of the spatial- and temporal-dilatations in the propagation fields of singularities in arbitrary motion, (ii) generalized formulation of the solution methods for aerodynamics and acoustics, and (iii) the introduction of a new sweep-technique to calculate the inducing fields of moving source- and doublet-surfaces. The methods developed here can also be inserted into the numerical computing procedures developed by others, using the steps described as subroutines to calculate the inducing functions of propeller blade elements.

2. SPATIAL- AND TEMPORAL-DILATATIONS IN THE RADIATION FIELDS OF SINGULARITIES IN ARBITRARY MOTION

The phenomena of spatial dilatations during the emission process from sources in translatory motions was first dealt with by A. Liénard [44] and E. Wiechert [45], who considered the motion of an electron in an electromagnetic field. The stretching factor derived by them is identical to that obtained by the theory of relativity and the Lorentz-dilatations.

In acoustics and aerodynamics one encounters similar dilatation processes when the sources motion becomes comparable to or higher than the speed of sound. In order to obtain results of general validity it is essential to allow for arbitrary orientations and arbitrary motion of the source elements in space, including in particular translatory, circular and helical motions. For the direct derivation of the dilatation factors it is necessary to prescribe the relative positions $P_0(r_0, \psi_0)$ of the moving source and the locations P of the field point in space at the time instant t_0 , and to determine the emitting position $P_v(r_v, \psi_v)$ of the source element at a time t_v , as illustrated in Fig. 1. From this a straight forward relation for the radiation quantities r_v and ψ_v is established. For the propeller problem it is essential to consider the following basic type of motions and the corresponding interrelations of the radiation quantities:

Translatory motion

$$(1 - Ma_S^2) r_v^2 - 2 r_0 Ma_S \cos \psi_0 r_v - r_0^2 = 0 \quad (2-1)$$

$$r_v \cos \psi_v - Ma_S r_v - r_0 \cos \psi_0 = 0$$

with r_v and ψ_v as unknowns.

Circular motion

$$r_v^2 - r_a^2 + 2 R r_a \sin \psi_a \cos \psi_v - R^2 = 0$$

$$r_v \cos \psi_v + r_a \sin \psi_a \sin \psi_v = 0 \quad (2-2)$$

$$R(\psi_0 - \psi_v) - Ma_w r_v = 0$$

with r_v , ψ_v , ψ_v as unknowns.

Helical motion

$$(1 - Ma_x^2)r_v^2 + 2r_a \cos\psi_a Ma_x r_v - \left\{ R_0^2 + r_a^2 - 2r_a \sin\psi_a R \cos\left(\psi - \psi_0 + \frac{Ma_\omega r_v}{R}\right) \right\} = 0$$

$$Ma_S \cos\psi_v = Ma_x \cos\psi_{vx} + Ma_\omega \cos\psi_{v\omega} \quad (2-3)$$

$$\cos\psi_{vx} = -\frac{x_v - x}{r_v}; \quad \cos\psi_{v\omega} = -\frac{r_a \sin\psi_a \sin\psi_v}{r_v}$$

with r_v , ψ_v , ψ_{vx} and $\psi_{v\omega}$ as unknowns.

Using these equations the position and orientation of the emission point P (r_v, ψ_v) of a source element is fully determined. Imposing now the kinematic relations one can derive the spatial and temporal stretching factors. The spatial stretching factors are defined under the conditions that all the signals from the effective emission element reach the field point simultaneously at time t_0 . The temporal stretching factors define the ratio of the time sequence or duration of signal emission compared to those at reception at the field point. For the stretching factors occurring in the propagation field one can define:

The spatial dilatations

$\sigma_V = \frac{dv_v}{dv_0}$ volume-stretching-factor	$\sigma_R _{1,2} = \frac{dr_v}{dr_{v0}}; \frac{dm_v}{dm_{v0}}$ shifting factor of dipole singularities
$\sigma_L = \frac{dl_v}{dl_0}$ longitudinal-stretching factor	$\sigma_\omega = \frac{d\psi_v}{d\psi_0}$ circumferential-stretching-factor
$\sigma_N = \frac{dn_v}{dn_0}$ cross-stretching-factor	$\sigma_X = \frac{dx_v}{dx_0}$ axial-stretching-factor

The temporal dilatations

$\sigma_D = \frac{dt_v}{dt_0}$ time sequence of signal emission from a moving source and reception at a medium fixed field point	$\sigma_D^* = \frac{dt_v}{dt_0} \Big _{Ma_E}$ time sequence of signal emission from a moving source and reception at a moving field point
----------------------------------------------------------------------------------------------------------------------------------	-------------------------------------------------------------------------------------------------------------------------------------------

These quantities will now be derived in the subsequent sections.

2.1 Spatial dilatations in the radiation fields of singularities in uniform translatory motion

Considering a singularity element of length dl_0 moving along a trajectory aligned with the coordinate x , with a velocity V_S in the negative x -direction the method of shrinking sphere as formulated by A. Liénard [44] and E. Wiechert [45] yields the following relations as illustrated in Fig. 2. These relations are set up conforming to the statements made in these contributions:

$$dl_v = dl_0 + Ma_S dr_{v1} - Ma_S dr_{v2} = dl_0 + Ma_S dr_v \quad (2-4)$$

With $dr_v = dl_v \cos\psi_v$ (Fig. 2) it follows:

$$dl_v = dl_0 + Ma_S dl_v \cos\psi_v \quad (2-5)$$

Hence

$$\sigma_V = \sigma_L = \frac{dl_v}{dl_0} = \frac{1}{1 - Ma_S \cos\psi_v} \quad (2-6)$$

In Fig 2 three cases are demonstrated for which $\sigma_V = 1$ and $\sigma_V \leq 1$.

For arbitrary orientation of the source element in space it is more convenient and instructive to follow the method described in [59]. The derivation of the spatial dilatations are based on the simple kinematic relations

$$\begin{aligned} x_v - x_o &= Ma_S r_v \\ h_v \sin \psi_v &= h_o \sin \psi_o \end{aligned} \quad (2-7)$$

and further relations connecting r_v , ψ_v to r_o and ψ_o . The derivation yields

$$\sigma_L = 1 + \frac{Ma_l \cos \psi_{vl}}{1 - Ma_S \cos \psi_v} \quad (2-8)$$

$$\sigma_N = \frac{1}{1 - Ma_n \cos \psi_{vn}} \quad (2-9)$$

$$\sigma_V = \sigma_L \cdot \sigma_N = \frac{1}{1 - Ma_S \cos \psi_v} \quad (2-10)$$

The stretching of a moving source element are shown in Fig. 3 for three different inclinations of it to the trajectory, maintaining however the same relative orientation between its centroid and the field point at the time instant t_o . Although the stretching factors σ_L and σ_N are different in the three cases, the resulting volume stretching σ_V remains constant. While σ_L implies a pure surface stretching, the dilatation factor σ_N contributes to a change in the flux through the surface, thus affecting the singularity strength at emission.

The stretching factor defining the relative shifts of the source-sink-combination of a dipole in translatory motion can be determined by σ_R under the condition that the signals from both the singularities meet the field point simultaneously at a time instant t_o . The undergoing-phenomena is illustrated in Fig. 4. The partial derivations of r_v with respect to m_o can be carried out easily and yields the following dilatation factors:

$$\sigma_{R1} = \frac{dr_v/dm_o}{|dr_v/dm_o|_{Ma_S=0}} = \frac{dr_v}{dr_{vo}} = \frac{1}{1 - Ma_S \cos \psi_v} \quad (2-11)$$

and

$$\sigma_{R2} = \frac{r_v (d\psi_v/dm_o)}{|r_v (d\psi_v/dm_o)|_{Ma_S=0}} = \frac{dm_v}{dm_{vo}} = \frac{1}{1 - Ma_S \cos \psi_v} \quad (2-12)$$

so that $\sigma_{R1} = \sigma_{R2} \equiv \sigma_R$.

2.2 Spatial dilatations in the radiation fields of singularities in circular and helical motion

If the singularity undergoes a purely circular motion then the Mach number $Ma_S = Ma_\omega$ and the kinematic condition connecting P_o to P_v reduces to:

$$R (\psi_o - \psi_v) = Ma_\omega r_v \quad (2-13)$$

Taking the partial derivatives of this equation with respect to ψ_o it yields:

$$1 - \frac{\partial \psi_v}{\partial \psi_o} = \frac{Ma_\omega}{R} \frac{\partial r_v}{\partial \psi_v} \cdot \frac{\partial \psi_v}{\partial \psi_o} \quad (2-14)$$

From Eq. (2-14) one obtains the relation

$$\frac{1}{R} \frac{\partial r_v}{\partial \psi_v} = - \frac{r_a \sin \psi_a \sin \psi_v}{r_v} = - \cos \psi_{v\omega} \quad (2-15)$$

Eq. (2-15) inserted in Eq. (2.14) leads to the stretching factor of emitting elements in circular motion.

$$\sigma_{\omega} = \frac{dl_v}{dl_0} = \frac{d\psi_v}{d\psi_0} = \frac{1}{1 - Ma_{\omega} \cos \psi_{v\omega}} \quad (2-16)$$

This expression can also be directly obtained from the Eq. (2-8) for σ_v , in which one is to put $Ma_S = Ma_L = Ma_{\omega}$ as the only motion of the singularity. It is evident that the effect of the spatial dilatation σ_{ω} will be present in the whole disturbance field except for field points along the axis of the circular trajectory, for which $\psi_{v\omega} = \pi/2$. While the effect of σ_{ω} on the sound field of propellers was recognized in [32] and [57], this phenomena is mostly overlooked by other acousticians. The significance of this stretching function is clearly illustrated in Fig. 5.

Considering now the helical motion of a singularity along a helix ξ , as in the case of a propeller blade element having rotational and forward motion, the following kinematic relations will be based on.

$$\begin{aligned} \xi_v - \xi_0 &= Ma_S r_v \\ x_v - x_0 &= Ma_x r_v \\ R_v (\psi_0 - \psi_v) &= Ma_{\omega} r_v \end{aligned} \quad (2-17)$$

The partial derivatives of these expressions with respect to x_0 , ψ_0 and ξ_0 and using the kinematic relations given in Eq. (2-1) one obtains the spatial dilatation of an emitting element describing helical motion

$$\sigma_x = \frac{1}{1 - Ma_x \cos \psi_{vx}} \quad (2-18)$$

$$\sigma_{\omega} = 1 + \frac{Ma_{\omega} \cos \psi_{v\omega}}{1 - Ma_S \cos \psi_v} \quad (2-19)$$

$$\sigma_v = \sigma_x \cdot \sigma_{\omega} = \frac{1}{1 - Ma_S \cos \psi_v} \quad (2-20)$$

The effective stretching of a square element under helical motion is demonstrated in Fig. 6, confirming at the same time the relations set up in the above equations.

Having established the spatial stretching functions of emitting elements in arbitrary motion, it is of essential interest to look into the effective radiation strength of the surface singularity distribution during emission. The surface stretching factor being denoted by σ_L and the cross-stretching being implied in σ_N the following relation for the emission quantities will hold:

For source distribution

$$\bar{S}_v \cdot d\bar{F}_v = (S_0 \cdot \sigma_N) \cdot (dF_0 \cdot \sigma_L) = S_0 dF_0 \sigma_v \quad (2-21)$$

For dipole distribution

$$\bar{D}_v d\bar{F}_v = [S_0 dF_0 \sigma_v^2] \cdot \{dm_0 \sigma_R\} \quad (2-22)$$

Normally the stretching factor σ_v is combined with the propagation radius r_v , thus yielding an effective radius having the relation

$$r_v^* = \frac{r_v}{\sigma_v} = r_v (1 - Ma_S \cos \psi_v) \quad (2-23)$$

or

$$r_v^* = r_0 (1 - Ma_S^2 \sin^2 \psi_0)^{1/2} \quad (2-24)$$

A universal curve of r_v^*/r_0 valid for all Mach numbers and all field points in space is depicted in Fig. 7.

2.3 Temporal dilatations in the propagation fields of singularities in arbitrary motion

The propagation radius r_v between the field point P and the emission point P_v being already known and the time of signal arrival at P being t_o , the emission time t_v is given by the relation

$$t_v = t_o - \frac{r_v}{a_\infty} \quad (2-25)$$

For a moving source element and a moving field point the time sequence of signal emission and signal reception will be given by the universal expression

$$\frac{dt_v}{dt_o} = 1 - \frac{1}{a_\infty} \left\{ \frac{dr_v}{dx_v} \cdot \frac{dx_v}{dt_v} \cdot \frac{dt_v}{dt_o} - \frac{dr_v}{dx_o} \cdot \frac{dx_o}{dt_o} \right\} \quad (2-26)$$

with $\frac{1}{a_\infty} \frac{dx_v}{dt_v} = Ma_S$; $\frac{1}{a_\infty} \frac{dx_o}{dt_o} = \tilde{Ma}_E$ (2-27)

$$\frac{dr_v}{dx_v} = \cos \psi_v ; \quad \frac{dr_v}{dx_o} = \cos \tilde{\psi}_v$$

Introducing these relations in Eq. (2-26) it yields

$$\frac{dt_v}{dt_o} \left\{ 1 - Ma_S \cos \psi_v \right\} = 1 + \tilde{Ma}_E \cos \tilde{\psi}_v \quad (2-28)$$

For a space fixed point the temporal dilatation factor σ_D will reduce to:

$$\sigma_D = \frac{dt_v}{dt_o} = \frac{1}{1 - Ma_S \cos \psi_v} \quad (2-29)$$

while for a moving field point with the Mach number component \tilde{Ma}_E in the plane of PP_oP_v one obtains

$$\sigma_D^* = \frac{dt_v}{dt_o^*} = \frac{1 + \tilde{Ma}_E \cos \tilde{\psi}_v}{1 - Ma_S \cos \psi_v} \quad (2-30)$$

The temporal dilatations σ_D and σ_D^* are the real Doppler factors and the process of their origin are illustrated in Fig. 8.

3. THE SOLUTION OF THE LINEARIZED WAVE EQUATION FOR AERODYNAMICS AND ACOUSTICS OF MOVING BODIES

Disturbance waves originating and propagating in an unbounded medium can be described by the wave equation, expressed in a medium fixed or moving reference system. If the x-axis of both the systems is laid along the trajectory and the origins of the two systems coincide at a time instant $\bar{t} = \hat{t} = 0$, then the following interrelations are given by the Galilean-transformation.

$$\bar{x} = \hat{x} + V_o \hat{t} ; \quad \bar{y} = \hat{y} ; \quad \bar{z} = \hat{z} ; \quad \bar{t} = \hat{t} \quad (3-1)$$

In a moving system with $V_o = V_S$ the substantial derivative is defined as

$$\frac{D_o}{Dt} = \left[\frac{\partial}{\partial \bar{t}} + V_S \frac{\partial}{\partial \bar{x}} \right] \equiv \frac{\partial}{\partial \hat{t}} \quad (3-2)$$

Thus the linearized wave equation reduces to the following form in a moving reference system:

$$\nabla^2 \varphi - \frac{1}{a_\infty^2} \frac{\partial^2 \varphi}{\partial \hat{t}^2} = \Omega \delta(\hat{e}_o) \delta(\hat{r}_o) \quad (3-3)$$

By using the relations of Eq. (3-1) the wave equation can be recast to the classical form in a medium fixed reference system:

$$\nabla^2 \psi - \frac{1}{a_\infty^2} \frac{\partial^2 \psi}{\partial \hat{t}^2} = \Omega \delta(\epsilon_0) \delta(\epsilon_0) \quad (3-4)$$

where the Dirac delta-function with the arguments

$$\begin{aligned} \hat{\epsilon}_0 &= x_v - x_0 - Ma_S r_v \\ \hat{\kappa}_0 &= t_v - t_0 - r_v/a_\infty \end{aligned} \quad (3-5)$$

determines the source positions t_0 or t_v , with the condition $\hat{\epsilon}_0 = 0$ and $\hat{\kappa}_0 = 0$, for which the wave equation becomes inhomogeneous. The disturbance function Ω can have the general expression

$$\Omega = \frac{1}{\rho_\infty} Q(t) + \frac{1}{\omega_v \rho_\infty} \nabla \cdot K(t) - \frac{1}{\omega_v \rho_\infty} \nabla \cdot \nabla \cdot G_{ij}(t) + \Psi \quad (3-6)$$

comprising sources, dipoles and quadrupoles while Ψ may contain all the non-linear terms of the wave equation. Because of the linear relations between ψ and \bar{s} , where

$$\bar{s} = \frac{\rho'}{\rho_\infty} = \frac{p'}{\kappa p_\infty} = \frac{1}{a_\infty^2} \frac{D\psi}{Dt} \quad (3-7)$$

the linearized wave equation is equally valid for the disturbance quantity \bar{s} , giving in a moving reference system

$$\nabla^2 \bar{s} - \frac{1}{a_\infty^2} \frac{D^2 \bar{s}}{Dt^2} = \Omega^* \delta(\hat{\epsilon}_0) \delta(\hat{\kappa}_0) \quad (3-8)$$

with $\Omega^* = \omega_v \Omega / a_\infty^2$.

In aerodynamics and acoustics of moving bodies in an unbounded medium, the generalized Navier Stokes equation can be expressed as a wave equation as derived by Lighthill [55], whereby the term Ω^* in Eq. (3-8) denotes the stress Tensor, defined as

$$\Omega^* = \frac{1}{\rho_\infty a_\infty^2} \frac{\partial^2 (\rho v_i v_j)}{\partial x_i \partial x_j} = \frac{1}{\rho_\infty a_\infty^2} \frac{\partial^2 T_{ij}}{\partial x_i \partial x_j} \quad (3-9)$$

Applying now the Greens theorem for moving bodies with the basic function as derived in [59] and assuming time dependent steady processes, one obtains the following solution for the pressure field:

$$\begin{aligned} \bar{s}(P) &= \frac{e^{-i\omega t}}{4\pi\rho_\infty a_\infty^2} \sum_{\mu} (-1)^{\mu+1} \left[\int_{F_0} \frac{\sigma_v}{r_v} \frac{\partial \bar{s}_0}{\partial n} e^{ikr_v} dF_0 + \right. \\ &\quad \left. + \int_{F_0} \bar{s}_0 \frac{\partial}{\partial n} \left\{ \frac{\sigma_v e^{ikr_v}}{r_v} \right\} dF_0 + \int_{V_0} \frac{\partial^2 (\rho v_i v_j)}{\partial x_i \partial x_j} \frac{\sigma_v}{r_v} e^{ikr_v} dv_0 \right]_{\mu} \end{aligned} \quad (3-10)$$

The three terms on the R.H.S. imply respectively the contributions from source, dipole and quadrupole singularities - the first two being surface distributions on the body while the third term comprises a volume distribution in the surrounding medium. In case of viscous flows the volume integral is of significance quite close to the body.

3.2 The formulation of the acoustic problem of moving bodies using pressure potential

The most general solution of the wave equation in terms of pressure potential was formulated by N. Curle [56] for space fixed singularities. The solution given in Eq. (3-10) can be recast to a similar form by breaking down the volume integral in the following way:

$$\int_{v_0} \frac{\partial^2 T_{ij}}{\partial x_i \partial x_j} \frac{dv_0}{r_v^*} = \int_{F_0} \frac{\partial (T_{ij})_0}{\partial x_j} \frac{e^{ikr_v}}{r_v^*} dF_0 + \int_{F_0} (T_{ij})_0 \frac{\partial}{\partial x_j} \left\{ \frac{e^{ikr_v}}{r_v^*} \right\} dF_0 \quad (3-11)$$

$$+ \frac{\partial^2}{\partial x_i \partial x_j} \int_{v_0} \frac{T_{ij}}{r_v^*} dv_0$$

with $T_{ij} = \rho v_i v_j$. Hence Eq. (3-11) contains three terms analogous to those in Eq. (3-10) and can be combined accordingly, thus retaining the basic character of Eq. (3-10). The complete solution of the pressure field of a moving body or surface takes the following form

$$\bar{s}(P) = \frac{e^{-i\omega t}}{4\pi\rho_\infty a_\infty^2} \sum_{\mu} (-1)^{\mu+1} \left[\int_{F_0} \frac{\partial (p' + T_{ij})_0}{\partial n} \frac{e^{ikr_v}}{r_v^*} dF_0 + \int_{F_0} (p' + T_{ij})_0 \frac{\partial}{\partial n} \left\{ \frac{e^{ikr_v}}{r_v^*} \right\} dF_0 + \frac{\partial^2}{\partial x_i \partial x_j} \int_{v_0} \frac{(T_{ij})_0}{r_v^*} e^{ikr_v} dv_0 \right]_{\mu} \quad (3-12)$$

This equation is directly applicable to find the acoustic pressure field generated by the moving body at field points P. For $Ma_\infty = 0$ the radius r_v^* reduces to r_v and Eq. (3-12) becomes identical to the solution derived by N. Curle [56] for space fixed singularities. For nonviscous steady flows the term T_{ij} drops out, thus simplifying Eq. (3-12) essentially.

3.3 The formulation of the aerodynamic problem for bodies in arbitrary motion

The solution of the wave equation in terms of pressure potential as given in Eq. (3-12) is very useful for acoustic problems but cannot be directly used for aerodynamic problems, where the variable p' is unknown and no boundary condition can be prescribed to this equation in its present form. If now the momentum equation is made use of having the simple relation:

$$\frac{1}{\rho_\infty a_\infty^2} \left[\frac{\partial}{\partial t} (\rho v_i) + \frac{\partial}{\partial x_j} (\rho v_i v_j) \right] = - \frac{\partial \bar{s}}{\partial x_i} \quad (3-13)$$

then Eq. (3-12) is converted to the following expression

$$\bar{s}(P) = \frac{e^{-i\omega t}}{4\pi\rho_\infty a_\infty^2} \sum_{\mu} (-1)^{\mu+1} \left[- \int_{F_0} \frac{D}{Dt} (\rho v_n) \frac{e^{ikr_v}}{r_v^*} dF_0 + \int_{F_0} (p' + T_{ij}) \frac{\partial}{\partial n} \left\{ \frac{e^{ikr_v}}{r_v^*} \right\} dF_0 + \frac{\partial^2}{\partial x_i \partial x_j} \int_{v_0} \frac{(T_{ij})_0}{r_v^*} e^{ikr_v} dv_0 \right]_{\mu} \quad (3-14)$$

For arbitrary motion of surfaces or bodies, as in the case of propeller blades undergoing helical motion it is convenient to use Eq. (3-14) directly or else Eq. (3-12) in an extended form, adapting it for the fulfillment of boundary conditions at the body surface. Expressions analogous to Eq. (3-14) has already been used by F. Farassat [38], deriving it however from the Ffowcs-Williams and Hawkins equation [58] using involved operational calculus.

The boundary conditions on a moving surface

When a surface $\zeta = F(x,y)$ has an arbitrary time dependent motion of small amplitudes superimposed on a constant convective velocity along the negative x-axis, then the movement imparted to the surrounding medium particles in a direction n normal to the surface can be described by the simple relation:

$$v_n(t) = \vec{n} \cdot \vec{v}(t) = \frac{D\zeta}{Dt} = \left[\frac{\partial \zeta}{\partial t} + v_s \frac{\partial \zeta}{\partial x} \right] \quad (3-15)$$

For applying the linearized theory the amplitude of v_n is assumed to be small compared to V_∞ or a_∞ except at the stagnation point of rounded leading edges. When using Eq. (3-14) the quantity ρv_n in the first term can be looked at as uniquely defined through the Eq. (3-15), thus obtaining the boundary condition sought for. For stationary nonviscous flows the term T_{ij} can be neglected and Eq. (3-14) will yield then a system of simultaneous equations for p' at the collocation points prescribed on the moving surface.

If Eq. (3-12) is used for the aerodynamical calculation in the conventional way, as is often done in the unsteady lifting surface theories, then the boundary condition is to be imposed by using the classical relation:

$$\varphi(P) = a_\infty^2 \int_{-\infty}^t \bar{s}_0 e^{-i\omega t_1} dt_1 = \frac{a_\infty^2}{V_\infty} e^{-i\omega t} \int_{-\infty}^x \bar{s}_0 e^{i\bar{k}(x-x_1)} dx_1 \quad (3-16)$$

mit $\bar{k} = k/Ma_x$. The boundary condition at the moving surface is given by:

$$\frac{1}{V_\infty} \frac{\partial \varphi}{\partial n} = \frac{v_n}{V_\infty} = \frac{1}{V_\infty} \left[\frac{\partial \zeta}{\partial t} + v_s \frac{\partial \zeta}{\partial x} \right] \quad (3-17)$$

Eqs. (3-16) and (3-17) yield the classical relation:

$$\frac{\vec{n} \cdot \vec{v}}{V_\infty}(P) = \frac{a_\infty^2}{V_\infty^2} e^{-i\omega t} \left[\frac{\partial}{\partial n} \int_{-\infty}^x \bar{s}_0(x_1) e^{i\bar{k}(x-x_1)} dx_1 \right] \quad (3-18)$$

wherein $\bar{s}(x_1) = s_0(x_1)e^{-i\omega t}$ has to be replaced by the integral expressions of Eq. (3-12) and leads to an integral equation for the unknown quantities p' and dp/dn .

4. A UNIFIED EXPOSITION OF THE NUMERICAL METHODS FOR PROPELLER AERODYNAMICS AND ACOUSTICS

For analyzing the propulsive efficiency and the acoustic properties of a propeller it is necessary to make first a detailed calculation of the aerodynamic coefficients or loading distributions of the blades including viscous drags. In a preliminary step, however, the loadings due to nonviscous flows are determined. To do this the well known numerical methods already developed for wings as cited in the references [61] till [69] are utilized. As the spatial dilatations of the emitting elements and their effect on the induced fields are to be based on the helical motion, the evaluations becomes somewhat complex.

If the propeller blade surfaces are divided into a number of panel elements, each element describes its own helical path, as is illustrated in Fig. 9. Denoting the location of a singularity surface as P_0 and a field point as P at time t_0 the position of the emitting element P_v from which the signals reach P at time t_0 can be easily obtained by using Eq. (2-3).

If nonviscous flow is considered using Eq. (3-14) the loading consists mainly of two terms, sources and dipoles. The inducing functions of moving source and doublet panels at a field point can be easily obtained by following the extended sweep-technique of the panel method [60] [69], whenever the orientations between the field point P and the emission point P_v are defined. An alternative method is to determine the dummy position of the singularity element by shifting it from P_v to \bar{P}_0 by an amount of Ma_{Gr_v} , such that the path line forms an angle ψ_v with r_v , and the orientation of the panel element with respect to the flow vector Ma_{Gr} remains unchanged. An equivalent sweep technique applied to the singularity panel will then yield the same inducing function as the real emitting panel at P_v . The determination of the inducing function will be illustrated in the following sections.

4.1 The sweep technique for the calculation of the inducing field of bodies and surfaces in motion

The method of calculating the inducing functions of a moving singularity surface will be illustrated first for the simple case of uniform translatory motion. The position of the singularity panel and of a field point at time t_0 as well as the location of the

effective emitting panel subject to the spatial dilatations are shown in Fig. 10. For sources or doublets distributed on a panel of area F_0 having uniform translatory motion at $Ma_S < 1$ the disturbance potentials at arbitrary field points in space can be described as follows, where the time factor $e^{-i\omega t}$ has been dropped out.

Source-panels

$$\psi_S = \iint_{F_0} \frac{S_0 e^{ikr_{v0}}}{r_v} dF_0 = \iint_{F_v} \frac{S_{v0} e^{ikr_v}}{r_v} dF_v \quad (4-1)$$

with $F_v = \bar{F}_v / \cos(\chi - \chi_v)$ and $s_v = \bar{s}_v \cos(\chi - \chi_v)$. The equivalent form yielding the same result would be

$$\psi_S = \iint_{F_0} \frac{S_0 e^{ikr_v}}{r_v^*} dF_0 = \iint_{F_0} \frac{S_0 e^{-i\tilde{k} \{Ma_S(x-x_0) - r_v^*\}}}{r_v^*} dF_0 \quad (4-2)$$

with $\tilde{k} = k/\beta^2 = \omega/(a_\infty \cdot \beta^2)$.

Doublet-panels

For doublet-panels with arbitrary axis orientation of the source-sink combination one obtains

$$\psi_D = \iint_{F_0} \frac{[S_0 \sigma_v^2] \{dm_0 \sigma_R\} e^{ikr_v}}{r_v^2} \left[\frac{-(x-x_0)\cos\hat{\chi} + \beta^2 h_0 \cos\psi \sin\hat{\chi}}{r_v} \right] dF_0 \quad (4-3)$$

Written in terms of the radiation quantities related to the effective emitting panel, this yields

$$\psi_D = \iint_{F_v} \frac{D_{v0} e^{ikr_v}}{r_v^2} \left[-(\cos\psi_v - Ma_S) \cos\hat{\chi} + \beta^2 \sin\psi_v \cos\psi \sin\hat{\chi} \right] dF_v \quad (4-4)$$

The equivalent form expressed in terms of the panel position at P_0 would be

$$\psi_D = \iint_{F_0} \frac{D_{00} e^{-i\tilde{k} \{Ma_S(x-x_0) - r_v^*\}}}{r_v^{*3}} \left[-(x-x_0)\cos\hat{\chi} + \beta^2 h_0 \cos\psi \sin\hat{\chi} \right] dF_0 \quad (4-5)$$

For unit source and doublet strengths the integral values in the above equations yield the inducing functions I_S and I_D , which are now to be determined at field points in space for singularity panels of arbitrary motion and orientation. For $Ma_S = 0$ all expressions in Eqs. (4-1) to (4-5) reduce to those of incompressible flow, and for ω or $k = 0$ the equations simplify to those of steady disturbance fields.

In order to treat the problem in a most general way a moving singularity surface element 1-2-3-4 at P_0 is considered, the surface having arbitrary orientation in space as shown in Fig. 11. The global and local reference systems are denoted by x, y, z and $\bar{x}, \bar{y}, \bar{z}$, where the \bar{x} - and \bar{x} -axes are aligned along the direction of the trajectory. With H as the normal from the field point to the plane of the panel surface an equivalent coordinate system R, θ, H may be introduced as shown in Fig. 11. Both the inducing functions I_S and I_D consist of surface integrals over F_0 or F_v , which can now be solved by letting the triangular segment $R^2 d\theta/2$ sweep around the contour 1-2-3-4 once. Thus the contribution of the panel area will be left over, the contributions of the areas outside it being canceling with each other. This method, which is commonly applied in electromagnetic fields was first used for aerodynamics in [61] and has been extended for moving singularities in [60] and [69]. If χ is the inclination of the singularity surface to the x -axis in the x - H -plane then one obtains the relations:

$$\begin{aligned} \bar{x} - \bar{x}_0 &= H \sin\chi + R_1 \cos\theta \cos\chi \\ h_0 &= \left[H^2 + R_1^2 - (H_1 \sin\chi + R_1 \cos\theta \cos\chi)^2 \right]^{1/2} \\ r_0 &= \left[H^2 + R_1^2 \right]^{1/2} \end{aligned} \quad (4-6)$$

$$r_v^* = \left[(\bar{x} - \bar{x}_0)^2 + \beta^2 h_0^2 \right]^{1/2} \quad (4-6)$$

$$dF_0 = R_1 dR_1 d\theta$$

In case of space-fixed singularity surfaces or for very small Mach numbers the sweep can be performed over the original surface element. In case of moving singularity surfaces either an auxiliary rotated surface F'_0 or the proper emitting surface F_v can be used in the sweep technique. In the latter case, however, a constant mean value v is attributed to the singularity strength S_v on F_v , which implies the effect of cross-stretching ϕ_N .

In the following the equivalent method using an auxiliary surface is illustrated. The auxiliary surface is introduced to obtain the quantity r_v^* and the integral values in the physical domain directly. If the singularity surface is rotated about the z-axis at C by an amount χ such that $\text{tg} \chi' = \beta \text{tg} \chi$ and the contour points 1-2-3-4 are displaced on to the auxiliary plane along the h_0 -lines as in Fig. 10, then the following relations are established.

$$\bar{x}' = \bar{x} ; \quad \bar{y}' = \beta \bar{y} ; \quad \bar{z}' = \beta \bar{z} \quad (4-7)$$

$$(\bar{x}' - \bar{x}'_0) = H' \sin \chi' + R'_1 \cos \theta' \cos \chi' \quad (4-8)$$

$$r_v^* = r'_0 = \sqrt{R_1'^2 + H'^2}$$

and

$$dF_0 = R_1 dR_1 d\theta = \frac{1}{\beta \beta_n} \{ R'_1 dR'_1 d\theta' \} \quad (4-9)$$

$$\frac{\partial}{\partial n} \left[\frac{\sigma}{r_v} \right] = \frac{\partial}{\partial n} \left\{ \frac{1}{r_v^*} \right\} = \beta_1 \frac{\partial}{\partial n'} \left[\frac{1}{r'_0} \right]$$

with

$$\frac{\partial}{\partial n} = \frac{\partial}{\partial H} ; \quad \frac{\partial}{\partial n'} = \frac{\partial}{\partial H'}$$

$$\beta_1 = \sqrt{1 - \text{Ma}_S^2 \sin^2 \chi} ; \quad \beta_n = \sqrt{1 - \text{Ma}_S^2 \cos^2 \chi} \quad (4-10)$$

$$\beta = \sqrt{1 - \text{Ma}_S^2}$$

Further

$$r_v = \frac{-\text{Ma}_S [H' \sin \chi' + R'_1 \cos \chi' \cos \theta'] + \sqrt{R_1'^2 + H'^2}}{\beta^2} \quad (4-11)$$

Now, writing Eq. (4-2) and Eq. (4-5) in terms of the variables R'_1, θ', H', χ' and putting $S_0 = 1$ and $D_0 = 1$ the inducing functions I_S and I_D can be obtained directly. For singularity panels in uniform translatory motion these will reduce to the following expressions:

Source field

$$I_S = \frac{1}{4\pi\beta\beta_n} \oint \int_0^{R'} \frac{R'_1 e^{ikr_v}}{[R_1'^2 + H'^2]^{1/2}} dR'_1 d\theta' \quad (4-12)$$

Doublet near-field

$$I_{DN} = -\frac{\beta_1 H'}{4\pi\beta\beta_n} \oint \int_0^{R'} \frac{R'_1 e^{ikr_v}}{[R_1'^2 + H'^2]^{3/2}} \{ C_1 + C_2 R'_1 \cos \theta' \} dR'_1 d\theta' \quad (4-13)$$

where

$$C_1 = \{ 1 + \text{Ma}_n^2 - \text{Ma}_n^2 \beta_1 \}$$

$$C_2 = \text{Ma}_n \text{Ma}_1 \beta_1 \ll 1$$

Doublet far-field

$$I_{DF} = \frac{1k\beta_1}{4\pi\beta^3\beta_n} \oint \int_0^{R'} \left\{ Ma_S \sin\chi' - \frac{H'}{\sqrt{R_1'^2 + H'^2}} \right\} \frac{e^{ikr_v}}{\sqrt{R_1'^2 + H'^2}} R_1' dR_1' d\theta \quad (4-14)$$

These integrals can be solved in the classical way as described in [61] yielding closed expressions in case of steady flows. The determination of I_S and I_D also follows directly by sweeping the emitting element F_v at its real location P_v .

4.2 Extension of the sweep technique for the calculation of the inducing functions of singularity surfaces in helical motion

In case of a singularity element having spiraling motion, the spatial stretchings of the effective emitting element arise both from translatory and circular motions. As has already been established, the effective dilatations are solely dependent on the resultant Mach number and on the spatial orientation of the element at the time t_v of emission, from which the signals reach a field point P simultaneously at time t_o . Once the position P_v of the emitting element is determined, the sweep technique can be applied to it directly to determine the inducing effect at the field point P . The relative positions of P, P_o and P_v with the spatial dilatation of F_v is illustrated in Fig. 12. In contrast to Fig. 9 the perspective view and the direction of rotation ω_o of the blades have been changed in order to obtain well defined projections of the elements concerned.

If the alternative method with the singularity surface F_o is used to calculate the inducing effect, then the element is to be placed at P_o , i.e. the end of the vector $Ma_S r_v$ extending from P_v , and forming an angle ψ with r_v , while keeping its orientation in space unchanged. Assuming now the tangent line to the helix at P_v to be a part of the trajectory, the method of auxiliary plane as illustrated in section 4.1 can be applied. The sweeping plane and the auxiliary surface element are shown in Fig. 12. The application of the method will be easier if the emitting points P_v are turned up each time through an angle $(\pi/2) - \psi_v$ to the vertical position and the field points P are correspondingly turned away through the same angle, retaining the relative orientations between them unchanged.

If Eqs. (3-12) and (3-14) are used to determine the acoustic and aerodynamic fields, the inducing functions obtained by the above method can be applied directly. If on the other hand the classical method for the aerodynamics of propellers are used one has to solve Eq. (3-18) for which the induced functions are to be determined for a number of positions of the field point in the space domain. In this case the field point is shifted from $-\infty$ to $P(x)$ in steps while holding the time t_o and the position of the singularity element at P_o constant. The application of this method is illustrated in Fig. 13. For the treatment of the aerodynamic problems of propellers in steady flow fields the inducing functions reduce to very simple expressions, since ω or k vanish, thus enabling one to apply the classical numerical techniques outlined already in [69].

4.3 Formulation of the numerical methods for propeller aerodynamics and acoustics

The solution of the linearized wave equation for aerodynamics and acoustics of bodies in arbitrary motion has been dealt with in section 3. The methods are based on the extended Green's theorem yielding integral equations, which are easily amenable to numerical treatment. The basis of the numerical treatment is the classical panel method [61], which however has to be extended in two ways, i.e. with regard to the effect of spatial- and temporal-dilatations in the propagation field and with respect to the complexity arising from the helical motion of the singularity elements. This is achieved by introducing the new sweep technique already developed for wing aerodynamics [60] [69] and by an extension thereof accounting for the helical motion of singularity surfaces. A third factor arises due to the change of the inflow velocity with changing radius on the propeller blades.

In the panel method the body surface is divided into a large number surface elements, which are denoted by F_{oj} , where j indicates the panel numbering. The collocation points on the body surface are indexed by i . The expressions for the inducing functions of sources and doublets, termed $I_{S|ij}$ and $I_{D|ij}$, implying the induced effect of panel j on the collocation point at i , can be evaluated once and for all. Rewriting Eqs. (3-14) and (3-18) in a general form the procedure for a direct numerical treatment is established. Assuming nonviscous steady flow fields, as in the case of propeller aerodynamics involving subsonic velocities only, the most general form of Eq. (3-14) becomes:

$$\sum_{j=1}^N \left[\frac{1}{4\pi} \int_{F_{oj}} \frac{\partial}{\partial n_j} \left\{ \frac{1}{r_v^*} \right\}_{ij} dF_o \right] \bar{s}_j - \bar{s}_i = \sum_{j=1}^N \left[\frac{1}{4\pi} \int_{F_{oj}} \left\{ \frac{1}{r_v^*} \right\}_{ij} dF_o \right] \left[\frac{\partial \bar{s}}{\partial n} \right]_j \quad (4-15)$$

In case of steady motion the momentum equation simplifies to

$$\frac{1}{\rho_\infty a_\infty^2} \left\{ v_{Sj} \frac{\partial}{\partial \bar{x}} (\rho_\infty v_n)_j \right\} = - \left[\frac{\partial \bar{s}}{\partial n} \right]_j \quad (4-16)$$

where $(v_n)_j = v_{Sj} \left[\frac{\partial \zeta}{\partial \bar{x}} \right]_j$ (4-17)

as imposed by the motion of the blade surface $\zeta = F(x, y)$ at a radius $R = \text{const.}$. The bracketed terms in Eq. (4-15) are the inducing functions already listed in Eqs. (4-12) and (4-13). Hence, one obtains a system of N simultaneous equations for the N unknowns s_j on the blade surface. The equation for the computational procedure reduces to

$$\sum_{j=1}^N [L_D]_{ij} \cdot \bar{s}_j - \bar{s}_i = \sum_{j=1}^N [I_S]_{ij} \cdot x_j \quad (4-18)$$

The quantities $x_j = -\partial \bar{s} / \partial n_j$ are known from Eqs. (4-16) and (4-17). This equation has already been applied in [38] using different derivations and numerical techniques for its solution.

If the classical approach is followed for the calculation of propeller aerodynamics, one has to rewrite Eq. (3-18) in the following form

$$\sum_{j=1}^N n_i \cdot \nabla \left[\frac{1}{4\pi Ma_x Ma_{Si}} \int_{-\infty}^{x_i} \left\{ \int_{F_{Oj}} \left(\frac{1}{r_v^*} \right)_{i,j} dF_o \right\} dx_1 \right] \left(\frac{\partial \bar{s}}{\partial n} \right)_i +$$

$$+ \sum_{k=1}^M n_i \cdot \nabla \left[\frac{1}{4\pi Ma_x Ma_{Si}} \int_{-\infty}^{x_i} \left\{ \int_{F_{Oj}} \frac{\partial}{\partial n_k} \left(\frac{1}{r_v^*} \right)_{i,k} dF_o \right\} dx_1 \right] \bar{s}_k = \frac{\vec{n}_i \cdot \vec{v}_{Si}}{v_{Si}} \quad (4-19)$$

Identifying the gradients operating on the expressions inside the square brackets as the inducing coefficients A_{ij} and B_{ik} and denoting the unknown source and doublet strengths by X_j and Y_k , Eq. (4-19) leads to a system of $N+M$ equations for the same number of unknowns. For the numerical calculation it is advantageous to recast the above equation into the more compact form

$$\sum_{j=1}^N n_i \cdot A_{ij} x_j + \sum_{k=1}^M n_i \cdot B_{ik} Y_k = \frac{\vec{n}_i \cdot \vec{v}_{Si}}{v_{Si}} \quad (4-20)$$

The numerical approach using Eq. (4-20) has been applied extensively to the aerodynamical problems of wings. One example is shown in Fig. 14. The aerodynamics of propellers can be treated in a similar way. Once the aerodynamic coefficients of the blade surfaces are completely defined they can be used to solve the acoustic problem in the classical way.

5. CONCLUSIONS

Starting from the fundamental equations of wave propagation from moving singularities an analysis is performed from which a computational procedure to solve the aerodynamic and acoustic problems of propellers in forward motion is developed. The treatment includes the spatial and temporal dilatations in the propagation field of singularities in arbitrary motion, a generalized solution of the linearized wave equation in terms of pressure potential and the extension of the sweep technique for calculating the induced fields of singularity surfaces undergoing helical motion.

The analysis results in establishing universal relations and characteristic properties in the radiation field and leads to a better understanding of the physical processes connected to the problem. As a consequence extremely simple methods for the calculation of the inducing functions of moving singularity surfaces could be derived. The sweep procedure for determining the inducing effects can be applied either to the effective emitting

surface or to the real singularity surface in an equivalent position. The numerical treatment of the propeller problems is then shown to be reducible to the same technique as that of the classical panel method. As a test case the pressure distribution on a moving wing is presented - the construction of a numerical code for the case of propeller motion is presently under preparation.

REFERENCES

I. Aerodynamics of propellers

- [1] Joukowski, N.E. Théorie Tourbillonnaire de Hélice Propulsive. Paris: 1929.
- [2] Betz, A. Eine Erweiterung der Schraubenstrahl-Theorie. Zeitschr. f. Flugtech. u. Motorluftschiffahrt (ZFM) 11 (1920), S. 105-110.
- [3] Drzewiecki, S. Théorie Générale de Hélice Propulsive. Paris: 1920.
- [4] Taylor, G.I. The rotational inflow factor in propeller theory. ARC, Rep. & Mem. 765 (1921).
- [5] Betz, A. Schraubenpropeller mit geringstem Energieverlust. Göttinger Nachrichten (1919), S. 193-217. Vier Abhandlungen zu Hydrodynamik und Aerodynamik (1927), S.68-92.
- [6] Glauert, H. An Aeroödynamic Theory of the Airscrew. ARC, R&M 186 (1922).
- [7] Pistolesi, E. Neue Ansätze und Ausführungen zur Theorie der Luftschrauben. Vorträge aus dem Gebiet der Hydro- und Aerodynamik, Innsbruck (1922) Ed. Th.v. Kármán and T. Levi Civita (1924), pp. 67-84.
- [8] Bienen, Th. Zur Theorie der Luftschrauben. Zeitschr. VDI 68 (1924), S. 1237-1242, S. 1315-1318. Collected Works of v. Kármán, Vol. 2 (1956), pp. 189-218.
- [9] Lauth, A. Elementare Ableitung der Geschwindigkeit von Kreis- und Schraubenwirbel. Annalen der Physik, 1916, pp. 671-682.
- [10] Troller, Th. Zur Wirbeltheorie der Luftschrauben. ZAMM, Bd. 8 (1928), pp. 426-430.
- [11] Goldstein, S. On the vortex theory of screw propellers. Proc. Roy. Soc. A123 (1929), pp. 440-465.
- [12] Glauert, H. Airplane Propellers. In W.F. Durand: Aerodynamic Theory, Vol. IV, pp. 167-269. Berlin: Springer Verlag, 1935.
- [13] Lock, C.N.H. Airscrew Theory. ARC, R&M 1746 (1936).
- [14] Weinig, F. Aerodynamik der Luftschraube. Berlin: Springer Verlag, 1940.
- [15] Theodorsen, Th. Theory of Propellers. New York: McGraw-Hill Company, 1948.
- [16] Alexandrow, W.L. Luftschrauben. Berlin: VEB Verlag Technik, 1954.
- [17] Tietjens, O. Beiträge zur Propellertheorie. Jahrbuch der WGL (1955), S. 236-245.
- [18] Runyan, H.L. Unsteady Lifting Surface Theory Applied to a Propeller and Helicopter Rotor. Ph. D. Thesis, Loughborough University, Loughborough, England (1973).
- [19] Hanson, D.B. Compressible Helicoidal Surface Theory for Propeller Aerodynamics and Noise. AIAA Journal Vol. 21, 6 (1983), pp. 881-889.
- [20] Farassat, F. A new aerodynamic integral equation for high speed rotating blades based on an acoustic formula in the time domain. To appear in the AIAA Journal, (1984) as Technical Note.

II. Acoustics of propellers

- [21] Lynam, E.J.H. The Emission of Sound by Airscrews.
ARC, R&M 624 (1919).
- [22] Bryan, G.H. The Acoustics of Moving Sources with Application to Airscrews.
ARC, R&M (1920).
- [23] Ernsthausen, W. The Source of Propeller Noise.
NACA TM 825 (1937); Luftfahrtforschung 13 (1936), pp. 433-440.
- [24] Ernsthausen, W. Der Einfluß aerodynamischer Eigenschaften auf Schallfeld und Strahlleistung einer Luftschraube.
Luftfahrtforschung, Bd. 18 (1941), pp. 289-303.
- [25] Gutin, L. On the Sound Field of a Rotating Propeller.
NACA TM 1195 (1948).
Physik. Zeitschrift d. Sowjetunion, 9 (1936), pp. 57-71.
- [26] Deming, A.F. Noise from Propellers with Symmetrical Section at Zero Blade Angle.
NACA TN 679 (1938).
- [27] Deming, A.F. Propeller Rotational Noise due to Torque and Thrust.
NACA TN 747 (1940).
- [28] Yudin, E.Y. On the Vortex Sound from Rotating Rods.
NACA TM 1136 (1947); Journ. Tech. Phys., Vol. 14 (1944), p. 561.
- [29] Hubbard, H.H. Sound from Two-Blade Propeller at Supersonic Tip Speeds.
Lassiter, L.W. NACA TN 1079 (1952).
- [30] Regier, A.A. Status of Research on Propeller Noise and its Reduction.
Hubbard, H.H. Jour. of Acous. Soc. Am., 25 (1953), pp. 395-404.
- [31] Garrick, I.E. A Theoretical Study of the Effects of Forward Speed on the
Watkins, C.E. Free-Space Sound Pressure Field Around Propellers.
NACA TR 1198 (1954).
- [32] van de Vooren, A.I. Noise Field of a Rotating Propeller in Forward Flight.
Zandbergen, P.J. AIAA Journ. 1 (1963), pp. 1518-1526.
- [33] Metzger, F.B. A Study of Propeller Noise Research.
Magliozzi, B. Aerodynamic Noise.
Towle, G. Ed. H.S. Ribner
Gray, L. Toronto: University Press, 1969.
- [34] Morfey, C.L. Rotating Blades and Aerodynamic Sound.
Journ. of Sound and Vibration, Vol. 28 (1973), pp. 587-617.
- [35] Hanson, D.B. Helicoidal Surface Theory for Harmonic Noise of Propellers in
the Far Field.
AIAA Journal 18 (1980), pp. 1213-1220.
- [36] Hanson, D.B. Influence of Propeller Design Parameters on Far Field Harmonic
Noise in Forward Flight.
AIAA Journal, Vol. 18 (1980), pp. 1313-1319.
- [37] Nystrom, P.A. A Numerical Technique for Calculation of High Speed Propellers
Farassat, F. with Advanced Geometry.
NASA TP 1662 (1980).
- [38] Farassat, F. Linear Acoustic Formulas for Calculation of Rotating Blade Noise.
AIAA Journal 19 (1981), pp. 1122-1130.
- [39] Morse, P.M. Theoretical Acoustics
Ingard, K.U. New York: McGraw-Hill International Book Co., 1968.
- [40] Goldstein, M.F. Aeroacoustics
New York: McGraw-Hill International Book Co., 1976.

III. Wave propagation from moving singularities

- [41] Doppler, C. Über den Einfluß der Bewegung auf die Erscheinungen der Äther-,
Luft- und Wasserwellen.
Abh. d. Böhmischen Ges. d. Wiss. 5 (1947), S. 295-309.
- [42] Voigt, W. Über das Dopplersche Prinzip.
Nachrichten von der Kgl. Ges. d. Wiss. Göttingen 2 (1887),
S. 41-51.

- [43] Lorentz, H.A. Electromagnetic Phenomena in a System Moving with any Velocity less than that of Light. Proc. Acad. Sci. Amsterdam 6 (1904), S. 809-831.
- [44] Liénard, A. Champ électrique et magnétique produit par une charge électrique concentrée en un point et animée d'un mouvement quelconque. L'Eclairage électrique 16 (1898), S. 5-14; S. 53-59; S. 106-112.
- [45] Wiechert, E. Elektrodynamische Elementargesetze. Annalen der Physik, Leipzig 4 (1901), S. 667-689.
- [46] Schott, G.A. Electromagnetic Radiation. Cambridge: Univ. Press, 1912.
- [47] Poisson, S.D. Mémoire sur la théorie du son. Jour. de l'École Polytechn. Ser. 1 14 (1808), S. 319-392.
- [48] Helmholtz, H.v. Theorie der Luftschwingungen in Röhren mit offenen Enden. Journ. f. reine und angewandte Mathematik 57 (1860), S. 1-72.
- [49] Kirchhoff, G. Zur Theorie der Lichtstrahlen. Berl. Bericht (1882), S. 663-395; Vorlesungen über Mechanik. Leipzig: B.G. Teubner, 1897.
- [50] Hönl, H. Über das Schallfeld einer gleichförmig-translatorisch bewegten punktförmigen Schallquelle. Annalen der Physik, Leipzig 43 (1943), S. 437-464.
- [51] Küssner, H.G. Lösungen der klassischen Wellengleichung für bewegte Quellen. ZAMM 25 (1945), S. 243-250.
- [52] Rott, N. Das Feld einer raschbewegten Schallquelle. Inst. f. Aerodynamik, Eidg. Techn. Hochschule, Zürich, Mitteilung Nr. 9 (1945).
- [53] Billing, H. Geradlinig bewegte Schallquelle. ZAMM 29 (1949), S. 267-274; AVA-Bericht Nr. 45/J/15 (1945).
- [54] Oestreicher, H.L. The Effect of Motion on the Acoustic Radiation of a Sound Source. Centr. Air. Docum. Off. (Washington); Tech. Data Digest 16 (1951).
- [55] Lighthill, M.J. On Sound Generated Aerodynamically. I. General Theory. Proc. Roy. Soc. A 211 (1952), S. 564-587.
- [56] Curle, N. The Influence of Solid Boundaries upon Aerodynamic Sound. Proc. Roy. Soc. A 231 (1965), pp. 505-514.
- [57] Lowson, M.V. The Sound Field of Singularities in Motion. Proc. Roy. Soc. A 286 (1965), S. 559-592.
- [58] Ffowcs Williams, J.E. Sound Generation by Turbulence and Surface in Arbitrary Motion. Phil. Trans. Roy. Soc. A 264 (1969), pp. 321-342.
Hawkings, D.
- [59] Das, A. Wellenausbreitung und Lösungsmethoden der Wellengleichung bei bewegten Störquellen. DFVLR-FB 83-07 (1983).
Wave Propagation and Methods of Solution of the Wave Equation for Moving Disturbance Sources. Technical Translation (english), ESA-TT-824, March 1984; NASA TM 77410 (1984).
- [60] Das, A. Wave Propagation from Moving Singularities and a Unified Exposition of the Linearized Theory for Aerodynamics and Acoustics. DFVLR-FB 84-17 (1984).

IV. Numerical Methods in Aerodynamics

- [61] Hess, J.L. Calculation of Potential Flows about Arbitrary Bodies. Smith, A.M.O. Progress in Aeronautical Sciences Vol. 8, Pergamon Press, 1967, pp. 1-138.
- [62] Labrujere, Th.E. An Approximate Method for Calculation of the Pressure Distribution on Wing-Body Combinations at Sub-Critical Speeds. Loeve, W. AGARD Conf. Proceedings Nr. 71 (1970).
- [63] Kraus, W. Das MBB Unterschall-Panel-Verfahren. Teil II: Das auftriebsbehaftete Verdrängungs-Problem in kompressibler Strömung. MBB-Bericht Nr. UFE 633-70 (1970).

- [64] Hess, J.L. The Problem of Three-Dimensional Lifting Potential Flow and its Solution by Means of Surface Singularity Distribution. *Computer Methods in Applied Mechanics and Engineering* 4 (1974), pp. 283-319.
- [65] Albano, E. Rodden, W.P. A Doublet-Lattice Method for Calculating the Lift Distribution on Oscillating Surfaces in Subsonic Flow. *AIAA-Journal* 7 (1969), pp. 279-285.
- [66] Jones, W.P. Moore, J.A. Simplified Aerodynamic Theory of Oscillating Thin Surfaces in Subsonic Flow. *AIAA-Journal* 11 (1973), pp. 1305-1309.
- [67] Geissler, W. Methods for Inviscid Subsonic Flows about Aircraft Configurations. VKI-Lecture Series, Unsteady Aerodynamics, March 1980.
- [68] Morino, L. Steady, Oscillatory and Unsteady Subsonic and Supersonic Aerodynamics. Production Version (SOUSSA-P1.1), Vol. I, Theoretical Manual, NASA CR 159130 (1980).
- [69] Kohlmeier, H.H. Eine direkte Berechnungsmethode für Störfelder bewegter Körper in kompressiblen Medien bei Unterschall-Machzahlen. DFVLR-IB 129 - 83/24 (1983); Dissertation, TU Braunschweig, 1984.
- [70] Chaussee, D.S. Kutler, P. User's Manual for Three-Dimensional Analysis of Propeller Flow Fields. NASA-CR 167959 (1983).

V. Some classical references

- [71] Rankine, W.J.M. On the Mechanical Principles of the Action of Propellers. *Trans. of Institution of Naval Architects*, Vol. 6 (1865) pp. 13.
- [72] Froude, R.E. On the Part Played in Propulsion by Differences of Fluid Pressure. *Trans. of Institution of Naval Architects*, Vol. 30 (1889), pp. 390-405.
- [73] Lamb, H. The Magnetic Field of a Helix. *Proc. of Cambridge Phil. Soc.*, Vol. 21 (1923), pp. 477-481.
- [74] Maxwell, J.C. *Treatise on Electricity and Magnetism*. New York: Dover Publication, 1873.
- [75] Föttinger, H. Neue Grundlagen für die theoretische und experimentelle Behandlung des Propellerproblems. *Jb. Schiffbautechn. Gesellschaft*, Bd. 19 (1918), S. 385-472.

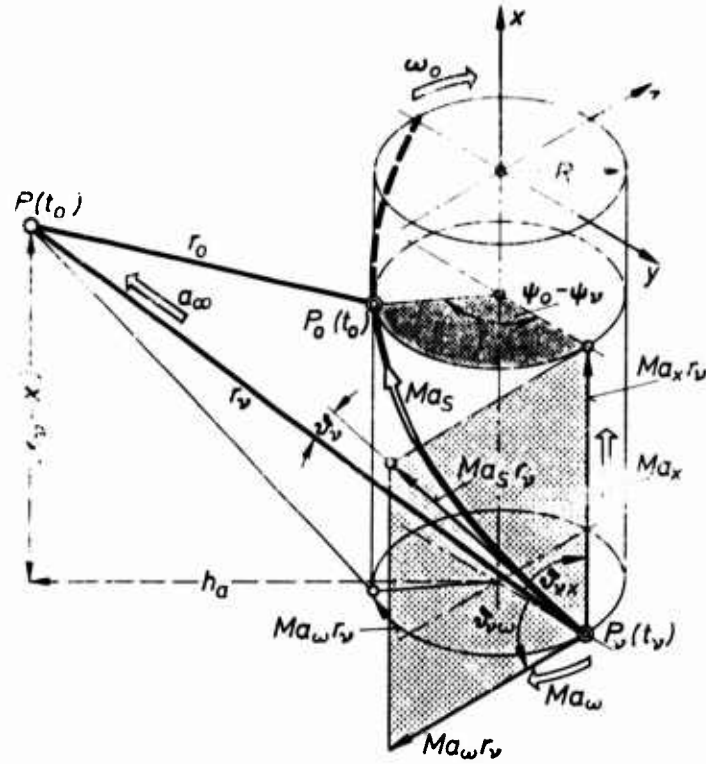


Fig. 1: The basic kinematic relations for disturbance propagation from a singularity-element in helical motion.

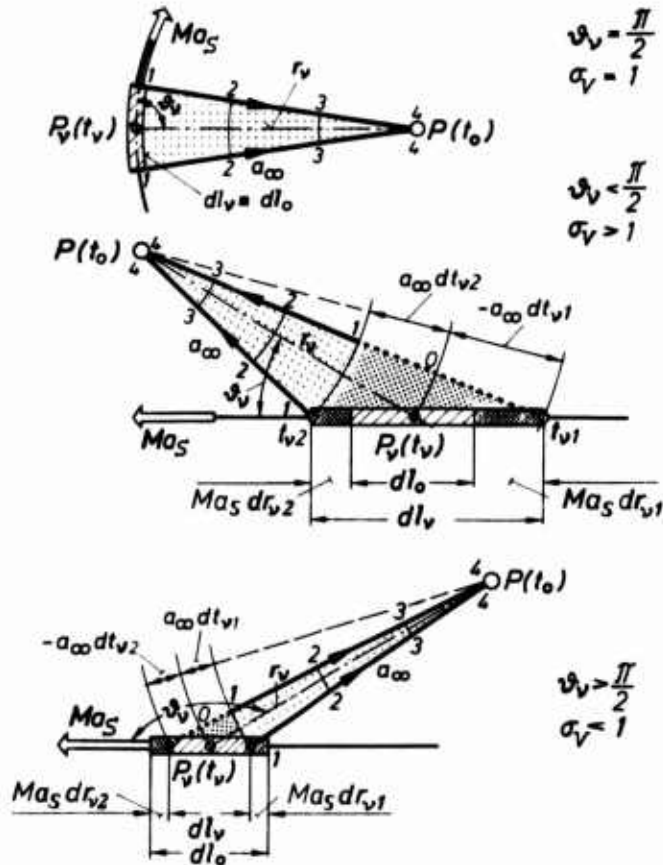


Fig. 2: The spatial dilatation factor σ_v of the emitting elements dl_v determined from the time sequences of the shrinking acoustic spheres propagating to the field point - the shifts $Ma_s dr_v$ and $a_\infty dt_v$ define the underlying basis of the Liénard-Wiechert Formula.

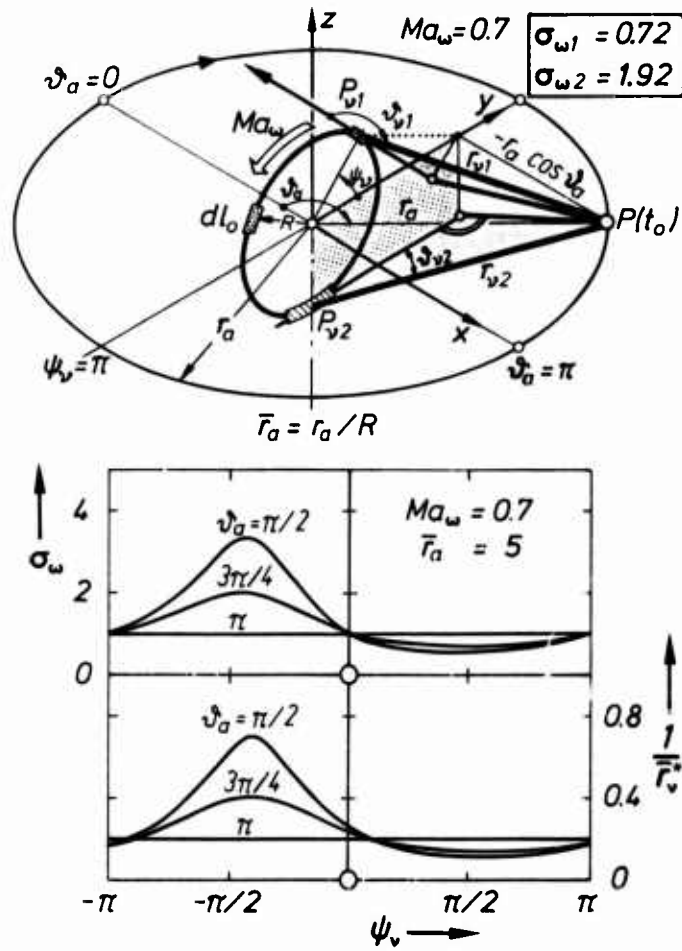


Fig. 5: The spatial dilatation factor σ_ω arising from the circular motion of a singularity element, thus influencing the radiation quantities both in the near-field and in the far-field.

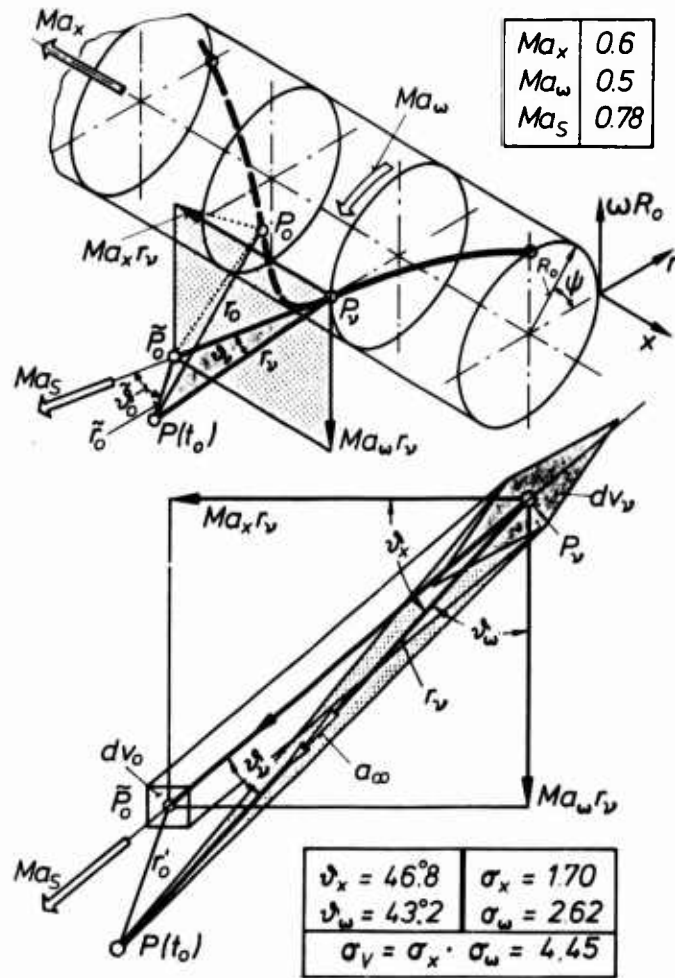


Fig. 6: The spatial dilatation factor σ_v of an emitting element in helical motion comprising axial- and circumferential stretchings σ_x and σ_ω .

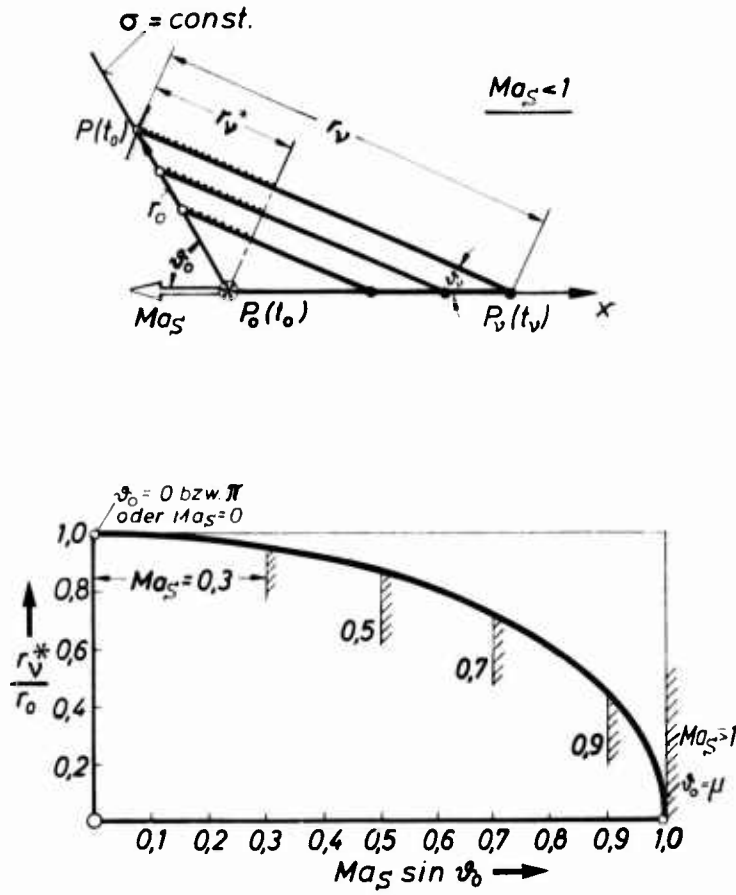


Fig. 7: Universal representation of the effective propagation radius $r_v^* = r_v/\sigma_v$ accounting for the spatial dilatation factor σ_v of singularity elements in arbitrary motion. (note: σ , r_v/r_0 and $r_v^*/r_0 = \text{const.}$ at field points on a ray $\vartheta_0 = \text{const.}$)

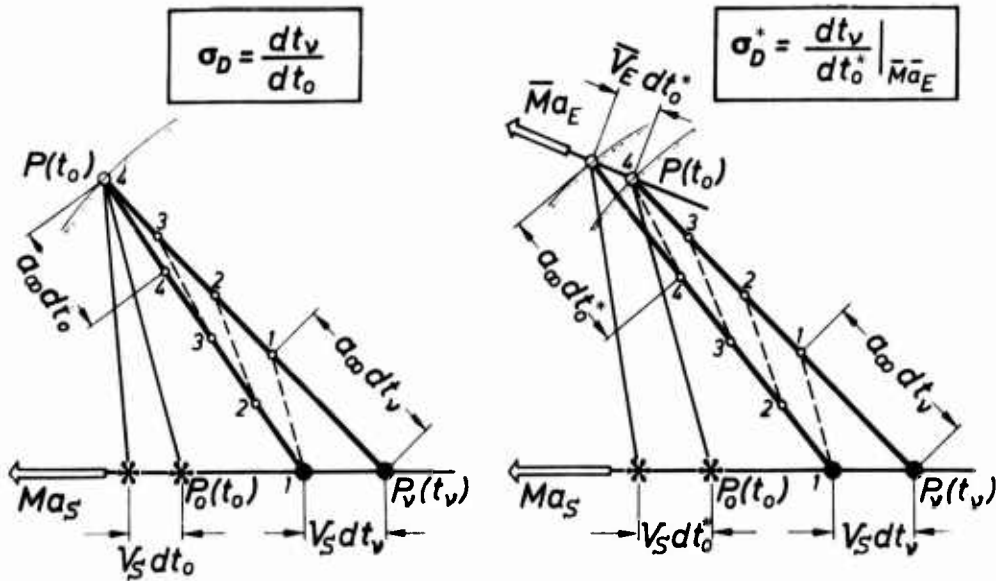


Fig. 8: The temporal influence functions σ_D and σ_D^* arising from the changed time sequence of signals passing through a fixed or moving field point in relation to the time sequence of emission from a moving singularity. ($\sigma_D = dt_v/dt_0$; $\sigma_D^* = dt_v/dt_0^*$)

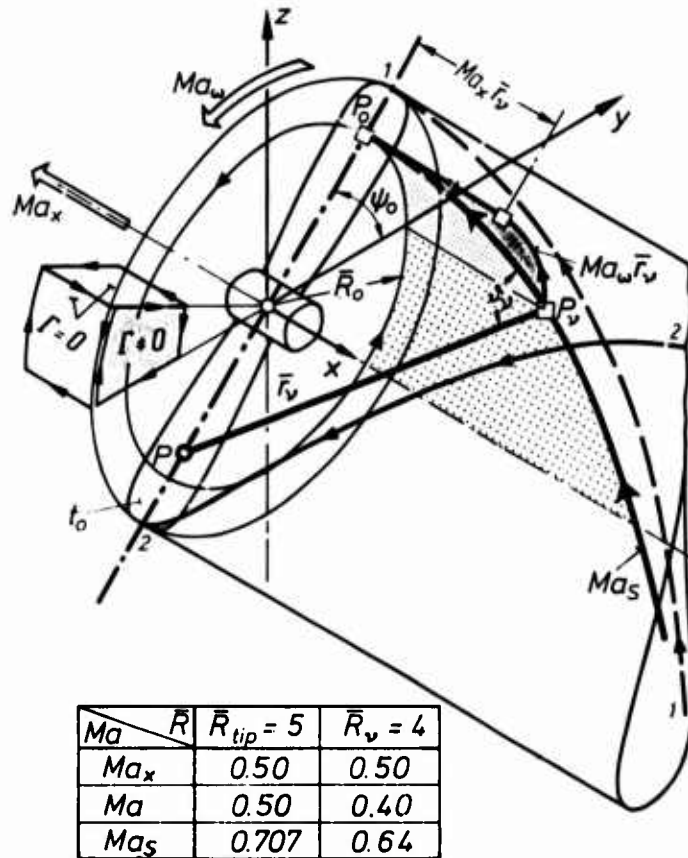


Fig. 9: The singularity elements and field points on propeller blades in helical motion and the corresponding kinematic relations for deriving the inducing functions. (note: irrotational flow condition in annular space and rotational flow condition in the cross planes)

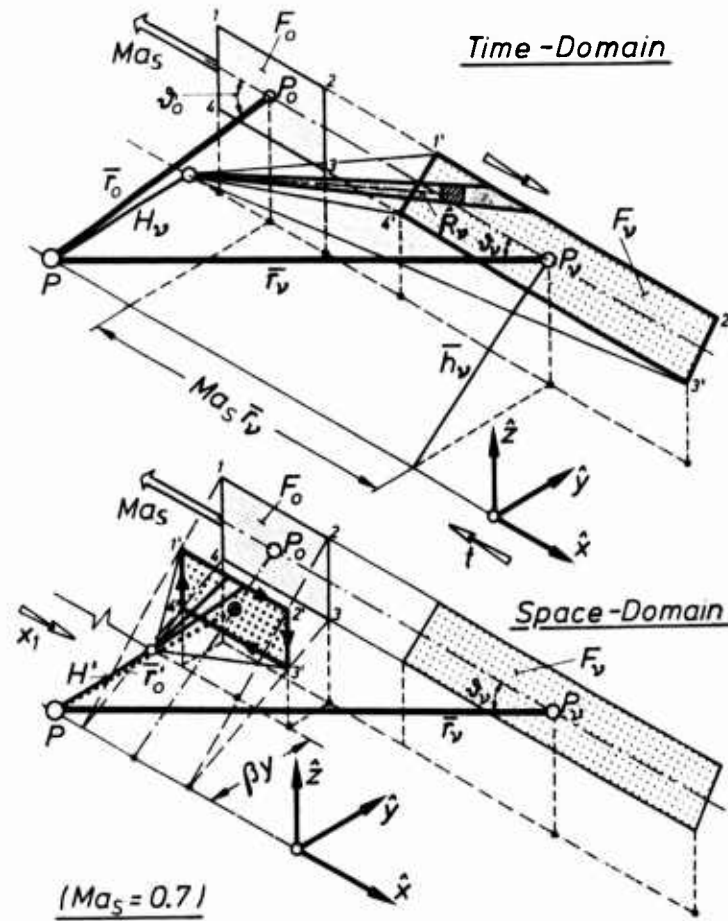


Fig. 10: Application of the sweep technique to derive the inducing field of a singularity surface in translatory motion:

- a) sweep of the effective emitting surface at P_v
- b) sweep of the moving source panel at P_0

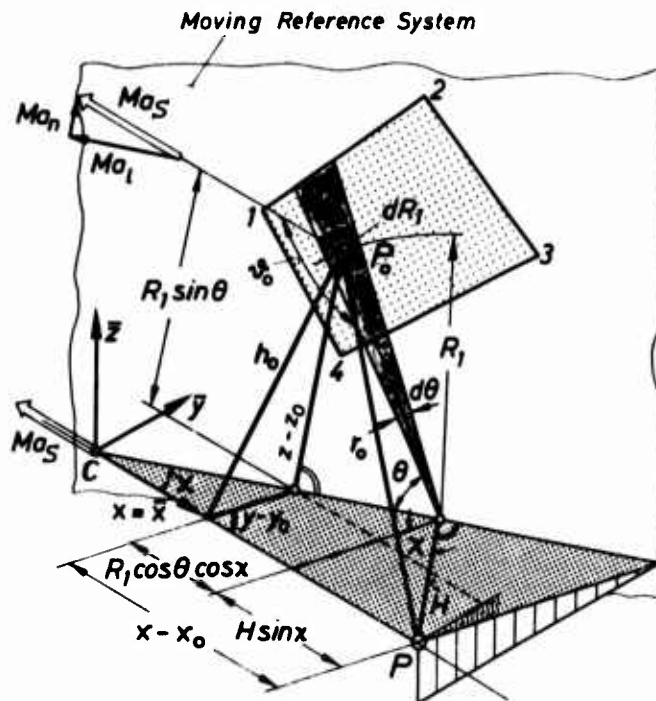


Fig. 11: Illustration of the sweep technique as applied to a moving source panel in arbitrary orientation in space and to the trajectory, implying the introduction of new coordinate system for the sweep.

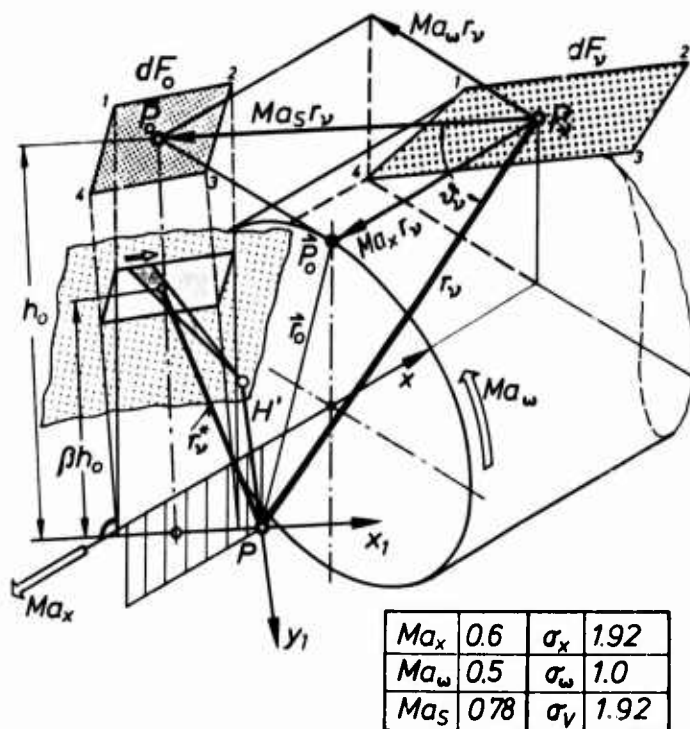


Fig. 12: Extension of the sweep technique for deriving the inducing functions of singularity surfaces in helical motion:
 a) sweep of the effective emitting surface at P_y
 b) sweep of an auxiliary surface after shifting \hat{y} the moving source surface to \hat{P}_0 .

Space-Domain

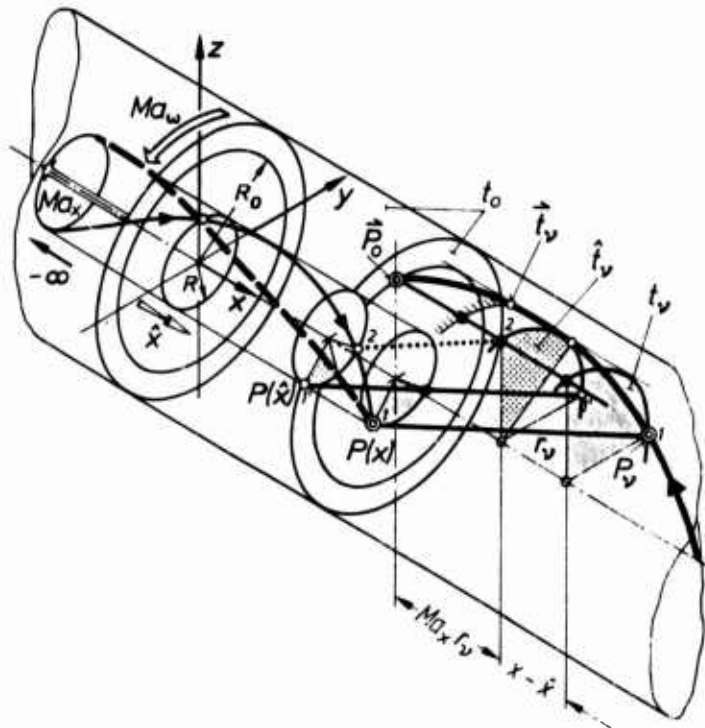


Fig. 13: Application of the sweep technique in the space-domain by holding the singularity element at its position P_0 at time t_0 and shifting the field point in steps from $\hat{x} = -\infty$ to its position $P(x)$ on the blade surface, where the classical boundary condition is to be fulfilled.

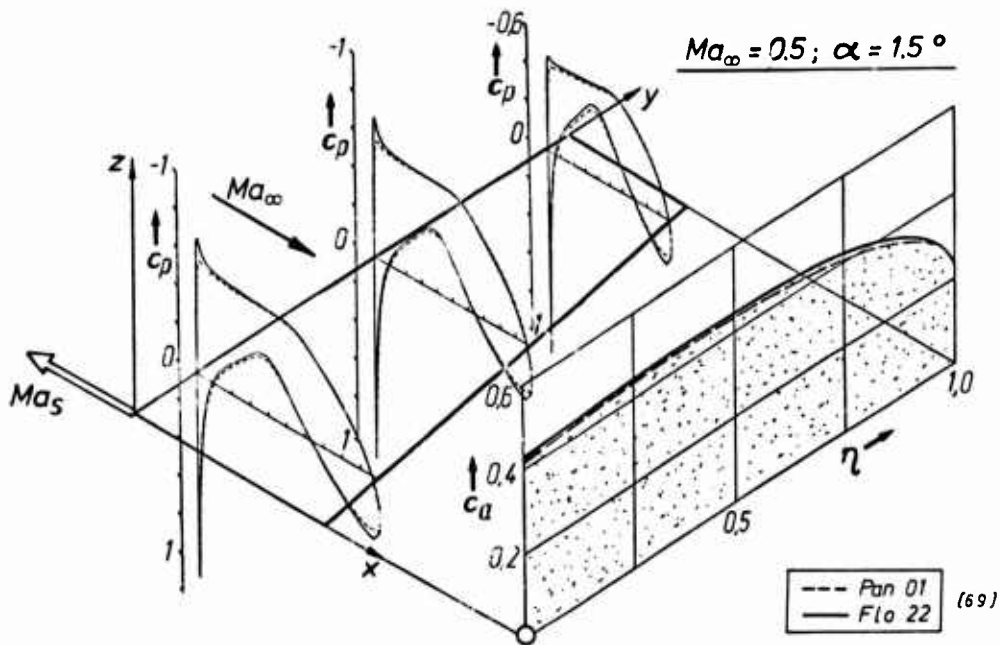


Fig. 14: Application of the numerical computational technique to a moving wing and comparison of the chordwise pressure distribution and spanwise lift distribution according to the linearized and non-linear theories. ($R = 10$, $\alpha = 0^\circ$, Airfoil RAE 2822)

**THEORETICAL ANALYSIS OF LINEARIZED ACOUSTICS AND AERODYNAMICS
OF ADVANCED SUPERSONIC PROPELLERS**

F. Farassat
Senior Research Scientist
NASA Langley Research Center
Aeroacoustics Branch, ANRD
Mail Stop 460
Hampton, VA 23665 U.S.A.

TABLE OF CONTENTS

ABSTRACT

- I. INTRODUCTION
- II. THE GOVERNING EQUATION AND ITS SOLUTION
- III. METHOD OF IMPLEMENTATION ON A COMPUTER AND SOME EXAMPLES
- IV. DERIVATION OF AERODYNAMIC INTEGRAL EQUATION
- V. CONCLUDING REMARKS

ABSTRACT

This paper presents the derivation of a formula for prediction of the noise of supersonic propellers using time domain analysis. This formula is a solution of the Ffowcs Williams-Hawkings equation and does not have the Doppler singularity of some other formulations. The result presented here involves some surface integrals over the blade and line integrals over the leading and trailing edges. The blade geometry, motion and surface pressure are needed for noise calculation. To obtain the blade surface pressure, the observer is moved onto the blade surface and a linear singular integral equation is derived which can be solved numerically. Two examples of acoustic calculations using a computer program currently under development at Langley Research Center are also presented.

I. INTRODUCTION

Advanced supersonic propellers are being considered for propulsion of future commercial airliners. The chief reason for this new interest in propellers is the high efficiency they offer at cruise speed of current subsonic aircraft. Two main areas of research in development of these propellers are acoustics and aerodynamics. The state-of-the-art of the 1970's is inadequate for prediction of the noise and aerodynamic performance of advanced propellers. New methods based on first principles are needed.

Advanced propellers have blades which run at transonic and supersonic speed over a substantial portion of the blade. The blade speed at the inboard region is subsonic. For noise prediction from subsonic sources, an efficient formulation by the author (called Formulation 1-A) exists.¹ An aerodynamic integral equation based on this result was derived by L. N. Long.² In this paper, we concentrate on the derivation of acoustic and aerodynamic formulations for transonic and supersonic sources. The governing differential equation for deriving these results is the Ffowcs Williams-Hawkins equation (FW-H equation).³

The results presented in here are closely related to those in references 4 and 5. First, the acoustic formulation is derived using the method of reference 4. The aerodynamic integral equation is then obtained by moving the observer onto the blade surface and finding the contribution of the sources near the observer analytically.⁵ Two examples of noise calculations for a supersonic propeller are presented.

II. THE GOVERNING EQUATION AND ITS SOLUTION

The governing equation is the FW-H equation written as follows:

$$\square^2 p' = \nabla_4 \cdot [\vec{Q} |\nabla f| \delta(f)] \quad (1)$$

where $Q = (-\vec{p}\vec{n}, M_n)$ and $\nabla_4 = (\nabla, 1/c \partial/\partial t)$. In this equation p' and p are the acoustic and the blade surface pressures, respectively, nondimensionalized with respect to $\rho_0 c^2$. The blade surface is described by $f(\vec{x}, t) = 0$. The local normal Mach number vector and unit outward normal are denoted \vec{M}_n and \vec{n} , respectively and $M_n = |\vec{M}_n|$. The function $\delta(f)$ is Dirac delta function. Note that only p and p' are nondimensional.

Below we will indicate the method of integrating equation (1). Some details can be found in reference 4. Let \vec{N} denote the unit normal to the surface $f=0$ in four dimensions. The direction of this vector is given by the four-gradient $\nabla_4 f = (\nabla f, 1/c \partial f/\partial t)$. The four-vector \vec{Q} is split into two vectors normal and tangent to the surface $f=0$ as follows

$$\vec{Q}_N = (\vec{Q} \cdot \vec{N}) \vec{N} \quad (2-a)$$

$$\vec{Q}_T = \vec{Q} - \vec{Q}_N \quad (2-b)$$

It is easily shown that

$$\vec{N} = \frac{1}{\alpha_n} (\vec{n}, -M_n) \quad (3)$$

$$\vec{Q}_N = \frac{-1}{\alpha_n} (p + M_n^2) (\vec{n}, -M_n) \quad (4-a)$$

$$\vec{Q}_T = \frac{1}{\alpha_n} M_n (1 - p) (\vec{M}_n, 1) \quad (4-b)$$

Equation (1) can now be written as

$$\begin{aligned} \square^2 p' = & \nabla_4 \cdot [\vec{Q}_N |\nabla f| \delta(f)] \\ & + \nabla_4 \cdot [\vec{Q}_T |\nabla f|] \delta(f) \end{aligned} \quad (5)$$

Note that the 4-divergence operator in the second term on the right of equation (5) does not operate on the delta function. This will result in the simplification of algebraic manipulations in the process of finding the solution of this equation. As will be seen below, the solution of equation (5) involves much algebra and any well-thought trick to reduce the algebra helps in obtaining the solution. This philosophy is applied in every step of the solution described here.

Basically, the second term on the right of equation (5) is easily interpreted in the solution using Green's function technique. The handling of the first term involves considerably more algebraic manipulations. We note that there are several kinds of discontinuities in the parameters of this problem which introduce line integrals in the solution of equation (5). These discontinuities are of the following kind:

- (i) There is a discontinuity of slope and therefore in M_n and angle θ (between radiation direction \vec{r} and local outward normal) at a sharp TE and LE of the blade,
- (ii) There is a discontinuity in surface pressure p at shock traces on the blade,
- (iii) Since only the outer high-speed portion of the blade is considered, the blade segment is not closed at the inboard section. The resulting edge is a discontinuity in the space.

To include the above discontinuities in the solution, we divide the outer portion of the blade into several contiguous open smooth surfaces across part or all of whose edges a discontinuity of the above kinds exists. Let k be a function such that $k=0$ and $f=0$ together describe the edge of one of these open surfaces. This new function is defined such that $f=0, k>0$ describe the points on the open surface. The FW-H equation for this open surface is then

$$\square^2 p = \nabla_4 \cdot [H(k) \vec{Q}_N | \nabla f | \delta(f)] + \nabla_4 \cdot [H(k) \vec{Q}_T | \nabla f | \delta(f)] \quad (6)$$

where $H(k)$ is the Heaviside function. We now describe the major steps in solving equation (6).

Steps of Algebraic Manipulations

Step 1: We use the Green's function of the wave equation in the unbounded space. The formal solution of equation (6) is

$$4\pi p'(\vec{x}, t) = \int \frac{1}{r} \nabla_4 \cdot [H(k) \vec{Q}_T | \nabla f | \delta(f) \delta(g)] d\vec{y} d\tau + \int \frac{1}{r} \nabla_4 \cdot [H(k) \vec{Q}_N | \nabla f | \delta(f) \delta(g)] d\vec{y} d\tau \quad (7-a)$$

$$\equiv I_1 + \int \frac{H(k)}{r^2} | \nabla f | \vec{Q}_N \cdot \nabla_4 r \delta(f) \delta(g) d\vec{y} d\tau - \int \frac{H(k)}{r} | \nabla f | \vec{Q}_N \cdot \nabla_4 g \delta(f) \delta'(g) d\vec{y} d\tau \quad (7-b)$$

$$\equiv I_1 + I_2 - I_3 \quad (7-c)$$

Here I_1 is the first integral in equation (7-a) and I_2 and I_3 are the integrals appearing as the second and third terms of equation (7-b). In going from equation (7-a) to equation (7-b), we have used an integration by parts as follows

$$\int \frac{\delta(g)}{r} \nabla_4 \cdot [H(k) \vec{Q}_N | \nabla f | \delta(f)] d\vec{y} d\tau = - \int H(k) | \nabla f | \delta(f) \vec{Q}_N \cdot \nabla_4 \left[\frac{\delta(g)}{r} \right] d\vec{y} d\tau \quad (8)$$

The right side then results in I_2 and I_3 . This operation is permissible since for finite (\vec{x}, t) , the subspace $f=0, g=0$ is finite in extent in the space. Thus, no other integral appears on the right side of equation (8). For the moment our work with I_1 and I_2 is finished. We concentrate on I_3 which involves $\delta'(g)$.

Step 2: We now utilize the following identity derived in appendix A of reference 4 to write I_3 in a form which no longer contains $\delta'(g)$ in the integrand:

$$\int q(\vec{y}, \tau) \delta(f) \delta'(g) d\vec{y} d\tau = - \int \nabla_4 \cdot (q \vec{A}) \delta(f) \delta(g) d\vec{y} d\tau \quad (9)$$

in which we have defined

$$\vec{A} = \frac{c}{\lambda^2} [-\alpha_n^2 (\vec{t}_1, 0) + (1 - M_n \cos \theta) (\vec{M}_n, 1)] \quad (10)$$

This expression for \vec{A} is indeed equal to that of reference 4. Note that \vec{t}_1 is the projection of \vec{r} on the local tangent plane of $f=0, \tau$ -fixed. The above identity gives

$$I_3 = - \int \nabla_4 \cdot \left[\frac{H(k)}{r} | \nabla f | (\vec{Q}_N \cdot \nabla_4 g) \vec{A} \right] \delta(f) \delta(g) d\vec{y} d\tau$$

(Cont'd)

$$\begin{aligned}
&= \int \frac{H(k)}{r^2} \left| \nabla f \right| (\vec{Q}_N \cdot \nabla_4 g) \vec{A} \cdot \nabla_4 r \delta(f) \delta(g) d\vec{y} d\tau \\
&= \int \frac{1}{r} \nabla_4 \cdot [H(k) \left| \nabla f \right| (\vec{Q}_N \cdot \nabla_4 g) \vec{A}] \delta(f) \delta(g) d\vec{y} d\tau \\
&\equiv I_{31} - I_{32}
\end{aligned} \tag{11}$$

We have now been able to get integrals which no longer contain derivatives of delta functions. Combining equations (7-c) and (11), we have shown that

$$4\pi p'(\vec{x}, t) = I_1 + I_{32} + I_2 - I_{31} \tag{12}$$

We write the integrals on the right side of equation (12) as follows

$$\begin{aligned}
I_1 + I_{32} &\equiv I'_1 \\
&= \int \frac{1}{r} \nabla_4 \cdot [H(k) \left| \nabla f \right| \{ \vec{Q}_T + (\vec{Q}_N \cdot \nabla_4 g) \vec{A} \}] \delta(f) \delta(g) d\vec{y} d\tau
\end{aligned} \tag{13-a}$$

$$\begin{aligned}
I_2 - I_{31} &\equiv I'_2 \\
&= \int \frac{H(k) \left| \nabla f \right|}{r^2} [\vec{Q}_N \cdot \nabla_4 r - (\vec{Q}_N \cdot \nabla_4 g) \vec{A} \cdot \nabla_4 r] \delta(f) \delta(g) d\vec{y} d\tau
\end{aligned} \tag{13-b}$$

so we have written equation (12) as

$$4\pi p'(\vec{x}, t) = I'_1 + I'_2 \tag{14}$$

Note that in all the above integrands, we have defined $\nabla_4 = (\nabla, 1/c \partial/\partial\tau)$ where $\nabla = \partial/\partial y_1$. Our next task is simplifying I'_1 and I'_2 .

Step 3: It is easily shown that

$$\nabla_4 r = (-\vec{P}, 0) \tag{15-a}$$

$$\nabla_4 g = \frac{1}{c} (-\vec{P}, 1) \tag{15-b}$$

By using \vec{Q}_N and \vec{Q}_T from equation (4) and some algebraic manipulations, we get

$$\vec{Q}_T + (\vec{Q}_N \cdot \nabla_4 g) \vec{A} = -\vec{B}' - (p + M_n^2) \vec{B} \tag{16}$$

where

$$\vec{B} = \lambda (\vec{M}_n, 1) - \lambda_1 (\vec{t}_1, 0) \tag{17-a}$$

$$\vec{B}' = M_n (\vec{M}_n, 1) \tag{17-b}$$

Note that \vec{B} and \vec{B}' are on surface $f=0$ in four dimensions. This fact is seen by observing that $\vec{B} \cdot \vec{N} = \vec{B}' \cdot \vec{N} = 0$. Also note that we have defined

$$\lambda = \frac{\cos\theta - M_n}{\tilde{\lambda}^2} \tag{18-a}$$

$$\lambda_1 = \frac{\cos\theta + M_n}{\tilde{\lambda}^2} \tag{18-b}$$

In addition, we can show that

$$\vec{Q}_N \cdot \nabla_4 r - (\vec{Q}_N \cdot \nabla_4 g) \vec{A} \cdot \nabla_4 r = \lambda(p + M_n^2) \tag{19}$$

Equation (14) can thus be written simply as follows

$$\begin{aligned}
4\pi p'(\vec{x}, t) = & - \int \frac{1}{r} \nabla_4 \cdot [H(k) |\nabla f| \vec{B}'] \delta(f) \delta(g) d\vec{y} d\tau \\
& - \int \frac{1}{r} \nabla_4 \cdot [H(k) |\nabla f| (p + M_n^2) \vec{B}'] \delta(f) \delta(g) d\vec{y} d\tau \\
& + \int \frac{\lambda H(k) |\nabla f|}{r^2} (p + M_n^2) \delta(f) \delta(g) d\vec{y} d\tau
\end{aligned} \tag{20}$$

This equation can be simplified enormously. We next write the 4-divergence terms in such a way that we can take advantage of the fact that the vectors \vec{B} and \vec{B}' lie on the surface $f=0$ in four dimensions. At this point we remark that the last integral in equation (20) is not the only integral in $p'(\vec{x}, t)$ whose integrand is of $O(1/r^2)$. The reason is that $\nabla_4 \cdot \vec{B}$, coming from the second integral contains terms of $O(1/r^2)$. It is crucial that we find explicitly all the terms of $O(1/r^2)$ for aerodynamic applications of our main acoustic result.

Step 4: To get the 4-divergence in the integrands of the first and second integrals in equation (20), it is not wise to use the Cartesian variables in the divergence operator ($\nabla, 1/c \partial/\partial\tau$). This would lead to lengthy expressions whose geometric interpretation is difficult. We use the invariant definition of divergence given in tensor analysis. We first take any convenient coordinate system (u^1, u^2) on the surface $f=0, \tau$ -fixed. We also introduce two other variables (u^3, u^4)= $(f, c\tau)$. In other words, we introduce the coordinate transformation

$$\begin{aligned}
(y_1, y_2, y_3, \tau) & \rightarrow (u^1, u^2, u^3, u^4) \\
& = (u^1, u^2, f, c\tau)
\end{aligned}$$

The natural base vectors $\vec{A}_i, i=1-4$ in this coordinate system are obtained in appendix B of reference 4. These base vectors are as follows:

$$\vec{A}_1 = (\vec{a}_1, 0) \tag{21-a}$$

$$\vec{A}_2 = (\vec{a}_2, 0) \tag{21-b}$$

$$\vec{A}_3 = \left(\frac{\vec{n}}{|\nabla f|}, 0 \right) \tag{21-c}$$

$$\vec{A}_4 = (\vec{M}, 1) \tag{21-d}$$

where \vec{a}_1 and \vec{a}_2 are the natural base vectors of the surface $f=0, \tau$ -fixed. In reference 4, it is also shown that $g(4)$, the determinant of the coefficients of the first fundamental form is given by

$$g(4) = \frac{g(2)}{|\nabla f|^2} \tag{22}$$

where $g(2)$ is the determinant of the coefficients of the first fundamental form of the surface $f=0, \tau$ -fixed, in surface coordinates (u^1, u^2).

In terms of the natural base vectors $\vec{A}_i, i=1-4$, the components of \vec{B} and \vec{B}' can be written as follows

$$\begin{aligned}
\vec{B} & = \lambda_1 (\vec{t}_1, 0) - \lambda [\vec{A}_3 - (\vec{M}_t, 0)] \\
& = (\lambda \vec{M}_t + \lambda_1 \vec{t}_1, 0) - \lambda \vec{A}_3 \\
& = (\lambda \mu^1 + \lambda_1 \alpha^1, \lambda \mu^2 + \lambda_1 \alpha^2, -\lambda, 0) \\
& \equiv B^i \quad i = 1 - 4
\end{aligned} \tag{23-a}$$

$$\begin{aligned}
\vec{B}' & = M_n (\vec{M}_t, 0) - M_n \vec{A}_3 \\
& = (M_n \mu^1, M_n \mu^2, -M_n, 0) \\
& \equiv B'^i \quad i = 1 - 4
\end{aligned} \tag{23-b}$$

In these equations, \vec{M}_t is the local tangential component of the Mach number vector \vec{M} and \vec{t}_1 is the projection of the radiation vector \vec{F} on the local tangent plane to $f=0$, τ -fixed. The components of \vec{M}_t and \vec{t}_1 in terms of the natural base vectors (\vec{a}_1, \vec{a}_2) of the surface $f=0$, τ -fixed, are denoted by μ^i and α^i , $i=1-2$, respectively.

The 4-divergence terms of equation (20) can now be written easily. First, however, we define the function k which describes the edge of the open surface as follows. We assume that this function is given as $k(u^1, u^2, \tau)$. This means that it is described as a time varying function of surface coordinates. This is done to take care of oscillating shock traces on the blade since we are not explicitly assuming that the edge curve described $f=k=0$ is time independent. The 4-divergence terms are as follows

$$\begin{aligned} \nabla_4 \cdot [H(k) |\nabla f| (p + M_n^2) \vec{B}] &= |\nabla f| H(k) (p + M_n^2) (B^i \Gamma_{ij}^j) \\ &+ \frac{\partial B^i}{\partial u^i} - \frac{1}{c} \frac{\partial \lambda}{\partial \tau} + |\nabla f| H(k) [B^i \frac{\partial}{\partial u^i} (p + M_n^2) - \frac{\lambda}{c} \frac{\partial}{\partial \tau} (p + M_n^2)] \\ &+ |\nabla f| |\nabla k| (p + M_n^2) (\lambda M_{av} + \lambda_1 \hat{\Gamma}_v) \delta(k) \quad i, j = 1-2 \end{aligned} \quad (24-a)$$

$$\begin{aligned} \nabla_4 \cdot [H(k) |\nabla f| \vec{B}'] &= |\nabla f| H(k) (\Gamma_{ij}^j B'^i + \frac{\partial B'^i}{\partial u^i} - \frac{1}{c} \dot{M}_n) \\ &+ |\nabla f| |\nabla k| M_{av} \delta(k) \quad i, j = 1-2 \end{aligned} \quad (24-b)$$

In these equations the tensor summations on i and j are used. The Christoffel symbol of the second kind is denoted by Γ_{ij}^k . The component of the local absolute velocity (with respect to the frame fixed to the undisturbed medium) of the edge curve $f=k=0$ in the direction of inward geodesic unit normal \vec{v} is M_{av} and $\hat{\Gamma}_v$ is the projection of the radiation vector of \vec{F} along \vec{v} . The geodesic normal \vec{v} is a vector normal to the edge of the open surface and tangent to the surface pointing inward. The rate of change of local Mach number for a point on the surface (with fixed u^1, u^2) is denoted \dot{M}_n . In the next step, we will begin to simplify the terms in equation (24).

Step 5: We note that

$$\begin{aligned} (B^1, B^2) &= \lambda \vec{M}_t + \lambda_1 \vec{t}_1 \\ &\equiv \vec{b} \end{aligned} \quad (25)$$

we can thus write

$$B^i \frac{\partial}{\partial u^i} = b \frac{\partial}{\partial \sigma_b} \quad (26)$$

where $b = |\vec{b}|$ and $\partial/\partial \sigma_b$ signifies the directional derivative in the direction of surface vector \vec{b} . Assuming that in terms of variables (u^1, u^2, τ) , the surface pressure is described by the function $p_B(u^1, u^2, \tau)$, we have

$$\begin{aligned} B^i \frac{\partial}{\partial u^i} (p + M_n^2) - \frac{\lambda}{c} \frac{\partial}{\partial \tau} (p + M_n^2) \\ = b \frac{\partial p_B}{\partial \sigma_b} - \frac{\lambda}{c} \dot{p}_B + 2M_n (b \frac{\partial M_n}{\partial \sigma_b} - \frac{\lambda}{c} \dot{M}_n) \\ \equiv E_0 \end{aligned} \quad (27)$$

Our next task is simplification of the following two terms in equation (24)

$$E_1 = B_i \Gamma_{ij}^j + \frac{\partial B^i}{\partial u^i} \quad (28-a)$$

$$E_2 = B'^i \Gamma_{ij}^j + \frac{\partial B'^i}{\partial u^i} - \frac{1}{c} \dot{M}_n \quad (28-b)$$

These expressions need considerable algebraic manipulations. The results are:

$$E_1 = E_{11} + \frac{1}{r} E_{12} \quad (29-a)$$

$$E_{11} = \frac{1}{c} \dot{\hat{\Omega}} \cdot \left[\frac{\dot{\vec{t}}_1 - \dot{\vec{M}}_t}{\tilde{\lambda}^2} + 2\lambda \dot{\vec{b}} - \left(\frac{1}{\tilde{\lambda}^2} + 2\lambda\lambda_1 \right) \dot{\vec{t}} \right] - \frac{1}{c} \left(2\lambda^2 - \frac{1}{\tilde{\lambda}^2} \right) \dot{M}_n$$

$$- 2b^2 \kappa_b - \kappa_1 \sigma_{11} - \kappa_2 \sigma_{22} + 2Hh_n \quad (29-b)$$

$$E_{12} = -2\lambda\lambda_1 (\cos\theta - M_n) \quad (29-c)$$

$$E_2 = \frac{1}{c} (\dot{\hat{\Omega}} \cdot \dot{\vec{M}}_t - \dot{M}_n) - M_t^2 \kappa_M + 2M_n^2 H \quad (29-d)$$

In these equations κ_1 and κ_2 are the principal curvatures, H is the mean curvature and κ_b and κ_M are the normal curvatures in the direction of \vec{b} and \vec{M}_t , respectively. Other symbols are defined as follows

$$\sigma_{11} = \frac{1}{\tilde{\lambda}^2} [(\tilde{\alpha}^1)^2 - (\tilde{\mu}^1)^2 + 2\tilde{\alpha}^1 \tilde{\mu}^1] \quad (30-a)$$

$$\sigma_{22} = \frac{1}{\tilde{\lambda}^2} [(\tilde{\alpha}^2)^2 - (\tilde{\mu}^2)^2 + 2\tilde{\alpha}^2 \tilde{\mu}^2] \quad (30-b)$$

$$\dot{\hat{\Omega}} = \dot{\vec{n}} \times \dot{\vec{\omega}} \quad (30-c)$$

$$h_n = \lambda M_n + \lambda_1 \cos\theta \quad (30-d)$$

where $\tilde{\alpha}^i$ and $\tilde{\mu}^i$, $i=1,2$, are the components of \vec{t}_1 and \vec{M}_t with respect to the unit basis vectors (\vec{a}_1, \vec{a}_2) in principal directions. Also we have used $\dot{\vec{\omega}}$ for the angular velocity of the surface.

We summarize our result obtained so far. We can now write equation (24) as follows

$$\nabla_4 \cdot [H(k) |\nabla f| (p + M_n^2) \vec{B}] = |\nabla f| H(k) (p + M_n^2) (E_{11} + \frac{1}{r} E_{12})$$

$$+ |\nabla f| H(k) E_0 + |\nabla f| |\nabla k| (p + M_n^2) (\lambda M_{av} + \lambda_1 r_v) \delta(k) \quad (31-a)$$

$$\nabla_4 \cdot [H(k) |\nabla f| \vec{B}'] = |\nabla f| H(k) E_2 + |\nabla f| |\nabla k| M_{av} \delta(k) \quad (31-b)$$

We now substitute these equations in equation (20). We obtain

$$4\pi p'(\vec{x}, t) = \int \frac{|\nabla f|}{r^2} H(k) (p + M_n^2) Q'_N \delta(f) \delta(g) d\vec{y} d\tau$$

$$+ \int \frac{|\nabla f|}{r} H(k) [(p + M_n^2) Q'_F + Q''_F + Q'''_F] \delta(f) \delta(g) d\vec{y} d\tau$$

$$- \int \frac{|\nabla f| |\nabla k|}{r} [(p + M_n^2) Q'_E + M_{av}] \delta(f) \delta(g) \delta(k) d\vec{y} d\tau \quad (32)$$

where we have defined

$$Q'_N = \lambda - E_{12}$$

$$= \lambda [2\lambda_1 (\cos\theta - M_n) + 1] \quad (33-a)$$

$$Q'_F = -E_{11}$$

$$= \frac{1}{c} \left(2\lambda^2 - \frac{1}{\tilde{\lambda}^2} \right) \dot{M}_n + \frac{1}{c} \dot{\hat{\Omega}} \cdot \left[\frac{\dot{\vec{M}}_t - \dot{\vec{t}}_1}{\tilde{\lambda}^2} - 2\lambda \dot{\vec{b}} - \left(\frac{1}{\tilde{\lambda}^2} + 2\lambda\lambda_1 \right) \dot{\vec{t}} \right] + 2b^2 \kappa_b + \kappa_1 \sigma_{11} + \kappa_2 \sigma_{22} - 2Hh_n \quad (33-b)$$

$$Q'_E = -E_0$$

$$= \frac{\lambda}{c} \dot{p}_B - b \frac{\partial p_B}{\partial \sigma_b} + 2M_n \left(\frac{\lambda}{c} \dot{M}_n - b \frac{\partial M_n}{\partial \sigma_b} \right)$$

$$= \frac{\lambda}{c} \dot{p}_B - b \frac{\partial p_B}{\partial \sigma_b} + 2M_n \left[\frac{1}{c} (\lambda \dot{M}_n - \dot{\hat{\Omega}} \cdot \dot{\vec{b}}) + \kappa_1 \tilde{\mu}^1 \tilde{B}^1 + \kappa_2 \tilde{\mu}^2 \tilde{B}^2 \right] \quad (33-c)$$

$$\begin{aligned}
 Q''_F &= -E_2 \\
 &= \frac{1}{c} (\dot{M}_n - \dot{\vec{n}} \cdot \dot{M}_t) + \kappa_M M_t^2 - 2HM_n^2 \quad (33-d)
 \end{aligned}$$

$$Q_E = \lambda M_{av} + \lambda_1 \hat{r}_v \quad (33-e)$$

In equation (32-c), we have denoted the components of \vec{M}_t and \vec{b} with respect to the unit basis vectors (\vec{a}_1, \vec{a}_2) along the principal directions as \vec{u}^i and \vec{B}^i , respectively.

In the next step, we give the interpretation of the following two integrals which are of the types appearing in equation (32)

$$J_1 = \int Q_1(\vec{y}, \tau) |\nabla f| H(k) \delta(f) \delta(g) d\vec{y} d\tau \quad (34)$$

$$J_2 = \int Q_2(\vec{y}, \tau) |\nabla f| |\nabla k| \delta(f) \delta(g) \delta(k) d\vec{y} d\tau \quad (35)$$

The first two integrals in equation (32) are of the type J_1 and the third integral is of the type J_2 . The interpretation of J_1 in various forms was given in several publications earlier.^{4,6} The interpretation of J_2 in three forms is discussed in appendix C of reference 4.

Step 6: We now integrate the delta functions in the integrals of equation (32). We start by discussing the integration of J_1 and J_2 given by equations (34) and (35). As we will see below, one can give various equivalent expressions for J_1 and J_2 .

When we have an integral involving the product of two delta functions with supports on two surfaces (properly speaking, hypersurfaces) $f=0$ and $g=0$, the resulting integral is over the subspace which is the intersection of the two surfaces. In the case of the surfaces $f=0$ ($k>0$) and the surface $g=0$, the visualization of the intersection subspace is actually quite easy. For a fixed (\vec{x}, t) and a given source time τ , the surface $g=\tau-t+r/c=0$ is a sphere with radius $c(t-\tau)$ and center at the observer position. The surface in the space generated by the intersection of $f=0$, $k>0$ and $g=0$ is denoted by $\Sigma: F(\vec{y}; \vec{x}, t) = [f(\vec{y}, \tau)]_{\text{ret}=0}$, $K(\vec{y}; \vec{x}, t) = [k]_{\text{ret}>0}$. This surface is constructed by letting the open surface move in space and finding its intersection with the collapsing sphere $g=0$ as τ varies from $-\infty$ to t . The intersection occurs only during some finite time intervals along a curve which we call the Γ -curve. The locus of these Γ -curves in the space is the Σ -surface (see reference 6 for more details).

The integral J_1 can then be written as

$$J_1 = \int_{\substack{F=0 \\ K>0}} \left[\frac{Q_1}{\Lambda} \right]_{\text{ret}} d\Sigma \quad (36)$$

where

$$\Lambda = [1 + M_n^2 - 2M_n \cos\theta]^{1/2} \quad (37)$$

The integral in equation (36) can also be written in two other forms using the following relation

$$\frac{d\Sigma}{\Lambda} = \left| \frac{dS}{1-M_r} \right| = \frac{cd\tau d\Gamma}{\sin\theta} \quad (38)$$

In this equation dS is element of the surface area of $f=0$, τ -fixed, and M_r is the Mach number in the radiation direction. Also $d\Gamma$ denotes the element of length of the Γ -curve.

In appendix C, of reference 4 we have shown that J_2 is an integral over the curve in space formed by the intersection of the edge of the open surface (described by $f=k=0$) and the collapsing sphere $g=0$. Let this curve be denoted as γ -curve. Then we have

$$J_2 = \int_{\substack{F=0 \\ K=0}} \left[\frac{Q_2}{\Lambda_o} \right] d\gamma \quad (39)$$

where

$$\Lambda_o = [M_p^2 \cos^2\psi + (1 - \vec{M}_p \cdot \vec{r}_p \sin\psi)^2]^{1/2} \quad (40)$$

In equation (40), ψ is the local angle between the edge of open surface and \vec{r} . Construct the local plane normal to this edge. Then \vec{M}_p is the projection of the local Mach number vector \vec{M} and \vec{r}_p is the unit vector along the projection of \vec{r} on this plane. Again we can use the following relation to write equation (39) in two other forms

$$\frac{d\gamma}{\Lambda_o} = \frac{dl}{|1-M_r|} = \frac{cd\tau}{|\cos\psi|} \quad (41)$$

where $d\ell$ is the element of length of the edge of the open surface given by $f=k=0$, τ -fixed.

Using equations (36) and (39), the final result of the present step is

$$\begin{aligned}
 4\pi p'(\vec{x}, t) = & \int_{F=0} \frac{1}{r^2} \left[\frac{1}{\Lambda} (p + M_n^2) Q_N' \right]_{\text{ret}} d\Sigma \\
 & + \int_{\substack{F=0 \\ K>0}} \frac{1}{r} \left\{ \frac{1}{\Lambda} [(p + M_n^2) Q_F + Q_F' + Q_F''] \right\}_{\text{ret}} d\Sigma \\
 & - \int_{\substack{F=0 \\ K=0}} \frac{1}{r} \left\{ \frac{1}{\Lambda_0} [(p + M_n^2) Q_E + M_{av}] \right\}_{\text{ret}} d\gamma
 \end{aligned} \tag{42}$$

In the next and final step of this section, we use the above equation to get the main result of this paper.

Step 7: We now assume that the supersonic portion of the blade shown in figure 1 is divided in three smooth open surfaces ABCHGF, FGHCDE and ABCDE. We apply equation (42) to each of these open surfaces and sum the results. We note that M_{av} and Q_E have opposite signs on BC, CH, CD and AF. The line integrals over these curves exactly cancel each other. Our final and main result of this paper is

$$\begin{aligned}
 4\pi p'(\vec{x}, t) = & \int_{F=0} \frac{1}{r^2} \left[\frac{1}{\Lambda} (p + M_n^2) Q_N' \right] d\Sigma \\
 & + \int_{F=0} \frac{1}{r} \left\{ \frac{1}{\Lambda} [(p + M_n^2) Q_F + Q_F' + Q_F''] \right\}_{\text{ret}} d\Sigma \\
 & - \int_{LE, TE} \frac{1}{r} \left\{ \frac{1}{\Lambda_0} [(p + M_n^2) Q_E + M_{av}]_{u+l} \right\}_{\text{ret}} d\gamma \\
 & - \int_{GEFG} \frac{1}{r} \left\{ \frac{1}{\Lambda_0} [(p + M_n^2) Q_E + M_{av}] \right\}_{\text{ret}} d\gamma \\
 & - \int_{\substack{\text{SHOCK} \\ \text{TRACES}}} \frac{1}{r} \left[\frac{\Delta p Q_E}{\Lambda_0} \right]_{\text{ret}} d\gamma
 \end{aligned} \tag{43}$$

In this equation we have defined

$$[(p + M_n^2) Q_E + M_{av}]_{u+l} = [(p + M_n^2) Q_E + M_{av}]_u + [(p + M_n^2) Q_E + M_{av}]_l \tag{44-a}$$

$$\Delta p = p_2 - p_1 \tag{44-b}$$

where the subscripts u and l stand for the upper and the lower surfaces of the blade. Also the subscripts 1 and 2 on p refer to the regions on each side of the shock trace as shown in figure 1. Note that in the last integral of equation (43), Q_E is calculated based on the unit normal \vec{v} pointing into region 2.

We can now look back and explain what we have achieved by all these manipulations. Although developed for supersonic propellers, equation (43) is valid for all blade speeds including subsonic speed, and steady or unsteady blade surface pressure. In addition, it can be used for near field as well as far field noise calculations. The observer can be stationary or in motion with the propeller.⁶ What is important, and this is the reason behind deriving this formulation, is that equation (43) does not have any of the nagging singularities of the other formulations of the solution to the FW-H equation for supersonic propellers. It must be mentioned that we are assuming here that the propeller blade is thin and is swept in such a way that both M_n and M_p are less than one everywhere. These conditions are satisfied for the current advanced supersonic propellers. Therefore, it is obvious that there has been a need for a formulation such as equation (43) to overcome the problems with the other formulations. One byproduct of this effort is that the accuracy in acoustic calculations improves considerably and there is also some saving in execution time on a computer.

It is seen that the derivation of equation (43) is rather lengthy. However, the final result is not much more complicated than some other useful results such as formulation 1-A (see reference 1). In the next section the application of equation (43) in prediction of the noise of high speed propellers will be discussed. We will refer to equation (43) as formulation 3.

III. METHOD OF IMPLEMENTATION ON A COMPUTER AND SOME EXAMPLES

In this section, we briefly describe how the main result of this paper, equation (43), is used for numerical work on a computer. We describe a program being developed at NASA Langley for high speed propeller noise prediction. First, the blade geometry, the blade surface pressure and the propeller

motion are specified. The blade is then cut into two segments. The inner segment runs fully at subsonic speed. The outer segment runs at transonic and supersonic speed.

To calculate the noise of the inner segment of the blade, a result called Formulation 1-A is always used. For the outer portion of the blade, the present formulation is used only if it is found that M_r , the Mach number in the radiation direction, is greater than $1-\epsilon$ for some point on this segment. Here ϵ is a small positive number usually taken as 0.05. If the observer position and time are such that this condition is not met for the outer portion, then Formulation 1-A is used again. It must be mentioned that Formulation 1-A executes faster on a computer than the present supersonic formulation. However, it suffers from Doppler singularities when $M_r=1$. The current computer program, therefore, optimizes the usage of the two formulations to speed up the execution time.

We now present several preliminary numerical results from a code under development at NASA Langley. Two examples for which experimental data were available are presented here. These examples were presented in NASA TP-1662 and correspond to figures 12 and 14 there.⁷ All the relevant operational and geometric data are given in the above technical paper. We mention here that the propeller used in the calculations is four bladed with a diameter of 0.65 m (2.2 ft). The measurements were performed in an anechoic tunnel running at a Mach number of 0.32. The helical tip Mach number is 1.17.

Figure 2 shows a comparison of measured and predicted acoustic pressure signatures by two methods. These correspond to figure 14 of reference 7. The old calculations were based on Formulation 1-A, and are taken from reference 7. The new calculation is based on a combination of Formulation 1-A and equation 22 as described above. As observed from this figure, the new pressure signature is smooth and agrees better with the measured signature. It must also be mentioned that the new code runs much faster than the old code used in reference 7. Figure 3 shows a comparison of acoustic spectra corresponding to figure 2. It is observed that, in contrast to the old calculation, there is now somewhat of an overprediction but the harmonic fall-off of the new calculation is much better than the old calculation. We must remind the readers of the preliminary nature of our results. At present, some of the overprediction is thought to be due to inaccuracies in numerical integration schemes used in the computer code.

Figure 4, which corresponds to figure 12 of reference 7, shows another comparison of measured and predicted acoustic signatures for a different observer position than that of figures 2 and 3. Again the smoothness of the new calculations must be noted. The agreement of the pressure signature for the new calculation compared with measured signature is reasonably good. Note that the measured signature was drawn by hand from an oscillograph picture which showed a dark band for many periods recorded on the screen. Thus the present comparison of signatures must not be considered ideal for the test of our theory. For this reason, more comparisons are planned in the future with other available and soon to be available measured data.

IV. DERIVATION OF AERODYNAMIC INTEGRAL EQUATION

In this section equation (43) will be used to derive an integral equation for aerodynamic calculations. It should be realized that since a linearized governing equation (FW-H equation) is utilized here, the results are valid only for propellers with thin blade sections. The derivation of our main result is similar to that of Long² who started with Formulation 1-A of the present author.

To derive the aerodynamic result, one must move the observer onto the surface of the blade. However, it can be shown that the first surface integral in equation (43) is divergent. In fact, it is of the type which is known as semi-convergent, that is, it can be given a value by regularizing the integral (or taking the principal value in some sense). It is helpful to recognize that there are many ways of regularizing divergent integrals leading to different analytic expressions for the aerodynamic integral equation which are all equivalent. The particular regularization selected must be tailored to numerical calculations. In the present derivation, a regularization of the near field term of the acoustic formula based on the collapsing sphere approach will be presented. This is done because the collapsing sphere approach is the preferred technique in noise calculations of bodies moving at transonic or supersonic speeds. The process is described as follows. Remove a small hole from the body surface $f = 0$ in such a way that the near field integral is convergent. This is possible because of the semi-convergence property of the integral. Next move the observer to the cap of the hole and evaluate the integral as the observer reaches the surface of the cap. The shape of the hole cut from the surface in this note is produced by the collapsing sphere of radius $r < \epsilon$ where $\epsilon > 0$ is a small fixed number. The observer is assumed to reach the surface when $r = 0$. The shape of the hole is shown in figure 5 for the observer on the supersonic portion of the blade.

It is easy to show that the near field term which is

$$I = \int \frac{1}{r^2} \left[\frac{(p+M_n^2)Q_N'}{\Lambda} \right]_{\text{ret}} d\Omega = \int \frac{c(p+M_n^2)Q_N'}{r^2 \sin\theta} d\Gamma dt \quad (45)$$

is now convergent. To see this, note that when the observer reaches the surface at time t , the corresponding collapsing sphere intersects the local tangent plane in a circle (Γ -curve) along which $\cos\theta = M_n$ (see equation (47-a), below, letting $\delta = 0$). Since Q_N' is proportional to λ and the latter is proportional to $\cos\theta - M_n$, the high order singularity of equation (45) is removed. We now must find the contribution of the cap of the hole which is of the shape shown in figure 5.

The limiting process to calculate the contribution of the cap is as follows. Take $\delta > 0$, fix ϵ and set the observer at a normal distance δ above the desired point on the surface at time t . Evaluate the integral in equation (45) and then let δ approach zero. Finally, let ϵ approach zero also. We assume $c(t-\tau) < \epsilon$ in the collapsing process of $g = 0$. Figure 6 shows the geometry of the collapsing sphere process at two times. The two planes are the local tangent planes. By expanding $q=p+M_n^2$ in a Taylor series in the vicinity of the observer position, we note that we must study the contribution of the cap to the integral

$$I = q_0 \int \frac{cQ_N'}{r^2 \sin\theta} d\Gamma dt \quad (46)$$

where q_0 is the value of q at the observer position. In the integral above, the time integration is over $c\tilde{\tau} < \epsilon$ where $\tilde{\tau} = t - \tau$. The above integral can be evaluated analytically as follows.

Referring to figure 6, we note that

$$\cos\theta = M_n + \frac{\delta}{c\tilde{\tau}} \quad (47-a)$$

$$R = r \sin\theta \quad (47-b)$$

$$\int_{t-\frac{\epsilon}{c}}^t \int_{r=ct}^{\dots} \dots \frac{cd\Gamma d\tau}{r^2 \sin\theta} = -2\pi \int_{\tau_1}^{\epsilon} \dots \frac{cd\tilde{\tau}}{r} \quad (47-c)$$

where τ_1 is the value of $\tilde{\tau}$ when the collapsing sphere leaves the body. From equations (46) and (47-c), the following is obtained

$$I/q_0 = -2\pi \int_{\tau_1}^{\epsilon} \frac{\lambda}{r} c d\tau - 4\pi \int_{\tau_1}^{\epsilon} \frac{(\cos\theta - M_n) \lambda \lambda_1}{r} c d\tau \equiv -2\pi I_1 - 4\pi I_2 \quad (48)$$

An easy way to integrate I_1 and I_2 is to introduce the new variable $z = \cos\theta$ and use equation (47-a). It is found that

$$I_1 = -\int \frac{dz}{2\alpha_n^2 - (z + M_n)^2} \quad (49)$$

$$I_2 = \int \frac{dz}{2\alpha_n^2 - (z + M_n)^2} + M_n \int \frac{2(z + M_n) dz}{[2\alpha_n^2 - (z + M_n)^2]^2} - 2\alpha_n^2 \int \frac{dz}{[2\alpha_n^2 - (z + M_n)^2]^2} \quad (50)$$

The limits of all these integrals are from $M_n + \delta/\epsilon$ to 1. The integrals in equations (49) and (50) can now be evaluated to yield

$$\frac{I}{q_0} = -2\pi \left[\frac{M_n - z}{2\alpha_n^2 - (z + M_n)^2} \right]_{M_n + \delta/\epsilon}^1 \quad (51)$$

After substituting the limits and letting $\delta \rightarrow 0$, we obtain

$$I = \frac{2\pi q_0}{1 - M_n} \quad (52)$$

Our main result is obtained by noting that p' on the left of equation (45) is in fact p . We now replace q_0 by $p + M_n^2$. Using equation (52), equation (43) can now be written as

$$4\pi \left[1 - \frac{1}{2(1 - M_n)} \right] p = \frac{2\pi M_n^2}{1 - M_n} + I_\epsilon \quad (53)$$

Here I_ϵ denotes all the acoustic integrals with the surface integrals evaluated on $f = 0$ with a hole of the shape shown in figure 5. If we also allow the observer to approach the surface $f=0$ from inside, i.e., from the region where $f < 0$, then equation (53) becomes

$$4\pi \left[1 + \frac{1}{2(1 - M_n)} \right] p = -\frac{2\pi M_n^2}{1 - M_n} + I_\epsilon \quad (54)$$

Combining equation (53) and (54), we obtain

$$4\pi \left[1 - \frac{\text{sgn}(f)}{2(1 - M_n)} \right] p = \frac{2\pi \text{sgn}(f) M_n^2}{1 - M_n} + I_\epsilon \quad (55)$$

where $\text{sgn}(f)$ is the signum function defined as

$$\text{sgn}(f) = \begin{cases} 1 & f > 0 \\ -1 & f < 0 \end{cases} \quad (56)$$

Equation (55) is the aerodynamic integral equation in time domain and is the main result of this section.

Equation (55) is a singular integral equation which must be solved to find the unknown surface pressure p . It was derived for application to advanced high speed propellers where the use of thin blade sections allows linearization of the aerodynamic problem. There is little hope of obtaining a closed form analytic designs. However, numerical techniques such as the Galerkin or collocation methods are available. The arbitrary motion of the blades in the present formulation will allow the study of nonuniform in-flow to the propeller. The experience of Long in solving the subsonic integral equation² indicates that the matrices involved in the inversion process are well-behaved. This is another important advantage of using integral equations in the time domain as compared to those derived in the frequency domain. The integral equation (55) is under study at NASA Langley presently.

V. CONCLUDING REMARKS

In this paper, we have given the derivation of a formula for the prediction of the noise of high speed propellers. This formula was derived to overcome some of the problems with earlier formulations when the source speed is supersonic. These problems include appearance of singularities, length of execution time on a computer and inaccuracy of the predicted numerical results. It is claimed that the new acoustic formulation presented here overcomes all these problems when properly used in a computer program.

In the last part of this paper a new integral equation is derived by using the main acoustic result, equation (43), and moving the observer onto the blade surface. This integral equation can be used to find the blade surface pressure and this can in turn be used as input to the acoustic program for noise prediction. Work on the study of this integral equation is in progress at NASA Langley. The initial results indicate that this integral equation can provide a viable alternative to existing methods of prediction of aerodynamic loads on the propeller blades.

REFERENCES

1. F. Farassat and G. P. Succi: The Prediction of Helicopter Rotor Discrete Frequency Noise, Vertica, Vol. 7, No. 4, 1983, 309-320.
2. Lyle N. Long: The Compressible Aerodynamics of Rotating Blades Using an Acoustic Formulation, NASA TP-2197, December 1983.
3. J. E. Ffowcs Williams and D. L. Hawkings: Sound Generated by Turbulence and Surfaces in Arbitrary Motion", Phil. Trans. of Roy. Soc. Lond., A264, 1969, pp. 321-342.
4. F. Farassat: The Prediction of the Noise of Supersonic Propellers in Time Domain - New Theoretical Results, AIAA Paper 83-0743, April 1983.
5. F. Farassat: A New Aerodynamic Integral Equation Based on an Acoustic Formula in the Time Domain, Technical Note, AIAA Journal, 1984, pp. 1337-1340.
6. F. Farassat: Theory of Noise Generation from Moving Bodies with an Application to Helicopter Rotors, NASA TR-451, December 1975.
7. P. A. Nystrom and F. Farassat: A Numerical Technique for Calculation of the Noise of High-Speed Propellers with Advanced Blade Geometry, NASA TP-1662, July 1980.

LIST OF SYMBOLS

\vec{A}_i $i=1-4$	The 4-vector tangent to the surface $f=0$, see equation (10)
\vec{a}_i $i=1-4$	The natural 4-D base vectors in the coordinate system u^i , $i=1-4$. $\vec{A}_1 = (\vec{a}_1, 0)$, $\vec{A}_2 = (a_2, 0)$
\vec{a}_i $i=1,2$	The local natural base vectors in the blade surface coordinate system (u^1, u^2)
\vec{a}_i $i=1,2$	The local unit base vectors in the principal directions on the blade surface
\vec{B}, \vec{B}'	The 4-vectors defined by equation (17), components in 4-D denoted B^i and B'^i , respectively
\vec{b}	$= \lambda \vec{M}_t + \lambda_1 \vec{e}_1$; $b = \vec{b} $
b_v	$\vec{b} \cdot \vec{v}$
c	speed of sound
$f(\vec{y}, \tau)=0$; $f(\vec{x}, t)=0$	The equation of the blade surface in the frame fixed to the undisturbed medium
g	$= \tau - t + r/c$
$g_{(2)}, g_{(4)}$	The determinant of the coefficients of the first fundamental form in u^i , $i=1,2$ and u^i , $i=1-4$, respectively
$H(k)$	Heaviside function
H	The local mean curvature of the blade surface, $H = H(u^1, u^2)$
h_n	$= \lambda M_n + \lambda_1 \cos \theta$
$K(\vec{y}, \vec{x}, t)=0$	$= [k(\vec{y}, \tau)]_{ret}$
$k=0$	The equation of a surface whose intersection with $f=0$ produces a finite open piece of the blade surface by relations $f=0$, $k>0$.
l	(in dl) length variable along the trailing edge, along perimeter of airfoil section at blade inner radius or along shock traces on the blade
\vec{M}	Local Mach number vector based on c , $M_n = \vec{M} \cdot \vec{n}$, $M_t = \vec{M} \cdot \vec{r}$
\vec{M}_p	The projection of the local Mach number vector on the local plane normal to the edges (e.g., TE) of the blade surface, $M_p = \vec{M}_p $
\vec{M}_t	The projection of \vec{M} on the local tangent plane of the blade surface for fixed source time τ , $M_t = \vec{M}_t = v_t/c$
\vec{N}	The 4-D unit vector normal to $f(\vec{y}, \tau) = 0$ described by $(\vec{n}, -M_n)/a_n$
\vec{n}, n_1	Unit normal to $f=0$, τ -fixed
p'	Acoustic pressure (nondimensional)
$p_B(\vec{n}, \tau)$	$\equiv p(\vec{y}(\vec{n}, \tau), \tau)$ blade surface pressure described in a frame moving with the blades (nondimensional)
Q'_N, Q'_F	See equations (33a, 33b)
Q'_F, Q'_F, Q'_E	See equations (33c-e)
\vec{r}, r_1	$= \vec{x} - \vec{y}$, $r = \vec{x} - \vec{y} $
\vec{r}, \vec{r}_1	Unit radiation vector \vec{r}/r
\vec{r}_p	Unit vector in the direction of the projection of \vec{r} on the local plane normal to the edges (e.g., TE) of blade surface, τ -fixed
S	(in dS) element of blade surface area, τ -fixed
t	Observer time
\vec{t}_1	The projection of the unit radiation vector \vec{r} on the local tangent to $f=0$, τ -fixed. Not unit vector, $ \vec{t}_1 = \sin \theta$
u^i $i=1-4$	$= (u^1, u^2, ct, f)$ where (u^1, u^2) are the blade surface coordinate variables
v_n, v_t	Local normal and tangential velocity of $f = 0$
\vec{x}	Observer position
\vec{y}	Source position

GREEK SYMBOLS

σ	$= (1 + M_n^2)^{1/2}$
α^i $i=1,2$	The contravariant components of \vec{t}_1 with respect to the local base vectors (\vec{a}_1, \vec{a}_2)
α^i $i=1,2$	The components of \vec{M}_t with respect to the base vectors in the principal directions (\vec{a}_1, \vec{a}_2)
γ	(in $d\gamma$) length variable along the intersection of an edge of $f=0$ (e.g., TE) and the collapsing sphere $g=0$
Γ	(in $d\Gamma$) length variable of the arc of intersection of surfaces $f=0$ and $g=0$
∇_4	The 4-D gradient $(\nabla_y, 1/c \partial/\partial\tau)$, $\nabla_y = \partial/\partial y_i$
$\delta(f)$	The Dirac delta function
θ	The angle between \vec{n} and \vec{F}
$\bar{\eta}$	The Lagrangian coordinate of a point on the surface $f=0$, τ -fixed

Other symbols defined in text.

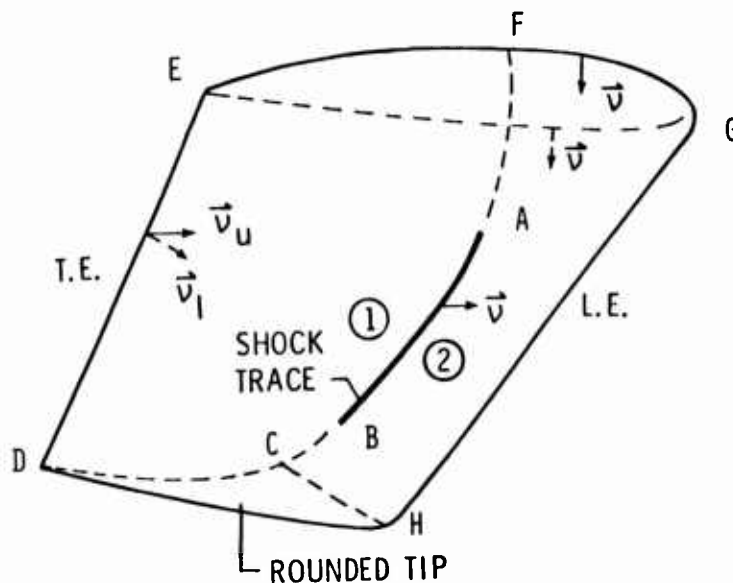


Figure 1.- The high speed portion of the propeller blade. The open surfaces forming this blade segment are shown.

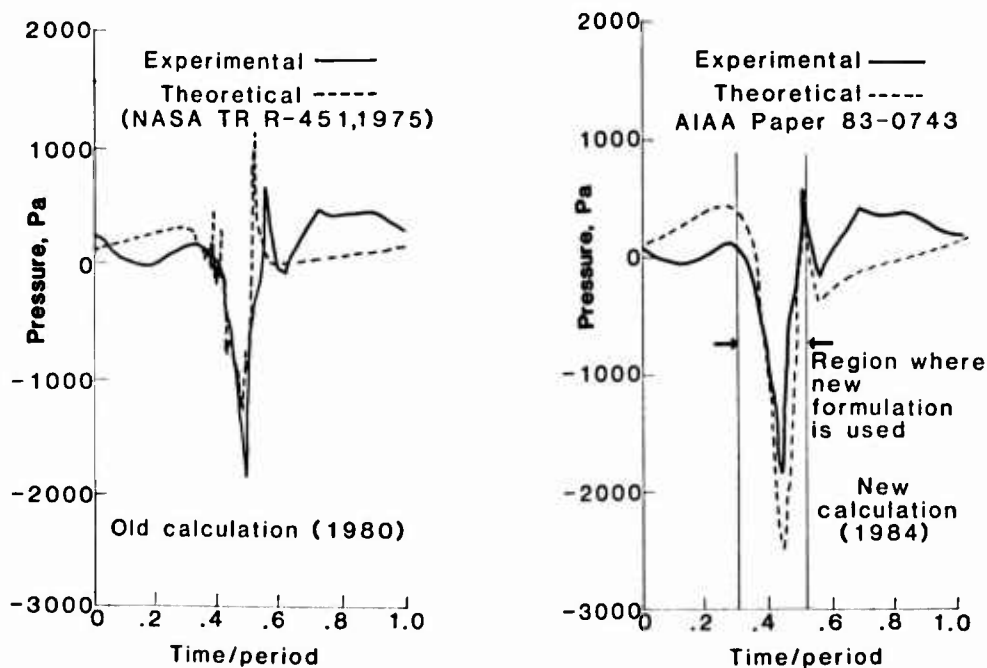


Figure 2.- Comparison of measured and predicted acoustic pressure signatures from the old (Formulation 1) and new (Formulations 1A and 3 (equation 43)) codes. See reference 7 for input data to acoustic program. The above figure corresponds to figure 14 of reference 7.

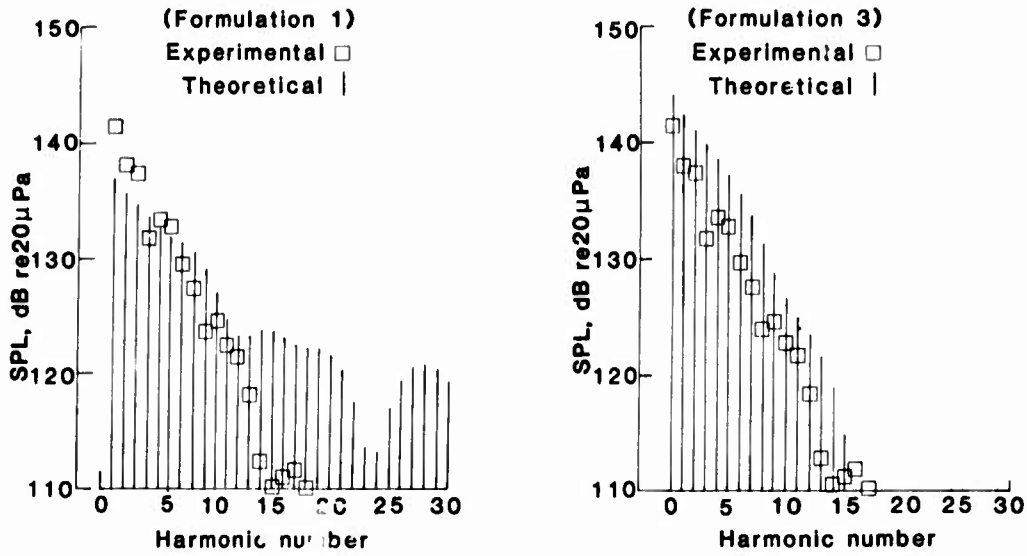


Figure 3.- Comparison of measured and predicted acoustic pressure spectra from the old and new code corresponding to figure 2 above.

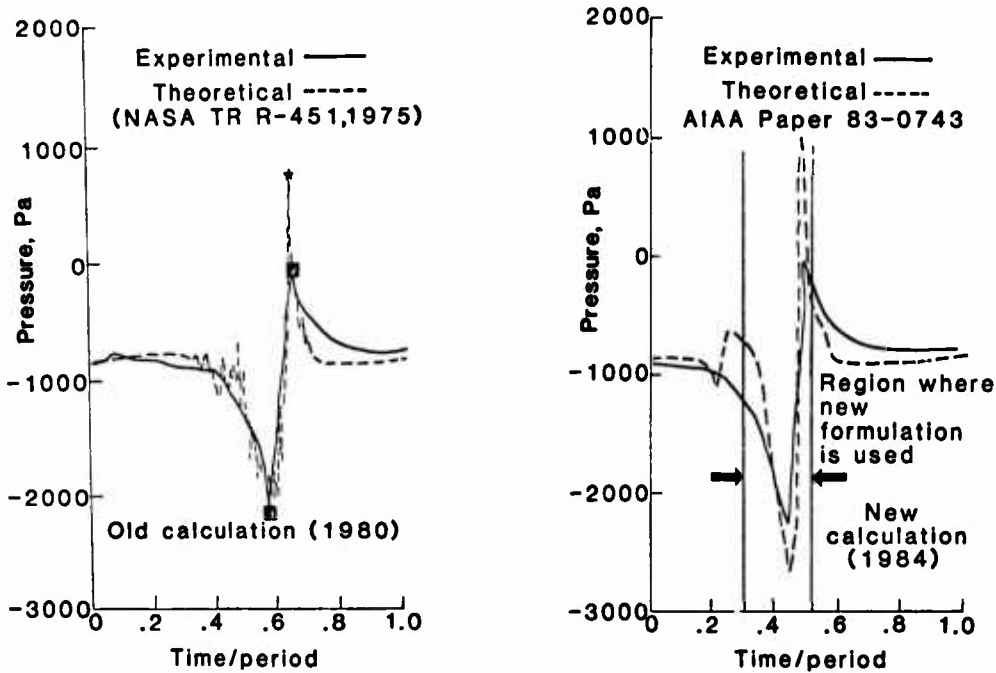


Figure 4.- Comparison of measured and predicted acoustic pressure signatures from the old and new codes. This figure corresponds to figure 12 of reference 7. See this reference for input data to acoustic code.

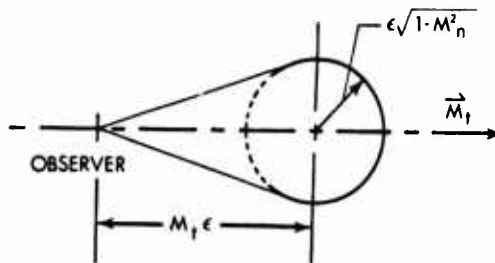


Figure 5.- The shape of the hole used in regularizing the divergent integral of equation (43) to obtain the aerodynamic integral equation.

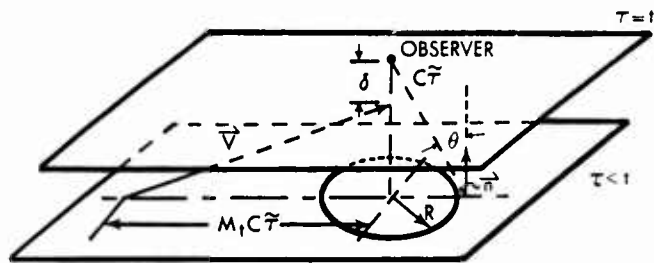


Figure 6.- The geometry of the intersection of the collapsing sphere with local tangent plane for the evaluation of the integral in equation (45).

A General Theory of Arbitrary Motion Aerodynamics
using an AeroAcoustic Approach

By

Lyle N. Long and George A. Watts
Lockheed California Company
Post Office Box 551
Burbank, California 91520

SUMMARY

This paper describes the theoretical aspects of a new unsteady aerodynamics method that uses time-domain aeroacoustic integral equations. Recent advances in theoretical aeroacoustics permit the development of general unsteady aerodynamics methods. The effects of thickness, compressibility, and arbitrary motions may be calculated for subsonic and supersonic flows. Most linearized unsteady aerodynamics methods today are limited to zero thickness effects and sinusoidal motion. The equations presented in this report will make it possible to develop computer codes for complex three-dimensional bodies, including not only complete aircraft configurations, but rotating propellers and helicopter blades as well. Panel methods for steady aerodynamics are widely used in the aircraft industry for such configurations, the present method should permit equally general configurations to be solved in unsteady motion, using a time-stepping procedure.

List of Symbols

c	Speed of sound
$f(\bar{x}, t)$	Function describing body surface (before linearization)
M	Mach number
M_n	Mach number in normal direction, $\bar{v} \cdot \hat{n} / c$
M_r	Mach number in radiation direction, $\bar{v} \cdot \hat{r} / c$
\hat{n}	Unit normal vector on body surface, $\nabla f / \nabla f $
\hat{n}_x	Unit normal vector evaluated at observer position, \bar{x} , i.e normal to the receiving surface
\hat{n}_y	Unit normal vector evaluated at source position, \bar{y} , i.e normal to the sending surface
p'	Pressure perturbation
P_{ij}	Compressive Stress Tensor
r	$ \bar{r} $
\bar{r}	Vector distance between source and observer, $\bar{x} - \bar{y}(\tau)$
\hat{r}	\bar{r} / r
t	Observer time
T_{ij}	Lighthill's Stress Tensor, $\rho u_i u_j + P_{ij} - c^2(\rho - \rho_0)\delta_{ij}$
\bar{u}	Fluid velocity
\bar{u}'	Fluid velocity perturbation
\bar{u}_1	Irrrotational component of velocity field
\bar{u}_2	Solenoidal (vortical) component of velocity field
u_n	$\bar{u}' \cdot \hat{n}$
\bar{v}	Velocity of body surface
v_n	$\bar{v} \cdot \hat{n}$
v_r	$\bar{v} \cdot \hat{r}$

\bar{x}	Observer location in frame fixed to undisturbed fluid
\bar{x}_0	Observer location for $\delta = 0$
$\bar{y}(\tau)$	Source location (in motion)
β^2	$1 - M^2$
β_n^2	$1 - M_n^2$
δ	Distance between observer and source (for ϵ - region)
$\delta(f)$	Dirac delta function
δ_{ij}	Kronecker delta
ϵ_1	One half the size of ϵ -region in y_1 direction
ϵ_2	One half the size of ϵ -region in y_2 direction
θ	$\arccos(\hat{n}_y \cdot \hat{r})$
ρ	Fluid density
ρ'	Fluid density perturbation, $\rho - \rho_0$
ρ_0	Density of undisturbed fluid
τ	$t - r/c$, Retarded time
$\bar{\omega}$	$\nabla \times \bar{u}'$, Vorticity

Subscripts:

ret expression is evaluated at retarded time, $\tau = t - r/c$

Notation :

sgn(a) $a/|a|$
 \oint Integration with a specific hole removed from surface of integration
 \square^2 Wave operator

[] Jump in quantity across body surface

INTRODUCTION

A renewed interest in propellers and helicopters, has fostered a reevaluation of aerodynamic methods for rotating blades. Advanced highly-swept blade geometries and high tip-speeds require fully three-dimensional aerodynamic methods. Classical lifting-surface methods are no longer adequate because they often assume a rectilinear mean velocity and harmonic motion for the perturbational velocity.

However, the very general aerodynamic methods required for rotating blades will also be of use in the development of aircraft. The present paper describes one such method based upon aeroacoustic integral equations. The method is a time-domain formulation, which is necessary for completely arbitrary motions. In addition, a time-domain formulation is a prerequisite to including nonlinear effects. This paper addresses mainly the linear aspects.

Certain aspects of propeller and aircraft dynamic behavior are often inadequately predicted during the design process. Some examples are : sub- or super-harmonic instabilities, limit cycle oscillations, single degree of freedom flutter, control system ineffectiveness, and battle-damage effects. The importance of predicting these effects increases when higher performance, lighter more flexible structures, and complex active control systems are used. Therefore, the designers tools must become more versatile and more accurate. The arbitrary motions aerodynamics method described herein responds to this challenge by permitting the calculation of time-accurate surface pressures on arbitrary bodies in arbitrary motions. In addition, because the

integral equations are derived from first principles, the proper role of the nonlinear aerodynamic terms is readily apparent.

The present paper describes the theoretical aspects of an arbitrary motions aerodynamics method. The major contributions of this paper are the presentation and discussion of the aeroacoustic equations. The paper also includes brief descriptions of the regularization of the singularity in the equations and an outline of a numerical solution procedure. Additional research in numerically solving the equations is under way. This work will be presented in the near future in another paper. Initially, the equations presented will be used to develop an arbitrary motion lifting surface method. Thickness effects will be included in the future, thus making the method the unsteady equivalent of the well-known panel methods currently used for steady aerodynamics.

Current unsteady aerodynamics methods become increasingly inaccurate as the reduced-frequency becomes large at Mach numbers approaching unity. In addition, these methods are often restricted to harmonic motions and the flutter speed must be determined through an iterative process. An arbitrary motions aerodynamics method will permit the direct calculation of flutter speeds. The method described in this paper will be valid for frequencies increasing without limit and the time stepping nature of the solution technique allows the treatment of systems with mechanical nonlinearities.

THE FLOWCS WILLIAMS-HAWKINGS EQUATION

The origin of the aeroacoustic approach can be traced to the Fflowcs Williams-Hawkings (FW-H) equation (Reference 1)

$$c^2 \square^2 (\rho - \rho_0) = \frac{\partial^2 T_{ij}}{\partial x_i \partial x_j} - \frac{\partial}{\partial x_i} (P_{ij} \frac{\partial f}{\partial x_i} \delta(f)) + \frac{\partial}{\partial t} (\rho_0 v_i \frac{\partial f}{\partial x_i} \delta(f)) \quad (1)$$

where :

$$\square^2 = \frac{1}{c^2} \frac{\partial^2}{\partial t^2} - \frac{\partial^2}{\partial x_i^2}$$

is the wave operator and :

$$T_{ij} = \rho u_i u_j + P_{ij} - c^2 (\rho - \rho_0)$$

is Lighthill's stress tensor. This equation is a combination of the complete nonlinear inhomogeneous conservation of mass and momentum equations. Generalized function theory is extremely useful in deriving the above equation. Reference 2 is a recent text on the subject and includes classroom lecture notes due to Farassat. It should also be pointed out that viscous effects are included in the compressive stress tensor, P_{ij} . The conservation equations are inhomogeneous because the fluid is assumed to occupy both the interior and exterior of arbitrary bodies. The inhomogeneous terms represent mass and momentum sources that will be used to satisfy the boundary conditions. The above equation is obtained by differentiating the inhomogeneous mass conservation equation with respect to t and the momentum conservation equation with respect to x_i . The latter is then subtracted from the former and rearranged such that only the wave operator is on the left-hand side. Writing the equations in this manner is referred to as the "acoustic analogy approach," which was pioneered by Lighthill (Reference 3). However, Lighthill was concerned with the noise due to turbulent jets in regions without solid surfaces and therefore neglected the last two terms in the above equation. Acousticians frequently use the above form of the equation to model aeroacoustic noise.

If the entire right hand side of the above equation were known, then one could presumably predict the radiated noise. However, these terms contain unknowns that must be determined before the noise can be predicted. Recently computational fluid dynamics methods have been used to predict Lighthill's stress tensor (Reference 4). In the past however, classical methods or experiments were used to determine the forcing functions, and then the above theory was used to predict the noise. A more appealing approach, especially for linear theory, is to use the above equations for both the aerodynamics and the acoustics. Both fields are governed by the above equation and recent research (Reference 5 and 6) has shown that this approach is possible. In addition, the nonlinear terms are included in the above equation. Therefore, if one wanted to include them in the aerodynamic and/or acoustic method, their proper roles are readily apparent.

Although the above equation is commonly referred to as the FW-H equation, there is a more general form that was not explicitly presented in the original paper. In equation

(1) the flow inside the body is assumed to be quiescent. For some applications, it may be useful not to make this assumption. The equation then becomes :

$$c^2 \square^2 (\rho - \rho_0) = \frac{\partial^2 T_{ij}}{\partial x_i \partial x_j} - \frac{\partial}{\partial x_i} [P_{ij} - \rho u_i (u_j - v_j)] \delta(f) \frac{\partial f}{\partial x_i} + \frac{\partial}{\partial t} [\rho (u_i - v_i)] \delta(f) \frac{\partial f}{\partial x_i}$$

where the brackets, [], indicate the jump in a flow quantity across the body surface. Of course, one should be careful not to infer too much from the above equation, it cannot contain as much information as the original four equations and four unknowns, as shown later on. The linearized, inviscid FW-H equation is :

$$\square^2 p' = - \frac{\partial}{\partial x_i} [p'] \delta(f) \frac{\partial f}{\partial x_i} + \frac{\partial}{\partial t} \rho_0 [u'_i] \delta(f) \frac{\partial f}{\partial x_i} \quad (2)$$

where : $p' = (\rho - \rho_0)/c^2 = \rho'/c^2$ and $[p'] = p'_2 - p'_1$, the jump in pressure across the surface, and $[u'_i]$ is the jump in the velocity across the surface. Again, the above equation does not assume quiescent flow inside the body. The primes denote perturbational quantities, and since only the linear equations will be discussed from here on, the primes will not be shown after this.

FARASSAT'S SOLUTIONS TO THE FW-H EQUATION

Farassat (Reference 7 and 8) has derived several useful integral equation versions of the previous equation using Green's functions. One of the most well-known is :

$$4\pi p(\bar{x}, t) = \frac{\partial}{\partial t} \iint_{\text{ret}} \left(\frac{\rho_0 c [u_n] + [p] \cos \theta}{c r |1 - M_r|} \right) dS + \iint_{\text{ret}} \left(\frac{[p] \cos \theta}{r^2 |1 - M_r|} \right) dS \quad (3)$$

where 'ret' signifies retarded time. That is, the integrands are evaluated at the emission time, $\tau = t - r/c$, instead of the reception time, t . Once again, this is not usually written explicitly with jump conditions. Instead, most researchers assume the internal flow to be quiescent, which yields :

$$4\pi p(\bar{x}, t) = \frac{\partial}{\partial t} \iint_{\text{ret}} \left(\frac{\rho_0 c v_n + p \cos \theta}{c r |1 - M_r|} \right) dS + \iint_{\text{ret}} \left(\frac{p \cos \theta}{r^2 |1 - M_r|} \right) dS \quad (4)$$

where now the p under the integral is the same as the p on the left hand side (when the singularity is properly accounted for) and the boundary condition $u_n = v_n$ has been applied.

The above equation is only one example of the integral form of the differential equation, other forms are available and should not be ruled out for practical applications. Reference 8 summarizes many of the existing integral equations for aeroacoustics. In particular, equations (15b) and (17b) of reference 8 are equivalent to equation (4) above, however, the integration is carried out over the intersection of the "collapsing" sphere and the body surface, instead of over the body surface in retarded time. Even though these other forms are sometimes difficult to use because one must determine these intersections, they may prove useful in certain aerodynamic applications. In addition, references 5 and 9 present equation (4) with the time derivative brought inside the integral.

Equation (4) appears to be very useful, since the pressure is the only unknown. The velocity is known from the boundary conditions. However, the above equation by itself is of limited utility for aerodynamics, since the internal flow has been specified and

there is no means of accounting for the wake development and consequently, there is no circulation or lift. This can be easily shown by letting the thickness of the body go to zero, which yields :

$$4\pi p(\bar{x}, t) = \frac{\partial}{\partial x_1} \iint_{ret} \left(\frac{[\rho] n_1}{r |1 - M_r|} \right) dS$$

which is one equation for two unknowns (p and $[\rho]$). And, there is no means of specifying the boundary conditions. This occurs because the pressure is uncoupled from the vortical part of the velocity field (in linearized theory). This can be shown using the well-known splitting theorem (Reference 10), where the velocity field is split into a solenoidal (vortical) and an irrotational part, i.e.

$$\bar{u} = \bar{u}_1 + \bar{u}_2 \quad \text{where} \quad \nabla \times \bar{u}_1 \equiv 0 \quad \text{and} \quad \nabla \cdot \bar{u}_2 \equiv 0$$

and it can be shown (Reference 10) that the homogeneous conservation laws become

$$\frac{1}{c^2} \frac{\partial p}{\partial t} + \rho_0 \nabla \cdot \bar{u}_1 = 0 \quad \rho_0 \frac{\partial \bar{u}_1}{\partial t} + \nabla p = 0 \quad \frac{\partial \bar{u}_2}{\partial t} = 0$$

which shows that the vortical velocity field is independent of the pressure (or acceleration potential) field. Only in nonlinear theory are the governing equations for the acoustic pressure coupled to the vortical or solenoidal velocity. Therefore, the vortical velocity can only be coupled to the pressure via the boundary conditions. This means that while specifying the boundary conditions in the FW-H equation does completely specify the thickness problem, it is not enough to solve the general lifting problem. Incidentally, in supersonic flows where the vortical field is unimportant (such as those with supersonic leading and trailing edges), the solution can be adequately represented by 'thickness' or irrotational terms. In this case equation (4) is a complete specification of the problem.

In a velocity potential formulation, such as those used in panel methods, one must distribute doublets over the body surface and the wake. Since the pressure jump across a wake is zero, one might assume that equation (4) is as general as the Green's theorem formulation of the velocity potential -- without requiring any integration over the wake. However, in the above formulation, the normalwash contributions are not included because they are due to the vortical velocity field. Therefore, the effects due to the wake (and consequently lift) are not included.

ARBITRARY MOTIONS AERODYNAMICS

Even though Equation (4) is not enough in itself to develop an arbitrary motions aerodynamics method, there are several options which will permit its use in such a method. One rather novel solution technique would be to use equation (3) to solve for the flow field in both regions simultaneously, i.e. inside and outside the body. A second technique might be to use the splitting theorem mentioned earlier. This would not change the operator on the pressure, but would effect the application of boundary conditions, since there would be another unknown (the normal component of the solenoidal velocity). This additional unknown would appear as another 'thickness' term in the integral equation (thickness is, of course, a misnomer in this case). However, in both of these approaches, one obtains more unknowns than equations. Thus one must use either the equations governing the internal flow or one of the conservation laws, in addition to the integral equation for the pressure.

As an aside, it should be pointed out that the method described in Reference 5 for predicting lift using equation (4) can be shown to be related to the two procedures just mentioned. However, instead of solving for the additional unknown that appears (i.e. the vortical velocity or the internal flow), these terms are approximated using a "conditioning" procedure. This conditioning was prompted by a recommendation of van Holten (Reference 11) that only the leading edge be placed at an angle of attack when using acceleration potential methods. The vortical component of the velocity would have such an effect, but it must be determined as part of the solution in a general prediction method. That is, even though this technique produced good results for uncambered, symmetrical blades and wings, it would be very difficult, if not impossible, to apply to arbitrary bodies.

The technique that will be described in this paper is an alternate approach, closely

related to classical unsteady aerodynamics methods, and utilizes the linearized conservation of momentum equation as the second equation. Its validity is easily demonstrated because of its relationship to well-known unsteady aerodynamics methods. The linearized inhomogeneous conservation of momentum equation is :

$$\rho_0 \frac{\partial \bar{u}}{\partial t} = -\nabla p + [\rho] \nabla f \delta(f) \quad (5)$$

which, for a field point off the surface is :

$$\rho_0 \frac{\partial \bar{u}}{\partial t} = -\nabla p$$

or

$$\rho_0 \bar{u}(\bar{x}, t) = - \int_{-\infty}^t \nabla p(\bar{x}, t') dt' \quad (6)$$

This equation can be combined with equation (4) to eliminate the pressure, p , thus giving an equation relating the fluid velocity, u , to the surface quantities: pressure jump, $[\rho]$ and normal velocity, v_n . The resulting equation describes the relation between an arbitrary surface loading and the downwash, unlike equation (4). Most importantly though, it accounts for the growth of a wake (which will simply be the body at previous times) and the generation of vorticity. Therefore, for a wing, the wake will lie in the plane directly behind the wing and for a propeller the wake will be formed by the helical path of the body.

In order to illustrate the origin of vorticity in the aeroacoustic approach, take the curl of equation (5) to get :

$$\rho_0 \frac{\partial \bar{\omega}}{\partial t} = \nabla f \times \nabla [\rho] \delta(f)$$

where :

$$\bar{\omega} = \nabla \times \bar{u}$$

which relates the rate of change of vorticity to the momentum sources on the surface. That is, vorticity is only generated at the surface. However, this vorticity must remain in its place of origin since there is no vorticity convection or diffusion included in these equations. Von Karman and Burgers presented similar relations for an incompressible fluid in Reference 12, where the fluid is assumed to have an arbitrary distribution of force. These forces, analogous to the source terms above, are the source of vorticity. Reference 12 also discusses (in different terminology) splitting the velocity of a perfect fluid into solenoidal and irrotational parts. The above relation also shows that for a constant pressure panel method, the vorticity is generated only at the panel edges, since the surface-pressure gradients are zero everywhere else. This is one illustration of how the method is related to the vortex lattice method.

Combining equations (4) and (6) gives :

$$4\pi\rho_0 \bar{u}(\bar{x}, t) = \nabla \iiint_S \left(\frac{\rho_0 c v_n + p \cos \theta}{c r |1 - M_r|} \right) dS_{ret} - \nabla \int_{-\infty}^t \iiint_S \left(\frac{p \cos \theta}{r^2 |1 - M_r|} \right) dS dt' \quad (7)$$

Applying the boundary condition,

$$u_n(\bar{x}, t) = v_n(\bar{x}, t)$$

gives

$$4\pi\rho_0 v_n(\bar{x}, t) = - \frac{\partial}{\partial n_x} \iiint_S \left(\frac{\rho_0 c v_n + p \cos \theta}{c r |1 - M_r|} \right) dS_{ret} - \frac{\partial}{\partial n_x} \int_{-\infty}^t \iiint_S \left(\frac{p \cos \theta}{r^2 |1 - M_r|} \right) dS dt' \quad (8)$$

where: \hat{n}_x is the surface normal at \bar{x} , the "observer" position (which is distinguished from \hat{n}_y the normal at \bar{y} , the "source" position). The above equation relates the time-history of the surface pressure and normal velocity of an arbitrary surface to the fluid velocity at a control point. Equation (8) was presented by Farassat in Reference 9, in a discussion of how the aeroacoustic equations relate to classical unsteady aerodynamics equations. It has not been proposed as the basis of an arbitrary motions

aerodynamics method before. Incidentally, once the surface pressure is known, equation (7) can be used to predict the velocity at any point in the flow field.

Notice that in this formulation the time history of the body's motion accounts for the wake effects of potential theory. The pressure jump is zero across a wake, but the effect from a pressure jump at that location (when the body was located there) lingers on after the body has moved. That is the pressure loading only exists for a certain amount of time, but after it is gone there remains a vortical velocity field. And as mentioned earlier, the governing equations for the pressure are decoupled from the vortical field, therefore only in the boundary and initial conditions can they be coupled. This effect accounts for the unsteady shedding of a vortex sheet in a very natural manner.

The above equations are unique in that thickness effects, compressibility, and arbitrary motions can be modeled by them. These equations should permit the development of unsteady aerodynamics methods that are very general compared to existing methods. Recent advances in computer technology and in theoretical aeroacoustics now permit very general methods to be developed. Of course the above equation must be regularized before it can be used in a numerical method, which means the singularity must be properly treated. The treatment of this singularity will be discussed in the next section.

If thickness effects are neglected, equation (8) becomes :

$$4\pi\rho_0 v_n(\bar{x}, t) = - \frac{\partial}{\partial n_x} \iiint_S \left(\frac{p \cos \theta}{c r |1 - M_r|} \right)_{ret} dS - \frac{\partial}{\partial n_x} \int_{-\infty}^t \iiint_S \left(\frac{p \cos \theta}{r^2 |1 - M_r|} \right)_{ret} dS dt'$$

which can be approximated by :

$$v_n(\bar{x}, t) = \frac{-1}{4\pi\rho_0} \frac{\partial}{\partial n_x} \int_{-\infty}^t \iiint_S \left(\frac{\beta^2 [p] \cos \theta}{r^2 |1 - M_r|^3} \right)_{ret} dS dt' \quad (9)$$

which is derived using a form of equation (4) with the time derivative taken inside the integral (see Reference 5) and assuming the acceleration of the body is small. The compactness of these equations is surprising considering their generality. Included within these equations is the incompressible, steady Biot-Savart law. They are valid for completely arbitrary motions at subsonic and supersonic speeds. Given the loading on a lifting surface anywhere in space and time the above equation will predict the velocity field due to that loading. Or inversely, which is how the above equation can be used, given the velocity of a body, the above equation will predict its time-accurate surface loading. The previous equation is closely related to those of Dat (Reference 13) and Kussner (Reference 14). Kussner, however, used a Lorentz transformation, which would only be useful for a body whose mean motion is rectilinear. The formulation of Kussner has formed the foundation of unsteady aerodynamics for many years. It is the basis for the kernel function approach (Reference 15) and the doublet lattice method (Reference 16), both of which assume a rectilinear mean motion and a harmonic perturbational velocity.

TREATING THE SINGULARITY

Of course the difficulty in using the above equations for aerodynamics is that they become singular unless treated properly. However, Reference 5 describes the appropriate regularization procedure for equations (3) and (4), which is analogous to the Cauchy principal value technique of Mangler (Reference 17). This same technique can be applied here to obtain the unsteady aerodynamic formulae. The proper approach is outlined below. The following analysis assumes subsonic motion and that the entire epsilon region is within the domain of influence of the control point. Since the regularization technique may vary with the numerical solution technique, the following is presented mainly to illustrate the procedure and the order of the principal value part.

In Reference 5, the surface integrals of equation (4) were broken into two regions, one around the singularity and one over the rest of the body as shown in Figure 1.

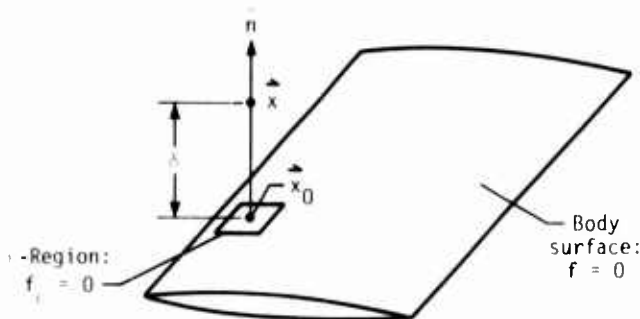


Figure 1.- ϵ -Region of Arbitrary Body

Assuming the pressure is constant over the "small epsilon" region, the integral can be evaluated analytically over this region. In reference 5, only the integration over a square was presented, since the final result was the same for square or rectangular regions. However, since the singularity will be of a higher order after taking the gradient shown in equation (7), this will no longer be true. Therefore, the integration will be performed over a rectangular region. Since this will have a relatively minor effect on analysis presented in Reference 5, only the final result will be presented here.

When the singularity is isolated within this rectangular region, equation (4) becomes :

$$4\pi p(\bar{x}_0, t) = \frac{\partial}{\partial t} \iint_{\text{ret}} \left(\frac{\rho_0 c v_n + p \cos \theta}{r |1 - M_r|} \right) dS + \iint_{\text{ret}} \left(\frac{p \cos \theta}{r^2 |1 - M_r|} \right) dS$$

$$+ \frac{2}{\beta_n^2} (\rho_0 v_n^2 + p) \lim_{\delta \rightarrow 0} \left[\text{sgn}(\eta_2) \tan^{-1} \left(\frac{|\eta_2| \beta_n \epsilon_2}{\delta \Gamma_2} \right) - \text{sgn}(\eta_1) \tan^{-1} \left(\frac{|\eta_1| \beta_n \epsilon_2}{\delta \Gamma_1} \right) \right]$$

$$+ \frac{2 M_n M_t}{\beta_n^2 \beta} (\rho_0 c^2 + p) \lim_{\delta \rightarrow 0} \left[\ln \left(\frac{\Gamma_2 + \beta_n \beta \epsilon_2}{\Gamma_1 + \beta_n \beta \epsilon_2} \right) - .5 \ln \left(\frac{\eta_2^2 + \beta^2 \delta^2}{\eta_1^2 + \beta^2 \delta^2} \right) \right]$$

where :

$$\Gamma_1 = \text{sqrt}(\eta_1^2 + \beta_n^2 \beta^2 \epsilon_2^2 + \beta^2 \delta^2)$$

$$\Gamma_2 = \text{sqrt}(\eta_2^2 + \beta_n^2 \beta^2 \epsilon_2^2 + \beta^2 \delta^2)$$

$$\eta_1 = -\beta_n^2 \epsilon_1 - M_n M_t \delta$$

$$\eta_2 = \beta_n^2 \epsilon_1 - M_n M_t \delta$$

and \iint indicates a region of the surface has been removed from the integral. In addition, this equation is valid only on the exterior of the body since it was assumed that $\delta > 0$ in the above. Consult Reference 5 to determine the correct signs for the interior values.

Now the above equation must be differentiated in the direction of the surface normal in order to use it in equation (8). For the epsilon region, the normal is

$$\hat{n}_x = (0, 0, 1).$$

Therefore,

$$\frac{\partial p}{\partial n_x} = \frac{\partial p}{\partial z} = \frac{\partial p}{\partial \delta}$$

Taking this derivative of the above equation and then taking the limit as the observer goes to the surface and substituting in equation (8) gives :

$$4\pi \rho_0 v_n(\bar{x}_0, t) = - \frac{\partial}{\partial n_x} \iint_S \left(\frac{\rho_0 c v_n + p \cos \theta}{c r |1 - M_r|} \right)_{ret} dS - \frac{\partial}{\partial n_x} \int_{-\infty}^t \iint_S \left(\frac{p \cos \theta}{r^2 |1 - M_r|} \right)_{ret} dS dt'$$

$$- \int_{-\infty}^t \frac{4 \theta}{\beta_n^4 \epsilon_1 \epsilon_2} (\rho_0 v_n^2 + p) dt'$$

$$+ \int_{-\infty}^t \frac{4 M_n^2 M_t^2 (\theta + \beta \epsilon_2)}{\beta_n^2 \epsilon_1 (\beta \epsilon_2 \theta + \beta^2 \epsilon_2^2 + \beta_n^2 \epsilon_1^2)} (\rho_0 c^2 + p) dt'$$

where :

$$\theta = \text{sqrt}(\beta^2 \epsilon_2^2 + \beta_n^2 \epsilon_1^2)$$

Incidentally, since this is linearized theory, the normal velocity, v_n , will always be small, (except near the leading edge where the theory is invalid). Therefore, the terms containing products of p and v_n and those with v_n squared could be neglected in a numerical scheme, which greatly simplifies the result. This inconsistency occurs because our differential equations were linearized but the boundary conditions were not. It is just more convenient to use the general expression $f(\bar{x}, t) = 0$ to describe the body.

The above equation is now amenable to numerical solution techniques. Unlike equation (4) which is an inhomogeneous Fredholm integral equation of the second kind, the above equation is a Volterra integral equation, which is typically more difficult to solve than the Fredholm equation.

NUMERICAL SCHEME

As mentioned earlier, the Lockheed-California Company is currently studying the most effective numerical schemes for solving the above equations. This section presents a brief sketch of how equation (9) is discretized. However, the procedure would also apply to equation (8), which includes thickness effects. In aerodynamic panel methods for steady flow, the surface of the body is approximated by a finite number of discrete panels. The dependent variable (usually velocity potential) is assumed to vary in some prescribed manner over each panel (e.g. constant, bilinear, etc.). This procedure could also be used for the equations described in this report. That is, the body could be approximated by panels of, say, constant pressure.

In addition, however, the pressure must be discretized as a function of time. For example, if the pressure distribution is assumed constant over a set of discrete emission time intervals, i.e.

$$[p(\bar{y}, \tau)] = \begin{pmatrix} [p(\bar{y})]^1 & 0 & \tau & \tau_1 \\ [p(\bar{y})]^2 & \tau_1 & \tau & \tau_2 \\ \vdots & & \vdots & \\ [p(\bar{y})]^{NT} & \tau_{NT-1} & \tau & \tau_{NT} \end{pmatrix}$$

then equation (9) could be written

$$v_n(\bar{x}, t)_1 = \sum_{k=1}^{NT} \frac{-1}{4\pi \rho_0} \frac{\partial}{\partial n_x} \int_{-\infty}^t \iint_S \left(\frac{\beta^2 [p]^k \cos \theta}{r^2 |1 - M_r|^3} \right)_{ret} dS dt'$$

where the superscript indicates emission time (not exponentiation) and where NT is the total number of time steps. Now for each emission time, the surface can be approximated by a finite number of constant pressure panels, giving :

$$v_n(\bar{x}, t)_i = \sum_{k=1}^{NT} \sum_{j=1}^{N_i} A_{ij}^k [p]_j^k$$

$$A_{ij}^k = \frac{-1}{4\pi \rho_o} \frac{\partial}{\partial n_x} \int_{-\infty}^t \int_S \left(\frac{\beta^2 \cos \theta}{r^2 |1 - M_r|^3} \right) dS dt'$$

and where NP is the total number of panels. Evaluating this at the control points (the centroid of each panel) gives a system of linear algebraic equations :

$$\begin{pmatrix} v_{n_i} \end{pmatrix} = \begin{bmatrix} A_{ij}^1 \end{bmatrix} \begin{pmatrix} [p]_j^1 \end{pmatrix} + \begin{bmatrix} A_{ij}^2 \end{bmatrix} \begin{pmatrix} [p]_j^2 \end{pmatrix} + \dots + \begin{bmatrix} A_{ij}^k \end{bmatrix} \begin{pmatrix} [p]_j^k \end{pmatrix}$$

rewriting gives :

$$\begin{pmatrix} [p]_j^k \end{pmatrix} = \begin{bmatrix} A_{ij}^k \end{bmatrix}^{-1} \left(\begin{pmatrix} v_{n_i} \end{pmatrix} - \begin{bmatrix} A_{ij}^1 \end{bmatrix} \begin{pmatrix} [p]_j^1 \end{pmatrix} - \begin{bmatrix} A_{ij}^2 \end{bmatrix} \begin{pmatrix} [p]_j^2 \end{pmatrix} - \dots \right) \quad (10)$$

Now, from causality, during the first time step only the first matrix will influence the solution, thus

$$\begin{pmatrix} [p]_j^1 \end{pmatrix} = \begin{bmatrix} A_{ij}^1 \end{bmatrix}^{-1} \begin{pmatrix} v_{n_i} \end{pmatrix}$$

which combined with an appropriate regularization procedure (as outlined above) will predict the pressure during the first time step. For subsequent time steps, equation (10) can be used, which contains only known information on the right hand side (i.e. the boundary condition and the pressure at previous time steps).

This is, of course, only an outline of a numerical scheme. It does not answer all the questions. For example, one must still determine the most appropriate variation of pressure over a panel. In fact, instead of prescribing some variation over the panel, one could assume the entire load exists along a line on each panel as in the doublet lattice method (Reference 16). Or one could concentrate the force at the centroid of each element as in Reference 18. This would be less accurate but would not require any quadrature.

Even though the numerical method is not described in detail, one can still make some general comments concerning the approach outlined above. First of all, the matrix of influence coefficients at the latest time step is the only one that must be inverted as shown in equation (10). In addition, this matrix will be either banded or diagonal due to the effect of the domain of influence. In effect, the pressure corresponding to the latest emission time has not propagated very far from its point of origin. Therefore, these panels will only influence themselves and, possibly, their immediate neighbors. This situation corresponds to piston theory (Reference 20), which is often used in unsteady aerodynamics. Piston theory gives a linear relation between the pressure and the velocity, i.e.

$$[p] = 2 \rho_o c v_n$$

If the latest matrix is a diagonal, and the effects from the panel edges do not effect the self-influence terms, then the elements of the matrix will be given exactly by this relation.

Another general comment corresponds to when the initial effects are relatively removed from the latest time step. The initial transients will then have a minor effect and in a numerical scheme could be ignored. Thus as the time-marching scheme progresses and the elements of the early matrices become small, they may be neglected. This is analogous to truncating the wake in steady panel methods. This will reduce the computer storage required by the program and means that a finite amount of computer storage will be required even for relatively large values of the observer time.

One final comment concerns the Kutta condition. The method described in this report is a time-accurate pressure or acceleration potential formulation and is based upon the linearized Euler equations. It is believed that this method will automatically satisfy the Kutta condition because vorticity is generated automatically, the wake is explicitly unloaded, and the initial conditions (or starting vortex) is included. The method is the compressible equivalent of an unsteady vortex lattice method that sheds vortex elements.

CONCLUSION

This paper describes a linearized, compressible, arbitrary motions aerodynamics method that uses aeroacoustic integral equations. The major contributions are the presentation and description of the equations and a treatment of the singular terms. The method is essentially a time-domain acceleration potential method. The majority of existing unsteady aerodynamics methods assume harmonic motion, which is inadequate to predict many preliminary design problems, as discussed in the introduction. A numerical scheme for solving the aeroacoustic equations using a time-stepping procedure is currently being investigated and will be described in a later paper.

This research represents the latest efforts by the Lockheed-California Company in the development of general arbitrary motions aerodynamics methods. Previous efforts have concentrated on incompressible methods, including pilot computer codes (Reference 21). This paper describes the theory for a subsonic and supersonic arbitrary motion aerodynamics method.

The aeroacoustic equations described above are valid at both subsonic and supersonic speeds, which makes the method even more useful. By solving the wave equation instead of the Prandtl-Glauert equation, the governing equation remains hyperbolic in both speed regimes. This is very important when one is solving flows that contain subsonic and supersonic regions, such as rotating blades with supersonic tip speeds. In addition, in subsonic steady flow one can ignore domain of influence effects, but in unsteady flow the domain of influence is important in both speed regimes.

Even though transonic and viscous effects are very important in aeroelasticity, it is believed that the method described will be useful because of its efficiency when compared to full non-linear methods. The aeroacoustic equations use the Green's function technique to convert the three-dimensional problem into a two-dimensional surface integration. Its role can be compared to that of steady aerodynamic panel methods. However, whereas most panel methods use linearized forms of the full-potential equation, the current method uses a linearized version of the Euler equations. Very sophisticated codes are currently available for solving the full-potential, Euler and Navier-Stokes equations, however, these codes are not yet efficient enough to be routinely used by designers of flight vehicles, especially to predict unsteady or arbitrary motion effects. Therefore, just as panel methods are heavily used for steady flows, especially for preliminary design, the method described in this report could be developed into a general arbitrary motion panel method and will be very useful for preliminary design.

REFERENCES

1. Ffowcs Williams, J.E. and Hawkins, D.L.: Sound Generation by Turbulence and Surfaces in Arbitrary Motion, Phil. Trans. Roy. Soc., London, Ser. A, [264], no. 1151, May 8, 1969, pp. 321-342. (also published in Aerodynamic Noise, AIAA Selected Reprint Series, Vol. XI, Ed. A. Goldburg, New York, July, 1970).
2. Kanwal, R.P.: Generalized Functions, Theory and Technique, Academic Press, New York, 1983.
3. Lighthill, M.J., On Sound Generated Aerodynamically. II. Turbulence as a Source of Sound, Proc. Roy. Soc., London, Ser. A, Vol. 222, no. 1148, Feb. 23, 1954, pp. 1-32.

4. Hardin, J.C. and Lankin, S.L.: AeroAcoustic Computation of Cylinder Wake Flow, AIAA J., Vol. 22, No. 1, Jan., 1984.
5. Long, L.N.: The Compressible Aerodynamics of Rotating Blades Based on an Acoustic Formulation, NASA TP-2197, Dec. 1983. (D.Sc. Dissertation from George Washington University).
6. Hanson, D.: Compressible Helicoidal Surface Theory for Propeller Aerodynamics and Noise," AIAA J., Vol.21, June, 1983, pp. 881-889.
7. Farassat, F.: Theory of Noise Generation from Moving Bodies with an Application to Helicopter Rotors, NASA TR R-451, 1975.
8. Farassat, F.: Linear Acoustic Formulas for Calculation of Rotating Blade Noise, AIAA J., vol.19, no. 9, Sept. 1981, pp. 1122-1130.
9. Farassat, F., Advanced Theoretical Treatment of Propeller Noise. Propeller Performance and Noise, VKI-LS 1982-08, Vol. I, Von Karman Institute for Fluid Dynamics, May, 1982.
10. Goldstein, M.E.: AeroAcoustics, McGraw-Hill, San Fransisco, 1976.
11. van Holten, Th.: The Computation of Aerodynamic Loads on Helicopter Blades in Forward Flight, Using the Method of Acceleration Potential, Rep. VTH-189, Tech. Hogeschool Delft Vliegtuigbouwkunde, Mar., 1975.
12. von Karman, Th. and Burgers, J.M.: General Aerodynamic Theory - Perfect Fluids, Vol. II, Division E, in Aerodynamic Theory Edited by W. F. Durand, Peter Smith Pub., Mass., 1976.
13. Dat, R.: Lifting Surface Theory Applied to Fixed Wings and Propellers, ESRO-TT-90, 1973.
14. Kussner, H.G.: General Airfoil Theory, NACA TM 979, June, 1941 (translation of: Luftfahrtforschung, Vol. 17, No. 11/12, Dec. 10, 1940, Verlag von R. Oldenburg, Munchen und Berlin).
15. Watkins, C.E., Woolston, D.S., and Cunningham, H.J.: A Systematic Kernel Function Procedure for Determining Aerodynamic Forces on Oscillating or Steady Wings at Subsonic Speeds, NACA TR R-48, 1959.
16. Albano, E. and Rodden, W.P.: A Doublet-Lattice Method for Calculating Lift Distributions on Oscillating Surfaces in Subsonic Flows, AIAA J., Vol. 7, No. 2, Feb., 1969, pp. 279-285. Also, Errata, AIAA J., Vol. 7, No. 11, Nov., 1969, p. 2192.
17. Mangler, K.W.: Improper Integrals in Theoretical Aerodynamics, Rep. No. 2424, British R.A.E., June, 1951.
18. Dowell, E.H., Curtiss, H.C., Scanlon, R.H., Sisto, F.: A Modern Course in AeroElasticity, Sijthoff and Noordhoff, Alphen aan den Rijn, The Netherlands, 1978.
19. Ueda, T. and Dowell, E.H.: A New Solution Method for Lifting Surfaces in Subsonic Flow, AIAA J., Vol. 20, No. 3, Mar., 1982.
20. Ashley, H. and Zartarian, G.: Piston Theory - A New Aerodynamic Tool for the AeroElastician, J. of the Aeronautical Sciences, Vol. 23, Dec., 1956, pp. 1109-1118.
21. Hassig, H.J.: Unsteady Aerodynamics for Active Control - Independent Research 1979 Year-End Report, Lockheed Report, LR 29279, May 30, 1980.

SUMMARY OF RECENT NASA PROPELLER RESEARCH

Daniel C. Mikkelson, Glenn A. Mitchell, and Lawrence J. Bober
National Aeronautics and Space Administration
Lewis Research Center
Cleveland, Ohio 44135

SUMMARY

Advanced high-speed propellers offer large performance improvements for aircraft that cruise in the Mach 0.7 to 0.8 speed regime. At these speeds, studies indicate that there is a 15 to near 40 percent block fuel savings and associated operating cost benefits for advanced turboprops compared to equivalent technology turbofan powered aircraft. The current status of the NASA research program on high-speed propeller aerodynamics, acoustics, and aeroelastics is described. Recent wind tunnel results for five eight- to ten-blade advanced models are compared with analytical predictions. Test results show that blade sweep was important in achieving net efficiencies near 80 percent at Mach 0.8 and reducing near-field cruise noise by about 6 dB. Lifting line and lifting surface aerodynamic analysis codes are under development and some results are compared with propeller force and probe data. Also, analytical predictions are compared with some initial laser velocimeter measurements of the flow field velocities of an eight-bladed 45° swept propeller. Experimental aeroelastic results indicate that cascade effects and blade sweep strongly affect propeller aeroelastic characteristics. Comparisons of propeller near-field noise data with linear acoustic theory indicate that the theory adequately predicts near-field noise for subsonic tip speeds but overpredicts the noise for supersonic tip speeds. A study of advanced counter-rotation turboprops indicates that there may be about a 9 percent additional block fuel savings compared to a single rotation systems at Mach 0.8.

LIST OF SYMBOLS

A	noise amplitude
C_p	power coefficient = $P/\rho_o n^3 D^5$
CR	counter rotation
D	blade tip diameter, cm (in)
dB	decibel
$dC_p/d(r/R)$	elemental power coefficient $C_p = \int [dC_p/d(r/R)]d(r/R)$
FPS	velocity in units of feet per second
J	advanced ratio, V_o/nD
M	Mach number
MPS	velocity in units of meters per second
M_l	local Mach number
M_o	free-stream Mach number
n	rotational speed, rpm
P	power, kW (ft-lb/sec)
R	blade tip radius, cm (in)
RPM	rotational speed, rpm
r	radius, cm (in)
SHP	shaft power, kW (hp)
SR	single rotation
T	thrust, N (lbf)
V_o	free-stream velocity, m/sec (ft/sec)
x	axial distance, cm (in)
$\beta_{3/4}$	propeller blade angle at 0.75 radius
η	efficiency = $(T \cdot V_o)P$
η_i	ideal efficiency = $(T_{ideal} \cdot V_o)P$
ρ_o	free-stream density, kg/m^3 (slugs/ft ³)
ϕ	phase angle
θ	ratio of total temperature to standard sea-level temperature of 518.7° R

INTRODUCTION

The free air propeller offers the potential of very high propulsive efficiencies for subsonic aircraft. This key propulsion component has been the object of many NACA/NASA research programs conducted throughout the history of the agency. From 1927 to about the mid 1950's NACA had an extensive propeller research effort. This research led

to many successful propeller powered aircraft with cruise speeds as high as Mach 0.6. From the mid 1950's to the mid 1970's there was about a 20-year hiatus in propeller research due to the success of turbojet and turbofan propulsion systems. These systems offered efficient flight at speeds from Mach 0.6 to 0.85 and cruise altitudes above most of the weather. The lower propulsive efficiencies of these systems compared to the early turboprops hardly mattered when the fuel costs were so low (near 10 cents per gallon). However, the world energy crisis of 1973 and 1974 changed all that and NASA began an initial modest effort to evaluate the need for a high-speed propeller research program. Both in-house and contractor studies indicated that at cruise speeds as high as Mach 0.8 an advanced high-speed turboprop powered aircraft would have a large performance advantage over an equivalent technology high bypass ratio turbofan. This superior performance could result in large block fuel savings, reduced life cycle costs, improved range, or other benefits for both future civil and military aircraft. To investigate these advantages a high-speed propeller research program was established at the NASA Lewis Research Center in 1976. This program has grown to encompass both experimental and analytical work into the aerodynamics, acoustics, and aeroelastics of advanced high-speed propellers. In the past, most of the research effort was directed toward developing advanced single-rotation propellers. More recently, however, the research work has been expanded to include advanced counter-rotation propellers which offer even higher performance potential. A possible future application of the technology from this program is illustrated by the photograph of Fig. 1 showing an advanced counter-rotation turboprop powered aircraft.

THEORETICAL ADVANTAGES OF TURBOPROPS

Propeller propulsion has some rather large efficiency advantages over more highly loaded propulsion systems. This can be shown by using simple momentum disk theory. Ideal propulsive efficiency is shown in Fig. 2 as a function of fan pressure ratio which is analogous to the commonly used propeller power loading (shaft horsepower divided by propeller diameter squared). These curves were derived for flight Mach numbers from 0.1 to 0.8 using simple momentum theory and represent only the losses associated with the acceleration of the fluid in the axial direction. The calculations assumed an adiabatic fan efficiency of 1.0 and included no viscous losses. The ranges in fan pressure ratio typical for each type of propulsor are indicated. Conventional low speed propellers generally are lightly loaded with fan pressure ratios up to about 1.03. Advanced propellers require more power to fly at higher speeds. Also, because of the low air density at the higher cruise altitudes, a higher power loading is required to keep the propeller diameter to a reasonable size. Fan pressure ratios for the higher-loaded advanced propellers will range from about 1.03 for single-rotation propellers of moderate loading to 1.10 for some of the more ambitious counter-rotation propeller designs. High bypass ratio turbofans are even more highly loaded with fan pressure ratios generally greater than 1.3.

The design point established for some initial advanced single-rotation turboprop engines included a power loading of 301 kW/m^2 (37.5 hp/ft^2) at 243.8 m/sec (800 ft/sec) tip speed and 10.668 km (35 000 ft) altitude. These conditions resulted in a design integrated fan pressure ratio of 1.047. The equivalent power loading of 301 kW/m^2 (37.5 hp/ft^2) is about three times the loading used on previous conventional propeller aircraft such as the Lockheed Electra/P-3. A typical advanced turbofan of comparable technology is projected to have a fan pressure ratio of about 1.6. Therefore (from Fig. 2) the ideal efficiency for the advanced turboprop at Mach 0.8 cruise would be 97 percent, while that for the comparable turbofan would be 80 percent. Thus, the turboprop exhibits an inherent 17 percent advantage. As seen in Fig. 2 this ideal advantage would be larger at lower flight speeds.

The simple momentum theory, however, does not account for the residual swirl loss in the wake of single-rotation propellers. This swirl is a loss that is unique to such propellers since it is not recovered by stators, as it would be in a fan engine or by a second rotor as it would be in a counter-rotation propeller. Therefore, the ideal propeller efficiency shown in Fig. 2 has to be corrected for this loss. The swirl loss is shown in Fig. 3 by comparing the basic axial momentum loss with the total induced loss for a configuration with an infinite number of blades. This loss is shown in Fig. 3 in terms of ideal propeller efficiency as a function of power loading. At the selected initial design power loading of 301 kW/m^2 (37.5 hp/ft^2) the swirl represents about a 7 percent performance penalty. However, it should be possible to eliminate this penalty if counter-rotation propellers are considered. This more mechanically complex approach is being investigated as an alternative propulsion concept in the NASA Advanced Turboprop Project (ATP) and will be discussed later in this paper.

A further efficiency correction for single-rotation propellers is the tip loss for a finite number of blades. Figure 3 shows that tip losses increase dramatically as the number of blades is reduced. At the higher power loadings the tip losses with two or four blades are excessive. With an eight blade propeller the tip losses are tolerable. For any number of blades, propeller efficiency increases as power loading is decreased. But such an increase in aerodynamic efficiency would require larger propeller diameters and thereby increase blade and gearbox weight. These considerations resulted in initial single-rotation propeller designs having eight blades and a power loading of 301 kW/m^2 (37.5 hp/ft^2). The tip loss for this design point is nearly 5 percent and the total loss (swirl and tip) above the axial momentum loss is about 12 percent. However, even with these two additional penalties, it is evident from Figs. 2 and 3 that the highly loaded single-rotation (SR) turboprop at Mach 0.8 still shows a significantly higher ideal efficiency than the high fan pressure ratio turbofan (85 percent versus 80 percent). As

is shown in the next section of this paper, this efficiency advantage for the turboprop would be even larger when comparisons include installed losses.

ADVANCED TURBOPROP POTENTIAL

A comparison of the installed cruise efficiency of turboprop-powered and turbofan-powered propulsive systems is shown in Fig. 4 over a range of cruise speeds. The efficiencies shown in the figure include the installation losses for both systems; namely, nacelle drag for the turboprop systems, and cowl drag and internal airflow losses for the fan stream of the turbofan systems. Conventional low speed turboprops have installed efficiency levels near 80 percent up to about Mach 0.5 but suffer from rapid decreases in efficiency above this speed due to increasing propeller compressibility losses. These losses are primarily the result of relatively thick blades operating at high helical tip Mach numbers.

The advanced high-speed turboprop has the potential to delay these compressibility losses to a much higher cruise speed and achieve a relatively high performance to at least Mach 0.8 cruise. Although high bypass ratio turbofans exhibit their highest efficiency at cruise speeds near Mach 0.8, their performance would still be significantly below that of the advanced turboprops. At Mach 0.8 the installed efficiency of turbofan systems would be approximately 63 percent compared to about 77 percent for the advanced single-rotation (SR) turboprop. Advanced counter-rotation (CR) high speed turboprops that recover the swirl losses would have an installed efficiency about 5 to 10 percent higher. At lower cruise speeds, the efficiency advantage of the advanced turboprop systems would be even larger.

A number of studies have been conducted by both NASA and industry to evaluate the potential of advanced high-speed turboprop propulsion for both civil and military applications. Numerous references to specific studies and summary results are listed in Ref. 1. The trip fuel savings trend shown in Fig. 5 plotted versus operating range is a summary of these studies. Installed efficiency levels similar to those shown in Fig. 4 for comparable technology advanced turboprops and turbofans were used in most of these studies. As shown in Fig. 5, trip fuel savings is dependent on aircraft cruise speed and range. At the bottom of the band, associated with Mach 0.8 cruise, fuel savings range from about 15 to 30 percent for advanced turboprop aircraft compared to equivalent technology turbofan aircraft. The larger fuel savings occur at the shorter operating ranges where the mission is climb and descent dominated. Because of the lower operating speeds encountered during climb and descent, turboprops have an even larger performance advantage than the advantage at Mach 0.8 cruise conditions. In a similar manner, a larger fuel savings is possible at Mach 0.7 cruise (represented by the top of the band in Fig. 5). At this lower cruise speed, fuel savings range from 25 percent to near 40 percent. Even larger fuel savings are possible by recovering the propeller swirl loss from these single-rotation turboprops. Counter-rotation is one promising concept for recovering swirl loss that is currently under investigation as part of the NASA Advanced Turboprop Project (ATP). Some results derived from a study of counter-rotation (Ref. 2) are shown in Fig. 5 for a 1300 nmi, Mach 0.8 counter-rotation turboprop aircraft. The gains in fuel savings over a single-rotation (SR) turboprop are of the same magnitude as the gains realized by reducing cruise speed from Mach 0.8 to Mach 0.7. This additional fuel savings gain projected for counter-rotation is about 8 to 10 percent.

ADVANCED DESIGN CONCEPTS

A model of an advanced high-speed SR turboprop propulsion system is shown in Fig. 6. The advanced propeller would be powered by a modern turboshaft engine and gear box to provide the maximum power to the propeller with a minimum engine fuel consumption. Propeller efficiency would be kept high by minimizing or eliminating compressibility losses. This would be accomplished by utilizing thin swept blades that would be integrally designed with an area ruled spinner and nacelle. Blade sweep would also be used to reduce noise during both take-off/landing and during high-speed cruise flight (Refs. 1, 3, and 4). Aircraft operations at high altitudes and Mach 0.6 to 0.8 requires much higher power than used on current propeller aircraft. A power loading about three to four times higher than existing technology low-speed turboprops would be needed to minimize propeller diameter and weight. Eight or ten blades are required to increased ideal efficiency at these higher disk loadings. In addition to these advanced concepts, a modern blade fabrication technique is needed to construct the thin, highly swept and twisted blades.

Since all of the advanced concepts used to minimize compressibility losses are interrelated, an integrated procedure is used to design high-speed propellers and nacelles (Refs. 1 and 5). The effects of applying these advanced concepts to a propeller design are shown in Fig. 7. This figure is based on a cruise condition of Mach 0.8 and shows the propeller blade Mach number as it varies from hub to tip. The Mach number at each radial location is called the section Mach number and is the vector sum of the axial and rotational components. Curve A represents the Mach number distribution encountered by the propeller operating in an unsuppressed flow field where the axial component is the free-stream Mach number. At the hub the section Mach number is slightly higher than the cruise speed of Mach 0.8. As the rotational velocity component becomes larger at increased radius, the relative Mach number increases until it reaches Mach 1.14 at the blade tip. This Mach number must be compared to the drag rise (or drag divergence) Mach number of each blade airfoil section to evaluate the propeller performance potential. The predicted drag rise Mach number (Fig. 7, curve B) was obtained from isolated two-

dimensional airfoil data for a high-speed propeller having thickness-to-chord ratios of about 15 percent at the hub and 2 percent at the blade tip. Across the entire radius the section Mach number (curve A) is higher than the drag rise Mach number (curve B). This represents a potentially large compressibility loss.

The advanced aerodynamic concepts of thin swept blades and an area ruled spinner and integrated nacelle design are effective in minimizing or eliminating these losses. In the outer portions of the propeller, the thin blades are swept to reduce the component of velocity normal to the blade airfoil section, similar to swept wing theory. With a sufficient amount of sweep the section Mach number (curve A) can be reduced to an effective Mach number (curve C) that is below the drag rise Mach number (curve B) in the outer portions of the blade. This procedure significantly reduces the compressibility losses in the blade tip region and can also be effective in reducing noise. In the hub region, the spinner-nacelle body is tailored to increase the effective nacelle blockage behind the propeller and reduce the local Mach number through the propeller plane. This effect is shown by the local surface Mach number distribution plotted for the spinner-nacelle body in Fig. 7 (without blade blockage effects) and the resulting effective section Mach number of curve D. Near the hub the effective section Mach number is suppressed far below the drag rise Mach number. With a large number of blades (8 in this example), the hub blade sections operate as a cascade and the additional Mach number suppression is necessary to prevent blade-to-blade choking. Area ruling the spinner between the blades gives further relief from choking by opening the flow area between the blades at the spinner.

In addition to maximizing the aerodynamic performance of the advanced turboprop, techniques for minimizing the near-field source noise during cruise operation have been developed to keep interior noise levels competitive with current wide body aircraft and to minimize the need for fuselage acoustic treatment. Since the blade relative tip Mach numbers are slightly supersonic as shown in Fig. 7 ($M_{Tip} \sim 1.14$) the initial approach for noise reduction was to add sweep and reduce the effective local section Mach number to below the section critical Mach number. The shock strength and, therefore, the resulting pressure pulse is thereby reduced. The initial blade designs with 30° tip sweep were expected to be somewhat quieter for this reason. A more advanced concept was incorporated in a 45° tip sweep design using the linear acoustic analysis of Ref. 6. A historical development of the application of acoustic theory to advanced propeller design is given in Ref. 7. The present theory predicts thickness (due to blade airfoil thickness distribution) and loading (due to pressure loads on the blade airfoil) noise components from each radial section of the blade. Thickness noise is generally the dominant noise source on a propeller operating with a slightly supersonic tip Mach number. By properly sweeping and stacking the blade it is possible to reduce near-field noise using the phase interference concept illustrated in Fig. 8. The noise from one propeller blade is the vector sum of the contributions of the sinusoidal wave (amplitude and phase angle) from each radial strip. The noise of the total propeller is the product of the vector sum and the number of blades. Sweeping the tip back causes its signal to lag the signal from the mid-blade region. This increase in phase angle causes partial interference and a reduction in noise. This phase interference concept was used in the acoustic design of the 45° swept propeller model (SR-3, Fig. 9) to reduce the near-field cruise noise. This concept should have application to both thickness and loading noise in the near and far fields.

PROPELLER MODEL DESIGNS

In a cooperative program between NASA Lewis Research Center and Hamilton Standard the concepts described above were used to design a series of propeller models for wind tunnel testing. The basic blade planforms pictured in Fig. 9 represent five propeller designs that have been wind tunnel tested. All of the propellers shown in the figure except the fourth one (SR-6) were designed by Hamilton Standard. The SR-6 was aerodynamically designed at the Lewis Research Center. The first three propellers shown in the figure (SR-2, SR-1M, and SR-3) have a blade tip speed of 244 m/sec (800 ft/sec), a cruise power loading of 301 kW/m² (37.5 hp/ft²) at Mach 0.8 and 10.668 km (35 000 ft), and eight blades. The last two propellers shown are ten-bladed models. The SR-6 has a design blade tip speed of 213 m/sec (700 ft/sec), and a cruise power loading of 241 kW/m² (30 hp/ft²); and the SR-5 has a design blade tip speed of 183 m/sec (600 ft/sec) and a cruise power loading of 209 kW/m² (26 hp/ft²). The blade planforms are identified by tip sweeps of 0°, 30°, 45°, 40°, and 60°. Here the tip sweep is approximately the angle between the blade mid-chord line at the tip of the blade and a radial line intersecting this line at the tip.

The straight blade and an initial 30° swept blade (not shown) were designed using established analyses (Ref. 8) that lack a refined methodology to design the twist of a swept blade. Tests of the initial 30° swept design indicated a retwist was required (which was actually a redistribution of the blade load from hub to tip). That became the modified 30° swept design shown in Fig. 9 (SR-1M). The 45° and 60° swept blades (SR-3 and SR-5) were designed for acoustic suppression as well as improved aerodynamic performance by tailoring the sweep and planform shape as described in Ref. 9. The Lewis propeller design (SR-6) was based on a different design philosophy, wherein the cruise design conditions were changed from those used for the first three propellers in order to increase predicted performance and lower noise. The design tip speed of this propeller was lowered to help reduce noise. The predicted performance lost by the lower tip speed was regained and possibly increased slightly by increasing the number of blades to 10 and lowering the power loading to 241 kW/m² (30 hp/ft²). The technique of lowering tip speed and power loading was also used with the SR-5 design. Its design point was

chosen to further reduce noise and obtain about the same predicted performance level as the eight-bladed models. More detailed discussions of the aero/acoustic design methodology represented by the SR-3 and SR-5 designs are presented in Refs. 6, 7, and 10.

The noise levels that were predicted at the time these blades were designed are listed in Fig. 9. The cruise noise predictions indicated a small reduction for 30° of sweep, a significant reduction for the aero/acoustic 45° swept design and the 40° ten-bladed design and a very large reduction for the 60° ten-bladed design.

Each photograph in Fig. 10 shows one of the five propeller models that was installed on the Propeller Test Rig (PTR) in the NASA Lewis 8- by 6-Foot Wind Tunnel. The tunnel (Ref. 11) has a porous wall test section to minimize any wall interactions. The PTR is powered by a 746 kW (1000 hp) air turbine using a continuous flow 3.1×10^6 N/m² (450 psi) air system routed through the support strut. Axial force and torque on the propeller are measured on a rotating balance located inside of an axisymmetric nacelle behind the propeller (Ref. 9). The propeller diameters range from 0.622 m (24.5 in) to 0.696 m (27.4 in).

PROPELLER AERODYNAMIC RESEARCH

Experimental Research

Experimental wind tunnel test results obtained with the eight-bladed propellers (Refs. 1, 5, 9, and 12) are summarized in Fig. 11. The net efficiencies of the 0°, 30°, and 45° swept blade designs are shown for Mach numbers from 0.6 to 0.85. Because the power coefficient and advance ratio are constant in this figure, the ideal efficiency is also constant as is shown by the upper dashed line. The ideal efficiency represents the performance of an optimally loaded propeller with no blade drag. The difference in Fig. 11 between the ideal efficiency line and the experimental performance curves represents viscous and compressibility losses, possible hub choking losses, and losses associated with a nonoptimum radial loading distribution. As the data curves show, those losses increase at the higher speeds due to increasing compressibility losses. However, the performance of the 45° swept blade decreased a smaller amount with increasing speed than the performance of propellers with less sweep. The 45° swept blade achieved a 3 percent performance gain over the straight blade design at Mach 0.8 and about a 4 percent gain at Mach 0.85. At the lower speeds of Mach 0.6 to 0.7 both swept blades had approximately a 2 to 3 percent efficiency advantage over the straight blade and the highest performing design had an efficiency that exceeded 81 percent. At speeds near Mach 0.6 the straight blade design may not have had an optimum twist distribution. Unpublished data with an identical blade shape constructed from graphite rather than steel (that apparently deflected to a more optimum twist distribution) had a net efficiency near the 45° swept design at Mach 0.6. The study level (shown on Fig. 11) of 79.5 percent efficiency at Mach 0.8 was the value used in projecting the large fuel efficiency and operating cost advantages of an advanced turboprop over an equivalent technology turboprop powered aircraft. The 45° swept propeller at this speed had an efficiency of 78.7 percent which was close to this study level.

By operating the eight-bladed 45° swept propeller at off design lower power loadings, higher efficiencies can be obtained at Mach 0.8. This is shown in Fig. 12 where net efficiency is plotted against advance ratio for several levels of power loading. The typical variation of efficiency with advance ratio at a constant power loading (i.e., constant C_p/J^3) is a peaked curve. The reduction from the peak with increasing advance ratio is due to (1) a combination of lower ideal efficiencies due to increased swirl and tip losses and (2) lower blade sectional lift to drag ratios (from increasing local angles-of-attack). The fall-off with decreasing advance ratio is due to increased compressibility losses associated with the higher tip rotational speeds and/or again lower blade section lift to drag ratios (from decreasing local angles-of-attack). The circle symbol in Fig. 12 represents the eight-bladed 45° swept propeller design point. The square symbol on the 80 percent power loading curve shows the design power loading and advance ratio of the ten-bladed 40° swept propeller (SR-6). The effect of operating the eight-bladed 45° swept propeller at this reduced power loading and increased advance ratio (3.06 to 3.5) was to increase efficiency about 0.3 percent. This reduced power loading would result in a 12 percent larger propeller diameter in an actual aircraft installation where power requirements are fixed. The eight-bladed 45° swept propeller obtained an efficiency of 79.7 percent at 80 percent power loading and 3.3 advance ratio and an efficiency slightly above 80 percent at 70 percent power loading.

A comparison of the eight- and ten-bladed propellers (Ref. 13) is shown in Fig. 13 where net efficiency is plotted versus Mach number. These data show both propellers operating at the ten-bladed propeller design power coefficient and advance ratio. The performance of the ten-bladed propeller was about 3/4 to 1 percent higher than that of the eight-bladed model from Mach 0.6 to Mach 0.75. This higher performance would be expected due to the higher ideal efficiency for a blade count increase from 8 to 10. For the eight-bladed propeller, the performance loss due to compressibility effects began above Mach 0.7 and increased gradually with increasing speed. The ten-bladed propeller, however, showed no performance loss up to a speed near Mach 0.75. Beyond this speed, the efficiency fell rapidly with increasing Mach number. By Mach 0.8, the efficiency had fallen 3 percent and was 1/2 percent below the eight-bladed model.

Since the rapid performance loss of the ten-bladed, 40° swept propeller was believed to be due to the onset of choking in the interblade region near the hub, a new flow visualization technique, called the paint flow technique, was developed and used to

determine the extent of interblade choking (Refs. 14 and 15). The paint flow technique consists of painting the propeller blades with a red undercoat and a white overcoat. Then with the propeller operating at the desired test condition, an upstream jet atomizer was turned on to produce a cloud of dioctyl-phthalate (DOP) particles. The DOP solvent then impinged on the rotating propeller blades and after about 30 min of testing caused the paint to flow, etching the surface airflow patterns into the surface of the blades.

The results of these paint flow tests with the ten-bladed propeller operating near design conditions at Mach 0.8 is shown in Fig. 14. The photographs indicate a rather extensive shock on both the pressure and suction sides of the propeller blade. The shock structure extends far from the hub region to near the blade mid-radius. The extensive shock structure indicates that hub choking was quite severe, and propagated outward over a considerable portion of the blade span. A low hub-to-tip ratio together with close blade spacing reduced the interblade flow area on this ten-bladed propeller and contributed to the choking problem. In addition, the larger propeller diameter of this model (0.696 m (27.4 in) compared to 0.622 m (24.5 in) for the SR-3) increased the blade root chord, and structural constraints prevented thinner root sections. Future efforts in spinner area ruling techniques (Ref. 8) to reduce the interblade root Mach number in combination with advanced controlled diffusion cascades, and the use of lighter, structurally superior, advanced composite blade material to achieve thinner root sections may be able to minimize these root section design problems.

Analytical Research

Advanced aerodynamic analysis methods for predicting high-speed propeller performance are being developed as a part of the NASA Propeller Research and Advanced Turboprop Programs (Ref. 8). The analysis methods (Fig. 15) range from simple short running lifting line programs such as the existing strip analysis for single-rotation propellers based upon Goldstein's work (Ref. 16) to very complex long running programs such as the lifting surface analysis that solves the five Euler equations (Refs. 17 to 19).

The existing Goldstein type strip analysis assumes the vortex wake is composed of a rigid helical vortex sheet, corresponding to the optimum span-wise loading of a lightly loaded propeller. The propeller is restricted to having straight blades and there is no provision for a nacelle since the vortex wake extends to the axis. Simple modifications have been made to existing analyses in an attempt to circumvent these restrictions. For example, the simple cosine rule is used to account for blade sweep and a radial gradient of axial velocity is used to account for the effect of the nacelle.

More recent lifting line analyses, such as the curved lifting line program (Ref. 20) and the propeller nacelle interaction program (Ref. 21) include a swept lifting line capability, and to varying degrees, the ability to account for the presence of the nacelle in the analysis.

The curved lifting line analysis represents the wake by a finite number of helical vortex filaments instead of the continuous sheet of vorticity used by Goldstein. Each filament has a constant pitch, but its location relative to the other filaments is arbitrary. The strengths of the individual wake filaments are related to the spanwise variations of the bound vortex strength. Since both of these are unknown, the blade and wake vortex strengths are solved simultaneously. This solution is made possible by placing the bound vortex along the quarter chord line and requiring the flow to be tangent to the blade mean camber line along the three-quarter chord line. With these conditions, the blade and wake vortex strengths can be computed. The lift coefficient of the blade at any radial location is then determined from the bound vortex strength at the same radius. Drag is provided by correlated two-dimensional airfoil data. The total induced velocity at any point in the flow field is obtained by summing the induced flow of the bound vortex and the trailing vortex system. In this analysis, the propeller blades are represented by curved lifting lines which can have any arbitrary shape. The nacelle shape is an infinite cylinder since the wake filaments cannot contract radially. However, a radially varying propeller inflow velocity can be accounted for. This analysis was originally applicable only to single-rotation propellers, but has now been recently extended to include counter-rotation propellers.

The propeller nacelle interaction analysis (Ref. 21) also represents the wake by a finite number of vortex filaments. However, this analysis allows the vortex filaments to be placed along stream surfaces so that they conform to the shape of an axisymmetric nacelle. This is accomplished in the analysis by the calculation of the inviscid flow around the nacelle alone, which locates the wake vortex filaments around the nacelle and determines the radial variation of the inflow velocity at the propeller. The induced velocity is determined by summing the induced flow from the individual filaments and the swept lifting line. The local blade lift and drag are determined from two-dimensional airfoil and cascade data contained in the program and the calculated local blade angle of attack. An optional step in the analysis allows the calculated blade forces to be used in a circumferentially averaged (axisymmetric) viscous compressible flow calculation to determine interblade and off-body velocities. This calculation can indicate whether the velocities are high enough to result in large shock wave losses, and can determine the drag of the nacelle in the presence of the propeller. The wake model in this analysis can be applied to both single and coaxial counter-rotation propellers. The propellers can have blades of any arbitrary shape and the nacelle can be any axisymmetric geometry.

Finite difference lifting surface analyses that can solve the complete three-dimensional flow field are also under development. These analyses require the generation of a complex grid system which conforms to the shape of the nacelle and propeller. The nacelle shape is required to be axisymmetric so that the flow between each two adjacent blades is the same, and it is only necessary to solve for the flow between two blades. Beyond the tips and upstream and downstream of the blades, the flow is assumed to be periodic. On all solid surfaces the flow is required to be tangent to the surface.

One lifting surface inviscid analysis that is under development for single-rotation propellers solves the single full transonic potential equation (Ref. 22). It requires the wake location to be defined and does not account for shock total pressure variation although it indicates the shock location. Another lifting surface technique is the Euler analysis (Refs. 18 and 19) which is being developed for both single- and counter-rotating propellers. The equations used in the Euler analysis are the five unsteady three-dimensional Euler equations. These govern the inviscid flow of a compressible fluid and can accurately represent the total pressure variation caused by shock waves and the work done by the propeller. This analysis requires no wake modeling and no two-dimensional airfoil data. This code has a significantly longer running time than the transonic potential analysis. These lifting surface analyses will be able to predict detailed pressure distributions on both sides of the propeller blade as well as the flow conditions in any portion of the off-body flow field.

The final type of analysis under development utilizes the time averaged Navier-Stokes equations. This analysis also does not require the wake location to be specified. Since this analysis includes viscous effects in the governing equations, it can predict important features of the flow not addressed by the inviscid analyses. These include details of the blade and nacelle boundary layers, blade tip flow, blade-nacelle corner flow and blade viscous wakes.

Such detailed three-dimensional results will be important tools for improving the aerodynamic, acoustic and structural performance of propellers through a better understanding of the complicated flow processes of advanced high-speed propellers.

Experimental to Analytical Comparisons

Although these lifting line and lifting surface programs are still under development, some comparisons of their results with wind tunnel experimental data obtained with a laser velocimeter (LV), a rotating force/torque balance and a flow survey probe on an eight-bladed, 45° swept propeller (SR-3) have been made (see also Ref. 23). These comparisons are intended to show the current status in the development of the programs.

The first analytical/experimental data comparisons were made with wind tunnel experimental data obtained using the laser velocimeter (LV) system. The laser velocimeter system was developed to obtain nonintrusive measurements of detailed velocities ahead of, in between, and behind propeller blades (Refs. 24 to 26). The laser system is shown in Fig. 16 installed in the NASA Lewis 8- by 6-Foot Wind Tunnel. The SR-3 propeller, spinner, and nacelle can also be seen in this figure.

This laser velocimeter system uses a 15-W argon ion laser which is operated at about one-third power. The system uses a four beam on-axis backscatter optic system. The measuring volume is moved axially and vertically within the wind tunnel by traversing the entire laser system and is moved horizontally by using a zoom lens assembly. The movement of the measuring volume is remotely computer controlled. The flow within the tunnel is artificially seeded with dioctyl phthalate (DOP). The four beam laser velocimeter is capable of measuring two velocity components simultaneously. The four beams were set up such that the planes defined by the two beams of each color were essentially orthogonal to each other and at nominally 45° to the horizontal plane of the wind tunnel. The axial and tangential components of velocity were obtained by making a measurement in the horizontal plane which passes through the propeller rotational axis. The axial and radial components of velocity were similarly obtained by making measurements in the vertical plane which passes through the rotational axis.

In Fig. 17, the laser velocimeter velocity data is compared with results from the curved lifting line analysis. The comparisons shown are for the eight-bladed, 45° swept (SR-3) propeller (shown in Fig. 16) operating at a tunnel Mach number of 0.8, a design advance ratio of 3.06, a corrected tip rotational speed ($V_t/\sqrt{6}$) of 280 m/sec (917 ft/sec), a helical tip Mach number of 1.15, a power coefficient of 1.8, and a blade angle setting at the three-fourths radius of 60.5°.

A color computer graphic technique similar to Refs. 27 and 28 was utilized to evaluate and compare the measurements and predictions of the highly three-dimensional exit flow from the propeller. At an axial station just behind the propeller, laser velocimeter (LV) circumferential surveys were taken at 17 radial positions located from 59 to 122 percent of the blade span. These data were used to generate the computer graphic presentations of Fig. 17 where shades of gray replace the color coding presented in Ref. 26. At each radial position, the data over the complete circumference for the eight blades was folded to a 45° segment to provide data in a single equivalent blade passage. The circumferential data was averaged to provide 30 circumferential values within this "equivalent" blade passage. The entire array of experimental data at 17 radial positions by 30 circumferential positions was interpolated to provide data at intermediate positions, color-coded and displayed on a color raster display. The

results were photographed and then reprocessed to gray shades to provide the results shown in the figure. The analytical results were processed in an identical manner. Velocities were predicted for the same 17 by 30 array of spatial positions, computer interpolated and graphically displayed.

Figure 17 presents the axial velocity field in the absolute reference frame seen by a stationary observer. The blade rotation in the figure is in the counterclockwise direction when viewed from behind the propeller looking forward. The axial velocity measured by the laser velocimeter clearly show the thick blade wakes and the tip vortex. The light gray region adjacent to the blade wakes is the high velocity from the suction surface. The maximum suction surface velocity occurs at about 0.9 of the tip radius. In making the comparison of the LV data with the results from the curved lifting line analysis, the viscous blade wakes must be ignored since they are not included in the analysis. The comparison also shows the analysis has a stronger predicted tip vortex because of the mathematical singularity present in the analysis at the tip. The general character of the flow field as measured is strikingly similar to the flow field predicted by the curved lifting line analysis. Some flow disturbances are noted beyond the blade tip. These velocity fluctuations may present a potential noise source. In general, the curved lifting line analysis shows good qualitative agreement with the experimentally measured LV data.

The SR-3 propeller test results obtained from the propeller test rig rotating balance and a flow survey probe are compared in Fig. 18 with the curved lifting line and the propeller/nacelle lifting line analytical codes. For consistency of comparison with experimental results, the analytical results account for the change in twist resulting from centrifugal forces generated by blade rotation. These data are presented over a range of advance ratios for a free-stream Mach number of 0.8. In the power coefficient curve, both analytical methods overpredict the power coefficient although the curved lifting line analysis more accurately predicts the level. Both methods deviate further from the data at both high and low advance ratios and are most accurate in the mid-range. The assumed variation of twist change with rotational speed affects the shape of the predicted power coefficient curve. The analysis prediction shown in Fig. 18 assumed that the twist varied with rotational speed squared and may be responsible for some of the discrepancy in the predicted and measured power coefficient results. For the efficiency curves, the curved lifting line analysis agrees well with the data while the propeller nacelle interaction analysis considerably underpredicts the efficiency at low advance ratios and considerably overpredicts the efficiency at high advance ratios. The differences between the results from the two methods appear to be primarily due to the different approaches used for obtaining lift.

Comparisons for radial distribution of loading are shown in Fig. 18(b) for the SR-3 propeller at a free-stream Mach number of 0.8 and an advance ratio of 3.06. The propeller nacelle interaction analysis more accurately predicts the loading distribution over most of the blade, deviating appreciably only in the outer 20 percent of the blade. The curved lifting line analysis overpredicts the loading inboard and underpredicts outboard, both by appreciable amounts.

A comparison of the analytical and experimental results recently obtained with the Euler lifting surface analysis can be seen in Figs. 19 to 21.

In Fig. 19, the predicted relative Mach number on the surface of the SR-3 propeller blades and between the blades is shown for the SR-3 propeller at a free stream Mach number of 0.8, an advance ratio of 3.06, and a blade angle of 61.3°. These data employ the same gray shading technique described for Fig. 17. The level of Mach numbers on the suction side of the blade near the nacelle surface at about the two-thirds chord indicates the presence of a shock wave at that location. On the pressure side of the blade, a shock wave is also indicated at about the same location. The middle portion of the figure shows the calculated Mach numbers between the blade passages near the hub and at 82 percent of the blade span. Near the hub, the shock wave is strong and spans the entire passage. At the 82 percent blade span location, the shock wave emanates from the suction surface near the trailing edge but becomes very weak near the pressure surface.

The results shown in Fig. 19 are in good qualitative agreement with laser velocimeter measurements presented in Ref. 26. One significant difference is the location of the shock wave. In the computed results, the shock wave originates closer to the trailing edge of the blade on the suction surface whereas the data of Ref. 26 indicates a shock wave location somewhat upstream of the trailing edge. This behavior is consistent with shock wave boundary layer interactions in other types of flow fields in which viscous effects cause the actual shock wave location to be upstream of the location predicted by inviscid analyses.

The Euler analysis results are next compared in Figs. 20 and 21 with experimentally measured propeller wake swirl angles and power coefficients at a free stream Mach number of 0.8. In Fig. 20, the Euler analysis values of swirl angle downstream of the propeller are compared with experimentally measured values of swirl angle obtained during the wind tunnel tests described in Ref. 9. These values were measured with an instrumented wedge mounted on a translating probe. Both the computed and measured values correspond to an axial location 0.21 propeller diameters downstream of the pitch change axis. Although the level of the predicted results is considerably higher than the experimental results, the radial variation of swirl is in reasonable agreement between the two sets of results. The swirl angle overprediction is approximately equal

to 4° whereas at a free stream Mach number of 0.6 (Ref. 15) the discrepancy was about 3° . Inasmuch as the Mach 0.6 discrepancy was presumed due to the lack of viscous effects in the analysis, the larger discrepancy at Mach 0.8 implies that a mechanism in addition to boundary layer growth is causing decreased flow turning. This mechanism could be due to the presence of the previously discussed shock wave located just upstream of the blade trailing edge. A shock wave boundary layer interaction resulting from this shock location would result in reduced blade loading and cause reduced swirl relative to a trailing edge shock wave location.

The compressor methodology of Ref. 29 was used to estimate the viscous losses at Mach 0.8 and a radius ratio of 0.52 where the solidity (chord/gap) is 1.0. The methodology is based on low speed cascade data and does not account for the presence or effects of shock waves. Because of shock losses, it was expected that the estimate of viscous effects would fall considerably short of the Euler analysis to data discrepancy. Surprisingly, the estimate falls only slightly short. The unusual behavior of the data near $r/R = 1.0$ was apparently caused by the tip vortex rollup. The analysis did not predict this feature of the flow because the mesh was too coarse in this region.

A comparison of the Euler computed and measured propeller power coefficients is shown in Fig. 21 for the SR-3 propeller at a Mach number of 0.8. Experimental results are taken from Ref. 9. The power coefficient (shown for three blade angle settings) was considerably overpredicted for each case shown. Since power coefficient is closely related to swirl angle, the over-prediction of power coefficient is consistent with the overprediction of swirl angle shown in Fig. 20.

PROPELLER ACOUSTIC RESEARCH

In order for an advanced turboprop aircraft to be competitive with an advanced turbofan aircraft, the turboprop fuselage interior should be equivalent in comfort (low levels of noise and vibration) to that of the turbofan aircraft. A quiet fuselage interior will be more difficult to achieve in the turboprop aircraft. This is because its fuselage may be in the direct noise field of the propeller whereas the inlet duct of a turbofan shields the fuselage from fan noise. In addition, the propeller tip vortex from a wing mounted tractor propeller induces significant wing surface pressure fluctuations that could be transmitted as structural borne noise to the fuselage interior (Ref. 30). Both of these areas are being investigated as part of the NASA propeller technology program; however, only the direct radiated noise will be covered in this paper. Advanced technologies are currently being evaluated to reducing propeller source noise and improving fuselage wall noise attenuation. Fuselage wall study results have shown improved wall attenuation potential with reduced weight penalty by using a double wall fuselage construction and lighter composite materials (Refs. 31 and 32). Reduced propeller source noise is being studied with propeller sweep and new acoustic analysis techniques.

The acoustic propeller analysis methods being used and under development by NASA are listed in Fig. 22 and include both steady and unsteady aerodynamic theory, along with several propagation models. The simplest acoustic code (A in Fig. 22) uses lifting line aerodynamics and two-dimensional airfoil data with the linear propagation theory of Farassat (Ref. 33). This analysis has been compared with propeller noise data and some results are presented later in this section of the paper. A more sophisticated analysis (B) developed and being used at Lewis is the three-dimensional nonlinear steady aerodynamics approach with linear time domain propagation (Ref. 34). This program uses the Denton code (Ref. 35) as adapted from a turbofan aerodynamics package and the Farassat time domain acoustic code for propagation from the steady loading and blade thickness sources. The above methods currently have only single rotation (SR) capability. The third analysis listed in Fig. 22 (C) is being developed under a Lewis grant to Texas A&M University. It will use the simpler lifting line analysis, two-dimensional airfoil data and the Farassat propagation theory to determine the steady loading effects of counter-rotating propellers. Unsteady aerodynamics need to be developed for this program to provide a more complete modeling of CR propeller flow fields.

A three-dimensional exact linear lifting surface theory is being developed under a Lewis contract to Hamilton Standard. A steady aerodynamics version will be developed first (D), followed by an unsteady version (G). The sound propagation model uses the linear frequency domain theory of Hanson (Ref. 36). The program will also contain an airframe flow theory which describes the installation effects of the fuselage, wing and nacelle. Boundary layer sound refraction effects on the fuselage (Ref. 37), and wing shielding of the noise propagation to the cabin are also planned to be included. A three-dimensional nonlinear steady aerodynamics method with a linear frequency domain sound propagation formulation (E) is under development in a Lewis contract program at General Electric. The aerodynamics are modified by a nonlinear Euler code (Refs. 18 and 19). This program will eventually include the installation effects on noise. Flow distortion resulting from airframe installation, as well as fuselage boundary layer and wing shielding effects are to be included in the program. Some initial unsteady aerodynamics capability (H) will also be added to this program by combining the aerodynamics of the actuator disk theory and the unloaded linear lift response theory.

A three-dimensional nonlinear steady aerodynamics approach (F) is being developed in a Lewis contracted program to Arvin/Calspan. This program will use the nonlinear Euler code to describe the near field and couple it to a linear integral analysis to extend the solution to the far field. The coupling is to be done on a cylindrical surface as in Ref. 38 and an iteration routine will provide the required matching of solutions

at the surface. This system will provide proper boundary conditions for the far field and allow nonlinear propagation effects in the near field.

Acoustic measurements have been made in the Lewis 8- by 6-Foot Wind Tunnel on several of the high-speed propeller models of Fig. 10. The noise data were obtained from pressure transducers located on the side-wall and ceiling of the tunnel. Acoustic results from tests of the SR-2, SR-1M, and SR-3 eight-bladed propellers are reported in Refs. 3 and 4, and results from tests of the SR-6 ten-bladed model are reported in Ref. 39. There were some initial concerns about the quality of the noise data obtained in this tunnel, however, the Refs. 3 and 4 results indicated that a relative comparison of noise levels measured in the tunnel for the various high-speed propellers would be valid.

The effect of blade sweep on propeller noise obtained from wind tunnel results is shown in Fig. 23. The maximum blade passage tone measured on the tunnel ceiling is plotted against the helical tip (total, including tunnel and rotational) Mach number. The data were obtained at approximately the design power coefficient by holding the advanced ratio constant. The helical tip Mach number was varied by changing tunnel and propeller rotational speed. In general, the noise of both swept and straight propellers increased rapidly as the helical tip speed approached Mach 1.0. At higher helical tip speeds the noise of all three propellers shown in Fig. 23 tended to level off. The aerodynamic sweep of the 30° swept propeller (SR-1M) produced a lower noise level than the straight propeller at the lower helical tip speeds. But this advantage decreased and eventually disappeared as the tip speed increased to Mach 1.2. The 45° sweep of the SR-3 propeller was tailored to provide additional noise reduction through increased sweep and acoustic phase cancellation. The success of this acoustic sweep design is evident from the data of Fig. 23. Over the complete test range the noise level of the 45° swept propeller was consistently lower than that of the straight or 30° swept propeller, being 5 to 6 dB lower than the straight propeller at the design tip Mach number of 1.14 and 7 to 9 dB lower at the lowest tip speeds that were tested.

In addition to wind tunnel measurements, flight noise tests have been made using propeller models mounted above the fuselage of the Jetstar aircraft (Fig. 24). Comparisons of flight and wind tunnel noise data using the SR-3 propeller are reported in Refs. 40 and 41. The good agreement of these comparisons is currently being reexamined to insure that all potential sources of differences between the two tests are properly understood. Flight noise tests have also been conducted with the SR-2 and SR-6 propellers.

The simpler lifting line aerodynamics and the linear acoustic propagation theory as derived from some earlier work of Farassat (Refs. 42, 43, and 44) were used to predict the noise of the three initial propeller models (Fig. 9) and the results are reported in Ref. 45. A comparison of this theoretical prediction with tunnel data for the eight-bladed straight propeller (SR-2) is shown in Fig. 25. Generally good agreement is shown with the model data at tip speeds up to around Mach 1.0. Above a helical tip Mach number of 1.0, the theory overpredicts the near-field noise. The linear theory does not predict the levelling off of the peak noise as shown by the data. This levelling off of propeller noise at supersonic helical tip Mach numbers was observed in older propeller tests (Ref. 46). At these speeds, shock waves can propagate from a rotating propeller blade and cause nonlinear acoustic sources. To address this source, an initial simple shock wave noise model was formulated at the NASA Lewis Research Center (Ref. 47). This model predicts the noise resulting from the shock pressure rise caused by the propeller tip alone. The shock pressure rise prediction for the eight-bladed straight propeller is compared to the data in Fig. 25. Although the shock wave model predicts a rather substantial peak in the noise level not measured in the tunnel data, it also predicts the levelling-off trend in noise at the higher supersonic tip speeds that agrees with the trend in the tunnel data. This predicted trend indicates that the nonlinear shock wave model may be a viable method to pursue for enhancing the future acoustic modelling of high-speed propellers.

The effects of installation environments on propeller noise are also being investigated. Flow field distortion due to the influence of wings, nacelle, and fuselage can have an important influence upon the noise generated by a propeller. Recent experiments using an adjustable lifting wing and the SR-3 propeller have been conducted in the Lewis 8- by 6-Foot Wind Tunnel as shown in Fig. 26. Time variations in the pressure on the propeller blades due to the flow distortion have been measured using flush mounted pressure transducers. Preliminary results with the blade mounted pressure transducer data have been reported in Ref. 48. The major conclusions observed so far are that local oscillatory pressure cancellation occurs on the propeller blades due to interaction of the acoustic propagation and the unsteady aerodynamics and that the presence of the propeller significantly influences the flow-field distortion induced by the lifting wing.

Also seen in Fig. 26 is one of the four microphone mounting plates used to measure the unsymmetrical noise field produced by the unsteady loading of the propeller by the flow field. The noise data are now being analyzed and will be presented in the near future. The presence of the wing has been observed to significantly change the noise radiation from the propeller.

PROPELLER AEROELASTIC RESEARCH

Three major goals of advanced high speed propeller designs are to maximize aerodynamic efficiency, minimize noise and assure structural integrity. The acoustic and

aerodynamic requirements of high speed propellers have resulted in propellers with thin, highly swept and twisted blades of low aspect ratio and high solidity operating in transonic flow conditions. To assure the structural integrity of these advanced propellers, the NASA propeller technology program includes both experimental and analytical aeroelastic research that is applicable to the unconventional geometry and transonic flow conditions of these propellers and can be used to improve existing and develop new aeroelastic analyses. The aeroelastic research areas that are being investigated as a part of the high speed propeller program are shown in Fig. 27. These areas include the phenomena of stall flutter, forced-excitation and classical flutter. Stall flutter occurs at low flight speed conditions when the local blade angle-of-attack is high and separated flow occurs, whereas classical flutter involves unstalled flow and usually occurs at higher flight speeds. Forced excitations occur at both low and high flight speeds and can be due to cross-winds, upwash, airframe flow field distortions, and angled inflow with respect to the propeller thrust axis.

The aeroelastic propeller analysis methods that are currently being used and under development as part of the NASA program are listed in Fig. 28. Both structural blade models and unsteady aerodynamic models are shown. The swept straight-beam model (A in Fig. 28) is part of a classical flutter analysis that used two-dimensional subsonic and supersonic cascade (F), and two-dimensional transonic airfoil unsteady aerodynamics with sweep corrections (G). This analysis is based on a modification to the analysis described in Ref. 49. Some results from this analysis have been compared with propeller flutter data and are presented later in this section of the paper. A swept curved-beam model (B) is part of a more comprehensive aeroelastic analysis which is still in development under a NASA contract with United Technologies Research Center (Ref. 50). This analysis (which is based on a modification to an existing helicopter rotor code) has forced response, stall and classical flutter capabilities. The unsteady aerodynamics used for forced response and classical flutter are two-dimensional quasi-steady (D), subsonic airfoil with sweep correction (H), and empirical airfoil for stall flutter (E).

A plate finite element structural model (C) is part of a more sophisticated analysis developed under a contract with Bell Aerospace Textron and is being used at Lewis for classical flutter analysis (Ref. 51). This code is an extended version of the NASTRAN code modified for flutter analysis of turbomachinery, including turboprops and turbofans. This classical flutter analysis will be modified in the near future to include forced response analysis of advanced propellers. It uses the same unsteady aerodynamics as the swept straight-beam classical flutter analysis (F and G). Some results from this code are also shown compared to experimental data later in this section.

An aeroelastic code being developed at Lewis will use the coupled normal modes and frequencies from a plate finite element structural program (C) and will include structural mistuning of blades. This code is planned to have forced response, stall and classical flutter capability. For classical flutter, the code will initially use the same unsteady aerodynamics as the swept straight-beam analysis (F and G). Later, a three-dimensional subsonic cascade unsteady aerodynamic code (I) which is being developed at Purdue University under a NASA grant will be substituted. Modified versions of the aerodynamic models from the swept curved-beam analysis will be used for stall flutter and forced response predictions.

Experimental aeroelastic research in progress at Lewis also includes work on forced excitation, stall flutter and classical flutter. Three of the high-speed propeller models are being used for this work: the eight-bladed unswept and 45° swept models (SR-2 and SR-3) and the ten-bladed 60° swept model (SR-5) (Fig. 10). These models, while having the same aeroacoustic characteristics and geometry as a large-scale design, are not, however, aeroelastically scaled. The experimental aeroelastic data that were obtained from them is, however, applicable to and is being used to help evaluate the accuracy of the aeroelastic analysis methods. Aeroelastic wind tunnel tests with the three models have been completed at freestream velocities from Mach 0 to 0.85 and at rotational speeds up to 9000 rpm. Stall flutter, classical flutter and forced response tests were done at NASA Lewis Research Center with an isolated nacelle model (Fig. 10) using all three propeller models. Also, a nacelle-wing-fuselage model (Fig. 29) was used at NASA Ames Research Center to obtain forced response data in a flowfield more representative of an aircraft installation. This was done with the eight-bladed unswept propeller model (SR-2). Similar tests are planned at Ames with the eight-bladed 45° swept model (SR-3).

The operating procedure used to conduct these experiments was to incrementally increase the propeller rotational speed, at a fixed blade pitch angle, thrust centerline pitch angle, and tunnel Mach number until a desired operating condition or limit was reached. The operating limits were blade stress, rotational speed, and rig power or vibration. The model was operated with the propeller thrust axis aligned with the freestream velocity for the flutter tests and at an angle-of-attack to the freestream velocity for the forced response tests. This angle-of-attack produced the aerodynamic excitation forces on the blades for the response study. Data were obtained from strain gauges installed on the surface of selected blades.

Some results from the propeller forced excitation tests at 0.8 Mach number are shown in Fig. 30. Comparisons between measured and predicted one-P vibratory blade stress are shown from the isolated nacelle tests for the eight-bladed unswept and 45° swept models and the ten-bladed 60° swept model. A comparison from the installed test (Fig. 29) is shown for the eight-bladed unswept model. The data presented were obtained

by an inboard uniaxial strain gauge and its location for the 45° swept blade is shown in the figure. For the isolated nacelle case shown in Fig. 30, the predicted value of one-P stress agreed well with the data for the unswept propeller but showed only reasonable agreement with the swept propeller data and tended to underpredict their measured stress levels. For the installed case, there were two analysis methods used. Both tended to overpredict the measured stress level.

The predicted values used in Fig. 30 were calculated by Hamilton Standard under contract to NASA Lewis using company developed codes that incorporated two-dimensional quasi-steady aerodynamics. The aerodynamics were combined with a beam analysis for the unswept propeller and a finite element analysis for the swept propeller models. Two different flow field calculations were used for the installed analysis. The first was the Douglas-Neumann Potential Flow Program (Ref. 52) which is a lifting surface method. It produced the stress ratio of 0.8 shown in Fig. 30. The second was a Hamilton Standard inhouse program that represented the fuselage by a Rankine solid and the wing by a lifting line. This method produced the lower stress ratio of 0.4 in Fig. 30. These results indicate that the more accurate flow field calculation of the lifting surface method resulted in a better prediction capability at Mach 0.8. However, at lower Mach numbers, the two methods produced more comparable results.

During high speed wind tunnel tests a classical coupled bending-torsion flutter phenomena was encountered with the ten-bladed 60° swept propeller model, SR-5 (Ref. 53). The other two propeller models experienced no flutter. The flutter was encountered over the tested Mach number range of 0.6 to 0.85 and occurred when the blade helical tip Mach number reached a value of about 1.0 over a range of blade angles and power loadings. A theoretical study made after this flutter experience suggested that sweep and aerodynamic cascade effects have a strong destabilizing influence on the flutter boundary. The theoretically predicted destabilizing effect of sweep on flutter was experimentally supported by the fact that only the most highly swept of the three tested propellers encountered flutter. To experimentally investigate the aerodynamic cascade effect, a five- and two-bladed configuration of the SR-5 model was subsequently tested. This experiment supported the theoretical predictions by showing that the flutter onset occurred at a lower helical tip Mach number when there were a larger number of blades on the rotor. These results are illustrated in Fig. 31 which shows the experimental flutter boundary for the ten- and five-bladed configurations at a selected blade angle of 69°. The flutter boundary data are shown in terms of the flutter onset rotational speed versus free-stream Mach number. Also shown are two theoretical predictions for the flutter boundary of the ten-bladed configuration. These boundaries were predicted by the swept straight-beam and the plate finite element classical flutter aeroelastic analysis codes that were described earlier in this section. Both of these analyses and the experimental data of Fig. 31 show the same trend of decreasing flutter rotational speed with increasing free-stream Mach number. Although the slopes of the experimental and calculated boundaries are different they are in reasonable agreement. However, the figure shows that both of the predicted boundaries are conservative, and increasingly underpredict the experimental boundary as the Mach number increases.

Future efforts in aeroelastics will be directed toward improving the existing analysis codes and developing new aeroelastic codes with better prediction capabilities and accuracy. Experimental to analytical comparisons will continue to be a primary tool to identify areas where the codes need improving. Future experimental work will include a model of the eight-bladed 45° swept propeller fabricated from composite materials (SR-3C). This model will soon undergo isolated forced response and flutter testing in the Lewis 8- by 6-Foot Wind Tunnel. Installed forced response testing in the Ames 14-ft tunnel is also planned for this model. These efforts will be followed by the testing of a new high-speed propeller model (SR-7) that is aeroelastically scaled from a 9-ft propeller design.

FUTURE TRENDS

The NASA advanced high-speed propeller research program has been primarily directed toward developing technology for high performing single-rotation (SR) tractor propellers. The performance results achieved with SR propeller models show that future advanced turboprop powered aircraft should be potentially far superior in performance to an equivalent turbofan powered aircraft. Wind tunnel model results have shown propeller efficiencies near 80 percent at Mach 0.8 with near-field cruise noise reductions with swept blades of about 6 dB. Further efficiency improvements and noise reductions may be possible with some of the advanced experimental and analytical technology work that is underway or planned as part of this research program. Two additional SR propeller models are currently being designed to address the speed range from Mach 0.7 to 0.8. The latest refinements to the evolving advanced analysis methods in aerodynamics, acoustics, and aeroelastics are being used to assist in the design of these models.

A number of attractive advanced turboprop concepts (Fig. 32) are being studied to further improve performance and reduce propeller noise. A single-rotation pusher propeller mounted at the rear of the aircraft fuselage (away from the cabin section) could reduce or possibly eliminate the potentially high cabin noise associated with a tractor wing-mounted configuration without incurring a weight penalty for cabin wall acoustic treatment. Advanced concepts that have the potential for recovering the residual swirl loss from SR turboprops could offer large improvements in propeller efficiency. Variable pitch stators behind a single-rotation propeller is one concept that offers increased efficiency through swirl recovery. Although the potential performance gains are not predicted to be as large as those for counter-rotation (CR) propellers, the stator

concept has the advantage of minimum complexity. However, the more complex CR propellers have the potential for recovering essentially all of the swirl losses. Advanced CR concepts that are being investigated as part of the NASA program include both pusher and tractor designs. One particularly unique pusher design is a gearless concept being investigated as part of a NASA contract program with General Electric. This concept eliminates the gearbox altogether but introduces the new concept of an integral counter-rotating power turbine.

The potential advantages of CR propellers over SR propellers is shown in Fig. 33 where ideal efficiency (optimum loading with zero blade drag) is plotted versus power loading for propellers operating at a typical Mach 0.8 cruise condition. The figure shows that performance gains by increasing blade count from 8 to 10 with SR propellers are rather small (about 1 percent) compared to the gains achievable by selecting CR over SR systems. At power loadings from 200 to 320 kW/m² (25 to 40 hp/ft²) the CR potential efficiency gains range from about 6 to 9 percent for equal total blade count. As power loading is further increased, the SR propellers suffer a larger performance loss compared to CR systems due primarily to increasing swirl losses. Therefore, CR propellers can be operated at much higher power loadings (with associated propeller diameter and weight reductions) than SR systems without large performance losses. In addition, CR propellers with total blade counts comparable to SR propellers should also reduce potential blade-to-blade choking losses incurred in the inboard region of the 8 to 10 blade SR propellers by providing a larger flow area between the blades.

A recent NASA sponsored study that compared SR and CR geared tractor turboprops for a Mach 0.8 commercial transport application is reported in Refs. 2 and 54. This study focused on evaluating a number of propeller and gearbox concepts on a 100-passenger, twin engine airplane with a 1300 nmi design mission. The concepts with the most attractive operating costs were an advanced six by six-bladed CR propeller with an in-line differential planetary gearbox and an advanced ten-bladed SR propeller with an offset compound idler gearbox.

The study results are summarized in Fig. 34. The advanced CR propeller system was projected to have an 8 percentage point higher efficiency due to swirl recovery and a higher blade count, with only a 17 percent increase in propeller weight and 1.6 dBA cruise interior noise increase. The compact one-stage differential planetary gearbox would be 15 percent lighter and have a 0.2 percent higher efficiency than the gearbox system required for SR turboprops. There did appear to be an increase in acquisition cost of 19 percent with the CR gearbox. However, CR propeller systems offered an almost complete (-80 to -100 percent) cancellation of aircraft torque and gyroscopic loads. Because of the slightly higher CR propeller interior noise (1.6 dBA) and lower frequency noise content, the cabin acoustic treatment weight would have to be increased by about 5 percent. Based on these performance and weight changes, a 9 percent block fuel savings and a 2.9 percent DOC reduction was estimated for an advanced CR system relative to a comparable SR system for the 1300 nmi design mission.

To verify the performance gains projected for advanced CR turboprops, NASA has planned and recently initiated an extensive CR wind tunnel program. The program includes the testing of several 0.62 m (two ft) diameter model propellers that include both tractor and pusher configurations. Figure 35 is a photograph of a 16-bladed CR model of a gearless pusher configuration installed on a 1119 kW (1500 hp) propeller test rig.

REFERENCES

1. Jeracki, R. J., Mikkelson, D. C., and Blaha, B. J., "Wind Tunnel Performance of Four Energy Efficient Propellers Designed for Mach 0.8 Cruise," SAE Paper 790573, 1979.
2. Weisbrich, A. L., Godston, J. and Bradley, E., "Technology and Benefits of Aircraft Counter Rotation Propellers," (HSER-8858, Hamilton Standard; NASA Contract NAS3-23043.) NASA CR-168258, 1982.
3. Dittmar, J. H., Blaha, B. J., and Jeracki, R. J., "Tone Noise of Three Supersonic Helical Tip Speed Propellers in a Wind Tunnel at 0.8 Mach Number," NASA TM-79046, 1978.
4. Dittmar, J. H., Jeracki, R. J. and Blaha, B. J., "Tone Noise of Three Supersonic Helical Tip Speed Propellers in a Wind Tunnel," NASA TM-79167, 1979.
5. Mikkelson, D. C., Blaha, B. J., Mitchell, G. A., and Wikete, J. E., "Design and Performance of Energy Efficient Propellers for Mach 0.8 Cruise," SAE Paper 770458, 1977.
6. Hanson, D. B., "Near Field Noise of High Tip Speed Propellers in Forward Flight," AIAA Paper 76-565, 1976.
7. Metzger, F. B., and Rohrbach, C., "Aeroacoustic Design of the Prop-Fan," AIAA Paper 79-0610, 1979.
8. Bober, L. J., and Mitchell, G. A., "Summary of Advanced Methods for Predicting High Speed Propeller Performance," AIAA Paper 80-0225, 1980.
9. Rohrbach, C., Metzger, F. B., Black, D. M., and Ladden, R. M., "Evaluation of Wind Tunnel Performance Testings of an Advanced 45° Swept Eight-Bladed Propeller at Mach Numbers from 0.45 to 0.85," NASA CR-3505, 1982.
10. Dugan, J. F., Jr., Gatzert, B. S., and Adamson, W. M., "Prop-Fan Propulsion - Its Status and Potential," SAE Paper 780995, 1978.
11. Swallow, R. J., and Aiello, R. A., "NASA Lewis 8- by 6-Foot Supersonic Wind Tunnel," NASA TM X-71542, 1974.

12. Mikkelson, D. C., and Mitchell, G. A., "High Speed Turboprops for Executive Aircraft, Potential and Recent Test Results," NASA TM-81482, 1980.
13. Jeracki, R. J., and Mitchell, G. A., "Low and High Speed Propellers for General Aviation - Performance Potential and Recent Wind Tunnel Test Results," NASA TM-81745, 1981.
14. Mitchell, G. A. and Mikkelson, D. C., "Summary and Recent Results from the NASA Advanced High-Speed Propeller Research Program," AIAA Paper 82-1119, 1982.
15. Stefko, G. L., Bober, L. J. and Neumann, H. E., "New Test Techniques and Analytical Procedures for Understanding the Behavior of Advanced Propellers," NASA TM-83360, 1983.
16. Goldstein, S., "On the Vortex Theory of Screw Propellers," Royal Society (London) Proceedings, Vol. 123, Series A, No. 792, 1929, pp. 440-465.
17. Chaussee, D. S., "Computation of Three-Dimensional Flow Through Prop Fans," NEAR TR-199, Nielsen Engineering and Research, Inc., 1979.
18. L. J. Bober, D. S. Chaussee and P. Kutler, "Prediction of High Speed Propeller Flow Fields Using a Three-Dimensional Euler Analysis," AIAA Paper 83-0188, 1983.
19. D. S. Chaussee and P. Kutler, "User's Manual for Three-Dimensional Analysis of Propeller Flow Fields," (FSI-80-04, Flow Simulations, Inc.; NASA Contract NAS3-22375.) NASA CR-167959, 1983.
20. Sullivan, J. P., "The Effect of Blade Sweep on Propeller Performance," AIAA Paper 77-716, 1977.
21. Egolf, T. A., Anderson, O. L., Edwards, D. E., and Landgrebe, A. J., "An Analysis for High Speed Propeller-Nacelle Aerodynamic Performance Prediction; Volume 1, Theory and Initial Application and Volume 2, User's Manual for the Computer Program," R79-912949-19, United Technologies Research Center, 1979.
22. W. H. Jou, "Finite Volume Calculations of Three-Dimensional Flow Around a Propeller," AIAA Paper 82-0957, 1982.
23. Bober, L. T., and Chang, L. K., "Factors Influencing the Predicted Performance of Advanced Propeller Designs," NASA TM-82676, 1981.
24. Serafini, J. S., Sullivan, J. R., and Neumann, H. E., "Laser-Velocimeter Flow-field Measurements of an Advanced Turboprop," AIAA Paper 81-1568, 1981.
25. R. J. Freedman and J. P. Greissing, "The Development and Utilization of a Laser Velocimeter System for a Large Transonic Wind Tunnel," NASA TM-82886, 1982.
26. H. E. Neumann, L. J. Bober, J. S. Serafini and L. K. Chang, "An Analytical and Experimental Comparison of the Flow Field of an Advanced Swept Turboprop," AIAA Paper No. 83-0189, 1983.
27. B. H. Anderson, C. W. Putt and C. C. Giamati, "Application of Computer Generated Color Graphic Techniques to the Processing and Display of Three Dimensional Fluid Dynamic Data," NASA TM-82658, 1981.
28. B. H. Anderson, C. W. Putt and C. C. Giamati, "Fluid Dynamic Data in Color and Three Dimensions," Mechanical Engineering, Vol. 104, No. 3, 1982, pp. 30-35.
29. I. A. Johnsen and R. O. Bullock, Editors, "Aerodynamic Design of Axial-Flow Compressors," NASA SP-36, 1965.
30. Miller, B. A., Dittmar, J. H., and Jeracki, R. J., "The Propeller Tip Vortex - A Possible Contributor to Aircraft Cabin Noise," NASA TM-81768, 1981.
31. Revell, J. D., Balena, F. J., and Koval, L. R., "Analytical Study of Interior Noise Control by Fuselage Design Techniques on High-Speed, Propeller-Driven Aircraft," (LR-29382, Lockheed-California Co.; (NASA Contract NAS1-15427.) NASA CR-159222, 1980.
32. Rennison, D. C., Wilby, J. F., and Marsh, A. H., "Interior Noise Control Prediction Study for High-Speed Propeller-Driven Aircraft," (BBN-4026, Bolt, Beranek, and Newman, Inc.; NASA Contract NAS1-15426.) NASA CR-159200, 1979.
33. Martin, R. M., and Farassat, F., "User's Manual for a Computer Program to Calculate Discrete Frequency Noise of Conventional and Advanced Propellers," NASA TM-83135, 1981.
34. Clark, B. J., and Scott, J. R., "Coupled Aerodynamic and Acoustic Predictions for Turboprops," presented at the 107th Meeting of the Acoustical Society of America, 6-10 May, 1984, Norfolk, Va.
35. Denton, J. D., and Singh, U. K., "Time Marching Methods for Turbomachinery Flow Calculation," in Application of Numerical Methods to Flow Calculations in Turbomachines, von Karman Institute for Fluid Dynamics Lecture Series 1979-7, von Karman Institute for Fluid Dynamics, 1979.
36. Hanson, D. B., "Compressible Helicoidal Surface Theory for Propeller Aerodynamics and Noise," AIAA Journal, Vol. 21, No. 6, 1983, pp. 881-889.
37. Hanson, D. B., and Magliozzi, B., "Propagation of Propeller Tone Noise Through a Fuselage Boundary Layer," AIAA Paper 84-0248, 1984.
38. Hawkings, D., "Noise Generation by Transonic Open Rotors," Research Paper 599, Westland Helicopters Limited, 1979.
39. Dittmar, J. H., Stefko, G. L., and Jeracki, R. J., "Noise of the 10-Bladed, 40° Swept SR-6 Propeller in a Wind Tunnel," NASA TM-82950, 1982.
40. Dittmar, J. H., and Lasagna, P. L., "A Preliminary Comparison Between the SR-3 Propeller Noise in Flight and in a Wind Tunnel," NASA TM-82805, 1982.
41. Mackall, K. G., Lasagna, P. L., and Dittmar, J. H., "In-Flight Acoustic Results from an Advanced Design Propeller at Mach Numbers Up to 0.8," AIAA Paper 82-1120, 1982.
42. Farassat, F., "Theory of Noise Generation from Moving Bodies with an Application to Helicopter Rotors," NASA TR R-451, 1975.
43. Farassat, F., "Discontinuities in Aerodynamics and Aeroacoustics - The Concept and Applications of Generalized Derivatives," Journal of Sound and Vibration, vol. 55, no. 2, 1977, pp. 165-193.

44. Farassat, F., Morris, C. E. K., and Nystrom, P. A., "A Comparison of Linear Acoustic Theory with Experimental Noise Data for a Small Scale Hovering Rotor," AIAA Paper 79-0609, 1979.
45. Dittmar, J. H., "A Comparison Between the Existing Propeller Noise Theory and Wind Tunnel Data," NASA TM-81519, 1980.
46. Hubbard, H. H., and Lassiter, L. W., "Sound From a Two-Blade Propeller at Supersonic Tip Speeds," NACA Rep. 1079, 1952.
47. Dittmar, J. H., and Rice, E. J., "A Shock Wave Approach to the Noise of Supersonic Propellers," NASA TM-82752, 1981.
48. Heidelberg, L. J., Dahl, M. D., and Rice, E. J., "Measurements of Periodic Blade Pressures on a Transonic Propeller with Nonuniform Inflow," presented at the 107th Meeting of the Acoustical Society of America, 6-10 May, 1974, Norfolk, Va.
49. Kaza, K. R. V. and Kielb, R. E., "Coupled Bending-Bending-Torsion Flutter of a Mistuned Cascade With Nonuniform Blades," NASA TM-82813, 1982.
50. Bielawa, R. L., Johnson, S. A., Chi, R. M. and Gangwani, S. T., "Aeroelastic Analysis for Propellers - Mathematical Formulations and Program User's Manual," NASA CR-3729, 1983.
51. Elchuri, V., and Smith, G. C. C., "Flutter Analysis of Advanced Turboprop Propellers," AIAA Paper 83-0846, 1983.
52. Hess, J. L., "Calculation of Potential Flow About Arbitrary Three-Dimensional Lifting Bodies," Report MDC-J5679-01, Douglas Aircraft Co., Inc., Oct. 1972.
53. Mehmed, O., Kaza, K. R. V., Lubomski, J. F., and Kielb, R. E., "Bending-Torsion Flutter of a Highly Swept Advanced Turboprop," NASA TM-82975, 1982.
54. Strack, W. C., Knip, G., Weisbrich, A. L., Godson, J., and Bradley, E., "Technology and Benefits of Aircraft Counter Rotation Propellers," NASA TM-82983, 1982.



Figure 1. - Advanced counter-rotation turboprop aircraft.

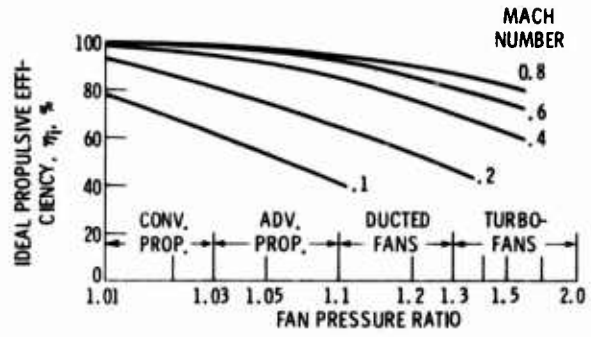


Figure 2. - Ideal propulsive efficiency as a function of fan pressure ratio.

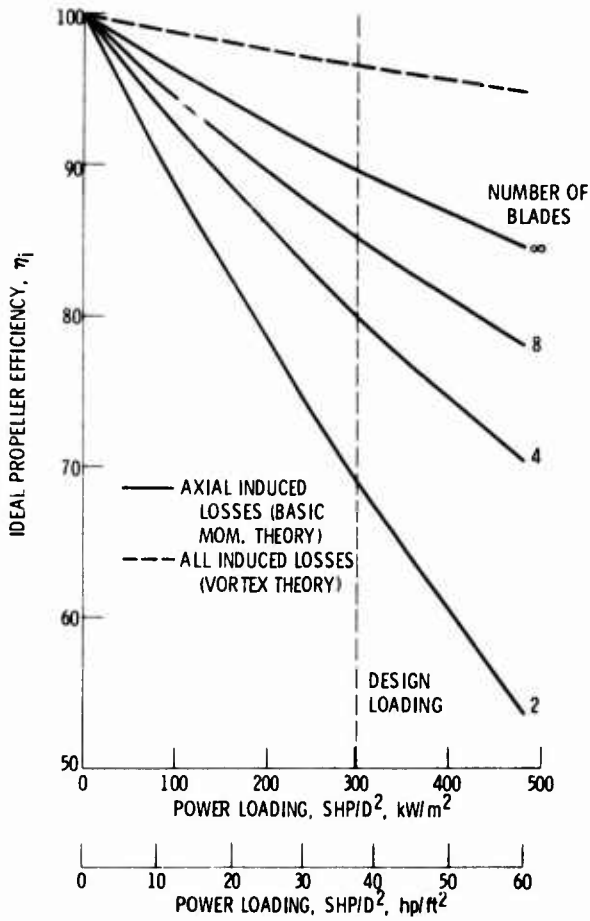


Figure 3. - Ideal single-rotation propeller efficiency; 0.8 Mach number at 10,668 km (35 000 ft) altitude and 243.8 m/sec (800 ft/sec) tip speed.

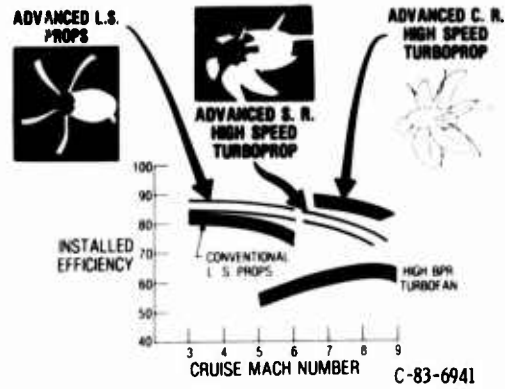


Figure 4. - Installed cruise efficiency trends.

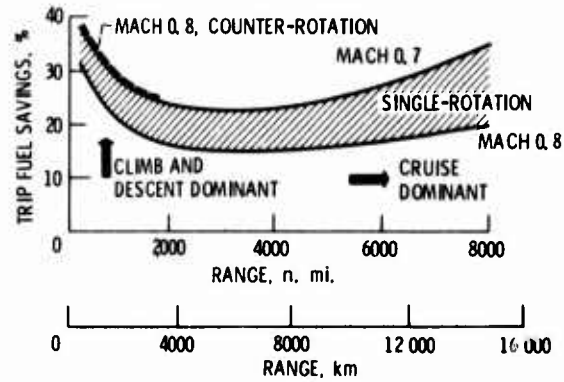


Figure 5. - Fuel savings trends of advanced turboprop aircraft over comparable turbofan aircraft.

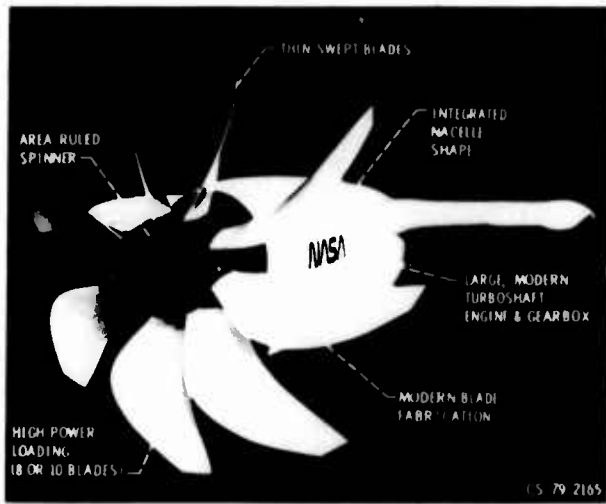


Figure 6. - Advanced turboprop propulsion system.

CURVE

- A SECTION MACH NUMBER, NO VELOCITY SUPPRESSION OR SWEEP
- B DRAG DIVERGENCE MACH NUMBER (NACA 16-SERIES)
- C SECTION MACH NUMBER WITH 30° TIP SWEEP
- D EFFECTIVE SECTION MACH NUMBER (WITH SUPPRESSION AND SWEEP)

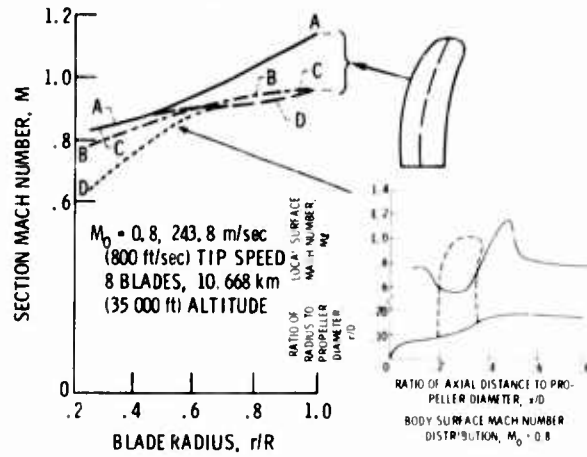


Figure 7. - Effects of advanced aerodynamic concepts on blade section Mach number distributions.

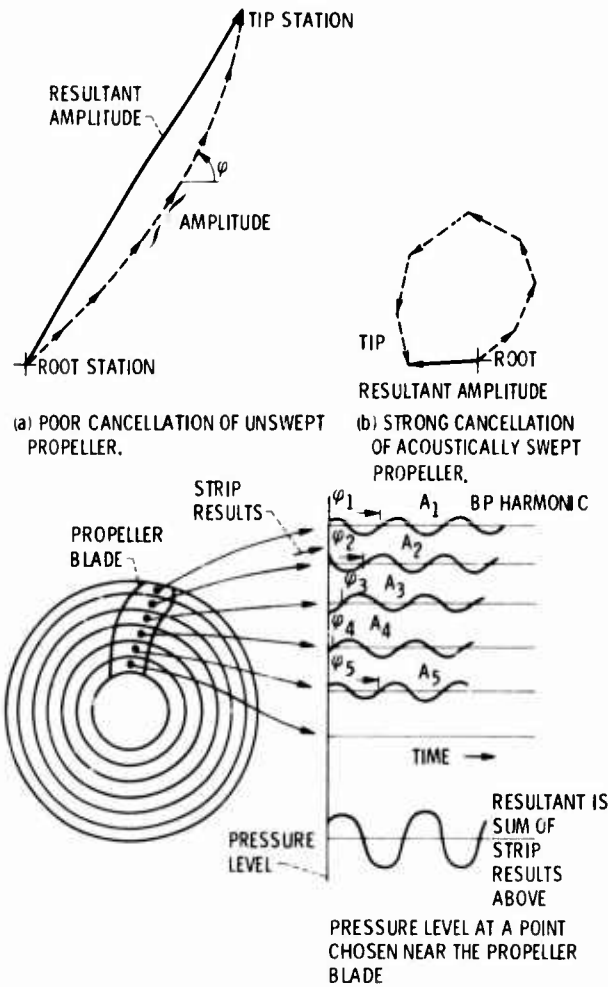


Figure 8. - Acoustic strip analysis technique for near-field noise reduction.

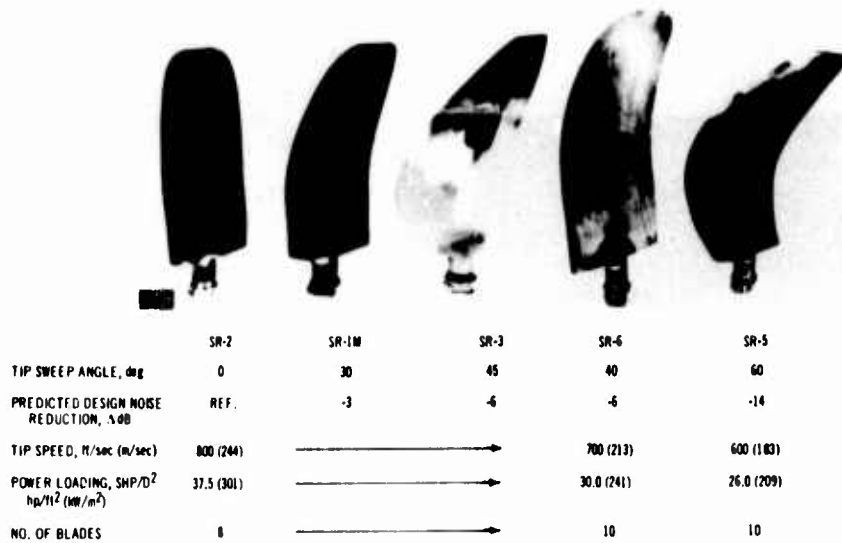


Figure 9. - Design characteristics and planforms of high speed propeller models.

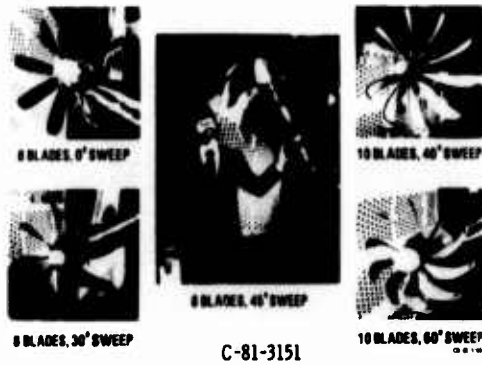


Figure 10. - Propeller models installed in the Lewis 8-by-4 foot wind tunnel.

AREA RULED SPINNER. $J = 3.06$, $C_p = 1.7$

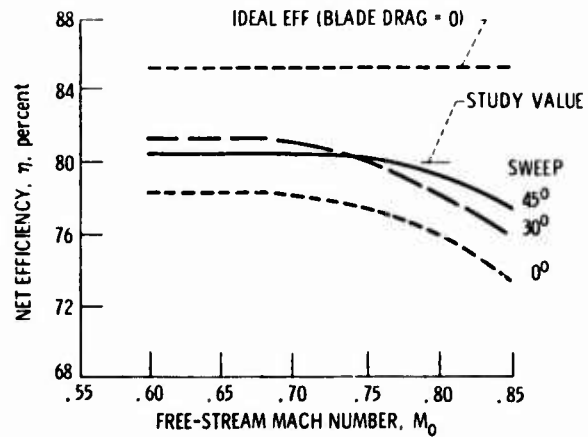


Figure 11. - Performance summary of 8-bladed propellers.

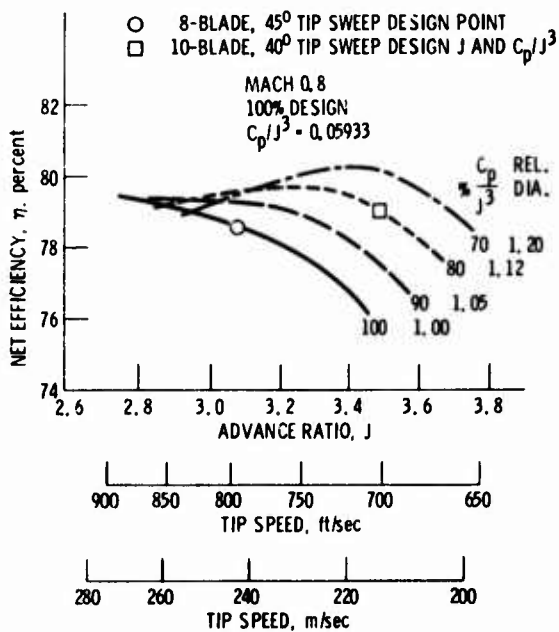


Figure 12. - Effect of power loading and advance ratio on performance of the 8-bladed 45° swept propeller (SR-3).

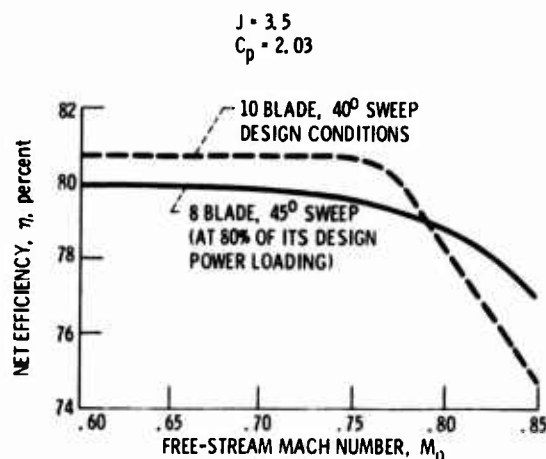


Figure 13. - Comparison of 8 and 10 blade performance.

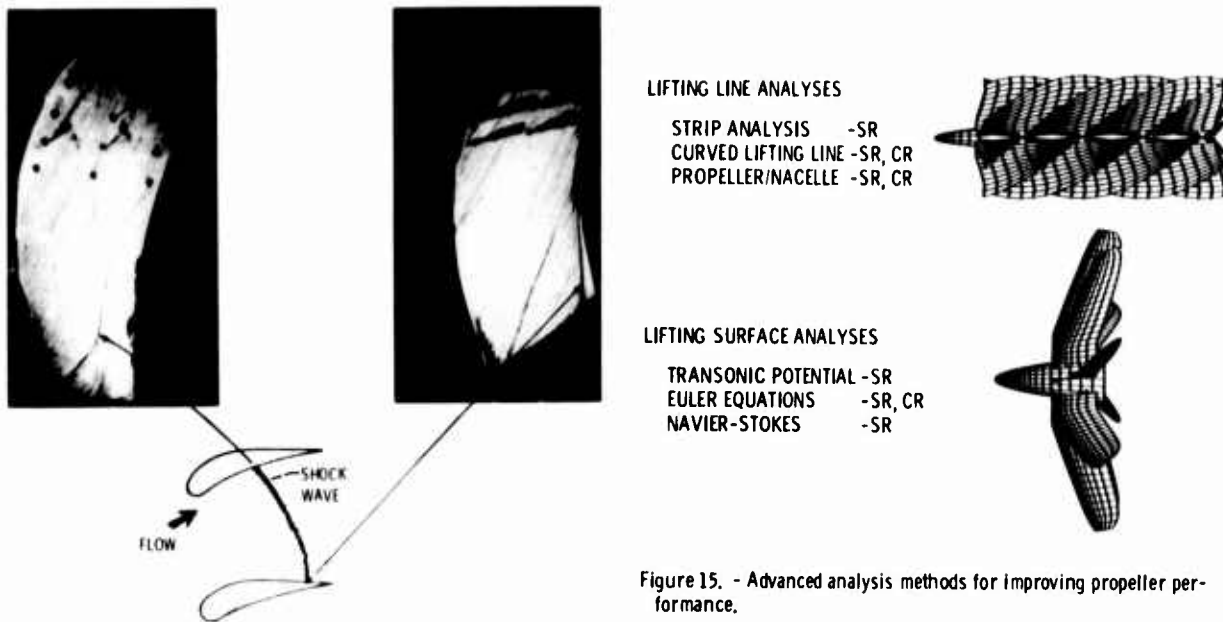


Figure 14. - Results from the paint flow visualization technique indicating the interblade shock structure on the 10-bladed, 40° swept propeller at Mach 0.8.

Figure 15. - Advanced analysis methods for improving propeller performance.



Figure 16. - Laser velocimeter in Lewis 8-by-6 foot wind tunnel.

SR-3 EXIT VELOCITY
AXIAL COMPONENT

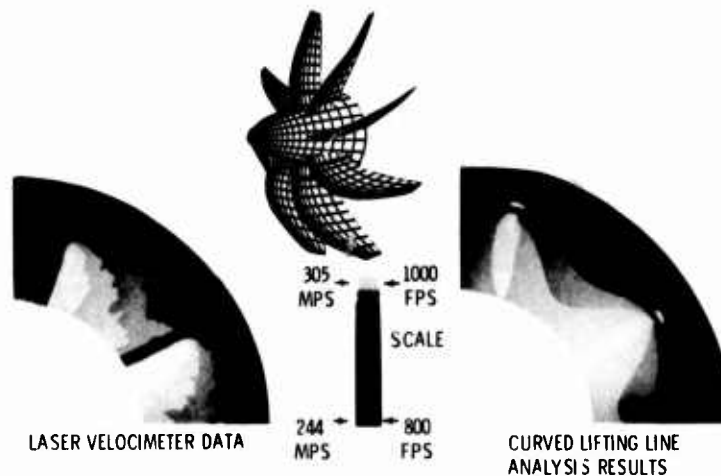
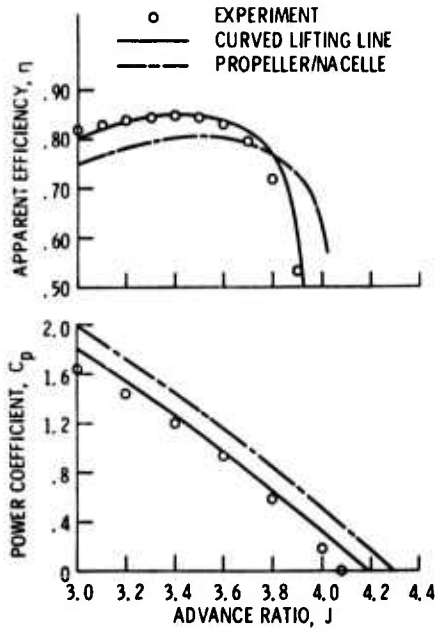
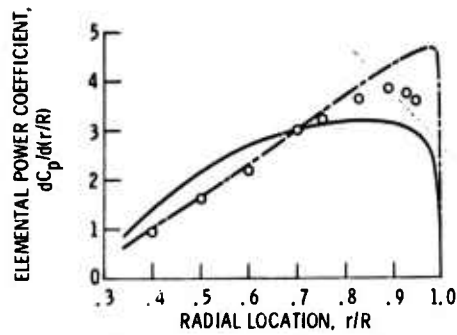


Figure 17. - Axial exit velocity comparisons between laser velocimeter data and curved lifting line analysis on the SR-3 propeller at Mach 0.80.



(a) Propeller performance. Blade angle at 3/4 radius equals 60.4°.



(b) Power loading distribution. Advance ratio equals 3.06.

Figure 18 - Comparison of lifting line analytical and experimental results for the SR-3 propeller at free stream Mach number of 0.8.

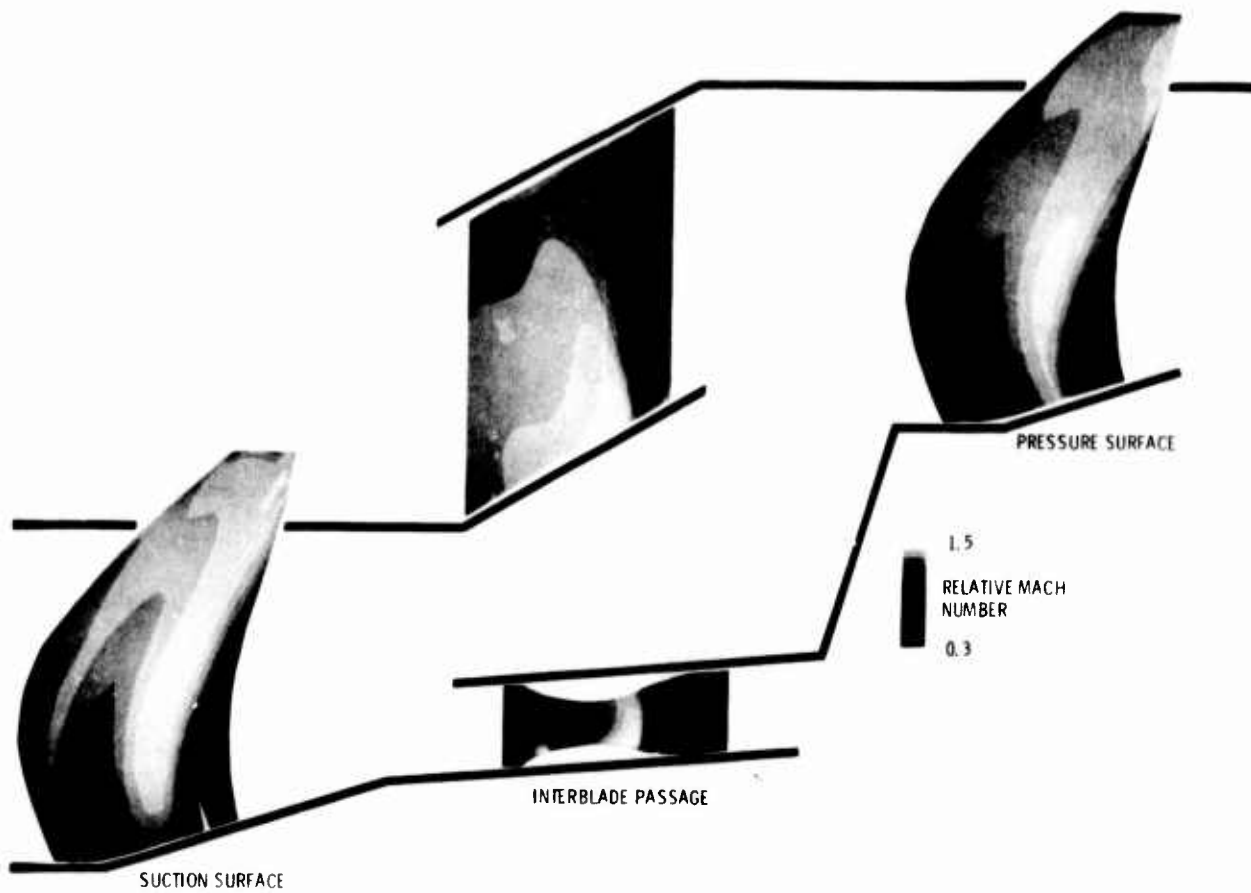


Figure 19. - Euler lifting surface analysis Mach number contours, SR-3 propeller at Mach 0.80, advance ratio 3.06, and blade angle at three-quarter radius 61.3.

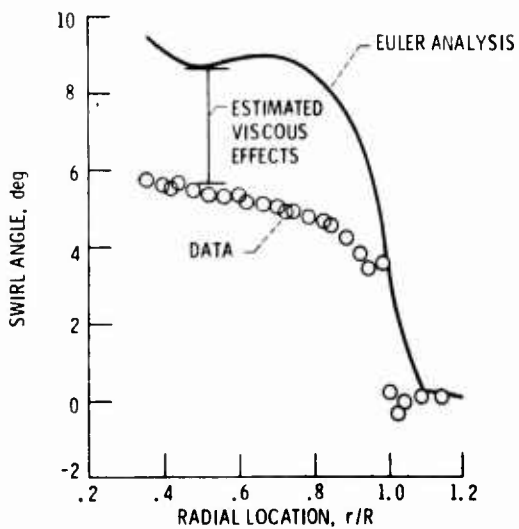


Figure 20. - Comparison of predicted and measured swirl angle downstream of the SR-3 propeller blade. Axial location, 0.21 diameters downstream of the pitch change axis; free stream Mach number, 0.8; advance ratio, 3.06; blade angle at three-quarter radius, 60.5°.

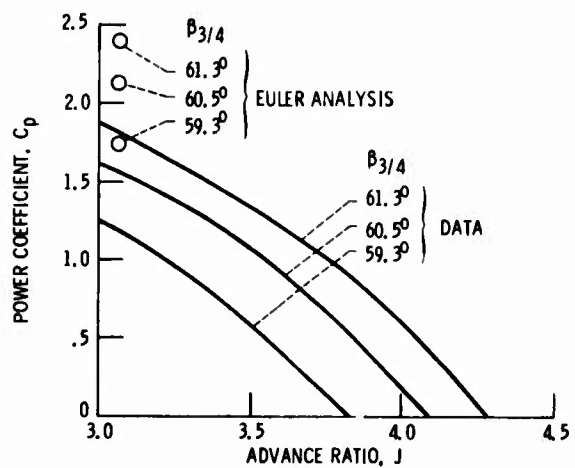


Figure 21. - Comparison of predicted and measured power coefficient for the SR-3 propeller. Free-stream Mach number, 0.8; advance ratio, 3.06.

APPROACH		STATUS
<u>STEADY AERODYNAMICS</u>		
(A) LIFTING LINE/2D AIRFOIL (SR)	LINEAR - TIME DOMAIN	CURRENT
(B) 3D NON-LINEAR (SR)	LINEAR - TIME DOMAIN	CURRENT
(C) LIFTING LINE/2D AIRFOIL (CR)	LINEAR - TIME DOMAIN	IN DEVELOPMENT
(D) 3D EXACT LINEAR (SR)	LINEAR - FREQUENCY DOMAIN	IN DEVELOPMENT
(E) 3D NON-LINEAR (SR)	LINEAR - FREQUENCY DOMAIN	IN DEVELOPMENT
(F) 3D NON-LINEAR (SR)	NON-LINEAR/LINEAR	IN DEVELOPMENT
<u>UNSTEADY AERODYNAMICS</u>		
(G) 3D EXACT LINEAR (SR)	LINEAR - FREQUENCY DOMAIN	IN DEVELOPMENT
(H) LINEAR LIFT RESPONSE- ACTUATOR DISK (SR)	LINEAR - FREQUENCY DOMAIN	IN DEVELOPMENT

Figure 22. - Acoustic Analysis Methods.

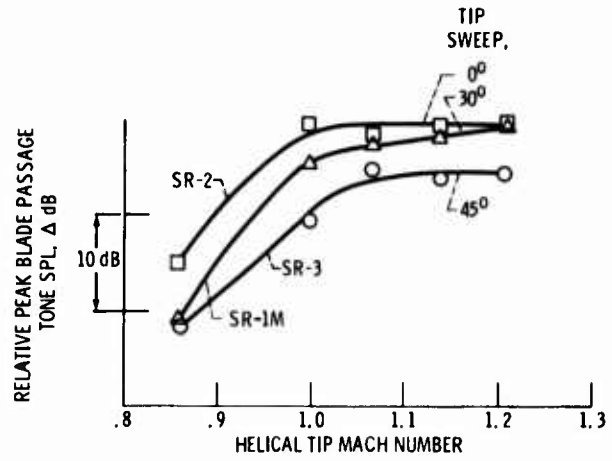


Figure 23. - Maximum blade passage tone variation with helical tip Mach number for 8-bladed propellers. (All at nominal advance ratio of 3.06.)



Figure 24. - Photograph of SR-3 propeller installed on the Jetstar aircraft for in flight noise measurements.

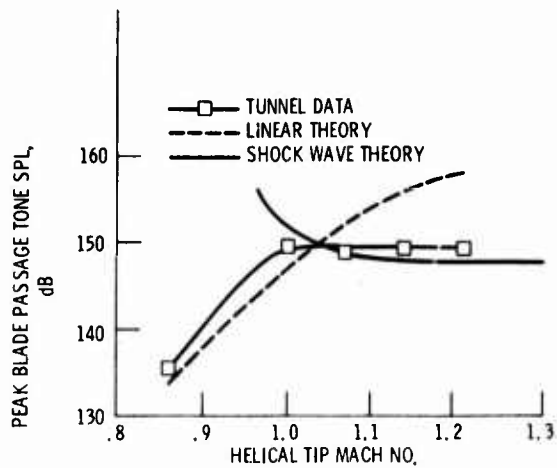


Figure 25. - Near field noise of the 8-bladed 0° swept propeller (SR-2) at 1.5 diameters from propeller tip.



Figure 26. - Photograph of the SR-3 (8 bladed, 45° swept) propeller installed for wing effects acoustic tests in the Lewis 8-by-6 foot wind tunnel.

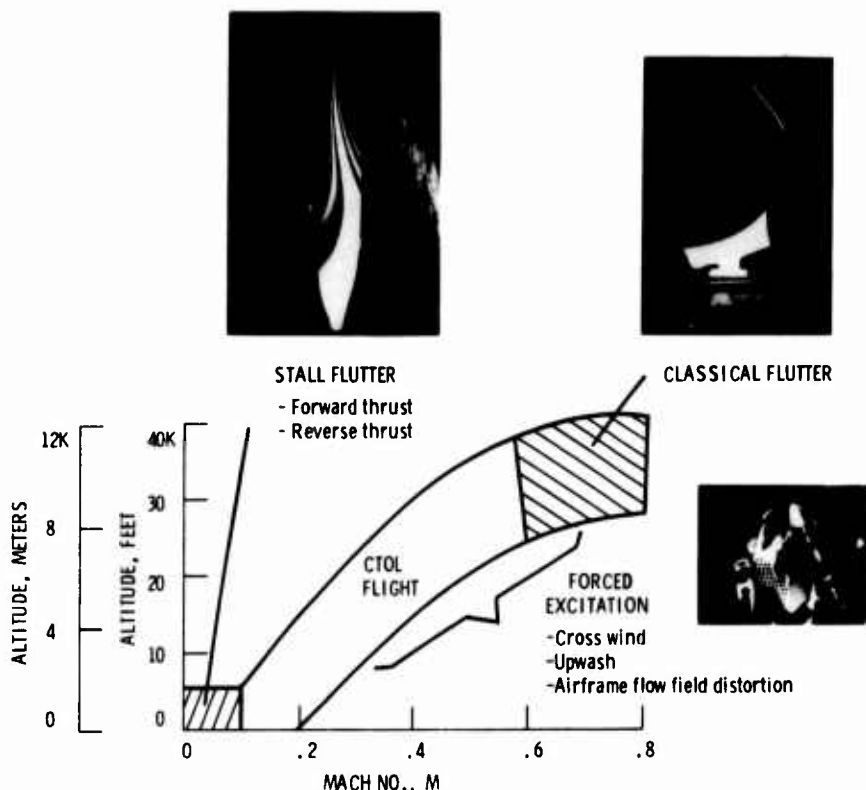


Figure 27. - Areas of propeller aeroelastic research.

METHOD	STATUS
<u>STRUCTURAL BLADE MODELS</u>	
(A) SWEEP STRAIGHT BEAM	CURRENT
(B) SWEEP CURVED BEAM	IN DEVELOPMENT
(C) PLATE FINITE ELEMENT	IN DEVELOPMENT
<u>UNSTEADY AERODYNAMIC MODELS</u>	
FORCED EXCITATION	
(D) 2D QUASI-STEADY	CURRENT
STALL FLUTTER	
(E) EMPIRICAL SUBSONIC AIRFOIL	CURRENT
CLASSICAL FLUTTER	
(F) 2D SUB AND SUPERSONIC CASCADE	CURRENT
(G) 2D TRANSONIC AIRFOIL	CURRENT
(H) 2D SUBSONIC AIRFOIL	CURRENT
(I) 3D SUBSONIC CASCADE	IN DEVELOPMENT

Figure 28. - Propeller aeroelastic analysis methods.



Figure 29. - Photograph of the SR-2C (8-bladed, 0° sweep) propeller installed on the semi-span aircraft model in the Ames 14-foot transonic wind tunnel.

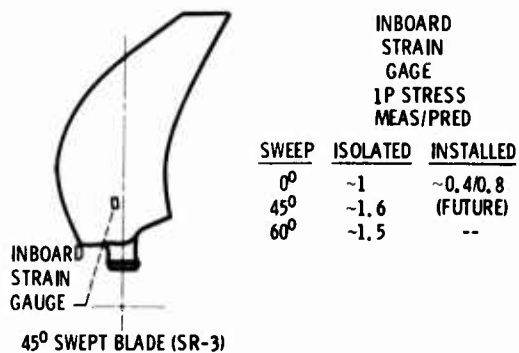


Figure 30. - Propeller forced excitation results at Mach 0.8

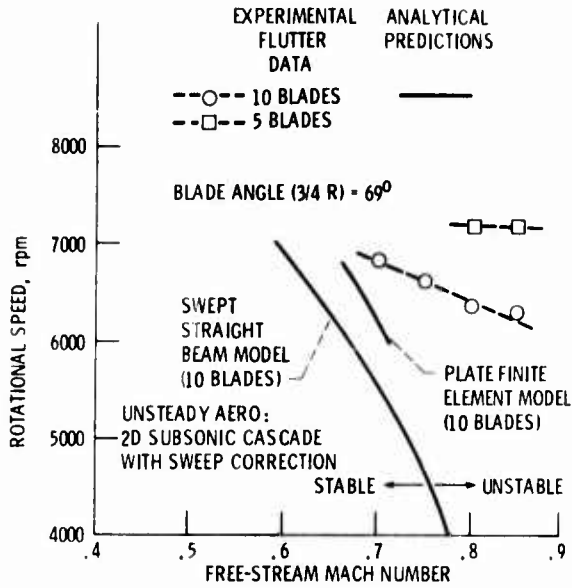


Figure 31. - A comparison of predicted and measured classical flutter boundaries of the 60° swept propeller model (SR-5).

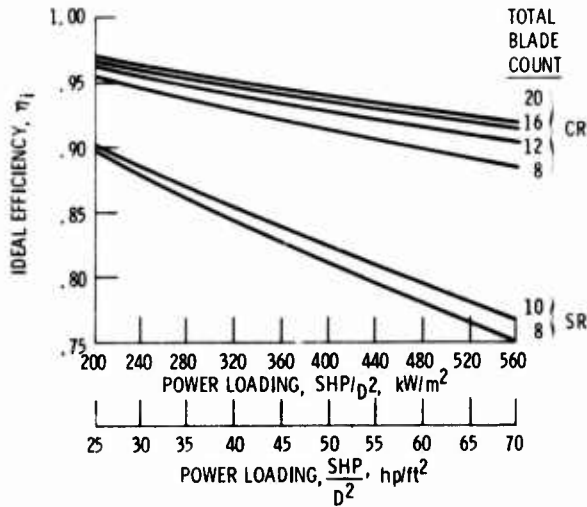


Figure 33. - Comparison of ideal efficiency for single- and counter-rotation propellers: $M_0 = 0.8$, altitude = 10,668 km (35,000 ft), tip speed = 244 m/sec (800 ft/sec).

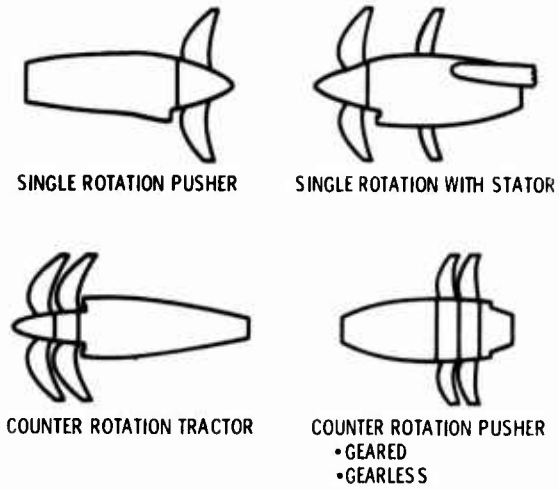
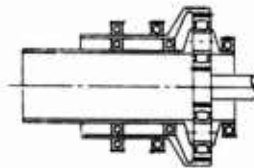


Figure 32. - Future advanced turboprop concepts.

ADVANCED CR PROPELLER
 $\Delta n_{CRP-SRP} +8$ PTS
 Δ PROPELLER WEIGHT +17 %
 Δ CRUISE NOISE +1.6 dBA



DIFFERENTIAL PLANETARY GEARBOX
 Δ GB WEIGHT -15 %
 Δ EFFICIENCY +.2 %
 Δ ACQUISITION COST +19 %



OVERALL INSTALLATION

Δ FUEL -9 %
 Δ DOC -2.9 %
 Δ CABIN ACOUSTIC TREATMENT +5 %
 Δ AIRCRAFT INSTALLATION LOADS (PROP GYRO MOMENT AND DRIVE TORQUE) -80 TO -100 %

Figure 34. - Advanced counter-rotation propeller potential.

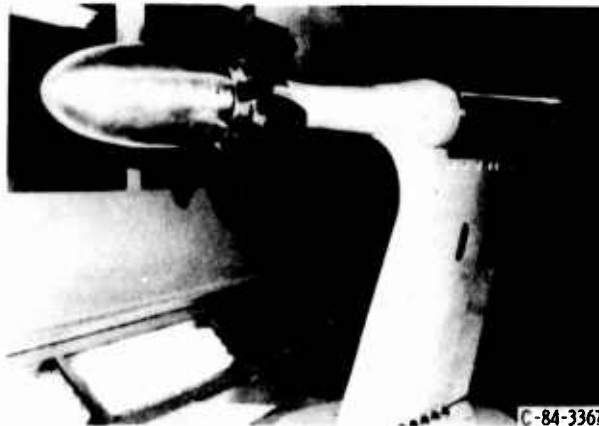


Figure 35. - Test model of the 16-bladed gearless pusher CR propeller.

COMPORTEMENT DYNAMIQUE D'UN "PROP-FAN"

par

J.M.Besson
Aérospatiale Société Nationale Industrielle
Division Hélicoptères
13725 Marignane Cedex, France

et

D.Petot
O.N.E.R.A.
B.P. 72
92322 Châtillon, France

RESUME

Un programme de recherches sur des hélices de conception nouvelle appelées "PROP-FAN" ou hélice pour avion rapide est mené en FRANCE. Dans ce cadre, des études d'un tel système sont effectuées et l'essai d'une maquette dans la grande soufflerie transsonique S1 de Modane est prévu en 1985. On présente ici les études aéroélastiques et dynamiques effectuées à ce jour sur cette maquette. Les particularités géométriques de la pale ont conduit à revoir les méthodes de calculs habituelles qui utilisent une aérodynamique bidimensionnelle et un modèle élastique fondé sur l'hypothèse poutre. Les différents essais et calculs effectués avec des éprouvettes représentatives de la pale de soufflerie montrent que les méthodes par éléments finis sont les plus adaptées pour déterminer les déformées statiques, et les modes à l'arrêt des pales. Un processus permettant le calcul des modes propres en rotation des pales (fréquences, déformées, amortissement) ainsi que le calcul de stabilité de l'hélice sur son support est exposé. Il met en jeu les méthodes par éléments finis, une méthode aérodynamique tridimensionnelle, et les méthodes habituellement utilisées pour le calcul des rotors d'hélicoptère.

1. INTRODUCTION

- Depuis quelques années, la propulsion par hélices connaît un "renouveau". Celui-ci est dû en grande partie à l'augmentation du prix du pétrole. De ce fait l'hélice qui, comparée au turboréacteur, présente jusqu'à environ Mach 0,6 un rendement meilleur est attractive. De plus des études menées aux ETATS UNIS depuis les années 1974 montrent qu'il est possible grâce à une géométrie appropriée d'étendre jusqu'à Mach 0,8, vitesse de croisière de la plupart des avions longs ou moyens courriers, le domaine où l'hélice reste performante. Ce nouveau concept appelé "PROP-FAN" ou hélice pour avion rapide doit permettre, à Mach 0,8, des gains de consommation de l'ordre de 10 à 25 % par rapport aux turboréacteurs.
- En FRANCE un programme de recherche sur le thème de l'hélice rapide mené par les services officiels français a débuté en 1982. Ce programme comprend le développement de méthodes de calculs et l'essai en soufflerie d'une maquette d'hélice (diamètre 1 m, 12 pales). Cet exposé présente les travaux effectués à ce jour concernant l'étude aéroélastique et dynamique de cette maquette : détermination des déformées et contraintes statiques, détermination des modes propres (fréquences, déformées, et amortissement) de l'hélice seule "Isolée", étude de la stabilité de l'hélice montée sur son support.

Ce type d'hélice présente des caractéristiques spécifiques notablement différentes de celles des hélices classiques. On peut citer entre-autres :

- La forme géométrique (grand nombre de pales à faible allongement),
- Une aérodynamique tridimensionnelle transsonique.

Ces différences obligent à revoir les méthodes de calcul traditionnelles.

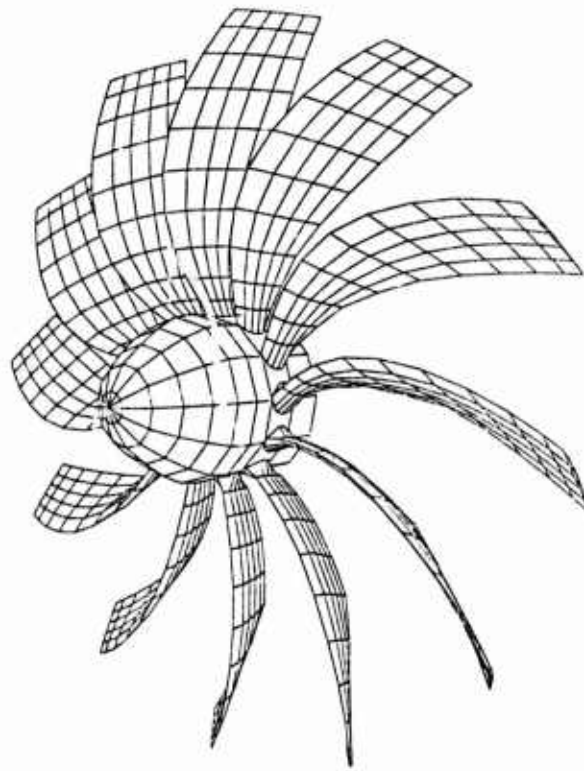


Fig. 1 Hélice "PROP-FAN"

2. PRESENTATION SUCCINCTE DES METHODES DE CALCUL UTILISEES POUR L'ETUDE DE LA MAQUETTE

On peut distinguer deux types de méthodes :

- Celles fondées sur des hypothèses restrictives mais bien adaptées aux calculs aéro-élastiques. Les principales hypothèses sont l'assimilation de la pale à une poutre et la prise en compte d'une aérodynamique bidimensionnelle. Ce type de modèle est habituellement utilisé pour les pales d'hélicoptère.
- Celles fondées sur le concept d'éléments finis beaucoup plus général mais qui ne prennent pas en compte les variations des efforts aérodynamiques résultant des déformations de la pale, variations qui sont à l'origine de l'amortissement des mouvements ou de certaines instabilités.

Ce paragraphe présente pour chaque type deux méthodes, en précisant leurs principales hypothèses, et le type de modélisation effectué pour l'étude de la maquette.

2.1. Méthode "Hélice Isolée"

. GENERALITES

La méthode consiste d'une part à calculer la déformée statique des pales sous l'action des efforts d'inerties et aérodynamiques, d'autre part à analyser les mouvements possibles autour de cette déformée (modes "naturels" ou encore modes "propres" avec les amortissements). Il n'est pas tenu compte en général des mouvements du centre du moyeu de l'hélice, ce centre étant supposé fixe. Cette méthode utilisée à l'Aérospatiale donne en général des résultats satisfaisants pour les rotors en composite d'hélicoptère [1].

. HYPOTHESES DE BASE

- La pale est assimilée à une "poutre"; autrement dit, toute section droite de la pale avant déformation reste plane après déformation (les sections droites étant les sections perpendiculaires à la ligne des 25 % des profils). Une conséquence directe est que la déformée d'une section est entièrement déterminée à partir de la déformée d'un de ses points (déplacements u , v , w et rotations θ_1 , θ_2 , θ_3).

- Le calcul des charges aérodynamiques se fait en admettant une aérodynamique quasi stationnaire et des caractéristiques de profil bidimensionnelles. Un calcul des vitesses induites, des incidences et des nombres de Mach locaux permet la détermination des coefficients aérodynamiques C_x , C_z , C_m par interpolation dans les fichiers de polaires de profils. Nous verrons au paragraphe 4 comment un fichier de polaire "Tridimensionnel équivalent", représentatif du fonctionnement de l'hélice a été généré.
- Hypothèse des petits mouvements autour de la position d'équilibre.

. MODELISATION

Une ligne caractéristique est la ligne des 25 % des profils qui, pour une hélice de "PROP-FAN" est courbe. Cette ligne sert de base à la définition de la pale. Ainsi le long de celle-ci sont précisés les types de profil, leurs positions angulaires, et les caractéristiques mécaniques (masse, raideurs, centre de gravité, inertie ...).

Ces caractéristiques sont calculées en considérant des matériaux homogènes "équivalents" pour le cas des stratifiées.

. RESOLUTION

En appelant X le vecteur constitué par les déplacements $(u, v, w, \theta_1, \theta_2, \theta_3)$

et les efforts (forces f_1, f_2, f_3 et moments m_1, m_2, m_3) le système à résoudre est du type $\frac{\partial x}{\partial r} = \text{fonction de } (x, \frac{\partial x}{\partial t}, \frac{\partial^2 x}{\partial t^2})$, r étant l'abscisse de la section considérée.

La première étape du calcul est la détermination de la déformée statique qui est indépendante du temps ($\frac{\partial x}{\partial r} = \text{fonction de } x$).

La méthode utilisée est non linéaire et s'effectue par une intégration numérique avec plusieurs itérations successives jusqu'à obtenir l'égalité entre les forces de liaison de la pale et les forces extérieures (centrifuges et aérodynamiques) dans la position déformée.

Puis le calcul des modes se fait en linéarisant les équations (hypothèse des petits mouvements) et en découpant la pale en tronçons successifs.

La solution générale est du type $\sum k_j e^{r_j t} Y_j$. Les r_j sont des nombres complexes qui s'écrivent $r_j = \alpha_j + i w_j$ où w_j est la pulsation propre du mode j et α_j le facteur d'amortissement ($\alpha_j < 0$). Les valeurs (α_j, w_j) s'obtiennent par une méthode numérique itérative.

2.2. Méthode "Hélice sur son support"

. GENERALITES

Un programme général a été mis au point qui calcule les équations globales de l'hélice sur sa nacelle et qui donne accès à un nombre important de résultats : traction de l'hélice, déformée de pale, modes et stabilité du montage. D'utilisation simple et rapide, il peut rendre de grands services pour les calculs de stabilité, sans toutefois donner avec précision la traction de l'hélice et les déformées des pales.

. HYPOTHESES DE BASE

- Le mouvement de l'axe de l'hélice est décomposé suivant la base des p modes de la nacelle (calculés ou mesurés).
- Le mouvement des pales est lui aussi décomposé suivant la base de ses n modes à l'arrêt (calculés ou mesurés). Il y a la possibilité de rentrer les modes de pale en rotation. Le programme ne peut rendre compte des effets du raidissement de la pale amenés par sa déformée sous l'action des forces centrifuges (qui se traduit par une raideur géométrique supplémentaire).

Cet effet s'introduit automatiquement si l'on utilise les modes en rotation. Il est négligeable pour une pale droite.

- La pale est assimilée à une poutre. Pendant la rotation et la vibration elle est supposée ne pas s'allonger.
- L'aérodynamique est linéaire, la portance étant en chaque tranche proportionnelle à l'incidence. Une aérodynamique non plus linéaire mais "affine" issue de méthodes plus sophistiquées peut également être prise en compte (voir paragraphe 4.3.) sous la forme :

$$C_z = C_{z_0} + \frac{\partial C_z}{\partial \theta} \cdot \Delta\theta \quad \Delta\theta \text{ Variation du calage de la section considérée.}$$

- Les équations utilisent les variables multicycliques de pales et les $(p + 3n)$ modes obtenus sont vus dans le repère fixe (les modes les plus élevés ne sont pas significatifs).

. MODELISATION

Les caractéristiques des pales sont introduites de façon similaire à la méthode "Hélice isolée" et les modes de pale le sont par la donnée de la déformée de la ligne des 25 % des profils. Le support est caractérisé par ses modes : fréquences, amortissement, masse généralisée et vibrations du centre de l'hélice.

. RESULTATS

Le programme détermine la traction de l'hélice, la déformée de la pale, les modes du montage et sa stabilité. L'utilisation est extrêmement aisée dans le cas de l'utilisation des modes de pale à l'arrêt, puisque toutes les configurations de vol sont directement accessibles. L'utilisation des modes de pale en rotation, plus précise, nécessite le calcul préalable de ces modes avec une autre méthode pour chaque configuration de vol.

Le programme calcule les équations du système complet sous la forme :

$$M_{\text{meca}} \ddot{X} + (A_{\text{meca}} + A_{\text{aéro}}) \dot{X} + (K_{\text{meca}} + K_{\text{aéro}}) X = F_{\text{meca}} + F_{\text{aéro}}$$

dans laquelle chaque matrice est accessible.

M = matrice de masse ; A = matrice d'amortissement et de couplage gyroscopique

K = matrice de raideur ; F = $\frac{\partial W}{\partial X}$ (travail des forces extérieures)

méca : provient de la mécanique ; Aéro : provient de l'aérodynamique.

Plusieurs formes d'instabilités peuvent être mises en évidence :

- flottement de précession des modes du bâti pour lequel la référence [5] a montré la sensibilité à la flexibilité des pales,
- flottement par couplage des modes récessifs de pale - mode du bâti,
- flottement classique battement-torsion mais qui dépend de l'aérodynamique utilisée

Par contre les flottements dus à l'action aérodynamique d'une pale sur l'autre (action type compresseur) échappent à l'analyse.

Ce programme a été utilisé et a prédit de façon satisfaisante les instabilités d'hélices et de rotors classiques d'hélicoptère à pale droite, à partir des modes de pale à l'arrêt [5].

2.3. Code de calculs SAMCEF (*)

. GENERALITES

Ce code de calcul développé par l'université de LIEGE est largement utilisé dans l'aéronautique. Il permet le calcul des fréquences propres de la pale en rotation dans le vide, et des déformées et contraintes statiques de la pale soumise aux efforts d'inertie et aérodynamiques. (Il s'agit de calculs "Hélice isolée").

* SAMCEF : Système d'Analyse des Milieux Continus par Eléments Finis

. MODELISATION

Dans le cadre des études d'hélice, les différentes modélisations ont été effectuées avec un seul type d'élément. Cet élément tridimensionnel isoparamétrique a été pris de degré 2 suivant les 3 directions. Le nombre de points de Gauss utilisés pour calculer en particulier la matrice de raideur est de 2 suivant les 3 directions. Pour les zones d'épaisseur faible, ce même élément a été utilisé en supposant un comportement de coque épaisse.

L'anisotropie des matériaux est prise en compte par la donnée d'une matrice 6×6 reliant les déformées et les contraintes.

Afin de diminuer la complexité du problème, les zones constituées par plusieurs plis ont été modélisées par un seul élément en épaisseur (cas du revêtement de la pale de soufflerie). Dans ce cas, les caractéristiques sont celles d'un matériau équivalent (voir ci-dessous).

. CARACTERISTIQUES DES MATERIAUX

Il est nécessaire de connaître les caractéristiques tridimensionnelles des matériaux. Celles-ci ont été déterminées théoriquement à l'aide d'une méthode d'homogénéisation par éléments finis [2]. Les caractéristiques calculées d'un pli ou d'un empilage sont celles d'un matériau homogène anisotrope équivalent. Un ajustement des valeurs a été effectué par identification entre des mesures de fréquences propres d'éprouvettes parallélépipédiques constituées des matériaux à étudier et des calculs par éléments finis correspondants.

. CALCULS

Les matrices suivantes sont calculées :

- K_0 matrice de rigidité linéaire
- $K(\sigma)$ matrice de rigidité géométrique (précontraintes dues aux efforts centrifuges de la position d'équilibre)
- M matrice de masse.

Les systèmes classiques sont ensuite résolus :

- en statique $F = (K_0 + K(\sigma)) q$
- en dynamique $(K_0 + K(\sigma)) \ddot{q} + M \dot{q} = 0$

2.4. Code de calcul ASTRONEF

. GENERALITES

Ce code de calcul développé par l'ONERA a aussi de multiples utilisations dans l'aéronautique. L'élément utilisé est spécifiquement adapté aux pales en composite ainsi qu'aux effets dus à la vitesse de rotation. Ainsi la modélisation nécessite peu d'éléments. Les calculs que l'on peut effectuer sont les mêmes qu'avec SAMCEF.

. MODELISATION

L'élément utilisé est un élément multicouche isoparamétrique et est dérivé d'un élément de coque épaisse. La pale est représentée en épaisseur par deux couches d'éléments, les degrés de liberté du modèle étant restreints à la surface moyenne de la pale.



Les fonctions d'interpolation sont quadratiques en surface et linéaires en épaisseur. Les éléments ainsi définis peuvent comporter plusieurs couches de matériaux composites quelconques.

. CARACTERISTIQUES DES MATERIAUX

De la même façon que pour SAMCEF le calcul se fait avec la théorie de l'homogénéisation mais le nombre de coefficients utilisés est moins important (E_1, E_2 les modules d'Young dans le plan de la pale, V_{12}, V_{21} les coefficients de Poisson, G_{12}, G_{13}, G_{23} les modules de Coulomb).

. CALCULS

Les calculs sont identiques à ceux menés avec le code de calcul SAMCEF mais une matrice supplémentaire K_C est déterminée. Cette matrice antisymétrique tient compte des effets de couplage dus aux forces de Coriolis. En dynamique le système à résoudre devient : $(K_0 + K(\sigma)) q + Kc\dot{q} + M\ddot{q} = 0$

3. CALCULS ET ESSAIS D'ÉPROUVETTES

Trois pièces appelées "éprouvettes" de forme comparable à la pale de la maquette de soufflerie ont été réalisées :

- massive en matériau homogène : Dural (voir Fig.2),
- massive en matériau composite : Carbone ,
- avec un longeron, un revêtement en carbone et un remplissage en mousse (Technologie similaire à la pale de la maquette de soufflerie).

Les essais et les calculs portent sur la détermination des fréquences propres de ces éprouvettes à l'arrêt, ainsi que les déformées sous des efforts statiques, le pied de pale étant encastré.

3.1. Modélisations effectuées par éléments finis

. CODE ASTRONEF

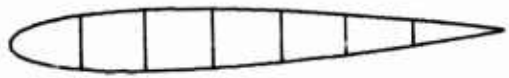
Les maillages pour les trois éprouvettes sont du type :



(élément multicouche ($\sigma_z \approx 0$))

. CODE SAMCEF

Pour les éprouvettes massives les maillages sont du type :



(éléments tridimensionnels)

(Voir Fig.3)

Pour l'éprouvette avec remplissage en mousse :



longeron mousse revêtement ($\sigma_z \neq 0$)

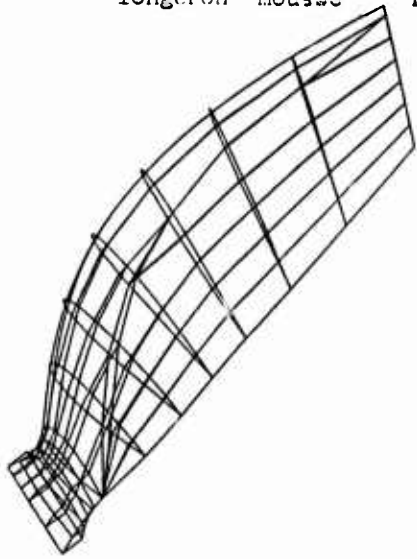


Fig. 3 : Modélisation éprouvette Dural
(SAMCEF)



Fig. 2 : éprouvette Dural

3.2. Méthode expérimentale

Les déformées modales pale encastrée ont été mesurées avec précision. Elles ont été déterminées par interférométrie, la pale étant excitée sur le mode à caractériser. Un faisceau laser est réfléchi par des pastilles rétrodiffusantes collées sur la pale (Voir Fig. 5). Les mesures ont été effectuées en chaque point suivant cinq directions. Leur combinaison permet le calcul des composantes du vecteur déplacement suivant les trois axes du trièdre de référence. Un exemple des déformées obtenues en essais est donné Fig. 4.

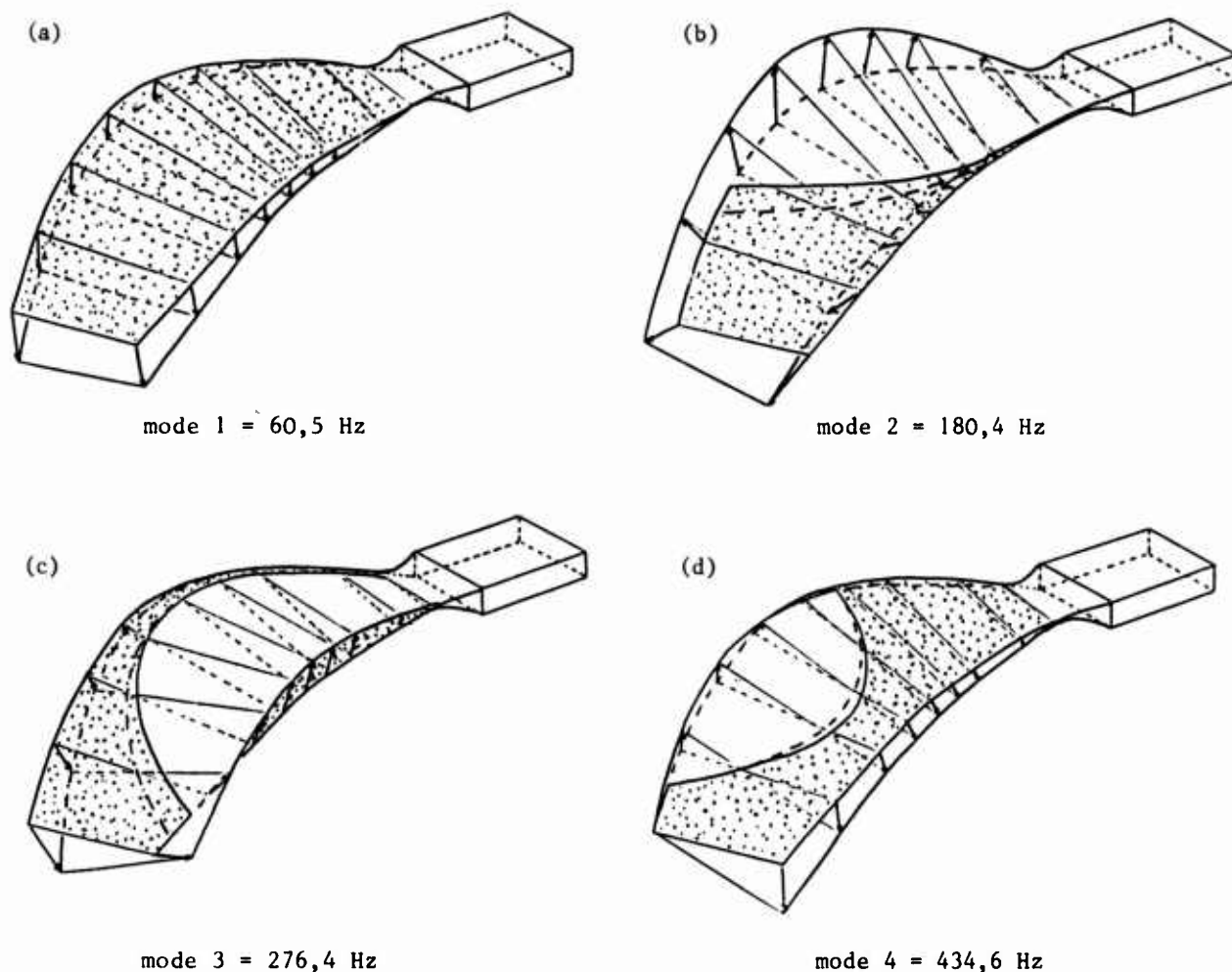


Fig 4 (a), (b), (c), (d) : Modes propres obtenus expérimentalement avec l'éprouvette en Dural. La partie visible de la pale au repos, est tachetée, et la partie visible de la pale dans une position extrême de la vibration est en blanc. Les traits continus sur la pale représentent l'intersection de ces deux pales, et les pointillés la ligne des points où la composante du vecteur vibration normale à la surface est nulle. On constate que les modes, mis à part le premier, ont des déformées complexes qui sont des combinaisons de mouvements de flexion et de torsion (pour les pales droites les modes sont en général nettement découplés). Cette particularité se retrouve sur l'ensemble des pales étudiées et elle est due à la forme en plan et au vrillage important.

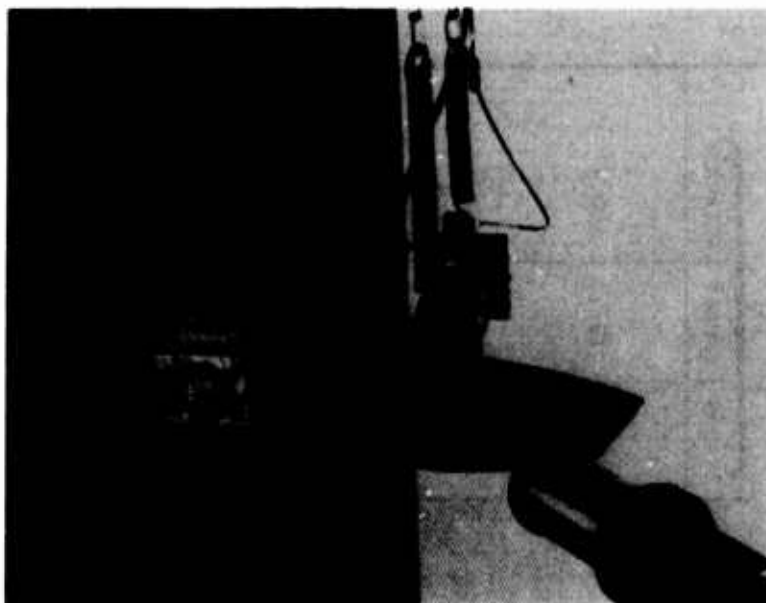


Fig. 5 : montage d'essai avec une éprouvette en stratifié carbone.

Des essais statiques ont été effectués. L'éprouvette est soumise à son extrémité à une force ponctuelle et les déplacements suivant les trois directions en différentes sections ont été relevés avec un palpeur.

3.3. Comparaisons calculs - essais

L'ensemble des calculs poutre (méthode "hélice Isolée"), des calculs par éléments finis (code SAMCEF et ASTRONEF) et les valeurs expérimentales des fréquences se trouvent dans le tableau ci-après.

Pour le calcul des éprouvettes en matériaux stratifiés, un paramètre fondamental est l'orientation des fibres. Un écart de quelques degrés modifie la valeur des fréquences et peut changer notablement les déformées modales. Or les outillages nécessaires à la fabrication de ces éprouvettes n'ont pas été prévus pour assurer une telle précision. De ce fait, cette incertitude peut être à l'origine de certains écarts calculs-mesures.

De l'ensemble de ces calculs et essais, les conclusions suivantes peuvent être tirées:

- Tout d'abord, et c'est une constatation, il est difficile de calculer les fréquences d'une telle pale. Ainsi pour les pales d'hélicoptère en composite, droites, les quatre premiers modes à l'arrêt sont en général obtenus à moins de 3 %, alors que pour ce type de pale la précision est de l'ordre de 10 %.
- La forme de la pale est sans doute à l'origine des écarts constatés avec la méthode poutre. En effet ces écarts sont du même ordre de grandeur entre la pale en dural où seule la forme intervient (matériau homogène) et la pale en carbone et mousse où la forme et l'anisotropie des matériaux interviennent.
- Les méthodes par éléments finis sont les plus adaptées à ce type de pale, mais il est nécessaire de connaître avec précision les orientations des fibres. Pour la modélisation, des éléments de coque épaisse multicouche peuvent être suffisants. Les calculs en rotation de ces éprouvettes avec ASTRONEF ont montré que la matrice de couplage K_c peut être négligée (déphasage inférieur au degré).

EPROUVETTE MASSIVE DURAL				EPROUVETTE MASSIVE CARBONE				EPROUVETTE CARBONE + MOUSSE			
Calculs				Calculs				Calculs			
Essais	Poutre		ASTRONEF	Essais	Poutre		ASTRONEF	Essais	Poutre		ASTRONEF
	SAMCEF				SAMCEF				SAMCEF		
60,5	58,4	63,3	64,6	89,3	78,4	82,3 (9 %)	93,8	103	102,5	107,3	106,4
180,6	165,5	190,9	191,6	160,3	176,5	170,7	170,0	220	210,4	204	203,4
276,4	216,4 (28 %)	281,1	288,9	365,6	238 (54 %)	364,8	359,2	328	373	348	368
434,6	390,9	468,2 (7 %)	472,3 (8 %)	390,6	400	386	415,2 (6 %)	490	662 (26 %)	550 (11 %)	433 (12 %)

Unités : Hertz ; Les valeurs entre parenthèses donnent pour chaque méthode l'écart maximal essais - calculs.

Les mêmes conclusions peuvent être déduites des essais statiques (voir Fig. 6). Un bon accord existe entre la méthode éléments finis (ASTRONEF) et les résultats expérimentaux. Et la méthode poutre ("hélice isolée") fournit des valeurs erronées surtout pour les déplacements suivant l'envergure de la pale. Toutefois aux 25 % de la corde, les déplacements les plus importants sont calculés de façon satisfaisante.

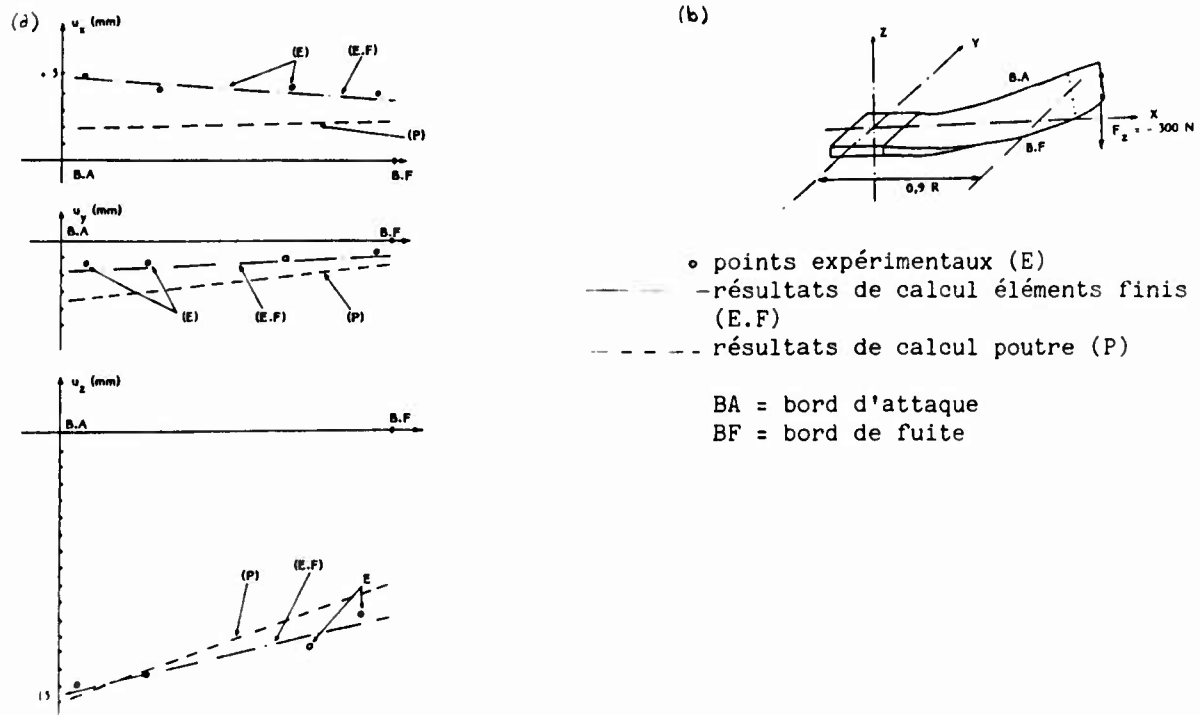


Fig. 6 (a), (b), : déplacements mesurés de la section 0,9 R sous un effort statique (épreuve en dural)

4. CALCUL DE L'HELICE MAQUETTE

4.1. Présentation du montage d'essai

La future hélice expérimentée appelée HT3, a un diamètre de 1 m et comporte 12 pales. Le support du montage d'essai est placé assez loin de l'hélice afin d'éviter des perturbations aérodynamiques (voir Fig. 7). Ce montage largement instrumenté (capteurs de pression, jauges, etc ...) permettra d'effectuer des recoupements calculs-mesures jusqu'à Mach 0,8 et une vitesse de rotation de 5200 Tr/mn.

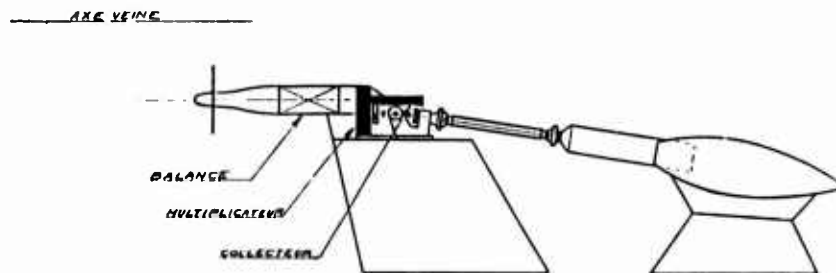


Fig. 7 : Montage d'essai de l'hélice HT3 à la soufflerie transsonique S1 de Modane

4.2. Principe de calcul

Suite aux calculs et essais sur éprouvettes, le processus suivant est prévu :

- Calcul de l'aérodynamique spécifique de l'hélice,
- Détermination des modes propres de la pale dans le vide et de sa déformée statique sous les efforts centrifuges et aérodynamiques par les méthodes éléments finis,
- Prise en compte par les modèles poutre des résultats précédents. Les caractéristiques mécaniques de la pale du modèle "hélice isolée" sont ajustées afin de retrouver les fréquences calculées dans le vide par éléments finis et après introduction de l'aérodynamique, de vérifier la déformée statique. Dans le modèle "hélice sur son support", les modes de la pale calculés par éléments finis sont introduits.
- Calcul avec les méthodes poutre des caractéristiques propres en rotation de "l'hélice isolée" et de "l'hélice sur son support".

4.3. Détermination de l'aérodynamique

La méthode de calcul qui s'est avérée la plus adaptée à ce type d'hélice est la méthode appelée "Surface Portante" [3]. Ses principales caractéristiques sont :

- Théorie tridimensionnelle,
- Hypothèse fluide parfait compressible.

Cette méthode fournit les répartitions de pression intrados et extrados directement utilisables par les éléments finis, et par intégration la répartition de C_z jusqu'au nombre de Mach de 0,63, limite de validité de la méthode. (Les répartitions jusqu'à Mach 0,8 ont ensuite été déterminées en supposant une évolution de la différence de pression intrados et extrados similaire à celle des ailes en attaque oblique). Pour les calculs dynamiques avec le vent, l'idée de base est de fournir aux programmes poutre suivant la déformée de la pale à l'instant considéré, les coefficients C_z que l'on obtiendrait en figeant la géométrie à cet instant avec la méthode "surface portante". Pour des petits mouvements autour de la position d'équilibre, la variation de C_z provient pour une grande part de la déformée en torsion. Ainsi, autour d'une configuration de base, plusieurs calculs de pale déformée en torsion ont été effectués et ont mis en évidence l'existence d'une loi linéaire liant les variations de C_z aux variations du vrillage :

$$C_z = C_{z_0} + \frac{\partial C_{z_0}}{\partial \theta} \cdot \Delta\theta \quad \text{avec } \Delta\theta \text{ variation du calage de la section considérée}$$

et $\frac{\partial C_{z_0}}{\partial \theta} = a(r)$ r abscisse de la section.

A chaque type de déformée en torsion de la pale correspond une fonction $a(r)$ mais ces fonctions se sont révélées très voisines (hormis la zone du pied de pale mais qui a peu d'influence sur les calculs dynamiques). Ainsi l'introduction de l'aérodynamique dans les programmes "hélice isolée" et "hélice sur son support" est possible, le ΔC_z local de la section r ne dépendant que de la déformée $\Delta\theta$ de cette même section.

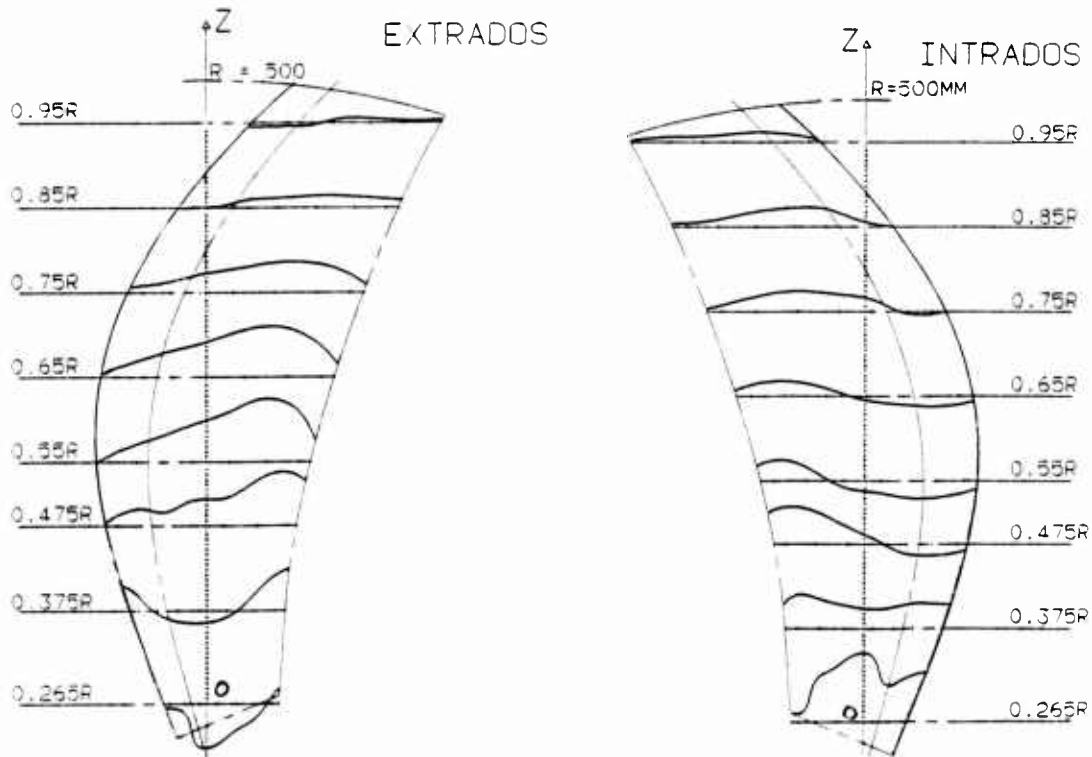
En final, pour une configuration de vol, on dispose de la répartition de C_z en envergure correspondant à la position d'équilibre ainsi que ses variations possibles autour de cette position.

4.4. Calcul de la déformée statique et de l'état de contrainte de la pale

Le code SAMCEF a été utilisé pour ces calculs (voir le maillage Fig. 9). L'aérodynamique est issue de la méthode "Surface Portante" et correspond à la position d'équilibre de la pale en rotation. Les différences de pression entre l'intrados et l'extrados ont été appliquées sur chaque face des éléments constituant l'intrados de la pale. Les performances d'une telle hélice étant particulièrement sensibles à la loi de vrillage des pales, celle de la pale au repos a été modifiée afin d'obtenir en rotation la loi adéquate. Pour ce faire plusieurs calculs itératifs éléments finis - "Surface Portante" ont été nécessaires. D'autre part la répartition massique et l'orientation des fibres ont été déterminées afin de minimiser les déformées en rotation.

Ainsi des calculs linéaires ont pu être possibles, les déformations n'étant pas trop importantes : un écart maximal de 10 % sur les contraintes et les déformées a été mis en évidence entre un calcul linéaire et un non linéaire (Au cours de la montée en régime, le calcul non linéaire effectue des calculs successifs des efforts centrifuges, des matrices de raideur ...).

Le calcul des contraintes (Voir Fig. 8) a permis de montrer la bonne tenue de cette pale aux efforts extérieurs. On note dans la partie courante, côté intrados, une zone importante en compression, mais avec des niveaux faibles.



Suivant O.Z : une graduation = 1 daN/mm²

Fig. 8 : Courbes des contraintes du revêtement de la pale HT3.
($\Omega = 4800$ tr/mn, Mach = 0,8)

4.5. Calculs dynamiques

Les modes propres en rotation dans le vide ont été déterminés avec SAMCEF
(Voir Fig. 9, 10, 11).

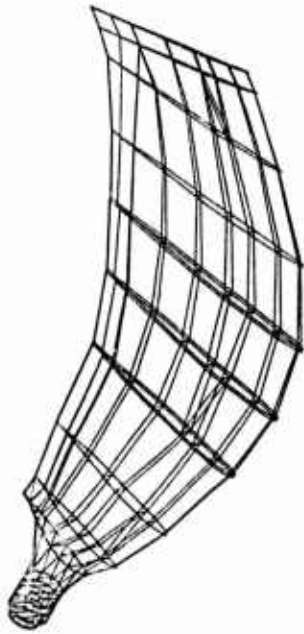


Fig. 9 : Maillage de la pale HT3
(SAMCEF)

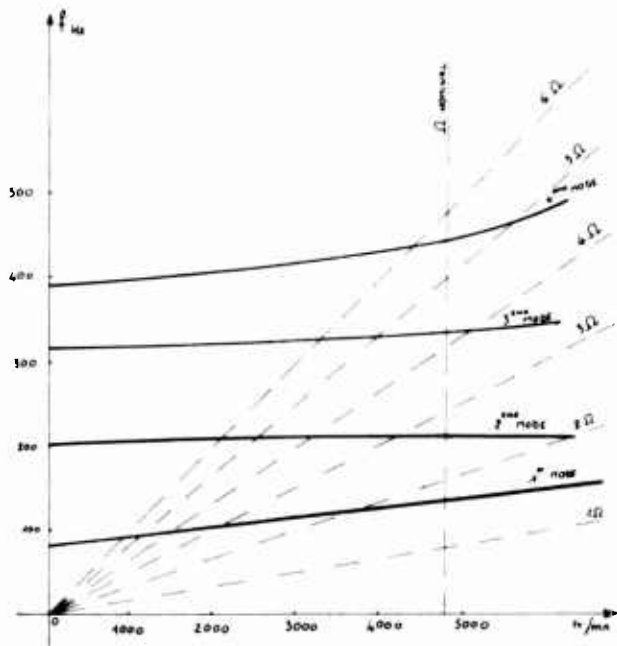
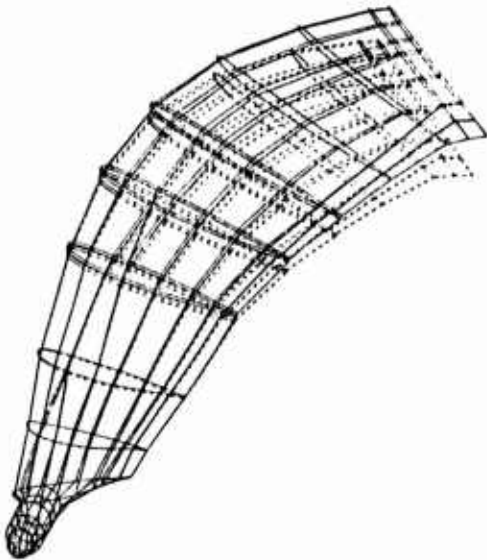


Fig. 10 : Diagramme de fréquences de la pale HT3 dans le vide

(a)



(b)

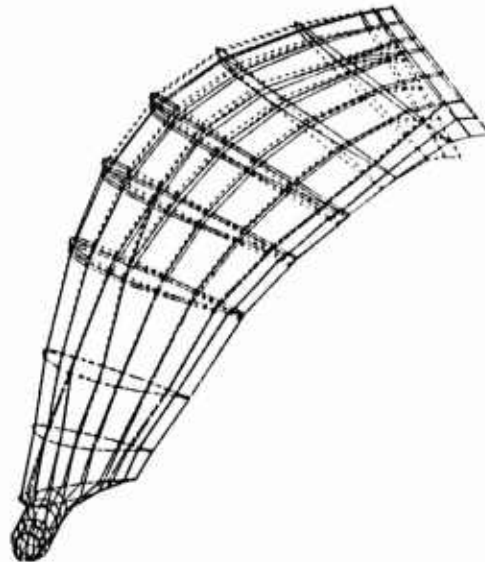


Fig. 11 (a), (b) : Exemples de déformée de modes en rotation dans le vide de la pale HT3
(modes 1 et 2)

Le diagramme des fréquences (voir Fig. 10) laisse présager un bon comportement dynamique ; au régime nominal, les modes ne se croisent pas, et ne croisent pas des multiples du régime, et ce tout particulièrement pour le premier mode.

L'ensemble des différents programmes nécessaires aux calculs dynamiques jusqu'à Mach 0,8 fonctionne et des vérifications et mise au point sont actuellement en cours. Néanmoins, les premiers résultats des modèles "hélice isolée" et "hélice sur son bâti" ne font pas apparaître d'instabilité.

5. CONCLUSIONS

Comme nous venons de le voir pour la maquette de soufflerie, les particularités géométriques d'une hélice de "PROP-FAN" compliquent nettement les calculs de prédiction (déformés et contraintes statiques, modes propres en rotation de la pale et de l'hélice sur son support). On ne peut pas utiliser telles que, les méthodes habituelles de calcul des hélices classiques ou des rotors d'hélicoptère. Le processus de calcul envisagé qui fait appel à différents programmes, aérodynamiques, éléments finis ..., a permis de calculer l'hélice de soufflerie. Les essais de cette hélice permettront d'évaluer pour chaque phase du processus la justesse des hypothèses. Ce n'est qu'après cette évaluation puis éventuellement des modifications que cette démarche sera validée. Toutefois son inconvénient majeur est sa complexité car l'utilisation de plusieurs codes de calcul importants est nécessaire. Mais le développement d'une méthode de calcul spécifique à ce type d'hélice ne pourra se faire que lorsque l'ensemble des hypothèses admissibles et l'ensemble des paramètres fondamentaux à prendre en compte seront bien connus.

Références

- [1] J.P. LEFRANCQ and B.MASURE (SNIAS)
 "A complete method for computation of blade mode characteristics and response in forward flight".
 "7th European Rotorcraft and Powered lift Aircraft Forum" - Garmisch - Partenkirchen, Sept. 1981.
- [2] MM. BEGIS et DUVAUT (INRIA)
 "Homogénéisation par éléments finis du module de comportement élastique des matériaux composites"
 Forum "Tendances actuelles en calcul des structures" - 1,2,3 Février 1982 Sophia Antipolis
- [3] J.M. BOUSQUET (ONERA)
 "Méthodes aérodynamiques utilisées en France pour l'étude des hélices pour avion rapide"
 55th meeting of the fluid dynamics panel symposium - 1,4 Octobre Toronto Canada
- [4] L. SIMON
 "A set of finite elements developed for the dynamic computation of composite helicopter blade".
 International conference on composite structures - Paisley (G.B) - September 1981.
- [5] J. COSTES - J. NICOLAS - D. PETOT
 "Etude de la stabilité d'une maquette de convertible" - Recherche Aérospatiale n° 1982-6.

**PERFORMANCE EVALUATION OF FULL SCALE
PROPELLERS BY WIND TUNNEL TEST**

by

D.J. Barber

Senior Engineer Advanced Design
The de Havilland Aircraft of Canada, Limited
Downsview, Ontario, Canada M3K 1Y5

SUMMARY

A large propeller test facility has been developed by de Havilland Aircraft of Canada for the National Research Council of Canada nine metre wind tunnel. The facility is described along with the propeller test rig features and associated drive system. Propeller performance measurement philosophy, test procedures and calibrations are discussed.

In cooperation with Dowty Rotol Ltd. and Hartzell Inc. two currently available propeller designs were tested. The two 8.5 foot diameter propellers suitable for a DHC Twin Otter size of aircraft provided an evaluation of alternative airfoil applications: the ARA-D series and NACA 16 series. Results have demonstrated propeller efficiencies close to manufacturers estimates for clean well finished blades. Forward and reverse thrust testing results are discussed with respect to aircraft application.

Prediction methods tend to over estimate efficiencies due to hardware features encompassing blade finish, blade-root/spinner juncture, spinner openings, erosion protection and deicer equipment. Typical results illustrating the influence on propeller performance of such features are given.

LIST OF SYMBOLS

C_T	= Thrust Coefficient - thrust/ $\rho n^2 d^4$	β	= Blade Angle
C_P	= Power Coefficient - power/ $\rho n^3 d^5$	ρ	= Freestream Density
d^p	= Propeller Diameter	η	= Efficiency - $J \times C_T / C_P$
J	= Advance Ratio - V/nd	σ	= ρ/ρ Standard Atmosphere
n	= Propeller Rotational Speed	μ	= micro
r/R	= Radius/Maximum Propeller Radius		
V	= Freestream Speed		

INTRODUCTION

Energy conserving aircraft design has highlighted the need for airframe manufacturers to develop a better understanding of propeller technology. Propeller technology improvements such as new airfoil types require assessment prior to application. Aircraft flight tests which are expensive do not readily determine propeller performance due to installation losses. Generally a propeller manufacturer supplies uninstalled estimated performance data to an airframe manufacturer neglecting the effects of protuberances and holes. These additional losses are both poorly documented and difficult to assess.

New experimental test facilities are required to validate propeller performance estimates for current designs and to test technology improvements proposed for future project aircraft. In the case of de Havilland Aircraft of Canada this has led to the development of a large scale test rig for accurately measuring propeller performance. Testing at large scale was considered desirable to avoid adverse Reynolds number effects and to allow accurate representation of design features which influence installed performance. The nine metre wind tunnel (30 x 30 foot working section) at the National Research Council of Canada in Ottawa provided a suitable environment for full scale propeller testing. The maximum tunnel speed is 105 knots which allows propeller design conditions for aircraft takeoff and climb to be accurately represented. Cruise conditions are simulated non-dimensionally at reduced propeller rotational speed although full compressibility effects are not present in this case.

Design and manufacture of the propeller test rig during the period 1979 - 1981 culminated in initial tests during 1981 to commission the facility. In cooperation with Dowty Rotol Ltd. and Hartzell Propeller, two currently available propeller designs were tested in 1981 - 1982. The Dowty Rotol propeller design utilizes the recently developed ARA-D airfoil sections. The Hartzell propeller currently used on the de Havilland Twin Otter aircraft utilizes the NACA 16 series airfoils. Both propellers are 8.5 feet in diameter. In 1982 an 8 foot diameter scaled Hamilton Standard propeller design for the de Havilland Dash 8 successfully completed performance assurance tests. Recently testing was carried out on two 8 foot diameter propellers utilizing de Havilland developed airfoils. Development of the propeller test rig and tunnel systems during this time has produced a useful facility which is available to other organizations.

Several aspects of the test work are covered within this paper. The facility is described along with rig design features and drive system. Measurement philosophy and procedure required to determine propeller characteristics are discussed. Propeller performance measurements are summarized for the Dowty Rotol and Hartzell propellers. Characteristic differences arising are discussed. The influence of details such as blade finish, spinner holes, external deicer boots and erosion shields are examined.

1. PROPELLER TEST RIG SPECIFICATION

During 1978 criteria for the rig power, torque and rotational speed were developed by examining current and future propeller applications. Meanwhile Pratt and Whitney Aircraft of Canada (PWC) looked at modifications required to convert existing power

turbine designs to cold compressed air drive.

A match of desirable running requirements and turbine/gearbox hardware for a propeller drive unit was established. PWC then modified an existing turbine to have cut back blading on the turbine combined with a modified inlet guide vane ring. The final design was aided by the availability of heated air at the nine metre wind tunnel. Heated air allowed turbine operation without aerodynamic restrictions and avoided potential icing problems on the nacelle exterior arising from sub-zero exhaust temperatures in humid conditions.

The highly modified turbine/gearbox was adapted from a PT6A-27 unit which provided appropriate gearing and torque levels for the test rig. The drive unit allows large scale testing of propellers absorbing up to 850 SHP or 2360 ft. lb. of torque at rotational speeds up to 2000 rpm.

2. PROPELLER TEST RIG FEATURES

The propeller test rig is shown installed in the 30 x 30 foot wind tunnel section in Figure 1. A streamline nacelle, 2.375 ft. in diameter containing the propeller drive unit is mounted centrally in the tunnel at the top of a main supporting strut. The propeller plane is about 11 feet ahead of the main strut.

A schematic of the test rig geometry is shown in Figure 2. The propeller and forward section of the nacelle are sting mounted from the main strut which in turn is mounted on a six component mechanical balance housed beneath the tunnel floor. Location of the propeller is close to the virtual centre of the balance to minimize interactions between components and to allow testing at the high yaw angles.

The nacelle aft section is supported by a main strut fairing which is bolted to the tunnel floor and is therefore "off balance". The aerodynamic drag of the nacelle aft section is therefore eliminated from the propeller thrust measurement.

The propeller drive unit is a compressed air driven turbine/gearbox assembly built by Pratt and Whitney Canada, Figure 3. Drive air for the unit is piped into the rig via a steam heat exchanger. The mechanical balance houses a low restraint air cross-over system to provide compressed air "on balance". Compressed air passes along the support sting from the main strut to enter an adjustable pressure reducer within a supporting plenum for the turbine unit. Typically at maximum power the turbine unit consumes 18 lb. of air per second at a 3 to 1 pressure ratio.

A remote lubrication system incorporating a water cooler built for this application allows continuous running of the turbine gearbox unit. The inlet of the turbine is a simple bellmouth with a centre body, located within the plenum downstream of the pressure reducer.

Exhaust air from the turbine flows out through a standard A-27 twin ported exhaust into the nacelle interior. The exhaust passes downstream inside the nacelle around the strut head to a single large diameter convergent nozzle at the rear of the nacelle. The nozzle is "on balance" and protrudes from the nacelle afterbody fairing which terminates with a semi-labyrinth seal.

The propeller is mounted on a standard PT6A-27 output shaft and runs at selected pitch angles. Blade pitch is adjusted manually through a barrel mechanism which allows simultaneous adjustment of all blades.

3. PROPELLER PERFORMANCE EVALUATION

The propellers were run at designated blade angles through a range of rotational speeds at specific forward speeds. Propeller performance was based on measurements taken instantaneously by the data acquisition system which provided on line real time data reduction. Several calibrations were required prior to the propeller testing, related to tunnel velocity, nacelle tare drag and residual exhaust thrust.

The nacelle forebody, the spinner and propeller were mounted together on the main balance so the buoyancy forces arising from interaction between these components were eliminated by mutual cancellation. This approach represents an important simplification relative to other test rigs in which the individual components are separately assessed.

The net thrust determined also includes the deficit due to the increased forebody skin friction drag caused by the slipstream and swirl effects. Independent estimates have judged this additional drag to be negligible.

The mechanical balance measured overall thrust and torque in one of two ranges. Low levels of thrust and torque are measured with the balance set in the V/STOL range where maximum levels measurable are 750 lb. and 1125 ft. lb. respectively, whilst maximum levels of 3000 lb. and 4500 ft. lb. can be measured on the normal range, when a 50% bias is added to the full scale ranges. The balance accuracy is equal or better than 0.1% of full scale.

Propeller rotational speed was measured using a magnetic speed pickup driven via a gearbox accessory drive.

Three base pressure measurements were made to establish base forces occurring within the nacelle afterbody between the forward nacelle section and the final nozzle plane. A simple semi-labyrinth seal attached to the afterbody and surrounding the final nozzle served to minimize any flow within the nacelle afterbody.

The most significant base pressure exists on the contracting exhaust duct upstream of the final nozzle. The two remaining pressure forces occur about the main strut head on the forward and aft diaphragms of the main nacelle structure. A differential transducer was used to determine the differential pressure between diaphragm faces and an absolute measurement of the forward diaphragm pressure was made relative to the wind tunnel ceiling static.

4. TUNNEL VELOCITY MEASUREMENTS

Propeller efficiency is directly dependent on forward speed and its measurement accuracy. A tunnel speed measuring system employing a ceiling static in the plane of the propeller has been shown to yield a freestream velocity independent of propeller loading and only requires correction for the solid blockage effect of the propeller and nacelle.

A pitot static calibration probe at the location of the propeller was used to calibrate a ceiling static in the same plane, and referenced to a total pressure at the exit of the settling chamber.

Calibration both with the tunnel empty and rig installed with and without propeller blades mounted was undertaken which allowed the corrections for blockage to be isolated. Blockage effects for nacelle and propeller were found to be less than 1% or less than 1/2% on forward speed.

During propeller test work velocity measurements using the ceiling static were compared with the reference tunnel system measurements with the appropriate classical corrections for a thrusting propeller and blockage applied. Except at high thrust loadings and during reverse thrust testing close agreement was normally obtained.

5. EXHAUST CALIBRATION

The exhaust nozzle contains an array of five pitot probes at the centroids of five equal areas and connected to individual transducers referenced to the tunnel ceiling static. Calibration of the exhaust nozzle was carried out with the propeller off and wind-off to avoid a nacelle external drag contribution. The turbine was removed for this calibration and replaced by a dummy unit to ensure flow path simulation. To simulate the turbine pressure drop a pressure reducing plate was inserted in the air supply line.

The nozzle thrust calibration was obtained by a linear regression fit correlating the pressures of the five pitot probes with the wind tunnel balance thrust measurements. During propeller performance tests the exhaust thrust was determined using this calibration and pressure measurements within the nozzle.

6. NACELLE DRAG TARE

The nacelle tare drag was determined prior to mounting the propeller. A dummy spinner without any cutouts for the blades was fitted to the forward nacelle and the drag determined at maximum tunnel speed.

7. PERFORMANCE CALCULATIONS

The net propeller thrust was computed on line along with shaft power and propeller efficiency. The steps in the thrust calculation are:

Exhaust Thrust	T_E	=	$C_1 P_E + C_2$
Nacelle Drag	D/q	=	$[D_M + P_E A_N + \Sigma (K_1 B_1 \dots)]/Q_M$
Propeller Net Thrust	T_N	=	$T_M - T_E + (D/q) Q_M - \Sigma (K_1 B_1 \dots)$
where:	P_E	=	average exhaust pressure
	D_M	=	balance measured drag
	A_N	=	exhaust area
	$K_1 B_1$ etc.	=	base forces
	T_M	=	balance measured thrust
	Q_M	=	tunnel dynamic pressure
	$C_1 C_2$	=	constants from thrust calibration.

The shaft power input to the propeller, SHP, was determined from the balance measured torque, T_Q , and the propeller rotational speed n , i.e.:

$$\text{SHP} = 2\pi \cdot n \cdot T_Q / 550$$

Tunnel velocity and density were calculated using compressible flow relations from the measured tunnel temperature, tunnel ceiling static pressure, and total pressure at the settling chamber exit plane.

Calculation of propeller coefficients and advance ratio in the conventional manner allowed propeller efficiency to be determined.

8. PROPELLER HARDWARE

Propeller performance tests were carried out on two 8.5 ft. diameter propellers supplied by Hartzell (U.S.) and Dowty Rotol (U.K.). The Hartzell propeller is an established design utilizing traditional NACA 16 series airfoils and is currently used on the DHC-6 Twin Otter aircraft. The three bladed propeller (blade designation T102820+0) has an activity factor of 115 and an integrated lift coefficient of 0.55, Figure 1. Maximum power absorption was 850 SHP at 2000 rpm with a torque limit greater than the PTR gearbox limit of 2360 ft. lb.

The Dowty Rotol propeller design utilizes the recently developed ARA-D airfoil sections which provide improved lift/drag ratios over a wider operating range than the NACA series 16 airfoils. Higher maximum lift coefficients allow narrower chord blades to

be used which reflect in weight and some performance improvements. A three bladed propeller (blade designation 3102 B080-351-1) with an activity factor of 80 was tested, Figure 4. The maximum design speed was 1750 rpm with maximum design power of 750 SHP and a torque limit of 2250 ft. lb.

Both propellers were finished to production standard with polyurethane paint, but without deicer boots. Surface finish was smooth, with a measured roughness in the 40 - 60 μ in range. The performance tests were carried out in this as supplied configuration. Additional tests with simulated surface roughness used strips of tape wound around the blade. Some limited tests with add on deicer boots, actual and simulated, established typical performance penalties. Full scale polyurethane add on erosion strips were also tested. Closure of the spinner cutouts were investigated using shim and/or metal tape to seal the blade root/spinner surface interface.

9. PROPELLER TEST RESULTS

Since the nine metre tunnel is a closed circuit type the propeller tends to drive the tunnel when the wind is off. However, near static tests at ≤ 15 knots illustrate the maximum thrust and shaft power achieved at near optimum blade angles, Figure 5. Note that the propellers have similar thrust capability up to the design limit of the Dowty propeller. The Hartzell propeller, with higher design limits, achieved a maximum thrust close to measuring capability of the balance.

Low blade angles were tested at low speeds representative of an aircraft in the ground roll phase of takeoff. Power coefficient data was strongly influenced by forward speed and propeller three dimensional effects at high rotational speeds (lowest advance ratio at each forward speed), Figure 6.

Propeller efficiency variation with advance ratio collapsed into unique curves for each blade angle, Figure 7. Wind off data, with the propeller circulating the tunnel air were included.

A full range of propeller blade angles was tested at 70 and 103 knots forward speed. At high power coefficient for a given advance ratio the power absorbed increased with forward speed. The data indicates a sensitivity to local blade Mach number effects coupled with three dimensional effects due to propeller rotational speed, Figure 8.

Although the above effects were present, a single efficiency map for the Hartzell propeller was derived using data from the test range of forward speed, Figure 9. Efficiency contours were smoothed and generally fell within 0.1 percent of experimental data. It is noted that the efficiency contours are acute angled in nature reflecting a narrow maximum lift/drag ratio range of operation for NACA 16 series airfoils. Although a maximum efficiency of 90% was measured, the high advance ratio required to use this performance demands aircraft design cruise speeds ≥ 300 knots. This propeller whilst providing good low speed performance, therefore has a high cruise design point. It is noted that the efficiency maps presented were developed from test data obtained at forward speeds up to 103 knots where compressibility effects on the blades are minimal. Furthermore, at substantially higher cruise flight conditions compressibility losses occur and cruise flight efficiencies may be significantly different from those shown.

Similar trends in power coefficient data were exhibited by the Dowty Rotol propeller. The increase in power absorption near maximum rotational speed was not as marked due to lower relative blade section Mach numbers as a result of the lower design tip speed. A single efficiency map covering the forward speed range of blade angle was also derived for the Dowty Rotol propeller, Figure 10. Characteristics of the contours were different to the NACA 16 series airfoil propeller. The efficiency contours were steeper leading to higher efficiency levels particularly at climb conditions or high disc loadings. The 89% efficiency contour is substantially broader and extends to lower advance ratios which may benefit aircraft long range cruise conditions.

At low advance ratios and disc loadings the propeller closely matches the higher activity factor Hartzell blade. Furthermore, performance at increasing disc loading reflects the high efficiency of the ARA-D sections.

Propeller performance at aircraft design points allow a rapid assessment of a potential propeller design application. However, if the propeller design and aircraft requirements are unrelated the merits of alternative designs are very much subject to the aircraft design points selected. Typical propeller efficiencies for a utility STOL aircraft application show that differences between Hartzell and Dowty propellers are small.

Aircraft Design Point	Propeller Efficiency		
	Hartzell	Dowty	DHC
Takeoff	0.560	0.560	0.600
Takeoff, WAT	0.720	0.720	0.730
Maximum Climb	0.755	0.760	0.765
Maximum Climb	0.815	0.838	0.845
Maximum Cruise	0.860	0.868	0.880
Long Range Cruise	0.865	0.870	0.882

The table includes results for a de Havilland propeller design recently tested. This propeller design offers improved performance at the takeoff and cruise points, although the propeller was not specifically designed for this application. When higher disc loadings are utilized both Dowty and de Havilland designs show substantial benefits over a broad flight envelope.

10. PERFORMANCE COMPARISON WITH ESTIMATES

Propeller test rig results have demonstrated efficiencies close to propeller performance estimates. A comparison of test results with estimates for selected aircraft design points is given in the following table.

Condition	η Ratio – Measured/Estimate	
	Dowty Rotol	Hartzell
Ground Roll	1.001	0.961
Second Segment Climb		
Sea Level	1.009	0.993
8000 Feet	0.983	0.979
Enroute Climb	0.989	0.990
High Speed Cruise	1.007	1.015
Long Range Cruise	1.006	1.018

When performance estimates are exceeded by experiment additional laminar flow under three dimensional conditions may have occurred. Compressibility losses occurring in actual cruise flight conditions also give high ratios of measured/estimated performance. Effects of blade finish, spinner juncture, and blade roots can result in efficiency overestimation.

The propeller test rig results have demonstrated repeatability within 0.2% on propeller efficiency depending on thrust levels. Back to back testing of a variety of blade root modifications have successfully isolated features giving improvements as low as 0.3% in efficiency.

11. REVERSE THRUST OF PROPELLERS

Reverse thrust provides braking which is particularly useful during adverse ground roll conditions. STOL aircraft design requires high levels of braking, both mechanical and/or aerodynamic. Test data were acquired for both Hartzell and Dowty propellers at blade angles through to nominal maximum negative values. Propeller speed was limited by tunnel flow conditions which caused unstable test rig operation depending on wind speed. Longitudinal oscillation of the rig occurred at high reverse thrust levels.

Although a large body of test data was acquired through fine pitch into reverse thrust, typical data is presented to illustrate important trends. Figure 11 shows reverse thrust levels obtained, in engineering units, for both Hartzell and Dowty designs at typically maximum reverse blade angles. The lower blade activity factor of the Dowty Rotol propeller provides less reverse thrust at these conditions where the blade has significant flow separation. However, the propeller design speed was achieved without severe rig instability indicating less abrupt stalling characteristics.

12. EFFECT OF DESIGN DETAIL FEATURES

Production propellers usually feature openings in the spinner shell allowing the propeller blade to operate from reverse pitch to feather. Large holes may be required depending on blade design. In addition, slotting to the spinner trailing edge to allow easy removal is common. At low blade angles, typical of aircraft takeoff and climb, the effect of sealing the spinner was either small or negligible. In cruise the propeller blade operates generally near maximum efficiency. Typically a 1% or more gain in efficiency was shown, Figure 12.

Blade finish can vary significantly depending on protective or erosion coatings used. Variations from 50 μ inches to 250 μ inch finishes have been experienced. Surface roughness for both propellers fell in the 45 - 60 μ inch range representing a very smooth finish. A tape was applied chordwise on the blade camber and face sides to simulate a blade with a rough coating. Typically the tape surface roughness was measured as 150 - 200 μ inches. Figure 13 illustrates an efficiency loss from 1 to 1½ percentage points over a range of blade angles. At takeoff and climb conditions where the blade operates below peak efficiency a 1 percentage point loss was shown. In cruise a 1½ percentage point loss was typical.

Externally mounted electrical deicer boots are common installations to propeller blades. Radial coverage can vary depending on requirements, but typical installations terminate at 40 - 75% of blade radius. A high radial coverage installation representative of a large commuter aircraft was simulated using layers of smooth tape wrapped around the leading edge. Protrusion of the boot was about 0.030 inches, which produced an aft facing step about 0.4% chord deep. Typical losses were 1 to 3 percentage points in efficiency, Figure 14. Maximum loss occurred near peak efficiency for all blade angles indicating a large loss of laminar flow conditions across the blade.

Full scale Goodrich deicer boots with tapered trailing edges extending to 42% blade radius, were bonded to one propeller. The effect of these shorter deicer boots was negligible, differences being within the tolerance of measurements, Figure 15. These results indicate that protruberances on the inner part of the blade may be tolerated. In addition, anti-erosion strips were bonded to the blades, extending from 42% radius to the blade tip. The 1 - 2% efficiency loss was indicative of a loss of laminar flow on the outer part of the blade. Discontinuities in blade profile such as a step, particularly on the outer part of the blade, can therefore cause a significant loss of performance. Feathered trailing edges on anti-erosion strips may avoid performance losses providing the resulting profile is smooth, such that premature flow transition is avoided.

13. CONCLUSIONS

The development of a large scale propeller test rig for the NRC nine metre wind tunnel has provided a valuable tool for studying propeller performance.

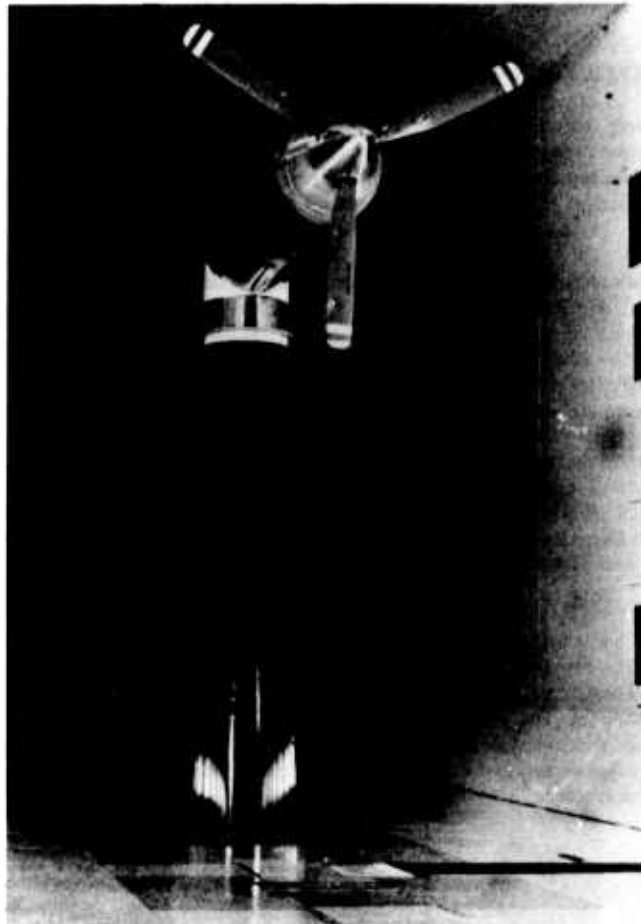
Test results have demonstrated propeller efficiencies close to performance estimates indicating that estimation methods can be successful. Prediction of blade angle to absorb power is not so accurate due to three dimensional flow effects. Usually prediction methods over estimate performance as they do not include installation features.

14. REFERENCES

1. Bocci, A.J. - "A New Series of Airfoil Sections Suitable for Aircraft Propellers," Aeronautical Quarterly, Volume 28, February 1977.
2. Borst, H.V., Elliot, D.A. Jr. and Sand, E. - "Summary of Propeller Design Procedures and Data," Volumes I - III, USAAMRDL Technical Report 73-34A, AD-774831, November 1973.
3. Rohrback, C. and Wainauski, H.S. - "Aerodynamic Characteristics of an Advanced Technology Propeller for Commuter Aircraft," AIAA-81-1565, July 1981.
4. Hoerner, S.F. - "Fluid Dynamic Drag," United States of America, S.F. Hoerner, 1965, pp. 1-1 to 20-18.
5. Pope, A. - "Wind Tunnel Testing," Second Edition, United States of America, John Wiley & Sons, Inc., 1954, pp. 1 to 511.

15. ACKNOWLEDGEMENTS

This work was jointly funded by the National Research Council of Canada, the Transport Research Centre of Transport Canada, and the de Havilland Aircraft of Canada, Limited. Dowty Rotol and Hartzell Propeller contributed propellers for test and permitted test data to be published. The drive unit was developed by Pratt and Whitney, Canada.



PROPELLER TEST RIG INSTALLED IN NRC 9M WIND TUNNEL

FIGURE 1

PROPELLER TEST RIG FOR 30x30 FT WIND TUNNEL

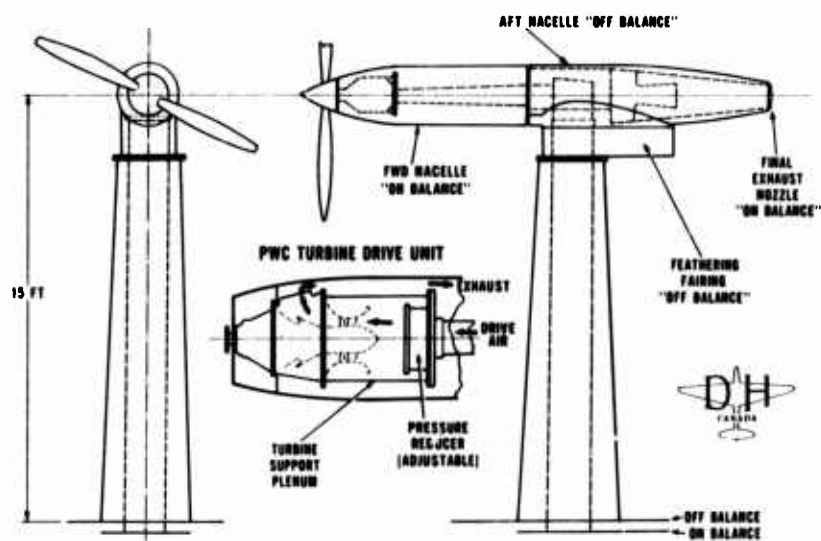
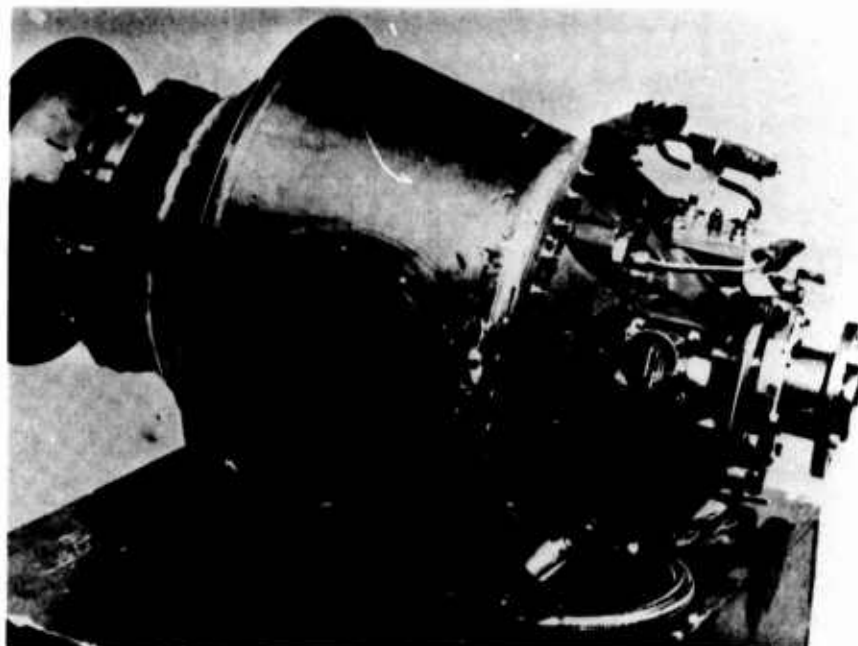
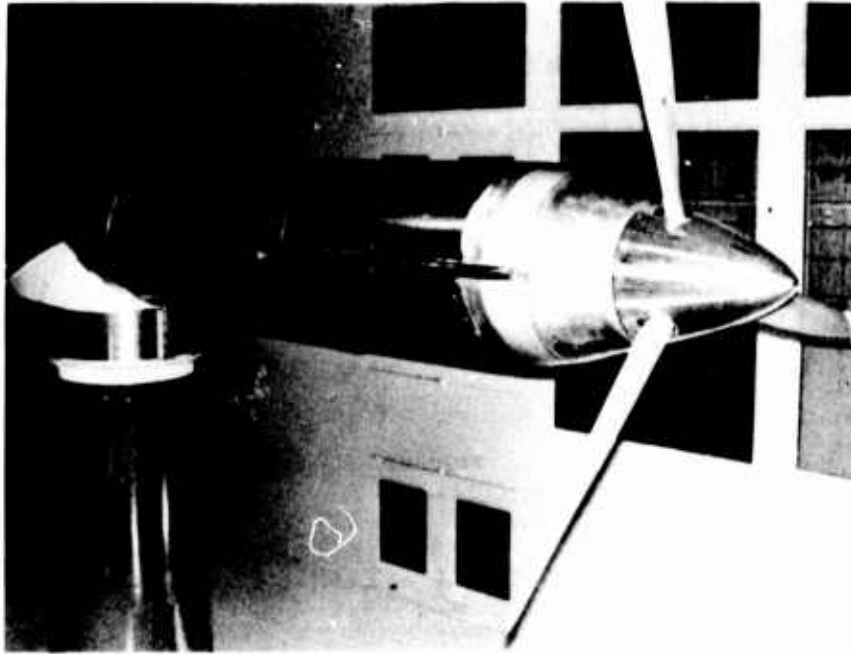


FIGURE 2



P.W.C. AIR DRIVE TURBINE/GEARBOX ASSEMBLY

FIGURE 3



DOWTY ROTOL PROPELLER INSTALLED ON TEST RIG

FIGURE 4

WIND OFF PERFORMANCE

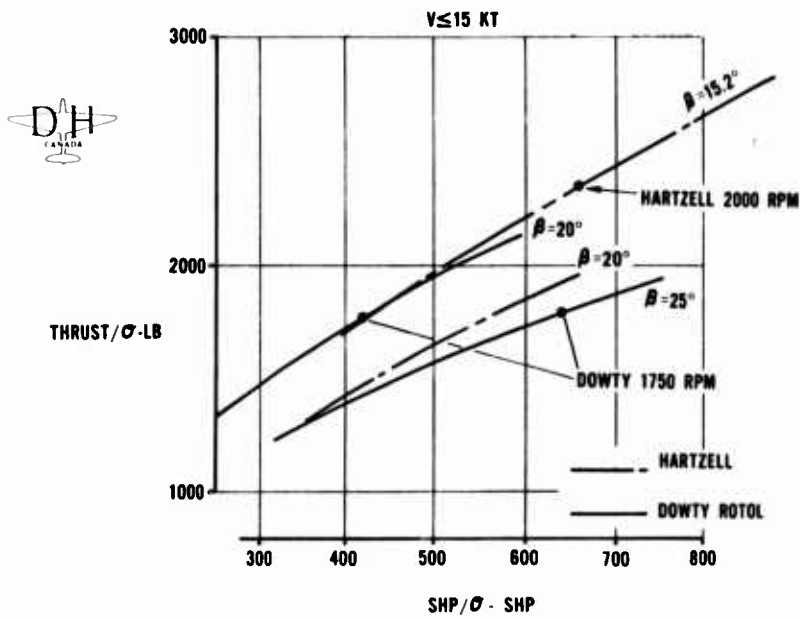


FIGURE 5

EFFECT OF FREESTREAM VELOCITY ON POWER ABSORPTION

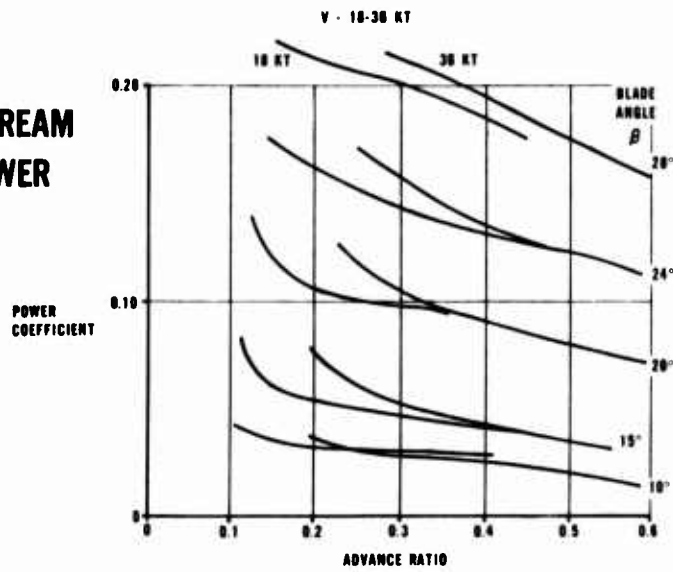


FIGURE 6

PROPELLER EFFICIENCY AT LOW FREESTREAM VELOCITY

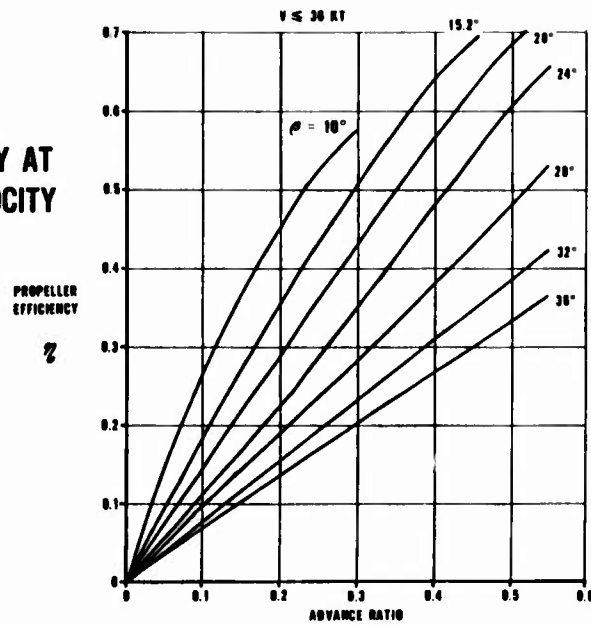


FIGURE 7

POWER COEFFICIENT AT VARIOUS FORWARD SPEEDS

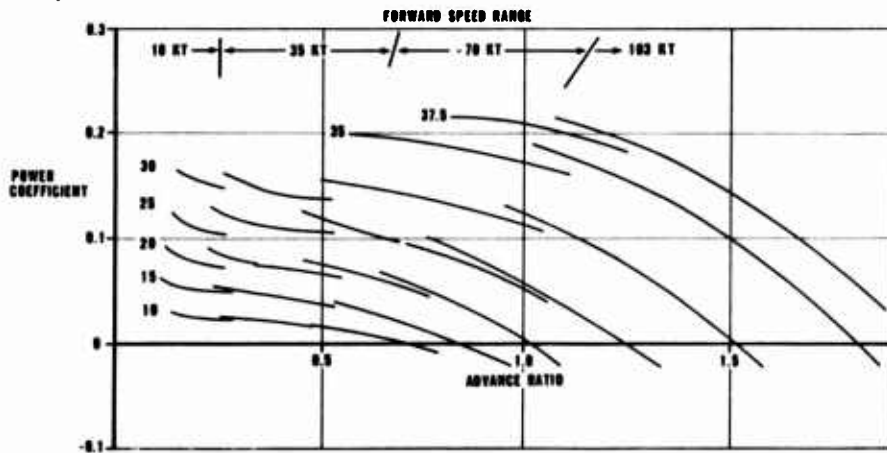


FIGURE 8

PROPELLER EFFICIENCY MAP NACA-16 AIRFOILS

3 BLADE HARTZELL PROPELLER
FREESTREAM MACH NUMBER ≤ 0.15

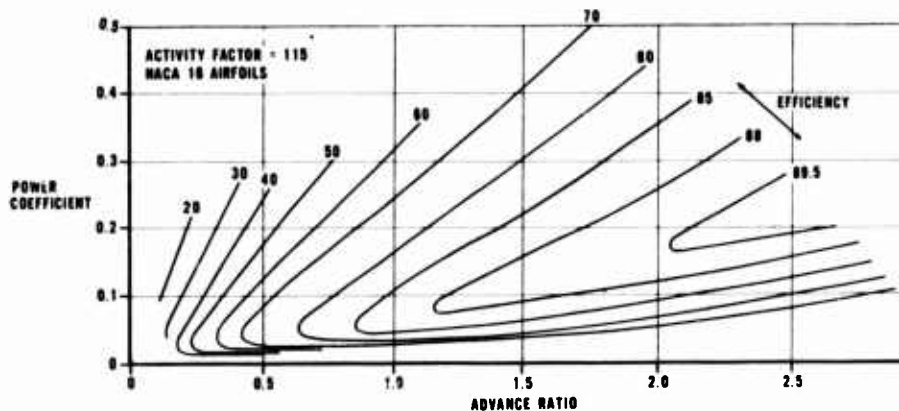


FIGURE 9

PROPELLER EFFICIENCY MAP ARA-D AIRFOILS

3 BLADE DOWTY ROTOL PROPELLER
FREESTREAM MACH NUMBER ≤ 0.15

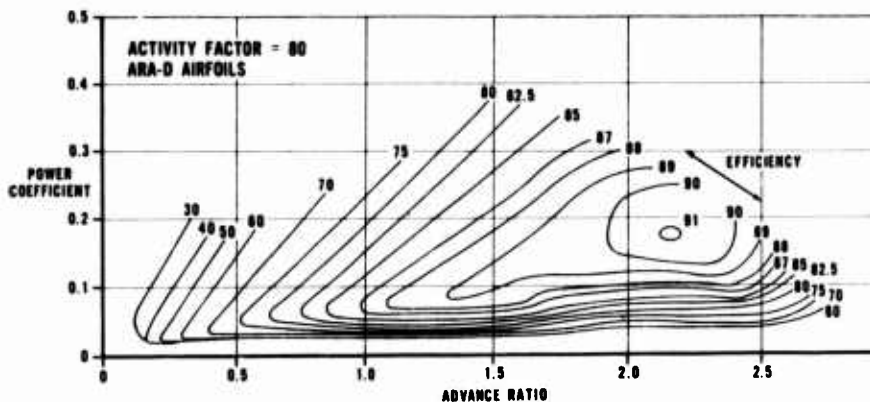


FIGURE 10

REVERSE THRUST COMPARISON

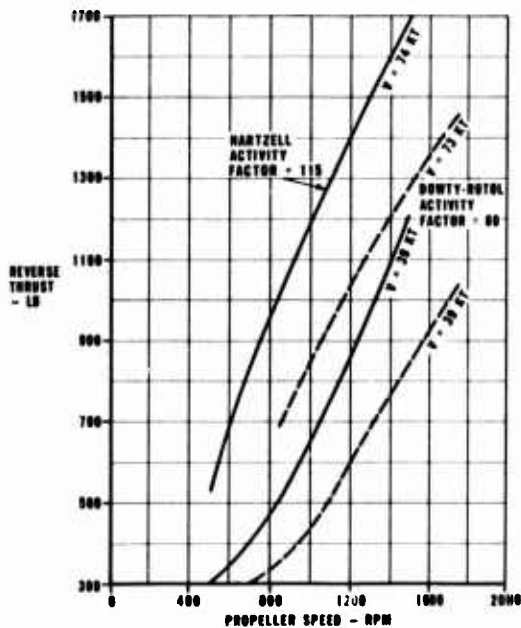


FIGURE 11

EFFECT OF SEALING SPINNER OPENINGS

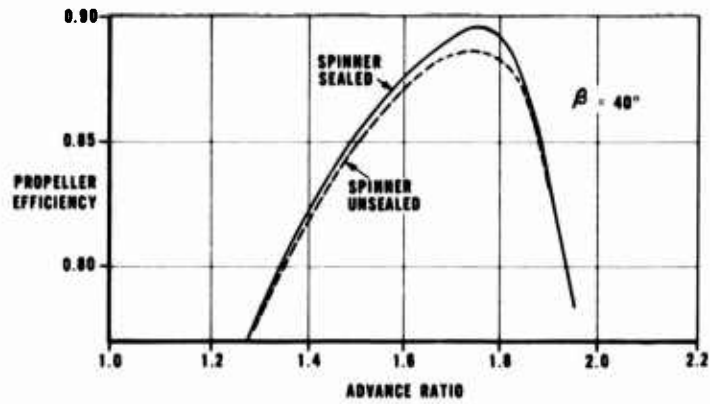


FIGURE 12

EFFECT OF BLADE FINISH ON PROPELLER EFFICIENCY

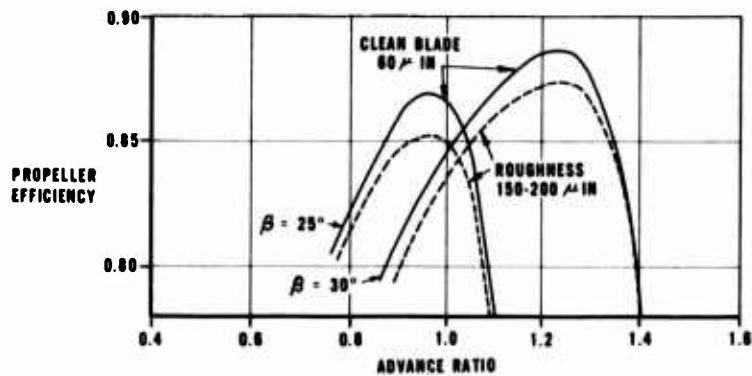


FIGURE 13

EFFECT OF EXTERNAL DEICER BOOTS

BOOT RADIAL COVERAGE $0.75 \gamma/R$

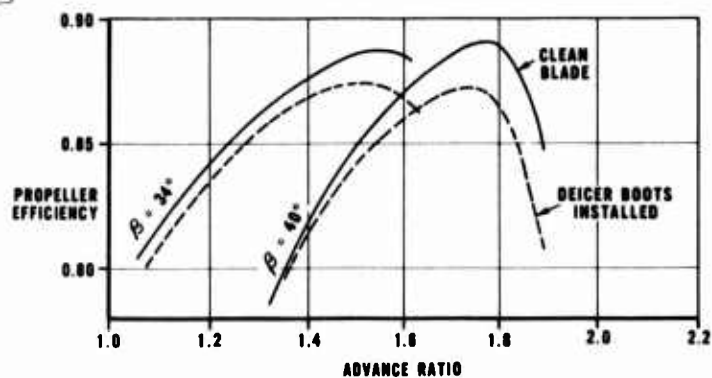


FIGURE 14

EFFECT OF EXTERNAL DEICER BOOTS AND EROSION STRIPS

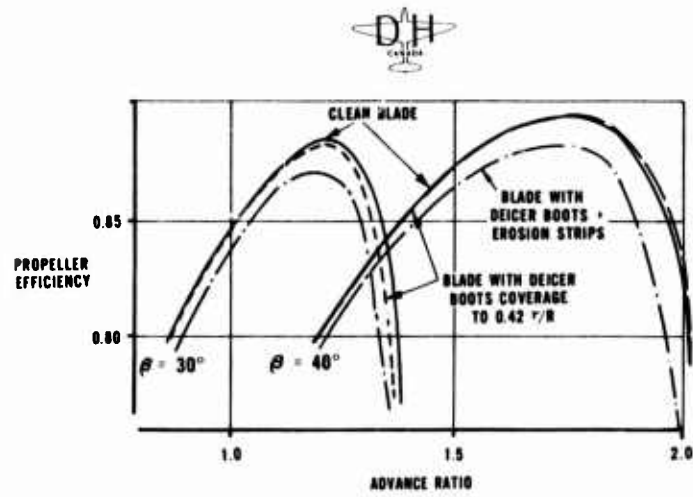


FIGURE 15

ETUDE DU SILLAGE 3D D'UNE HELICE AERIENNE

D. FAVIER, C. MARESCA

Institut de Mécanique des Fluides, LA03 du C.N.R.S.
1, rue Honnorat, 13003 Marseille, FRANCESOMMAIRE

L'analyse du sillage proche et lointain d'une hélice aérienne quadripale opérant à différents paramètres de fonctionnement et suivant différents calages, a été réalisée par anémométrie à fils chauds. Des lois empiriques de synthèse donnant la vitesse de translation axiale des tourbillons marginaux, le taux de contraction radiale du sillage, ainsi que la limite de stabilité du système tourbillonnaire engendré, sont établis en fonction de l'azimut de rotation et pour une gamme étendue de paramètres de fonctionnement allant du régime de traction nulle au régime de traction maximum. Pour un régime de fonctionnement donné, la détermination du champ 3D des vitesses induites est effectuée en différentes sections aval du sillage et conduit à une caractérisation détaillée de la géométrie et de l'intensité tourbillonnaire associées, en fonction de l'azimut et de la distance axiale à l'aval du plan de rotation.

NOTATIONS

A, B	: coefficients intervenant dans la loi de contraction (1)
a_F, b_F	: vitesses axiales induites déduites de la théorie de Froude
α	: angle d'incidence des profils, $\alpha = \alpha_0 + \theta_V$, (deg)
α_0	: calage géométrique à $\xi = 0.7$, (deg)
b	: nombre de pales, $b = 4$
c	: corde des profils, (m)
C	: couple exercé sur les pales, (Nm)
γ	: paramètre de fonctionnement, $\gamma = V_\infty / nD$
Γ_p, Γ	: circulation sur la pale ou dans le sillage, m^2/s
D, D_0	: diamètres de l'hélice et du moyeu ($D = 0.85$ m; $D_0 = 0.14$ m)
ξ	: rayon réduit, $\xi = r/R$
k_1, k_2	: coefficients intervenant dans la loi de translation (3)
λ	: paramètre d'avancement, $\lambda = V_\infty / \omega R = \gamma/\pi$
n	: nombre de t/sec de l'hélice
OXYZ	: système de référence défini sur la Figure 2
P	: puissance fournie à l'hélice, $P = 2 \pi n C$ (watts)
ψ	: azimut de rotation de la pale, (deg)
ψ_b	: azimut de périodicité, $\psi_b = 360^\circ/b$, (deg)
ψ_s	: azimut d'instabilité du sillage lointain, (deg)
r	: abscisse suivant le rayon de la pale, (m)
R	: rayon de l'hélice, ($R = 0.425$ m)
χ	: coefficient de puissance, $\chi = P/\rho n^3 D^5$
S	: aire d'une section droite du sillage, (m^2)
T	: traction exercée sur les pales, (N)
τ	: coefficient de traction, $\tau = T/\rho n^2 D^4$
U, V, W	: composantes de vitesse dans le système OXYZ, Fig.2
V_∞	: vitesse à l'infini amont, (m/s)
ω	: vitesse angulaire de rotation, (rd/s)

INDICES SUPERIEURS

" — "	: grandeurs relatives à la section $\xi = 0.7$
" ~ "	: grandeurs adimensionnées par ωR

INDICES INFERIEURS

o	: grandeurs adimensionnées par V_∞
t	: grandeurs relatives au tourbillon d'extrémité
F	: grandeurs déduites de la théorie de Froude

1. INTRODUCTION

Les méthodes de prévision des charges aérodynamiques subies par les pales d'hélices aériennes, de rotors d'hélicoptères, ou d'éoliennes, sont généralement développées sur la base d'une modélisation géométrique, aussi réaliste que possible, du sillage aval proche ou éloigné du plan de rotation (voir Réf. (1) à (4)).

En ce qui concerne les méthodes de mise en équilibre, basées sur des lignes ou des surfaces portantes représentant la pale et appliquées à des rotors en vol stationnaire^{(5), (6), (7)}, celles-ci font appel à une géométrie initiale figée du sillage qui est prescrite par des lois de synthèse déduites de l'expérience. La mise en équilibre du sillage, sous l'action du champ des vitesses induites résultantes, permet ensuite d'obtenir une optimisation des charges aérodynamiques qui sont plus proches des charges réelles. De même, les méthodes visant à modéliser l'effet de souffle d'une hélice^{(8), (9)}, nécessitent généralement la prise en compte d'une loi de contraction radiale du sillage en fonction de la distance aval, également déduite de l'expérience.

Dans le but de valider et d'améliorer les méthodes de calcul de ce type, la présente étude a donc été entreprise à l'I.M.F.M. avec pour principal objectif la détermination précise des trajectoires tourbillonnaires marginales et des champs 3D de vitesses induites associées à différents régimes de fonctionnement d'une hélice quadripale.

Après avoir décrit les conditions d'essais de l'hélice maquette utilisée et les techniques expérimentales mises en oeuvre pour l'exploration du sillage, la première partie de cette étude est consacrée à l'établissement de lois synthétiques permettant de définir avec précision la géométrie du sillage correspondant à un fonctionnement donné de l'hélice. Cette démarche s'inspire de travaux analogues^{(10), (11)} réalisés sur une grande variété de configurations de rotors (par variations du nombre de pales, de leur forme en plan, du vrillage, ...) dans le cas du vol stationnaire ($V_\infty = 0$), pour lequel la géométrie du sillage associée est alors indépendante du paramètre d'avancement ($\gamma = V_\infty / \omega R$). Dans la seconde partie, les champs de vitesses axiale, radiale et tangentielle, induits en différentes sections aval du sillage proche et lointain ($0.2 \leq Z/R \leq 2.0$), seront plus particulièrement étudiés dans le cas d'un fonctionnement à coefficient de traction τ constant.

2. CONDITIONS D'ESSAIS ET MOYENS DE MESURES

Les essais sont conduits dans la soufflerie subsonique S1 de l'I.M.F.M. à veine ouverte (section elliptique : $3,3 \times 2,2 \text{ m}^2$; courant uniforme $V_\infty \leq 45 \text{ m/s}$) et équipée d'un banc rotor muni de jauges de contraintes qui permettent la mesure globale des efforts aérodynamiques (traction et couple) subis par les pales. Une vue du montage dans la veine d'essais de l'ensemble hélice, mât de support, dispositif de déplacement de sondes, est donné sur la photo de la Figure 1.

L'hélice utilisée est une maquette d'hélice aérienne, quadripale, de type MARQUIS dont les pales sont définies par la série de profils NACA 64A408 caractérisés par des lois de distribution de corde, d'épaisseur et de vrillage suivant le rayon réduit ξ , indiquées sur le tableau ci-après :

ξ	0,176	0,300	0,400	0,500	0,600	0,700	0,800	0,900	1,00
e/c	0,187	0,091	0,085	0,082	0,080	0,073	0,052	0,051	0,051
t = c/R	0,205	0,292	0,280	0,242	0,203	0,174	0,155	0,143	0,134
θ_v (°)	28,3	20,8	15,1	9,66	4,53	0,00	- 4,5	- 8,3	- 11,5

La visualisation de l'écoulement est réalisée par des filets de fumée émis en amont de l'hélice et éclairés par un flash stroboscopique synchronisé avec la fréquence de rotation des pales. Un système caméra-vidéo-magnétoscope permet la visualisation des lignes d'émission issues des extrémités de pale à une phase ωt quelconque de la rotation. Cette technique, également utilisée pour l'étude de sillages de rotors⁽¹²⁾, permet en particulier de visualiser l'écoulement dans des régions très proches des pales ($Z/R < 0,1$) qui ne peuvent être explorées par intrusion de sondes dans l'écoulement.

L'exploration du sillage est effectuée à l'aide d'une sonde anémométrique à fils croisés (DISA 55R51), montée sur un dispositif de déplacement à 3 degrés de liberté, et opérant suivant le principe de recombinaison de deux mesures 2D successives pour restituer la vitesse 3D (voir Réfs. (12), (13)). En un point de mesure quelconque du sillage ($Z/R > 0,1$), les 3 composantes de vitesse axiale W , radiale U , et tangentielle V , peuvent ainsi être déterminées en fonction de l'azimut, dans un système d'axe fixe OXYZ lié à la sonde comme l'indique la Figure 2.

L'acquisition des données azimutales (800 échantillons par période) et leur traitement graphique sont réalisés par l'intermédiaire d'un analyseur multicanaux couplé à un mini ordinateur HP9845B. L'enregistrement est initié à chaque révolution à partir du top fourni par une cellule photoélectrique incorporée au boîtier d'hélice, et s'effectue sur 20 cycles successifs de révolution. Chacune des composantes U , V , W relatives à un point du sillage, peut de plus être représentée par une décomposition en série de Fourier à l'ordre 10 en fonction de l'azimut de rotation.

En ce qui concerne la détermination des trajectoires tourbillonnaires marginales, celle-ci s'effectue suivant une technique au fil chaud développée à cet effet pour l'analyse des sillages de rotors⁽¹²⁾. Dans cette méthode, la sonde préalablement positionnée dans une section aval $Z = Cte$ est déplacée radialement depuis l'extrémité de pale vers le moyeu jusqu'à ce que soit localisé avec précision le passage du tourbillon sur le détecteur (pic de vitesse axiale, maximum de turbulence). Un exemple de profils de vitesse axiale en fonction de la phase ωt , enregistrés au cours d'un déplacement radial de la sonde depuis l'extérieur du sillage ($r/R = 1,01$) vers le moyeu ($r/R = 0,88$), est donné sur la Figure 3, où le tourbillon d'extrémité peut être localisé à $r_t = 0,93R$ et $\psi_t = 72^\circ$.

La trajectoire tourbillonnaire marginale est ainsi complètement déterminée par la mesure des paramètres Z_t , r_t , ψ_t localisant le tourbillon dans le champ aval. De plus, la méthode permet de déterminer pour le sillage lointain un azimuth d'instabilité ψ_s , lié à l'âge du tourbillon, pour lequel le sillage perd sa permanence de forme en raison de la diffusion visqueuse et de l'interaction tourbillonnaire. La précision dans la détermination des coordonnées spatiales du noyau tourbillonnaire est de l'ordre de 1 mm (soit environ $R/400$) par cette technique au fil chaud.

De façon à déterminer les caractéristiques de fonctionnement global de l'hélice, et permette l'analyse des sillages associés à ces différents régimes, les mesures de traction et de couple ont été effectuées dans une gamme aussi étendue que possible du paramètre $\gamma = V_\infty/nD$ obtenu par combinaison des variations de V_∞ et n . La Figure 4 présente les variations du coefficient de traction τ que l'on peut ainsi réaliser en fonction de γ ($0.2 \leq \gamma \leq 1.1$) pour différents calages moyens des pales α_0 ($23^\circ \leq \alpha_0 \leq 32,5^\circ$).

3. TRAJECTOIRES TOURBILLONNAIRES MARGINALES

Selon la méthode précédemment décrite, les lignes tourbillonnaires ont été déterminées au fil chaud pour trois calages de pale distincts $\alpha_0 = 23^\circ$; 27° ; $32,5^\circ$ pour différents paramètres de fonctionnement $\gamma = 0,34$; $0,44$; $0,53$; $0,63$; $0,75$; $0,82$; $0,89$; $0,97$. Les limites de variations de ces deux paramètres (α_0, γ) , et les courbes de fonctionnement $\tau = \tau(\alpha, \gamma)$ de la Figure 4, fixent donc également les limites de validité des lois de synthèse décrites ci-après, qui donnent l'évolution des coordonnées (r_t, Z_t) du tourbillon issu de l'extrémité de pale, en fonction de l'azimut. Ces lois empiriques sont déduites des valeurs expérimentales par une méthode de lissage direct de moindres carrés. Dans certains cas, et pour les régions proches des pales, les mesures au fil chaud ont été doublées et recoupées par les résultats déduits des visualisations.

3.1. Contraction radiale r_t/R

Pour des azimuths croissants allant jusqu'à l'azimut ψ_s d'apparition des instabilités, la coordonnée radiale du tourbillon d'extrémité a été synthétisée par la relation :

$$\left\{ \begin{array}{l} r_t/R = A + (1-A)e^{-\psi/B} \quad \text{pour} \quad 0 \leq \psi \leq \psi_s \\ \text{avec :} \quad A(\alpha_0, \gamma) = P_A(\gamma) + \alpha_0 Q_A(\gamma) \\ \quad \quad \quad B(\alpha_0, \gamma) = P_B(\gamma) + \alpha_0 Q_B(\gamma) \end{array} \right. \quad (1)$$

où les termes dépendant de γ sont des polynômes du second degré de la forme :

$$\begin{array}{ll} P_A = a_0 + a_1\gamma + a_2\gamma^2 & ; \quad Q_A = a'_0 + a'_1\gamma + a'_2\gamma^2 \\ P_B = b_0 + b_1\gamma + b_2\gamma^2 & ; \quad Q_B = b'_0 + b'_1\gamma + b'_2\gamma^2 \end{array}$$

pour l'hélice étudiée et dans la gamme des paramètres considérés, ces coefficients ont pour valeurs :

$$\begin{array}{lll} a_0 = 0,836692 & ; & a_1 = 0,113536 & ; & a_2 = 0,079580 \\ a'_0 = -0,002059 & ; & a'_1 = -0,000298 & ; & a'_2 = -0,001806 \\ b_0 = 161,727490 & ; & b_1 = 60,400684 & ; & b_2 = -28,530729 \\ b'_0 = -4,160263 & ; & b'_1 = 3,816861 & ; & b'_2 = -0,523051 \end{array}$$

Les Figures 5 et 6 donnent l'évolution des coefficients de contraction A et B du sillage dans la gamme de variation des paramètres α_0 et γ considérés.

L'azimut ψ_s correspondant au début de la zone de sillage lointain où la lanière tourbillonnaire devient spatialement instable (et où la précision dans la détermination de r_t au fil chaud décroît rapidement), a également pu être synthétisé comme une fonction de α_0 et de γ par la relation :

$$(\psi_s - \psi_b)/(b\psi_b) = (1/4) [8,5 - \alpha_0/10 - \gamma(2 + \gamma)] \quad (2)$$

où ψ et α_0 s'expriment en degrés, et $b\psi_b = 360^\circ$.

Les courbes d'évolution de $r_t/R = r_t/R(\psi)$ déduites de l'expression (1), ainsi que les valeurs expérimentales brutes utilisées pour le lissage, sont présentées sur les Figures 7, 8, 9, respectivement pour $\alpha_0 = 23^\circ$; 27° ; $32,5^\circ$, et pour différentes valeurs de γ variant de 0,34 à 0,97. Pour chaque calage considéré, ces courbes font apparaître une contraction radiale d'autant plus forte que γ est faible (c'est à-dire que la charge est élevée). De même, l'instabilité du sillage lointain apparaît à des azimuths d'autant plus grands que γ est faible.

Il est à remarquer que pour les faibles valeurs de γ , cette instabilité ψ_s intervient lorsque la contraction est pratiquement achevée. En posant $\epsilon = ((r_t/R)_s - A)/A$, on a en effet : $\epsilon = 0,22\%$; $0,21\%$; $0,20\%$ respectivement pour $\alpha_0 = 23^\circ$; 27° ; $32,5^\circ$, et à $\gamma = 0,44$. En revanche, pour les fortes valeurs de γ , les instabilités apparaissent nettement avant la valeur asymptotique de contraction finale; on a par exemple $\epsilon = 0,8\%$; $1,1\%$; $1,8\%$ respectivement pour $\alpha_0 = 23^\circ$; 27° ; $32,5^\circ$ et à $\gamma = 0,89$.

On notera également que la forme de l'expression (1), tout comme les courbes d'évolution des Figures 7 à 9, présentent bien une allure similaire à celles qui sont obtenues^{(10), (11)} pour des sillages de rotors en vol stationnaire (où $V_\infty = 0$), pour lesquels :

$$r_t/R = 0,78 + (1 - 0,78)e^{-B'\psi}$$

où l'exposant de contraction B' n'est fonction que du coefficient de traction.

3.2. Translation axiale Z_t/R

La loi de synthèse qui a été dégagée pour la coordonnée axiale du tourbillon d'extrémité, présente également une forme analogue à celle proposée^{(10), (11)} pour les rotors en vol stationnaire, et s'écrit :

$$\left\{ \begin{array}{l} Z_t/R = k_1 (\psi/\psi_b) \quad \text{pour} \quad 0 \leq \psi \leq \psi_b \\ Z_t/R = k_1 + k_2 \{ (\psi/\psi_b) - 1 \} \quad \text{pour} \quad \psi_b \leq \psi \leq \psi_s \end{array} \right. \quad (3)$$

où les azimuts sont exprimés en degrés; $b \psi_b = 360^\circ$; ψ_s est donnée par l'expression (2); et où les coefficients k_1 et k_2 sont des polynômes de degré 3 en fonction de λ et de α_0 , de la forme suivante :

3.2.1. Coefficient k_1 :-

On considère le rapport $X = \lambda / \lambda_T = \gamma / \gamma_T$ comme variable du fonctionnement aérodynamique; le paramètre d'avancement λ_T (correspondant au régime de traction nulle $\tau = 0$) est donné (14) par :

$$\lambda_T = \gamma_T / \pi = \xi_t \bar{\alpha}$$

où les quantités surlignées désignent des valeurs correspondant à la section moyenne $\xi = 0,7$ de la pale.

Le coefficient k_1 , qui détermine la translation axiale du tourbillon jusqu'à la première interaction avec la pale suivante ($\psi = \psi_b$), s'exprime alors sous la forme :

$$k_1 = \frac{Z_0 + Z_1 X + Z_3 X^3}{\lambda_T / \pi^2} \quad (4)$$

$$Z_1 = P_{Z1}(\alpha_0) + \gamma Q_{Z1}(\alpha_0)$$

$$Z_3 = P_{Z3}(\alpha_0) + \gamma Q_{Z3}(\alpha_0)$$

expressions où les termes P_{Z1} , Q_{Z1} , P_{Z3} , Q_{Z3} sont des polynômes en α_0 ($\alpha_0 = \bar{\alpha}$ pour l'hélice étudiée) du type :

$$P_{Z1} = P_{10} + P_{11} \alpha_0 ; \quad P_{Z3} = P_{30} + P_{31} \alpha_0 + P_{32} \alpha_0^2$$

$$Q_{Z1} = Q_{10} + Q_{11} \alpha_0 + Q_{12} \alpha_0^2 ; \quad Q_{Z3} = Q_{30} + Q_{31} \alpha_0$$

Dans la gamme de paramètres (α_0, γ) étudiés, ces coefficients prennent les valeurs suivantes:

$$\begin{aligned} P_{10} &= -0,033433 ; & P_{11} &= 0,025844 \\ Q_{10} &= -0,010462 ; & Q_{11} &= 0,001152 ; & Q_{12} &= -0,000014 \\ P_{30} &= -0,031699 ; & P_{31} &= -0,005434 ; & P_{32} &= -0,000057 \\ Q_{30} &= -0,000092 ; & Q_{31} &= -0,000118 \end{aligned}$$

3.2.2. Coefficient k_2 :-

D'une manière analogue, le coefficient k_2 , qui détermine le pas de la trajectoire hélicoïdale des tourbillons du sillage lointain jusqu'à l'instabilité $\psi = \psi_s$, s'exprime par :

$$k_2 = \frac{Z'_0 + Z'_1 X + Z'_2 X^2 + Z'_3 X^3}{Z'_0 \lambda_T (1 + Z'_{01} \alpha_0)} \quad (5)$$

$$Z'_1 = P'_{Z1}(\alpha_0) + \gamma Q'_{Z1}(\alpha_0)$$

$$Z'_2 = P'_{Z2}(\alpha_0) + \gamma Q'_{Z2}(\alpha_0)$$

$$Z'_3 = P'_{Z3}(\alpha_0) + \gamma Q'_{Z3}(\alpha_0)$$

expressions où les termes indépendants de γ sont des polynômes en α_0 du même type que précédemment :

$$\left\{ \begin{aligned} P'_{Z1} &= P'_{10} + P'_{11} \alpha_0 + P'_{12} \alpha_0^2 ; & Q'_{Z1} &= Q'_{10} + Q'_{11} \alpha_0 \\ P'_{Z2} &= P'_{20} + P'_{21} \alpha_0 + P'_{22} \alpha_0^2 ; & Q'_{Z2} &= Q'_{20} + Q'_{21} \alpha_0 \\ P'_{Z3} &= P'_{30} + P'_{31} \alpha_0 + P'_{32} \alpha_0^2 ; & Q'_{Z3} &= Q'_{30} + Q'_{31} \alpha_0 \end{aligned} \right.$$

Relations dans lesquelles les coefficients prennent, pour la gamme de paramètres (α_0, γ) étudiés, les valeurs ci-dessous :

$$\begin{aligned} Z'_{00} &= 1,081463 ; & Z'_{01} &= -0,011464 \\ \left\{ \begin{aligned} P'_{10} &= 0,099112 ; & P'_{11} &= -0,0088495 ; & P'_{12} &= 0,0003534 \\ Q'_{10} &= 0,004341 ; & Q'_{11} &= 0,0016975 \end{aligned} \right. \\ \left\{ \begin{aligned} P'_{20} &= -0,118670 ; & P'_{21} &= 0,017929 ; & P'_{22} &= -0,0001366 \\ Q'_{20} &= -0,006505 ; & Q'_{21} &= -0,002547 \end{aligned} \right. \\ \left\{ \begin{aligned} P'_{30} &= 0,0395547 ; & P'_{31} &= -0,0059765 ; & P'_{32} &= 0,0000456 \\ Q'_{30} &= 0,0021666 ; & Q'_{31} &= 0,0008496 \end{aligned} \right. \end{aligned}$$

Il est à noter que des relations de forme similaire, c'est-à-dire fonction de γ , λ_T , et de $\bar{\alpha}$, ont été proposées (14), (15) pour déterminer le pas réduit des tourbillons du sillage. Toutefois, dans ces relations la coordonnée axiale Z_t est supposée indépendante de l'azimut ψ , et le pas des tourbillons est considéré comme constant depuis le plan de rotation jusqu'à l'infini aval (c'est-à-dire que $k_1 = k_2$, ce qui représente une hypothèse nettement restrictive, puisque les résultats présents indiquent que k_1 est toujours nettement inférieur à k_2).

Les variations des coefficients k_1 et k_2 ainsi obtenus à partir des expressions (4) et (5) sont données sur les Figures 10 et 11 en fonction des paramètres α_0 et γ .

La vitesse de translation axiale du tourbillon d'extrémité qui se déduit alors de l'expression (3) en fonction de l'azimut ψ , est présentée sur les Figures 12, 13, 14 respectivement pour $\alpha_0 = 23^\circ$; 27° ; $32,5^\circ$. Pour chaque calage, ces courbes mettent clairement en évidence l'accroissement de translation axiale du tourbillon lorsque γ augmente (c'est-à-dire que la charge diminue).

Il apparaît également que la limite d'instabilité ψ_s ne concerne, suivant la coordonnée axiale Z , que des sections du sillage lointain voisines de $Z = 2R = D$, et ceci quel que soit le calage considéré.

4. CHAMP DE VITESSES 3D DES SILLAGES ASSOCIES

A partir des caractéristiques globales du fonctionnement $\tau = \tau(\gamma)$ de la Figure 4, les trajectoires tourbillonnaires et les champs de vitesses induites ont été analysés pour un coefficient de traction constant de l'hélice. Pour chacun des calages moyens $\alpha_0 = 23^\circ; 27^\circ; 32,5^\circ$, le paramètre de fonctionnement a donc été sélectionné aux valeurs respectives $\gamma = 0,44; 0,63; 0,89$, pour permettre de maintenir constant et égal à $\tau = 0,16$ le coefficient de traction (voir Figure 4).

Les trajectoires tourbillonnaires associées à ce coefficient de traction constant, $\tau = 0,16$, sont regroupées sur la Figure 15 qui représente les variations des coordonnées $r_t/R = r_t/R(\psi)$ et $Z_t/R = Z_t/R(\psi)$ du tourbillon d'extrémité pour chacun des 3 couples de paramètres (α_0, γ) sélectionnés.

Contrairement au cas du rotor en vol stationnaire, pour lequel un coefficient de traction C_T donné détermine une géométrie unique du sillage (coefficients A, B, k_1, k_2 , fonctions de C_T), les résultats de la Figure 15 mettent en évidence des géométries de sillage totalement différentes pour chaque couple de paramètres (α_0, γ) . On observe en effet une contraction radiale d'autant plus forte que le calage est faible. Par voie de conséquence, lorsque le calage décroît la vitesse de translation axiale des tourbillons diminue également.

Sur la Figure 15, est également représentée (par des tirets) la limite azimutale d'instabilité ψ_s du sillage lointain. Bien que l'hélice fonctionne à coefficient de traction constant, on remarquera que la limite d'instabilité est d'autant plus éloignée du plan de rotation que le calage est faible ($\psi_s \approx 360^\circ$, soit 4 tourbillons consécutifs pour $\alpha_0 = 32,5^\circ$; tandis que $\psi_s \approx 540^\circ$, soit 6 tourbillons consécutifs pour $\alpha_0 = 23^\circ$).

Il est également à noter sur les résultats de la Figure 15, que le paramètre γ qui constitue le paramètre universel vis-à-vis des efforts globaux à calage donné (voir courbes $\tau = \tau(\gamma)$ à iso- α pour différentes valeurs de n sur la Figure 4), apparaît aussi comme le paramètre caractéristique de la géométrie du sillage associé. En effet, les courbes obtenues pour $\alpha_0 = 32,5^\circ$ et $\gamma = 0,89$ indiquent que les trajectoires en r/R et Z/R sont en parfaite coïncidence, quelle que soit la manière dont on réalise le paramètre γ par variations de n et V_∞ (ici n = 35,7 t/s et $V_\infty = 27$ m/s; ou n = 22,7 t/s et $V_\infty = 17,2$ m/s).

Les lignes tourbillonnaires marginales étant déterminées pour l'hélice opérant à $\tau = C_{ste}$, le choix de 5 plans de coupe $Z/R = C_{ste}$ du sillage où ont été mesurées les vitesses 3D, a été effectué en fonction de l'âge du tourbillon par rapport à la pale l'ayant émis, et pour une distance aval variant de $Z/R = 0,2$ à $Z/R = 2,0$.

Un exemple de distribution des vitesses radiale, tangentielle et axiale (U_0, V_0, W_0) adimensionnées par la vitesse amont V_∞ , et mesurées en fonction de ψ en 15 stations radiales Z/R est donné sur les Figures 16A ($Z/R = 0,221$) et 16B ($Z/R = 1,239$) pour $\alpha_0 = 23^\circ$; $\gamma = 0,44$.

4.1. Champ de vitesses moyennes.

Pour chaque calage envisagé, il a été possible, à partir des mesures de vitesses 3D réalisées aux 5 sections aval, de restituer le champ moyen d'écoulement en fonction de Z/R et ceci jusqu'à une distance d'environ un diamètre à l'aval du plan de rotation. Les Figures 17A et B donnent, en fonction du rayon réduit $\xi = r/R$, les distributions de vitesse axiale moyenne $W_0 = W/V_\infty = 1 + a$ (où a représente la vitesse axiale induite W_1/V_∞), obtenues dans les 5 plans de coupe pour $\alpha_0 = 23^\circ$ et $32,5^\circ$. Lorsque Z/R croît, ces résultats mettent en évidence l'évolution de la contraction résultant du tourbillon d'extrémité, et font apparaître un accroissement des vitesses induites d'autant plus grand que le calage est faible (c'est-à-dire que la charge augmente).

En outre, ces résultats permettent de vérifier certains résultats classiques déduits des théories de Froude de la quantité de mouvement axiale. Les relations de Froude permettent en effet d'établir⁽¹⁶⁾ le taux de contraction finale du sillage sous la forme :

$$S_\infty / S_H = (1 + a_F) / (1 + 2a_F) \quad (6)$$

où S_H et S_∞ représentent l'aire des sections dans le plan de l'hélice et à l'infini aval, et où la vitesse axiale induite a_F est donnée par :

$$2a_F = (1 + 8 \tau / \pi \gamma^2)^{1/2} - 1 \quad (7)$$

Dans la section S_∞ située à l'infini aval, la vitesse induite b_F vérifie de plus la relation $b_F = 2a_F$. La conservation du débit dans chaque section aval $Z = C_{ste}$ permet alors de déterminer^{(8), (9)} une loi de contraction de type exponentielle par :

$$(S/S_H)_F = S_\infty / S_H + (1 - S_\infty / S_H) e^{-C_N \cdot Z/R} \quad (7)$$

où S est l'aire de la section courante à l'abscisse Z, et où l'exposant de contraction est donné⁽⁸⁾ par une loi empirique en fonction de la traction (ici $C_N = 1,105$ pour $\tau = 0,16$).

Pour les deux couples de paramètres $(\alpha_0 = 23^\circ; \gamma = 0,44)$ et $(\alpha_0 = 32,5^\circ; \gamma = 0,89)$, les Figures 18A et B montrent les résultats ainsi obtenus^o (courbes en pointillés) sur la contraction (S/S_H) et sur la vitesse axiale $\bar{W}_F = (1 + a)(S_H/S)$, à partir des expressions (6) et (8).

Sur ces Figures, les résultats obtenus par la théorie de Froude sont confrontés aux mesures présentes (courbes continues), pour lesquelles la vitesse axiale moyenne $\bar{W}_0 = 1 + a$ est déduite des résultats des Figures 17A et B, et le rapport des sections à l'abscisse courante Z se déduit des lois (1) et (3) par $(S/S_H) = (r_t/R)^2$.

La comparaison de ces résultats fait apparaître des contractions du sillage nettement plus fortes que celles déduites de la théorie de Froude. Cependant, les vitesses axiales \bar{W}_0 présentent également des niveaux plus élevés que ceux de Froude, si bien que le débit volumique se trouve conservé et pratiquement égal à celui de Froude dans toute la zone de sillage explorée, à savoir $0,2 \leq Z/R \leq 2,0$. L'évolution du rapport D/D_F montre en effet que le débit déduit des mesures ($D = (r_t/R)^2 \cdot \bar{W}_0 \cdot \pi R^2 V_\infty$) représente bien le débit de Froude ($D_F = (S/S_H)_F \cdot \bar{W}_F \cdot \pi R^2 V_\infty$), à moins de 4 % près, pour chaque section $Z = C_{ste}$ et dans les deux conditions de α_0 et γ étudiées.

4.2. Champ de vitesses instantanées

A partir de la mesure des composantes $U = U(r/R, \psi)$ et $V = V(r/R, \psi)$, la vitesse radiale résulte

tante $(U^2 + V^2)^{1/2}$ dans un plan de coupe aval du sillage peut être représentée en fonction de r/R et à toute phase de la période $0^\circ \leq \omega t \leq 90^\circ$. En admettant une symétrie de révolution pour les 4 zones interpailes, les cartes d'écoulement du champ radial résultant peuvent être restituées à toute phase de la rotation ($0^\circ < \omega t < 360^\circ$) et pour chaque plan de coupe $Z/R = \text{Cste}$.

Les Figures 19, 20, 21 donnent des exemples du champ radial résultant ainsi restitué dans les conditions $\alpha_0 = 23^\circ$; $\gamma = 0,44$, et pour les 3 plans aval $Z/R = 0,221$ (Fig. 19); $Z/R = 0,597$ (Fig. 20); $Z/R = 1,880$ (Fig. 21). Sur chaque Figure, la vitesse résultante est tracée suivant 15 abscisses radiales et avec un incrément d'azimut de rotation $\Delta\psi = 4,5^\circ$. Pour chaque azimut ψ , les composantes U_R et V_R de cette vitesse résultante se déduisent des composantes U et V mesurées par la rotation :

$$U_R = U \cos\psi + V \sin\psi \quad V_R = V \cos\psi - U \sin\psi$$

Bien que ce mode de représentation ne fasse pas intervenir la composante axiale, il permet cependant de décrire avec précision l'écoulement radial qui se développe à un instant quelconque à l'aval des pales. En particulier, le passage du tourbillon d'extrémité dans chaque plan $Z/R = \text{Cste}$, ainsi que la contraction radiale qu'il engendre, sont clairement matérialisés sur ces cartes. Outre les deux zones marginales influencées par le moyeu et par l'extrémité de pale, les cartes confirment la présence, dans la région moyenne des pales, d'une zone d'écoulement neutre assez peu perturbée.

En outre, à partir du champ radial résultant précédemment obtenu, il est possible de déterminer la circulation du tourbillon marginal par intégration, dans chacune des sections aval considérées, des vitesses tangentes à un contour fermé englobant le noyau tourbillonnaire. Comme l'indique la Figure 22, le centre du tourbillon est préalablement localisé en (r_t, ψ_t) pour un plan $Z/R = \text{Cste}$ donné, et la circulation Γ_{tot} du tourbillon résulte alors de la circulation Γ_ω due à la composante de rotation ωr relative à la section r considérée, et de la circulation Γ_i due aux vitesses V_r et V_t tangentes au contour fermé (ds, dr) comme le montre la Figure 22.

Le calcul des circulations Γ_i a ainsi été effectué dans chacune des 5 sections aval étudiées, et la Figure 23 en donne un exemple relatif au calage $\alpha_0 = 32,5^\circ$. Pour un plan $Z/R = \text{Cste}$ donné, la circulation Γ_i est représenté sur cette Figure en fonction de la longueur des contours fermés, tels que $ds = dr$, et de dimension croissante (ds variant de 2 à 17 cm). L'accroissement de la longueur ds avec l'abscisse Z/R croissante correspond à une augmentation du rayon tourbillonnaire, qui dans ce cas varie de 2 cm à 5 cm lorsque Z/R croît de 0,203 à 1,819. Ces résultats montrent que la circulation Γ_i augmente avec la dimension du contour, puis tend vers une valeur quasiment constante pour des contours de dimension suffisamment grande, avant de redécroître. Dans chaque plan $Z/R = \text{Cste}$, la circulation du tourbillon a donc été calculée par la relation $\Gamma_{\text{tot}} = \Gamma_i + \Gamma_\omega$ (voit Fig. 23) où la dimension $ds = dr$ du contour a été sélectionnée pour correspondre à la valeur constante du contour de Γ_i .

Par ailleurs, la distribution de circulation liée à la pale a été calculée à l'aide de la théorie tourbillonnaire classique⁽¹⁴⁾, qui permet de déterminer la circulation $\Gamma_p = \Gamma_p / \omega R^2$ et les vitesses induites axiale, $\tilde{w}_i = w_i / \omega R$, et tangentielle, $\tilde{u}_i = u_i / \omega R$, sur la pale par les relations :

$$\begin{cases} \tilde{\Gamma}(\xi) = ikt(\lambda^2 + \xi^2)^{1/2} / \{1 + (h/H_1)kt(\lambda^2 + \xi^2)^{1/2}\} \\ \tilde{w}_i(\xi) = \xi(h/H_1)\tilde{\Gamma}(\xi) \quad ; \quad \tilde{u}_i(\xi) = -h\tilde{\Gamma}(\xi) \end{cases} \quad (9)$$

où $k = 1/2(dc/di)$ et $t = c/R$ sont fonctions des coefficients de portance des profils et de la géométrie de la pale; H_1^2 est le pas moyen des tourbillons du sillage lointain qui se déduit du coefficient k_2 par $H_1 = bk_2/2\pi$; l'angle $i(\xi)$ de l'écoulement incident et la fonction h étant définis par :

$$i(\xi) = \alpha_0 + \theta_V - \text{Arctg}(\lambda/\xi) \quad ; \quad h(\xi) = b/4\pi\xi \chi_B$$

où le coefficient χ_B est donné⁽¹⁴⁾ par :

$$\chi_B(\xi, \lambda) = (2/\pi) \cdot \text{Arccos}(e^{-b(1-\xi)/2\lambda})$$

La distribution de circulation $\Gamma_p = \tilde{\Gamma}_p \omega R^2$ sur la pale ainsi calculée par (9) en fonction du rayon réduit $\xi = r/R$, est donnée sur la Figure 24 pour les deux calages $\alpha_0 = 23^\circ$ et $32,5^\circ$, et fait apparaître un maximum de circulation situé dans les deux cas au voisinage de $\xi_0 = 0,5$. Ce niveau maximum $(\Gamma_p)_{\text{max}}$ de circulation sur la pale est comparé, sur la Figure 25, à l'évolution de la circulation du tourbillon marginal précédemment obtenu dans le sillage en fonction de Z/R et pour $\alpha_0 = 32,5^\circ$. Ces résultats montrent que pour une distance aval suffisante ($Z/R > 0,4$), le maximum de circulation sur la pale se trouve concentré dans le tourbillon d'extrémité ($\Gamma_{\text{tot}} = 0,97 (\Gamma_p)_{\text{max}}$ à $Z/R = 0,494$). Lorsque la distance axiale Z/R augmente, l'intensité du tourbillon diminue en raison de la diffusion turbulente; cette intensité tourbillonnaire représente encore 78 % de $(\Gamma_p)_{\text{max}}$ dans le sillage lointain à $Z/R = 1,819$.

5. CONCLUSIONS

L'analyse du sillage proche et lointain d'une hélice aérienne quadripale opérant à différents paramètres de fonctionnement et suivant différents calages a été réalisée dans cette étude par une méthode anémométrique à fils chauds. Pour des distances aval allant jusqu'à un diamètre d'hélice, les trajectoires tourbillonnaires marginales et les champs de vitesses 3D ont été déterminés dans une gamme étendue de paramètre de fonctionnement allant de régimes voisins de la traction nulle à des régimes proches de la traction maximum.

Il a ainsi pu être établi des lois empiriques de synthèse sur la contraction radiale du sillage et sur la translation axiale des tourbillons d'extrémité, qui définissent avec précision la géométrie du sillage associé à un régime de fonctionnement propulsif quelconque ($\alpha_0, \lambda, \tau > 0$) de l'hélice étudiée. Il est à noter que ces lois empiriques présentent une certaine analogie avec celles établies pour les sillages de rotors en vol stationnaire, mais font intervenir des coefficients A, B, k_1, k_2 dépendant des paramètres du fonctionnement (γ, α_0) et liés à la présence d'une vitesse non nulle à l'infini amont.

La limite azimutale de validité de ces lois est donnée par une relation empirique qui détermine l'azimut d'instabilité ψ_s , à partir duquel le sillage et les tourbillons marginaux perdent leur permanence de forme sous l'action de la diffusion et de l'interaction tourbillonnaire.

Pour un régime de fonctionnement de l'hélice à $\tau = \text{Cste}$, la mesure des champs de vitesses 3D a permis une description détaillée de l'écoulement de sillage associé, pour des azimuts quelconques de la

rotation complète $0^\circ \leq \omega t \leq 360^\circ$. L'établissement de cartes d'écoulement du champ radial résultant a en outre permis de déterminer l'évolution de la circulation du tourbillon marginal en fonction de la distance aval. Lorsque cette distance varie de $0,5R$ à $2,0R$, l'intensité concentrée dans le tourbillon d'extrémité représente de 95 % à 80 % du maximum de circulation liée à la pale.

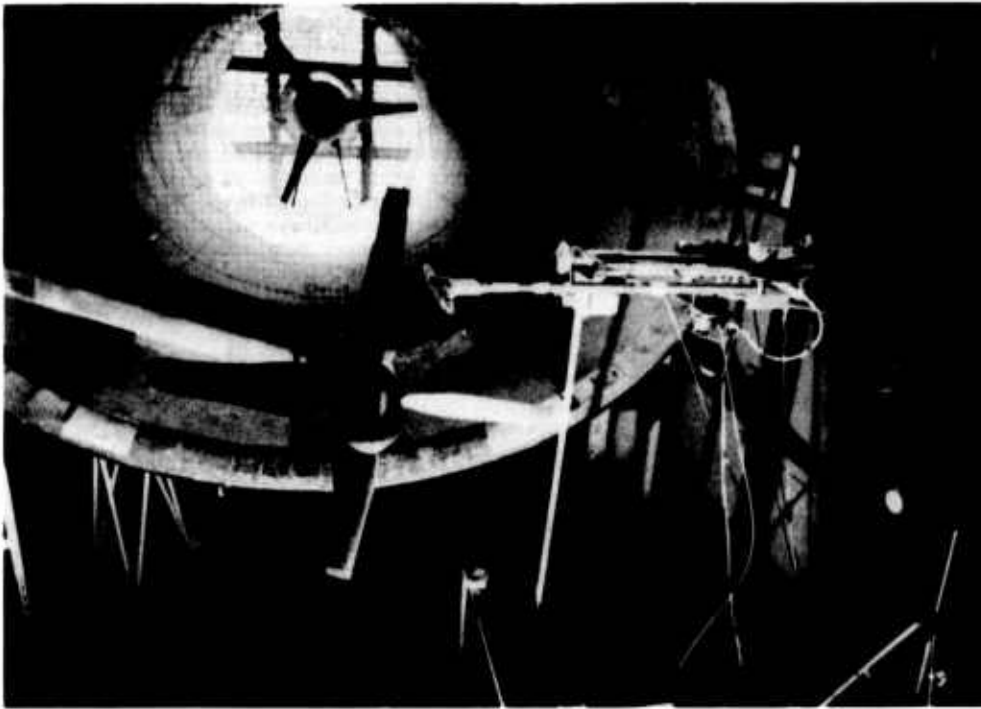
Pour l'hélice étudiée, il apparaît donc que la modélisation géométrique du sillage associé ainsi obtenue, constitue une configuration suffisamment complète pour servir de base à des programmes de mise en équilibre et de calcul des performances (méthodes similaires à celles développées pour les rotors en vol stationnaire et fondées sur la théorie tourbillonnaire et la relation de Biot et Savart). Toutefois, pour permettre une généralisation des lois de contraction et de translation proposée ici pour l'hélice étudiée, il s'avère nécessaire de systématiser les explorations de sillages associés à d'autres configurations d'hélice prenant notamment en compte la variation de paramètres tels que : le nombre de pales, la loi de vrillage, la géométrie des profils et des extrémités de pale.

REMERCIEMENTS.

Cette étude a été réalisée avec l'appui de la Direction des Recherches, Etudes et Techniques (Convention 81/278) que les auteurs tiennent à remercier.

REFERENCES

- (1) AGARD : "Prediction of Aerodynamic Loads on Rotorcraft", AGARD-CP N°334, Fluid Dynamics Specialists' Meeting, London, May 1982.
- (2) J.M. BOUSQUET : "Hélices adaptées au vol transsonique - Amélioration des méthodes de calcul", Convention D.R.E.T. N°3/3463 AY008, Décembre 1981; voir aussi 17° Colloque AAAF, Grenoble, Novembre 1980.
- (3) R. HIRSCH, T.S. LUU : "Remarques sur l'évolution des méthodes de calcul des hélices et rotors", 19° Colloque AAAF, Marseille, Novembre 1982.
- (4) C. BERGER, P. CALVET, M.S. ZAHNAN : "Etude des performances d'une éolienne en présence d'un gradient de vent", 19° Colloque AAAF, Marseille, Novembre 1982.
- (5) A.J. LANDGREBE, T.A. EGOLF : "Prediction of Helicopter induced Flow Velocities using the Rotorcraft Wake Analysis", 32nd A.H.S. Forum, Washington, May 1976.
- (6) J.M. POURADIER, E. HOROWITZ : "Aerodynamic Study of a Hovering Rotor", 6th European Rotorcraft and Powered Lift Forum, Bristol, September 1980.
- (7) J.M. SUMMA, D.R. CLARK : "A Lifting Surface Method for Hover/Climb Airloads", A.H.S. Forum Proceedings, Washington, D.C., May 1976.
- (8) W.Z. STEPNIOWSKI : "Rotary-Wing Aerodynamics", Vol.1, NASA-CR-3082, 1979.
- (9) C. KIRRMANN, A. ROUSSEAU, M. YERMIA : "Calcul du souffle moyen d'une hélice et de son influence sur les performances d'un avion", 19° Colloque AAAF, Marseille, Novembre 1982.
- (10) A.J. LANDGREBE : "An Analytical and Experimental Investigation of Helicopter Rotor Hover Performance and Wake Geometry Characteristics", AMRDL Technical Report 71-24, June 1971.
- (11) J.D. KOCUREK, J.L. TANGLER : "A Prescribed Wake Lifting Surface Hover Performance Analysis", Journal of AHS, Vol.22, N°1, January 1977.
- (12) C. MARESCA, N NSIMBA, D. FAVIER : "Prédiction et vérification expérimentale du champ des vitesses d'un rotor en vol stationnaire", AGARD-FDP ou Prediction of Aerodynamic Loads on Rotorcraft, London, May 1982.
- (13) D. FAVIER, C. MARESCA : " Champ aérodynamique à l'aval d'une hélice aérienne", Convention D.R.E.T. 81/278, Etude N°1, Mars 1983.
- (14) R. SIESTRUNCK : "Le développement moderne de la théorie de l'hélice", Edition Gauthier-Villars, Paris, 1947.
- (15) R. PELISSIER : "Note sur la théorie tourbillonnaire de l'hélice à pas aérodynamique constant", Journal de Mécanique, Vol.10, N°2, 1971.
- (16) P. REBUFFET : "Aérodynamique expérimentale", Editeur C. Béanger, Paris, 1958.



Montage hélice et système d'exploration



Acquisition de données SOLAR 16/40

Figure 1

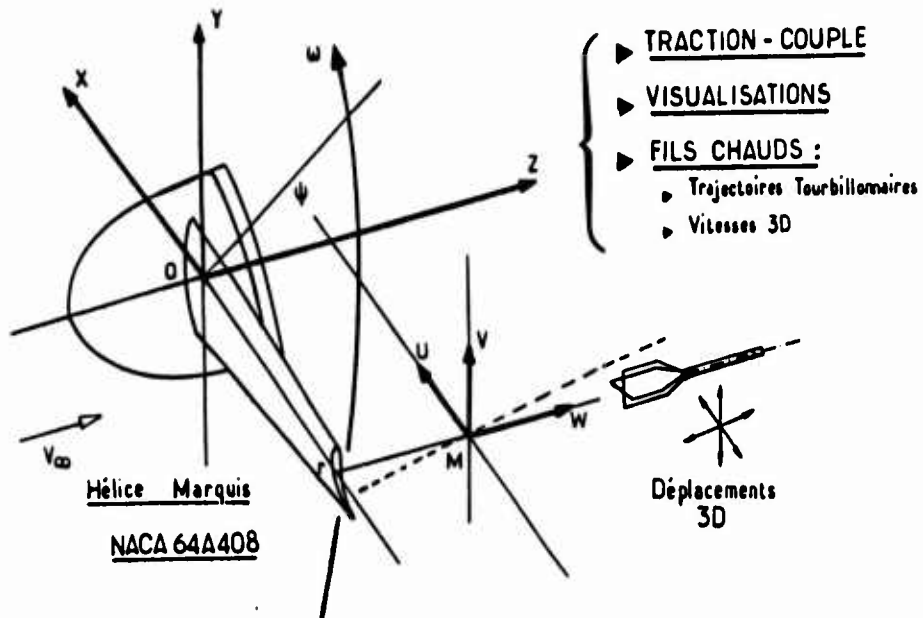


Figure 2

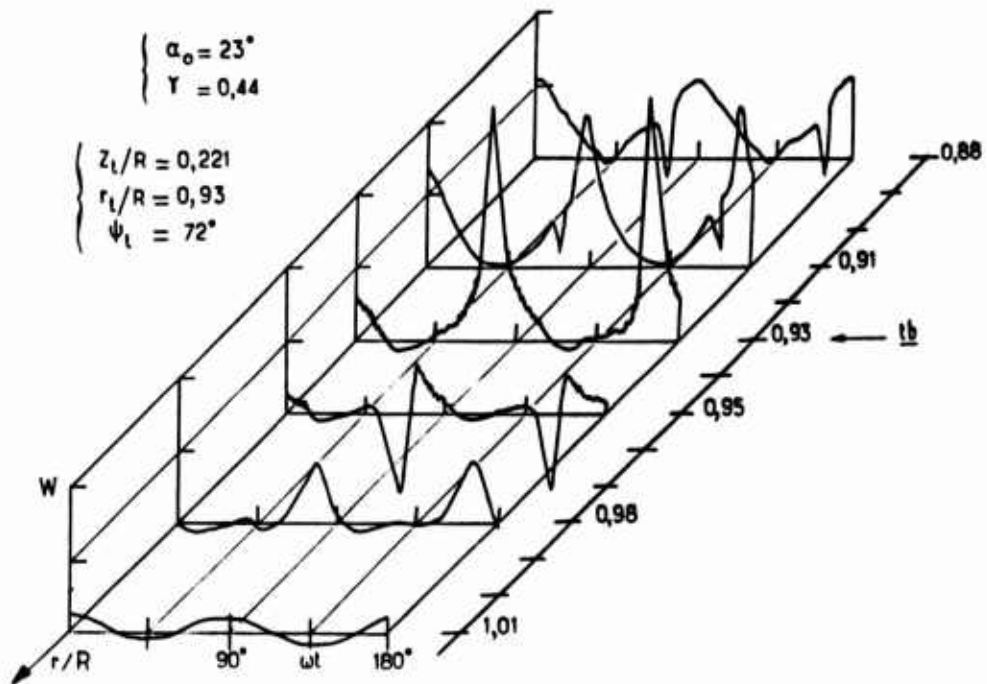


Figure 3

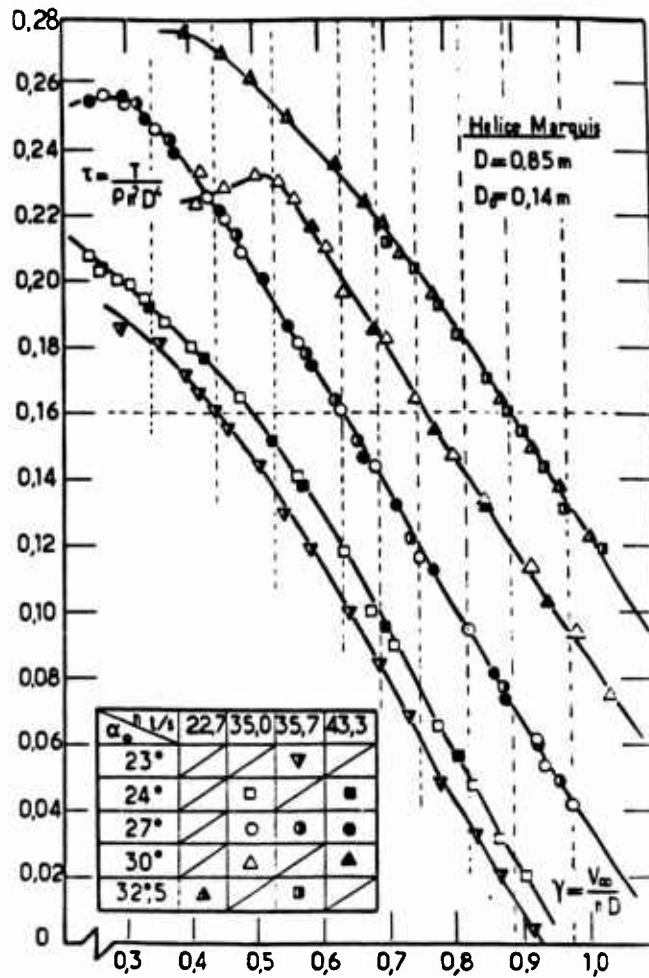


Figure 4

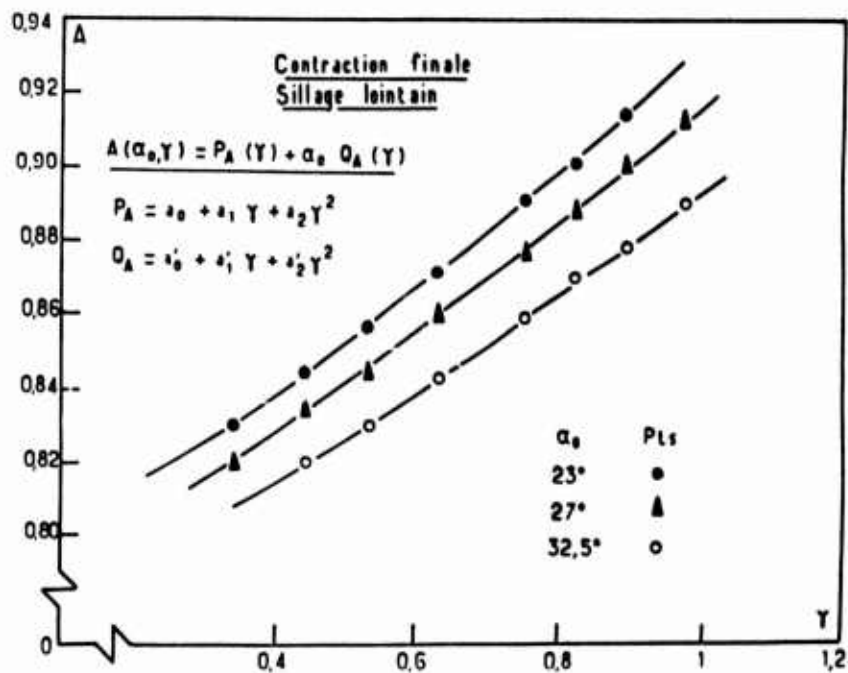


Figure 5

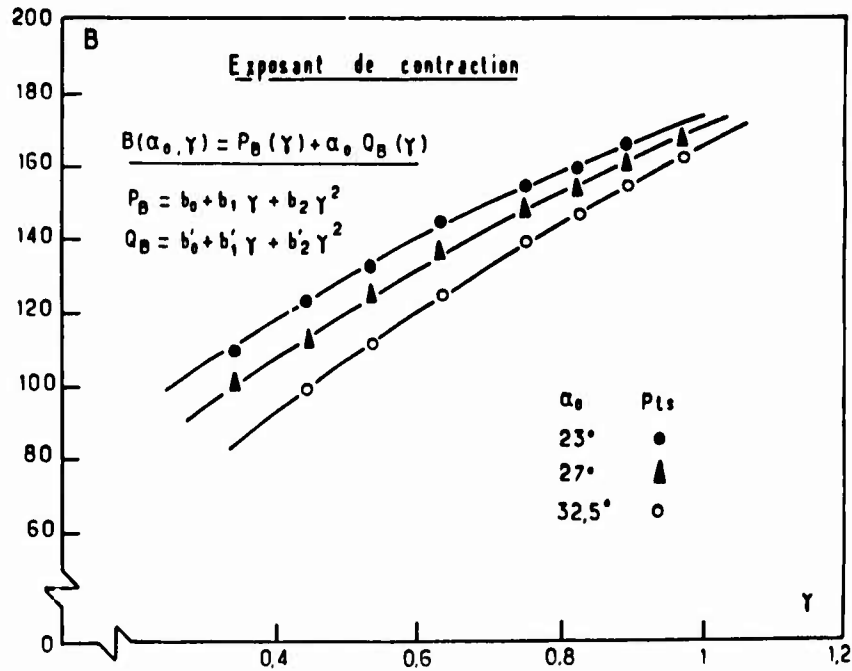
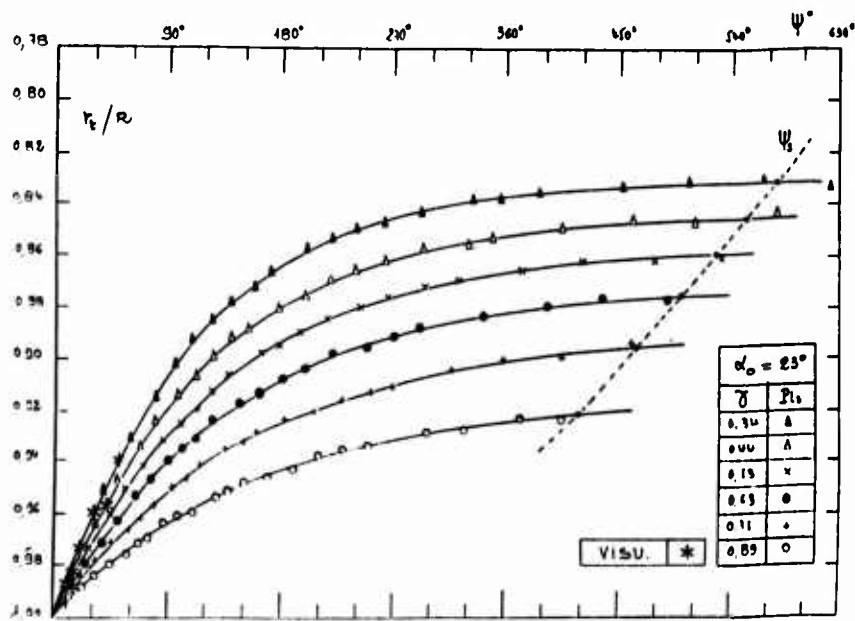


Figure 6



Distances radiales des trajectoires tourbillonnaires.

Figure 7

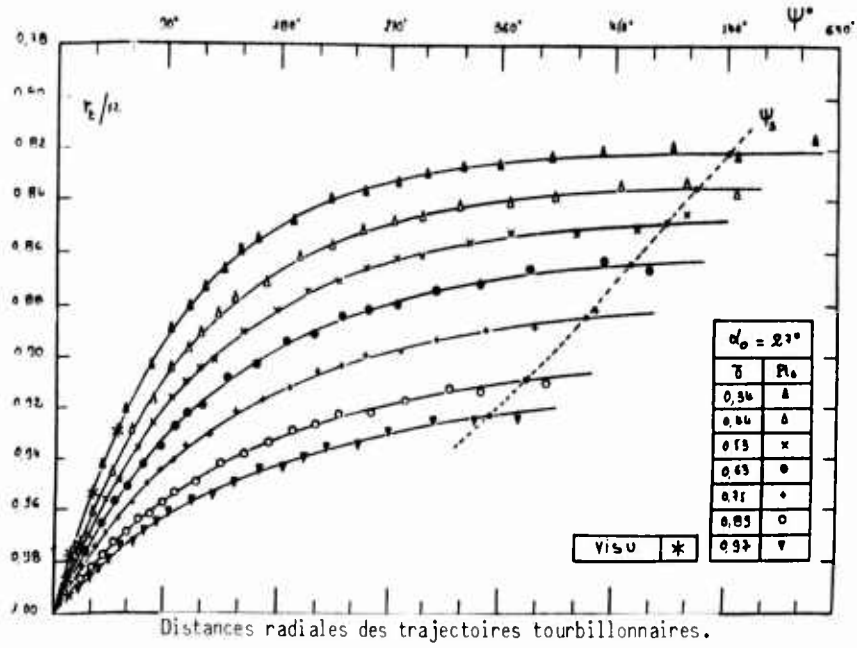


Figure 8

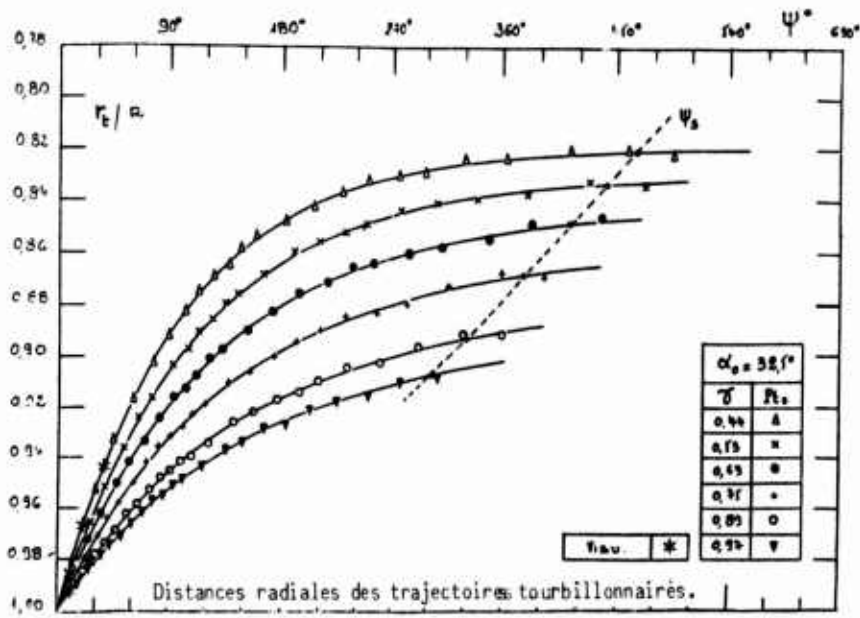


Figure 9

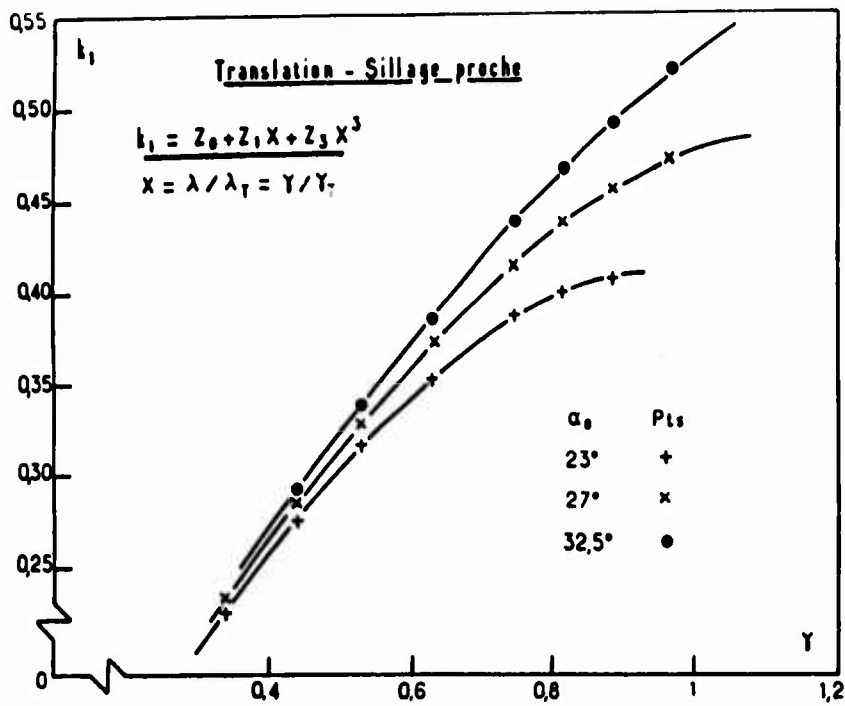


Figure 10

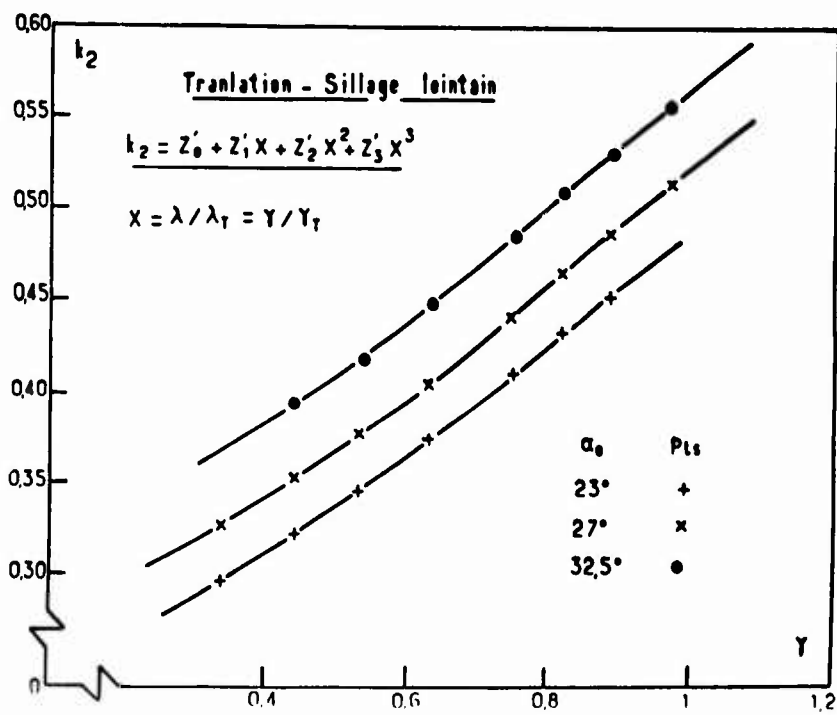


Figure 11

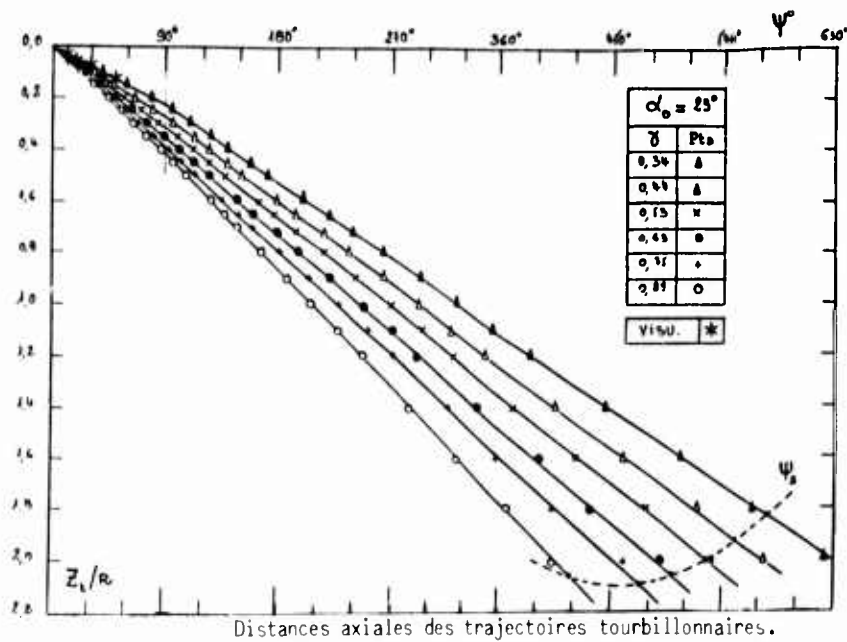


Figure 12

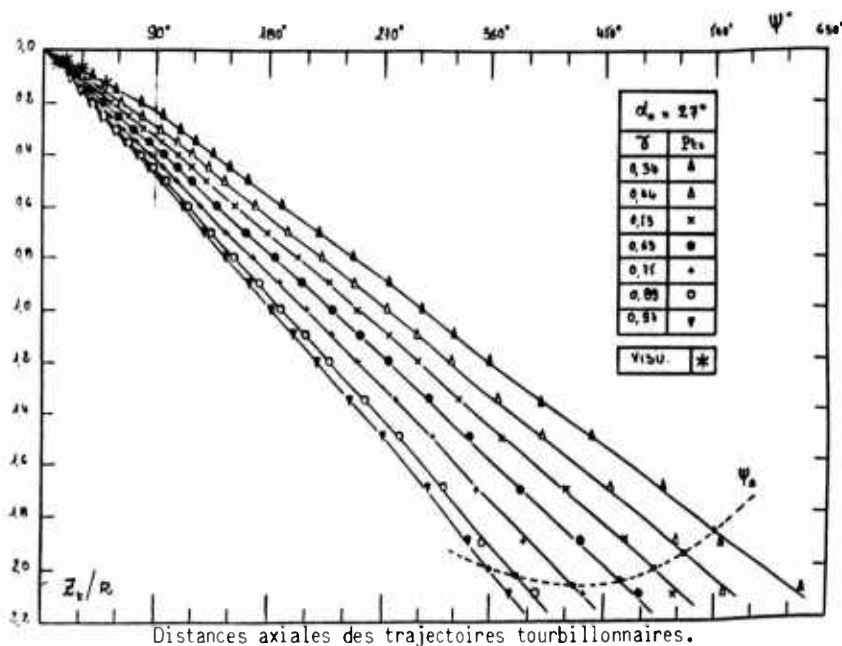


Figure 13

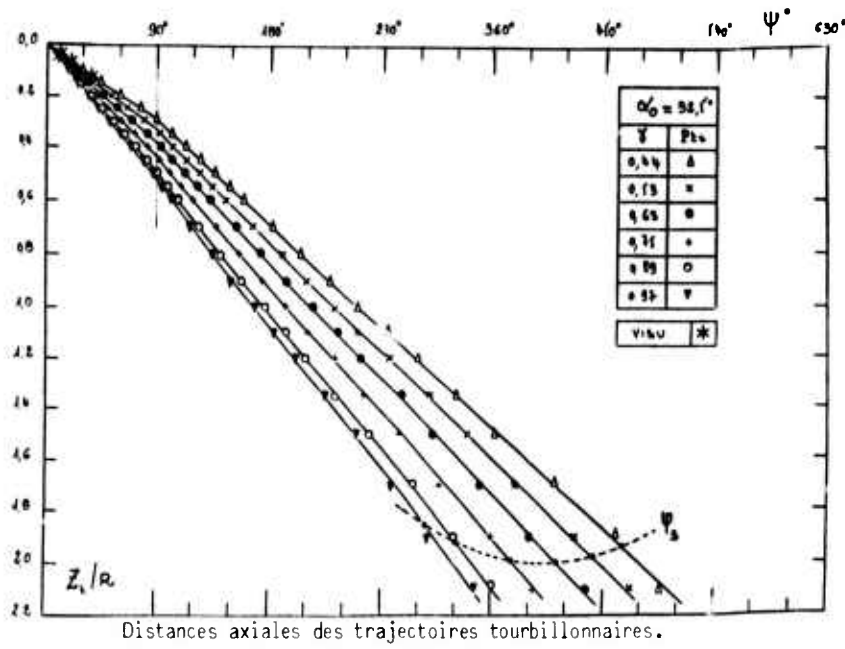


Figure 14

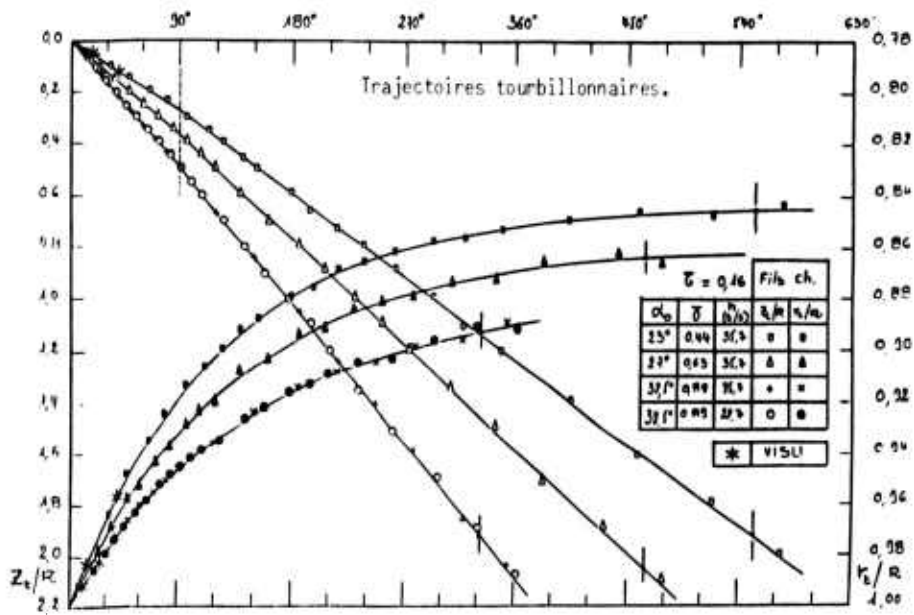


Figure 15

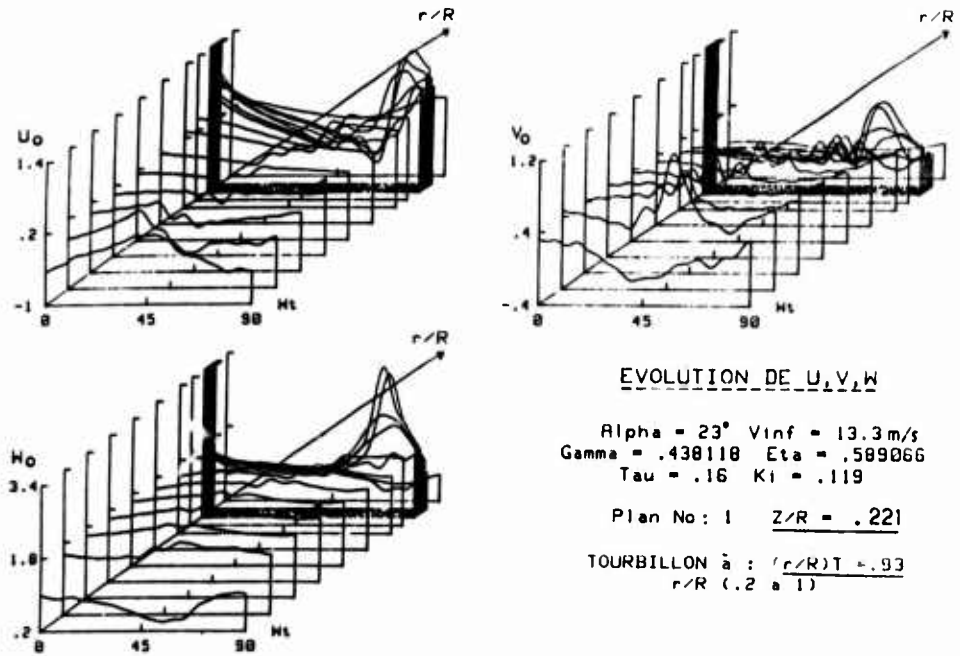


Figure 16A

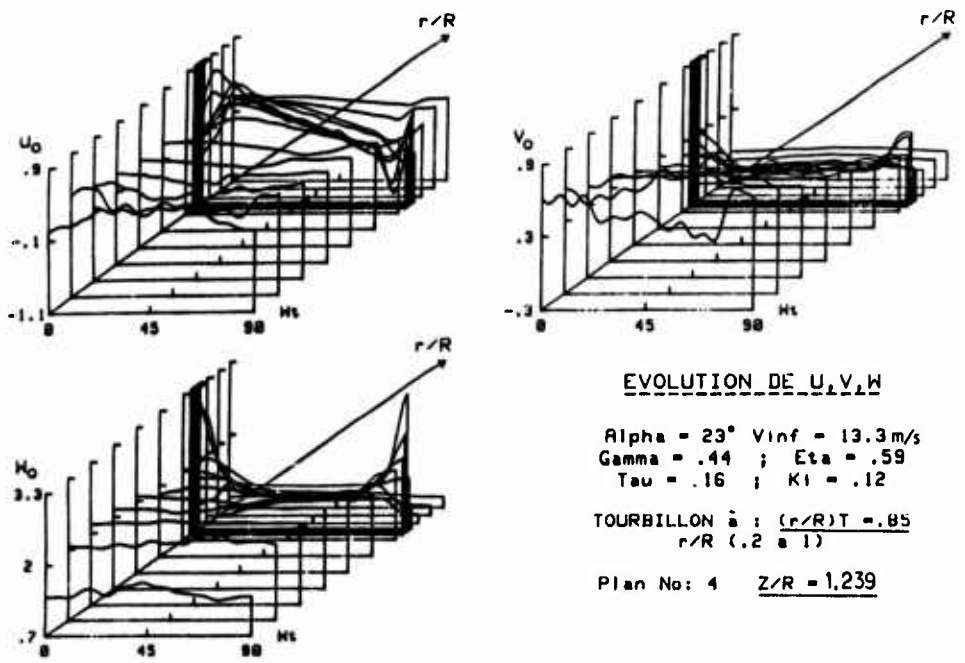


Figure 16B

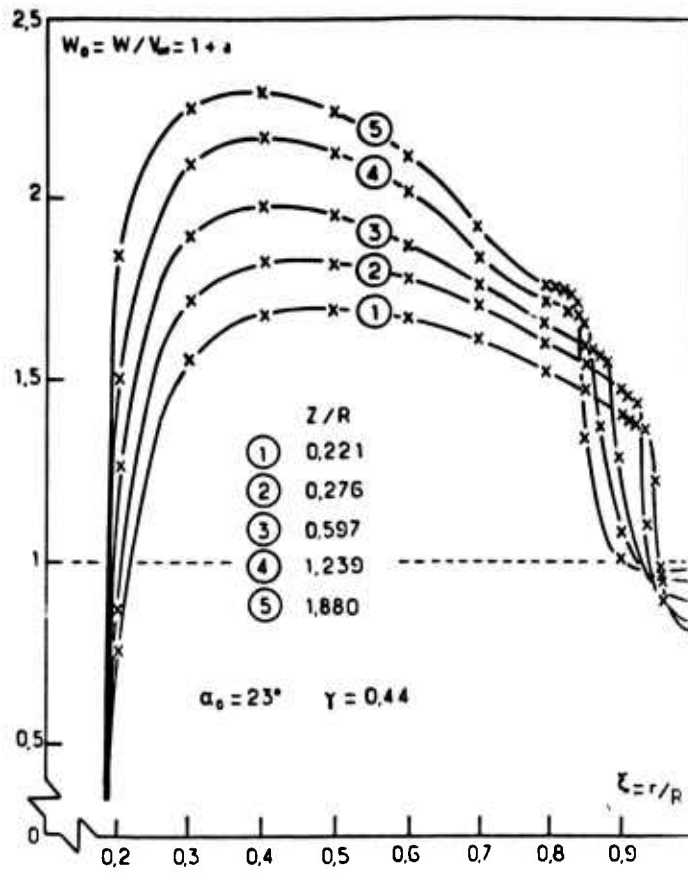


Figure 17A

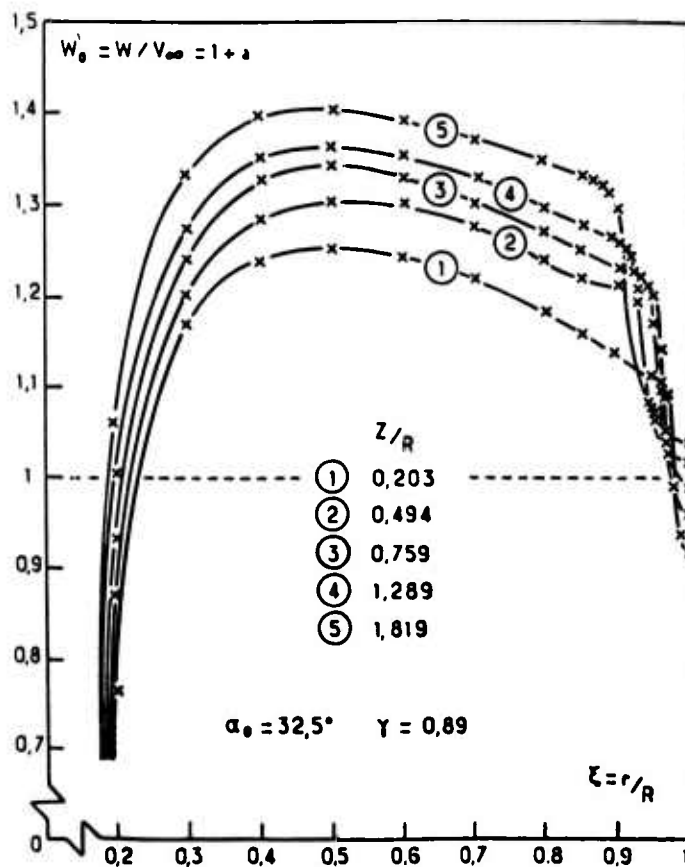


Figure 17B

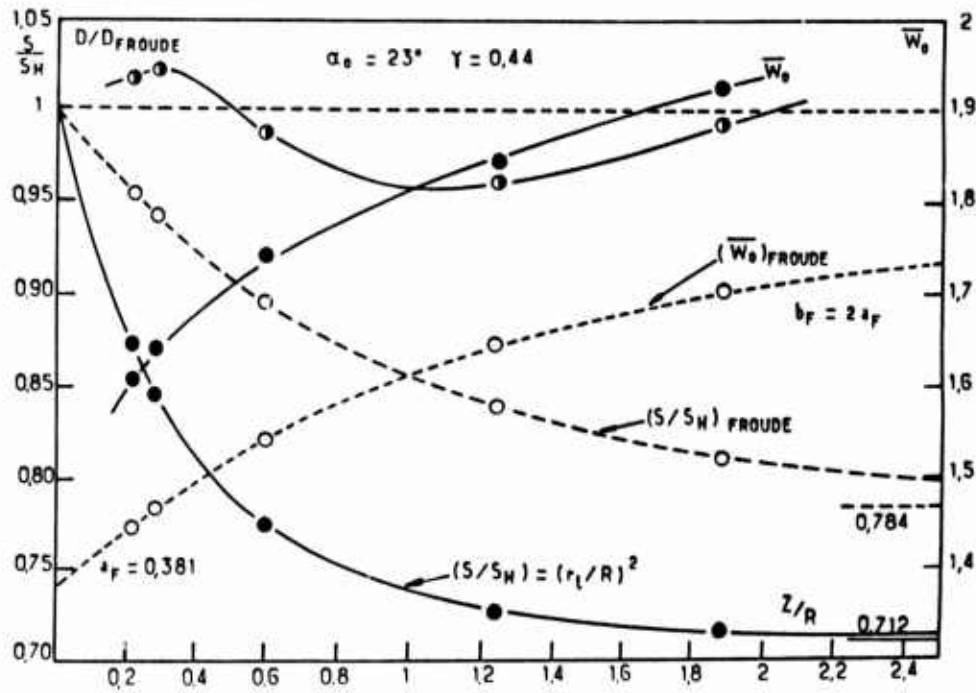


Figure 18A

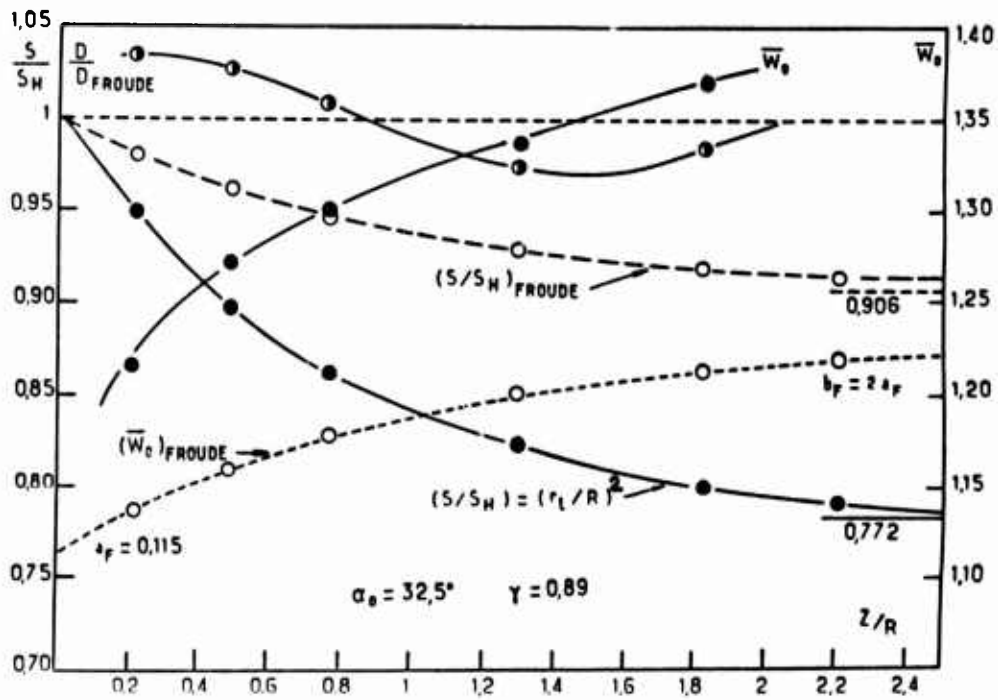


Figure 18B

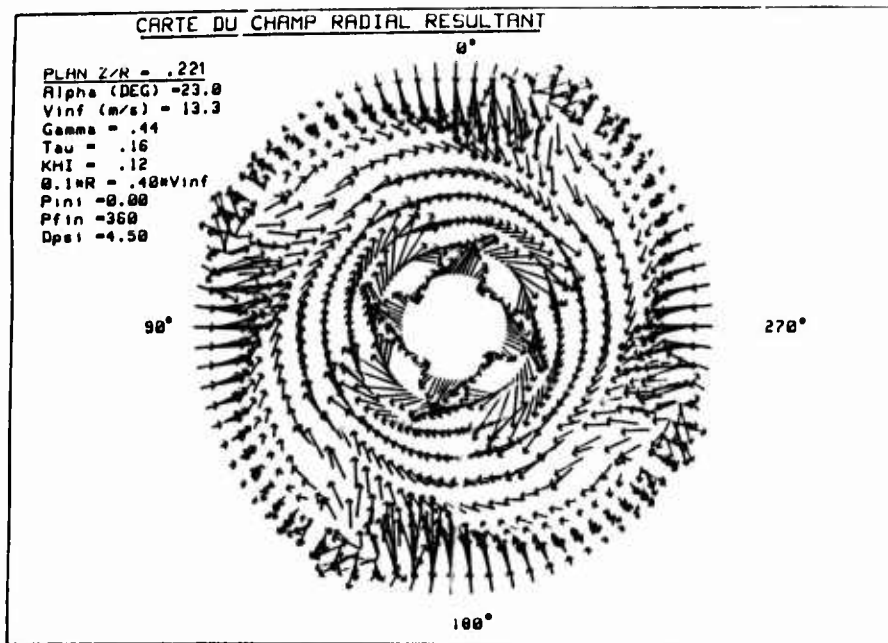


Figure 19

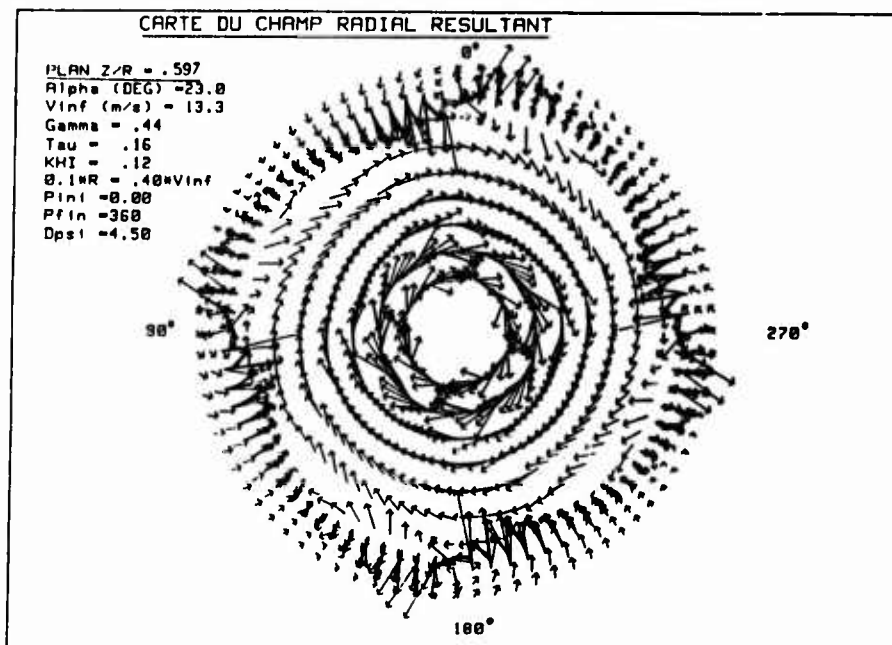


Figure 20

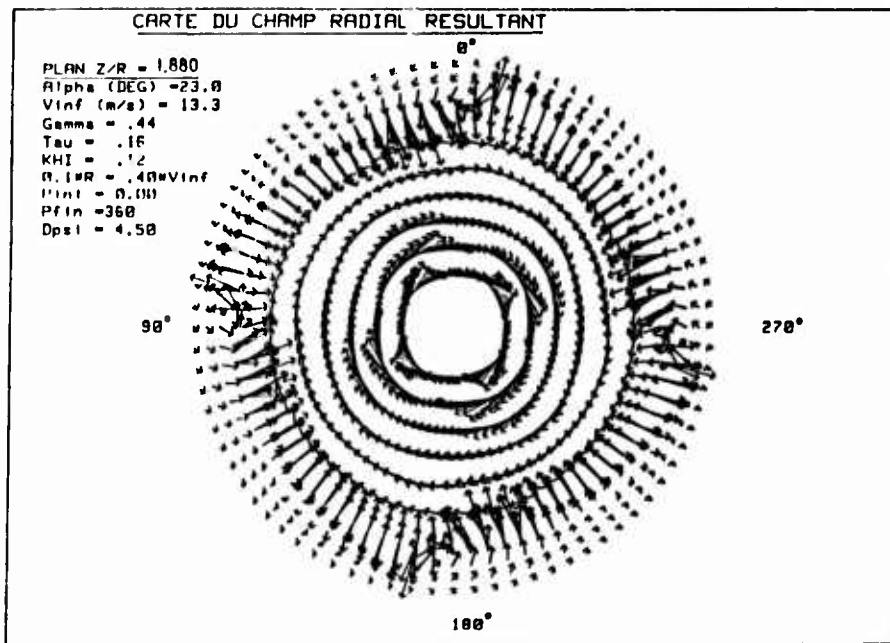
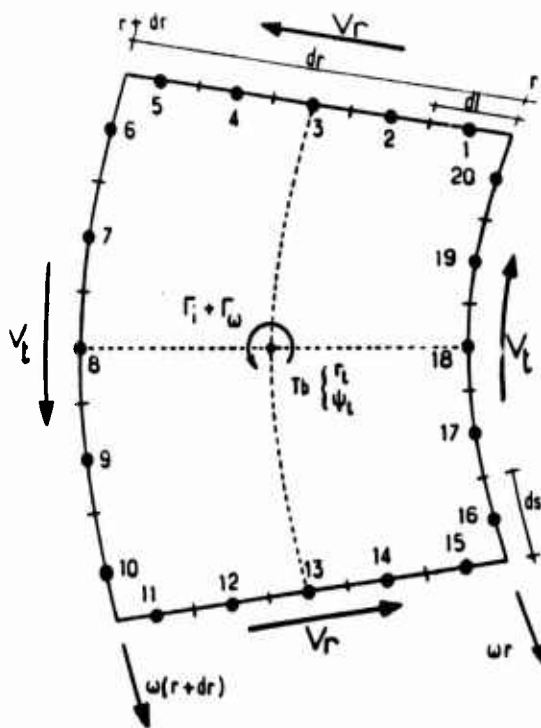


Figure 21



$$\Gamma_{TOT} = \int_1^5 V_{r_i} dl + \int_{11}^{15} V_{r_i} dl$$

$$+ \int_6^{10} V_{t_i} ds + \omega(r+dr) ds$$

$$+ \int_{16}^{20} V_{t_i} ds - \omega r ds$$

$$ds = dl = dr/5$$

$$\Gamma_{TOT} = \Gamma_i + \Gamma_\omega$$

$$\left\{ \begin{array}{l} \Gamma_i = \int_1^5 V_{r_i} dr/5 + \int_6^{10} V_{t_i} dr/5 \\ \quad + \int_{11}^{15} V_{r_i} dr/5 + \int_{16}^{20} V_{t_i} dr/5 \\ \Gamma_\omega = \omega(dr)^2 \end{array} \right.$$

Figure 22

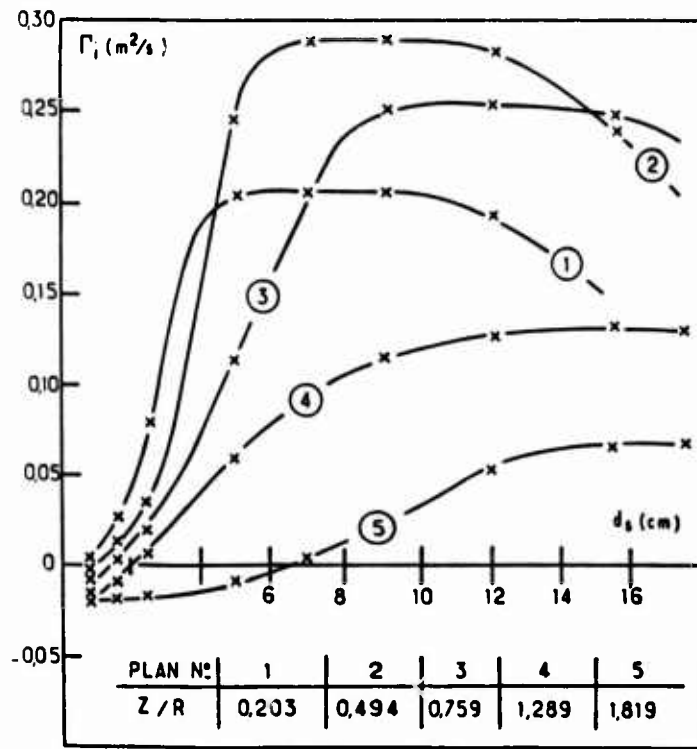


Figure 23

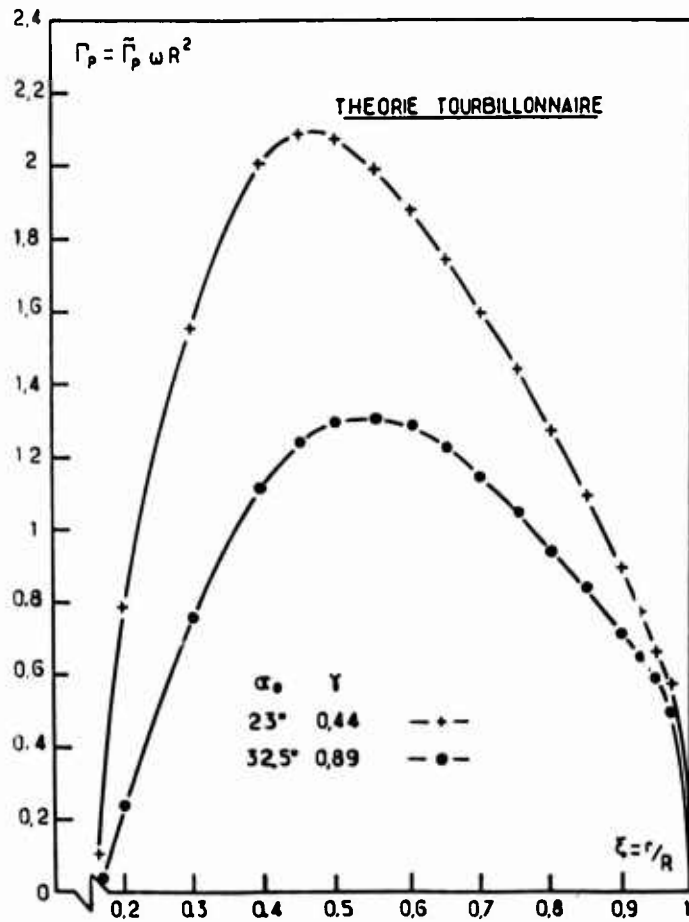


Figure 24

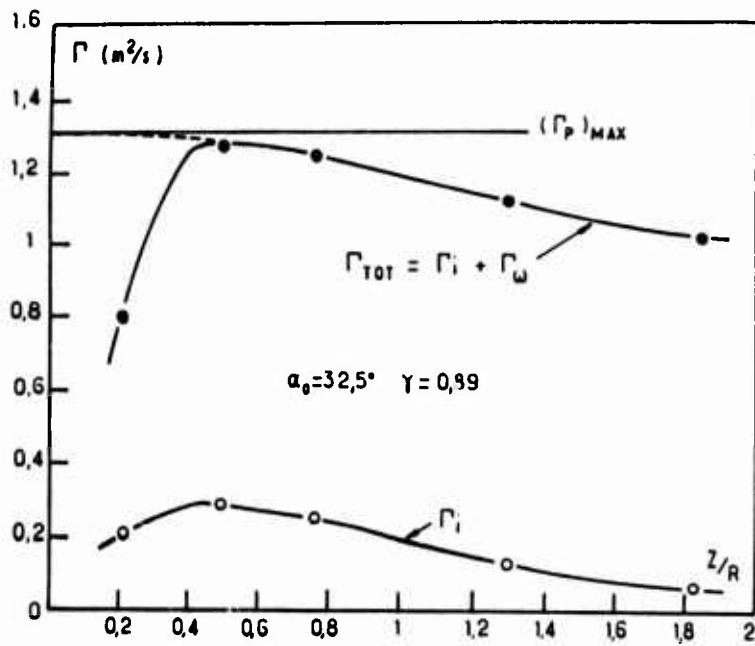


Figure 25

INVESTIGATIONS OF MODERN GENERAL AVIATION PROPELLERS

H. Zimmer
Dornier GmbH, Friedrichshafen

R. Hoffmann
Hoffmann-Propellers, Rosenheim

K. H. Horstmann
DFVLR, Braunschweig

SUMMARY

After a period of stagnation in the years following WW II an accelerated movement towards propeller propulsion has taken place in recent years. Because of its inherent propulsive advantages the propeller propulsion has a considerable development potential. Initial analyses of the state-of-the-art of propeller technology in the General Aviation field by means of flight and windtunnel tests as well as by aerodynamic and acoustic calculations have shown possibilities for improvement, mainly in the lower and medium speed range. Improved propellers were designed and analysed theoretically and experimentally. Newly designed supercritical airfoils with high lift-to-drag ratios at high lift were used. To find the optimum blade shapes associated with minimum superevelocities, also several tip shapes were analysed. After windtunnel tests the best of the propeller designs was selected for full scale flight test. A set of experimental propellers for the Do 228 Experimental aircraft was developed, constructed and tested. Improvements were achieved in the whole flight regime. The experience of this propeller development program was used to design a high performance high speed General Aviation propeller for $M = 0.6$ flight.

NOTATION

c	Chord length	β	Twist distribution [$^{\circ}$]
c_d	Drag coefficient	δ	Blade angle [$^{\circ}$]
c_l	Lift coefficient	η_K	Wing flap angle [$^{\circ}$]
$c_{l_{max}}$	Maximum lift coefficient	η_V	Uninstalled propulsive efficiency
c_p	Pressure coefficient		
c_p^*	Critical pressure coefficient		
G	Aircraft mass [kg]		
H	Altitude [m]		
M	Mach number		
n	Turnrate [RPM]		
P	Power [SHP, kW]		
r, R	Radius [m]		
Re	Reynolds number		
T	Thrust [kp, N]		
V	Velocity [$\frac{m}{s}$, $\frac{km}{h}$]		
V_d	Downwash at blade station [$\frac{m}{s}$]		
x, y	Propeller coordinate system		

Abbreviations

AF	Activity Factor
BMFT	Federal Minister of Research and Technology
DFVLR	German Aerospace Research Agency
FL	Flight number
TNT	New Technology Wing
TQ	Engine Torque [%]
TWB	Transonic Windtunnel Braunschweig
UYS	University of Stuttgart
ZKP	Civil Component Experimental Program

1. INTRODUCTION

During WW II the propeller propulsion reached a standard, which was quite high, as is shown, for instance, by the flight performance of the Do 335 aircraft according to figure 1. With the appearance of jet engines the propeller propulsion experienced a certain stagnation but due to the fact that the latter represents the optimum and therefore the most economical type of aircraft propulsion, there is great emphasis all over the world both to improve propeller propulsion in the low and medium speed range and to extend its application to significantly higher velocities than are currently used.

In recent years considerable efforts have been made to improve the performance of General Aviation aircraft, mainly by an improved wing design. One example is the New Technology Wing (sponsored by the BMFT), which showed excellent performance in flight test and therefore was introduced into the Do 228 series production aircraft (figure 2).

The aim of the present study (also sponsored by the BMFT) was therefore to use this aerodynamic background to establish improved propeller designs. This study was performed in cooperation between DORNIER (prime contractor), HOFFMANN (propeller manufacturer), DFVLR and the University of Stuttgart. The major steps of this development program are summarized in figure 3. The goal of the study was a thrust improvement and noise reduction of the propeller by specific aerodynamic measures at a given diameter, power and rotational speed. A four-bladed propeller was developed and optimized. Also a three-bladed version was analysed. The study should lead to a propeller, which could be certified on the Do 228 (figure 2) to enhance its shortfield and also hot-and-high performance. The main steps of the study according to figure 3 were carried out in the timeframe October 1978 through April 1982. Since then certification work and preparation of the series production have been done. In this report emphasis is placed on the aerodynamic design aspects and the effects on propeller performance. Also some features concerning the adopted light weight blade construction are described. For more detailed results and also for the theoretical and experimental acoustic properties references [1] and [2] are recommended.

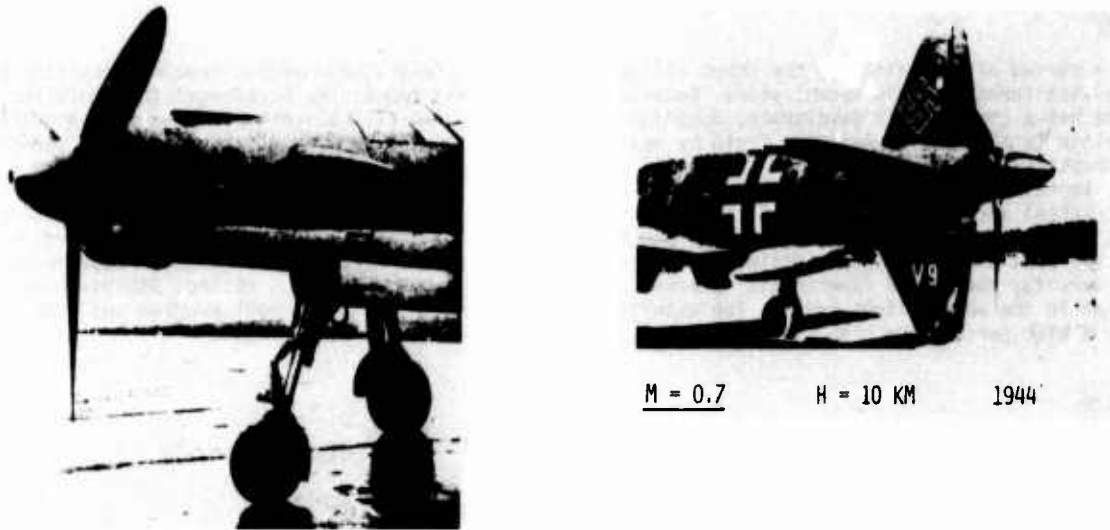


Figure 1: Dornier Do 335 aircraft



Figure 2: Dornier Do 228 aircraft

Besides the full scale propeller tests windtunnel test were carried out on one third scale model propellers. Two propellers of the flight test series were also tested in model scale. Fig. 5 shows the DFVLR model propeller test stand with a model propeller equipped with bent tips. Also the acoustic test set up can be seen. During the study five model propellers were constructed and tested [3], [4].

2.2 Theoretical analysis

In the aerodynamic analysis of the known propellers and also for the design of the improved ones the mathematical model depicted in figure 6 was used. This method (an extended version of [5]) is a blade element vortex wake method, where the radial contraction and the axial displacement of the blade tip vortices is

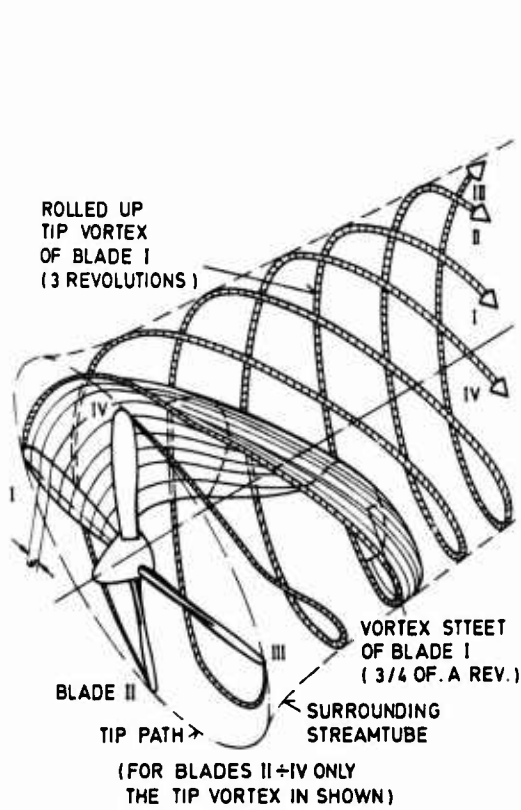


Figure 6: Mathematical model used in the propeller calculation

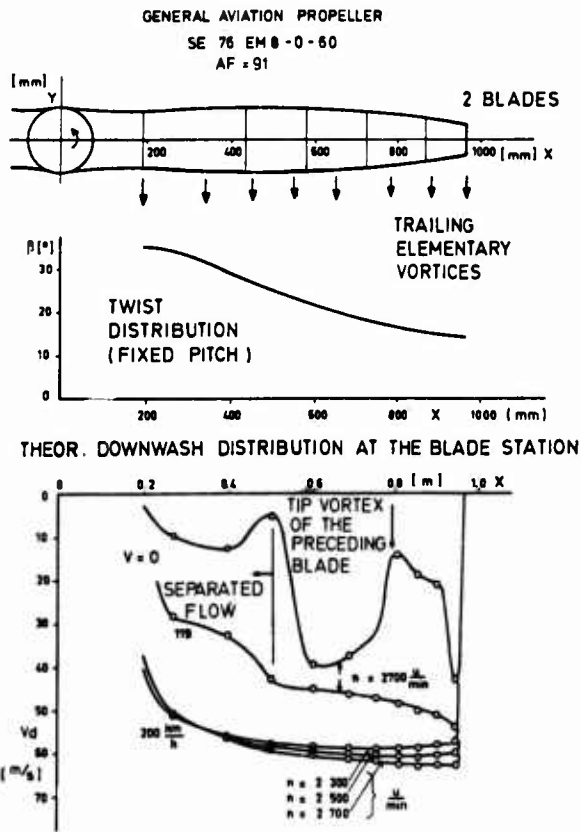


Fig. 7: Downwash distribution at the blade station of a two-bladed General Aviation propeller

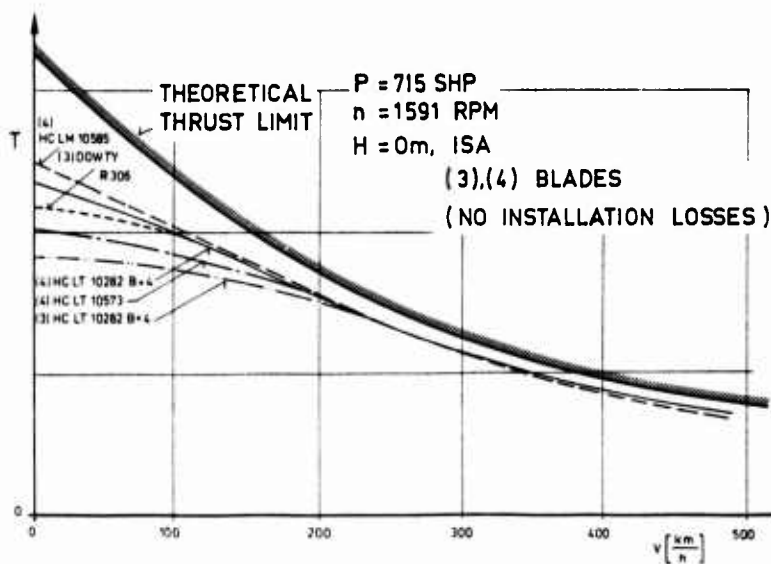


Figure 8: Thrust dependence of flight velocity for several General Aviation propellers

prescribed and where the vortex wakes of the several blades adjust themselves freely in axial direction according to the local downwash. This method proved useful for the design and analysis of a variety of different propellers and rotors in the whole power range. The results of this modelling of the propeller flowfield is illustrated on a fixed pitch General Aviation propeller in the 150 kW power class according to figure 7. There the calculated downwash distributions are given for static condition, climb and cruise flight at 3 turnrates. In the static case the downwash in the tip region is very irregular due to the strong blade-tip vortex interaction and at the inboard portion of the blade the downwash has broken down due to flow separation. In the climb condition an inner separated region is still discernible, but in cruise flight a near optimum constant downwash is present. All the other distributions of interest, e. g. local lift, drag, circulation, thrust, moment and also the corresponding

CIVIL COMPONENT EXPERIMENTAL PROGRAM

DEVELOPMENT OF AN IMPROVED GENERAL AVIATION
PROPELLER IN THE 500 - 600 KW POWER RANGE

1. ANALYSIS OF THE STATE OF THE ART (DO, HO,
DFVLR, UYS) THEOR., EXP., 2-D, 3-D

2. DEVELOPMENT OF IMPROVED AIRFOILS
(DFVLR, UYS)

3. OPTIMIZED BLADE SHAPE (DO)

4. DESIGN, CONSTRUCTION, TEST OF MODEL
PROPELLERS (DO, HO, DFVLR)

5. DESIGN, CONSTRUCTION, TEST OF FULL-SCALE
PROPELLERS (DO, HO)

Figure 3: Major steps of the ZKP-Development Program

2. ANALYSIS OF THE CURRENT PROPELLER TECHNOLOGY

2.1 Experimental analysis

In the first step according to figure 3 an analysis of the current propeller technology was done. It was very helpful that the possibility was given to flight test eight available propellers in the time frame of the study on the Do 228 Experimental Aircraft. Figure 4 shows seven out of the eight propellers tested.

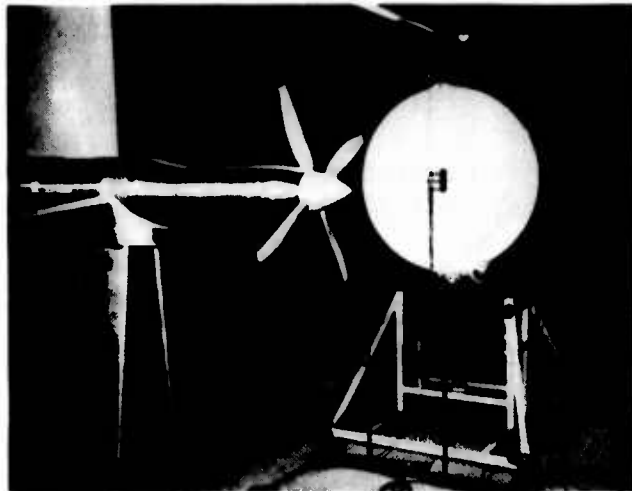
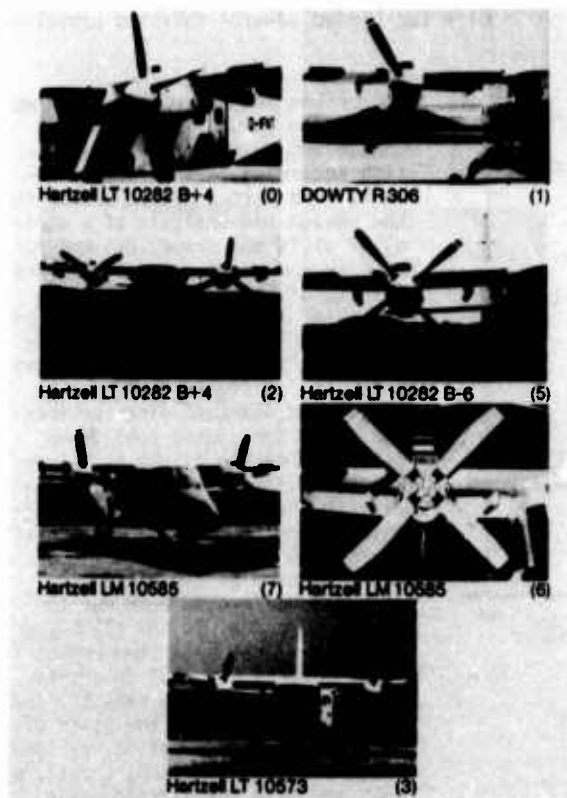


Figure 5: DFVLR Model propeller test stand

Figure 4: Candidates of the propeller flight test

Besides the full scale propeller tests windtunnel test were carried out on one third scale model propellers. Two propellers of the flight test series were also tested in model scale. Fig. 5 shows the DFVLR model propeller test stand with a model propeller equipped with bent tips. Also the acoustic test set up can be seen. During the study five model propellers were constructed and tested [3], [4].

2.2 Theoretical analysis

In the aerodynamic analysis of the known propellers and also for the design of the improved ones the mathematical model depicted in figure 6 was used. This method (an extended version of [5]) is a blade element vortex wake method, where the radial contraction and the axial displacement of the blade tip vortices is

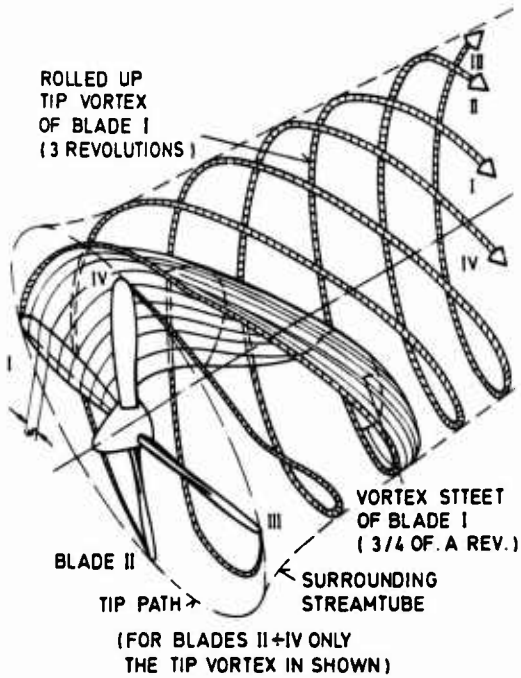


Figure 6: Mathematical model used in the propeller calculation

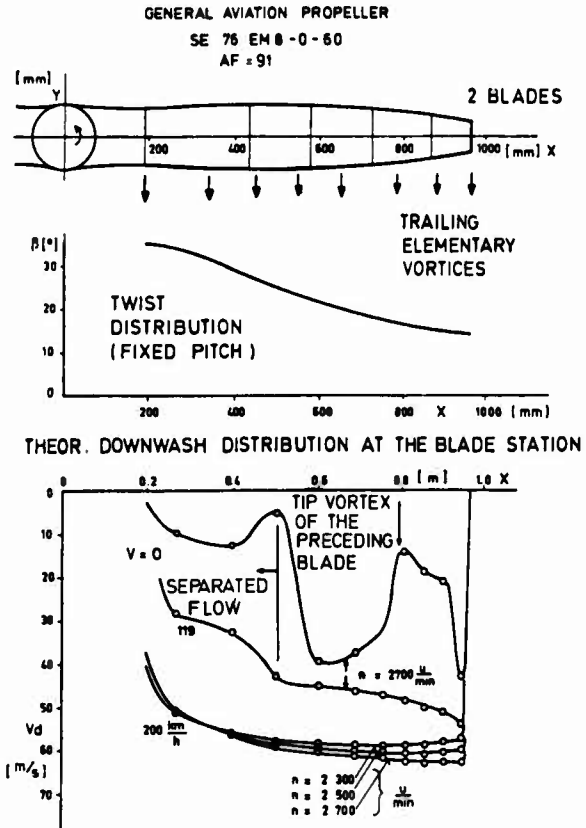


Fig. 7: Downwash distribution at the blade station of a two-bladed General Aviation propeller

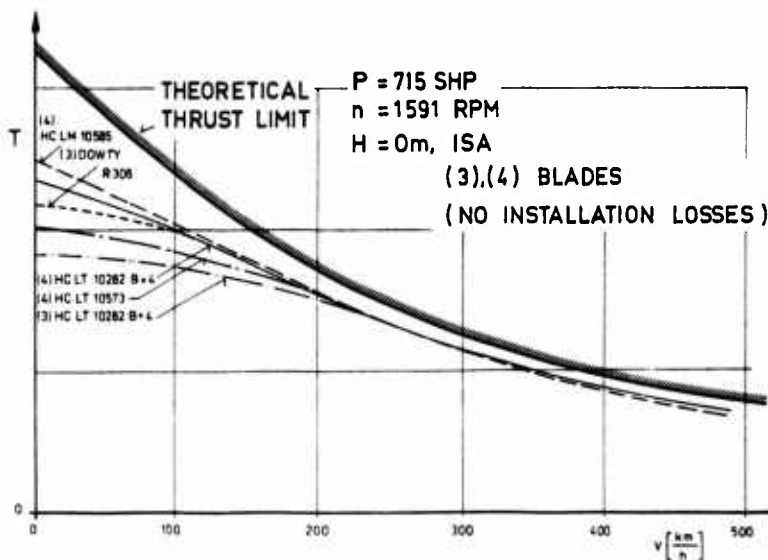


Figure 8: Thrust dependence of flight velocity for several General Aviation propellers

prescribed and where the vortex wakes of the several blades adjust themselves freely in axial direction according to the local downwash. This method proved useful for the design and analysis of a variety of different propellers and rotors in the whole power range. The results of this modelling of the propeller flowfield is illustrated on a fixed pitch General Aviation propeller in the 150 kW power class according to figure 7. There the calculated downwash distributions are given for static condition, climb and cruise flight at 3 turn-rates. In the static case the downwash in the tip region is very irregular due to the strong blade-tip vortex interaction and at the in-board portion of the blade the downwash has broken down due to flow separation. In the climb condition an inner separated region is still discernible, but in cruise flight a near optimum constant downwash is present. All the other distributions of interest, e. g. local lift, drag, circulation, thrust, moment and also the corresponding

coefficients are calculated using the local aerodynamic profile characteristics which are given.

Several of the tested propellers were analysed this way. A characteristic result is shown in figure 8, where the thrust, depending on flight velocity, for several General Aviation propellers is compared with the theoretical limit. From this figure the conclusion can be drawn, that in the lower and medium speed regime an improvement should be possible. In the present study two reference propellers were considered. Since the Do 228 Experimental Aircraft was originally equipped with Hartzell LT 10282 B+4 propellers, this type is named reference propeller 1 (figure 4, version (0)) and since the propellers Hartzell LT 10573 were introduced into the Do 228 series, this type is named reference propeller 2 (figure 4, version (3)).

3. FOCUS OF THE PRESENT DEVELOPMENT PROGRAM

In order to develop a propeller with improved performance the blades should have a favourable lift to drag ratio in the whole working range. To achieve this, the following aspects were given particular attention:

- The profiles along the whole blade must have favourable aerodynamic characteristics
- Careful design of the blade root area
- Careful desing of the blade tip region

In order to achieve a noise reduction despite the increased thickness of the composite blade structure in comparison with the reference metal blade, a blade design with minimum superevelocities was worked out. Minimum superevelocity in tangential direction was achieved by a roof top type pressure distribution of the profiles in the outer blade region and minimum superevelocity in axial direction was achieved by optimizing the blade tip region for a smooth downwash distribution by reducing the tip vortex circulation strength and by increasing the loading of the inner blade region. The design condition for the propeller was the single engine climb case of the Do 228 aircraft.

4. AIRFOIL DEVELOPMENT

4.1 Design features for the outer propeller blade sections

For a low drag airfoil development two design features are important [6]:

- Avoiding local supersonic regions with strong drag inducing shocks
- Extending the region of laminar boundary layer on both surfaces as much as possible

Except in the case of high loaded blades the first requirement in general can be fulfilled. Due to the small thickness of outer propeller sections the second one, however, leads to an airfoil with a very sharp leading edge with the risk of an abrupt stall behaviour and a corresponding low maximum lift coefficient. To avoid this sharp leading edge the laminar boundary layer region has to be limited to a certain value depending on other requirements. Especially on the lower surface it is convenient to limit the laminar boundary layer region. Due to the higher flow velocity it is more efficient with regard to the drag to realize a large laminar boundary layer region on the upper surface.

For a high static thrust a high maximum lift coefficient, especially at the radial position $r/R \approx 0.8$ with a Mach number $M \approx 0.6$, is required. Therefore the small local supersonic flow field existing near the leading edge on the upper surface should be extended to about 15 % of the chord length. This is attainable by a reduction of contour curvature at the leading edge and a relatively high curvature at the rear part of the supersonic region.

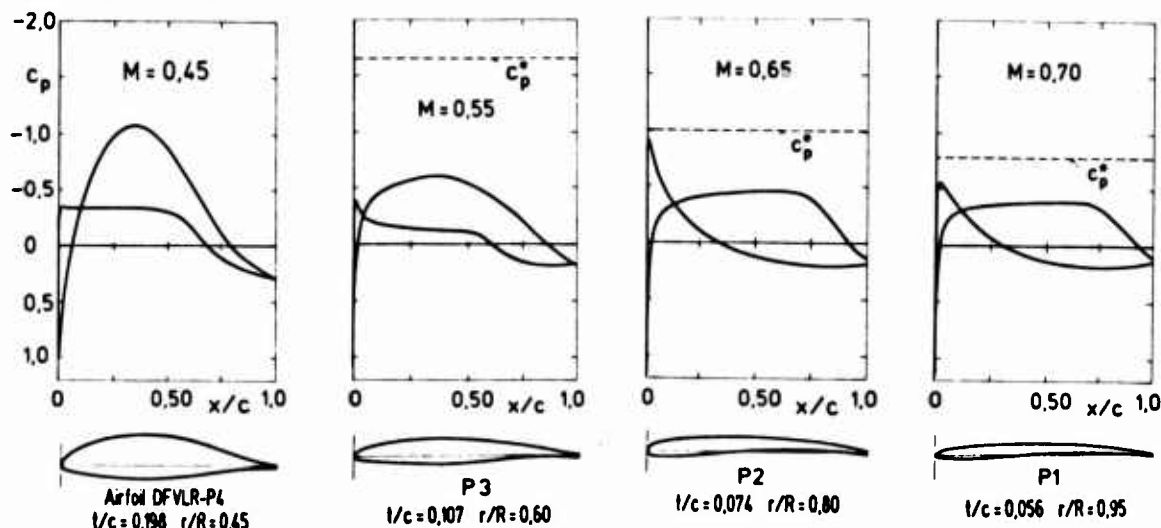


Figure 9: Calculated pressure distributions for different radial blade sections at cruise conditions ($c_1 = 0.3$, $Re = 2.5 \cdot 10^6$)

Unfortunately this typical curvature distribution, first described by Wortmann [7], considerably reduces the lift coefficient range of the low drag bucket due to laminar boundary layer at climb and cruise conditions. The high curvature at $10 \pm 15\%$ chord length causes downstream an additional destabilisation of the laminar boundary layer.

Fig. 9 shows the contours of four airfoils designed for different radial blade positions and the calculated pressure distribution at cruise conditions.

For the airfoils DFVLR-P1 and P2 laminar boundary layers up to 80% on the upper surface and 10% ÷ 20% on the lower surface can be expected. At climb conditions (not shown) the laminar flow region on the upper surface is only insignificantly reduced and on the lower surface it is considerably extended. The airfoils P3 and P4 are designed for smaller laminar boundary layer regions on the upper surface and larger regions on the lower surface.

4.2 Airfoil design and analysis methods

Developing the four airfoils shown, two methods are used. The inverse problem which needs the prescribing velocity distribution on the airfoil as input and which leads to the airfoil contour and to the aerodynamic coefficients has been solved by a modified computer code from Eppler and Somers [8]. This very efficient code for incompressible flow has been extended to subsonic flow by Radespiel [9] who introduced a combination of two different compressibility rules. The Eppler/Somers code is based on a conformal mapping procedure in its design part and on a higher order panel/boundary layer interaction method in its analysis part. A number of options can be specified in the design part such as extent of upper and lower surface pressure plateaus at specified angles of attack, extent and behaviour of recompression in the rear part, trailing edge angle, etc.

For transonic flow the Bauer/Garabedian/Korn/Jameson method (BGK III) was used [10], [11], which is based on a finite difference approximation of the full potential equation in a transformed mesh to fulfill the exact boundary conditions. In the BGK III as well as in the modified Eppler/Somers code the viscous effects are taken into account by adding the boundary layer displacement thickness to the airfoil contour.

4.3 Windtunnel

The experimental investigations have been carried out in the Transonic Windtunnel Braunschweig (TWB) of the DFVLR [12]. The windtunnel is of the blow-down type and especially suited for airfoil tests at subsonic and transonic flows in the Mach number range of $M = 0.3$ to 0.9 . The rectangular test section of 34 cm by 60 cm with slotted walls at the top and the bottom allows testing of airfoil models with chord lengths of 10 cm to 20 cm and a span of 34 cm. This results in

- windtunnel height/airfoil chord ratios of 0.6 to 3.0 and
- geometric aspect ratios of 3.4 to 1.7

which are common in airfoil investigations. In this case 12.5 cm chord length models have been used. The width of the slots has been optimized for zero blockage corrections. This has led to an open area ratio of 2.35%.

In a routine investigation the subsequent data are provided from the experiment

- static pressure on the airfoil contour at approximately 50 locations on the contour
- total and static pressure in the wake at approximately 360 locations

Lift and pitching moment coefficient are evaluated from the contour pressure, drag coefficient from the wake traverse pressures.

As in all other transonic windtunnels the turbulence and especially the high noise level considerably influence the laminar boundary layer development, but an indication of the transition location shift or an amount of drag increase can not be given.

4.4 Experimental results

The drag polars of the airfoils DFVLR-P1 and P2 at different Mach numbers are shown in fig. 10. For comparison the polars of a NACA 16-series airfoil taken from the reference propeller 1 and also tested in the TWB are included in the figures. All figures show that the low drag lift coefficient range of the DFVLR-airfoils is much larger than that of the reference airfoil. Additionally, the drag of the DFVLR airfoil is lower. At cruise conditions the difference amounts to $\Delta c_d = 0.001 \div 0.003$ (10% ÷ 30%). For cruise and climb and partly for take-off conditions the polars cover the required lift coefficient range of low drag.

The ranges of low drag are mainly characterised by complete subsonic flow or by local supersonic flow fields without a severe drag inducing shock. Since the windtunnel flow is disturbed by noise and turbulence the size of the laminar boundary layer region on the airfoil is small and therefore has only a minor influence on the measured polar.

Characteristic performance boundaries of the three airfoils are shown in fig. 11. The maximum lift coefficients of the DFVLR airfoils are significantly higher than those of the reference airfoil. The drag boundaries $c_d = 0.01$ and 0.015 cover a much larger M - c_l -area. The operational conditions of cruise and climb are completely inside the $c_d = 0.01$ -boundary.

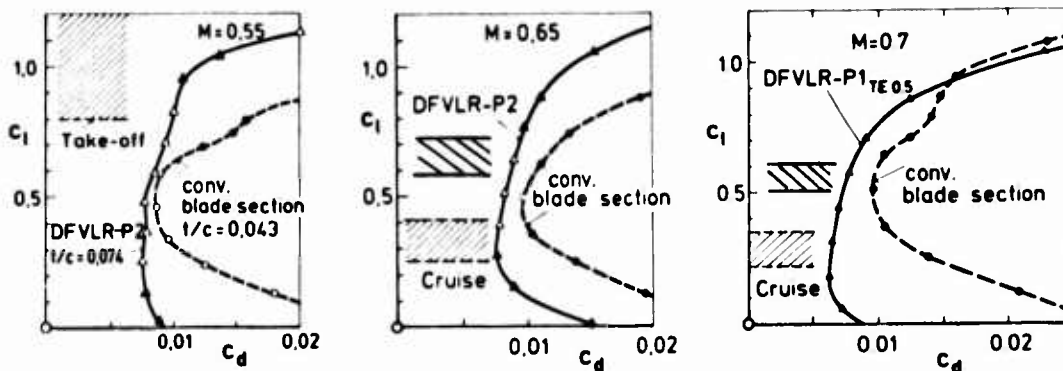
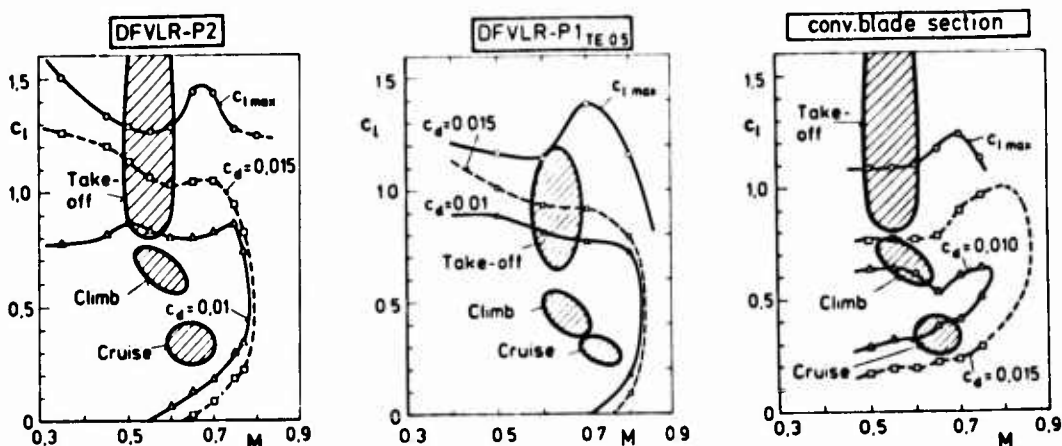
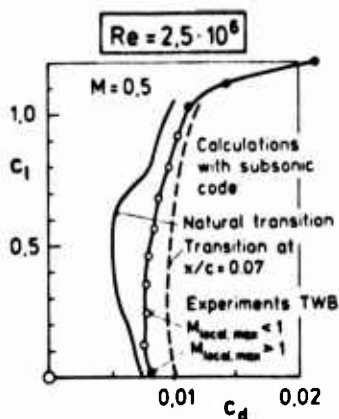
Experiments TWB, $Re=2.5 \cdot 10^6$, $\Delta M_{local,max} < 1$ 

Figure 10: Measured drag polars of different airfoils

Figure 11: Maximum lift coefficients and constant drag lines of different airfoils ($Re = 2.5 \cdot 10^6$)

As mentioned above the windtunnel turbulence and especially the high noise level force transition considerably more upstream than in free flight. To illustrate this problem fig. 12 shows a comparison of polars from windtunnel measurements and two different calculations, with free transition and with transition at $x/c = 0.07$. The calculated drag polar with free transition clearly shows the laminar low drag bucket in the lift coefficient range $c_l = 0.25 \div 0.75$. The measured polar curve shows drag coefficient values between those of the two calculated polars. This leads to the two assumptions that inspite of the presence of turbulence and high noise level a certain region of laminar boundary layer exists and that in free flight a considerable lower drag could be attained.

Figure 12: Comparison of the measured and calculated drag polars of the airfoil DFVLR-P2

4.5 Airfoils for the blade root

As was shown in [13] the usable lift in the hub region of a rotating propeller is increased by the suction effect caused by the Coriolis acceleration working on the boundary layer material. To take advantage of this effect, high lift FX-airfoils were used in the hub region ([14], also private communication) with a two-dimensional maximum lift coefficient up to $c_{l,max} = 2.0$. The definition airfoils for the blade to be developed are shown together in figure 13. These were used in a numerical lofting procedure to define the blade shape.

The radial distribution of the maximum lift coefficient of the new airfoils in comparison to those of reference propeller 1 together with the influence of rotation is shown in figure 14. Near the hub a local maximum lift coefficient of $c_{l,max} = 3$ is obtained.

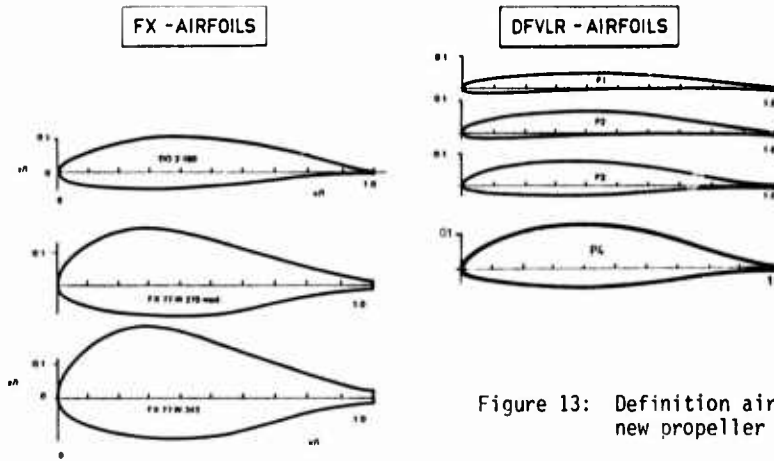


Figure 13: Definition airfoils for the new propeller design

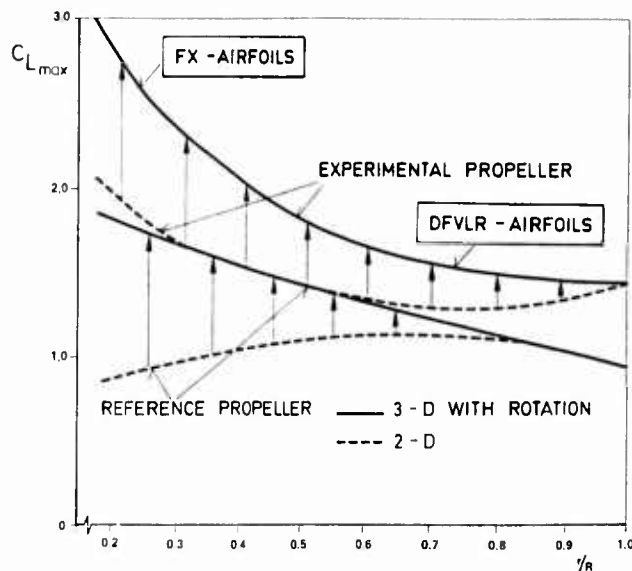


Figure 14: Influence of rotation on maximum lift for different propellers

5. OPTIMIZED BLADE SHAPES

5.1 Blade tip devices

A variety of blade tip devices were already proposed and analysed (e. g. [15]). A review of the work done in this field was also undertaken in order to find the optimum blade shape.

Experimental results on bent-tips in model scale (figure 5) and full scale (300 kW power range) were analyzed. The results showed that the tip devices caused a shift of the propulsive efficiency curve to higher velocities, so that in the lower and medium speed range a slight propulsive efficiency degradation is observed. Only for high velocity low thrust cases the propulsive efficiency is improved. Also flight test results on Bi-blades in the 150 kW power range were analysed. Some beneficial aerodynamic effects were found, but this configurations had inherent structural problems.

To summarize the analysis of different tip devices, it was shown in accordance with the results gained during the development of the New Technology Wing (figure 2) that a nonplanar configuration cannot be as efficient as a planar one. So it was of aerodynamical and acoustical interest to analyse planar swept tips, which prove effective on fixed wings (figure 2) and on helicopter rotors which are relatively lightly loaded when compared with propellers. Results of this part of the study are given in section 6.

5.2 Blade planform optimization

With the aerodynamic characteristics of the selected profiles according to figure 13 and 14 a blade planform variation was carried out using the mathematical model of figure 6 in order to find the optimum blade shape. Several analysed planform shapes can be seen on figure 15.

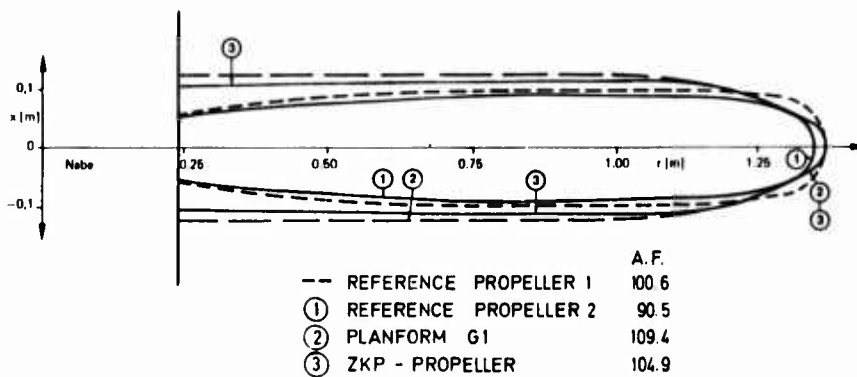
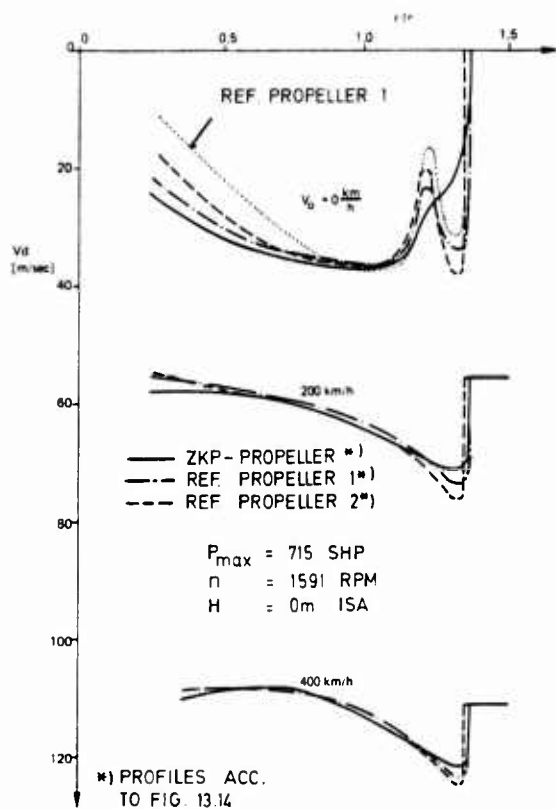


Figure 15: Several analysed blade planforms



A second optimization criterion besides the overall thrust was the downwash distribution according to the above mentioned reasons. Figure 16 shows the influence of several blade planforms on the downwash distribution for the three conditions of main interest, i. e. static condition, climb and cruise flight. The distributions of the conventional planform shapes show the typical kinks in static condition due to the strong blade-vortex interaction. Also in climb and cruise flight the relatively strong tip vortices induce quite a high downwash peak at the outer end. Finally the ZKP-planform was selected because the blade-vortex interaction is greatly reduced - which is due to the relatively small tip vortex circulation strength - and because a more uniform downwash is present at the inner blade area which is due to increased loading there. Also in climb and cruise flight the downwash peaks are significantly reduced. This effect of a reduced intensity of the wake vortex system circulation also proved effective in reducing noise.

After the optimum blade shape had been established with a twist distribution optimized for the single engine climb speed, the usual performance characteristics were calculated for a four-bladed and a three-bladed propeller. In figure 17 the theoretical thrust of these two versions are compared with the performance of the propellers already analysed in figure 8. According to these results the four-blade version shows a considerable improvement in efficiency especially in the lower and medium speed regime. Because the three-blade version still ranks at the high edge of the current technology, this version is also of interest because of the potential to reduce the propeller mass without degradation in performance.

Fig. 16: Influence of blade planform on downwash distribution

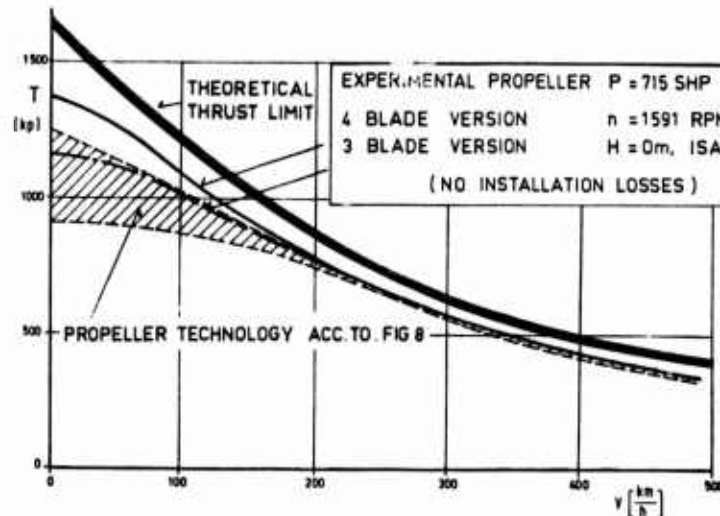
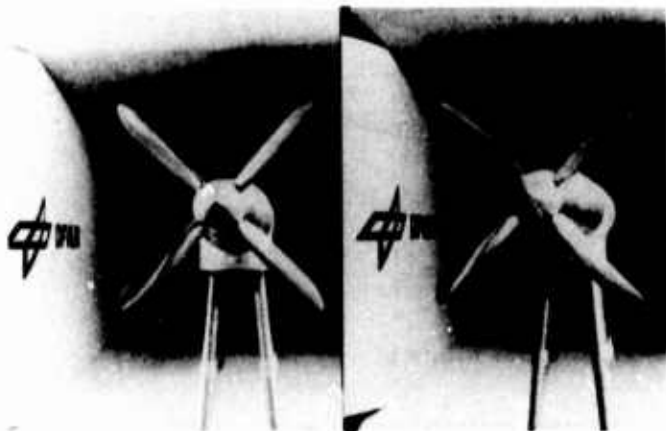


Figure 17: Thrust vs flight velocity of the developed four- and three-blade propeller in comparison with current propellers

6. DESIGN, CONSTRUCTION AND TEST OF THE MODEL PROPELLERS



After the blade shape had been specified, two model propellers were designed and constructed in aluminium by numerical machining. These propellers (figure 18) had identical profiles (figure 13) and twist distribution. The only difference was that model propeller 5 had swept tips.

Figure 18: Model propeller 4 (left) and 5 (right)

Figure 19 shows a comparison of the calculated and measured power and thrust of model propeller 4 dependent on blade angle. It shows that the required power is quite accurately predicted, but that the theoretical thrust for high power loading is not obtained in the experiment. This can be explained by the fact that in the calculation the aerodynamic characteristics for the full scale Reynolds Number were used. In effect the full scale propeller tests carried out later met the predictions exactly.

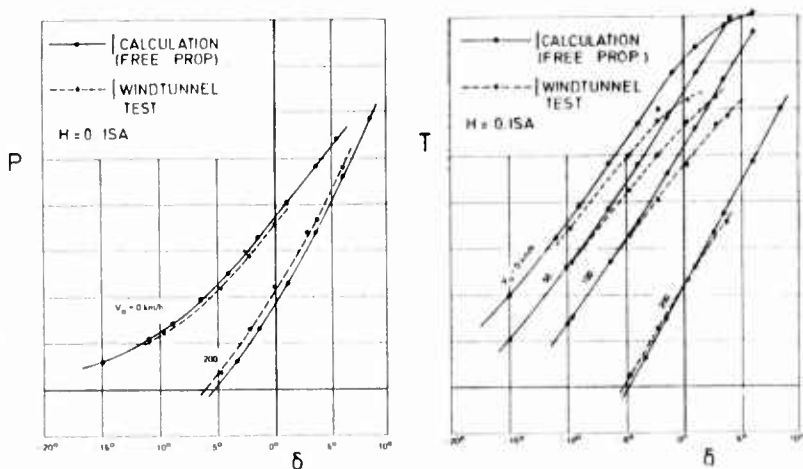
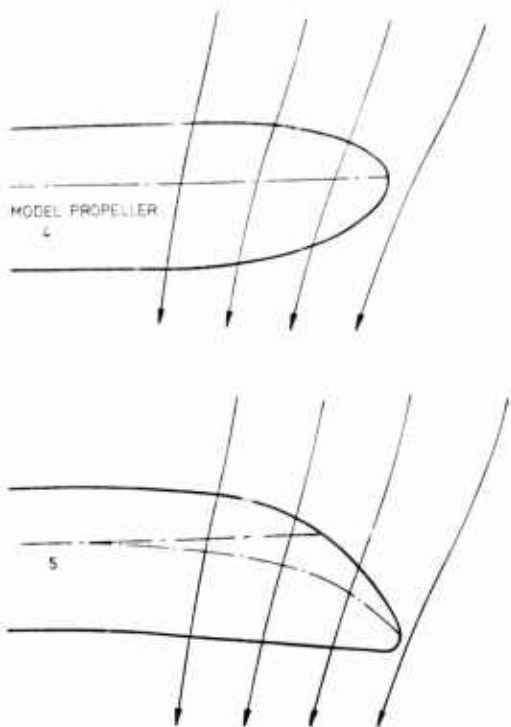


Figure 19: Comparison of the theoretical and experimental required power and thrust of model propeller 4 dependent on blade angle



The measurements of model propeller 5 showed that this version had almost the same performance as model propeller 4. Where differences occurred they were always small and in favour of model propeller 4. The acoustic properties of model propeller 5 were such that for low power loading the noise emission was lower than that of No. 4 (in accordance with helicopter rotor experience) but for high power loading the swept tips produced more noise than the straight ones. This behaviour can be explained by the local flow field in the tip region as shown schematically in figure 20. Due to the increasing downwash contraction with increasing power loading the swept tips become aerodynamically unswept while the straight tips become aerodynamically swept forward. Because of this positive effect the straight tips of model propeller 4 were selected for the full scale propellers.

Figure 20: Flow field in the tip region of model propeller 4 and 5 under high load condition (schematically)

7. DESIGN, CONSTRUCTION AND TEST OF THE FULL SCALE PROPELLERS

7.1 Design and construction of the blades

The comparatively voluminous blades had to be constructed with a very light structure, because metal blades would have been too heavy. Therefore the blades were designed and built with a relatively inexpensive wood-composite structure. This type of construction is a modern development of the technology widely used on German and British aircraft during WW II.



Figure 21: Root section (left) and tip section (right) of the blade structure without the composite shell

This technology proved a high reliability and durability even under harsh environmental conditions (e. g. Hovercraft) up to 4.000 kW. Experience over several decades is at hand. Figure 21 shows the blade structure before the composite outer shell is applied. The blade shank and the root region is made of highly densified red-beech wood. This material has the strength of aluminium with half its specific weight. The blade retention system is integrated into the shank such that these blades can easily be exchanged against the metal blades on standard Hartzell hubs. The blade retention system also was subjected to the appropriate certification tests.

On figure 21, at the root section, the foam filled leading and trailing edges are visible, also the transition of the densified wood (dark) to pine wood, which represents the load carrying structure of the outer blade. Also the metal erosion resistance strip is discernible. This structure is machined after a master blade, surrounded by a fiber reinforced plastic shell to carry torsional loads, and is slightly corrected - if needed - using numerically machined templates.

7.2 Test of the full scale propellers

The propellers were adapted to the control system of the Garrett TPE 331-5 engines and tested in the four-blade and three-blade version according to figure 22.

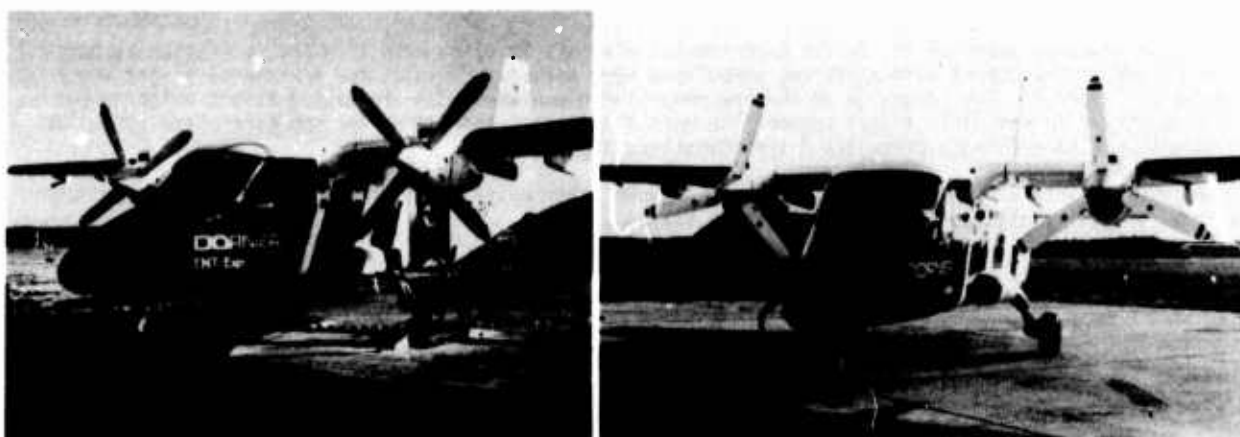


Figure 22: The developed propellers on the Do 228 Experimental Aircraft

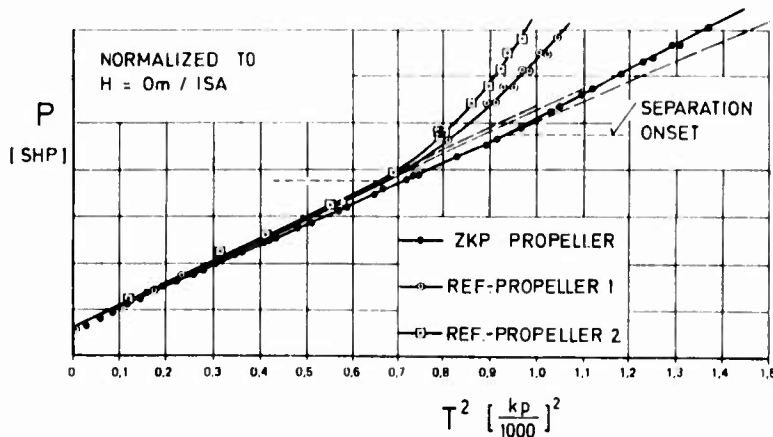


Figure 23: Static thrust measurements for different propellers on the Do 228 Experimental Aircraft

The static thrust was measured on the Do 228 Experimental Aircraft with different propellers installed. Results can be seen on figure 23, where the squared thrust is shown dependent on the required power for the three most interesting four-blade propellers. The deviation from the straight lines indicates beginning flow separation in the inner propeller region. It is evident that the ZKP-propeller produces more thrust at a given power setting, also flow separation onset starts later and is apparently very weak, so the blade root design proves to be effective.

The propeller thrust was also reduced from the accelerated roll tests according to figure 24. Here also the advantage of the ZKP propeller is evident.

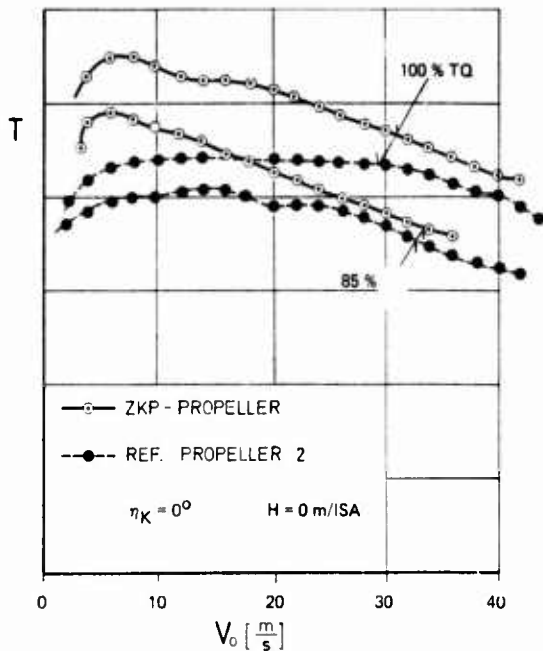


Figure 24: Thrust dependent on velocity for different propellers reduced from the taxi tests

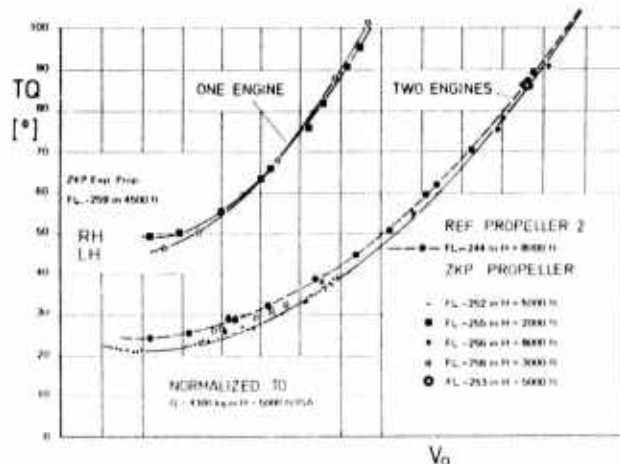


Figure 25: Required power in stationary horizontal flight of the Do 228 Experimental Aircraft equipped with different propellers

Finally the required power of the Do 228 Experimental Aircraft in climb condition and in stationary horizontal flight when equipped with different propellers were measured. Results for horizontal flight are compared in figure 25. The advantage of the new propeller diminishes with increasing flight velocity but remains positive in the whole flight regime. The main flight test results of the new four-blade propeller in comparison with reference propeller 2 are summarized in figure 26.

In the range of interest the propeller thrust at a given power measured by the different methods mentioned above was generally within $\pm 5\%$ of the expected values.

FLIGHT TEST RESULTS ZKP-PROPELLER - REFERENCE PROPELLER 2:

- STATIC THRUST + 19 %
 - CLIMB VELOCITY
 - ON TWO ENGINES + 6 - 7 %
 - ON ONE ENGINE + 10 - 16 %
 - CRUISE VELOCITY + 2 %
 - RANGE + 3 %
- ARTIFICIAL EROSION HAS NEGLIGIBLE INFLUENCE
FOR EQUAL THRUST NOISE AND VIBRATION ARE REDUCED
REVERSE- AND AIRSTART-CHARACTERISTICS ARE IMPROVED

Figure 26: Main flight test results of the new four-blade propeller compared with reference propeller 2

8. DEVELOPMENT OF A HIGH SPEED GENERAL AVIATION PROPELLER

With the experience gained in the previously described development program a high performance relatively highly loaded propeller for the $M = 0.6$ cruise flight regime was designed for a new project. The profiles P1 through P3 according to figure 9 were moved further inboard and another new inboard section was designed. Some geometrical characteristics are shown on the left hand side of figure 27. Because of the favourable aerodynamic high speed characteristics according to figure 10 and 11 the profiles P1 and P2 can tolerate the much higher load in cruise condition ($c_1 = 0.5 \div 0.7$) with only a small drag increase as indicated in figure 10. So the calculated propulsive efficiency of this propeller is quite high as can be seen on the right hand side of figure 27.

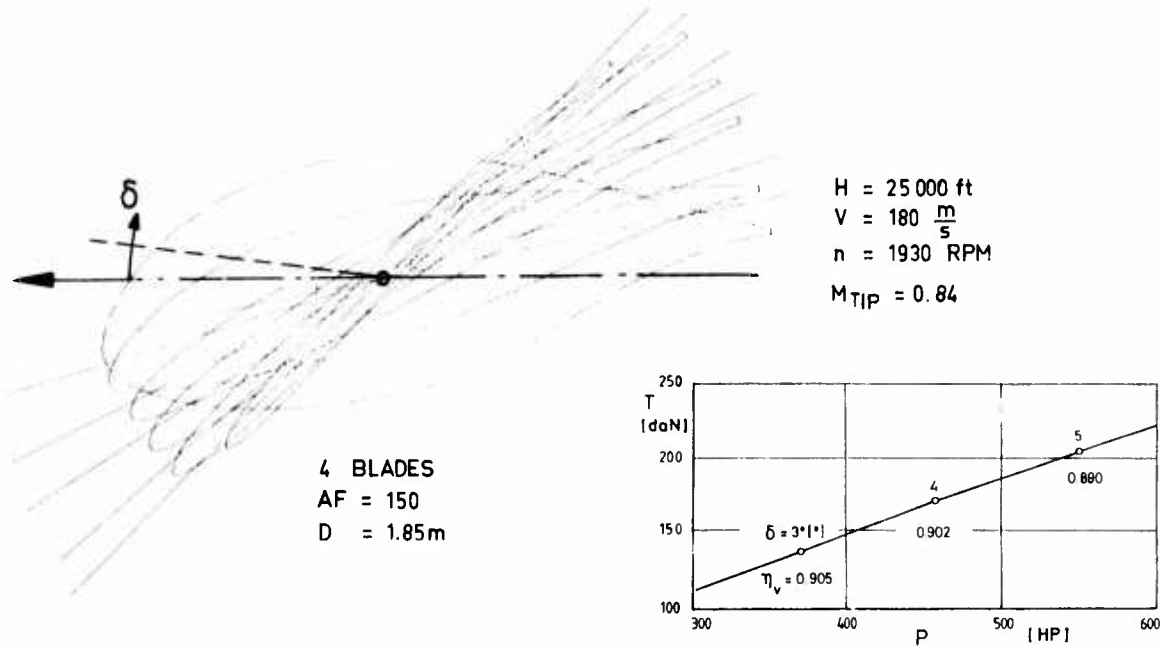


Figure 27: Geometrical characteristics and cruise performance of a high speed General Aviation propeller

8. REFERENCES

- [1] H. Zimmer, J. U. Borchers, H. Friedel:
Entwurf, Bau und Erprobung eines Experimentalpropellers in der Leistungsklasse 750 PS.
Jahrestagung der DGLR, DGLR-Nr. 82-066, Stuttgart, 5. - 7. Okt. 1982
- [2] H. Zimmer, R. Hoffmann:
Ein verbesserter Propeller für Flugzeuge der Allgemeinen Luftfahrt.
3. BMFT-Statusseminar, Hamburg, 2. - 4. Mai 1983
- [3] W. Böddener, W. Stäger:
Aerodynamische Messungen an 1:3-Modellpropellern im 3m-Niedergeschwindigkeitskanal Göttingen -
Vorläufige Ergebnisse des zweiten Meßabschnittes.
DFVLR-Bericht IB 157-80 C23, 1980
- [4] W. Böddener, W. Stäger:
Weitere aerodynamische Messungen an Modellpropellern im 3m-Niedergeschwindigkeitskanal Göttingen.
DFVLR-Bericht Nr. 16 100-81 C29, 1981
- [5] H. Zimmer:
The Rotor in Axial Flow.
AGARD Conference Proceedings No. 111, Aerodynamics of Rotary Wings, Marseille, 13. - 15. Sept. 1972
- [6] K. H. Horstmann, H. Köster, A. Quast:
Entwicklung von vier Profilen für einen Experimentalpropeller in der Leistungsklasse 750 PS.
Paper No. 82-067 presented at the Annual Meeting of DGLR, 1982, Stuttgart, Germany
- [7] F. X. Wortmann, J. M. Drees:
Design of Airfoils for Rotors.
Paper presented at the CAL/AVLABS 1969 Symposium on Aerodynamics of Rotary and VTOL Aircraft,
Buffalo, N. Y., USA
- [8] R. Eppler, D. M. Somers:
A Computer Program for the Design and Analysis of Low-Speed Airfoils.
NASA TM 80210, 1980

- [9] R. Radespiel:
Erweiterung eines Profilberechnungsverfahrens im Hinblick auf Entwurfs- und Nachrechnungen von Laminarprofilen bei Verkehrsflugzeugen.
DFVLR IB 129-81/15, 1981
- [10] F. Bauer, P. Garabedian, D. Korn, A. Jameson:
Supercritical Wing Sections II.
Springer-Verlag Berlin - Heidelberg - New York, 1975
- [11] F. Bauer, P. Garabedian, D. Korn:
Supercritical Wing Sections III.
Springer-Verlag Berlin - Heidelberg - New York
- [12] E. Stanewsky, W. Puffert-Meißner, R. Müller, H. Hoheisel:
Der Transsonische Windkanal Braunschweig der DFVLR.
z. Flugwiss. Weltraumforsch. 6 (1982), pp. 398-408
- [13] H. Himmelskamp:
Profiluntersuchungen an einem umlaufenden Propeller.
Mitteilungen aus dem Max-Planck-Institut für Strömungsforschung, Göttingen, Nr. 2, 1950
- [14] F. X. Wortmann:
Tragflügelprofile für Windturbinen.
Seminar und Statusreport Windenergie, 22. - 24. Okt. 1978, Jülich, ISSN 0344-5798
- [15] J. P. Sullivan, L. K. Chang, C. J. Miller:
The effect of proplets and Bi-Blades on the Performance and Noise of Propellers.
SAE-Paper No. 810600, Business Aircraft Meeting and Exposition, Wichita, Kansas, April 7-10, 1981

AERODYNAMIC AND STRUCTURAL ASPECTS OF PROPELLER AND DRIVE
FOR A 1/5 SCALE WIND TUNNEL PROGRAMME

by

R.M. Bass

Dowty Rotol Ltd. Gloucester, U.K.

B. Munniksma

National Aerospace Laboratory NLR, Amsterdam, The Netherlands

J. van Hengst

Fokker B.V., Schiphol-Oost, The Netherlands

SUMMARY

The paper describes the development of a model propeller and its calibration in association with an axisymmetric nacelle in the NLR low speed tunnel in Amsterdam before testing on a complete 1/5 scale model of the Fokker F50 in the DNW (German-Dutch wind tunnel). The calibration so obtained, allowed the required operating propeller conditions to be set up on the complete F50 model. The influence of Reynolds number on propeller performances is discussed and some data presented showing the good agreement obtained, after correction for scale effects, between experimental model results and full scale prediction. A previously unsuspected and unavoidable vibration originating in the reduction gear train of the drive unit gave rise to high propeller blade stresses, ultimately leading to a blade failure. In order to continue running with minimum delay, new propeller blades with high internal damping were manufactured from composite materials, and the programme was successfully concluded.

NOMENCLATURE

D	Propeller Diameter
R	Blade tip radius
r	Local blade radius
S _p	Propeller disc area
ρ	Free Stream air density
v	Velocity
M _H	Blade helical tip Mach number
β _{0.7R}	Blade pitch angle at 0.7R
ε _o	Swirl angle relative to axial direction
q	Total head
D _S	Drag of strut
D _N	Drag of nacelle
F _{NET}	Propeller net thrust
F _J	Jet Thrust
F _{BAL}	Balance force
P	Shaft Power
n	Propeller Rotational Speed (revs/sec)
J	Advance Ratio. $\frac{v_o}{nD}$
C _p	Power coefficient $\frac{P}{\rho n^3 D^5}$
C _T	Thrust coefficient $\frac{F_{NET}}{\rho n^2 D^4}$
T _c	Thrust coefficient $\frac{F_{NET}}{qS_p}$
η	Propeller efficiency $\frac{F_{NET} v_o}{P}$
Suffices	
o	Free stream
L	Local

1.0 INTRODUCTION

During the development phase of a propeller driven aircraft, much attention has to be paid to the aerodynamics and the stability and control characteristics of the aircraft as affected by the propeller slipstream, this is especially true at take-off, climb-out and landing, where slipstream effects can be quite large. A wind tunnel test was initiated to study the influence on stability and control of the propeller slipstream and the opportunity was taken to acquire some near field noise data by installing microphones in the fuselage in the region of the propeller plane of rotation (see Ref. 1).

The model propeller used for this investigation was designed to represent the aerodynamic configuration of a 4-bladed propeller at that time proposed for the full scale aircraft. The investigation was planned to be conducted on a 1/5 scale model of the F50 in the 8 x 6 m. DNW at the North East Polder, in the

Netherlands, so that full advantage could be taken of the high Reynolds number capability of this tunnel (see Figure 1). In order to calibrate the propeller and drive unit, preliminary tests were carried out on an isolated axisymmetric nacelle in the 3 x 2 m low speed wind tunnel (LST) of the NLR in Amsterdam. During the testing of the complete F50 model, a totally unexpected mechanical excitation was encountered, emphasizing the need to consider all aspects of the combination of propeller and drive unit when designing powered models of propeller installations. This paper addresses itself to the development of a model propeller, its construction, vibrational behaviour, and its performance calibration in isolation before testing on the complete F50 model in the DNW.

2.0 DESCRIPTION OF THE TEST RIG AND PROPELLER

The test rig used in the low speed tunnel and shown in Figure 2, consists essentially of an isolated nacelle, mounted by means of a faired strut on the balance located beneath the wind tunnel floor. The propeller is 4-bladed with a diameter of .762 m and an activity factor of 90. It is a 1/5 scale model of the four bladed propeller at that time proposed for the full scale aircraft.

2.1 Nacelle and Strut

The metal nacelle is a slender body of revolution housing:

- a drive unit and gearbox,
- a Lebow torquemeter installed between propeller and gearbox, and
- an exhaust duct with a ASME nozzle connected to the turbine exhaust of the drive unit.

The maximum cross sectional area and the total length of the nacelle are kept the same as those of the nacelle with a faired inlet of the 1/5 scaled F50 model. The conical front part of the nacelle blends at the forward end with the 15° cone of the spinner and is smoothly faired at the rear from the cylindrical mid part. The rear part of the nacelle incorporates a faired boattail in order to ensure a uniform flow in the ASME nozzle.

The strut is a steel box covered by a profiled resin fairing. A NACA-6 series thickness distribution was selected to shape the strut cross sectional contour. All the required piping, leads and wirings to control the drive unit run through the strut.

The drive unit is a single stage turbine driven by compressed air with a maximum air consumption of 2.27 kg/s at 17 bar. The turbine motor and output shaft are coupled through a planetary reduction gear system giving a maximum propeller speed of rotation of 7500 r.p.m. At this speed, the power delivered at the propeller shaft amount to 133 kW. A special air supply system was designed in order to avoid abrupt pressure and mass flow changes of the drive air, which would give rise to excessive gearbox torques. Furthermore, this system was set up in such a way that very precise control of the drive unit was attained.

In order to ensure that the drive air ducting did not interfere with the balance a special airbridge was used. The airbridge contains three flexible couplings of which each has two degrees of freedom. From extensive balance calibrations, it was established that the drive air pressure and temperature inside the airbridge had no effect on the balance calibration. Related to the maximum propeller thrust, the repeatability of the balance was found to be within 0.1 %. The accuracy of the built-in torquemeter was about the same order.

2.2 Propeller

2.2.1 Metal Model Propeller

In the interests of speed of manufacture, accurate scaling, and close dimensional tolerances, the model propellers were made with metal blades machined all over by a numerically controlled cutter. The blades were machined from a forged bar of light alloy and finished to within a tolerance band of $\pm .001$ " (0.025 mm). The general construction of the model propeller followed a well tried design indicated quite clearly in Figure 3. The light alloy hub is in two halves, the rear part is retained on the driveshaft by a retaining nut extended forward into a stem, tapped to receive a screw holding the spinner into position against the front half of the hub. The retaining nut imposes no axial constraint on the front half of the hub, which is held to the rear half by four pairs of bolts, each pair being associated with a blade root. The blades are clamped by their shanks between the two halves of the hub. Close tolerances on the blade shank diameter and the hub bores together with the flexibility of the hub between the bores ensure that every blade is gripped sufficiently tightly to prevent change of pitch angle under the influence of the centrifugal twisting moment experienced when running.

Pitch angle was set by slackening the bolts of each blade successively, setting the angle and re-tightening without disturbing the other three blades. It was found convenient to remove the propeller from the model and make use of an existing pitch adjusting jig as shown on Figure 4. This jig consisted of a spigot on which the propeller was mounted and a straight edge at the appropriate radius (0.7R), which could be set to within $0^\circ \pm 5'$. Each blade was then adjusted in turn until the leading and trailing edges of its concave pressure face were in contact with the straight edge.

The time taken to remove the propeller, adjust the blade angles and replace it on the model was about 15 minutes in the LST, where the model was readily accessible, and about 30 minutes in the large DNW where access to the model involved bringing extra equipment into the tunnel.

2.2.2 Composite Blades

Following a blade failure of the metal propeller arising from gearbox-induced vibrations discussed below in Section 5.0, it became necessary to change the elastic properties of the blades. To enable the propeller to operate in this unexpectedly hostile environment it was therefore rebladed with blades made from carbon fibre reinforced plastic.

In a scale model, the dimensions of the blade are fixed from the outset and the elastic and vibration characteristics of a metal blade follow as a matter of course. The very small change obtainable by working to upper or lower dimensional tolerances, or varying the dimensions within this band along the blade are insignificant, and faced by an unexpected destructive vibration, the exciting cause of which cannot be removed, the only course is a change of material. The choices offered are steel, titanium or a fibre reinforced composite. At the particular time when there was an urgent need of replacement blades, machining facilities were heavily committed to other work, and the delay in manufacturing two sets of metal blades was unacceptable. Attention was therefore directed to composite blades for which a large body of experience existed. Analysis of the natural frequencies of a blade made from carbon fibre reinforced epoxy resin indicated that there was no problem from mechanical or aerodynamic excitation, and blades from this material were therefore manufactured. Composite blades offer a number of advantages for model work, and their use is likely to increase, particularly for the larger sizes of model. It is therefore of interest to describe in some detail the construction of the blade.

The particular blade under consideration consists of thirty nine layers of .014" (0.0355mm) thick carbon fibre laminae with fibres all running from root to tip. The radial lengths of the laminae decrease from the surfaces to the centre of the blade so that only three laminae run the full length of the blade, two on one outer surface, suction side, and one on the other, pressure side. A cross section at the root would cut all laminae. This stack of unidirectional carbon fibres is covered on each face by a single layer of .012" (0.305mm) thick crossply carbon cloth with its weave running at 45° to the radial line.

One of the most critical regions in composite blade construction, full scale or model, is the attachment of the non-metallic aerofoil to a metallic root for retention in the hub. The design adopted in the model under discussion is a simple and well tried approach as illustrated in Figure 5. A rectangular slot extending into a truncated wedge is milled into a cylindrical light alloy blade shank. The root ends of the carbon laminae are inserted into the rectangular slot, the layers are separated into two equal thicknesses and a solid metal wedge placed in position as indicated in the figure. The whole assembly of carbon fibres and metal root is placed in the blade mould, impregnated with epoxide resin and cured. After curing, the fibres, prevented from collapsing by the solid wedge, form an immovable joint, keyed to the metal shank, which does not rely on adhesion alone for its strength.

This construction, used in the model propeller, resulted in a larger shank diameter than was the case with the metal blade, and exact scaling of the blade/spinner intersection was no longer possible. The larger shank also necessitated a small change in spinner contour line to contain it. The rear diameter of the spinner however, remained unchanged. Since this model was built, a much smaller root attachment has been developed in which a cone rather than a wedge is used.

2.2.3 Structural Properties

The use of anisotropic composite materials in blade construction allows the elastic properties of the blade as a whole to be very considerably modified, by adjusting the direction of the fibres in individual laminae, without change to external dimensions. The presence of the outer single layers of cross-ply carbon cloth has the effect of raising the natural torsional frequency from 662 Hz to 965 Hz, giving it essentially the same torsional properties as its metal counterpart. Flexural frequency can be lowered by substituting glass for carbon in other layers, but there was no case for doing so in the present instance.

The satisfactory behaviour of the composite blade is indicated by a consideration of the natural frequencies of the main fundamental modes of vibration of both blades shown below:

	Flexural (Hz)	Torsional (Hz)
Light Alloy Blade	149	970
Composite Blade	189	965

The increased flexural frequency confers no benefit in this particular case, only moving this mode even further from the operating range of the propeller.

Although the absolute stiffness of the composite blade, both flexurally and torsionally, is lower than its metal counterpart, the lower density, 54 %, compensates for this in the establishment of the natural frequencies of these modes. However, because of the lower stiffness, the static loading imposed by the aerodynamic and centrifugal loads can result in deflections which require a correction to blade angle not needed in the case of metal blades.

Arising from the centripetal acceleration, propeller blades experience two moments about the radial axis along which the blade aerofoil is distributed. One of these, centrifugal twisting moment, always acts in the sense to rotate all the elementary aerofoils of the blade towards fine or flat pitch, and the other, the centrifugal straightening moment, tends to untwist the blade and align all its elements along the chord line of the most inboard element, having the net effect of a moment towards coarse pitch.

In addition to these two, an aerodynamic moment is present which varies in magnitude and sign with operating conditions. The combined result of these moments is an effective change of pitch angle which can, as in the present case, be as high as 0.9°. The calculation of blade deformation and appropriate aerodynamic corrections presents no particular difficulties.

2.2.4 Safety Aspects of Composite Blades

The higher damping and improved fatigue properties of composite material, together with their failure modes, confer a very high degree of safety. Failure is normally a progressive phenomenon beginning with delamination, and any material shed from a blade is of low density and not likely to produce severe secondary damage. Evidence of failures is not easily acquired, but the following incidents illustrate the point. A 20" (508mm) diameter fan rotor running at 12000 RPM with carbon fibre reinforced blades was struck by a large metal foreign body. The blades disintegrated into a cloud of black smoke, leaving the rotor carrying what resembled a ring of shaving brushes. The glass reinforced stators immediately behind

were undamaged except locally where struck by the foreign body. In a second incident, a model propeller of identical construction and root retention to the model discussed in this paper, was struck while running at 7000 RPM by a piece of foam acoustic lining with a hardboard backing which had come loose from the tunnel wall. The only obvious damage to the blade was a very localised area of delamination at the composite/metal junction. The third case occurred as a result of a gross aerodynamic overload in which a similar model propeller with glass rather than carbon reinforced blades, driven by a synchronous electric motor, was effectively locked at a relatively low rotational speed and high blade angle, while the velocity of the tunnel, operating at two atmospheres, was increased to a high value. The resulting windmilling forces and moments applied to the blade caused them to twist sufficiently to cause a torsional delamination at the root. Propeller speed was increased to 8000 RPM and it was only when it became obvious from thrust and torque values, that the propeller was not operating normally, that the tunnel was shut down and the damage, as shown in the photograph of Figure 6 was found.

These three cases, together with the known behaviour of full scale propellers subjected to destructive testing, confirm the complete suitability from safety aspects of fibre reinforced resins as materials for model propeller blades.

2.3 Instrumentation

To protect the test rig and drive unit against excessive dynamic loading, bearing temperatures and vibration levels were measured at a number of critical locations. Accelerometers were installed on the bearing houses of the torquemeter (No. 1 and 2) and the gearbox output shaft (No. 3). Accelerometer No. 4 was installed on the nacelle/strut junction and served as a means of detecting vibrations of the strut. A diagram of these and the associated data logging and analysis system is shown in Figure 8.

In addition to measurements of force and torque, temperature and total and static pressures were measured in the jet pipe in order to determine the thrust contribution of the jet from the turbine exhaust. The air mass flow supplied to the drive unit was measured by means of a sonic venturi. For propeller slipstream flow surveys a fixed 34-tube total pressure rake could be installed on top of the nacelle behind the propeller plane of rotation, and also a three hole "cobra-probe" installed in a traversing device was available. During all tests, the local dynamic head in the propeller slipstream was measured by means of a pitot static tube located at 70 % of the propeller radius 0.465 diameters behind the propeller plane of rotation. Figure 7 shows a photograph of the rig in the test section of the LST ready for flow survey measurements.

3 TEST SCHEME AND DATA REDUCTION

The testing of the isolated propeller on the axisymmetric nacelle was carried out in the 3 x 2 m low speed tunnel (LST) of the NLR at Amsterdam. This tunnel has a maximum speed of 85 m/s (165 kts). The main objectives of the isolated propeller tests were to establish:

- (1) drive unit operating procedure in order to ensure the safety of the unit during the DNW tests.
- (2) "thrust minus drag" data of the propeller nacelle arrangement in order to set up the required propeller thrust on the complete aircraft model.

Since the whole propeller rig including the strut was metric the propeller thrust was evaluated from overall balance forces as measured in the following test steps:

- the strut alone at various tunnel speeds.
- the strut + nacelle without propeller at wind-off and wind-on (40, 55, 70 and 85 m/s) and exhaust jet pressure ratios, simulating different drive unit exhaust thrust conditions.
- the strut + nacelle + propeller at tunnel speeds of 0, 40, 55, 70 and 85 m/s with different propeller blade angles and rotational speeds varying from windmilling up to 7000 r.p.m.
- slipstream flow surveys at some representative power cases.

The propeller net thrust term was defined:

$$F_{NET} = F_{BAL} + D_{NS} + \Delta D_{NS} - F_J \quad (1)$$

where:

- F_{BAL} = the overall balance
- F_J = the turbine exhaust thrust
- D_{NS} = the basic nacelle and strut drag due to free stream
- ΔD_{NS} = the additional nacelle and strut drag due to the propeller slipstream.

The drive unit turbine exhaust thrust, F_J , was measured at several nozzle pressure ratios at wind-off condition. The basic nacelle and strut drag D_{NS} was derived from wind-on and wind-off measurements at various nozzle pressure ratios. The additional nacelle and strut drag ΔD_{NS} was calculated using data from the slipstream flow survey. In this computation, the friction drag part and the induced drag part were calculated from the increment of dynamic head and the swirl angle as measured in the slipstream.

The propeller thrust coefficients T_c and C_T were based on the net thrust as defined in eq.(1). The propeller torque coefficient was based on the torquemeter readings corrected for the friction of the propeller bearings. This correction was a linear function of r.p.m. and appeared to be small. At 6500 r.p.m, the bearing torque was equal to 0.7 Nm showing a hysteresis of ± 0.13 Nm, which corresponded to about 0.5 % ± 0.09 of the relevant propeller torque.

In addition to the standard wind tunnel corrections such as blockage, compressibility etc., the data were also corrected for slipstream effects using the approach derived by Glauert. The value of the Glauert

correction for the tested propeller in the 3 x 2 m LST amounts to approximately 2.5 % in velocity, i.e. J, in the high thrust regime at 40 m/s tunnel speed. This correction drops to 0.8 % in the high thrust regime at 85 m/s tunnel speed.

4.0 DISCUSSION OF TEST RESULTS

4.1 Tare Forces

Tare forces were measured on the nacelle without propeller blades and faired with a solid spinner. Measurements were made at several tunnel speeds, including $v_o = 0$ m/s. The jet exhaust pressure ratio was varied from zero up to a value corresponding to the maximum power setting of the drive unit. The drag of the nacelle and strut was derived from these data, assuming that the jet thrust was not influenced by the external flow.

Figure 9 shows the measured tare forces of the various components expressed as a percentage of the propeller net thrust for a blade pitch angle, $\beta_7 = 30.3^\circ$. As can be seen from this figure, the basic drag of nacelle and strut D_{NS} ranged from 1 - 5 % of the propeller net thrust, whereas the jet thrust contributed to about 5 - 10 % for the relevant power case.

The additional drag term ΔD_{NS} was calculated using the information of the slipstream flow survey as well as the results from the different test steps. The drag term ΔD_{NS} included a friction and an induced drag term. The contribution of friction was derived from the extra drag of nacelle and strut due to increased total head of the slipstream. The induced drag of the strut due to swirl in the slipstream was calculated by considering the strut as a wing with a spanwise twist distribution corresponding to the measured swirl distribution along the strut. This induced drag was corrected for the fact that in reality an untwisted strut was submerged in a swirling flow and a drag component orientated in the direction of the nacelle centre line was determined. This induced drag component, acting in the direction of thrust, could be expressed as a linear function of T_c . The final results of this calculation showed that ΔD_{NS} amount approximately 0.2 % of the propeller thrust coefficient.

4.2 Propeller Performance

From measurements on the complete configuration, the propeller net thrust was determined by correcting the balance force for jet thrust and nacelle and strut drag. The propeller performances in terms of the coefficients C_D and C_m are shown as a function of the advance ratio J in Figures 10 and 11. It is seen that for each tunnel speed tested, a single curve exists. That "fanning out" of the curves at the lower values of J, is mainly due to variations of the local Mach number of the blade, was substantiated by calculation using a conventional strip analysis programme, the results of which are shown in Figure 12. In this programme use has been made of measured full scale 5" (127mm) chord aerofoil characteristics for a wide range of Mach numbers.

The variation of Mach and Reynolds number with tunnel speed and propeller rotational speed is given in Figures 13 and 14. Figure 13 shows the relation between advance ratio, J, and the helical tip Mach number, M_H , for a number of propeller rotational speeds and the four tunnel velocities tested. Figure 14 presents the variations of the Reynolds number, based on a blade chord at $.7R$, with tunnel velocity and propeller rotational speed. It is seen from these figures that, as an example, for an advance ratio of $J = .70$ the helical tip Mach number changes from $M_H = .539$ to $.741$ when the tunnel velocity changes from 40 m/s ($Mo = .118$) to 55 m/s ($Mo = .162$), and Reynolds number correspondingly changes from 3.72×10^7 to 5.07×10^7 .

With the available strip analysis programme, a comparison between experimental and calculated values can only be made if the Reynolds number and the power absorption of the propeller in the computer model are the same as those of the test. Model dimensions and the measured shaft powers were fed into a programme written for the full scale propeller. Thereupon, the results were corrected for Reynolds number from full to model scale according experimental data on Reynolds number influence, as indicated in Reference 2. Figure 15 shows the effect of Reynolds number correction on the calculated thrust polars. The dashed lines and solid lines represent the uncorrected data and the data corrected from full to model scale respectively. From this figure, it can be concluded, that the effect of Reynolds number is mainly a shift of the whole curve. However, it is emphasized that available data for Reynolds number correction at high thrust and power conditions were limited. Hence, at high thrust the relevant correction is less reliable.

Figure 16 gives a comparison between experimental and calculated thrust coefficients. In this figure it can be seen that for $v_o = 40$ m/s and $J < 0.5$ the calculated thrust coefficient still increases with decreasing advance ratio whereas the measured thrust coefficient decreases. Incipient propeller blade stall occurred at these small values of J as was indicated also by slipstream flow surveys.

Also given in Figure 16 are the relevant calculated blade angles, as an overall average value, to which the programme iterates for the given shaft power absorption. The differences between the actual and theoretical blade angles as given in the figure are $30.3^\circ - 29.5^\circ = .8^\circ$ and $44.3^\circ - 43.4^\circ = .9^\circ$ respectively.

Figure 17 shows a typical comparison between measured and calculated model propeller efficiency for a blade angle $\beta_{7R} = 30.3^\circ$. It is seen that in most cases the calculated and the experimental data agree within a ± 1 % band.

4.3 Slipstream Flow Surveys

The flow characteristics of the slipstream were measured by means of a traversing three hole probe, a so called "Cobra probe", and a fixed pitot rake located at respectively $.082D$ and $.486D$ behind the propeller plane of rotation.

Total head distributions for a blade pitch angle of $\beta_{7R} = 30.3^\circ$ and a tunnel velocity of 40 m/s are shown in Figures 18a and 18b obtained from the Cobra probe and the fixed rake respectively. Figure 19 shows the swirl angle distribution as measured by the Cobra probe. From both total head distributions shown in Figure 18 it can be concluded that at an advance ratio of 0.458 there is a local stall in a region .5R to .75R of the blade span. The swirl angle distribution shown in Figure 19 however, suggests that this region lies between the spinner and .55R blade span. That blade stalling had taken place at this condition was already indicated by the reduction in C_T as shown in Figures 11 and 16.

From the calculations as discussed in the previous section and shown in Figure 12 it was found that blade stall most likely occurs in the region from spinner to .45R blade span. Taking the results of the calculation as a baseline indication it is at the present not yet clear why the swirl angle and total head distributions of the cobra probe do not agree with one another at this condition. It may be questioned whether a three hole probe, is an adequate probe for flow survey studies in the complex slipstream of a propeller. The reason why the fixed pitot rake located at .486D behind the plane of rotation do show a total head loss in an annulus from .5R to .75R from the nacelle centreline at this condition, is also not fully understood. Radial cross flow components in the slipstream might possibly explain why the area of separated flow from the blades moved outward.

From Figure 20, it is seen that at .082D as well as .486D behind the plane of rotation, the propeller slipstream extends to .95R of the blade span. In this respect it is noted that the sign reversal of the swirl angle in the swirl distribution of Figure 19 gives an indication of the spanwise locations of the helical tip vortex and so of the spanwise extension of the propeller slipstream. In comparison to the propeller disc area, the nacelle cross sectional area increases from 2.9 % at the plane of rotation to 5.5 % at the location of the Cobra probe and to 10.8 % at the position of the fixed pitot rake. These nacelle cross sectional area changes are relatively small and will have no major influence on the changes of the slipstream streamtube.

The measurements suggest that the contraction of the slipstream takes place earlier than was predicted by theory. Theoretical predictions, based on an approach by Theodorsen, show that to at least 5D behind the plane of rotation the streamtube converges and the dynamic head increases correspondingly. Figures 20 and 21 present measured and calculated slipstream characteristics. Very large differences exist between measured and calculated results. The measured total heads (at .082D as well as .486D) are almost as high as those calculated for the fully developed slipstream at 5D behind the plane of rotation. The same can be said for the swirl angles measured at .082D which approximate those computed at 5D behind the plane of rotation. In the calculations the effect of nacelle blockage on the flow in the plane of rotation was taken into account, however, the effect of increasing nacelle diameter aft of the propeller was not considered. For this reason the calculated streamtube may be somewhat smaller than its measured equivalent.

It may be concluded that the test results are in contradiction with the classical slipstream model results based on Theodorsen. The convergency of the streamlines appears to have taken place in an area at or just behind the plane of rotation. This seems to be in agreement with the theorem of G. Schouten (Reference 3) who stated that the calculated increase in static pressure behind a rotating propeller is the result of a wrong approximation of the vortex system leaving the propeller blades. In the classical theoretical model, the vortex sheet that leaves a blade is assumed to become a helical surface flat in spanwise direction. Assuming however that this vortex sheet rolls up as it does behind a wing, Schouten shows that if no increase in static pressure behind the propeller occurs, there will also be no convergency of the streamlines. The results of the slipstream flow survey tend to concur with this theory.

5.0 BLADE FAILURE

5.1 Failure and Fracture Investigation

During initial test runs on a complete model of the F50 in the DNW tunnel, one of the blades from the port propeller failed at the root and as a result, the front part of the port engine nacelle and some parts of the windtunnel were also damaged. Figure 22 shows photographs of the damage of the port propeller and nacelle structure. The failure occurred at a blade pitch angle of 30° , a tunnel speed of 85 m/s and a propeller rotational speed of 6200 r.p.m.

Fracture surface examination revealed that the blade had failed at the root due to fatigue cracking. The position of the crack was at the radius run-out from the blade airfoil to the circular root section at the leading edge. The fatigue cracking was initiated from two principal origins which were situated approximately 30° , clockwise around from the blade root chord as shown by the arrows in Figure 23. The fatigue cracking had propagated across approximately 60 % of the section before the final fracture occurred.

Figure 24 gives an overview of the fractured surface and its position with respect to the root airfoil section. Also shown in Figure 24 is the resulting force, F_R , which is located approximately .63R above the crack. F_R is perpendicular to the growth direction of the fatigue crack. Examination of the remaining three blades of the port propeller showed fatigue cracks at similar positions. On the starboard propeller only one blade was found which showed a positive crack indication at the root.

As part of the normal blade design procedure the static stress levels in the blade root (in points 1 thru 5 of Figure 24) had been estimated for maximum loading conditions. A very large safety factor of 5.0 was demonstrated between the estimated static stresses and the specified stress properties of the aluminium alloy of which the blades were manufactured. Based upon the measured crack growth rate, an approximation was made of the level of the corresponding dynamic stresses which must have occurred. It was found that these stresses were well beyond the fatigue strength of the material. A chemical analysis test showed that the composition of the alloy met the material specification.

From this extensive factor examination, it was concluded that:

- the fatigue failure was the result to high dynamic stresses, probably caused by resonance
- an alternating resultant force F_R could not have caused the fatigue crack, since F_R acts perpendicular to the direction of the crack growth

- the position of the cracks suggested that they were initiated by an edgewise vibration mode of the propeller blades; the crack growth was in the direction of the blade chord at radial station .7R
- neither the quality of the selected aluminium alloy nor the manufacturing and finishing process of the blade could be considered to be the cause of failure.

5.2 Overall Dynamic Characteristics of the Rig

In an early stage of the design of the test rig, a study was made concerning the dynamic behaviour of the rig with and without propeller. This study showed that the significant rig frequencies were all well outside the normal operating range of the propeller rotational speeds. It was also shown that the rig was free from dynamic instability problems such as whirl flutter.

Before the start of the test programme, as discussed in sections 4 and 5, an overall check of the rig was performed which included the measurements of model excitations due to unbalance or aerodynamic interactions between the propeller and the nacelle and strut. Test instrumentation and measuring equipment are discussed in section 2.3 and shown in Figure 8. Figure 25 shows how well the 1P vibration levels of the failed propeller lay within the limits defined by the motor manufacturer. The effect of tunnel velocity on the vibration levels was negligible and so was the effect of running the rig without the torque meter installed as in the configuration during the DNW tests.

A typical frequency spectrum corresponding to Figure 25 is shown in Figure 26. A 2.7P (propeller order) frequency component and its higher harmonics were found to be dominant. This 2.7P frequency can be related to the ratio of the propeller shaft gear wheel to the idle gears i.e. 89/33, see Figure 27. These drive gear frequency components were considered to be harmless to the propeller. The starboard propeller/drive unit combination was also subjected to a limited number of test runs at angles of attack of -6° (nose down) and $+20^\circ$ (nose up). Only small increments of the 1P excitation levels were measured.

From these test it was concluded that the rig excitation due to unbalance forces and 1P propeller loads were low and hence, the rig was accepted for further propeller performance testing.

5.3 Straingauge Test

The origin of the fatigue failure of the blade could not be established from the aforementioned investigations and check-outs. Moreover, it is noted that a very similar set of propeller blades and spinners have run for many hours without malfunctions on other Dowty Rotol programmes however, the propellers were driven by either an electric or hydraulic motor.

Using two of the remaining sound blades, together with two spares, it was decided to go back to the LST in Amsterdam and to carry out a straingauge test. The straingauges were cemented to the blades around the root and to the blade airfoil at positions shown in Figure 28. Sliprings were installed behind the propeller hub.

Since the number of slipring channels limited the straingauges to three per run, an initial survey was carried out at low blade pitch (15°) to establish the straingauges giving the highest stresses. Further runs were then carried out at 24° and 30° blade pitch and at 0 and 40 m/s tunnel speed. The 24° blade pitch condition was also tested at an angle of attack of 5° .

The tests showed that the stress levels in the blade as well as at the root did not change very much by varying the tunnel speed or the angle of attack. Figure 29 shows the results of straingauge Nr. 2 and Nr. 8. The stresses measured by the root straingauges were higher than those measured by the blade gauges. For the three conditions given in Figure 29, a mean line was drawn and Figure 30 shows how the stresses increase rapidly with blade angle.

Many frequencies were present in the usable range of propeller rotational speeds from 4000 to 7000 rpm. The high stresses however were dominated by two frequencies, 2.7P, which varies with rpm and a constant 730 Hz. Frequency spectra of straingauge Nr. 2 and Nr. 6 are given in Figure 31. The 2.7P is generated by the drive gearbox as discussed earlier. Where the 730 Hz comes from is at yet still not known. It was concluded that the fatigue damage to the blade was caused by these two forcing frequencies.

A Campbell plot as illustrated in Figure 32 shows how propeller blade resonances occur where blade fundamentals or overtones intersect propeller orders. These, if excited, are always accompanied by sharp increments in stress level. In this installation no high stresses attributable to this was observed. Therefore it was considered that the forcing frequencies were transmitted by the engine/gearbox and that no resonance were excited.

If the data of Figure 30 are extrapolated up to higher blade pitch angles (dashed lines), very high stresses can be obtained. Taking into consideration the running time of the port propeller at blade pitch angles of 40 and 44, (is equal to 18 minutes) in the tests before the blade failure, it is most likely that during this time, an adequate number of stress cycles have to be accumulated to cause the fatigue cracks.

6.0 CONCLUDING REMARKS

The detailed structural investigation of the propeller and drive uncovered the presence of two quite unexpected forcing frequencies, one at 2.7 times propeller rotational speed, and one at a constant 730 Hz independent of speed. The former gave rise to the higher stresses and was clearly related to meshing frequency in the gearbox, but the source of the latter has not been identified. The only way in which any high stresses could be induced in the area in which failure occurred, was by an acceleration along the rotational axis of the propeller with the blades at a coarse pitch. It is therefore concluded that in the model the excitation showed itself as an axial vibration of the propeller shaft.

A large amount of experience of running model propellers on electric and hydraulic drives has been acquired without any significant vibratory stresses. Both of these drives, the electric motor in particular, have a high inertia and stiffness and it is likely that the low inertia of the air drive and gearbox was partially responsible for the transmission of high accelerations to the propeller.

The propeller was not straingauged before testing because the factors of safety were so large and no dangerous resonances in the normal modes were present. This would have been confirmed if a straingauge study had been carried out at this time, but unacceptably high stresses would still have occurred because the area where cracks started would not have been examined since in all the previous experience of Dowty Rotol, high stresses in a chordwise sense have not been encountered. In such a case where structural changes to the blade cannot be made and the excitation cannot be removed, the only solution is a change of blade material and the advantages of composites for this situation have already been discussed.

The foregoing emphasizes the importance of considering not only the normal excitations experienced by all propellers but also unlikely ones arising from the drive. It is clearly desirable to obtain at the earliest possible stage, a very thorough knowledge of the dynamic properties of a rig which may be associated with a number of different models in order that all factors can be properly taken into account in the design of the propeller.

REFERENCES

1. Zandbergen, T., Sarin, S. and Donnelly R.P., Propeller Noise Measurements in the DNW on the Fuselage of a Twin Engine Aircraft Model. AIAA 84-2367.
2. Bass, R.M., Techniques of Model Propeller Testing. SAE Paper 830750, April 1983.
3. Schouten, G., Static Pressure in the Slipstream of a Propeller, AIAA Paper 82-4055 and Journal of Aircraft Vol. 19 No. 3 March 1982.

ACKNOWLEDGEMENTS

The authors wish to thank Fokker B.V., NLR and Dowty Rotol Ltd., for permission to publish the quoted data.

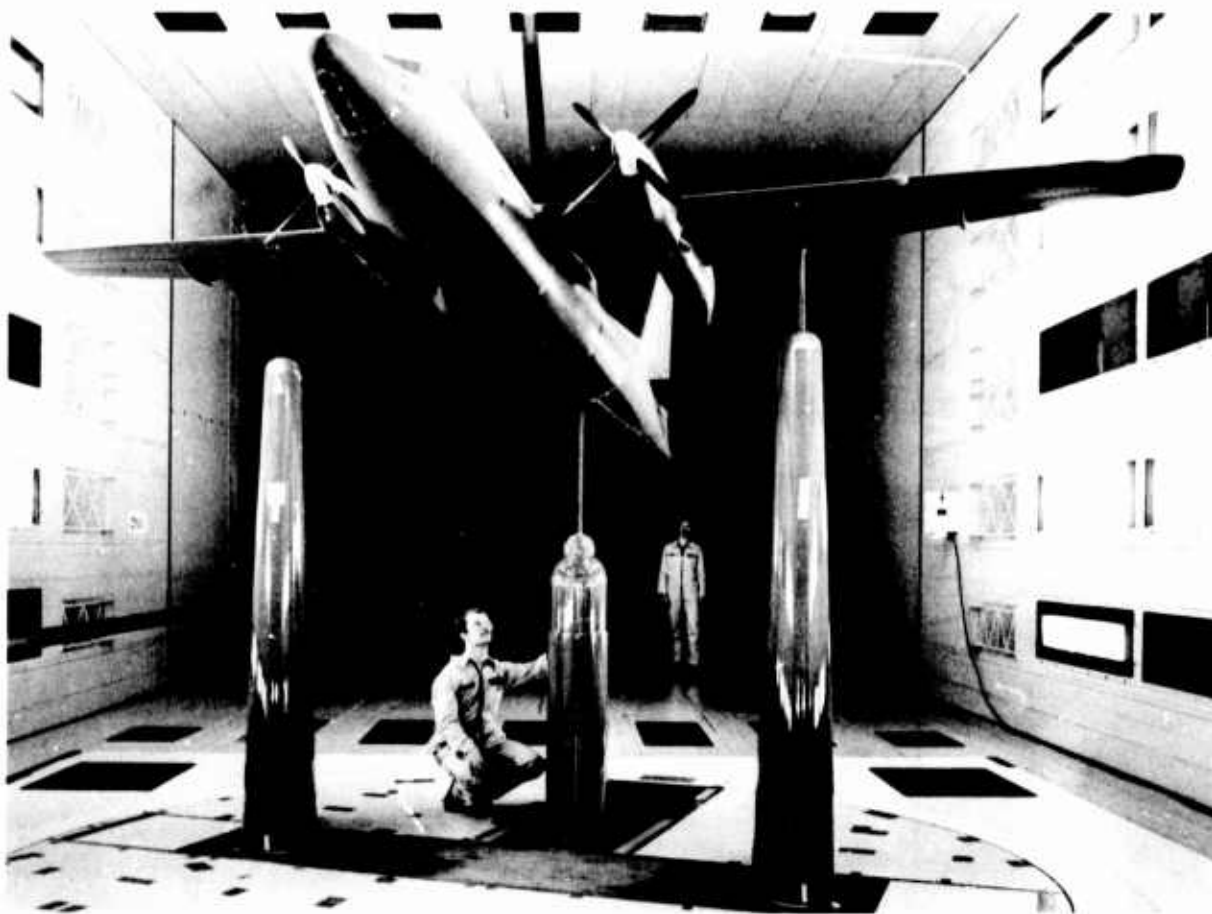


Fig. 1 Complete F-50 model in DNW

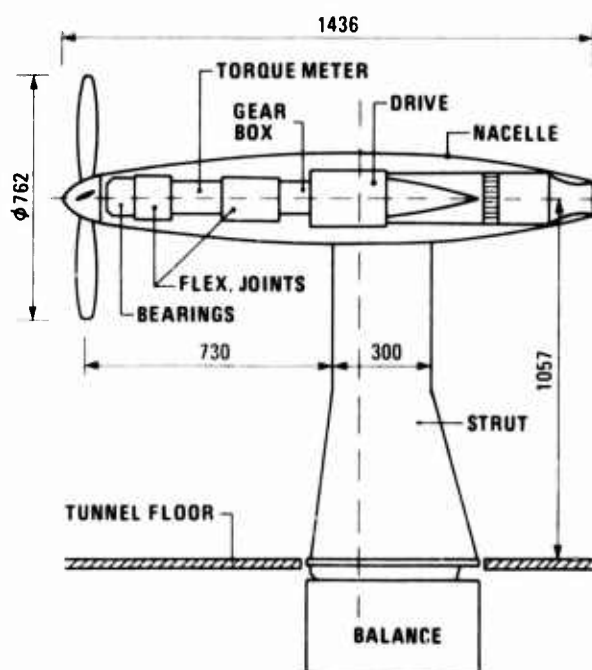


Fig. 2 Schematic of propeller test rig

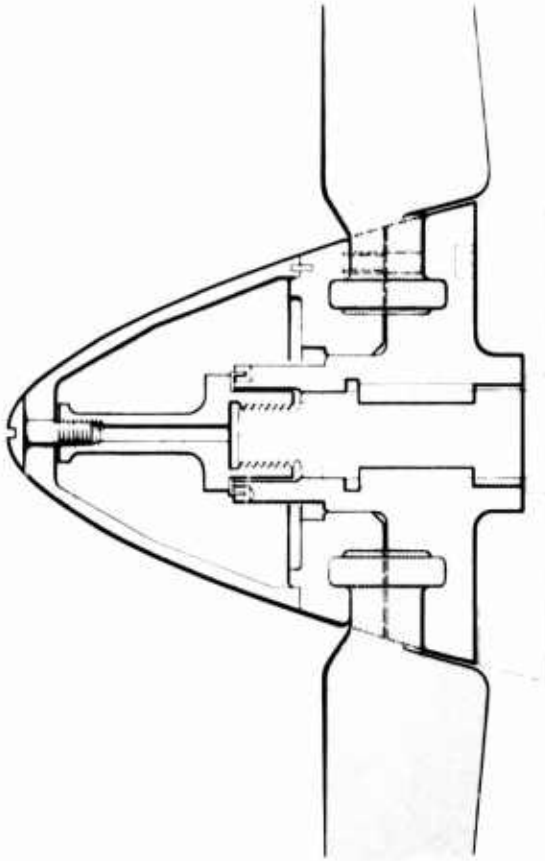


Fig. 3 Model propeller hub assembly

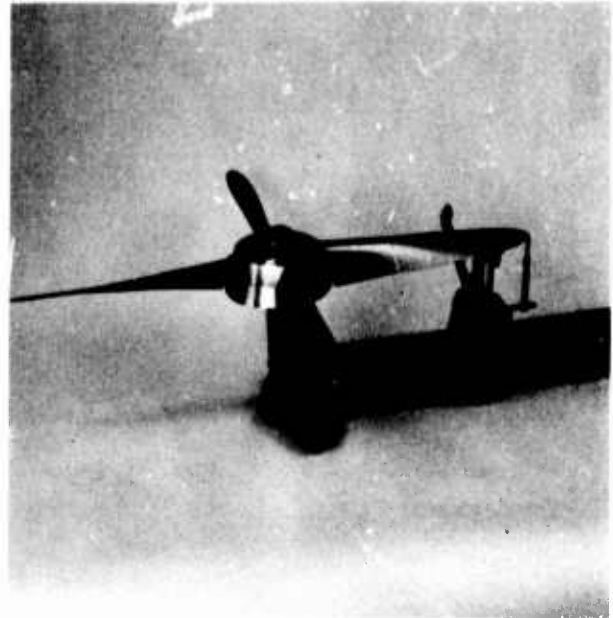


Fig. 4 Blade angle setting jig

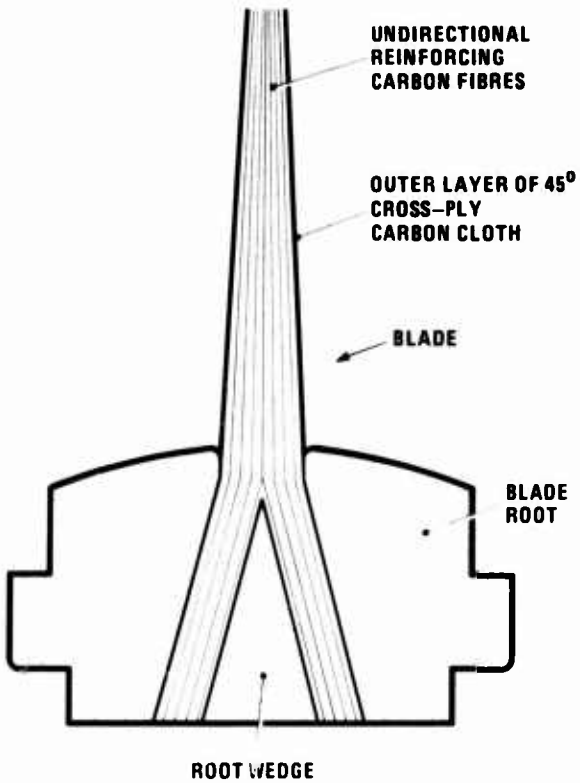


Fig. 5 Root attachment of composite blade



Fig. 6 Damaged composite blade subsequently run at 8000 rpm

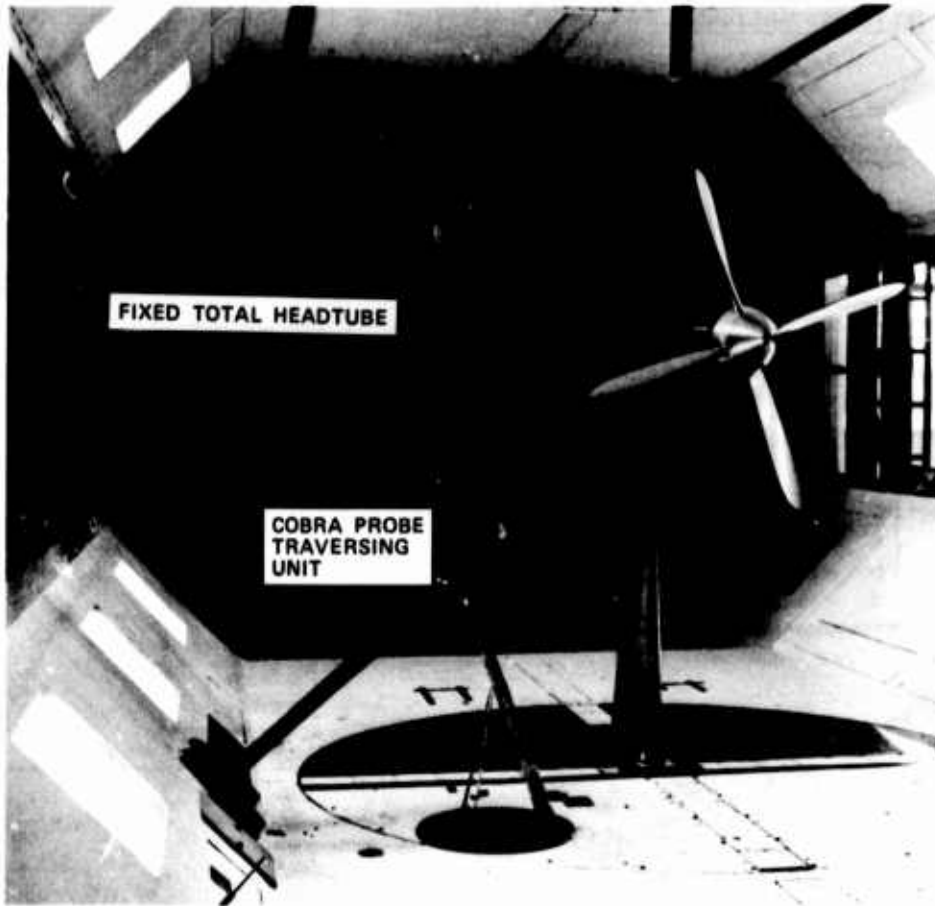


Fig. 7 Propeller test rig in the low speed wind tunnel (LST)

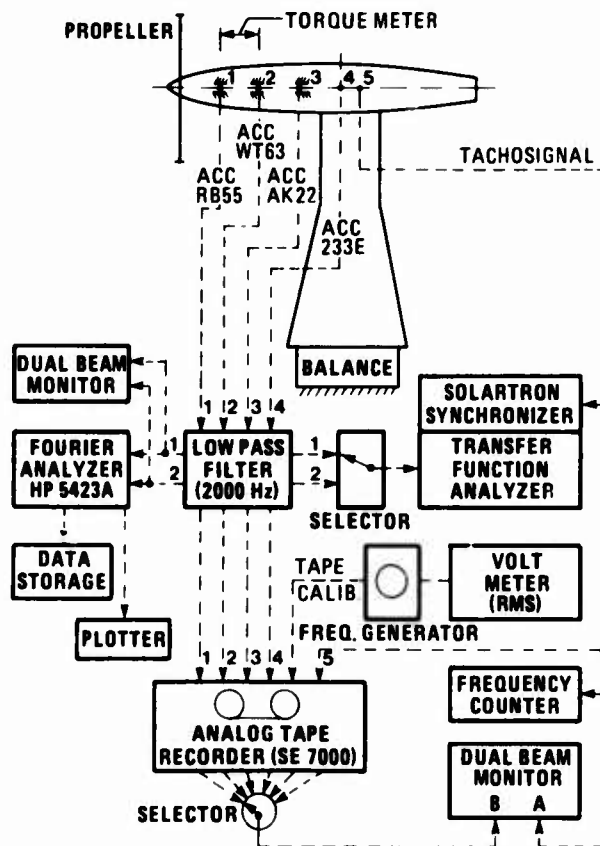


Fig. 8 Instrumentation and block diagram equipment for vibration diagnosis

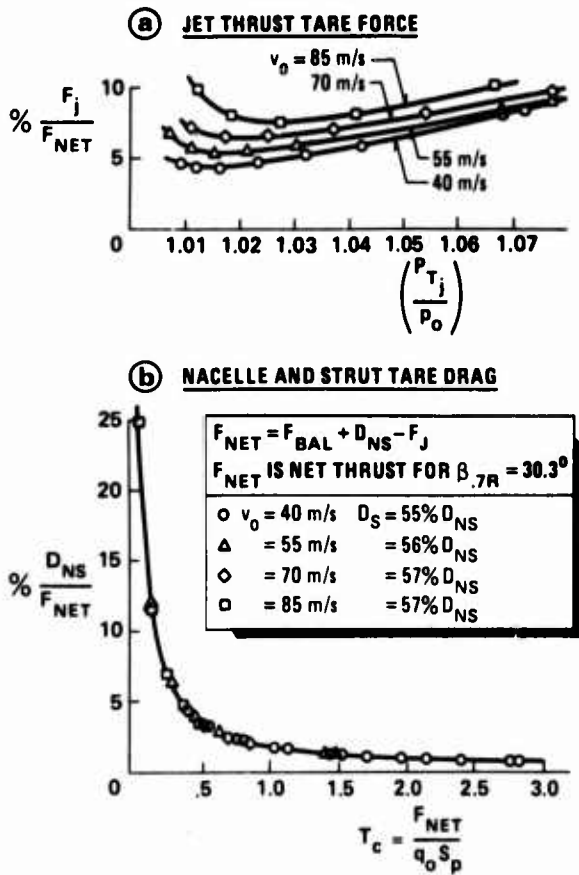


Fig. 9 Measured tare forces

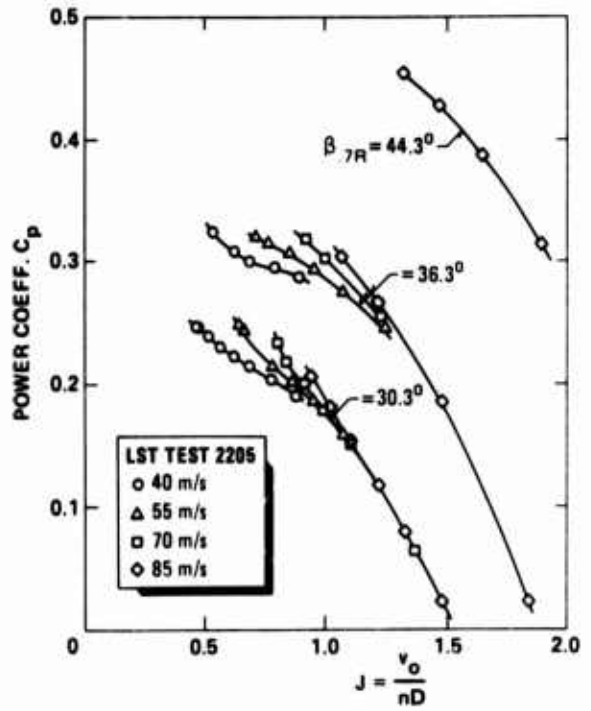


Fig. 10 Typical propeller power characteristics measured

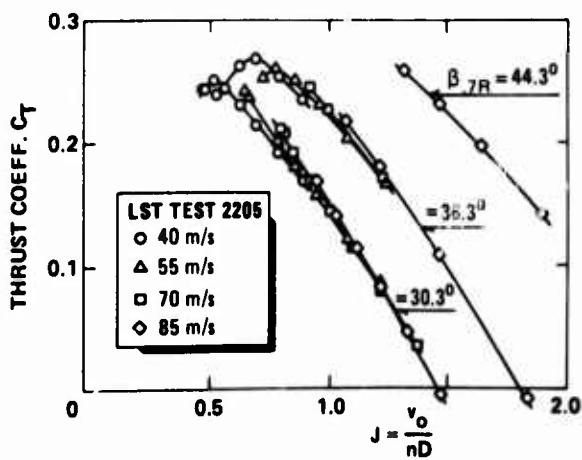


Fig. 11 Typical propeller thrust characteristics measured

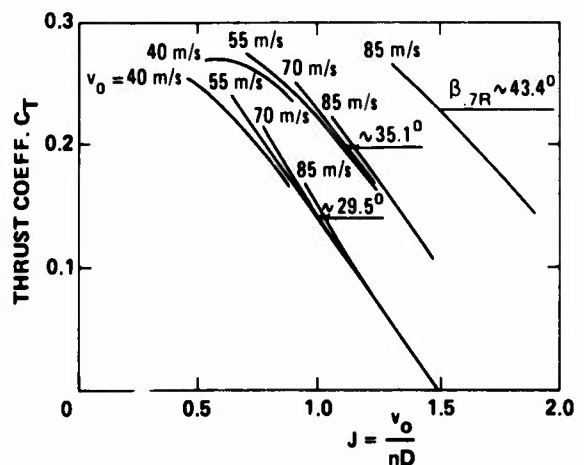


Fig. 12 Typical propeller thrust characteristics calculated

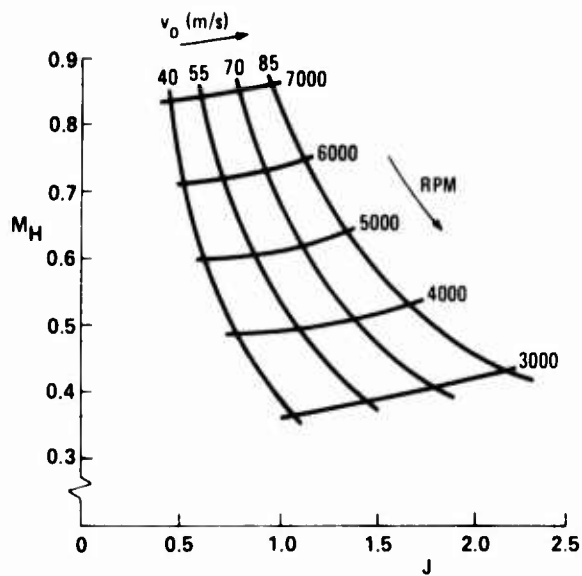


Fig. 13 Relation between blade tip Mach number and advance ratio J

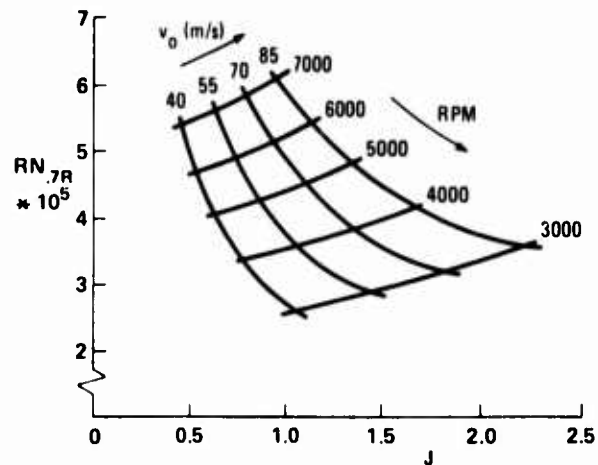


Fig. 14 Relation between blade Reynolds number at $0.7R$ and advance ratio J

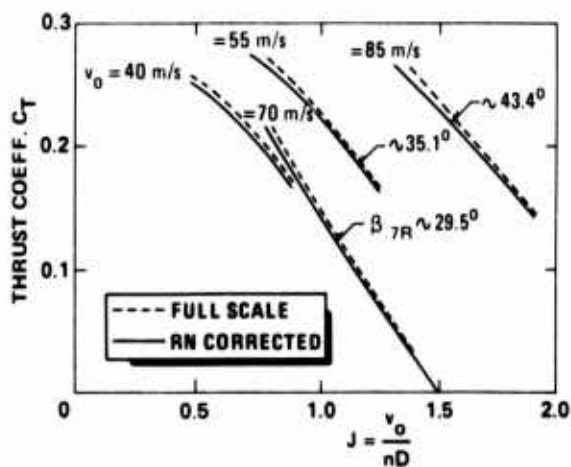


Fig. 15 Correction of full scale values to model scale

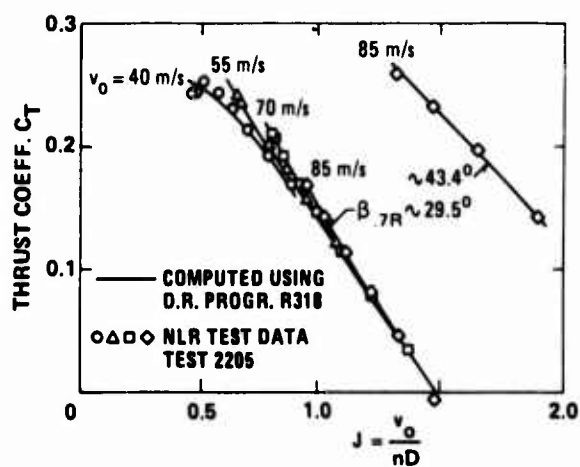


Fig. 16 Comparison of measured and calculated thrust coefficient

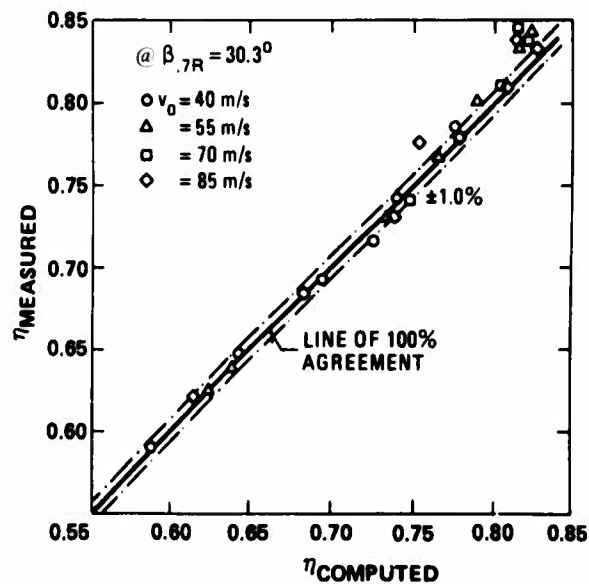


Fig. 17 Comparison of measured and calculated efficiency

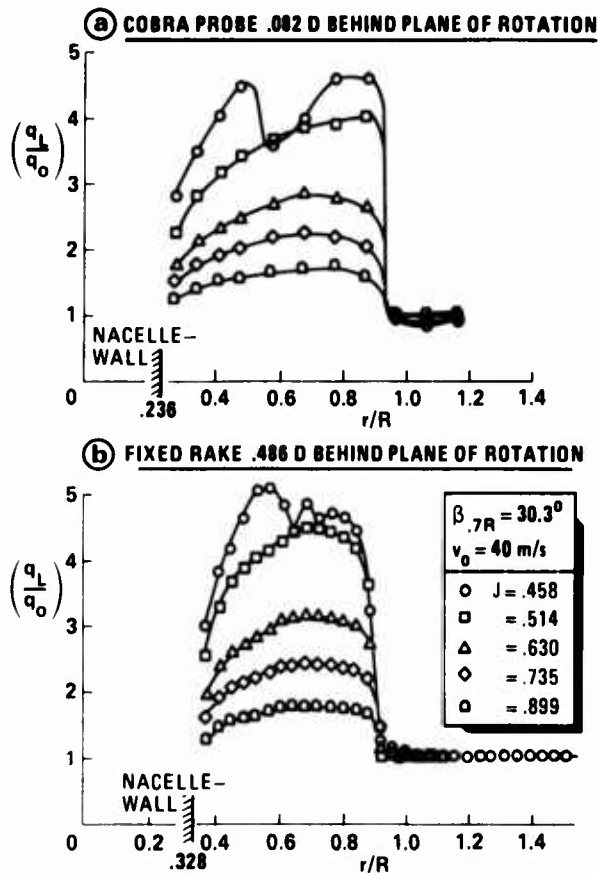


Fig. 18 Total head wake survey

COBRA PROBE AT 0.082 D BEHIND ROTATION PLANE

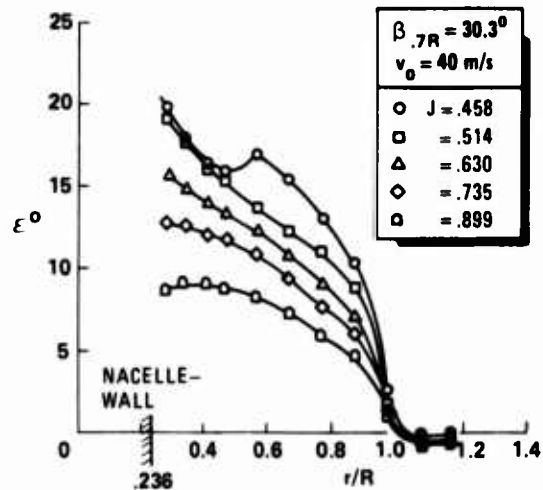


Fig. 19 Wake swirl angles

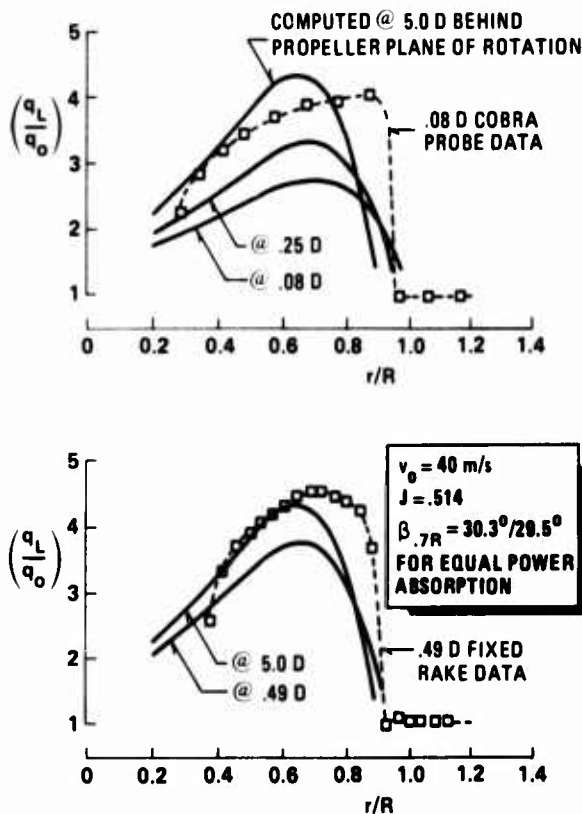


Fig. 20 Comparison between measured and calculated total heads

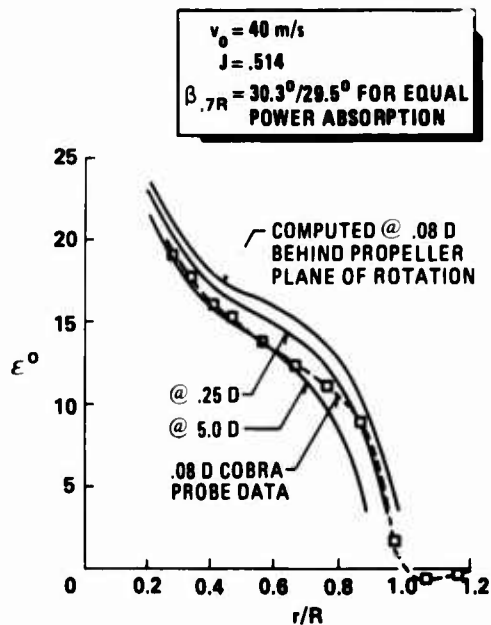


Fig. 21 Comparison between measured and calculated swirl angles

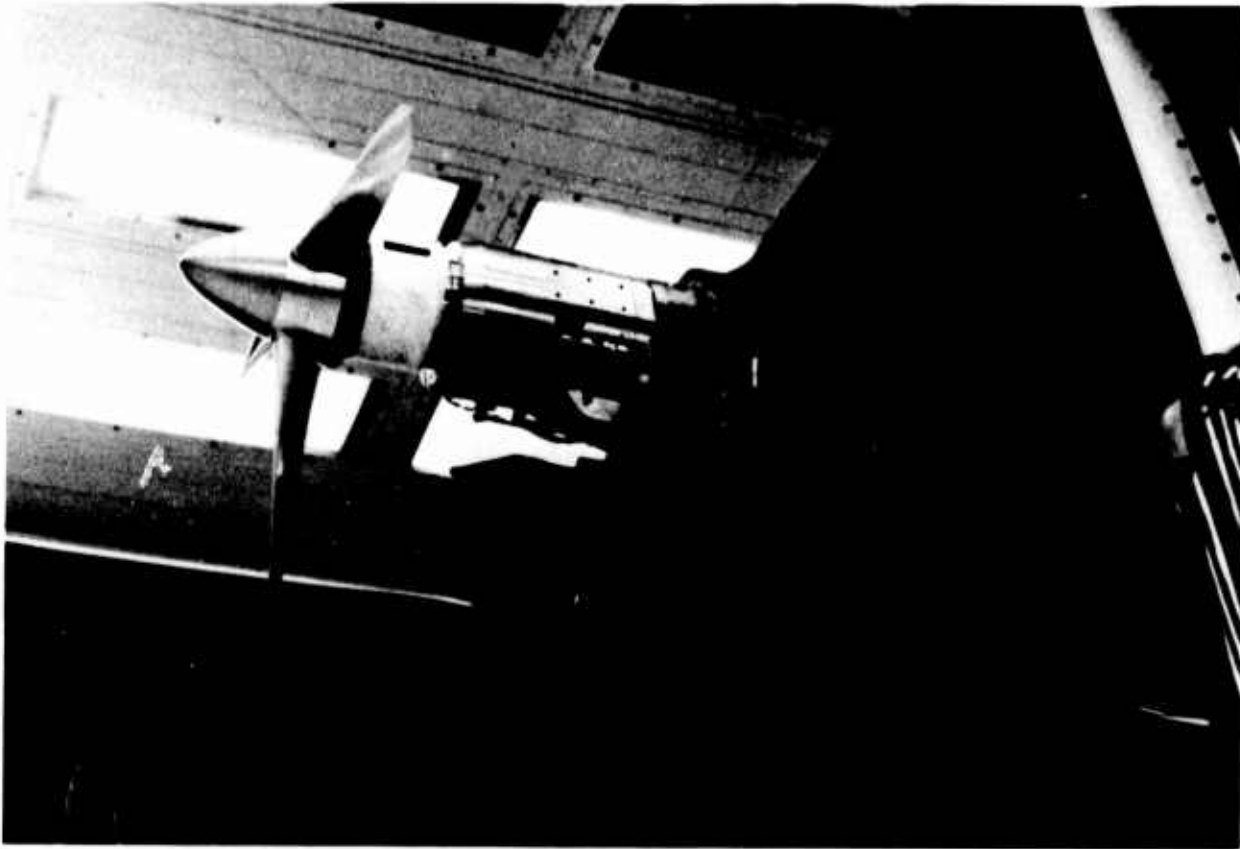


Fig. 22 Damage to F-50 model



Fig. 23 Fracture surface

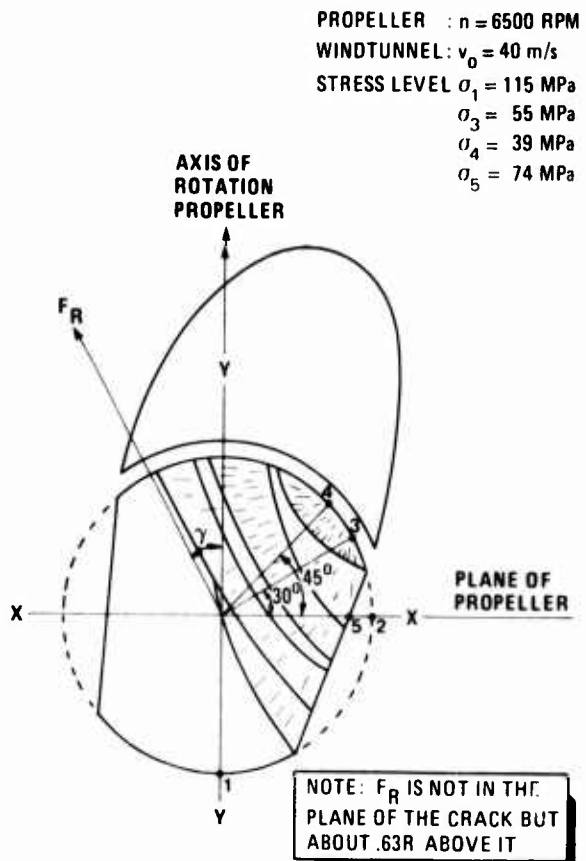


Fig. 24 Estimate static stresses in the blade foot

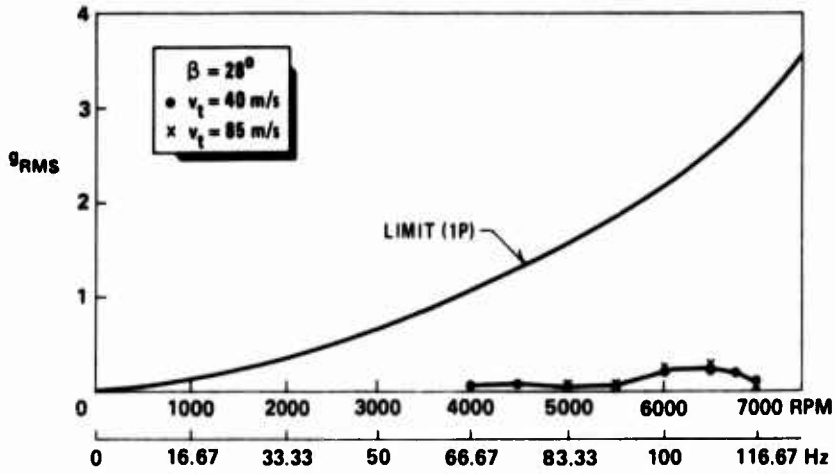


Fig. 25 1 P acceleration measured on drive casing

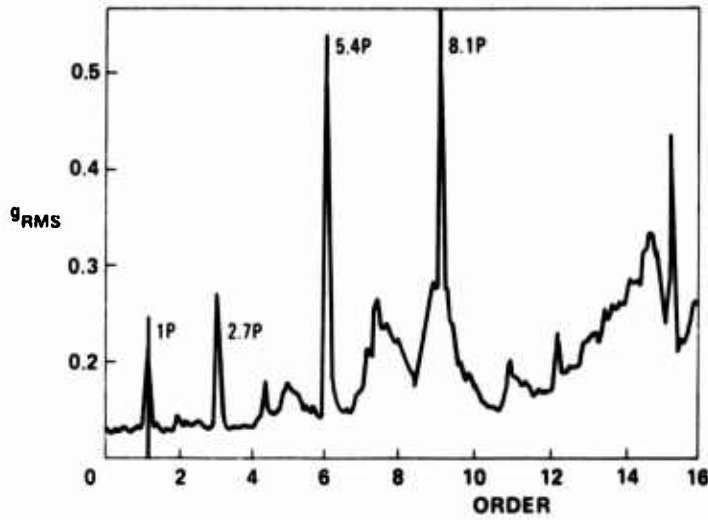


Fig. 26 Typical spectrum of accelerations of drive casing

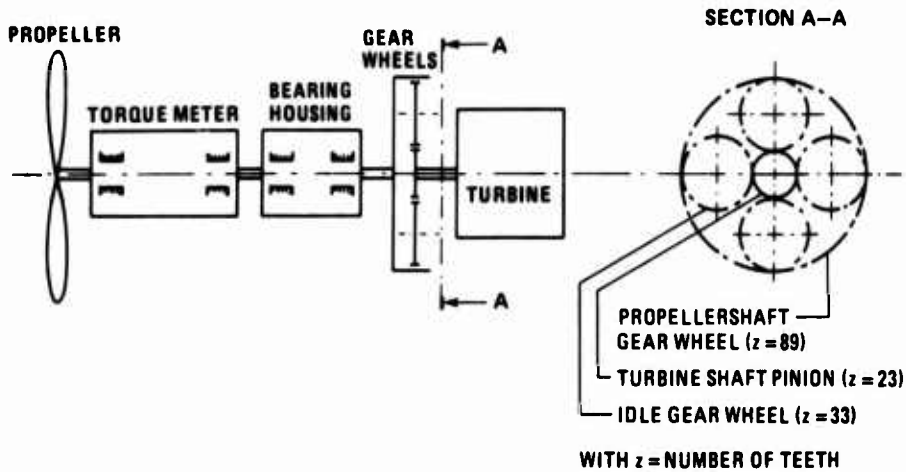


Fig. 27 Reduction gear train

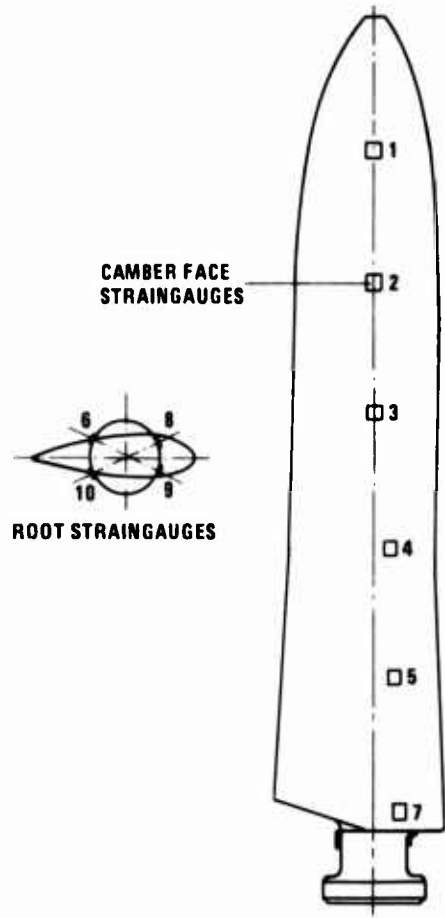


Fig. 28 Position of strain gauges on metal blade

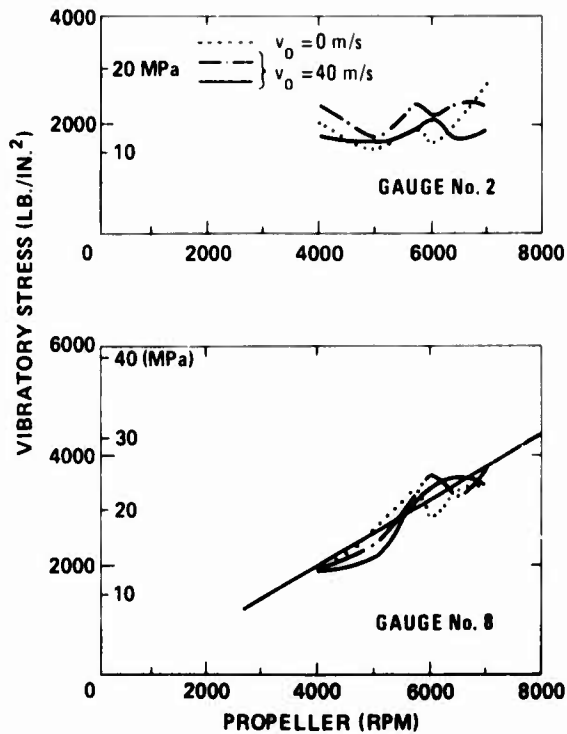


Fig. 29 Vibratory stresses at gauge 2 and 8

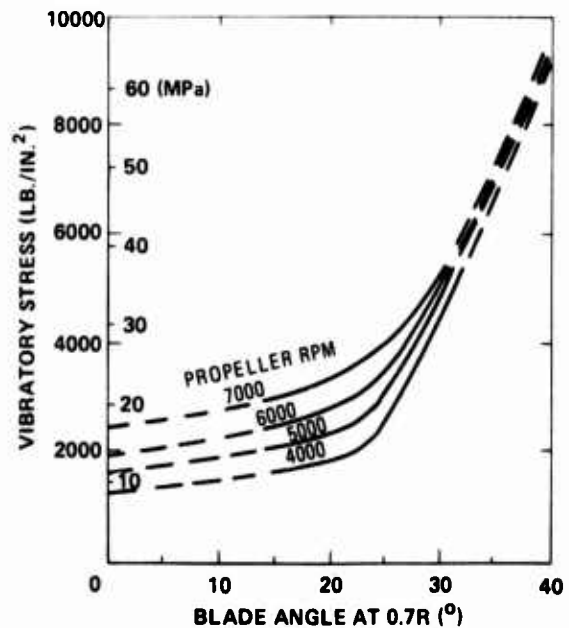


Fig. 30 Variation of root stress with blade angle

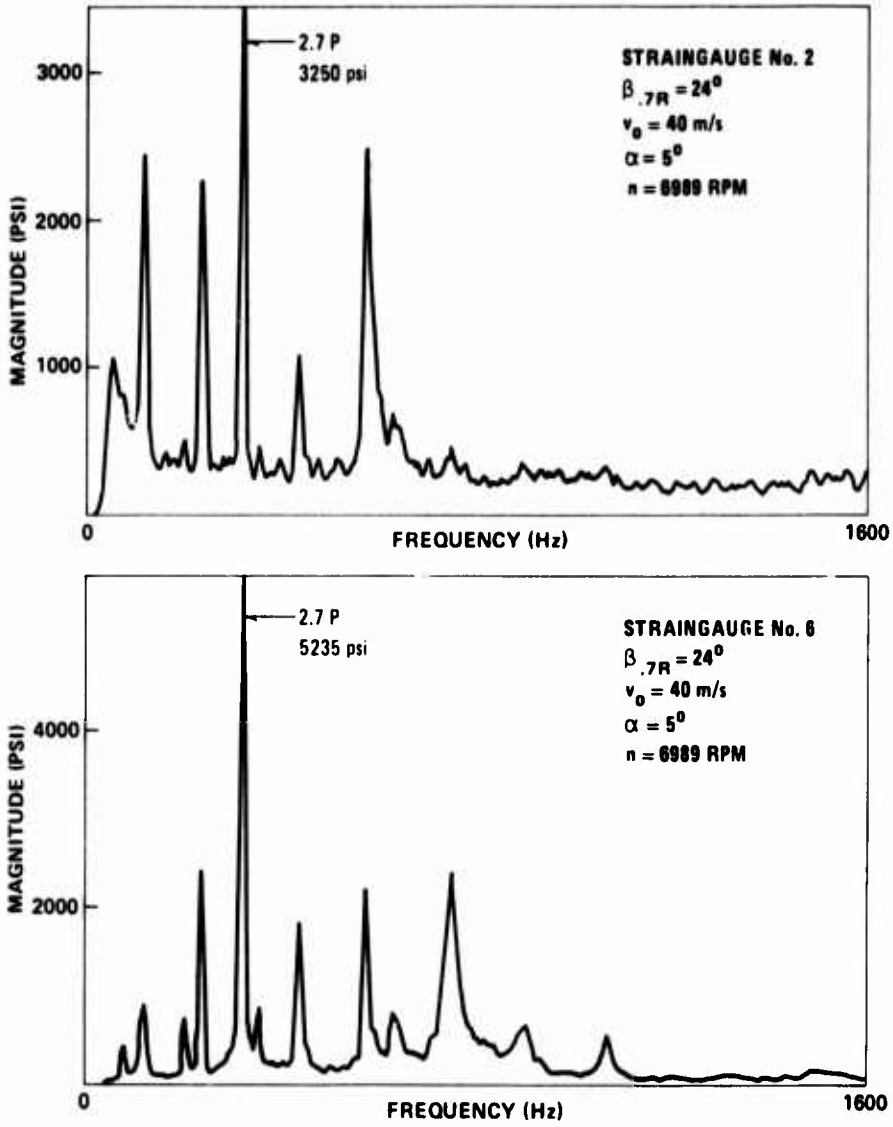


Fig. 31 Spectra of blade stresses

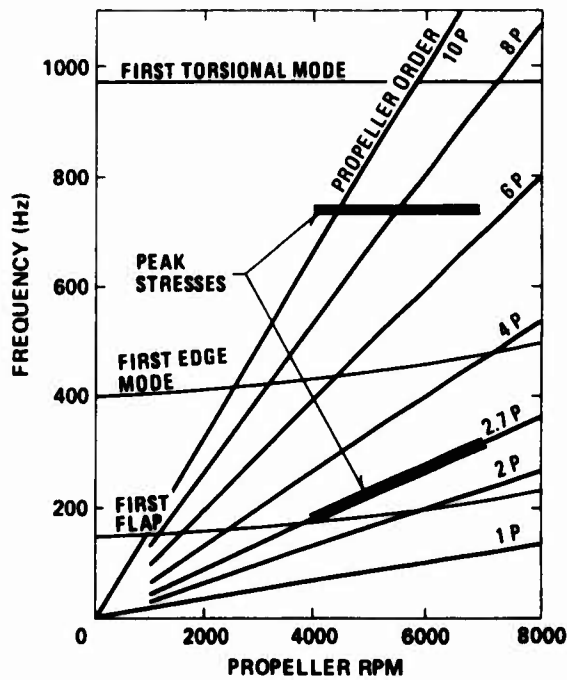


Fig. 32 Campbell diagram for metal blade

SOME CONSIDERATIONS IN PROPELLER AND AIRFRAME INTEGRATION

by

B. Eggleston

Manager of Advanced Design

The de Havilland Aircraft of Canada, Limited
Downsview, Ontario, Canada M3K 1Y5

SUMMARY

The paper reviews selected items of R and D at de Havilland Aircraft of Canada, Limited in support of propeller driven transport aircraft. The topics include the design of new propeller airfoils, two-dimensional tests of selected airfoils, and estimates are presented of the resulting benefits in propeller performance. The application of numerical optimization to the aerodynamic design of propellers is also reviewed. Some results from wind tunnel tests of airframe/propeller installations are presented showing the benefits of alternative nacelle shapes and the merits of high versus low wing locations on a transport aircraft.

LIST OF SYMBOLS

C_D	=	Drag coefficient
$C_{D_{MIN}}$	=	Minimum drag coefficient
$\Delta C_{D_{NAC}}$	=	Increment in drag coefficient due to a nacelle
C_L	=	Lift coefficient
$C_{L_{BAL}}$	=	Lift coefficient derived from balance measurements
$C_{L_{MAX}}$	=	Maximum lift coefficient
C_{L_P}	=	Lift coefficient derived from pressure integration
C_{M_P}	=	Pitching moment derived from pressure integration
D	=	Drag
L	=	Lift
L/D	=	Lift/drag ratio
M, No	=	Mach number
R, Re, No	=	Reynolds number

INTRODUCTION

There are strong economic and competitive pressures to improve the operating costs and fuel consumption of new and existing aircraft. Powerplants are one of the key ingredients in achieving these improvements and this requires airframe manufacturers to develop a comprehensive knowledge of factors influencing powerplant performance and the associated installation penalties. The turbo-prop is generally accepted as the best type of propulsion for small short range aircraft, but more recently developments in advanced propellers indicate that large, propeller driven transports cruising at speeds up to Mach 0.8 are possible in the next generation of transport aircraft. Thus, modern propeller technology and installation effects on performance are now of widespread interest throughout the aircraft industry.

In the case of de Havilland Canada R and D programs on propeller driven aircraft have included the design of several new airfoils specifically for a STOL propeller. These were integrated into a propeller design which recently has been tested at large scale along with other existing propeller designs, as will be reported elsewhere at this meeting, reference 1. An important aspect of these investigations has been assessing the degradation in propeller efficiency caused by departures from ideal airfoil profiles as caused by "real-life" requirements. These could arise from excessive manufacturing tolerances, from externally added features such as deicer boots or erosion shields, or from the distributed roughness caused by the erosion coat paints used on composite blades.

This paper will highlight several topics related to turbo propeller installations. The design of airfoils suitable for a STOL propeller will be reviewed and some results of two-dimensional airfoil tests will be presented and compared with data from other sources. The application of numerical optimization to propeller aerodynamic design will be discussed with examples given of designs suitable for lightly loaded aircraft. In conclusion the paper will review some results of wind tunnel model tests which investigated the effect of nacelle shape on the interaction losses between a propeller slipstream, a nacelle, and the wing of a complete aircraft configuration.

1. PROPELLER AIRFOIL DESIGN

Due to a lack of interest in propellers the subject of propeller airfoil design stagnated for years until a noteworthy paper by Bocci of ARA working for Dowty Rotol, reference 2. His work showed that the application of modern airfoil design methods could yield substantial gains in maximum lift, and also widen the ranges of lift and Mach number over which high lift/drag ratios could be maintained. Since that time other manufacturers have developed their own airfoils, eg. reference 2. On reviewing the performance of the available new technology airfoils, DHC decided that an in-house effort could yield further improvements, as the designs would be tailored more closely to DHC requirements for a STOL propeller.

The airfoil sections along a propeller blade experience very wide variations in local conditions of Mach number, lift coefficient and Reynolds number, as summarized in Figure 1 for a typical STOL propeller. In the past the propeller manufacturers have used one or two families of NACA standard airfoil, to cater to these variations, but clearly it is better to tailor the airfoil designs to suit local conditions at each radius. Given the wide availability of reliable computational methods for airfoil analysis and design, which now include supercritical flow and viscous effects, the design of tailored airfoils no longer presents an unduly formidable task.

The DHC propeller R and D program involved the design and test of four airfoils of 4, 6, 13 and 21% maximum thickness/chord ratio shown in Figure 2. The first airfoil to be designed was of 6% thickness, suitable for about 80 - 85% of the maximum radius of a STOL propeller. The airfoil was designed using inverse methods to meet several operating conditions, using a NACA 16 profile as a starting point. The DHC design did not place undue emphasis on C_{Lmax} , i.e. pure static thrust, and the lowest aircraft speed considered critical was 60 knots. The design task was to minimize the strength of shocks on either surface while obtaining the longest run of laminar flow possible. As a consequence the airfoil has lower camber than designs elsewhere, which should provide superior climb and cruise performance.

The next airfoil designed was of 21% thickness suitable for 20 - 30% of the maximum radius of a STOL propeller, placing it immediately ahead of the engine air intake. Although this region of the blade does not contribute substantially to thrust, or to the overall propeller efficiency, high performance is needed locally because the pressure rise through the propeller boosts engine performance significantly. Thus the airfoil has to achieve high lift/drag ratios when operating near maximum lift during takeoff and climb, while still retaining low drag at the low lift coefficients appropriate to cruise. The resulting airfoil design used some aft loading and a moderately concave pressure recovery on the upper surface to give a long run in the pressure distribution favourable to laminar flow.

It is desirable for the exterior surface of a propeller blade to be smooth and wave free, which requires that the airfoils must change in a progressive fashion radially along the blade. In order to achieve this, DHC constructed the intermediate airfoils by decomposing the 6% and 21% thick airfoils into thickness and camber distributions which could be mixed linearly, then the best combination at any station found using the airfoil analysis program. The intermediate 13% thick airfoil was constructed in this manner. In the case of the 4% thick airfoil this was obtained by suitably scaling the camber and thickness of the 6% thick design, with additional thickness added on the lower surface "chin" to weaken shocks at cruise.

The wind tunnel models of the 4, 6, 13 and 21% thick airfoils are shown in Figure 2. It was found subsequently when it came to lofting a complete propeller blade that additional airfoils of 18 and 24% thickness were needed to obtain suitable control of airfoil shapes along the blade. These additional airfoils were derived from the tested airfoils as discussed previously.

2. MODELS AND TEST TECHNIQUES

The wind tunnel models of the airfoils were tested in the NAE 0.38 m x 1.5 m two-dimensional wind tunnel, shown schematically in Figure 3. The models were supported by pins at their ends set into balances in the tunnel walls. In the case of the two thinner airfoils, strength considerations required the pins to be made integral with the ends and the use of 17-4PH steel as material for the models.

The models were instrumented for surface pressure measurements along their centrelines. The lift and pitching moments were computed from the integrated pressures and checked against wall balance values with generally good agreement except near the stall, Figure 4.

The model drags were determined using a traversing wake rake with averaging of values from three probes. The pressure tapings on the centreline were ahead of probe #1, causing premature transition and increasing the drag measured at this location, Figure 5. If this influence was removed by averaging data from only probes #2 and #3, the values of best lift/drag ratios could be improved by up to 5%.

The NAE 0.38 m x 1.5 m wind tunnel is of the blow-down type so there are minimum operating limits on the stagnation pressures, and hence Reynolds numbers, achievable in the test section at any given Mach number. As a consequence the airfoil sections were usually tested at Reynolds numbers slightly greater than full scale values (see for example the subsidiary scale on Figure 11).

3. PROPELLER SECTION TESTS

3.1 Maximum Lift

The experimental results obtained for maximum lift coefficients are presented in Figure 6 as functions of Mach number. Each curve has a heavy lined region which indicates the typical range of Mach numbers during takeoff for a STOL propeller. If the strip analysis values for the takeoff lift coefficients given in Figure 1 are compared with the experimental results, it can be seen that the two-dimensional values were slightly lower than required. However this was not considered serious, as rotational flow phenomena on propellers are known to enhance C_{Lmax} above 2-D test values. Furthermore this was confirmed subsequently by recent complete propeller tests which indicate improvements in static thrust of up to 8% over a propeller with conventional airfoils, at similar activity factors.

3.2 Lift/Drag Ratios

The experimental values of lift/drag ratio for the four airfoils at typical climb and cruise conditions are presented in Figures 7 and 8 respectively. Again on each curve the typical operating ranges of lift coefficients are shown by the heavily lined regions.

A STOL propeller is relatively lightly loaded which results in a wide separation between the operating lift coefficients at takeoff, climb and cruise. The climb conditions noted in Figure 7 show that the airfoils operate close to their peak lift/drag ratios, which confirms the final airfoil designs were well matched to this requirement. The cruise cases given in Figure 8 show a substantial reduction in the operating lift coefficients, causing the airfoils to operate well below their peak lift/drag ratios. Nevertheless the values obtained in the tests were generally substantially better than equivalent conventional airfoils, as shown later in Section 4.

At this time no other propeller airfoils have been tested in the NAE 0.38 m x 1.5 m wind tunnel, so comparisons can only be made with data from other wind tunnels. This is acknowledged to be of uncertain value, as the test techniques, turbulence levels and Reynolds numbers could be significantly different. With those reservations, a comparison for 6% thick airfoils at climb conditions is made in Figure 9 for ARAD airfoils from reference 2, and for Hamilton Standard airfoils from reference 2. Bearing in mind that the DHC airfoil has lower camber than the other two, these results indicate its performance is quite competitive, particularly at lower lift coefficients.

3.3 Influence of Profile Disturbances

Practical propeller blades often depart from idealized contours in order to accommodate features such as leading edge erosion shields and externally applied deicer boots. Also the painted surfaces which are applied for erosion protection can introduce a significant distributed roughness. DHC were concerned about potential losses in performance arising from such features so the two-dimensional airfoil investigations included studies of these effects.

In the tests the deicer boots were represented by building up layers of metal tape, with a profile as sketched in Figure 10. The distributed roughness was simulated by applying strips of tape in a chordwise direction, with a tape having a surface roughness of about 180 μ . in.

As an illustration, Figure 11 shows the effects of profile disturbances on the minimum drag of the 13% thick airfoil. The distributed roughness caused an increase of C_{Dmin} of about 30%, while the boot with a step caused C_{Dmin} to be increased by 50%. In tests on the other DHC airfoils, similar penalties were observed and tests on a full scale propeller with similar features represented showed losses in efficiencies in accordance with the two-dimensional penalties. These results serve to emphasize the need for propeller manufacturers to maintain extremely careful control of blade profiles and to have a smooth surface finish in order for the full benefits of modern airfoils to be realized in practise.

4. PROPELLER DESIGN

4.1 Benefits of New Technology Airfoils

The section data for the DHC airfoils were adapted to suit a propeller analysis program used by DHC, reference 4. The experimental results were used without any modifications being applied for the beneficial effects of rotational flow, although such procedures are commonly used by the propeller manufacturers in adapting NACA data.

In order to illustrate the gains from the new airfoils a propeller design similar to the Dash 8 geometry was optimized for conventional airfoils, using NACA 65 series airfoils out to 50% of radius and NACA 16 airfoils over the outer radius. Next, keeping the same blade geometry and without reoptimizing twist, the propeller performance was estimated using the DHC airfoils. The resulting variations of lift/drag ratio across the propeller blade are presented in Figure 12 for a climb case, and in Figure 13 for a cruise case.

In the climb case the new DHC airfoils show substantial gains in lift/drag ratios for stations inboard of about 80% maximum radius. Outboard of this location the NACA 16 airfoil data in the program are superior, although they may have been "massage'd" to reflect tip effects. The overall gain in climb efficiency for the new DHC airfoils represents about a 1% increase in thrust. In the cruise case the DHC airfoils show significant gains inboard of 87% maximum radius, while again the NACA 16 data are superior outboard. The overall gain in cruise efficiency from the new airfoils represents about a 0.25% increase in cruise thrust. It should be noted that propellers using the new airfoils would benefit from further reoptimization of planform, thickness and twist, so that the above increases represent quite conservative estimates of the potential gains.

4.2 Propeller Design By Numerical Optimization

The optimization of propeller blade characteristics is usually done by skilled professionals using a "cut-and-try" process with a strip analysis program. This can be an economical approach to blade design when the requirements are close to past experience. DHC have investigated an automated approach to propeller design based on numerical optimization methods, such as described in reference 4, in order to speed up this process for unusual designs.

The numerical optimization approach is based on perturbing the blade characteristics in directions which will minimize an objective function. The objective function can include multiple design points, each suitably weighted to reflect their relative importance,

$$\text{i.e. } F_B = K_1/\eta_1 + F_2/\eta_2 + K_3/\eta_3 + \dots \text{ etc.}$$

The objective function could also be expanded to include structural factors such as stress levels at critical operating conditions, if of interest. Any constraints on blade chord, or thickness can be included in the objective function as penalty functions which become active as these limits are approached.

The DHC optimization program uses a strip analysis method and the chords and twist angles at ten radial stations are used as variables. The optimizer is a gradient method which perturbs each variable in turn to determine derivatives, followed by an overall change in the variables in their optimum directions, subject to the applied constraints. Note that this approach has the advantage of using the strip analysis method directly for performance calculations and it does not require separate analysis of induced and profile losses.

The procedure outlined above has been used to design several small lightly loaded propellers, including a model aircraft propeller (1971) and the ultra-light aircraft propellers (1978 and 1980) shown in Figure 14. Further discussion on the procedure can be found in reference 6.

5. PROPELLER-AIRFRAME INSTALLATION EFFECTS

The integration of propellers and engine nacelles with an airframe involves many design/layout compromises in addition to purely aerodynamic considerations. In the early stages of Dash 8 development a multi-purpose half model was tested, Figure 15, to obtain aerodynamic/pushion data for use in preliminary configuration studies. The model was tested with a wide variety of nacelle shapes, Figure 16, and also with alternative high and low wing configurations, Figure 17. For power-on studies a model propeller was first calibrated on an isolated test stand and then driven by an electric motor in the model. The aircraft model used a 39% chord single slotted flap and it had a wing of aspect ratio twelve (12).

The half model tests gave data on the drag increments for adding various nacelles to a clean wing. Typical results for a wing with undeflected flaps and the propellers-off are presented in Figure 18 for a case with a low wing, and for a high wing layout with alternative "long" and "short" nacelles. The best configuration found at climb lift coefficients was the high wing with long nacelles projecting past the wing trailing edge, while at cruise conditions its drag was very similar to the short nacelle configuration. It was found that both nacelle configurations tested on the high wing were significantly better than the low wing arrangement at all conditions studied.

The half model was tested with the calibrated propeller in place at various flap angles to determine the effects of power-on lift, drag, pitching moment and propeller thrust recovery. Also maximum lift was measured for high and low wing arrangements, Figure 19, showing the improved lift carry-over on the fuselage with a high wing layout gave up to 10% more maximum lift.

The overall effect of wing location and nacelle geometry on performance was assessed by using the model polars and maximum lifts to predict the maximum climb weights with an engine failed, for a Dash 8 sized aircraft. The aircraft polar was synthesized using results from the half model with power-on combined with results for a propeller-off case, to which were added drag increments for the control deflections required to trim out the asymmetric power effects and the drag of a feathered propeller. The maximum lift coefficients of the aircraft were based on the half model values at zero thrust coefficient, with an increase of 10% to allow for scale effects and the 'g'-break occurring in a FAA stall demonstration. The results are presented in Figure 20 as a function of flap angle. The high wing/long nacelle configuration was found superior for flap deflections up to 10°, which are the most critical deflections for WAT limited performance, and for enroute engine failed performance. In all cases the low wing configuration was markedly inferior to both high wing layouts, and the size of the penalties appear too large to be offset by any structural weight benefits of a low wing layout.

6. CONCLUSIONS

Many factors are important in achieving improved performance with turboprop aircraft. Some of the most significant items discussed in this paper are noted below.

Modern technology airfoils can provide significant improvements in performance over earlier types of propeller airfoils. However, achieving these improvements will require tighter control of manufacturing tolerances, including waviness, and it precludes the addition of external features which significantly disturb the blade airfoil shapes. Blade smoothness is important in achieving high performance, and protective paints should be very smooth.

Wind tunnel investigations of nacelle geometry undertaken in support of Dash 8 studies, showed significant benefits from long nacelles extending beyond the wing trailing edge. The high wing location was found to confer significant benefits in maximum lift and overall aircraft performance.

7. REFERENCES

1. Barber, D.J. - "Performance Evaluation of Full Scale Propellers By Wind Tunnel Tests," AGARD Conference Paper 14, October 1984.
2. Bocci, A.J. - "A New Series of Airfoil Sections Suitable for Aircraft Propellers," Aeronautical Quarterly, Volume 28, February 1977.
3. Rohrback, C. and Wainauski, H.S. - "Aerodynamic Characteristics of an Advanced Technology Propeller for Commuter Aircraft," AIAA-81-1565, July 1981.
4. Borst, H.V. - "Summary of Propeller Design Procedures and Data," USAAMRDL Technical Report 73-34C, AD-776998, November 1973.
5. Bernstein, S. - "Feasibility of Propeller Design for General Aviation By Numerical Optimization," SAE Paper 760477, April 1976.
6. Eggleston, B. - "Design of a Propeller for an Ultra Light Aircraft," Third Canadian Symposium on Advanced Technology Light Aircraft, October 1979.

8. ACKNOWLEDGEMENTS

The work described in this paper was jointly funded by the PILP Office of the National Research Council of Canada, the Transportation Development Centre of Transport Canada, and by de Havilland Aircraft of Canada, Limited. The author wishes to acknowledge the valuable contributions made to this work by his colleagues at DHC, notably D.J. Barber, R.J.D. Poole and D.C. Oswald.

**TYPICAL OPERATING CONDITIONS ON A STOL PROPELLER
DESIGNED FOR 300 KT CRUISE**

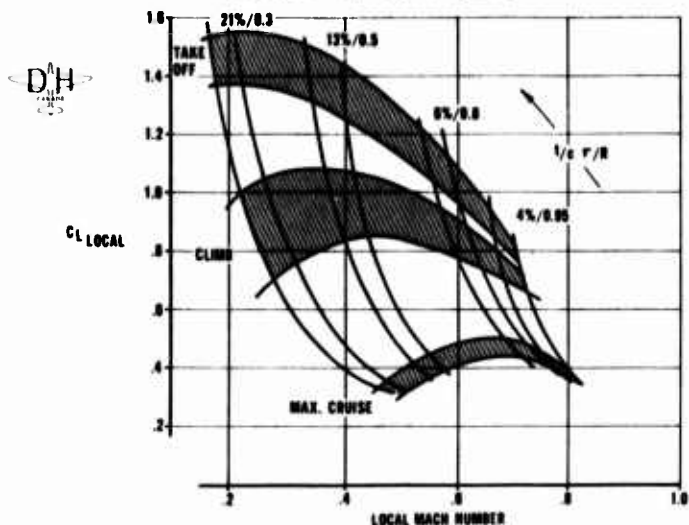


FIGURE 1

**AIRFOIL WIND TUNNEL MODELS
4%, 8%, 13% & 21% THICKNESS/CHORD**

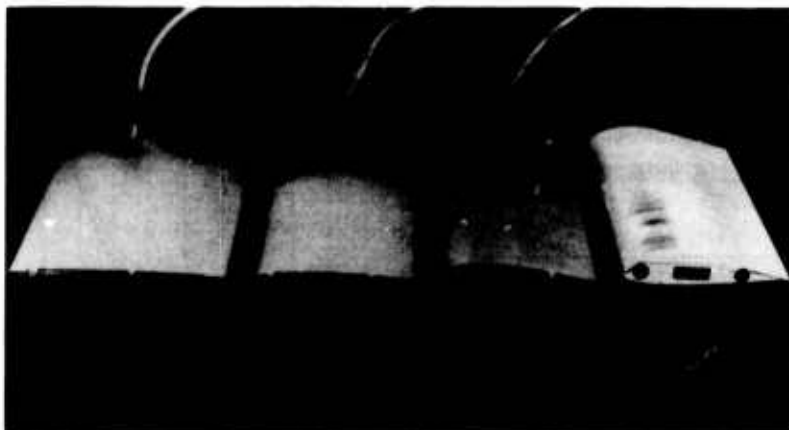


FIGURE 2

**CUTAWAY DIAGRAM
OF NAE 0.38 METRE x 1.5 METRE
TWO-DIMENSIONAL WIND TUNNEL**

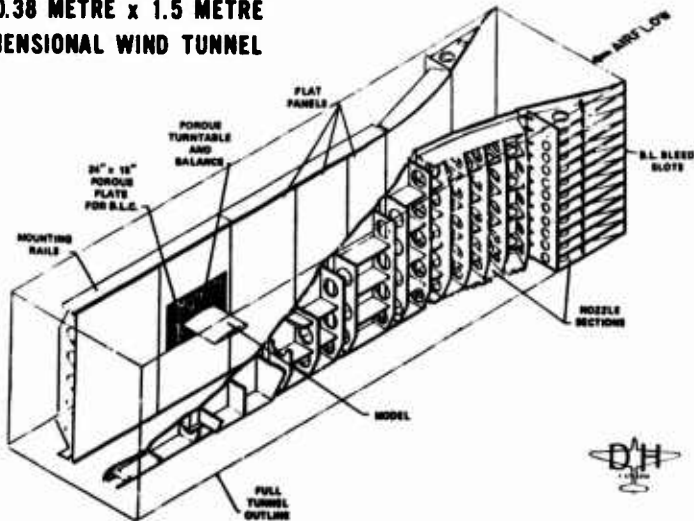


FIGURE 3

COMPARISON OF LIFT DATA FROM BALANCE AND PRESSURE INTEGRATION



MACH NUMBER: 0.4
REYNOLDS NUMBER: 3×10^6

- — ○ C_L BALANCE DURING PRESSURE RUN
- △ — △ C_L PRESSURE INTEGRATION
- — □ C_L BALANCE DURING FORCE RUN

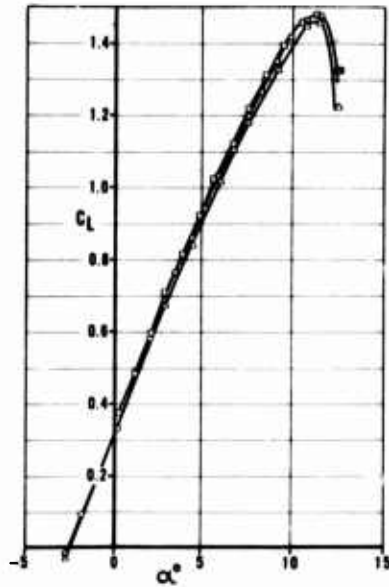


FIGURE 4

SPANWISE VARIATION IN DRAG



MACH NUMBER: 0.50
REYNOLDS NUMBER: 2.5×10^6

- — ○ PROBE 1
- △ — △ PROBE 2
- — □ PROBE 3
- + - - - + AVERAGE (PROBES 1,2,3)

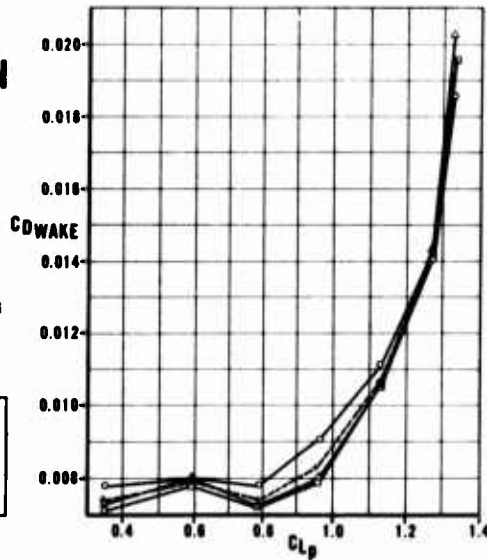


FIGURE 5

MAXIMUM LIFT AT TAKEOFF

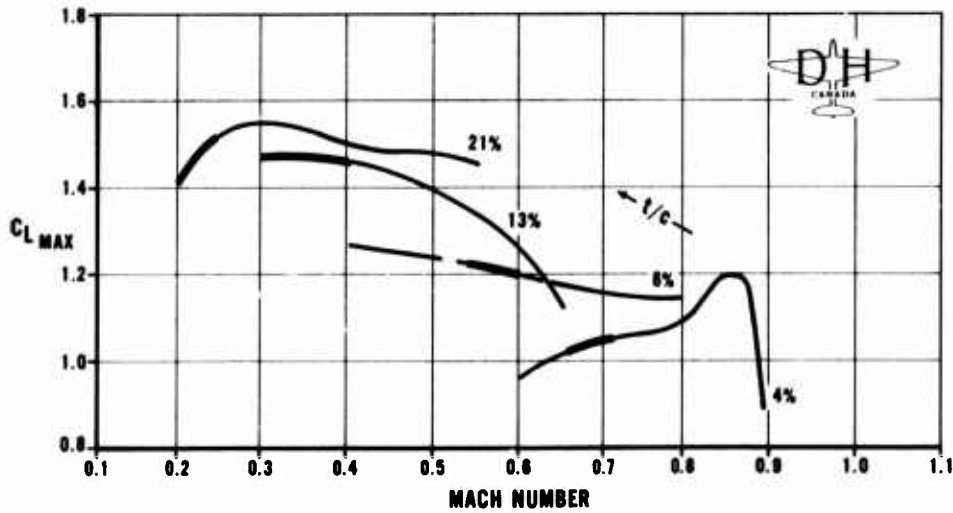


FIGURE 6

CLIMB LIFT/DRAG RATIOS

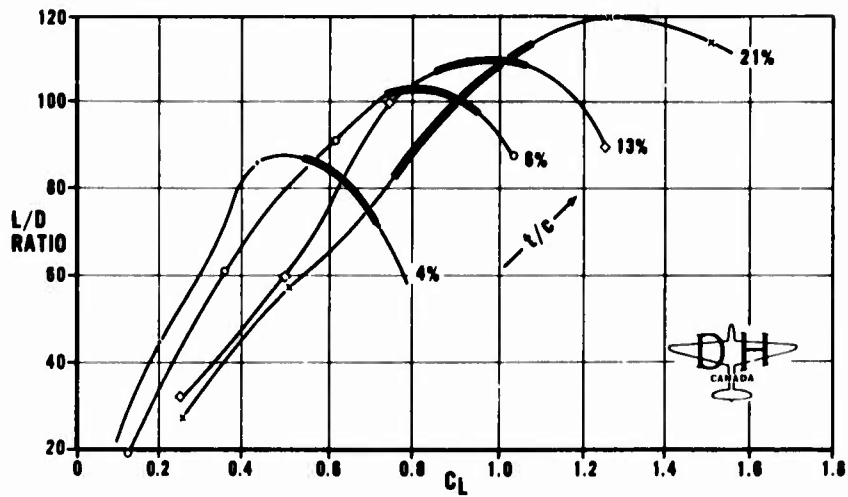


FIGURE 7

CRUISE LIFT/DRAG RATIOS

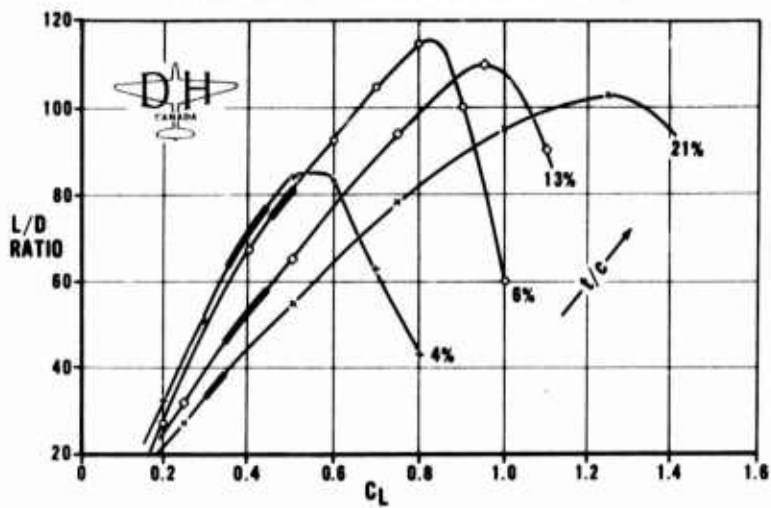


FIGURE 8

COMPARISON OF CLIMB LIFT/DRAG RATIOS

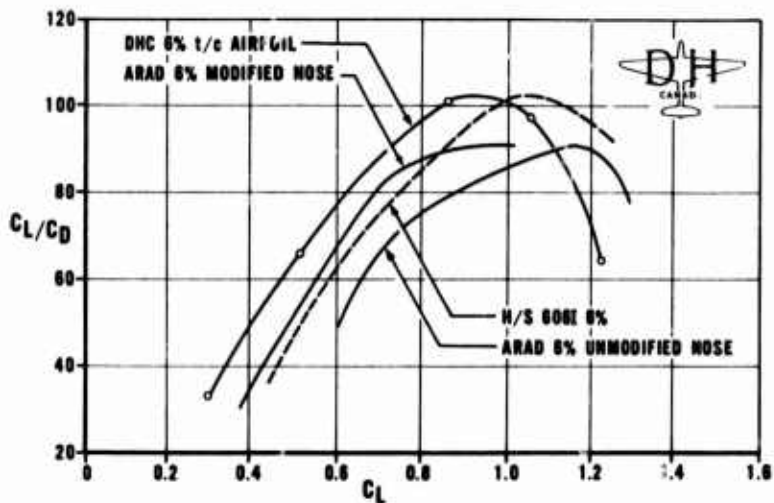


FIGURE 9

GEOMETRY OF LEADING EDGE BOOT & STEP ON A FULL SCALE PROPELLER

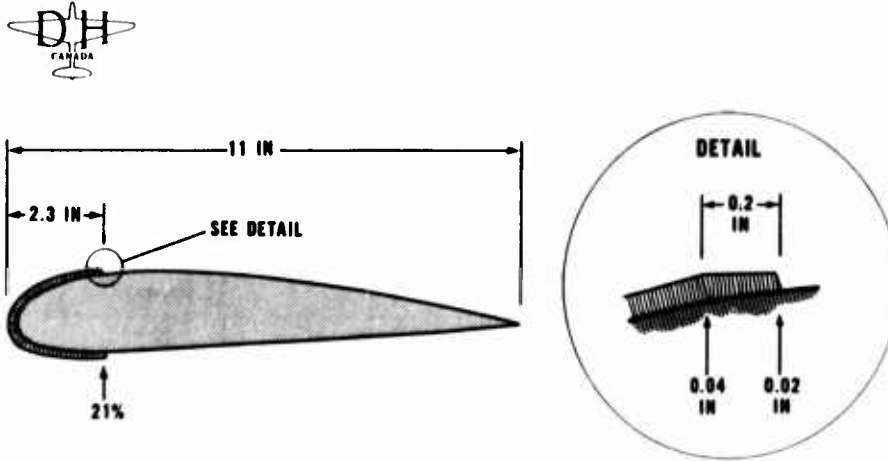


FIGURE 10

INFLUENCE OF MODEL FINISH, MACH NUMBER AND REYNOLDS NUMBER ON $C_{D\text{MIN}}$

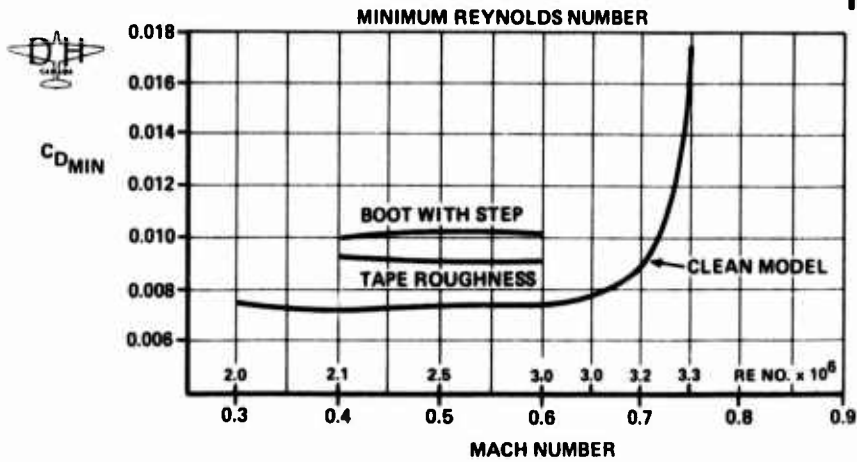


FIGURE 11

LIFT/DRAG RATIO ACROSS PROPELLER RADIUS AT CLIMB CONDITIONS

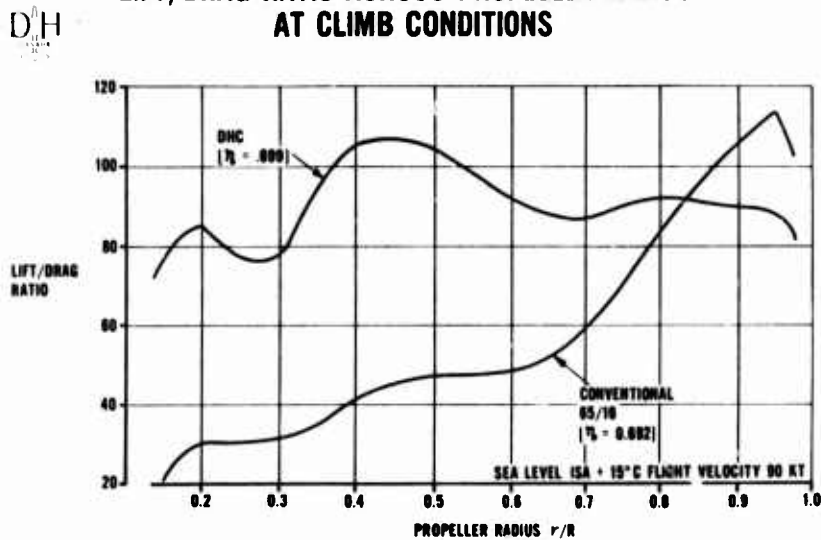


FIGURE 12

**LIFT/DRAG RATIO ACROSS PROPELLER RADIUS
AT CRUISE CONDITION: 260 KT AT 20,000 FT**

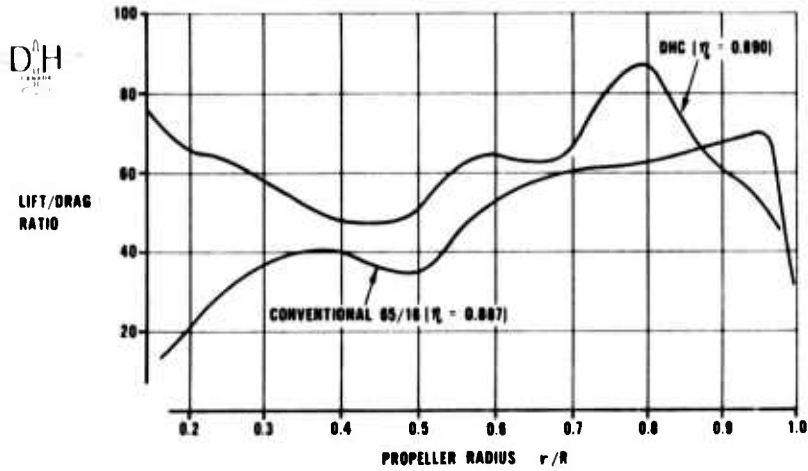


FIGURE 13

OPTIMIZED ULTRA-LIGHT AIRCRAFT PROPELLERS

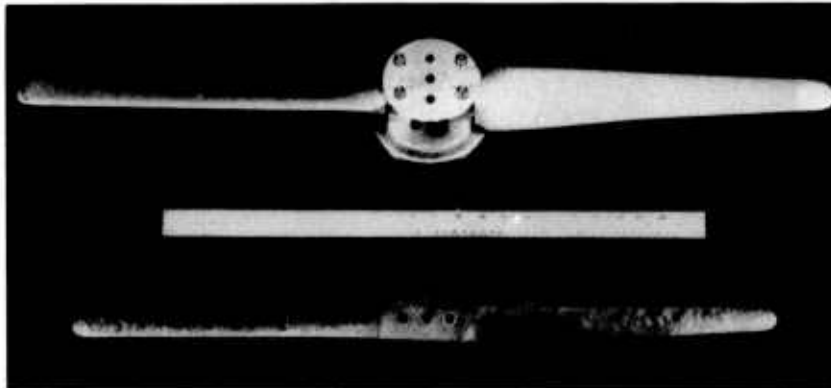


FIGURE 14

**EARLY DASH 8
3-D HALF-MODEL**

(WTBY)



IN 6 x 9 FT
LOW SPEED WIND TUNNEL



FIGURE 15

NACELLE CONFIGURATIONS TESTED

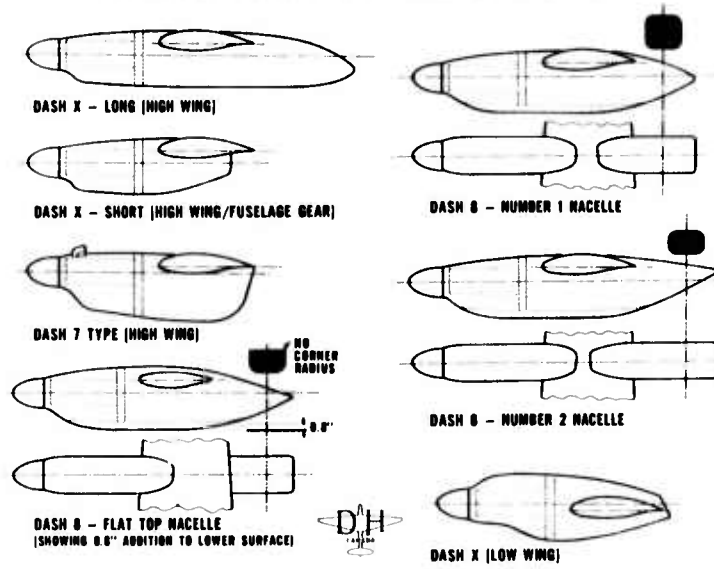


FIGURE 16

DASH 8 EARLY WIND TUNNEL MODEL LOW WING CONFIGURATION

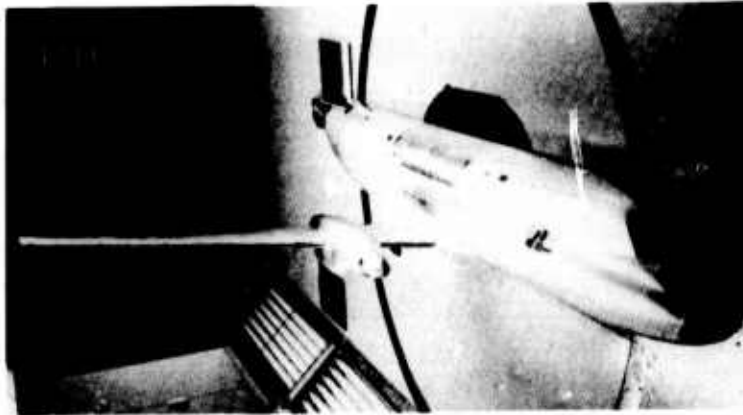


FIGURE 17

COMPARISON OF NACELLE DRAGS, FLAPS 0° AND PROPS OFF

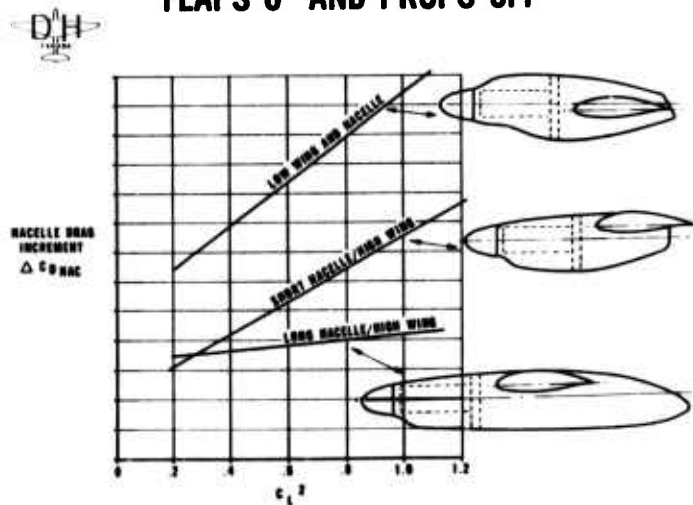


FIGURE 18

INFLUENCE OF WING LOCATION ON $C_{L\text{MAX}}$

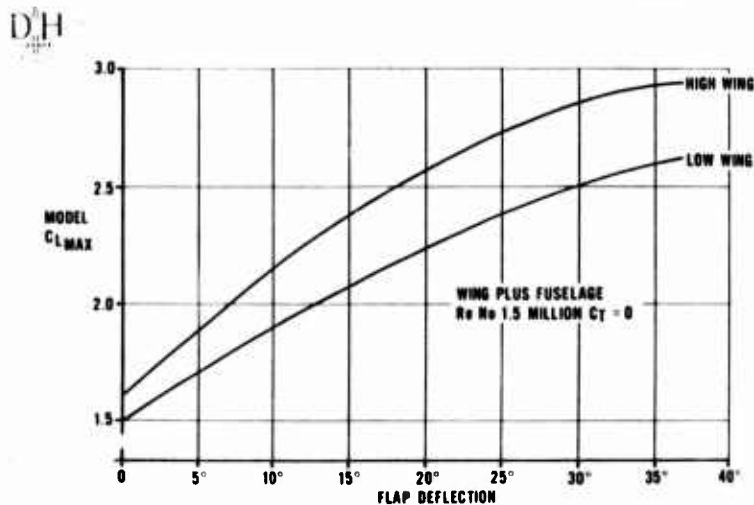


FIGURE 19

MAXIMUM CLIMB WEIGHTS BASED ON POWERED MODEL TEST RESULTS FOWLER FLAP 39% CHORD

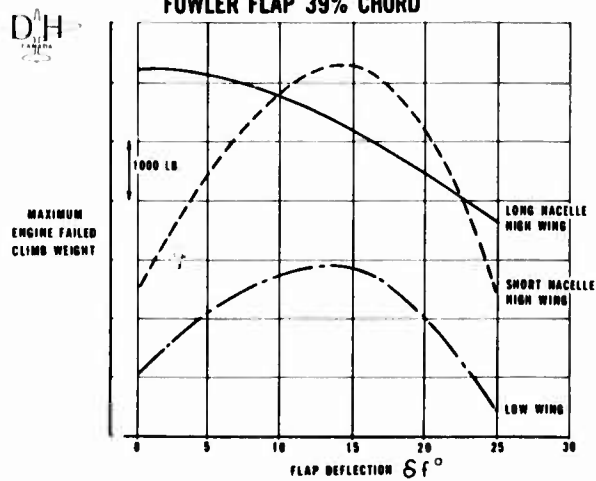


FIGURE 20

LES PROBLEMES D'INTEGRATION DES HELICES A LA CELLULE D'UN AVION
ET, PLUS PARTICULIEREMENT, D'UN BIMOTEUR DE FORTE PUISSANCE

Par

René TAISSAIRE

Ingénieur

Chef de Service Principal

Division des Etudes Avancées

AVIONS MARCEL DASSAULT-BREGUET AVIATION

78, quai Carnot - 92214 ST-CLOUD (FRANCE)

0. INTRODUCTION

L'intégration des hélices à la cellule de l'avion dont elles assurent la propulsion pose essentiellement des problèmes d'interactions.

En effet, l'ensemble que constitue l'avion équipé de ses moteurs et de ses hélices ne saurait être représenté par la simple addition de deux sous-ensembles constitués respectivement par le système de propulsion et par la cellule, considérés séparément et indépendamment l'un de l'autre : c'est que le champ aérodynamique de l'avion modifie, d'une part, les caractéristiques du système propulsif, et que la mise en oeuvre du système propulsif modifie, d'autre part, les caractéristiques propres au "planeur".

L'intensité de ces influences mutuelles, régies par des lois physiques qui, comme on va le voir, peuvent en général s'exprimer par des règles relativement simples, est d'autant plus grande que le souffle des propulseurs est plus puissant.

C'est, en règle générale, le cas des bimoteurs développant de fortes tractions, objet principal de cet exposé, et en particulier celui, très typique, de l'avion patrouilleur maritime "Atlantic" (figure n° 1).

1. RAPPEL DES COEFFICIENTS SANS DIMENSION CARACTERISANT LE FONCTIONNEMENT DE L'HELICE ET DES RELATIONS QUI EXISTENT ENTRE EUX

Avant d'aborder l'analyse des interactions entre le système propulsif et la cellule, il nous a semblé nécessaire de rappeler la nature et la définition des paramètres d'entrée et de sortie qui caractérisent le fonctionnement d'une hélice et les relations qui existent entre eux. Ceci nous a également permis, au passage, de préciser nos notations.

Ainsi, pour des conditions de fonctionnement en vol ou en soufflerie bien définies, nous avons désigné par :

V la vitesse aérodynamique ;

ρ la masse volumique de l'air ambiant ;

N le régime d'un moteur (généralement exprimé en nombre de tours/minute) ;

$n = \frac{rN}{60}$ le régime d'une hélice (en tours/seconde) ;

r le taux de réduction entre moteur et hélice ;

W la puissance absorbée sur l'arbre hélice ;

T la traction correspondante sur l'arbre ;

θh le pas de l'hélice, calage d'une section de référence par rapport au plan de rotation perpendiculaire à l'arbre ;

D le diamètre de l'hélice.

Dans ces conditions, on démontre assez facilement que les deux paramètres non-dimensionnels

$$\chi = \frac{W}{\rho n^3 D^5}$$

$$\text{et } \tau = \frac{T}{\rho n^2 D^4}$$

ne sont fonction que du pas θh et du paramètre sans dimension $\gamma = \frac{V}{nD}$

θh et γ permettent en effet de définir de façon univoque l'incidence aérodynamique de toute section d'une pale, et par conséquent les coefficients aérodynamiques non-dimensionnels C_z et C_x locaux qui lui correspondent.

L'intégration des puissances et des tractions locales élémentaires qui en résultent fournit les valeurs de la puissance absorbée et de la traction restituée au niveau de l'arbre de l'hélice.

C'est ce que montre la figure n° 2, sur laquelle le calcul des coefficients χ et τ , dont on veut montrer qu'ils ne dépendent que de θh et de γ , a été simplifié pour des raisons de clarté : le fait d'avoir négligé, dans la démonstration, l'influence des vitesses induites par la nappe tourbillonnaire n'en change en effet ni le principe, ni le résultat, parce que les modifications locales d'incidence qui en résultent au niveau d'une section donnée ne dépendent elles-mêmes que de θh et de γ .

Pour mémoire, nous rappellerons que le rendement de l'hélice sur l'arbre s'écrit, pour une valeur donnée du pas θh :

$$\eta = \frac{\text{Puissance effectivement restituée sur l'arbre}}{\text{Puissance fournie par le moteur}} = \frac{T \times V}{W} = \frac{\gamma \times \tau}{\chi}$$

η est donc lui-même une fonction de γ et de θh .

La figure n° 3 montre l'allure des réseaux de courbes χ , τ et η en fonction de γ et de θh .

2. LE CHAMP AERODYNAMIQUE DE L'AVION INFLUE SUR LE FONCTIONNEMENT DE L'HELICE

Si l'on veut analyser correctement le fonctionnement d'une hélice en présence de la cellule de l'avion, on doit considérer que tout se passe comme si l'hélice était introduite au sein d'un champ de vitesses aérodynamiques identique à celui que créerait la cellule en l'absence du système propulsif.

Une simplification très acceptable de ce concept consiste à estimer qu'en fait, l'infini amont est constitué, pour l'hélice montée sur l'avion, par le champ aérodynamique qui régnerait à l'emplacement de celle-ci, mais en son absence.

En général, on peut admettre, avec une bonne approximation, que l'écoulement, à cet endroit, est assimilable à un écoulement continu homogène, présentant par rapport à l'écoulement réel à l'infini amont une sous-vitesse relative $u = u/V$, où u est la moyenne des sous-vitesses locales induites, à l'emplacement du disque-hélice, par la présence du fuseau-moteur.

L'influence de cette sous-vitesse se traduit, dans ces conditions, par une modification des courbes caractéristiques théoriques de l'hélice consistant, toutes choses égales par ailleurs, à transformer le paramètre γ en $\gamma(1-u)$.

En présence d'un fuseau-moteur de dimensions relatives importantes par rapport à celles de l'hélice, cette correction est tout à fait nécessaire. A titre d'exemple, elle est de l'ordre de 4 % pour les hélices de l'Atlantic, montées sur des fuseaux-moteurs dont le maître couple a une surface égale à 16 % de la surface du disque hélice.

Cette influence peut être évaluée :

- soit par des calculs basés sur des méthodes semi-expérimentales ;
- soit par comparaison directe entre les résultats de deux séries d'essais en soufflerie effectués avec deux types de montage d'hélice différents :
 - le premier, sur un fuseau d'interaction minimale (minimum body, figure n° 4a),
 - le deuxième, sur une maquette du fuseau réel (figure n° 4b).

Ces deux figures représentent une maquette d'hélice de l'Atlantic de 900 mm de diamètre.

3. LE SOUFFLE DES HELICES MODIFIE LE CHAMP AERODYNAMIQUE DE L'AVION PAR LA CREATION DE SURVITESSES LONGITUDINALES ET NORMALES

En tout point de l'espace, la mise en oeuvre du système propulsif de l'avion introduit, par rapport au vecteur-vitesse aérodynamique local du "planeur", une survitesse qui modifie à la fois le module de ce vecteur et sa direction, c'est-à-dire la déflexion locale, et dont on peut dire qu'elle est la somme d'une composante "longitudinale", colinéaire au vecteur-vitesse initial, et d'une composante "normale", définie en grandeur et direction dans un plan normal à ce dernier.

En analysant la nature de cette survitesse, on constate qu'elle est, en fait, constituée par la superposition de deux survitesses de nature différente :

- l'une, directement liée au souffle de l'hélice, a pour composantes longitudinale et normale celles du système tourbillonnaire hélicoïdal qui s'échappe de l'hélice, compte tenu, par ailleurs, des modifications de direction que lui impose sa rencontre avec le plan de l'aile ;
- la deuxième, qui n'est liée au souffle d'hélice que d'une manière indirecte, correspond au champ tourbillonnaire engendré au niveau de la voilure par la modification de répartition de portance en envergure imputable aux survitesses directes.

La figure n° 5 résume cette situation dans le cas d'une hélice ayant un pas à gauche, c'est-à-dire tournant dans le sens anti-horaire lorsqu'on la regarde de l'arrière.

Déterminer par le calcul le champ complet des survitesses ainsi définies, et en déduire l'influence sur les caractéristiques aérodynamiques de l'avion n'est, pour l'instant, qu'un objectif assez lointain.

Par contre, on connaît bien les paramètres de similitude simples dont on doit, sur le plan expérimental, respecter les valeurs pour retrouver sur une maquette les coefficients aérodynamiques non-dimensionnels correspondant à une configuration et à des conditions de vol données sur l'avion.

4. LE COEFFICIENT SANS DIMENSION C_T EST A LA FOIS REPRESENTATIF DES SURVITESSES LONGITUDINALES ET DE LA PLUS GRANDE PART DES SURVITESSES NORMALES

Pour réaliser en soufflerie la similitude exacte par rapport au vol, il faut, en toute rigueur, respecter sur la maquette les valeurs des deux paramètres sans dimension :

τ/γ^2 , lié à la traction T sur l'arbre,

et χ/γ^2 , lié à la puissance sur l'arbre W.

La première de ces deux quantités est, en général, exprimée un peu différemment, à l'aide d'un paramètre qui lui est proportionnel, et qui est l'homologue du coefficient de traînée C_x sur le plan de la traction d'hélice, puisqu'il est défini par :

$$C_T = \frac{T}{\rho/2 V^2 S}$$

où S est la surface de référence de la maquette. Il est immédiat de montrer, à partir des définitions de τ et de γ , que, pour une hélice donnée :

$$C_T = \frac{2 D^2}{S} \frac{\tau}{\gamma^2}$$

Si l'on se place à présent dans les hypothèses simplifiées de la théorie de Froude (écoulement par tranches dans un tube de courant ayant pour section celle du disque hélice au niveau de ce dernier, et sur les parois duquel règne la pression statique ambiante), on peut aisément relier C_T à la survitesse relative moyenne longitudinale $u = \frac{W}{V}$ à l'infini aval par la relation :

$$C_T = \frac{\pi D^2}{4 S} \times u (2+u)$$

Il suffit pour cela (figure n° 6) d'appliquer le théorème des quantités de mouvement sur une surface de contrôle entourant le disque hélice, au voisinage immédiat de celui-ci, puis d'appliquer successivement la relation de Bernoulli dans les parties amont et aval du tube de courant considéré.

On peut, de même, démontrer que le paramètre χ/γ^2 est en relation avec le champ des survitesSES normales. Cependant, ces dernières sont, pour leur majeure part, indirectement reliées à C_T par l'intermédiaire des échappements tourbillonnaires provoqués par la modification des portances locales dues aux survitesSES longitudinales créées par les hélices.

Dans les variations de déflexion locale liées au souffle d'hélice, la part imputable à C_T est ainsi, finalement, beaucoup plus importante que celle liée à χ/γ^2 .

Pour en fournir un exemple précis, nous avons résumé sur la figure n° 7 les résultats moyens de mesures de déflexions locales effectuées sur une maquette motorisée au 1/15 de l'"Atlantic", à l'aide de six clinomètres répartis symétriquement à l'emplacement du bord d'attaque de l'empennage horizontal (mais évidemment en l'absence de celui-ci).

L'influence de C_T sur la déflexion moyenne est considérable sur la partie gauche de l'empennage, et beaucoup plus modeste, sur sa partie droite. Cela résulte évidemment du sens de rotation anti-horaire des deux nappes tourbillonnaires issues des hélices, qui, à leur intersection avec le bord d'attaque de l'aile, provoque une forte déviation du souffle, vers la gauche au-dessus du plan des cordes de la voilure, et vers la droite en-dessous de celui-ci.

5. INFLUENCE DU SOUFFLE D'HELICE SUR LES COEFFICIENTS ET LES DERIVEES AERODYNAMIQUES DE L'AVION

Ainsi, pour un couple de valeurs données de l'incidence α et du dérapage β , chacun des coefficients aérodynamiques non-dimensionnels de l'avion est fonction de C_T et de χ/γ^2 .

Pour reproduire en soufflerie les conditions réelles, il faudrait donc pouvoir réaliser simultanément la similitude de ces deux paramètres. Notons que, dans les rares cas où elle peut être assurée, cette similitude parfaite est en général obtenue pour des valeurs de θh et de γ assez différentes de celles du vol.

Dans les autres cas, c'est-à-dire presque toujours, il faut donner la priorité absolue à la similitude de C_T , dont on a vu l'influence prépondérante sur le champ aérodynamique.

Celle-ci est d'ailleurs confirmée par les résultats de nombreuses études paramétriques qui montrent qu'à C_T constant, l'influence des variations de χ/γ^2 est très faible.

Finalement, l'identification aérodynamique de l'avion interactionné par l'hélice se traduit :

- pour ce qui concerne les coefficients aérodynamiques longitudinaux, par des réseaux de courbes :

\bar{C}_z ($\alpha, C_T, \delta m$), dites courbes unitaires "motorisées";

\bar{C}_z ($\chi, C_T, \delta m$), dites polaires "motorisées";

\bar{C}_m ($C_z, C_T, \delta m$, centrage), dites courbes de stabilité longitudinale "motorisées";

- et pour ce qui concerne les coefficients aérodynamiques latéraux et transversaux, par des réseaux de courbes :

$$\begin{aligned} \overline{C_n}(\beta, \delta n, \delta l, C_T); \\ \overline{C_y}(\beta, \delta n, \delta l, C_T); \\ \overline{C_l}(\beta, \delta n, \delta l, C_T). \end{aligned} \quad \text{établis pour différentes valeurs de l'incidence}$$

La barre qui surmonte les symboles représentant ces coefficients non-dimensionnels indique qu'ils tiennent compte de l'effet de la motorisation.

Quelques explications complémentaires sont nécessaires en ce qui concerne $\overline{C_x}$:

Si l'on désigne par $\Delta \overline{C_x}$ le supplément de C_x dû à la motorisation, on peut écrire, pour une valeur donnée de l'incidence :

$$\overline{C_x} = C_x + \Delta \overline{C_x} - C_T$$

où C_x est le C_x "planeur", et C_T est mesuré sur l'arbre hélice.

En désignant par C_T propulsif (C_T prop) la quantité :

$$C_T \text{ prop} = C_T - \Delta \overline{C_x}$$

on peut écrire finalement :

$$\overline{C_x} = C_x - C_T \text{ prop}$$

Pour évaluer $\Delta \overline{C_x}$, et donc C_T prop, on peut :

- utiliser des méthodes semi-expérimentales basées sur l'hypothèse que le rapport $\frac{C_T \text{ prop}}{C_T}$ n'est fonction que du paramètre γ et des dimensions relatives du fuseau-moteur par rapport au disque hélice,
- ou bien effectuer des essais en soufflerie permettant de mesurer d'une part C_T sur l'arbre hélice à l'aide d'une balance interne, d'autre part $\overline{C_x}$ et C_x à l'aide d'une balance externe, comme sur la maquette du fuseau de l'Atlantic équipée d'une hélice de 900 mm de diamètre, représentée sur la figure n° 4 (b).

Quantitativement, l'influence du souffle des hélices sur certains coefficients aérodynamiques peut être très importante aux vitesses faibles et aux régimes des moteurs élevés.

Sur l'"Atlantic", chacun des deux moteurs développe au décollage, dans les conditions d'atmosphère standard au niveau de la mer, une puissance maximale voisine de 6 000 CV absorbée par une hélice quadripale d'un diamètre légèrement inférieur à 5 m.

Durant cette phase de vol, la diminution de stabilité longitudinale due à la motorisation est très sensible, mais le fait que l'avion accélère de façon continue la rend plus tolérable que dans le cas le plus critique, qui est celui de la remise des gaz à l'atterrissage.

Au cours d'une telle manoeuvre, la diminution de stabilité, liée à l'augmentation de la puissance, est en effet quasi-instantanée. Elle est, d'autre part, plus importante qu'au décollage, parce que la vitesse est plus faible et que, de ce fait, le niveau maximal de C_T à plein régime est plus élevé.

A la masse d'atterrissage, très usuelle, de 30 T, et à un centrage très voisin de la limite AR, la figure n° 8 montre l'influence d'un tel niveau de C_T sur les courbes $\overline{C_z}$ ($\overline{C_m}$, δm). On voit qu'il en résulte une diminution de marge statique égale à plus de 10 % de la corde moyenne aérodynamique, c'est-à-dire une perte de stabilité considérable.

C'est cette condition critique qui détermine le centrage-limite AR de l'"Atlantic", comme certainement celui de tout autre bimoteur de forte puissance.

Traduite en termes de braquages d'équilibre en fonction de la vitesse, la perte de stabilité due à la motorisation est mise en évidence sur la figure n° 9 qui, pour deux valeurs extrêmes du centrage, permet une comparaison entre les courbes δm (V_c) correspondant respectivement, en vol horizontal rectiligne, au ralenti de vol et au régime de croisière maximale, en configuration d'approche. La différence de pente entre ces deux courbes, autre façon d'exprimer la différence de stabilité statique longitudinale entre les deux cas de motorisation considérés, est, on le voit, très importante.

Cette planche est aussi très instructive en ce qui concerne l'influence de la motorisation sur le C_{zmax} .

La masse de l'avion étant bien identifiée pour chacun des essais, on a pu en déduire, en effet, que le passage du ralenti vol au régime de croisière maximale fait augmenter C_{zmax} de :

$$\Delta \overline{C_{zmax}} = 0,5 \text{ en configuration de décollage}$$

et de :

$$\Delta \overline{C_{xmax}} = 0,65 \text{ en configuration d'approche.}$$

Ouvrons ici une brève parenthèse pour rappeler l'exemple particulièrement spectaculaire de l'influence du souffle des hélices sur le C_{zmax} de l'avion S.T.O.L Bréguet 941, dont la conception même était basée sur le souffle intégral, à l'aide de quatre hélices contrarotatives, d'une voilure très fortement

hypersustentée par des volets triples, s'étendant sur toute son envergure. Pour un braquage de volets de l'ordre de 100° et pour les plus grandes valeurs praticables de C_T , la valeur du C_z maximum de cet avion, mesurée en vol, était supérieure à 5.

Revenons à l'"Atlantic" pour montrer à présent l'influence de C_T sur les coefficients aérodynamiques latéraux et transversaux de cet avion. Nous l'avons résumée sur la figure n° 10 pour la configuration d'approche.

On voit sur cette figure que, pour des valeurs du C_T de remise des gaz de l'ordre de 0,4, la diminution de stabilité de route $C_{n\beta}$ et celle de l'effet dièdre $C_{l\beta}$ sont respectivement de l'ordre de 35 % et de 55 %. L'influence de la motorisation sur les dérivées aérodynamiques latérales et transversales est donc elle-aussi très importante aux basses vitesses.

On pourrait, enfin, constater que l'efficacité des gouvernes de profondeur et de direction est affectée de façon significative par une augmentation du C_T .

Dans l'écriture des équations générales de la mécanique du vol, il est donc bien évidemment nécessaire de prendre en compte cette variation des coefficients aérodynamiques en fonction du taux de motorisation, en introduisant leurs dérivées partielles par rapport à C_T .

6. ROLE PRIMORDIAL DES INTERACTIONS DUES AU SOUFFLE DES HELICES DANS LA DETERMINATION DE LA VMC D'UN BIMOTEUR DE FORTE PUISSANCE

Rappelons succinctement que la vitesse minimale de contrôle VMC est la vitesse conventionnelle en dessous de laquelle, en cas de panne du moteur le plus critique, en configuration de décollage train sorti, l'équilibrage latéral et transversal de l'avion n'est plus possible.

La démonstration en vol de la VMC peut être effectuée à dérapage nul, à condition de ne pas dépasser 5° d'inclinaison latérale.

Nous allons à présent établir une comparaison entre deux appareils, de caractéristiques géométriques identiques, mais différant par leur type de motorisation : l'un est biréacteur, l'autre biturbopropulseur, et la poussée F , fournie par chacun des réacteurs du premier, est identique à la traction T fournie par chacune des hélices de l'autre sur son arbre. La distance $|ym|$ de l'axe de poussée au plan de symétrie est la même que celle de l'axe de traction au plan de symétrie.

Nous verrons plus loin que, pour l'avion à hélices, le cas critique de panne, du point de vue de la VMC, est celui de la panne du moteur droit.

Nous allons donc supposer que, dans un cas comme dans l'autre, c'est le fonctionnement de ce moteur qui est interrompu.

Pour le biréacteur, le couple de lacet dû à la panne est égal, dans ces conditions, au produit $F|ym|$, avec les conventions de signes habituelles. Nous supposons que, pour annuler ce couple, la gouverne de direction est braquée à fond dans le sens > 0 ($\delta n_{\max} > 0$). La dérivée partielle $C_{n\delta n}$ étant < 0 , l'équilibre en lacet à VMC, à dérapage nul, s'écrit :

$$F \cdot |ym| + \frac{P}{2} \frac{1}{VM_c^2} \text{ S.b. } C_{n\delta n} \delta n_{\max} = 0$$

$$\text{d'où : } VMC = \sqrt{\frac{-F|ym|}{P/2 \text{ S.b. } C_{n\delta n} \cdot \delta n_{\max}}}$$

Le cas de panne d'un turbopropulseur est plus complexe (figure n° 11).

En effet, les échappements tourbillonnaires issus de la "bosse" de portance provoquée sur la voilure par les survitesses de l'hélice gauche engendrent, sur l'empennage vertical, une succion vers la gauche, qui se traduit par une augmentation du moment de lacet $T \cdot |ym|$ directement dû à la traction.

D'autre part, le pas de l'hélice étant à gauche comme sur l'"Atlantic" la partie du souffle située au-dessus de l'aile est également déviée vers la gauche et la déflexion latérale moyenne qui en résulte donne à nouveau naissance à une augmentation du moment de lacet de même signe.

On voit bien que c'est lorsque la panne se produit à droite que les trois effets s'ajoutent et c'est donc bien ce cas qui est le plus défavorable du point de vue de la VMC.

Aussi, sur un avion comme l'Atlantic, le moment de lacet réel dû à la panne du moteur droit est supérieur de plus de 50 % au couple de base, $T \cdot |ym|$.

Pour en revenir à notre comparaison initiale, on constate donc que pour obtenir la même VMC sur les deux avions, il faut doter l'avion à hélices d'une gouverne de direction bien plus efficace que celle du biréacteur. C'est une caractéristique très importante à laquelle il faut, sur ce type d'avion, attacher une attention particulière dès le stade de la conception.

CONCLUSIONS

Par ces quelques rappels très simples, nous avons essayé de mettre en évidence, aussi clairement que possible, l'intime imbrication de l'aérodynamique du système propulseur avec celle de la cellule de tout avion à hélices, et plus particulièrement d'un bimoteur de forte puissance.

Le dimensionnement des empennages et des gouvernes d'un tel appareil est largement tributaire du soin apporté à définir l'influence de la motorisation sur l'ensemble de ses caractéristiques aérodynamiques dans tout le domaine de vol, mais surtout aux basses vitesses associées à de fortes tractions d'hélices.

Un tel résultat ne peut être obtenu que grâce à des essais de maquettes motorisées conçues pour permettre la réalisation de la similitude des CT et, en particulier, dans les cas de vol les plus critiques.

Figure 1 AMD-BA Avion "ATLANTIC"

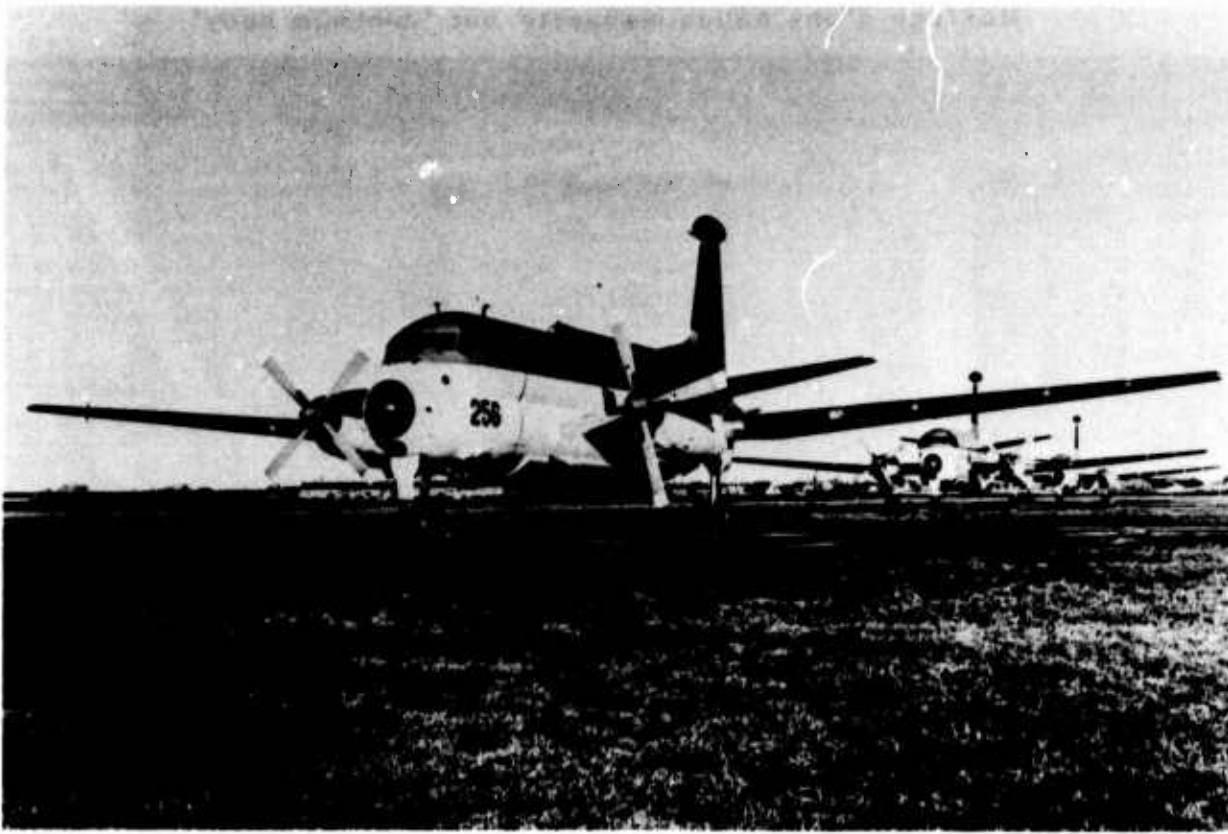


Figure 2

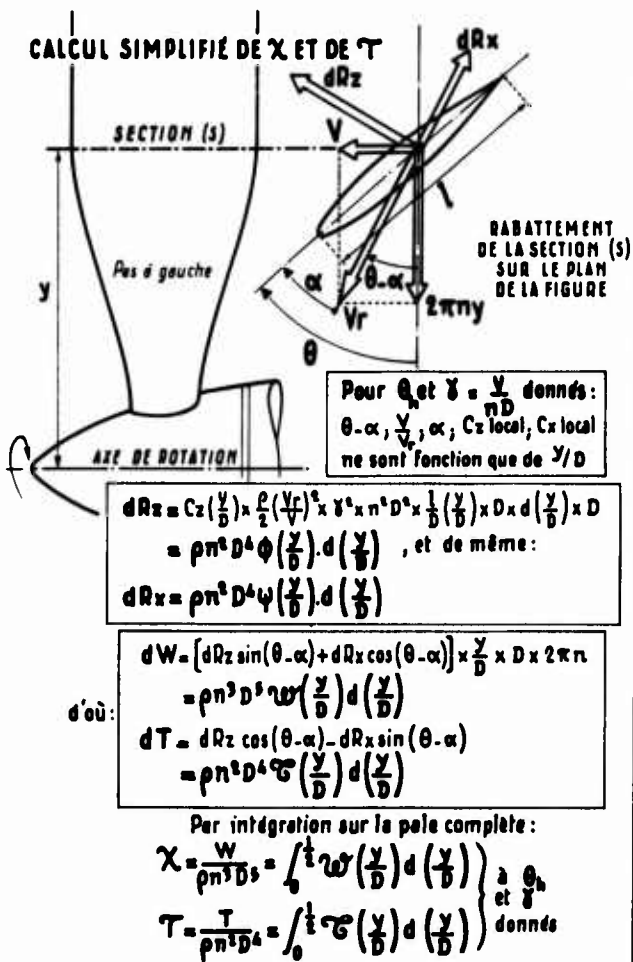


Figure 3

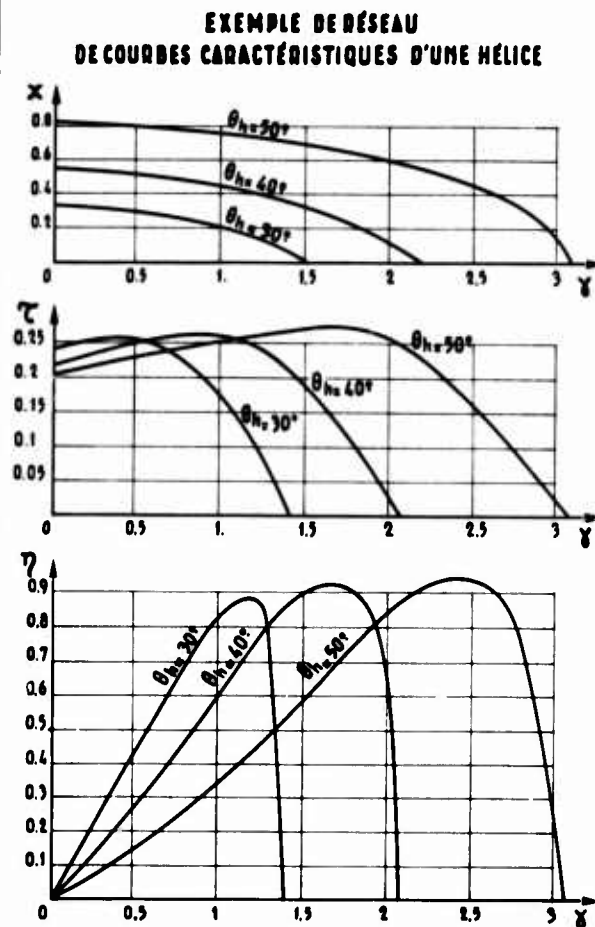


Figure 4(a)

Montage d'une hélice maquette sur "minimum body"

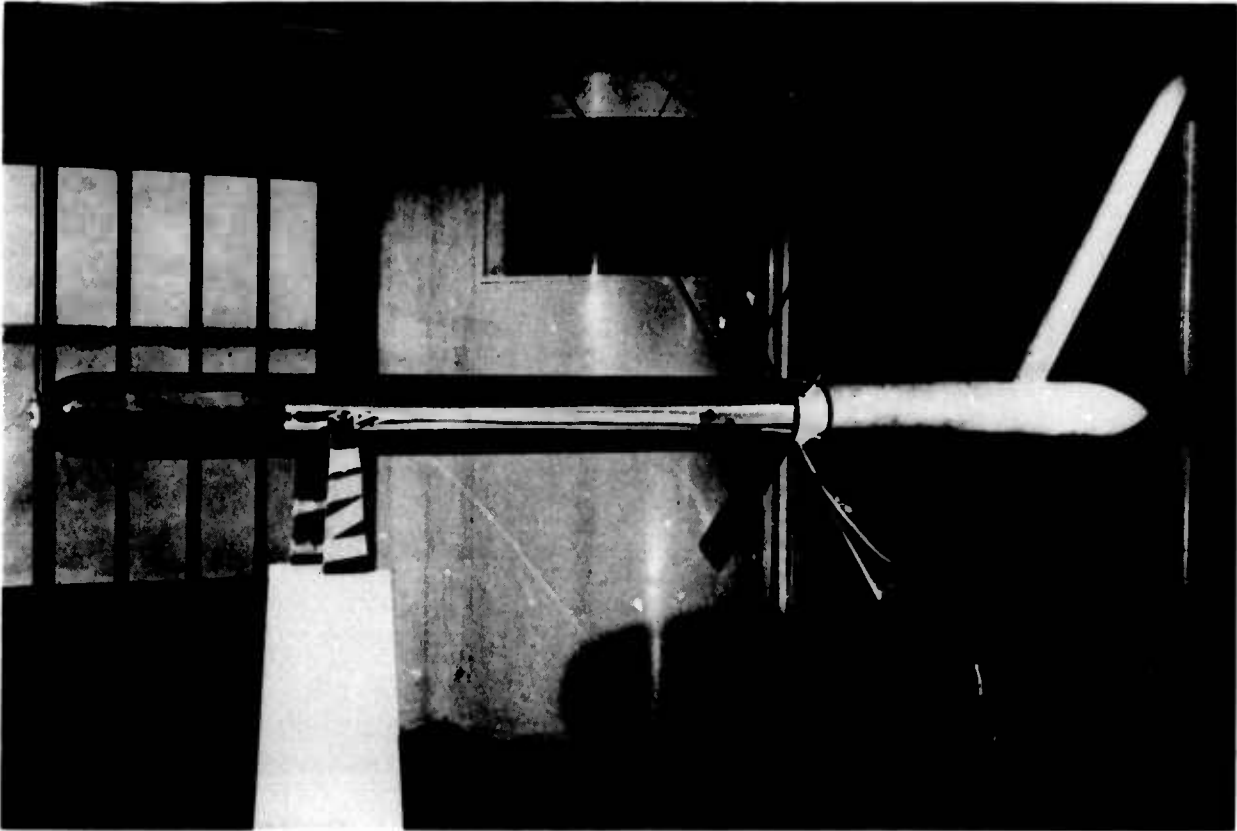
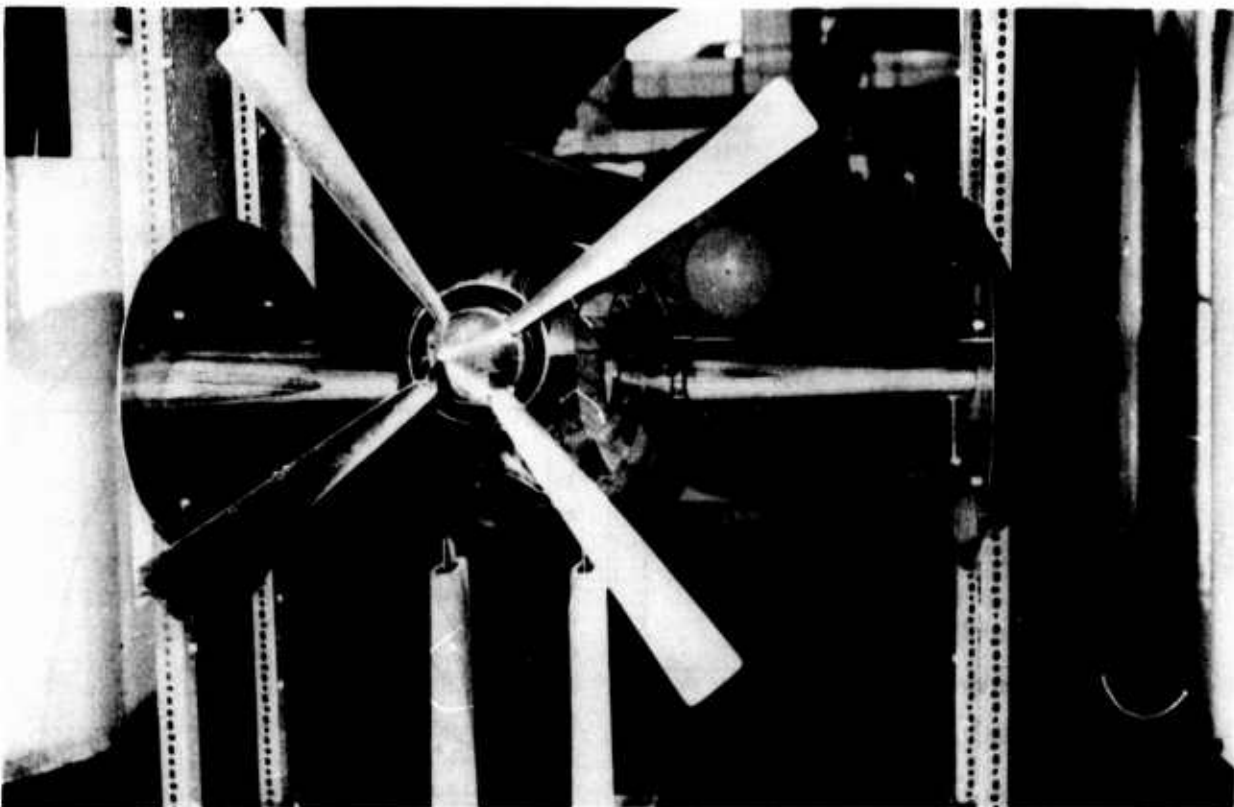


Figure 4 (b)

Montage d'une hélice maquette sur une maquette de fuseau de l'avion



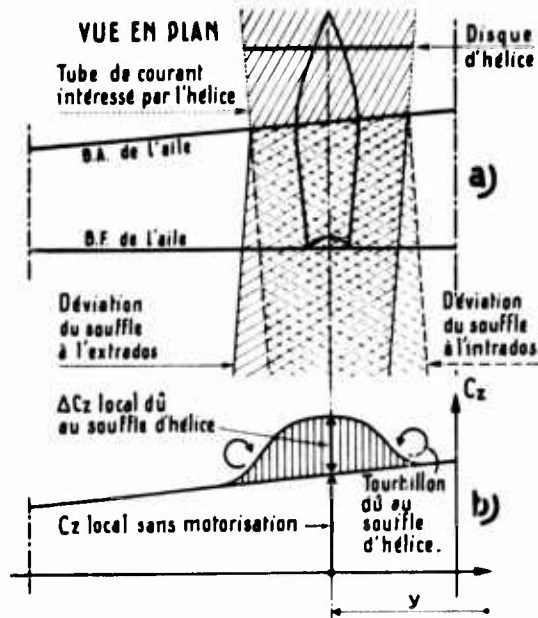


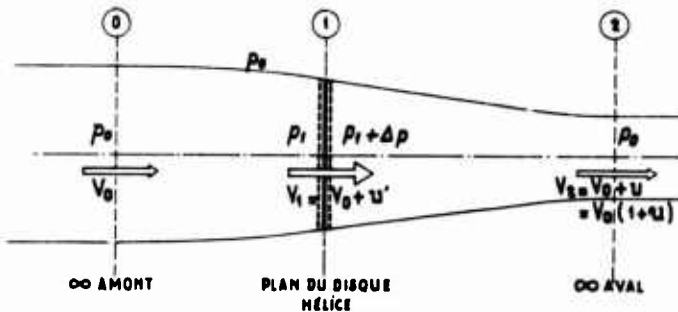
Figure 5

**INTERACTIONS
HÉLICE-VOILURE**
pour une hélice ayant un pas à gauche.

- a) - Déviaton du souffle par le bord d'attaque de l'aile.
- b) - Influence des survitesses d'hélice sur les C_z locaux de la voilure.
- Système tourbillonnaire associé à ces survitesses.

Figure 6

RELATION ENTRE LE PARAMÈTRE DE TRACTION C_T ET LA SURVITESSE RELATIVE LONGITUDINALE MOYENNE u EN AVAL DE L'HELICE



Théorème des quantités de mouvement en ① :

$$m V_1 - m V_0 = 0 = -\Delta p \cdot S_h + T$$

avec S_h : surface du disque hélice
 T : traction sur l'arbre

Equations de Bernoulli :

Entre ① et ② : $p_0 + \frac{\rho}{2} V_0^2 = p_1 + \frac{\rho}{2} V_1^2$

Entre ① et ② : $p_1 + \frac{\rho}{2} V_1^2 = p_2 + \frac{\rho}{2} V_2^2$

d'où : $p_1 - p_2 = \Delta p = \frac{\rho}{2} (V_2^2 - V_0^2) = \frac{\rho}{2} V_0^2 u (2+u)$

et $T = \Delta p \cdot S_h = \frac{\rho}{2} V_0^2 S_h u (2+u)$

d'où $C_T = \frac{T}{\frac{\rho}{2} V_0^2 S} = \frac{S_h}{S} u (2+u)$

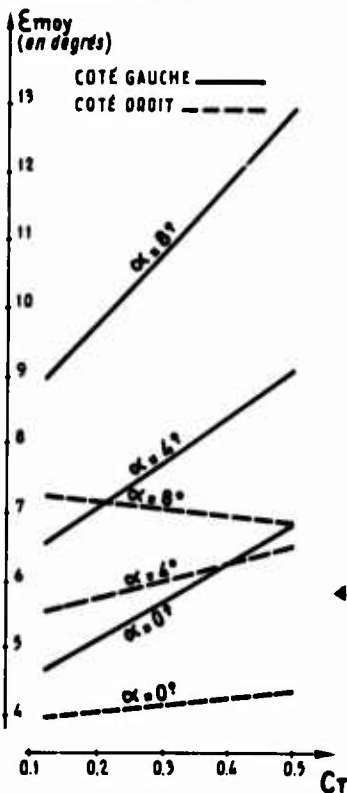


Figure 7

ATLANTIC
MAQUETTE MOTORISÉE AU 1/15^e
DÉFLEXION MOYENNE
AU DROIT DE L'EMPENNAGE HORIZONTAL

POSITION DES CLINOMETRES

← RESULTATS DES MESURES

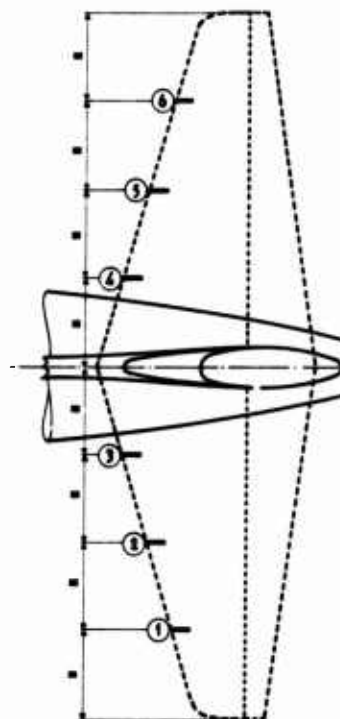


Figure 8

ATLANTIC - MAQUETTE MOTORISÉE AU 1/15^e
 INFLUENCE DE C_T SUR LA STABILITÉ LONGITUDINALE
 ET SUR L'EFFICACITÉ DE GOUVERNE DE PROFONDEUR
 EN CONFIGURATION D'APPROCHE

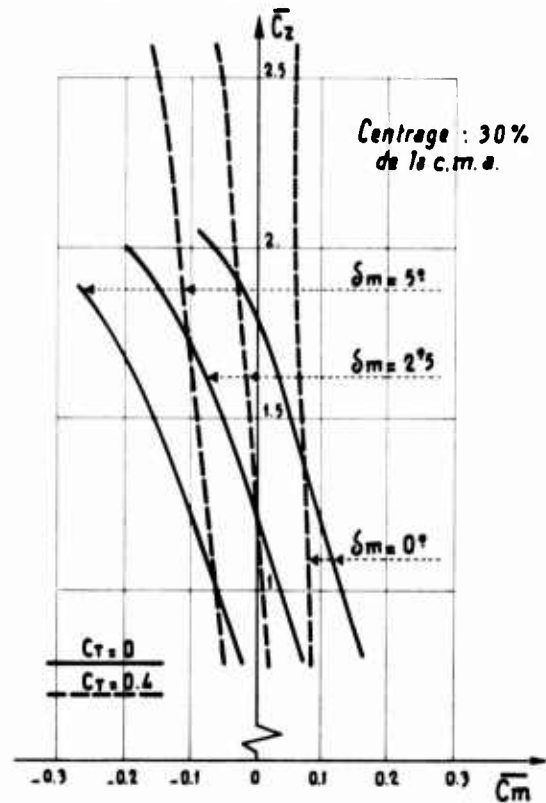


Figure 9

ATLANTIC

EXEMPLE D'INFLUENCE DE LA MOTORISATION
 SUR LES BRAQUAGES D'ÉQUILIBRE EN PALIER

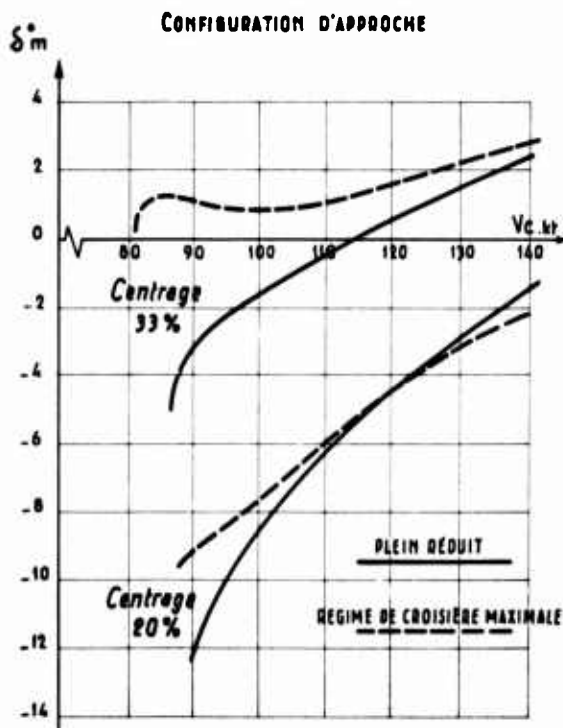


Figure 10

ATLANTIC
 VARIATIONS DE $\bar{C}_{n\beta}$ ET $\bar{C}_{l\beta}$ EN FONCTION DE L'INCIDENCE α
 ET DE LA MOTORISATION EN CONFIGURATION D'APPROCHE

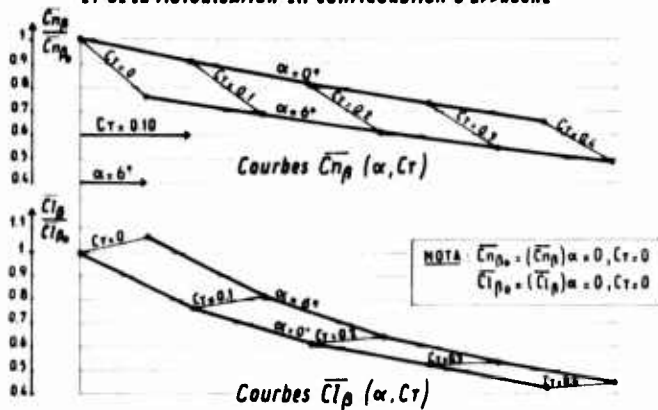


Figure 11

PANNE DU TURBOPROPULSEUR DROIT AU DÉCOLLAGE

DÉTERMINATION DE LA VMC

LES HÉLICES ONT TOUTES DEUX UN PAS À GAUCHE

EN CAS DE PANNE DU MOTEUR DROIT,
 LES COUPLES DE LACET DUS :

- Au couple direct $T \cdot |y_m|$
- A la déflexion du souffle E_h
- A l'influence du tourbillon (t) sur la dérive.

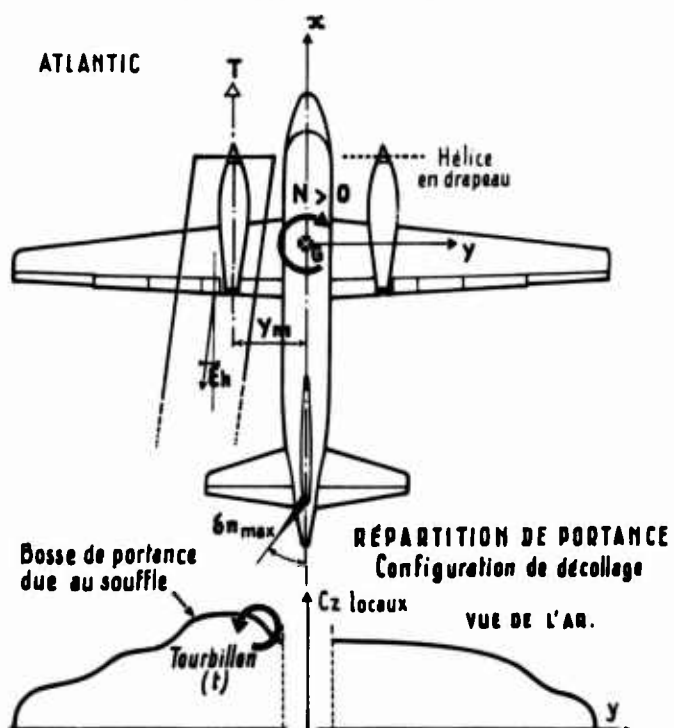
S'AJOUTENT.

LE COUPLE DÙ A LA PANNE EST ÉGAL A :

$$K \cdot T \cdot |y_m| \quad \text{avec } K > 1$$

$$\text{et } VMC = \sqrt{\frac{K \cdot T \cdot |y_m|}{\rho \cdot S \cdot b \cdot C_{n\beta} \cdot \delta n_{max}}}$$

Nota : Pour un avion à réaction $K=1$



**WIND TUNNEL INVESTIGATION OF THE INTERACTION OF PROPELLER
SLIPSTREAM WITH NACELLE/WING/FLAP COMBINATIONS**

By

A. S. Aljabri and A. C. Hughes
Lockheed-Georgia Company
86 S. Cobb Drive
Marietta, Georgia 30063

SUMMARY

Until recently it was sufficient to define the propeller slipstream by the average velocity induced across the propeller disk. With the advent of the highly loaded propfan and the accompanying concern for the effect of the slipstream on aircraft components, it has become imperative that the nature of the slipstream and its interaction with aircraft components be known. This paper describes a series of wind tunnel tests performed to improve the understanding of this complex aerodynamic interaction. The tests were conducted using a conventional propeller operating at low subsonic speeds.

Complementary theoretical and experimental studies were used to investigate the interaction effects. Results from wind tunnel tests on propeller/nacelle, propeller/nacelle/wing, and propeller/nacelle/wing/flap combinations are presented here. Force, pressure, and wake survey data from the test allow the slipstream characteristics, including its distortion by the wing and flap, to be obtained. The important parameters which govern the slipstream shape and induced velocities are identified and techniques are developed for estimating slipstream drag and the torque absorbed by a wing immersed in the slipstream. An improved understanding of the effects of wind tunnel walls on propeller powered testing is also presented.

LIST OF SYMBOLS

c	Blade chord
C_d	Airfoil section drag coefficient
C_l	Airfoil section lift coefficient
C_{li}	Airfoil section design coefficient
C_p	Power coefficient
C_T	Thrust coefficient
D	Propeller diameter
J	Advance ratio
n	Propeller rotational frequency in revolutions per second
P	Power
Q	Torque
R	Propeller radius
r	Radial distance to blade element
T	Thrust
V_o	Freestream velocity
V_e	Effective resultant velocity
V_R	Resultant velocity
w	Induced velocity
w_a	Axial component of induced velocity
w_t	Tangential component of induced velocity
x	Fraction of tip radius
α	Angle of attack
α_i	Induced angle of attack
β	Geometric pitch angle of zero lift line
Δ	Small quantity or change
ϵ	Swirl angle
η_p	Propeller efficiency

- ρ Mass density of air
- ϕ Angle formed by V_R and horizontal plane
- ω Propeller rotational frequency in radians per second

INTRODUCTION

High-speed turboprops, or propfans, have been proposed to power transport aircraft that cruise at high subsonic speeds. Significant benefits in terms of fuel-efficient operation and reduction of life-cycle cost are expected from the use of propfans on advanced transport aircraft. Critical to the realization of these benefits is the understanding, prediction, and treatment of the complicated aerodynamic interaction between the slipstream produced by these highly-loaded propellers and aircraft components, especially the wing.

A wing-mounted turboprop/nacelle demands special attention to installation design because of the much greater aerodynamic interaction between the propeller slipstream, the nacelle, and the wing. There are two important aerodynamic characteristics of this type of installation that must be distinguished and understood. First, installed propeller performance including slipstream characteristics is required. This demands a reliable data base for the isolated propeller.

Second, changes in the performance of the wing due to the presence of nacelle and slipstream need to be determined. The slipstream gives rise to both swirl and increased dynamic pressure, and an understanding of both effects is necessary to treat the slipstream/wing interaction. The wing also has a straightening effect on the slipstream which results in a portion of the swirl being recovered in the form of thrust. Improved methods are needed to assess the amount of torque absorbed and the thrust recovered by the wing. A detailed experimental approach was pursued to obtain fundamental aerodynamic information regarding the interaction of the slipstream with the nacelle and wing. Although this paper emphasizes wind-tunnel testing and data reduction techniques, analytical methods have been developed and applied to gain understanding of installation effects and are compared with the test results.

TEST DESCRIPTION

Tests were conducted on an isolated propeller (to provide baseline information), a propeller/nacelle/wing configuration and a propeller/nacelle/wing/flap configuration. Surface pressure, force and wake survey data were obtained for angles of attack from 0 to 4 degrees and advance ratios from 0.6 to 1.0 at blade angles of 22.4 and 24 degrees. These tests were conducted in the Lockheed-Georgia 30-inch by 43-inch wind tunnel at a nominal dynamic pressure of 10.0 pounds per square foot.

WIND TUNNEL MODEL AND INSTRUMENTATION

The model consists of a symmetric wing with a NACA 0018 section and a symmetric nacelle. The wing has a 30-inch span and the nacelle maximum diameter is 2.5 inches. The nacelle was mated to the wing such that its centerline was coincident with the wing chord line with no fillets or fairing at the intersection. The test used a four-bladed propeller of 11.2-inch diameter. The planform and twist distributions of the blades are described in Reference 1. The propeller was powered by an electric motor housed in the nacelle. The ratio of propeller disc area to the tunnel cross-sectional area was 0.07. A photograph showing the model mounted in the tunnel for testing is presented in Figure 1.

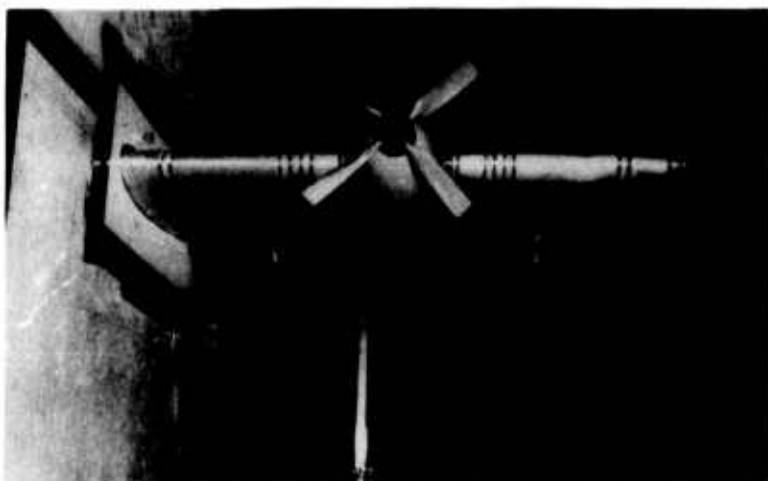


Figure 1. Propeller/Nacelle/Wing/Flap Installed in the Model Test Facility

The wing contains 210 static pressure taps, positioned in chordwise rows and spanwise stations so as to give good definition in high gradient regions. Forces and moments were measured by a strain gauge balance located beneath the floor of the tunnel. Wake survey data were also obtained and are discussed in detail in the next section.

Wake surveys were made at three vertical planes aft of the propeller plane: 0.7 inch (as close to the propeller plane as practical), 11.2 inches (one propeller diameter) and 22.4 inches (two propeller diameters). The survey instrumentation consists of a 7 probe, 5 holes-per-probe survey rake with the probes spaced 0.5 inch apart. A 0.5-inch-square cartesian grid was used except in the slipstream boundary region where the grid was 0.2 inches.

RESULTS AND DISCUSSION

WING PRESSURE DISTRIBUTIONS AND SPAN LOADINGS

When producing thrust, a propeller increases the axial velocity of the air flowing through the rotor disk area and gives the flow within the slipstream a tangential velocity component, producing a swirling flow. These changes in the flow interact with downstream aircraft components, such as the nacelle and wing, thus affecting their aerodynamic performance. In turn, the propeller slipstream is distorted by the aircraft components that it washes.

The effect of the propeller super-velocity on the wing increases its lift but does not change the lift coefficient based on the local dynamic pressure. The swirl, however, does change the lift coefficient because it causes a direct change in the local angle of attack. Since the swirl is not constant but varies with distance from the propeller centerline, the change in lift coefficient varies accordingly at each spanwise station. On the portion of the wing where the swirl causes upwash, the section angle of attack is effectively increased causing local suction peaks. Since the lift force is normal to the onset flow direction, the lift vector is rotated forward giving a component in the thrust direction. On the downwash side, the section angle of attack is reduced giving a smaller force, which detracts from, but does not eliminate, the net thrust recovery.

The above observations were verified by the test results. Wing surface pressure distributions at the critical stations are presented in Figure 2. The span loadings, shown in Figure 3, are typical of propeller slipstream-washed wings and show an increase in loading behind the up-going blade and a reduction in loading behind the down-going blade.

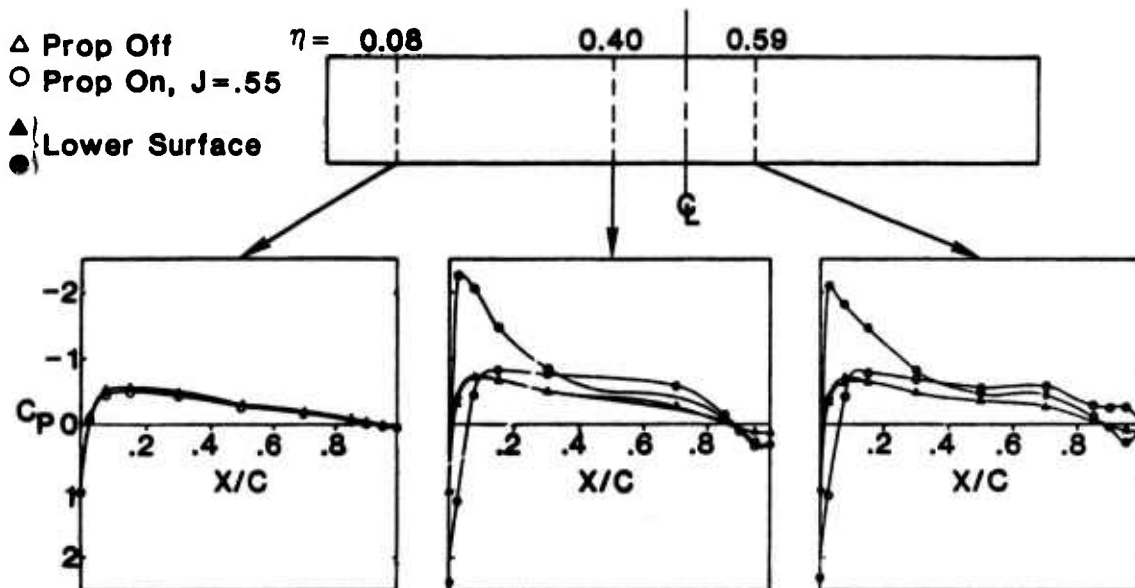


Figure 2. Wing Section Pressure Distributions

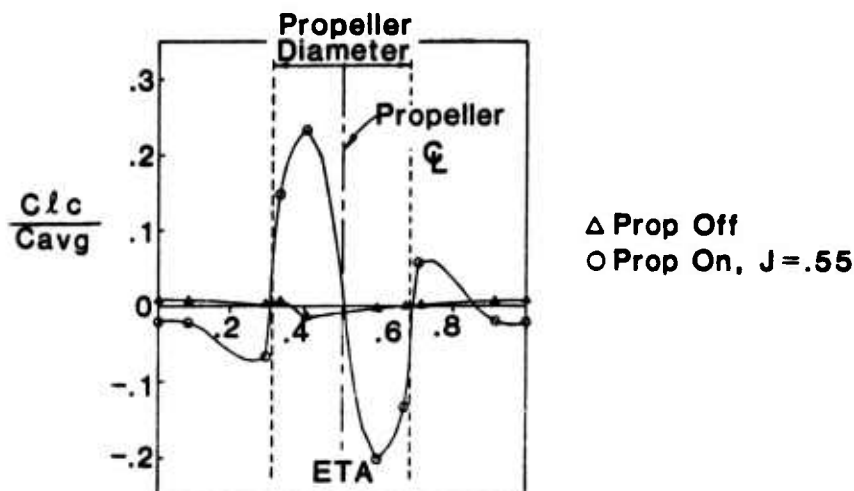


Figure 3. Spanwise Load Distribution

FORCE DATA

Force data were obtained for all the configurations tested. Figure 10 presents the isolated propeller thrust coefficient, C_T , versus advance ratio, J , obtained from both the balance and from the wake surveys. The agreement between the force and wake survey data is excellent. In addition, the predicted free air C_T vs J for the same conditions is shown. The differences between the free air and tunnel data are prominent at low advance ratios where the mass flow in the slipstream is high. The reasons for the differences in free air and tunnel data are discussed in detail later.

WAKE SURVEY ANALYSIS

Lockheed employs a well established technique to obtain wake survey data. When using five-holed probes it is important that they be properly calibrated and that an empty tunnel survey be obtained to establish baseline conditions. Reference 2 gives further details on wake survey procedures and data analysis using these probes.

Wake surveys are used to determine the radial and streamwise variation of the slipstream properties and to locate the slipstream boundary. In critical areas such as the slipstream boundary region, a sufficiently fine grid is selected to precisely define the location and magnitude of the high gradient regions.

Wake Survey Data Analysis: The data were reduced to provide the three components of the wake velocity and the total pressure, from which the circulation, kinetic energy, and vorticity within the wake were computed. Maps of these aerodynamic parameters were made to help visualize the nature of the propeller wake. The radial variation of the propeller thrust coefficient gradient, power coefficient gradient, blade section lift and blade section drag coefficients were derived from the wake survey data. Integration of these gradients radially produced propeller thrust and power coefficients. Wake data also allowed the torque in the slipstream at any given survey station to be determined. Therefore, the slipstream torque calculated from data in one plane immediately in front of, and a second plane behind the wing, allowed the torque absorbed by the wing to be calculated. This gives a measure of the amount of de-rotation that the wing has imparted to the slipstream.

FLOW VISUALIZATION FROM WAKE SURVEY

Isolated Propeller/Nacelle

The wake survey data provide visualization of the slipstream flow and its interaction with other components. Figure 4 presents the results from the propeller/nacelle test at an advance ratio of 0.6 and zero angle of attack. Illustrated is a crossflow map at three locations downstream from the propeller plane. The arrows represent the vector sum of the tangential and radial velocities, with their length indicating the magnitude of the vector at that point. Clearly, the tangential velocity, which represents swirl in the slipstream, is dominating. The radial velocity is generally weak. The map vividly marks the slipstream boundary by the absence of swirl outside the boundary.

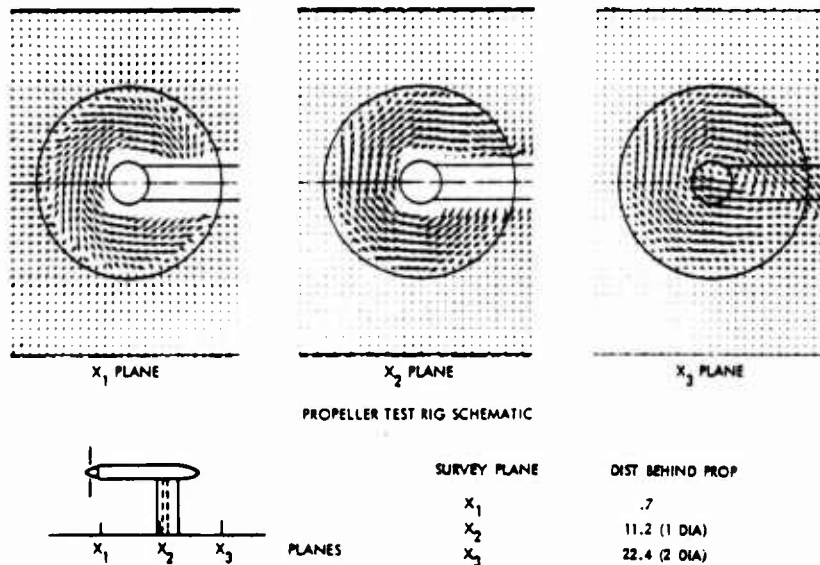


Figure 4. Isolated Propeller Crossflow Vector Maps at 0.6 Advance Ratio

The strong slipstream contraction can be seen immediately behind the propeller with some additional contraction at one diameter behind the propeller plane. At two diameters behind the propeller plane there is no further evidence of contraction, but still the slipstream boundary remains distinct.

The radial flow outside the slipstream immediately behind the propeller is indicative of the free stream following the shape of the contracting slipstream rather than entrainment. The strong vortex system bounding the slipstream precludes entrainment of the surrounding flow. No radial flow is present at the two downstream locations because at these stations the contraction gradient is very small.

Figure 5 shows the corresponding axial and transverse velocity map viewed from beneath the model. The vortex system bounding the slipstream induces a velocity upstream and is seen as a reduction in the magnitude of the freestream just outside the slipstream edge. The radial distribution of axial velocity is also shown. There is an increase, as expected, in axial induced velocity with downstream position, but the increase is not discernible beyond one propeller diameter downstream of the propeller plane.

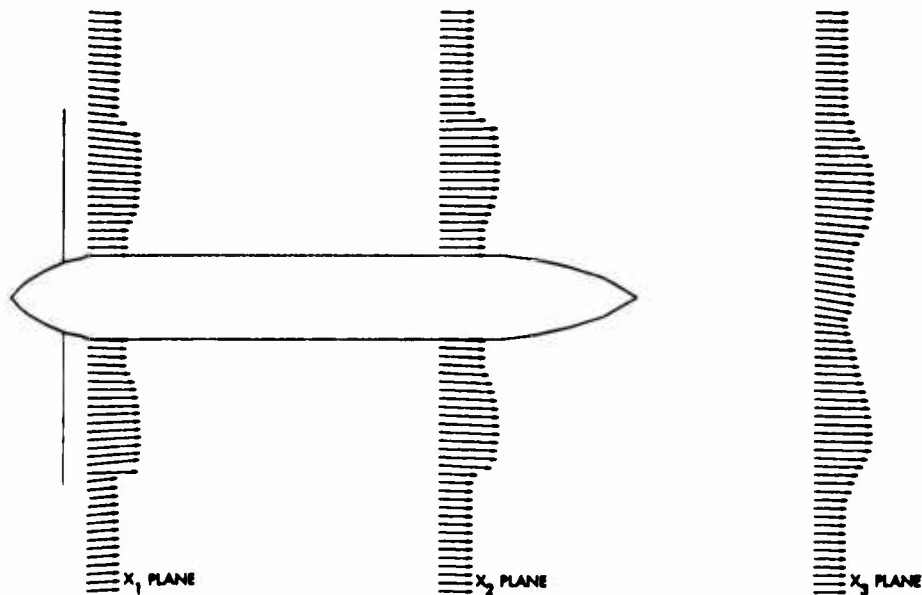


Figure 5. Isolated Propeller Velocity Profiles at 0.6 Advance Ratio

Slipstream/Wing Interaction

The slipstream/wing crossflow map is shown in Figure 6. The slipstream is no longer axisymmetric in the presence of the wing but is "sheared" spanwise in opposite directions on the upper and lower surfaces. The shearing is in the direction of the crossflow and increases as the slipstream progresses along the wing chord reaching a maximum at the trailing edge. Figure 7 shows the total pressure map at both one diameter downstream of the propeller plane and behind the wing trailing edge. Once again, the shearing of the flow is revealed. Note the steep pressure gradient at the slipstream boundary at the one-propeller-diameter plane, while in the downstream plane the pressure gradient is reduced showing a rather thicker slipstream boundary, but still distinct.

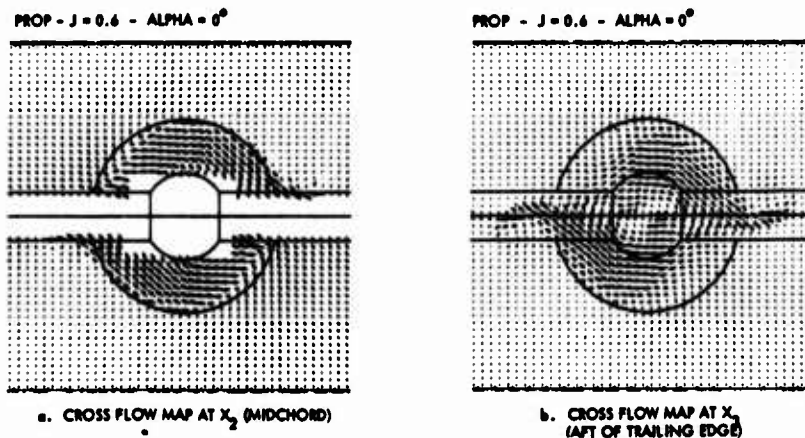


Figure 6. Cross Flow Map Showing Shearing of the Slipstream by the Wing

Except for the shearing, the slipstream remains remarkably preserved. It is still contracted and maintains a strong boundary with the swirl contained within it. A pair of strong vortices are shed from the junction of the wing surface and the edge of the slipstream, which is indicative of the high gradient of spanwise load on the wing. On one side, the wing experiences an upwash and thus a lift increase and conversely a download is experienced by the wing on the other side. Outside of the slipstream the wing experiences no loads as it is of symmetric section and is at zero angle of attack.

Slipstream/Wing/Flap Interaction

Wake survey data shows that the addition of the slotted flap to the wing causes major changes to the slipstream (Figure 8). The swirl is removed and there is no longer a distinct slipstream boundary. The mutual interaction between the slipstream and the wing/flap is no longer limited to the slipstream but includes the surrounding flow field as well, which is deflected downwards. Once again, vortices are shed indicating a rapid change in the spanwise load distribution on the wing, but as shown, they are much stronger for the wing with the slotted flap.

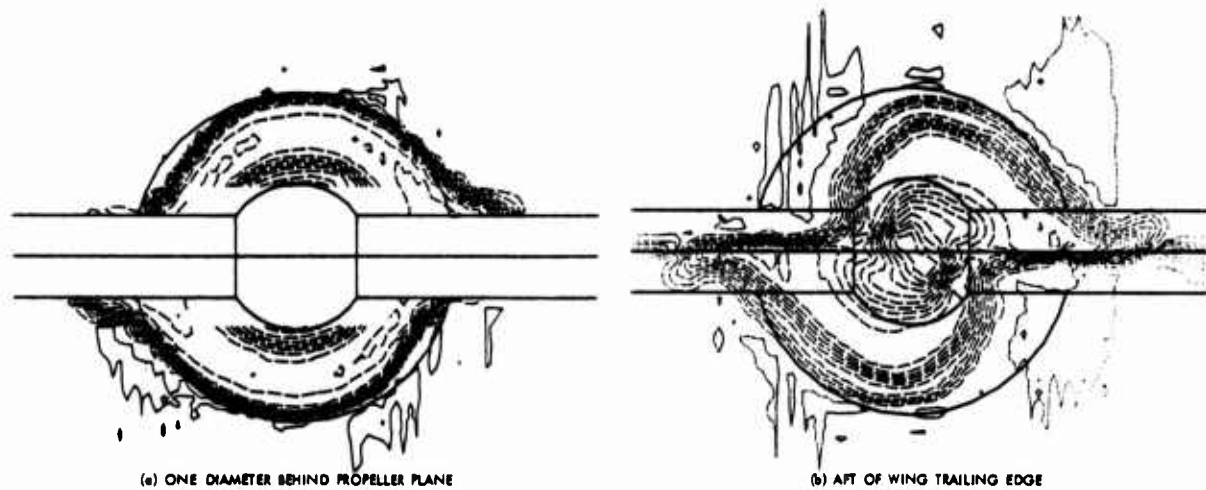


Figure 7. Total Pressure Maps Showing Slipstream Distortion by the Wing

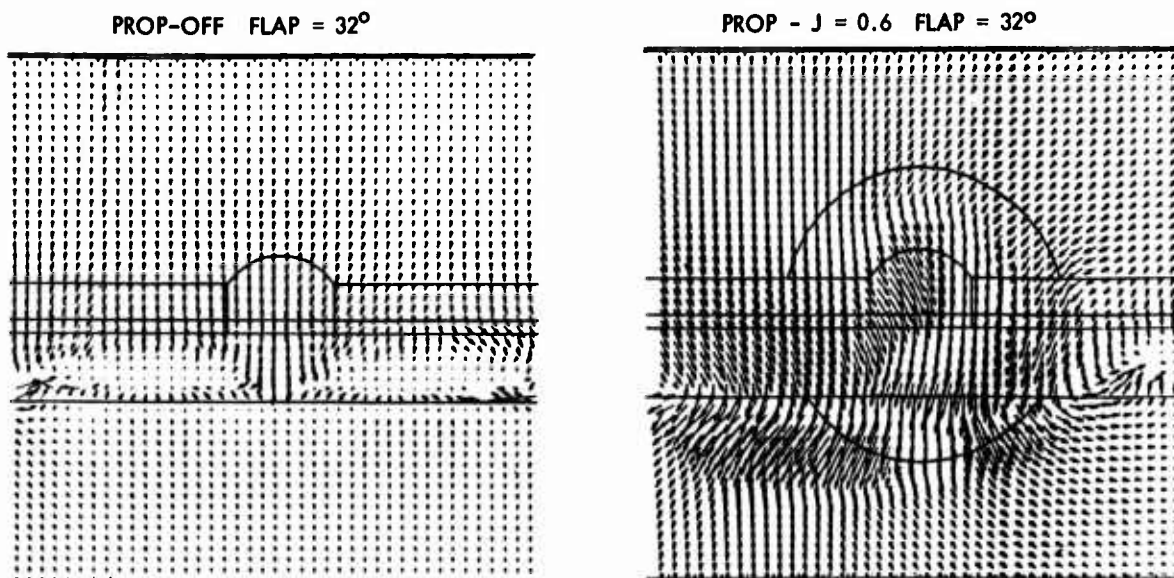


Figure 8. Effect of Slipstream on Nacelle/Wing/Flap Combinations

PERFORMANCE CALCULATIONS FROM WAKE SURVEY

Slipstream Characteristics

The slipstream immediately behind the propeller contains sufficient information to determine propeller performance including the radial distribution of the propeller aerodynamic characteristics. Careful analysis of the slipstream data using Glauert's momentum-vortex theory (Reference 3) gives good results. The fundamental relations used in the evaluation of the elementary blade performance are presented here for convenience, the details can be found in References 4 and 5.

$$dC_T/dx = \pi(r/R)J^2 w_a (1+w_a)$$

$$dC_P/dx = \pi^2(r/R)^2 J^2 w_t (1+w_a)$$

where; dC_T/dx is the elemental thrust coefficient, and dC_P/dx is the elemental power coefficient.

As may be seen from the above expressions there are three quantities to be determined from the experimental data in order to define the propeller characteristics. They are w_a , the induced axial velocity; w_t , the induced tangential velocity; and r/R , the nondimensional radius of the propeller at which they are applied. With reference to the diagram in Figure 9, it is seen that when these three quantities are obtained, all of the other characteristics may be readily derived.

Determination of Axial And Tangential Induced Velocities

When developing an expression for the section thrust coefficient, it should be noted that as the air flows through the plane containing the blades, it experiences a sudden increase in static pressure and undergoes a tangential acceleration while its axial velocity remains unchanged. As the air moves downstream of the propeller plane, the static pressure increase gradually drops, being transformed into an axial and tangential velocity until finally (far downstream), the velocity increments are twice their value at the propeller plane, while the static pressure is reduced to its freestream value.

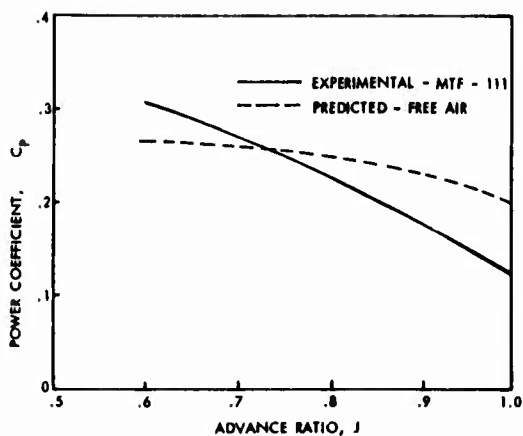
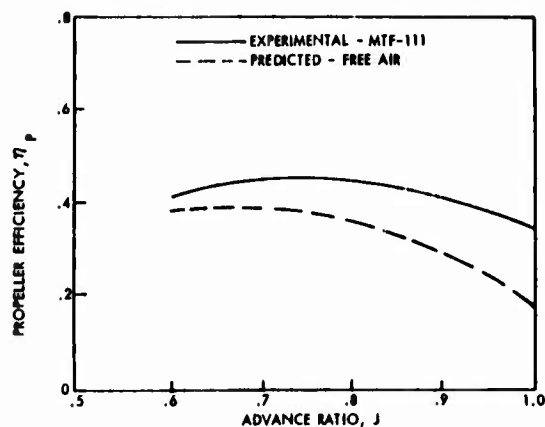
Figure 11. C_p versus J Comparisons

Figure 12. Propeller Efficiency versus J Comparisons

COMPARISON OF FREE AIR PREDICTIONS AND TUNNEL DATA

Comparisons between wake survey test data and theoretical predictions are shown in Figures 13 thru 15 for an advance ratio of 0.6. All three wake parameters, axial induced velocity, w_a , tangential induced velocity, w_t and swirl angle show close agreement in the shape of the radial distribution, although they differ significantly in magnitude.

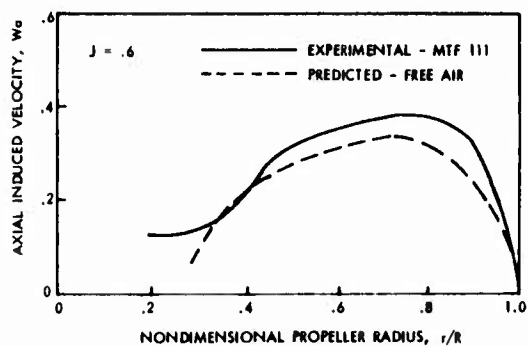


Figure 13. Induced Axial Velocity Comparisons

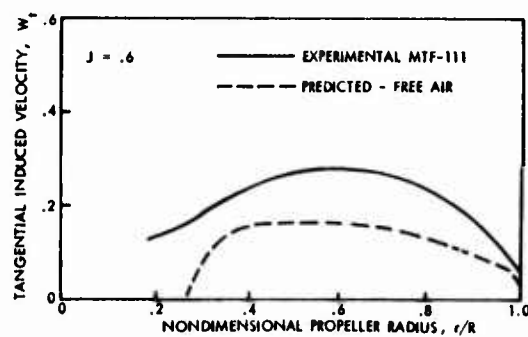


Figure 14. Tangential Velocity Comparison

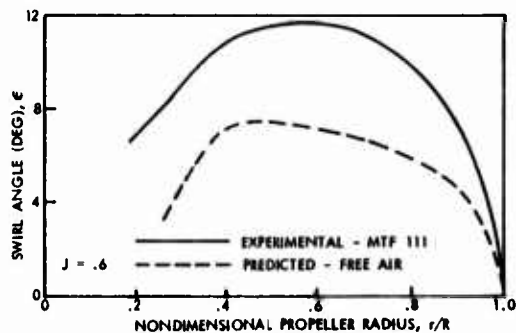


Figure 15. Swirl Angle Comparisons

It has long been known that propeller characteristics obtained from wind tunnel tests tend to be optimistic compared to results obtained in free air. The analysis of the isolated propeller wake survey data has provided some detailed insight into this subject. Again, referring to Figure 9, once w_a and w_t have been obtained, all of the other important parameters may be readily derived.

A comparison of parameters predicted for free air with results from the present test indicate the following:

(1) The primary effect of the tunnel wall constraint is to reduce the induced angle, thereby increasing the thrust. The induced angle change has an effect more akin to reducing the Activity Factor rather than merely reducing the advance ratio. The increased thrust also increases the power absorbed, but since the induced angle is reduced, the efficiency is increased. Induced angle comparisons are shown in Figures 16 and 17 for radial distribution and variation with advance ratio, respectively.

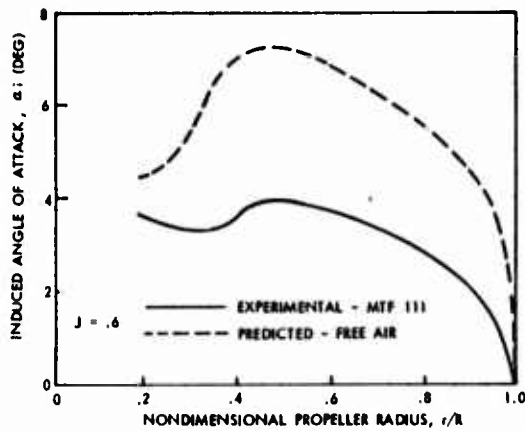


Figure 16. Induced Angle Comparison

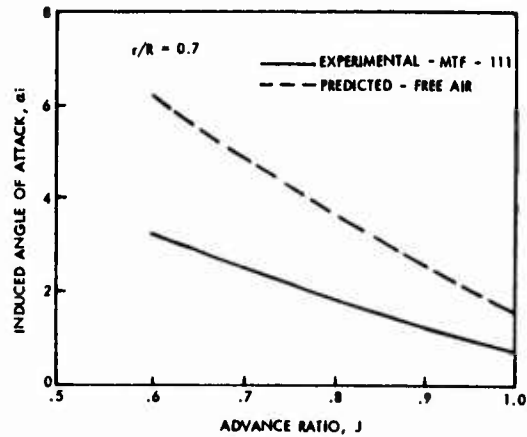


Figure 17. Induced Angle Comparison

(2) A comparison of the predicted and measured section C_l distribution is shown in Figure 18. The effect of the reduction in induced angle is to increase the local C_l , as would be expected.

(3) A comparison of predicted and measured section drag polars for the 0.7 radius station is shown in Figure 19. The correlation is considered excellent considering that the prediction method cannot account for laminar separation or the differences in actual airfoil sections on a well-used model propeller and the loft ordinates. The drag levels are very high due to the extremely low section Reynolds numbers. The Reynolds numbers for the model as tested ranged from 100,000 to 200,000. For reference, the predicted polars for a full-scale propeller operating at the same pitch angle and advance ratios is included. It is worth noting that the very low Reynolds numbers not only cause an increase in drag, and therefore a loss in efficiency, they also cause a significant increase in swirl angle.

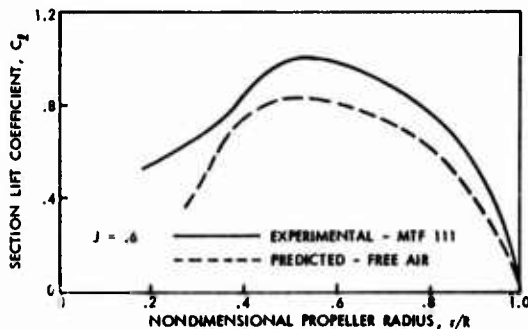


Figure 18. Section Lift Coefficient Comparison

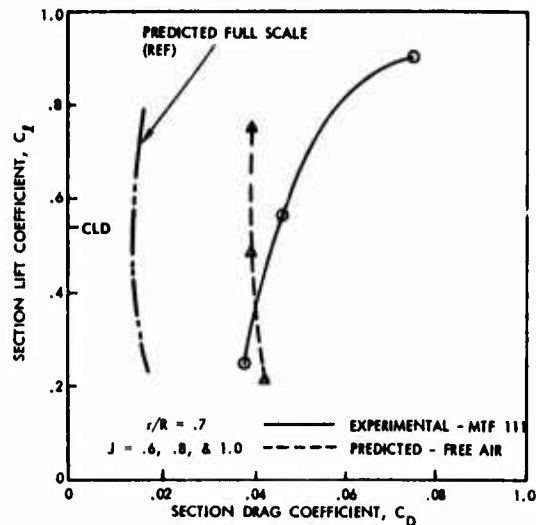


Figure 19. Section Lift and Drag Coefficient Comparison

SLIPSTREAM/COMPONENT INTERACTION

Having derived a method of obtaining propeller characteristics from wake survey data, it appeared that this method might provide an approach to the derivation of the elusive slipstream lift and drag increments. Figure 20 shows the thrust loss at the survey plane completely behind the models in terms of an increment in C_d . If the prop off C_d of the region influenced by the slipstream is subtracted from the increment due to the thrust loss, the result would be the drag due to the slipstream. Inherent in this approach is the assumption that the thrust represented by the slipstream will remain constant for at least two propeller diameters downstream, unless the slipstream is modified by some object that disturbs it.

The modified slipstream downstream of the model contains information relative to both thrust and power. It was observed that the power loss was greater than the thrust loss which provides an indication of the thrust recovery due to the straightening of the flow. These effects are shown by the dashed line in Figure 20. This particular approach applied the isolated propeller efficiency to the C_p remaining at the downstream plane to obtain a downstream thrust that would have occurred had there been no swirl recovery.

It is of interest to note that, for the wing, the net thrust loss becomes negative at the higher advance ratios. This is not too surprising considering that the Reynolds number based on the wing chord was only 700,000. At such low Reynolds numbers, the turbulence generated by a running propeller would create an effective increase in Reynolds number and significantly reduce the section drag. The thrust recovered from straightening the swirl was greater than the drag created by the very small increase in local velocity.

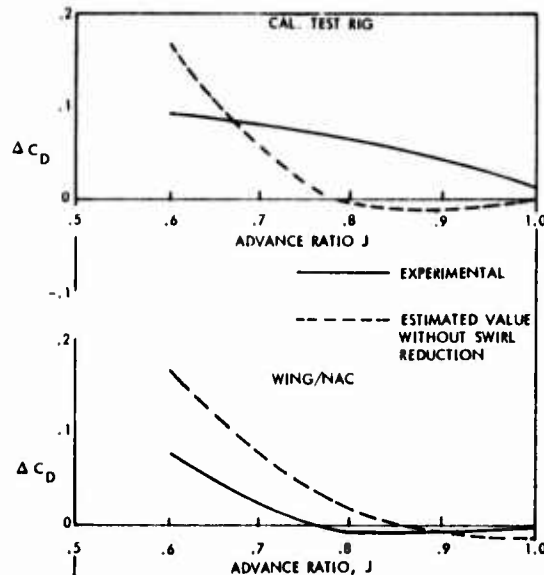


Figure 20. Slipstream/Component Interaction

CONCLUSIONS

(1) The analysis of propeller characteristics obtained from experimental data has been significantly advanced by the development of a method of extracting propeller characteristics from wake survey data. This method provides details of the aerodynamics of running propellers previously unavailable from experiment. It is also useful for obtaining the effects of the interaction of the slipstream and components of the aircraft washed by the slipstream.

(2) The wing had a much larger shearing effect on the slipstream than expected. There is a significant spanwise migration of the slipstream in the direction of rotation on both the upper and lower surface. The boundary of the slipstream remains intact, although distorted. These effects should be considered when selecting the rotation direction of a tractor propeller installation.

(3) An improved understanding of the effects of wind tunnel wall constraints on propeller performance has been obtained. The fact that the tunnel changes the entire propeller vortex system rather than only changing the effective advance ratio has a significant impact on the interpretation of scale model propeller test data.

REFERENCES

1. Aljabri, A. S., "Prediction of Propeller Slipstream Characteristics," Lockheed Engineering Report LG79ER0120, October 1979.
2. Hackett, J. E.; Phillips, C. G.; Lilley, D. E.: "Three-Dimensional Wake Flow Measurements for a Wing and a Bluff, Car-Like Body," Lockheed Engineering Report LG81ER0201, submitted to the Georgia Institute of Technology under Subcontract 1-E-16-655 and NSF Grant No. ENG-79-00891, August 1981.
3. Glauert, H.: "Airplane Propellers. The Vortex Theory," Vol. IV, Div. L, Ch. VI of Aerodynamic Theory, W. F. Durand, ed., Julius Springer (Berlin), 1935.
4. Goldstein, S., "On the Vortex Theory of Screw Propellers," Proceedings of the Royal Society of London, Series A, Vol. 123, No. 792, April 6, 1929.
5. McCormick, B. W., Jr., Aerodynamics of V/STOL Flight, Academic Press, New York, 1967.

AN ASYMPTOTIC THEORY FOR THE INTERFERENCE OF
LARGE ASPECT RATIO SWEEPED WINGS AND MULTIPLE
PROPELLER SLIPSTREAMS

R. K. Prabhu*

Department of Mechanical Engineering and Mechanics
Old Dominion University, Norfolk, VA 23508

C. H. Liu[†]

Analytical Methods Branch
NASA Langley Research Center, Hampton, VA 23665

S. N. Tiwari[#]

Department of Mechanical Engineering and Mechanics
Old Dominion University, Norfolk, VA 23508

SUMMARY

This paper presents an asymptotic method for the analysis of the interference of multiple tractor propeller slipstream with large aspect ratio swept wings. It is assumed that the height of the slipstream is of the order of the wing chord and its spanwise extent is of the order of the wing span. Three different flow regions are identified by employing different stretching transformations. Asymptotic expansions are made in each of the three regions, using the chord-to-span ratio as the small expansion parameter. The details of the nonuniform flow in the slipstream enter into the wing sectional analysis. In the outer limit, the wing shrinks to a swept lifting line, and the slipstream reduces to a thin sheet of jet carrying the momentum gain from the propeller. The curvature of this jet sheet results in a pressure difference which is represented by a vortex sheet. The governing equations are solved by discretization. Several examples are considered for which experimental data are available. Comparison of the present results with the experimental data as well as other numerical solutions showed generally good agreement.

1. INTRODUCTION

The cost of aviation fuel has gone up substantially in the last decade and is expected to be on an ever increasing trend. Added to this is the uncertainty regarding the supplies. These factors combined with the national concern over energy conservation have lead aircraft designers as well as the operators to give prime importance to fuel efficient propulsion systems for the future aircraft. Prior to the so-called oil crisis in 1973, the fuel cost was a relatively small fraction (about 25%) of the direct operating cost, and it was of less concern to the designers/operators. Today, however, it is claimed that this fraction has risen to about 60%, and that it is the major part of the aircraft operating cost (ref. 1).

Before jet engines appeared on the scene, only propellers provided propulsive force to aircraft. As flight speeds increased, the propellers posed serious problems of rapidly decaying propulsive efficiency and increasing noise and vibration levels. As a result, more powerful and efficient jet engines took over and dominated the scene, and the propellers were neglected for many years. It is well known that the old technology propellers are the most efficient mode of propulsion up to a Mach number of about 0.6. The interest generated in the propeller technology since the oil crisis has lead to the development of the prop-fan, which is claimed to operate at an aerodynamic efficiency of about 80% at a Mach number of 0.8 (ref. 2).

With the prospect of the use of prop-fans on transport airplanes, there has been concern regarding the associated problems. The interference of slipstreams with other parts of the airplane, in particular with the wing, is one of the major problem areas. With the flight speeds going up to $M=0.8$, compressibility effects can no longer be neglected. The flowfield behind the propeller is highly rotational and effects of vorticity in the slipstream cannot be ignored. Therefore the problem in its complete form is quite complex. Consequently considerable efforts - analytical, numerical and experimental - are being made to understand the rather complex flowfield associated with wing-slipstream interference.

The problem of determining the influence of the propeller slipstream on wing lift has been studied quite extensively in the past, and a considerable literature is available. Because of the highly nonuniform nature of the flow in the slipstream, the problem is essentially a nonlinear one; as a result, the work done during the 1930's was based on approximate and semi-empirical methods (refs. 3 and 4). These methods yielded satisfactory results in the speed - power range for which they were

*Graduate Research Assistant

[†]Research Scientist

[#]Eminent Professor

developed. Koning (ref. 5) gave an analytical treatment for a wing in a propeller slipstream based on the lifting line theory. It was assumed that the increment in velocity in the slipstream was small. Ferrari (ref. 6) developed what is generally referred to as the classical lifting line theory for wings in slipstreams. The main assumptions were that (i) the slipstream was in the form of a circular cylindrical tube extending to infinity both upstream and downstream, (ii) the velocity in this tube was uniform (U_j), and (iii) the relation between the lift and angle of attack for the wing sections was obtained by considering them to be in uniform flows with velocities U_j and U_∞ for sections inside and outside the slipstream tube, respectively. One of the drawbacks of this theory is the third assumption. It is obvious that the lift produced by an airfoil would depend on the jet height. Ting and Liu (ref. 7) employed the method of images and studied the lifting characteristics of thin airfoils in a nonuniform parallel streams. This method can be used to determine the lift of an airfoil in a uniform jet. Chow, et al. (ref. 8) numerically investigated the two-dimensional nonuniform flow past an airfoil by solving the Euler equations. These results brought out the fact that the lift of an airfoil depends not only on the jet height but also on the nonuniformity in the approach stream. Recognizing this fact, Kleinstein and Liu (ref. 9) made some improvements to the classical theory. The lift data for the wing sections within the slipstream was obtained by employing the methods of refs. 7 and 8, and was used in the classical theory. However, the assumptions (i) and (ii) of the classical theory were still retained while computing the downwash due to trailing vortices. These results demonstrated the effects of modifying the assumption (iii) mentioned earlier.

There were other attempts to improve upon the classical theory of Ferrari. Rethorst (ref. 10) employed the Weissinger approach and developed a lifting surface theory. Wu and Talmadge (ref. 11) and Cumberbatch (ref. 12) extended Rethorst's method to wings extending through multiple jets. Jameson (ref. 13) modeled wide slipstreams by rectangular and elliptic jets, and by using the standard imaging technique developed a lifting-surface theory. In all these analyses one of the main assumptions was that the velocity was uniform in the jet (representing the slipstream).

Ting, et al. (ref. 14) scrutinized the assumptions of the classical lifting line theory, and suggested a new approach to solve the problem. It was recognized that the height of the slipstream is of the order of the wing chord, and the spanwise spread of the combined multi-propeller slipstream is of the order of the wing span. Three different flow regions were identified by employing different stretching transformations. Asymptotic expansions were made by using the reciprocal of the wing aspect ratio ($1/AR$) as the small parameter. This analysis showed that the details of the nonuniform stream enter primarily into the local sectional analysis; behind the wing, the slipstream acts like a thin jet sheet which supports a pressure difference across itself. By solving the governing integral equation, the wing lift distribution was determined. Maarsingh (ref. 15) made an evaluation of this method by comparing these results with the data obtained from some specially designed experiments (ref. 16). Some differences between the two sets of results were found, and these are suspected to be due to inaccuracies in the lift-curve slope data that was used in the computations of ref. 15.

Ribner and Ellis (ref. 17) considered slipstreams of arbitrary cross section, and, instead of the standard imaging technique, represented the slipstream boundary by vortex sheets, and proceeded on the basis of lifting line theory. Lan (ref. 18) developed a method based on the quasi-vortex-lattice method and a two-vortex-sheet representation of the slipstream. Both of these methods accounted for the rotation in the slipstream.

With the availability of high speed computers and efficient CFD techniques, there has been a new trend in the approach to the solution of the wing slipstream interaction problem. Numerical techniques have been employed to solve the linearized potential flow equations, full potential equations, and Euler equations.

Rizk (ref. 19) investigated the propeller slipstream - wing interference problem at transonic speeds. It was noted that a nearly uniform slipstream interacting with a thin wing allows the perturbations to be potential although the undisturbed flow within the slipstream is rotational. The resulting potential flow (boundary value) problem for transonic flow was solved by a finite-difference scheme. In general, however, the assumptions made in this work may not be fully valid; for example, the nonuniformity in the slipstream may be large enough to cause potential flow assumptions to yield erroneous results.

Chandrasekaran and Bartlett (ref. 20) modified the Hess panel code to handle the effects of the propeller slipstream. The slipstream boundary was modeled by a system of ring vortices, and the effects of swirl in the slipstream was included. A comparison of the results with experimental data showed some differences, which were attributed to viscous and compressibility effects as well as to uncertainties in the estimation of the flowfield behind the propeller.

Narain (ref. 21) and Samant, et al. (ref. 22) made assumptions similar to those of Rizk regarding the slipstream, but did not assume that the perturbations were small. Instead, the problem was investigated on the basis of the full potential flow equations with a rigid boundary for the slipstream tube. These results compared reasonably well with available experimental data; however, it should be recognized that the advantage of using the accurate full potential equation is sacrificed by the approximation of irrotational flow.

Whitfield and Jameson (ref. 23) solved the three-dimensional Euler equations coupled with the energy equation. The Euler equations had force terms included to simulate the propeller effects. The viscous effects were accounted for, although approximately, by coupling the three-dimensional Euler equations with the two-dimensional inverse integral boundary layer equations. In spite of these sophistications, the spanwise lift distribution obtained by this analysis failed to show good agreement consistently with the experimental data of Welge and Crowder (ref. 24). This method, however, provides detailed information on velocity and other flow quantities in the entire computational domain. As may

be expected, such an effort would require a large computer memory and a considerable amount of computing time. For example, the computer code developed by Whifield and Jameson required 900,000 words of memory and 341 seconds of computing time on Cray-1S computer for a relatively coarse (96x16x16) grid.

The asymptotic method has been a powerful tool in the analysis of large aspect ratio wings (ref. 25). This method is a simple analysis, and provides better physical insight into the problem. The asymptotic method has also been used in an analysis of unswept wing-slipstream interference (ref. 14). The purpose of the present study is to present an asymptotic method for the analysis of the interference on a large aspect ratio swept wing with multi-propeller slipstream. It is assumed (as in ref. 14) that the height of the slipstream is of the order of the wing chord, and that its width is of the order of the wing span. By employing different stretching transformations, three different regions are identified. Expansions are introduced in each region by using the ratio of the chord to the span as the small parameter. The details of the nonuniformities in the slipstream enter in the two-dimensional flow past wing sections normal to the lifting line. The spanwise component of the velocity is shown not to affect the sectional lift data. For the outer solution, the wing planform reduces to a swept lifting line, and the propeller slipstream behind the wing reduces to a thin sheet carrying the sectional momentum gained through the propellers. The curvature of this sheet results in a pressure difference across itself, which is represented by a vortex sheet. The governing equations are solved by a discretization procedure. Several examples are considered for which experimental results are available. Present results are compared with these experimental data as well as other numerical results.

2. MATHEMATICAL FORMULATION

Consider a large aspect ratio swept wing in a uniform flow (figure 1). Propellers placed ahead of the wing produce slipstreams which flow past the wing. It is assumed that the wing geometry and the velocity distribution in the slipstream are known. The problem is to determine the lift distribution on the wing as influenced by the slipstream.

In the present analysis, the flow is considered to be steady, incompressible and inviscid. This amounts to a considerable simplification; however, the resulting problem is nonlinear due to the nonuniform flow in the slipstream, and the governing equations are the Euler equations.

In the analysis that follows, two right-handed Cartesian coordinate systems are used. The (x,y,z) system has the x -axis in the direction of the free stream and the z -axis in the lift direction. The (x',y',z') system is obtained by rotation of the first system through the quarter chord sweep angle Λ about the z -axis. It should be noted that the z' -axis is identical to the z -axis and that the y' -axis lies along the quarter-chord line of the wing planform.

In the absence of the wing, it is assumed that the undisturbed velocity field can be written as follows:

$$\vec{V}(x/c_0, y/s, z/c_0) = i U_\infty \quad (\text{ahead of the propellers}) \quad (1a)$$

$$= i U(y/s, z/c_0) \quad (\text{behind the propellers}) \quad (1b)$$

where i is the unit vector in the x -direction. This amounts to assuming that there is a jump in the axial velocity across the propellers and that there is no swirl in the propeller stream. The velocity field around a propeller is quite complex. There is inflow ahead of the propeller. There is a pressure jump and not a velocity jump across the propeller. The velocity field in the slipstream is periodic rather than steady because of the finite number of blades, and has swirl component in addition to an increased axial velocity. In spite of this, the drastic idealization implied in equation (1) for the velocity field around the propellers is quite common, and springs from the fact that detailed treatment of the swirl and periodicity in the stream makes the problem extremely complex. Attempts have been made by several workers to take into account the effects of the swirl in a simplified manner by assuming that the swirl only introduces a change in the spanwise distribution of the sectional angle of attack. In the absence of any superior (yet simple) approach, this method is adopted in the present study. It is required that $U(y/s, z/c_0) \rightarrow U_\infty$ for large $|z|$.

The analysis starts by making the assumption that for large aspect ratio wings with multiple tractor propellers, the height (h) of the slipstream behind the propellers is of the order of the mid-chord c_0 , whereas the spanwise spread ($2l$) of the combined propeller slipstreams is of the order of the wing span $b=2s$. Thus there are two length scales c_0 and b in the problem; hence, different stretching transformations are possible. Following the classical analysis for large aspect ratio wings, the outer region is introduced with the corresponding stretched variables $\tilde{x}, \tilde{y}, \tilde{z}$ defined as follows:

$$\tilde{x} = x/s, \quad \tilde{y} = y/s \quad \text{and} \quad \tilde{z} = z/s \quad (2)$$

With $\tilde{x}, \tilde{y}, \tilde{z}$ fixed and $AR \rightarrow \infty$ or $\epsilon \rightarrow 0$ where $\epsilon = c_0/s$ the wing shrinks to a line and the undisturbed velocity becomes

$$\vec{V} = i U_{\infty} \quad (\text{ahead of the wing}) \quad (3a)$$

$$= i U_{\infty} \quad (\text{behind the wing except on the cut } z=0) \quad (3b)$$

The momentum gained by the stream in passing through the propeller is now contained in this thin sheet which acts very much like a jet flap. The spanwise distribution of the momentum in this sheet is given by

$$J(\tilde{y}) = \rho c_0 \int_{-\infty}^{\infty} U(U - U_{\infty}) d\tilde{z} \quad (4)$$

All the details of the flow past the wing section are lost in this outer limiting process. The inner region with the inner variables \hat{x} , \hat{y} and \hat{z} defined by the following transformation is introduced to recover these details.

$$\hat{x} = x'/c_0, \quad \hat{y} = y'/s \quad \text{and} \quad \hat{z} = z'/c_0 \quad (5)$$

The following relations exist between the variables $(\hat{x}, \hat{y}, \hat{z})$ and (x', y', z') :

$$x' = \hat{x} \cos \Lambda + \hat{y} \sin \Lambda, \quad y' = \hat{y} \cos \Lambda - \hat{x} \sin \Lambda \quad \text{and} \quad z' = \hat{z} \quad (6)$$

Now, the undisturbed velocity behind the propellers can be expressed as

$$\begin{aligned} \vec{V}(x/c_0, y/s, z/c_0) &= i U(y/s, z/c_0) \\ &= i U[(y' \cos \Lambda - x' \sin \Lambda)/s, z'/c_0] \\ &= i U[(\hat{y} \cos \Lambda - \epsilon \hat{x} \sin \Lambda), \hat{z}] \\ &= i [U(\hat{y} \cos \Lambda, \hat{z}) - \epsilon \hat{x} \tan \Lambda \frac{\partial U}{\partial y}(\hat{y} \cos \Lambda, \hat{z}) + \dots] \\ &= i U(\hat{y} \cos \Lambda, \hat{z}) \quad \text{for } \epsilon \ll 1 \end{aligned} \quad (7)$$

The undisturbed stream for the inner region, therefore, is given by (in the transformed coordinate system)

$$\vec{V} = [U(\hat{y} \cos \Lambda, \hat{z}) \cos \Lambda, U(\hat{y} \cos \Lambda, \hat{z}) \sin \Lambda, 0] \quad (8)$$

The analysis of the flow in the propeller stream behind the wing requires the introduction of another region (called the third region) with the corresponding variables \bar{x} , \bar{y} and \bar{z} defined as follows:

$$\bar{x} = x/s, \quad \bar{y} = y/s \quad \text{and} \quad \bar{z} = z/c_0 \quad (9)$$

In this region, the undisturbed velocity is given by

$$\vec{V} = i U(y/s, z/c_0) = i U(\bar{y}, \bar{z}) \quad (10)$$

Equations (3), (8) and (10) represent the undisturbed velocity field for the three regions considered. The effect of the presence of the wing is to introduce disturbances in these flowfields. The disturbances in velocity and pressure depend on the small parameter $\epsilon = c_0/s$ which, in turn, is related to the reciprocal of the wing aspect ratio. In the following sections, these disturbances are introduced in the flowfields of the three regions, and the governing equations are derived. The solution obtained in each region is matched with the others, and a solution for the entire problem is obtained.

2.1 The Inner Region

The disturbances in velocity components and pressure for the inner region are expanded in power series of ϵ as follows:

$$\hat{u}(\hat{x}, \hat{y}, \hat{z}, \epsilon) = \hat{u}^{(0)}(\hat{x}, \hat{y}, \hat{z}) + \epsilon \hat{u}^{(1)}(\hat{x}, \hat{y}, \hat{z}) + \dots \quad (11a)$$

$$\hat{v}(\hat{x}, \hat{y}, \hat{z}, \epsilon) = \hat{v}^{(0)}(\hat{x}, \hat{y}, \hat{z}) + \epsilon \hat{v}^{(1)}(\hat{x}, \hat{y}, \hat{z}) + \dots \quad (11b)$$

$$\hat{w}(\hat{x}, \hat{y}, \hat{z}, \epsilon) = \hat{w}^{(0)}(\hat{x}, \hat{y}, \hat{z}) + \epsilon \hat{w}^{(1)}(\hat{x}, \hat{y}, \hat{z}) + \dots \quad (11c)$$

$$\hat{p}(\hat{x}, \hat{y}, \hat{z}, \epsilon) = \hat{p}^{(0)}(\hat{x}, \hat{y}, \hat{z}) + \epsilon \hat{p}^{(1)}(\hat{x}, \hat{y}, \hat{z}) + \dots \quad (11d)$$

The undisturbed velocity components given by equation (8) and the disturbance quantities given by equation (11) are substituted in the continuity and the momentum equations. Upon equating the coefficients of like powers of ϵ on either side of the equations, the following leading equations are obtained:

$$\frac{\partial \hat{u}^{(0)}}{\partial x} + \frac{\partial \hat{w}^{(0)}}{\partial z} = 0 \quad (12)$$

$$(U \cos \Lambda + \hat{u}^{(0)}) \frac{\partial \hat{u}^{(0)}}{\partial x} + \hat{w}^{(0)} (U \cos \Lambda + \hat{u}^{(0)}) \frac{\partial \hat{u}^{(0)}}{\partial z} = -\frac{\partial \hat{p}^{(0)}}{\partial x} / \rho \quad (13a)$$

$$(U \cos \Lambda + \hat{u}^{(0)}) \frac{\partial \hat{v}^{(0)}}{\partial x} + \hat{w}^{(0)} (U \sin \Lambda + \hat{v}^{(0)}) \frac{\partial \hat{v}^{(0)}}{\partial z} = 0 \quad (13b)$$

$$(U \cos \Lambda + \hat{u}^{(0)}) \frac{\partial \hat{w}^{(0)}}{\partial x} + \hat{w}^{(0)} \frac{\partial \hat{w}^{(0)}}{\partial z} = -\frac{\partial \hat{p}^{(0)}}{\partial z} / \rho \quad (13c)$$

If a stream function $\hat{\psi}^{(0)}(\hat{x}, \hat{y}, \hat{z})$ is defined such that

$$\frac{\partial \hat{\psi}^{(0)}}{\partial z} = U \cos \Lambda + \hat{u}^{(0)} \quad (14a)$$

$$\frac{\partial \hat{\psi}^{(0)}}{\partial x} = -\hat{w}^{(0)} \quad (14b)$$

then equation (12) is automatically satisfied. Now, it should be noted that equations (13a) and (13c) do not involve the v-component of the velocity, and that by eliminating the pressure, they can be reduced to the two-dimensional vorticity transport equation

$$(U \cos \Lambda + \hat{u}^{(0)}) \omega_x + \hat{w}^{(0)} \omega_z = 0 \quad (15)$$

where

$$\omega = \frac{\partial \hat{w}^{(0)}}{\partial x} - (U \cos \Lambda + \hat{u}^{(0)}) \frac{\partial \hat{u}^{(0)}}{\partial z} = -\left(\frac{\partial^2 \hat{\psi}^{(0)}}{\partial x^2} + \frac{\partial^2 \hat{\psi}^{(0)}}{\partial z^2} \right) \quad (16)$$

A combination of equations (14a), (14b) and (15) results in

$$\frac{\partial \hat{\psi}^{(0)}}{\partial z} \omega_x - \frac{\partial \hat{\psi}^{(0)}}{\partial x} \omega_z = 0 \quad (17)$$

This implies that ω is a function of $\hat{\psi}^{(0)}$ only, or equivalently ω is constant along $\hat{\psi}^{(0)} = \text{constant}$ (i.e., along the projection of the streamlines on the $y = \text{constant}$ plane). Thus, the problem reduces to solving the Poisson equation

$$\omega(\hat{\psi}^{(0)}) = -\left(\frac{\partial^2 \hat{\psi}^{(0)}}{\partial x^2} + \frac{\partial^2 \hat{\psi}^{(0)}}{\partial z^2} \right) \quad (18)$$

This equation applies to the flowfield behind the propellers. In the plane of the propellers, the disturbances due to the wing section may be neglected. Consequently, the boundary condition at the propeller plane would be

$$\hat{\psi}^{(0)} = \int_0^{\hat{z}} U \, d\hat{z} \quad (19)$$

The other boundary conditions are (i) far away from the airfoil $\hat{u}^{(0)}$ and $\hat{w}^{(0)}$ tend to zero, (ii) on the airfoil the normal velocity component is zero, and (iii) at the trailing edge of the airfoil the pressure is continuous (which is equivalent to the Kutta condition). Note that in this problem, y appears only as a parameter.

The solution of equation (18), or the equivalent equations (12), (13a) and (13c), with the above boundary conditions can be obtained by a suitable numerical technique. Results would yield the values of the velocity components $\hat{u}^{(0)}$ and $\hat{w}^{(0)}$ everywhere in the field including on the airfoil surface.

The \hat{y} -momentum equation (13b) may be rewritten as follows:

$$\left[(U \cos \Lambda + \hat{u}^{(0)}) \frac{\partial}{\partial \hat{x}} + \hat{w}^{(0)} \frac{\partial}{\partial \hat{z}} \right] (U \sin \Lambda + \hat{v}^{(0)}) = 0$$

$$\frac{\partial}{\partial \hat{s}} (U \sin \Lambda + \hat{v}^{(0)}) = 0 \quad (20)$$

where $\frac{\partial}{\partial \hat{s}} = (U \cos \Lambda + \hat{u}^{(0)}) \frac{\partial}{\partial \hat{x}} + \hat{w}^{(0)} \frac{\partial}{\partial \hat{z}}$. Note that $\frac{\partial}{\partial \hat{s}}$ is the derivative along the projection of the streamline in the \hat{x} - \hat{z} plane. Equation (20) implies that $(U \sin \Lambda + \hat{v}^{(0)})$ remains constant along the streamlines projected on the \hat{x} - \hat{z} planes. Since the airfoil is one such streamline it is concluded that $(U \sin \Lambda + \hat{v}^{(0)})$ is a constant on the airfoil. Let U^* be the velocity far ahead of the airfoil on the zero streamline. Then, it is evident that $U^* \sin \Lambda = (U \sin \Lambda + \hat{v}^{(0)})$. Note that, even though $(U \sin \Lambda + \hat{v}^{(0)})$ is a constant on the airfoil, both $U \sin \Lambda$ and $\hat{v}^{(0)}$ being functions of \hat{z} , vary along the airfoil surface.

The pressure coefficient c_p on the airfoil defined by

$$c_p = (p - p_\infty) / (1/2) \rho U_\infty^2 \quad (21)$$

can be reduced to

$$c_p(\hat{x}, \hat{z}) = [U^{*2} \cos^2 \Lambda - (U \cos \Lambda + \hat{u}^{(0)})^2 - (\hat{w}^{(0)})^2] / U_\infty^2 \quad (22)$$

Hence the difference $\Delta c_p = (c_{p_u} - c_{p_\lambda})$ is given by

$$\Delta c_p(\hat{x}) = c_{p_u}(\hat{x}, \hat{z}_u) - c_{p_\lambda}(\hat{x}, \hat{z}_\lambda) = - \{ (U \cos \Lambda + \hat{u}^{(0)})^2 + (\hat{w}^{(0)})^2 \} / U_\infty^2 \quad (23)$$

where $\{ \}$ represents the difference between the top and the bottom surfaces of the airfoil. The section lift coefficient c_λ is obtained by integration of $\Delta c_p(\hat{x})$ along the chord. Thus, it is seen that the lift obtained by the solution of equation (13) is not affected by the spanwise component of the velocity. In summary, the governing equations for the inner solution are the continuity and momentum equations (12) and (13) with the appropriate boundary conditions. The solution of these would yield the lift of the airfoil which is independent of the spanwise velocity component. This lift is a function of the sectional angle of attack, and may be written as follows:

$$\lambda(\alpha, \hat{y}) = (1/2) \rho U_\infty^2 c(\hat{y}) c_\lambda(\alpha, \hat{y}) \quad (24)$$

Notice that in this relation \hat{y} appears only as a parameter.

2.2 The Third Region

In the analysis of the third region, i.e., in the propeller stream far behind the wing, the stretched coordinates \bar{x}, \bar{y} and \bar{z} defined by equation (9), and the undisturbed velocity defined by equation (10) are used. The perturbation velocity components and the pressure are expressed in power series of ϵ as follows:

$$\bar{u}(\bar{x}, \bar{y}, \bar{z}, \epsilon) = \bar{u}^{(0)}(\bar{x}, \bar{y}, \bar{z}) + \epsilon \bar{u}^{(1)}(\bar{x}, \bar{y}, \bar{z}) + \epsilon^2 \bar{u}^{(2)}(\bar{x}, \bar{y}, \bar{z}) + \dots \quad (25a)$$

$$\bar{v}(\bar{x}, \bar{y}, \bar{z}, \epsilon) = \epsilon \bar{v}^{(1)}(\bar{x}, \bar{y}, \bar{z}) + \epsilon^2 \bar{v}^{(2)}(\bar{x}, \bar{y}, \bar{z}) + \dots \quad (25b)$$

$$\bar{w}(\bar{x}, \bar{y}, \bar{z}, \epsilon) = \epsilon \bar{w}^{(1)}(\bar{x}, \bar{y}, \bar{z}) + \epsilon^2 \bar{w}^{(2)}(\bar{x}, \bar{y}, \bar{z}) + \dots \quad (25c)$$

$$\bar{p}(\bar{x}, \bar{y}, \bar{z}, \epsilon) = \epsilon \bar{p}^{(1)}(\bar{x}, \bar{y}, \bar{z}) + \epsilon^2 \bar{p}^{(2)}(\bar{x}, \bar{y}, \bar{z}) + \dots \quad (25d)$$

These perturbation components and the undisturbed velocity given by equation (10) are substituted in the continuity and momentum equations. The subsequent analysis would be identical to the analysis performed in ref. 14 while studying the third region behind unswept wings. Therefore these details are not given here, but only the major conclusions from this analysis are listed below:

- (i) To the first order, there is no pressure discontinuity or change in streamline inclination across the jet sheet.
- (ii) The momentum integral $J(\bar{y})$ remains constant with respect to \bar{x} .
- (iii) To the second order, there is a pressure difference across the jet sheet given by

$$\Delta \bar{p}^{(2)} = \bar{p}^{(2)}(\bar{x}, \bar{y}, 0+) - \bar{p}^{(2)}(\bar{x}, \bar{y}, 0-) = - \epsilon \frac{\partial \bar{u}^{(1)}}{\partial x}(\bar{x}, \bar{y}, 0) J(\bar{y}) \quad (26)$$

where

$$\bar{u}^{(1)} = \bar{w}^{(1)} / U_\infty$$

Equation (26) is the familiar result of the thin jet approximation that states the pressure difference across the sheet is equal to the product of the momentum in the jet sheet and its curvature. These results will be used in the analysis of the outer region that follows.

2.3 The Outer Region

The undisturbed velocity in the outer region is uniform (equations (3a) and (3b)), hence, the flowfield away from the wing and the propeller streams is irrotational. The disturbance velocity field can therefore be described by a velocity potential $\Phi(x, y, z, \epsilon)$ which satisfies the Laplace equation

$$\left(\frac{\partial^2}{\partial x^2} + \frac{\partial^2}{\partial y^2} + \frac{\partial^2}{\partial z^2} \right) \Phi = 0 \quad (27)$$

Bernoulli's equation provides an expression for the pressure disturbances as

$$\bar{p} = (1/2) \rho U_\infty^2 [1 - |\vec{i} + \nabla \Phi / U_\infty|^2] \quad (28)$$

Equations (27) and (28) are the governing equations in the outer region. As the first step towards the solution, Φ is expanded in a power series of ϵ as

$$\bar{\Phi}(\bar{x}, \bar{y}, \bar{z}, \epsilon) = \epsilon \bar{\Phi}^{(1)}(\bar{x}, \bar{y}, \bar{z}) + \epsilon^2 \bar{\Phi}^{(2)}(\bar{x}, \bar{y}, \bar{z}) + \dots \quad (29)$$

where both $\bar{\Phi}^{(1)}$ and $\bar{\Phi}^{(2)}$ in turn satisfy the Laplace equation (27). Next the velocity and pressure disturbances are also expanded in power series of ϵ as follows:

$$\bar{u}(\bar{x}, \bar{y}, \bar{z}, \epsilon) = \epsilon \bar{u}^{(1)}(\bar{x}, \bar{y}, \bar{z}) + \epsilon^2 \bar{u}^{(2)}(\bar{x}, \bar{y}, \bar{z}) + \dots \quad (30a)$$

$$\bar{v}(\bar{x}, \bar{y}, \bar{z}, \epsilon) = \epsilon \bar{v}^{(1)}(\bar{x}, \bar{y}, \bar{z}) + \epsilon^2 \bar{v}^{(2)}(\bar{x}, \bar{y}, \bar{z}) + \dots \quad (30b)$$

$$\bar{w}(\bar{x}, \bar{y}, \bar{z}, \epsilon) = \epsilon \bar{w}^{(1)}(\bar{x}, \bar{y}, \bar{z}) + \epsilon^2 \bar{w}^{(2)}(\bar{x}, \bar{y}, \bar{z}) + \dots \quad (30c)$$

$$\bar{p}(\bar{x}, \bar{y}, \bar{z}, \epsilon) = \epsilon \bar{p}^{(1)}(\bar{x}, \bar{y}, \bar{z}) + \epsilon^2 \bar{p}^{(2)}(\bar{x}, \bar{y}, \bar{z}) + \dots \quad (30d)$$

Thus

$$\bar{u}^{(1)} = \frac{\partial \bar{\Phi}^{(1)}}{\partial x}(\bar{x}, \bar{y}, \bar{z}) / s \quad (31a)$$

$$\tilde{v}^{(1)} = \frac{\tilde{\phi}^{(1)}(\tilde{x}, \tilde{y}, \tilde{z})}{y} / s \quad (31b)$$

$$\tilde{w}^{(1)} = \frac{\tilde{\phi}^{(1)}(\tilde{x}, \tilde{y}, \tilde{z})}{z} / s \quad (31c)$$

$$\tilde{p}^{(1)} = -\rho U_{\infty} \frac{\partial \tilde{\phi}^{(1)}(\tilde{x}, \tilde{y}, \tilde{z})}{\partial x} / s \quad (31d)$$

The unknown $\tilde{\phi}^{(1)}$ is a solution of the Laplace equation. It is obtained by distributing the singularities along the line $x-m|y|=0$, and on the plane $z=0$, $x-m|y|>0$, and by matching with the solutions of the inner and the third regions respectively. Note that m is the tangent of the wing quarter chord sweep-back angle.

By an analysis of the inner region it was shown that the wing section at a spanwise station \tilde{y} produces a lift force $\lambda(\alpha, \tilde{y})$. This implies that there is a vortex distribution along the lifting line $x-m|y|=0$. The strength $\Gamma(\tilde{y})$ is related to the lift $\lambda(\alpha, \tilde{y})$ as follows:

$$\begin{aligned} \Gamma(\tilde{y}) &= \lambda(\alpha, \tilde{y}) / \rho U_{\infty} \quad \text{for } \tilde{y} < 1 \\ &= (1/2) U_{\infty} c(\tilde{y}) c_{\lambda}(\alpha, \tilde{y}) \end{aligned} \quad (32)$$

The spanwise variation of Γ requires the presence of a trailing vortex sheet extending downstream from the lifting line. This is the well known vortex system of lifting line theory.

By a matching with the solution of the third region, it was shown that, to a first approximation, there is no discontinuity in either the pressure or the streamline inclination across the jet sheet behind the wing. Therefore, the first order outer solution $\tilde{\phi}^{(1)}$, is not affected by the propeller stream behind the lifting line. Based on this first order analysis, the flow in the outer region is described by the potential due to $\Gamma(\tilde{y})$ and the associated trailing vortex system, and is given by

$$\tilde{\phi}^{(1)} = \frac{1}{4\pi} \int_{-1}^1 \frac{\tilde{z} \Gamma(\tilde{\eta})}{(\tilde{y}-\tilde{\eta})^2 + \tilde{z}^2} \left\{ 1 + \frac{\tilde{x}-m|\tilde{\eta}|}{R} \right\} d\tilde{\eta} \quad (33)$$

where $R^2 = [(\tilde{x}-m|\tilde{\eta}|)^2 + (\tilde{y}-\tilde{\eta})^2 + \tilde{z}^2]$. Upon approaching the lifting line (i.e., for small $\tilde{x}-m|\tilde{y}|$ and \tilde{z}), the inner limit of $\tilde{\phi}^{(1)}$ is obtained. This yields the downwash $\theta(\tilde{x}-m|\tilde{y}| \rightarrow 0, \tilde{y}, 0)$. By matching with the inner solution, the effective angle of attack at each spanwise station is obtained as

$$\alpha(\tilde{y}) = \alpha_g(\tilde{y}) - \epsilon \tilde{\theta}^{(1)} = \alpha_g(\tilde{y}) - \tilde{\theta} \quad (34)$$

The circulation $\Gamma(\tilde{y})$ given by equation (6), now becomes

$$\Gamma(\tilde{y}) = (1/2) U_{\infty} c(\tilde{y}) c_{\lambda}(\alpha_g - \tilde{\theta}, \tilde{y}) \quad (35)$$

Equations (34) and (35) are the required governing equations for the first order analysis. Note that in this analysis, the effect of the nonuniform flow in the slipstream enters only in the sectional analysis.

The first order analysis discussed so far is valid for $\epsilon \rightarrow 0$, or $AR \rightarrow \infty$. It was shown in the analysis of the third region that terms proportional to $J(\tilde{y})$ appear in the second order analysis; hence it is necessary that $J(\tilde{y})$ be of the order of 1.0 for the first order theory to be valid. It is well known (ref. 25) that the first order theory for large aspect ratio wings in uniform flow gives satisfactory results for wings of aspect ratio as low as 1.0. Hence, only the contribution of the momentum in the propeller stream will be considered in an extension of the present analysis.

At the outset it is noted that $\tilde{\phi}^{(1)}$ is an odd function in \tilde{z} . It was shown by an analysis of the third region that $\tilde{p}^{(1)}(\tilde{x}, \tilde{y}, \tilde{z})$ is continuous across $\tilde{z}=0$. Hence it is concluded that

$$\tilde{p}^{(1)}(\tilde{x}, \tilde{y}, \tilde{z}=0) = 0 \quad (36)$$

In view of equations (31a) and (31d), it may also be stated that behind the wing

$$\tilde{u}^{(1)}(\tilde{x}, \tilde{y}, \tilde{z}=0) = 0 \quad (37)$$

However, because of the vorticity $d\Gamma(\tilde{y})/d\tilde{y}$ on the plane $\tilde{z}=0$ behind the wing, $\tilde{v}^{(1)}$ is discontinuous across the jet sheet and is given by

$$\tilde{v}^{(1)}(\tilde{x}, \tilde{y}, \tilde{z}=0+) = d\Gamma(\tilde{y})/d\tilde{y} = -\tilde{v}^{(1)}(\tilde{x}, \tilde{y}, \tilde{z}=0-) \quad (38)$$

Nevertheless $[\tilde{v}^{(1)}]^2$ is continuous across the jet sheet. Furthermore, since $\tilde{\theta}^{(1)}$ is continuous, $\tilde{w}^{(1)}$ is also continuous across the jet sheet.

Next, upon considering the $O(\epsilon^2)$ terms in the Bernoulli equation the following equation is obtained:

$$\tilde{p}^{(2)}/\rho = -U_\infty \tilde{u}^{(2)} - [(\tilde{v}^{(1)})^2 + (\tilde{w}^{(1)})^2]/2 \quad (39)$$

Since $[\tilde{v}^{(1)}]^2$ and $\tilde{w}^{(1)}$ are continuous, the pressure difference across the sheet is given simply by

$$\begin{aligned} \Delta \tilde{p}^{(2)} &= \tilde{p}^{(2)}(\tilde{x}, \tilde{y}, \tilde{z}=0+) - \tilde{p}^{(2)}(\tilde{x}, \tilde{y}, \tilde{z}=0-) \\ &= -\rho U_\infty [\tilde{u}^{(2)}(\tilde{x}, \tilde{y}, \tilde{z}=0+) - \tilde{u}^{(2)}(\tilde{x}, \tilde{y}, \tilde{z}=0-)] \end{aligned} \quad (40)$$

This discontinuity in $\tilde{u}^{(2)}$ is equivalent to a vorticity distribution $\gamma(\tilde{x}, \tilde{y})$ on the jet sheet and, in view of equation (26), $\gamma(\tilde{x}, \tilde{y})$ can be expressed as follows:

$$\gamma(\tilde{x}, \tilde{y}) = -\epsilon \tilde{\theta}_x^{(1)}(\tilde{x}, \tilde{y}, 0) J(\tilde{y}) / \rho U_\infty s = -\tilde{\theta}_x(\tilde{x}, \tilde{y}, 0) J(\tilde{y}) / \rho U_\infty s \quad (41)$$

At the lifting line, $\tilde{\theta}$ is not zero (i.e., the jet sheet has a non-zero inclination at the lifting line). This would require a vertical force of magnitude $J(\tilde{y})\epsilon\tilde{\theta}^{(1)}$ at the lifting line. To account for this force, a circulation distribution $\Gamma_J(\tilde{y})$ is introduced along the lifting line. The magnitude of this circulation is given by

$$\Gamma_J(\tilde{y}) = -J(\tilde{y})\epsilon\tilde{\theta}^{(1)} / \rho U_\infty = -J(\tilde{y})\tilde{\theta} / \rho U_\infty \quad (42)$$

Thus, in this limited second order analysis, referred to as the systematic analysis in ref. 14, the vortex system consists of the circulation $\Gamma(\tilde{y})$ along the lifting line, the circulation $\Gamma_J(\tilde{y})$ which accounts for the change in the inclination of the jet sheet on passing over the wing, and a distribution $\gamma(\tilde{x}, \tilde{y})$ behind the wing, which accounts for the curvature of the jet sheet. This system of vortices produces a downwash distribution $\theta(\tilde{x}, \tilde{y})$ which is obtained from the following velocity potential:

$$\begin{aligned} \Phi(\tilde{x}, \tilde{y}, \tilde{z}) &= \frac{1}{4\pi} \int_{-1}^1 \frac{\tilde{z}\tilde{\Gamma}(\eta)}{\tilde{z}^2 + (y-\eta)^2} \left(1 + \frac{\tilde{x}-m|\eta|}{R}\right) d\eta + \frac{1}{4\pi} \int_{-1}^1 \frac{\tilde{z}\Gamma_J(\eta)}{\tilde{z}^2 + (y-\eta)^2} \left(1 + \frac{\tilde{x}-m|\eta|}{R}\right) d\eta \\ &+ \frac{1}{4\pi} \int_{-1}^1 \int_{|\eta|}^{\infty} \frac{\tilde{z}\gamma(\xi, \eta)}{\tilde{z}^2 + (y-\eta)^2} \left(1 + \frac{(\tilde{x}-\xi)}{\sqrt{[(\tilde{x}-\xi)^2 + (y-\eta)^2 + \tilde{z}^2]}}\right) d\xi d\eta \end{aligned} \quad (43)$$

The downwash is related to the unknown quantities by the following relations:

$$\Gamma(\tilde{y}) = (1/2)U_\infty c(\tilde{y}) c_{\alpha_g} [\alpha_g(\tilde{y}) - \tilde{\theta}(\tilde{x}, \tilde{y})], \quad \tilde{x} + m|\tilde{y}| \quad (44)$$

$$\Gamma_J(\tilde{y}) = -J(\tilde{y})\tilde{\theta}(\tilde{x}, \tilde{y}) / \rho U_\infty, \quad \tilde{x} + m|\tilde{y}| \quad (45)$$

$$\gamma(\tilde{x}, \tilde{y}) = -J(\tilde{y})\tilde{\theta}_x(\tilde{x}, \tilde{y}) / \rho U_\infty s \quad (46)$$

These are the governing equations for the unknowns $\Gamma(\tilde{y})$, $\Gamma_J(\tilde{y})$ and $\gamma(\tilde{x}, \tilde{y})$.

3. METHOD OF SOLUTION

The governing equations for the unknowns $\Gamma(\tilde{y})$, $\Gamma_J(\tilde{y})$ and $\gamma(\tilde{x}, \tilde{y})$ are the equations (44) - (46) together with the equation (43) for the downwash angle θ required in the solution. The downwash angle computed by equation (43) on the lifting line at the wing centerline is infinite because of the discontinuity in the slope of the lifting line at the wing root. This is familiar problem in the swept wing analysis. Rigorous studies of swept wings in uniform flow by Cheng, et al. (refs. 27 and ref. 28) have shown that the induced velocity approaches infinity like the logarithm of the distance from the centerline. This behavior does not allow computation of the spanload at the wing centerline of symmetrically swept wings. Thurber (ref. 29) studied swept wings with curved centerlines having zero sweep at the wing centerline and zero tip chord (crescent wings) in uniform flow. This planform has limited application in the present context.

The method developed by Lan (ref. 30) is employed here to compute the downwash from equation (43). This method starts with the Weissinger velocity potential, and, placing the lifting line on the quarter-chord line, computes the downwash at the three-quarter-chord line. A brief description of this method is presented here.

Consider the first integral on the right-hand side of equation (43). This is the potential due to $\Gamma(y)$ along the lifting line, i.e.,

$$\Phi_1 = \frac{1}{4\pi} \int_{-1}^1 \frac{z\Gamma(\eta)}{z^2 + (y-\eta)^2} \left(1 + \frac{(x-\xi)}{R}\right) d\eta \quad (47)$$

where $R^2 = (x-\xi)^2 + (y-\eta)^2 + z^2$ and tildes are dropped for convenience. The origin for the co-ordinate axes is assumed to be at the mid-root chord. Also

$$\xi = -c_0/4 + m|\eta| \quad (48)$$

$$x = -c_0/4 + c(y)/2 + m|y| \quad (49)$$

These expressions are introduced in equation (47), and the resulting expression is expanded for small $c(y)$. By retaining only first order terms in the expansion, and differentiating them with respect to z , the required expression for θ_1 (evaluated at $z=0$) is obtained as

$$\theta_1(x, y, 0) = \frac{1}{4\pi} \int_{-1}^1 \frac{\Gamma(\eta)}{(y-\eta)^2} \left(1 + \frac{x-m'|\eta|}{R_1} + \frac{c(\eta)}{4} \frac{(y-\eta)^2}{R_1^3}\right) d\eta \quad (50)$$

where $m' = m - (c_0/4)(1-\lambda)$ is the tangent of the mid-chord sweep, and $R_1^2 = (x-m'|\eta|)^2 + (y-\eta)^2$. The right hand side of equation (50) is integrated by parts to arrive at the following expression for θ_1 :

$$\theta_1(x, y, 0) = \frac{1}{4\pi} \int_{-1}^0 \frac{Q(\eta)}{y-\eta} \frac{d\Gamma(\eta)}{d\eta} d\eta + \frac{1}{4\pi} \int_0^1 \frac{P(\eta)}{y-\eta} \frac{d\Gamma(\eta)}{d\eta} d\eta \quad (51)$$

The functions $P(\eta)$ and $Q(\eta)$ are defined in ref. 30. More details of the derivation are available in ref. 31. Next, a coordinate transformation is introduced, changing η into ϕ , and the integrals are reduced to finite sums by discretizing $\Gamma(y)$. Thus equation (51) reduces to the following:

$$\theta_1(x_i, y_i, 0) = \frac{1}{4\pi} \sum_{k=1}^N \Delta\Gamma(\eta_k) \left\{ \frac{P(\eta_k)}{y_i - \eta_k} - \frac{Q(\eta_k)}{y_i + \eta_k} \right\} \quad (52)$$

$$\text{where } \eta_k = (1 - \cos \phi_k)/2, \quad \phi_k = (2k-1)\pi/2N, \quad k = 1, 2, \dots, N \quad (53a)$$

$$y_i = (1 - \cos \phi_i)/2, \quad \phi_i = (i-1)\pi/N, \quad i = 1, 2, \dots, N \quad (53b)$$

By writing $\Delta\Gamma(\eta_k) = \Gamma(y_{k+1}) - \Gamma(y_k)$, equation (52) may be expressed as

$$\theta_1(x_i, y_i, 0) = \sum_{k=1}^N \Gamma(y_k) A(i, k) \quad (54)$$

This is the required expression for the downwash due to the $\Gamma(y)$ distribution. A similar expression is obtained from the second integral on the right-hand side of equation (43), i.e.,

$$\theta_2(x_i, y_i, 0) = \sum_{k=1}^N \Gamma_J(y_k) A(i, k) \quad (55)$$

The vortex sheet behind the wing is assumed to extend downstream from the wing trailing edge. The continuous distribution $\gamma(x,y)$ is replaced with a finite number (M) of discrete vortices of strength $\gamma_\lambda(y)$ located at x_λ , $\lambda=1,2,\dots,M$ behind the wing. Each of these vortices is further represented in the same manner as $\Gamma(y)$ is discretized, so that the jet sheet behind the wing is represented essentially by a vortex lattice. The downwash computed from this system of vortices is expressed as

$$\theta_3(x_i, y_j, 0) = \sum_{\lambda=1}^M \sum_{k=1}^N \gamma_\lambda(y_k) B(i, j, k, \lambda) \quad (56)$$

Equations (54) - (56) together provide an expression for the downwash angle in terms of the unknown $\Gamma(y_k)$, $\Gamma_j(y_k)$ and $\gamma_\lambda(y_k)$, $k=1,2,\dots,N$; $\lambda=1,2,\dots,M$. This expression is used in the discretized versions of equations (44) - (46), and the resulting set of simultaneous equations are solved for the unknowns. More details of the analysis and method of solution may be found in ref. 32.

The lift-curve slope required in equation (44) is to be obtained by solving equation (18) or the equivalent equations (12), (13a) and (13c). However, in the present analysis, a potential flow method, based on an extension of the method of Ting and Liu (ref. 7), has been employed. This method is found to give results which compare reasonably well with the solution of Euler equations.

The analysis presented thus far is applicable to incompressible flows. A limited extension is made to account for the compressibility effects by introducing the Prandtl-Glauert factor $\beta = \sqrt{1-M_\infty^2}$ at appropriate places in the expressions for Φ , equation (43), as well as in the lift-curve slope in equation (44). A rigorous treatment of the nonuniform compressible flow past a wing section would require the solution of the Euler equations coupled with the energy equation. However, it is observed that the nonuniformities in the slipstreams at high speeds would be relatively smaller than at low speeds. Hence, it is hoped that the Prandtl-Glauert correction, which is known to provide excellent corrections to the lift of airfoils in uniform subcritical flow, will provide a reasonable correction in the present case where the approach flow is not uniform.

4. RESULTS AND DISCUSSION

The spanwise lift distribution and total lift have been computed for several configurations and compared with available experimental data. As the first example, the configuration tested by Stuper (ref. 33) is considered. In these experiments, the wing was rectangular and spanned the wind tunnel walls. The ratio of chord to geometric span was 5.25. A slipstream simulator was placed centrally ahead of the wing. The ratio of the slipstream radius to the wing chord was 0.3, and the velocity ratio of the slipstream was 1.36. Figure 2 shows the spanwise distribution of the incremental lift non-dimensionalized with incremental lift as obtained by strip theory. Present theoretical results are also shown in the figure. It is observed that there is a good agreement between the two results, particularly in the region of the slipstream. Viscous effects at the jet boundary might have contributed to the discrepancy around $(y/r)=1.0$. Experimentally measured large values of incremental lift for $(y/r)>1.0$ could not be explained, but are suspected to be partly due to the tunnel wall interference.

As the second example, the configuration tested by Possio (ref. 34) is considered. In this example, the wing had a taper ratio of 0.5 and an aspect ratio of 6.5. A single model propeller was placed ahead of the wing. Several sets of data are available with varying velocity ratio and angle of attack. Figure 3 shows the spanwise lift distribution for the wing alone, and for the wing with the slip streams of velocity ratio 1.4 and 1.6. In these tests only the incremental total lift coefficients were measured. The present theoretical values of $\Delta C_L = 0.068$ and 0.098 compare very well with the corresponding experimental values of 0.07 and 0.10.

In the next example considered, the wing (tested by Maarsingh ref. 16) had a rectangular planform with aspect ratio of 7.9. Two simulators were placed on each side of the wing at 42% and 79% of the semispan. The simulated slipstream radius was 0.28 times the wing chord. Tests results are available for the wing alone and for the wing with slipstreams having velocity ratios of 2.0 and 3.0. Figure 4 shows the spanwise lift distribution for the test configurations obtained by the present analysis. Figure 5 shows the spanwise distribution of incremental lift (ΔC_L) due to the jets for the two velocity ratios, compared with the experimental values. The results computed by Maarsingh (ref. 15) using Ting's method (ref. 14) are also shown in this figure. It should be noted that the present method degenerates into Ting's method for unswept wings. However, there are some minor differences between the present results and those of Maarsingh (ref. 15). These differences are suspected to be primarily due to the inaccurate expression used for the sectional lift curve data used in ref. 15. The figure shows that the present results compare well with the experimental data.

In the examples considered so far, only unswept wings at very low speeds were considered, compressibility effects were neglected, and there was no swirl in the slipstream. The next configuration considered was tested by Welge and Crowder (ref. 23) in the NASA Ames 14-foot tunnel. The wing had an aspect ratio of 7.0 and a quarter-chord sweepback of 32 degrees. Figure 6 shows the wing geometry. The wing had a discontinuity in the trailing edge sweepback angle. For the purpose of the present analysis, this wing has been replaced with an equivalent simple swept wing shown in figure 6 by the dashed lines. The slipstream simulator was driven by compressed air, and provided a jet which had a total pressure profile very close to what is observed in a prop-fan slipstream. Figure 7 shows the properties of the jet at $M_\infty=0.8$. The radial distribution of the total pressure ratio, the resulting velocity ratio, and the corresponding spanwise momentum distribution are shown in this figure. The simulator had adjustable vanes which could be set to obtain a swirl angle distribution

typical of what is found in a slipstream. The measured radial distribution of the swirl angle in the jet is also included in the figure. Tests results are available for $M_\infty=0.7$ and 0.8 , with and without the jets.

The spanwise load distribution obtained by the present method as well as by the experiments for the wing alone at $M_\infty=0.8$ and $\alpha=3.28$ degrees are presented in figure 8. (The span load parameter c_{l_x}/c_{mac} used in figures 8-11, is the local lift coefficient c_l multiplied by the ratio of local chord c to the mean aerodynamic chord c_{mac} .) There is good agreement between the two results at wing outboard stations; but the agreement is not as good at stations close to the wing root. It should be noted that the test configuration had a body at the center, and the wing planform was modified near the wing root. These details were not simulated in the present analysis. Some of the differences between the present results and the experimental data at the inboard stations may be attributed to these differences.

The effect of the jet without swirl on the spanwise load distribution at $M_\infty=0.8$ and $\alpha=3$ degrees is illustrated in figure 9. The experimental data, the results obtained by the present analysis and the solution of Euler equations (ref. 23) are included in this figure. It should be noted that the jet is a rather weak jet with a maximum total pressure ratio of 1.075. As a result, the jet does not modify the load distribution significantly. It can be observed from the figure that the incremental lift values obtained by the present analysis agree closely with the experimental data. A comparison of the Euler solution (ref. 24) with experimental data shows a trend similar to that which was observed earlier - at the wing inboard stations there is good agreement, but at the outboard stations there is some discrepancy. Nevertheless, the incremental lift values obtained by this method also compare well with the experimental data.

The effect of the swirl in the jet on the spanwise load distribution at $M_\infty=0.8$ and $\alpha=3$ degrees is illustrated in figure 10. The experimental data are available for the wing with jet having nominal swirl angles of 7 degrees up inboard and 7 degrees down inboard. These experimental data are shown in figures 10a and 10b for the up inboard and down inboard swirl distributions respectively. Present results and the computed results from ref. 23 are also included in these figures which bring out the interesting effect of the swirl in the slipstream on the spanwise load distribution. Quantitative agreement between the Euler solution (ref. 23) and the experiments is good at stations close to the wing root; the agreement is not as good at the outboard stations. In contrast, a comparison of the present results with the experiments shows good agreement at the outboard stations but not as good agreement at stations close to the wing root. This discrepancy in the results near the wing root may be attributed to the differences between the theoretical model used in the present analysis and the actual wind tunnel model. A closer examination of figures reveals that the present results agree with experimental data qualitatively; but quantitatively, the present analysis seems to slightly overpredict the effect of the swirl. Similar observations can be made by a study of figure 11 which also illustrates the effect of swirl at $M_\infty=0.7$ and $\alpha=3$ degrees.

5. CONCLUSIONS

The problem of the interference of multiple propeller slipstreams with large aspect ratio swept wings is treated by the method of asymptotic expansions. While this is only a first order theory, the important second order contributions from the propeller slipstream are included in the analysis. The method is quite versatile in the sense that it can handle slipstreams of any given velocity distribution. The time dependence of the velocity field in the slipstream is neglected. The increased axial velocity and the swirl component in the slipstream are of primary concern in the present analysis. One of the assumptions that the spanwise extent of the slipstream was of the order of the wing span, was not satisfied in the examples considered; but the results do not seem to be affected noticeably. Viscous effects are neglected; but the compressibility effect is accounted for by the Prandtl-Glauert factor.

Several examples are considered for which experimental data are available, and in each case spanwise lift distribution is obtained by the present method, and compared with the corresponding experimental data. In most of the cases the agreement between the two results is very good. In the first example, the differences between the experimental data and the present results are suspected to be partly due to the tunnel wall interference in the measurements. In the last example considered, the experimental configuration had a body on the centerline; also the wing planform was modified near the wing root. These details were not simulated in the present analysis. It is suspected that these differences have resulted in the difference in the two sets of results.

In the present analysis, the effect of the swirl in the slipstream is accounted for by assuming that the swirl only changes the local angle of attack. This approach yields results which compare well qualitatively with the experimental data. However, the method seems to slightly overpredict the effect of swirl on the spanwise load distribution.

A comparison was made between the present results and the numerical solution of Euler equations. The numerical solution of Euler equation requires a large computer memory and extensive computing effort. It, however, provides details of the flowfield in the entire computational domain. But the present method is simple, requires relatively small computational effort, and gives spanwise lift distributions that compare favorably with experimental data.

ACKNOWLEDGEMENT

This research work was supported by NASA/ODU Research Foundation Cooperative Agreement NCC1-65. The authors would like to thank Mr. Richard J. Margason, Head of NASA Langley Analytical Methods Branch, for his keen interest and many helpful suggestions during the course of this work.

REFERENCES

1. Ludemann, S.G., "Prop-fan Powered Aircraft - An Overview," SAE Paper No.820957, 1982.
2. Arndt, W.E., "Fuel Efficient And Mach 0.8 Too," Lockheed Horizon, Issue 10, Spring 1982, pp.26-34.
3. Smelt, R. and Davies, H., "Estimation of Increase in Lift Due to Slipstream," British ARC R and M 1788, 1937.
4. Millikan, C.B., "The Influence of Running propellers on Airplane Characteristics," Journal of Aeronautical Sciences, Vol.7, No.3, January 1940, pp.85-106.
5. Koning, C., "Influence of the Propeller on other Parts of the Airplane Structure," Aerodynamic Theory, Vol.IV, Edited by W.F.Durand, Division M, Dover Publication, New York, 1963.
6. Ferrari, C., "Propellers and Wing Interaction at Subsonic Speeds," Aerodynamics Component of Aircraft at High Speed, Edited by A.F.Donovan and H. C. Lawrence, Sec. D, Ch. 3. Princeton University Press. Princeton, N.J., 1957.
7. Ting, L. and Liu, C.H., "Thin Airfoil in Nonuniform Parallel Streams," NYU Rep. AA 68-20, New York Univ., July 1968, Also Journal of Aircraft, Vol.6, No.2, March-April 1969, pp.173-175.
8. Chow, F., Krause, E., Liu, C.H., and Mao, J., "Numerical Investigations of an Airfoil in a Nonuniform Stream," Journal of Aircraft, Vol.7, No.6, Nov.-Dec. 1970, pp.531-537.
9. Kleinstein, G. and Liu, C.H., "Application of Airfoil Theory for Nonuniform Streams to Wing-Propeller Interaction," Journal of Aircraft, Vol.9, No.2, Feb. 1972, pp.137-142.
10. Rethorst, S., "Lift on a Wing in a Propeller Slipstream as Related to Low-Speed Flight," Aeronautical Engineering Review, October 1958, pp.42-48.
11. Wu, T.Y. and Talmadge, R.B., "A Lifting Surface Theory for Wings Extending Through Multiple Jets," Report No.8, Vehicle Research Corporation, Pasadena, California, August 1961.
12. Cumberbatch, E., "A Lifting Surface Theory for Wings at Angles of Attack Extending Through Multiple Jets," Report No.9, Vehicle Research Corporation, Pasadena, California, July 1963.
13. Jameson, A., "Analysis of Wing Slipstream Interaction," NASA CR-1632, 1970.
14. Ting, L., Liu, C.H., and Kleinstein, G., "Interference of Wing and Multiple Propellers," AIAA Paper 71-614, Palo Alto, Calif., 1971; Also AIAA Journal, Vol.10, No.7, July 1972, pp.906-914.
15. Maarsingh, R.A., "Calculation of the Lift Distribution on a Wing in Jets or Slipstreams using Ting's Method," NLR TR 73151C, National Aerospace Laboratory, Netherlands, Oct. 1973.
16. Maarsingh, R.A., "Evaluation of Ting's Method for the Calculation of the Lift Distribution on a Wing in Propulsive Jets," NLR TR 80078U, National Aerospace Laboratory, Netherlands, Nov. 1979.
17. Ribner, H.S. and Ellis, N.D., "Aerodynamics of Wing Slipstream Interaction," Transactions of the Canadian Aeronautics and Space Institute, Vol.5, No.2, Sept. 1972, pp.56-63.
18. Lan, C.E., "Wing-Slipstream Interaction with Mach Number Nonuniformity," Journal of Aircraft Vol.12, No.10, October 1975, pp.759-760.
19. Rizk, M.H., "Propeller Slipstream/Wing Interaction in the Transonic Regime," AIAA Paper 80-0125, January 1980.
20. Chandrasekaran, B. and Bartlett, G., "Method for Calculating Effects of a Propfan on Aircraft Aerodynamics at Subsonic Speeds," AIAA-83-1216, Presented at the AIAA/SAE/ASME 19th Joint Propulsion Conference, Seattle, Washington, June 1983.
21. Narain, J.P., "A Transonic Analysis of Propfan Slipstream Effects on a Supercritical Wing," AIAA Paper 83-0186, January 1983.
22. Samant, S.S., Yu, N.J., and Rubbert, P.E., "Transonic Flow Simulation of Prop-Fan Configurations," AIAA Paper 83-0187, January 1983.
23. Welge, H.R. and Crowder, J.P., "Simulated Propeller Slipstream Effects on a Supercritical Wing," NASA CR-152138, June 1978.
24. Whitfield, D.L. and Jameson, A., "Three-dimensional Euler Equation Simulation of a Propeller-Wing Interaction in Transonic flow," AIAA Paper 83-0236, January 1983.

25. Van Dyke, M., "Lifting Line Theory as a Singular Perturbation Problem," Sudaer No.165, Stanford University, Stanford, California, August 1963.
26. Van Dyke, M., "Perturbation Methods in Fluid Mechanics," The Parabolic Press, Stanford, California, 1975.
27. Cheng, H.K., Meng, S.Y., Chow, R. and Smith, R.C., "Transonic Swept Wing Studied by the Lifting Line," AIAA Journal, Vol.19, No.8, August 1981, pp.961-968.
28. Cheng, H.K., Chow, R., and Melnik, R.E., "Lifting Line Theory of Swept Wing Based on Full Potential Theory," Journal of Applied Mathematics and Physics, Vol.31, 1981, pp.481-496.
29. Thurber, J., "An Asymptotic Method for Determining the Lift Distribution on a Swept-back Wing of Finite Span," Communications on Pure and Applied Mathematics, Vol.18, 1965, pp.733-756.
30. Lan, C.E. and Fasce, M.H., "Application of an Improved Nonlinear Lifting Line Theory," Journal of Aircraft, Vol.14, No.4, April 1977, pp.404-407.
31. Fasce, M.H., "Application of a Improved Nonlinear Lifting Line Theory," M.S. Thesis, Department of Aerospace Engineering, University of Kansas, March 1975.
32. Prabhu, R. K., "Studies on the Interference of Wings and Propeller Slipstreams," Ph.D. Thesis, Department of Mechanical Engineering and Mechanics, Old Dominion University, September 1984.
33. Stuper, J., "Effects of Propeller Slipstream on Wing and Tail," NACA TM No.874, 1938.
34. Possio, C., "Experimental Investigation of Propeller Wing Interference," Aerotecnica, Vol.26, 1946, pp.73-77.

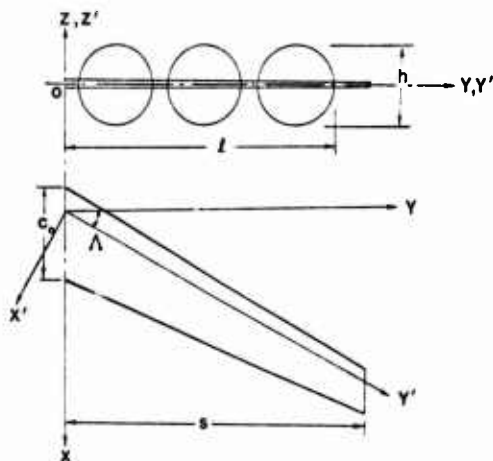


Fig. 1 Schematic of the Physical Problem

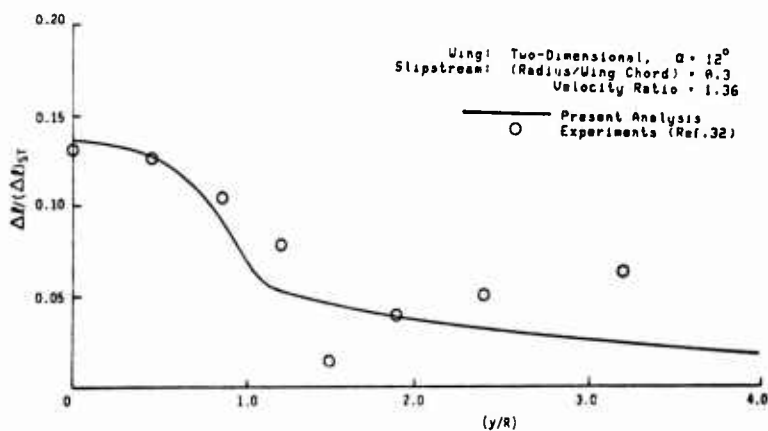


Fig. 2 Additional Lift Distribution due to Slipstream on a Two-dimensional Wing

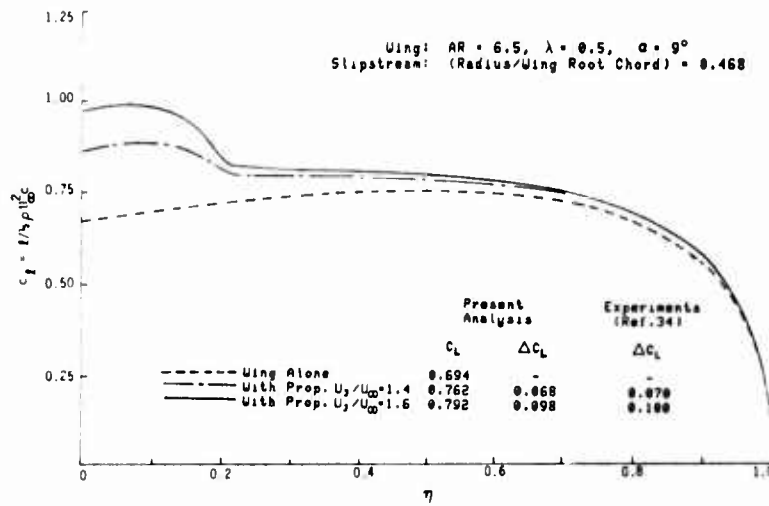


Fig. 3 Spanwise Lift Distribution on a Tapered Wing with and without the Slipstream

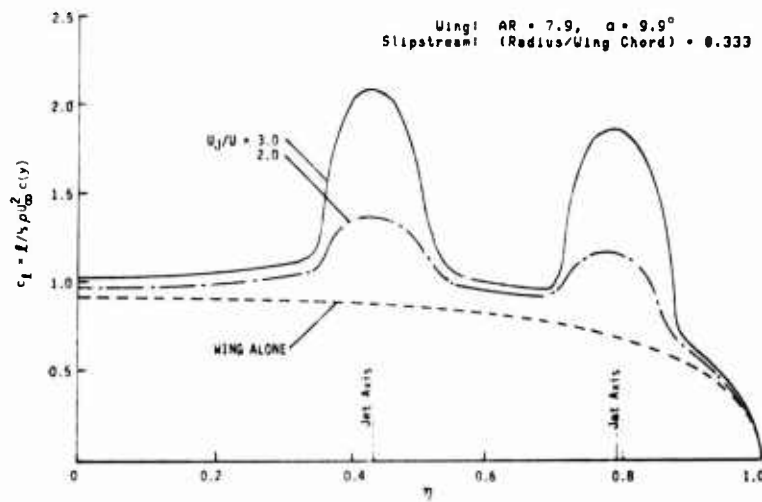


Fig. 4 Spanwise Lift Distribution on a Rectangular Wing with and without the Slipstream

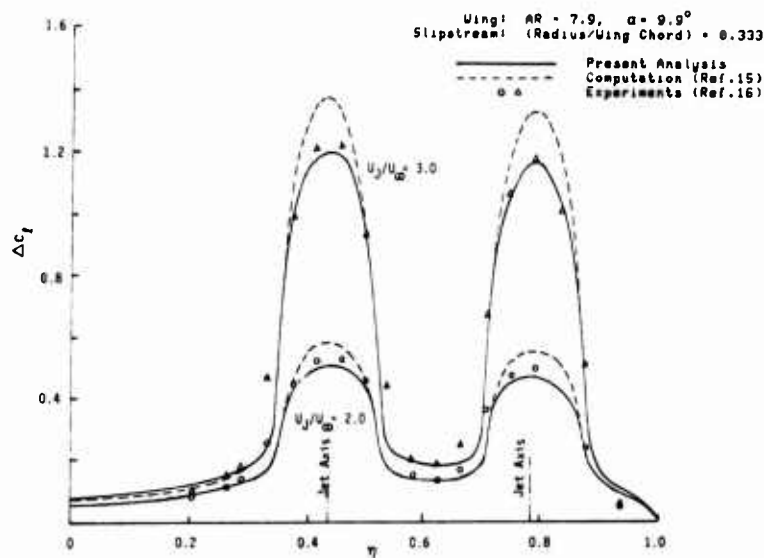


Fig. 5 Additional Lift Distribution due to Slipstream

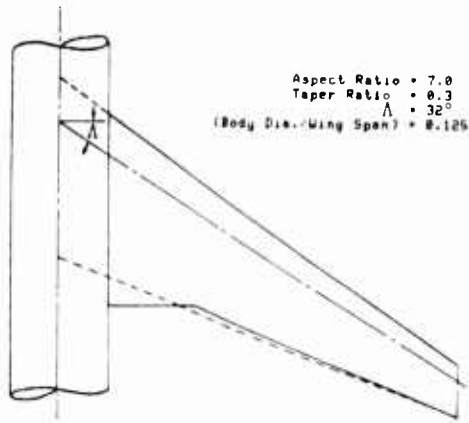


Fig. 6 The Swept Wing Geometry

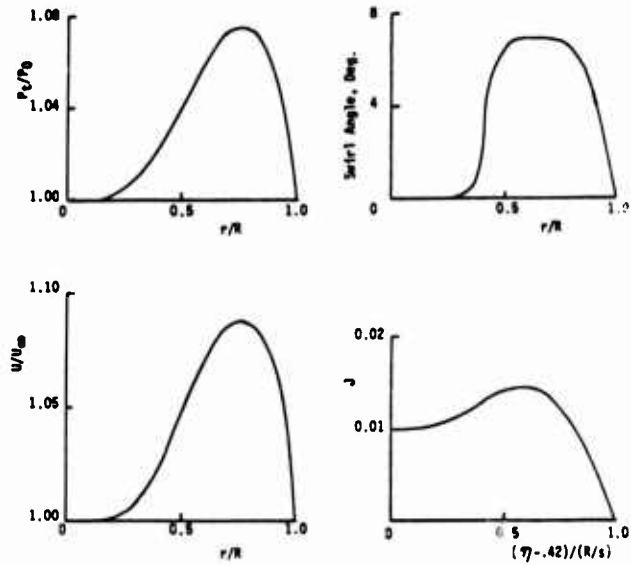


Fig. 7 The Properties of the Jet at M = 0.8

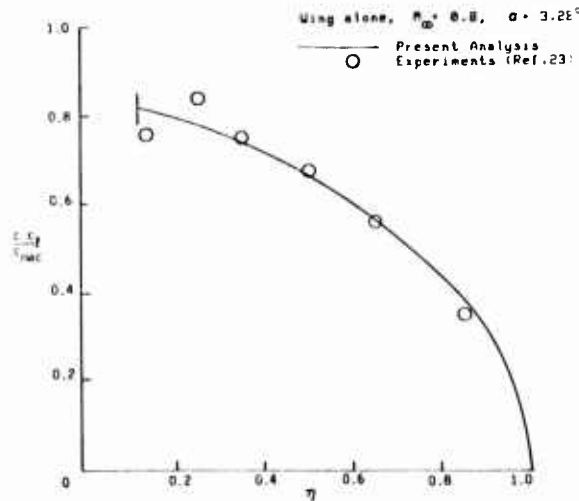


Fig. 8 Spanwise Load Distribution on the Wing alone

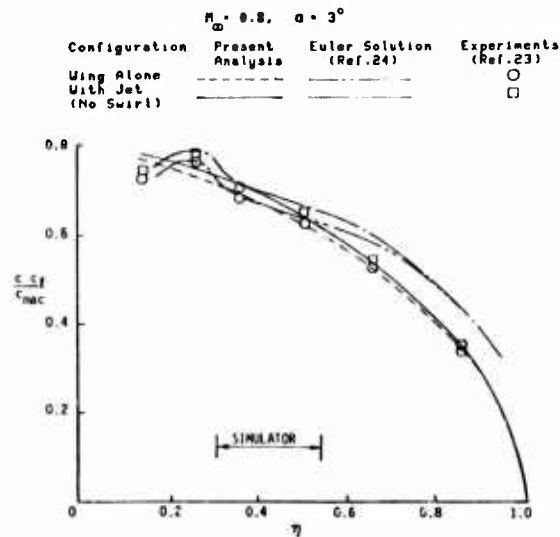


Fig. 9 Effect of the Jet on the Spanwise Load Distribution

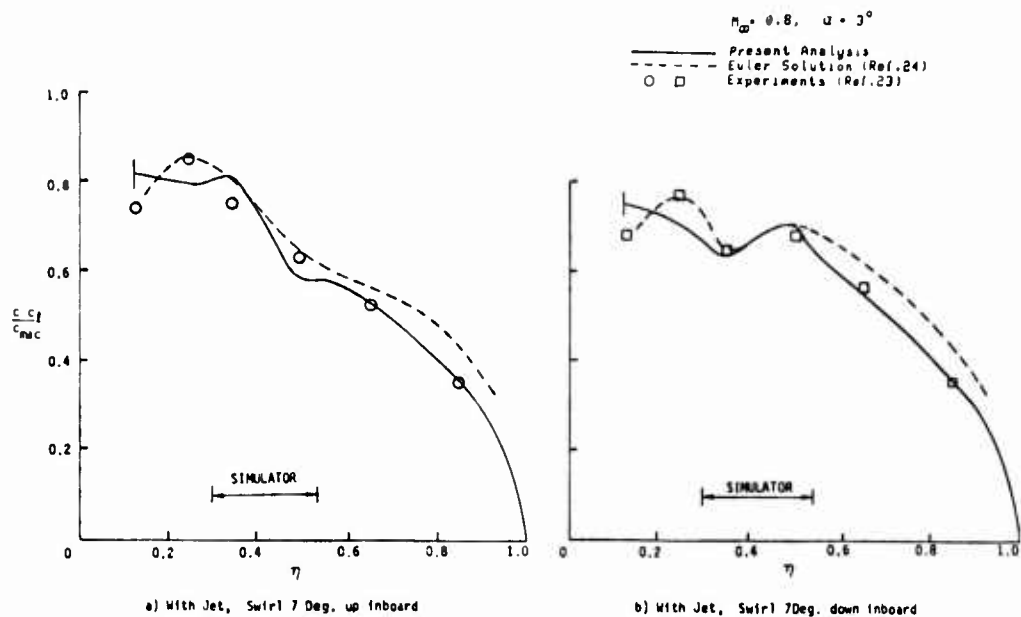


Fig. 10 Effect of the Swirl on the Spanwise Load Distribution

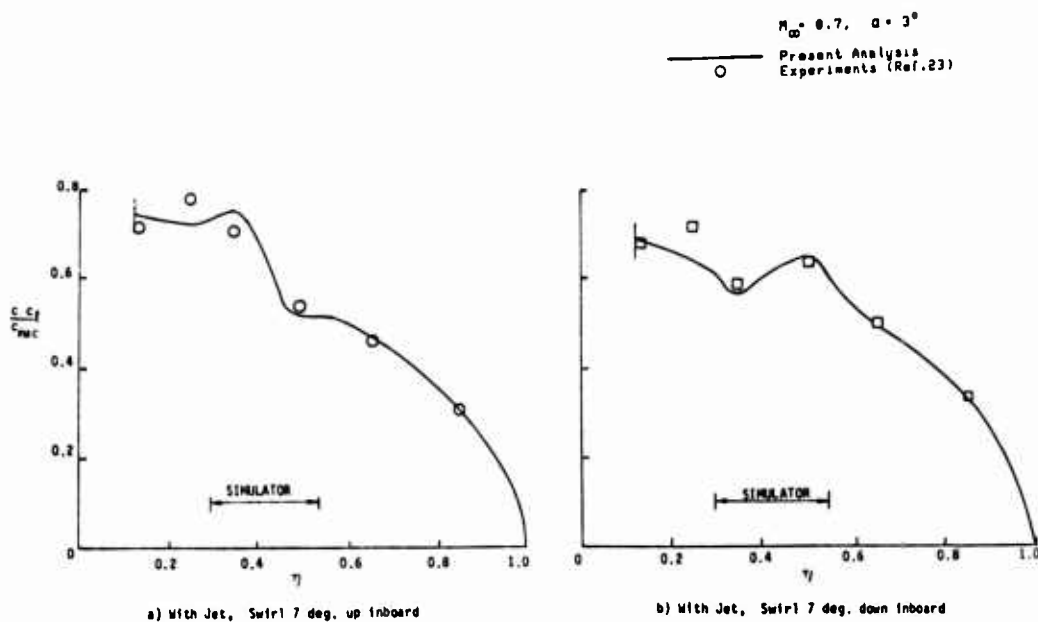


Fig. 11 Effect of the Swirl on the Spanwise Load Distribution

DEVELOPMENT OF MODERN TURBOPROP ENGINES

by

H.I.H.Saravanamuttoo
 Professor and Chairman
 Department of Mechanical and Aeronautical Engineering
 Carleton University
 Ottawa, Canada
 K1S 5B6

Proposals for propfan commercial aircraft operating at high cruise speeds pose requirements for advanced turboprops of high power. The history of turboprops for long range operation is briefly reviewed and the requirements for future engines are discussed. Considerable gains in the thermodynamic cycle can be realized, and the development of high performance gas generators should be a straightforward process. Transmission designs for high power engines may be extremely difficult and may result in novel engine configurations. It appears likely that a more modest goal of M 0.7 cruise for shorter haul aircraft could be attained with much less risk while still achieving major gains.

INTRODUCTION

The rapid escalation of fuel costs in the mid 70's caused a serious re-appraisal of fuel efficiency in commercial aircraft applications, where the impact on operating economics was very high. Military users were also seriously concerned with both the amount and cost of fuel required for normal operations. Although at the present time the upward trend in fuel prices has halted, this can at best be a lull in what is a potentially very unstable system. It is therefore important to continue the search for high fuel efficiency.

NASA sponsored several major studies which clearly demonstrated that advanced turboprops combined with propfans, capable of operating at high propeller efficiency at flight Mach Numbers of 0.80, offered substantial gains in fuel economy over turbofans. The aircraft studies were largely based on the premise that speeds should be similar to those of existing turbofan powered aircraft, both for reasons of passenger appeal and integration with air traffic control systems. It was clearly recognized that extensive research in the aerodynamic and structural problems of propfans was required, along with methods for reducing cabin noise to an acceptable level comparable to existing airline standards.

The purpose of this paper is to review turboprop developments covering the past, present and future in the hope of clarifying problem areas and potential solutions.

HISTORICAL BACKGROUND

Turboprops were first introduced to airline service in April 1953, when the Vickers Viscount entered service with British European Airways, powered by four Rolls Royce Darts. The passenger appeal of the Viscount was very high, because of its low noise and vibration levels relative to existing piston engined aircraft; this was particularly apparent on routes where BEA's competitors had long claimed the major portion of the traffic. As an example, between the summer of 1952 and 1954 BEA's share of the traffic from London-Copenhagen-Stockholm increased from 26.7% to 46.2% (1). It is interesting to note from (1) that Viscounts were used on non-stop sectors as long as London-Rome and London-Lisbon. Air Canada (then TransCanada Air Lines) was one of the earliest users of Viscounts, and the Viscount was a major part of their fleet for many years; a notable sector flown at dead of night was Toronto-Winnipeg in 3 hrs 50 minutes.

PRECEDING PAGE BLANK-NOT FILMED

The Lockheed Electra, powered by four Allison 501 turboprops, entered service with Eastern Airlines in January 1959. The Electra had a much higher cruise speed than the Viscount, and was capable of continuous cruise at Mach 0.6. It is interesting to recollect that in the post World War II piston airline market, the dominant manufacturers were Lockheed and Douglas with Boeing lying a distant third. The major US airlines basically decided that the fuel economy of the turboprop could not compensate for the lack of passenger appeal compared with jet aircraft and the Electra was only modestly successful. The seat miles per gallon progression from the DC6B, through the Electra to the early 707 and 747 is shown in Fig. 1 from (2). The Electra, however, spawned the extremely successful P3 Orion ASW aircraft which achieved huge sales around the world and is still in production with the T56 turboprop which was the military version of the Allison 501.

There was a major controversy in the mid Fifties regarding the most appropriate propulsion systems for long haul, intercontinental aircraft required to replace the existing piston engined aircraft such as the Super Constellation and DC7C. One school of thought favoured the turboprop because of its better fuel economy, and this led to the development of the Bristol Britannia powered by Bristol Proteus turboprops. The Britannia was large and comfortable for its day and was well known for its low noise, being given the enviable nickname of "The Whispering Giant". The Britannia was the only Transatlantic turboprop developed in the Western World; its entry into service was disappointingly delayed partially due to icing problems with the reverse flow engines, and it had only a very short period of superiority over the piston aircraft before it was superseded by the faster and more productive pure jets. It is amusing to recall, however, that when the 707-120 first entered service and had to make technical stops at both Boston and Iceland, it was in fact faster to cross non-stop on the slower turboprop! The only other transatlantic turboprop to be used was the Russian TU 114, a civil counterpart of the Bear bomber. This was a truly remarkable aircraft and it would be well worth doing some historical research into Aeroflot's commercial operations. The TU 114 was notable for its extremely high speed, extremely powerful engines and contra-rotating propellers. Jane's quoted the TU 114 as having a maximum speed of 590 mph (M 0.88) and a maximum cruising speed of 497 mph at 32,800 ft (M 0.74). If these seem barely credible, a world record for a 25,000 kg payload over a 5000 km circuit at a speed of 545 mph was established in April 1962. The power was supplied by 4 Kuznetsov NK 12 turboprops of approximately 12,000 ehsp, driving eight bladed contra-rotating propellers of 18.3 ft diameter. Despite the remarkable performance, the TU 114 did not remain in service for very long before being superseded by aircraft such as the Il-62; there may well be a lesson to be learned from history.

Perhaps the most interesting of all the turboprops, however, was the Vickers Vanguard. The Vanguard was probably the first real attempt to design an 'airbus' type aircraft, with a capacity of 139 passengers, a maximum payload range capability of 1830 miles and a cruise speed of 425 mph at 20,000 ft (M 0.61). The Vanguard was powered by four Rolls Royce Tyne turboprops of about 5500 ehsp. A paper by Dyment (3) on the selection of the Vanguard makes very interesting reading in the light of the current interest in fuel economy, as fuel burn was hardly even mentioned for a very fuel efficient aircraft. The sad fact remains that only BEA and TransCanada Airlines bought a total of about 40 Vanguards. The writer always enjoyed flying in Vanguards and was of the opinion that a unique solution to the noise problem was achieved, with all the noise transferred to the passenger cabin! Despite its commercial failure the Vanguard was a good work horse, and it too provides a useful lesson in history. Salient data for the faster turboprops are given in Table 1. Data extracted from Air Canada timetables (1961 and current) compare the scheduled times for Viscount, Vanguard and modern jets on sectors of varying lengths; even at a stage length of around 1000 miles the Vanguard was only 27 minutes slower than current schedules.

The long range, high speed turboprops generally show a gloomy picture. In the case of the short haul aircraft the picture is quite different. Notable successes have been achieved by the Fokker F27, HS748 and Viscount, all powered by the Rolls Royce Dart. After 25 years in service the F27 is still in production and is now being offered in considerably upgraded form as the Fokker 50, repowered with the Pratt and Whitney of Canada PW124. Similarly the HS 748 has led to a stretched derivative, the BAC ATP, also to be powered by the PW 124. In the commuter market a large number of turboprops such as the DHC6 Twin Otter, Shorts 330 and 360, Fairchild-Swearingen Merlin and Embraer Bandeirante have been sold. The most widely used engine has been the PWC PT-6, followed by the Garrett 331. There is now much activity in the turboprop market for commuter aircraft in the 30-50 seat range with the two prime contenders at the present time being the PW 100 series and the GE CT7, based on the highly successful T700 turboshaft.

POWER REQUIREMENTS

The NASA goal of a cruise speed of M 0.8 at 30,000 ft plus leads immediately to some major problems with regard to availability of suitable engines. Studies by many independent sources have all shown that the potential fuel gains of the propfan compared with an equivalent technology turbofan are of the order of 20-30 per cent. While there are still many aerodynamic and installation problems to be overcome, the potential gains are so large that even if they are not fully realized significant gains can still be expected. Fig. 2 from (4) shows the gains predicted by several different studies over a range of stage lengths; perhaps the most noticeable feature is that at lower Mach Numbers the advantage of the propfan is even more marked. Fig. 3 shows the cruise power required for cruise at M 0.8 and 0.6 at 30,000 ft, showing the effect of reduction in propeller efficiency. It is clear that the risks of lower than expected propeller efficiency are much higher at M 0.8 and combined with the already high power required may result in a significant power increase, fuel demand, and increase in structural weight. The very nature of the propfan means that aircraft will use either two or four engines, and three engine installations appear to be impractical. With the current trend towards twin engine aircraft, it appears likely that a twin propfan aircraft would be desirable for most transport applications.

It is not always appreciated how large the power requirements are, especially when compared to the 6000 eshp which is about the largest value in use. Goldsmith and Bowles (5) investigated the design of a propfan powered version of a DC9-80, and the power required per engine came to about 16,500 eshp. A Boeing study by Davenport (6) for a M 0.8, 1800 mile range, 180 passenger aircraft resulted in a power of 31,000 eshp per engine. This study, in fact, showed only about 10% saving in fuel and the author concluded that the drag and weight uncertainties were great enough to have a decisive influence on the propfan's economic potential. Egglestone (7) studies the requirements for propfan powered STOL aircraft operating up to M 0.7; even for a twin engine aircraft with a maximum TOW of 51,000 lb capable of carrying 50 passengers for 345 miles from 2000 ft strips, the take off-power was no less than 9500 SHP per engine.

Goldsmith and Bowles (5) pointed out that current aircraft such as the DC9-80 cruise substantially slower than M 0.8 and Fig. 4 shows the effects of Mach Number on both range and fuel burn, showing clearly the greater advantage at reduced Mach Numbers.

It seems probable that the propfan may best be aimed at relatively small (100-150 seat) transports with cruise speeds in the range of M 0.7, close to current operational speeds of B737/DC9. Aircraft of this class may require engine powers in the range of 10,000 eshp, which represents a considerable increase in the power capability of turboprops but one which does not present huge risks. Fig. 5, from (8) indicates the power requirements for twin engine transports. The long endurance ASW mission represents a considerable market for advanced turboprops; an increase in cruise Mach Number from 0.6 to 0.7 would permit faster transit times and time on station. Even without propfans, using conventional propellers, a new version of the T56 currently under development could give an increase in time-on-station of 2.3 hours (9).

CYCLE CONSIDERATIONS

The turboprop was never developed to the same level of aerodynamic sophistication as the turbofan, and current turboprop cycles are quite modest in terms of both pressure ratio and maximum cycle temperature. Considerable gains could readily be achieved using current technology.

It must be remembered, however, that prop-fans operate at extremely high by-pass ratios, perhaps 30 or more, and it immediately follows that for a given cruise thrust the gas generator flow will be much lower than would be required for the equivalent turbofan. While new turbofans such as the V2500 use pressure ratios of around 36, these would not be feasible in a propfan gas generator because of the very small size of the rear stages of blading if axial compressors were used; this could be overcome by the use of a centrifugal compressor at the high pressure end, as is already being developed in both the GE27 and PW 3005 turboprops in the 5000 shp class. The relatively small high pressure turbine blades could not use the same sophisticated cooling techniques currently in use in large turbofans, so it would be necessary to operate at a somewhat lower maximum cycle temperature.

Quite apart from the reduction in cycle parameters, the effects of small size cause aerodynamic penalties due to relatively large clearances, relatively thick compressor leading edges and turbine trailing edges, and the use of lower aspect ratios because of blade strength requirements, resulting in increased secondary flow losses. Thus, in performing detailed cycle calculations it is very important to make appropriate allowances for the penalties resulting from small size.

Figures 6 and 7, taken from Morris (10), illustrate this clearly. With no size effect, Fig. 6 suggests pressure ratios of over 30 and turbine inlet temperatures of 2600 F (1700 K) for low specific fuel consumption. Based on a cruise power of 1300 eshp at 25000 ft and 350 mph, however, an optimum pressure ratio of 20 at 2600 F is shown, with a pressure ratio of 30 showing a considerable degradation of both specific fuel consumption and specific power. In fact, at a pressure ratio of 15 and a turbine inlet temperature of 2000 F (1365 K) there is a negligible penalty on sfc and this was chosen as the design point for the PW 100. Brooks and Hirschkrone (11) reviewed advanced turboprops for commuter aircraft in the 30 and 50 passenger size class and arrived at values of 17 and 2300 F for the smaller aircraft and 20 and 2400 F for the larger aircraft. A recent study by Hirschkrone and Davis (12) of advanced turboprops for long endurance ASW aircraft proposed values of 22 and 2400 F (1590 K), presumably for an engine of similar power to the T56. Banach and Reynolds (8), investigating gas generators for a M 0.8, 120 passenger twin with 12000 shp engines suggested values of around 30 and 2240 F (1500 K). The studies referred to above were carried out by different design teams from Pratt and Whitney of Canada, GE and Pratt and Whitney and show quite good agreement. It appears that GE are rather more aggressive with regard to turbine inlet temperature; a balance has to be struck between performance and durability.

It is clear that there is no inherent difficulty in producing a fully acceptable gas generator. In view of the very high development costs of a totally new engine program it is worth considering whether an existing core may provide a suitable gas generator. Both the CF6 and RB 211 cores have been used with notable success as gas generators for industrial and marine engines in the 25-35000 shp class. Banach and Reynolds considered the possibility of using HP compressors from the F100 and PW 2037 programs, but found the resulting sfc to be 11.8 and 5.2% worse than for the optimized turboprop. The core of the V2500 turbofan, with a pressure ratio of 20 on a single-spool could provide an attractive gas generator for a turboprop of around 12-14,000 SHP.

The possibility of using more complex thermodynamic cycles involving heat exchange and intercooling has been examined at regular intervals during the last thirty years. The Bristol Theseus, built before the Proteus, was the first turboprop to use a heat exchanger but it never went into production. The heat exchanger, although offering gains in fuel economy, leads to a heavier and bulkier installation. The US Navy investigated the use of a regenerative engine similar to the T56, designated the T78, as far back as 1964, intended for use in long endurance patrol aircraft; this engine was successfully tested, showing over 35% improvement in sfc at the design condition (16) but did not go into service. More recently, GE under subcontract to Lockheed re-examined cycles for a similar long endurance mission (12); it was concluded yet again that a simple cycle turboprop of advanced design (22, 2400 F) was superior to both a regenerative turboprop (13, 2400 F) and a regenerative/intercooled turboprop (22, 2400 F). Using the conventional turboprop as a base, the mission fuel + engine weight was 9.5% higher for the regenerative cycle and 18.7% higher for the regenerative/intercooled cycle, combined with an increase in nacelle drag. It seems clear that if these more complex cycles can not show a gain on this long duration mission they are unlikely to be competitive for higher speed commercial transports.

CANDIDATE CONFIGURATIONS

At the period when the earlier large turboprops were designed pressure ratios achievable on a single spool compressor were limited to about 10, and the Tyne achieved the highest pressure ratio in service of 14 using a twin-spool compressor. Modern developments in compressor aerodynamics using multiple rows of variable stators, pioneered by GE on the J79, permit much higher pressure ratios on a single spool. The LM 2500 industrial derivative of the CF 6 demonstrated a pressure ratio of 16, and the inner core of the V2500 is capable of a pressure ratio of 20 in 10 stages. These developments give the engine designer much greater flexibility than in the past, and an advanced turboprop with pressure ratios of 15-25 could be laid out in four basic configurations as shown in Fig. 8.

(i) Fixed turbine

This approach has been very widely used on the T56, Dart, 331 and Astazou. Although the fixed shaft unit is essentially intended for fixed speed operation, some reduction in speed for fuel economy is possible. The Series IV T56, for example, can increase rotational speed by 3% for hot day take-off and reduce speed by 5% for low altitude loiter at 500 ft and 210 kt (13). The mechanical design is simplified, but at very high pressure ratios efficiency penalties may result from the fact that the propeller and compressor must operate at the same speed. Transient response on approach is excellent because the compressor need not be accelerated to increase power.

(ii) Free turbine, single spool compressor

This configuration is also very widely used on the PT6, T700, and T64 and was pioneered on the Proteus. The use of a free turbine opens up the market to both turboprop and turboshaft versions which is important in widening the potential sales base. Power setting is controlled by fuel flow to the gas generator and the propeller speed can be set independently of the compressor speed. This permits variation of propeller rpm with flight speed, which is attractive both from fuel economy and internal noise points of view. Reduction in power requires reduced compressor speed, so the compressor must be accelerated to restore power; it is not anticipated that this will present any significant problems.

(iii) Twin spool compressor, propeller driven by LP turbine

The Tyne is the only turboprop to have entered service in this configuration, but this approach has been proposed by both PW (14) and GE (15) for advanced turboprop. The LP compressor is coupled to the propeller, and it would probably be necessary to incorporate variable stators to accommodate variable propeller speeds. This compressor arrangement would suffer less penalty from propeller speed restrictions than the single shaft engine, as only part of the compression system is affected.

(iv) Twin spool compressor with free turbine

At the present time the PW 100 is the only turboprop using this configuration, although it is also used in the Gem turboshaft and a variety of industrial derivatives of aero engines. In many ways this seems the ideal situation regarding design and operational flexibility, as compressor and propeller speeds are completely independent. The mechanical design, however, becomes more complex with the introduction of three shafts rather than two. It is worth noting that the Tyne is in production as a marine engine, with a free turbine and rear drive; this configuration would be ideally suited to a pusher type arrangement.

It is not possible to make categorical statements regarding the best arrangement, and this would clearly depend on the past experience of the particular design team and the power rating. It does appear, however, that all four configurations are quite viable; as the pressure ratio increases the twin-spool compressor becomes more likely.

TRANSMISSION CONSIDERATIONS

The development of suitable high power transmissions is a major requirement for the introduction of the propfan into airline service. The T56 and Tyne represent the highest power turboprops built in the western world, and the most experience has been gained on the more than 14000 T56 engines which have accumulated over 100 million flight hours. Experience with these high power gearboxes has been good, but considerably higher powers will be required in the future. These successful gearboxes were designed some twenty years ago, and there have been major advances in stress analysis and design technology which will have a major impact on the design of new gearboxes. From the airline point of view it is clear that the propeller/gearbox combination should not present any significantly different maintenance cost or problem compared with the fan and thrust reverser on conventional turbofans. Studies (16) have shown that this goal can be achieved, but there is no doubt there will be airline scepticism until this has actually been demonstrated.

The design of the gearbox will be heavily dependent on whether a single propeller or contra-props are used. Up to about 10,000 shp it is not anticipated that the gearbox will be excessively difficult to design and develop. Allison (17) have tested a 12,000 shp gearbox, driven by a pair of T56 engines. They suggest that at high powers the specific weight of the gearbox may increase from about 0.1 lb/hp for the T56 to about 0.15 lb/hp at 30,000 shp. The next generation of gearboxes will be designed to achieve a life in regular operation of 25,000 hr or more.

As power requirements increase, alternative arrangements may find favour. GE, for example, are proposing a revolutionary counter-rotating 'unducted fan' which entirely dispenses with a gearbox. This requires considerable technology advances to build a turbine with contra-rotating rotors and no stators. Another possibility, suggested by Rolls Royce (18) is the dual cycle engine which combines a turbofan with a geared propfan; this configuration would lead to some loss of propulsive efficiency but a substantial reduction in gearbox power. The general arrangement of such an engine is shown in Fig. 9.

Another possible solution is torque limiting of the engine at take-off conditions, with the power limited to the maximum cruise rating at altitude. As the aircraft climbs and the density decreases the throttle is opened to maintain constant power. This was proposed as far back as 1956 on the Bristol Orion; with a cruise power of 3500 eshp at 350 mph and 30,000 ft, the power available at SLS was 8,000 eshp. The Orion was torque limited to maintain constant power with altitude, a notable feature being the ability to offer the SLS rating for all airfield elevations and temperatures. Financial restrictions in the mid Fifties resulted in the UK Government only supporting one large turboprop, and the Orion was dropped in favour of the Tyne. There is no doubt that this approach would be valuable to-day in tackling the problem of excessive gearbox powers.

The inlet arrangement to the compressor is strongly dependent on the gearbox arrangement, which may be in line with an annular intake (e.g. Dart, Tyne) or offset (e.g. T56, T64, PW100, 331). Recent aircraft studies have suggested the use of rear mounted pusher propellers, examples being the Beech Starship and the Gates Learjet/Piaggio projects. Similar arrangements have been proposed for large aircraft. This is obviously an attractive method of isolating the propeller noise from the passenger cabin but it may bring structural and installation problems. From the engine viewpoint, however, it presents a good solution to the intake design, especially for higher flight speeds, and can readily be met using a rear drive arrangement such as exists on the Marine Tyne.

CONCLUSIONS

The advanced turboprop provides a means of achieving significant reductions in fuel burn relative to turbofans of the same level of technology. Power requirements are in excess of those actually in service or available, and the technical risks involved may make engines in the 10-15,000 shp range a logical starting point. The goal of 0.8 Mach Number set by NASA may be too ambitious and an aircraft capable of M 0.7 for use on shorter routes may be a better proposition. The engine technology certainly exists and very high performance gas generators, with considerable advances in cycle parameters over existing turboprops, could be developed in the normal time frame for new engines. The transmission represents the biggest unknown at the higher power levels, but would not be a major problem for powers of about 10,000 shp.

For aircraft intended for service in the early 1990s, the engine selection and start of development must take place in the immediate future.

ACKNOWLEDGEMENTS

The author would like to thank NSERC for their financial support and Ken Bunker for his assistance.

TABLE I

<u>Aircraft</u>	<u>Max T.O.W.</u> (lb)	<u>Powerplant</u> (ehp)	<u>Max Cruise</u> (mph)	<u>Range</u> (miles)	<u>Passengers</u>
Brittania	185,000	4 Proteus x 4450	357/30000	5300	139
Electra	116,000	4 Allison x 4050	405/22000	2770	74-98
TU 114	396,800	4 NK12 x 12,000	497/32800	6200	120-220
Vanguard	146,500	4 Tyne x 5500	425/20000	3100	139

TABLE II

	<u>Viscount</u>	<u>Vanguard</u>	<u>DC9/727</u>
Toronto-Winnipeg	3 hr 50 min	2 hr 55 min	2 hr 28 min
Toronto-Chicago	1 55	1 35	1 28
Montreal-Toronto	1 30	1 15	1 5

REFERENCES

1. Some Maintenance Aspects of Viscount Operation
E.R. Major
Journal of Royal Aeronautical Society, Vol. 60, Sept. 1956,
pp. 605-617.
2. The Significance of Propulsion in Commercial Aircraft Productivity
B.N. Torell
Aeronautical Journal, Dec. 1975, pp. 537-549.
3. Selection of the Vickers Vanguard by Trans-Canada Air Lines
J.T. Dymont
Canadian Aeronautical Journal, May 1958, pp. 149-155.
4. The Regeneration of the Turboprop
J.F. Coplin
Aeronautical Journal, Jan. 1984, pp. 427-434.
5. Potential Benefits for Propfan Technology on Derivatives of
Future Short-to-Medium Range Transport Aircraft
I.M. Goldsmith, J.V. Bowles
AIAA Paper 80-1090, June 1980.
6. Fuel Saving Potential of Mach 0.8 Twin Engine Propfan Transports
F.J. Davenport
Canadian Symposium on Energy Conserving Aircraft, National Research
Council of Canada, Oct. 1977.
7. Prospects for Energy Conserving STOL Transports Using Propfans
B. Eggleston
Ibid
8. Turboprop Engine Propulsion for the 1990s
H.J. Banach and C.N. Reynolds
AIAA Paper 81-16848, Aug. 1981.
9. A New Generation T56 Turboprop Engine
W.L. McIntire
ASME Paper, 84-GT-210, June 1984.
10. The Pratt and Whitney PW100 - Evolution of the Design Concept
R.E. Morris
Canadian Aeronautics and Space Journal, Vol. 28, Sept. 1982
11. A Review of Commuter Propulsion Technology
A. Brooks and R. Hirschcron
SAE Paper 820716, May 1982.
12. Advanced Turboprop Engines for Long Endurance Naval Patrol
Aircraft
R. Hirschcron and R.H. Davis
ASME Paper 82-GT-217, March 1982.
13. A T56 for the 1990s
Flight International, 15 Jan. 1983.
14. Some Aspects of Propfan Propulsion Systems Analysis
R.W. Owens and W.W. Ferguson
SAE Paper 821358, Oct. 1982.
15. Alternative Concepts for Advanced Energy Conservative Transport
Engines
R. Hirschcron and R.E. Neitzel
SAE Paper 780550, 1978.
16. Evolution of the Turboprop for High Speed Air Transportation
G.E. Holbrook and G. Rosen
ASME Paper 78-GT-201.
17. Next Generation Turboprop Gearboxes
W.L. McIntire and D.A. Wagner
ASME Paper 82-GT-236.
18. Large Turbofans to the Year 2000
M.R. Williams
Aeronautical Journal, Jan. 1984.

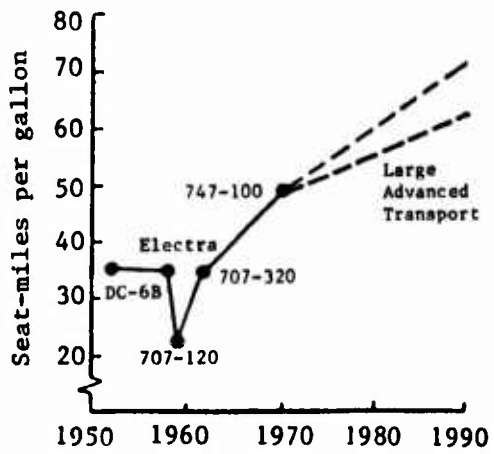


FIG. 1

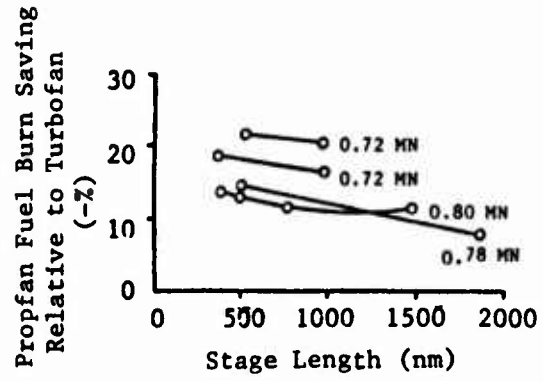


FIG. 2

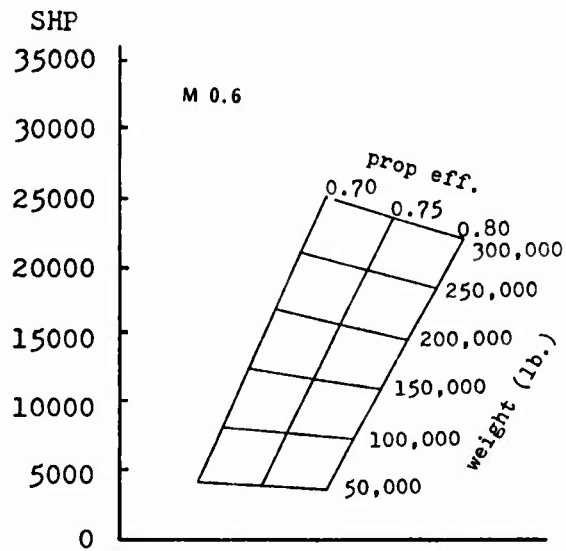
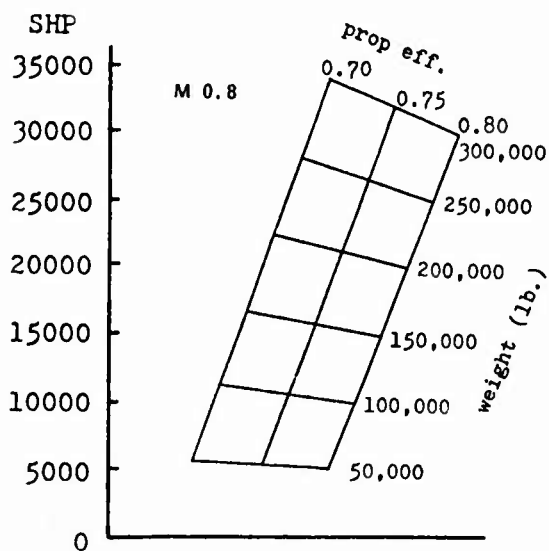


FIG. 3

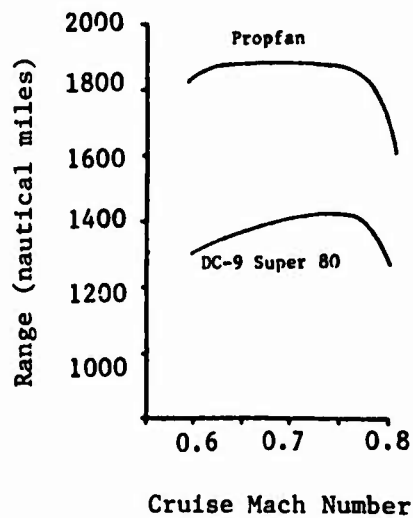
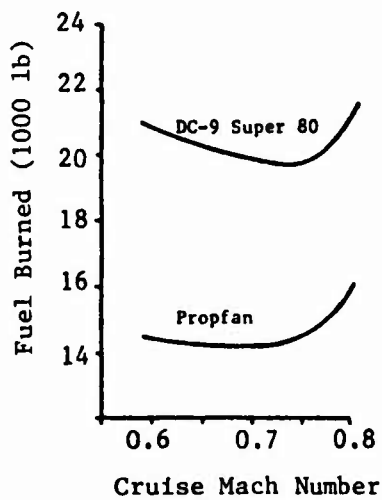


FIG. 4

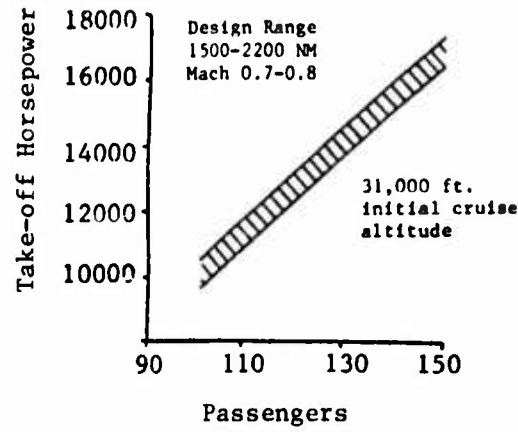


FIG. 5

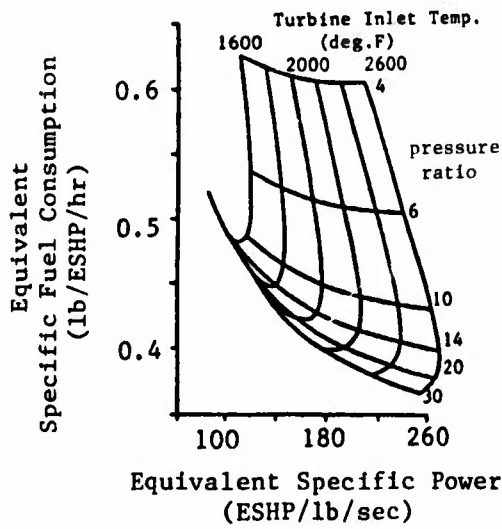


FIG. 6

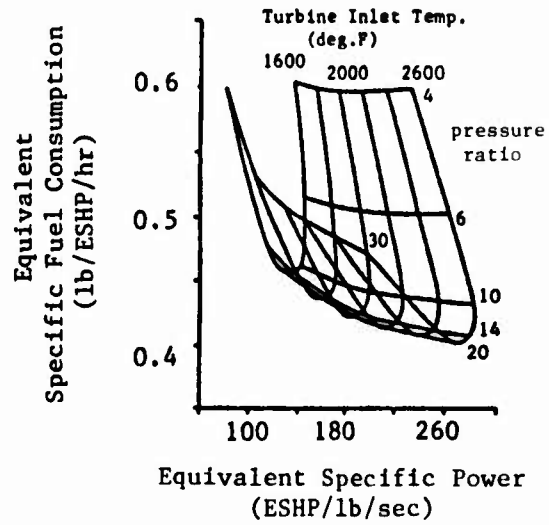


FIG. 7

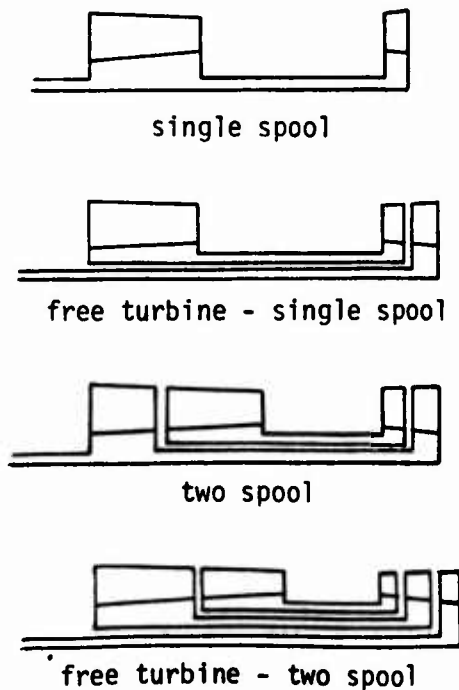


FIG. 8

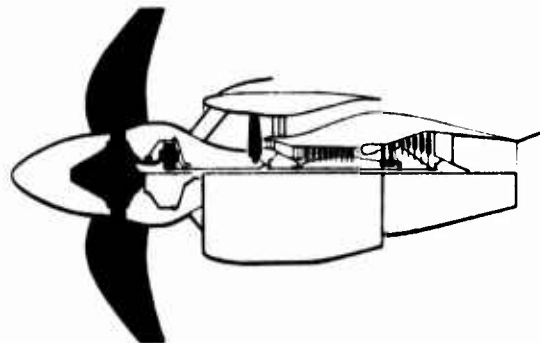


FIG. 9

AEROACOUSTIC WINDTUNNEL MEASUREMENTS ON PROPELLER NOISE

by
 F.-R. Grosche and H. Stiewitt
 DFVLR Institute for Experimental Fluid Mechanics
 Bunsenstrasse 10, D-3400 Göttingen, F.R.G.

SUMMARY

Model tests were conducted in a low speed windtunnel to determine the sound radiation of 5 propellers with different blade designs including variations of thickness ratios, blade profiles, blade planforms and blade tip configurations. The diameter of the propellers was 0.9 m, the propeller speed was kept constant. The tip Mach number was $M_T = 0.66$ and the helical tip Mach number varied between 0.66 and 0.69. The main objectives were to investigate the effects of blade geometry on near-field and far-field noise and to locate the dominant sound sources in the propeller plane, radiating to the observer, by means of a highly directional microphone system. The results include:

- Comparisons of noise spectra of different propeller configurations
- Near-field sound pressures as function of axial distance from the propeller plane
- Directivity of sound radiation from the moving blades.

LIST OF SYMBOLS

a_c (m/s)	sound velocity, $a_0 \approx 340$ m/s
b (m)	half-width of diffraction image $b \approx 3\lambda$
C_T	thrust coefficient $C_T = T/(\rho n^2 d^4)$
d (m)	propeller diameter, $d = 0.9$ m
f (Hz)	sound frequency
l (m)	chord length of propeller blades
M_T	propeller tip Mach number $M_T = \pi \cdot d \cdot n / a$
M_{hT}	propeller helical tip Mach number
n (1/s)	propeller speed
r (m)	radial coordinate
R (m)	propeller radius
T (N)	propeller thrust
U_∞ (m/s)	free stream velocity
X (m)	axial coordinate
L (dB)	sound pressure level (SPL)
δ^* (deg)	blade angle measured at $r = 254$ mm
λ (m)	acoustic wave length
ρ (kg/m ³)	density of air
BPF (Hz)	blade passing frequency $BPF \approx 80$ Hz

1. INTRODUCTION

Earlier investigations e.g. [1-4] have demonstrated that the acoustic data provided by static propeller tests are not always representative for the propeller noise radiated under real flight conditions. This is due to additional sound components which are caused mainly by the distortions of the inflow to the propeller plane due to the absence of the mainflow which results from the forward speed of the aircraft. Therefore, acoustic propeller tests with simulation of forward velocity by a wind tunnel flow have become a more and more accepted technique, particularly if one intends systematic studies of the sound source mechanisms and of possibilities of noise reduction. Results of experiments with a small scale propeller model (41 cm diameter) in the 3x3 m² low speed windtunnel of DFVLR Göttingen are presented in [4]. They show a marked effect of the inflow conditions (e.g. pusher versus tractor propeller) and exhibit the generation of high frequency tones caused by periodic laminar vortex shedding from the propeller blades. Based on the experience gained in this investigation, a more extensive test program was conducted in the meantime with larger model propellers and a more elaborate set-up. The tests were connected with the development of an advanced propeller for commuter type aircraft which was carried out by Dornier Aircraft Co. in cooperation with Hoffmann Propeller Co., University of Stuttgart and DFVLR [5]. In the context of this work, the sound radiation and aerodynamic performance of 5 model propellers-including 2 new designs - was investigated. Main objectives of the acoustic measurements were

- to determine effects of blade geometry on noise generation
- to check noise prediction procedures

- to locate the dominant sound sources within the propeller plane, radiating to the observer
 - to provide model data for the assessment of scale effects by comparison with flight test results and with model experiments at different scale [6, 7].
- The results of the aerodynamic measurements are given in Ref. [8].

2. EXPERIMENTS

2.1 Test set-up

The experiments were conducted in the open test section of the low speed windtunnel of DFVLR Göttingen which has a square nozzle of 3 m by 3 m exit area and a test section length of 6 m. The maximum wind velocity is $U_\infty \approx 65$ m/s. Walls, ceiling and floor of the measuring chamber around the test section were covered with sound absorbing material (polyurethane foam). The lower limiting frequency of this sound absorbing treatment was ≈ 400 Hz.

The model propellers, diameter $d = 0.9$ m, were driven by an electric motor enclosed in a streamlined nacelle which was equipped with a 3-component balance for determining thrust and torque of the propeller simultaneously with the acoustic measurements. The streamlined fairings of the nacelle and of its supporting struts were not mechanically connected to the balance. The balance measured therefore only the aerodynamic forces and moments acting on the propeller and spinner. The maximum speed of the electric motor was 5000 rpm and the maximum power was 65 KW. Fig. 1 and Fig. 2 show the test rig and its installation in the windtunnel.

2.2 Acoustic instrumentation

Fig. 3 illustrates the test set-up and the acoustic instrumentation. Three types of acoustic measurements were carried out:

Near-field measurements were made at a distance $0.14 d$ from the blade tips ($d =$ propeller diameter) by means of an in-flow microphone equipped with a nose cone for suppression of flow noise. The microphone was mounted on a traversing unit - see Fig. 4 - which allowed to vary the microphone position in axial direction between $0.5 d$ upstream and $1.0 d$ downstream of the propeller plane. The relative distance $0.14 d$ corresponds to the distance between the cabin wall and the propeller tips of the Dornier experimental aircraft used for flight tests [7]. This enables one to compare the model results with full scale measurements and to estimate the excitation of the fuselage wall by the propeller noise.

The acoustic far field was measured by four microphones outside of the windtunnel flow. The microphones were located at a distance $3 d$ from the propeller axis at angles between -15 deg. and $+30$ deg. relative to the propeller plane, see Fig. 3.

An acoustic mirror telescope [4, 9] was used as a highly directional microphone to investigate the sound radiation from different parts of the propeller disk in direction to the observer. A concave mirror of 1.6 m diameter was installed - as shown in Fig. 3 - at 4 m distance from the propeller. The contour of the mirror is a part of an ellipsoid of revolution which has focal points on the mirror axis at 0.57 m and 4.0 m distance from the center of the mirror. Thus, if a microphone is located at the focal point close to the mirror, the sound radiated to the mirror from the close vicinity of the second focal point will be concentrated on this microphone by reflection from the mirror surface. Also, the sound emanating from other volume elements not too far from the second focal point will be focused by the mirror on microphones positioned at proper points in the vicinity of the first focus.

The spatial resolution of the system is limited mainly by the diffraction of the sound waves at the edge of the mirror, since the wave lengths for the frequency range of interest are not very large as compared to the mirror diameter. Therefore, the spatial resolution improves with sound frequency. The diameter of the diffraction image of a point source is proportional to the acoustic wave-length. For the system used here the half-width of the diffraction image is $b \approx 3 \lambda$, see [9]. Also, the spatial resolution of the mirror system is much higher in directions normal to the mirror axis than in the direction of the axis, compare [4, 9].

Utilizing these characteristics of the elliptical mirror, the three microphones No. 1, 2, 3 shown in Fig. 3 were mounted in front of the mirror in such positions that microphone 1 received mainly the sound radiated to the mirror by the lower part of the propeller disk and microphone 2 and microphone 3 received the sound from the central and upper part respectively. The mirror system was located downstream of the propeller at the angle of 15° to the propeller plane, see Fig. 3a, since this was considered to be approximately the angle of maximum noise radiation.

The signals of all microphones were simultaneously recorded on tape and were analyzed later by means of a constant-bandwidth narrowband spectrum analyzer. The same instrument was used on-line for quick-look and for comparison with the results of the later off-line data processing.

2.3 Model propellers

All propellers investigated had 4 blades, variable pitch and a propeller diameter $d = 0.9$ m which is $1/3$ of the diameter of the full scale propeller [7]. The blade designs may be characterized briefly as follows:

- No. 1: Conventional thin blade sections, rounded blade tips. This propeller was used as reference propeller, see [5].
- No. 2: Experimental blades with thicker sections and angular blade tips.
- No. 3: Same blades as No. 2, but with "Q-Tips", that is the tips were bent back by 90 deg to form end-plates for the pressure surface of the blade, see Fig. 4. (This photo also shows the acoustic mirror telescope. The three microphones in front of the mirror are equipped with polyurethane-foam windshields to reduce the flow noise caused by secondary flows outside the test section).
- No. 4: Newly developed blades with advanced high lift profiles and optimized planform. This is the "ZKP-propeller" in ref. [5], see there for details.
- No. 5: Same design as No. 4, but blade tips swept back to reduce compressibility effects. Fig. 5 shows propellers No. 4 and No. 5 mounted on the test rig. Details can also be found in ref. [5].

The radial distributions of maximum relative thickness of the blades are given in Fig. 6. In the outer region, $r/R > 0.5$, the blades of propellers No. 4 and No. 5 are thicker than the blades of propellers No. 2 and No. 3, and these in turn are thicker than the blades of propeller No. 1.

The blade planforms of propeller No. 1 and No. 4 are shown in Fig. 15 of [5]. Near the tip, the blades of No. 4 (and No. 5) have smaller chord compared to No. 1 in order to minimize the strength of the tip vortex, as explained in [5].

2.4 Measurements

Since this investigation was aimed mainly at the effects of blade geometry for a given tip Mach number similar to the one anticipated for the operation of full scale propeller, all measurements reported in this paper were made at constant propeller speed $n = 4773$ rpm ≈ 80 rps equivalent to a tip Mach number $M_T = 0.66$. Free stream velocity was varied between $0 < U_\infty \leq 58$ m/s, thus helical tip Mach number varied between $0.66 \leq M_{hT} < 0.69$. Blade angle δ^* was also varied between 15 deg. and 30.8 deg. to obtain data for different thrust coefficients.

Nearfield measurements and farfield measurements were carried out separately and the traversing mechanism for the nearfield microphone was removed during the farfield measurements (including the tests with the acoustic telescope) in order to avoid measuring errors due to reflections.

3. RESULTS

The results of the nearfield measurements comprise the effects of propeller blade geometry on the tonal noise components. They give a comparison of experiment with prediction, and they illustrate the dependence of the tone noise levels on the axial distance from the propeller plane. The farfield results also show the effects of blade geometry on the tonal noise components. The results of the directional microphone measurements demonstrate the difference in sound radiation between the blades advancing to and receding from the observer.

3.1 Acoustic Near-Field

Fig. 7 shows two typical spectra measured at $0.14 d$ distance from the blade tips in the propeller plane, and $0.5 d$ downstream at the same radial position. The tonal components in the plane of the propeller are up to 25 dB higher than the broad-band noise floor which is in part due to the background noise of the tunnel. The repeatability of the tone levels was in the order of ± 1 dB.

The spectrum obtained at the position $0.5 d$ downstream of the propeller plane exhibits much lower tonal peaks, the higher harmonics of the BPF being masked by the background noise. This already indicates that the rotational noise levels at the side of the fuselage decrease sharply with increasing distance from the propeller plane.

Comparison of different propellers

The tone SPLs of all propellers measured with the same flow conditions and blade angle are given in Fig. 8. The propellers with the same profiles and chord distributions, but different blade tip configuration - prop. No. 2 and No. 3, and prop. No. 4 and No. 5, respectively - generate almost exactly the same nearfield sound pressures. Thus, the blade tip modifications (Q-tip, swept back-tip) seem to have practically no effect on the acoustic near-field at the given test conditions. Similar findings are published in [10]. Significant differences in the near-field SPLs occur in Fig. 8 between the thin-bladed propeller No. 1 and all the other propellers at the blade passing frequency, and between propellers No. 2/No. 3 and all the other propellers at the higher harmonics of the BPF. These results are essentially corroborated by Fig. 9 and Fig. 10 which display the SPL values of the blade passing frequency and of its 4th harmonic as functions of thrust of the model propeller. (1000 N thrust is equivalent to a thrust coefficient $C_T = 0.19$). For the BPF, all propellers except No. 1 generate approximately the same SPLs at a given thrust, the levels increasing by about 10 dB from zero thrust to maximum thrust equivalent to a thrust coefficient $C_T \approx 0.25$. For the 4th harmonic, propellers No. 2 and No. 3 produce about 5 dB higher SPLs in the nearfield than the other propellers. The new propeller designs No. 4 and No. 5 differ appreciably only at zero thrust, where the swept-back

propeller No. 5 produces less noise than propeller No. 5 with straight blades. Considering the fact that the thickness/chord ratio of the propeller No. 4 and No. 5 is higher than the thickness ratio of the other propellers (see Fig. 6), a positive effect of the new profiles and planforms of propellers No. 4 and No. 5 on the near-field noise can be recognized.

Comparison of experiment with prediction

A prediction scheme for the near-field propeller noise was developed by Dornier Co. [11] on the basis of [12, 13, 14]. Fig. 11 shows predicted SPL values of tonal components and broad-band noise in comparison to a measured spectrum obtained with the reference propeller (No. 1) at a thrust coefficient $C_T = 0.05$. The agreement is quite satisfactory. Unfortunately no comparisons exist at the time being for higher loading and for the other propellers.

Dependence of near-field SPL on axial distance from the propeller plane

Fig. 12 illustrates the variation of tone SPLs with axial position at the same radial distance $d = 0.14$ from the propeller tips as in Figs. 7-11. The SPL values of the BPF and of its 1. and 2. harmonic are plotted against the axial distance x/d from the propeller plane for measurements with the propellers No. 4 and No. 5. Blade angle was $\delta^* = 30.75$ deg and thrust coefficients were $C_T = 0.24$ for propeller No. 4 and $C_T = 0.23$ for propeller No. 5. Similar results were obtained also at other conditions. The maximum SPLs do not occur in the propeller plane but slightly upstream at $x/d \approx 0.1$. According to [15], this can be explained by interference between the thickness noise and loading noise components. With increasing distance from the maximum, the SPLs decrease within half a propeller diameter by approximately 15 dB for the BPF and by almost 30 dB for the 2. harmonic.

3.2 Acoustic Far-Field

Fig. 13 gives a typical example of the far-field spectra obtained by the microphone located at 15 deg downstream of the propeller plane, see Fig. 3. As compared to the near-field spectra, the tone/background noise ratio is smaller and the tone SPLs vary less systematically with the number of the harmonic. The latter may be due to interference effects caused by sound reflections at parts of the experimental set-up. Therefore we consider the far-field data to be less accurate than the near-field results. Fig. 14 and Fig. 15 present - in analogy to Fig. 9 and Fig. 10 - the variation of SPL values with propeller thrust for the blade passing frequency and for its 3. harmonic. For the sake of clarity of the graphs, regression analysis was applied to the measured data which was far more extensive than the near-field data, and only the straight lines obtained by regression are plotted for the 5 propellers in Figs. 14 and 15. The standard deviation of the data was in the order of ± 2 dB.

According to Fig. 14 there is no significant difference in sound generation between all the propellers except No. 1 for thrust values > 600 N, $C_T > 0.11$. The slope of SPL versus thrust is steeper for the thin bladed reference propeller No. 1. Thus it appears to be more noisy at high thrust values than the other propellers, and to generate about the same SPL as propellers No. 2, 4, 5 at low thrust. The slope of SPL versus thrust is about the same for propellers No. 2 and No. 3, and for propellers No. 4 and No. 5 respectively. This indicates in accordance to the near-field results that the modifications of the propeller tips are of minor importance as compared to the general geometry of the blades.

The results for the 3. harmonic of the BPF support this statement, see Fig. 15. They show a significantly lower gradient of SPL versus thrust for propellers No. 2 and No. 3 than for the other propellers. Also, the differences in absolute SPLs are greater between the propellers at the 3. harmonic than at the BPF, compare with Fig. 14, and the new propellers No. 4 and No. 5 appear to be less noisy than the others over most of the thrust range. These findings again agree qualitatively with the near-field results given in Figs. 9 and 10.

A more detailed analysis of the far-field data is required, since the measured noise levels depend in fact not only on the thrust coefficient but also to some extent on the particular combinations of advance ratio, blade angle and flow Mach number (propeller speed is constant). Thus, the far-field results presented in Fig. 14 and Fig. 15 should be considered as preliminary and as showing only the general trends.

3.3 Sound source location

Typical results of the measurements with the acoustic mirror telescope are given in Fig. 16 and Fig. 17 which show the spectra of the propeller noise received by mirror-microphones No. 1 and No. 3, respectively. As already pointed out in section 2.2, the propeller noise radiated to the mirror from the lower part of the propeller disk is focused on microphone 1, and the noise from the upper part of the propeller disk is focused on microphone 3. Comparing Fig. 16 and Fig. 17 we find that for frequencies $f > 4.5$ kHz (which are equivalent to $f > 1.5$ kHz for the full scale propellers because of the model scale 1 : 3) the intensity of the sound received from the upper part of the propeller plane, where the propeller blades move towards the mirror telescope, is about 20 dB higher than the intensity of the sound received from the lower part of the propeller plane, where the blades are receding from the telescope. The level difference of 20 dB means that the noise radiated to the observer (telescope) by the approaching blades is by a factor of 100 stronger than the noise radiated by the receding blades. Thus, practically all the high

frequency noise comes from the blades approaching the observer.

This effect can be explained by the well known convective amplification of the noise radiation of moving sources. According to theory - see e.g. [16] - the difference in noise radiation of dipole sources approaching to or receding from the observer with Mach number M_S is

$$\Delta L = 20 \log \left(\frac{1 + M_S}{1 - M_S} \right)^2$$

For a rough estimate we assume the noise sources of the propeller blades to be concentrated at 0.8 of the propeller radius, $r_S = 0.8 R$. The source Mach number is then $M_S = 0.8 M_T$, and with the constant tip Mach number $M_T = 0.66$ of our tests (see section 2.4) one obtains

$$\Delta L \approx 20,$$

which agrees with the experimental result for frequencies $f > 4.5$ kHz.

At lower frequencies, the measured difference ΔL decreases and becomes practically zero for the BPF and its 1. harmonic, while it is still approximately 10 dB for the 2. harmonic of the BPF. This effect is to be expected because of the decrease of spatial resolution of the mirror telescope with increasing acoustic wave length, see section 2.3.

4. CONCLUDING REMARKS

The following conclusions may be drawn from the results of these model tests:

- At the given helical tip Mach numbers $M_{HT} \leq 0.69$, the sound radiation of the propellers investigated is determined mainly by the thickness ratios, planforms and profiles of the blades. Modifications of the blade tips were of minor importance.
- Measured near-field spectra agree well with theoretical prediction
- Near-field SPLs at constant, small radial distance from the propeller plane decrease rapidly with axial distance from the propeller plane. This is particularly true for the harmonics of the blade passing frequency. The maximum SPLs occur slightly upstream of the propeller plane, in accordance with theoretical prediction.
- The propeller blades radiate high frequency noise mainly in their direction of motion. This can be explained by the convective amplification of the noise emission of moving sources.

5. REFERENCES

- [1] F.B. Metzger and B. Magliozzi,
New Directions in Aircraft Propulsor Noise Research
Society of Automotive Engineering, Business Aircraft Meeting, Wichita, Kansas,
April 8-11, 1975.
SAE-Paper 750515
- [2] F.B. Metzger and B. Magliozzi,
Progress Report on Propeller Aircraft Fly over Noise Research
Society of Automotive Engineering, Business Aircraft Meeting, Wichita, Kansas,
April 6-9, 1976
SAE-Paper 760454
- [3] R.J. Pegg, B. Magliozzi, F. Farassat,
Some Measured and Calculated Effects of Forward Velocity on Propeller Noise
ASME-Paper 77-GT-70 (1977)
- [4] F.R. Grosche and H. Stiewitt,
Investigation of Rotor Noise Source Mechanisms with Forward Speed Simulation
AIAA-Journal Vol. 16, No. 12, Dez. 1978, pp 1255-1261
- [5] H. Zimmer, R. Hoffmann, K.H. Horstmann,
Investigations of Modern General Aviation Propellers
AGARD Fluid Dynamics Symposium on "Aerodynamics and Acoustics of Propellers"
Toronto, Canada, 1-4 October 1984
AGARD Conference Reprint No. 366, Paper 16
- [6] H. H. Heller and M. Kallergis,
Full-Scale and Model-Scale Windtunnel Test on the Near-field Noise Characteristics
of Aircraft Propellers
AGARD Fluid Dynamics Symposium on "Aerodynamics and Acoustics of Propellers"
Toronto, Canada, 1-4 October 1984
AGARD Conference Reprint No. 366, Paper 27

- [7] I.U. Borchers, P. Bartels, H. Zimmer, F.-R. Grosche,
Akustische Untersuchungen im Rahmen der Entwicklung des ZKP-Experimentalpropellers
der Leistungsklasse 750 PS
FASE/DAGA '82, Fortschritte der Akustik,
- [8] W. Stäger and W. Böddener,
Weitere aerodynamische Messungen an Modellpropellern im 3-m-Niedergeschwindigkeits-
Windkanal Göttingen
DFVLR Internal Report 16 100 - 81 C 29 (1981)
- [9] G. Chicocchia and F.-R. Grosche
Shear layer effects on the performance of an acoustic mirror microphone system
DFVLR-Forschungsbericht 79-30 (1979), 101 paper, 71 fig., 15 ref.
- [10] W.C.G. Trebble, J. Williams, R.P. Donnelly
Some Aeroacoustic Windtunnel Measurements, Theoretical Predictions, and Flight-Test
Correlations on Subsonic Aircraft Propellers
AGARD Fluid Dynamics Symposium on "Aerodynamics and Acoustics of Propellers"
Toronto, Canada, 1-4 October 1984
AGARD Conference Reprint No. 366, Paper 25
- [11] I.U. Borchers, H. Zimmer, P. Bartels, G. Mühlbauer, H. Köster, F.-R. Grosche,
F.X. Wortmann,
Entwurf, Bau und Erprobung eines verbesserten Propellers für Flugzeuge der Allgemeinen
Luftfahrt
Dornier-Bericht, 2. BMFT Statusseminar Luftfahrtforschung und Luftfahrttechnologie,
Garmisch-Partenkirchen, 8./9. Okt. 1980
- [12] I.E. Garrick, C.E. Watkins
A Theoretical Study of the Effect of Forward Speed on the Free Space Sound-Pressure
Field Around Propellers
Report 1198, National Advisory Committee for Aeronautics, Washington, D.C. 1953
- [13] R.A. Arnoldi,
Propeller Noise Caused by Blade Thickness
Report R-0896-1, United Aircraft Corporation Research Department, East Hartford,
Conn. 1956
- [14] F.W. Barry, B. Magliozzi,
Noise Detectability Prediction Method for Low Tip Speed Propellers
Techn. Report AFAPL-TR-71-37, Wright-Patterson Air Force Base, Ohio, 1971
- [15] J.B.H.M. Schulten,
Aeroacoustics of Wide-Chord Propellers in Non-Axisymmetric Flow
AIAA-Paper-84-2304, Oct. 1984
- [16] H.V. Fuchs
Aeroacoustic Measuring Technique in or Outside Turbulent Flows
AGARD Report No. 686, August 1979

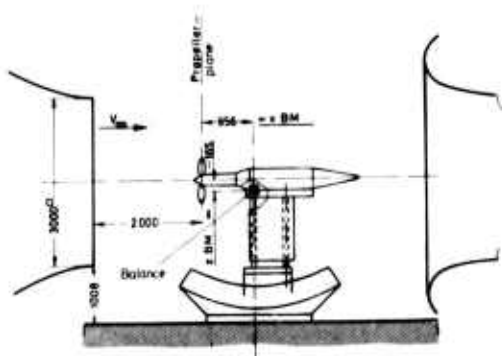


Fig. 1 Propeller test rig

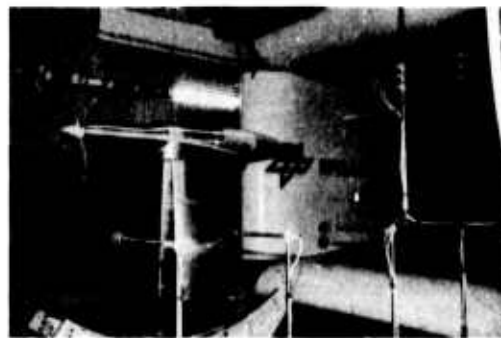


Fig. 2 Test rig in the windtunnel

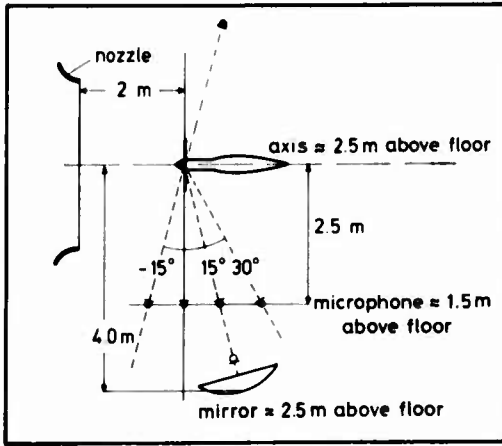


Fig. 3a Test set-up, plan view

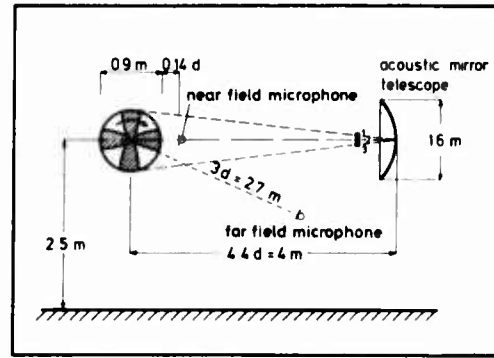


Fig. 3b Test set-up, front view



Fig. 4 Propeller No. 3 (with Q-Tips) and acoustic mirror telescope

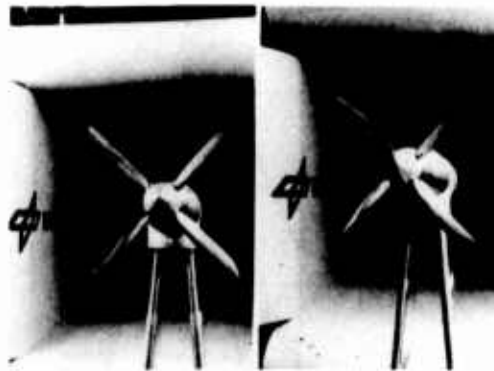


Fig. 5 Propellers No. 4 (left) and No. 5 (right)

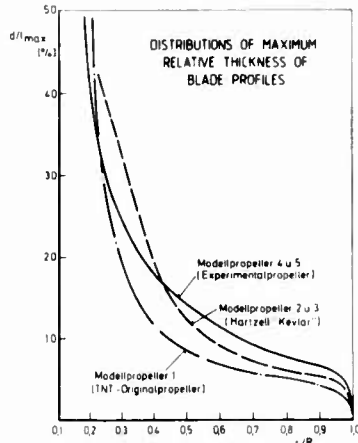


Fig. 6 Radial distributions of maximum relative blade thickness of the propellers investigated

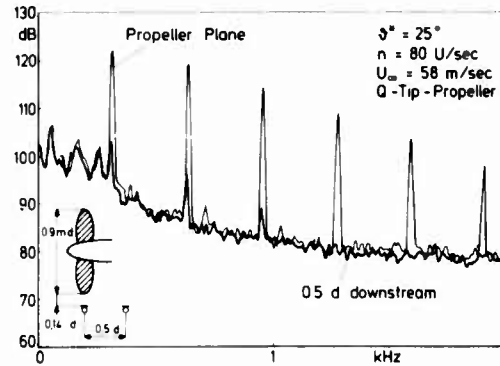


Fig. 7 Typical near-field noise spectra of propeller No. 3, thrust coefficient $C_T \approx 0.023$

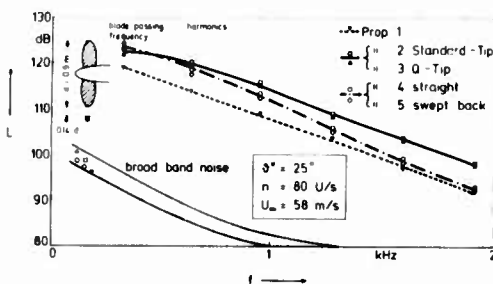


Fig. 8 Comparison of tone SPLs of all propellers at same blade angle and flow conditions

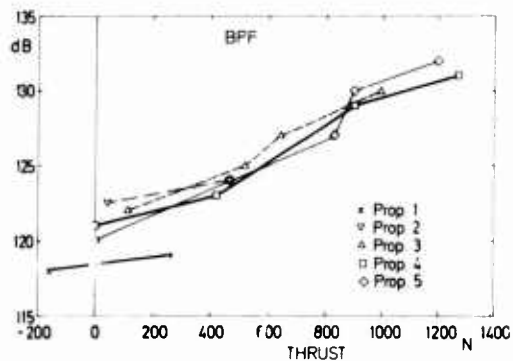


Fig. 9 Near-field SPLs of the BPF as functions of propeller thrust. Microphone position as in Fig. 8

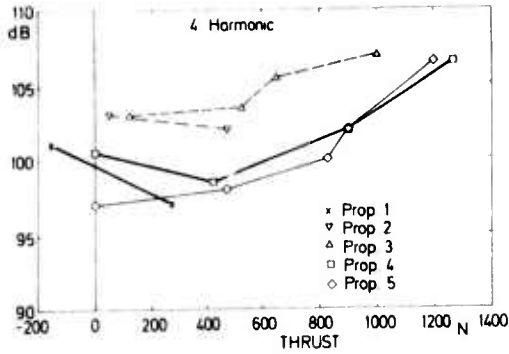


Fig. 10 Near-field SPLs of the 4. harmonic of the BPF as functions of thrust. Microphone position as in Fig. 8

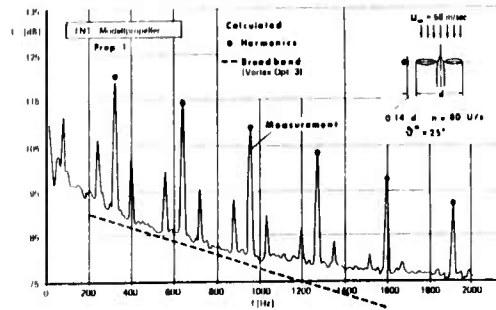


Fig. 11 Comparison between measured and predicted near-field noise spectra

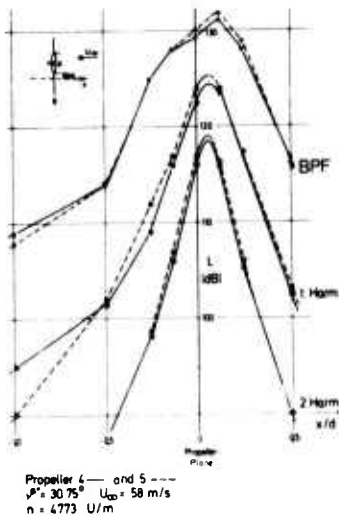


Fig. 12 Variation of near-field SPL with distance x/d from the propeller plane

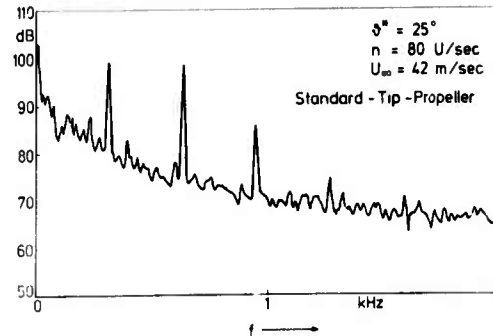


Fig. 13 Typical far-field noise spectrum of propeller No. 2, thrust coefficient $C_T \approx 0.09$

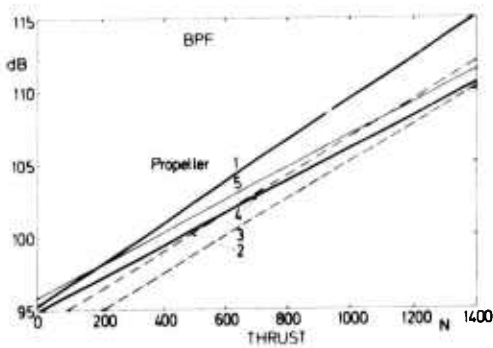


Fig. 14 Far-field SPLs of the BPF as functions of propeller thrust. Measured at 15° downstream of propeller plane

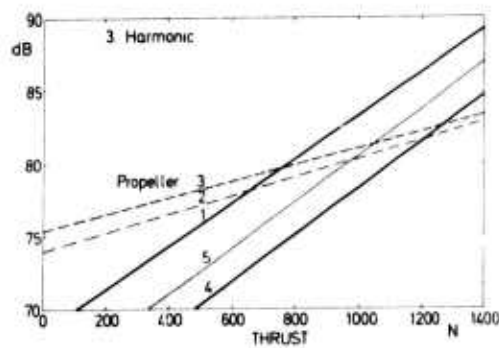


Fig. 15 Far-field SPLs of the 3. harmonic of the BPF as functions of propeller thrust

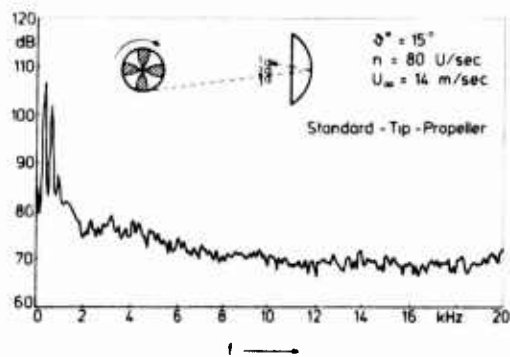


Fig. 16 Spectrum of the sound radiated by the propeller blades receding from the acoustic mirror telescope (sound received by microphone No. 1)

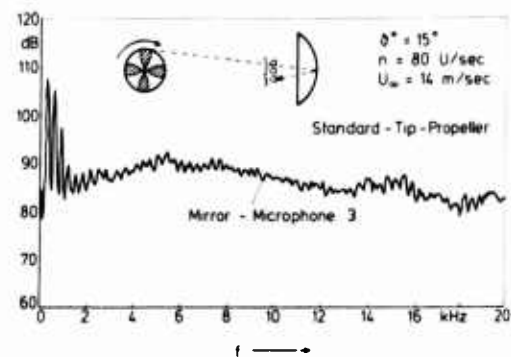


Fig. 17 Spectrum of the sound radiated by the propeller blades advancing towards the acoustic mirror telescope (Sound received by microphone No. 3)

**SOME AEROACOUSTIC WINDTUNNEL MEASUREMENTS,
THEORETICAL PREDICTIONS, AND FLIGHT-TEST CORRELATIONS
ON SUBSONIC AIRCRAFT PROPELLERS**

by

W.J.G. Trebble

Aerodynamics Dept., R.A.F., Farnborough, UK

J. Williams

Aeronautics and Astronautics Dept., Southampton University, UK
(Formerly of R.A.F., Farnborough)

R.P. Donnelly

Noise Engineer, Dowty Rotor Ltd., Gloucester, UK

SUMMARY

An analysis is presented of the results of an integrated research programme on subsonic aircraft propeller noise carried out jointly by the Royal Aircraft Establishment and Dowty-Rotor Ltd. (1979-'83), with participation by Shorts (1979-'81), and with support from the Department of Industry throughout. The research work combined acoustic windtunnel experiments on propellers at model-scale and full-scale with aircraft flight tests and theoretical predictions, centred primarily around the Dowty R.292 four-bladed propeller (ARAD-sections) as fitted specially to the Shorts 330 aircraft, while enabling direct comparison also against the standard Hartzell S.330 five-bladed propeller (NACA 64-sections). Supplementary noise experiments on other propellers and allied theoretical prediction studies, involving also British Aerospace (HS 748 aircraft) and Southampton University (Aeronautics Dept), have been taken into account in the present paper.

1. INTRODUCTION

An integrated research programme involving windtunnel, theoretical and flight studies on aircraft propeller noise (far-field and near-field) was started at the Royal Aircraft Establishment¹ during 1979, in conjunction with Dowty Rotor and Shorts, relating to feeder-line aircraft in particular but with light and heavy aircraft also borne in mind. Acoustic measurements were first made at full-scale for the Hartzell S.330 five-bladed propeller with classical NACA 64-sections, both in the RAE 24ft anechoic tunnel and in flight on the Shorts 330 aircraft. More extensive measurements soon followed for a Dowty R.292 four-bladed propeller with modern ARAD-sections, not only at full-scale in the 24ft tunnel and on the Shorts 330 aircraft, but also at 1/4-scale on a geometrically similar propeller-model in the RAE 1.5m acoustic tunnel. The 1/4-scale model was shown to have closely similar noise-spectra characteristics and aerodynamic performance coefficients to those of the full-scale propeller. Moreover, substantially better noise measurements proved attainable in the new 1.5m tunnel than in the old 24ft tunnel, though perforce at smaller model scale².

For the prediction of propeller noise spectra, the then available theoretical frameworks were investigated and computer programs were developed by Dowty, to examine separately and conjointly the basic blade rotational contributions to discrete-frequency levels, from steady aerodynamic loading (Garrick and Watkins), unsteady aerodynamic loading (Lowson) and blade-thickness air-volume displacement (Succi/Hawkings). The broadband noise contribution, manifested conventionally as a low-level region peaking somewhat at frequencies of the order of 10 times the blade-passing-frequency (BPF), had to be estimated by purely empirical formulae (Magliozzi) which seemed too inaccurate.

Since mid-1981², RAE and Dowty Rotor have jointly carried out further data analysis, windtunnel experiments, flight tests and theoretical prediction developments concerning propeller noise characteristics in the near-field and far-field. The research was naturally centred round Dowty propeller concepts, for which details and design experience were readily available. Supplementary noise experiments and theoretical studies, involving also British Aerospace (HS748) and Southampton University (Aeronautics Dept.) were included in this integrated research programme on propeller aeroacoustics before its termination in 1983 because of organisational changes at RAE.

This AGARD paper attempts primarily an analysis of the results now available from the foregoing research programme, with only brief reference to the many essential advances in the windtunnel, flight-test and theoretical techniques developed for this research^{1,2,3}. The aeroacoustic windtunnel experiments are reviewed (Section 2) with specific regard to full-scale propeller-nacelles in the 24ft anechoic tunnel, model propeller-nacelles in the 1.5m acoustic tunnel, and a complete twin-propeller aircraft model of the Shorts 330 in the 24ft tunnel. Our analysis of the windtunnel results (Section 3) first assesses the experience gained on correlation of propeller noise and allied aerodynamics at model and full-scale. Then appraisals follow of the observed effects of propeller axis inclination to the mainstream, blade-surface roughness application, some blade geometry changes, blade-number/solidity variation and airframe installation interference. Empirical parametric relations are derived for the fundamental BPF tone level SPL_1 at a near-field location, in terms of the propeller power coefficient C_p , helical tip Mach number M_{th} , mainstream Mach number M_0 , and blade number B . The decay of the near-field noise level SPL_q of the harmonic tones with increasing harmonic number q is also correlated simply in terms of q and M_{th} .

The flight research trials carried out at RAE Bedford airfield on the Shorts 330 aircraft and the B.Ae. HS.748 aircraft are noted³. However, because of space limitations, discussion is limited to only a few flight-tunnel and flight-theory correlations of the near-field and far-field noise characteristics as investigated on these two aircraft.

The basic theoretical frameworks employed for the practical prediction of propeller discrete-frequency noise components are discussed in respect of both near-field and far-field applications, while broadband noise estimation problems are also summarised for completeness (Section 4). Correlations between our theoretical predictions and experimental results are presented for the several Dowty propeller designs investigated, with additional comments on allowance for airframe installation effects (Section 5). Mention is made of some current research on propeller aerodynamics and noise at Southampton University in conjunction with Dowty Rotor, with RAE co-operation in respect

of test facilities and experience, and strongly encouraged by the continuing support of the Department of Industry.

2. AEROACOUSTIC WINDTUNNEL RESEARCH PROGRAMME

2.1 Full-Scale Propeller-Nacelles in 24ft Anechoic Tunnel

Full-scale windtunnel tests on operational propellers are desirable not only for prediction and correlation of flight-test results from the same installed propellers, but also to establish and improve the range and validity of propeller research at model scale. The open-jet test-section of the 24ft anechoic tunnel (7.3m diameter) fortunately has a quiet powered nacelle (1.2m diameter and 4m length) powered by a 1200 kW three-phase electric motor, specifically designed for driving medium-size propellers (Fig.1). The existing nacelle-rig, mounted from the two-component lower-balance in the floor of the tunnel, allows thrust to be measured along the tunnel airstream axis, while lift arising from any non-axisymmetric interactions or from the permissible tilting of the thrust axis (up to 10°) can also be measured.

Noise measurements were made using 6mm microphones traversed to provide an array of near-field and far-field positions, as illustrated in Fig.1, the microphones were equipped with ogival nose cones and aligned into wind, or with standard protective grill and axis normal to tunnel centre-line, according to their location inside or outside the mainstream. The positioning of the nearest microphone to the propeller was chosen to give a representation of the typical full-scale clearance between the propeller tip and the side of the aircraft fuselage.

Aeroacoustic experiments using the full-scale propeller-nacelle rig in the 24ft anechoic tunnel were first made in 1979/80 on three alternative propellers also tested in flight on the Short's 330 aircraft. The Hartzell five-bladed propeller of the production aircraft has conventional NACA 64-series sections and standard tips⁴, the Hartzell 'Q-tip' version of this has its tips bent as lower-surface end-plates in the direction of rotation, and the Dowty four-bladed propeller has modern ARA-D sections and standard tips ($D_p = 2.8\text{m}$)^{2,5}. Later complementary tunnel/flight experiments also included the Dowty four-bladed R.212 propeller with classical NACA 16-series sections as fitted to the B.Ae. HS 748 aircraft ($D_p = 3.7\text{m}$)⁶.

Naturally, the full-scale tunnel investigations were carried out over the blade test conditions recommended and permitted by the propeller manufacturer. Typically (Dowty R.292), both noise and performance measurements were made at rotational speeds varied from 1100 to 1700 rev/min for a range of practical blade settings β , at mainstream speeds of about 30 m/s and 50 m/s EAS, thoroughly covering the values of blade helical tip-speed and advance-ratio $J (= U_0/nD_p)$ relevant to low-speed operation. Also, to simulate the higher values of J appropriate to cruise conditions, extra performance measurements were made at coarser blade settings with lower rotational speeds at the tunnel maximum airspeed ($U_0 = 50\text{ m/s}$). Sometimes the tests have been limited by the total combined electrical load (2000 kW) available for powering simultaneously the tunnel-drive fan and the test propeller. The experimental results are referred to briefly under the relevant items of Section 3.

2.2 Model-Scale Propeller Nacelles in 1.5m Acoustic Tunnel

The aeroacoustic research on this propeller-nacelle pedestal-rig in the 1.5m acoustic tunnel takes advantage of the greater flexibility and accessibility of the model and rig than possible with the remote full-scale propeller in the 24ft anechoic tunnel, permitting more varied and more rapid testing at much less running costs. The compact quiet drive is provided by a three-phase variable-frequency electric motor housed in a cylinder of 140mm diameter with a length of 400mm (Fig.2). The long nacelle provides ample space for the installation of strain-gauge links for the measurement of torque and thrust, to complement tachometer readings of rotational speed. Experience has shown that over 100 Nm of torque can be produced by this water-cooled motor without the creation of excessive heating. Upper test limits have been determined solely by the propeller manufacturers recommendation that the maximum rotational speed should not exceed 8000 rev/min and that the blades should not be allowed to enter into a flutter mode, which is a condition clearly identified by a sudden change in noise quality with the generation of multi-tones of sub-harmonics of the blade-passing frequency. In general, the model propeller investigations were made at rotational speeds from about 4000 to 8000 rev/min at mainstream speeds of 30 m/s and 50 m/s EAS, for a range of practical blade settings β 0.7, more than covering the range of blade-tip helical Mach number and aerodynamic incidence appropriate to full-scale propeller operation in low-speed flight. In addition, performance measurements were made at coarser blade settings with lower rotational speeds at the tunnel maximum airspeed of 57 m/s EAS, to simulate the blade spanwise loading distributions relevant to cruise conditions.

Noise measurements were made using 6mm condenser microphones, primarily in the plane of the propeller disc; at near-field positions representative of the distance between the propeller tip and practical fuselage side (typically $1.44 R_p$ from the propeller axis); and at far-field positions limited by working-chamber boundary consideration (typically $4.17 R_p$ from the propeller axis). Since the near-field microphone was of necessity positioned inside the airstream, it was equipped with an ogival nose cone aligned directly into wind. The far-field microphone, in the anechoic working-chamber but well outside the mainstream flow, was provided with a standard protective grill and directed with its axis normal to the tunnel centre-line. To investigate the variation in signal with the fore-and-aft location of the measuring point relative to that at the disc plane, some linear traverses were carried out parallel to the tunnel centre-line, as illustrated by Fig.2

During the period 1980-83, basic 1/4-scale model experiments were first carried out on the Dowty R.292 four-bladed propeller ($D_p = 0.7\text{m}$), with ARA-D type sections and with the spanwise distribution of chord/thickness/twist shown in Fig.3. The experimental results, obtained with the propeller axis at zero inclination to the airstream and with a minimum-size nacelle to streamline the electric drive motor, provide the main background to our initial discussion and parametric analysis of basic propeller characteristics relating to aerodynamic performance, far-field noise and near-field noise (Sections 3.1 and 3.2).

Wake traverse surveys behind the model propeller indicated that the centre of the blade loading was at 85% to 90% radius, which agreed with Dowty Rotol theoretical predictions. Local Mach number in this outboard region of the blade is high, and implied that some reduction in propeller noise level could be effected simply by unloading the outboard region by shape modifications from the standard tip. The spear tip configuration Dowty R.292S (Fig.3) represents one possible design change which has now been tested, again as a 1/4-scale model in the 1.5m acoustic tunnel (Section 3.5).

To check the effects of a significant change in blade geometry from the modern ARA-D section blades of the

Dowty R.292, the Dowty R.212 four-bladed propeller with NACA-16 section blades (Fig.3) was next investigated using a 1/5-scale model ($D_p = 0.74\text{m}$) in the 1.5m acoustic tunnel⁶. Here, apart from thrust/torque and noise measurements some relevant wake studies were undertaken and completed.

The influence of propeller axis inclination to the tunnel mainstream, represented for practical convenience here by yaw (ψ) of the axisymmetric body in the horizontal plane, was investigated on the Dowty R.292 model⁷, particularly as regards noise in the disc plane near-field ($r = 1.6 R_p$); with microphones located directly above the propeller axis ($\theta = 0^\circ$), directly to the side ($\theta = 90^\circ$) and directly below ($\theta = 180^\circ$). All three microphones were translated as appropriate when the propeller axis was inclined from the mainstream direction ($\psi = 0^\circ$ to 10°), so as to maintain the same geometrical positions in the new propeller disc plane with nominally their original distances from the propeller disc periphery. Some differences in propeller axis inclination effects experienced by RAE during model and full-scale tunnel tests on other propellers have been noted (Section 3.3).

The influence of blade surface roughness was again examined mainly on the Dowty R.292 model⁷, though experience on other propellers warrant comparison (Section 3.4). Allied comments on the effects of propeller scale, slipstream turbulence and other inflow disturbances have at this stage to be of a qualitative nature based on our accumulated experience to date on various models and full-scale operational propellers.

Any reduction in blade tip speed, to radically reduce noise at source, implies in practice increased solidity of the propeller to maintain the same disc loading in the absence of further radical improvements in blade design. Consideration has therefore been given to propellers with increased number of blades, while still taking advantage of modern ARA-D type sections (Section 3.6). The effect of the number of blades (3, 4, 6 and 8) has been investigated on a new Dowty Rotor model ($D_p = 0.68\text{m}$), using the R.320-type blade geometry illustrated in Fig.3. Here the measurements of aerodynamic and noise characteristics were made at propeller rotational speeds from 4,700 to 6900 rev/min (max. allowable) at mainstream speeds of the 1.5m acoustic tunnel of 30, 40, 50 and 60 m/s for a range of blade settings between 12.5° and 45° . Again some performance measurements were made at the coarser blade settings with lower rotational speeds at the higher tunnel speeds, to simulate the higher J-values appropriate to cruise conditions.

2.3 Complete Aircraft Model in 24 ft Anechoic Tunnel

A 1/4-scale model of the Shorts 330 aircraft was constructed at RAE Farnborough for aeroacoustic experiments in the 24ft anechoic tunnel, with the twin R.292 four-bladed propellers (standard tip, $D_p = 0.7\text{m}$) already tested in the 1.5m acoustic tunnel, to investigate installation effects associated with the presence of a practical wing-fuselage-nacelle combination. The model (Fig.4) with cropped wing tips to increase tunnel jet-boundary clearance, was hung from the three-component overhead mechanical-balance to provide total lift, along-wind force (thrust-drag) and pitching moment, in addition to the propeller-nacelle strain-gauge recordings for axial thrust and torque. Noise measurements were again made using 6mm condenser microphones fitted with forward-facing nose-cones; six near-field microphones were mounted just outside the fuselage side-wall at useful comparative locations inside and fore-and-aft of the propeller disc plane, as in the full-scale flight tests. A far-field microphone was mounted directly below the model ($r/R_p = 5.6$) and traversed along a linear track fore-and-aft parallel to the tunnel test-section centre-line. The acoustic instrumentation and analysis techniques for these complete-model experiments in the 24ft anechoic tunnel follow those for the pedestal propeller-nacelle models in the 1.5m acoustic tunnel.

The permitted model testing time (May 1982) allowed only part of the planned aero-acoustic measurements and model configuration changes to be undertaken, before termination of this RAE propeller research programme. Nevertheless, extensive measurements were completed with the flaps retracted and with the flaps fully-down, in each case with the wing struts and undercarriage housing either fitted or absent, the tail-unit being retained throughout for aerodynamic reference. Both noise and performance tests were made for propeller rotational speeds varied from 4000 to 6000 rev/min, at mainstream speeds of 30 m/s and 50 m/s, with three blade-angle settings ($\beta = 17^\circ, 22^\circ, 27^\circ$), and at three aircraft attitudes ($0, 5^\circ, 10^\circ$). Measurements were carried out with the twin propellers rotating together (anti-clockwise viewed from front), and some with the starboard or port propeller only rotating. Data reduction and allied interpretation has not yet been completed for all these results, but some comments can be made about the airframe installation effects (Section 3.7).

3. ANALYSIS OF WINDTUNNEL RESULTS

3.1 Correlation of Propeller Aerodynamics at Model and Full-Scale

Investigations with the 1/4-scale model of the Dowty R.292 propeller in the 1.5m acoustic tunnel and with the full-scale propeller in the 24 ft anechoic tunnel have been made over the wide range of blade angle setting from $\beta_{0.7} = 10^\circ$ to 45° at airspeeds up to about 50 m/s. For practical tunnel testing, the minimum airspeed ($U_{nom} = 0$) is that induced in the tunnel solely by the propeller slipstream, the additional constrictions in the circuit of the 1.5m tunnel resulting in somewhat lower minimum airspeeds than those experienced with the full-scale propeller in the 24ft tunnel. Naturally, on the 1/4-scale model the rotational speed has to be increased by a factor of 4 over that for the full-scale model to give the same blade tip-speed. The model thrust balance measures the total axial load on the nacelle and propeller and thus indicates a small nacelle drag (4N at 50 m/s) in the absence of the propeller. The value of the installed thrust with the model propeller operating has thus been obtained by adding the value of this nacelle tare drag to the measured thrust (ranging up to 1000N). For the full-scale propeller tests, similar corrections are applied to the total along-wind force to allow for the tare drag of the nacelle and nearby balance struts.

From the power (deduced from the torque) and thrust measurements made at various blade settings between $\beta_{0.7} = 10^\circ$ to 45° , the power coefficient ($C_p = \text{Power}/\rho n^3 D_p^5$) and thrust coefficient ($C_T = \text{Thrust}/\rho n^2 D_p^4$) are evaluated as functions of the advance ratio ($J = U_0/nD_p$) for mainstream speeds of about 30 m/s and 50 m/s at least. In Fig.5, interpolated values of C_p and C_T relating to the R292 propeller are cross-plotted against blade-setting for J-values of 0.4, 0.8 and 1.2. These results indicate generally good agreement between the model and full-scale propeller, though there is some discrepancy (of the order of 1° in blade setting) under low loading conditions at $J = 1.2$ (i.e. when $C_p < 0.1$). The peak efficiency ($\eta = JC_T/C_p$) occurs at relatively low thrust loadings of the propeller, particularly with coarse blade settings. For example, the peak efficiency of 86% observed at a blade setting of 35° actually occurs when the model thrust is only 90N ($C_T = 0.12$) so that there an error of 1N would change the peak efficiency value by 1%.

At a fixed blade setting, the propeller results should exhibit a unique relationship between C_p (or C_T) and J,

irrespective of speed unless there arise flow changes associated with the differences in Reynolds number or Mach number. However, it is observed that at low values of J (i.e. high rotational speed) there is some increase in the values of C_p and C_T at fixed values of J with increase in mainstream speed. Presumably, these differences result from the fact that both a higher rotational speed and tip Mach number is required in the faster airstream to maintain the same value of J . For example, with $J = 0.6$, helical tip Mach numbers (M_h) of 0.47 and 0.78 would be required at airspeeds of 30 m/s and 50 m/s. Identical trends were also evident during 1/5-scale and full-scale testing of the Dowty R.212 propeller, in the 1.5m tunnel and 24ft tunnel respectively, both as regards the good agreement between model and full-scale at the same test speed (i.e. same tip Mach number) and the noticeable increase in both C_p and C_T at fixed J with increase in mainstream speed.

This implies that, at least for highly-loaded conditions, it is preferable to make aerodynamic performance investigations at the correct Mach number, even though this may entail model testing at reduced scale in order to make the tests in a facility with a suitable speed range. However, from our experience, we could not yet justify reductions to much below one-fifth scale (e.g. to one-tenth) for reliable full-scale prediction, as distinct from basic research studies. More generally, any differences in spinner/root geometry and blade deformation characteristics associated with scaling demands seem likely to be much more important than changes in blade Reynolds number, especially at highly-loaded conditions and high tip Mach numbers.

For fundamental propeller studies and for propeller installation considerations, the propeller wake explorations are also of interest. The possible occurrence of contrasting pressure distributions in the slipstream is illustrated in Ref.6 for the R.212 model propeller. Under low thrust loading conditions pertaining to a fine blade setting ($\beta = 9.3^\circ$), the peak pressure ($C_p = \bar{p} - p_0 / q_0$) occurs at some 45% radius with a tendency to negative thrust loading in the tip region; the peak pressure moves out to 80% radius for the highly loaded conditions, while more uniform pressure distributions are produced at intermediate loading. Comparison of the pressure distribution at two streamwise stations also confirms the anticipated contraction in slipstream diameter with rearward movement behind the propeller disc. Extensive propeller wake investigations, both windtunnel and theoretical, have recently been completed by Tadghighi and Hurst at Southampton University for the R.292 model propeller with variation of the tip shape and the number of blades.

3.2 Correlation of Propeller Noise at Model and Full-Scale

The noise characteristics of the Dowty R.292 full-scale propeller under axial flow conditions in the 24ft anechoic tunnel are discussed extensively in Section 5 of Ref.2. Basically, it should be noted that the highest value of tonal SPL occurs at the blade-passing-frequency (BPF), but that significant tones also exist at multiple harmonics of that frequency ($q \times \text{BPF}$). Moreover, the SPL of the BPF tone rises significantly with increases in blade-tip Mach number M_h and in blade-angle β , while there are usually complementary growth in the number and levels of the measurable harmonic tones with increasing M_h .

Typical one-third octave spectra in both the near-field and far-field for the quarter-scale model at 4800 and 6400 rev/min show very similar trends to the corresponding full-scale results at 1200 and 1600 rev/min though the blade settings differ slightly for the two propellers². Moreover, both propellers exhibit the phenomenon of a rise in the high-frequency content of the broadband noise levels at low blade setting (i.e. when the propeller is lightly loaded). The spectra can be compared usefully at a constant Strouhal number ($S = fD_p/V_{tip}$) for nearly identical blade settings, e.g. for $\beta = 21\frac{1}{2}^\circ$ in Fig.6. Here the blade-passing frequency for the four-bladed propeller occurs at $S = 4/\pi$. Comparisons made at equivalent full-scale frequencies of 1200 and 1600 rev/min show good agreement in the spectra except in the range $5 < S < 20$. To some extent the discrepancy in this region is attributable to the intrusion of tunnel background noise in the 24ft tunnel tests particularly at the lower rotational speed of 1200 rev/min, but the high turbulence level in the 24ft tunnel (0.5%) as against 0.25% may also be adversely affecting propeller broadband noise at frequencies below 2 or 3 kHz. There is some supporting evidence of this effect from some recent acoustic research on helicopter rotors, and confirmation may be possible from further investigation with the model propeller.

Typical comparisons of narrow-band spectra for the model and full-scale propellers are shown in Fig.7 at both near-field and far-field microphones, with a tunnel airspeed of 30 m/s. Again a blade setting of $\beta = 21\frac{1}{2}^\circ$ is chosen and the spectra at equivalent full-scale rotational speeds of 1200 and 1600 rev/min are illustrated. For the near-field microphone $r/R_p = 1.4$, there is good correlation between the measured values of the sound pressure levels of the various tonal harmonics in the spectra particularly at the higher rotational speeds, though again the broadband noise is noticeably larger for the full-scale propeller.

Values of the near-field SPL for the Dowty R.292 propeller at the fundamental blade-passing-frequency (BPF), derived from the tunnel measurements over a large range of blade settings and rotational speeds at $r/R_p = 1.4$, have been plotted in Fig.8 against the following parametric expression in terms of the power loading C_p and the helical tip Mach number M_h for mainstream Mach number M_0 up to 0.15.

$$\text{SPL}_1 = 162 + 10 \log_{10} (M_h^8 C_p^2) - 40 M_0.$$

There is very good parametric correlation on this basis and very good agreement (within ± 2 dB) between the results for the model and full-scale propeller at appropriately scaled distances. Additionally, the fall-off of the noise level of the various harmonics below the SPL of the fundamental tone are plotted against M_h in Fig.9 for $r/R_p = 1.4$. Over the range $0.65 < M_h < 0.87$, the SPL of the q^{th} harmonic (frequency = $q \times \text{BPF}$) correlates reasonably for both full-scale and model in the form

$$\text{SPL}_q = \text{SPL}_1 - 25(q - 1)(0.95 - M_h)$$

Corresponding comparisons of the far-field noise measurements ($r/R_p = 4.2$) are complicated by the effects of low-frequency reflections from the nearby acoustic curtain in the 24ft tunnel. Certainly, the far-field results at model scale appear to be far more orderly than the measured values (uncorrected) for the full-scale propeller. In Ref.2, a simple correction formula has been deduced for the effect of this reflection on the SPL of the tones for the full-scale propeller; Fig.7b lists both measured and corrected values of the tone SPL values. Broadly speaking, application of the correction gives appreciably better agreement between the results for the full-scale and quarter-scale propellers.

The 'far-field' station in our present tunnel tests ($r/R_p = 4.2$) is arguably so-called, in the sense that the instantaneous differences between the distances of the individual blade tips from the noise measurement position may be small but still of the same order as the wavelengths of primary interest, thus possibly resulting in constructive or

destructive acoustic interference with signal integration. This contrasts with conditions at the near field station ($r/R_p = 1.4$); where the noise signal is so dominated by the contribution from the closest blade tip that the other three blades make little contribution to the overall signal. Consequently, the variations of these 'far-field' spectra could be more complex than those of the near-field spectra, while the rate of fall-off SPL tone level with harmonic number at $r/R_p = 4.2$ could be somewhat different from that experienced at $r/R_p = 1.4$, as illustrated by comparison of Fig.7a and Fig.7b.

Similar comparative measurements of near-field and far-field noise for the Dowty R.212 (NACA 16) propeller at 1/5 scale in the 1.5m tunnel and full-scale in the 24 ft tunnel likewise showed excellent parametric correlation and good agreement between model and full-scale, as discussed in Section 3.5. The acoustic advantages to be gained from model testing in the quieter 1.5m tunnel are clearly demonstrated in Fig.7. Even at an equivalent rotational speed as low as 1000 rev/min full-scale and the high tunnel speed of 50 m/s, there is little contamination of the model propeller noise signal by the 1.5m tunnel background noise, though the corresponding full-scale propeller noise is completely swamped by the background noise in the 24ft tunnel. As with aerodynamic considerations (Section 3.1), it is advisable to make acoustic investigations near the correct M_h and M_o even if reduced model-scale is entailed. But from our experience we could not yet justify reductions to much below one-fifth scale (e.g. to one-tenth) if reliable prediction of full-scale noise spectra is required.

3.3 Influence of Propeller Axis Inclination

The influence of propeller thrust-axis inclination (upwards) relative to the direction of the oncoming airstream was first investigated at full-scale in the 24 ft anechoic tunnel, by noise measurements at two near-field microphone positions in the propeller disc plane. One station, at $r/R_p = 1.8$, was to the down-going side of the propeller disc, i.e. 'advancing blade' position with axis inclination, and the microphone remained in the same position when the propeller was tilted. The other station (at $r/R_p = 1.4$) was always located immediately below the propeller disc, being moved as the propeller attitude was altered so that its position remained in the inclined plane of the propeller disc and 0.6m outside its periphery.

Narrow-band noise spectra from the two microphones are presented for the Dowty R-292 propeller in Figs.10, with $\alpha = 0, 5^\circ$ and 10° , for a propeller blade setting $\beta = 24.5^\circ$, rotational speed of 1600 rev/min and airspeed of 30 m/s. Measurements made for other propeller test conditions indicate similar trends for the effect of propeller-axis attitude on noise levels. Although the development of an asymmetric inflow into the propeller disc with increase in incidence might well be expected to lead to an increase in propeller noise, little effect is observed consistently, on this propeller, at either microphone position. In contrast, some significant incidence effects had been observed during tests on the Hartzell full-scale propeller, particularly for the microphone mounted under the propeller where increases of up to 5 dB in the tonal SPLs had been recorded when incidence was raised from 0 to 10° .

A more extensive study of the influence of propeller axis inclination to the airstream was therefore undertaken on the Dowty R.292 propeller model in the 1.5m tunnel, for practical convenience by yaw ψ of the axi-symmetric propeller nacelle in the horizontal plane⁷. Two microphones were located in the disc plane near-field ($r/R_p = 1.51$ & 1.58) directly above and below the propeller axis ($\theta = 0^\circ$ & 180°) respectively. A third microphone was located directly to the side of the propeller axis ($\theta = 90^\circ$), at a greater distance ($r/R_p = 1.66$) for practical reasons. All three microphones were translated as necessary when the propeller axis was yawed away from the mainstream direction ($\psi = 0^\circ$ to 10°), so as to maintain the same geometrical positions in the new propeller disc plane with nominally their original clearance distances from the closest blade tip.

A typical comparison of narrow-band spectra obtained from these microphones at $\psi = 0^\circ$ to 10° is provided by Fig.11, for the datum blade setting $\beta = 20^\circ$. Overall, for a range of rotational speeds and tunnel speeds, the microphone above the propeller axis exhibits some 2 dB rise in the SPL of the fundamental tone due to 10° yaw, and similar rises in at least the second and third harmonics, but sometimes by up to 10 dB at higher harmonics where the SPL-values are relatively low. These rises may be expected from the increases in relative airspeed and in effective blade incidence leading to high loading as the 'advancing blade' passes closest to the 'above' microphone ($\theta = 180^\circ$), and from possible unsteady loading effects. The microphone to the side ($\theta = 90^\circ$) also exhibits greater SPL with yaw, though less significant than those for the microphone above. In contrast, the microphone below the propeller axis often exhibits lower tonal SPL-values with yaw, while any rises in SPL are insignificant, possibly because the 'retreating' blade with reduced relative airspeed and blade incidence then passes closest to this microphone.

3.4 Influence of Blade Surface Roughness

The sensitivity of the aerodynamic and noise characteristics of the quarter-scale R.292 propeller model to blade surface conditions was examined for the test condition $\beta = 23^\circ$, $U_o = 50$ m/s and $\psi = 0^\circ$ (axial flow), over the rotational speed range 4,000 to 7,200 rev/min⁷. For comparison with clean surface conditions, Ballatini roughness (0.25mm diam.) was applied liberally to the blade pressure and suction surfaces in turn. Expectedly, the surface roughness application to the pressure side only, caused little deterioration in aerodynamic performance; while additional application to the suction surface reduced C_T by as much as 0.03 and C_p by rather less, leading to a noticeable reduction in η (JC_T/C_p) below the clean blade values of Fig.5. Such drastic roughening of the blade suction surface beyond the needs of transition fixing may induce noise effects because of excessive thickening of the suction surface boundary-layer and possible unsteady or separated flows. Comparisons of narrow-band noise spectra (Fig.12) show tone level increases due to roughening of only 1 or 2 dB in the low harmonics. The broadband noise levels at frequencies above 1 kHz tend to increase by up to 4 dB with the roughening of the suction surface.

An earlier application of conventional transition strips to both surfaces of the clean blades on the R.292 model propeller, at 10% chord aft of the leading-edge, does not appear to have caused any significant changes in the SPL-values of the fundamental tone and harmonics, nor in the broadband noise at high frequencies (Fig.13). At this time, we have little full-scale experience of the effects of blade roughness or damage on the noise characteristics, since all the propellers tested in the 24ft tunnel were in excellent condition, without protuberances from possible anti-icing or anti-erosion devices.

3.5 Blade Geometry Effects

The Hartzell 5-bladed propeller (NACA 64-sections) has the same diameter (2.7m full-scale) as the Dowty R.292 4-bladed propeller (ARAD-sections) and broadly gives the same overall aerodynamic performance. The acoustic characteristics naturally differ in that the frequencies of the BPF tone and harmonics of the Hartzell are 1.25 times

those of the Dowty. Unweighted values of the near-field SPL for the Hartzell at its fundamental BPF satisfy a similar parametric correlation to that for the Dowty in terms of C_p , M_h and M_o ; but appear to be 2 or 3 dB lower from 24ft tunnel measurements in the disc plane⁴. This could reflect the inherently lower blade-loading by some 20% of the Hartzell with its classical blade section, requiring of course the individual blade area outside its $0.2 R_p$ section to be little different (lower by only 3%) despite its larger number of blades. When frequency-dependent subjective weighting is applied, the subjective reductions in the SPL of the low frequency tones are less favourable towards the Hartzell, because its blade passing frequency is 1.25 times that of the Dowty. Then, under some practical conditions of propeller thrust and rotational speed, both the A-weighted level of the predominant fundamental tone and the A-weighted overall level L_A of the whole spectrum can be a few dB(A) higher for the 5-bladed Hartzell than the 4-bladed Dowty. It is also relevant to note that the attenuation of the SPL_1 for the fundamental tone with rearward movement of the near-field microphone behind the disc plane tends to be less marked with the Hartzell than the Dowty.

The Dowty R.212 4-bladed propeller (NACA 16 sections) also exhibits similar noise characteristics, with good agreement established between full-scale and 1/5-scale windtunnel measurements (Fig.14). The empirical parametric relation for the BPF tone level SPL_1 , in terms of C_p , M_h and M_o , closely matches that quoted for the Dowty R.292, within an accuracy better than ± 2 dB except at very high helical tip Mach number ($M_h > 0.85$). The fall-off in the noise level SPL_q of the propeller-model harmonics with increasing harmonic number q correlates well with the relation

$$SPL_q = SPL_1 - 21(q-1)(0.95-M_h)$$

i.e. the decay is slightly less than for the Dowty R.292.

Other related results for another four-bladed propeller, with different R.320-type blades (ARAD sections), are discussed later in connection with considerations of the blade number. Altogether, the foregoing results imply that blade section shape changes have had little effect on the tonal strength for a prescribed aerodynamic performance, except at the extremities of the propeller operating range.

Two specific changes in blade-tip geometry have been investigated, as simple attempts towards the reduction of noise without significant deterioration in aerodynamic performance. The Hartzell 'Q-tip' version of their 5-bladed propeller has the standard tips bent through 90° in the direction of rotation, thus essentially providing 3% reduction in blade span and lower surface tip-end plates. Full-scale investigations made in the 24ft tunnel exhibited no noticeable improvement over the standard-tip propeller as regards noise and a slight deterioration in aerodynamic performance. This was later confirmed by RAF flight-test results on the Shorts 330 aircraft.

The Dowty 'spear-tip version' of the R.292 4-bladed propeller was designed with the intention of reducing noise by off-loading the blade tips; effected by a substantial change in chord distribution and some reductions in thickness/chord ratio near the tip, but minor changes in twist (Fig.3). Comparative investigations made on a 1/4-scale model in the 1.5m tunnel showed that the tone levels for the 'spear-tip' version R.292S are about 1 dB lower than those for the standard tip when compared at the same helical tip Mach number and same C_p . In particular, the earlier parametric relation for the noise level SPL_1 of the BPF tone at the near-field station again applied to an accuracy within ± 2 dB (Fig.8c). Additionally, the earlier parametric relation for the fall-off in harmonic tone level with harmonic number q applied to both the 'spear-tip' and 'standard tip' versions of R.292, over the range $0.65 < M_h < 0.87$, up to the maximum mainstream Mach number ($M_o < 0.15$) of the tunnel tests (Fig.9)

3.6 Effects of Variation of Blade Number/Solidity

A matched set of model propellers (0.68m diam.) with different multiples of identical R.320-type blades were constructed for the investigation of the effects of varying the number of blades, i.e. increasing the propeller solidity, in the 1.5m tunnel over a range of β° , rev/min and U_o . Two hubs were completed, so that configurations containing three, four, six and eight blades could readily be assembled. The hub diameters (181mm in each case) had to exceed the propeller motor diameter (140mm) in order to accommodate safely the large number of blades, so a long chamfered sleeve was fitted on the motor to blend in with the hubs.

The power and thrust coefficients of the four propellers are compared in Fig.15 at a constant blade setting of 25° . As mentioned previously, the relationship between the aerodynamic coefficients C_p (or C_T) and J is not independent of mainstream speed because of Mach number effects, but for clarity the values for the four-bladed and six-bladed propellers have been omitted at mainstream speeds other than 30 m/s. As might well be expected from augmenting induced flow effects with greater blade number, i.e. aggravating the influence of the downwash from the preceding blade on the following blades, increase of the number of blades at a fixed blade setting effectively reduces the blade aerodynamic incidences with resultant losses in both the power absorption per blade and the thrust per blade. This is accompanied by some reduction in efficiency, so that (at $\beta = 25^\circ$) the peak efficiency has been reduced from 82% for the three-bladed propeller to 74% for the eight-bladed propeller. However, at constant J , the reduction is less marked when the optimum blade-settings for each configuration are considered, though these still amount to some 5% reduction in efficiency at $J = 1$.

The noise spectra for the four propellers are basically similar to those already discussed, with of course a proportional increase in the fundamental frequency (at a prescribed rev/min) as the blade number is increased (Fig.16). But there is simultaneously a general reduction in the number of significant tones and lowering of their SPLs with increasing blade number at the same blade angle. An empirical analysis has been made to determine the main parameters affecting the SPL of the BPF fundamental tone at a near-field location ($r/R_p = 1.44$). As before², this parametric correlation first demonstrates that the BPF noise intensity I_1 is proportional to the square (C_p^2) of the power coefficient throughout the propeller speed range. Interpolation of the propeller noise levels at $C_p = 0.15$ and plotting against blade number B indicates that the noise intensity varies inversely as the fourth power (B^4) of the blade number, provided that the helical tip Mach number M_h does not exceed 0.7. Similarly, noise intensity is seen to vary with the eighth power (M_h^8) of the helical tip Mach number. In addition, there remains then some contribution from the mainstream Mach number (M_o), so that the following overall parametric formula is implied

$$SPL_1 \text{ of BPF} = [182 + 10 \log_{10}(M_h^8 C_p^2 B^{-4}) - 20 M_o] \text{ dB}$$

Comparison between the measured SPL_1 and estimates by this parametric formula are shown in Fig.17, and the SPL_1 -values are predicted to within some 2 dB for the model propellers with three, four, six or eight blades. The greatest discrepancies mainly occur at very low mainstream speed (nominally zero) when the propellers operate with the most disturbed inflow conditions.

Here it is relevant to recall the slightly different parametric formula derived earlier for the four-bladed R.292 model with carbon-fibre or glass-fibre blades, namely

$$\text{SPL}_1 \text{ of BPF} = [162 + 10 \log_{10} (M_h^8 C_p^2) - 40 M_0]$$

which does agree very well with the multi-blade formula for $B=4$ at $M = 0.2$. Since there is an implication that the SPL_1 of these early R.292 carbon-fibre blades is more dependent on mainstream Mach number than the R.320-type metal blades, it should be noted also that the hub/tip diameter ratio of the former is 0.22 compared with 0.27 for the latter, possibly contributing to some changes in the radial distribution of loading. Additionally, the multi-bladed dural propellers have root sections which are much thicker (near circular) than those of the composite R.292 model propellers. But perhaps this comparison serves better to illustrate the difficulty of accepting fundamental deductions from parametric relations derived by regression analysis without established theoretical affinity of the type discussed later (Sections 4 & 5).

3.7 Airframe Installation Effects

Although analysis of the aeroacoustic research on the 1/4-scale model of the Shorts 330 aircraft with wing-mounted twin propellers in the 24ft tunnel has not yet been completed (Section 2.5, Fig.4), some results relevant to propeller nacelle installation effects can be illustrated here. It will be recalled that six near-field microphones were mounted just outside the fuselage, together with one far-field traversing microphone. Measurements of noise and aerodynamic performance were made with the flaps retracted and with the flaps fully down, in each case with the wing-struts and undercarriage-housing either represented or absent.

Near-field noise spectra at the upper and lower microphone stations, for either single propeller or twin propellers operating, show that the propeller furthest from the microphone made little contribution to the signal strength. This is not surprising since the closest tip position for the 'far' propeller is some 6 or 3 times further away than that of the 'near' propeller for the upper or lower microphone stations respectively. After making allowance for the increased distances from the major noise source, there appears to be about 10 dB attenuation associated with shielding (absorption/diffraction) of the far propeller by the wooden fuselage.

Typical near-field spectra obtained with the twin propellers operating at a prescribed blade-angle are illustrated in Fig.18 for three microphone locations. Empirical parametric analysis as earlier, for the SPL of the fundamental BPF tone, again offers a useful standard of correlation in terms of the blade helical tip Mach number M_h , the power loading C_p and the mainstream Mach number M_0 (Fig.19). Specifically, for the starboard microphone locations and $\beta = 22.5^\circ$,

$$\text{SPL}_1 = 169 \text{ or } 157 + 10 \log_{10} (M_h^8 C_p^2) - 40 M_0$$

the larger and smaller values of the initial constants being relevant to $r/R = 1.37$ (upper mic.) and $r/R_p = 2.05$ (lower mic.) respectively.

Such analysis further reveals BPF noise levels around 7 dB higher on the complete aircraft model at $r/R_p = 1.37$ when compared with those for an isolated propeller-nacelle model at $r/R_p = 1.44$. The fuselage reflections could be expected to give about 6 dB of this increase in tonal signal level, while the somewhat closer position of the microphone position to the installed propeller disc could account for the extra 1 dB. Moreover, from the RAF flight experiments on the Shorts 330 aircraft, the corresponding SPL_1 levels for the BPF tone lie encouragingly close to those given by the foregoing parametric relation (Fig.20).

The changes in tone levels associated with the combined incorporation of the wing-struts and the undercarriage housing on the aircraft model do not appear to be significant at the starboard microphone stations, near the upgoing propeller tip; but SPL reductions are noticeable at the lower port microphone station, e.g. 3 dB decrease (Fig.18), where the microphone is at fuselage-base level near the downgoing propeller tip. Flap deflection leads correspondingly to a noticeable increase of tone levels at this lower port microphone. Again, expectedly, aircraft incidence causes SPL level increases in respect of tones and broadband noise at this lower port microphone, while there are some decreases in tone levels at the upper starboard microphone. But it should be recalled that the noise levels of the 'upper starboard' at zero incidence are not only about 10 dB higher than those for the 'lower port' but also than those for the 'lower starboard'. Unfortunately, the results for the 'upper port' microphone proved unreliable because of a technical fault.

4. BASIC THEORETICAL PREDICTION CONSIDERATIONS

4.1 General Background

Windtunnel and flight testing techniques inherently can supply powerful noise prediction methods, if the specific propellers can be made available either at full-scale or model-scale as previously discussed. Also empirical parametric formulae, derived as earlier from broad physical concepts and available propeller test data, can offer simple useful tools to indicate practical noise trends and to isolate unusual results quickly. However, to ensure reliable clarification of primary noise sources and to predict logically the character of noise variations with changes in propeller running conditions or in propeller geometry, well-defined theoretical frameworks should be employed with experimentally-justified elements.

The theoretical prediction frameworks employed here for correlation with measured free-field noise spectra contain discrete-frequency (tone) components generated by rotational blade steady-loading associated with thrust and torque, by rotational blade-thickness leading to displaced air-volume, and by blade unsteady-loading associated with inflow non-uniformities or cyclic pitch variation. Non-linear 'quadrupole-type' noise relevant to local transonic flows is neglected at this time, as insignificant for our straight-bladed propellers operating normally at helical tip Mach numbers M_h below 0.85. The non-discrete 'broadband' noise components conventionally attributed to viscous flow effects become significant at the higher frequencies ($> 4 \times \text{BPF}$), but in practice still have to be estimated largely from empirical formulae. Finally, propeller axis inclination to the mainstream and airframe installation interference can affect the noise characteristics through changes which should be predicted not only in the installed propeller aerodynamics but also in the acoustic propagation conditions locally.

These individual prediction aspects will be discussed briefly in respect of near-field and far-field needs (Sections 4.2 to 4.6), before proceeding to an appraisal of some practical correlations between such theoretical predictions and sample experimental results from our windtunnel and flight measurements (Section 5).

4.2 Steady-Loading and Thickness Noise (Near-Field)

Our earlier near-field prediction method² for discrete-frequency noise produced by rotational steady blade-loading followed the calculation procedure formulated by Watkins and Durling⁸, which was based on the Garrick and Watkins extension⁹ of the classical Gutin theory to cover forward flight. A computer program involving spanwise integration of blade loading was developed and applied by Dowty Rotol, to produce predictions of the tone SPL values (BPF and harmonics) at typical fuselage-side positions. But the possible significance of blade-thickness noise contributions, even at moderate subsonic tip-speeds ($M_t > 0.7$), was soon appreciated as a result of the theoretical developments by Hawkings and Lawson¹⁰ from the Ff. Williams-Hawkings (FW-H) acoustic analogy. With the quadropole terms ignored (subsonic tips), the FW-H analogy effectively provides a relation for the time-dependent acoustic pressure $p(x,t)$ produced at a spatial location x by a propeller blade source element, comprising a linear sum of contributions $p_L(x,t)$ and $p_T(x,t)$ generating steady-loading and thickness noise. A practical solution is achieved by employing Green's function and retarded-time concepts, with the propeller blade sub-divided into separate small compact source elements. The loading-noise contribution usefully sums a far-field term ($p_{L_f} \propto 1/r$) and an extra near-field term ($p_{L_n} \propto 1/r^2$).

The present predictions of steady-loading and thickness noise have been based therefore on Succì's developments¹¹ of a subsonic time-domain calculation procedure and computer program. This first sub-divides the propeller blade into a mesh comprising many compact sources of loading and thickness noise, then calculates their combined-pressure signals at any selected location, and finally performs a Fourier analysis of this time-dependent signal to evaluate the noise-spectrum amplitude values (SPL_q) at the blade-passing frequency and its harmonics. The input data requires the mesh definition, the blade planform geometry and section profiles, the radial distribution of thrust and torque loadings, and the chordwise distribution of pressure loading.

A much simplified calculation procedure, originally recommended by Hawkings for lifting-rotor far-field noise predictions, has recently been modified and improved by Tadghighi and Williams⁷ at Southampton University for propeller applications. This SU-Hawkings procedure has provided steady-loading and thickness noise estimates more rapidly and in close agreement with Succì-type calculations even at typical near-field (fuselage) locations. Additional mention should be made of further theoretical advances in propeller discrete-frequency noise technology, with regard to both time-domain and frequency-domain calculations for high-speed propellers, particularly those by Farassat and Hanson.

4.3 Steady-Loading and Thickness Noise (Far-Field)

Our earlier far-field prediction method for discrete frequency noise also employed Garrick and Watkins treatment⁹ for rotational steady-loading distributions across the propeller blade span, including forward speed effects. But the simplified calculation procedure followed Magliozzi¹² in assuming a point-loading approximation usually at 80% radius ($0.4 D_p$), to avoid spanwise integration complexities in addition to the absence of near-field terms. Thereby, the datum sound pressure level SPL_q of the resulting steady-loading tone for each q th harmonic of the BPF ($f_q = q BN/60$) can be expressed algebraically in terms of the following parameters, at unit normalised radial distance:-

- B the number of blades, N the rev/min; θ the acoustic ray angle;
- M_t the rotational tip Mach number, M_a the flight airspeed Mach number;
- T the propeller thrust, P the aerodynamic power, D_p the diameter.

Of course, when the acoustic radiation involves conventional spherical spreading only, then the tone SPL_q -value at far-field distance r from the propeller follow simply as $SPL_q - 20 \log_{10} r$.

The present predictions of both steady-loading and thickness noise in the far-field mostly use the basic Succì or SU-Hawkings methods as outlined already for near-field noise prediction (Section 4.2). For correlation with windtunnel results, where there is no relative movement between the microphone receiver and the propeller model, while sound atmospheric attenuation over such small distances is negligible, the required far-field calculation procedure is identical to the near-field calculation for aircraft-bied microphones without installation interference. For correlation with flight results, the required far-field calculation procedure relating to ground-based microphones must allow for relative aircraft movement (Doppler shift), apart from atmospheric attenuation and any environmental/installation effects.

4.4 Unsteady-Loading Noise

As discussed in Ref.2, unsteady loading noise prediction is based on the work of Lawson and Ollerhead¹⁴, again using a point-loading approximation usually at 80% radius; but with load fluctuations from the average steady load (L_0), comprised of rotational components of amplitude L_n for each n^{th} harmonic of the rotational frequency. These random-phased unsteady-loading harmonics are assumed to have amplitudes proportional to L_0 and decaying as n^{-k} , such that $L_n = C L_0 n^{-k}$, with the constants C and k originally taken as 0.261 and 1.61 respectively following Magliozzi's correlation with noise tests done statically on model propellers¹². The SPL_q of each unsteady loading tone can then be expressed algebraically in terms of parameters similar to those arising in the discussion of far-field steady-loading noise, but here several unsteady-loading harmonics can contribute to one sound harmonic. Magliozzi suggested some rough corrections to allow for the reduction of propeller inflow-turbulence levels and hence of unsteady loading as flight airspeed rises. Typical quoted reductions are substantial, as much as 15 dB for 50 m/s airspeed, so leaving some doubt as to their accuracy for forward speed predictions.

Later evaluations¹³, using data from uninstalled propellers rather than the earlier installed, also resulted in revised coefficients, involving a steeper roll-off of the higher harmonic levels against harmonic number (for frequency $> 4 \times$ BPF) and noise-level reductions of up to 5dB at the lower harmonics. Usually unsteady-loading effects are considered only in relation to far-field noise prediction, but their possible importance for near-field noise must also be borne in mind, especially at low blade-tip speeds and with practical airframe installations.

4.5 Broadband Noise

The broadband noise formulae so far applied have been purely empirical and Magliozzi's prediction procedure¹² has been employed here to provide the third-octave spectrum contributions (far-field). The frequency f_p for peak 'broadband noise' SPL is derived from a predetermined peak Strouhal number:-

$$f_p \times (\text{blade thickness}) / (\text{blade-section helical speed at } 0.7 \text{ span}).$$

The peak SPL value is then obtained from an algebraic expression in terms of Θ , M_t , T and total blade area. The broadband noise prediction is then completed by incorporation of a prescribed third-octave spectral shape about the peak. However, correlations of predictions by Magliozzi's procedure with windtunnel results, suggest that the broadband noise is in general over-predicted by the order of 10 dB, especially in the higher frequency regions (above 5 x BPF) where it has most effect on the total noise signature. Fortunately, other theoretical work, relating mostly to helicopter or fan blades, has led to more promising correlations with test data, while broadband noise is quoted as being caused mainly by random turbulent disturbances (environmental or blade-generated) interacting with the rotating blades.

4.6 Installation Effects

The free-field acoustic characteristics of an isolated propeller in axial mainstream flow may be modified in practice by propeller non-axisymmetric inflow changes caused by propeller axis inclination to the mainstream (aircraft incidence), wing/fuselage or test-rig flow interference, and spurious inflow turbulence (natural or propeller-generated). A first-order estimate of such axis-inclination and flow-interference effects may be derived by assuming an overall upwash influence on the inflow, which generates cyclic aerodynamic changes in the relative airspeed and incidence of the blades. Circumferential positions of maximum and minimum loads arise where the additional cross-flow component in the propeller disc plane opposes or acts with the blade rotational velocity, resulting in increases or decreases respectively of the blade loading noise component and possibly of the blade-thickness noise also at high M_h or M_o .

In the near-field, the maximum and minimum loading noise positions can be taken to be the same circumferentially as for the aerodynamic loading changes, if retarded-time effects are ignored, so that the loading-noise changes can be calculated directly. However, the Succi computer program offers a more accurate treatment, in that two sinusoidal grading distributions at 90° phase difference and with prescribed factors FC and FS are incorporated to represent the nett loading pattern, then being used within the retarded-time/loading noise calculations.

External fuselage noise is measured with the microphones flush-mounted in the surface or just-outside³, and acoustic reflection effects off the fuselage can increase the recorded SPL-levels compared with free-field values. This augmentation may vary according to the type of microphone installation, boundary-layer effects and acoustic ray incidence at the particular microphone; but 6 dB is assumed for our later correlations since most of the relevant data is for forward-facing pitot microphones located close to the fuselage surface and near the propeller disc plane. Extraneous noise at the fuselage microphones from other non-propeller sources could be due to the fuselage boundary-layer flow (ESDU 75021 prediction), wing/fuselage junction flow distortion, and the power-plants. Although these may not influence the measured SPL-values at the BPF and lower harmonics of the propeller, they can certainly affect the measured broadband levels at higher frequencies.

For the far-field, acoustic propagation of the propeller-generated noise can be influenced by airframe reflection, shielding or flow refraction. But with large diameter propellers, rather than compact jet engines, the effects may be less significant and are not included here for any correlations with flight tests. Atmospheric attenuation effects during propagation to the distant ground microphones can be allowed for by standard published procedures (SAE). The ground level microphones (zero ground clearance) used by RAE for flight research on noise³ provide theoretically less than 1 dB distortion of noise spectra from ground reflections (concrete surface) for frequencies up to about 4 k Hz, while the recorded SPL are consistently augmented then by 6 dB relative to free-field values. In contrast, the conventional certification microphones at 1.2m height (often above grass) are subject to considerable variability in ground reflection effects, especially at the low harmonics, though some estimates of this can be attempted (ESDU prediction).

5. CORRELATIONS BETWEEN THEORY AND EXPERIMENT

5.1 Near-Field Correlations (Isolated Propeller)

Our early analysis² for the full-scale Dowty R.292 propeller (ARAD-sections) in the 24ft tunnel, e.g. Fig.21 ($r/R_p = 1.4$ in disc plane), revealed that the predicted BPF and usually the 2 x BPF tones were usually dominated by the steady-loading contribution as estimated by the Watkins & Durling method or by the Succi/Hawkings treatments. The 3 x BPF tone mostly exhibited more or less equal contributions from steady-loading and thickness noise sources, as given also by the Succi/Hawkings treatments, while for the higher harmonics the thickness contribution became increasingly dominant. Overall, the predicted tone levels (steady-loading and thickness) appeared to agree remarkably well with the measured values (+ 1 to -3 dB error) up to 4 x BPF, and in some cases up to 8 x BPF (Fig.21). Shortfall in the noise predictions at higher frequencies were probably associated with the 24 ft tunnel-drive or test-rig noise rather than the true propeller noise.

More extensive correlations now cover both the full-scale and model-scale results for the Dowty R.292 propeller in the 24ft tunnel and the 1.5m tunnel respectively, for the R292S 'spear-tip' version at model-scale, for the R.212 propeller (NACA 16-sections) at both full-scale and model-scale, and for the Dowty Multi-blade model with R.320-type blades (ARAD-sections), over a total M_h range of 0.43 to 0.9. For clarity, the correlations are shown here mainly as 'Differences' of Tone-level SPL, with overpredictions positive, namely

$$\Delta \text{SPL}_p = \text{Prediction (Succi method)} - \text{Measured (Tunnel)}$$

for each of the first three or four harmonics, and plotted against M_h over the blade-angle ranges tested.

For the R.292 model, the Differences ΔSPL_p vary mostly between 0 and -2 dB at the BPF, to between -1 and -3 dB at 4xBPF (Fig.22). For the R.292S model, the underpredictions become more marked, with ΔSPL still between 0

and -3 dB at the BPF but deteriorating to between -2 and -6 dB by 3xBPF (Fig.23). This implies that the practical noise improvements from the spear tip modification are less than those predicted by the Succi method, possibly because of deficiencies in the blade loading calculations and effects of blade flexibility. Also, at the lowest blade angle ($\beta = 14.5^\circ$) for both model propellers, the underpredictions tend to become worse, with ΔSPL_p between -2 and -5 dB on the R.292 model, and between -2 and -8 dB on the R.2925 model, up to 4xBPF. Other complementary predictions by the simpler SU-Hawkings procedure⁷ are in close agreement with those by the Succi method.

For the full-scale R.212 propeller, corresponding correlations imply Differences ΔSPL_p mostly between +1 and -3 dB at and above $\beta = 17.3^\circ$, again with some deterioration to between -1 and -5 dB at the lowest blade angle ($\beta = 9.8^\circ$). For the R.212 model, ΔSPL_p lies between 0 and -3 dB at the BPF, deteriorating to between -1 and -5 dB by 3xBPF, though with less worsening of agreement than before at the lowest blade angle ($\beta = 9.5^\circ$). Such poorer correlation at low blade angles on both the R.212 and R.292 propellers are probably due to the occurrence of negative C_L 's at the tip sections and flow discontinuities with the low blade loading, which aggravates spurious noise as the blade-tips move towards negative thrust.

The Multi-blade series of model propellers have been studied with 3, 4, 6, and 8 identical blades over the range $\beta = 15^\circ$ to 30° , $M_h = 0.5$ to 0.72 , at $U_0 = 30$ m/s and 50 m/s. For constant values of power coefficient C_p and advance ratio $J (= U_0/nD_p)$, the tone SPL-values at the BPF or harmonics can fall significantly with increasing blade number, typically by 15 dB and 25 dB at the BPF and 2xBPF respectively as the blade number is raised from 3 to 8; see also Section 3.6. Nevertheless the Differences ΔSPL_p between tone-level predictions (Succi) and measurements (1.5m tunnel) remain mostly between +1 and -1 dB for the BPF and 2xBPF tones (Fig.24), confirming that the predicted substantial changes in the tone levels from 3 to 8 blades closely follow the measured data. For the 3xBPF tone the correlation becomes much poorer with the 6 and 8-blade models; this could be expected because the measured SPL-values at the relevant higher frequencies become immersed in the tunnel background noise and are also possibly influenced by the unsteady-loading and broadband-noise contributions not included in these predictions.

Overall, the Multi-blade series of model propellers with their stiffer metal blade construction exhibit better correlation between discrete frequency noise prediction and experiment than the R.292 and R.212 models with their composite blade construction. The latter's greater blade flexibility allows more blade untwist when running, thus moving their loading further outboard and increasing the noise generated. Inclusion of practical untwist in the noise prediction calculations does usually improve the theoretical correlation with noise measurements at the higher rotational speeds, so more detailed analysis seems justified.

5.2 Far-Field Correlations (Isolated Propeller)

As reported earlier², third-octave analyses of far-field spectra from 24ft tunnel tests on the full-scale Dowty R.292 propeller were first compared with appropriate total noise predictions by Magliozzi's computational procedure involving contributions from steady-loading (Garrick & Watkins), unsteady loading (Lowson and Ollerhead) and broadband noise (empirical). Individual measured narrow-band tone levels were then compared with discrete-frequency noise elements predicted from steady-loading (Succi/Hawkings) and thickness (Succi/Hawkings) and unsteady loading (Lowson and Ollerhead). The predicted tone level at the BPF and often at the 2 x BPF is dominated by the steady-loading contribution, though this prediction can be a few dB below the measured tone (e.g. Fig.25). The 3 x BPF tone is predicted to contain contributions of equal importance from both the steady-loading and thickness sources (Succi/Hawkings), and the combined predicted intensity may even just exceed the measured tone, except at low rotational speeds where the tone becomes submerged in the propeller-broadband or tunnel background noise contributions. The predictions for the 4 x BPF and higher tones tend to be dominated by the thickness-noise contribution except again at low rotational speeds.

The unsteady-loading predictions only become significant for the harmonics from 5 x BPF upwards, when the predicted values are near to the measured tone values at low blade angles, but are usually below at high blade angles. Presumably these unsteady-loading predictions are reduced further (by several dB) if Magliozzi's later evaluation¹³ for the unsteady loading harmonics is adopted, corresponding to uninstalled rather than installed propeller characteristics. Moreover, the current choice of static conditions as a datum for this unsteady-loading treatment cannot be accepted as reliable, even if of practical necessity at this time, because gross reductions to the resulting SPL estimates then have to be applied to allow for the substantial removal of ingested turbulence when airspeed is raised to 10 kn or beyond.

The broadband noise contributions from the Magliozzi empirical formula usually dominate the predicted third-octave spectra at frequencies above 4 x BPF. However, even with an arbitrary reduction of 10 dB in the predicted level of the broadband noise, the correspondingly reduced estimates for the associated third-octave spectra contributions around 1 kHz still give levels as much as 6 dB higher than the measured values. Admittedly, at very high frequencies (above 5 kHz) the number and amplitude of predicted unsteady-loading harmonics can raise the effective third-octave levels there.

5.3 Influence of Propeller-Axis Inclination

For the Dowty R.292 propeller model in the 1.5m tunnel with a change in propeller axis inclination ψ from 0 to 10° , the three near-field microphones were located directly above, below and to-the-side in the disc plane. After allowing for small differences in the microphone distances, as discussed in Section 3.4, the noise levels with inclination could there be expected to be respectively a maximum (advancing blade), a minimum (retreating blade) and unchanged. Some theoretical predictions of these inclination effects have been attempted by applying an extended Succi treatment incorporating simple cyclic blade-loading variation, as mentioned already in Section 4.6.

Fig.26 compares the measured and predicted values of ΔSPL_ψ at $\psi = 10^\circ$ over that at $\psi = 0^\circ$, plotted against M_h for the first four harmonics at the top and bottom microphones. While there is fairly good correlation between the predicted and measured changes at 50 m/s airspeed, the predicted effect at 30 m/s increasingly falls short (in magnitude) of the measured effect as the harmonic number rises. This theoretical shortfall in predicting inclination effects may well be due to the exclusion of unsteady-random-loading noise from the Succi procedure, which can become more dominant at low speeds. Additionally, the simplified assumptions relating to coincidence of the max-min loading and noise positions could be supplemented by including more sophisticated retarded-time considerations. Similar correlations for upwash effects on the full-scale aircraft at higher airspeeds (Section 5.4) also provide encouraging support for the 50 m/s results quoted here.

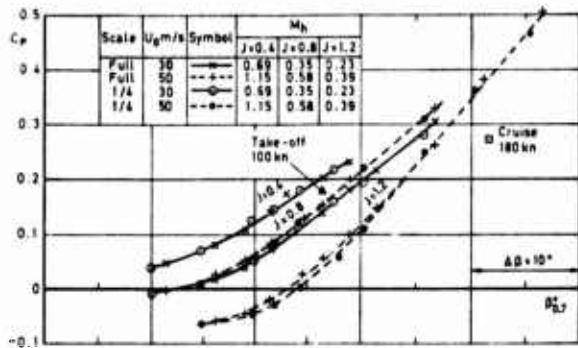
5.4 Installation Effects on Aircraft Near-Field Noise

As a practical aircraft analysis, the narrow-band and third-octave spectra from flight measurements at the fuselage-mounted microphones on the Shorts 330 aircraft (Fig.20) have been correlated with our predictions of discrete frequency noise by the Succi method, broadband noise by the Magliozzi empirical relation, and boundary-layer noise by the FSDU method. The upflow and fuselage reflection corrections due to installation effects on tone noise are taken as ± 1.5 dB and $+ 6$ dB respectively. For the high-power/low-speed conditions during take-off, the SPL estimates for the first four harmonics then compare well (Fig.27) with both the high (max) and low (min) values of test SPLs at the port and starboard microphones respectively - corresponding to the downgoing and upgoing blades closest to the fuselage side. The broadband noise estimates show appreciable overprediction at the higher frequencies with the assumed installation effects included, while the boundary-layer noise estimates seem also significant. At cruise conditions, good correlations for the tone levels have likewise been obtained, but the broadband noise then tends to be underpredicted. In comparison with the noise spectra measured on the complete model in the 24 ft tunnel, some differences at the higher frequencies have been attributed to the presence of engine noise in the flight tests.

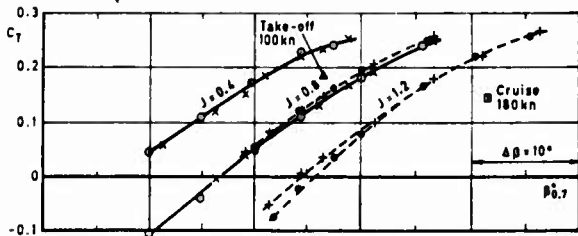
In making similar correlations for the B.Ae. HS748 aircraft under cruise flight conditions, the nett upflow angle of about 5° into the propellers was used to estimate the differential corrections to the noise levels of the port and starboard microphones (instead of nominal ± 1.5 dB). Again the tone SPL estimates are good up to the fourth harmonic (Fig.28). There is reasonable agreement for the installed broadband noise up to frequencies of 3 kHz, although the estimated boundary-layer noise lies about 10 dB above this.

LIST OF REFERENCES

1. J. Williams, W.J.G. Trebble: Some British research on propeller noise characteristics under low-speed windtunnel and aircraft flight conditions. RAE TM Aero 1843 (1980).
2. W.J.G. Trebble, J. Williams and R.P. Donnelly: Comparative acoustic windtunnel measurements and theoretical correlations on subsonic aircraft propellers at full-scale and model-scale. RAE TM Aero 1909 (1981).
3. M.R.P. Law and J. Williams: Flight noise research with 4-bladed Dowty R.292 propellers and 5-bladed Hartzell propellers on Shorts 330 aircraft. RAE Report to be issued.
4. W.J.G. Trebble: Investigation of the noise field in the vicinity of a 5-bladed propeller of 2.81m diameter in the 24ft tunnel. RAE TM Aero 1993 (1984).
5. W.J.G. Trebble: Investigation of the effect of blade-tip shape on aerodynamic performance and noise characteristics of a 0.7m diameter propeller. RAE TM Aero 1974 (1983).
6. W.J.G. Trebble: Investigation of the aerodynamic performance and noise characteristics of a 1/5th scale model of the Dowty R.212 propeller. RAE TM Aero 1983 (1983). Others to be issued.
7. H. Tadghighi, J. Williams: Some theoretical noise prediction developments and complementary acoustic windtunnel measurements for a subsonic aircraft propeller (Dowty R.292). Southampton Univ. AASU Memo 84/8 (1984).
8. C.E. Watkins, B.J. Durling: A method for calculation of free-space sound pressures near a propeller in flight, including consideration of the chordwise blade loading. NASA TN 3809 (1956).
9. I.E. Garrick, C.E. Watkins: A theoretical study of the effect of forward-speed on the free-space sound-pressure field around propellers. NACA Report 1198 (1954).
10. D.L. Hawkins, M.V. Lawson: Noise of high speed rotors. AIAA Paper 75-540 (1975).
11. G.P. Succi: Design of quiet efficient propellers. SAE Paper 790548 (1979).
12. B. Magliozzi: V/STOL rotary propulsion system noise prediction and reduction. USA Report FAA-RD-76-49 (1976).
13. B. Magliozzi: V/STOL rotary propulsion noise prediction model update and evaluation. USA Report FAA-RD-79-107 (1979).
14. M.V. Lawson, J.B. Oilerhead: Studies of helicopter rotor noise. USA AVLABS Tech. Report 68-80 (1969).

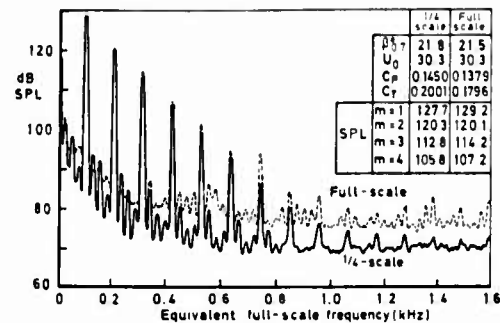


(a) Power coefficient $C_p = \text{power} / \rho n^3 D^5$

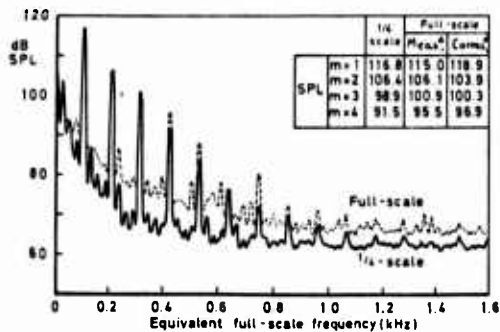


(b) Thrust coefficient $C_T = \text{thrust} / \rho n^2 D^4$

Fig 5 a&b. Performance comparison between model and full-scale propellers



(a) $r/R = 1.44$



(b) $r/R = 4.17$

Fig 7 a&b. Noise spectra comparison between full-scale and 1/4-scale normalised to 1600 rev/min; $U_{nom} = 30 \text{ m/s}$

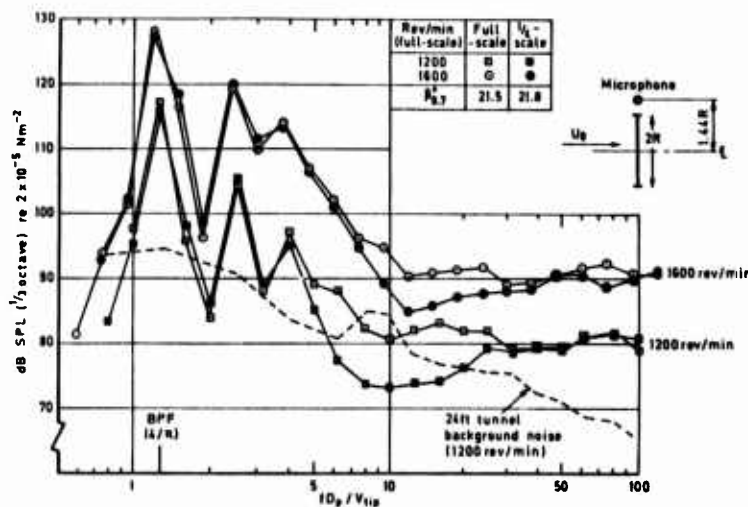
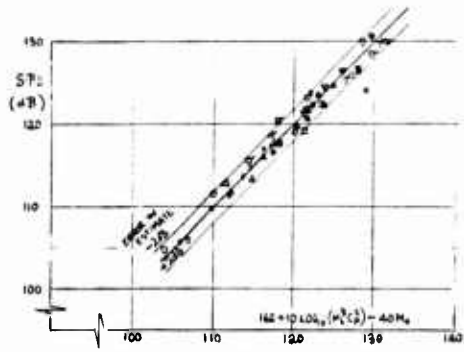
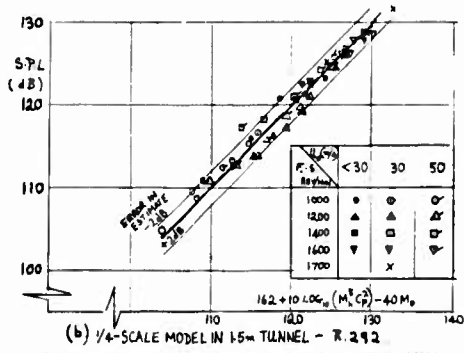


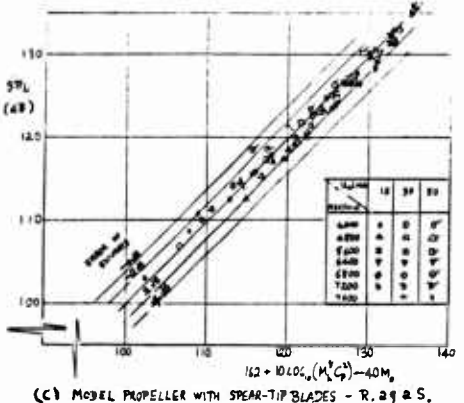
Fig 6. Comparison of noise spectra of model and full-scale propellers $U_0 = 30 \text{ m/s}$; $r/R = 1.44$



(a) FULL-SCALE PROPELLER IN 24FT TUNNEL - R. 292



(b) 1/4-SCALE MODEL IN 1.5M TUNNEL - R. 292



(c) MODEL PROPELLER WITH SPEAR-TIP BLADES - R. 292 & S.

FIG 8. SOUND PRESSURE LEVEL OF BLADE-PASSING-FREQUENCY $\theta = 90^\circ$, $r/R = 1.44$ - NEAR FIELD

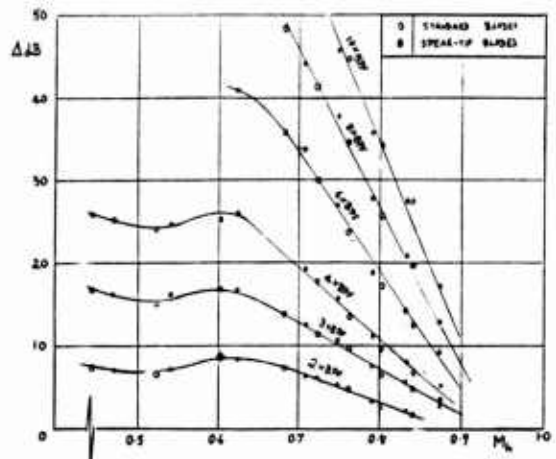


Fig 9. Reduction in SPL of tonal harmonics below SPL of blade-passing-frequency. $\beta = 19.5^\circ$, $U_0 = 50$ m/s (EAS), $M_0 = 0.147$, noise spectra at $r/R = 1.44$, $\alpha = 90^\circ$

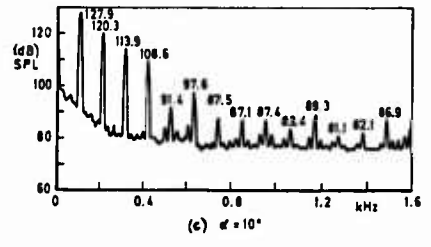
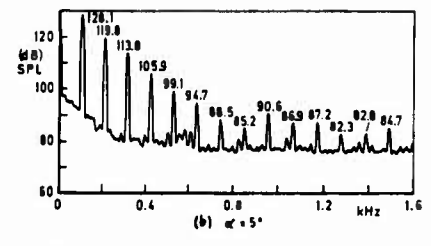
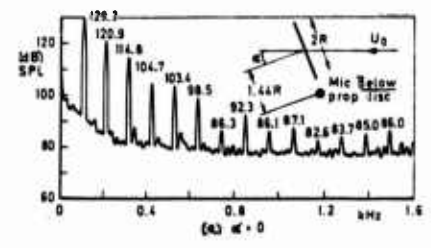


Fig 10 a-c, $\beta = 24.5^\circ$; 1600 rev/min; $U_0 = 30$ m/s; $r/R = 1.44$; $\theta = 90^\circ$ Full-scale propeller in 24ft tunnel at incidence

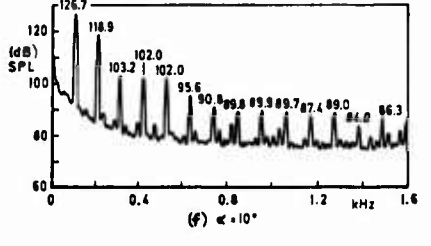
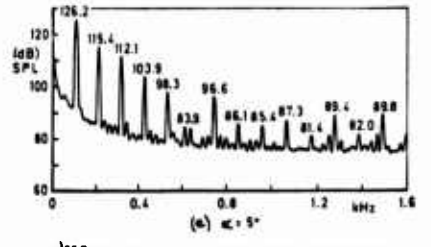
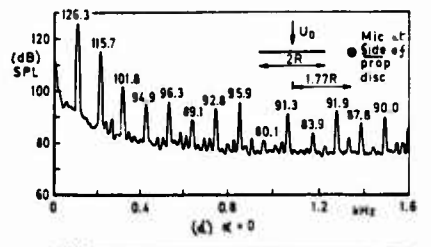


Fig 10 d-f, $\beta = 24.5^\circ$; 1600 rev/min; $U_0 = 30$ m/s; $r/R = 1.77$ Full-scale propeller in 24ft tunnel at incidence

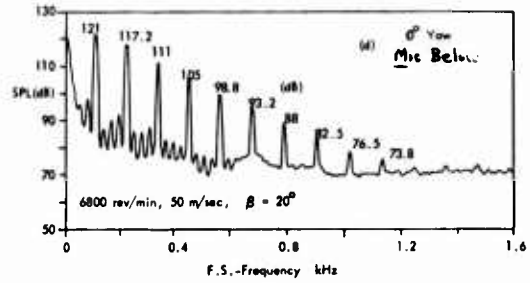
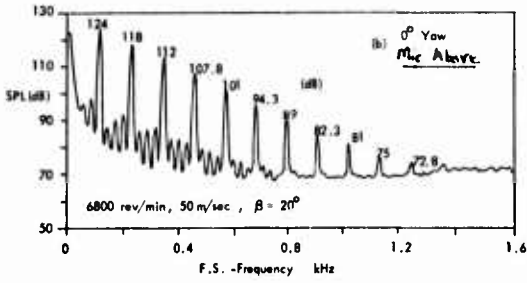
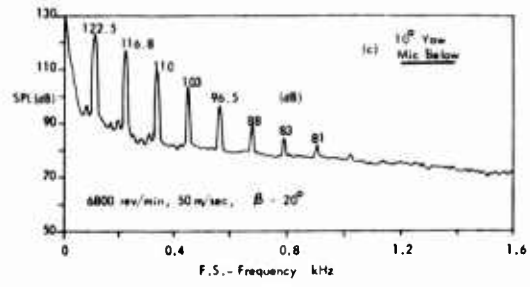
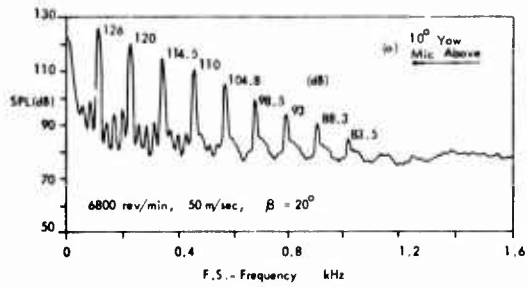


FIG 11 a, b INFLUENCE OF PROPELLER INCLINATION ON NEAR-FIELD NOISE OF R. 292 MODEL PROPELLER

FIG 11 c, d INFLUENCE OF PROPELLER INCLINATION ON NEAR-FIELD NOISE OF R. 292 MODEL PROPELLER

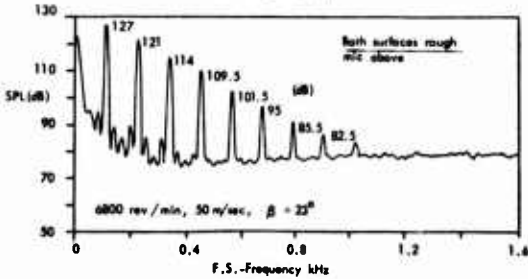
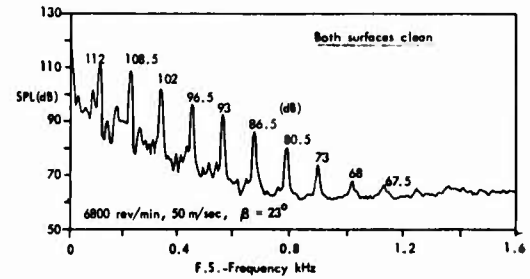
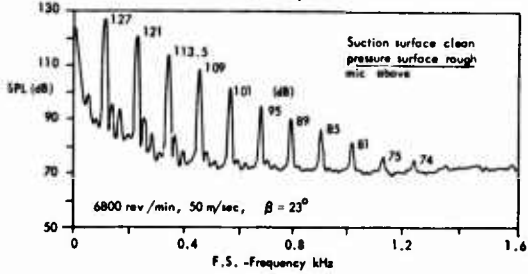
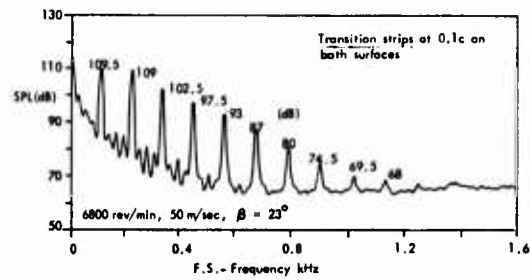
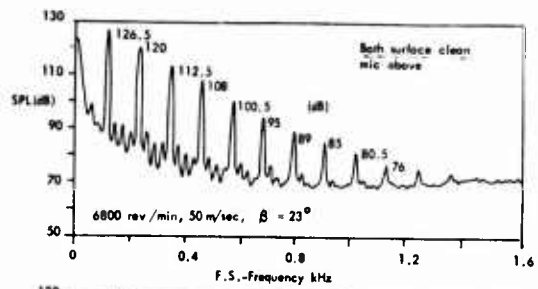


FIG 13 INFLUENCE OF TRANSITION STRIP ON FAR-FIELD NOISE OF R. 292 MODEL PROPELLER.

FIG 12 INFLUENCE OF BLADE SURFACE ROUGHNESS ON NEAR-FIELD NOISE OF R. 292 MODEL PROPELLER

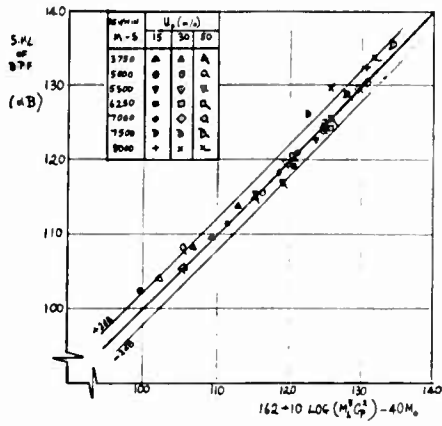


Fig. 14(a) Sound pressure level of blade passing frequency R.212
r/R = 1.44, θ = 90°

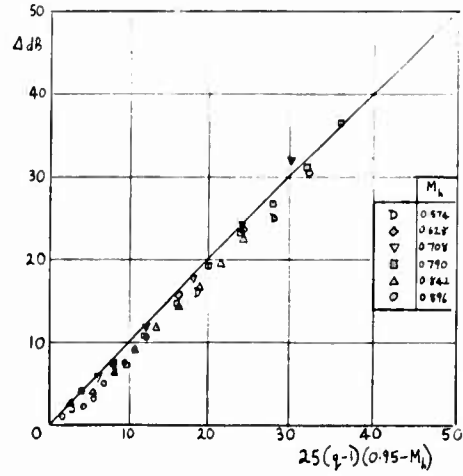


FIG 14(b) REDUCTION IN SPL OF TONAL HARMONICS BELOW SPL OF BPF.
FOUR-BLADED R212 PROPELLER, B = 17.3°, U₀ = 50 m/s EAS
NOISE SPECTRA AT r/R = 1.44, θ = 90°

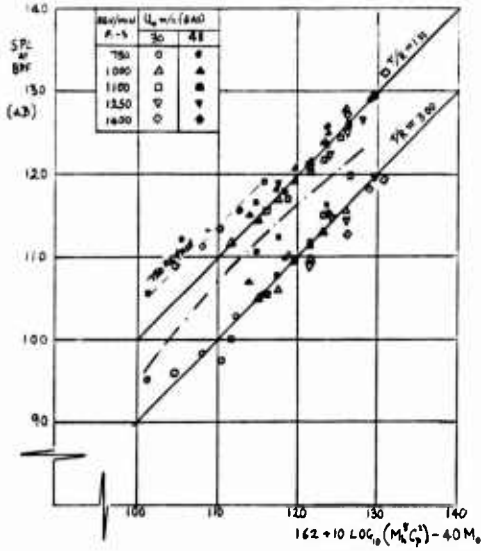
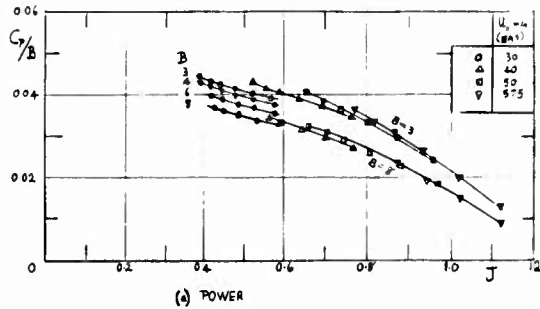
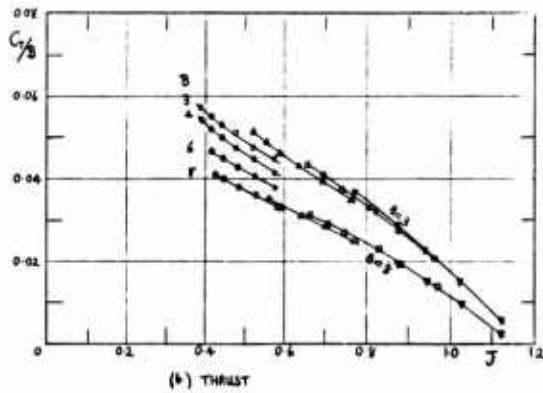


FIG 14(c) COMPARISON OF MEASURED SPL AT BPF WITH PARAMETRIC FORMULA
FOR FULL-SCALE R212 PROPELLER



(a) POWER



(b) THRUST

Fig 15. Effect of number of blades on power and thrust θ_{0,7} = 25°

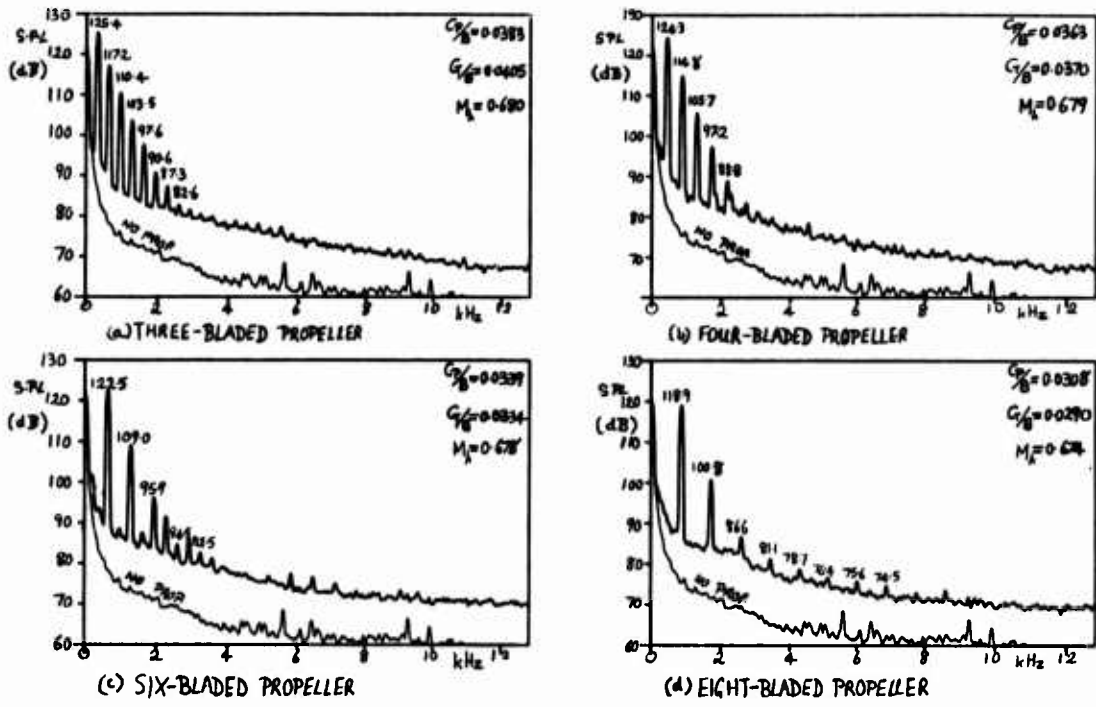


Fig 16. Effect of blade-number on noise spectra.
 $\beta = 25^\circ$; 6460 rev/min; $U_0 = 50$ m/s (EAS)

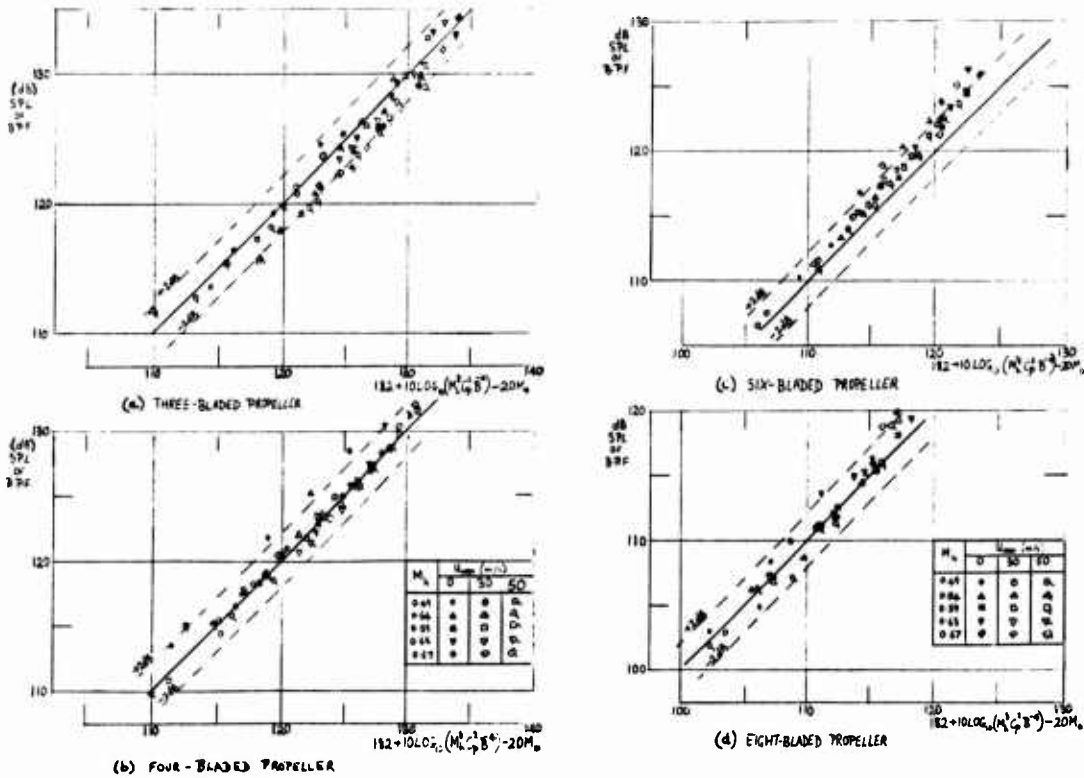


Fig 17. SPL of multi-blade propellers at $r/R = 1.44$; $\theta = 90^\circ$

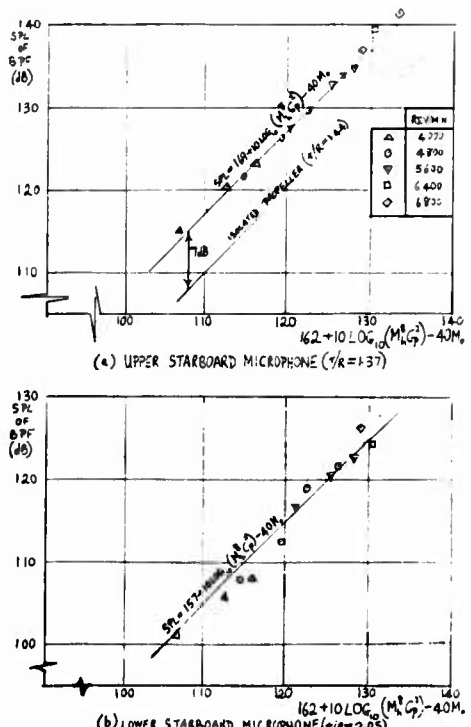
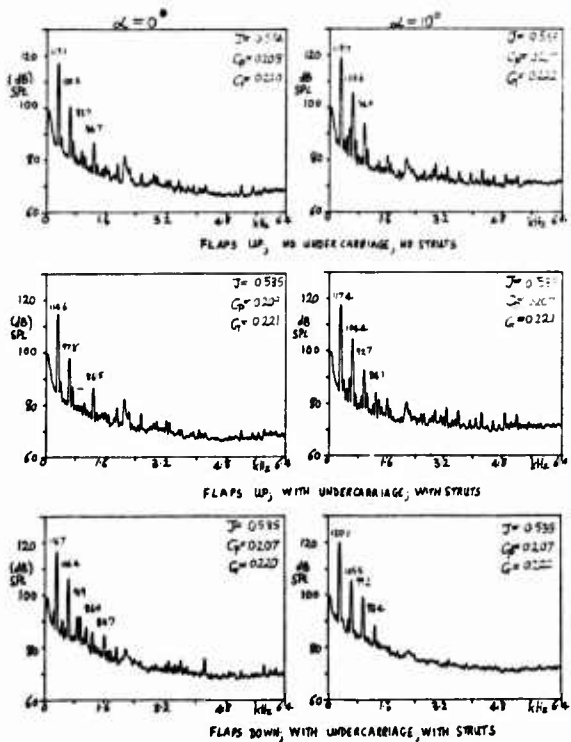
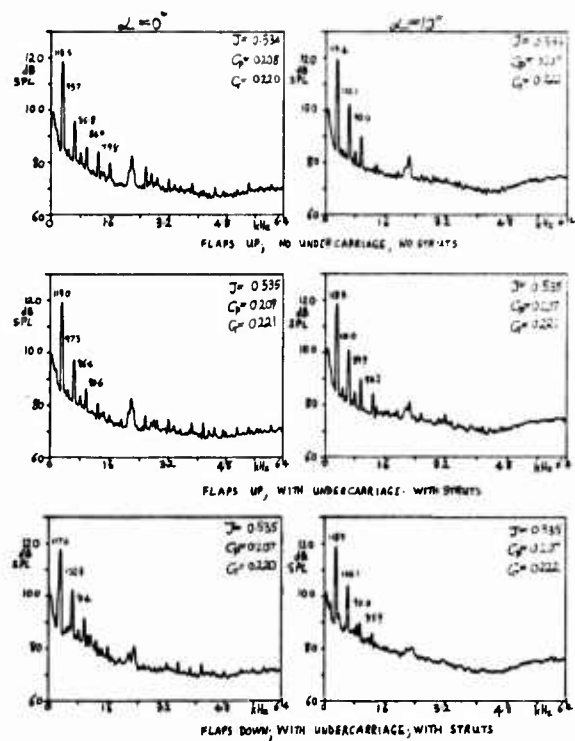
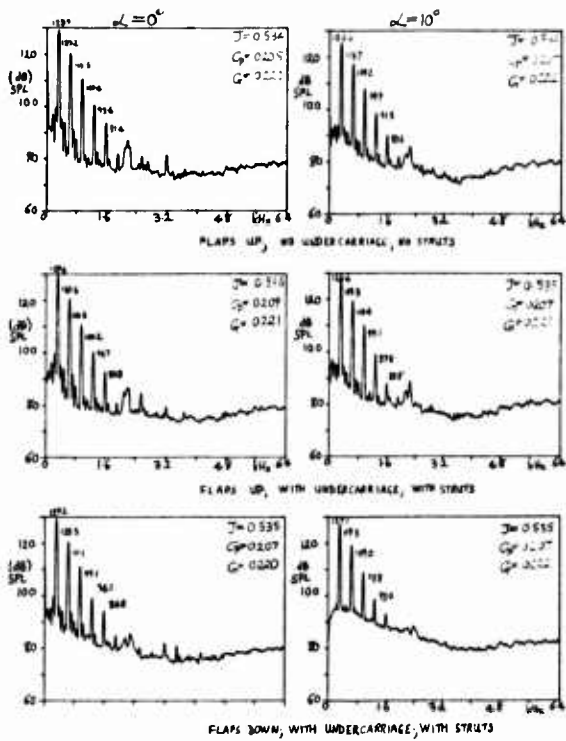


FIG 18(c) NOISE SPECTRA AT LOWER PORT STATION ($\beta/R=2.05, \beta/R=0$)
 $\beta=27.5^\circ, 4800 \text{ REV/MIN}, U_\infty=30 \text{ m/s (EAS)}$

FIG 19. SOUND-PRESSURE-LEVEL OF BLADE-PASSING-FREQUENCY TONE

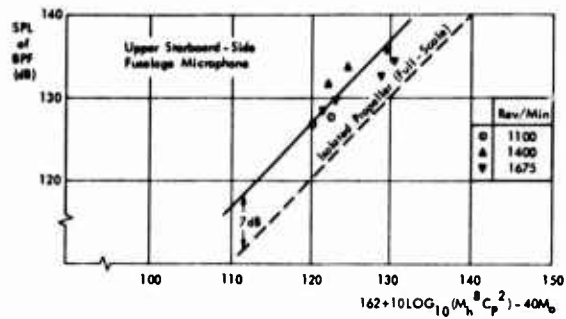
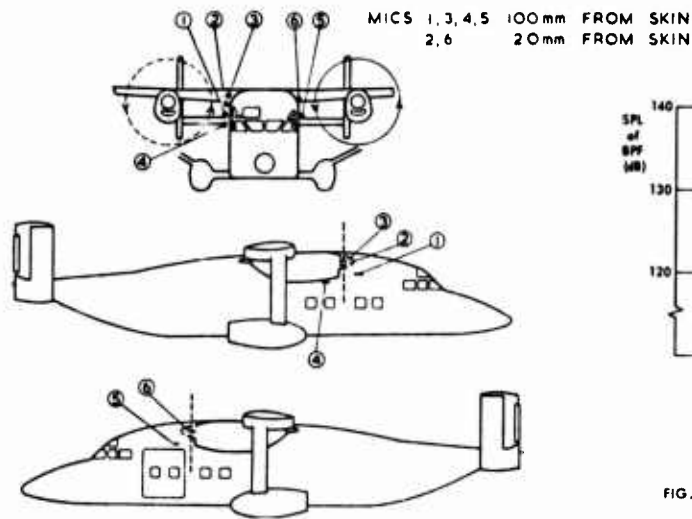


FIG. 20. FLIGHT MEASUREMENTS ON SHORTS 330 AIRCRAFT

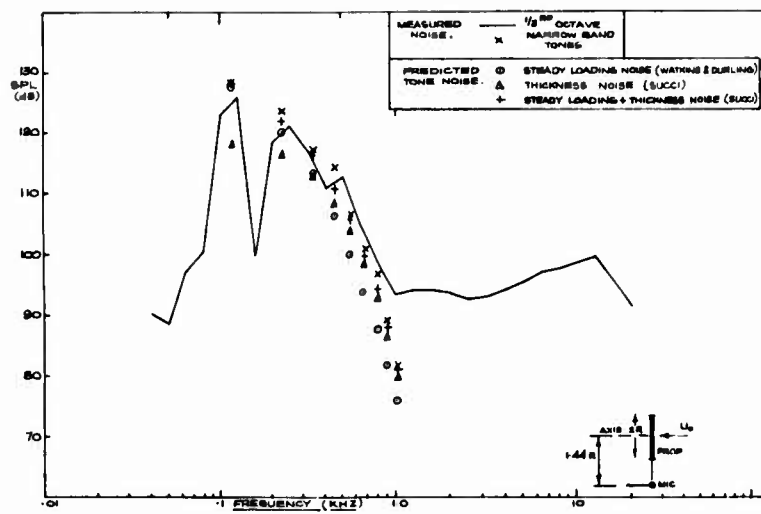


FIG. 21. COMPARISON OF MEASURED TONES AND 1/3RD OCTAVE NOISE WITH PREDICTED TONES FOR FULL SCALE R202 PROPELLER IN 24 FT TUNNEL
 $\beta = 21.6^\circ$; 1695 RPM; $U_0 = 30$ m/s; $\theta = 90^\circ$; $r/R = 1.44$ - NEAR FIELD.

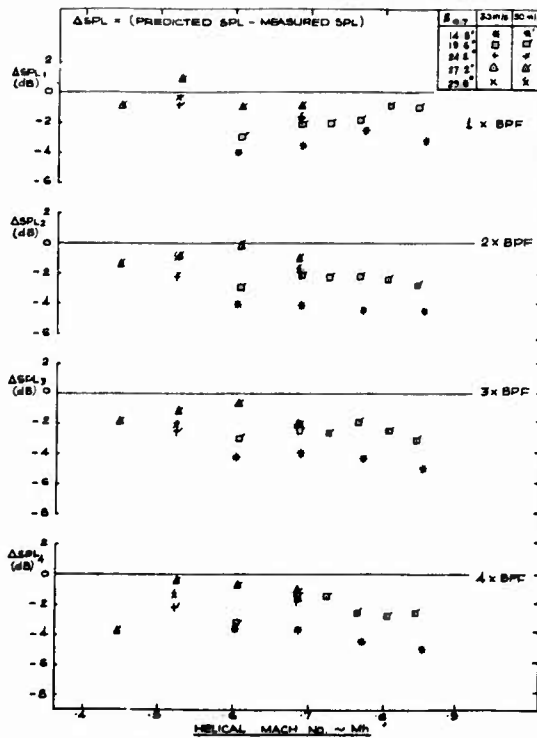


FIG. 22. CORRELATIONS BETWEEN MEASURED AND PREDICTED SPL'S AT THE FIRST FOUR HARMONICS OF BLADE PASSING FREQUENCY FOR 1/4 SCALE R202 PROPELLER IN 1.8M TUNNEL. $\theta = 90^\circ$; $r/R = 1.44$ - NEAR FIELD.

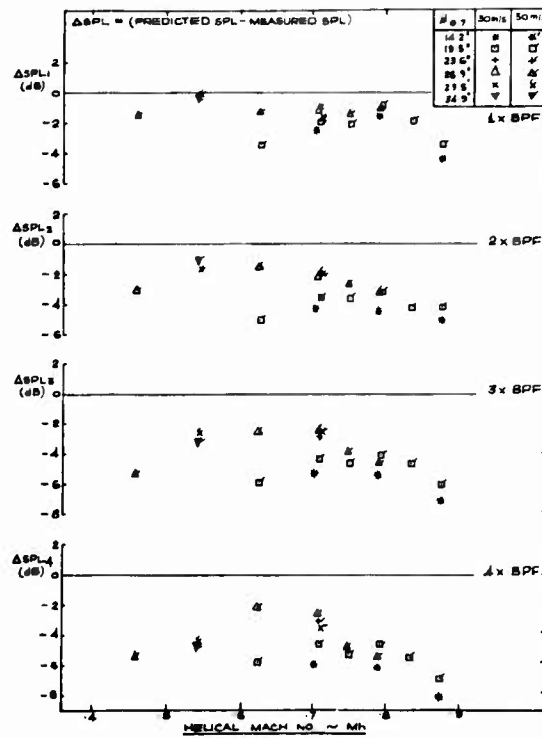


FIG. 23. CORRELATIONS BETWEEN MEASURED AND PREDICTED SPL'S AT THE FIRST FOUR HARMONICS OF BLADE PASSING FREQUENCY FOR 1/4 SCALE R202 PROPPELLER IN 1.8M TUNNEL. $\theta = 90^\circ$; $r/R = 1.44$ - NEAR FIELD.

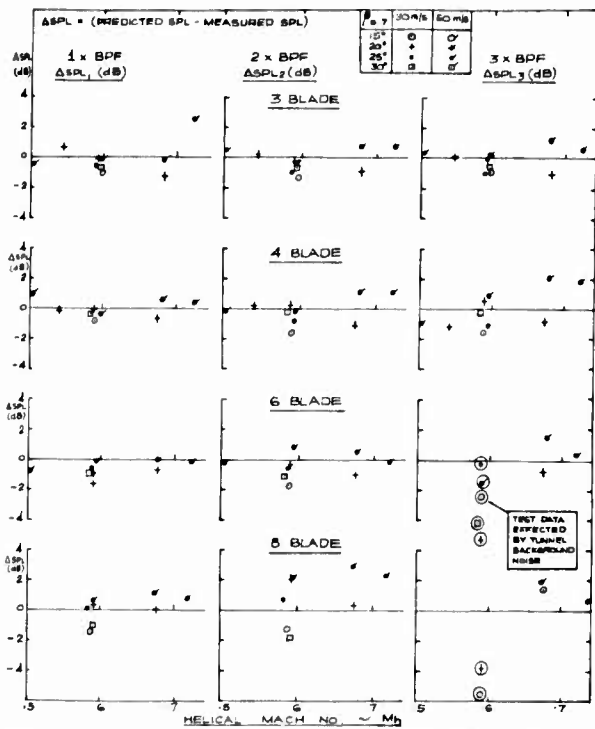


FIG 24. CORRELATIONS BETWEEN MEASURED AND PREDICTED SPLs AT THE FIRST THREE HARMONICS OF BLADE PASSING FREQUENCY FOR MULTIBLADE R202 TYPE MODEL PROPELLER IN 1.8m TUNNEL $\beta_0 = 30^\circ$; $r/R = 1.44$ - NEAR FIELD.

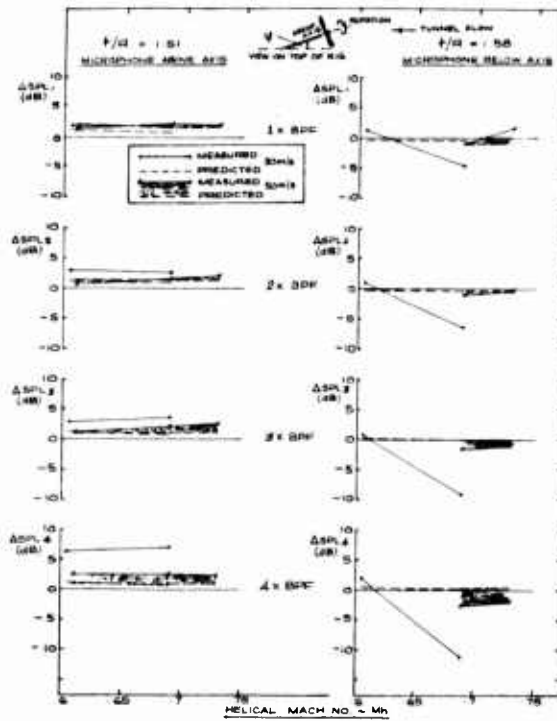


FIG 25. COMPARISON OF MEASURED AND PREDICTED INFLUENCE ON NOISE OF PROPELLER AXIS INCLINATION, FOR R202 MODEL PROPELLER IN 1.8m TUNNEL INFLOW ANGLE (ψ) = 0 AND 10; $\beta_0 = 50^\circ$; $\beta_0 = 20^\circ$

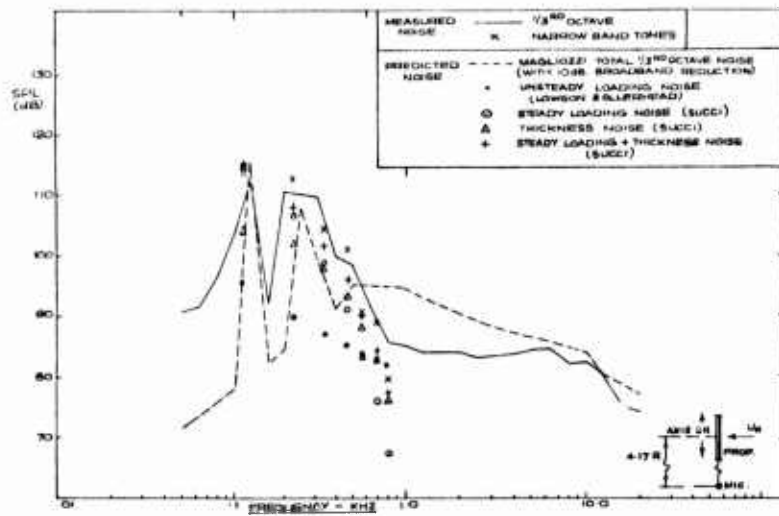


FIG 26. COMPARISON OF (CORRECTED) MEASURED AND PREDICTED TONES AND 1/3RD OCTAVE NOISE FOR FULL SCALE R202 PROPELLER IN 24 FT TUNNEL. $\beta_0 = 21.5^\circ$; 1682 R.P.M; $U_0 = 25$ M/S; $\beta_0 = 90^\circ$; $r/R = 4.17$ - FAR FIELD

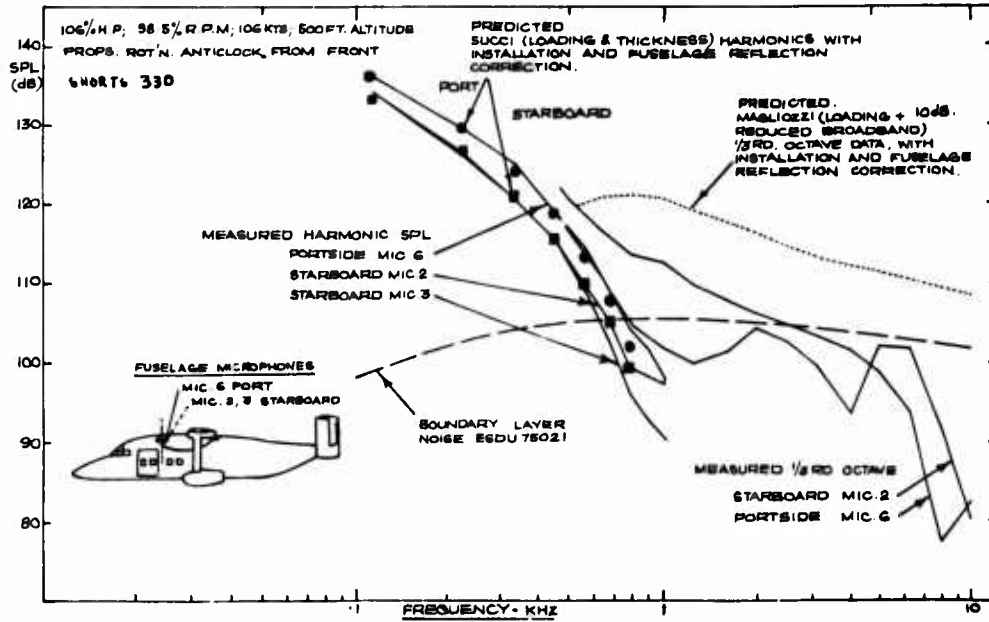


FIG. 27. COMPARISON OF MEASURED AND PREDICTED INSTALLED NOISE AT EXTERNAL FUSELAGE MICROPHONES, FOR S4330 AIRCRAFT FITTED WITH FULL SCALE R882 PROPELLERS.

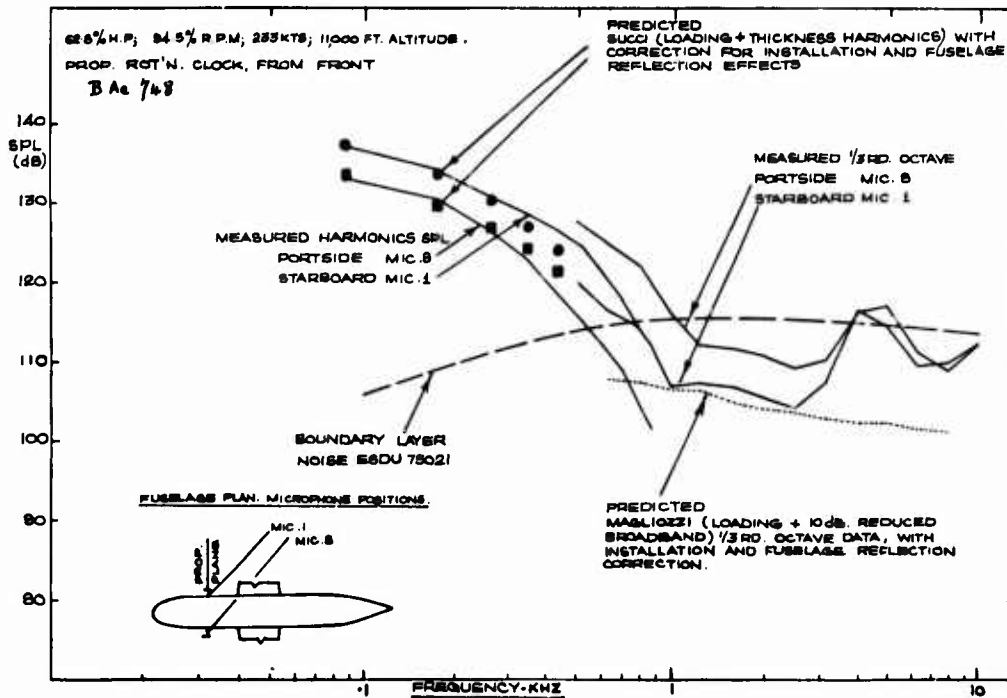


FIG. 28. COMPARISON OF MEASURED AND PREDICTED INSTALLED NOISE AT EXTERNAL FUSELAGE MICROPHONES, FOR BAe 748 AIRCRAFT FITTED WITH FULL SCALE R812 PROPELLERS.

AN INVESTIGATION OF IN-FLIGHT NEAR-FIELD PROPELLER NOISE GENERATION AND TRANSMISSION

by

H. Bonneau
Technical Consultant EngineerD.F. Wilford
Staff Aerodynamicist

and

L.K. Wood
Aerodynamicist
Pratt and Whitney Canada Inc.
P.O. Box 10
Longueuil, Quebec, Canada J4K 4X9

SUMMARY

In-flight near-field propeller noise measurements, made on a General Aviation turbo-prop aircraft, are reported for a range of propeller operating conditions, and are shown to be well defined and reproducible. Measurements have been made at 8 exterior microphones; 2 located on a wing mounted boom, and 6 embedded in, and flush with the aircraft fuselage. Interior noise levels are also presented.

Measured propeller harmonic levels are compared to first principles calculations of near-field noise, using a modified version of the Farassat computer program, in which the blade surface pressure is described using the known aerodynamic properties of the blade (NACA 16) airfoil sections. The first few; i.e. the dominant harmonic levels of propeller noise are shown to be well predicted, while higher harmonic levels are underpredicted.

The 'transmission loss' between exterior and interior noise levels is shown to be relatively constant for varying propeller operating conditions and at two different locations along the length of the fuselage.

Interior noise levels are also shown for the aircraft in gliding flight at various forward velocities, with both engines at idle and propellers feathered. A method of interpolating these measurements is discussed, which allows the interior noise due only to the forward velocity of the aircraft, to be determined. The transmission loss for this component is also discussed.

Finally, interior noise levels are presented for a series of ground static tests with engine mounts of various different stiffnesses. Changing engine mounts stiffness is shown to have little effect on interior noise levels, suggesting that there is no significant noise transmission through the engine support structure.

INTRODUCTION

The subject of propeller noise has received wide attention because of its direct impact on passenger comfort, and therefore on the acceptance of propeller driven passenger aircraft. Several computer codes are currently available for calculating propeller and rotor noise, and a comparison of three of these is presented by Korkan in Reference 1. The first, by Woan and Gregorek (Reference 2) has been compared with in-flight data in Reference 3. The other two are by Farassat, as described in Reference 4. Hanson (References 5 and 6) has also derived a method for computing rotor noise in the frequency domain, rather than in the time domain, as in the above methods. However, Korkan's evaluation shows calculations of OASPL to be different by as much as 6dB. The primary objective of the current work was therefore to make first principles near-field propeller noise calculations and to assess their accuracy by comparison with in-flight measured noise data.

One other area of great current interest is that of aircraft interior noise. References 7 and 8 discuss strategies which can be used in aircraft design to reduce interior noise, and for example, Reference 9 discusses some recent research on this subject. Reference 10 also discusses the impact of engine mount stiffness on interior noise, which is also discussed in the present work.

COMPUTATIONAL METHOD

The computer program used in the present study, the so-called Farassat program to calculate the discrete frequency noise of conventional and advanced propellers, employs a Finite Difference scheme to solve the governing Ffowcs Williams-Hawkings wave equation. The computing algorithm and a discussion of the details of the methodology are included in Reference 11. A general review of this subject is contained in Reference 12, including a description of the Ffowcs Williams-Hawkings equation and the physical significance of various simplifying assumptions. In particular, so-called thickness and loading noise are often separately identified, each corresponding to one of two source terms in the Ffowcs Williams-Hawkings equation. Thickness noise is a function only of the propeller blade geometry, and loading noise of the propeller blade surface pressure distribution. Two inputs are therefore fundamentally required in a noise calculation of this type: an exact description of the propeller blade surface geometry, and of the surface pressure field.

The propeller blade geometry (maximum thickness, chord, camber, twist, leading edge displacement and airfoil type (NACA 16)) were all known at 10 radial locations, sufficient to allow accurate interpolation between them. The blade surface pressure was calculated based on the theory of wing sections as described in Reference 13; which considers the wing loading to consist of 3 separate and independent terms:

- 1) The load distribution corresponding to the blade section thickness at zero angle of attack.
- 2) The distribution corresponding to the section mean line (having zero thickness) at its ideal angle of attack.
- 3) The additional load distribution caused by an angle of attack different from the ideal value.

The blade pitch angle (which along with the twist distribution specifies the airfoil section angle of attack) was calculated for each flight condition (altitude, propeller RPM, power and aircraft forward speed) using a conventional propeller strip analysis method.

Adding or subtracting the velocity increment ratios, corresponding to the latter two loading components above, gives the velocity over the blade surface pressure and suction surfaces from which the blade surface pressure field is calculated.

Surface pressures were calculated in the above manner at the centre coordinates of (15x15) quasi rectangular elements at which the Ffowcs Williams-Hawkings difference equation is solved. Absorbed power was also computed by the Farassat program and in all cases was in excellent agreement with the measured value used to compute the blade pitch angle. For example, a typical result was a computed power absorption of 214.9 SHP blade as opposed to a measured value of 216.7 SHP/blade. This agreement is an important check on the consistency of the calculation.

In summary, both the propeller blade geometry and pressure loading were accurately reproduced in the noise calculation; the first through a detailed knowledge of the propeller blade design and the second by using the well known and experimentally verified properties of the single family of blade airfoil sections from which the propeller was comprised. Discrete frequency noise calculations are presented in the following section and compared with measured values for a variety of flight conditions.

DISCRETE FREQUENCY NOISE MEASUREMENTS

All tests were conducted using a Pratt and Whitney Canada experimental twin engine turbo-prop aircraft. Measurements were conducted in level flight at 16,000 feet altitude and no difficulties were encountered in stabilizing aircraft and propeller operating conditions. Noise measurements were made at the microphone locations indicated in figure 1 and specified in table 1. Two microphones with nose cones (Bruel and Kjaer 4124 and UA 0385) were installed on a wing mounted boom, six microphones (Bruel and Kjaer 4134) were installed flush with the aircraft fuselage and two (Bruel and Kjaer 4133) were installed inside the aircraft. The fuselage microphones were calibrated immediately prior to installation and all other microphones immediately before and immediately after each test flight.

Position	X ₁ (Metres)	X ₂ (Metres)	X ₃ (Metres)
F1	- 1.912	0.092	0
F3	- 1.806	0.297	- 1.831
F5	- 1.806	0.297	- 2.523
F6	- 1.806	0.297	- 3.609
B1	+ 2.50	0	- 0.77
B2	+ 2.50	0	- 1.55

Table 1: EXTERIOR MICROPHONE LOCATIONS

Measured noise levels were determined to be reproducible by repeating various test conditions in each of three flight tests. Discrete frequency noise levels measured at the boom microphone, B1, were found to vary, typically by ± 1.7 dB (95% confidence); at the fuselage microphones F1, F2 and F3 by ± 0.8 dB and at the interior microphones I2 and I5 by ± 2.0 dB. A single investigation of the repeatability of third octave levels measured at one interior microphone, I2, showed these to be repeatable to within 1.0 dB.

Examples of discrete frequency spectra measured at each microphone location are shown in figure 2, from which it can be seen that at microphone B1, propeller harmonic levels are of the order of 30 dB above broadband, and at all other external microphones are of the order of 20 dB above broadband. Typically from 2 to 10 harmonic levels are clearly resolved. At the interior microphones I2 and I5, the harmonic levels are similarly approximately 20 dB above broadband.

For each test condition, narrow band spectra, such as those shown in figure 2, were determined by linearly averaging three spectra, each corresponding to 4 seconds of recorded data and located at approximately the beginning, middle and end of each 90 second recording. In this way, while all spectra are calculated from only 13% of the recorded data, they are representative of the complete noise recording.

Also, any extreme variation in spectral content (none was observed) would be made evident by this procedure.

For completeness, the noise signal itself is shown in figure 3. The 'y' scale is arbitrary while the time scale shows the full analyzer memory (400 msec), and also that portion corresponding to a single spectral analysis (40 msec). As can be seen, the propeller harmonic noise is clearly resolved (with a time period of 10.54 msec, corresponding to a propeller RPM of 1895.5). However, the uniformity of the signal can not be easily assessed. To investigate this, figure 3c shows the same plot, but after the data has been filtered through a 100 Hz 1/3 octave band pass filter. Figure 3c shows the variation of propeller noise at the fundamental of the blade passing frequency (BPF) to be of constant amplitude.

To summarize, great care has been taken to ensure that quoted noise levels are accurate and reproducible. Test measurements have been repeated up to three times, in different flight tests, and in each case, average spectra have been generated which are representative of the complete noise recording, rather than an instantaneous and small portion of it. Measured harmonic levels have been shown to be accurate to within a 90% confidence interval of less than ± 2 dB.

Measured propeller harmonic levels for condition 5 are shown in figures 4, 5 and 6. Condition 5 is for 2 propellers operating at 1900 RPM and at four different engine power settings. Conditions 3 and 4, for which similar figures are not shown, are for 2 and 1 propellers operating at 650 SHP and at four different propeller RPM.

Measurements for condition 5 have been analyzed in greatest detail; harmonic levels have been determined for each of the three tests conducted, labelled B5, C5 and D5. Measurements at microphone B1 are shown in figure 4, represented by open and closed circles (O, \odot , \bullet). As can be seen, the three sets of measurements are in good overall agreement, despite the fact that the harmonic levels for data set C5 correspond to a reduced aircraft speed, due to an engine installation modification to the aircraft. Harmonic levels for the other two flights are in agreement to within ± 0.7 dB as previously stated. However, for flight test C5, the levels of higher harmonics are slightly lower, and including these reduces the level of agreement to ± 1.7 dB.

Also shown in figure 4 are harmonic levels computed as discussed previously. Computed levels are shown as crosses (x), and are almost exactly linear in propeller harmonic number, n. This reproduces the observed approximately linear decrease in measured harmonic levels (a linear decrease is the simplest dependence that can be ascribed to the measured levels). The agreement between the first few measured and computed levels (n = 1 through 4) is seen to be very good but levels at higher harmonic numbers are seen to be significantly underpredicted.

Measurements at microphone F1 are shown in figure 5, and at microphone F3 in figure 6. For these cases, no correction has been applied to account for pressure doubling at the reflecting fuselage surface. Figure 5 shows trends similar to those seen in figure 4, for the boom microphone. The measured levels are in good overall agreement (to within ± 1.7 dB), and fall approximately linearly with increasing harmonic number. If 6 dB is added to the computed levels to account for pressure doubling, the measured and computed levels are also found to be in good agreement, although the computed levels fall off more quickly than measured, as was seen in figure 4.

Measurements at microphone F3 are seen in figure 6 to be at the limit of resolution. The measured levels no longer fall linearly with increasing harmonic number, but in fact remain approximately constant, suggesting contamination from background noise in levels n = 2 and above.

An important objective of the present work was to evaluate the accuracy of the noise prediction method. An evaluation for condition 5 is shown in figure 7a, based on the levels listed in table 2.

Spectra at each microphone position are evaluated in two ways. Firstly, OASPL, being the logarithmic sum of all harmonic levels, is an overall figure which can be used to determine the accuracy of the method for calculating the magnitude of propeller noise. Secondly, a slope has been calculated by fitting best straight lines through both the measured and computed harmonic levels. (As has been discussed, the calculated levels are almost exactly linear in harmonic number, and a linear variation is the simplest dependence which can be ascribed to the measured levels.)

In figure 7, discrete points are measured values at various microphones (with 6 dB subtracted to correct for pressure doubling at fuselage microphones) and solid lines connect the predictions. As can be seen, the measured and computed trends in OASPL are very close. In particular, the noise prediction method accurately reproduces the increase in OASPL with increasing engine power at all microphone positions. However, the slope, or spectrum shape, is very poorly reproduced. At microphones B1 and F1 the measured slope is only approximately half that predicted, and at microphones F3 and F4, it is underpredicted by almost 8 dB (per harmonic number). However, the slopes are predicted in the correct order; ie., the slope at microphones F3 and F4 is correctly predicted to be greater than at microphone B1, which is in turn greater than at microphone F1.

Conditions 3 and 4 show the same behaviour. Values of OASPL and slope are shown in figure 7b and listed in table 3. As in figure 7a, computed OASPL's for microphone F1 are slightly overpredicted and for microphone B1 are slightly underpredicted. Computed OASPL for microphones F3 and F4 are on average well predicted, but in contrast to figure 7a, the results at these two microphones are asymmetric, being lower on the port side of the aircraft (F4) than on the starboard (F3). The slope or spectrum shape, shows stronger dependence on RPM in figure 7b than on engine power in figure 7a; values are again overpredicted by the noise prediction method, and seriously overpredicted at microphones F3 and F4, but as in figure 7a are predicted in the correct order.

In summary, the noise prediction method is shown to be reasonably successful in calculating the near field noise around a propeller. OASPL is calculated to within 1.5 dB on average at several different locations around the propeller, spanning a wide range of noise directivity. However, spectrum shape is not

well predicted, the computed fall off in harmonic levels being always greater than measured.

INTERIOR NOISE

Noise levels were also measured inside the aircraft at two locations, both at the centre of the fuselage at ear height, one just forward of the wing leading edge at the front of the passenger area, and the other approximately three feet forward of this in the rear of the aircraft cockpit. The aircraft interior was standard, with the exception of two racks of data acquisition equipment, and in particular, side wall treatment was of normal fabric covered panels. Typical results are shown for conditions 5 in figure 8. As can be seen from the figure, both interior and exterior third octave spectra have characteristic shapes. Above 500 Hz, the exterior spectra are flat, while for the interior spectra the third octave levels fall smoothly up to approximately 6 kHz. This results in a transmission loss (the difference between the interior and exterior spectra) which increases with increasing frequency, as shown.

To determine the behaviour of the transmission loss with changing propeller operating conditions, measurements at conditions 5 (1900 RPM and 800 to 500 SHP) are shown in figure 9, based on unweighted third octave spectra. As can be seen, the transmission loss results are very similar at each of the different propeller operating conditions, there being no discernable variation with changing engine power. For this reason, average transmission loss results have been calculated and are shown as solid lines in figure 10 for both interior microphone locations.

The shapes of the two graphs in figure 10 appear similar and in fact are the same to within an experimental uncertainty of ± 2 dB. The average dependence of transmission loss on third octave band number, N , in the linear region is given by:

$$T = 3.22 N + 7.15$$

Figure 10 also compares the above average transmission loss results with similar measurements made in gliding flight. For these tests, the aircraft was flown at nominally constant airspeed, with both engines at idle and both propellers feathered. This is done to determine the noise 'floor' below which interior noise can not be reduced. As can be seen in figure 10, the transmission loss results at the location of microphone 15 are the same in gliding flight as in powered flight, while at the location of 12 the levels are approximately 5 dB higher. This is thought to be due to the fact that microphone 12 is closer to the aircraft windshield, through which a disproportionate amount of noise enters the aircraft. Despite this, the fact that transmission loss measurements are in one case the same in gliding flight as in powered flight, and in another case are similar, is considered to confirm the applicability of an average transmission loss to a wide range of propeller operating conditions.

As has been stated above, noise measurements were made in gliding flight to determine the contribution to interior noise due only to the forward motion of the aircraft ie., with no contribution from the propeller/engine combination. However for reasons of safety, both engines were operated at idle power and both propellers were feathered. The gliding flight measurements may therefore contain a residual engine noise component, and should more accurately be considered an upper bound to the airspeed generated component of interior noise.

Measurements during gliding flight were made at three different airspeeds (112, 145 and 170 knots), at nominally 16000 feet altitude. In order to extrapolate measured interior noise spectra to airspeeds corresponding to powered flight (170 to 210 knots), a procedure suggested in Reference 14 has been used, in which each third octave level is held to vary as $H(1 - M_0)$, where H is altitude and M_0 is the Mach Number corresponding to the aircraft forward speed. In the present case because the altitude was kept approximately constant at 16000 feet, the above degenerates to a linear dependence on aircraft forward speed, which is confirmed by measured third octave levels, to within 1 dB at all frequencies. Measurements also reveal that third octave spectra measured at the two interior microphones give the same dependence on aircraft forward speed. Therefore, an average interior noise spectrum for gliding flight is shown in figure 11, for an aircraft Mach number of 0.32, a typical cruise value being 0.35. In fact, the value of 0.35 occurs within the range of Mach number achieved in gliding flight tests so that no extrapolation of the results is necessary to obtain the forward speed interior noise component for cruise flight.

As can be seen, figure 11 shows the forward speed component to be broadband in nature, peaking at approximately 200 Hz. More important, a comparison with spectra for powered flight (each at the same value of aircraft Mach number and altitude) reveals the forward speed component to be always less than the powered flight spectra by at least 8 dB, and on average by 10 dB (above 200 Hz). These measurements therefore suggest that non-discrete frequency interior noise inside a twin engine turbo-prop aircraft is not significantly generated by the forward speed of the aircraft, but is dominated by noise generated by the propeller and engine; in the former case by the vortex sheet shed by each propeller blade, and in the latter case mainly by the engine exhaust.

In a final series of tests, measurements were made during a ground static noise and vibration survey to determine the dependence of interior noise on engine mount stiffness. The purpose of this was to further investigate the transmission of propeller noise into a turbo-prop aircraft interior.

It has been previously concluded by several investigators that an important mechanism for discrete frequency noise transmission is through the engine mount structure. In the present testing, measurements have been obtained with three different sets of engine mounts, one set having infinite stiffness (solid steel) and the other two having half and twice normal mount stiffness. Noise measurements were made at four locations inside the aircraft and vibration measurements were made at four accelerometer locations on the engine and engine mount frame. The test matrix again covered a wide range of propeller operating conditions including take-off, cruise and approach power settings. Typical interior spectra are shown in figure 12, and to ensure representative spectra, they have again been obtained as an average of three

separate scan analyses. As can be seen, the spectra (and OASPL) are dominated by the first two propeller harmonic levels. The maximum uncertainty associated with these is ± 0.5 dB. The time variation of all acoustic signals was also investigated and was similarly found to be stable.

Four interior microphones were employed, labelled M6 through M9 in figure 13. Microphone M6 was in the location of microphone 12 used in the previously discussed flight test. Microphone M7 was directly below this, in the geometrical center of the fuselage (rather than at ear height) and microphone M8 was in the same plane as M6 and M7, but was placed approximately three inches from the fuselage wall. Microphone M9 was in the location of microphone 15.

Comparison of measurements made with the three different sets of engine mounts show that the harmonic level at the fundamental propeller blade passing frequency changed very little with varying engine mount stiffness. On average the difference, as a result of changing engine mount stiffness, is 2.4 ± 0.7 dB at microphones M6 and M7, with the noise level being lowest at all test conditions with the steel mounts installed and approximately the same with either set of 'soft' mounts. The average difference in OASPL is 1.7 ± 0.8 dB. These results suggest that the engine and engine mount structure are not a significant noise transmission path in the particular aircraft studied.

CONCLUSIONS

In conclusion, the present paper summarizes the findings of some noise investigations carried out by Pratt and Whitney Canada. A first principles method of calculating near field propeller noise has been shown to be successful in calculating OASPL, and useful as a guide for determining discrete frequency noise in the near field. Measured propeller noise transmission loss through the cabin wall has been shown to be unchanged over a wide range of propeller operating conditions (from take-off to flight idle power). Non-discrete frequency noise has been shown to be dominated by the propeller and the engine and not significantly influenced by the forward speed of the aircraft. Finally, it was found that interior noise was not reduced by changing engine mount stiffness, in this instance.

REFERENCES

1. Korkan K.D.; "A Study of Theoretical Propeller Acoustic Methodologies", AIAA 83-0742.
2. Woan C.J. and Gregorek G.M.; "The Exact Numerical Calculation of Propeller Noise". AIAA 78-0028.
3. Gregorek G.M., Woan C.J., and Korkan K.D.; "Acoustic Evaluation of Three Turbo Propellers" SAE 83-0733.
4. Farassat F.; "The Prediction of the Noise of Supersonic Propellers in Time Domain - New Theoretical Results", AIAA 83-0743.
5. Hanson D.B.; "The Influence of Propeller Design Parameters on Far-field Harmonic Noise in Forward Flight", AIAA 79-0062.
6. Hanson D.B.; "Near Field Frequency Domain Theory for Propeller Noise", AIAA 83-0688.
7. Waterman E.H., Kaptein D and Sarin S.L.; "Fokker's Activities in Cabin Noise Control for Propeller Aircraft", SAE 830736.
8. Metzger F.B.; "Strategies for Aircraft Interior Noise Reduction in Existing and Future Propeller Aircraft" SAE 810560.
9. Mixson J.S., Farassat F. and Leatherwood J.D.; "Interior Noise Considerations for Advanced High-Speed Turboprop Aircraft"; J. Aircraft, Vol. 20, No. 9, Sept. 1983, p. 791.
10. Unruh J.F.; "Specification, Design, and Test of Aircraft Engine Isolators for Reduced Interior Noise". AIAA 830718.
11. Martin R.M. and Farassat F.; "User's Manual for a Computer Program to Calculate Discrete Frequency Noise of Conventional and Advanced Propellers", NASA TM 83135.
12. Farassat F.; "Linear Acoustic Formulas for Calculation of Rotating Blade Noise" AIAA 800996R.
13. Abbott I.H. and Von Doenhoff A.E.; "Theory of Wing Sections", Dover Publications LC 60-1601.
14. Moses N.M. and Roxner T; Private Communication.

MICROPHONE		B1	SPLo(dB)		OASPL(dB)		SLOPE		
SHP	COND	#	PROPS	MEASURED	PREDICTED	MEASURED	PREDICTED	MEASURED	PREDICTED
800	5	2		125.2	126.3	126.7	127.9	- 2.8	- 5.0
700	5	2		123.6	125.2	125.3	126.8	- 3.1	- 5.1
600	5	2		122.8	123.7	124.3	125.1	- 3.2	- 5.4
500	5	2		120.4	122.1	122.1	123.5	- 3.3	- 5.5
MICROPHONE F1									
800	5	2		130.0	129.6	133.5	131.9	- 2.2	- 3.8
700	5	2		128.7	128.4	132.6	130.6	- 2.0	- 3.8
600	5	2		127.0	126.9	130.8	129.0	- 2.1	- 4.0
500	5	2		126.6	125.2	129.5	127.3	- 2.2	- 4.0
MICROPHONE F3, F4.									
800	5	2		118.4	119.5	119.0	119.7	- 5.1	- 12.9
700	5	2		116.8	118.4	117.4	118.6	- 4.8	- 12.9
600	5	2		116.5	117.2	117.0	117.4	- 5.5	- 13.1
500	5	2		116.2	115.9	116.7	116.1	- 3.9	- 13.3

Table 2: MEASURED AND PREDICTED NOISE LEVELS FOR CONDITION 5

MICROPHONE		B1	SPLo(dB)		OASPL(dB)		SLOPE		
RPM	COND	#	PROPS	MEASURED	PREDICTED	MEASURED	PREDICTED	MEASURED	PREDICTED
2000	B3	2		126.2	124.7	128.7	126.7	- 3.6	- 4.55
	B4	1		125.2		127.3		- 2.9	
1900	B3	2		123.6	124.4	125.2	125.9	- 3.0	- 5.25
	B4	1		123.3		124.7		- 4.0	
1800	B3	2		122.7	123.7	124.4	124.8	- 3.7	- 6.22
	B4	1		121.0		122.7		- 4.3	
1700	B3	2		121.2	123.2	123.1	124.1	- 4.8	- 7.32
	B4	1		117.2		119.6		- 4.3	
MICROPHONE F1, F2.									
2000	B3	2		126.0	127.3	131.5	130.2	- 1.6	- 2.90
	B4	1		128.5		132.7		- 1.9	
1900	B3	2		128.5	127.6	132.5	129.8	- 1.8	- 3.80
	B4	1		129.4		133.0		- 2.3	
1800	B3	2		128.9	127.7	131.7	129.3	- 2.7	- 4.91
	B4	1		129.2		131.3		- 3.2	
1700	B3	2		128.6	127.8	130.8	129.1	- 3.2	- 5.93
	B4	1		128.6		130.6		- 3.6	
MICROPHONE F3, F4.									
2000	B3	2		117.3	118.6	118.0	118.9	- 4.4	- 11.9
	B4	1		121.1		121.5		- 8.1	
1900	B3	2		114.4	117.8	115.1	118.0	- 4.5	- 13.0
	B4	1		121.1		121.5		- 8.1	
1900	B3	2		114.4	117.8	115.1	118.0	- 4.5	- 13.0
	B4	1		120.8		121.1		- 9.9	
1800	B3	2		115.1	116.7	116.2	116.9	- 5.1	- 14.3
	B4	1		119.2		119.6		- 8.3	
1700	B3	2		115.0	115.8	114.7	115.9	- 6.4	- 15.7
	B4	1		117.9		118.4		- 8.5	

Table 3: MEASURED AND PREDICTED NOISE LEVELS FOR CONDITIONS 3 AND 4

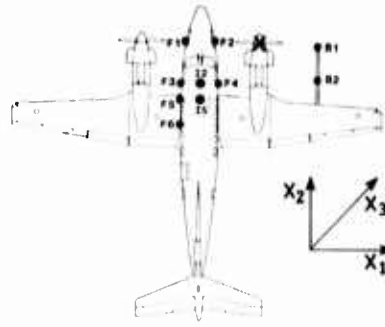


Fig. 1: MICROPHONE LOCATIONS

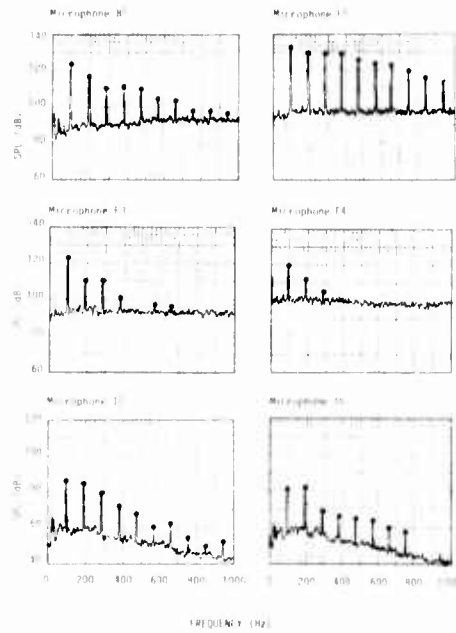


Fig. 2: EXAMPLES OF IN-FLIGHT MEASURED SPECTRA SHOWING PROMINENCE OF DISCRETE FREQUENCY PROPELLER NOISE

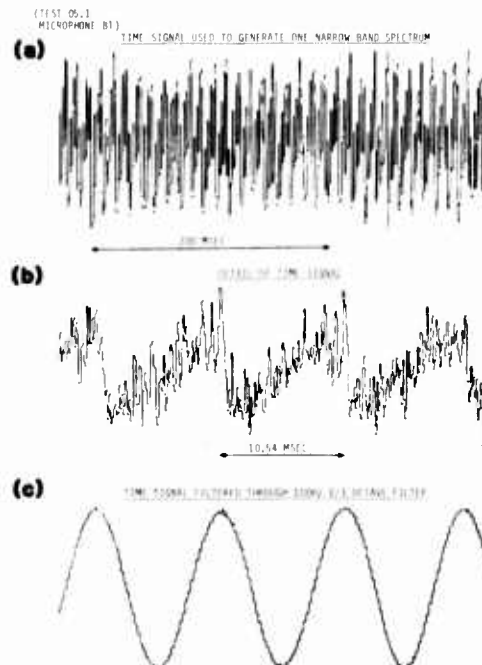


Fig. 3: MEASURED TIME DEPENDENCE OF PROPELLER NOISE

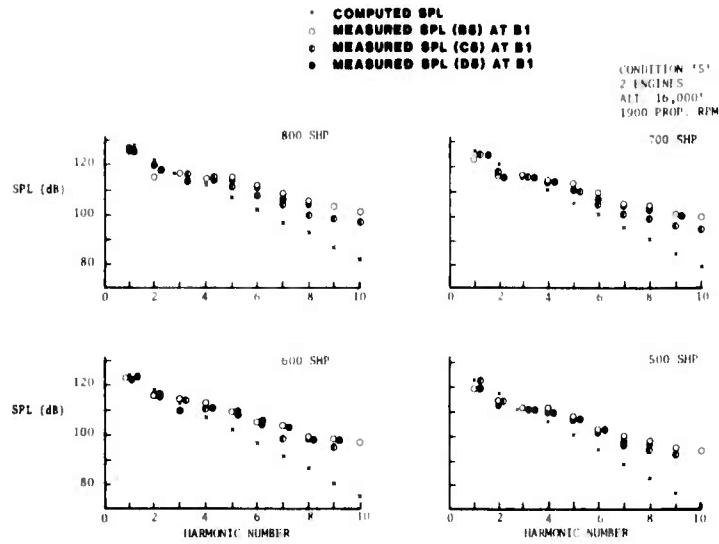


Fig. 4: COMPARISON OF MEASURED AND COMPUTED DISCRETE FREQUENCY NOISE AT MICROPHONE B1

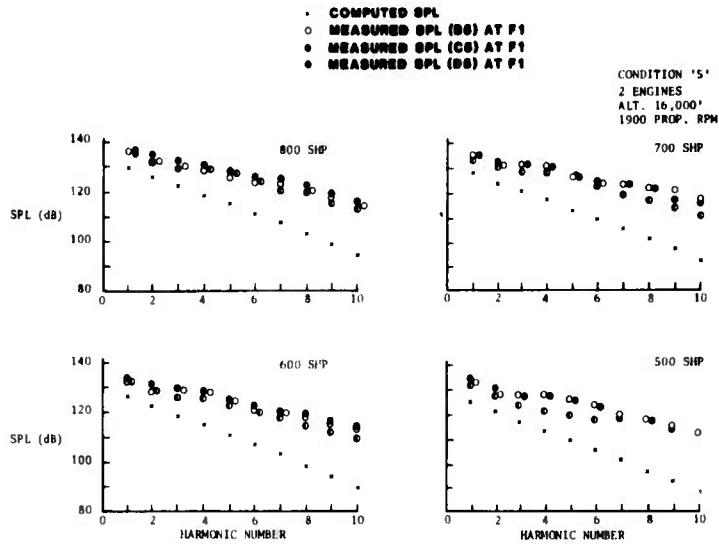


Fig. 5: COMPARISON OF MEASURED AND COMPUTED DISCRETE FREQUENCY NOISE AT MICROPHONE F1

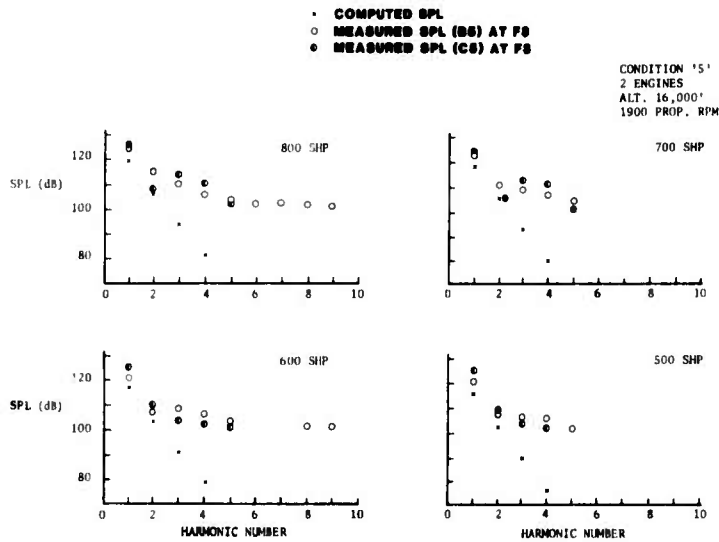


Fig. 6: COMPARISON OF MEASURED AND COMPUTED DISCRETE FREQUENCY NOISE AT MICROPHONE F3

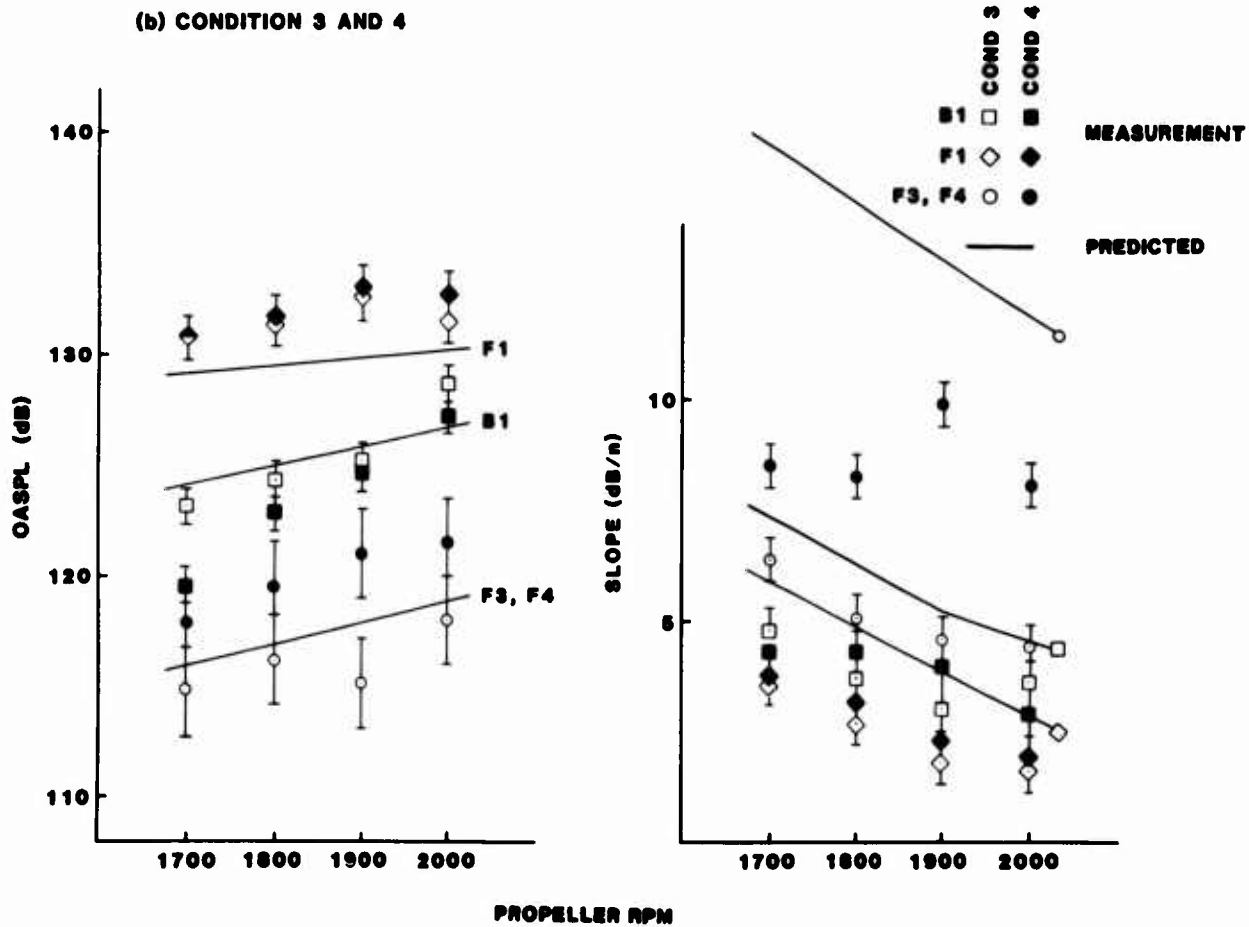
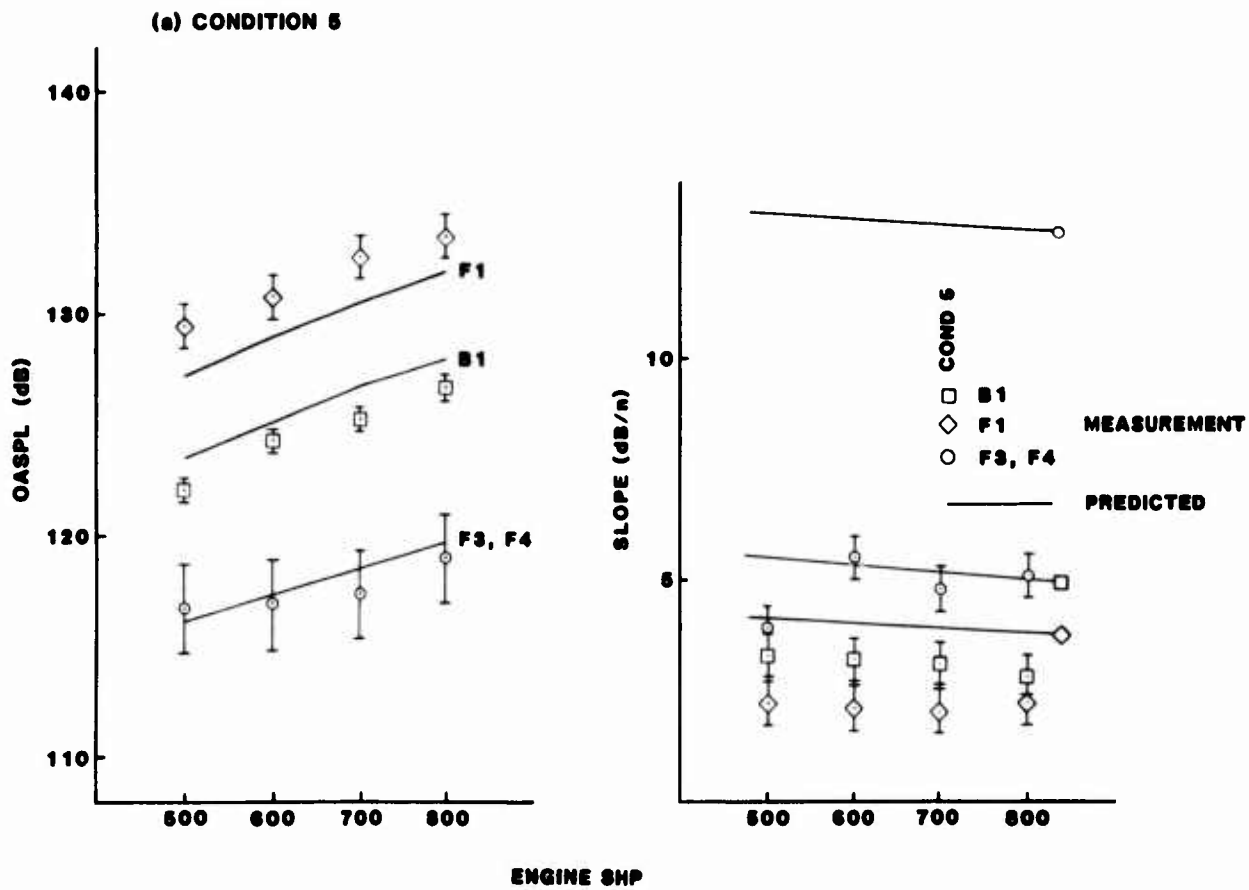


Fig. 7: EVALUATION OF NOISE PREDICTION METHOD

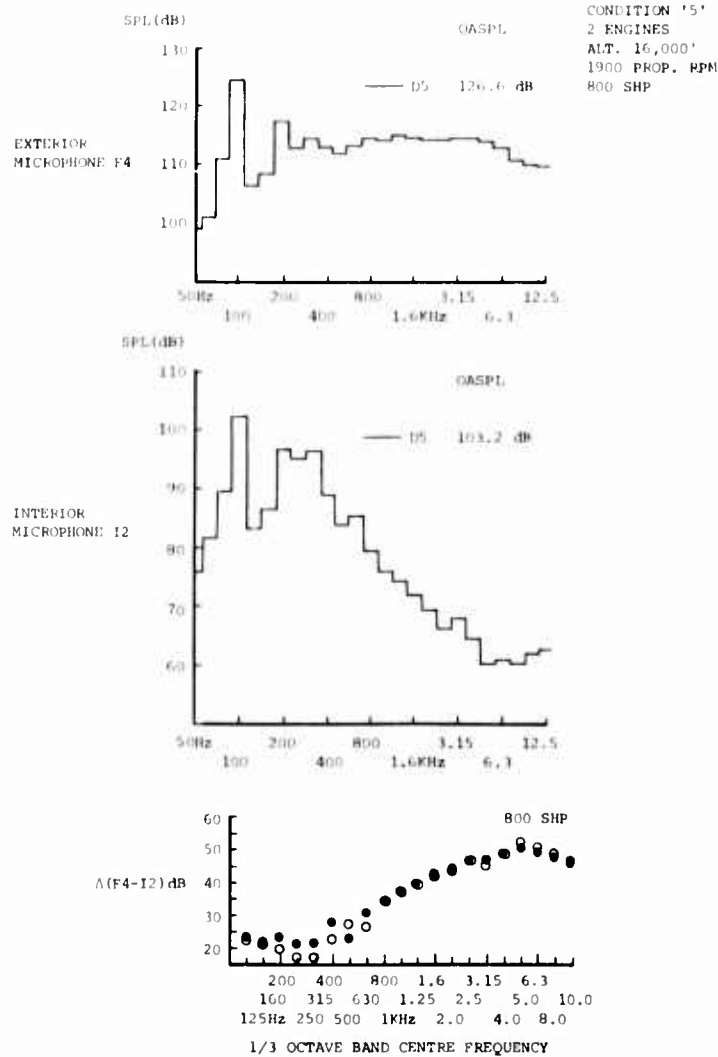


Fig. 8: THIRD OCTAVE SPECTRA AND TRANSMISSION LOSS FOR CRUISE FLIGHT

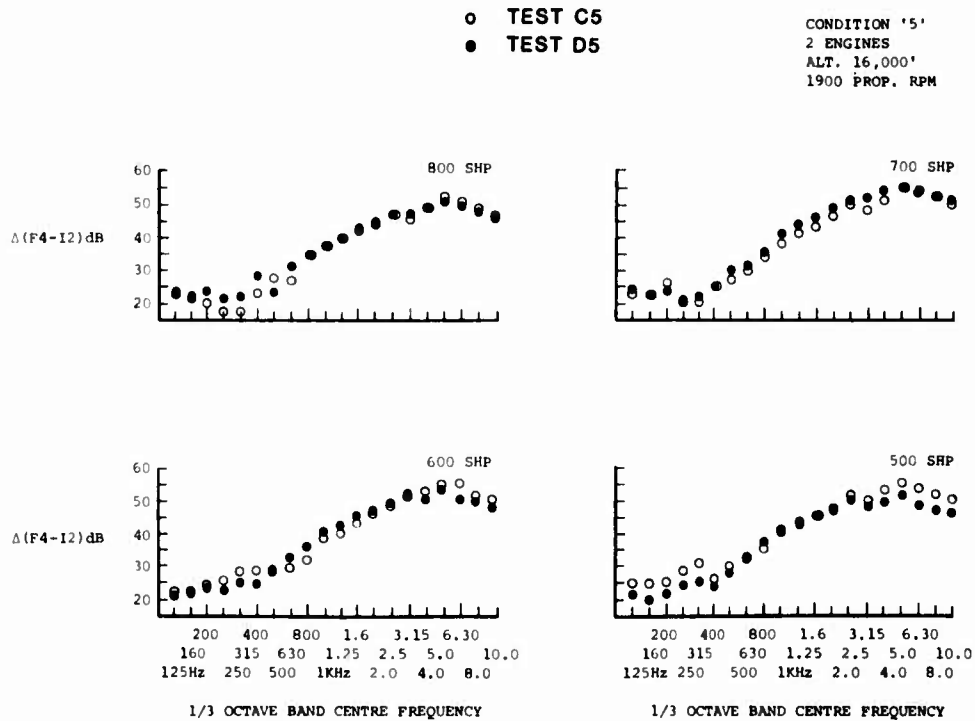


Fig. 9: MEASURED TRANSMISSION LOSS AT A VARIETY OF TEST CONDITIONS

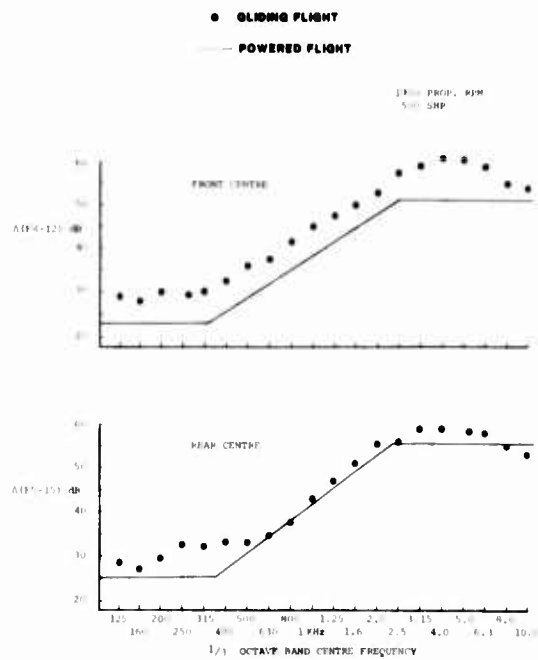


Fig. 10: AVERAGE TRANSMISSION LOSS FOR POWERED FLIGHT AND COMPARISON WITH MEASUREMENTS IN GLIDING FLIGHT

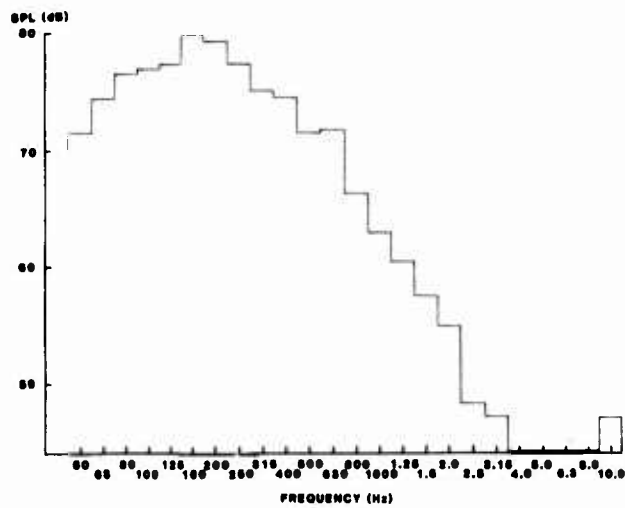


Fig. 11: ESTIMATED INTERIOR NOISE SPECTRA DUE ONLY TO AIRCRAFT FORWARD SPEED

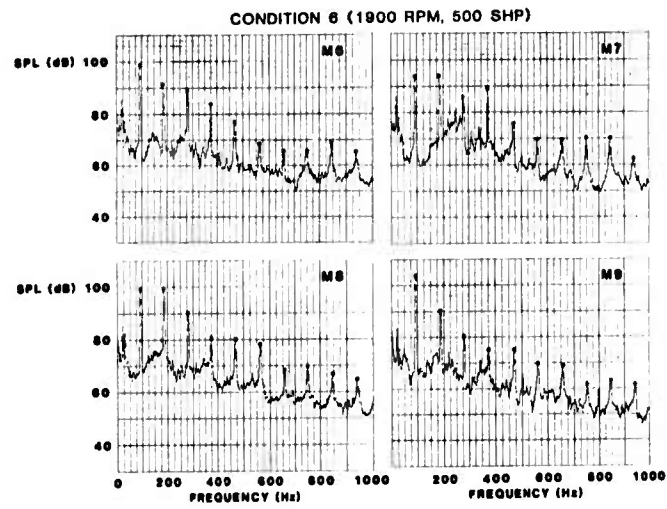


Fig. 12: EXAMPLES OF SPECTRA MEASURED IN A GROUND STATIC TEST

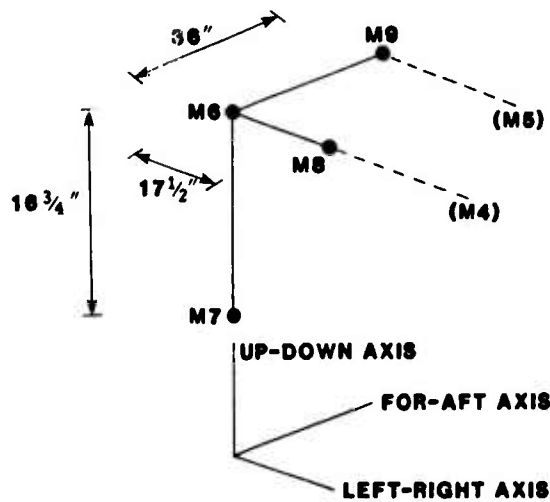


Fig. 13: INTERIOR MICROPHONE LOCATIONS

**FULL-SCALE FLIGHT AND MODEL-SCALE WIND TUNNEL TESTS ON THE NEARFIELD
NOISE CHARACTERISTICS OF AIRCRAFT PROPELLERS**

Heller, H., Kallergis, M., and Gehlhar, B.
Abteilung Technische Akustik im Institut für Entwurfsaerodynamik
Forschungsbereich Strömungsmechanik
Deutsche Forschungs- und Versuchsanstalt für Luft- und Raumfahrt e.V. (DFVLR)
Bienroder Weg 53, 3300 Braunschweig, W.-Germany

ABSTRACT

Flight noise tests employing a single-engine Cessna T 207 aircraft with an array of wing-mounted microphones were conducted to investigate nearfield acoustic characteristics of a 3-blade variable pitch propeller under different operational conditions, varying helical blade tip Mach-number, propeller advance ratio, and blade loading. A special technique to minimize the engine exhaust influence on the propeller signature had been developed for this purpose. Supplementary, yet much more extensive tenth-scale tests were performed in the 'DFVLR One-Meter Acoustic Tunnel' again in the acoustic nearfield of propellers with 2 to 6 blades over a substantial range of operational, partially interdependent, parameters, such as helical blade tip Mach-number, blade pitch angle setting, blade incidence angle, rotational plane attitude, and ambient temperature. These data could also be compared to some third-scale results for geometrically identical propellers. Especially the model tests allowed an exact quantification of the effect of the various parameters on the ensuing harmonic and subharmonic propeller-noise spectra.

1. INTRODUCTION

Interior noise of propeller-driven aeroplanes is dominated by propeller acoustic radiation due to the physical proximity of the rotating-blade tips to the fuselage. Considering aeroplanes with wing-mounted engines in particular, it is quite common to position the propellers at clearances of 10 to 20 % of the diameters between the tips and the airframe. When mounted on the wings - rather than at the tail-end of the aircraft - the full "blast" of the propeller acoustic nearfield is felt by the aircraft-skin (and - so to speak - by the skin of the passengers, being only a few feet away from the spinning propellers, albeit somewhat protected by a low-transmission-loss fuselage).

The advent of the propfan, with its near sonic tip-speeds, is not going to lessen the problem; until then, and in the foreseeable future, the small business and the commuter aeroplanes, as well as the medium-weight to heavy transport-category aircraft will utilize conventional or (however) "advanced" propellers with comparatively low tip-speeds, taking advantage of the propeller's proven aerodynamic efficiency and frugal consumption of gasoline.

A thorough understanding of the acoustic behavior of propellers, in their dependence on geometric and operational parameters is necessary both for nearfield (passenger comfort) and farfield (community annoyance) conditions, when attempting to develop and design acoustically acceptable propeller-driven aeroplanes.

Several studies to this extent have been initiated in the DFVLR Braunschweig Research Center /1-13/, following a two-tier approach of full-scale flight, and model-scale wind tunnel experiments. The intent of this paper is to provide a progress-report on some ongoing studies, related specifically to the nearfield acoustics of General-Aviation propellers.

2. EXPERIMENTAL PROGRAMS

Both the full-scale flight and the model-scale wind tunnel tests were designed to obtain nearfield data under conditions, where the source (i.e. the propeller) and the receiver (i.e. the microphone) had fixed positions with respect to each other at realistic conditions with the propeller "flying" through the air (inherent in the flight-test or properly simulated in the tunnel tests). Furthermore, both test-series were to yield a maximum of results by controlled variation of relevant operational parameters. It was, however, not possible to directly, and quantitatively compare the tests, and the ensuing results, since the test-propeller geometries at full-scale and at model-scale were different. On the other hand, equivalent trends and similar acoustic characteristics were expected to occur for both test types, thus tying them together in a meaningful way.

Some of the model-test data however, could be checked against results available from prior, originally unrelated, wind tunnel experiments, where an exact geometric replica of the propeller of larger dimensions had been tested, thus providing information on the scalability of model-data, and hence on their overall validity.

2.1 Full-scale Flight Tests

2.1.1 Test Specifics

The test-aircraft, a single-engine Cessna T 207 with a 6-cylinder engine of 212 kW rated power was equipped with an array of 8 flow-exposed 1/2-inch B&K condenser-microphones with nose-cone protection (Fig. 1). During test-evaluation the basic microphone arrangement was checked for its aerodynamically-induced self-noise characteristics; to this end, the sensors were exposed to quiescent air by mounting and flying them on an (engine-less) glider plane (Fig. 2). The aircraft was equipped with a 3-blade variable pitch McCauley propeller (type 90 DFA-10) of 2.03 m diameter with a rated-maximum rotational speed of 2600

Fig. 3 shows the measurement array and the microphone positions, 1 m behind the propeller-plane. One further microphone was installed 0.2 m to the side of the engine-exhaust outlet. Blade pitch angle and propeller-RPM were determined by means of a photodiode, which registered the light off a reflecting patch on one propeller-blade. Microphone- and photodiode-signals were recorded synchronously on a multitrack on-board tape-recorder. Blade-loading - which is related to the aircraft-performance - was varied by climbing or descending at otherwise constant flight- and rotational-speed with corresponding blade-pitch settings in an atmosphere of constant temperature. Since the flight-speed during the experiments was generally held at 50 m/s, the flow-conditions around the microphones and hence the self-noise remained unchanged.

The results reported in the following are presented mostly in the (sound-pressure) time-domain, rather than in the frequency domain.

2.1.2 Test Results

(a) Separation of Engine-exhaust and Propeller-noise

A general problem in studying nearfield propeller noise phenomena on aeroplanes with piston-engines lies in the usual coincidence of the engine-exhaust harmonics and the propeller harmonics. An attempt has therefore been made to electronically separate the two sources in order to obtain the "clean", i.e. uncontaminated propeller-signal. For this purpose, the noise at the engine-exhaust orifice is monitored; after appropriate adjustment in amplitude (to account for the propagation path attenuation from the exhaust to the wing-tip microphone) and in phase, its signal is subtracted from the combined propeller/exhaust signal. Fig. 4 illustrates the process. Here (a) shows the engine-exhaust pressure signature of the 6 cylinder-engine, as measured very close to the exhaust-outlet, the repetitive pattern for each 6 peaks being clearly discernible; (b) then represents the combined signature; (c/left) shows both the contaminated total signature with the (adjusted) exhaust signature superimposed and (c/right) the "clean" signature of the propeller only, after exhaust-noise subtraction.

It is of interest to try and identify the exhaust-contribution within the narrowband spectra. In Fig. 5 the exhaust-related "discretes" may be discerned in the combined spectrum. In this case, it seems, that at the particular microphone location (wing-tip) these discretes would play a minor role. The results presented in section (b) below pertain to the uncontaminated ("clean") propeller-signatures.

(b) Uncontaminated Propeller Noise

Influence of helical blade tip Mach-number: Fig. 6 shows pressure time-histories as observed on microphone M1, located at a distance of 2.2 propeller-diameters to the left of the propeller-hub (facing forward), and 11° aft of the propeller-plane. The helical blade tip Mach-number was varied from 0.70 to 0.83 with the pitch-settings remaining unchanged at 18.2° and 13.6°. Here the blade pitch is defined as the angle at the 75% radial station between the plane of rotation and the blade chord. This Figure inherently illustrates the effect of a blade tip-speed (rotational speed) change, since all test-results were obtained at the same forward flight speed but at different rotational speeds.

For helical blade tip Mach-numbers (HTM) between 0.70 and 0.73, the pressure signal exhibits a somewhat sinusoidal shape. The peak-to-peak amplitude is nearly the same at both HTMs, while at HTMs from 0.76 to 0.79 the peak pressures grow in magnitude and assume an increasingly impulsive character. At the same time, the peak-to-peak amplitude increases. The essential change in the signal occurs at a HTM of 0.83, where the negative peak pressure amplitude exceeds the positive one, although the latter too has grown in magnitude, such marked peaks having their origin in the advent of compressibility-effects.

Influence of blade pitch angle setting: Fig. 7 shows signatures for a constant HTM of 0.83 at microphone-position M1, as function of the blade-pitch angle (affecting both axial and circumferential forces). With growing angle, both the peak-to-peak amplitude and the signal width at zero-pressure crossing increase, resulting in higher sound levels. For the highest blade pitch angle of 18.2°, the pressure amplitude is twice that at the lowest angle of 12.9°. On the other hand, the ratio of the signal width at the 3-dB-down-point (half amplitude) and the peak-to-peak amplitude remains approximately constant.

Fig. 8 shows more clearly - within a direct comparison - the pitch-angle effect for

otherwise constant conditions at HTMs of 0.83 and 0.73, resp., again at microphone M1. Finally, plotting the peak-to-peak amplitudes vs. the blade-pitch angle for conditions of a high HTM (equal to 0.83) shows these to grow with that angle (Fig. 9).

Influence of radiation direction: Although covering only a small fraction of the azimuthal range around the propeller (11° to 24° , where the rotational plane corresponds to 0°), some information on the pressure signature directivity characteristics may be obtained. Fig. 10 shows corresponding results; it should be kept in mind, however, that the microphone/propeller-hub distances vary from about 1.5 D (microphone M6) to 2.2 D (microphone M1), where D stands for propeller-diameter, such that directivity and nearfield/ farfield transition effects are intermingled. Proceeding then from M6 to M1 (distance and directionwise), one observes a conspicuous change in signal-character: the "Mike 6-signal" is characterized by pronounced positive pressure peaks, by far exceeding the negative portion, while the "Mike-1-signal" shows a more symmetrical positive/negative energy distribution. In the absence of results from more measurement points around the propeller, no definitive answer to the reason for such variations in the signature-characteristics may be given.

2.2 Model-scale Wind Tunnel Tests

2.2.1 Test Specifics

Supplementing the full-scale flight-tests on propellers, and allowing - after all - a much wider range of parameter-variations, model-scale tests in specially suited (i.e. acoustically treated) wind-tunnels are necessary. The DFVLR has recently designed and built an acoustic wind tunnel (Fig. 11) in its Braunschweig Research Center, providing a quiet and low turbulence ($<0.25\%$) flow emanating from a $1 \times 1 \text{ m}^2$ nozzle at speeds of up to 65 m/s into an anechoic ($f_{\text{limit}} = 124 \text{ Hz}$) chamber of $7.5 \times 7.5 \times 3.5 \text{ m}^3$. This facility is presently used for extensive model tests on aircraft-propellers.

Fig. 12 shows the general set-up, positioning the test-propellers one nozzle width downstream of the nozzle. A close-up of the propeller drive-system, consisting of two tandem electric motors of 7 kW total power at rotational speeds up to 20,000 RPM, appears in Fig. 13. The test propellers of 0.273 m diameter and fixed geometry allow variation of blade number (2 to 6, see Fig. 14) and blade pitch setting; rotational speed in conjunction with tunnel flow speed provides helical blade tip Mach-numbers in excess of 0.9 (for the 2-blade propeller at high advance-ratio).

The test propellers corresponded in their blade-form and profile to those used in a propeller-developmental program conducted by the DORNIER company in close cooperation with the 'Propellerwerke Hoffmann', and the DFVLR /14, 15/. In this program, various propellers were to be tested at 1:3 model-scale in the DFVLR-Göttingen 'Three-meter Low Speed Tunnel', and selected ones under 1:1 full-scale flight conditions on the DORNIER TNT-experimental aeroplane.

For the subject model-experiments in the DFVLR Braunschweig One-meter Acoustic Tunnel, one propeller was selected for testing at 1:10 scale, a planform and profile-sections appearing in Fig. 15, twist-, blade-chord-, and thickness- distribution in Fig. 16. The propeller-blades were made of carbon-fiber, thus minimizing mass while still providing a sufficiently accurate surface-finish. Although the in-flow microphone (a nose-cone protected B&K 1/4-inch diam condenser microphone) could be freely moved in axis-parallel and lateral directions, the majority of the tests occurred at an in-plane position of 2 propeller-diameters from the center of the hub (equal to 1.5 diameter to the side from the rotating tips).

The test arrangement allows variation of the attitude of the propeller-plane with respect to the prevailing tunnel-flow direction (within $-7.5^\circ/+15^\circ$); furthermore, the tunnel-flow temperature could be varied from a starting temperature up to a maximum steady-state temperature by switching off the tunnel-flow cooler and letting the temperature climb. The starting-temperature roughly corresponds to the prevailing ambient (summer-temperature e.g. 15° C , winter-temperature lower), while maximum temperatures of about 35° C could be achieved.

Several farfield microphones, outside the free-jet tunnel-flow were positioned at lateral distances of about 10 propeller-diameters, but no data-reduction for these has yet been performed. However, a lateral, through the shear-layer, sweep was made to explore sound-signal variations with growing distance from the rotating blade-tips when also passing the highly turbulent free-shear flow regime.

In addition to measuring rotational speed and instantaneous blade position by means of a photo-diode/reflecting pad arrangement, the propeller total thrust could be determined by means of a force-gauge appropriately positioned on the support-pylon; however no direct measurement of power or torque was possible, other than inferring these from the voltage and current drawn by the electric motors.

2.2.2 Test Results

Most of the test-results pertain to one lateral nearfield measurement point only (in-plane one propeller-diameter from the tips to the right, when looking towards the propeller from upstream), and are presented in the frequency domain. Depending on the band analysed, either 0 to 6, 0 to 12, and 0 to 25 kiloHertz, the analysis bandwidths for the narrowband spectra were 12.5 Hz, 25 Hz and 50 Hz, resp.

(a) Subharmonic Spectra

While it is known that the harmonic spectra of propellers - in addition to showing the basic blade number times rotational speed related discrete frequencies - exhibit subharmonics (between the rotational frequency harmonics), these have been tied to unavoidable manufacturing differences of the blades and to more or less random flow incidence irregularities or attitude changes. Although this reasoning is certainly true, it is difficult to quantify such effects. If the amplitude of such subharmonics (related to a once-per-revolution event) are substantially below the fundamental "blade-passage"-spectrum, they may be ignored. However, as the model-tests showed, the subharmonic spectrum may approach, or even exceed the harmonic spectral levels, thus contributing or even dominating the overall propeller-noise spectrum. While the relative importance of such subharmonic spectra might also depend on the absolute scale of a propeller (perhaps relatively less important for full-scale propellers), their appearance and magnitude should still be a function of geometric and operational parameters.

Hence, the available experimental data was systematically screened for information on the parametric dependence of subharmonic characteristics, mostly for the 2-blade model rotor.

Influence of Advance Ratio: Fig. 17 shows spectra of the 2-bladed propeller at a blade-pitch angle (BPA) setting of 20° at the 75 % radial station under conditions of constant helical blade tip Mach-number (HTM) of 0.75 for blade-tip advance ratios (AR) of, respectively 0.10, 0.15, 0.20, and 0.25. This change in AR corresponds to effective blade-incidence angles at the 75 % radial station of, respectively, 9.3° , 6.5° , 3.7° , and 1.0° (since there exists a 5° -twist between the 75 % radial station and the blade tip), indicating that high blade incidence angles with correspondingly high lift (approaching flow-separation and/or causing thick wakes) tends to emphasize the subharmonic spectrum. In the top-frame of Fig. 17, for the highest blade-incidence angle, the subharmonic spectrum exceeds the harmonic one. Fig. 18 shows corresponding results for a HTM of 0.85, where for diminishing blade-incidence angles an amplitude drop of the subharmonic spectrum occurs.

Influence of Helical Tip Mach-number: Maintaining on the other hand, a BPA of 20° as well as an AR of 0.2 (i.e. blade-incidence angle equal to 3.7°) at HTMs of 0.65, 0.75, 0.85, and 0.97, as shown in Fig. 19, illustrates the increasing importance of the subharmonic spectrum also with Mach-number. (Note however, that the relative importance tends to diminish with growing Mach-number as the comparison for HTMs of 0.8 and 0.97 indicates.)

Influence of Blade Pitch Angle Setting: Comparing spectra at corresponding AR but different BPAs of 20° and 27° , maintaining however the HTM at 0.75, shows the higher BPA to cause relatively more intense subharmonic spectra (Fig. 20). This is readily explained by the different effective blade-incidence angles at the same AR. Specifically, at an AR of 0.15 the incidence angle is 6.5° for a BPA of 20° , and 13.5° for a BPA of 27° ; likewise at an AR of 0.20, the number-pairs are $3.7^\circ/20^\circ$ vs. $10.8^\circ/27^\circ$, while at an AR of 0.25 the number-pairs are $1^\circ/20^\circ$ vs. $8^\circ/27^\circ$. Hence, expectedly, it is the local flow-conditions in terms of the effective blade-incidence angle (rather than the advance ratio) which determines the relative importance of a subharmonic spectrum. Accordingly, spectra should - for different blade pitch settings - be compared on the basis of the blade-incidence angles, in order to yield similar harmonic and subharmonic spectra.

Influence of Blade Number: While the dependence on operational parameters of the subharmonic spectral characteristics could best be demonstrated on a 2-bladed propeller (as illustrated in the previous 4 Figures), since 2 blades in their geometries or settings might be distinctly different, looking at 3-, 4- or more blade propellers, there could exist more similarity between 2 or 3 blades, rather than all 3 or 4 blades being distinctly different.

The purpose of presenting Fig. 21, where spectra of a 2-, 3-, and 4-bladed propeller are shown for otherwise identical blade-settings and operational conditions (BPA= 23.5° , AR = 0.15, HTM = 0.65) is merely to indicate that indeed there is one (subharmonic) discrete tone between the harmonic tones each for the 2-blade propeller, two then for the 3-blade propeller and three for the 4-blade propeller, as should be expected. It seems, however, that the relative importance of a subharmonic spectrum diminishes with growing blade number. It is of interest to note, that the level-envelopes of the harmonics are independent of blade-number.

(b) Harmonic Spectra

This section serves to illustrate the characteristics of the harmonic (rather than the subharmonic) spectra in their dependence on operational parameters. Data will be presented in spectral-envelope form, depicting the harmonic peak-levels only.

Influence of Blade Number: Varying the number of blades (from 2 to 6) at otherwise constant operational conditions yield essentially identical harmonic envelopes. Fig. 22 shows such envelopes for BPA-settings of 23.5° and an AR of 0.2 for HTMs ranging from 0.45 to 0.85. The harmonic levels follow constant HTM-line essentially independent of the number of blades. Mach-number certainly has the overriding influence.

Influence of Blade Pitch Angle: Testing the behavior of the harmonic levels for 2 different blade-pitch angles (20° and 27°) demonstrated again the local blade incidence angle to be the decisive physical quantity. Fig. 23 shows, for 2 helical blade tip Mach numbers of 0.75 and 0.65, the harmonic envelopes for respectively two combinations of blade-pitch and advance-ratio. If these combinations cause the same local blade incidence angle, then the levels are identical.

Influence of Helical Blade Tip Mach-Number: Maintaining blade-number, advance-ratio and blade pitch-setting (and thus blade incidence angle), an increase in the helical blade tip Mach-number expresses itself in a pronounced level-growth and the appearance of ever more harmonics. Fig. 24 exemplifies this behavior on the example of a 2-bladed rotor, with an AR of 0.2, and a BPA of 20°, resulting in a blade incidence angle of 3.7°. (The Figure also contains not directly comparable data for a lower HTM of 0.56 too, but here AR was 0.25, with an ensuing incidence angle of 1.0°.)

Influence of Blade Incidence Angle: To illustrate the decisive role of the blade incidence angle - at respectively constant helical blade tip Mach numbers -, Fig. 25 shows for HTMs of 0.56, 0.65, 0.75, and 0.85 spectral envelopes for the 2-blade propeller, where advance ratio and blade pitch setting combinations were selected to cover blade incidence angles ranging from 1.2° up to 13.5°. Within each (approximately) constant HTM, the harmonic levels order themselves according to the blade incidence angle with higher incidence angles causing higher levels. The relative increase seems approximately independent of HTM.

Influence of Rotational Plane Attitude: The effect of unsymmetrical inflow into the propeller plane, corresponding to an aircraft attitude change with respect to the main inflow direction, has been tested by changing the attitude within (a) a small range from -0.6° to +2.5°, and (b) a large range from -7.5° to +15°, where 0° corresponds to a dead-on inflow into the propeller-plane. Here the microphone remained at a fixed position, lateral to the plane of rotation and one propeller-diameter distance from the rotating tip.

A positive attitude-change indicates an inclination towards the microphone, and vice versa. Rotational direction, as seen from the front (with the microphone to the right) was - as always - counterclockwise.

The results are presented in the following two Figures. Fig. 26 shows for the 2-blade propeller at constant AR of 0.2, BPA of 23.5° and HTM of 0.75 the rather small, yet systematic, changes in spectral envelope caused by attitude-variations from -0.6° to +2.5°. The changes correspond to approximately 0.5 to 1 dB per degree of attitude change, with negative attitudes being more noisy than positive ones.

This tendency is more obvious from Fig. 27 depicting results for rather pronounced attitude-changes between -7.5° and +15°. Data are shown for two HTMs of 0.9 and 0.7, for the same AR and BPA-settings, whereby - very roughly - an overall 0.5 dB per degree of attitude change is observed. This behavior is readily explained, since higher levels are observed when an attitude change causes the blade-incidence angle of the blade moving towards the microphone to increase.

Influence of Ambient Temperature: The helical blade tip Mach-number is known to decisively determine propeller noise-levels. HTM itself depends, of course, on propeller rotational speed, forward flight speed, and speed-of-sound, hence on the ambient temperature. It is thus possible to achieve the same HTM through various combinations of these 3 quantities.

Fig. 28 illustrates - for 3 respectively constant HTMs of 0.7, 0.8 and 0.9 - the effect of an ambient temperature change from 15°C to 30°C on the harmonic levels. Inspecting the 3 sets of data-pairs, one finds, for example, that the ambient temperature of 15°C requires a rotational speed of 272 Hz (at a flow-speed of 46.7 m/s) to obtain a HTM of 0.7, while the temperature of 30° requires correspondingly 279.3 Hz (at a flow-speed of 47.9 m/s). Although, then, the HTM is the same, the harmonic levels differ fairly substantially with a growing tendency with harmonic number. The corresponding effects at higher HTMs are less pronounced, in that the level-difference reduces to about 2 dB for a HTM of 0.8, and to about 1 dB for a HTM of 0.9.

Reverting back to the HTM = 0.7 data, one finds the rather substantial level-difference to be accompanied (if not caused) by a fairly small rotational speed change of less than 3%. Such a change at a full-scale situation would correspond to an RPM-change from 1630 to 1675 per minute, or a tip-speed change from 240 m/s to 233, for example. The chord-based Reynolds-number for the model-tests at the two test-conditions were, respectively, 0.313 million at 15°C and 0.297 million at 30°C, corresponding to a 5% change.

One might thus tentatively conclude, that helical blade tip-speed, rather than helical blade tip Mach-number, determines propeller-noise characteristics. Unfortunately, no test data at constant tip-speed for various ambient temperatures are presently available.

2.2.3 Pressure Time-history (waveform) and Ensuing Spectrum

Some initial evaluation of the relationship between the waveforms and the corresponding narrow-band sound pressure level spectra from the tenth-scale model test, employing the 2-blade propeller, show the typical change in waveform with helical blade tip Mach-number; raising HTM from 0.7 to 0.9 changes the waveform from a "shallow", somewhat sinusoidal or cupped-triangular shape to a distinctly impulse-type shape with pronounced negative peaks and very narrow pulse-widths (Fig. 29). At the same time, the peak-to-peak amplitude grows from about 80 Pa to 450 Pa, while the corresponding harmonic spectra show an increasing number of harmonics, together with the characteristic rise of the harmonic-level envelope with growing HTM.

2.2.4 Comparison with Third-scale Data

The model-test data reported so far and acquired in the DFVLR-Braunschweig One-meter Acoustic Tunnel relate to a scale-factor of 10. However, third-scale data were available for a geometrically identical 4-blade propeller of scale 1:3, obtained in the DFVLR-Göttingen Three-meter Wind Tunnel /16/. In this case, acoustic signals were measured with a microphone only 0.14 diameters to the side of the propeller tips; this distance corresponded to a full-scale situation, where the propeller tips were that close to the fuselage. Within the tenth-scale tests, it was possible to exactly match the geometric and operational conditions of the third-scale test, so that a direct quantitative comparison is possible, at least for the first few rotational harmonics.

The results for 2 conditions are shown in Fig. 30, where the harmonic spectra for the tenth-scale tests are displayed, and the harmonic levels of the third-scale tests drawn in as short horizontal lines. TABLE I shows the geometric and operational conditions for the comparison, indicating that advance ratios and helical blade tip Mach-numbers were matched exactly, as well as the nondimensional measurement distances. Fig. 30a, where comparative data are shown for a blade-pitch angle of 20°, exhibits agreement within 1 or 2 dB for all six harmonics, while Fig. 30b, displaying comparative data for not exactly matched blade-pitch angle settings of 25° (tenth-scale) and 25.4° (third-scale) shows better agreement for the first 4 harmonics, with a subsequent - probably systematic - discrepancy for higher harmonics (fifth and sixth). This discrepancy could be tied to the - albeit slight - differences in blade angle.

Fig.	Scale	Prop Diam (m)	Tunnel 1-m BS 3-m GÖ	Blade Pitch Angle	Rot. Speed (1/s)	Flow Speed (m/s)	Adv. Ratio	Hel. Tip Mach-Nbr.	Distance Tip to Mike	
									Dim. (m)	Nondim.
30a	1:10	0.273	1 m	20°	265	58	0.255	0.683	0.038	0.14 D
	1:3	0.91	3 m	19.6°	79.5	58	0.255	0.684	0.127	0.14 D
30b	1:10	0.273	1 m	25°	265	58	0.255	0.683	0.038	0.14 D
	1:3	0.91	3 m	25.4°	79.5	58	0.255	0.684	0.127	0.14 D

TABLE I: Propeller Operational Conditions for Tenth-scale/Third-scale comparisons

In all, the scaling from tenth- to third-scale yield satisfactory results, lending credibility to small-scale tests, and indicating further that the Reynolds-number may play a minor role. It seems important however to match test-conditions very precisely to obtain quantitatively reliable results.

It should be noted, that a somewhat better criterion on the scalability of propeller-noise data from small-to-large scale would be a check on the basis of the respective pressure waveforms - rather than of the spectra - since similarities or dissimilarities become more obvious in a time-domain representation.

3. DISCUSSION

Both full-scale flight and tenth-scale (as well as third-scale) wind tunnel tests on General Aviation propeller nearfield acoustics mostly in the plane of rotation, or slightly aft, exhibit certain common characteristics. Helical blade tip Mach-number has the most pronounced effect both on the pressure time history of the propeller nearfield signature and on the ensuing sound pressure level spectrum. While at relatively low helical blade tip Mach-numbers (HTM), say around 0.70 to 0.73, the waveform (pressure time history) exhibits a more sinusoidal or triangular pattern, increasing the HTM towards and up to values of 0.83 (flight tests) or 0.97 (wind tunnel tests) causes the waveforms to assume a distinctly impulse-type shape, with pronounced negative peaks, and rapidly growing pressure peak-to-peak amplitudes, indicating the advent of compressibility effects and the predominance of thickness noise. In correspondence to the increasingly more needle-type waveform the harmonic spectra are characterized by a growing number of discrete components, totally dominating the spectrum at high helical Mach-numbers.

The tenth-scale propeller tests revealed certain characteristics of the subharmonic spectra (i.e. the once-per-revolution discretely and multiples thereof), being a function of both geometric and operational conditions. The relative amplitudes of the subharmonic discretely are largest for low advance-ratios (causing relatively larger blade-incidence angles). In fact, the subharmonic spectral levels may exceed those of the harmonic spectrum; the relative importance of the subharmonic spectrum - as compared to the harmonic one - seems to increase with helical blade tip Mach-number. Also, more-bladed propellers are less prone to a predominance of subharmonic components than those with fewer blades. However, subharmonic spectral levels may also depend on the absolute scale of the propeller, such that at model-scale manufacturing or blade geometric differences may have a more pronounced effect than if a large-scale propeller is considered.

Harmonic levels are independent of blade number; as verified in the small-scale tunnel tests, the level-envelopes are essentially the same, whether 2-, 3-, 4-, 5- or 6-bladed propellers are tested for otherwise matched conditions. Testing (2-blade) propellers at different advance ratios and blade-pitch angle setting, such that the ensuing blade incidence angles are the same, yields identical harmonic levels. Hence, a low blade-pitch at high advance ratio may generate the same harmonic spectrum as a high blade-pitch at a low advance ratio. Thus, it is the (local) flow incidence at the given helical blade tip Mach-number, that determines levels, rather than an advance ratio or a blade pitch angle setting by itself.

Blade loading (as dependent on the blade-pitch angle at given rotational and flight speeds) distinctly changes the pressure time waveform and the ensuing harmonic spectrum. Its influence becomes stronger with helical blade tip Mach-number.

Even minor attitude changes of the propeller rotational plane with respect to the onflow direction - as occurring during ascending or descending flight - causes perceptible level changes. Approximately 0.5 to 1 dB per degree attitude change was observed, whereby a negative attitude (turning the rotational plane away from the observer point) was to cause the higher levels. Such a situation would exist under a take-off/climb condition with the observer on the ground.

Keeping all other operational conditions constant, but varying the ambient temperature caused fairly pronounced effects on the harmonic levels, more so at lower helical blade tip Mach-numbers, than at the higher ones. For a HTM of 0.7, for example, a change in ambient temperature from 15°C to 30°C raised levels by 3 to 6 dB for the first few harmonics. However, maintaining the HTM at different ambient temperatures inherently requires an adjustment of the rotational and flow ("forward-flight") speed, if advance ratio is also maintained. This then, for the lower temperature yields an effectively lower tip speed (rather than tip Mach-number). Therefore, at lower HTMs, where compressibility effects are not yet present, it is the (helical) tip speed, and not so much the helical tip Mach-number, which determine the noise levels. At higher HTMs close to 0.9 and above, where compressibility effects occur, the Mach-number - rather than the tip-speed - determine the levels; hence for the same HTM, even when ambient temperature and ensuing rotational and flow speeds differ, the same harmonic levels occur.

An important justification for scaled-model tests lies in the scalability of results towards full-scale. In aerodynamics, the Reynolds-number (in addition to the Mach-number) determine scalability. Reynolds-number may only be ignored, if defined separation-lines on whatever body exist, or if the onflow is highly turbulent, such that no (Reynolds-number sensitive) transition phenomena occur. In case of propeller aeroacoustics, opinions differ upon the effect of Reynolds-number. Within the wind tunnel model tests, it was possible to evaluate geometrically identical propellers of scale 1:10 and 1:3 with respect to a full-scale propeller (whose data however were not in a form to allow comparisons). Matching geometric and operational parameters for the two tests yielded rather encouraging results, in that the harmonic levels up to the first four to six agreed within 1 or 2 dB. However, no waveform comparison, representing the much more sensitive criterion, or a full-frequency-range spectral comparison was possible. Still, comparing propellers of diameter 0.273 m and 0.91 (considering that GA propeller diameters of 1.8 m are quite common, thus being only a factor of 2 off), and showing harmonic-level agreement, must, at the very least, be considered as encouraging to proceed with the small-scale tests, with the expectation to obtain quantitatively scalable results.

REFERENCES

- /1/ Heller, H.; Kallergis, M.; Ahlswede, M.; Dobrzynski, W.: "Rotational- and Vortex-noise of Propellers in the 100 to 150 kW Class." AIAA 5th Aeroacoustics Conference, Paper No. 79-0611, Seattle/Wash., 1979.
- /2/ Dahlen, H.: "Vergleichsmessungen zur Lärmzertifizierung von Propellerflugzeugen." DAGA 1980, Proceedings, S. 277, VDE-Verlag, 1980.
- /3/ Dobrzynski, W.: "Interferenzwirkung durch Bodenreflexion bei Fluglärm-messungen an Propellerflugzeugen." DFVLR Forschungsbericht, FB 81-28, 1981.
- /4/ Kallergis, M.; Ahlswede, M.: "Identity of Propeller Aircraft Flyover Noise Signatures Acquired by Several Microphones in Close Proximity." Proceedings INTERNOISE 1981, Amsterdam, Vol. 2, Page 881.

- /5/ Ahlswede, M.; Anders, K.-P.: "Collection and Evaluation of Propeller Aircraft Noise Certification Data." DFVLR-Mitteilung 81-20, 1981.
- /6/ Dobrzynski, W.: "Bodenreflexionseffekte bei Fluglärm-messungen." Zeitschrift für Flugwissenschaften (ZFW) 5, 1981/6, Page 367.
- /7/ Neubauer, R.F.: "Über die Schallabstrahlung von Modellpropellern." FASE/DAGA 1981, VDE-Verlag, 1982.
- /8/ Dahlen, H.; Heller, H.: "Repeatability and Reproducibility of Flyover Noise Measurements of Propeller-driven Aircraft." Proceedings INTERNOISE 1981, Amsterdam, Vol. 2.
- /9/ Heller, H.: "Propeller Aircraft Noise Certification and Flight Testing." DFVLR-Mitteilung 82-16, 1982.
- /10/ Dahlen, H.: "Statistical Significance Testing for the Proof of Aeroplane Noise Control Measures." Proceedings INTERNOISE 1983, Edinburgh.
- /11/ Neubauer, R.F.; Kallergis, M.: "Die Trennung von Propeller- und Auspuffgeräusch bei Propellerflugzeugen im Überflug." 11. ICA, Paris, Juli 1983, Paper 1.7.7.
- /12/ Kallergis, M.; Neubauer, R.F.: "Propeller Nearfield and Noise Radiation to the Farfield." Proceedings INTERNOISE 1983, Edinburgh, Juli 1983.
- /13/ Heller, H. et al: "Field Evaluation of Newly Proposed ICAO-ANNEX 16 Take-off Noise Certification Procedure for Propeller-driven Aeroplanes not Exceeding 5700 kg." DFVLR-FB 83-34, 1983.
- /14/ Borchers, I.V.; Zimmer, H.; Bartels, P.: "Entwurf, Bau und Erprobung eines verbesserten Propellers für Flugzeuge der Allgemeinen Luftfahrt." Bericht 2. BMFT Status Seminar 'Luftfahrtforschung und Luftfahrttechnologie', Garmisch-Partenkirchen, Oktober 1980.
- /15/ Zimmer, H.; Borchers, I.V.; Friedel, H.: "Entwurf, Bau und Erprobung eines Experimentalpropellers in der Leistungsklasse 750 PS." DGLR-Jahrestagung, Stuttgart, Oktober 1982, Bericht Nr. 82-066.
- /16/ Grosche, F.R; Stiewitt, H.; Höfer, H.R.: "Akustische und aerodynamische Windkanaluntersuchungen an 5 Modellpropellern im 3-m Niedergeschwindigkeits-Windkanal der DFVLR Göttingen." DFVLR-Interner Bericht IB 222-82 A30, 1982.

ABBREVIATIONS AND SYMBOLS

HTM or M_{Hel}	:	Helical Blade Tip Mach-number
BPA or β	:	Blade Pitch Angle Setting
AR or λ	:	Advance Ratio
BIA or $\Delta\beta$:	Blade Incidence Angle
BS	:	Braunschweig
GÖ	:	Göttingen



Fig. 1 Test Aircraft CESSNA T 207 with Microphone Array

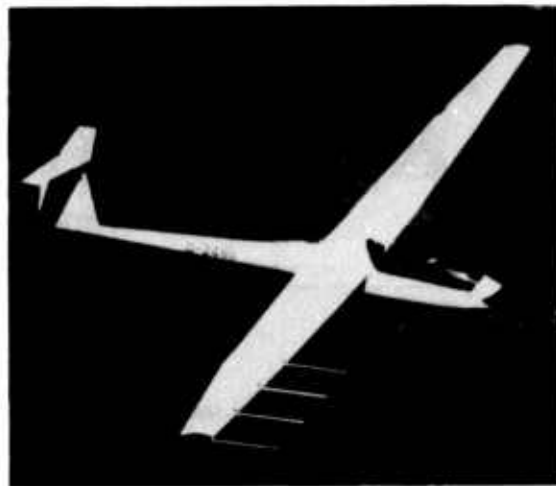


Fig. 2 Self-noise Evaluation of Glider-wing-mounted Sensors (Microphones with Nose-cone Protection)

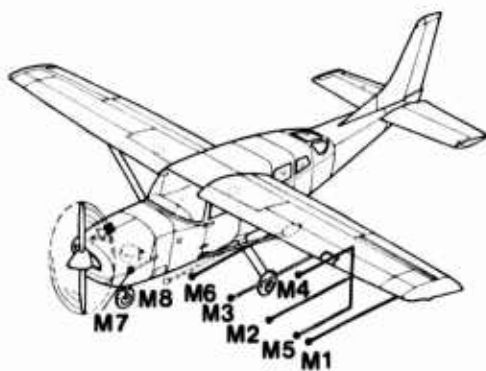


Fig. 3 Schematic of Test Aircraft with Microphone Designations and Positions

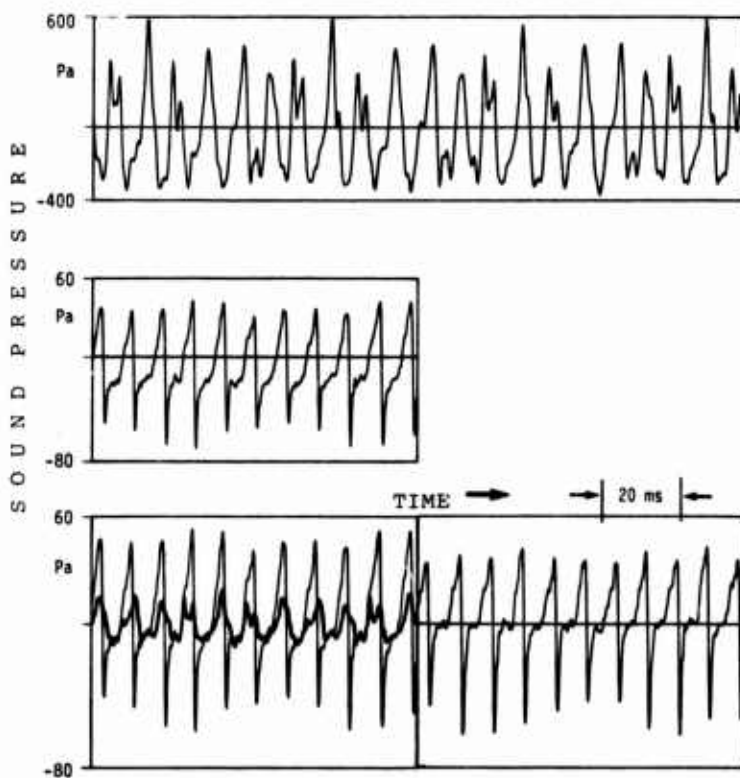
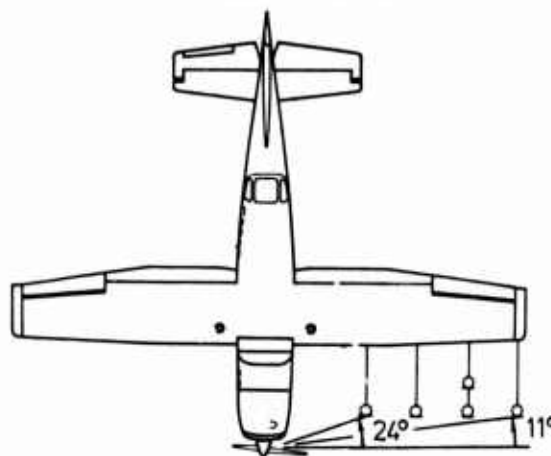


Fig. 4a Exhaust Pressure Signature of 6-Cylinder Piston Engine

Fig. 4b Combined Propeller/Engine Exhaust Signature

Fig. 4c Combined Signature (left) and Clean Propeller Signature (right)

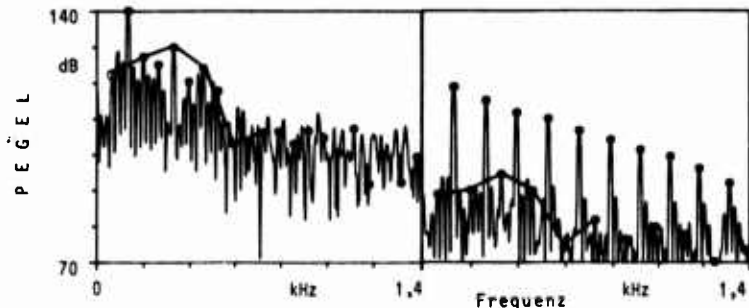


Fig. 5 Narrowband Spectra: Engine Exhaust (left) and Combined Engine/Propeller Signature (right)

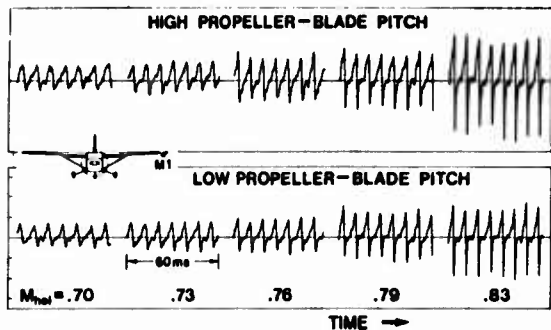


Fig. 6 Propeller Noise Pressure Time Histories for Respectively High (18.2°) and Low (12.9°) Blade Pitch Angle Settings at Various Helical Blade Tip Mach-numbers

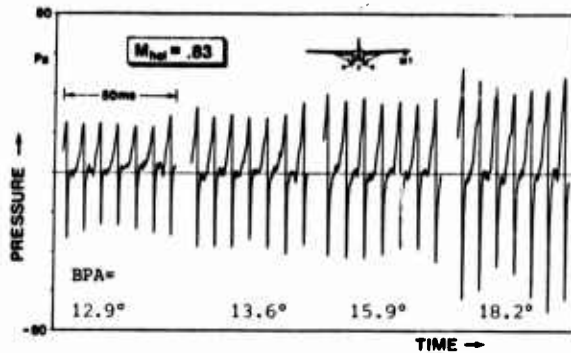


Fig. 7 Propeller Noise Pressure Time Histories at Constant Helical Blade Tip Mach-number for Various Blade Pitch Angle Settings

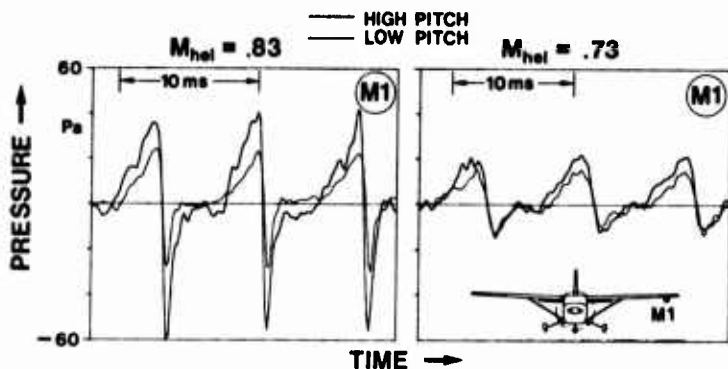


Fig. 8 Comparison of Propeller Noise Pressure Time Histories at Stretched Time-scale for Combinations of High (18.2°) and Low (12.9°) Blade Pitch Angle Settings and Helical Blade Tip Mach-numbers

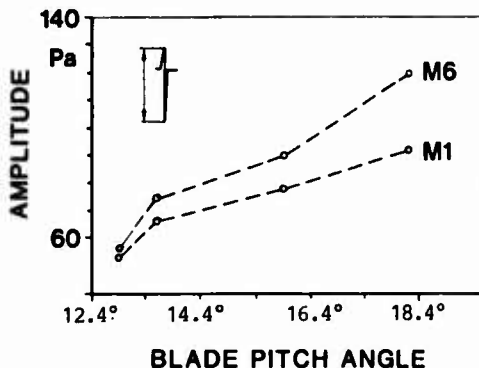


Fig. 9 Peak-to-peak Amplitudes of Propeller Noise Pressure Time Histories at Constant Helical Blade Tip Mach-number of 0.83 as Function of Blade Pitch Angle Settings

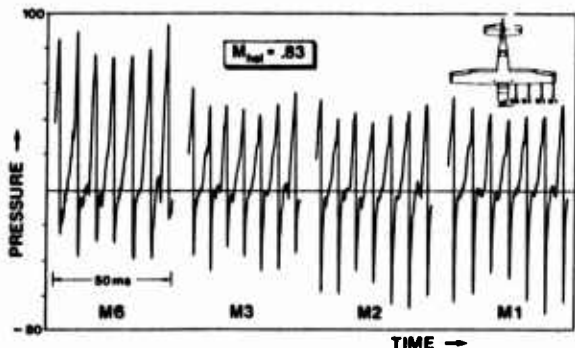


Fig. 10 Propeller Noise Pressure Time Histories for Constant Operating Conditions at Various Microphone Locations

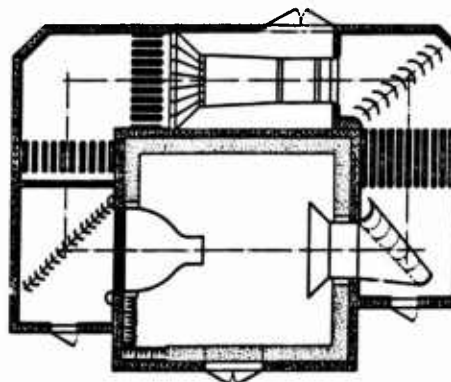


Fig. 11 Plan View of DFVLR-Braunschweig One-Meter Acoustic Tunnel (with Open Test Section. Nozzle-Width 1 m

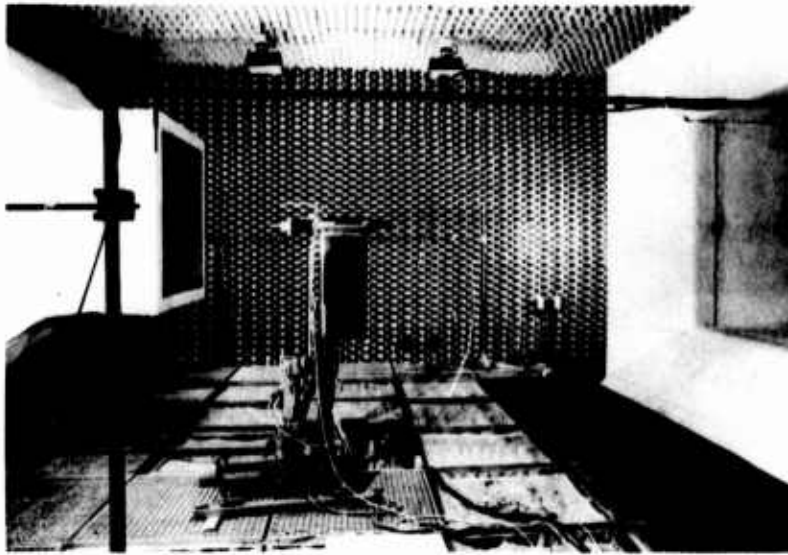


Fig. 12 DFVLR-Braunschweig One-Meter Acoustic Tunnel with Model-propeller Test Setup

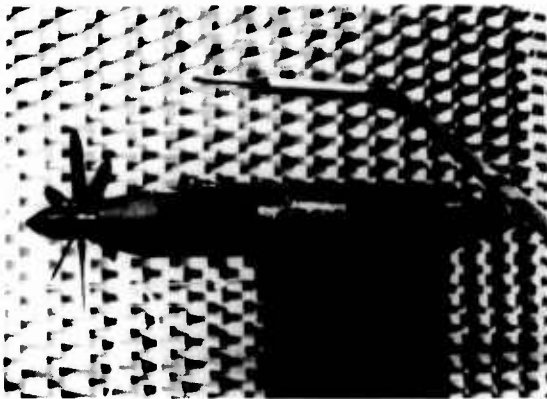


Fig. 13 Propeller Test Stand and Measurement-microphone

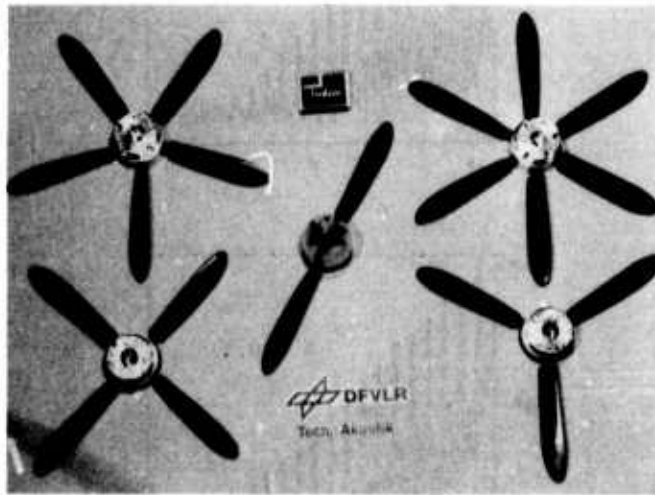


Fig. 14 Test Propellers with 2 to 6 Blades, Propeller Diameter 0.273 m

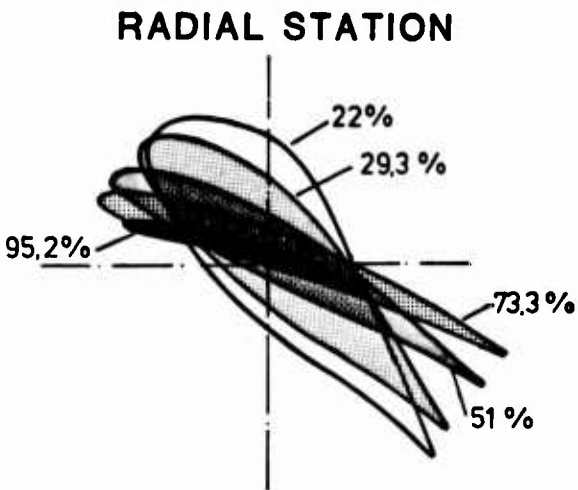


Fig. 15 Test Propeller Planform and Profile-sections

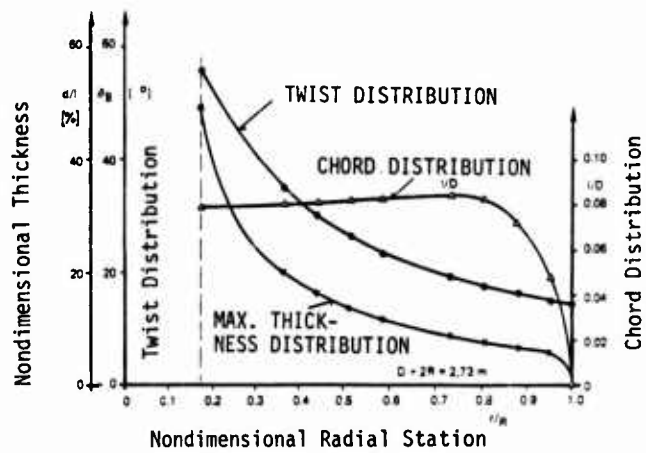


Fig. 16 Test Propeller Twist-, Chord-, and (maximum) Thickness Distribution vs Radial Station (from /15/)

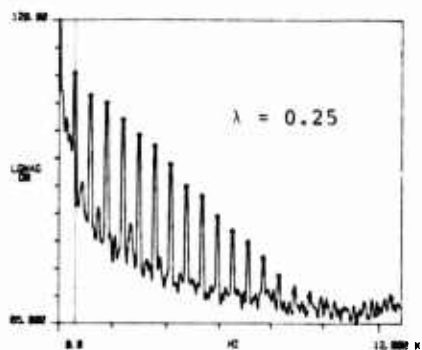
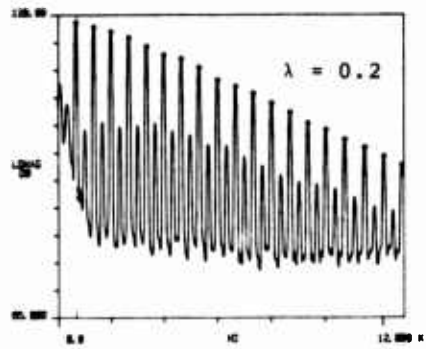
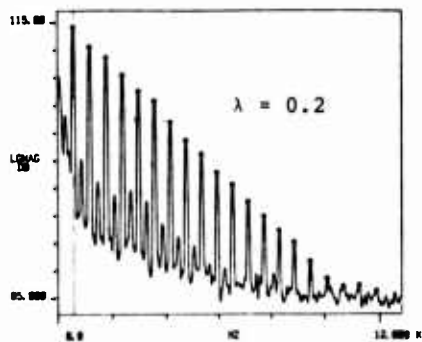
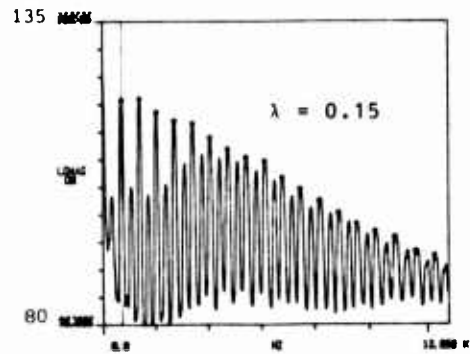
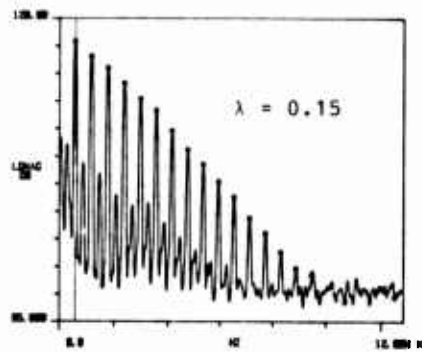
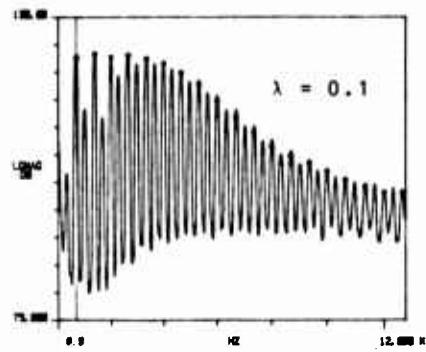
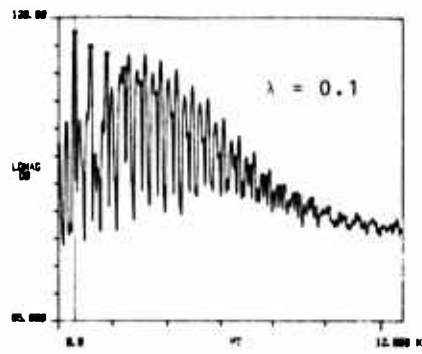


Fig. 18 Subharmonic Spectral Characteristics for 2-Blade Propeller at Constant Blade Pitch Angle Setting of 20° and Helical Blade Tip Mach-number of 0.85 for Various Advance Ratios

Fig. 17 Subharmonic Spectral Characteristics for 2-Blade Propeller at Constant Blade Pitch Angle Setting of 20° and Helical Blade Tip Mach-number of 0.75 for Various Advance Ratios

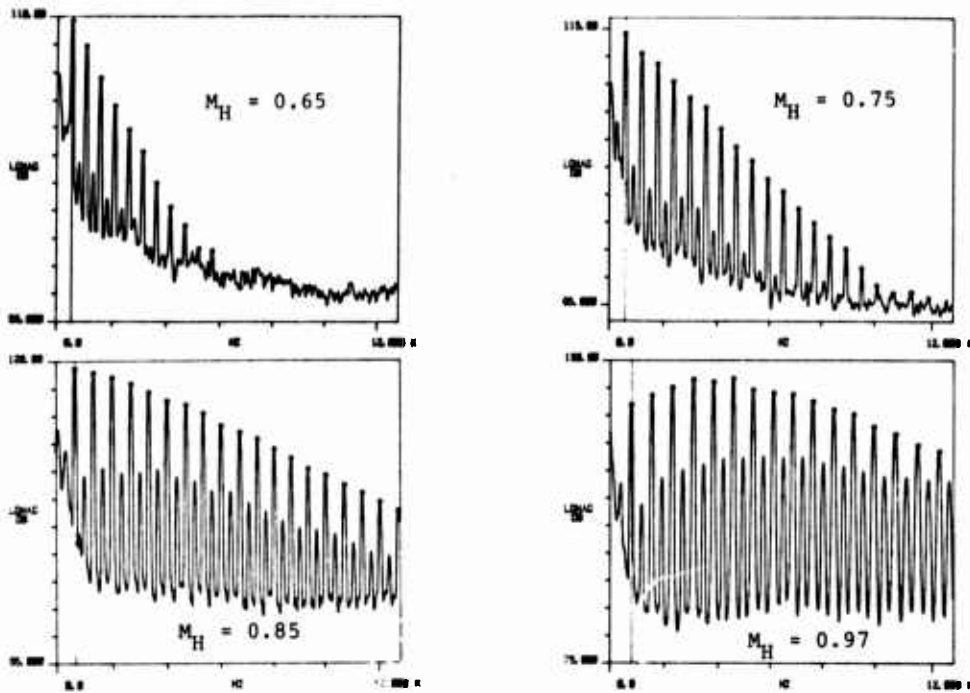


Fig. 19 Subharmonic Spectral Characteristics for 2-Blade Propeller at Constant Blade Pitch Angle Setting of 20° and Constant Advance Ratio of 0.2 for Various Helical Blade Tip Mach-numbers

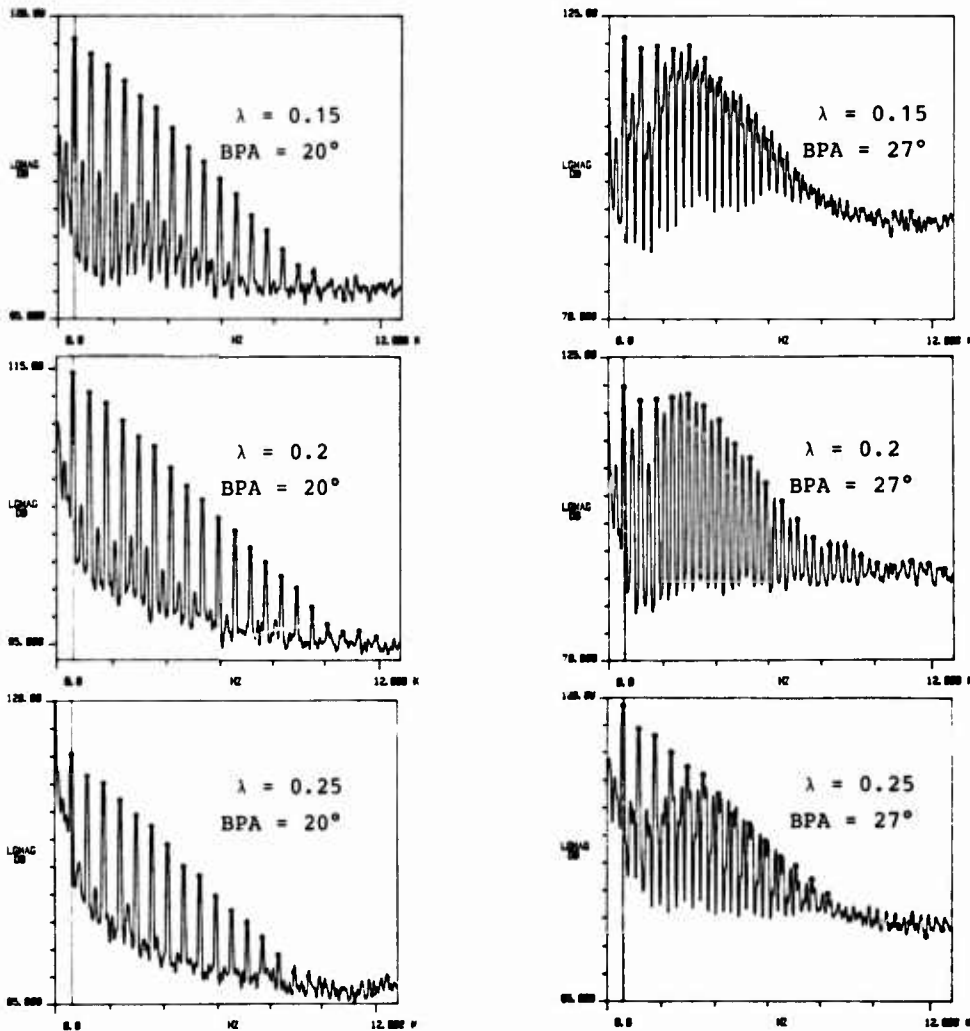


Fig. 20 Subharmonic Spectral Characteristics for 2-Blade Propeller at Constant Helical Blade Tip Mach-number of 0.75 and Constant Blade Pitch Angle Settings of 20° (left) and 27° (right) for Various Advance Ratios

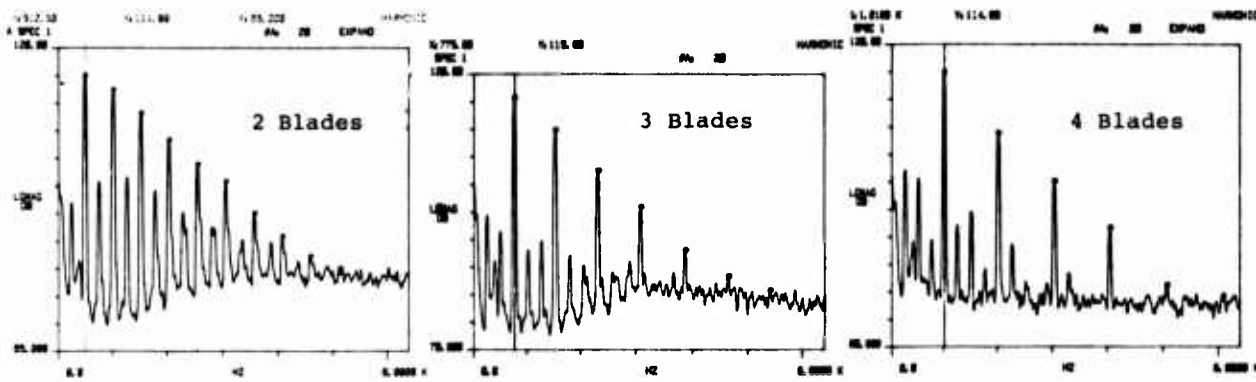


Fig. 21 Subharmonic Spectral Characteristics at Constant Advance Ratio of 0.15, Blade Pitch Angle Setting of 27°, Helical Blade Tip Mach-number of 0.64 for 2-, 3-, and 4-Blade Propellers

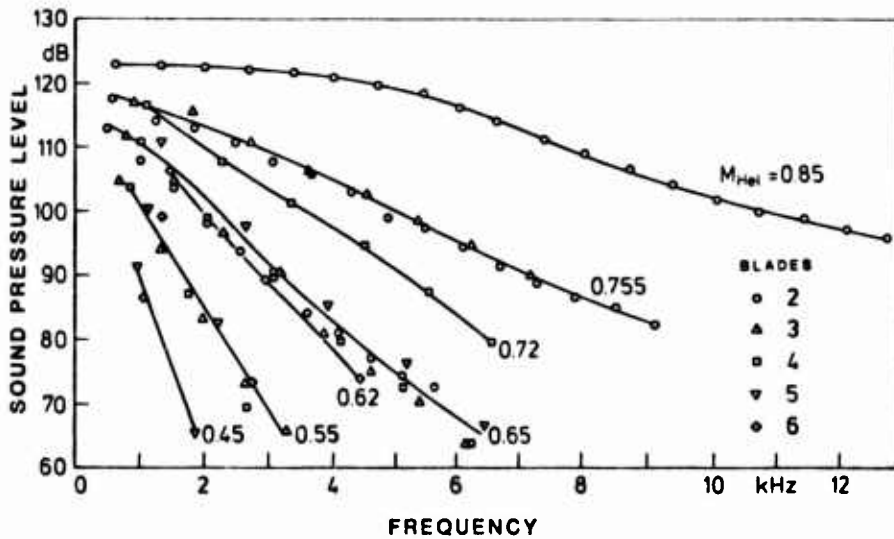
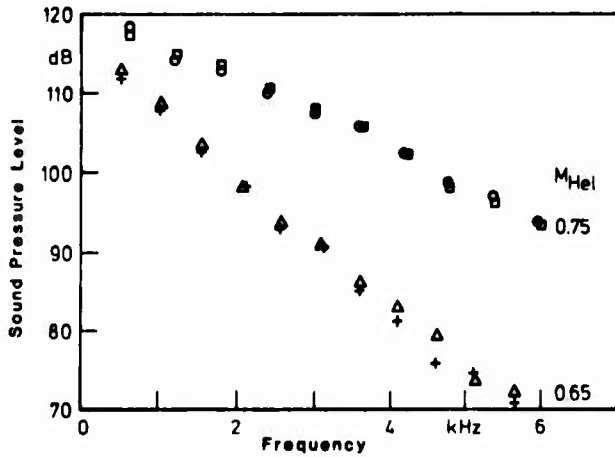


Fig. 22 Influence of Blade Number on Harmonic Levels at Various Helical Blade Tip Mach-numbers for Constant Advance Ratio of 0.2, and Blade Pitch Angle Setting of 23.5°



	λ	β	$\Delta\beta$
○	0.25	20°	9°
□	0.10	27°	9.3°
△	0.25	27°	8.0°
+	0.1	20°	8.0°

Fig. 23 Influence of Advance Ratio and Blade Pitch Angle Settings on the Harmonic Levels of a 2-Blade Propeller at two Helical Blade Tip Mach-numbers

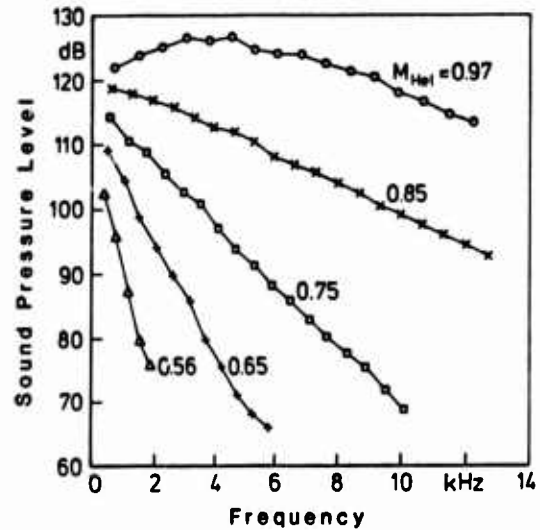


Fig. 24 Influence of Helical Blade Tip Mach-number on the Harmonic Levels of a 2-Blade Propeller for Constant Advance Ratio of 0.2 and Blade Pitch Angle Setting of 20°

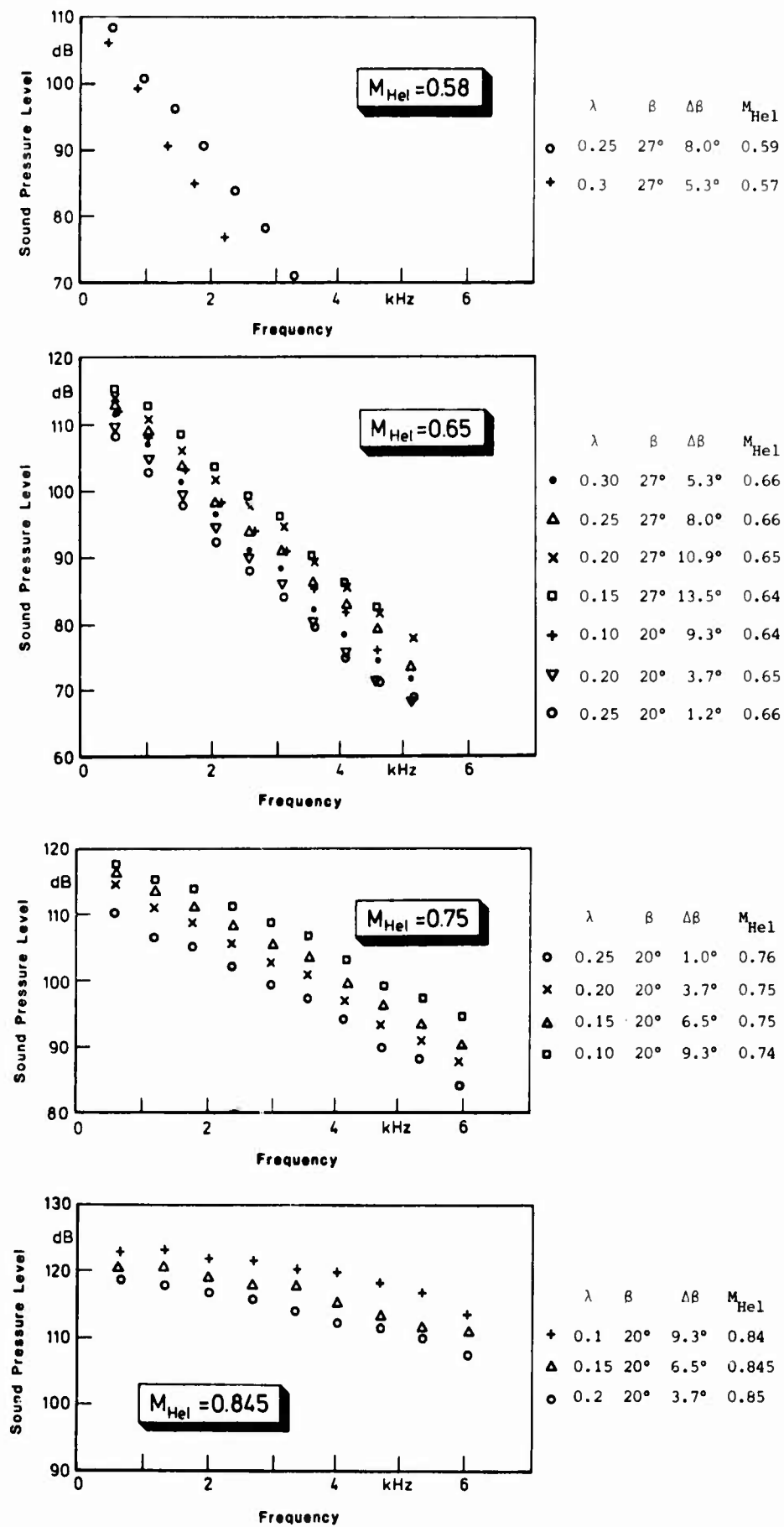


Fig. 25 Influence of Blade-incidence Angle $\Delta\beta$ in Particular (and other Parameters as in the Legends) on the Harmonic Levels of a 2-Blade Propeller for Various Helical Blade Tip Mach-numbers

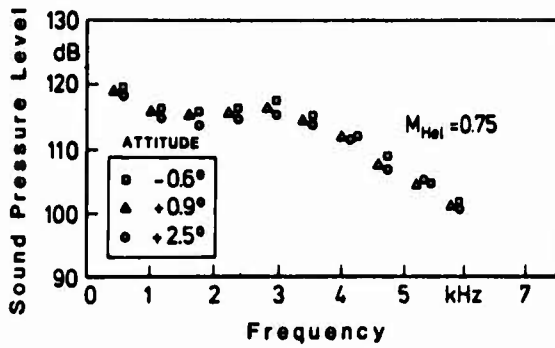


Fig. 26 Influence of Minor Propeller Rotational Plane Attitude Variation for a 2-Blade Propeller at Fixed Lateral In-plane Microphone Position for Constant Operating Conditions

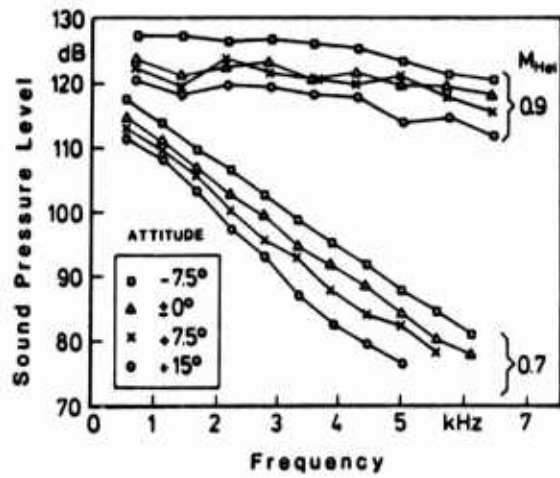


Fig. 27 Influence of Major Propeller Rotational Plane Attitude Variations for a 2-Blade Propeller at Fixed Lateral In-plane Microphone Positions for two Helical Blade Tip Mach-numbers

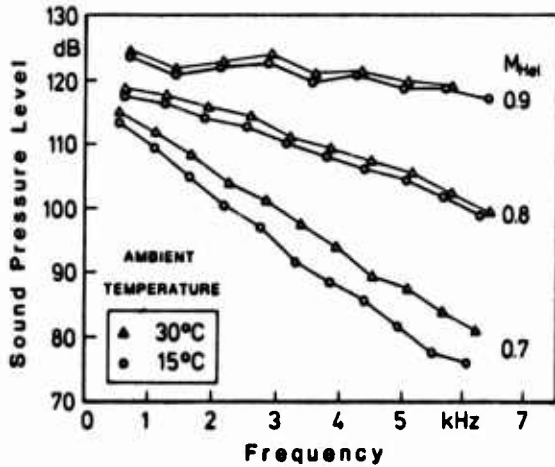
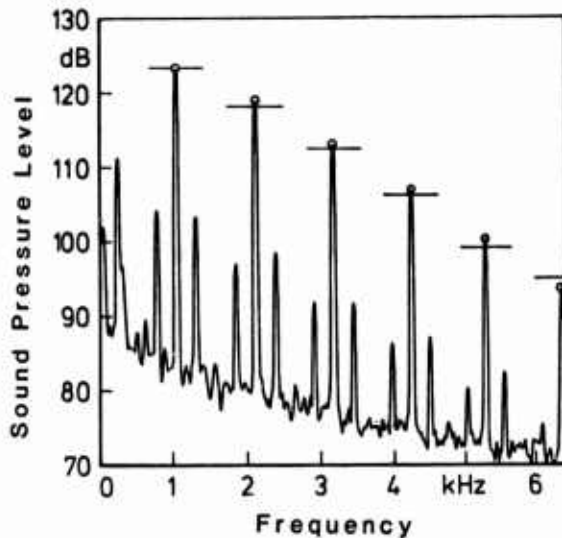
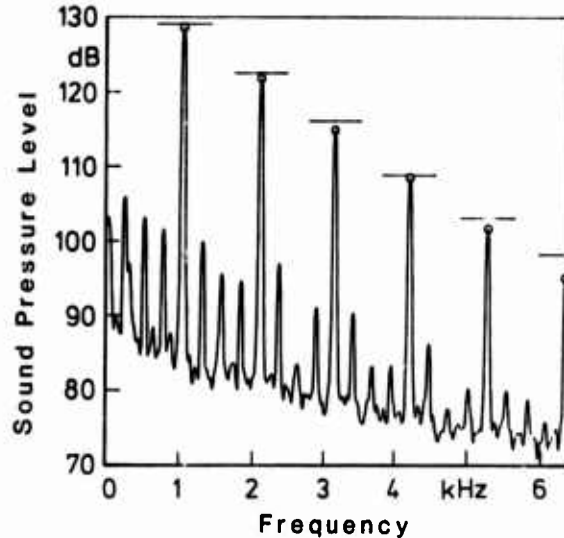


Fig. 28 Influence of Ambient Air Temperature for Constant Helical Blade Tip Mach-numbers of 0.7, 0.8, and 0.9



(a) Blade Pitch Angle Setting 20° (1:10 Scale) and 19.6° (1:3 Scale)



(b) Blade Pitch Angle Setting 25° (1:10 Scale) and 25.4° (1:3 Scale)

Fig. 30 Harmonic Level Comparison of 4-Blade Propellers of Scale 1:3 and 1:10 under Matched Geometric and Operational Conditions: Helical Blade Tip Mach-number 0.68, Advance Ratio 0.255. (Spectrum and Circles Correspond to Tenth-scale Propeller of 0.273 m Diam., Horizontal Lines to Third-scale Propeller of 0.91 m Diam.)

Note: Fig. 29 on subsequent page!

FREQUENCY SPECTRUM

PRESSURE WAVEFORM

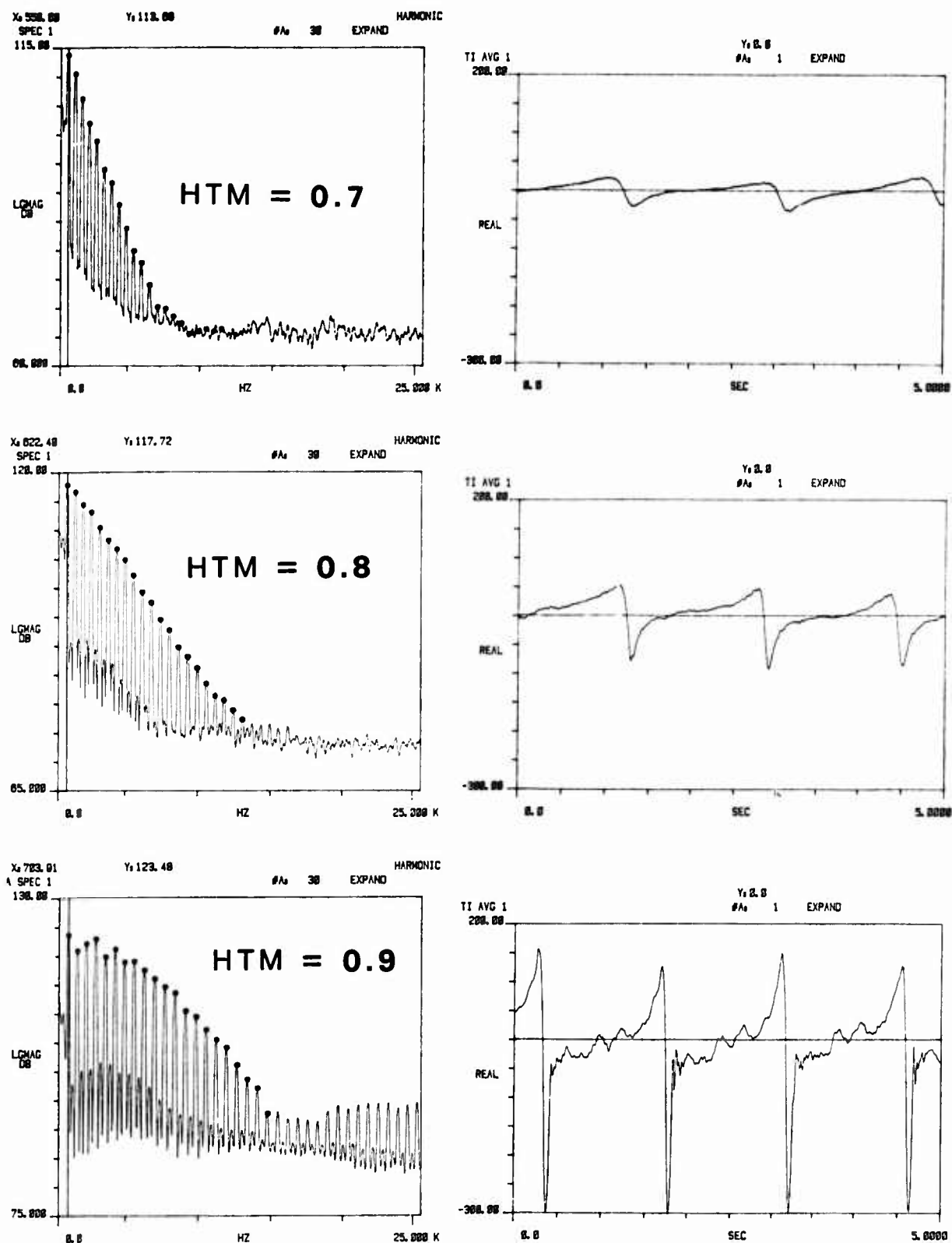


Fig. 29 Frequency Spectra and Corresponding Pressure Time Histories (Waveforms) in the Plane of Rotation, at a Distance of 1 Diameter of 2-Blade Propeller with Blade Pitch Angle Setting 23.5° and Advance Ratio of 0.2

CABIN NOISE REDUCTION FOR A NEW DEVELOPMENT
TURBOPROP COMMUTER AIRCRAFT

BY

A. CARBONE, A. PAONESSA, AERITALIA SAIPA, POMIGLIANO D'ARCO, ITALY

L. LECCE, F. MARULO, ISTITUTO PROGETTO VELIVOLI, NAPOLI, ITALY

SUMMARY

The program followed to attain an interior noise level similar to turbofan aircraft in a new design turboprop commuter is described. The need for an early consideration, in the definition phase of the aircraft, of the acoustic requirement for configuration development is stressed, along with some peculiar characteristics of this program. After a brief presentation of features of the aircraft related to interior noise control, the analytical and experimental models developed in the course of program are discussed. Some of the results of the studies are presented, clarifying the impact that they have had on the configuration of the aircraft. The output of three structural analysis theoretical procedures is compared to experiments. Two of these procedures, the panel-stringer periodic model, and a simplified FEM analysis, are found adequate to represent experimental findings. The cylindrical shell-frame model is found not representative of test results. Sidewall treatment performance is discussed, with reference to theoretical and experimental results. The noise reductions measured in a furnished fuselage are compared to data obtained without interior treatment. Future developments and recommendations for additional work are discussed.

1. INTRODUCTION

Reduction of interior noise in propeller driven aircraft to levels comparable to those obtained in turbofan transports has been recognized by several institutions as a leading factor in the acceptance from the travelling public of new generation turboprop aircraft (1).

This paper presents some of the results obtained so far in the program that has been started with the purpose of developing the acoustic configuration of a new design turboprop commuter well in advance of its introduction in service.

The aircraft program is the ATR-42, a joint development of Aeritalia of Italy and Aerospa tiale of France.

Several studies are presently under way on the interior noise reduction of propeller aircraft. The vast majority of published works was originated by the recognized need for research in this field, to develop technology required to make feasible the advent of propfan. Some work has been performed to quiet existing aircraft, civil and military. The research aimed to control of propfan noise has provided several results concerning the noise source, the mechanism of noise generation (2) and transmission (3) to the fuselage, the means for reducing internal noise acting on the source (1), (4). These results have been partly used in new commuter aircraft. In addition, a large effort is under way to fully model the relationship between internal and external noise and to validate the theoretical results. No studies are available in the technical literature, to the knowledge of these authors, concerning correlation of theory with full scale results. Little is published on means being studied to achieve noise reductions larger than those given by conventional primary fuselage structures and add-on systems, without increasing the sidewall mass to unrealistic values.

Some reports exist on noise reduction programs performed on existing aircraft (5), whose main indication is the need for working at the same time on the several factors affecting internal noise, because of the relatively small effect of each.

The propfan research follows the goal of achieving a full understanding of all the mechanisms involved, given the time frame considered for this propulsion technology.

The work on existing aircraft is more concerned with achieving some practical results, soon.

The program described in this paper follows an approach that is much closer to what is being done on noise attenuation of existing aircraft. Having dealt with this problem at a much earlier stage of aircraft life, however, has brought to the development of theoretical and experimental tools whose main purpose is to assist in taking decisions on aircraft configuration before production starts and to allow development of interior noise attenuation technology.

2. PROGRAM DESCRIPTION

Interior noise control of ATR-42 has been considered from the first phases of aircraft configuration definition. Achievement of a maximum level of 78 dBA-aisle seat, passenger head position, typical cruise condition -, the aim set for this airplane in a fully developed acoustic configuration, was soon understood to be possible only giving due consideration to the following items:

- A - The general configuration of aircraft
- B - The external noise sources
- C - The structural configuration of the fuselage

- D - The cabin interior
- E - The internal noise sources

AIRCRAFT GENERAL CONFIGURATION

Propeller distance from fuselage is an obvious factor in determining the noise level set on cabin exterior. However, the strong influence that it exerts on the vertical stabilizer size requires a convinced commitment toward the acoustical quality of the aircraft to let it to be influenced by noise considerations. The selected distance of propeller tip from fuselage skin is 0.82 m, corresponding to a distance to propeller diameter ratio of 0.207, one of the largest values for this class of aircraft.

Structural vibration excitation of noise is a well known effect to turboprop aircraft manufacturers. The G222, a medium sized military transport powered by two General Electric T64 engines with Hamilton Standard three bladed propellers and, alternatively, by two Rolls-Royce Tyne's with BADG four blade propellers, presents an increasing internal noise from the wing section to the rear that has been explained with the excitation of its low tail by propeller wakes. This led to the recommendation for a high tail configuration, that is the solution selected for the aircraft.

PROPELLER SELECTION

Tip speed, diameter, blade number, blade load distribution and planform shape are the main factors that influence both noise generation and propulsive efficiency and, some of them, weight. These factors were evaluated with the manufacturers resulting in the selection of Hamilton Standard 14SF, 3.96m diameter, four blade propeller.

FUSELAGE STRUCTURE

Fuselage sidewall construction has a strong effect on low frequency propeller tone transmission to cabin interior as demonstrated by analysis of stiffened panel dynamic response. Consideration of interior noise in fuselage sidewall design led to theoretical and experimental developments treated in some detail in following sections.

CABIN INTERIOR

Differences found in flight tests performed on G222 in one configuration having thermal insulation blankets on fuselage structure and in a so-called VIP version featuring an elastically suspended sidewall trim and a commercial transport type interior, with seats, carpets and overhead bins, provided a first insight in the acoustic performance of interior treatment. Since the intended sidewall construction of ATR-42 was so much different from G222, it was decided that a theoretical and experimental development of cabin interior, based on the close modelling of configurations being considered, was needed.

INTERNAL SOURCES

This item has also received attention from the beginning of program. It will not be discussed in this work.

3. ANALYTICAL DEVELOPMENTS

Priority has been given to the development of analytical tools, capable of a detailed representation of fuselage structure dynamic behaviour and of effects on fuselage response of add-on systems like vibration absorbers and damping. Sidewall treatment insertion loss and cavity acoustical modes have also been modelled.

These models can become parts of a more general procedure for the analysis of sound transmission inside the fuselage. Such a development will be attempted once experience gained in this production program will have shown the limits of validity of each tool and indicated more appropriate analysis techniques, as reported afterward.

In the following, models of the dynamic behaviour of the structure and of sidewall treatment transmission loss are discussed.

FUSELAGE STRUCTURE DYNAMICS

In recent years some analytical methods to predict aircraft interior noise have been developed, among which (6), (7), (8). A very useful analysis of limitations and capabilities of these methodologies is reported in (9) and (10), that with their 171 and 135 references give a wide overview of contemporary research status. Here it is of interest to point out that to allow a numerical evaluation of interior noise these procedures have to make some simplifying assumptions of the configuration of the structure under analysis. If this can be acceptable for preliminary evaluations of noise transmission inside fuselage, when attempting a detailed analysis of structure dynamics for design purpose it is of importance to have the capability to model the contribution of all structural components, consistently with limitations posed by computation power availability.

After a critical evaluation of methods being developed (14), it was decided to implement the structural dynamic analysis methodologies developed by Sen Gupta (11), (12), (13). These techniques combine transfer matrix and wave approach (TMWA) to derive closed form solutions of the displacement of a periodic structure under acoustic pressure excitation.

Two computerized procedures have been realized, based on these methods: PESAL (14) and NAT-DASC (15), (16).

For a detailed discussion of the methods, reference should be made to Sen Gupta work. Program PESAL allows studies of the modal dynamic response of the fuselage interframe periodic structure, assuming it to be flat, infinite and simply supported by two infinitely rigid elements simulating fuselage frames (figure 1), taking into account the structural details of panel and stringer, under pressurization loads. Curvature effects are simulated by a fictitious plane stress increase. The acoustic field excitation used in ATR-42 studies has a white noise spectrum and infinite trace velocities along the circumferential and longitudinal directions.

Program NAT-DASC calculates the modal dynamic response of the "Cylindrical shell-frame" periodic structure, taking into account, among the various parameters, pressurization effects and warping, non-symmetry and excentricity of frame section (figure 2).

A white noise spectrum, infinite trace velocity along both directions, acoustic excitation is usually considered.

These models have been applied, (14), (15), (16), to the analysis of some fuselage structures. Interesting results were obtained (16) using NAT-DASC program to compare the "base line" and "advanced" fuselage configurations of the three aircraft studied in (8), with conclusions similar to those found with different methodologies.

Program PESAL has been used to perform a parametric study of the ATR-42 fuselage structure configuration, on which selection of some structural parameters was based. This followed experimental corroboration obtained by flat panel model tests. Some of these results are presented in a following section.

Program NAT-DASC has not been used in fuselage configuration definition, lacking an experimental confirmation of its results. A later comparison of NAT-DASC outputs with data obtained in the fuselage section test, documented in the following, has shown strong differences, leading to the conclusion that the procedure cannot be used in fuselage design studies.

SIDEWALL TREATMENT TRANSMISSION LOSS

The sidewall treatment (fiberglass batting, blanket cover, trim panel, air gap, septa) effect has been described with reference to Beranek and Work model (17). The fuselage, the trim panel and the septa (including blanket covers) are assumed in the calculations as limp masses. Transmission in the sidewall treatment is considered normal to the wall. The resulting computer program, NAT-TPL, after being found in agreement with experimental results on flat panel treatments, has been used to perform trades on different configurations and materials of the sidewall for selection of the aircraft solution. Some results are discussed in a following section.

4. EXPERIMENTAL DEVELOPMENTS

The experimental program has been established with the main purpose of developing the acoustic configuration of fuselage sidewall structure and add-on systems, namely the thermoacoustical insulation, the interior trim panels with their mounting, damping and vibration absorber devices.

Most of the studies are performed on a full scale fuselage section, 6 bay long (3.25 m). Part of the sidewall structure and add-on system work has been done on flat panels.

FLAT PANEL VIBRATION TEST

Two test articles are available, resembling structural solutions being traded.

Each article is made up of a panel, having the width of a fuselage bay, and of seven stringers spaced as on the aircraft. Damping is applied at the two shortest edges to reduce wave reflections at these discontinuities. The sample is attached to very rigid frames on the two long edges, and is free at the two short. This installation simulates the infinitely long, rigid frame, stringer/panel model described in the analytical model section.

A modal analysis is performed on the centre bay, using the Single Point Transfer Function technique.

SIDEWALL TREATMENT FLAT PANEL TRANSMISSION LOSS

The same test articles and a similar fixture as in previous test are used. ABS trims, of different surface densities, are bolted to the rigid fixture. Fiberglass blankets with covers typical of aircraft applications can be installed in the trim/panel gap. Fixture is connected to the edges of a window opened on one wall of a semi-anechoic chamber, 1.5 x 1.5 x 1.5 m.

Acoustic excitation is obtained through a loudspeaker system driving an acoustic horn resting on the sample fixture (fig. 3). One external microphone at the tip of a probe mounted at center of the horn reads sound pressure on sample surface.

Several microphones are mounted inside the chamber. Chamber walls are lined with constant thickness fiberglass providing absorption characteristics as in a typical furnished aircraft.

This set-up is used to acoustically test sidewall treatments coupled to the fuselage panel.

FUSELAGE SECTION TEST

The test article (fig. 4) duplicates the fuselage structure construction, including windows and floor structure.

Or some tests only one window row was present, with window glass changed with an aluminum panel of the same mass as the glass.

The interior of the test article (fig. 5) can resemble the various solutions taken under consideration for the aircraft. The baseline configuration consists of three longitudinal beams for each side, elastically suspended on the frames, to which ceiling panels, baggage bins, and the lateral trim panels are attached. Acoustical effects of seats and carpeting are simulated by some foam material distributed in the test article (fig. 6).

The test section is terminated at each end by a reinforcing flange riveted to the skin, through which the article is suspended to the holding structure.

The test rig is designed to allow section pressurization. The cylinder is closed at the two ends (fig. 7) by heavy caps - about 350 Kg. each - bolted to flanges, 9 PSI being max allowed pressure differential. The caps are connected by means of a spring system to the fixture, with a resulting isolation above 20 Hz. The suspension system is designed so to allow longitudinal motion of one section end to avoid loads not present on aircraft. The interior of the end caps is covered with 0.1 m deep fiberglass.

Two types of tests are performed on the fuselage section, modal analysis and noise reduction.

Figures 8, 9 are schematics of the instrumentation used. Figure 10 shows the test article assembled on the fixture, with the point force and the acoustical excitation in place.

The single point force excitation is provided by an electrodynamic shaker having a force output of about 40 N. The acoustic excitation is given by two pairs of high and low frequency electrodynamic drivers installed on the rear wall of a box having the opposite side open. The box is placed with its open side close, but not in touch, to the fuselage skin.

In the modal test, acceleration at about 200 points has been measured, using 2 gr accelerometers for panel and 11 gr accelerometers for frame vibration tests.

In the acoustic test 9, 1/2 inch pressure type microphone (fig. 6) are used inside and 7, 1/4 inch pressure type microphones outside the fuselage, reading skin pressure. One external microphone is flush mounted at the center of a window with its membrane tangent to window skin, its body being inside the fuselage at the interior pressure. Rear side of membrane is vented outside.

The other external microphones are installed with membrane perpendicular to fuselage skin. One of them is mounted near the flush microphone to provide an indication of the installation effect, that is applied to the readings of remaining external microphones.

All tests are performed using a semi-automated procedure started by the test operator during the data acquisition phase. Data are stored on the magnetic mass memory of the test dedicated computer, a Sel 32/35, for the following analysis and presentation.

5. DISCUSSION OF RESULTS

Theoretical and experimental studies have been conducted, that are still under way for certain aspects, having the main purpose of providing information for selection of fuselage structural and interior elements having an impact on the interior noise of the aircraft.

Contribution to the definition of fuselage structure configuration has been given on the basis of results obtained by the panel/stringer theoretical model, confirmed by flat panel tests available at the time configuration was frozen. Later, data collected during modal testing of fuselage section brought to the decision to add shear ties between frames and panels where they lacked in the baseline configuration. Development of sidewall treatment has been based on theoretical analysis and on the output of tests performed on flat panels and on the fuselage section. This test article, still undergoing experimentation, is the heart of the development program under discussion. It is used to understand the effects of modifications to the baseline. In addition, it is providing results for the development of damping and vibration absorber technology. Lack of previous experience in the use of such experimental methodology does not allow yet to take the output of this test as an absolute estimate of aircraft behaviour. In particular, model scale effects are not clear at this moment. Still it is felt that, if used for the purpose of deriving comparisons among different acoustical solutions, the results of this experimentation are reliable. Although the program being discussed has not as its main purpose the development and the validation of theoretical procedures, results obtained can be used to infer limits and merits of the analytical approach used.

FLAT PANEL VIBRATION ANALYSIS

Two possible configurations of fuselage interframe structure have been realized with test articles consisting of flat panels with stringers mounted at a constant pitch, 0.12 m and 0.24 m respectively.

The panel resonant frequency, as found in the test and from program PESAL analysis, in the no pressurization case, is as follows

PANEL	STRINGER PITCH (m)	FRAME PITCH (m)	RESONANT FREQUENCY (Hz)	
			THEOR.	EXPER.
1	0.12	0.53	124	122
2	0.24	0.53	78	77.7

Measured and calculated transfer functions are compared in fig. 11. It should be noted that the theoretical transfer function refers to a uniform acoustic pressure field excitation, the measured transfer function to an impulsive type excitation.

More modes are present in the experimental transfer function with respect to theory.

This is explained with the not perfect realization on the test article of assumptions contained in the theoretical model. Namely, test article is not infinite in length, giving rise to resonances in the direction perpendicular to stringers in particular the 48 Hz mode. Production tolerances introduce non uniformities that make the structure non periodic. Figures 12, 13 show theoretical results concerning the effect of pressurization. Vibration level is practically not affected, 1st mode frequency increases with in plane panel stresses.

Figure 14, shows the importance of stringer spacing and damping on vibration response. For the structure analyzed, subject to pressurization, inter-stringer panel first resonance frequency is well above stringer frequency, also at the higher stringer pitch values considered. This makes the first periodic structure mode to be influenced by stringer behaviour, and then effective vibration reductions are obtained by just increasing the damping of the stringer. First mode amplitude is practically not affected by panel damping. As a result of this study and of an evaluation of panel radiation efficiency variation with stringer spacing, a pitch smaller than required by purely structural considerations was selected in order to reduce resulting acoustic power radiation inside the fuselage and to increase resonant frequencies.

FUSELAGE SECTION STRUCTURE ANALYSIS

Several studies, (7), (10), (18), concerning aircraft interior noise have evidenced the need for performing modal analysis of the fuselage structure as a means for a better understanding of acoustic transmission inside the fuselage. Examples of this approach are reported in (19), (20).

An experimental modal analysis can provide the following results:

- 1 - Definition of structure natural frequencies
- 2 - Mode shape analysis and contribution of various structural elements
- 3 - Loss factors associated to modes
- 4 - Definition of factors having an effect on the use of noise attenuation devices like vibration absorbers, damping materials, anti-vibration mounts for the interior furnishing.

An experimental modal analysis using the single point transfer function technique of fuselage structure has been performed (21) on the fuselage section test article. Theoretical modal analyses have also been performed by the NAT-DASC periodic cylindrical structure procedure and by a finite element method. The experimental analysis has first evaluated some effects concerning the test set-up. The six rigid body frequencies of test article have been determined, all being below 15 Hz. Two excitation types, one vertical on the fuselage bottom and a second horizontal at window height, both at panel/frame interfaces, have been tried. The horizontal excitation has been selected, more modes and with higher amplitudes being generated. Three different pick-up arrangements have been used to the purpose of defining contributions of various structural elements. Test has covered frequency ranges from 50 to 500 Hz. Pressurized and unpressurized conditions have been tested. A strong influence of structure asymmetries like windows on one side only, floor, fuselage cross-section shape and non uniform distribution of frame shear-ties, has been evidenced in the mode shapes.

Mode amplitudes at window locations and at the fuselage crown intersections with frames having no shear-ties appear to be much larger than at frame locations where shear-ties are present and no window is adding its mass to the moving structure. The parts of the fuselage located under the floor move with very small amplitudes.

A comparison has been made of resonant frequencies and loss factors of the first modes, for the bare fuselage structure, with and without pressurization, as well as for the furnished fuselage. It confirms the expected effect of pressurization on resonant frequencies, shown for one mode in Figure 15. A large impact on mode frequencies is found by adding the sidewall treatment, overhead bins and ceiling, and masses simulating items attached to interior holding secondary structure and hand carried baggage. The analysis of mode shapes in this case has given some difficulties, a larger number of acceleration readings than for the bare structure being more appropriate. Mode loss factor increases by a ratio of two, in the average. Modal density, considering only the larger amplitude modes, is smaller in the case of the furnished fuselage, with three modes in the range 50-80 Hz that are completely missing.

A comparison of experimental modal analysis data with theoretical predictions has been performed. Mode shapes and frequencies have been calculated using the program NAT-DASC and the program Nastran.

Program NAT-DASC describes the behaviour of an infinite cylinder with circular frames at a constant pitch. Frame parameters as in the fuselage section have been used, with no possibility to simulate non uniformities due to shear ties actual distribution.

Panel parameters are those of test article, with added the smeared mass of stringers and windows. No possibility exists in this program to simulate floor structure.

Figure 16 provides the calculated transfer function frame acceleration - acoustic pressure, the latter being associated to an acoustic field with infinite trace velocities in the two directions.

Modes predicted by the program have no similarity with modes found experimentally, being fewer and with different frequencies.

Program Nastran has been used to describe the forced response to a pressure field, equivalent to the one considered in the NAT-DASC analysis, of a structure being a simplified simulation of the test article. It consists of one frame with attached masses on both sides equal to those of panels, stringers and windows present in the two adjacent half bays. The actual distribution of shear ties on the frame is duplicated, and the floor structure is introduced.

Figure 17 compares mode shapes of first modes found theoretically with FEM and experimentally, for the non pressurized, unfurnished fuselage.

Figure 18 compares mode frequencies, theoretically calculated with FEM, and experimental.

Table 1 provides the list of resonant frequencies found with the two theoretical models and experimentally.

Some agreement and general resemblance of FEM theory and experiment outputs is visible in these comparisons.

Present formulation of NAT-DASC procedure has not been found adequate for studies of fuselage structure configuration.

As a result of the experimental investigation of dynamic behaviour of structure, the decision has been taken to use shear ties all along frame, in order to decrease panel motion. In addition, modal information is being used in understanding fuselage noise reduction and in developing means for reducing interior noise.

SIDEWALL TREATMENT TRANSMISSION LOSS

The sidewall treatment acoustic performance has been studied theoretically using the procedure NAT-TPL described in a preceding chapter, and experimentally with results from the semi-anechoic chamber facility; it is to be noted that the experimental set-up is finalized to read a "Noise Reduction" parameter, obtained as the difference between external sound pressure level and the average of the levels at some microphones in the chamber. Semi-anechoic chamber room constant is similar to that of typical commercial aircraft interior, at the middle-high frequencies. This set-up is meant to furnish the relative effects of different sidewall treatments at the speech interference frequencies. At lower frequencies, dimensions of chamber and possible effects of curvature on sidewall treatment performance advise to use a different approach for this particular evaluation. Test on the fuselage section has provided this information.

To the purpose of comparing experimental results with those from the theory, a "Transmission Loss" parameter was derived from test data using sound pressure readings close to double wall structure.

Some comparisons are shown in figures 19, 20. It is clear that agreement greatly improves for configurations including fiberglass blankets in the gap between trim and stringer-skin structure. This may be caused by the fuselage panel and the trim panel being simulated in the analytical procedure as limp masses.

Agreement in the configurations that include fiberglass is consistently good at the frequencies of interest. Instrumentation dynamic range limitations and some possible leakage effects can explain the large differences at high frequencies.

The analytical procedure and the experiments have been used to accomplish a trade on effects like distribution of the mass between trim and blankets, air-gap/fiberglass sequence, fiberglass density, thickness and flow resistance.

Results have confirmed solutions presently used on commercial aircraft. Specifically, low density, high flow resistance materials are found to provide best compromise between weight and attenuation, wherever space available for treatment allows to obtain requested isolation effectiveness with blanket thicknesses smaller or equal to trim/structure gap.

FUSELAGE BEHAVIOUR WITH ACOUSTIC EXCITATION

Acoustic tests are being performed on the fuselage section, with various interior configurations, to the purpose of developing understanding of optimum solutions for items of furnishing having an effect on interior noise. In addition, effect of structural modifications and add-on systems - damping, vibration absorbers - can be checked. Other model tests of a similar nature have been conducted (7), (18). The intent in these cases has been to validate theoretical prediction methods and to obtain experience on heavy double wall systems.

Results of experiments on the fuselage section cannot be simply extrapolated to full scale aircraft, reason being the scale effects inherent to this test. At this time scale effects can be identified as follows:

- A - Geometry. Cross section of test article is full scale, length is 3.256m, versus 10.2 m of aircraft fuselage, from forward baggage compartment partition with passenger cabin to aft cabin-galley partition.
Low frequency structural modes, probably below propeller noise fundamental frequency, and acoustics of the cabin are influenced.
- B - Source. Level distribution and phase relationship of sound on fuselage surface are different from aircraft.
Noise is generated on one side only of test article. Effect of asymmetry of real acoustic field (1) on the two sides of fuselage is not taken into consideration.
Absolute level of excitation has been determined to be unimportant up to 130 dB, limit of the source system used, other than for usual noise floor problems at the low amplitudes.

Some of above factors can be investigated using the same test set-up. A better understanding will be developed at the completion of flight tests on aircraft.

Effect of pressurization on noise transmission inside the fuselage is taken into consideration in this test, differently from the other mentioned above (7), (18).

This effect is mainly determined by fuselage structure response and by the larger characteristic resistance of the receiving space.

Figure 21 reports the Noise Reduction functions for a furnished configuration of test article, with and without pressurization. Acoustic excitation used to derive these data is white noise. The reduction of attenuation in the pressurized condition varies with frequency, being larger at higher frequencies.

This result, and other similar obtained during the program, demonstrate the need for including pressurization among parameters to be taken into account in model tests.

Figure 22 presents accelerations measured on the elastically suspended secondary structure holding the interior and on the lateral trim panel, both ratioed to acceleration measured on a frame, at the point of attachment of anti-vibration mount. Below 250 Hz trim panel vibration is much larger than motion transmitted through the elastic suspension. Acoustic excitation from fuselage panels and trim panel resonances cause these differences. At higher frequencies, attenuation provided by acoustic insulation blankets in configurations typical for this class of aircraft makes the lateral panel motion similar to vibration input, in the average.

Table 2 presents an analysis on the Noise Reduction spectrum of furnished and bare fuselage section configurations, where frequencies at which attenuation is in a dip are compared to main structure and interior resonances. Analysis is based on 1.25 Hz bandwidth spectra. Both configurations were pressurized. The correspondence between attenuation minima and some of acoustical and structural resonances is good.

COMMENTS TO RESULTS

Data presented in this section allow to draw some comments on the problem of Interior Noise prediction of a turboprop aircraft.

Low frequency Noise Reduction prediction is the area of greater concern. It has a large impact on the accuracy of dBA and OASPL predictions of the Interior Noise, and this is the frequency range where simplifying assumptions in the description of the source, the dynamic behaviour of structure and interior trim, and the cabin and sidewall treatment acoustics can induce discrepancies with respect to the reality of the aircraft.

Experimental modal analysis performed on the bare and furnished fuselage section has shown the importance of a detailed description of the main structure, that should consider also the attached mass-spring system of the interior furnishing.

The level of detail required appears to be higher than in prediction procedures presently under development.

On the contrary, the good correlation obtained in this program between acoustic mode frequencies predicted using a simplified approach, and measurements, shows that predictions of the receiving space acoustic behaviour, especially when performed considering the actual cabin geometry (7), should be of much less concern.

Obviously the presence of several tones in the source spectrum makes the calculation of Interior Noise highly uncertain, even if more detailed analysis methods were made available. However, procedures that included more details than presently available could provide a better understanding of the extremes of the range in which the real interior noise parameters would fall. Such procedures, in addition, could be very useful in the design of the acoustic configuration of the fuselage.

It is with this perspective that, as suggested by Sen Gupta (13), studies will be started by the authors, on the integration of FEM and TMWA methods for a more detailed description of the primary fuselage structure.

6. CONCLUSIONS

The program has been discussed for the development of the acoustic configuration of a turboprop commuter aircraft. The analytical and experimental tools employed have provided valuable information for definition of structure and sidewall treatment of fuselage. Limits of these tools have been evidenced, that do not allow their use for a reliable prediction of fuselage attenuation in flight. Flight tests that are planned in 1985 will provide a better understanding of their limits and of ways for widening their capabilities.

REFERENCES

- 1 - F.B. METZGER "Strategies for Aircraft Interior Noise Reduction in Existing and Future Propeller Aircraft" SAE Technical Paper 810560, 1981.
- 2 - D.B. HANSON "Near Field Frequency-Domain Theory for Propeller Noise" AIAA 8th Aeroacoustics Conference, 1983.
- 3 - D.B. HANSON "Shielding of Prop-Fan Cabin Noise by the Fuselage Boundary Layer" Journal of Sound and Vibration, 92 (4), 1984.
- 4 - B. MAGLIOZZI "Synchrophasing for Cabin Noise Reduction of Propeller Driven Airplanes" AIAA 8th Aeroacoustics Conference, 1983.
- 5 - E.H. WATERMAN "New Means of Reducing Propeller Induced Cabin Noise" Proceedings of Institute of Acoustics (U.K.), Spring Conference, 1981.
- 6 - L.D. POPE, D.C. RENNISON, C.M. WILLIS, W.H. MAYES "Development and Validation of Preliminary Analytical Models for Aircraft Interior Noise Prediction" Journal of Sound and Vibration, 82 (4), 1982.
- 7 - L.D. POPE, E.G. WILBY, C.M. WILLIS, W.H. MAYES "Aircraft Interior Noise Models - Sidewall Trim, Stiffened Structures and Cabin Acoustics with Floor Partition" Journal of Sound and Vibration, 89 (3), 1983.
- 8 - J.D. REVELL, F.J. BALENA, L.R. KOVAL "Analytical Study of Interior Noise Control by Fuselage Design Techniques on High-Speed Propeller - Driven Aircraft" NASA CR-159222, 1978.
- 9 - E.H. DOWELL "Master Plan for Prediction of Vehicle Interior Noise" AIAA Paper 79-0582, 5th Aeroacoustics Conf. Seattle, 1979.

- 10 - J.F. WILBY: "Propeller Aircraft Interior Noise" Von Karman Lectures Series on "Propeller Performance and Noise" 1982.
- 11 - G. SEN GUPTA "Natural Flexural Waves and the Normal Modes of Periodically - Supported Beams and Plates" Journal of Sound and Vibration, 13 (1), 1970.
- 12 - H.H. NIJIM, G. SEN GUPTA "Response of Frame-Stiffened Cylinders to Random Pressure Fields" BOEING Doc. D6-44721, 1978.
- 13 - G. SEN GUPTA "Reduction of Cabin Noise During Cruise Conditions by Stringer and Frame Damping" AIAA Journal, 17 (3), 1979.
- 14 - L. LECCE, F. MARULO, A. CARBONE, S. MANDARINI "Sul Problema della Riduzione del Rumore a basse-medie frequenze all'interno di fusoliere mediante modificazione dei parametri strutturali. L'Aerotecnica, Missili e Spazio, Vol. 63, No. 4, 1982.
- 15 - L. LECCE, F. MARULO "Dynamic Analysis of Periodically Frame-Stiffened Cylinders" (In Italian) Report SPER 82-85, Istituto di Progetto Velivoli University of Naples, June 1982.
- 16 - L. LECCE, F. MARULO, A. CARBONE, A. PAONESSA "Theoretical and Experimental Results relative to Dynamics Response of Fuselage Structures to Acoustic Excitation (In Italian) L'Aerotecnica, Missili e Spazio. Vol. 62, No.4, dicembre 1983.
- 17 - L.L. BERANEK, G.A. WORK "Sound Transmission Trough Multiple Structures Containing Flexible Blankets" The Journal of the Acoustical Society of America, 21 (4), 1949.
- 18 - J.S. MIXSON, F. FARASSAT, J.D. LEATHERWOOD, R. PRYDZ, J.D. REVELL "Interior Noise Considerations for Advanced High - Speed Turboprop Aircraft" Journal of Aircraft, 20 (9), 1983.
- 19 - D.L. GEJSLER "Experimental Modal Analysis of an Aero-Commander Aircraft" NASA CR 165750, 1981.
- 20 - F.B. METZGER - Private Communication, 1983.
- 21 - A. PAONESSA, S. MANDARINI, L. LECCE, F. MARULO "Experimental Modal Analysis on a Full Scale Partial Fuselage of a Turboprop Aircraft" in Italian, Proceedings 7th AIDAA National Conference, 1983.

MODE	FEM (FRAME MODEL) (Hz)	NAT - DASC (CYLINDER MODEL) (Hz)	EXPERIMENTAL RESULTS (Hz)
1 2 A	12.3		
1 2 S	18.7		
1 3 A	37.9		55.2
1 3 S	54.1	20	58.6
1 4 A	70.3		66.9
1 4 S	97.6		
1 5 A	110.1		93.4
1 5 S	141.6	65	
1 6 A	151.1		
1 6 S	168.7		
1 7 A	211.6	145	

A = Antisymmetric
S = Symmetric

TABLE 1 - Fuselage section mode frequency -
Theoretical and experimental -

BARE FUSELAGE			FURNISHED FUSELAGE		
STRUCTURE MODE (Hz)	ACOUSTIC MODE (Hz)	NOISE REDUCTION DIP (Hz)	STRUCTURE MODE (Hz)	ACOUSTIC MODE (Hz)	NOISE REDUCTION DIP (Hz)
61.4				60	63
74.4				70	69
79.2				72	
87.2	84	84	80.9	73	78
95	97		91.5	90	87
115.8	115	114	94.5	105	
129	126	126	115.5	117	117
131.8			126	129	129
144.1	145	144	135.4		
148.5			137.3	137	
154.5			142.1	141	141
158.9	159	156	143.5		
162			150.2	155	156
169.6	168	168		163	
174				165	
178.3	180		173	174	
182				180	
188.7		186	193	198	195
194.3	192		206.5	207	
198	198		224.5	225	
206.9	204	210		240	240
235.6	235	240	255.8		
248.1			261.9	258	
249.4	250			276	276
259.4	264	258			
271.9					
273.1	276				

TABLE 2 - Fuselage section Noise Reduction
Analysis -

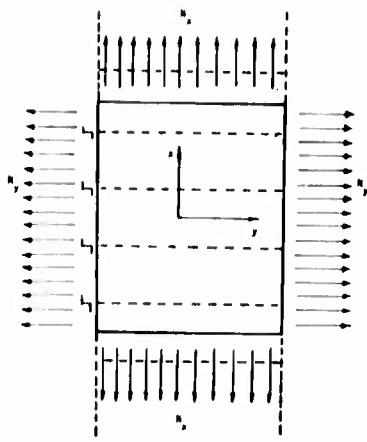


Fig. 1 - Model stringer - panel

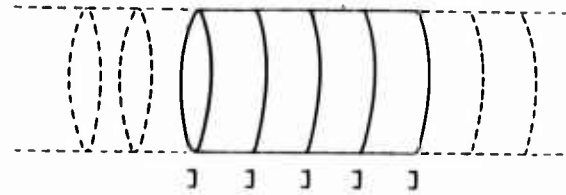


Fig. 2 - Model cylindrical shell - frame

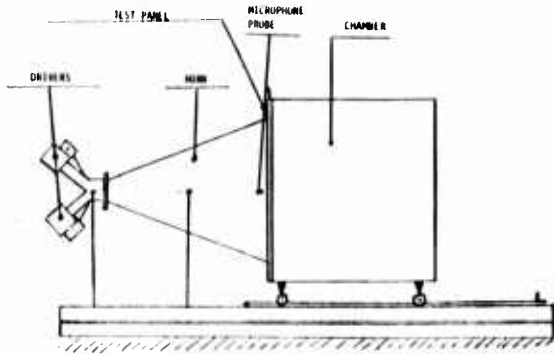


Fig. 3 - Semi-anechoic chamber facility

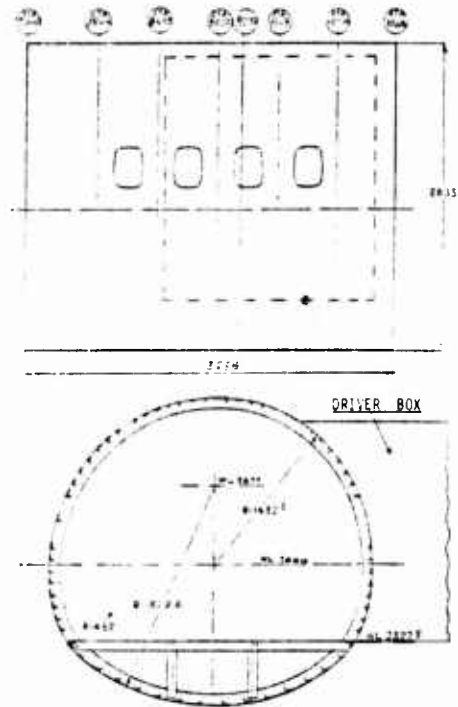


Fig. 4 - Fuselage section test article



Fig. 5 - Fuselage section interior

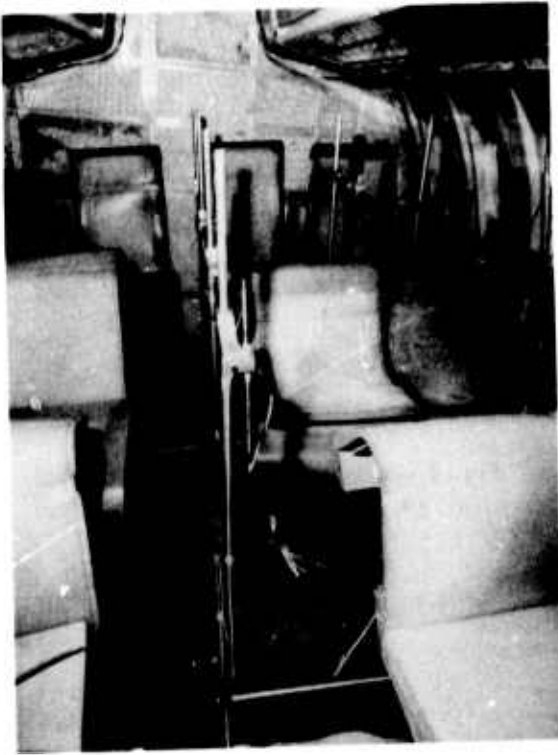


Fig. 6 - Furnishing configuration and microphone arrangement

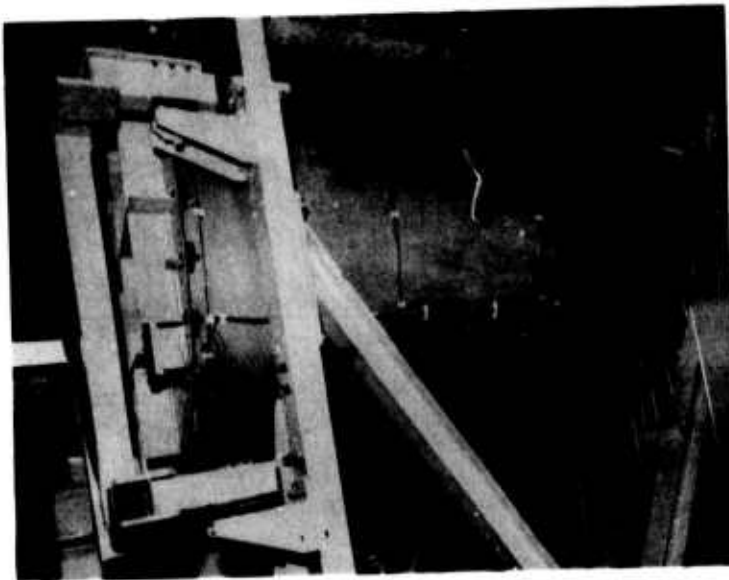


Fig. 7 - Fuselage section installation

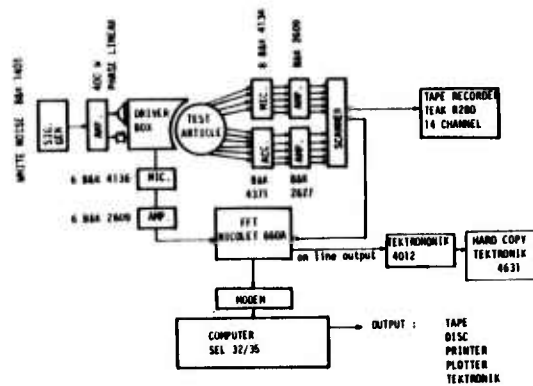


Fig. 8 - Acoustic excitation test - instrumentation schematic

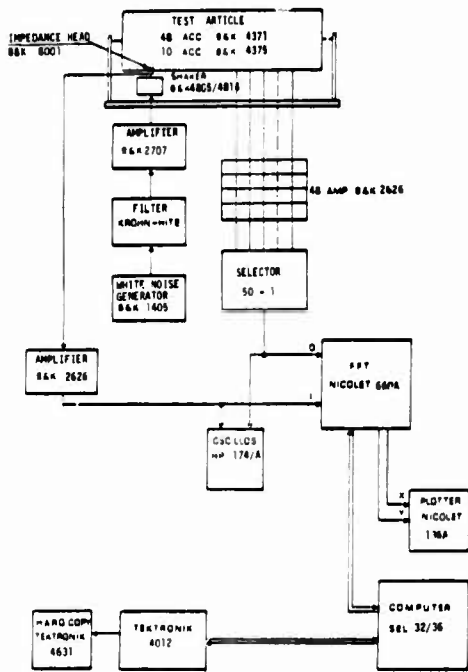


Fig. 9 - Point force excitation test-instrumentation schematic

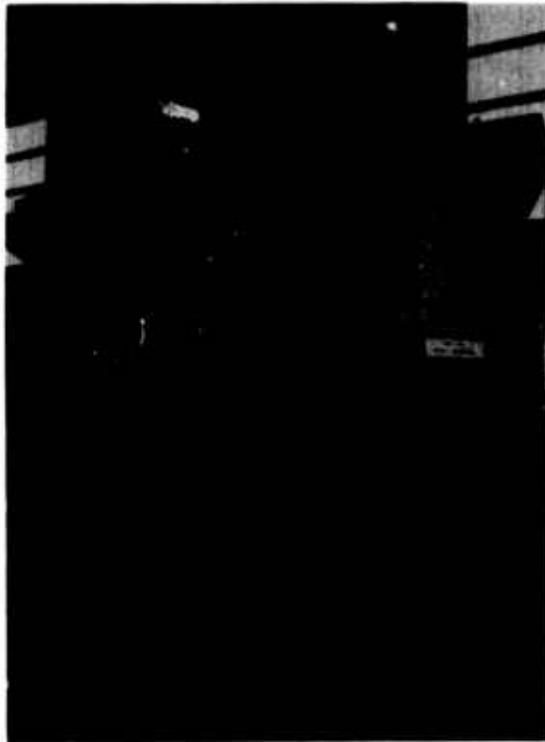


Fig. 10 - Fuselage section test set-up

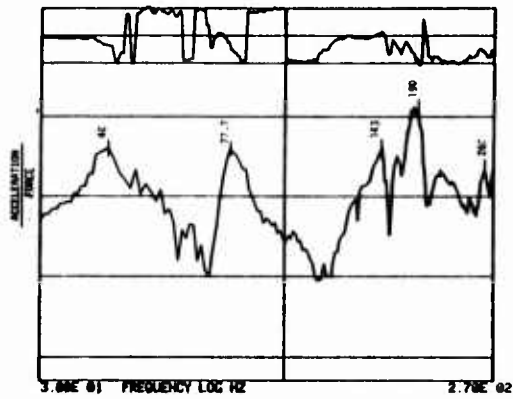
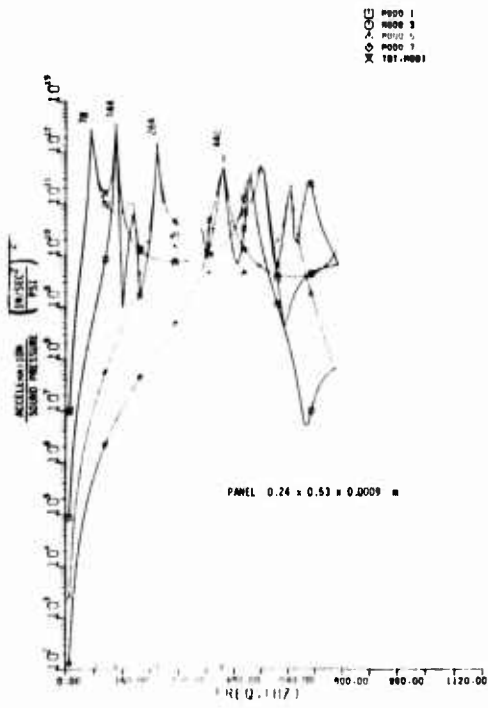


Fig. 11 - Flat panel theoretical and experimental Transfer Functions

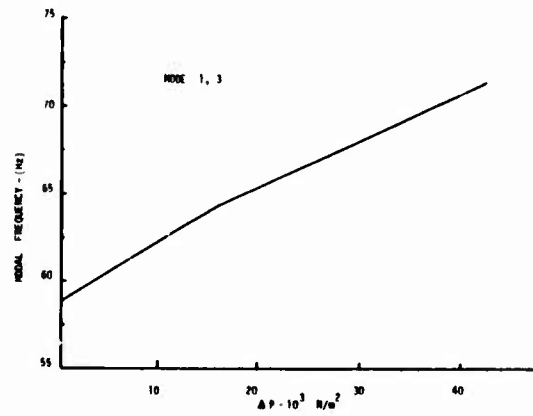
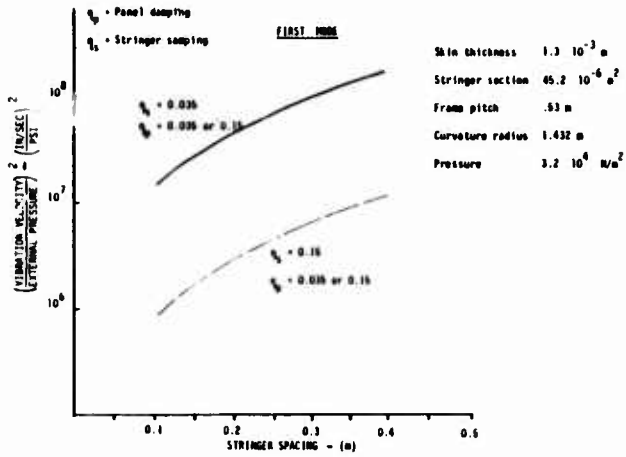
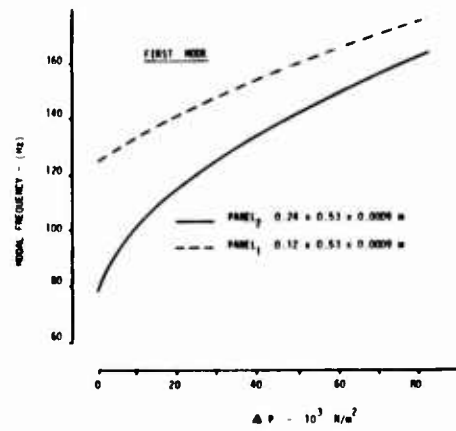
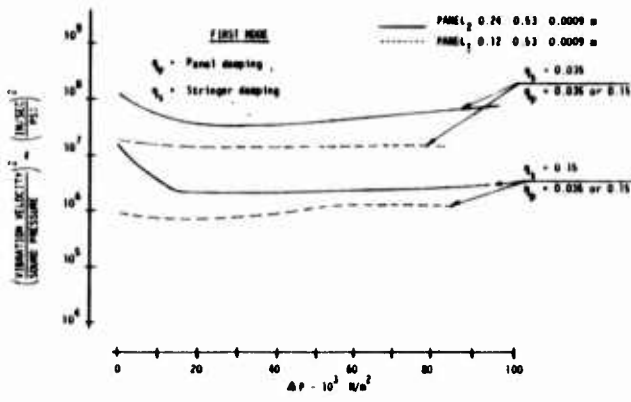


Fig. 14 - Stringer spacing and damping effects on panel response - theoretical

Fig. 15 - Pressurization effect on fuselage resonance frequency - experimental

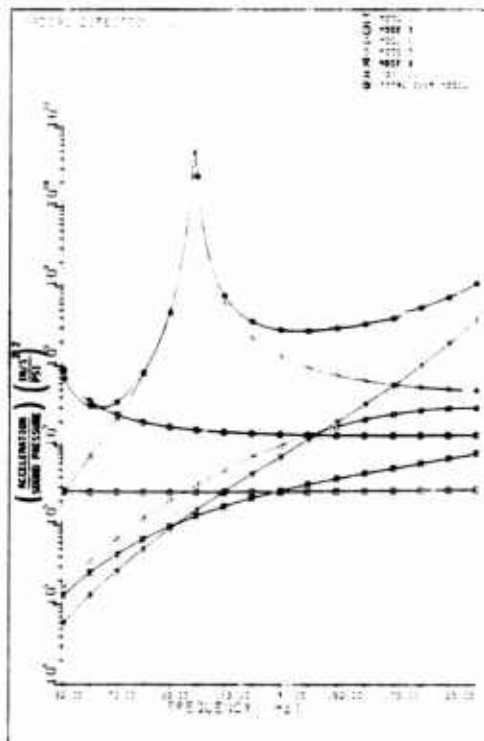


Fig. 16 - Cylinder - frame theoretical transfer function

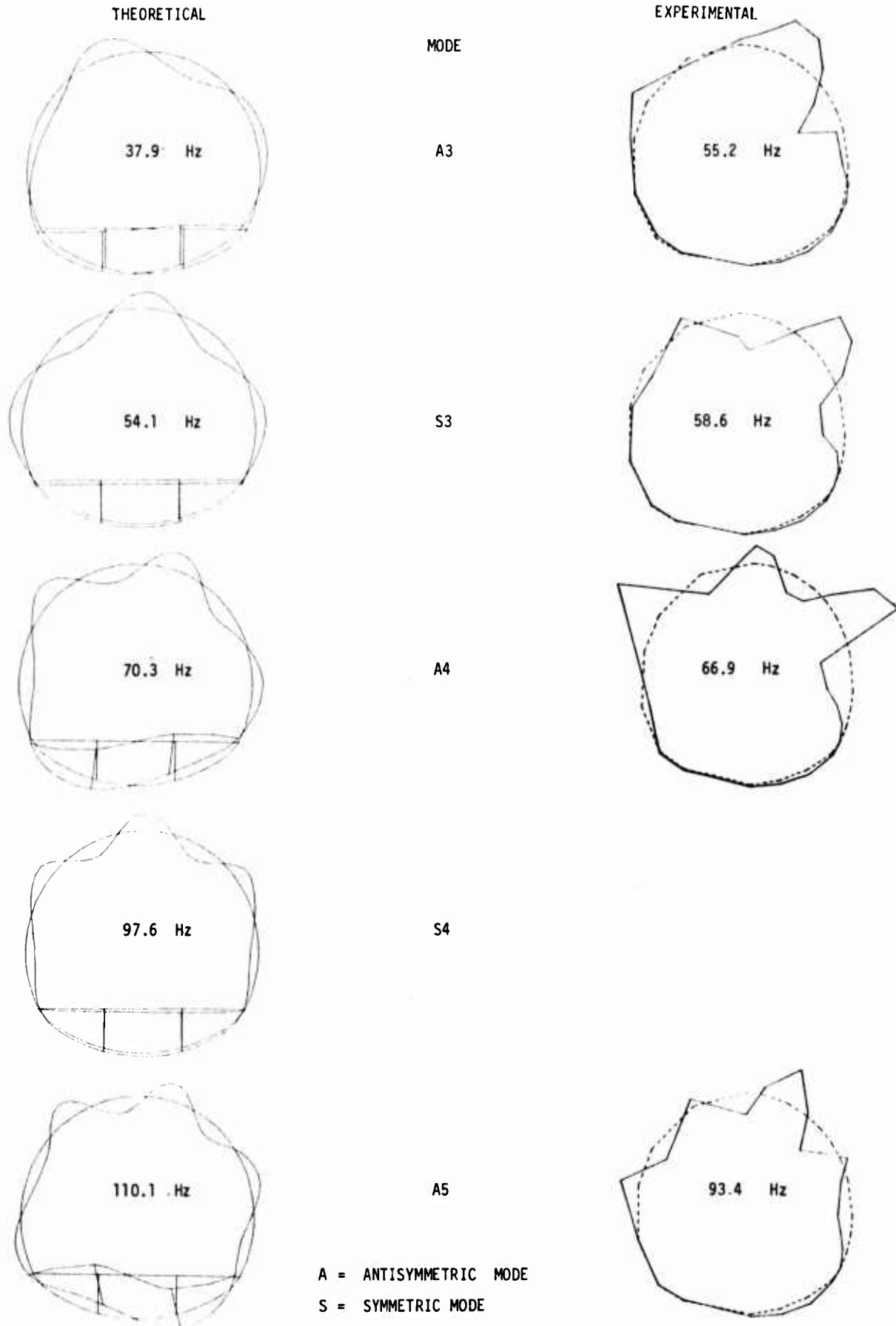


FIG. 17 - Mode shapes of fuselage section -
Theoretical (Nastran) and Experimental -

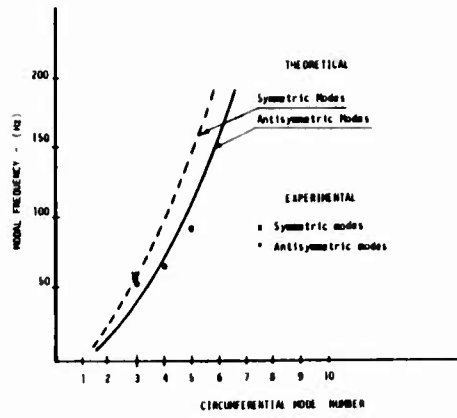


Fig. 18 - Mode frequencies - theoretical (Nastran) and experimental

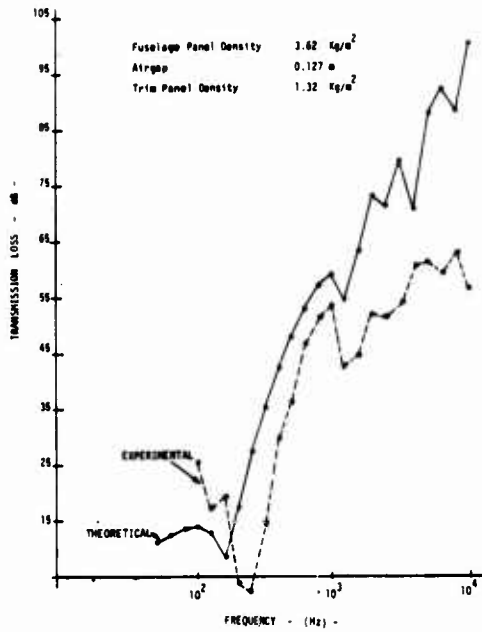


Fig. 19 - Sidewall treatment, no fiberglass. Theoretical and experimental Transmission Loss

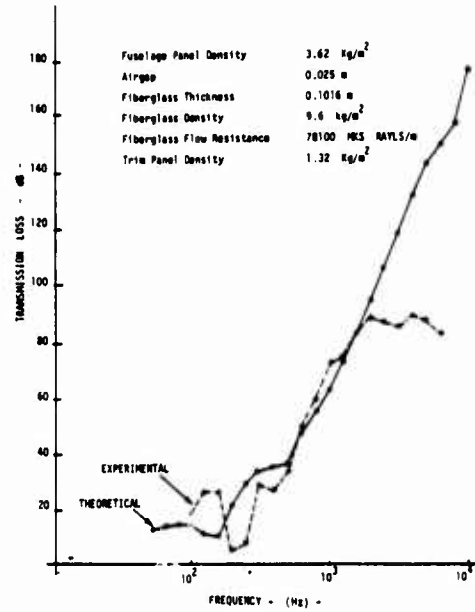


Fig. 20 - Sidewall treatment with fiberglass. Theoretical and experimental Transmission Loss

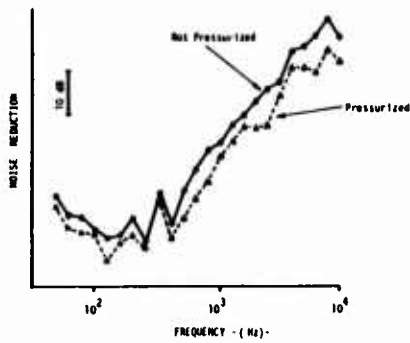


Fig. 21 - Pressurization effect on furnished fuselage section attenuation

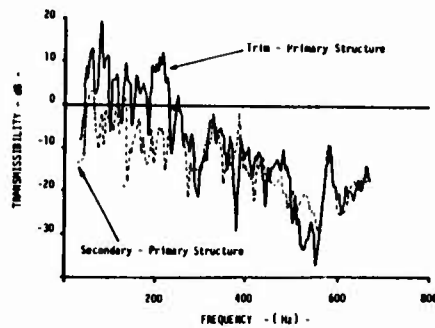


Fig. 22 - Trim panel and AVM Acceleration transmissibility

PROPELLER AIRCRAFT CABIN VIBRATION AND
NOISE-EXCITATION, SOURCES, AND PATHS

R.E. Donham, F.J. Balena,
E.Z. Bochary, and O.K. Liehr
Lockheed-California Company
Burbank, California

SUMMARY

The potential sources and paths by which the propeller produces structural responses resulting in vibration and noise in the cabin of a transport aircraft are discussed. New low-cost, convenient experimental and analytical techniques are described for evaluating the excitations; propeller airborne pressures on the fuselage shells, slip-stream-induced forces on the wing and tail, and oscillatory forces on the propeller. The techniques described make use of ground determined structural signatures to relate forces with vibrations or noise, and of propeller signatures from flight tests which define the vibro-acoustic contributions of individual propellers.

INTRODUCTION

The advanced turboprop-propulsion system, addressed in a NASA Aircraft Energy Efficiency (ACEE) program (Ref. 1), describes a significant part of that program making the internal vibration and noise environments competitive with those of turbofan aircraft. Vibration and noise are closely related, inasmuch as vibration of the fuselage shell and floor produce the noise heard in the cabin.

The background of a more hostile environment, in terms of propeller torque and advancing tip Mach number, indicates that every source and every path by which vibration and noise enter the cabin must be considered in designing advanced turboprop aircraft.

Until recently, we have dealt with the most obvious source, the oscillatory pressures on the fuselage shell, airborne from the adjacent propeller. It is toward the understanding and evaluation of all excitations and their structural and vibroacoustic effects that this paper is addressed. New experimental and analytical techniques are described for evaluating the propeller input forces on the fuselage shell, the slip-stream-induced forces and moments on the wing and tail, propeller blade/engine forces and moments as well as the contributions of each, separately, to the structural responses, including the noise and vibration in the cabin. With the excitation forces and responses evaluated in magnitude and phase, design approaches to controlling structural fatigue and the vibro-acoustic environment can be enunciated logically.

Flight tests, ground tests, and theoretical analyses have been carried out to investigate the following propeller aircraft input sources/paths:

- o Airborne/fuselage
- o Wing in slip-stream
- o Tail in slip-stream
- o Propeller forces/moments
- o Multiple propellers

PROPELLER SIGNATURES

Test Signatures

As reported in reference 2, the acoustic and vibration propeller signatures measured on a Navy/Lockheed P-3C four-propeller patrol aircraft were validated by using them to predict the noise levels at 12 test locations for later test runs at the same altitude and speed.

To determine propeller acoustic or vibration signatures from test data, knowing the propeller phase angles, it is, in theory, necessary only to measure the sound pressure (or vibration) vector at four different known combinations of propeller phases to find the signatures. In practice the accuracy is improved by using more data points in a least-squares determination, which is included in the computer code LOCKPHASE, a FORTRAN program developed for signature analysis.

Figures 1, 2, 3, 4, and 5 show the theory and results of these LOCKPHASE analyses, using flight test data. Figure 6 and 7 shows that both the average noise and vibration minimize at the same phase angles. Figures 8 and 9 show the improved 1/3 octave from flight tests results both acoustically and vibrationally obtained using LOCKPHASE angles. These are shown as pressures in psf (pounds/square foot) and velocities in in/sec (inches/second).

Additional conclusions on propeller signatures from reference 2 follow.

- 1) Outboard propellers are significant contributors to the noise and vibration in the fuselage (pointing up the probable importance of the wingborne excitations).
- 2) Smaller synchrophase errors (than the observed ± 5 -degree propeller shaft angle phase variations) are desirable to achieve optimum noise/vibration conditions; the eight- and ten-blade propfans will require still more accuracy.
- 3) Much of the wide variability of noise measurements for a given multipropeller airplane can be attributed to differences in phase angles; no future propeller-powered airplane vibroacoustic tests should ever be made without accurately measuring and accounting for the relative propeller phase angles.

Although the use of propeller signatures has an immediate payoff in its ability to predict optimum phase angles for minimum overall or weighted sound and vibration levels, its most promising use is as a tool for separating and evaluating the vibroacoustic source and path systems. In this respect they are used in conjunction with structural signatures, as described in the following section.

EXPERIMENTAL STRUCTURAL SIGNATURES

An exploratory test was conducted at Lockheed in May 1980 to determine whether and under what conditions tap signatures can be used to determine vibroacoustic transfer paths, in lieu of the alternative more difficult ground vibration tests. It was concluded from these simple tests that transient inputs can be used to investigate vibration and noise transfer functions and transfer paths with such apparently linear systems as the P-3 structure. The precautions taken for this test should continue to be observed, e.g., to select conditions of low ambient noise level, to make on-the-spot analyses with portable analyzer equipment to check the quality of the data, to select hammer masses appropriate to the local mass being excited, and to make multiple taps at each location to maximize the signal, rejecting taps showing overloads or poor input force time history. The primary check on the data quality is the coherence.

GROUND MECHANICAL EXCITATIONS OF THE P-3 AIRCRAFT STRUCTURE

Until recently, primarily the airborne transmission of propeller noise and vibration has been studied. The next step in the methodical noise and vibration control process is the investigation of structureborne propagation paths. To be successful, low cost and convenient experimental techniques are needed to facilitate the acquisition of an empirical data base. A promising test technique is the impulse method which uses an instrumented hammer to excite the structure.

Impulse hammers are widely used in modal studies of structures for the determination of prominent mode shapes and modal damping. To use hammers on such massive and complicated structures as transport aircraft raises a number of questions. Can sufficient force be imparted to the large mass of the aircraft throughout the frequency range of interest? Do nonlinearities exist which render the test method useless? It also has been questioned whether measurable cabin noise radiation may be produced from a distant input point.

A Lockheed P-3C aircraft was used to compare two methods for the mechanical excitation of aircraft structure to verify their interchangeability. An electrodynamic shaker, using three different signal types, and an impulse hammer were compared as mechanical exciters for the aircraft. Both methods produced comparable frequency response and transfer function measurements. The shaker must be used with caution to prevent the generation of a significant airborne noise component. The hammer is not as sensitive to this limitation but an adequate number, at least 50, impulses must be made at each input point to reach a sufficiently high confidence level for the measurement.

Figures 10 and 11 shows the excitation points which are implicitly selected to provide input sources/paths related to airborne/fuselage, wing in slip-stream, tail in slip-stream, propeller forces/moments and multiple propellers.

Test Objective

The design of a propeller-driven aircraft with an acceptable cabin noise environment requires as a first step an understanding of the noise source and its propagation path characteristics. Existing aircraft may be used to measure noise path parameters and establish a useful data base. One approach to the determination of the transmission efficiency of structureborne noise is to employ a means of vibratory excitation that generates little airborne noise. This requirement can be, at least, partially met by the use of electrodynamic shakers and impulse hammers that can excite the aircraft structure in the frequency range where the cabin noise problem is the greatest. Electrodynamic exciters are the traditional tools used for this type of a problem, but their use requires a great degree of care, their setup is a laborious process, and they cannot be connected to every part of the aircraft. However, impulse hammers provide a very flexible approach that can easily be used on virtually any part of the aircraft and permit rapid data acquisition. Hammers, however, have not been used in the past on such complex structures and in frequency regimes where structural modal analysis was not the primary consideration.

It was necessary, therefore, to design and conduct a test which allows the direct comparison of shakers to impulse hammers as mechanical exciters for a complex aircraft structure. The test objective then was to measure the structureborne noise transmission and radiation characteristics of a P-3C aircraft when the engine, wing, fuselage, and empennage are excited by electrodynamic shakers and impulse hammers.

Force Inputs

A P-3 aircraft structure was excited by two different methods, an electrodynamically driven shaker and an impulse hammer.

The shaker was supported by a test stand and located under each of the input points. In the case of the fuselage sidewall input points (numbers 801 and 901) the shaker was mounted horizontally. A 220 Newton M-B shaker was connected by an instrumented shaft to suitable mounting plates that were bolted to the structure.

The connecting shaft was instrumented with a strain gauge. The force calibration was performed by Specialized Testing Services of Burbank, CA. A Hunter Model L-30 spring type gauge was used to measure a steady force while the output voltage was recorded.

A 1.4 kg instrumented impulse hammer with a 44 Shore A hardness tip was used to tap the structure at the input points. The hammer was made and calibrated by PCB Piezotronics, Inc. of Buffalo, NY. The force gauge-hammer assembly PCB Model 086B20 was calibrated as a system by the pendulum impact method.

Instrumentation

Four microphones and seven accelerometers were installed on the P-3C to measure its structural and acoustical response to the mechanical excitations. The sensors were laid out according to the schematic presented in Figure 12.

The microphone systems consisted of Bruel & Kjaer condenser microphones connected with short cables to their power supplies then linked with 30 meter cables to variable gain Ithaco preamplifiers. The accelerometer systems were made up of Endevco piezoelectric accelerometers joined by 30 meter cables to Endevco charge amplifiers that were coupled to variable gain Ithaco preamplifiers.

The microphone systems were calibrated end-to-end by a Bruel and Kjaer Model 4320 pistonphone after they were suspended 0.3 meter (12 inches) away from the fuselage sidewall. The accelerometer systems were calibrated by a Bruel & Kjaer Model 4291 calibrator prior to their installation. The four sidewall accelerometers (A1 to A4) were installed on the outside of the fuselage. They were attached with double backed tape on the frames at the fuselage stations. Accelerometers A5 and A6 were mounted on the floor above the front spar and A7 was on the rear spar.

Test Conditions and Data Acquisition

The test was conducted on November 20 and 21, 1982 at Burbank, California. A current production aircraft P-3C S/N 5753 was located in a production stall and the shaker control, signal conditioning, and tape-recording equipment was housed in the adjacent service building.

The shaker could be controlled to provide single frequency sinusoidal, swept sinusoidal, random, and square wave inputs to the structure. Single frequency sinusoidal inputs were used at 68.75, 136.0, and 204.7 Hz to correspond to the 4P, 8P, and 12P propeller orders of the P-3C. A rate of one Hz per second was used for the sinusoidal sweep which started at 60 Hz and ended at 215 Hz. The random input was a white noise signal which was filtered to concentrate the exciting force in the frequency regime of interest. A square wave input was utilized to simulate a harmonic spectrum but the results were not analyzed due to its poor second harmonic content.

Prior to the actual data acquisition, the shaker or the hammer excitations were applied until optimum gain settings were made on all transducer preamplifiers. During the shaker tests, steady state conditions were maintained for one minute while the swept sine tests required three minutes. The hammer tests required 50 impulses to obtain the desired amount of signal averaging. The random error is inversely proportional to the square of the number of averages, reference 4.

The force input level from the shaker or, in turn, from the hammer was recorded simultaneously with the four-microphone and seven-accelerometer outputs on a RACAL FM 14 track tape-recorder. The remaining two tracks were used to record an IRIG time code and the voice annotation.

For logistical reasons and aircraft availability constraints, not all the input types were used at all the input points. Table No. 1 lists the test conditions and shows the actual input types used.

Results

The sinusoidal inputs are around 153 dB, which is equivalent to 45 Newtons (10 pounds) of peak force, while the tap and random inputs average about 140 dB, i.e., 10 N (2.2 pounds)/Hz. Example of transfer functions and coherences between the microphones and accelerometers and the force input at the fuselage sidewall are shown on Figures 13 to 16.

Microphone and accelerometer 1 are both close to the input point and show a strong response to all the excitations, excellent correlation with all inputs, and coherence functions near unity.

In general, the data from the inputs show very good correlation among all the responses with very good coherence functions indicating adequate signal to noise ratios. There seems to be only one prominent structural mode that was excited; it is at 120 Hz.

On the logarithmic scale

$$1 \text{ Newton} = 120 \text{ dB,}$$

$$1 \text{ Pascal} = 94 \text{ dB, and}$$

$$1 \text{ g} = 120 \text{ dB}$$

The frequency response, or transfer function, was measured in terms of acceleration/force and (sound pressure level)/force. The transfer functions then are expressed in units of g/N and Pa/N. To illustrate this with a numerical example, suppose the transfer function is -73 dB with a force input of 153 dB, the transfer function for accelerations would be:

$$-73 \text{ dB} = \frac{80 \text{ dB}}{153 \text{ dB}} \text{ or } \frac{0.01 \text{ g}}{45 \text{ N}} \text{ or } \frac{0.1 \text{ g}}{10 \text{ lb}}$$

and for the sound pressure levels

$$-73 \text{ dB} = \frac{80 \text{ dB}}{153 \text{ dB}} \text{ or } \frac{0.2 \text{ Pa}}{45 \text{ N}} \text{ or } \frac{0.2 \text{ Pa}}{10 \text{ lb}}$$

Table 2 summarizes part of the acoustic data experimental results for a constant force input of 100 pounds at various input locations for each microphone.

The magnitude of these noise contributions in decibels can be compared with the following pressure equivalents, from ref. 2:

0.084	psf	=	106	dB
0.042	psf	=	100	dB
0.021	psf	=	94	dB
0.0105	psf	=	88	dB
0.0052	psf	=	82	dB

PROPELLER FORCES

Oscillatory forces on the propeller itself are difficult to estimate. Nonuniform inflow, due to angle of attack, will produce significant once-per-revolution (1P) loads on the blade, and curved flow will cause 2P blade loads. While these modify the airborne pressures on the shell, the 1P loads are not transmitted as oscillations into the mounts if the propeller has more than two blades, and the 2P loads are not transmitted as oscillations if the propeller has more than three blades. A four-blade propeller will transmit 4P oscillations from 3P, 4P, and 5P blade loads, and a ten-blade propeller will transmit 10P oscillations from 9P, 10P, and 11P blade loads. The higher-frequency blade load content exists for nonlinearities producing impulsive-type inputs, such as blade passage through locally nonuniform airflow or discontinuous occurrences like blade stall or shock-induced separation in part of the blade load cycle.

Panel methods have been under development during the last 20 years to permit three-dimensional aerodynamic methods to be applied to flow field analysis. QUADPAN (Quadrilateral Panel) is an advanced subsonic panel method, developed by Lockheed-California Company, reference 5.

Figures 17, 18, and 19 shows the P-3 QUADPAN model and plots of the calculated vertical velocity fields for the numbers 3 and 4 propeller planes for one condition. The propeller gear box steady (0P) and unsteady (4P) forces and moments, due to propeller blade aerodynamic calculations using the QUADPAN velocity field components, are given on Table 3. These are for a rigid blade assumption and presently are not correlated with test data. The strength of these 4P gear box loads, compared with Table 2, suggests that the degree of isolation provided by the engine mounts at 4P (68 Hz) is important to cabin vibration and noise.

The upwash effects of the wing system are found to be important to the 1P propeller blade loads. Amplification of the free stream angle of attack by 1.34 times for the outboard propellers and 1.48 times for the inboard propellers as derived from QUADPAN compares favorably with the 1.30 and 1.60 factors deduced from propeller measurements.

The nacelle and flowing inlet descriptions in QUADPAN are the dominant factors influencing the higher harmonic aerodynamic propeller blade loads. Quasi-static calculations, using the in-flow velocity fields, all three components, over the propeller disc in combination with the propeller blade geometry for various combinations of power and angle of attack are given for all four propellers in Table 3.

Test/correlations are underway, as well as investigations of engine mount isolation at 4P (68 Hz) for low strain levels.

CONCLUSIONS

- o The comparison between different mechanical exciters of the P-3C aircraft structure verifies interchangeability between electrodynamic shakers and impulse hammers, provided adequate safeguards are present in the case of the shaker to prevent additional noise path contamination and an adequate number of taps are made in the case of the hammer to provide the necessary signal to noise ratios.
- o QUADPAN results indicate that nacelle/inlet and wing system can produce nonuniform flow fields which results in 4P aerodynamic propeller blade loads such that support forces and moments may be important to cabin vibration and acoustic levels.
- o Wing and tail propeller slipstream excitations can be important to the P-3 based on mechanical excitation test results.
- o The linear superposition of propeller vibration and acoustic signatures, coupled with the highly linear response of the P-3 system, makes it very likely that indirect force analysis methods can be applied, reference 3.
- o The sources/paths that influence cabin vibration and noise probably varies considerably between configurations. Mechanical excitation techniques may be useful in providing some quantification of the relative importance of each source/path for a specific existing configuration.

REFERENCES

1. Dugan, J.F., et al, "The NASA High-Speed Turboprop Program," SAE Tech. Paper 801120, October 1980
2. Johnston, J.F., Donham, R.E. and Guinn, W.A., "Propeller Signatures and Their Use," AIAA Journal of Aircraft, Volume 18, Number 11, November 1981
3. Johnston, J.F. and Donham, R.E., "Attenuation of Propeller-Related Vibration and Noise," AIAA Journal of Aircraft, Volume 19, Number 10, October 1982
4. Bendat, J.S. and Piersol, A.G., Engineering Applications of Correlation and Spectral Analysis,: John Wiley and Sons, 1980
5. Youngren, H.J., Bouchard, E.E., Coopersmith, R.M. and Miranda, L.R., "Comparison of Panel Method Formulations and Its Influence on the Development of QUADPAN, an Advanced Low Order Method," AIAA Applied Aerodynamics Conference, July 13-15, 1983, Danvers, Mass.



Figure 1 P-3 Aircraft Measurement Locations

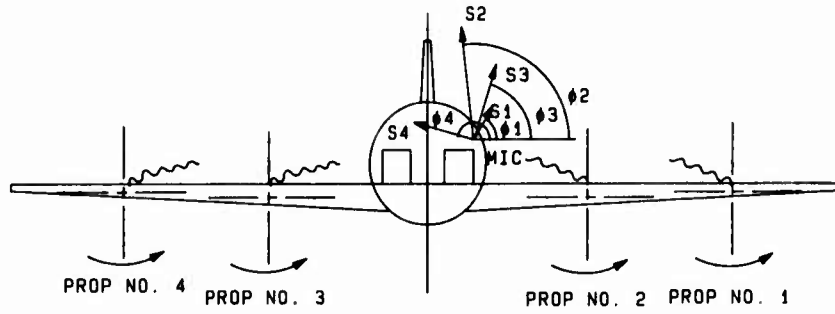


Figure 2. Propeller Signatures

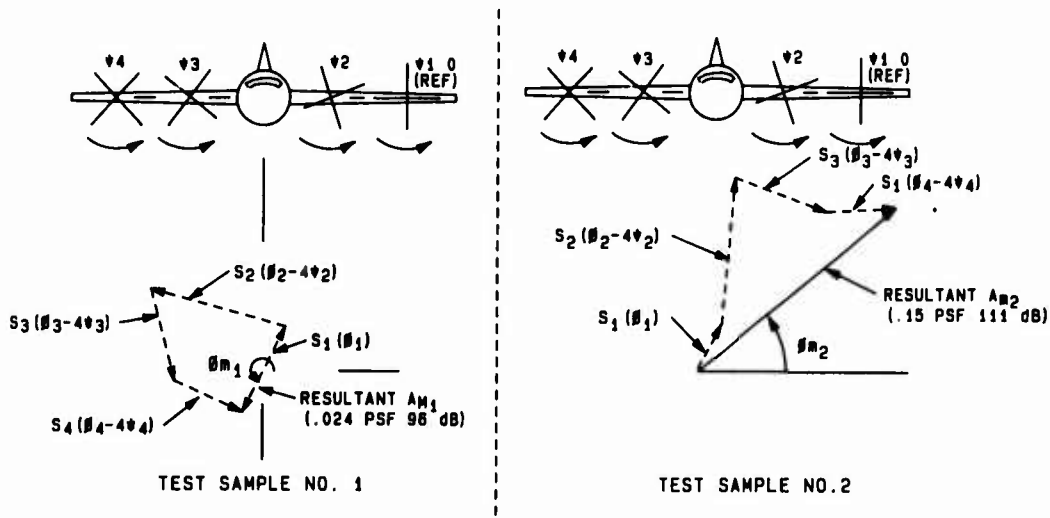


Figure 3. How Signatures Add

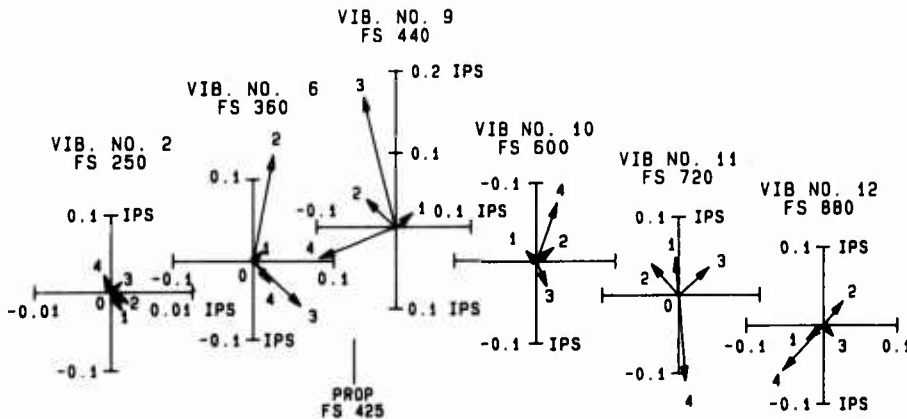


Figure 4. 68-Hz Vibration Signatures Along Centerline

MIC NO. 2 FS 255 FLT ENGR MIC NO. 6 FS 340 NAVCOM/TACCO MIC NO. 9 FS 450 MIC NO. 10 FS 620 SENSO 1/2 MIC NO. 11 FS 720 R R BEAM MIC NO. 12 FS 880 R R OBS

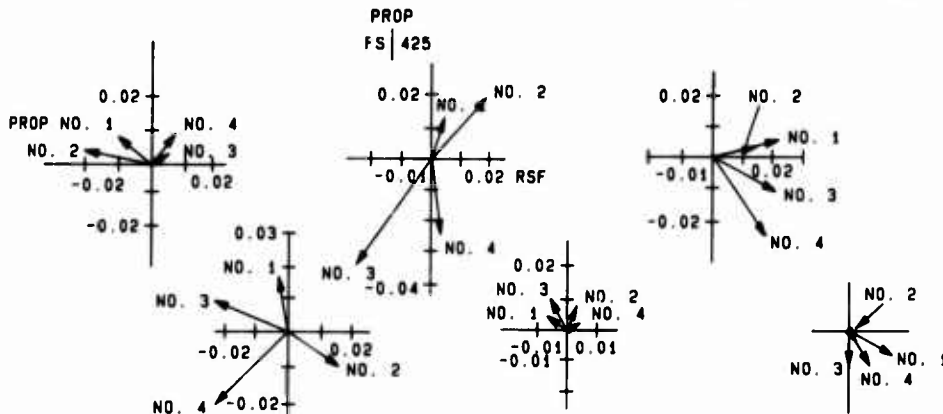
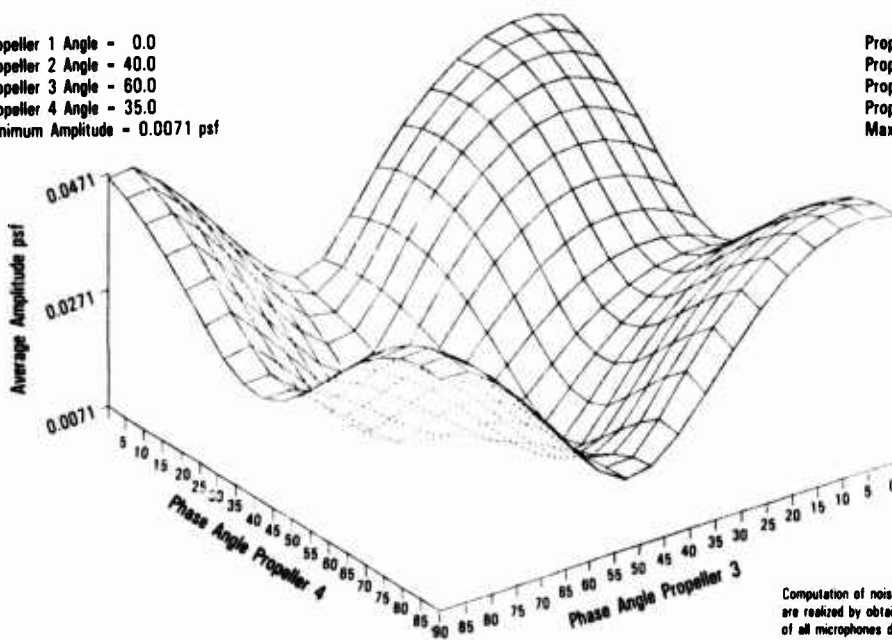


Figure 5. Signatures Along Centerline: 68-Hz Noise, P-3C Aircraft

Propeller 1 Angle - 0.0
 Propeller 2 Angle - 40.0
 Propeller 3 Angle - 60.0
 Propeller 4 Angle - 35.0
 Minimum Amplitude - 0.0071 psf

Propeller 1 Angle - 0.0
 Propeller 2 Angle - 40.0
 Propeller 3 Angle - 10.0
 Propeller 4 Angle - 0.0
 Maximum Amplitude - 0.0513 psf

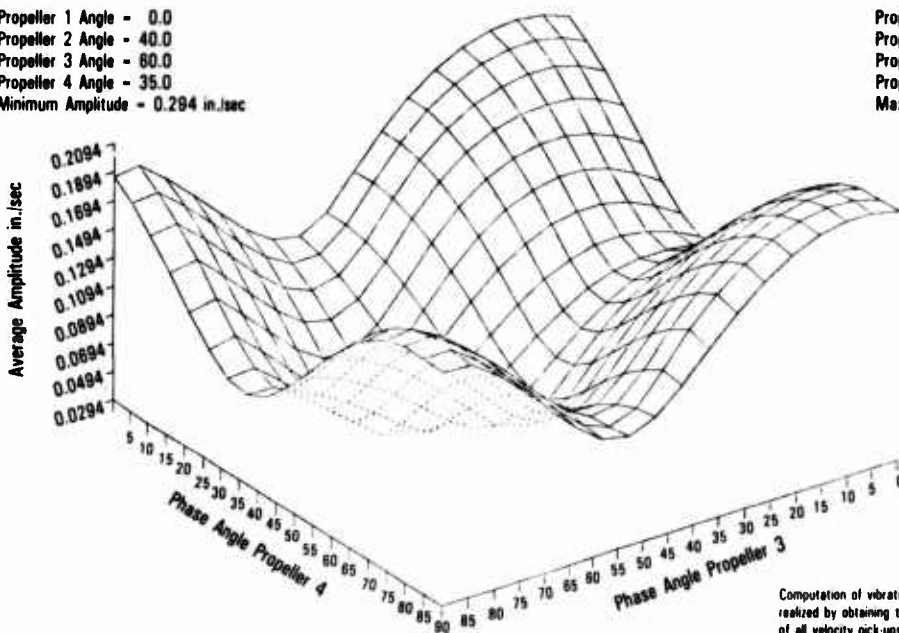


Computation of noise amplitude levels are realized by obtaining the average amplitudes of all microphones during the rotation of the propellers at five (five) degree intervals, when referenced to propeller 1.

Figure 6. P-3C Lockphase Analysis Int. Pred. at Rnd. Cuts 68 Hz ~ Noise Levels

Propeller 1 Angle - 0.0
 Propeller 2 Angle - 40.0
 Propeller 3 Angle - 60.0
 Propeller 4 Angle - 35.0
 Minimum Amplitude - 0.294 in./sec

Propeller 1 Angle - 0.0
 Propeller 2 Angle - 40.0
 Propeller 3 Angle - 10.0
 Propeller 4 Angle - 85.0
 Maximum Amplitude - 0.2097 in./sec

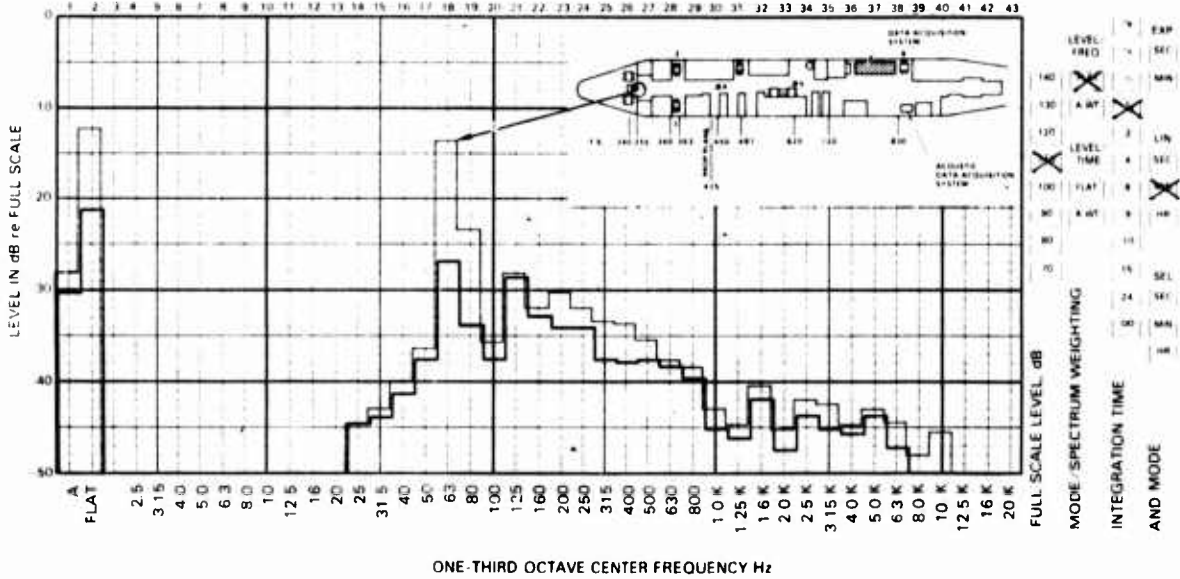


Computation of vibration amplitude levels are realized by obtaining the average amplitudes of all velocity pick-ups during the rotation of the propellers at five (5) degree intervals, when referenced to propeller 1.

Figure 7. P-3C Lockphase Analysis Int. Pred. at Rnd. Cuts 68 Hz ~ Vibration Levels

DESCRIPTION **LOCKHEED CALIFORNIA COMPANY ACOUSTICS** ID NO **Plot# 1**
 Project P S/N 5748 Test 15 TDR 10
 Run 2 Condition NATOPS Measurement 13001
 Start time 10:27:48.000 Stop time 10:28:48.000
 Run 9 Condition NR LOCKPHASE Measurement 13001
 Start time 11:33:04.000 Stop time 11:34:04.000
 Test date 5/05/83 G.S. run date 7/26/83

NATOPS				LOCKPHASE					
TSHP	2470	2800	2780	2660	TSHP	2800	2810	2830	2710
TIT	862	896	894	878	TIT	906	930	926	912
WF	1400	1480	1440	1400	WF	1360	1400	1400	1370

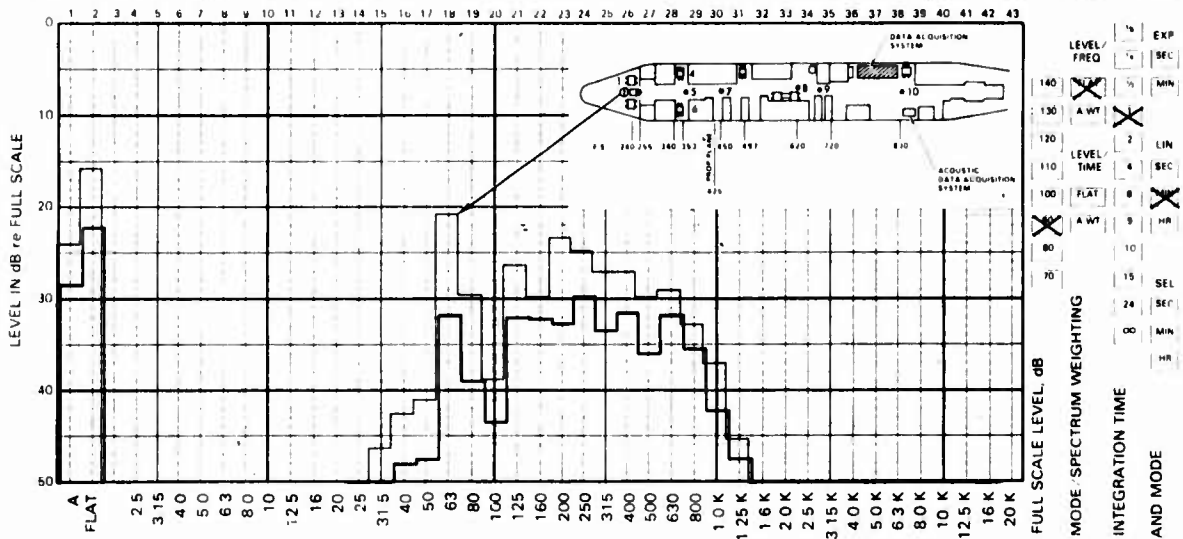


ONE-THIRD OCTAVE CENTER FREQUENCY Hz

Figure 8. Lockheed California Company Acoustics

DESCRIPTION **LOCKHEED CALIFORNIA COMPANY VIBRATION** ID NO **Plot# 2**
 Project P S/N 5748 Test 15 TDR 14
 Run 2 Condition NATOPS Measurement 22002
 Start time 10:27:48.000 Stop time 10:28:48.000
 Run 9 Condition NR LOCKPHASE Measurement 22002
 Start time 11:33:04.000 Stop time 11:34:04.000
 Test date 5/05/83 G.S. run date 8/02/83

NATOPS				LOCKPHASE					
TSHP	2720	2800	2780	2660	TSHP	2800	2810	2830	2710
TIT	862	896	894	875	TIT	906	930	926	912
WF	1400	1480	1440	1400	WF	1360	1400	1400	1370



ONE-THIRD OCTAVE CENTER FREQUENCY Hz

Figure 9. Lockheed California Company Vibration

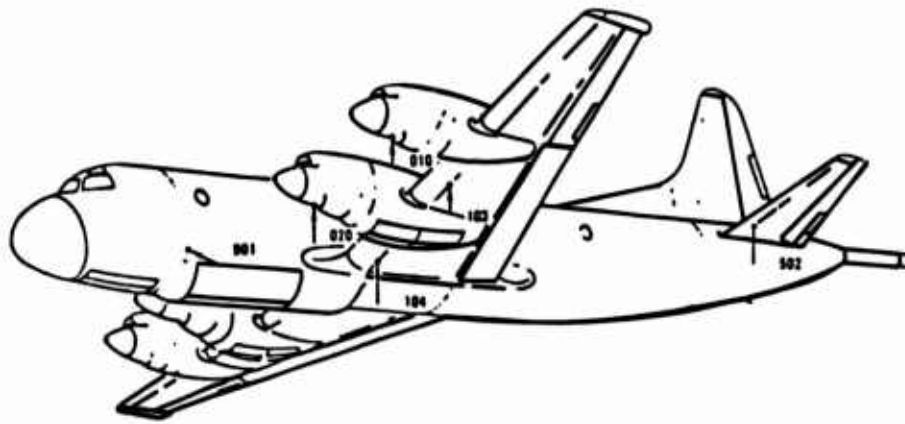


Figure 10. P-3C Shaker and Tap Test Input Locations - Right Side

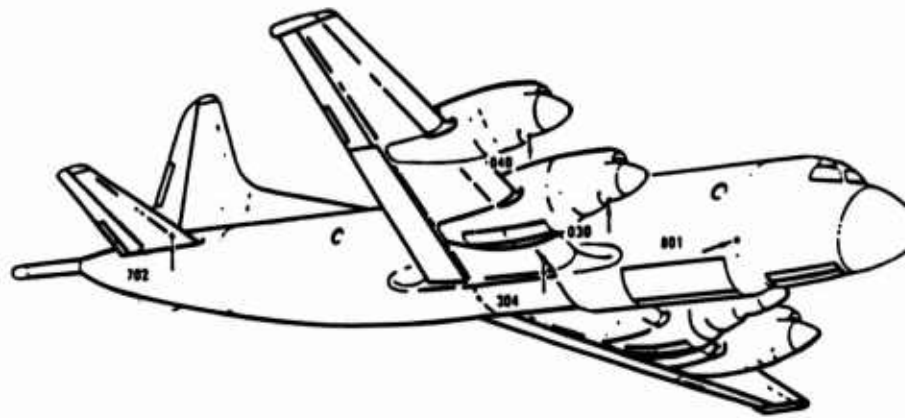


Figure 11. P-3C Shaker and Tap Test Input Locations - Left Side

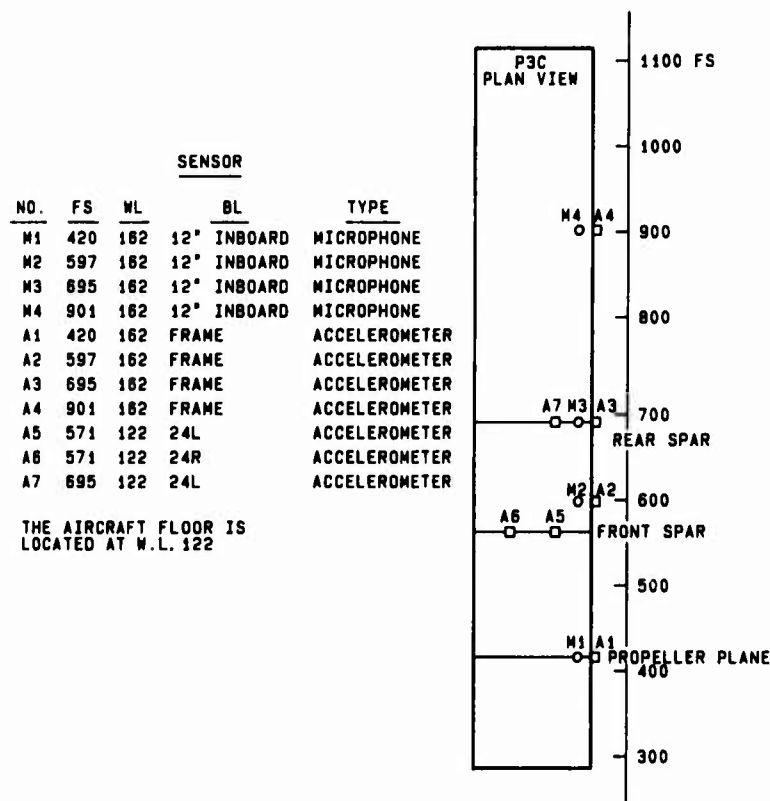


Figure 12. Microphone and Accelerometer Location

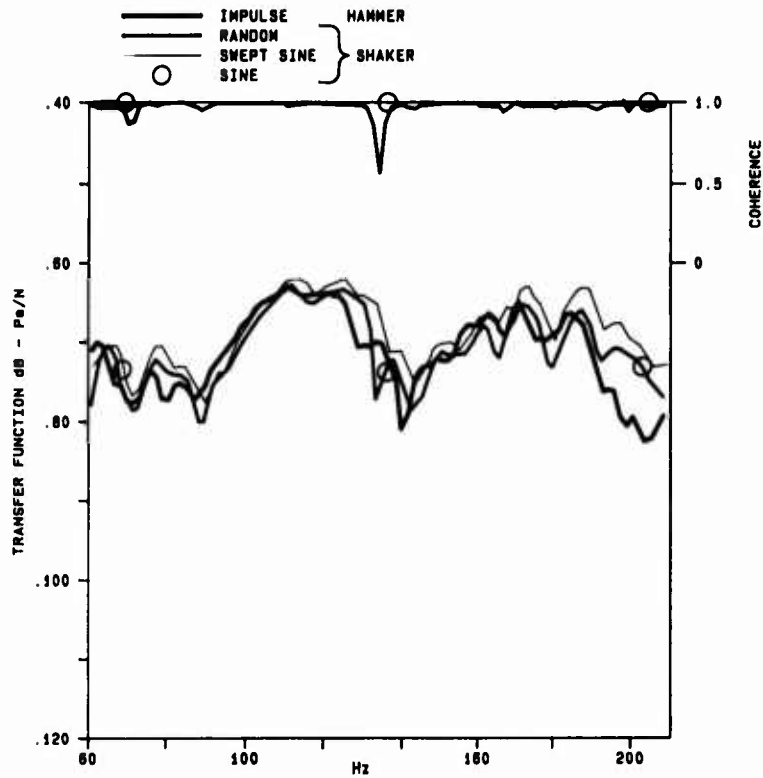


Figure 13. Transfer Function and Coherence Between Microphone 1 and Force Input at the Fuselage Sidewall, Input Location No. 901

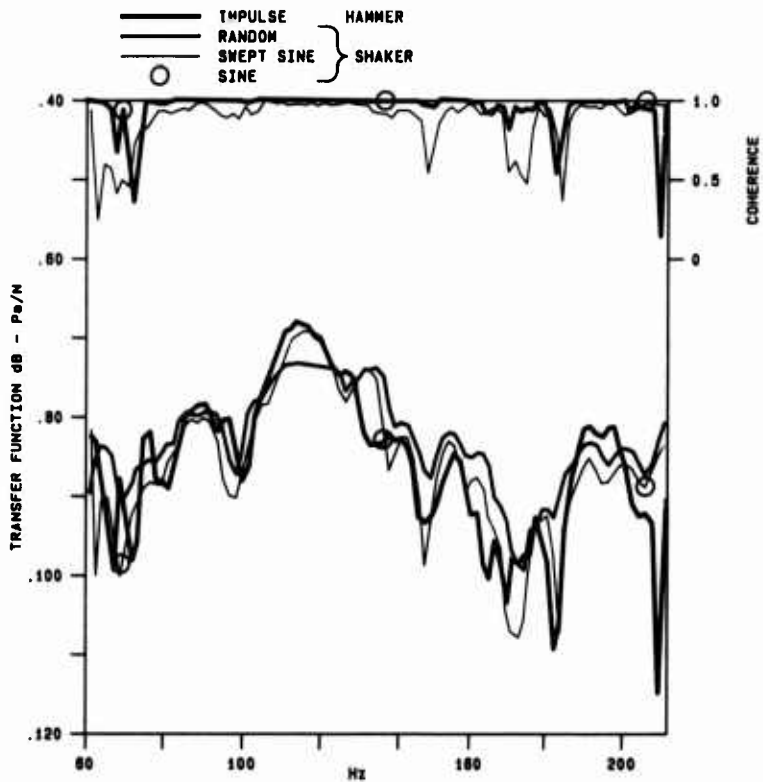


Figure 14. Transfer Function and Coherence Between Microphone 2 and Force Input at the Fuselage Sidewall, Input Location No. 901

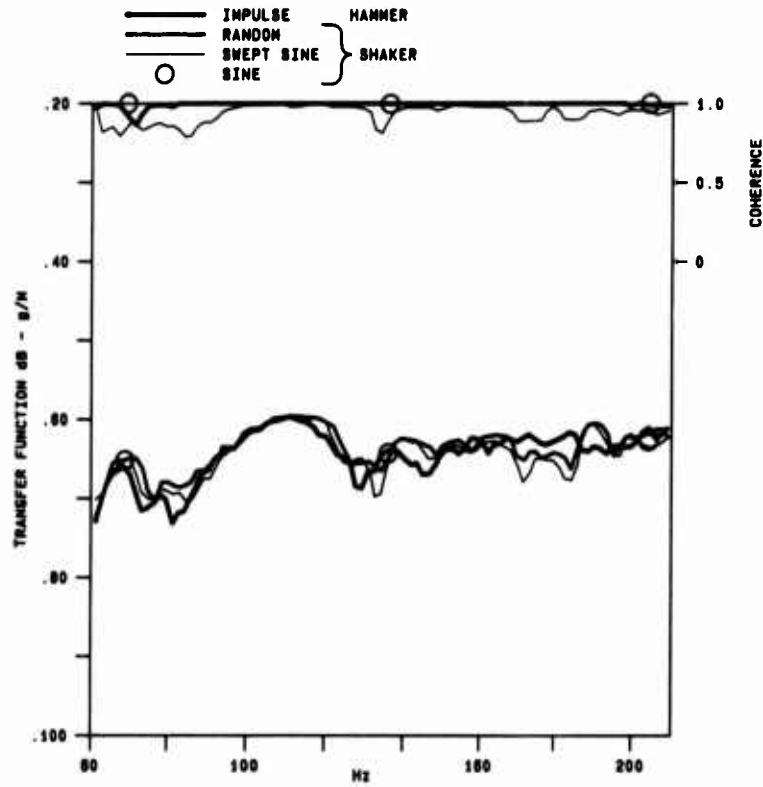


Figure 15. Transfer Function and Coherence Between Accelerometer 1 and Force Input at the Fuselage Sidewall, Input Location No. 901

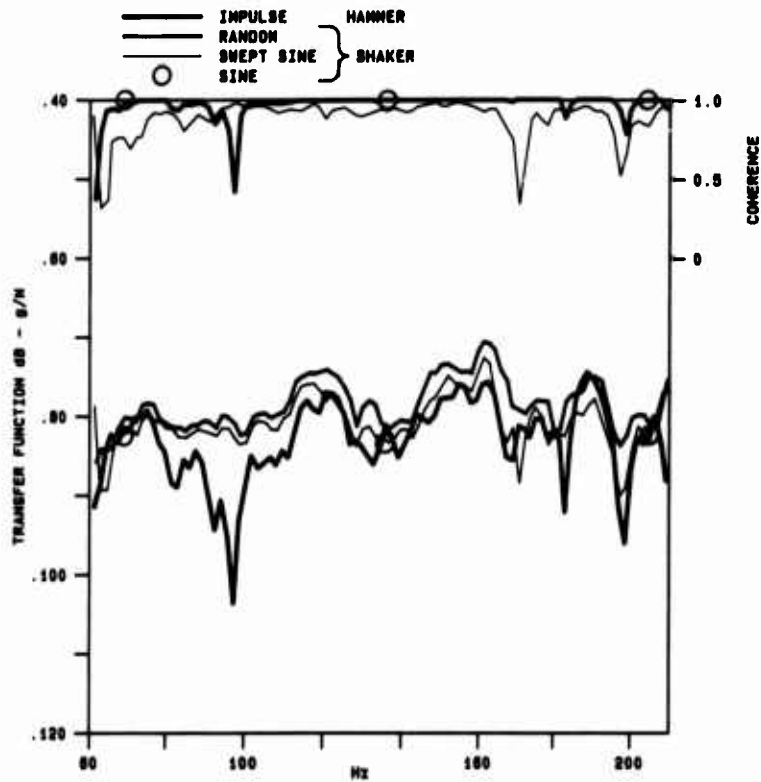


Figure 16. Transfer Function and Coherence Between Accelerometer 2 and Force Input at the Fuselage Sidewall, Input Location No. 901

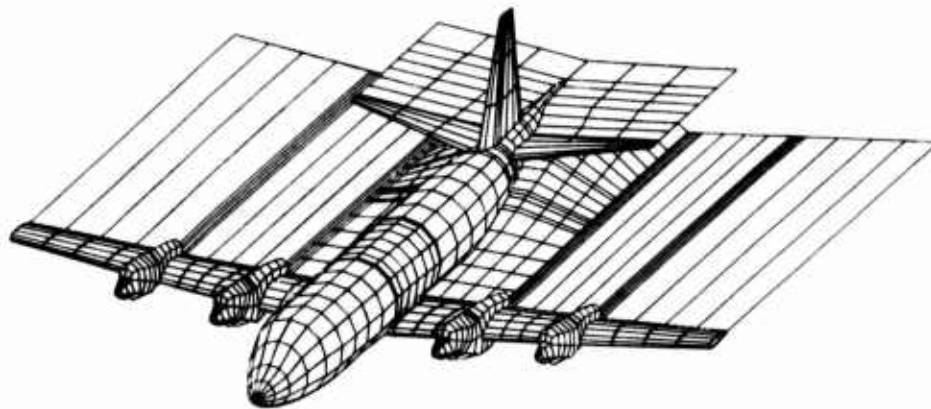


Figure 17. Quadpan Model of P-3C

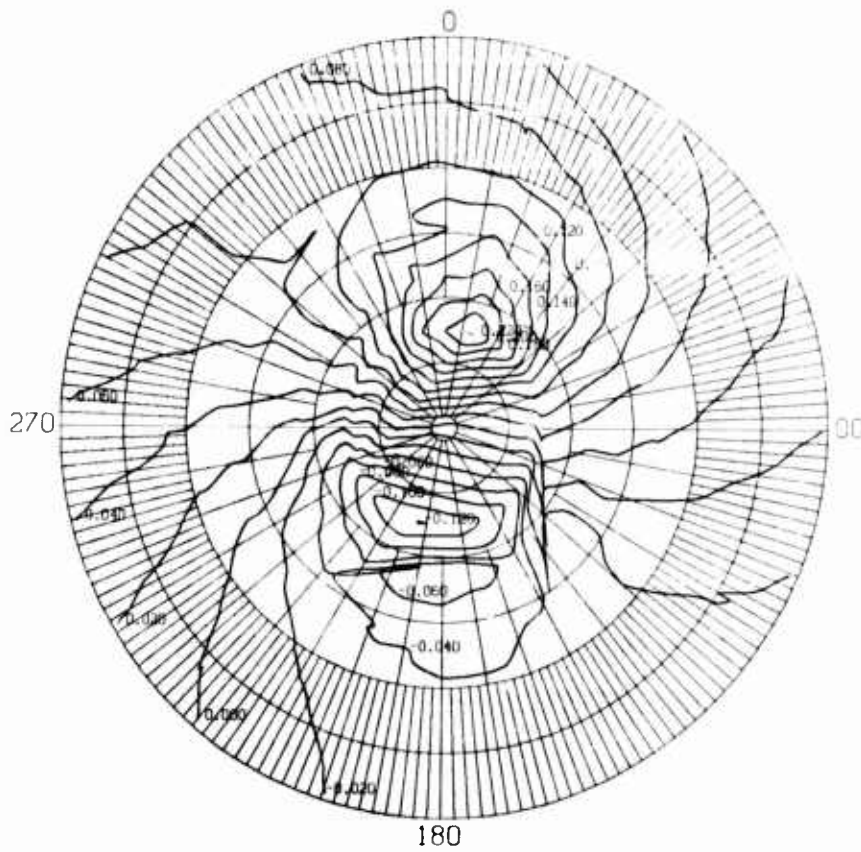


Figure 18. P-3C Propeller Plane No. 3 Velocity Survey Vertical Velocity Ratio

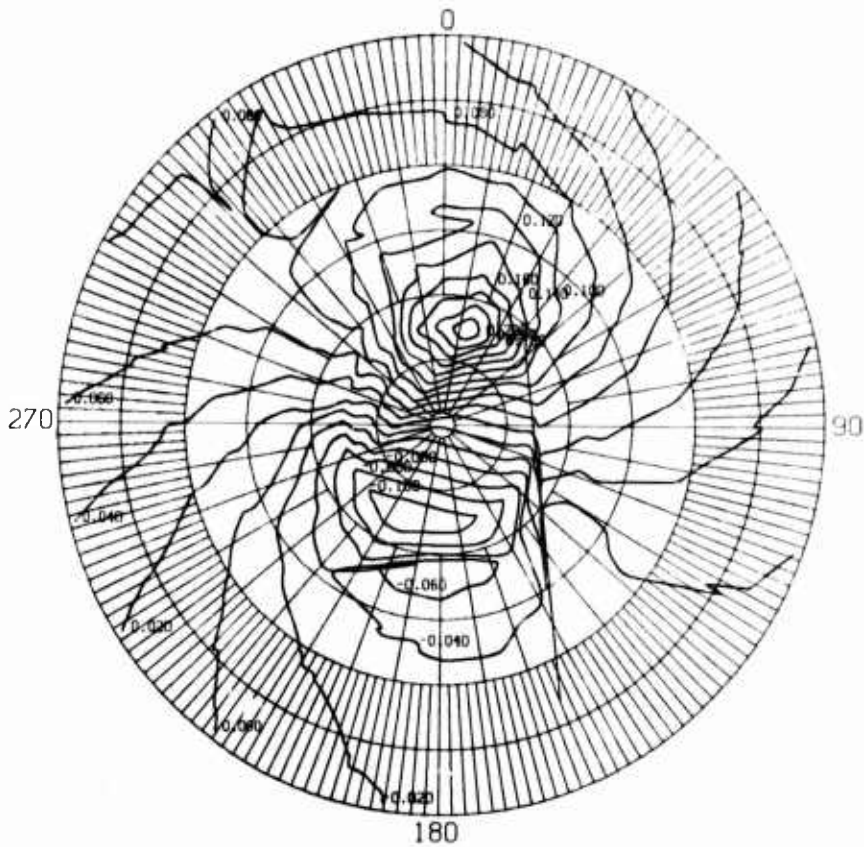


Figure 19. P-3C Propeller Plane No. 4 Velocity Survey Vertical Velocity Ratio

TABLE 1. TEST CONDITIONS FOR THE MECHANICAL EXCITATIONS OF THE P-3 AIRCRAFT STRUCTURE

INPUT POINT NO.	INPUT LOCATION	HAMMER IMPULSE	RANDOM	INPUT TYPE SHAKER	
				SWEPT SINE	SINE
901	FUSELAGE SIDEWALL, LEFT	X	X	X	X
502	STABILIZER ROOT, LEFT	X	X	X	X
104	WING ROOT, LEFT	X		X	X
020	INBOARD ENGINE NACELLE, LEFT	X		X	X
010	OUTBOARD ENGINE NACELLE, LEFT			X	X
103	WING BETWEEN NACELLES, LEFT		X	X	X
030	INBOARD ENGINE NACELLE, RIGHT			X	X
040	OUTBOARD ENGINE NACELLE, RIGHT			X	X
801	FUSELAGE SIDEWALL, RIGHT		X	X	X
702	STABILIZER ROOT, RIGHT		X	X	X

TABLE 2. MEASURED P-3 ACOUSTIC TRANSFER FUNCTIONS AT 68 Hz
(dB LEVELS FOR 100 LB FORCE)

EXTERNAL EXCITATION:

MICROPHONE	FUSELAGE AT PROPELLER PLANE	GEAR BOX OF INBD. NACELLE	FUS.-INB'D NAC. WING FRONT BEAM	FRONT BEAM HORIZ. STAB. ROOT
#1	100	71	81	69
#2	75	88	88	79
#3	87	88	83	91
#4	78	88	83	73

TABLE 3

LOCKHEED P3C ORION AIRCRAFT
MACH = 0.39, SEA LEVEL, THRUST = 1900 LB
FIXED HUB AXES
CRUISE POWER DISTORTION PATTERN FOUND WITH ENGINE INLET FLOW
UNITS LB, FT-LB AND DEG

-----SHEAR-----				-----MOMENT-----						
LIFT-		RIGHT		-YAW-		PITCH		--TORQUE--		THRUST
-OP--	--4P-	-OP--	-4P--	-OP--	-4P--	-OP--	-4P--	-OP--	-4P--	--4P--
ALFA = INCIDENCE = 0, UNIFORM FLOW										
0	0	0	0	0	0	0	0	8867	0	0
ALFA = INCIDENCE = 0, UNIFORM FLOW										
278	0	-1	0	-957	0	13	0	8810	0	0
NO. 1 PROP, ALFA = 0, INCIDENCE = 0, CRUISE POWER DISTORTION										
157	175	-133	203	-1197	304	238	325	8516	391	125
NO. 1 PROP, ALFA = 1, INCIDENCE = 0, CRUISE POWER DISTORTION										
575	195	-68	194	-2511	347	581	338	8479	366	115
NO. 1 PROP, ALFA = 0, INCIDENCE = 0, ZERO POWER DISTORTION										
33	216	-189	285	-1035	367	38	491	8433	579	183
NO. 1 PROP, ALFA = 0, INCIDENCE = -3, ZERO POWER DISTORTION										
-706	192	-169	229	1732	326	55	410	8340	458	148
NO. 2 PROP, ALFA = 0, INCIDENCE = 0, CRUISE POWER DISTORTION										
196	160	45	161	-1135	239	949	277	8517	401	116
NO. 2 PROP, ALFA = 1, INCIDENCE = 0, CRUISE POWER DISTORTION										
661	191	100	160	-2610	337	1279	328	8453	417	118
NO. 2 PROP, ALFA = 0, INCIDENCE = 0, ZERO POWER DISTORTION										
71	204	-15	268	-993	329	804	468	8428	608	190
NO. 2 PROP, ALFA = 0, INCIDENCE = -3, ZERO POWER DISTORTION										
-665	184	18	214	1766	316	874	395	8354	498	155
NO. 3 PROP, ALFA = 0, INCIDENCE = 0, CRUISE POWER DISTORTION										
289	166	236	162	-1684	259	1561	285	8504	394	109
NO. 3 PROP, ALFA = 1, INCIDENCE = 0, CRUISE POWER DISTORTION										
758	198	302	161	-3169	355	1928	335	8415	389	101
NO. 3 PROP, ALFA = 0, INCIDENCE = 0, ZERO POWER DISTORTION										
134	206	156	273	-1452	323	1333	456	8415	600	183
NO. 3 PROP, ALFA = 0, INCIDENCE = -3, ZERO POWER DISTORTION										
-599	187	189	218	1277	326	1408	400	8357	492	150
NO. 4 PROP, ALFA = 0, INCIDENCE = 0, CRUISE POWER DISTORTION										
156	184	327	209	-1223	387	1722	376	8504	397	109
NO. 4 PROP, ALFA = 1, INCIDENCE = 0, CRUISE POWER DISTORTION										
586	203	369	199	-2589	399	1994	373	8457	368	97
NO. 4 PROP, ALFA = 0, INCIDENCE = 0, ZERO POWER DISTORTION										
17	227	258	327	-1038	483	1543	577	8394	616	184
NO. 4 PROP, ALFA = 0, INCIDENCE = -3, ZERO POWER DISTORTION										
-717	209	282	263	1685	487	1569	519	8303	492	152

XPROP Steady and Vibratory Hub Loads

THE STATE OF THE ART
IN
PROP-FAN AND TURBOPROP NOISE

Mr. Frederick B. Metzger
United States of America

Hamilton Standard
Windsor Locks, CT 06096 USA

ABSTRACT

This paper briefly summarizes the evolution of propeller noise research from 1919 to the present. The early experimental and analytical work to understand and predict propeller noise is discussed. Emphasis is placed on understanding source noise. However, the major advances in cabin comfort assessment and design of airplane fuselage and cabin trim to improve passenger comfort are briefly described. Emphasis is on the recent noise research work on the Prop-Fan, a many bladed relatively small diameter unshrouded rotor with swept blades that will allow future transports to cruise efficiently at speeds equal to modern turboprop transports. The most recent Prop-Fan concept, a counter rotation version with even greater efficiency potential than the Prop-Fan with a single blade row is also discussed.

INTRODUCTION

Propeller noise has been the subject of research for at least 60 years. Because of the complexity of the subject it appears appropriate to divide the present discussion into five time periods. The first period from 1919 to 1939 is marked by the discovery of propeller noise and the initial theoretical work on its prediction. The second time period from 1940 to 1945 was a period of experimental work to understand and control the interior noise of long range military aircraft. The third period from 1946 to 1958 was a period where significant progress was made in both analytical and experimental areas. In the fourth period from 1959 to 1969 much less work was conducted because of the advent of turbojet transport aircraft. The fifth period from 1970 to the present was marked by a level of effort in the early part of the period which resulted in some significant results, particularly in the understanding of noise of turboprop aircraft during takeoff and landing. Later in this period, propeller noise research gained importance due to the interest in development of advanced fuel efficient turboprop transports. This was the result of the OPEC imposed oil embargo and the recognition that fuel was becoming scarce and, as a result, higher in cost. Also, as a result of airline deregulation, there was a new interest in turboprop commuter aircraft. In the later part of this period emphasis was placed on the Prop-Fan, a many bladed, small diameter, unshrouded propulsor. In the following discussion the highlights of the propeller noise control work in each of the above time periods will be discussed with the emphasis on the recent Prop-Fan activity.

DISCUSSION

1919 to 1939

As early as 1919 Lynam and Webb¹ recognized that propellers caused acoustic disturbances at large distances. They appear to be the earliest researchers who attempted to devise an analytical model for the noise generated by a propeller.

This period of propeller noise research was marked by limitations in experimental work imposed by a lack of adequate instrumentation. However, observations on the behavior of propeller noise under static and flight conditions were made and Prandtl in 1921 observed the difference between noise of a propeller run, first in a large room and then run in a wind tunnel.² He found that the propeller operating in the room reingested part of its own "vortex" system and produced a clearly noticeable impure tone. The same propeller operating in a wind tunnel did not produce the characteristic siren tone heard in the large room because the slipstream from the propeller had been smoothed out by travel through the tunnel before it again passed through the propeller. As will be seen later, it was not until the 1970's that the interaction of the propeller with disturbances from the atmosphere and from ground vortices was clearly recognized as a major cause of noise observed when a propeller or other propulsor is operated statically.

Gutin is the most famous theoretician in this time period and is noted for his publication in 1936 of a theory for noise due to steady aerodynamic forces on propeller blades.³ Deming in 1937 and 1938 published reports^{4, 5} on the importance of blade thickness for predicting the noise of a propeller. The work of Gutin and Deming is the foundation for prediction of thickness and loading related noise, the two linear tone components of propeller noise that dominated the attention of propeller noise researchers until the 1970's. Stowell and Deming in 1935⁶ also recognized the importance of the broadband noise component of propeller noise. They attributed this component to the shedding of vortices from the propeller blades. In summary, it can be seen that the major components of propeller noise, i.e., loading, thickness and broadband noise were recognized in the 1919 to 1939 time period.

1940 to 1945

An indication of the direction that propeller noise took in this period can be derived from a review of the book by Beranek, et al published in 1944.⁷ Here the work that had begun in November 1940 to establish methods for reducing noise in long range bombers is summarized. The similarity of the measurements made during this program to those made routinely in current acoustic research is remarkable. The importance of reducing noise at frequencies above 300 Hz to improve communication in an aircraft was established experimentally in this program. The ability of improved fuselage treatment to reduce this high frequency noise was pointed out as a major finding of the program.

1946 to 1958

This was a very productive period for both analytical and experimental propeller noise work. The interest in aviation which developed during the 1940 to 1945 time period resulted in the expansion of both airline transportation and the market for general aviation aircraft. Therefore it is not surprising that there were increased demands for control of noise around airports and within the cabins of the new aircraft.

In the analytical area Garrick and Watkins⁸ made substantial improvements in loading noise prediction and Arnoldi⁹ developed a better formulation for thickness noise prediction on the basis of the work of Billings.¹⁰ This was the period when the computer became available for routine scientific computation and the works of Garrick and Watkins and of Arnoldi were computerized. The efforts to reduce noise in the far field around airports caused an interest in the broadband noise component during this time period. Yudin¹¹ was the first to provide a prediction procedure for this component which is particularly important in large conventional turboprops where the loading and thickness tone levels are low relative to the broadband component. With the addition of this component, mathematical models for the three dominant components of conventional propeller noise (loading, thickness, and broadband) were available for use in design of quiet propellers.

This was a period of extensive experimental work. Hubbard made substantial contributions to the general understanding of ways to reduce propeller noise. He conducted extensive tests over a range of tip speeds including Mach 1 which even today provide reference information for study of propeller noise. In one of his many papers¹² Hubbard reported on correlation of measurements with theoretical predictions done with an extension of Gutin's theory to the near field. In 1976 data from this test series was found valuable by Hanson¹³ as a check on the accuracy of new theoretical procedures developed for prediction of Prop-Fans which may operate at transonic tip speeds during cruise.

By 1948 the work of Hubbard and his co-workers,¹⁴ had been evaluated on an aircraft. This was a modification of a Stinson L-5 liaison type airplane¹⁵ selected as being representative of personal type airplanes in the 150 to 200 horsepower class. It appears that the motivation for this work was the reduction of noise around general aviation airports. In this installation, two relatively narrow blades were replaced by five paddle type blades. The propeller of the standard aircraft was directly driven by the engine while the propeller of the modified aircraft was gear driven at a lower tip speed. Also the engine exhaust noise was reduced by use of a tuned chamber muffler. A rather remarkable noise reduction of 20 dB was achieved by this modification. Even more impressive is the comparison of the noise of the modified airplane with power on and power off. The aircraft with power on was found to be only 5 dB noisier with power on than with power off. Performance of this installation was claimed to be as good or better than the standard aircraft, but the weight penalty was not acceptable. A similar program was also reported in 1957^{16, 17} where a de Havilland Otter was modified to reduce detectability in a military mission. Noise data from this program indicates that the propeller noise for the Otter was (like that of the L-5) reduced to a level close to the nonpropulsor noise. Also in the case of the Otter, the mechanical gearbox noise was found to contribute at higher frequencies.

By 1955 high power turboshaft engines were available and efforts were under way to design quiet turboprops to take advantage of such power. Kurbjun reported on work to suppress the far field noise during takeoffs and landings¹⁸. The turboprop tested by Kurbjun had four-blades, and was 10 ft. in diameter. It absorbed 1250 SHP and operated at a tip Mach number of 0.79. These are not unlike the operating parameters of conventional turboprops of today. Kurbjun's 1955 work was followed by a radical approach to propeller design, a 7.2 ft. diameter three-blade configuration operating at a tip Mach number of 1.2. Kurbjun states¹⁹ that this turboprop, which is shown in Fig. 1 was designed to operate at a forward Mach number of 0.95 at an altitude of 40,000 ft. and to absorb 2500 horsepower at sea level conditions. In Ref. 19 the results of static acoustic tests of this configuration were compared with those from the previous test of the more conventional design of Ref. 18. It was found that the supersonic turboprop produced approximately 14 dB more noise than the conventional turboprop and produced a flatter noise spectrum. While these high levels are not surprising with the present understanding of propeller noise, the results of these tests were discouraging enough to prevent further investigation of supersonic tip speed designs until the 1970's.



Figure 1. The 7.2-foot diameter, three-blade propeller mounted on a turbine-driven airplane (Ref 19)

1959 to 1969

Dominance of jet propulsion in commercial transport aircraft and the lack of interest in turboprop noise control in military aircraft contributed to a drastic reduction in propeller noise control research in this time period. Noise predictions were done in this period by empirical or theoretically based procedures developed prior to 1959.

One related development in this time period does, however, deserve some discussion, i.e., the development of standardized methods for rating the noisiness of various types of aircraft sounds. Kryter²⁰ in 1959 proposed the Perceived Noise concept which was based on the loudness concept of Stevens.²¹ In this concept the relative annoyance of noise in various frequency ranges is summed to produce a single number called the Perceived Noise Level. Because of the airport noise problem, the interest in refining this procedure was intensified. In 1962 Kryter reported results of tests where subjects rated the relative noisiness of turboprop and turbojet aircraft sounds.²² He concluded that there was probably another annoyance factor not included in the perceived noise calculation, that of the pure-tone component or "whine." In later developments²³ Kryter added the tone correction and duration correction to Perceived Noise Level to produce the Effective Perceived Noise Level unit which was called out in the Federal Aviation Administration aircraft noise certification regulation (FAR 36) of 1969.²⁴ The tone correction attempts to account for the fact that sounds containing tones are more annoying than those without tones. The duration correction attempts to account for the fact that sounds of longer duration are more annoying than those of shorter duration.

Conventional Turboprops after 1970

The implementation of the aircraft noise certification requirements gave a new impetus to the scientific study of aircraft noise control. However, due to the dominance of the turbofan in the aircraft market, turboprop noise related research was conducted on a rather low level in the early 1970's. Nevertheless, in this time period valuable work was conducted in both military and commercial areas. An example of this is the Y03A developed by Lockheed as a low detectability reconnaissance aircraft. The Y03A was quite successful, but the propeller acoustic design was empirical. Also, it was found in extensive experimental work that the propeller noise dominated the aircraft noise signature, regardless of the propeller used. Because of this, the U.S. Air Force sponsored experimental and analytical work to put the design of such propellers on a more scientific footing.^{25, 26} Unfortunately, it was not recognized until 1974, during the Air Force sponsored low detectability propeller research contracts, that the steady loading and thickness noise of a propeller were not the only important noise components for a quiet propeller installation. In Ref. 27 Griffith and Revell concluded that the nonuniform loading of the propeller which is associated with aircraft angle of attack and upwash over the wing and also the interaction of the propeller wakes with the wing (such as rotor stator interaction in a turbofan engine) were the dominant noise mechanisms of the Y03. It was believed at this time that these mechanisms would be of negligible importance in conventional turboprops. However, recent analysis indicates that the angle of attack effects must be considered for accurate evaluation of the annoyance of noise at low speed certification conditions.

The work of Barry and Magliozzi sponsored by the U.S. Air Force in 1970 relied to a great extent on the work of previous researchers for the noise prediction procedure published as Ref. 26. Barry and Magliozzi were constrained to conduct tests of various propeller concepts under static conditions. They found that their experimental results did not agree with their prediction procedure which included steady loading, thickness and broadband noise components. The agreement was improved when they added unsteady loading effects. In this same time period, the quiet turboprop for the de Havilland Dash 7 STOL transport was under development. Tests in that program showed dramatic differences between turboprop noise under static conditions versus flight conditions. Barry and Magliozzi reported these results in Ref. 26, and it was recommended that further work be conducted to establish forward flight corrections. It was not until 1976 that results were reported from a definitive test program to explore the influence of forward flight on turboprop noise.^{28, 29} In this program noise measurements and propeller blade surface pressure measurements were made on a de Havilland DHC-6 Twin Otter which showed conclusively the dominant mechanism of noise generation under static conditions and how this mechanism was affected by forward flight. As shown in Fig. 2 pressure transducers were flush mounted on a single blade of the Twin Otter turboprop. Magnetic tape recordings of the output from these transducers plus a once-per-revolution reference signal and microphone outputs from wing tip mounted microphones provided the information needed to understand the noise generation mechanism.

The most revealing information is obtained from plots such as that at the right of Fig. 2. Each line of this plot is the output of a pressure transducer for one blade revolution. Succeeding revolutions are slightly displaced downwards to present a time history variation of the pressure on the blade. The once-per-revolution signal is used to "lock" the plot in a stationary reference frame. Thus the circumferential location can be seen where a disturbance is "felt" by the blade. Disturbances that persist for many revolutions produce tonelike noise components (the energy of pure tones exists at only one frequency, but the disturbances interacting with a rotor produce a peak in the noise spectrum resembling a tone but having a finite band width) and disturbances that occur for a very small portion of a revolution produce high frequency tonelike components. Fig. 3 shows time history pressure plots for the test aircraft as it moves from static to flight conditions during a takeoff. It can be seen that a strong disturbance occurs at the circumferential location closest to the fuselage (sample number 38). This is caused by a vortex generated on the aircraft fuselage. A second persistent disturbance occurs at the circumferential location nearest the ground (sample number 75). This is caused by a vortex generated on the ground under the aircraft. These disturbances are seen in Fig. 3 to disappear as the aircraft picks up speed for takeoff. Although not important for noise generation, it is interesting to note the nonuniform inflow caused by aircraft angle of attack which can be clearly seen in the inboard sections of the blade at the upper right of Fig. 3 during climb. The measured noise generated under static and flight conditions is shown in Fig. 4. Here it can be seen that the tonelike noise components which dominate the static spectrum are dramatically reduced at the flight condition. This is due to the reduction of circumferentially fixed persistent disturbances that disappear as an aircraft moves from static to forward flight conditions. Hanson³⁰ has postulated that even under ideal conditions where no vortices can form to be ingested by a propeller, the turbulent eddies that normally occur in the atmosphere can give rise to tonelike noise components. Hanson postulates a sinklike flow passing through the propeller under static conditions. As shown in Fig. 5 the eddies which are attracted to the

propeller must be reduced in cross section and stretched in order to pass through the propeller disc. These narrow elongated eddies will produce tonelike noise components as the propeller "chops" through them. In contrast, the sinklike flow does not occur in flight and therefore, as shown in Fig. 5, the eddies that pass through the propeller disc are not elongated and do not generate noise. Under flight conditions the dominant noise components are then the steady loading and thickness tone noise components and broadband noise.

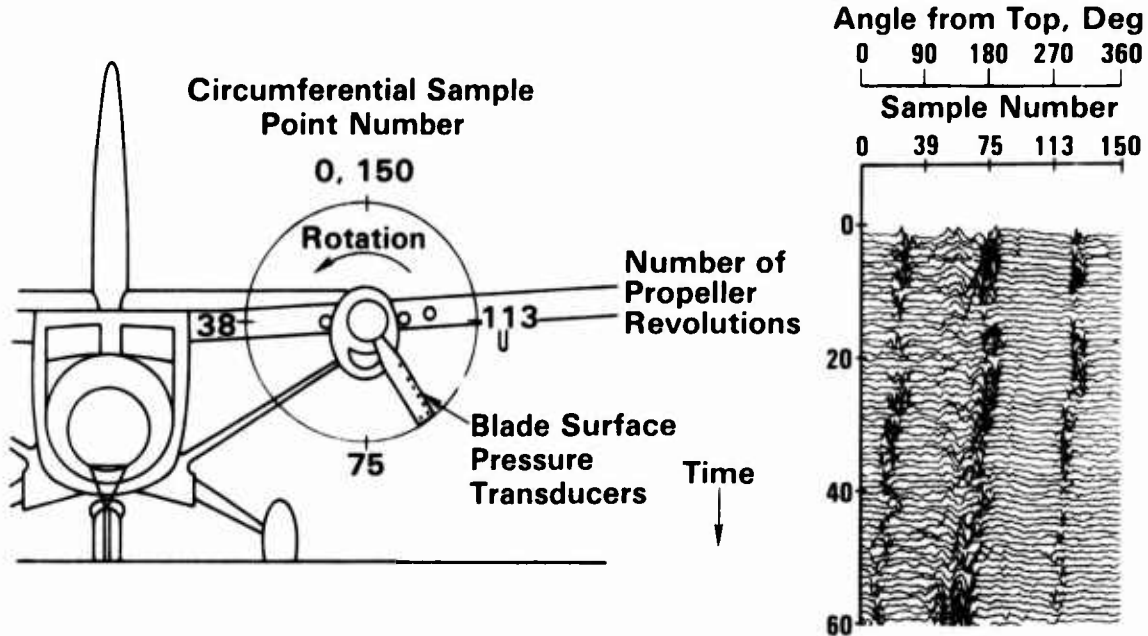


Figure 2. Relationship of blade position and time history plots (Ref 29)

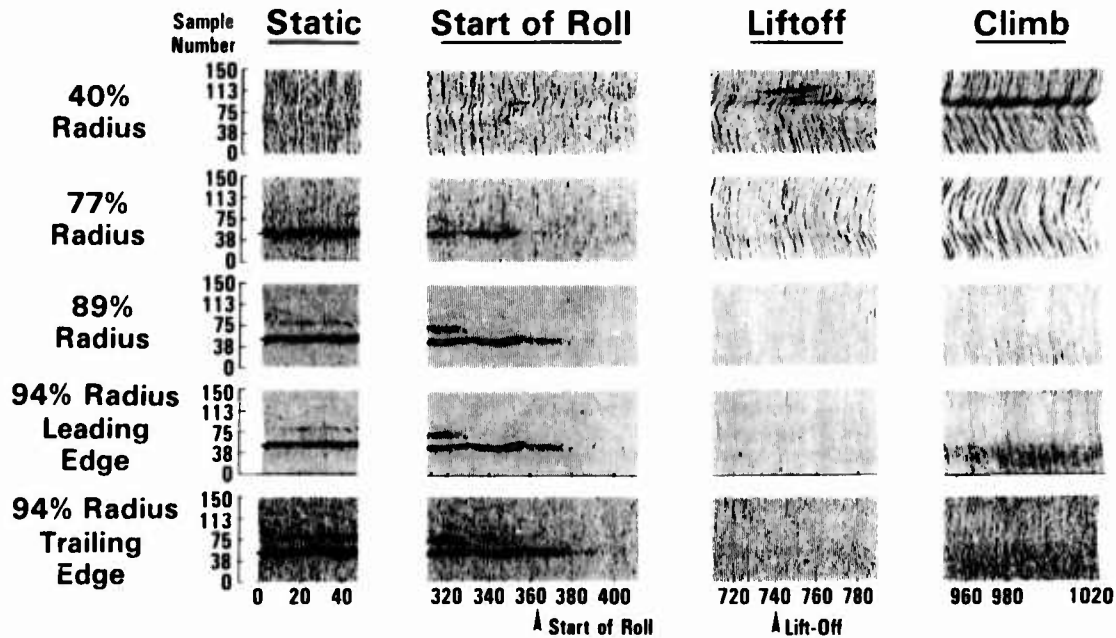


Figure 3. Blade surface pressure time history takeoff at 97.5% RPM (Ref 29)

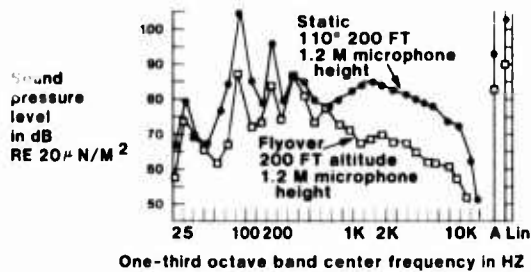


Figure 4. Static and flight noise spectra at 90° RPM (Ref 29)

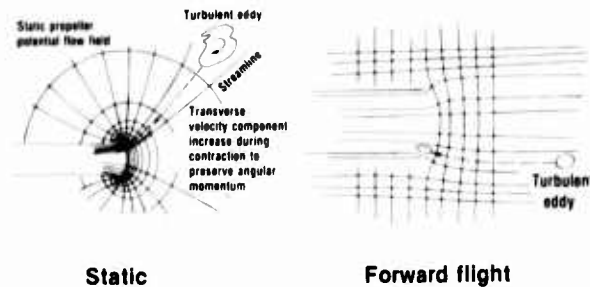


Figure 5. Forward flight effects

The development of the quiet turboprop for the de Havilland Dash 7 was a very important milestone in this time period.^{31, 32} The Dash 7, shown in Fig. 6, is a 50 passenger STOL transport which was designed with the objective of meeting an extremely low noise goal of 95 PNdB at a distance of 500 ft. during takeoff. Extensive static and flight tests on many propeller configurations were used to optimize the design of the low tip speed, lightly loaded, four blade turboprops that are now in service on this aircraft. An indication of the success of the design can be seen by the fact that the noise levels are 13 dB below the certification limits at takeoff.

At the present time there is a renewed interest in turboprop aircraft of all sizes. This is due to the recognized fuel efficiency of the propeller relative to that of turboprops or turbojets and to the recent airline deregulation activity which has caused substantial expansion of the commuter airlines.

The new large commuter airplanes shown in Fig. 7 carry 30 to 60 passengers and are just now beginning to enter airline service. Propellers for these airplanes were designed to be the optimum considering certification noise, cabin noise, performance and weight. All of the new turboprops developed for these airplanes incorporate blades with new airfoil sections that allow blade chord to be reduced to reduce weight while achieving improved takeoff performance without compromising cruise performance. Most of the designs incorporate a narrow thin elliptical blade tip and a twist distribution to unload the tip in order to minimize noise. While most of the new commuters use four blades, the British Aerospace ATP has six blades to further reduce noise.



Figure 6. DeHavilland Dash 7 quiet Stoll transport

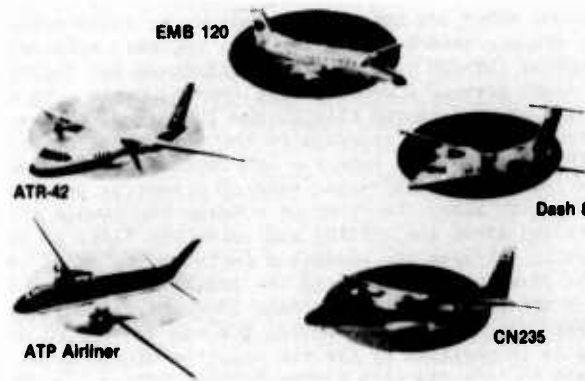


Figure 7. New commuter airplanes

In the general aviation area the industry is continuing to modify existing aircraft designs and to design new aircraft to meet the FAR 36 requirements which were imposed in 1975.³⁴ The most common method of reducing propeller noise in this class of aircraft is to increase the number of blades to maintain performance with a smaller diameter and hence achieve a tip speed reduction at a given RPM. The use of a thin elliptical tip shape on blades having a twist distribution that unloads the tip appears to have been incorporated in some recent aircraft.

Recent Advances in Conventional Turboprop Transport Cabin Noise Control

Prior to the introduction of jet transports, passengers accepted high cabin noise levels in reciprocating engine propeller driven airplanes because there was no alternative. In the jet transports, cruise at high altitude where fuselage boundary layer noise is minimized and the change to broadband jet noise generated by the engines rather than the strong low frequency tones of the propeller or reciprocating engine improved cabin comfort dramatically. The traveling public now expects similar comfort levels in new turboprop driven airplanes. Fig. 8 shows the relative quiet of jet transports relative to propeller transports. In fact, as Fig. 8 shows, the quietest part of a jet transport is about 10 dB quieter than a turboprop transport. In Fig. 8 Overall and A-weighted test data throughout the aircraft are presented. High Overall or A-weighted levels are an indication of reduced passenger comfort. NASA studies have indicated that levels of less than 82 dBA are considered very comfortable by the traveling public.³⁵ More recently NASA tests³⁶ using listeners to rate the comfort of mixtures of broadband noise and tone noise such as those encountered in turboprop transports have shown that the existence of tones in the cabin noise spectrum decreases the comfort level for a given A-weighted sound pressure level. Figure 9 from ref. 36 shows that this penalty can be negligible to a maximum of 5 dBA. Therefore turboprop transport cabins with strong tone noise contributions may have to be reduced below 82

dBA to be judged comfortable by the traveling public. The existing turboprop transports are seen in Fig. 8 to have levels that generally exceed the comfortable region. In general, the noise in a multi-engine turboprop transport peaks in the passenger cabin near the plane of rotation with levels dropping rapidly immediately ahead of and behind the plane of rotation and then dropping more gradually toward the rear of the cabin. Jet aircraft with engines mounted on either side or above the rear of the cabin are seen to produce very high levels. These high levels were primarily experienced in early versions of such aircraft. As Fig. 8 shows, however, these aircraft are even quieter at some locations than the aircraft with wing mounted engines. This quiet area occurs primarily at the front of the cabin, the location farthest from the engines. The levels in aircraft with wing mounted engines do not reach the high or low extremes of the aircraft with aft mounted engines but appear to meet the NASA comfort level requirements quite well. In these aircraft the higher levels are found near the rear of the cabin and are probably due to fuselage boundary layer excitation or engine jet noise. In summary, it appears that a reduction of 5 to 10 dB in overall and A-weighted levels is needed in turboprop transports to approach the comfort level of the large jet transports, particularly those with wing mounted engines.

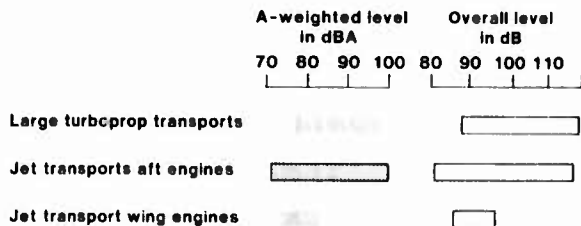


Figure 8. Range of cabin levels in transport aircraft



Figure 9. Effect of propeller tones on cabin comfort (Ref 36)

The reduction of cabin noise in turboprop driven airplanes has been a difficult problem. As Fig. 10 shows, the installation of trim panels in the cabin may actually reduce rather than increase the noise reduction. This is because the added mass of trim panels and other conventional acoustic treatment is only effective at frequencies higher than the dominant tones of turboprops. Fokker has recognized this problem and has been successful in reducing cabin noise of the F-27. The treatment used consists of many elements which act together to reduce the cabin noise more than 7 dBA. Initially, the F-27 was fitted with dynamic absorbers (spring mass systems) attached to the fuselage frames tuned to blade passage frequency (RPM/60 x 4). This modification was incorporated in the F-27 many years ago to help control the blade passage frequency noise in the cabin. As the travelling public demanded lower cabin noise as the length of commuter flights has increased, Fokker has developed an improved noise control system.^{37, 38} This consists of the elements shown in Fig. 11. The major feature of the new system is a vibration isolated interior consisting of wall panels, luggage bins and ceiling. This system forms a classical double wall noise reduction barrier that is more effective pound for pound than a single wall of the same mass. In order to enhance the double wall effectiveness, fiberglass blankets have been installed above the ceiling and below the floor to suppress resonances in these reverberant areas. In order to suppress the adverse effects of the stiff coupling created by the narrow air gap between the outer fuselage structure and the inner trim system, dynamic absorbers are attached to the trim panels. These are tuned to blade passage frequency, two times blade passage frequency and three times blade passage frequency. To complete the new trim panel system a window was mounted directly on the panel. This is in addition to the two existing window panels used in previous F-27 construction. The final detail in this new trim system is the anti-rattle provision. This consists of resilient pads mounted at any point where two adjacent rigid components in the cabin could touch. Vibration of such components due to excitation by turboprop noise or vibration is a known contributor to the discomfort of many turboprop transports.

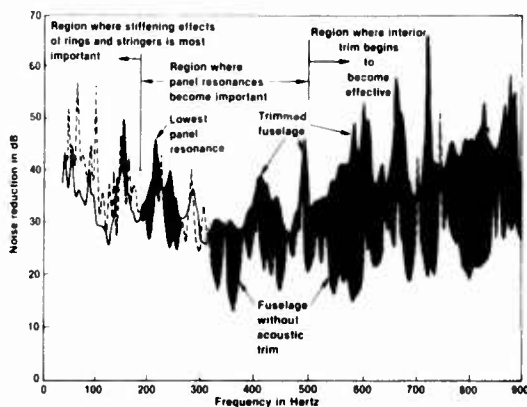


Figure 10. Noise reduction of typical turboprop aircraft



Figure 11. Cabin noise reduction features of new Fokker F-27's (Ref 38)

The Prop-Fan

Introduction - The occurrence of fuel shortages and increased fuel cost and the threat of future worsening conditions for air transportation caused NASA to sponsor studies of the advanced turboprop (Prop-Fan) beginning in 1975. This propulsion system, shown in Fig. 12, differs dramatically from existing turboprops. The turboprop has three to six blades; the Prop-Fan generally has eight to twelve blades. The turboprop has straight blades with relatively thick airfoil sections; the Prop-Fan has swept back blades with thin airfoil sections to enhance performance and reduce noise. The turboprop cruises at no more than 0.65 Mach number; the Prop-Fan is designed to cruise at 0.7 to 0.8 Mach number. The diameter of the Prop-Fan is about 40 percent smaller than that of the turboprop for a given horsepower. For maximum performance, the Prop-Fan makes use of advanced turbine engines of the kind being used in modern turbofans. Performance is also enhanced by use of a spinner and nacelle aerodynamically contoured to reduce compressibility losses by retarding the high velocity flow through the root sections of the Prop-Fan blades.

Utilizing predicted aerodynamic performance data, weight estimates, and noise projections, several NASA sponsored studies by both engine and airframe manufacturers have concluded that significant fuel savings should be achieved by a Prop-Fan aircraft operating at 0.7 to 0.8 Mach number, as compared with a high bypass ratio turbofan aircraft. With these encouraging results, NASA, with the support of industry, has conducted a research technology effort to establish the design criteria for this new propulsion system.

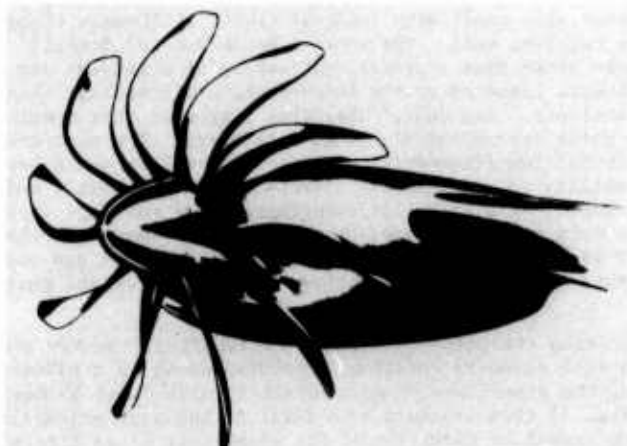


Figure 12. Prop-Fan propulsion system

The objective of this work has been the development of Prop-Fan configurations with high efficiency and low noise. Turboprops in the past that operated at the transonic relative tip speeds of the Prop-Fan at cruise showed performance losses and high noise levels. As Fig. 13 shows, conventional turboprops suffer performance losses at cruise Mach numbers greater than 0.6. The single rotation Prop-Fan configuration of Fig. 12 improves on this performance. Recently, there has been increased emphasis in the NASA Advanced Turboprop Program on the counter rotation (CR) Prop-Fan shown in Fig. 14.³⁹ As shown in Fig. 13, this Prop-Fan configuration is expected to operate at even higher efficiency than the single rotation (SR) Prop-Fan because the downstream blade row recovers the residual swirl induced by the upstream blade row. Until recently, Prop-Fan concepts have incorporated a gearbox. This is consistent with past turboprop systems. Studies are now under way to establish the feasibility of a CR Prop-Fan that eliminates the gearbox. This is a pusher configuration with gas generator exhaust flow passing through two counter rotation turbines with the Prop-Fan blades attached directly to each turbine stage. In order for this system to work, the Prop-Fan diameter is minimized to achieve a maximum RPM at an acceptably low tip speed for acoustic reasons. The turbine is increased in diameter as much as possible to enhance its efficiency at the same RPM as the Prop-Fan. It is recognized, however, that there is some loss of efficiency for both the Prop-Fan and turbine over that achieved in geared systems. Furthermore, the relatively high tip speed operation of the nongearred system may cause high noise levels at certification conditions.

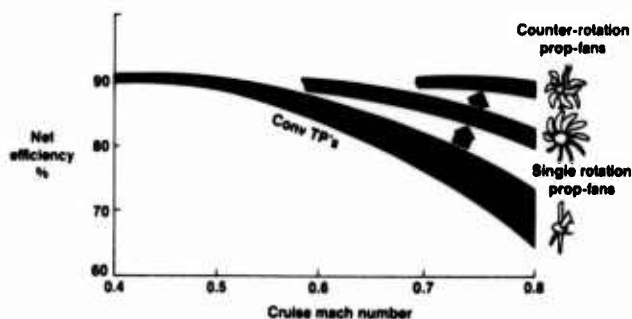


Figure 13. Turboprop efficiency trends

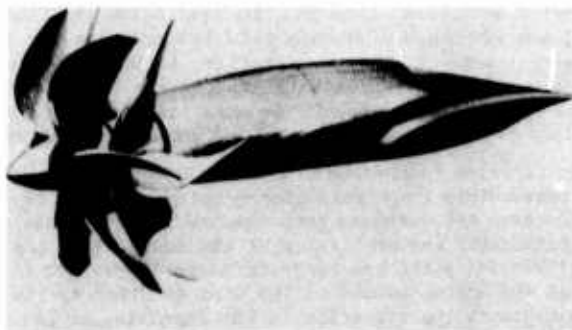


Figure 14. Counter rotation Prop-Fan

Cabin Comfort - From the beginning of the Prop-Fan program cabin comfort research has been an integral part of the program. Both experimental and analytical work has been conducted in a coordinated effort where the experimental results are used to guide the development of improved source noise prediction procedures. Also intensive efforts have been made to understand the cabin noise control problem and establish prediction procedures that allow development of lightweight fuselage wall treatment systems. NASA has sponsored work to evaluate the potential for optimizing existing fuselage walls which consist of (1) an outer fuselage skin with attached stringers and frames, (2) inner acoustic trim panels which are seen by the passengers, (3) multi-layer windows, and (4) fiberglass acoustic and thermal insulation blankets between the inner and outer walls. The objective of the NASA sponsored work is to take a fresh look at fuselage wall noise transmission using the structural analysis procedures which have been developed recently. These include (1) the Modal Analysis techniques which appear particularly suited to treatment of the low frequency noise problems of turboprop aircraft,^{40, 41} (2) the extension of classical transmission loss analysis, now used in architectural acoustics, to treat the case of a cylindrical pressurized aircraft cabin,⁴² and (3) the investigation of extensions of the statistical energy analysis techniques which have been successful in analyzing spacecraft noise transmission problems.⁴³ New experimental techniques such as computerized modal analysis are also available to develop a more fundamental understanding of the noise transmission through aircraft fuselages. These techniques⁴⁴ have already proved successful in reducing the noise and vibration in a new generation of fuel efficient automobiles in the United States. The application of new materials such as composites has been shown in preliminary tests to be particularly effective for reducing transmission of low frequency noise. In Ref. 45 Getline shows in tests how the resonant frequency of the panel can be raised and how low frequency noise reduction can be increased substantially without increasing the panel weight. In Ref. 46 Lorch shows that an outer skin panel with integral ribbed stiffeners (Isogrid) can be used to improve transmission loss of a fuselage wall. The work of Henderson and Nashif⁴⁷ is also promising. Using their concepts it has been shown that a proper combination of stiffness and damping for lightweight constrained layer damping treatment cemented on the inner surface of fuselage skin panels reduces the noise of propeller aircraft interiors. Sen Gupta⁴⁸ has also suggested that damping treatment can be precisely tuned to reduce the noise transmission through a fuselage. The most recent work still under way combines the modal approach for low frequencies with the statistical energy approach at high frequencies and includes the ability to estimate the effects of cabin acoustic modes in predictions of cabin noise. Laboratory experiments on a Fairchild/Swearingen Metro fuselage with different double wall treatment⁴⁹ have established a data base for correlations with improvements to the Koval methods⁴² and the methods of Wilby and Pope.⁵⁰ In summary, it appears that the work now under way will provide the guidance necessary to achieve greater noise reduction with minimum weight penalties in Prop-Fan transport designs.

Two other concepts are receiving attention as a means for reducing Prop-Fan aircraft interior noise: Synchrophasing^R, and shielding with opposite rotation. Synchrophasing is a patented principle which locks the phase relationship of the propellers on an aircraft to each other by means of an automatic control system. As shown in Fig. 15 this has been beneficial in the past primarily for eliminating the highly annoying beats which are caused by operation of the propellers on an aircraft at slightly different speeds. Claims have also been made that selection of the proper phase relationship between propellers can also reduce the noise level in the aircraft. Until recently it was believed that such reductions would be achieved over a small area inside the aircraft with other adjacent areas showing no improvement or an actual increase in noise. However, tests over the past several years show that a precision synchrophaser set to hold a phase relationship between propellers, as established by a test, can be used to reduce the level in a large area near the plane of rotation without substantially increasing noise in adjacent areas. Work is currently under way to evaluate the potential of precision synchrophasing by use of new data analysis procedures.^{51, 52} These procedures rely on computer analysis of measurements obtained in flight tests to select the optimum phase angles. These new analysis techniques allow evaluation of the noise reduction achievable with a given phase holding accuracy. Limited experiments reported in Ref. 52 indicate that an accuracy of $\pm 3^\circ$ to $\pm 5^\circ$ is required to achieve meaningful noise reductions in conventional turboprop transports. Reductions of peak A-weighted levels in four engine airplanes of up to 14dB and in two engine airplanes of up to 5dB appear possible. Reductions of space average A-weighted levels in four engine airplanes of up to 8.5dB and in two engine airplanes of up to 3dB appear possible. The greater reductions possible in four engine airplanes is due to the greater possibility for four noise sources to cancel. In Prop-Fan transports, it is expected that Synchrophasing will be incorporated as a noise reduction system.

The second concept which has not been exploited for noise reduction of turboprop aircraft cabins is the use of opposite rotation, i.e., the propellers on the port side of the aircraft rotate counter clockwise and the propellers on the starboard side rotate clockwise (or vice versa), plus use of the wing to shield the fuselage from airborne noise. As Figure 16 indicates, the approaching blade creates the noise heard by a listener. This is the airborne noise that drives the fuselage surface and in turn causes the propeller noise heard in the cabin. By installing turboprops or Prop-Fans with direction of rotation such that the blades move up as they approach the fuselage in a low wing installation the noise generated must pass "through" the area below the floor of the cabin before reaching the inhabited space. Thus, the advantage of double wall construction for reduced noise may be achieved with no additional acoustic treatment penalty. Finally, if wing sweep were increased near the fuselage, the inboard section of the wing would provide shielding of the cabin walls. Even the normal wing sweep of a high subsonic cruise Mach number transport is expected to provide beneficial shielding effects that may reduce the fuselage treatment weight needed to achieve a comfortable cabin.

In addition to the reduction of airborne noise, another source of cabin noise is being studied at this time. This is structureborne noise. Figure 17 indicates schematically the concepts being considered. The airborne path treated in almost all propeller aircraft cabin noise control is that associated with the excitation of the fuselage by the airborne noise generated by the propeller. Three structureborne paths are conjectured in Figure 17: (1) engine or propeller vibration is transmitted through the engine mounts to the wing and then to the fuselage, (2) propeller wakes excite the wings which transmit the vibration to the fuselage, or (3) propeller wakes excite the tail surfaces which transmit the vibration to the fuselage. Evidence of structure borne noise was established in a test program conducted jointly by Hamilton Standard, Lockheed and deHavilland using a Dash 7. Measurements were made in flight with microphones flush mounted on the fuselage surface and in the cabin. The airplane was first flown with all four engines operating. It was then flown with inboard engines

operating and then with just the outboard engines operating. As Figure 18 shows, running just the outboard engines reduced fuselage surface noise (as expected) by 13dB but did not reduce cabin noise appreciably. Note that the exterior level for inboard engines operating alone is higher than that for all engines because of the higher power used to maintain air speed. It is believed at this time that the noise caused by the propeller wakes interacting with the wing is dominating the cabin noise (particularly blade passage frequency) when the outboard engines are operating alone. In another test program, NASA conducted static tests on a deHavilland Twin Otter.⁵³ Results indicated that structureborne noise in the aft cabin was about 5 dB lower than airborne noise. Additional research is now underway to explore this area further with the long range objective of quantifying the magnitude of structure borne noise in Prop-Fan airplanes and if necessary, defining measures to control it.

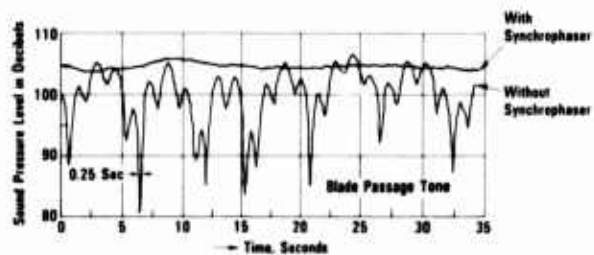


Figure 15. Typical effect of current synchrophasers on cabin noise (Ref 52)

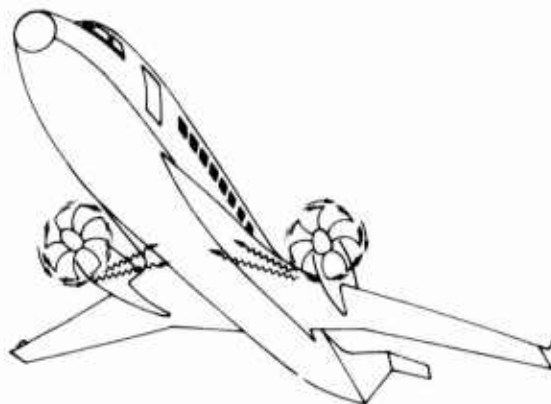


Figure 16. Opposite rotation cabin noise reduction concept

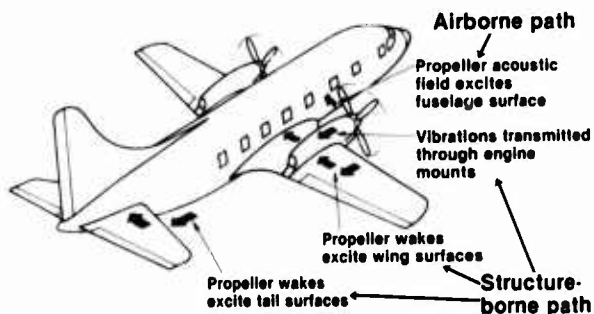


Figure 17. Candidate transmission paths for propeller noise

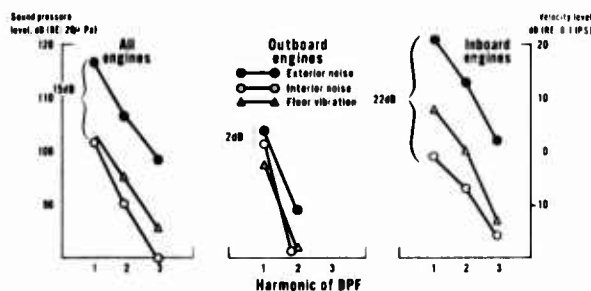


Figure 18. Comparison of exterior and interior noise to floor vibration DHC-7 port side prop-plane 9500 ft 10% RPM

Prop-Fan Source Noise Prediction - As shown in Figure 19, five Prop-Fan models have been designed and built in model scale. SR-1 thru SR-5 were designed by Hamilton Standard with much of the design and manufacture of these Prop-Fans supported by NASA contract. The SR-6 was designed by NASA and built by Hamilton Standard under NASA contract. Two additional single rotation Prop-Fans are now in design and manufacture: the SR-7 and SR-8. The SR-7, like the other single rotation models is designed for 0.8 Mach number cruise. The SR-8 is a dedicated 0.7 Mach number design. The acoustic methodology used in design of these models has evolved since 1975 when the SR-1 and SR-2 were designed using an empirical method which was based on available test data and the idea that tip sweep could be used to alleviate the effects of transonic tip speed. This was necessary because the existing theoretical noise prediction methodology was not capable of evaluating the supersonic helical tip speed operation of the Prop-Fan at cruise or the effects of blade sweep. In the SR-1 design, the features included to minimize noise were a reduction in airfoil thickness and a moderate amount of sweep. The reduction in thickness was expected to reduce the near field noise in cruise since propeller noise theory showed that thickness related (monopole) noise was a dominant part of the noise of existing propellers operating at high tip speed. The moderate amount of sweep incorporated was expected to lower the effective Mach number at which the blade airfoils operate and, therefore, reduce the excess noise which had been observed in conventional propellers when they operate at helical tip Mach numbers exceeding the critical Mach number of the blade airfoils (the operating Mach number of an airfoil at which local flow over the surface reaches sonic velocity). Unfortunately, in 1975, when SR-1 and SR-2 were designed, the effect of these features could not be accurately analyzed without an appropriate theory.

The SR-2 design is exactly like the SR-1 except the SR-2 has no blade sweep. This model was built as a reference design to establish the benefits of advanced swept blades relative to conventional unswept blade planform. SR-2, however, had thin airfoil sections and eight blades so it was expected to have higher efficiency and produce less noise than a conventional four-blade propeller.

The SR-1M has the same moderately swept planform of the SR-1. However, it has different twist and camber distributions which were established as a result of analysis of the aerodynamic wind tunnel data from SR-1.

In 1976, a theory was developed by Hanson¹³ which allowed prediction of near field noise of Prop-Fans operating at high subsonic speed. Similar approaches were taken by Farassat⁵⁴ and by Schmitz and Yu.⁵⁵ This work was based on the Ffowcs-Williams Hawkins "acoustic analogy"⁵⁶ in which the equations of fluid motion are cast into a wave equation for acoustic pressure. Two components of noise are calculated in this theory: (1) monopole (thickness) noise, which is determined by the blade airfoil section thickness distribution; and (2) dipole (loading) noise, which is determined by the pressure loading distribution on the surface of the blade. A third, second order term in the Ffowcs-Williams Hawkins equation (the quadrupole source term) was ignored in this early theoretical development because it was believed to be small relative to the monopole thickness term. Of course, the lack of the quadrupole source should not be surprising as none of the propeller and rotor noise prediction procedures which existed in 1976 had ever included this source. In the formulation of this theory, Hanson assumed that the Prop-Fan blades travel along helical surfaces defined by the forward flight speed of the aircraft and the angular velocity of the Prop-Fan. This method does not treat the nonlinear quadrupole source. This method is a time domain method, i.e., the acoustic pressure wave form generated by a blade is calculated and then the frequency spectrum of the noise is obtained by Fourier analysis.

Figure 20 shows schematically the input requirements, computations, and output of the computer program which make use of the above described theory. For Prop-Fan loading noise predictions, the chordwise variation in pressure is based on the chordwise loading distribution of airfoils of the type used in the Prop-Fan design. This new method was used in the design of a second generation model, the SR-3. For the design of the SR-3, a generalized chordwise loading distribution was used. For thickness noise calculations, the actual blade thickness distribution is the input to the program.

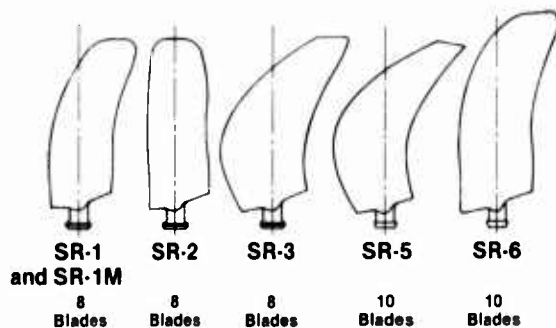


Figure 19. Prop-Fan blades untwisted platform comparison

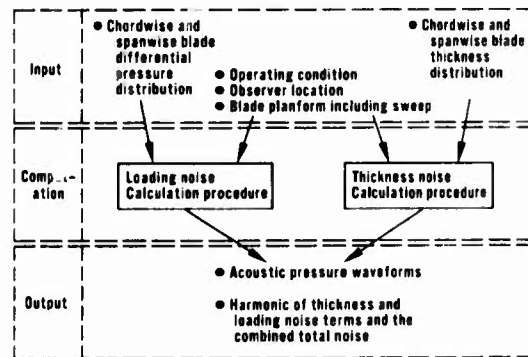


Figure 20. Prop-Fan linear time domain noise prediction procedure

The basic output of the program is the acoustic pressure waveform at a specified point in space assumed to be moving forward at the same speed as the Prop-Fan. The harmonic components of noise obtained from a Fourier analysis of this waveform are also an output. Thus, it is possible to calculate the noise at the location of a fuselage near a Prop-Fan as the aircraft is flying at cruise speed. For the SR-3, the primary noise reduction feature of the design was the blade sweep which was optimized using the theory described above. This sweep optimization utilized the concept of destructive interference of noise from different spanwise stations of the Prop-Fan blade. This concept is based on the fundamental assumption of linear acoustics that the acoustic pressure at any observer position can be calculated as the sum of contributions from each element of the source volume and surface area. To be done correctly, the summation (or integration) process must account for the amplitude and phase of the elemental contributions. If source dimensions of the blades are greater than about 1/2 the wavelength of interest (i.e., if the source is "acoustically non-compact"), then at some observer positions, elemental signals from different portions of the source will arrive out of phase. The net noise will then be reduced by self-interference below the level which would be obtained if the source dimension were very small ("acoustically compact"). Although the term "acoustically non-compact" is relatively new, the principle has been known for many years. For example, in Gutin's original theory for propeller noise,³ the appearance of Bessel functions and the polar directivity pattern result from phase variation around the propeller circumference. For most conventional turboprop designs, chordwise and spanwise phase variations can be neglected at blade passing frequency (number of blades times rotation speed). However, for the Prop-Fan, the combination of high Mach number, many blades, and large chord require that chordwise and spanwise phase variations be included.

The phase interference concept is most clearly illustrated with reference to the effect of sweeping a blade platform as suggested by Figure 21. At blade passing frequency, the noise from any strip of the blade is simply a sinusoidal wave with an amplitude and phase angle. The noise from one blade is simply the vector sum of the contributions from each strip and the noise of the total Prop-Fan is the product of the vector sum and the number of blades. The effect of sweeping the tip back is to cause the signal from the tip to lag (increased phase angle) the signal from the mid-blade region, thus causing partial interference and a reduction in net noise.

For the SR-3 design, a short form version of the Time Domain Method was developed in 1976 which included a graphical version of the concept discussed above. In this graphical procedure, the strip noise contributions are treated as vectors in the complex plane having amplitude and phase angle. Then, the summation of the contributions from the strips is performed by adding the vectors head-to-tail, as shown at the right of Figure 21. It can be seen that a lack of variation in phase angle in the individual contributions from several spanwise locations on the blade would vectorially add up to a value no different from the total length of the vectors (analogous to the resultant noise). This is the

general result for unswept and slightly swept Prop-Fan blades. However, by varying the amplitude and phase of the noise produced by the various spanwise stations on the blade, substantial reduction in the resultant amplitude can be achieved, as shown in the phase plot at the right of Figure 21. This is the result for a Prop-Fan blade with substantial blade sweep. An indication of the effect of sweep on the vector plots for the SR-2 unswept versus the SR-3 swept blade designs can be seen in Figure 22.

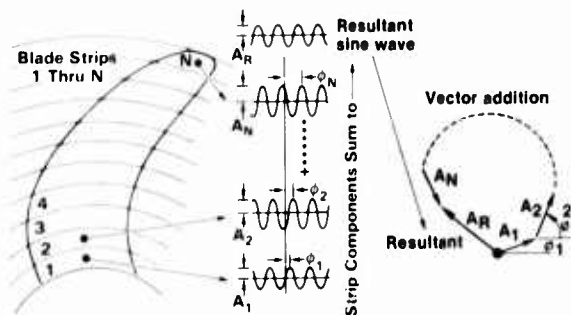


Figure 21. Acoustic strip analysis concept (Ref 58)

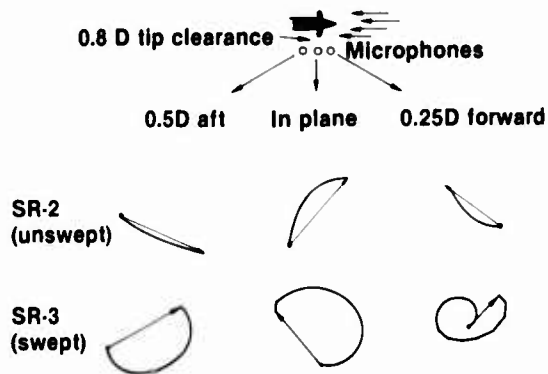


Figure 22. Prop-Fan phase plots

In 1977, a Frequency Domain Method was developed for predicting Prop-Fan noise.⁵⁷ This method was found to be more efficient for design of Prop-Fans where the blade passage frequency is dominant.

Late in 1977, Hanson developed a quadrupole prediction theory⁵⁷ and was able to show at the end of 1977, by use of a simplified nonlifting aerodynamic model, that the quadrupole noise is an important noise source in Prop-Fans with unswept or slightly swept blades operating at transonic tip speeds. The addition of the quadrupole component to the linear monopole and dipole components calculated by the Frequency Domain Method was shown to improve the correlation with Prop-Fan acoustic test data.

Throughout 1978 the major Prop-Fan Methodology development consisted of establishing a working procedure for including the quadrupole component in the Prop-Fan Acoustic Design Procedure. Figure 23 shows a block diagram of the method which was put into practice for design of the SR-5 model. The transonic airfoil design program at the upper left of Figure 23 is used to generate the data set which consists of the chordwise thickness distribution of an airfoil, the pressure distribution on the surface of an airfoil and the quadrupole distribution in the air surrounding an airfoil. A Fourier Transform Program is used to generate the Data Sets needed for noise calculations by the Frequency Domain Noise Prediction Program at the lower right of Figure 23. In addition, the Fourier Transform Program can be used to generate plots of frequency domain loading and thickness noise functions which are required for optimizing airfoil shape to reduce noise. The application of this part of the method is discussed in Reference 58.

The Prop-Fan Performance Analysis Program at the upper right of Figure 23 is used to define the lift coefficient distribution for the Prop-Fan configuration and operating condition being considered. This information is used by the Frequency Domain Noise Prediction Program to predict the cases for the Acoustic Data Sets which are a function of thickness, camber, operating lift coefficient, and operating Mach number of the airfoils making up the Prop-Fan blade. The Frequency Domain Noise Prediction Program calculates monopole, dipole, quadrupole, and total noise. To generate a frequency spectrum, any number of harmonics of blade passage frequency may be calculated. Also, the harmonics may be calculated for several observer locations to define the directivity of the Prop-Fan. In order to ensure that the input to the program is correct, the program plots the planform of the blade being evaluated. Phase plots for each harmonic and each location calculated are diagnostic output which is particularly important in optimizing the sweep distribution of a Prop-Fan blade during the design process.

Waveforms for the acoustic pressure pulse generated by a blade are also an output of the program. These are important diagnostic aids which can be compared with measured acoustic pressure pulses to establish areas of deficiency of the methodology.

The Prop-Fan Frequency Domain Noise Prediction Method described above predicts free-field noise. On an airplane where noise levels on the fuselage surface are predicted, the levels are influenced by the presence of the fuselage and the shielding of the aircraft boundary layer. This subject has been addressed by Hanson^{59,60} and McAninch.^{61,62} The latest and most complete analysis of these effects is summarized in Reference 59. The theory of Reference 59 models a distributed rotating source (the Prop-Fan) propagating sound through a boundary layer of arbitrary profile to an infinitely long rigid cylinder (the fuselage) in the near field. A sample of the calculated correction factors for conditions encountered in the flight test of Prop-Fan models on a Lockheed-Jetstar test vehicle (to be described later) are shown in Figure 24. This is an "unwrapped" fuselage surface showing the predicted measured level of blade passage frequency relative to a prediction in the free-field for an eight blade Prop-Fan at a cruise Mach number of 0.79 and a tip rotational Mach number of 0.816. Thus at forward locations, it can be seen that the measured level would be substantially lower than the free-field prediction due to propagation through the boundary layer. Behind the rotor plane of rotation, the measured level should exceed the free-field level by 3dB due to the pressure amplification associated with the presence of the fuselage.

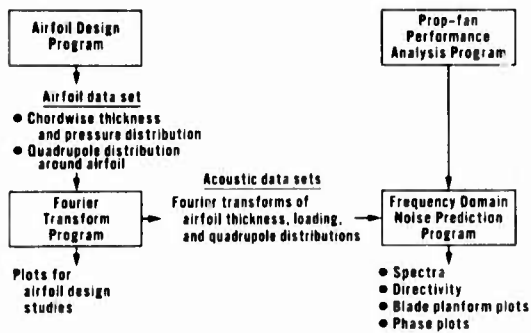


Figure 23. Prop-Fan frequency domain noise prediction method

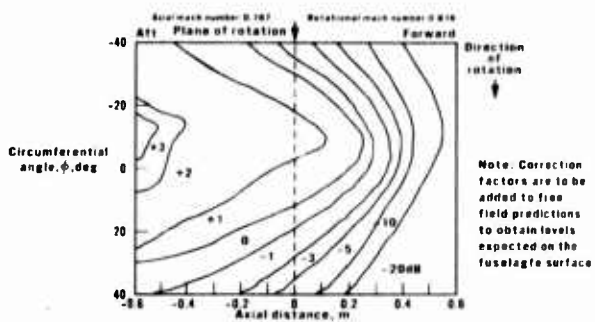


Figure 24. Sample calculated correction factors for the Jetstar fuselage at blade passage frequency for an eight blade Prop-Fan (Ref 60)

The most recent thrust in Prop-Fan noise theory is the application of more fundamental procedures for predicting performance and/or noise. One direction being pursued is the application of the Euler equations of fluid motion. One example of these programs is that developed by Bober et al.⁶³ Work to apply these programs to Prop-Fan noise prediction is still in the early stages. However, it is clear that calculations based on the Euler equations currently require large computers and take a long time to run per case. A second approach now being pursued is the compressible lifting surface theory for aerodynamic and noise predictions.⁶⁴ This is a unified theory applicable to acoustics, unstalled flutter and steady performance of unshrouded propulsors. It accounts for effects of blade interference, thickness and three-dimensionality. The noise theory described above developed by Hanson is already in use for design and evaluation of Prop-Fans. The performance aspects of the theory are now being developed.

The latest noise methodology task in the Prop-Fan area relates to the counter rotation configuration discussed earlier. As shown in Figure 25, there are several new mechanisms to be addressed in the predictions. The most obvious addition is the interaction between rotors. There is both an acoustic interaction associated with two coherent sources located close together and an aerodynamic interaction caused by potential and viscous wake interaction. As in the wing mount installation, the wing and nacelle influence the flow field at the Prop-Fan and these influences must be considered in noise predictions. In addition, the non-uniform flow caused by the engine exhaust and the pylon must be included in the tail mount Prop-Fan noise prediction. A block diagram of the procedure under development at Hamilton Standard for counter rotation noise predictions is shown in Figure 26. It can be seen that all of the above effects are included in this procedure.

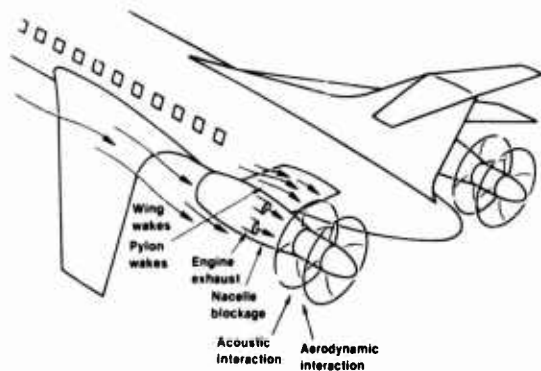


Figure 25. Factors affecting counter rotation Prop-Fan noise

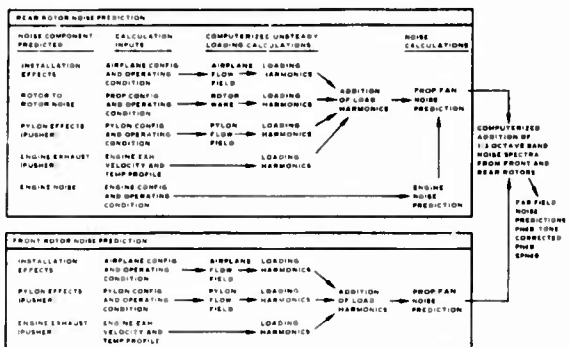


Figure 26. Counter rotation Prop-Fan noise prediction method

The above discussion is written in the framework of near-field noise prediction. This is certainly an important aspect of the Prop-Fan as it influences cabin comfort. However, a Prop-Fan airplane must satisfy the international certification limits on far-field noise. However, satisfying these limits has not been considered as difficult as the cruise noise control since Prop-Fans operate at takeoff and landing at subsonic tip speeds, like conventional turboprops. There are, of course special calculations required for certification predictions. For these calculations, the ground reflection effects associated with the direct and reflected sound reaching the measuring microphone mounted 4 ft. from the ground must be included in the calculation. An indication of the importance of the inclusion of ground reflection corrections for accurate predictions of conventional turboprop transports can be seen in Figure 27. Here it can be seen that the ground reflection effects suppress the blade passage frequency tone in the 63 Hz band, enhance the tone at two times blade passage frequency and enhance all of the higher frequency tones and broadband noise. The predicted free-field Effective Perceived Noise Level would be 97.2 while the prediction with ground reflection would be 98.3. For Prop-Fan transports the effects on Effective Perceived Noise Level seen in Figure 27 are enhanced because of the dominance of the low frequency tones in the Prop-Fan noise spectrum.

Far field Prop-Fan noise predictions now include the effects of the airplane flow field, particularly the effects of wing circulation, which cause the load on the "up going" blades to be different from that on the "down going" blades. Also for sideline noise predictions, the attenuation of sound propagating near the ground in excess of that which would occur due to normal propagation through a homogeneous atmosphere is now included for accurate certification level predictions. Prediction of both the effects of the airplane flow field (installation effects) and excess ground attenuation are in the development stages. Refinement in the installation effects calculations is expected in the near future as better airplane flow field calculation procedures are developed. Refinement in excess ground attenuation calculations is expected as new turboprop airplane test data becomes available.

Prop-Fan Experiments - Both wind tunnel and flight tests of single rotation Prop-Fan models have been conducted. In 1978 acoustic tests of the SR-1, SR-2 and SR-3 Prop-Fan models were conducted under NASA Contract in the Acoustic Research Tunnel at the United Technologies Research Center.⁶⁵ This open jet tunnel with an acoustically treated test section is shown in Figure 28.

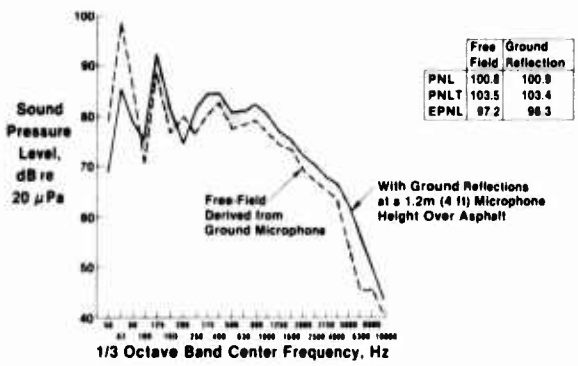


Figure 27. Effects of ground reflections on turboprop airplane noise

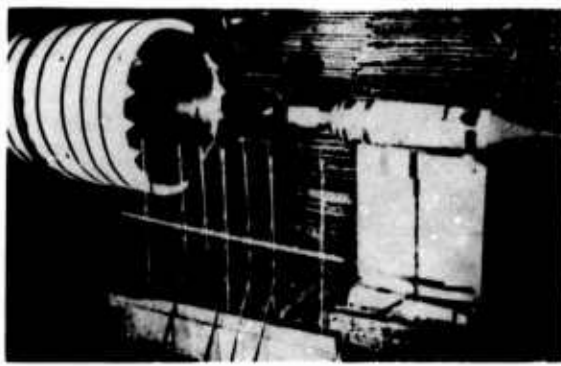


Figure 28. Prop-Fan model set up for acoustic test

Acoustic data were obtained at locations along lines parallel to the axis of the tunnel (also the axis of Prop-Fan rotation) at four distances: 0.4, 0.8, and 1.6 Prop-Fan diameters and at 10 ft.

The curves of Figure 29 show the peak level of the 8P harmonic at a tip clearance of 0.8 Prop-Fan diameters as a function of tip helical Mach number for a constant loading of approximately 37 SHP/Blade. At high tip speeds, this loading approaches the level of lift coefficient for a Prop-Fan at the cruise condition. Therefore, this data was considered an indication of the noise reduction potential of the SR-3 design. It can be seen in Figure 29 that the SR-3 is about 10dB lower in level than the SR-2 at supersonic tip helical Mach number. These benefits are seen in test points up to 1.21 tip helical Mach number. Wind tunnel tests have also been conducted at NASA Lewis in the 6 ft. x 8 ft. Transonic Wind Tunnel^{66,67} which confirm the benefits of blade sweep at high cruise Mach number.

The curves of Figure 30 show the trend of 8P harmonic with tip helical Mach number in the far field 10 ft. from the axis of rotation for a constant load of 37 SHP/Blade. At 0.7 to 0.8 tip helical Mach number, the reduction of 5dB for the swept SR-3 blade relative to the unswept SR-2 is considered particularly important as this is the operating regime during take-off and landing where regulations must be satisfied for aircraft noise certification. These results confirmed that Prop-Fan configurations designed to reduce near field noise in cruise are also beneficial in reducing far field noise at take-off and landing conditions.

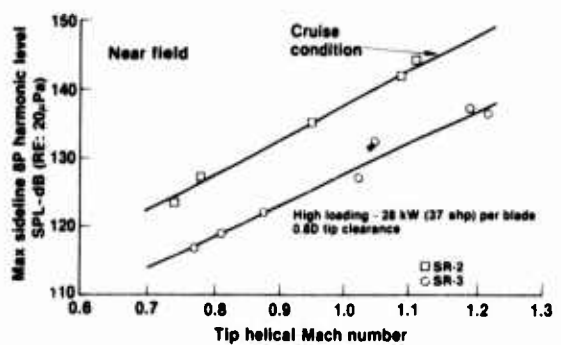


Figure 29. Maximum sideline 8P harmonic for a two blade configuration high loading ~28 KW (37 shp) per blade 0.8D tip clearance (Ref 65)

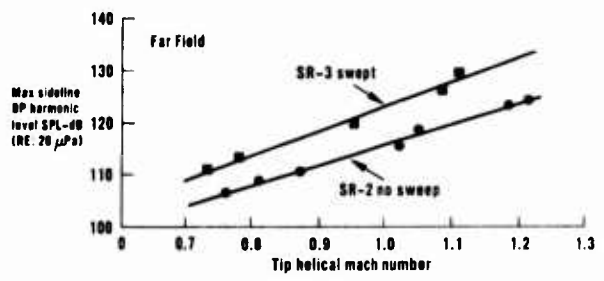


Figure 30. Maximum sideline 8P harmonic for a two blade configuration high loading ~28 KW (37 shp) per blade 4.4D tip clearance (Ref 65)

In 1981 and 1982 flight tests were conducted on the SR-2 and SR-3 driven by an air turbine drive mounted above the fuselage of Lockheed Jetstar as shown in Figure 31. Initial tests conducted in 1981 used an array of microphones on the fuselage surface as shown in Figure 32 to acquire amplitude and phase information useful for cabin soundproofing research. Initial data reduction showed that levels were lower than predictions and led to the discovery by Hanson⁵⁹ that the sound was attenuated by propagation through the fuselage boundary layer. In the 1982 tests, a microphone boom was mounted above the Prop-Fan as shown in Figure 32 to minimize boundary layer effects. Analysis of the data from this program is fully documented in References 68 thru 74 and in Reference 60. The following is a brief summary of the results.



Figure 31. Model Prop-Fan installed on Jetstar



Figure 32. Microphone boom and fuselage surface microphones on Jetstar

Figure 33 shows the comparison of SR-2 and SR-3 noise measurements. Figure 33A shows the comparison of directivity (0 is in the plane of rotation). It can be seen that (as in the earlier wind tunnel tests) the swept blade SR-3 produces less noise than straight blade SR-2. Figure 33B shows that this is true for the upper harmonics as well as the blade passage frequency noise. These are data from the boom microphones where the boundary layer effects are minimized. The differences between the boom and fuselage surface measurements is indicated in Figure 34. Note that the boom and fuselage microphones compared are slightly displaced as the Prop-Fan axis of rotation is down tilted. It can be seen that the effects expected by Hanson⁵⁹ are generally confirmed, i.e. the boundary layer attenuates noise substantially ahead of the plane of rotation. In Reference 60, the measured fuselage levels are compared with fuselage surface predictions (including Hanson's boundary layer corrections). As shown in Figure 35, at the 0.787 Mach number condition, the correction appears to be insufficient at forward microphones but at the 0.713 and 0.62 Mach number conditions the correction appears promising. Further work is under way to improve the high cruise Mach number amplitude correction and to evaluate the phase accuracy of the procedure. Phase accuracy is considered necessary for design of fuselage wall soundproofing using advanced theoretical procedures.

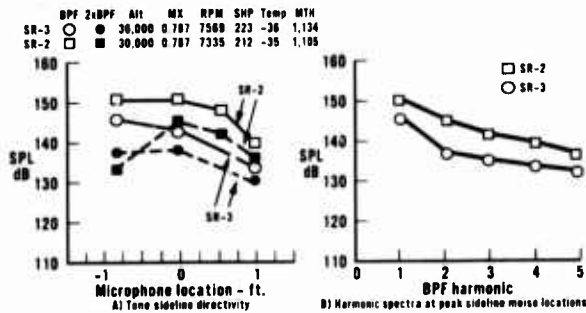


Figure 33. Comparison of SR-2 and SR-3 noise measurements boom microphones, design point operating condition (Ref 74)

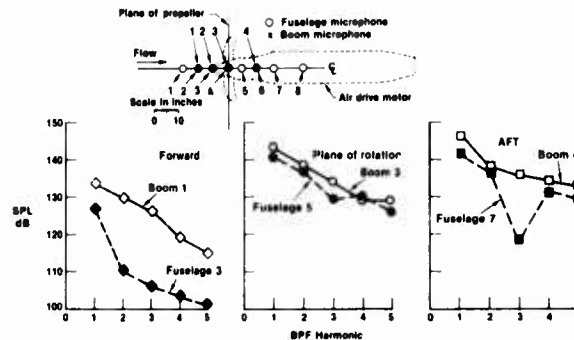


Figure 34. Comparison of boom and fuselage measurements of SR-3 harmonic spectra design point operating condition (Ref 74)

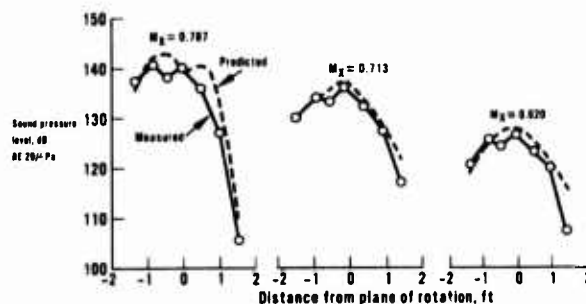


Figure 35. Comparison of measured and calculated sound pressure levels at the Jetstar fuselage for SR3 (Ref 60)

A comparison of prediction and measurement at the SR-3 cruise design point is shown in Figure 36. The boom microphone data corrected for pressure amplification due to the presence of the boom is shown compared to free-field predictions using Hanson's Frequency Domain Method.⁷⁵ The agreement can be seen to be quite good considering that the Prop-Fan is a highly swept wide chord blade operating at transonic tip speed. All of the noise components contribute to the total. Figure 37 shows the comparison of the peak near field directivity point predictions and measurements for the SR-2 and SR-3 (corrected to free field) as a function of tip helical Mach number. Again, the agreement is quite good. As noted before, the SR-3 shows the benefits of sweep at the high helical Mach numbers encountered at cruise. However, some benefits can be seen for the SR-3 even at lower helical Mach number⁸¹.

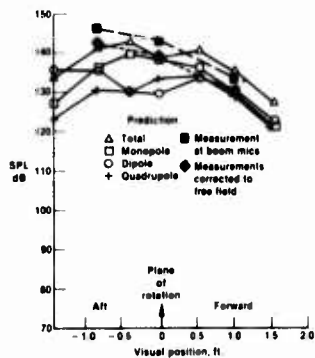


Figure 36. Comparison of measured and predicted BPF tone sideline directivity SR-3 operating at design point condition (Ref 74)

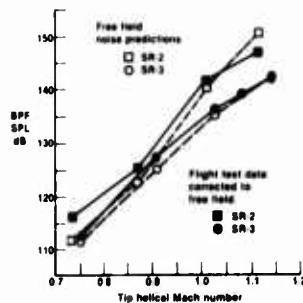


Figure 37. Comparison of measured and predicted peak sideline tone levels vs. M_{th} for the SR-2 and SR-3 boom microphones, constant $C_p \sim 1.9$ and $J \sim 3.1$ (Ref 74)

Counter Rotation Testing - The interest in the enhanced efficiency of the counter rotation version of the Prop-Fan described earlier has encouraged not only development of noise methodology but also acoustic tests. One test series was conducted in 1982 and 1983 using the Fairey Gannet Anti-Electronic Warfare airplane shown in Figure 38. This airplane is unique in that each of the blade rows is driven by a separate turbine engine. Thus, the front or rear blade row can be shut down for experimental purposes. For the test series, a boom (seen in the foreground of Figure 38) was mounted on the wing. Flush mounted microphones on the boom were used to acquire inflight near field noise data at various cruise conditions. Also, as shown in Figure 39, data was acquired at various locations farther from the Gannet in "station keeping" tests conducted jointly by Hamilton Standard and NASA using a NASA Learjet with microphones mounted on the nose and wing tip. In another part of the test series, far field data was acquired in flyover tests. The data from this comprehensive test series is still being evaluated. However, some initial results will be discussed below.



Figure 38. Fairey Gannet modified for acoustic tests



Figure 39. Fairey Gannet in station keeping acoustic test with Learjet

Figure 40 shows the circumferential directivity measured with a near field boom mounted microphone. This circumferential directivity had been anticipated based on the experimental work by Hubbard⁷⁶ and the analytical work by Hanson and Magliozzi reported in Reference 39. The data shown in Figure 40 was obtained with a stationary microphone boom while the crossover point of the front and rear rotors was shifted circumferentially by operating the two rotors at different RPM's. This circumferential directivity leads to difficulties in interpreting noise spectra from counter rotating systems because the spectrum seen when the BPF is at a peak has the harmonics of a 4 blade propeller but when the BPF is a minimum, the spectrum has the harmonics of an 8 blade propeller. These effects become less pronounced at higher frequencies as can be seen in Figure 40.

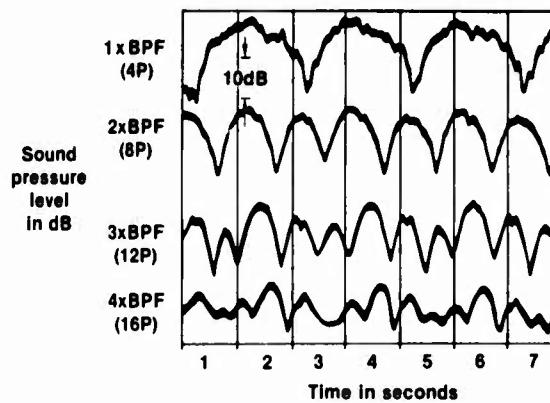


Figure 40. Gannet CRP circumferential directivity - June 1983 Test Data

The most serious question regarding counter rotation propulsors is the amount of aerodynamic interaction which causes noise in excess of that which would exist if the two rotors only generated the acoustic interaction noise associated with two coherent sources operating close to each other. In the near field, an indication of this excess can be seen in Figure 41. Figure 41 compares the near field harmonic levels for the summation of front and rear rotor noise spectra (obtained by operating each separately) with the spectrum of the two rotors operated together as a counter rotation system. Although it is recognized that the Gannet was operating at different flight speeds for the single and counter rotation tests, there is clearly an excess noise above the third harmonic. In the far field, the aerodynamic interaction is more difficult to evaluate due to the uncertainty introduced by the source moving past a stationary microphone. However, Figure 42 suggests that aerodynamic interaction exists above 2 times blade passage frequency (about 200 Hz). Unfortunately, the Gannet engines or airframe noise appear to mask the high frequency components so the far field flyover data is less useful than the near field boom microphone data or the far field station keeping data.

The Gannet is a conventional counter rotation turboprop and is lightly loaded when compared to the loading envisaged for a counter rotation Prop-Fan. Therefore, it is difficult to anticipate how the interaction identified above will impact these new designs. This is the subject of current intensive effort. One attempt to obtain data more relevant to the Prop-Fan has been reported by Block.⁷⁷ This data indicates that a substantial amount of interaction ahead of the plane of rotation occurs for a counter rotation Prop-Fan consisting of two blade rows each having four unswept SR-2 blades. Unfortunately, these tests were also limited to light blade loadings and low forward speeds so further experiments and analysis will be required to establish the interaction penalty for heavily loaded counter-rotation Prop-Fans.

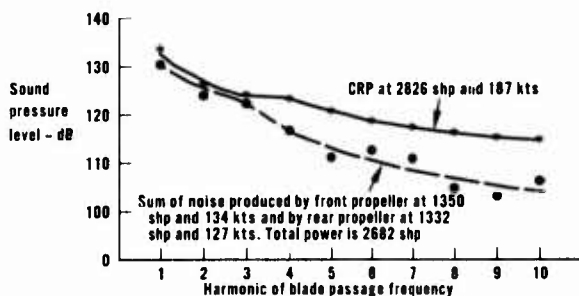


Figure 41. Comparison of measured noise of CRP operation with the summation of noise measured from individual operation of the front and rear propellers

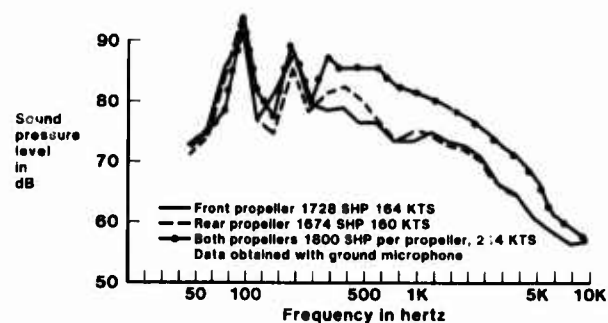


Figure 42. Fairey Gannet far field flyover noise comparison

Concluding Remarks

Propeller acoustic research has been conducted for more than 60 years. The work of the pioneers who developed source noise prediction procedures has been a valuable basis for more recent researchers who have had the advantage of more advanced mathematical tools and fast running computers. Nevertheless, there continue to be unsolved mysteries in accurate prediction of Prop-Fan and turboprop noise. In particular, the recent interest in counter rotation Prop-Fans has added a new complexity to the prediction process because of the aerodynamic interaction between blade rows. More conventional turboprops such as those now being introduced on large commuter airplanes appear to be better understood noise producers. However, the noise of these turboprops is still a challenge for the engineers designing fuselage wall treatment to improve cabin comfort. In the fuselage soundproofing area as in the Prop-Fan source noise prediction area, additional research will be needed before predictions can be made with complete confidence.

Acknowledgement

Some of the information in this paper has appeared before. It has been revised and expanded to highlight some of the important work and include recent research results. The present report is of necessity an account of the research in propeller noise as viewed by one person. Therefore, the author wishes to apologize for omission of many additional contributors to the understanding of propeller noise. The author gratefully acknowledges the contributions of his colleagues at Hamilton Standard to this report, particularly B. Brooks, Dr. D. B. Hanson, B. Magliozzi and D. Parzych. Also the financial assistance of NASA and the FAA for support of acoustic research on propellers and the Prop-Fan is gratefully acknowledged.

References

1. Lynam, E. J. H.; and Webb, H.A.: "The Emission of Sound by Airscrews," 1919 Advisory Committee for Aeronautics (London) R&M No. 624.
2. Prandtl, L.: "Remarks on Aircraft Noise," 1921 Zeitschrift fur Technische Physik 2, 244-245 (In German).
3. Gutin, L.: "On the Sound Field of a Rotating Airscrew," 1936 Zhurnal Tekhnicheskoi fiziki 6, 899-909 (In Russian) Translated as 1948 NACA TM 1195.
4. Deming, A. F.: "Noise From Propellers with Symmetrical Sections at Zero Blade Angle," 1937 NACA TN 605.
5. Deming, A. F.: "Noise from Propellers with Symmetrical Sections at Zero Blade Angle II," 1938 NACA TN 679.
6. Stowell, E.Z.; and Deming, A.F.: "Noise from Two Blade Propellers," T.R. No. 526, NACA, 1935.
7. Beranek, L.L.: Principles of Sound Control in Airplanes, OSRD No. 1543, The Murrey Printing Company, Cambridge, Mass., 1944.
8. Garrick, J.E.; and Watkins, C.E.: "A Theoretical Study of the Effect of Forward Speed on the Free-Space Sound-Pressure Field Around Propellers," NACA Report 1198, August 31, 1953.
9. Arnoldi, R. A.; and Taylor, H. D.: "Propeller Noise Caused by Blade Thickness," United Aircraft Corporation Report R-0896-1, January 10, 1956.
10. Billings, H.: "AVA Monographs; Part R - Modern Aeronautical Acoustics Part R-2 Sources of Sound in Motion," July 1, 1947.
11. Yudin, E. Y.: "On the Vortex Sound from Rotating Rods," NACA Tech. Memo 1136, National Advisory Committee for Aeronautics, Washington, D.C., 1947.
12. Hubbard, H. H.; and Regier, A. A.: "Free-Space Oscillating Pressures Near the Tips of Rotating Propellers," NACA Report 996, February 18, 1949.
13. Hanson, D.B.: "Near Field Noise of High Tip Speed Propellers in Forward Flight," AIAA Paper 76-565, July 1976.
14. Hicks, C. W.; and Hubbard, H.H.: "Comparison of Sound Emission from Two-Blade, Four-Blade, and Seven-Blade Propellers," NACA TN No. 1354, 1947.
15. Vogeley, A. W.: "Sound-Level Measurements of a Light Airplane Modified to Reduce Noise Reaching the Ground," NACA Technical Note No. 1647, July 1948.
16. Johnston, G. W.: "The Reduction of the External Noise Level of Otter UC-1 Aircraft," July 30, 1957, The de Havilland Aircraft of Canada Ltd. Report No. D.H./24, Office of Naval Research Nour 2160(00).
17. Johnston, G. W.; and Law, A.: "The Reduction of the External Noise Level of Otter UC-1 Aircraft Part 2," December 31, 1958, The de Havilland Aircraft of Canada Ltd. Report No. D.H./37, Office of Naval Research - continuation of work carried out in 1947 under Contract Nour 2160(00).
18. Kurbjun, M. C.: "Noise Survey of a 10-Foot Four Blade Turbine-Driven Propeller Under Static Conditions," NACA Technical Note 3422, July 1955.
19. Kurbjun, M. C.: "Noise Survey of a Full-Scale Supersonic Turbine Driven Propeller Under Static Conditions," NACA Technical Note 4059, July 1957.
20. Kryter, K. D.: "Scaling Human Reactions to the Sound from Aircraft," Journal of the Acoustical Society of America, 31, 1415-1429, July 1957.
21. Stevens, S. S.: "Calculation of the Loudness of Complex Noise," J. Acoustical Society of America, 28, 807-832 (1956).
22. Kryter, K. D.; and Pearsons, K.S.: "Judgment Tests of the Sound from Piston, Turbojet and Turbofan Aircraft," Sound Volume 1, No. 2, pp. 24-31, March-April 1962.
23. Kryter, K.D.: "Some Effects of Spectral Content and Duration on Perceived Noise Level," Journal of the Acoustical Society of America Volume 35, No. 6, June 1963.
24. Anon.: "Federal Aviation Regulations Part 36 Noise Standards: Aircraft Type and Airworthiness Certification" (14CFR Part 36) Nov. 1969.

25. Anon.: "Data Analysis Package, Low Noise Propeller Technology Demonstration," Four Volumes, Contract F 33615-73-C-2045, December 1973.
26. Barry, F.W.; and Magliozzi, B.: "Noise Detectability Prediction Method for Low Tip Speed Propellers," Tech Report AFAPL-TR-71-37, Wright Patterson Air Force Base, Ohio June 1971.
27. Griffith, E. D.; and Revell, J. D.: "The Quiet Airplane Paradox and Its Theoretical Explanation," paper presented at the 87th Meeting of the Acoustical Society of America, April 23, 1974.
28. Metzger, F.B.; et al: "Progress Report on Propeller Aircraft Flyover Noise Research, : SAE Paper 760454, April 1976.
29. Magliozzi, B.: "The Influence of Forward Flight on Propeller Noise," NASA CR-145105, February 1977.
30. Hanson, D. B.: "Spectrum of Rotor Noise Caused by Atmospheric Turbulence," Journal of the Acoustical Society of America, Vol. 56, No. 1, July 1974, pp. 110-126.
31. Metzger, F. B.; and Magliozzi, B.: "Noise Characteristics of Quiet Propellers for STOL Aircraft," Proceedings of the Purdue Noise Control Conference, July 15, 1971.
32. Cicci, F.; and Toplis, A. F.: "Noise Level Measurements on a Quiet Short Haul Turboprop Transport," SAE Technical Paper 760455, April 1976.
33. Anon.: 1970 U.S. Air Force Propeller Product Support Program, Hamilton Standard Document HSPC 69A02.
34. Anon.: "Federal Aviation Regulations Part 36 Noise Standards," Aircraft Type and Airworthiness Certification, Appendix F, "Noise Requirements for Propeller-Driven Small Airplanes," Jan. 1975.
35. Anon.: "1975 Ride Quality Symposium," NASA TM X3295, DOT-TSC-OST-7540, November 1975.
36. Mixson, J. S.: "Sources, Control, and Effects of Noise from Aircraft Propellers and Rotors," NASA TM 81971, March 30, 1981.
37. Waterman, E. H.: "New Means of Reducing Propeller Induced Cabin Noise," Proceedings of Institute of Acoustics (U.K.) Spring Conference 1981.
38. Waterman, E. H.; et al: "Fokker's Activities in Cabin Noise Control of Propeller Aircraft," SAE Paper 830736, April 1983.
39. Strack, W. C.; et al: "Technology and Benefits of Aircraft Counter Rotation Propellers," NASA TM 82983 October 1982.
40. Dowell, E. H.; et al: "Acoustoelasticity: General Theory,, Acoustic Natural Modes and Forced Response to Sinusoidal Excitation, Including Comparisons with Experiment," Journal of Sound and Vibration, 52, 519-542, 1977.
41. Vaicaitis, R.; et al: "Noise Transmission - Turboprop Problem, AIAA Paper 79-0645, March 1979.
42. Koval, L. R.: "Effects of Cavity Resonances on Sound Transmission into a Thin Cylindrical Shell," Journal of Sound and Vibration, 59, 22-33.
43. Wilby, J. F.; and Scharton, T. D.: "Acoustic Transmission Through a Fuselage Sidewall," NASA CR 132602.
44. Nifske, D. J.; et al: "Structural-Acoustic Analysis of the Automobile Passenger Compartment Using Finite Element Methods," General Motors Research Publication GM R-3015, June 11, 1979.
45. Getline, G. L.: "Low-Frequency Noise Reduction of Lightweight Airframe Structures," NASA CR-145104, August 1976.
46. Lorch, D. R.: "Noise Reduction Measurements of Integrally Stiffened Fuselage Panels," AIAA Paper 80-1033, June 1980.
47. Henderson, J. P.; and Nashif, A. D.: "The Effect of Stringer Width and Dampng on the Response of Skin-Stringer Structures," ASME Journal of Engineering for Industry, Feb. 1972.
48. SenGupta, G.: "Current Developments in Interior Noise and Sonic Fatigue Research," The Shock and Vibration Digest, Vol. 7, No. 10, October 1975.
49. Prydz, R. A.; et al.: "Evaluation of Advanced Fuselage Design Concepts for Interior Noise Control on High Speed Propeller-Driven Aircraft NASA CR 165960, September 1982.
50. Pope, L. D.; and Wilby, E. G.: "Analytical Prediction of the Interior Noise for Cylindrical Models of Aircraft Fuselages for Prescribed Exterior Noise Fields," NASA CR 165869, April 1982.
51. Johnston, J. F.; et al: "Propeller Signatures and Their Use - For Control of Cabin Noise and Vibration of Multiple Engine Aircraft," AIAA Paper 80-1035, June 1980.
52. Magliozzi, B.: "Synchrophasing for Cabin Noise Reduction of Propeller Driven Airplanes, : AIAA Paper 83-0717, April 1983.
53. Metcalf, V. L.; and Mayes, W. H.: "Structureborne Contribution to Interior Noise of Propeller Aircraft," SAE Paper 830735, April 1983.

54. F. Farassat: "Theory of Noise Generation from Moving Helicopter Blades with an Application to Helicopter Rotors," NASA TR-R-451, National Aeronautics and Space Administration, Washington, D.C., December 1975.
55. Schmitz, F. H.; and Yu, Y. H.: "Theoretical Modeling of High Speed Helicopter Impulsive Noise," J. American Helicopter Society, Vol. 24, No. 1, January 1979.
56. Ffowcs-Williams, J. E.; and Hawkings, D. L.: "Sound Generated by Turbulence and Surfaces in Arbitrary Motion," Phil. Trans. Roy. Soc. London Series A, Vol. 264, 1969.
57. Hanson, D. B.; and Fink, M. R.: "The Importance of Quadrupole Sources in Prediction of Transonic Tip Speed Propeller Noise," Journal of Sound and Vibration,, Volume 62, January 1979.
58. Hanson, D. B.: "The Influence of Propeller Design Parameters on Far Field Harmonic Noise in Forward Flight," AIAA Paper 79-0609 March 1979.
59. Hanson, D.B.: "Shielding of Prop-Fan Cabin Noise by the Fuselage Boundary Layer," Hamilton Standard Engineering Report, HSER 8165, August 24, 1981; Also Journal of Sound and Vibration on March 8, 1984.
60. Hanson, D.B.; and Magliozzi, B.: "Propagation of Propeller Tone Noise Through a Fuselage Boundary Layer," AIAA Paper 84-0248, 1984.
61. McAninch, G. L.: "A Note on Propagation through a Realistic Shear Layer," Letter to the Editor in Journal of Sound and Vibration, Vol. 88, No. 2, pp. 271-274, 1983.
62. McAninch, G.L.; and Rawls, J.W. Jr.: "Effects of Boundary Layer Refraction and Fuselage Scattering on Fuselage Surface Noise from Advanced Turboprop Propellers," AIAA Paper 84-0249, January 1984.
63. Bober, L. J.; et al: "Prediction of High Speed Propeller Flow Fields Using a Three-Dimensional Euler Analysis," NASA TM 83065, AIAA 830188, January 1983.
64. Hanson, D. B.: "Compressible Helicoidal Surface Theory for Propeller Aerodynamics on Noise," AIAA Journal Volume 21, Number 6, June 1983, p.881.
65. Brooks, B. M.; and Metzger, F. B.: "Acoustic Test and Analysis of Three Advanced Turboprop Models," NASA CR-159667, 1980.
66. Dittmar, J.H.; and Jeracki, R. J.: "Additional Noise Data on the SR-3 Propeller," NASA TM81736, 1981.
67. Dittmar, J. H.: "A Comparison between an Existing Propeller Noise Theory and Wind Tunnel Data," NASA TM81519, 1980.
68. Brooks, B. M.: "Jetstar Propeller Flight Test Program - Preliminary Data Analysis"; prepared for NASA-Dryden Flight Research Center (contract NAS4-2766), 1981. (Also published as Hamilton Standard Engineering Report HSER 8207).
69. Anon.: "Jetstar Propeller Flight Test Program - Preliminary Data Report"; prepared for NASA-Dryden Flight Research Facility (contract NAS4-2822) by Hamilton Standard, 1983.
70. Mackall, K. G.; et al: "In-Flight Acoustic Results from an Advanced-Design Propeller at Mach Numbers to 0.8," AIAA Paper 82-1120, 1982.
71. Lasagna, P.L.; et al: "In-Flight Acoustic Test Results for the SR-2 and SR-3 Advanced Design Propellers," AIAA Paper 83-1214, 1983.
72. Balombin, J. R.; and Loeffler, I. J.: "In-Flight Measurement of High-Speed Turboprop Noise," NASA Paper 83-83327, 1983.
73. Brooks, B.M.: "Analysis of Jetstar Prop-Fan Acoustic Flight Test Data," prepared for NASA-Dryden Research Facility (contract NAS4-2822), 1983. (Also published as Hamilton Standard Engineering Report 8882.)
74. Brooks, B.M.; and Mackall, K. G.: "Measurement and Analysis of Acoustic Flight Test Data for Two Advanced Design High Speed Propeller Models," AIAA Paper AIAA-89-0250, January 1984.
75. Hanson, D.B.: "Near Field Frequency Domain Theory for Propeller Noise," AIAA Paper AIAA-83-0688, April 1983.
76. Hubbard, H.H.: "Sound from Dual Rotating and Multiple Single-Rotating Propellers," NACA Technical Note 1654, July 1948.
77. Block, P.J.W.: "Installation Noise Measurements of Model SR and CR Propellers," NASA TM85790, May 1984.
78. Metzger, F.B.: "Progress and Trends in Propeller/Prop-Fan Noise Technology," AIAA Paper 80-0856, May 1980.

Supplementary References

1. Nystrom, P.A.; and Farassat, F.: "A Numerical Technique for Calculation of the Noise of High Speed Propellers with Advanced Geometry," NASA TP 1662, 1980.
2. Farassat, F.: "Linear Acoustic Formulas for Calculation of Rotating Blade Noise," AIAA Journal Volume 19 Number 9, September 1981, pages 1122-1130.
3. Farassat, F.; and Succi, G.P.: "A Review of Propeller Discrete Frequency Noise Prediction Technology with Emphasis on Two Current Methods for Time Domain Calculations," Journal of Sound and Vibration (1980) 71 (3) page 399-419.
4. Farassat, F.: "Advanced Theoretical Treatment of Propeller Noise," Proceedings of the Von Karman Institute Lecture Series on Propeller Performance and Noise 1982-08 Volume 1, May 1982.
5. Farassat, F.: "The Prediction of the Noise of Supersonic Propellers in Time Domain - New Theoretical Results," AIAA Paper 83-0743, April 1983.

APPLICATION OF ACTIVE NOISE CONTROL TO MODEL PROPELLER NOISE

M. Salikuddin, H. K. Tanna, R. H. Burrin and W. E. Carter
 Lockheed-Georgia Company
 Marietta, Georgia 30063

SUMMARY

The applicability of "active noise control" to reduce cabin noise of turboprop aircraft is demonstrated by conducting several laboratory experiments. The principle of active noise control is to reduce the noise radiated from a primary source by superimposing a signal from a secondary source, which is made identical in amplitude but opposite in phase to the primary sound signal. A computer controlled algorithm was developed to implement this concept in a free-field environment, in which, the noise from the primary source (eventually the propeller) and the noise measured at several locations on a representative surface (eventually the fuselage) were used to create the input for the secondary source. Experiments using a number of sinusoidal signals were conducted. An average noise reduction of 8 to 14 dB was achieved on the surface in the frequency range of 200 to 1000 Hz. Next the concept was applied to the propeller problem where the sound signal contains many discrete tones at harmonics of the blade-passage frequency. For this purpose, a pre-recorded time history of a 1/10-scale model propeller was used to drive the primary source. An average noise reduction of about 15 dB was observed at the first two blade passage frequencies, and 12 dB and 5 dB reductions were observed at the 3rd and 4th blade passage frequencies, respectively. Finally, the active noise control concept was applied to a 1/10th scale propeller, installed in an anechoic chamber with flight simulation facility. A substantial amount of noise reduction was achieved on the model fuselage surface.

1. INTRODUCTION

The fact that the high-speed turboprops offer significantly higher propulsion efficiency compared to that of the high-bypass-ratio turbofan engines has been well established[1]. However, before the potential fuel savings associated with the advanced turboprops can be realized in practice in future aircraft designs, several important technological problems must be solved[2]. One of the serious problems is concerned with the aircraft cabin noise. It is widely recognized that the cabin or interior noise of propeller-driven aircraft is significantly more annoying than the noise environment inside a jet-powered aircraft. An effective control of interior noise for large turboprop aircraft is a major obstacle in aeroacoustics, mainly because of the high levels of low-frequency discrete tones generated by the turboprops. This problem is in fact so critical for propfan aircraft that a satisfactory solution leading to an acceptable degree of passenger discomfort is one of the major factors that will determine the future of this class of aircraft.

Several solutions for the control of "air-borne" and "structure-borne" interior noise of turboprop aircraft are currently being pursued within the government and industry[3]. For air-borne cabin noise, these solutions range from the conventional concept of developing improved fuselage soundproofing methods to the more sophisticated techniques such as the use of "synchrophased" propellers to minimize the near-field noise signature impinging on selected parts of the fuselage structure. However, each of these solutions is accompanied by severe penalties and/or limitations. The soundproofing concept incurs significant economic and weight penalties. The propeller synchrophasing technique[4] requires an accurate automatic control of the propellers such that a predetermined phase relationship between the circumferential blade locations of the propellers is maintained. Although this technique has been successful in reducing the annoying variations in noise levels, known as "beats", inside the cabin of multi-engine turboprop airplanes, its effectiveness has so far been limited. This is mainly because the blade phase-holding or synchronization ability, to an accuracy better than 10°, is currently restricted significantly by electronic and mechanical control problems.

In view of the drawbacks associated with the above methods, an alternative method, commonly known as "Active Noise Control," is proposed to determine its applicability in reducing the interior noise of propeller/propfan aircraft. The basic principle of active noise control is to reduce the noise radiated from a primary source (in this case, the propeller or propfan) by using a secondary sound source. If the secondary sound signal can be made identical in amplitude but opposite in phase to the primary sound signal, then a complete cancellation can be achieved within certain regions of the space surrounding the two sources.

Although the idea of active noise control was first developed almost 50 years ago, its practical implementation did not start until 1973[5]. Most of the successful implementation of this technique, so far, is restricted to attenuate noise levels inside the air ducts by various ways[6-13]. However, there is a need to implement the active noise control concept in the free-field to attenuate noise levels in a near-field region. Some preliminary work in this direction has been done[14-16] to reduce the noise level in hallways or chambers. However, its application has not yet been directed toward the interior noise reduction for propeller driven aircraft.

The possible application of this principle to a real aircraft is shown schematically in Figure 1, where the noise generated by the propeller is desired to be minimized at the fuselage surface using a secondary source installed through the nacelle and facing toward the fuselage surface. The input to the secondary source can be determined by using the propeller signal measured at a remote location least affected by the secondary source. This signal can be modified in amplitude and phase so that the secondary source output reaching the fuselage surface would meet the active noise control requirements of reducing the blade passage tone and its harmonics.

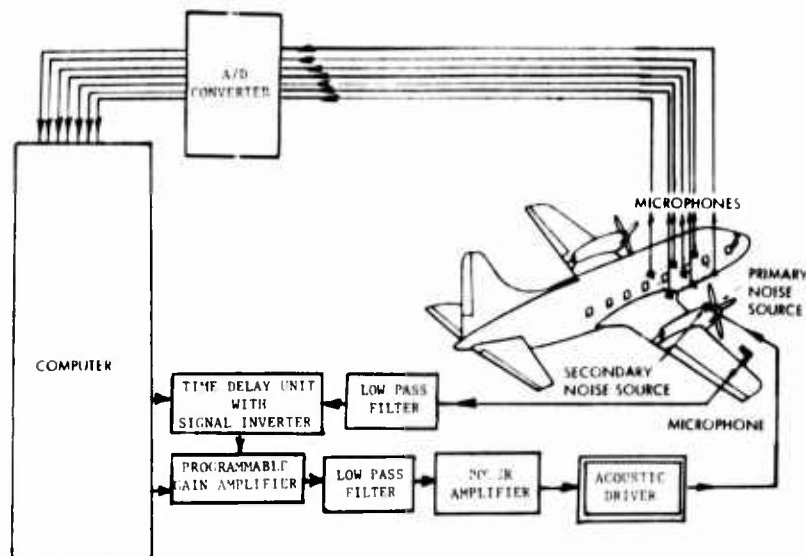


Figure 1. Computer-controlled analog active noise control system with feedback loop for propeller aircraft.

The objective of this paper is to demonstrate the applicability of "active noise control" to reduce the cabin noise of turboprop aircraft by conducting several laboratory experiments. These experiments were conducted using (1) discrete-frequency sinusoidal signal, (2) simulated propeller noise, and (3) noise generated by a 1/10th scale C-130 model propeller with simulated flight as the primary noise source. In each case an acoustic driver was used as the secondary source.

2. ACTIVE NOISE CONTROL SYSTEMS

Two separate systems were developed to implement the active sound control concept in a free-field environment. In these systems, the signal generated by the primary source (eventually the propeller) and the noise measured at several locations on a representative surface (eventually the fuselage surface) were used to create the input for the secondary source. The primary noise source in the initial study of discrete-frequency sinusoidal signals consisted of an acoustic driver excited by the electronic signal from an oscillator. The same signal was also used to "create" the input for the secondary source. For the simulated propeller noise experiments, the oscillator was replaced by an analog tape recorder on which the pre-recorded propeller noise tape was played. The output of the tape recorder was used for primary and secondary noise sources. Finally, for the model propeller experiments, where the propeller itself was the primary source, the input to the secondary source was obtained by measuring the propeller noise at a remotely mounted microphone, least affected by the secondary noise. Before feeding the secondary input signal to the secondary source, it was first inverted and then modified appropriately in amplitude and phase.

2.1 DIRECT SEARCH SYSTEM

In the direct search system, the secondary source input signal was fed to a modifier in which the signal was first inverted and then the modifications in amplitude and phase were introduced as desired. The modified signal was then fed to the secondary source. The resultant noise due to the primary and secondary sources on a representative surface were measured by several microphones mounted on it. These microphone outputs were connected to a computer through an analog to digital converter. An average mean-square value of these signals was computed, which was a representative measure of the noise level on the surface.

The operational procedure consisted of varying the phase of the input signal to the secondary source in small steps while keeping the amplitude fixed. The corresponding average noise levels were noted. From this operation an optimum phase value corresponding to the minimum average noise level was determined. Then, using this optimum phase value, the amplitude of the secondary source input was varied in steps, and the corresponding average noise levels were noted. From this exercise an optimum amplitude level corresponding to a minimum average noise level was determined. Hence, the optimum phase and amplitude values could be used for the secondary source input signal for achieving a minimum average noise level at the representative surface. The phase and amplitude of the secondary source were varied either manually, as shown in Figure 2, or using a computer. The circuit diagrams for the computer operated systems were similar to those shown in Figures 1 and 3, except the feedback process was switched off.

2.2 COMPUTER CONTROLLED OR AUTOMATIC SEARCH SYSTEM

The direct search system seemed to be simple and straightforward. However, any change in the primary noise required a complete new determination of the optimum amplitude and phase for the secondary source

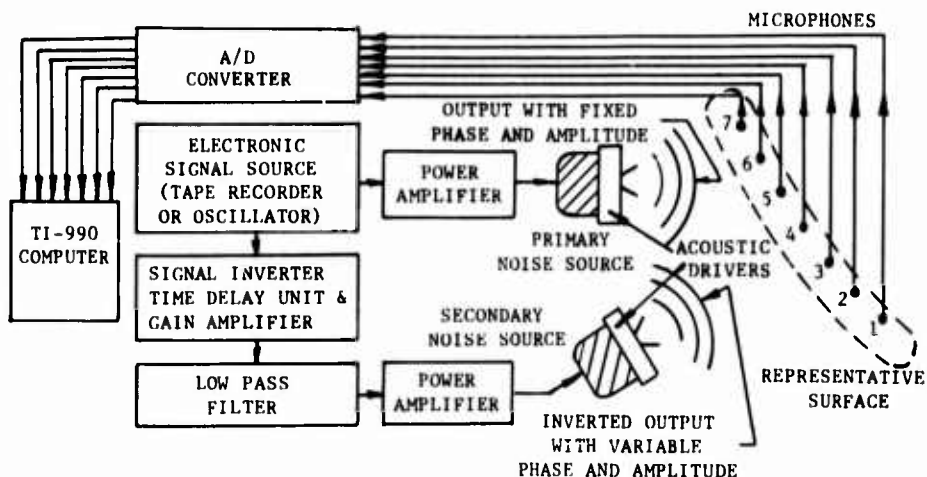


Figure 2. Manually operated direct search analog active noise control system.

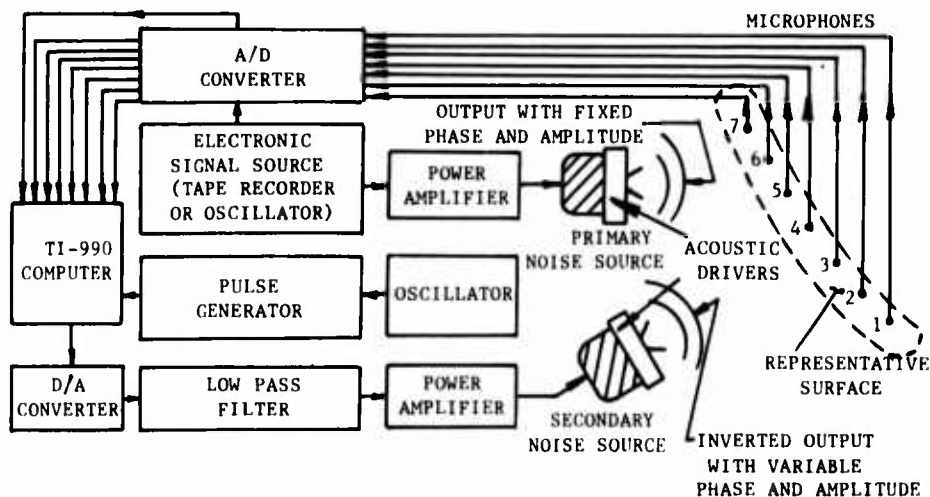


Figure 3. Computer controlled digital active noise control system with feedback loop.

input signal. Therefore, this system is not practical for an unsteady or quasi-steady type of primary noise source. Consequently, an automatic search system controlled by a computer was developed.

In this system a gradient technique was applied to determine the optimum values of amplitude and phase for the secondary source input. The secondary source input signal was first inverted. Then, initially, this signal was arbitrarily modified by the computer, both in amplitude and phase, and then fed to the secondary source. In the control process, the resultant signals due to both sources measured by several microphones on a representative surface were input to the computer via analog-to-digital converters. The average noise level of these signals was then computed and used to determine the appropriate modification to the input signal for the secondary source that would minimize the average noise level at the surface. The entire feed-back loop was computer controlled (see Figures 1 and 3). The algorithm converged rapidly, thus allowing fast generation of the required secondary source input.

The principle of the computer-controlled minimization technique can be illustrated as follows. The average noise level, $F(A, \phi)$, at the representative surface is a function of secondary source input amplitude A and the phase difference ϕ between the primary and secondary signals. Therefore, if a minimum

of F exists, then the gradients $(\partial F/\partial A)_\phi$ and $(\partial F/\partial \phi)_A$ would be zero at the optimum values of A and ϕ . To determine the optimum value of ϕ , it is evident that if $(\partial F/\partial \phi)_A$ is positive, the phase ϕ must be lowered and vice-versa until $(\partial F/\partial \phi)_A$ becomes zero. Similarly, if $(\partial F/\partial A)_\phi$ is positive, the amplitude A must be reduced and vice-versa until $(\partial F/\partial A)_\phi$ becomes zero. The algorithm was written on this principle, such that the two gradients were evaluated first time by varying A and ϕ arbitrarily. Then the subsequent modifications were introduced from the sign of the gradients thus evaluated and the process was continued until a minimum value of F was obtained.

The amplitude and phase modifications could be achieved, either by all digital processing using a digital computer (see Figure 3) or by analog systems. The analog systems consisted of an amplitude multiplier and a delay unit (see Figures 1 and 2). For direct search systems the modifier units were operated either manually or by a computer with external input, whereas, for automatic search systems, these units were programmable and were computer controlled.

In principle, the smallest step for ϕ (i.e., $\Delta\phi$), using the all digital system, was controlled by the sampling rate which was introduced using an oscillator. However, for the digital system to complete one cycle of operation, which consisted of the digitization of primary source input, modifications of its phase and amplitude, conversion of the modified data into analog signal, digitization of signals from the surface microphones, etc., the computer needed a finite amount of processing time, $\Delta\tau$. Therefore, the highest sampling rate, S , was controlled by the computer operation time, $\Delta\tau$ (i.e. $S_{\max} = 1/\Delta\tau$), and the smallest delay for the secondary signal input in this algorithm could not be less than $\Delta\tau$. For the noise minimization at a frequency f , the smallest step to the phase ϕ is

$$(\Delta\phi)_{\min} = 2\pi f \Delta\tau = 2\pi f / S_{\max}$$

Therefore, fine phase resolutions at higher frequencies could be achieved only if $\Delta\tau$ is very small. However, for most of the mini-computers used in this case, a fine phase resolution was not possible for higher frequencies. As an example, for the computer used in this study, the highest sampling rate, S_{\max} , was only about 9 KHz, which resulted in a phase resolution of $(\Delta\phi)_{\min} = 0.04f$ (degree). This gave a phase resolution of 20° for a signal of 500 Hz.

To obtain very fine phase resolutions, a continuously variable audio delay line was developed. Figure 4 shows a block diagram of the audio delay line, which contains a bucket brigade device, which

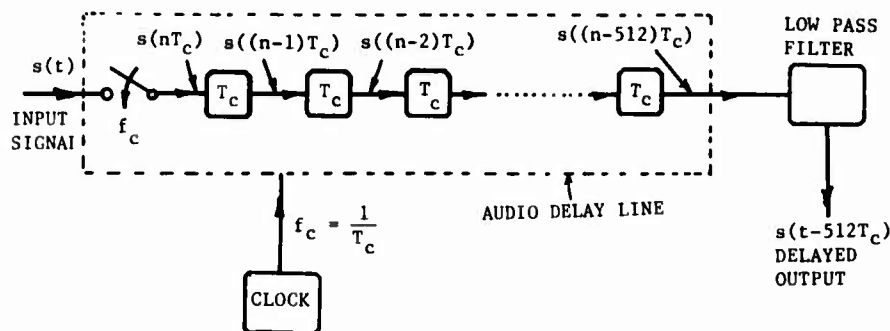


Figure 4. Block diagram of time delay system.

acted as a discrete-time transversal delay line. The continuous input signal, $s(t)$, was sampled at a rate f_c determined by an external clock source. The sampled signal was a stair-stepped discrete time signal $s(nT_c)$, where $T_c = 1/f_c$. The bucket brigade device had a fixed number of delay units, 512, so that the input signal was delayed by 512 T_c (i.e. $s_d(nT_c) = s((n-512)T_c)$). After passing through the delay line, the signal $s_d(nT_c)$ was low pass filtered to eliminate the stair-stepped discrete-time quantization effects to produce the continuous-time signal $s_d(t)$, where $s_d(t) = s(t-512T_c)$.

As indicated, the time delay introduced by the audio delay line was completely determined by f_c . For the current study, a waveform generator with frequency range of 0 - 20 MHz and frequency resolution of .000001 Hz was used. Changes in the time delay, $\Delta\tau$, as small as 1 μ sec were easily obtainable. Therefore, for $\Delta\tau = 1 \mu$ sec, the phase resolution was $(\Delta\phi)_{\min} = 2\pi f \times 10^{-6}$ radians, where f was the frequency of the input signal to the delay unit. For a 500 Hz input signal, this phase resolution became 0.18° , which was more than adequate for the purpose.

A programmable gain amplifier with very high gain resolution was also developed for the amplitude modification function. The amplifier gain, controlled by the computer, was as small as .005 volts/volt.

3. EXPERIMENTAL RESULTS

Two separate sets of experiments, one with simulated primary source and the other with a real model propeller as the primary source, were conducted in this study. The experimental results were obtained by using direct search as well as automatic search systems.

The direct search system was used to optimize the delay (phase) and amplitude of the secondary source input for the following reasons. (1) An optimum location for the secondary source with respect to the primary source was determined such that a maximum overall noise reduction was obtained on the

representative surface, while there was no increase in the noise level at any point on that surface. (2) The direct search system could indicate whether a single minimum for the average noise level existed or not. The simple gradient technique to get the minimum could be used for a function with a single minimum. For functions with multiple minima, the simple gradient technique needs to be modified to search all the minima before converging to the real minimum. (3) The direct search system was used to validate the automatic search system.

The experimental results presented in this section involve the following parameters. The time delay introduced to the input signal of the secondary source is expressed as τ (ms). For discrete frequency signal, the time delay is related to its phase, ϕ in degrees. The amplitude of the secondary source output is normalized with respect to that of the primary source and is termed as power ratio ψ . The average noise level measured on the representative surface is normalized with respect to the average noise level due to the primary source only (i.e. average noise level without active control.) This parameter is termed as relative noise level Λ . Without active control Λ becomes unity.

3.1 ACTIVE NOISE CONTROL FOR DISCRETE-FREQUENCY SINUSOIDAL SIGNAL

The experimental set up used for this case consisted of two acoustic drivers, one of which was the primary noise source and the other was the secondary noise source. Seven 1.27 cm B&K microphones were mounted on a representative surface in the free-field (see Figure 5). The input to the drivers and the

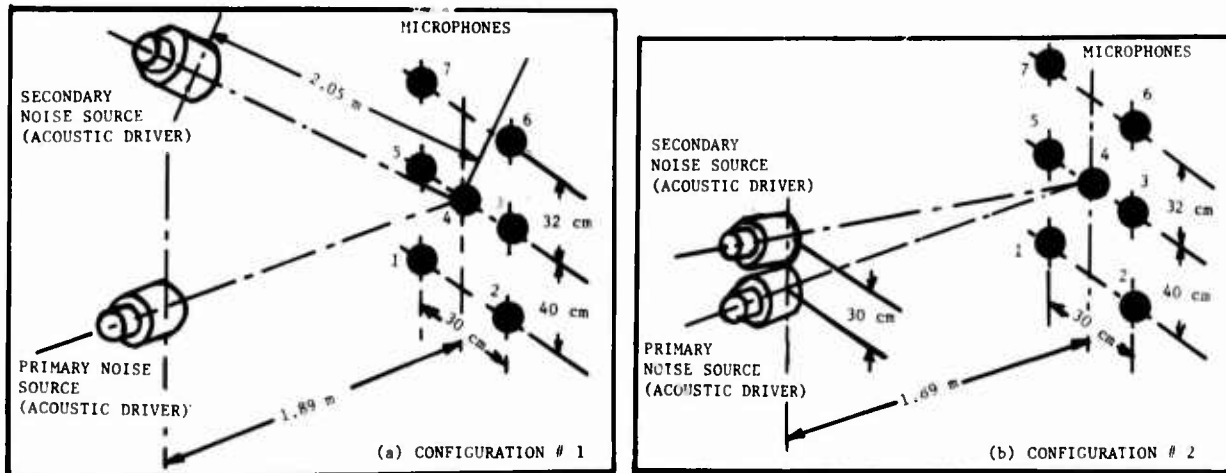


Figure 5. Experimental arrangement for simulated propeller active noise control with two configurations of secondary source, (a) secondary source far from primary; (b) secondary source close to primary.

output from the microphones were connected to the active noise control systems that were discussed in section 2. The results were obtained for discrete-frequency sinusoidal signals as input to the primary source.

The experimental results for this case are divided into two groups. Preliminary results were obtained using the direct search technique to determine the optimum configuration for the secondary source with respect to the primary at which the optimized average noise level for the whole representative surface was a minimum. The second set of results was obtained with the optimum configuration, by direct search as well as by automatic search techniques. These results were used to validate the computer controlled or automatic search algorithm as well as to determine the effectiveness of the active noise control concept.

3.1.1 PRELIMINARY RESULTS

To determine the optimum configuration for the experimental set up for which the active noise control was most effective, a parametric study was conducted by varying the location of the secondary source. The results presented here are for the cases in which the secondary source was placed at two different positions keeping the primary source location fixed.

Figure 6 shows the variation of the average noise level as well as the noise levels at each individual microphone location with respect to the phase, ϕ , of the secondary source input for a sinusoidal signal of 239.5 Hz. The input levels for both the sources were kept the same in this case (i.e. $\psi = 1$). Although a minimum for the average noise level was reached at $\phi = 180^\circ$, no reduction in noise level was obtained. The secondary source for this test was located away from the primary source (configuration #1 in Figure 5(a)) and, therefore, an optimum phase for one microphone location was not optimum for another, due to the individual phase relationship. This can be easily observed in Figure 6, where the minimum noise levels for each microphone occurred at different phase angles. These minimum noise levels for individual microphones are significantly lower than the noise levels without active control. However, the average noise level at $\phi = 180^\circ$ due to all the microphones was not lower than the average level due to the primary source. Therefore, while the noise levels were attenuated at some locations on the representative surface, there were other positions where the noise levels were increased above the primary noise level at the optimum condition.

Similar results, presented in Figure 7 for a sinusoidal signal of 1000 Hz, confirm the above conclusion, except that the average noise level at the optimum phase ($\phi = -80^\circ$) in this case was slightly lower than the level without active control (i.e., $\Lambda = 0.72$).

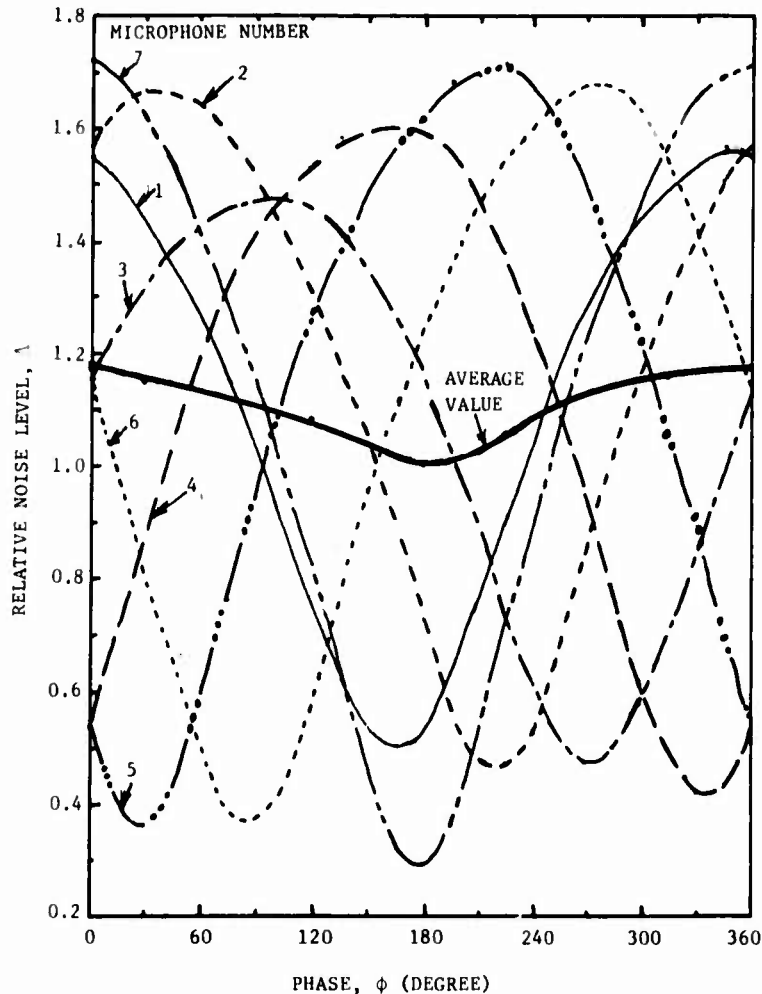


Figure 6. Variation of noise levels at individual microphone locations and the average noise level with respect to the phase, ϕ of the secondary source input for configuration #1, the power ratio, $\psi = 1$; primary source output being a 239.5 Hz discrete frequency sinusoidal signal.

The above results led to further investigations to achieve noise reductions at every point on the surface. When the secondary source was located at configuration #1, which was away from the primary source, it was obvious that the phase relationships between the primary and secondary signals at individual points on the surface were not identical. To maintain a constant phase relationship at every point on the surface, both primary and secondary sources must be placed precisely at the same location. However, physically this was not realizable. Therefore, the secondary source was then placed on a horizontal plane which contained the primary source and as close to it as possible (i.e. orientation #2 as shown in Figure 5(b)). For this configuration the average attenuations achieved were very high; but more importantly, attenuations of nearly uniform magnitude were achieved everywhere on the surface at the same optimum condition. As an example, in Figure 8 the noise levels at several locations on the surface, as well as the average noise level for a 239.5 Hz sinusoidal signal, are plotted with respect to phase ϕ of the secondary source input, keeping $\psi = 1$. Clearly a substantial noise reduction was achieved at each microphone position on the surface, and thereby, an equal amount of noise reduction was achieved on the average level. In addition, the optimum phases for minimum noise at individual points, as well as for average noise level, were more or less equal. Therefore, this orientation of the secondary source was considered to be the optimum.

To establish an optimization procedure for the direct search technique the effect of phase and amplitude variations on average noise level Λ were further studied for several discrete-frequency sinusoidal signals. For 239.5 Hz, the results are presented in Figure 9. In Figure 9(a) the average noise levels, Λ , are plotted with respect to ϕ at several fixed secondary source input levels (ψ). For each ψ , a minimum was obtained at about $\phi = 180^\circ$, even though these minimum levels were different in magnitude. The lowest minimum was obtained for $\psi = 0.6$. Figure 9(b) shows the average noise level distribution with respect to ψ at several fixed ϕ . Here one arrives at the same conclusion as that of Figure 9(a), except that there was no common minimum of Λ with respect to ψ for all the fixed phases. However, minimum average noise levels were obtained at phase angles around $\phi = 180^\circ$ which was established as the optimum phase in Figure 9(a). Therefore, in the direct search technique, it was essential to determine the optimum phase first for a fixed ψ ; and then, keeping this optimum phase fixed, the power ratio ψ was to be optimized.

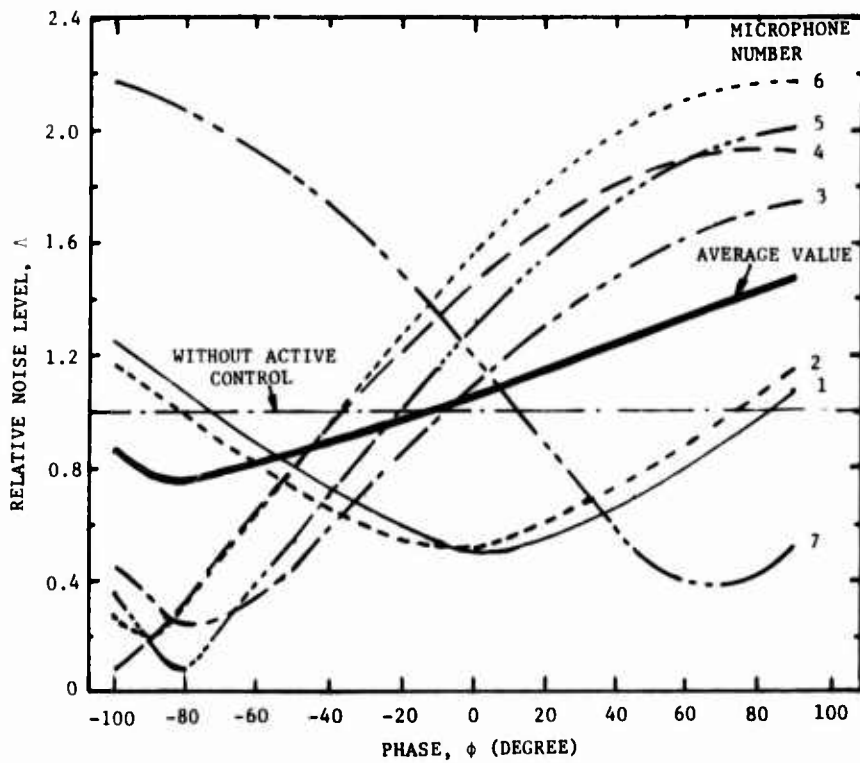


Figure 7. Variation of noise levels at individual microphone locations and the average noise level with respect to the phase, ϕ of the secondary source input for configuration #1; the power ratio, $\psi = 1$; source output signal being a 1000 Hz discrete frequency sinusoidal signal.

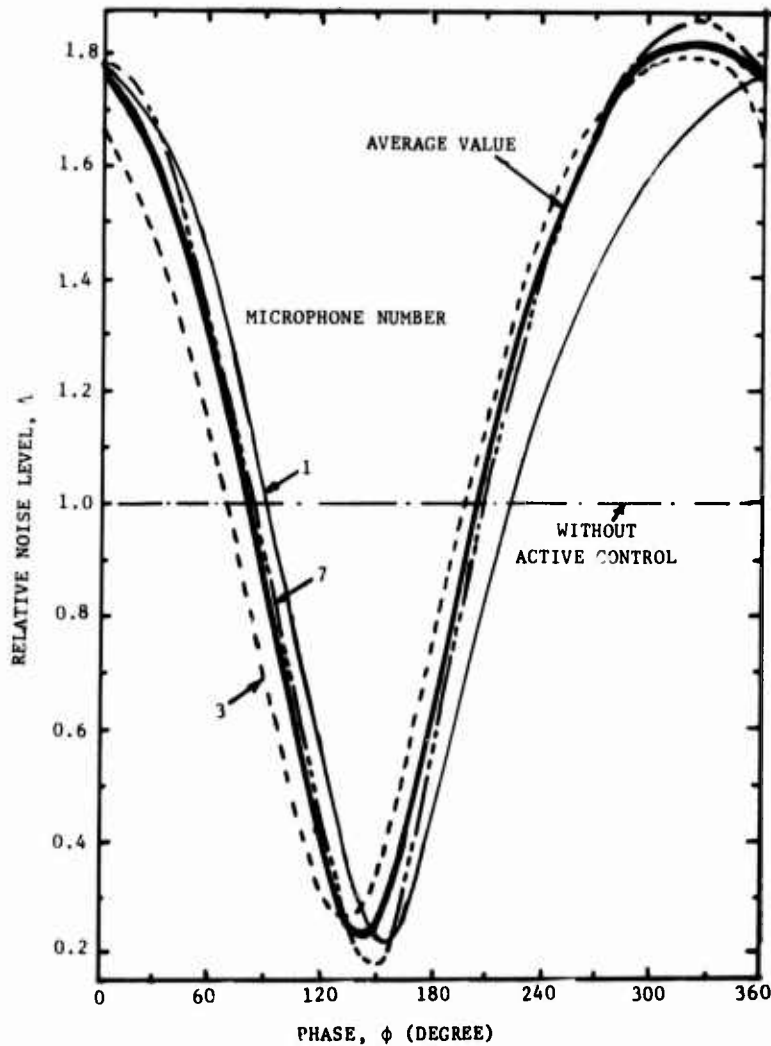


Figure 8. Variation of noise levels at individual microphone locations and the average noise level with respect to the phase, ϕ of the secondary source input for configuration #2; the power ratio, $\psi = 1$; primary source output being a 239.5 Hz discrete frequency sinusoidal signal.

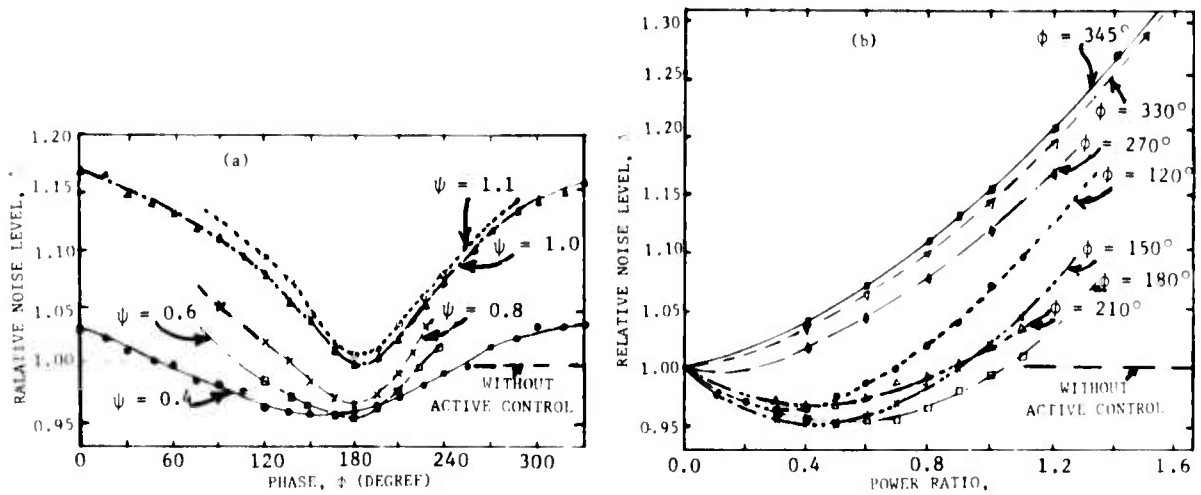


Figure 9. Noise level variation (a) with respect to ϕ at fixed ψ and (b) with respect to ψ at fixed ϕ for configuration #1; primary source output being a 239.5 Hz discrete frequency sinusoidal signal.

Examination of Figures 6 through 9 highlights another important feature, that, for discrete-frequency noise, only a single minimum existed for the average noise level distribution with respect to ϕ and ψ . This behavior simplified the automatic search technique significantly.

3.1.2 VALIDATION OF AUTOMATIC SEARCH SYSTEM

To establish the effectiveness of the computer controlled minimization algorithm (i.e. automatic search technique), experiments using a number of sinusoidal signals were conducted. The computer controlled automatic search technique was used to determine the maximized attenuations at various frequencies. The attenuations thus obtained were compared with the values determined by the direct search technique. The agreement was excellent. As an example, for 500 Hz, shown in Figure 10, an average

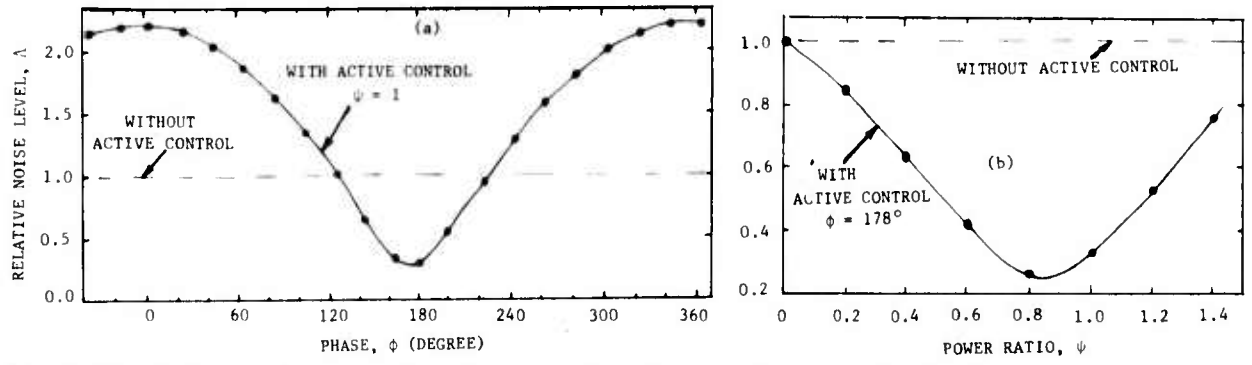


Figure 10. Variation of average noise level (a) with respect to ϕ at $\psi = 1$ and (b) with respect to ψ at an optimum phase value $\phi = 178^\circ$, primary source output being a 500 Hz discrete frequency sinusoidal signal.

attenuation of 12 dB (i.e. $\Lambda = .25$) was obtained at $\phi = 178^\circ$ for $\psi = 1$ by the direct search technique. This attenuation was further increased to 13 dB ($\Lambda = .225$) by varying the secondary source amplitude at $\phi = 178^\circ$ (see Figure 10(b)). The average attenuation of 13 dB thus obtained by the direct search technique at 500 Hz agreed very well with that derived by the automatic search technique, shown in Figure 11. This figure shows an average noise reduction of 8 to 14 dB on the surface in the frequency range 200 to 1000 Hz. It is interesting to note that, at a single point on the surface, attenuations as high as 50 to 60 dB could be achieved at some frequencies.

3.2 ACTIVE NOISE CONTROL FOR SIMULATED PROPELLER NOISE

The next step was to determine if the concept could be applied to propeller noise where the sound signal contains many discrete tones at harmonics of the blade-passage frequency. The experimental set up used for this case was same as that used for discrete-frequency sinusoidal signal tests except that the oscillator was replaced by a tape recorder, the output of which was the simulated propeller noise. For this purpose, a pre-recorded time history of propeller noise from a 1/10-scale C-130 model propeller was used as input to the primary source (acoustic driver).

The propeller signature recorded on the tape contained dominant noise levels at the blade passage frequency and its first three harmonics, as shown in Figure 12(a). The sound pressure levels (SPL) of the harmonics are 13 to 20 dB lower than the fundamental. However, when this signal was fed to the primary or secondary noise source (i.e. acoustic driver) and the spectral outputs of the microphones were

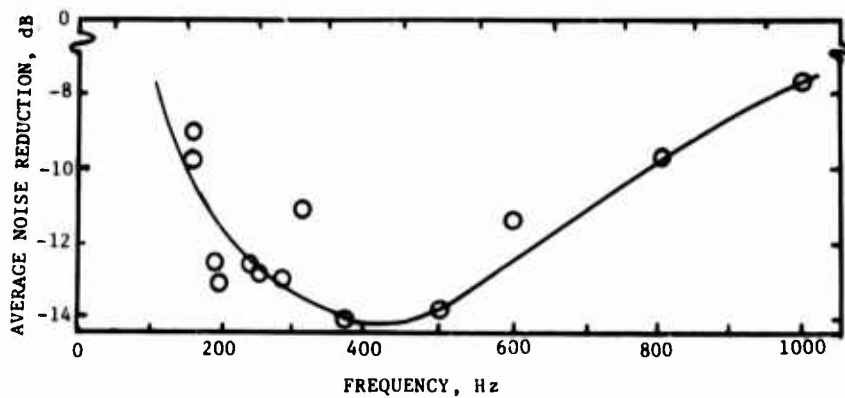


Figure 11. Maximized average attenuations at various discrete frequencies achieved by active noise control.

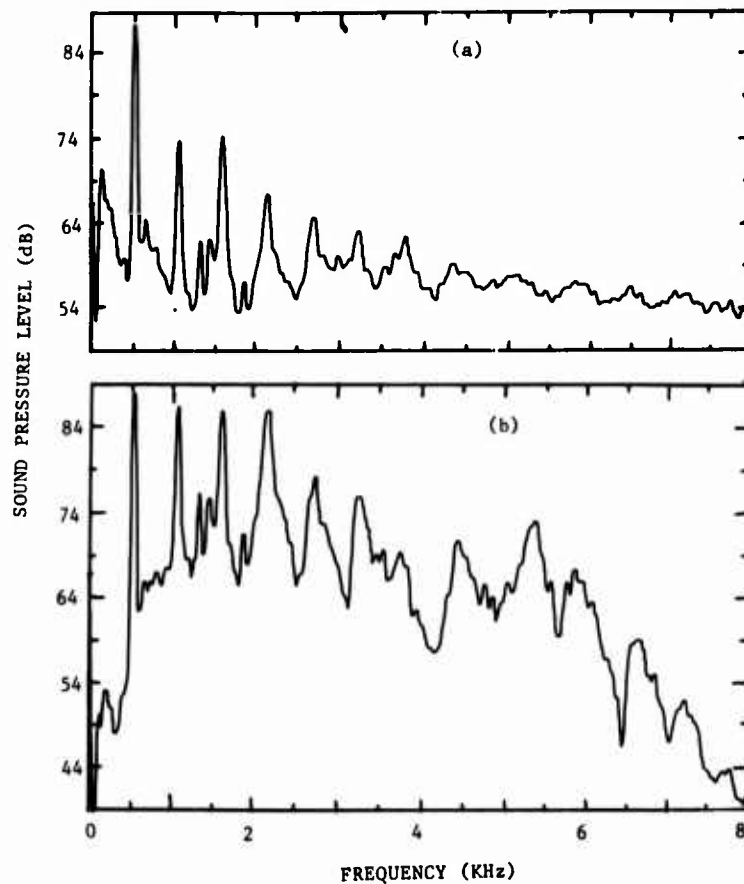


Figure 12. Spectral distribution of propeller noise; rotational speed of the propeller = 8,250 rpm without flight simulation; (a) directly measured from a model propeller; (b) output of secondary source (acoustic driver) with propeller noise as input to it.

examined, the SPLs of the harmonics seemed to be as high as the fundamental, as shown in Figure 12(b). This was apparently due to the characteristics of the acoustic driver used in this case which generated the harmonics of the fundamental frequency. Therefore, the noise levels observed in the free field were the sum of the propeller noise and the harmonics generated by the acoustic driver.

Two distinct approaches were taken to implement the active control to the simulated propeller noise. In one case, the harmonics were attenuated individually by separating them prior to feeding the signal to the secondary source. In the second approach, the complete noise signature was utilized to attenuate all the harmonics simultaneously.

3.2.1 ATTENUATION OF INDIVIDUAL HARMONICS

In this approach the tape recorded propeller noise for secondary source input is fed through a number of low and high pass filters to separate each of the four harmonics and then each of the harmonics is modified individually for its maximum attenuation. Finally these modified signals are mixed together and

fed to the secondary source for active control. The average noise level for each harmonic is used separately for the modification of the corresponding input to the secondary source. Therefore, the noise levels measured by individual microphones are Fourier transformed to separate the noise level of each harmonic.

Since only two active control electronic systems were available at the time, attenuation of only the first two blade passage harmonics was attempted. The active noise control results were excellent. For two microphone locations, the results with and without active control are shown in Figure 13 in terms of

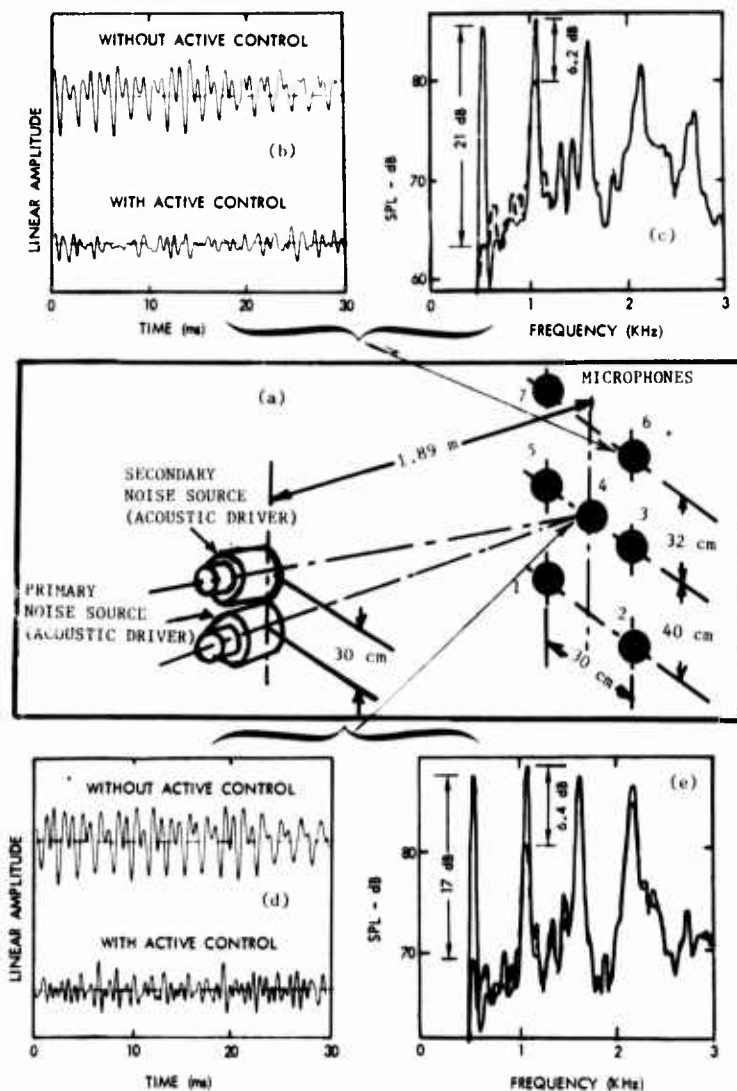


Figure 13. Effect of active noise control on propeller noise signature and noise level reduction at first two blade passage frequencies for simulated propeller noise experiment; rotational speed of the propeller = 10200 rpm, simulated flight speed = 75 m/s; (a) experimental set up; (b) and (c) microphone location #6; (d) and (e) microphone location #4.

signal time histories and spectral levels. In general, the attenuation at various microphone positions ranged from 10 to 25 dB for the fundamental tone and from 4 to 8 dB for the first harmonic.

3.2.2 ATTENUATION OF COMPLETE NOISE SIGNATURE

In this approach, the noise signature, as a whole, is inverted first and then modified appropriately prior to feeding to the secondary source. Before applying the automatic search technique for active noise control, the direct search technique was again used here to determine the maximum attenuation and the corresponding optimum conditions for the secondary source input (see Figure 14). This was done to determine if a similar single minimum characteristic for single tones still existed for a primary signal with multiple tones. Figure 14 clearly shows that this is indeed the case. The computer controlled algorithm for the automatic search technique was then validated by comparing these results with those obtained by the automatic search technique.

At the optimized condition shown in Figure 14, the output of all the microphones mounted on the representative surface was examined. Typical results are shown in Figures 15 and 16. Figure 15 indicates the effect of active control on propeller noise signature as observed at one of the microphone locations. The frequency domain results for two microphone locations are shown in Figure 16. A noise reduction of 13 to 17 dB is observed at the first two blade passage frequencies, and 12 to 14 dB and 5 to 9 dB reductions are observed at the 3rd and 4th blade passage frequencies, respectively.

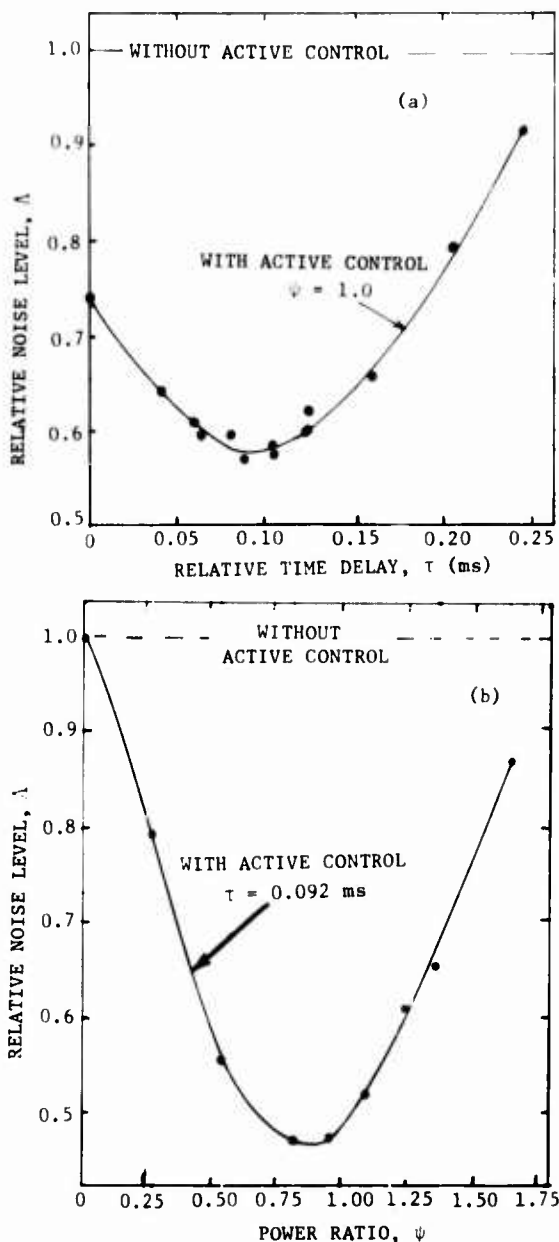


Figure 14. Variation of average noise level (a) with respect to τ at $\psi = 1$ and (b) with respect to ψ at an optimum delay of $\tau = 0.092$ ms, primary source output being the simulated propeller noise with rotational speed = 10200 rpm and simulated flight speed = 75 m/s.

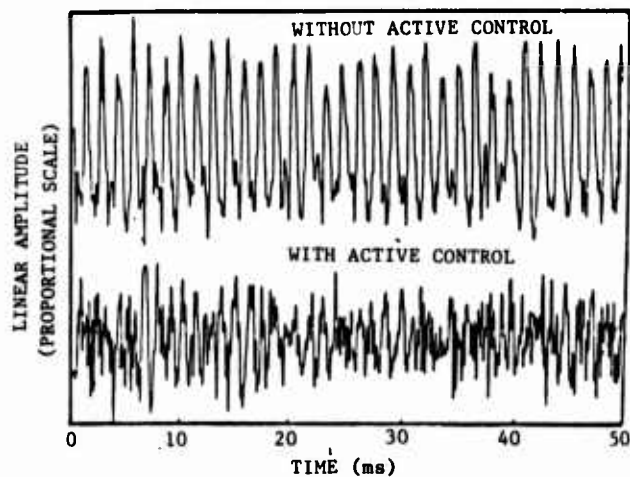


Figure 15. Effect of active control on propeller noise signature for simulated propeller noise experiment; rotational speed of the propeller = 10200 rpm; simulated flight speed = 75 m/s.

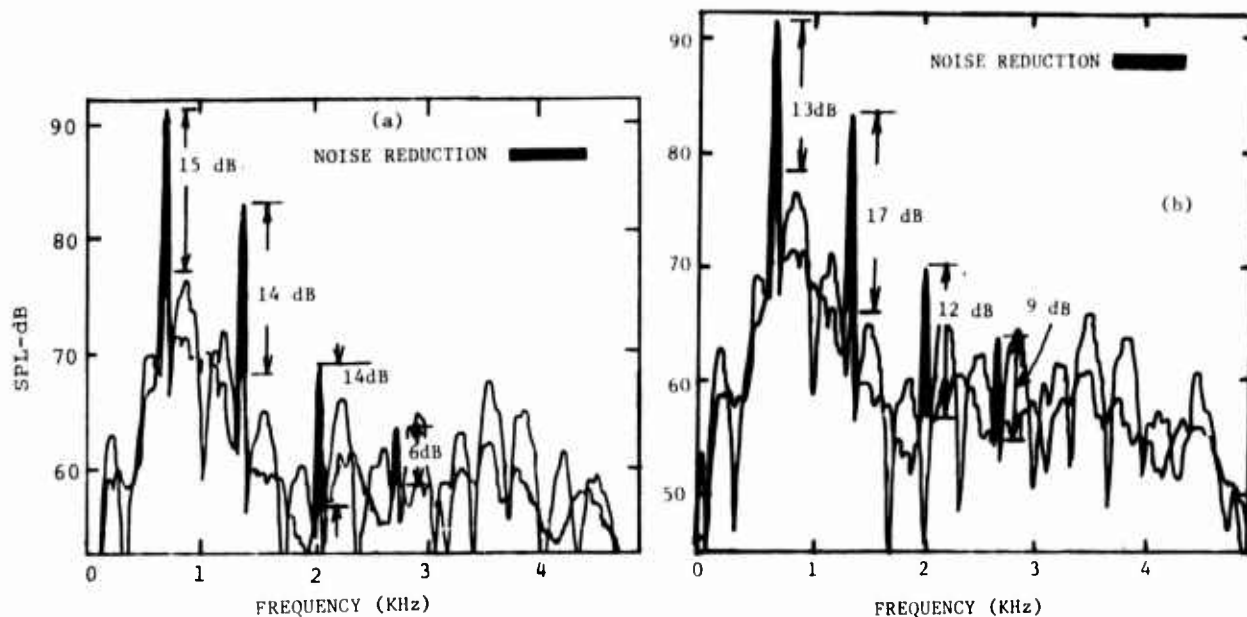


Figure 16. Reduction of noise levels at first four propeller blade passage frequencies due to active noise control for simulated propeller noise experiment; rotational speed of the propeller = 10200 rpm, simulated flight speed = 75 m/s; (a) microphone location #4; (b) microphone location #6.

3.3 ACTIVE NOISE CONTROL FOR A REAL MODEL PROPELLER

To provide the final proof of the validity of the active noise control concept, experiments using a 1/10-scale C-130 model propeller were conducted in the Lockheed anechoic wind tunnel. The test arrangement is shown in Figure 17. In this case, the input to the secondary source was obtained by measuring the propeller noise at a remotely mounted microphone, least affected by the secondary source.

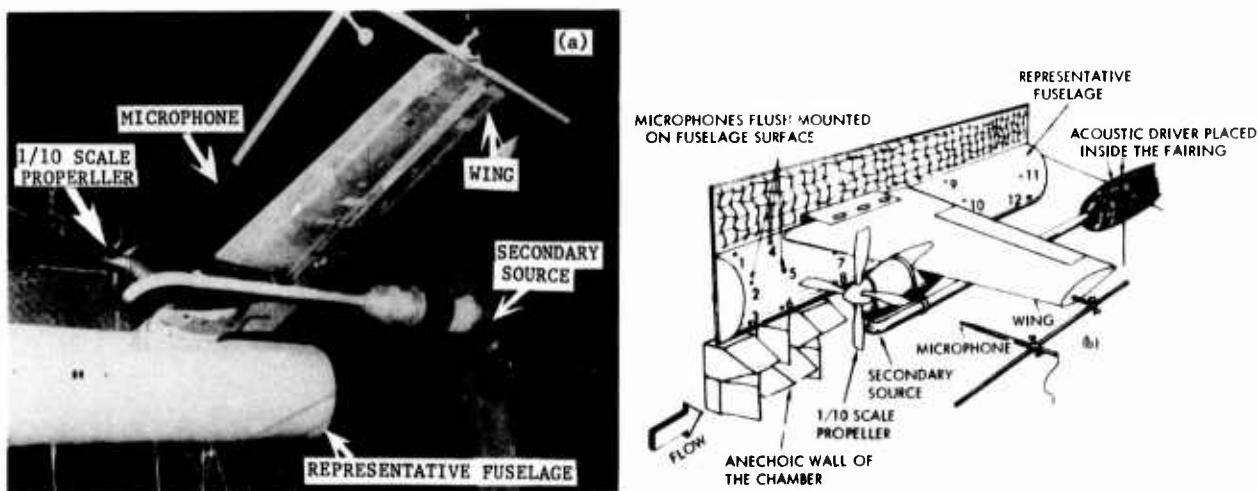


Figure 17. Arrangement for active noise control experiment using a 1/10-scale C-130 model propeller; (a) photographic view; (b) schematic view.

The propeller was run at various rotational speeds with different simulated flight velocities. A significant noise reduction was achieved at various microphone locations. The average noise level attenuation obtained by the direct search technique is shown in Figure 18. In addition, the active noise control results for a typical test condition at one microphone location are shown in Figure 19. The pressure-time histories, shown in Figure 19(a) clearly indicate that the peak amplitudes of fluctuating pressure are reduced drastically by applying active noise control. While the noise reduction for the fundamental blade passage frequency is significant, as shown in Figure 19(b), the levels for the other tones did not reduce significantly as compared to the simulated propeller test results (see Figure 16). The possible reasons for such results are discussed next.

It was observed from the preliminary tests that a maximum noise reduction was achieved when the secondary source was placed close to the primary. However, for the real propeller tests, the secondary noise was fed through a tube located behind the propeller and underneath the nacelle (see Figure 17). This

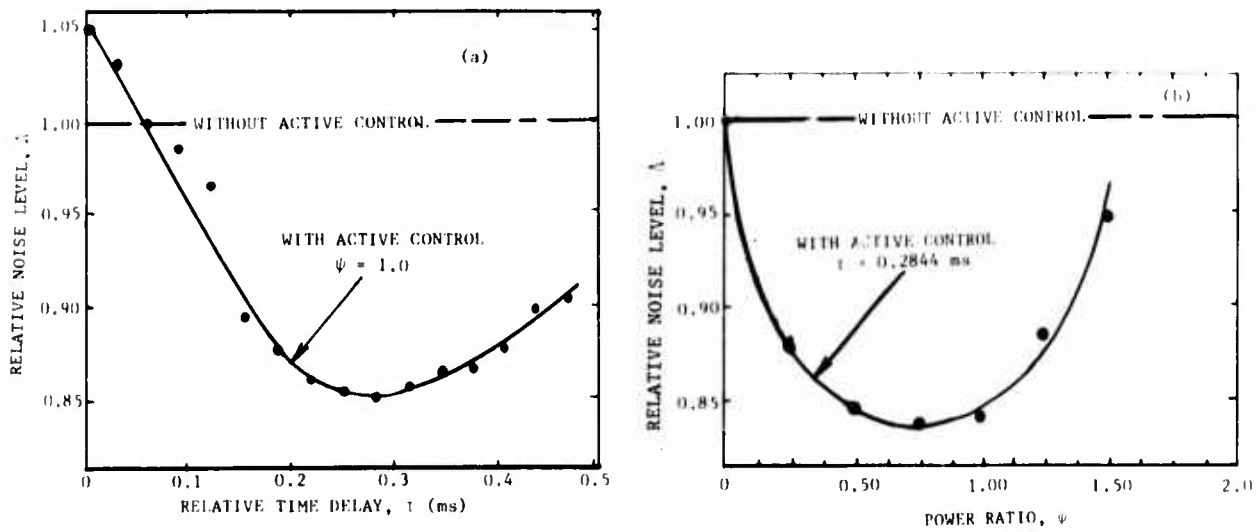


Figure 18. Variation of average noise level (a) with respect to τ at $\psi = 1$ and (b) with respect to ψ at an optimum delay of $\tau = 0.2844$ ms, primary source being a 1/10 scale model propeller with rotational speed = 10200 rpm and simulated flight speed = 75 m/s.

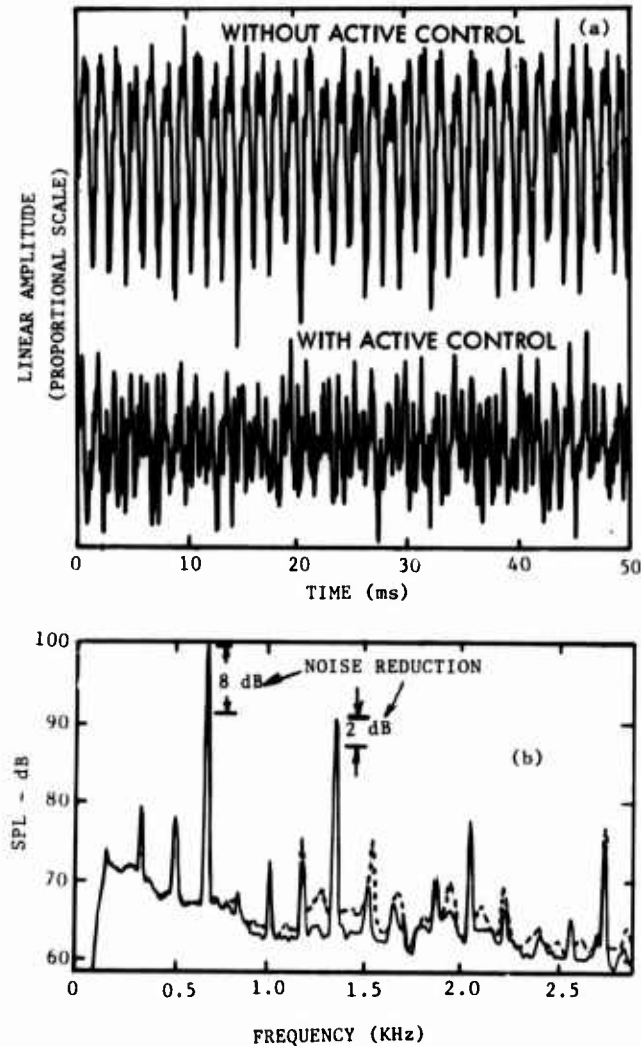


Figure 19. Active noise control for a 1/10-scale model propeller noise experiment; rotational speed = 10200 rpm, simulated flight speed = 75 m/s; (a) effect of active control on propeller noise signature; (b) reduction of noise levels at first four blade passage frequencies.

position was considerably off-center of the propeller, about 4 inches compared to its diameter of 16 inches. This may be one reason for the poor result. Since the overall propeller noise is focused from its center, it is expected that a better noise reduction would be achieved by introducing the secondary sound at the propeller axis through the nacelle.

For the simulated propeller noise tests, identical signals were fed to the primary and secondary sources and both the sources were also identical acoustic drivers. Therefore, the output of these sources were very similar, and this resulted in a very effective active noise control in this situation. On the other hand, for the real propeller tests, the secondary source output was affected by two adverse factors: (a) possible contamination of the primary noise measurement by the secondary noise, and (b) distortion of the secondary signal due to the non-flat amplitude and the non-linear phase responses of the acoustic driver and associated ductwork. For these reasons, the secondary source output was considerably different from that of the primary source output which was the noise of a real propeller in this case. Hence, an effective application of active noise control in this case needs to overcome the above problems. To minimize these problems, individual active control electronic systems for each tone could be used. Each tone could be appropriately modified after being separated by band pass filters. These modified signals could then be mixed together before being fed to the secondary source.

4. FUTURE WORK

In summary, it is indicated that "active noise control" is indeed a viable technique to reduce the noise levels inside a propeller or propfan aircraft. To exploit this concept, further work is necessary.

Even though the experimental results obtained in the laboratory environment are very encouraging, the implementation of active noise control on a real full-scale propeller aircraft is quite involved. A lot of hardware planning is clearly needed. In particular, the requirements associated with (a) the secondary noise source, (b) the microphone placement on the fuselage surface, and (c) the various electronic equipment, such as the computer, programmable delay unit, power supplies, etc., need to be studied and resolved.

REFERENCES

1. J. F. Dugan, B. A. Miller, E. J. Graber, and D. A. Sagerser The NASA High-Speed Turboprop Program NASA TM-81561, 1980.
2. An Accelerated and Enhanced Advanced Turboprop Program A report prepared by NASA (OAST) at the request of the Committee on Science and Technology, U. S. House of Representatives, 1981.
3. F. B. Metzger Strategies for Aircraft Interior Noise Reduction in Existing and Future Propeller Aircraft SAE Paper No. 810560, 1981.
4. J. F. Johnston, R. E. Donham and W. A. Guinn Propeller Noise Signatures and Their Use Journal of Aircraft, Vol. 18, No. 11 1981.
5. M. A. Swinbanks The Active Control of Sound Propagation in Long Ducts Journal of Sound and Vibration, Vol. 27, No. 3, 1973.
6. M. J. M. Jessel and G. A. Mangiante Active Sound Absorbers in an Air Duct Journal of Sound and Vibration, 23(3), 383-390, 1972.
7. G. A. Mangiante Active Sound Absorption Journal of Acoustical Society of America, Vol. 61, No. 6, June 1977.
8. J. H. B. Poole and H. G. Leventhall An Experimental Study of Swinbank's Method of Active Attenuation of Sound in Ducts Journal of Sound and Vibration, 49(2), 257-266, 1976.
9. J. H. B. Poole and H. G. Leventhall Active Attenuation of Noise in Duct Journal of Sound and Vibration, Letter to the Editor, 57(2), 308-309, 1978.
10. Kh. Eghtesadi and H. G. Leventhall Active Attenuation of Noise: The Chelsea Dipole Journal of Sound and Vibration, 75(1), 127-134, 1981.
11. Kh. Eghtesadi and H. G. Leventhall Active Attenuation of Noise: The Monopole System Journal of Acoustical Society of America, 71(3), March 1982.
12. M. Berengier and A. Roure Broad-Band Active Sound Absorption in a Duct Carrying Uniformly Flowing Fluid Journal of Sound and Vibration, 68(3), 437-449, 1980.
13. G. E. Warnaka and J. Tichy Acoustic Mixing in Active Attenuators Inter-noise, 1980.
14. C. F. Ross A Demonstration of Active Control of Broadband Sound Journal of Sound and Vibration, 74(3), 411-417, 1981.
15. C. F. Ross An Algorithm for Designing a Broadband Active Sound Control System Journal of Sound and Vibration, 80(3), 373-380, 1982.
16. C. F. Ross An Adaptive Digital Filter for Broadband Active Sound Control Journal of Sound and Vibration, 80(3), 381-389, 1982.

ACKNOWLEDGEMENTS

The work presented in this paper was accomplished as a part of Lockheed's Internal Research and Development Program. The authors are thankful to Dr. K. K. Ahuja for many useful discussions with him.

ROUND TABLE DISCUSSION

Mr. Lars Ohman, NAE

Gentlemen, we are now in the concluding phase or the grand finale of this most interesting symposium. Let me first introduce the members of the Round Table Discussion Panel. To my immediate left you have Dr. Hank Tijdeman who is Head of the Fluid Dynamics division of NLR Amsterdam, next to him is Derek Peckham, Superintendent of the Design Methods Division of the Aerodynamics Department of the RAE in Farnborough England and next to him is Peter Sacher, Head of the Theoretical Aerodynamics Department of the Military and Helicopter Division of MBB in Munich, and at the far end is Professor Geoff Lilley, who until recently was Professor of Aeronautics and Astronautics at the University of Southampton. The procedure for this RTD will be as follows: each of my colleagues here will give a short summary of one of the sessions of the Symposium in the order that they were given in the program. After that, the floor is yours. Judging by your very active participation during the course of the Symposium, I think that we can expect a very lively RTD discussion as well. With this I pass the floor over to Dr. Tijdeman.

Dr. Tijdeman

As far as the development of advanced propellers is concerned, roughly a distinction in the following phases can be made:

- (1) an exploratory phase, that started in the mid 70's,
- (2) an assessment and development phase, that (at least in some nations) is going on at present,
- (3) an application phase, in which the advanced propeller technology is ripe for application (1990?).

A similar development as sketched here we have seen before in the supercritical wing technology. It can be stated that the latter technology should not have been possible without the invaluable contribution of computational fluid dynamics. In my opinion the same is true for the advanced propeller technology. The application of 2-D advanced airfoils, obtained via CFD methods, has been demonstrated in a number of papers presented in our meeting, namely paper 5 (Bocci), 6 (Rodde, Cuny, Thibert), 14 (Barber), 16 (Zimmer, Hoffmann) and 30 (Metzger). Computational methods for 3-D propellers clearly are in a less-development stage. The 3-D methods for propellers can be classified in the following groups: (1) methods for axisymmetric flow, including axisymmetric installation effects like hubs and spinners, (2) methods for nonsymmetrical flow (the usual situation for installed propellers) and (3) methods to compute dynamic loads. The axisymmetric flow case, in which we have "steady" loads relative to the rotating axis system of the propeller, is of importance for the aerodynamical design and analysis of the propeller itself. Moreover, valuable information about the wake can be obtained. The "steady" loads also form the input for the noise computations.

In Fig. 1 it has been attempted to list the various methods presented in our meeting in order of the degree of sophistication. In the most advanced method the Navier-Stokes equations are solved. Such a solution is mentioned in the NASA overview paper (12). Impressive results, based on solutions of the full Euler equations were presented in the paper by Bousquet (2) and the earlier mentioned NASA overview (12). Solutions of the full potential equation were given in papers (2) and (3). The class of methods mentioned so far are of a non-linear nature. As a next category, in which small perturbations are assumed, a number of papers (7, 9, 10, 11) presented methods based on the linearized Euler equations and finally there were some other papers (5, 12, 16) based on simpler approximations.

The effect of the wake on aircraft components, an important aspect of propeller propulsions, has been treated in the papers by Lilley and Emarati (20), Prabhu (22) and Eshelby (8).

My guess is that for the aerodynamic analysis of advanced propellers non-linear methods are required, while for the design mode a linearized method will be sufficient.

The nonsymmetric flow case, requiring a time-dependent computation, gives as a result the time-dependent loads on the propeller (1-P and multiple P-loads) and time-dependent contents of the wake, being important as a source of excitation for AC-components. Most of the methods presented in our meeting were based on the linearized Euler-equations (see Fig. 2). These methods are closely related to methods using the acceleration potential. My estimate is that for advanced, installed propellers a non-linear method is required, because the disturbances cannot be considered to be small. (I would like to have the opinion of the audience on this matter.)

With respect to the computation of dynamic loads, I refer here to so-called motion-induced loads. These loads are important for whirl-flutter studies (which can be treated in a quasi-steady way) and blade-flutter (which requires a fully unsteady approach). Here the guess is that linear methods, if linearized around the correct "mean steady" flow field, will do the job.

One of the main problems associated with the application of propellers is the noise problem. Noise computations require as an input the "steady" aerodynamic loads on the propeller and the "time-dependent" loads due to flow nonsymmetry. The noise field generated by the propeller then can be determined. A complicated additional step is the translation into interior noise, taking into account the transmission through the fuselage structure.

All the noise prediction methods presented here (see Fig. 4) are based on the linearized Euler equations or acceleration potential equation. It is estimated that for noise predictions linearized theory is sufficient to obtain results for practical applications.

To conclude this short summary on the computational aspects, it can be stated that further development of the computational "tools" is essential for a successful development of the advanced propeller technology. These "tools" should be able to treat rather complex flow patterns. However it is not necessary to start at zero level: the last decade an enormous development in CFD methods and computer technology has taken

place, which implies that there is an excellent base for further developments. It will be clear also that still a lot of work has to be done in this area.

FIG. 1 :

METHODS FOR AXISYMMETRIC FLOW

("STEADY" LOADS ON PROPELLER)

- PURPOSE: - DESIGN
 - ANALYSIS
 - INPUT FOR NOISE COMPUTATIONS

<u>METHODS:</u>	<u>PAPER:</u>	<u>WAKE STRUCTURE*</u>
- Navier-Stokes Equations	12 Mikkelson c.s.	PART OF SOLUTION
- Full-Euler Equations	2 Bousquet 12 Mikkelson c.s.	
- Full-Potential Equation	2 Bousquet 3 Luls, Lollercandy	
- Linearized Euler Equations/Lifting Surface	7 Schulten 9 Das 10 Farassat 11 Long, Watts	INHERENTLY INCLUDED
- (Curved) Lifting Line & Simpler	5 Bocci 12 Mikkelson 16 Zimmer, Hoffmann	TO BE PRESCRIBED

non-linear
LINEAR

* Effect of Wake on A/C components in Paper 8 (Eshelby), 20 (Lilley, Emarati), 22 (Prabhu)

ESTIMATE: Non-Linear Method (Incl. B.L.- Effect) for Propfan Essential

FIG. 2 :

METHODS FOR NON-SYMMETRIC FLOW

- PURPOSE: - Time-Dependent Loads on Propeller a.o. 1-P Loads)
 - Excitation of A/C
 - Input for Noise Computations

<u>METHODS :</u>	<u>PAPER :</u>
- Navier-Stokes Equations	Not Presented
- Full Euler Equations	
- Full Potential Equation	
- Linearized Euler; Accel. Potential	7 Schulten 9 Dass 10 Farassat 11 Long, Watts
- Lifting Line	30 Metzger

ESTIMATE : Probably Non-Linear Approach Required for Propfan

FIG. 3 :

METHODS FOR DYNAMIC LOADS

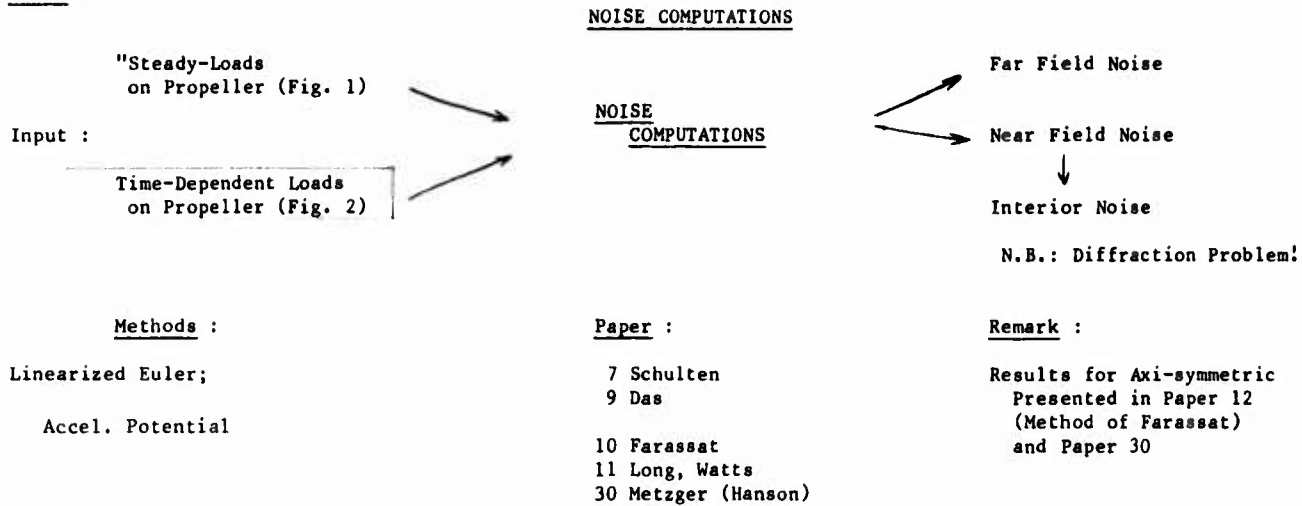
Motion-Induced

- Low-Frequency (Quasi-Steady) : Whirl Flutter
 Higher-Frequency (Unsteady) : Blade Flutter

No Methods Presented.

ESTIMATE : Linear Methods Applicable (If Linearized Around Correct "Mean Steady" Flow Field

FIG 4 :



ESTIMATE : Linearized Methods will Suffice

Mr. D. H. Peckham, RAE

I wish to highlight just a few points on propeller testing, mainly from the performance point of view. Firstly, the revival of interest in propellers has meant that an increasing number of windtunnels are being used for propeller testing. Also, the attempts to squeeze a few percent more efficiency out of propellers has increased the need for accuracy in such experiments. Inevitably, it seems to me, rigs for propeller testing are quite bulky. Even if the nacelle is a streamlined shape, there still has to be a substantial support strut, and sometimes in addition, a further strut bringing in power supplies. Now, not only do such rigs introduce substantial blockage, they can also give asymmetric blockage. Clearly, this affects the flow distribution in the plane of the propeller. Also, as mentioned by Dr. Williams, the wakes from such rigs may still persist to some extent around the tunnel circuit. I cannot recall any speakers actually presenting evidence on the flow quality upstream of their rigs, that is, in the plane of the propeller under test. The effects of blockage and flow distribution may not be serious in comparative tests, but such effects would have to be accounted for when one needs to establish, as accurately as possible, the performance of a full-scale propeller in relation to performance guarantees. Another point, I cannot recall any mention of tunnel wall corrections, nor anybody brave enough to present results on the same propeller in both open and closed jet working sections; I do not know how important this question is. I would be interested to hear later on any comments from members attending this symposium.

There were some mentions of Reynolds number effects, roughness effects and effects of leading edge de-icing equipment. With the Reynolds number of even full scale propellers being on the low side, one can expect that we are in a Reynolds number range where quite large effects can be expected between model scale and full scale Reynolds numbers. A figure of half a million Reynolds number was mentioned a number of times as the desirable minimum value. I cannot recall that being challenged.

Finally, we have been warned of some of the dangers in propeller testing by Mr. Bass, and I don't think that he is more accident-prone than other workers in the field; perhaps he is more open about his experiences. I think that his advice on avoiding damage, not only to the propellers, but also to the wind tunnels in which they are being tested was very valuable.

Mr. P. Sacher, MBB

I will try to summarize the main topics of Session 3, that is Propeller-Air Frame Interaction. I will stress five different points. First of all, the requirements derived from contributions of the papers from industry. Secondly, the question of how to achieve optimum propeller air frame installations. Then the evaluation of an experimental data base which is of course necessary for the development of new computer codes. Last but not least, some few words about the shortcoming of the prediction methods of the present time.

We have had five different papers; two contributions came from industry and the rest were from research institutes and universities. Of course, the papers from industry were more directed towards project applications, those from research were devoted more or less to theoretical development or fundamental measurements providing a data base. First some words about the contributions from industry. The main objective was the experimental determination of propeller airframe installation effects on realistic aircraft shapes. The most important aspect is the fact that not only the isolated propeller nacelle performance must be improved for example by the development of new 2-D shapes using recently developed numerical methods. The whole geometric arrangement of nacelle wing body needs careful optimization. The requirements from industry result in an optimization process. This process should achieve first of all minimum nacelle drag installation increment by optimal positioning and shaping the nacelle in combination with the selected wing plan form. Secondly, an optimum L/D and minimum induced drag during cruise, thirdly, maximum lift for design of a selected high lift flap system and concerning this last topic, I refer to the well known applications of upper and lower surface blowing systems using jets which seems to

have much similarity. In addition to the three preceding points, the influence of the engine installation especially in the case of engine failure, the effect of longitudinal, lateral and directional stability of the whole aircraft must be carefully worked out and in detail like the presentation of Mr. Taiseire has shown. How to achieve optimum propeller airframe installation? As in many other cases, the experimental investigations and theories must go together. There are obviously too many parameters in wind tunnel testing for systematic variations. There is the shape of the nacelle, short or long, the shape of the wing, twist, camber, planform and so on, and there is the position of the nacelle - high or low, even the location ahead of the wing or a pusher arrangement is not yet clear. Concerning this variety, I refer to the excellent paper from the de Havilland written by Mr. Eggleston. The second problem is the large quantity of measured data. We need, of course, at least force measurements, as a minimum to realize aircraft performance. Secondly, pressures for evaluating loads and local interference effects. We need in addition the whole flow field for validation of newly developed theoretical tools and of course, also for the basic understanding of the physics of the mixed flow. An example for this last class of experimental investigations was the presentation by Aljabri. As an outcome of the present meeting, I should say that there is a clear need for analytical and numerical methods for predicting installation effects. For validation of this method, there is also a need for an experimental data base like the experiments of Prof. Lilley, which were simplified enough in geometry that we can obtain isolated effects due to parametric variations, but complex enough to represent a real aircraft shape at least in basic form. Following those lines, we have had three papers from research and universities showing three different approaches for evaluating prediction methods.

The first was based on linearized potential flow using so-called panel methods. Taking account of the propeller slip stream, they should have an extension of course to rotational effects, but problems arise also due to the deflected slipstream which rolls up like a jet in cross flow. A data base has been shown at least for a pusher arrangement. Secondly there was an evaluation of propeller nacelle performance analysis using a very detailed flow field measurement technique. This wake survey in different planes shows clearly the development of swirl in the slipstream and analyzes the slipstream wing interactions in detail. This flowfield data could be used for evaluating the applicability of newly developed Euler codes. That means the development of flowfield prediction methods. The effect of wind tunnel wall interference, especially at angle of attack and the effect of the wind tunnel model support should be investigated separately and more in detail. The third investigation was based on steady incompressible Euler equations. This theory is an asymptotic zonal approach for the interference of large aspect ratio wings including sweep. This looks quite promising to save money in comparison with the full 3-D Euler solutions as Mr. Brabhu has shown in his excellent presentation. I'll recommend to read his detailed written version.

A short summary of short-comings. In the applications of these theoretical methods all results, shown at the present meeting, suffer first of all from the restriction to purely inviscid flow. For me it is hard to understand why the result of the flow mixing process, like the propeller slipstream which influences in addition the boundary layer significantly, could be prescribed correctly using inviscid flow models. But it seems to work at least for engineering purposes. Secondly, potential flow theories are restricted to irrotational flow. So far, we need at least the solution of the Euler equations which exist in principle, but we have seen only the incompressible case in this session. So we require the development of full 3-D compressible Euler solutions and we need a high speed computer capacity with extremely large direct access memory. Available codes have still to be improved concerning users comfort in mesh grid generation, the development of much faster parallel algorithms, extension to viscous effects, and extension also to unsteady flow phenomena. To conclude, this last class of prediction methods was unfortunately not covered by the present meeting. So far, the picture obtained is not complete and from my position working personally in the wing design field, I would have been interested to see in addition consequences of engine installations to the main wing design parameters, such as twist, camber for a given planform to result in optimum L/D for cruise conditions.

Prof. G. Lilley

Thank you, Mr. Chairman. As you know, I was asked to address you at this, the last stage of the symposium, on the problems on propeller acoustics, and I am sitting in for Dr. Leif Bjorno. It also gives me an opportunity, Mr. Chairman, to perhaps atone myself for my dismeansors of the earlier part of the week in not presenting my written version of my own paper. I hope that this does form some kind of atonement. On the general problem of the acoustical side of aircraft development, I presume that most people in the aircraft design field will feel that they have done a very good job over this last decade in relation to the low noise levels generated by the present day turbofan aircraft, and the very good levels of comfort that have been achieved in those aircraft. All of us, the passengers, have enjoyed that. It is therefore quite clear that for any reason we wish to introduce a new form of powerplant, we have still got to clearly keep the progress going in not providing in any way any deterioration in comfort and noise inside the cabin or any increase in external noise level in relation to community noise. Thus, we can say the current generation of aircraft have set standards which are extremely challenging for any future developments in aircraft propulsion. In addition to the problems of the low noise levels of the current generation of turbofan aircraft, we also have the success of the smaller commuter-type turbo-prop aircraft of the Dash 7 type. Might I just remind you that in the UK recently we had an inquiry in relation to building a city center STOL port in the center of London in the east London docks. The inspector, after listening to all the various comments by those who wanted to build the STOL port, operate the STOL port, and the community living around, came up with the recommendation to government that a STOL port should be built there provided the aircraft would have a noise level of the standard of the Dash 7. This recommendation is a major break-through and presents a great challenge and opportunity for anybody wanting to operate an aircraft in that environment with its tremendous potential that it offers the aircraft industry. The Dash 7 will clearly be replaced sometime in the future by an aircraft of a larger type to improve economics, but the noise level has got to be of the same standard as that of the Dash 7. This type of small commuter aircraft, 100 seats maybe going up to a 120 seats, with a noise level no greater than the Dash 7, is going to be, I am sure, a severe challenge. There is one further aspect of this question concerning community noise, which I think it is worth making at this stage. Let me very briefly remind you that the perceived noise level that we use today was arrived at by the onset of the jet engine

into the aircraft noise scene which were then turboprop or propeller driven aircraft. It was felt on the subjective side that the noise scales that we should be talking about should be comparable with the kind of subjective noise which we experienced in the case of propellers. Thus, the comparability of the propeller noise of the 1950's was compared with the jet noise for the engines which were coming into vogue, and the subjective scale of noise, known as PNdB, was therefore introduced. Later with the variations of powerplant we came on to use the EPNdB, and that of course appears in noise certification. I just make the point that introducing into the noise scene a different type of noise source, and I am not here suggesting, in any way, that a prop-fan is going to be a real problem in this respect, but nevertheless, demands a word of caution in respect of comparability with current noise standards. People's attitude to noise changes extremely slowly. If you introduce a totally different noise source into the community, even though you might argue in terms of decibels that this is comparable with some other noise, you may find that the public will not agree and accept it. This might well mean that the noise certification level and the rules that we have for present turbo fan aircraft, and indeed current propeller aircraft, may need changing and so introduce new certification for prop-fan aircraft. One has to be aware of this problem in trying to make absolutely certain that the prop fan is acceptable. In this I refer to both cabin and external noise.

I now come to the papers presented at the conference which gave us a very excellent summary and review of the high level of research and development on the aerodynamics and acoustics of propellers that has been going on in the past decade. As has been mentioned before, the research on the propeller to some extent took a dip in the late 1960's and 70's because of the concentration of effort in getting the turbo fan to its current low noise level. It is only from about 1975 onwards that we have had this resurgence of research interest into the noise of the propeller and the introduction of the idea of improved performance and reduced noise by sweeping the tips which comes about with the prop-fan. We started off this Session 4 with an excellent review paper on the engine development scene by Dr. Saravanamuto. He gave us a very unbiased view of the types of engine development which were going to be required for advanced propeller fan aircraft. We all benefited from that introduction. This was followed by the very excellent papers both dealing with propeller performance and propeller noise by a number of groups; these included Dr. Grosche and his colleagues from Göttingen, Prof. John Williams and his colleagues at Farnborough, Dr. Wilford and his colleagues from Pratt and Whitney and Dr. Heller and his colleagues from DFVLR in Braunschweig. All of these papers concentrated on what can be measured inside the windtunnel and how reduced data compare with full scale. I do wish to make one very important point: acoustic wind tunnels have only been in operation for about the last decade, treating this problem of noise measurement and tunnel noise calibration seriously. All of these windtunnels are by no means perfect. The wind tunnel measurements require a calibration scale. Therefore, it is absolutely essential to have good full scale flight data to make that very detailed comparison. We all know, however, how very difficult it is to get good full-scale reliable data. The various authors gave us very frank pictures of what they can achieve on the model scale in the windtunnel and the reliability in relation to full-scale prediction. Clearly, we have a good picture of the state of the art, but a lot of work still needs to be done. The papers of the above authors will repay very careful study. I perhaps have some preference and leaning to the advances some authors have made compared with others, but all the papers presented give us a very good state of the art in what can be achieved from acoustic windtunnels at the present time.

Of no less importance is of course the problem of the structure. The structural engineer requires to know what is the nature of the excitation on the outside of the fuselage shell. This he relies very much on the work I have mentioned above in relation to noise levels that are either measured in flight, measured in the windtunnel and then predicted for the real airplane. Clearly, considerable progress has been made on this problem of the structural evaluation, and the excitation of this highly complex structure. Here again, one has seen the close connection between the best available methods, and finite element methods especially, for predicting the noise and structural excitations, as well as performing large scale experiments and showing the comparison and the differences between calculation and measurement. We had some very excellent papers by Carbone and colleagues and Dr. Donham from Lockheed and his colleagues on the present position, as well as the problems that remain and the chances for getting the noise level down in the cabin to acceptable levels. I think all would agree that a lot more needs to be done, especially with regard to the prop-fan in order to be confident that we can achieve noise levels inside the cabin and a level of noise comfort comparable to what we experience today with the turbo fan airplane.

Dr. Metzger of Hamilton Standard gave us a very good review of the position reached in the state of the art of noise prediction on the prop fan. This paper again emphasizes the need to take flight measurements, and to analyze and compare them against available prediction methods. It is only by such methods that we can hope to optimize the design of the prop fan to not only meet the very stringent demands on performance, but also to get low noise levels, both in the far field as well as in the near field affecting the cabin. A very fine review paper. I am sure Dr. Metzger's paper will be seen as an important state of the art paper, and therefore to present the complete noise scene which involves so many research groups, perhaps some acknowledgment to certain other workers and groups in the field may be deserving. Finally, we learned from the Lockheed group with a paper presented by Dr. Salikuddin and his colleagues in relation to what can be achieved by active noise control. This is obviously a very new and novel approach to the problem of aircraft cabin noise. It has a lot of possibilities, as well as problems and whether it is going to be able to cope adequately and effectively, with the kind of noise sources that we get from the prop-fan remains to be seen. But at least the kind of initial results that have been achieved are very encouraging and this type of active noise control is obviously a technique needing careful assessment. The whole problem of course, is to integrate this technology into an aircraft, and to determine its effect on performance, especially with respect to the added weight.

Perhaps there are problems in its application to an actual aircraft design, but for the present, I am sure that everybody will want to keep their options open and indeed encourage further work in this field.

Mr. Ohman, NAE

I want to remind you that this session is being recorded and I want you to give your name and your affiliation when you speak. Who will be the first on?

M. Poisson-Quinton, ONERA

I want to comment briefly about wind tunnel testing at full-scale: my question is how to reduce a high risk venture with a prop-fan configuration? We have spoken about that during all this meeting. One solution is of course to try to have a full-scale testing of the nacelle in the largest existing tunnels before flight: NASA-Ames is of course the largest for low speed only (take-off, climb, landing); it will be possible to put even a full-scale aircraft inside the new 120' x 80' section in some years. We have also spoken about the German/Dutch DNW and the RAE 24 foot low-speed tunnels; at the NAE, you have also made some full-scale low-speed research in your very fine tunnel in Ottawa.

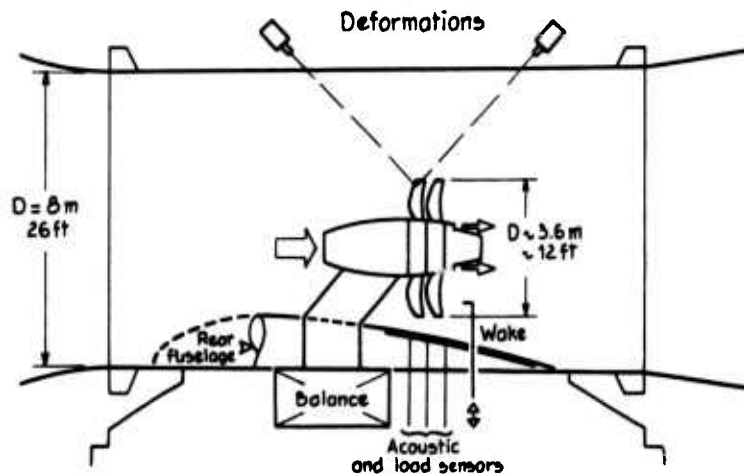
On the French side, we have the S1 Modane tunnel, 8 m. diameter, where it is possible not only to look at the low-speed tests, but also to run at the cruise conditions, up to Mach 0.85.

Such expensive tests, of course, would be made after theoretical predictions, structural testing and small-scale testing, to validate a prop-fan nacelle before experimental flight. At first, in a full-scale test, you have to look at the prop-fan characteristics (nacelle alone) to measure the local loads on blades, blade twist and deformation, etc; this is very important to check the calculation of the deformation including the flutter prediction, mainly with the new composite materials. The main measured parameters are thrust, power, RPM, Mach number and dynamic pressure; the second phase would be devoted to the prop-fan/airframe interaction, either on the wing behind the prop-fan, or on the local rear-fuselage near an aft-mounted prop-fan. The main measurements are the flow analysis around the wing (lift and pressure drag, etc.), the near field noise and the acoustic fatigue measured on a full scale part of the fuselage (including some absorbing material testing).

We have looked at such tests in the S1 tunnel at ONERA: we have made some calculations for a power loading of about 300 kW per square metre on a propeller at Mach 0.8: it is possible to test a propeller diameter up to about 12 feet in this tunnel with a simulated altitude: 15000 ft.

Now, if we look (see figure) at a full-scale "pusher" nacelle with counter-rotating propeller, such as the General Electric project for example, in the S1 Modane tunnel, where it is possible to run between 0.2 and about 0.8 Mach number, the main objective would be a validation before flight for safety and environment problems (structural integrity, propeller aeroelastic and dynamics, noise signature and acoustic fatigue, vibration attenuation development, etc.); moreover for the engine manufacturer, it is very important also, at full-scale and in a very realistic environment, to analyse the gas-turbine behaviour as well as some inlet/exhaust problems, its mechanical behaviour (operation of the variable pitch system, etc.).

This is a very ambitious long term proposal, but in the meantime, we have launched at ONERA a very modest programme (described by Mr Bousquet at this meeting), which is the first step to developing a testing methodology and to have good measurements (including noise signature), on a 1 m. diameter propeller, to be tested fall 1985 in our S1 Modane tunnel. One of our objectives will be the correlation between theory and experiments; our programme is limited by money and by the power of our existing gas turbine, but it would open the way to more ambitious, and perhaps cooperative, programmes.



FULL SCALE COUNTER ROTATION PUSHER
in S₁ Modane w.t.
0.2 < Mach < 0.85

M. Bucciantini, ALITALIA

Only two small observations regarding the topics that we have had in this very interesting symposium. First of all, I am not particularly a specialist in this field, my activity in the company has been in the airframe, aerodynamic design. First observation regards the prop fans. The prop fan is now a field for tomorrow for commercial transportation. The reason we have understood in the step ahead from turbo fan to prop fan is to increase the thrust to a new level without increasing the disk diameter. Therefore, the increase in number of blades, increase in chord, increase in dynamic pressure with the rotational speed. What I have not seen is another idea which I propose today. To increase the number of stages: instead of having at maximum two counter-rotating propellers, having four or six. Four might be feasible, two in front and two at the end of the nacelle. That could alleviate the strength and aerodynamic problems due to high Mach number. Second observation regards the noise. We have seen the noise for the civil aircraft in future is more and more demanding. We have seen that one way is to optimize the structure as my colleague at Aeritalia has shown, in order to reduce the noise amplification in the cabin. Another system I have not seen previously is to absorb the noise during the way which propagates it from the source to the various points. I have certain experience in military aircraft where the noise is reduced for two reasons; for the pilot to enable him to have a most quiet environment to fulfill his task and for the equipment. The general way the noise is reduced is to absorb it by anti-vibration devices such as rubber. The equipment has its anti-vibration mounting both in the equipment airframe interface and inside itself. Therefore, another idea for the civil aircraft is to put absorbant devices like foam or rubber in the points where the noise passes from the source to the cabin.

Mr. Larry Bober, NASA, Lewis

I want to thank Mr. Poisson-Quinton for endorsing the NASA advanced turboprop program in his comments. For those of you that may not be familiar with what is going on in the entire program, NASA has a program called the Propfan Test Assessment Program which follows very carefully Mr. Poisson-Quinton's comments on the approach which should be followed. As I mentioned in my presentation, NASA for some time has been developing analysis methods and has been doing small scale testing of propellers both isolated and installed. The PTA, or Propfan Test Assessment Program, is aimed at exploring full scale feasibility. As the first part of the program a 9 foot diameter propeller is being designed and fabricated by Hamilton Standard under contract to NASA Lewis. This 9-foot diameter propeller will first be tested isolated and in fact before the 9-foot diameter model is tested, a 2-foot diameter aeroelastically scaled model will be tested in wind tunnels.

Mr. L. Ohman, NAE

Is this single rotation?

Mr. Bober, NASA Lewis

Yes, single rotation. A Mach .8 design as are most of the others. The large-scale testing will be done for an isolated propeller first. In fact, the Modane tunnel is being considered for this testing. After that full scale installed static testing will be done, followed by wind tunnel testing with a full scale installed configuration and the NASA Ames tunnel is being looked at for that testing. The final part of the program will involve flight testing an installed single rotation propeller on the wing of a Gulfstream American aircraft. This PTA program's prime contractor is Lockheed, Georgia. The flight test program is planned for 1987.

Mr. L. Ohman, NAE

Thank you very much Mr. Bober, it sounds like we should have lots of interesting results in a few years. Perhaps we should already start planning for our next propeller symposium.

Mr. Landon, ARA, UK

I am concerned that accurate results are obtained in small scale model tests in the face of lack of simulation of those models. This I don't think has been mentioned by any of the authors in these last few days. I am particularly concerned about one aspect. We are fortunate that cruise Reynolds numbers can be nearly matched by atmospheric wind tunnels and also that model propellers can be made in such a way that the aeroelasticity can be matched, but I am concerned that the centrifugal effects on the boundary layer may have a very important effect and I would be very pleased to receive some comments from the panel on this point.

Mr. L. Ohman, NAE

Would anyone like to comment on the centrifugal force on boundary layer. We have some boundary layer specialists in the audience.

Mr. Bober, NASA Lewis

I will comment since nobody else seems ready to say anything. One of the main reasons for trying to develop a 3-D Navier Stokes analysis for propellers is to gain a better understanding of the three-dimensional boundary layers including centrifugal effects and we are pursuing this approach.

Prof. Lilley, Southampton University

The problem in wind tunnel testing of propellers is to be confident of the state of the boundary layers on the rotating blades and hence, by comparison with theory, to predict the effects at full scale. This problem is compounded when noise measurements are made and an extrapolation to full scale Reynolds number is required. More effort is required in this field.

Mr. A. Bagnall, Rolls Royce Derby

I thought I would say what we are trying to do with propellers. We have begun to realize the advantage of the propeller, especially the counter-rotation one, where you get 25% increase in efficiency. That makes a mockery of the half and one percent efficiencies we try to scrape at the moment with component efficiency of our turbo fans. We really need to know what configuration our engine is going to be so that we can start doing some design research work for the prop fan. To do that, although we may not actually consider making the propeller ourselves, we need to understand how the propeller works. We have been trying to apply our design and analysis tools (for turbomachinery inside an annulus) to work for a propeller. What we would like to do is to have a method that we can use to design propeller blades and then we would be able to test a variety of configurations with different numbers of blades and single rotation and counter rotation and get an idea of the noise impacts. Obviously you would want to go to counter rotation (if you can solve the noise problems) because of its greater efficiency, but the engine configuration of course is dependent on that. I would like to show, if possible, some work we have been doing with our design and analysis methods. We have been using a 3-D Denton code, which is a time marching unsteady Euler equation and it iterates in time to end up with the steady solution. I want to show a comparison we did with the SR3. We effectively put the propeller in a wind tunnel and had a boundary out here somewhere, and these diamonds show the NASA test Mach numbers and we are just showing that we have got the right sort of flow Mach number because we are agreeing with that to a certain extent. We were able to show with our 3-D program that there was indeed choking at the root of this blade. If we just look at the cross-section through the propeller, the left-hand picture has a straight annulus and then we have area ruling in the right-hand picture. You can see that the Mach number

reduces. That is perhaps more apparent if I show a picture where we look down on it and you can see that in the left-hand picture there is choking, the unity Mach number, across the passage; with the area ruling you get the reduction in Mach number through the passage. We really are only in the beginning stages of doing this, and we haven't developed the codes specifically for dealing with propellers as yet. Though this would not be a significantly difficult thing to do for a single rotation, I think, it would be very difficult to do the counter rotation complete with some sort of idea of the unsteady effects, and interactions of one rotor with the next. That is what we really would like to do, but that is many years in advance from here.

Mr. L. Ohman, NAE

May I ask those who have shown slides or viewgraphs to submit copies of them for the record.

Dr. H. Heller, DFVLR

I would like to address the problem of propeller acoustic testing in either hard walled tunnels, or open-jet test-section tunnels. We realize that there is a need for both kinds. We need to do hard walled tunnel testing to achieve high cruise speed Mach numbers (say on the order of 0.6, 0.7, or 0.8). But if we do so, we face problems of reflections in the tunnel and the question is: do we fully understand all the problems related to reflections in tunnels?

On the other hand, tests in open jet wind tunnels are much to be preferred. Here then we must ask ourselves: Do we fully understand the transmission of sound through the shear layer if we want to obtain far-field noise data? Furthermore, what is the role of the flow quality?

There are tunnels with excellent flow qualities and there are tunnels with not so excellent flow qualities; how sensitive then is propeller noise to in-flow turbulence in the typical aerodynamic tunnel? As far as scaling is concerned and the problem has been addressed and treated by one of the previous speakers we at the DFVLR have some experience in the DNW obtained in a joint project with the US Army on helicopter high speed impulsive noise, and blade vortex interaction impulsive noise; here it had been shown that scaling by a factor of 7 from model to full-scale flight tests was rather perfect. Depending, I guess, on the particular phenomenon one is looking at, scaling can indeed be achieved in high quality tunnels such as the DNW. On the other hand, the DNW is not a high speed facility, top speed for the open jet being only 85 meters per second. We hope to get more experience in terms of scaling in the upcoming joint DFVLR/FAA tests in December 1984 that I mentioned yesterday in my paper, where we will test a full scale propeller in the DNW and compare data to flight tests that have been conducted already. We then intend to run an experiment where we use the same geometry of the propellers tested in the DNW at a smaller scale - perhaps 1:10 - in our Braunschweig 1 meter acoustic tunnel. We will see how well that will scale and then gain confidence in small scale testing.

Finally, I would just like to advocate utilization of the excellent aerodynamic and acoustic qualities of the DNW in any further aeroacoustic testing, such as on prop-fans, for example, when we are interested in the low speed aspects complementing very well in other high quality tunnels - albeit with a closed test-section - such as the one in Modane.

Mr. L. Ohman, NAE

We are running out of time. I think I can only entertain one more comment or question.

Mr. Bass, Dowty Rotol

I would like to make a couple of very brief points if I may. Firstly, I would like to endorse Mr. Peckham's remarks that wind tunnel techniques with respect to small models need rather more attention. The only correction currently available for solid wall tunnels is that due to Glauert. In a series of experiments in the 8 foot by 6 foot tunnel at Farnborough which has slotted walls, we closed them so we could use Glauert, since we didn't want to deal with the open situation. It was a fairly lightly loaded propeller and the correction was so small that it could be ignored. This may not by any means be true where you get much higher disk loading in terms of power per unit area. The second point I would also like to endorse is Dick Landon's remarks about centrifugal effects. We did a series of experiments in which we were able to keep the blade tip Mach number constant and the Reynolds number constant and vary only rpm. We saw a very large difference in performance which apparently depended only on rpm and, by inference, centrifugal effects. I don't understand it at the moment and this work needs repeating, but there is something there which I think may well keep us entertained for some time to come.

Mr. L. Ohman, NAE

At this point, I am sorry, we have to terminate our discussion. Thank you very much for your very active participation in this discussion. I now turn the floor over to our Panel Chairman for the concluding remarks.

Dr. Roberts

When AGARD plans a symposium, it tries to choose a topic that is both relevant and timely, one that will attract good important papers of interest to a broad audience. On the basis of these criteria, I believe that this has been a successful meeting. Clearly, much has happened in the propeller world in the past 10 years, both in the fundamental understanding of propeller aerodynamics and acoustics and in the evolution of new concepts such as the prop fan and the unducted fan. It was our hope that this symposium would review this progress and I feel that we have been successful to a degree in this regard. We must thank all of the authors for their contributions, and the session chairmen for their good management of the symposium and I would like to thank you, the audience, for participating to the degree that you have in the discussions. A successful meeting requires not only an interesting subject, but a great deal of preparation and hard work on the part of the organizers. I would like you to join me in congratulating

and thanking particularly Mr. Lars Ohman who is both the host nation Coordinator and the Program Chairman for this meeting. A vote of thanks is also due to our Executive Secretary, Mr. Bob Rollins and to his assistant Anne Marie Rivault and to the Canadian staff from DeHavilland and ISTS who provided the equipment, and to the Canadian Imperial Bank of Commerce who provided the projectionists. Finally, our thanks to the team of interpreters, Miss Davis and Miss Dana, and to Major Bergeron, who have worked so hard to provide us with fast and accurate interpretation of the presentations and we thank you. Before closing the meeting, I would like to use the opportunity to tell you of the Fluid Dynamics Panel program for next year, 1985. I have it on a viewgraph here. We have two symposia planned. The first will be in May of 1985 at Gottingen, Germany; this is a joint meeting with the Flight Mechanics Panel of AGARD. The subject is Unsteady Aerodynamics: Fundamentals and Applications to Aircraft Dynamics, and it will have sessions on Unsteady Aerodynamics, Dynamic Stability Parameters and various applications to aircraft in different situations. The second symposium is planned in October of 1985. It will be held in Athens, Greece and it will be a NATO restricted conference on Store Airframe Aerodynamics. Additionally, we have two five-day Special Courses. The first will be in April at the von Karman Institute on Cryogenic Technology for Wind Tunnel Testing and the second in May of 1985 which will be held at VKI and subsequently in August at the NASA Langley Research Center in the US, and this will be a Special Course on Aircraft Drag Prediction and Reduction. If these meetings are of interest to you, and I think that they should be, or to your colleagues, please include them in your plans for 1985. If you need further information about these activities or any other Fluid Dynamics Panel activities or other AGARD activities, please write to Bob Rollins; you have his address on the green program sheet for this meeting. It now remains for me just to formally close this symposium. I thank you all for your participation and wish you all a safe journey home.

REPORT DOCUMENTATION PAGE

1. Recipient's Reference	2. Originator's Reference	3. Further Reference	4. Security Classification of Document						
	AGARD-CP-366	ISBN 92-835-0374-0	UNCLASSIFIED						
5. Originator	Advisory Group for Aerospace Research and Development North Atlantic Treaty Organization 7 rue Ancelle, 92200 Neuilly sur Seine, France								
6. Title	AERODYNAMICS AND ACOUSTICS OF PROPELLERS								
7. Presented at	the Fluid Dynamics Symposium in Toronto, Canada, 1-4 October 1984.								
8. Author(s)/Editor(s)	Various		9. Date February 1985						
10. Author's/Editor's Address	Various		11. Pages 468						
12. Distribution Statement	This document is distributed in accordance with AGARD policies and regulations, which are outlined on the Outside Back Covers of all AGARD publications.								
13. Keywords/Descriptors	<table> <tr> <td>Propellers</td> <td>Acoustics</td> </tr> <tr> <td>Aerodynamics</td> <td>Design</td> </tr> <tr> <td>Aircraft propeller noise</td> <td></td> </tr> </table>			Propellers	Acoustics	Aerodynamics	Design	Aircraft propeller noise	
Propellers	Acoustics								
Aerodynamics	Design								
Aircraft propeller noise									
14. Abstract	<p>→ The purpose of the Symposium to which this publication pertains was to provide a state-of-the-art review of the aerodynamic design and testing of modern propellers, acoustic and vibration environmental problems and their solutions, and considerations in the integration of the propeller(s) and airframe. <i>Propellers have again</i></p> <p>Propellers have recently become a focus of attention after have been neglected for many years. The efficient use of propellers as a propulsion medium up to Mach 0.6 was realised at the expense of high noise and vibration. Since the mid-1970s there have been many developments, including the propfan which, with an aerodynamic efficiency of 80% at Mach 0.8 now seriously challenges the fanjet. The advent of the supercritical airfoil is another significant development beginning to influence propeller design. <i>Topics include (to p. v)</i></p> <p>The papers contained in this publication were presented at the AGARD Fluid Dynamics Panel Symposium held in Toronto, Canada, on 1-4 October 1984.</p>								

<p>AGARD Conference Proceedings No.366 Advisory Group for Aerospace Research and Development, NATO AERODYNAMICS AND ACOUSTICS OF PROPELLERS Published February 1985 468 pages</p> <p>The purpose of the Symposium to which this publication pertains was to provide a state-of-the-art review of the aerodynamic design and testing of modern propellers, acoustic and vibration environmental problems and their solutions and considerations in the integration of the propeller(s) and airframe.</p> <p>Propellers have recently become a focus of attention after</p> <p>P.T.O</p>	<p>AGARD-CP-366</p> <p>Propellers Aerodynamics Aircraft propeller noise Acoustics Design</p>	<p>AGARD Conference Proceedings No.366 Advisory Group for Aerospace Research and Development, NATO AERODYNAMICS AND ACOUSTICS OF PROPELLERS Published February 1985 468 pages</p> <p>The purpose of the Symposium to which this publication pertains was to provide a state-of-the-art review of the aerodynamic design and testing of modern propellers, acoustic and vibration environmental problems and their solutions and considerations in the integration of the propeller(s) and airframe.</p> <p>Propellers have recently become a focus of attention after</p> <p>P.T.O</p>	<p>AGARD-CP-366</p> <p>Propellers Aerodynamics Aircraft propeller noise Acoustics Design</p>
<p>AGARD Conference Proceedings No.366 Advisory Group for Aerospace Research and Development, NATO AERODYNAMICS AND ACOUSTICS OF PROPELLERS Published February 1985 468 pages</p> <p>The purpose of the Symposium to which this publication pertains was to provide a state-of-the-art review of the aerodynamic design and testing of modern propellers, acoustic and vibration environmental problems and their solutions and considerations in the integration of the propeller(s) and airframe.</p> <p>Propellers have recently become a focus of attention after</p> <p>P.T.O</p>	<p>AGARD-CP-366</p> <p>Propellers Aerodynamics Aircraft propeller noise Acoustics Design</p>	<p>AGARD Conference Proceedings No.366 Advisory Group for Aerospace Research and Development, NATO AERODYNAMICS AND ACOUSTICS OF PROPELLERS Published February 1985 468 pages</p> <p>The purpose of the Symposium to which this publication pertains was to provide a state-of-the-art review of the aerodynamic design and testing of modern propellers, acoustic and vibration environmental problems and their solutions and considerations in the integration of the propeller(s) and airframe.</p> <p>Propellers have recently become a focus of attention after</p> <p>P.T.O</p>	<p>AGARD-CP-366</p> <p>Propellers Aerodynamics Aircraft propeller noise Acoustics Design</p>

having been neglected for many years. The efficient use of propellers as a propulsion medium up to Mach 0.6 was realised at the expense of high noise and vibration. Since the mid-1970s there have been many developments, including the propfan which, with an aerodynamic efficiency of 80% at Mach 0.8 now seriously challenges the fanjet. The advent of the supercritical airfoil is another significant development beginning to influence propeller design.

The papers contained in this publication were presented at the AGARD Fluid Dynamics Panel Symposium held in Toronto, Canada, on 1—4 October 1984.

ISBN 92-835-0374-0

having been neglected for many years. The efficient use of propellers as a propulsion medium up to Mach 0.6 was realised at the expense of high noise and vibration. Since the mid-1970s there have been many developments, including the propfan which, with an aerodynamic efficiency of 80% at Mach 0.8 now seriously challenges the fanjet. The advent of the supercritical airfoil is another significant development beginning to influence propeller design.

The papers contained in this publication were presented at the AGARD Fluid Dynamics Panel Symposium held in Toronto, Canada, on 1—4 October 1984.

ISBN 92-835-0374-0

having been neglected for many years. The efficient use of propellers as a propulsion medium up to Mach 0.6 was realised at the expense of high noise and vibration. Since the mid-1970s there have been many developments, including the propfan which, with an aerodynamic efficiency of 80% at Mach 0.8 now seriously challenges the fanjet. The advent of the supercritical airfoil is another significant development beginning to influence propeller design.

The papers contained in this publication were presented at the AGARD Fluid Dynamics Panel Symposium held in Toronto, Canada, on 1—4 October 1984.

ISBN 92-835-0374-0

having been neglected for many years. The efficient use of propellers as a propulsion medium up to Mach 0.6 was realised at the expense of high noise and vibration. Since the mid-1970s there have been many developments, including the propfan which, with an aerodynamic efficiency of 80% at Mach 0.8 now seriously challenges the fanjet. The advent of the supercritical airfoil is another significant development beginning to influence propeller design.

The papers contained in this publication were presented at the AGARD Fluid Dynamics Panel Symposium held in Toronto, Canada, on 1—4 October 1984.

ISBN 92-835-0374-0

AGARD

NATO  OTAN

7 RUE ANCELLE · 92200 NEUILLY-SUR-SEINE
FRANCE

Telephone 745.08.10 · Telex 610176

**DISTRIBUTION OF UNCLASSIFIED
AGARD PUBLICATIONS**

AGARD does NOT hold stocks of AGARD publications at the above address for general distribution. Initial distribution of AGARD publications is made to AGARD Member Nations through the following National Distribution Centres. Further copies are sometimes available from these Centres, but if not may be purchased in Microfiche or Photocopy form from the Purchase Agencies listed below.

NATIONAL DISTRIBUTION CENTRES

BELGIUM

Coordonnateur AGARD — VSL
Etat-Major de la Force Aérienne
Quartier Reine Eli
Rue d'Evere, 1140

ITALY

Aeronautica Militare
Ufficio del Delegato Nazionale all'AGARD
3 Piazzale Adenauer
00144 Roma/EUR

CANADA

Defence Scientific
Dept of National
Ottawa, Ontario

LUXEMBOURG

Ministère

DENMARK

Danish Defence
Ved Idrætspar
2100 Copenhagen

FRANCE

O.N.E.R.A. (I)
29 Avenue d
92320 Chât

GERMANY

Fachinform
Physik, Ma
Kernforsch
D-7514 E

GREECE

Hellenic Air Force
Research and Development Direct
Holargos, Athens

ICELAND

Director of Aviation
c/o Flugrad
Reyjavik

Defence
Station Square House
St Mary Cray
Orpington, Kent BR5 3RE

UNITED STATES

National Aeronautics and Space Administration (NASA)
Langley Field, Virginia 23365
Attn: Report Distribution and Storage Unit

THE UNITED STATES NATIONAL DISTRIBUTION CENTRE (NASA) DOES NOT HOLD STOCKS OF AGARD PUBLICATIONS, AND APPLICATIONS FOR COPIES SHOULD BE MADE DIRECT TO THE NATIONAL TECHNICAL INFORMATION SERVICE (NTIS) AT THE ADDRESS BELOW.

PURCHASE AGENCIES

Microfiche or Photocopy

National Technical
Information Service (NTIS)
5285 Port Royal Road
Springfield
Virginia 22161, USA

Microfiche

ESA/Information Retrieval Service
European Space Agency
10, rue Mario Nikis
75015 Paris, France

Microfiche or Photocopy

British Library Lending
Division
Boston Spa, Wetherby
West Yorkshire LS23 7BQ
England

Requests for microfiche or photocopies of AGARD documents should include the AGARD serial number, title, author or editor, and publication date. Requests to NTIS should include the NASA accession report number. Full bibliographical references and abstracts of AGARD publications are given in the following journals:

Scientific and Technical Aerospace Reports (STAR)
published by NASA Scientific and Technical
Information Branch
NASA Headquarters (NIT-40)
Washington D.C. 20546, USA

Government Reports Announcements (GRA)
published by the National Technical
Information Services, Springfield
Virginia 22161, USA



Printed by Specialised Printing Services Limited
40 Chigwell Lane, Loughton, Essex IG10 3TZ

ISBN 92-835-0374-0

